

nature

THE INTERNATIONAL WEEKLY JOURNAL OF SCIENCE

Pole to pole

How ice sheets in the north drove climate variability in the south during the Last Glacial Maximum **PAGE 351**

PHYSICS

QUANTUM INTERNET

Can teleportation enhance network security?

PAGE 289

NEUROSCIENCE

IN THE LINE OF FIRE

Ketamine targets neuronal bursts to tackle depression

PAGES 304, 317 & 323

ANIMAL BEHAVIOUR

THE WISDOM OF CROWDS

Life in large groups makes wild magpies smart

PAGES 303 & 364



NATURE.COM/NATURE

15 February 2018

Vol 554, No. 7692

THIS WEEK

EDITORIALS

MESSAGES Keep marriage proposals and animal authors out of papers **p.276**

WORLD VIEW Train PhD students to use critical-thinking skills **p.277**



BEETLEBUM Insect squirts from rear end to escape predators **p.279**

SpaceX ignites big dreams

The successful launch of the Falcon Heavy rocket was a stunning moment that opens the way for commercial exploration of deep space.

When David Bowie revealed the inspiration for his breakthrough hit 'Space Oddity', it came as a surprise to many: not the Apollo missions to the Moon but the film *2001: A Space Odyssey* (Kubrick, 1968). And it's easy to see why: the film's ballet of the spinning space station and dark themes about our place in the Universe has a distinct aesthetic appeal.

Does space travel still inspire? The continuing high profile of the International Space Station (ISS) and the welcome early steps of China and others aside, an extraordinary thing has happened. For much of the public, humanity's adventures in space have become history, something people used to do in the old days. (Exhibit A: the Space Shuttle, once a means to escape the surly bonds of Earth, is now a museum piece.)

But spaceflight suddenly seems futuristic again. How else to explain the reaction to the spectacle of last week's successful maiden launch of Falcon Heavy, the giant rocket built by Elon Musk and his company SpaceX. The hashtag generation has witnessed its own moment of inspiration writ large in the heavens.

The launch wasn't perfect, but it still came across as a stunning synchrony of power and control. The 27 Merlin engines blazed to lift their giant cargo towards the sky, accompanied by cheers and whoops on the ground. And then, with exquisite control, the side boosters separated, back-flipped in tandem towards Earth and settled on landing pads at Florida's Cape Canaveral Air Force Station with a rapid volley of ear-splitting sonic booms.

The Saturn V rocket NASA created in the 1960s for the Apollo missions remains the most powerful rocket ever built. But since Apollo there has been an almost 50-year hiatus in missions to take people beyond low Earth orbit. The successful launch of the Falcon Heavy will surely mark the beginning of the end of this hiatus. It is nothing short of historic, and Musk deserves enormous credit. Yes it was flashy — gimmicky, even — but there was substance behind the style.

Not without his faults, Musk has nevertheless shown himself to be a visionary with verve, can-do grit, a dash of genius and an abundance of hubris. SpaceX has roundly confounded many naysayers and upended the launcher industry. Tesla, Musk's electric-vehicle company, faces enormous challenges, but has still helped to persuade many in the automotive industry that fossil-fuel engines belong in museums alongside the shuttle.

Musk's goals for space are characteristically audacious. He intends SpaceX's Dragon capsule to carry people later this year, and Falcon Heavy's less powerful sibling — the Falcon 9 workhorse — to ferry astronauts to the ISS.

But it is the void beyond on which all sights are now set. Commercial companies have finally cracked access to deep space. Access to interplanetary trajectories — and the decisions about where to head — is no longer limited to governments. Musk wants to take people to Mars, which still seems a long shot — but space tourism

suddenly feels like a more realistic prospect.

Together, Musk and his rocket are showing what a combination of big ideas and big money can achieve, and so inspiring the next generation to dream big. Still, for all the thrill of the new, it's worth remembering just how much last week's launch — like so much in

"Access to interplanetary trajectories is no longer limited to governments."

science — builds on the achievements of others. Falcon Heavy took off from the historic Launch Complex 39A (LC-39A) at the Kennedy Space Center on Merritt Island in Florida, from where the Apollo Moon landings also began their journeys.

And although Musk's choice of test payload — his own cherry-red Tesla Roadster with a mannequin at the wheel and playing 'Space Oddity' on a loop — received as much attention as the rocket that carried it, SpaceX is not the first to put a car into space. From LC-39A, NASA did the same. Then it landed its car on the Moon. And then it drove it around. Not bad for the old days. ■

Climate conflict

Many studies that link global warming to civil unrest are biased and exacerbate stigma.

The people of Cape Town, South Africa, are enduring a terrible drought, and the resulting water shortages could soon force authorities to turn off the taps. Could civil unrest follow? When southern Brazil experienced a similar shortage in 2015, stories circulated about the authorities running drills to prepare a response to desperate people attacking water infrastructure. And a study published last year of some 1,800 riots in sub-Saharan Africa over 20 years concluded that drought can indeed be a powerful contributor to civil disorder (C. Almer *et al.* *J. Environ. Econ. Manage.* <http://doi.org/ckdj>; 2017).

Such retrospective analyses raise two questions related to cause and effect: did climate change alter the weather? And did the change in the weather provoke the conflict? Only a solid yes to both can justify bold statements that global warming promotes violence — and establishing this answer is difficult, if not impossible, in many cases.

That hasn't stopped such controversial claims being made. A decade ago, the United Nations went as far as to state that climate warming and desertification were one of the causes of the Darfur conflict in Sudan, which started in 2003 and led to the deaths of up to half a million people over five years of revolt. That daring claim, based on

sketchy information, met with harsh criticism and outright disbelief from researchers familiar with the region. But it also triggered growing interest in climate–conflict research.

Results so far are largely ambiguous and have been frequently questioned by political scientists, economists, social scientists and climate experts, on various grounds. This week, a systematic review of the literature highlights one problem: efforts to find links between climate and social conflict are hampered by a severe sampling bias, including a statistically and politically dubious focus on mainly African countries formerly under British colonial rule.

The study, published in *Nature Climate Change*, states what critics have long suspected: conclusions that climate change is triggering violent conflict cannot be generalized, and are hard to substantiate even in individual cases (C. Adams *et al.* *Nature Clim. Change* <http://doi.org/ckfw>; 2018). Researchers are drawn to regions that experience violence, rather than to those where climate change is most severe, they write. And the countries that are easiest to study — because of historical links, language and ease of transport — are often prioritized over nations that might experience more climate change or more violence, but are less convenient for research. (Kenya is a good example: it is one of the most studied countries, yet it is not near the top of the list in terms of either violence or climate impacts.)

Skewed results pay a disservice to science and can undermine peace-keeping efforts. Climate change is never the sole cause of war, violence, unrest or migration. Syria and Jordan have both been stricken by drought this decade. But it's clear that different social, political and economic factors in the two nations explain why people are desperate to flee from Syria and not from Jordan.

Done correctly, climate–conflict research is certainly valuable. As a

global human enterprise, any science must be concerned with social justice and peace. Rigorous investigation into how climate change might affect — and perhaps violently disrupt — societies or human civilization at large has its place. But first, researchers in the field must improve their methods.

There is a political implication to this sampling bias, too. To search for climate–conflict links in places where violent struggle is taking place, or has only recently ended — and to pursue such research with a geographical bias towards a few, relatively accessible regions in Africa — threatens to stigmatize troubled countries as being prone to even more instability in the future. With a view to social justice in science, this would be grossly undesirable. And it is a flawed approach to answering important questions about the socioeconomic and political conditions in which climate-related conflict is likely to emerge. Instead, scientists must consider whether peaceful responses to climate change are the norm in most countries.

There is a yawning disconnect between the needs of countries in the developing world, many of which sit on the front line of climate change, and the priorities of scientists in the developed world who carry out most of the research. To address this, climate researchers must seek fresh opportunities to provide decision-makers in the developing world with the kinds of data and projections that they most need — including attribution studies, which aim to assess the extent to which specific weather events are due to climate change. This will help the most vulnerable societies mobilize to adapt to climate change, and will offer some much-needed security. ■

“Climate change is never the sole cause of war, violence, unrest or migration.”

Personal papers

From proposals to gripes, scientists sneak messages into their papers.

To mark St Valentine's Day, *Nature* this week published a collection of stories of romance kindled and sealed by science (see go.nature.com/2foalrk). One describes a science writer who was asked to investigate unusual crystals in a particle collider, and on her arrival there, was surprised by her partner, who proposed; another concerns a palaeontologist who stashed an engagement ring in a stream bed.

Then there are the declarations and proposals buried in the acknowledgements of a scientific paper. What could be more romantic than an analysis of the cooling power of a fridge? Answer: an analysis of the cooling power of a fridge that ends with the words: Will you marry me?

That's how Rui Long, a PhD student in engineering at Huazhong University of Science and Technology in Wuhan, China, proposed to his partner Panpan Mao, in a paper published online last month in *Physica A: Statistical Mechanics and its Applications*.

He is not the first: a similar line in the acknowledgements of a 2015 *Current Biology* paper describing a new dinosaur sent viral the proposal of Caleb Brown to his girlfriend and fellow museum scientist Lorna O'Brien. The proposal method has its risks: it relies, of course, on the person being proposed to actually reading the acknowledgements. (In at least one case, an anxious proposer had to ask his partner to try again.) There are other more serious concerns: that the person proposed to will feel coerced. Many critics argue against public proposals — from those in YouTube videos to hijacked sporting events — for this reason.

Proposals are certainly not the only messages that scientists have smuggled into their academic acknowledgements. Funding agencies have been 'thanked' for steering research by refusing

previous applications, and scolded for not paying their bills. Sports fans have slipped in references to favourite teams, and imaginary people have been credited to pay homage to popular culture, such as *The Simpsons* TV show and, in one case, the thrash-metal band Slayer.

Even the text of the paper is not immune. Peer reviewers, it seems, must be on the lookout for striking similarities to lines from *Star Wars* — and, infamously, everybody missed that an interloper had drawn a stick man fishing in a water tank in a schematic diagram included in a 1955 paper in the *Journal of the American Chemical Society*.

Authorship of papers is also ripe for mischief making. *Physical Review Letters* published a paper in 1973 written by the US physicist and mathematician Jack Hetherington and F. D. C. Willard. Willard — who subsequently published as a sole author — was Hetherington's cat. And in 2001, materials scientist Andre Geim co-authored a *Physica B: Condensed Matter* paper on Earth's rotation with “H. A. M. S. ter Tisha”. (It's not clear how the hamster contributed.) Various groups of authors have claimed in their papers that the order in which their names appear was determined by non-standard methods, including in one case, a 25-game croquet series.

Tinkering with the names on academic publications should not be undertaken lightly. South Korea announced earlier this month that it was widening an investigation into the possibility that some scientists added the names of their children and other relatives. In certain cases, the practice is thought to be intended to give the children an edge when applying to university, a highly competitive process in which, it seems, a publication record might help (see *Nature* 554, 154–155; 2018).

How common are personal messages in papers? A straw poll of *Nature's* manuscript editors failed to produce any confirmed examples in our pages. But at least one has slipped through. In an online discussion of the practice from 2011, microbiologist Rosie Redfield writes: “I once thanked Howard Ochman for ‘pharmacological support’ on a theory paper (in *Nature*!). He had given me a pound of excellent coffee beans.” We checked, and it's true. But no more, please. As our guidelines to authors state: focus on the science, and avoid the risks and distractions of personal messages that might misfire. ■



Train PhD students to be thinkers not just specialists

Many doctoral curricula aim to produce narrowly focused researchers rather than critical thinkers. That can and must change, says **Gundula Bosch**.

Under pressure to turn out productive lab members quickly, many PhD programmes in the biomedical sciences have shortened their courses, squeezing out opportunities for putting research into its wider context. Consequently, most PhD curricula are unlikely to nurture the big thinkers and creative problem-solvers that society needs.

That means students are taught every detail of a microbe's life cycle but little about the life scientific. They need to be taught to recognize how errors can occur. Trainees should evaluate case studies derived from flawed real research, or use interdisciplinary detective games to find logical fallacies in the literature. Above all, students must be shown the scientific process as it is — with its limitations and potential pitfalls as well as its fun side, such as serendipitous discoveries and hilarious blunders.

This is exactly the gap that I am trying to fill at Johns Hopkins University in Baltimore, Maryland, where a new graduate science programme is entering its second year. Microbiologist Arturo Casadevall and I began pushing for reform in early 2015, citing the need to put the philosophy back into the doctorate of philosophy: that is, the 'Ph' back into the PhD. We call our programme R3, which means that our students learn to apply rigour to their design and conduct of experiments; view their work through the lens of social responsibility; and to think critically, communicate better, and thus improve reproducibility. Although we are aware of many innovative individual courses developed along these lines, we are striving for more-comprehensive reform.

Our offerings are different from others at the graduate level. We have critical-thinking assignments in which students analyse errors in reasoning in a *New York Times* opinion piece about 'big sugar', and the ethical implications of the arguments made in a *New Yorker* piece by surgeon Atul Gawande entitled 'The Mistrust of Science'. Our courses on rigorous research, scientific integrity, logic, and mathematical and programming skills are integrated into students' laboratory and field-work. Those studying the influenza virus, for example, work with real-life patient data sets and wrestle with the challenges of applied statistics.

A new curriculum starts by winning allies. Both students and faculty members must see value in moving off the standard track. We used informal interviews and focus groups to identify areas in which students and faculty members saw gaps in their training. Recurring themes included the inability to apply theoretical knowledge in statistical tests in the laboratory, frequent mistakes in choosing an appropriate set of experimental controls, and significant difficulty in explaining work to non-experts.

Introducing our programme to colleagues in the Johns Hopkins life-sciences departments was even more sensitive. I was startled by the oft-expressed opinion that scientific productivity depended more

on rote knowledge than on competence in critical thinking. Several principal investigators were uneasy about students committing more time to less conventional forms of education. The best way to gain their support was coffee: we repeatedly met lab heads to understand their concerns.

With the pilot so new, we could not provide data on students' performance, but we could address faculty members' scepticism. Some colleagues were apprehensive that students would take fewer courses in specialized content to make room for interdisciplinary courses on ethics, epistemology and quantitative skills. In particular, they worried that the R3 programme could lengthen the time required for students to complete their degree, leave them insufficiently knowledgeable in their subject areas and make them less productive in the lab.

We made the case that better critical thinking and fewer mandatory discipline-specific classes might actually position students to be more productive. We convinced several professors to try the new system and participate in structured evaluations on whether R3 courses contributed to students' performance.

So far, we have built 5 new courses from scratch and have enrolled 85 students from nearly a dozen departments and divisions. The courses cover the anatomy of errors and misconduct in scientific practice and teach students how to dissect the scientific literature. An interdisciplinary discussion series encourages broad and critical thinking about science. Our students learn to consider societal consequences of research advances, such

as the ability to genetically alter sperm and eggs.

Discussions about the bigger-picture problems of the scientific enterprise get students to reflect on the limits of science, and where science's ability to do something competes with what scientists should do from a moral point of view. In addition, we have seminars and workshops on professional skills, particularly leadership skills through effective communication, teaching and mentoring.

It is still early days for assessment. So far, however, trainees have repeatedly emphasized that gaining a broader perspective has been helpful. In future, we will collect information about the impact that the R3 approach has on graduates' career choices and achievements.

We believe that researchers who are educated more broadly will do science more thoughtfully, with the result that other scientists, and society at large, will be able to rely on this work for a better, more rational world. Science should strive to be self-improving, not just self-correcting. ■

Gundula Bosch directs the R3 Graduate Science Initiative at Johns Hopkins Bloomberg School of Public Health in Baltimore, Maryland. e-mail: gbsch@jhu.edu

PUT THE
PHILOSOPHY
BACK
INTO THE
DOCTORATE
OF
PHILOSOPHY.

SEVEN DAYS

The news in brief

POLICY

Harassment policy

Institutions that receive grant monies from the US National Science Foundation (NSF) must now inform the agency if they find that anyone funded by an NSF grant has committed sexual harassment. The policy, which the NSF announced on 8 February, also requires institutions to report if researchers are placed on administrative leave related to harassment allegations or findings, and to lay out clear rules defining inappropriate behaviour. The requirements will take effect after a 60-day public-comment period ends. US government research agencies generally do not require grant recipients or their employers to disclose sexual-harassment allegations or findings. See go.nature.com/2euvrrr for more.

POLITICS

US budget request

Funding for the US National Institutes of Health and the National Science Foundation would remain flat in fiscal year 2019, under the budget request released on 12 February by President Donald Trump. But his plan would slash funds for the Environmental Protection Agency to US\$6.1 billion — the lowest level since the 1990s — ending the agency's climate research. The proposal would also gut climate programmes at the National Oceanic and Atmospheric Administration and cancel five Earth-observing missions or instruments at NASA. See page 284 for more.

Research threat

Philippine President Rodrigo Duterte has declared that the seas around the country are off-limits to foreign

researchers. In a press conference on 9 February, Duterte said he would order the navy to fire on any foreign vessels found extracting resources from the Philippines' exclusive economic zone (EEZ). Under a 1982 United Nations treaty, countries have exclusive economic rights to an area extending 200 nautical miles (370 kilometres) from their shores, but foreign research vessels are often granted access. A spokesperson for Duterte said that future missions should be done by Filipinos; this would cut off nations that have previously done research in the area, such as China, Japan, South Korea and the United States. The Philippines' EEZ

includes the seismically active Benham Rise, which the nation renamed the Philippine Rise last year.

PUBLISHING

Leadership row

More than 70 members of the editorial board of the *Journal of Molecular Medicine* have quit over a disagreement with the publisher about the appointment of a new editor-in-chief. The journal's long-time editor-in-chief, German pharmacologist Detlev Ganten, retired last year. Journal editors recommended Martin Lohse of the Max Delbrück Center for Molecular Medicine in Berlin as his successor.

But the publisher, Springer Nature, instead appointed Ari Waisman, an immunologist at the Johannes Gutenberg University of Mainz in Germany. (*Nature's* news team is editorially independent of Springer Nature, which also publishes *Nature*.) As of 13 February, the *Journal of Molecular Medicine* listed 23 remaining editorial board members on its website.

Preprint server

The American Geophysical Union launched a major preprint server for the Earth sciences on 8 February. The Earth and Space Science Open Archive is a free community site for posting pre-publication findings, as well as conference



THOM BAUR/REUTERS

Falcon Heavy soars into the record books

SpaceX in Hawthorne, California, launched the most powerful commercial rocket ever on 6 February. Its 27-engine Falcon Heavy rocket lifted off from NASA's Kennedy Space Center in Florida and propelled founder Elon Musk's electric sports car into a looping orbit around the Sun. Two of the rocket's three boosters successfully returned to Earth and landed,

marking another step towards SpaceX's goals of reusability. The third booster, however, crashed into the Atlantic Ocean when some of its engines did not ignite as planned. SpaceX streamed live images of Musk's car as it moved farther and farther from Earth, until a final engine burn sent it on a course that will eventually take it out near Mars.

presentations such as posters. A competing preprint server, EarthArXiv, has been operating since last October under the auspices of the Center for Open Science in Charlottesville, Virginia. They are the first major initiatives to test whether Earth scientists will embrace the open-posting model pioneered by sites such as the arXiv physics server.

EVENTS

Gender pay gap

Women who work at the Wellcome Trust — one of the world's largest biomedical charities — earn a median salary that is 21% lower than that of their male colleagues, the London-based organization said on 7 February. The gap is slightly wider than Britain's overall gender pay gap of 18%. Organizations in the United Kingdom that employ more than 250 people are now required by law to publish such information on pay. "We see our gender pay gap as one important measure of how much more we have to do to become a truly inclusive place to work," the trust said in a statement.

Taiwan earthquake

Officials have started recovery efforts following an earthquake that struck the east coast of Taiwan on 6 February,



killing 17 people and injuring at least 285. The US Geological Survey measured the earthquake at magnitude 6.4. The quake's epicentre occurred 18 kilometres north of Hualien, the most severely affected area. It caused major damage to some buildings, including a 12-storey residential complex that is now tilted (**pictured**) after the first four floors gave way. Taiwan experiences frequent quakes because it lies close to the intersection of three tectonic plates. As *Nature* went to press, Hualien was still experiencing aftershocks.

Isotope process

On 8 February, the US Food and Drug Administration approved a new technology for producing a common medical isotope without the use of enriched uranium. Technetium-99m is used

in roughly 80% of medical-imaging procedures in the United States, but the country has relied entirely on foreign imports for the past three decades. The global market has been rocked by shortages in recent years, however, caused in part by reactor closures abroad. NorthStar Medical Radioisotopes in Beloit, Wisconsin, uses naturally occurring molybdenum-98, which absorbs neutrons in a nuclear reactor and becomes molybdenum-99 — a source material that decays into technetium-99m.

FUNDING

Science budget cuts

The Brazilian government will freeze 10% of the budget for its Ministry of Science, Technology, Innovation and Communications, according to an analysis released on

6 February by the Brazilian Society for the Advancement of Science. The government announced an overall budget cut on 2 February, but it was several days before each ministry could confirm how much it would have to give up. The move will drain 477 million reais (US\$145 million) from the 4.6 billion reais already authorized for the ministry in 2018. Science minister Gilberto Kassab promised not to apply those cuts to research institutes for now, in the hope that the freeze will be at least partly reversed in the coming months.

PEOPLE

Astronomy move

The University of Turku in Finland terminated the employment contract of astrophysicist Christian Ott on 7 February. Ott resigned from the California Institute of Technology in Pasadena last year after the institution determined he had committed gender-based harassment of two graduate students. The University of Turku announced on 1 February that it had hired Ott, but reversed the decision after astronomers inside and outside Finland criticized the appointment. Through his lawyer, Ott declined to comment publicly on the matter.

Popular science

The Royal Institution of Great Britain has appointed a new director, it announced on 8 February. Civil engineer Shaun Fitzgerald will lead the London-based organization, which promotes public engagement in science and is known for its Christmas Lectures. His predecessor, gerontologist Sarah Harper, left the 219-year-old organization last September after less than four months in the job.

➔ **NATURE.COM**

For daily news updates see:
www.nature.com/news

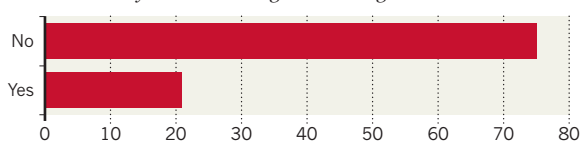
TREND WATCH

A survey of UK institutions reveals that many of them do not have policies to address the misuse of metrics such as impact factors in academic evaluations. The 2012 Declaration on Research Assessment (DORA), a global accord that aims to eliminate such misuse, urges hiring and grant panels to assess the quality of research papers rather than the journals in which they are published. Out of 96 institutions surveyed, 75 said that they hadn't signed DORA or didn't have a research-metrics policy.

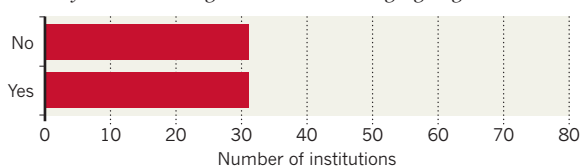
SHAKING UP METRICS CULTURE

Only 21 UK research organizations out of 96 said in a survey that they had signed the San Francisco Declaration on Research Assessment (DORA), which promotes the responsible use of research metrics.

Has your research organization signed DORA?



Is your research organization considering signing DORA?



Number of institutions

NEWS IN FOCUS

POLICY Trump's budget request for 2019 leaves science funding mostly flat **p.284**

ASTRONOMY South Africa braces itself for flood of data from telescope array **p.286**

POLICY US National Science Foundation sets sexual-harassment policy **p.287**



QUANTUM INTERNET Physicists aim to harness the power of entanglement **p.289**

EDDIE MOORE/ALBUQUERQUE JOURNAL/ZUMA WIRE



Forests of ponderosa pine (*Pinus ponderosa*) may never recover from a megafire that burned through New Mexico's Jemez mountains in 2011.

ENVIRONMENT

Tree rings reveal wildfire risk for southwestern US

Historical record points to climate patterns that prime the region for intense fire seasons.

BY CALLY CARSWELL

Ellis Margolis's desk is covered in slices of wood. They're scattered around his computer, piled in cardboard boxes and stacked on shelves. The tree rings and burn scars imprinted in the wood help the ecologist and other scientists predict the potential for future fires in the southwestern United States by understanding the blazes of the past.

This year, as Margolis and his colleagues at the US Geological Survey (USGS) in Santa Fe,

New Mexico, go into the field to expand their data set, the work feels like a race against time. Snowpack is dangerously low in many parts of Arizona and New Mexico, setting the stage for exceptionally dry conditions that fuel these conflagrations. The biggest wildfires in New Mexico's recorded history have erupted in just the past decade, torching hundreds of thousands of hectares across the state, including in the mountains Margolis studies. "The lack of snow is scary," he says. "We're set up for a big fire year if things don't change

dramatically."

Storms that could deliver game-changing amounts of precipitation are unlikely, according to a 6 February federal water-supply forecast. And preliminary results from the network of sampling sites across two of New Mexico's mountain ranges suggest that future blazes — even as soon as this summer — could be even bigger than recent megafires.

Since the late 1970s, researchers have used tree rings and fire scars to reconstruct the fire history of an area and to understand how ►

► climate drives conflagrations. Tree growth rings vary in width with annual precipitation, providing a record of past climates. And when blazes burn a tree without killing it, they leave scars that can be dated along with the rings.

Initially, researchers tried to understand how frequently fires had burned individual stands of trees, says Tom Swetnam, a fire ecologist at the University of Arizona in Tucson who is now based in New Mexico. Land-management agencies such as the US National Park Service and the US Forest Service had followed strict fire-suppression policies for decades, but they were beginning to recognize fire's ecological benefits. The agencies wanted to know how fire had behaved historically, so they could use it as a tool to promote forest health.

As scientists built fire chronologies, patterns emerged. Forests in Arizona, New Mexico, western Texas and northern Mexico all tended to burn in the same years, for instance. And Swetnam eventually linked active fire years to La Niña phases, or periods of cooling in the Pacific Ocean's equatorial waters, that dried out the Southwest¹.

Multiple studies on mid-elevation forests of ponderosa pine (*Pinus ponderosa*) in Arizona and New Mexico found² that before widespread fire suppression, low-intensity fires had burned through these stands roughly every decade. Fire helped to maintain the open

structure of ponderosa stands, and without it the forests grew thick with trees. This made them more vulnerable to big, hot fires.

One such blaze ignited in New Mexico's Jemez Mountains in June 2011, when a tree fell on a power line. Dubbed the Las Conchas fire, it torched about 63,000 hectares, making it the largest blaze in New Mexico's recorded history

"The lack of snow is scary. We're set up for a big fire year if things don't change dramatically."

at the time. It burned incredibly hot, and killed so many trees in certain areas that scientists are unsure whether the forest will ever grow back. In some ways, the Las Conchas fire was an outlier. Its severe temperatures were unusual, says Craig Allen, a USGS fire ecologist based in the Jemez Mountains, especially in areas where ponderosa pines were totally incinerated.

Yet, in other ways, fires on the scale of Las Conchas may be consistent with historical norms. For instance, Margolis says, researchers don't have a good grasp of whether the size of the blaze was truly exceptional.

This is one of the questions that Margolis has pursued by systematically sampling trees across the Jemez Mountains, and in expanding a similar network in the Sangre de Cristo Mountains outside Santa Fe. "It's so basic," he says, "but it takes a lot of data to get

there." Although his analysis of the Jemez data isn't complete, Margolis sees strong evidence that fires as big as Las Conchas, or even twice its size, have occurred for centuries. The implication: "We should be more freaked out that the fires can get even bigger," he says.

This year, it's the potential for fire in the Sangre de Cristo Mountains that really worries Margolis. Many of the area's forests haven't burned in more than 100 years, an unnaturally long dormant period, according to fire histories he's reconstructed. That means the mountains are stocked with fuel.

Widespread fires of the past burned on the heels of extremely dry winters that followed two to three wet winters. That's exactly the pattern New Mexico is currently experiencing, because 2016 and 2017 were relatively wet.

"If we had a Las Conchas fire outside of Santa Fe, it would be devastating," Margolis says. The fire itself could threaten life and property. The loss of vegetation would leave the area vulnerable to post-fire flooding that could wipe out roads and clog vital water infrastructure with debris. "We're sitting on this powder keg," he says. ■

1. Swetnam, T. W. & Betancourt, J. L. *Science* **249**, 1017–1020 (1990).
2. Margolis, E. Q., Huffman, D. W. & Iñiguez, J. M. *Southwestern Mixed-Conifer Forests: Evaluating Reference Conditions to Guide Ecological Restoration Treatments*. Ecological Restoration Institute Working Paper No. 28 (2013).

POLICY

Trump budget underwhelms

Many major science agencies would see flat funding.

BY LAUREN MORELLO, GIORGIA GUGLIELMI, SARA REARDON, JEFF TOLLEFSON & ALEXANDRA WITZE

Confusion reigned on 12 February, as US President Donald Trump released his budget request for the 2019 fiscal year.

Just four days earlier, the Congress had lifted mandatory caps on government spending, sending the Trump administration scrambling at the last minute to revise its budget proposal. The White House abandoned its original plan to seek a 27% funding cut for the National Institutes of Health (NIH), a 29% decrease for the National Science Foundation (NSF) and a 22% reduction for the Department of Energy (DOE) Office of Science, holding their funding steady. But the details of Trump's vision for

many agencies remain fuzzy, frustrating science advocates.

"The big headline is that at the eleventh hour, [the White House] backed away from their intention of dramatically scaling back on basic research," says Matt Hourihan, director of the research and development budget and policy programme at the American Association for the Advancement of Science in Washington DC. But science agencies aren't out of the woods yet, he warns. Even in a budget that seems to support basic science, "they're still going after programmes, like environmental programmes, that they believe fall outside the purview of government", Hourihan says.

Among other things, the Trump request would cut the US Environmental Protection Agency (EPA) budget to its lowest level since

the early 1990s, gut climate-change research at the National Oceanic and Atmospheric Administration (NOAA) and axe five Earth-observing missions and instruments at NASA.

And although biomedical research holds steady under Trump's final 2019 plan, policy watchers remain sceptical of the president's intentions. The White House may have reversed course on potential cuts to the NIH and NSF, but Trump still opposes any funding increases for non-military programmes, says Jennifer Zeitzer, director of legislative relations for the Federation of American Societies for Experimental Biology (FASEB) in Bethesda, Maryland. "I think it'd be really generous to read that suddenly NIH and NSF are a priority for this administration," she says.

Trump is seeking US\$34.8 billion for the NIH — roughly equal to the level in 2017, the last year for which Congress and the White House agreed on a final budget (see 'Roller-coaster ride'). But the White House wants that money to go further than it does now, by creating three new institutes within the NIH. Among them would be the National Institute for Research on Safety and Quality, which would replace the \$324-million Agency for Healthcare Research and Quality within the Department of Health and Human Services.

The NSF would also see flat funding under the Trump plan, with a budget of \$7.47 billion.

ROBERT NICKELBERG/GETTY

That figure includes \$2.2 billion that the White House added at the last minute, which it says would support basic scientific research, education programmes, upgrades to research facilities in Antarctica and elsewhere, and cross-disciplinary research activities. But it has not provided a more detailed explanation of how that money would be allocated.

Trump's final proposal for 2019 would boost spending across the NSF's 7 research directorates by 2%, to \$6.151 billion. But it would cut, by 56%, funding for the construction of research platforms — such as the agency's suite of telescopes — and the acquisition of scientific instrumentation. The budget for that account would drop from \$215 million in 2017 to \$95 million in 2019.

NASA would abandon the International Space Station under the Trump plan, which calls for the space agency to terminate its contribution to the 15-nation facility in 2024, after the current US commitment ends. The administration wants NASA to explore how to turn space-station operations to private industry in 2025, but the plan is unlikely to fly with many members of Congress.

The proposed budget would also cancel the Wide-Field Infrared Survey Telescope (WFIRST), which is designed to hunt for exoplanets and dark matter. It has been planned as NASA's next big astrophysics mission after the James Webb Space Telescope, which is due to launch next year.

A recent independent review found that WFIRST's cost could not be kept beneath the \$3.2-billion cap set by NASA (see go.nature.com/2btsw3z), and the agency has been working to revise the mission's design to reduce its price. US astronomers ranked WFIRST the top large mission in a 2010 survey of science priorities for the next decade.



Trump's budget would boost funding for research on fossil fuels, such as coal used in this power plant.

"Cancelling WFIRST is an unqualified disaster for the astronomical community," says Jon Morse, chief executive of the BoldlyGo Institute in New York City and former head of astrophysics at NASA. If the Congress does not move to continue the mission, "this would be the first time in the history of astrophysics decadal surveys dating back to the 1960s that the highest-priority mission wasn't accomplished".

Overall, NASA would receive \$19.9 billion under the Trump plan, a 1.3% increase from the 2017 level. The agency's science directorate would receive \$5.895 billion, a 2.3% increase.

Funds for basic research at the DOE's Office of Science would remain flat, at \$5.4 billion. Basic energy sciences would see a nearly 2%

increase, to \$1.85 billion, but the big winner would be advanced scientific computing, whose budget would rise by nearly 42%, to \$899 million. The nuclear-fusion project ITER, under construction in France, would receive \$75 million — \$25 million above the 2017 level.

For the second year in a row, the White House is proposing to kill the Advanced Research Projects Agency—Energy, which supports high-risk energy research. The agency received \$306 million in 2017, but the Congress is split over its future. The House's 2018 funding bill for the DOE would have eliminated the agency, whereas Senate appropriators approved a funding boost, to \$330 million.

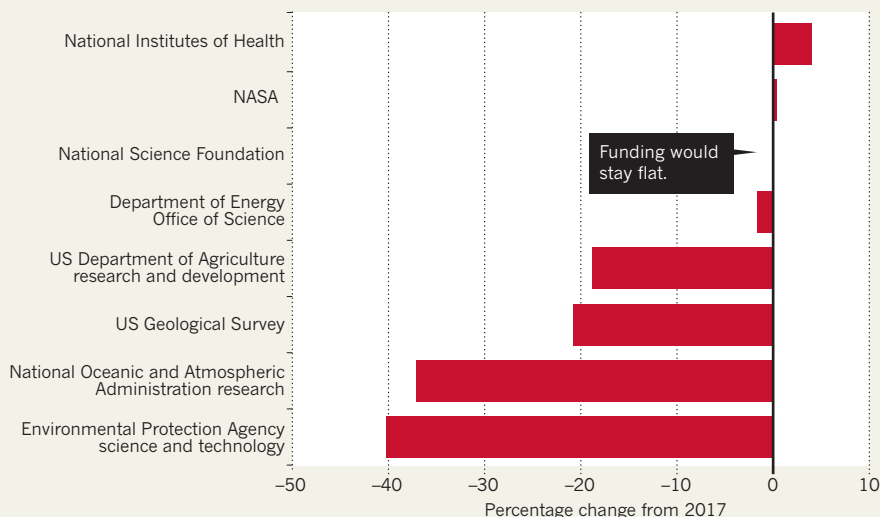
Climate-change programmes would take hits across multiple agencies. The Trump budget would eliminate funding for global-warming research at the EPA, whose overall funds would drop to \$6.1 billion, from \$8.1 billion in 2017. The plan would eliminate competitive grants for climate-change research at NOAA, and halt research to better understand how global warming is affecting the Arctic. The agency's overall budget would fall by 20%, to \$4.6 billion.

It is not clear how Congress will receive the Trump plan. So far, lawmakers have largely rejected the president's ongoing push for major cuts at federal science agencies. The 9 February budget deal, for example, included a provision to boost NIH spending by \$2 billion in 2018 — even though the bulk of the government is operating under a temporary spending plan that expires in late March.

Michael Lubell, a physicist at the City College of New York, says that with the spending cap for 2019 now lifted, science agencies will be competing with other parts of the federal government for extra cash. That process is just beginning. "There are a lot of feeders at the trough," Lubell says. "Time will tell." ■

ROLLERCOASTER RIDE

US President Donald Trump's proposed 2019 budget would hold research funding steady at some agencies, but others would be in line for deep cuts compared with 2017 levels — the last year for which Congress and the White House agreed on a final funding deal.



SOURCE: AMERICAN ASSOCIATION FOR THE ADVANCEMENT OF SCIENCE

DISEASE ERADICATION

Plan to end yaws disease queried

Bid fails to account for wild primates as hosts of infection.

BY LUCAS LAURSEN

Global health officials are intensifying efforts to eradicate yaws, a disfiguring skin disease that infects more than 64,000 people a year in 14 African and south-east Asian countries. But some critics say that the plans could fail, because they don't take into account discoveries in the past few years that wild primates harbour the bacterial infection.

Public-health officials met in Geneva, Switzerland, last month to discuss how to expand the eradication programme in 6 of the 14 countries in which yaws is endemic. But they did not discuss the part played by wild animals. "Even if this is not the main cause of re-emerging yaws nowadays, it would jeopardize global eradication," says Sascha Knauf, who studies neglected tropical diseases at the Leibniz Institute for Primate Research in Göttingen, Germany.

Five years ago, the World Health Organization (WHO) committed to eradicating yaws by 2020, motivated in part by the discovery that it can be treated using an easy-to-administer oral antibiotic, azithromycin. The WHO estimated that the initiative would cost at least US\$100 million. At the time, public-health officials thought that the disease occurred only in humans. Eradicating a disease that affects only people is much easier than one that also occurs in wild animals.

However, Knauf reported in 2011 (ref. 1) and 2013 (ref. 2) that gorillas, chimpanzees, baboons and smaller primates in several West and Central African countries were infected with the same bacterium that causes yaws (*Treponema pallidum pertenue*).

Epidemiologist Michael Marks at the London School of Hygiene and Tropical Medicine says that scientists have not yet shown that humans can catch the disease from primates. Even so, "it would be remiss not to pay attention to it", he says.

The WHO is still waiting for such proof, says its medical officer for the disease, Kingsley Asiedu. In the meantime, Asiedu says, "we are not taking that into account, because there has not been proof of an epidemiological link between those yaws-like cases that have been found in primates and in humans". ■

1. Knauf, S. *et al. Vet. Pathol.* **49**, 292–303 (2011).
2. Knauf, S., Liu, H. & Harper K. N. *Emerg. Infect. Dis.* **19**, 2058–2060 (2013).



The MeerKAT array of radio dishes will soon double its capacity.

DATA HANDLING

South Africa readies for data deluge

Nation seeks to retain control over its information.

BY SARAH WILD

Data scientists in South Africa are preparing to be inundated by a flood of information that is due to crash over them when the country's biggest radio telescope doubles the scale of its operations in March.

A terabyte-an-hour data deluge, which would fill more than three DVDs a minute, will flow from a network of radio dishes called the MeerKAT array. Currently consisting of 32 operational dishes, the array will expand to 64 next month.

The impending flood of data is just a trickle compared with what will arrive after 2020, when international astronomers begin to expand MeerKAT to form part of the Square Kilometre Array (SKA). That will be the world's largest radio telescope, and astronomers are trying to develop the expertise to handle torrents of data ahead of its full opening in 2026. South African data scientists also want to transfer their expertise to areas such as Earth observation and bioinformatics.

"We are building a system that empowers scientists, so that they can be part of processing the data — a system that allows the researchers to work with the data itself and work with the analytics, as if it was on their desktops," says astronomer Russ Taylor, who divides his time between the University of Cape Town in South Africa and the University of the Western Cape in the same city.

The MeerKAT array is designed to collect relatively weak radio signals from space and combine them to extract more information. To convert it into the first phase of the SKA, engineers will initially add another 136 dishes to the MeerKAT site in the Northern Cape province of South Africa, and connect them to 130,000 antennas scattered across Western Australia.

NUMBER CRUNCHING

Data from the SKA will be shared with scientists from ten partner countries. But for now, South Africa is keen to retain control of its MeerKAT data rather than exporting them to other countries that already have data-processing infrastructure, says Taylor.

MUJAHID SAFODIEN/AFP/GETTY

This is partly because distributing data is very expensive. “Fibre optics to connect two points in urban areas cost thousands of US dollars per mile,” says Ugo Varetto, acting executive director at Australia’s Pawsey Supercomputing Centre in Perth, which crunches and stores data from existing radio telescopes dotted over Australia. “In extreme environments or underwater, that’s hundreds of thousands of dollars.”

Astronomers also highly value the data produced by their telescopes and don’t want to send them elsewhere, says J. J. Kavelaars, group leader at the Canadian Astronomy Data Centre in Victoria, British Columbia. “All the effort of collecting the observations is expressed in those data files. Sending those data out of your jurisdiction is like shipping diamonds overseas for cutting,” he says.

Because the astronomy data sets will be very large and will sit in geographically separate databases, scientists need to develop software tools to access them and bring them together in an efficient manner, says Mattia Vaccari, a data scientist at the University of the Western Cape. Taylor says he hopes that other African countries could use the same tools to develop their own cloud-based infrastructure.

EXPLORING APPLICATIONS

Within South Africa, others seek to take advantage of the data-crunching capabilities that the country is developing. These could be used for applications such as monitoring water resources or urbanization across the continent, says Val Munzami, head of the South African National Space Agency in Pretoria.

Health-care officials would also like to get involved. Glaudina Loots, director of health innovation in the South African government’s Department of Science and Technology, says that her unit plans to “piggyback” on the astronomy investment and data infrastructure. “Part of that is earmarked for precision medicine. If you can’t handle the data, and have to export it out of the country, then you start running into problems,” she says.

“South Africa has one of the best hands in the game at this point,” says Tony Beasley, an astronomer and head of the US National Radio Astronomy Observatory in Charlottesville, Virginia. “In terms of deployed science infrastructure, South Africa is way ahead.” ■

POLICY

US agency targets sexual harassment

The National Science Foundation says institutions must disclose when grant recipients have violated policies.

BY ALEXANDRA WITZE

Any institution receiving grant monies from the US National Science Foundation (NSF) must now inform the agency if it finds that anyone funded by the grant proposal has committed sexual harassment. The policy will take effect once a 60-day public-comment period has ended.

Until now, “we haven’t had a requirement on universities to report a [harassment] finding or when they’ve put someone on administrative leave” during a harassment investigation, says France Córdova, the NSF director. “We didn’t have the channel to find out what’s at the end of an investigation.”

The reporting requirement comes in the wake of numerous sexual-harassment scandals in the sciences. It is a rare move among US federal research agencies, which generally do not require grant recipients or their employers to disclose sexual-harassment allegations or findings.

“It’s a big step in the right direction,” says Erika Marín-Spiotta, a biogeochemist at the University of Wisconsin–Madison who is co-leading a US\$1.1-million initiative funded by the NSF to combat sexual and other forms of harassment in the sciences. But Marín-Spiotta says that agencies must do more to develop truly protective policies. Among other things, the NSF policy does not address what happens if an institution never completes an investigation.

“At the end of the day, if the employing institution doesn’t do its job, those who are affected will still be in a very difficult situation,” says C. K. Gunsalus, who specializes

in research integrity at the University of Illinois at Urbana-Champaign.

The NSF notice, dated 8 February, is addressed to the heads of universities and colleges and other organizations that receive NSF funds. It requires them “to report findings of sexual harassment, or any other kind of harassment regarding a PI [principal investigator] or co/PI or any other grant personnel”. And it requires the institution to report if the PI or co-PI is placed on administrative leave relating to a harassment finding or investigation.

The notice also says that the NSF expects awardee organizations to lay out clear stand-

If the employing institution doesn’t do its job, those who are affected will still be in a very difficult situation.

ards for harassment-free workplaces, and processes by which students and others can report problems. Workplaces are defined to include conferences and remote fieldwork sites, where students and young researchers are often most vulnerable. The agency will solicit public feedback on the new rule in the coming weeks, through a posting in the *Federal Register*.

Córdova says that the burden of investigating harassment complaints typically rests with the institution that employs the person in question. The NSF accepts voluntary reports through its Office of Diversity and Inclusion, but “we get vanishingly few complaints”, she says.

Others note that institutions have differing policies on what constitutes sexual harassment; behaviour that might be ▶



TOP NEWS



Critics attack study that rewrote human arrival in Americas
go.nature.com/2ezc7cr

MORE NEWS

- Few UK universities have adopted rules against impact-factor abuse
go.nature.com/2f1ohge
- Fish’s sea-floor shuffle illuminates origins of walking
go.nature.com/2f0a8ou
- Researchers describe their nerdy proposals
go.nature.com/2f0alrk

NATURE PODCAST



Refocusing ageing research, a transportable atomic clock, and researching while pregnant
nature/podcast

► punished at one university — such as sexual relationships between faculty members and students — might not be at another. In 2016, investigators at the University of Rochester concluded that cognitive-sciences professor Florian Jaeger did not violate university policies on sexual harassment. A separate university-commissioned investigation reported last month that Jaeger had had sexual relationships with four prospective, current or former students, and that these did not violate university policies.

In a response to that report, Jaeger said the relationships were consensual and that he did not sexually harass any students.

UNDER SCRUTINY

Like other federal agencies, the NSF is under pressure from the US Congress to strengthen its response to sexual harassment. In January, the House of Representatives' science committee asked the Government Accountability Office to look into sexual harassment involving federally funded researchers at agencies including the NSF, NASA, the Department of

Energy and the National Institutes of Health.

The action in Congress was prompted in part by an investigation at Boston University in Massachusetts. The university found that one of its professors, David Marchant, had violated campus policies on sexual harassment while on NSF-funded field-work in Antarctica. (Marchant denies that he engaged in inappropriate behaviour, and he is appealing against the university finding, his lawyer says.)

Some scientific societies have stepped up their policies against sexual harassment in recent years. Last September, the American Geophysical Union (AGU) changed its integrity and ethics policy to classify discrimination, sexual harassment and bullying as professional misconduct.

The fact that a funding agency is taking action is crucial, says Robin Bell, a geophysicist at the Lamont-Doherty Earth Observatory in Palisades, New York, and AGU president-elect. "Linking reporting of harassment to funding is the next step the scientific enterprise can take to stop bullying and harassment by making the consequences clear," she says.

Meg Urry, an astronomer at Yale University in New Haven, Connecticut, agrees. "I think it will make a big impact," she says. "Grant money is very important to scientists and their institutions, so this policy will

definitely help change the culture."

But much remains to be done to further protect those who have been harassed and to lessen the roadblocks to reporting, says Marin-Spiotta. "You could imagine a postdoc thinking, my advisor's going to lose all the funding I need to do my work," she says.

One possible solution, she says, could be to route funding directly to students or postdocs, or to their academic department, rather than to their principal investigator. ■

CORRECTIONS

The News story 'Super-invasive crayfish revealed to be a genetic hybrid' (*Nature* **554**, 157–158; 2018) incorrectly stated that Julie Jones was the first to identify marbled crayfish in Madagascar. In fact, another team made the discovery; Jones and her team were the first to survey the species there.

The News story 'Israeli fossils hint at early migration' (*Nature* **554**, 15–16; 2018) gave the wrong URL for reference 1. It should have been <http://dx.doi.org/10.1126/science.aap8369>.

The Editorial 'Maths revision' (*Nature* **554**, 146; 2018) mistranslated the name of the Leibniz Institute. It is actually the Leibniz Institute for Information Infrastructure.



Stephanie Wehner is part of the team trying to build a true quantum network across Europe.

THE ENTANGLED WEB

BY DAVIDE CASTELVECCHI

Quantum physics can already make communications super-secure. But exploiting some of its strangest properties could take these networks to the next level.

Before she became a theoretical physicist, Stephanie Wehner was a hacker. Like most people in that arena, she taught herself from an early age. At 15, she spent her savings on her first dial-up modem, to use at her parents' home in Würzburg, Germany. And by 20, she had gained enough street cred to land a job in Amsterdam, at a Dutch Internet provider started by fellow hackers.

A few years later, while working as a network-security specialist, Wehner went to university. There, she learnt that quantum mechanics offers something that today's networks are sorely lacking — the potential for unhackable communications. Now she is turning her old obsession towards a new aspiration. She wants to reinvent the Internet.

The ability of quantum particles to live in undefined states — like Schrödinger's proverbial cat, both alive and dead — has been used for years to enhance data encryption. But Wehner, now at Delft University of Technology in the Netherlands, and other researchers argue

MARCEL WOGRAM FOR NATURE

that they could use quantum mechanics to do much more, by harnessing nature's uncanny ability to link, or entangle, distant objects, and teleporting information between them. At first, it all sounded very theoretical, Wehner says. Now, "one has the hope of realizing it".

Proponents say that such a quantum internet could open up a whole universe of applications that are not possible with classical communications, including connecting quantum computers together; building ultra-sharp telescopes using widely separated observatories; and even establishing new ways of detecting gravitational waves. Some see it as one day displacing the Internet in its current form. "I'm personally of the opinion that in the future, most — if not all — communications will be quantum," says physicist Anton Zeilinger at the University of Vienna, who led one of the first experiments on quantum teleportation¹, in 1997.

A team at Delft has already started to build the first genuine quantum network, which will link four cities in the Netherlands. The project, set to be finished in 2020, could be the quantum version of ARPANET, a communications network developed by the US military in the late 1960s that paved the way for today's Internet.

Wehner, who is involved in the effort, is also coordinating a larger European project, called the Quantum Internet Alliance, which aims to expand the Dutch experiment to a continental scale. As part of that process, she and others are trying to bring computer scientists, engineers and network-security experts together to help design the future quantum internet.

Many technical details still need to be sorted out, and some researchers caution that it is too early to say exactly how much a quantum internet might deliver. But by thinking about security early, Wehner says that she hopes to avoid the vulnerabilities that the Internet inherited from ARPANET. "Maybe we have a chance to do it all right from the start."

QUANTUM KEYS

The first proposals for quantum modes of communication date back to around the 1970s. Stephen Wiesner, then a young physicist at Columbia University in New York City, saw potential in one of the most basic principles of quantum mechanics: that it is impossible to measure a property of a system without changing it.

Wiesner suggested that information could be encoded in the states of objects such as isolated atoms, whose 'spins' can point up or down — like the 0 and 1 of classical bits — but can also be in both states simultaneously. Such units of quantum information are now commonly called quantum bits, or qubits. Wiesner pointed out that because the properties of a qubit can't be measured without changing its state, it is also impossible to make exact copies or 'clones' of one². Otherwise, someone could extract information about the state of the original qubit without affecting it, simply by measuring its clone. This prohibition later became known as quantum no-cloning, and it turns out to be a boon for security, because a hacker cannot extract quantum information without leaving a trace.

Inspired by Wiesner, in 1984, Charles Bennett, a computer scientist at IBM in Yorktown Heights, New York, and his collaborator Gilles Brassard, at the University of Montreal in Canada, came up with an ingenious scheme by which two users could generate an unbreakable encryption key that only they know³. The scheme depends on the fact that light can be polarized, so that the electromagnetic waves oscillate either in a horizontal or a vertical plane. One user converts a random sequence of 1s and 0s into a quantum key encoded in those two polarization states and sends it streaming to another person. In a sequence of steps, the recipient measures the key and establishes that the transmission was not disturbed by the measurements of an eavesdropper. Confident in the security of the key, the two parties can then scramble any message made up of classical bits — an image, for example — and send it just as they would any other encrypted message over the conventional Internet, or any other channel.

In 1989, Bennett led the team that first demonstrated this 'quantum key distribution' (QKD) experimentally⁴. Today, QKD devices that use similar schemes are commercially available and typically sold to financial or government organizations. ID Quantique, for example, a company founded in 2001 in Geneva, Switzerland, built a quantum link that has been protecting the results of Swiss elections for more than ten years.

Last year, China's Micius satellite, the brainchild of physicist Pan Jianwei of the University of Science and Technology of China in Hefei, made some of the flashiest demonstrations of the approach. Using a variant of Bennett and Brassard's protocol, the spacecraft created two keys, then sent one to a ground station in Beijing and another to Vienna as it passed overhead. An on-board computer then combined the two secret

keys to create a new one, which it beamed down classically. Armed with their private keys, the Vienna and Beijing teams could unscramble that combined key by essentially subtracting their own, and so learn the other's secret key. With both keys, one team could decrypt a transmission that the other team encrypted with its key. Last September, Pan and Zeilinger used this approach to set up the first intercontinental video chat to be secured in part with a quantum key⁵.

Satellites such as Micius could help to address one of the main challenges in making today's quantum communications secure:

distance. The photons needed to create an encryption key can get absorbed by the atmosphere or — in the case of ground networks — by an optical fibre, which renders quantum transmission impractical after several tens of kilometres.

Because quantum states cannot be copied, it is not an option to send multiple copies of a qubit in the hope that at least one will arrive. So, at the moment, creating long-distance QKD links requires building 'trusted nodes' to act as intermediaries. If a person were to hack into a trusted node, which handles keys in both their quantum and classical forms, they would be able to copy the keys without being detected — and so, of course, could the government or company operating the node. This is true both for trusted nodes on the ground and for Micius. "The satellite knows everything," Pan says. But passing satellites could cut down on the number of trusted nodes that are needed to connect distant points.

Pan says that trusted nodes are already a step forward for some applications, because they reduce the number of spots where a network is vulnerable to attack. He has also led the creation of the extensive Beijing-Shanghai quantum-communication backbone. Launched in September, this connects 4 cities with 32 trusted nodes using more than 2,000 kilometres of optical fibre, and is being tested for banking and commercial communications, such as linking up the data centres of Internet-shopping giant Alibaba, Pan says.

QUANTUM CONNECTIONS

But networks that involve trusted nodes are only partly quantum. Quantum physics plays a part only in how the nodes create the encryption key; the subsequent encryption and transmission of information is entirely classical. A true quantum network would be able to harness entanglement and teleportation to transmit quantum information over long distances, without the need for vulnerable trusted nodes.

One of the main motivations for building such networks is to enable quantum computers to talk to each other, both between countries and across a single room. The number of qubits that can be packed into any one computing system may be limited, so networking the systems together could help physicists to scale them up. "At this point, it's fair to say that probably you'll be able to build a quantum computer with maybe a couple of hundred qubits," says Mikhail Lukin, a physicist at Harvard University in Cambridge, Massachusetts. "But beyond that, the only way to do this is use this modular approach, involving quantum communications."

On a larger scale, researchers envision a quantum-computing cloud,

**"MAYBE WE HAVE
A CHANCE TO DO IT
ALL RIGHT FROM
THE START."**

with a few highly sophisticated machines that are accessible through a quantum internet from most university labs. “The extra cool thing is that such cloud quantum computing is also secure,” says Ronald Hanson, an experimental physicist at Delft. “People at the server are unable to know what kind of program you’re running and the data you have.”

Researchers have come up with a plethora of other proposals for Internet applications — such as auctions, elections, contract negotiations and speed trading — that could exploit quantum phenomena to be faster or more secure than their classical counterparts.

But the biggest impact of a quantum internet could be on science itself. Synchronizing clocks using entanglement could improve the precision of Global Positioning System-like navigation networks from metres to millimetres, some researchers say. And Lukin and others have proposed using entanglement to combine distant atomic clocks into a single clock with vastly improved precision, which he says could lead to new ways of detecting gravitational waves, for example. In astronomy, quantum networks might link distant optical telescopes across thousands of kilometres, to effectively give them the resolution of one dish spanning the same distance. This process, called very long baseline interferometry, is applied routinely in radio astronomy, but operating in optical frequencies requires timing precision that is currently out of reach.

SPOOKY SECURITY

In the past decade or so, experiments pioneered by Christopher Monroe⁶, a physicist at the University of Maryland in College Park, and others have demonstrated some of the fundamentals needed to build a truly quantum network, such as teleporting information encoded in qubits from one place to another (see ‘Creating a quantum internet’).

To see how teleportation (also proposed by Bennett and Brassard⁷) works, imagine two users: Alice and Bob. Alice holds a qubit, which could be a trapped ion or some other quantum system, and wants to transfer the information stored in it to Bob. As luck would have it, Alice and Bob come into possession of two ‘proxy’ particles — also qubits — that are entangled with each other. If Alice can entangle her qubit and proxy particle, the qubit will, by extension, also become entangled with Bob’s particle. To do so, Alice performs a particular kind of joint measurement on her two particles. She then shares the results of that measurement (which are ordinary, classical data) with Bob. To complete the teleportation process, Bob then uses that information to manipulate his particle so that it ends up in the same state as Alice’s qubit originally was.

For practical purposes, it doesn’t matter how Alice and Bob obtain the entangled proxy particles. They could be individual atoms delivered in a briefcase, say, or photons beamed to the pair by a third party. (One of Micius’s experiments last year sent entangled pairs of photons to two ground stations in China over a record distance of more than 1,200 kilometres.) Alice and Bob could also entangle the qubits they hold, by sending photons out to interact at a third location.

The beauty of quantum teleportation is that the quantum information does not technically travel along the network. The photons that do travel are just used to establish a link between Alice and Bob so that quantum information can then be transferred. If one pair of entangled photons fails to establish a connection, another pair will. This means that the quantum information is not lost if photons are.

LINK AND REPEAT

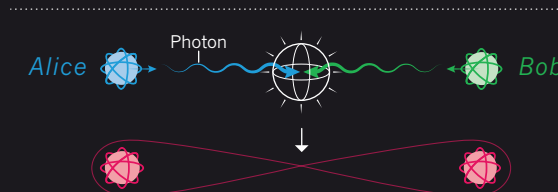
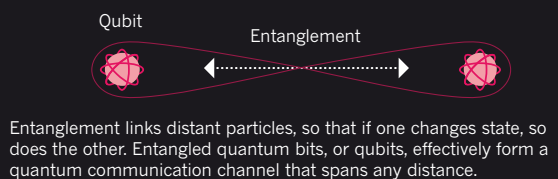
A quantum internet would be able to produce entanglement on demand between any two users. Researchers think that this will involve sending photons through both fibre-optic networks and satellite links. But connecting distant users will require a technology that can extend the reach of entanglement — relaying it from user to user and along intermediate points.

One way in which such a quantum repeater could work was proposed in 2001 by Lukin and his collaborators⁸. In their scheme, small quantum computers that can store qubits and do simple operations on them are used to entangle a qubit at an upstream station with one downstream.

CREATING A QUANTUM INTERNET

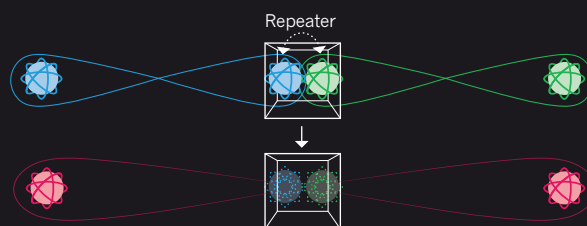
Researchers expect that a fully quantum network will need to establish entangled links between any two users. Quantum information will then be teleported from one to the other, transferring the information without transmitting it over the network.

ESTABLISHING ENTANGLEMENT



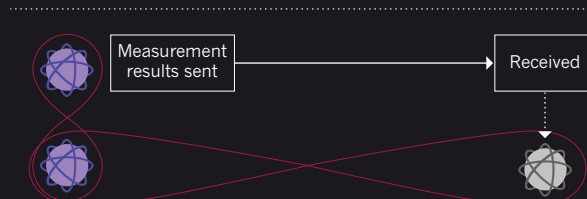
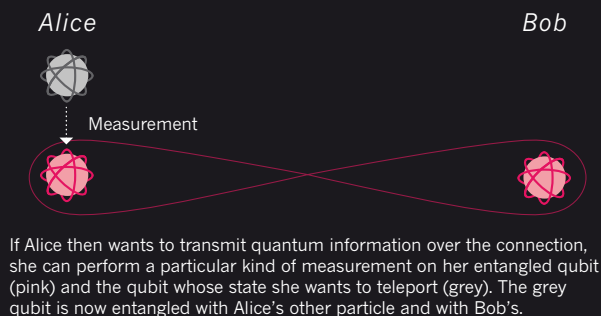
To create a link, Alice can emit a photon towards Bob from her qubit. Bob does the same towards Alice. Because the photons are entangled with their original qubits, when they interact, Alice's and Bob's qubits become entangled, too.

LONG-DISTANCE LINKS



If Alice and Bob are far away from one another or not directly connected, one or more quantum repeaters will be needed to establish entanglement. Here, one qubit in the repeater is entangled with Alice's qubit, and the other with Bob's. By performing an operation on the two qubits it holds, the repeater creates entanglement between Alice's and Bob's qubits.

TELEPORTING INFORMATION



Alice then sends information about the measurement to Bob, which can be done over the conventional Internet. With that information, Bob can perform an operation on his qubit that places it in the same state as Alice's second qubit was originally. The quantum state of Alice's particle — its quantum information — has been teleported.



Part of an experiment to investigate diamond-based systems as quantum-internet nodes at Delft University of Technology in the Netherlands.

Repeated application of this ‘entanglement swapping’ process along a path in a network would eventually produce entanglement between any two users.

In 2015, Hanson and his collaborators showed how to build one leg of a network when they linked two qubits built from single-atom impurities in diamond crystals and separated by 1.3 kilometres⁹. Photons emitted by the two qubits travelled towards an intermediate station, where they then interacted, establishing entanglement. “It shows that one can really establish entanglement — strong, reliable entanglement — between two distant quantum-information processors,” says Seth Lloyd, a physicist at the Massachusetts Institute of Technology in Cambridge.

Researchers are investigating other ways to construct and manipulate qubits, including using individual ions suspended in a vacuum — pioneered by Monroe and others — as well as systems that pair up atoms and photons bouncing between two mirrors inside a cavity.

Like Hanson’s diamond system, these qubits could be used to build both quantum repeaters and quantum computers. Fortunately for people hoping to ramp up quantum communications, the requirements for a repeater may be less demanding than those for a fully fledged quantum computer. Iordanis Kerenidis, a quantum-computation researcher at the University of Paris Diderot, made this argument at a workshop on quantum repeaters in Seefeld, Austria, last September. “If you tell experimentalists that you need 1,000 qubits, they are going to laugh,” he said. “If you tell them you need ten — well, they laugh less.”

The prospect of creating a quantum internet is now becoming a problem of systems engineering. “From an experimental point of view, people have demonstrated various building blocks” for quantum networks, says Tracy Northup, a physicist at Austria’s University of Innsbruck whose team works on cavity qubits and is part of Wehner’s pan-European Quantum Internet Alliance. “But putting them together in one place — we all see how challenging it is,” Northup says.

For the moment, Wehner’s alliance is still at an early stage and looking for public funding as well as corporate partners. In the meantime, the Dutch demonstration network, led by Hanson, has been moving forward. Hanson and his colleagues have been improving the speed of their systems, which in the 2015 experiment entangled just 245 qubit pairs over the equivalent of about 9 days. Another crucial challenge has been to reliably convert photons from the visible wavelengths that come out of the diamond qubits to longer, infrared ones that can travel well along optical fibres; this is tricky because the new photon still has to carry the quantum information of the old one, but without the possibility of cloning it. Earlier this year, Hanson and his colleagues achieved this by making photons interact with a laser beam of longer wavelength¹⁰. That technique would enable qubits to be linked over distances of tens of kilometres over fibre.

Hanson’s team is now building a link between Delft and The Hague, a good 10 kilometres away. By 2020, the researchers hope to have connected up four Dutch cities, with a station at each site acting as a quantum repeater. If successful, the project would be the world’s first genuine quantum-teleportation network. The group aims to open it up to other teams interested in performing quantum-communications experiments remotely, much like IBM’s Quantum Experience, which allows remote users access to a rudimentary quantum computer.

The network could be a test bed for researchers hoping to fix some of the Internet’s flaws, not least the ease with which users can forge or steal identities. “The idea that you could join a network without establishing identity is a problem from early on,” said Robert Broberg, a network engineer from the telecommunications equipment giant CISCO, at the Seefeld meeting. Wehner and others have proposed quantum techniques that would allow users to prove their identity by certifying that they own the correct secret code (a series of classical bits) without ever transmitting it. Instead, the user and the server use the code to create a sequence of qubits and send them to a ‘black box’ in between. The black box — which could be, say, a cash machine — can then compare the two sequences to see whether they match, without ever knowing the underlying code.

But some researchers caution against overselling the potential reach of the technology. “Today’s Internet will never be entirely quantum, no more than computers will ever be all-quantum,” says Nicolas Gisin, a physicist at the University of Geneva in Switzerland and a co-founder of ID Quantique. And it could be that many of the things people hope to achieve with quantum networks could be done with more conventional technologies. “Sometimes, something looks like a great idea at first, and then it turns out to be easily achievable without a quantum effect,” says Norbert Lütkenhaus, a physicist at the University of Waterloo in Canada who is helping to develop standards for the future quantum internet.

Time will tell whether the promise of the quantum internet will materialize. As far as we know, teleportation is a phenomenon that, although physically possible, does not occur in nature, Zeilinger says. “So this is really new for humanity. It might take some time.”

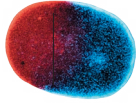
Wehner’s familiarity with both physics and network security has made her a point of reference for people in the field. And after having done much work on hard-core quantum theory, she is relishing the opportunity to shape these future networks. “For me,” she says, “this is really full circle.” ■

Davide Castelvecchi is a senior reporter for Nature in London.

1. Bouwmeester, D. *et al.* *Nature* **390**, 575–579 (1997).
2. Wiesner, S. *SIGACT News* **15**, 78–88 (1983).
3. Bennett, C. H. & Brassard, G. *Proc. IEEE Int. Conf. Comput. Syst. Signal Process.* **1**, 175–179 (1984).
4. Bennett, C. H. & Brassard, G. *SIGACT News* **20**, 78–80 (1989).
5. Liao, S.-K. *et al.* *Phys. Rev. Lett.* **120**, 030501 (2018).
6. Moehring, D. L. *et al.* *Nature* **449**, 68–71 (2007).
7. Bennett, C. H. *et al.* *Phys. Rev. Lett.* **70**, 1895–1899 (1993).
8. Duan, L.-M., Lukin, M. D., Cirac, J. I. & Zoller, P. *Nature* **414**, 413–418 (2001).
9. Hensen, B. *et al.* *Nature* **526**, 682–686 (2015).
10. Dréau, A., Tcheborateva, A., El Mahdaoui, A., Bonato, C. & Hanson, R. Preprint at <https://arxiv.org/abs/1801.03304> (2018).

COMMENT

PALAEoANTHROPOLOGY How did we get here and where do we go next? **p.296**



ART Biomedical powerhouse raided for patterns **p.298**

CONSERVATION US bill puts an economic gloss on extinctions **p.300**

HISTORY Snapshot recalls Rosalind Franklin's carbon work **p.300**

BRANDON THIBODEAU/ANZENBERGER/EVINE



Studies of ageing have tended to focus on lifespan rather than on years of good health.

Find drugs that delay many diseases of old age

Simply extending lifespan is not enough. We need treatments that boost resilience to multiple age-related diseases, argue **Ilaria Bellantuono** and 12 co-signatories.

By 2050, the number of people over 60 years old is expected to reach 2 billion worldwide, or 22% of the population. In 2015, it was 12% of the population. And for many, a longer life will mean more years of chronic diseases, such as arthritis, type 2 diabetes, cancer and Alzheimer's disease.

In Europe, for example, the estimated life expectancy for women born in 2014 is 1.6 years longer than for those born in 2006; for men, it is 2.3 years longer. But the

women born in 2014 can expect 0.7 fewer years of good health, and the men zero (see 'More years of what?'). As this trend continues, health-care and other costs are expected to soar.

A class of drugs called geroprotectors might be able to delay the onset of concurrent age-related diseases (multimorbidity) and boost resilience. In various animal models, these drugs can ward off problems of the heart, muscles, immune system and more. And in

2014, investigators reported the results of the first clinical trial of a geroprotector in people over 65: the drug, RAD001, boosted immune responses to an influenza vaccine¹.

More than 200 compounds have now been classified as geroprotectors. But various factors are preventing these drugs from reaching the clinic.

Here we set out three steps required to speed up translation. These have been distilled over the past three years by ►

► a network of academic and industry scientists, clinicians and regulators called COST Action BM1402: MouseAGE. The network, which is funded by the European Union, has worked with other experts in these domains worldwide.

MATURING FIELD

Over the past decade, understanding of the physiological changes that occur as people age has improved a great deal.

Common mechanisms seem to underpin several age-related diseases, including diabetes, Parkinson's disease and Alzheimer's. A review of more than 400 studies of people and animal models indicates that similar mechanisms underlie six conditions². These can involve DNA damage, such as that caused by free radicals; cellular senescence (in which cells stop dividing and start secreting inflammatory factors); or inflammation and autophagy (the degradation of organelles, misfolded proteins and so on)².

This may explain why people over 65 are at a higher risk than younger people of developing more than one disease at the same time. In the United States, 7 out of 10 people over 65 with diabetes will die of heart disease, for instance.

It is also becoming clear that one age-related disease can accelerate the onset of others. A 2014 study³ showed that people older than 75 who already had diabetes, say, were more than twice as likely to develop another disease over the next three years than those who were healthy at the beginning of the study.

Also, between one-quarter and half of people over the age of 80 become frail. The accumulation of deficits makes it harder for them to recover from an infection, fall or other minor stressor⁴. It is unclear whether multimorbidity leads to frailty or vice versa, or whether they are independent.

Until now, ageing research has focused mainly on single diseases, or on delaying death. This means that the fundamental mechanisms of ageing as targets for the treatment or prevention of several age-related conditions are being missed. What's more, patients with multimorbidity are being exposed to many drugs at once, often with adverse effects⁵.

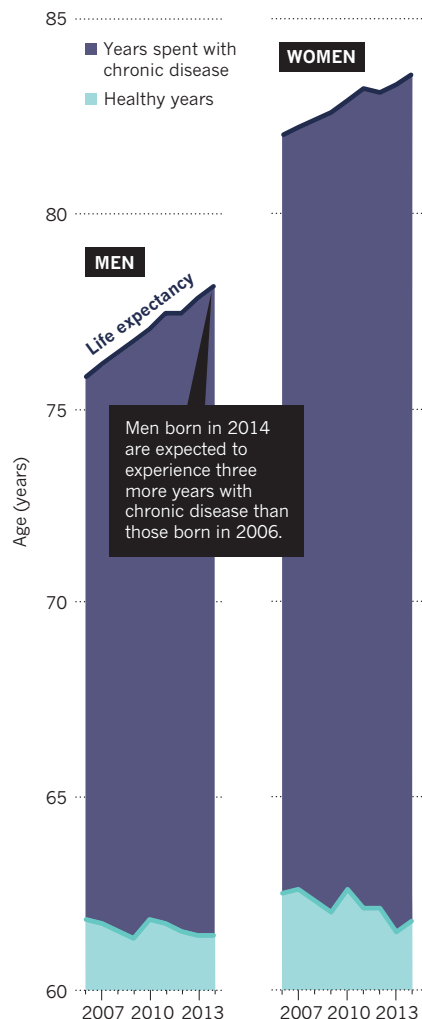
THREE STEPS TO TRANSLATION

Research in mice over the past few years suggests that it might be possible to delay the decline of many tissues and the onset of disease. Drugs such as rapamycin, metformin or senolytics (which remove senescent cells), can slow the development of cataracts, osteoarthritis, osteoporosis, the loss of muscle mass and can improve cardiac function^{2,6–8}.

If these are to become useful in people, three advances must be made.

MORE YEARS OF WHAT?

In Europe, men and women are living longer. They are also spending more years with chronic conditions such as diabetes, cancer and Alzheimer's disease.



Agree on definitions. For drugs to be approved for clinical use, developers must first identify the indication — the condition that enables investigators to obtain authorization to test a drug treatment in people. Professional organizations, such as the International Association of Gerontology and Geriatrics, must agree on definitions of multimorbidity and frailty. And institutions such as the World Health Organization (WHO) and the US Centers for Medicare and Medicaid Services (CMS) need to accept this consensus. (The CMS issues codes that affect people's ability to claim health insurance for the treatment of a particular condition.)

There is no standardized definition of multimorbidity. Some researchers use the term to describe the co-occurrence of 2 diseases, some 5, others 13 and so on. This makes it hard to compare studies and to establish which diseases have a higher chance of occurring together.

Agreeing to a definition will require:

working out which of the 5 or 10 most burdensome age-related diseases, say, to prioritize; which of these are most likely to associate together; the timing of development of each disease with respect to the others in the cluster; and the identification of the pathways associated with their common pathogenesis.

Likewise, there is no consensus on the definition of frailty, although clinicians and researchers are generally in agreement about its usefulness as a clinical term. Nor are there standardized assessments of frailty. Some describe a person as frail if they show three or more of the following: weakness, slowness, low levels of physical activity, self-reported exhaustion and unintentional weight loss. A more quantitative approach attempts to capture the accumulation of deficits (including hearing loss, low mood and dementia) in a 'frailty index'^{9,10}.

Over the past three years or so, at least six major international societies have held meetings to try to encourage scientists and clinicians to reach a consensus on the definition of frailty¹¹. These have involved the International Association of Gerontology and Geriatrics and the International Academy of Nutrition and Aging, among others. Such efforts should be scaled up and accelerated with the leadership of a coordinating body such as the WHO, the US Food and Drug Administration (FDA) or the European Medicines Agency (EMA).

Improve animal models. There are many mouse models for type 2 diabetes, Alzheimer's disease, stroke, cardiovascular diseases, osteoarthritis and osteoporosis¹². However, to save costs and time, the desired pathology is generally induced when lab mice are 2 to 6 months old. (The average lifespan for the most commonly used lab mouse is 22 months.) Researchers might delete a key gene, for instance, or remove a particular organ (such as the ovaries) to induce a disease (such as osteoporosis). This means that the effects of cellular ageing on disease progression are rarely taken into account.

We urge investigators to develop mouse models in which diseases are induced in aged animals.

Some researchers have proposed models of multimorbidity that use certain strains in which the ageing process is accelerated. Mice that have had the DNA-damage-repair gene *Ercc1* deleted, for example, develop dysfunction in multiple tissues¹³. Again, we recommend that such phenotypes are induced in older mice.

So far, the few attempts that have been made to develop mice models for age-related multimorbidity have met many challenges; in some cases, genetic alterations expected to worsen conditions have improved them.

It could be that researchers need to delete multiple genes, with one gene — or several

genes — linked to each specific disease. Ultimately, other species, such as dogs or baboons, might provide better models for multimorbidity.

Even if the creation of mouse models for age-related multimorbidity proves too difficult, mice could still be used in initial testing, to confirm how a candidate geroprotector works, to observe the effect of a drug on tissue dysfunction and to study individual diseases in isolation.

It might be easier, however, to establish good mouse models of frailty.

The application of a frailty-assessment tool that considers 31 parameters, from grip strength to body weight (but not cognition) showed in 2014 that C57BL/6J mice develop mild frailty with age¹⁴.

To develop models of more severe frailty, we recommend that, just as with morbidity, researchers characterize transgenic mouse models of premature ageing. As well as strains in which *Ercc1* is deleted, investigators could study mouse models of genetic disorders that result in premature ageing, such as for Werner syndrome or Hutchinson–Gilford syndrome, but induce the gene deletion in animals that are older than 12 months. We also urge investigators to characterize models in which the fundamental mechanisms of ageing, such as inflammation or telomere maintenance, are disrupted. Certain telomerase-knockout mice that have critically short telomeres, for instance, develop multiple deficits by the time the mice reach 6–12 months old.

In all such efforts, we encourage researchers to try to assess frailty in response to clinically relevant stressors, such as immobilization, surgery or the administration of chemotherapy or radiotherapy.

Agree on desired metrics. Assessing geroprotectors in preclinical trials and in the clinic requires that investigators establish which attributes to measure in model organisms and in patients.

We recommend that investigators focus

first on how to assess drugs' effects on frailty, which will enable the design of clinical trials that are short and cost-effective. We also urge researchers to prioritize measurements that signal a tangible benefit for patients, because this will facilitate the regulatory approval required to test geroprotectors in the clinic. For example, measuring a person's ability to walk for 400 metres is preferable to measuring muscle mass because it improves her or his ability to live independently. Researchers should then identify the best correlates for these measurements in their study organisms.

Various tools provide a starting point for monitoring resilience in frail elderly people. These include qualitative assessments obtained by asking individuals about their levels of fatigue, pain, weight loss and so on, or tests that monitor mobility such as gait speed or how long it takes a person to stand up and walk a certain distance. Regulatory authorities are especially likely to accept 'improvement in mobility' as a target. Mobility is a good predictor of disability, time spent in hospital, mortality and health-care expenditure¹⁵. It is easy to measure and its relationship to clinically meaningful change is well understood.

We also advocate the development of better metrics of frailty in animals. Measurements that capture the health of the cardiovascular, cognitive, metabolic, neuromuscular and musculoskeletal, and immunological systems should be made, along with other assessments of weight loss, responses to stressors and endurance, for example. Genomics and proteomics could be used to identify biomarkers for monitoring the early effects of interventions.

All these advances will require infrastructures that enable scientists to work collaboratively using standardized methodologies. An example of the kind of thing that's needed is INFRAFRONTIER, an EU-funded research network of interconnected mouse clinics that has been developed over

the past ten years for those working on mouse genomes.

IMMEDIATE ACTION

Proof-of-concept clinical studies could demonstrate the value of geroprotectors as boosters of resilience in frail patients within the next decade. In fact, we ask industry, academic scientists and regulatory bodies, such as the FDA and EMA, to work together to pursue preclinical testing and clinical trials in frail patients with conditions such as chronic obstructive pulmonary disease, hip fractures and cancer immediately — even before standardized definitions of frailty and multimorbidity are thrashed out.

Instead of waiting ten years or so for multiple diseases to develop, researchers (using metrics such as mobility and time in hospital) might be able to demonstrate an effect within a few weeks. If successful, such studies could catalyse efforts to advance definitions, animal models and the characterization of measurable outcomes against which to test the drugs.

Many factors have stopped discoveries about geroprotectors from changing patients' lives. These include: the need for many stakeholders to work together; industry's tendency to focus on the short term; and the way researchers' performance is evaluated (numbers of papers published carries more weight than time spent helping the community establish definitions, for instance). With an ever-increasing ageing population, and the social and health-care systems of many nations close to crisis point, we must take a different approach. ■

Ilaria Bellantuono is a professor at the MRC–Arthritis Research UK Centre for Integrated research into Musculoskeletal Ageing, University of Sheffield, UK.
e-mail: i.bellantuono@shef.ac.uk

1. Mannick, J. B. *et al. Sci. Transl. Med.* **6**, 268ra179 (2014).
2. Figueira, I. *et al. Mech. Ageing Dev.* **160**, 69–92 (2016).
3. Melis, R., Marengoni, A., Angleman, S. & Fratiglioni, L. *PLoS ONE* **9**, e103120 (2014).
4. Clegg, A., Young, J., Iliffe, S., Olde Rikkert, M. & Rockwood, K. *Lancet* **381**, 752–762 (2013).
5. Maher, R. L., Hanlon, J. & Hajjar, E. R. *Expert Opin. Drug Saf.* **13**, 57–65 (2014).
6. Zhu, Y. *et al. Aging Cell* **14**, 644–658 (2015).
7. Jeon, O. H. *et al. Nature Med.* **23**, 775–781 (2017).
8. Farr, J. N. *et al. Nature Med.* **23**, 1072–1079 (2017).
9. Mitnitski, A. B., Mogilner, A. J. & Rockwood, K. *ScientificWorldJ.* **1**, 323–336 (2001).
10. Fried, L. P. *et al. J. Gerontol. A Biol. Sci. Med. Sci.* **56**, M146–M156 (2001).
11. Morley, J. E. *et al. J. Am. Med. Dir. Assoc.* **14**, 392–397 (2013).
12. Drechsler, S. *et al. Mech. Ageing Dev.* **160**, 54–68 (2016).
13. Weeda, G. *et al. Curr. Biol.* **7**, 427–439 (1997).
14. Whitehead, J. C. *et al. J. Gerontol. A Biol. Sci. Med. Sci.* **69**, 621–632 (2014).
15. Cummings, S. R., Studenski, S. & Ferrucci, L. *J. Am. Med. Assoc.* **311**, 2061–2062 (2014).

A full list of co-signatories accompanies this article online (see go.nature.com/2bkouvk).



Children visit a resident of a Japanese nursing home.



VALERIE KUYPERS/EPA/REX/SHUTTERSTOCK

A 1.8-million-year-old skull discovered in Dmanisi, Georgia, is one of the oldest hominin fossils found outside Africa.

PALAEOANTHROPOLOGY

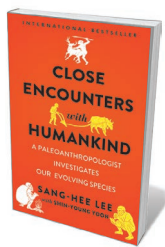
Back to the present

María Martín-Torres weighs up an original study on human origins and evolution.

Many people assume that palaeo-anthropology deals only with the past. The thinking goes that, beyond a curious, somehow romantic interest in the early accounts of our ancestors, there is not much that this discipline can add to the understanding of present-day humans. South Korean palaeoanthropologist Sang-Hee Lee disputes that view in *Close Encounters with Humankind*. She shows us to ourselves as the living (and, importantly, still changing) outcome of a wonderful interplay between biology and natural selection over the roughly 6 million years since hominins diverged from the chimpanzee lineage.

Avoiding the usual narrative, from bipedal ape-like creature to complex behaviour, Lee offers an original journey along our singular evolutionary path. When did our ancestors lose their fur? Did the taste for meat change our destiny? Was farming a blessing or a curse? Is altruism unique to us? Succinctly and engagingly, Lee revisits these and other key questions about the story of our evolving species — and gives some unconventional answers.

Notably, she supports multiregionalism. This is the theory that modern humans originated in many places simultaneously, in contrast to the 'out of Africa' model that posits a single origin for our species. Thus, she counters the sometimes rigid interpretations of the fossil record propounded in a literature dominated by the English language and the Western scientific community. In her book, Asia makes a comeback as a birthplace of modern humans and their ancestors. Lee reminds us that the Dmanisi hominin fossils from the republic of Georgia are as old as the earliest *Homo* fossils found in Africa; and that *Homo erectus* might have originated in Asia and migrated "back into Africa" to give



Close Encounters with Humankind: A Paleoanthropologist Investigates Our Evolving Species
SANG-HEE LEE
W. W. Norton: 2018.

rise to later *Homo* species. She also discusses the Denisovans, the mysterious hominins that coexisted with modern humans and left behind extensive DNA, but few fossils. She refers to them as "Asian Neanderthals" to highlight how the reconstruction of European hominins' evolutionary story should not be disconnected from that of their Asian cousins.

Not everything in *Close Encounters with Humankind* is about the past. Are humans still evolving? It's commonly thought that our interaction with the world through culture and technology (such as clothes, tools or medicines) has buffered the pressure on our bodies to adapt biologically to the environment. Lee challenges this view and traces a cascade of other evidence for ongoing human evolution. She points to studies on skin colour as evidence.

Dark skin is thought to have evolved in the first furless hominins in Africa, to protect against the ultraviolet radiation in intense direct sunlight. Hominins living in higher latitudes, went this line of reasoning, would be exposed to less UV radiation,

and so would need less-active melanocytes (the cells that produce the pigment melanin). That might largely explain the lighter skin of populations in regions farther from the Equator. However, studies by geneticist Iain Mathieson, now at the University of Pennsylvania in Philadelphia, and his colleagues on a large ancient-DNA sample from western Eurasian populations revealed that the light skin of Europeans is due to a new gene variant that emerged no more than 4,000 years ago (I. Mathieson *et al. Nature* 528, 499–503; 2015). They link these populations' lighter skin to the rise of agriculture and sedentary communal lifestyles, a view Lee favours.

As she shows, the shift to agriculture led to a diet based on processed grains and starches, which is deficient in many nutrients, including vitamin D. This deficiency forces the body itself to synthesize the vitamin — a metabolic process requiring the absorption of UV through the skin. The mutation for paler skin in Europeans pinpointed by Mathieson would maximize the UV absorption in populations facing low vitamin D intake. With this example, Lee emphasizes how culture — in this case, agriculture and a change in diet — might even have accelerated evolution.

Farming also led to a population explosion, despite increased vulnerability to infectious disease in settled communities. The availability of cereals allowed earlier weaning of infants, and meant women could give birth at shorter intervals. The resulting population increase brought higher genetic diversity, “the raw material of evolution”. Another demonstration of how our biology is still subject to change is the lactase mutation that has allowed some humans over at least the past 5,000 years to digest milk into adulthood. This eccentricity, less common in East Asia (predominantly China), became a key advantage for pastoralists and might represent an additional mechanism for overcoming the scarcity of vitamin D, because cow's milk is rich in the nutrient.

Moreover, living in communities is central to our species' success. As Lee notes, large groups became essential to survival because they offer assistance, to offset the difficulties of giving birth to big-brained babies and caring for them through a long infancy. Modern humans are also the longest-living primate species: three generations can overlap in time. Individuals stay ‘useful’ beyond their reproductive period by taking care of their children's offspring and even unrelated infants. As Lee states, the concept of

“European hominins’ evolutionary story should not be disconnected from that of their Asian cousins.”



The site near Beijing where the 750,000-year-old ‘Peking Man’ *Homo erectus* fossils were found.

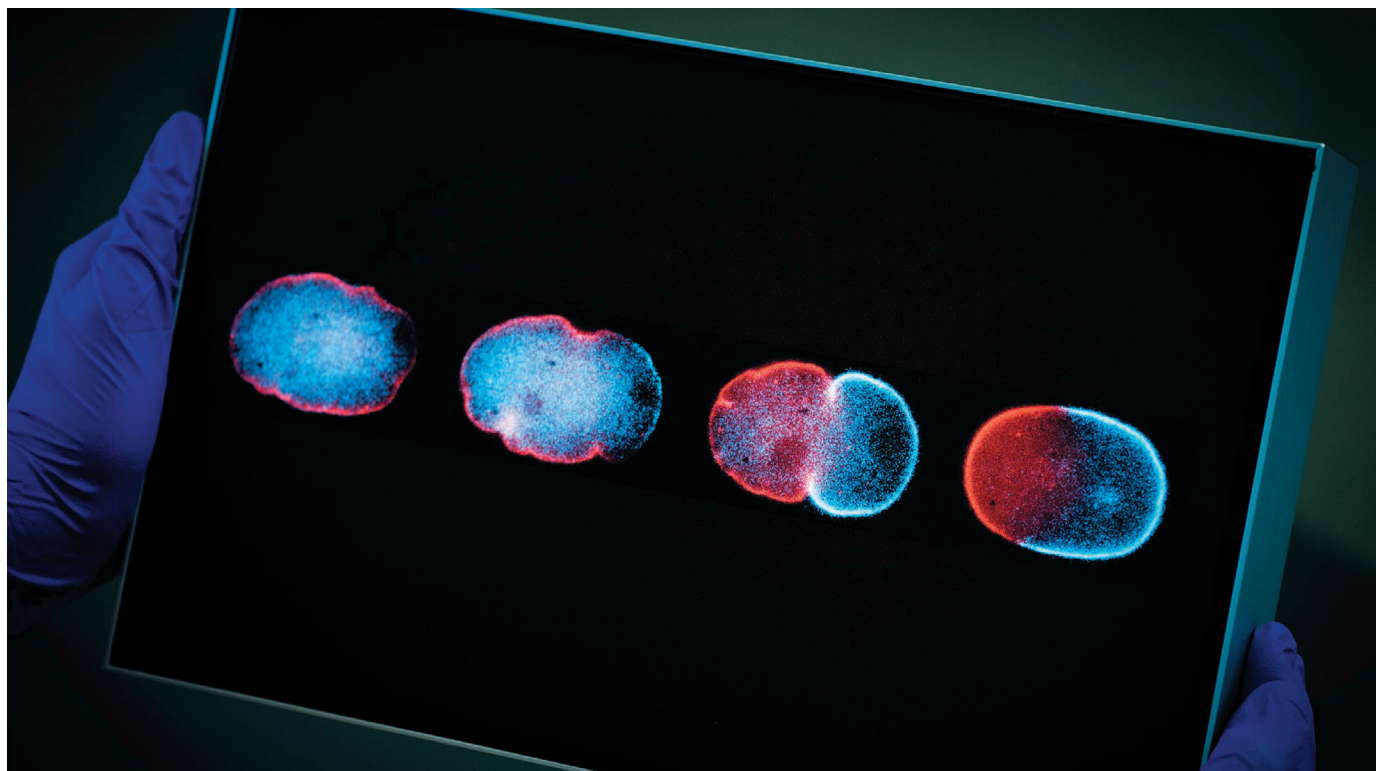
“fictive kin” (close bonds with those outside family or marriage) is unique to humans. She notes the remains of an elderly hominin in Dmanisi, dated to 1.8 million years ago, that evidently survived for some time without teeth, at a time without sophisticated tools or the knowledge of how to control fire. That could indicate that the hominin was treated with compassion by the group: the fossil could be the earliest evidence of human altruistic behaviour.

Lee's style is breezy. A chapter entitled ‘King Kong’ discusses *Gigantopithecus*, the puzzling gigantic ape found in China that might have coexisted with *Homo erectus* from 1.2 million to 300,000 years ago. ‘Breaking Back’ looks at back pain as a trade-off of bipedalism. That accessibility sometimes risks over-simplifying, and occasionally strays into territory where

every trait seems to have a function or to have evolved for a use.

Yet, ultimately, Lee will inspire even experts with her efforts at elucidating a field often seen as arid and inscrutable. *Close Encounters with Humankind* emphasizes how much the past matters. Our 6-million-year story has been massively shaped by chance and a changing environment. Lee shows that, now more than ever, our decisions can shape the future of Earth and its inhabitants, including ourselves. ■

María Martín-Torres is a palaeoanthropologist, director of the National Research Centre on Human Evolution (CENIEH) in Burgos, Spain, and an honorary reader at University College London.
e-mail: maria.martinon@cenieh.es



FIONA HANSON

Lightbox images showing the development of a nematode worm (*Caenorhabditis elegans*), one of the complex cellular systems studied at the Crick Institute.

ARTS

The quest for order

Philip Ball tours a cross-disciplinary exhibition exploring patterns in bioscience.

In 2016, a steel-and-glass spaceship landed next to St Pancras railway station, London's gateway to Europe. From the start, the biomedical powerhouse that is the Francis Crick Institute set out to put its stamp on a district already home to University College London, the Wellcome Trust and *Nature*. But how to carve out a cultural niche in an area buzzing with scientific and artistic activity?

Deconstructing Patterns is part of that endeavour. This collaboration between the Crick's scientists, established artists and young people from a community arts programme has created works inspired by what's going on in the institute's labs. As curator Bryony Bengel-Abbott told me, the theme of patterns was chosen because a quest for order and regularity underlies the Crick's research into various extremely complex systems. These range from genome-sequence analysis to *Drosophila* neurology and the development of the nematode worm *Caenorhabditis elegans*.

It's not clear how much of that comes across in the exhibits. A discussion of, say, the role of transcription factors or forces

in myosin-actin networks in guiding development presents a communication challenge, no matter how beautifully illustrated with micrographs of stained cells. But the displays' pedagogical ambitions are also undermined for the right reason: artists have other agendas. However laudable the efforts to suggest that artists and scientists share a goal of making sense of life's complexity, this exhibition reveals that they ask different questions and find different answers.

This is most evident in the collaboration between the *C. elegans* team in the Polarity and Patterning Networks Laboratory, led by Nate Goehring, and young filmmakers from the 1A Arts project. This partnership began last year with a one-day workshop in which the scientists shared their work with a group of teenagers aged 14 to 17, some without a science background. "Our aim was to get them thinking about how animals develop, and expose them to some key concepts," says Goehring. "That is, symmetry and asymmetry, the importance of breaking symmetry to

Deconstructing Patterns

Francis Crick Institute, London.
Until 1 December.

generate different types of cell and specifying geometric axes, the need to assign different cell identities, and how simple spatial rules can give rise to complex form." The researchers devised exercises using building blocks connected in different ways to illustrate how morphology and symmetry can arise from local, algorithmic rules.

What the 1A Arts team came up with was quite different: a short, metaphorical narrative film about the transformative experience of an office worker caught in a repetitive regime. Despite the absence of explicit scientific content, Goehring was pleased with the result. "It was great to see them take advantage of their artistic freedom to come up with something entirely their own," he says, adding that the young people nevertheless "clearly internalized the core concepts — the importance of disrupting uniformity, defining identity, rules". In that regard, he says that he sees aspects of the principles of developmental morphology reflected in the film.

Deconstructing Patterns showcases two other collaborations. In the more evocative of these, Australian artist Helen Pynor — a

biology graduate whose work explores, often viscerally, themes relating to living matter such as human organs — filmed Crick researcher Iris Salecker describing the development of the *Drosophila* neural circuitry for vision. Only Salecker's hands and arms are visible, and there is no soundtrack to explain what we're seeing. This silent, manual choreography is mesmerizingly beautiful. It also captures the eloquence and sophistication of the unconscious gesture — and the limitations of language alone for expressing scientific ideas.

"The scientific story is about the movement of things in space, and hard to convey in words," says Pynor. Salecker's use of body and gesture, Pynor adds, "fills in some of the gaps, even metaphorically, between verbal language and spatial meaning". Viewers learn nothing about fruit-fly vision from this film, but they do learn a great deal about the roles of spatial conceptualization and the sense of dynamic process involved in thinking about this complicated system.

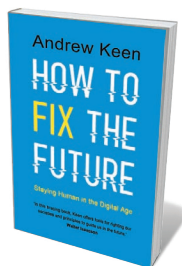
As Pynor notes, science does not take place in some abstracted universe where the observers have a disinterested distance from their subject. Instead, as she puts it, "the love of scientists for their subject, the presence of their own bodies in dialogue with the bodies they study, and ... their aesthetic sensitivity, are all layered into their research". Salecker, meanwhile, says the film revealed that her team's research is "in essence a 3D dynamic structural problem, and that we are limited by our imagery and language. This insight will influence how we present data in the future."

The exhibition also brought together award-winning poet Sarah Howe, sound artist Chu-Li Shewring and Greg Elgar, former head of the Crick's Advanced Sequencing team. The team's quest to "find meaning in noise" had an obvious appeal to Shewring. Her installation allows viewers to experience a sound composition within acoustic "hoods" that are suspended from the ceiling; included is a reading of Howe's poem 'A New Music', inspired by conversations with Elgar.

"Alphabet of us, cipher deciding the exact moment genes flip on and where", Howe's poem begins. The words, fugitive in Shewring's soundscape, suggest that representations of the genome are moving beyond the static, deterministic metaphors of a 'book of life'. Shewring was keen to keep interpretation open and uncertain, aptly reflecting the dance between prescriptiveness and contingency in the dynamic unfolding of genetic information. As a first step towards a more sophisticated public image of the genome, I'll settle for that. ■

Philip Ball is a writer in London, and author of *Patterns* in *Nature*.
e-mail: p.ball@btinternet.com

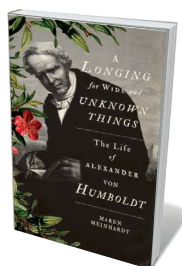
Books in brief



How to Fix the Future

Andrew Keen ATLANTIC (2018)

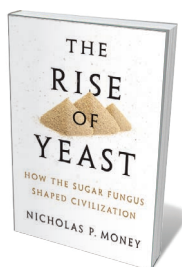
Silicon Valley insider Andrew Keen has long been calling out the "disturbingly centralized, unequal, and creepy" aspects of the digital revolution. In this acerbic, articulate global survey of human-centred solutions, he examines best practice in consumer choice, education, innovation, regulation and social responsibility. His journey takes in digital investor John Borthwick's call for antitrust regulation and "human-centric design"; lessons from China, Estonia and Singapore in how, or how not, to digitize; and distinct signs of cognitive clarity in no-tech schooling. An invigorating mix of principle and vision.



A Longing for Wide and Unknown Things

Maren Meinhardt HURST (2018)

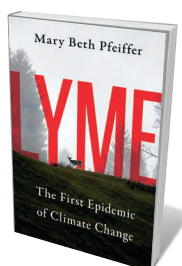
The heroic narrative is a poor fit for Alexander von Humboldt (1769–1859), argues Maren Meinhardt in her subtle biography. An editor at *The Times Literary Supplement*, Meinhardt paints the polymath as a creature of "contradictions and ambiguous achievements" firmly rooted in German Romanticism. Ever striving for the top, whether climbing Ecuador's Chimborazo mountain or writing *Cosmos* (1845), he often found his reach exceeding his grasp; even his personal life seems oddly indeterminate. An intriguing companion read to Andrea Wolf's *Invention of Nature* (Knopf, 2015; see *Nature* **525**, 31; 2015).



The Rise of Yeast

Nicholas P. Money OXFORD UNIVERSITY PRESS (2018)

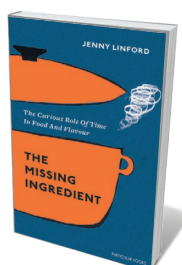
Yeasts are firmly embedded in the substrate of human culture. The sugar fungus *Saccharomyces cerevisiae* is, of course, central to the making of wine, beer, bread and biofuels; and other members of this unicellular eukaryotic clan are used as 'lab rats' in molecular genetics, or help produce drugs such as the antimalarial artemisinin. They're all over (and inside) us, too. Botanist Nicholas Money's effervescent tour is packed with delights, such as illustrations by Charles Tulasne, the "Audubon of fungi", or the revelation that yeasts and humans share a common ancestor (and hundreds of genes).



Lyme: The First Epidemic of Climate Change

Mary Beth Pfeiffer ISLAND (2018)

"This is an illness that has been minimized, underestimated, and politicized." Thus says investigative reporter Mary Beth Pfeiffer on Lyme, the tick-borne disease now on the march in North America, Europe and Asia. As Pfeiffer's hard-hitting study reminds us, non-specific symptoms and other complexities make tackling Lyme a formidable challenge (see also J. G. Logan *Nature* **552**, 174; 2017). She nimbly interweaves numerous strands of research — into the influence of climate change on the Lyme invasion, the disease, the pathogen, the vectors and the harrowing impacts borne by some sufferers.



The Missing Ingredient

Jenny Linford PARTICULAR (2018)

Time is the key ingredient in the culinary lab, argues Jenny Linford, cleverly reframing every step of the 'food chain' as poised on the clock's tick. From this perspective, we see classic veal stock as a 24-hour marathon, perfectly roasted coffee as a 4-minute drama and exquisitely fresh, consummately cooked sole as a mad sprint from boat to plate. Linford hardly draws breath as she zips from the time it takes for grated wasabi to develop its piquant kick (5 minutes) to the moment sauerkraut reaches peak fermentation. **Barbara Kiser**

Correspondence

Don't let triage put a gloss on extinctions

Conservation triage, the prioritization of conservation efforts by explicit economic accounting, may not be used to determine listing decisions under the US Endangered Species Act of 1973. This could change with the proposed US H.R.717 Listing Reform Act that has been submitted to Congress (see also go.nature.com/2e6s8fo and go.nature.com/2bftgd4).

The bill proposes to “preclude the listing of a species as threatened due to the likelihood of significant, cumulative economic effects that would result from such listing or from the likely resulting designation of critical habitat of the species”. Economic effects include those relating to public and private lands, property values, the provision of public services, employment and revenues available for governments. This triage process would effectively legitimize species extinctions by ruling out conservation programmes that conflict with economic interests.

Conservation triage puts a mathematical gloss on extinctions, presenting them as neutral outputs of optimization algorithms and branding itself as effective science that is based on data and not dogma. It is crucial to oppose the ‘new conservation’ paradigm: it is performing a conceptual triage on conservation itself.

Guillaume Chapron *Swedish University of Agricultural Sciences, Uppsala, Sweden.*

Yaffa Epstein *Uppsala University, Sweden.*

José Vicente López-Bao *Oviedo University, Spain.*
guillaume.chapron@slu.se

Pakistan heading for groundwater crisis

The United States, China, India, Iran and Pakistan together account for more than 60% of

the groundwater that is removed worldwide each year. Pakistan alone withdraws 6.6%, amounting to 65 cubic kilometres annually — 10 km³ more than is replaced each year by natural processes.

Pakistan, as a leading exporter of water-intensive crops such as rice, uses more global groundwater (29%, based on 2010 estimates) for agricultural exports than any other country (C. Dalin *et al. Nature* **543**, 700–704; 2017). It recycles just 1.2% of its urban wastewater, whereas China and India reuse 71% and 22% of theirs, respectively (A. L. Thebo *et al. Environ. Res. Lett.* **12**, 074008; 2017). Wastewater that is dumped into natural streams or used in irrigation ultimately finds its way into groundwater.

To improve management of Pakistan's groundwater and avert a crisis, research is urgently needed into the impact of these practices on the quality and quantity of groundwater.

Muhammad Arif Watto,
Safdar Bashir, **Nabeel Khan Niazi** *University of Agriculture Faisalabad, Pakistan.*
arifwatto@yahoo.com

Add societal impact to the syllabus

We agree that societal impact should be rated more highly in scientific publishing and research evaluation (*Nature* **553**, 5; 2018). To this end, we suggest that ways to achieve it should be introduced as an important component of curricula at higher-education institutions.

Degree theses and university classes in academic publishing are generally structured with bibliometric output in mind because that is the main driver of tenure and promotion. They rarely touch on the merits of societal impact. This monotheistic evaluation of academic pursuits means that few faculty members make time for public outreach. Even new journals for applied

excellence address a symptom of insufficient societal impact in research, not the cause.

Instead of relying solely on papers and citations as proxies for impact, funders and research organizations need to broaden their assessments of scientific output. They should also acknowledge other important outputs, such as developments in scientific products and services, important data sets, platforms and software, as well as their influence on policy.

Sascha Friesike *Vrije Universiteit Amsterdam, the Netherlands.*

Benedikt Fecher *Alexander von Humboldt Institute for Internet and Society, Berlin, Germany.*

Gert G. Wagner *Max Planck Institute for Human Development, Berlin, Germany.*
fecher@hiig.de

Maximize impact of Earth observations

To address challenges such as climate change, disaster resilience and the security of water and food, it is crucial for countries, organizations and individuals to work together to coordinate Earth observations. They need to ensure that these are sustained, and share data to inform decision-making (see, for example, G. Huadong *Nature* **554**, 25–27; 2018). As secretariat director of the Group on Earth Observations (GEO), I can vouch for the group's progress in realizing the global Earth observatory envisaged by Markku Kulmala (see *Nature* **553**, 21–23; 2018).

Over the past decade, the GEO community of 105 national governments and 118 partners has been building the Global Earth Observation System of Systems (GEOSS). Collaboration on more than 70 targeted activities is under way in the GEO programme (see go.nature.com/2nvvgo6). This coordinates and integrates observations from space-based and *in situ* platforms, fills data gaps, and increases capacity across a range

of geographical, thematic and cross-cutting areas (including several that Kulmala mentions). GEOSS has already brokered more than 400 million open-data and information resources from some 5,000 providers (www.geoportal.org).

We welcome extra partners from countries, international organizations, research institutes, academia and the private sector to join us in this endeavour and in helping to fulfil the actions and resources for which Kulmala calls.
Barbara J. Ryan *Group on Earth Observations (GEO), Geneva, Switzerland.*
bryan@geosec.org

Japanese photo of Rosalind Franklin

I happened upon a snapshot of Rosalind Franklin — whose landmark papers in *Nature* contributed to the unravelling of DNA's structure in 1953 — in a Japanese journal of carbon science (see S. Sonoda *Tanso* **3**, 133–136; 1953). It seems fitting to have rediscovered it this year, which marks 60 years since Franklin's death at the age of 37.

Franklin's earlier work on the structure of graphite was known worldwide in the carbon field (for a review, see P. J. F. Harris *Interdiscip. Sci. Rev.* **26**, 204–210 2001). Japanese carbon researcher Susumu Sonoda visited her in London in 1953, after she had completed her two-year study of DNA at King's College London and had moved on to investigate tobacco mosaic virus at Birkbeck College, London. He was travelling around Europe and the United States to interact and exchange ideas with fellow carbon researchers.

Sonoda discussed the problems of carbon graphitization with Franklin. With her permission, he then took a photo (see go.nature.com/2eeg2tx) to illustrate his report for *Tanso*.

Yoshihiko Watanabe *Kyoto, Japan.*
watanabe_yosh@yahoo.co.jp

SPACE PHYSICS

The origin of pulsating auroras

Spectacular light shows in Earth's atmosphere called pulsating auroras are directly linked to processes in space. After decades of research, the full chain of events that creates such auroras has been observed. [SEE LETTER P.337](#)

ALLISON N. JAYNES

The Northern and Southern lights, also known as auroras, are as varied as the colours they display in the night sky. Discrete auroras are the kind that typically grace our desktops and calendar covers, and that are produced a few thousand kilometres above Earth's surface. By contrast, pulsating auroras that are created tens of thousands of kilometres away, in the equatorial region of the magnetosphere — the area around Earth that is dominated by the planet's magnetic field. For decades, it has been suggested that pulsating auroras are the result of interactions between magnetospheric electrons and electromagnetic waves called chorus waves that send electrons careering towards Earth's atmosphere along magnetic-field lines^{1–3}. On page 337, Kasahara *et al.*⁴ report direct evidence for this process using observations both from Earth's surface and from a spacecraft positioned on a field line.

Because magnetic fields are invisible to the human eye, the prediction of where a field line hits Earth and where that same field line exists out in space — a task known as magnetic-field-line mapping — is extremely difficult⁵. Luckily, electrons that move around Earth tend to follow these field lines closely. When these particles interact with chorus waves, they can be directed into a region of the upper atmosphere called the ionosphere, where they often generate auroral light. This allows us instantly to see the footprint of the associated field lines.

In addition, if we have an observation platform at a precise location out in space, we can detect the chorus waves that caused the electrons to head towards the atmosphere and see fluctuations in the electron population that arise from the oscillation of the waves. The trick is to get the ground-based and space-based observations to line up at the right time and place, and to have instruments sensitive enough to view both processes simultaneously. This feat has eluded observers ever since the theory of pulsating-aurora generation was developed^{6,7}.

The first challenge is to have an instrument capable of making the *in situ* measurement of electrons in space at the required resolution. The Arase spacecraft⁸, launched by the Japan Aerospace Exploration Agency in late 2016,

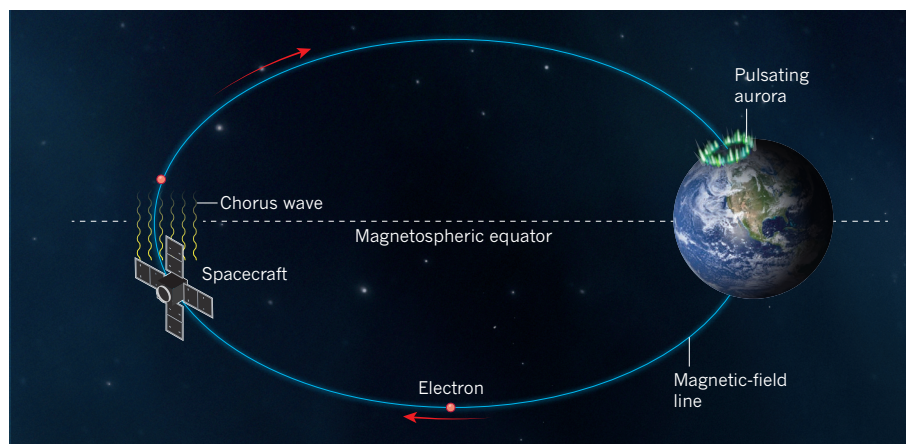


Figure 1 | Pulsating-aurora generation. Kasahara *et al.*⁴ report evidence for a mechanism that explains the occurrence of blinking patches of light in Earth's atmosphere called pulsating auroras. In a region surrounding Earth known as the magnetosphere, electrons are trapped by the planet's magnetic field and travel (red arrows) along magnetic-field lines. When these particles interact with electromagnetic waves called chorus waves, which are generated in the equatorial region of the magnetosphere, they can be directed towards Earth's atmosphere, where they produce auroral light. The authors detected the interactions between the chorus waves and the electrons using the Arase spacecraft⁸, which was positioned on the relevant field line.

carries just such an electron detector, which was designed to observe electrons within a narrow window around a magnetic-field line. The spacecraft is also equipped with instruments to detect chorus waves. Kasahara and colleagues analysed data from the spacecraft to uncover fluctuations in the electron population and the associated chorus waves.

The next obstacle was to determine where the field line threading the position of the spacecraft would hit the ground. Magnetic-field models are now sophisticated enough to be able to inform researchers of the approximate location of a field-line footprint in Earth's atmosphere, generally with higher accuracy when the level of geomagnetic activity (magnetic storms) is low. In the vicinity of this footprint, Kasahara *et al.* looked for a corresponding pulsating-aurora signal — namely, variations in auroral-light intensity that matched the fluctuations in the electron population. They identified such a signal in measurements from an all-sky imager based in central Canada⁹, which essentially records black-and-white video of the hemispherical view of the sky above (see Figure 2 of the paper⁴).

Thanks to Kasahara and colleagues, we can

see the complete process of pulsating-aurora generation for the first time: the fluctuations in an electron population out in space; the chorus waves responsible for these fluctuations; and the variations in auroral-light intensity from the ground (Fig. 1). The last part is somewhat analogous to watching an image on an old-fashioned television, where the ionosphere is the 'screen' onto which electrons are projected. Despite this simple picture, researchers are aware that the ionosphere probably changes the incoming signal — a detail that will no doubt be scrutinized in future studies.

Kasahara *et al.* carried out an analysis in which they correlated the electron fluctuations and chorus waves in space with the pulsating-aurora signals seen by the all-sky imager on the ground. This step revealed the precise location in the atmosphere in which the field-line footprint resides. Such a technique has incredible potential to test and refine our current magnetic-field models by comparing the modelled footprint location to the observed location. In the future, magnetic-field-line mapping might well rely on a similar methodology to gain insight into magnetic topology — the structure and linkage of field lines.

There is one caveat, however: clear skies are required to see and measure the pulsating-aurora signals, so Earth's terrestrial weather needs to cooperate. Furthermore, the chorus waves contain components of different frequency that interact with magnetospheric electrons in different ways depending on the energy of the particles. This affects which particles end up travelling down to Earth's atmosphere. These details are directly related to geomagnetic activity and have not yet been

fully quantified. There is still a rich body of research to be carried out regarding the mysterious pulsating auroras. ■

Allison N. Jaynes is in the Department of Physics and Astronomy, University of Iowa, Iowa City, Iowa 52242, USA.
e-mail: allison-n-jaynes@uiowa.edu

1. McEwen, D. J., Yee, E., Whalen, B. A. & Yau, A. W. *Can. J. Phys.* **59**, 1106–1115 (1981).
2. Nishimura, Y. *et al. J. Geophys. Res. Space Phys.*

116, A11221 (2011).

3. Jaynes, A. N. *et al. J. Geophys. Res. Space Phys.* **118**, 4884–4894 (2013).
4. Kasahara, S. *et al. Nature* **554**, 337–340 (2018).
5. Pulkkinen, T. I. & Tsyganenko, N. A. *J. Geophys. Res.* **101**, 27431–27442 (1996).
6. Coroniti, F. V. & Kennel, C. F. *J. Geophys. Res.* **75**, 1279–1289 (1970).
7. Davidson, G. T. *J. Geophys. Res.* **84**, 6517–6523 (1979).
8. Miyoshi, Y. *et al. J. Phys. Conf. Ser.* **869**, 012095 (2017).
9. Mende, S. *et al. Space Sci. Rev.* **141**, 357–387 (2008).

ANIMAL BEHAVIOUR

Brainpower boost for birds in large groups

Whether intelligence is selected for in species that have a complex social life is debated and hard to test. Cognitive performance and associated reproductive success are now linked to group size in wild magpies. [SEE LETTER P.364](#)

ANDREW WHITEN

Observations of primates' everyday lives led the psychologist Nicholas Humphrey to make a revolutionary proposal¹ in 1976 to explain primate intelligence. Before then, it had been commonly assumed that these animals' cleverness was an adaptation to their physical niches, reflected in their need for sophisticated skills in realms such as foraging, navigation or avoiding predators. Humphrey suggested instead that the complex social dynamics experienced when such animals live in a group become the main selective force driving the evolution of primate intelligence. On page 364, Ashton *et al.*² offer support for Humphrey's social-intelligence hypothesis, in a study of wild Australian magpies (*Cracticus tibicen dorsalis*, also known as *Gymnorhina tibicen dorsalis*).

The causal relationships between social complexity, intelligence and reproductive success proposed by Humphrey inspired a generation of primatologists, who uncovered unexpected sophistication in monkeys' and apes' social knowledge and political manoeuvrings^{3–5}. However, these discoveries arguably made it difficult to test Humphrey's hypothesis directly, because intelligence — both in social interactions and in non-social realms, such as foraging or tool use — and social complexity were revealed to be composed of many components^{4,5}. Primate social complexity, like intelligence itself, was found to be extraordinarily complex.

In 1995, primatologist Robin Dunbar suggested⁶ that focusing on the typical group size of a species as a proxy for social complexity, and on its brain size instead of intelligence,

might resolve the dilemma of how to test Humphrey's ideas. Both measurements were available for a range of primates — and, as predicted, a positive relationship was found between these factors. Multiple teams replicated the finding, using a range of related variables — for example, measuring the relative sizes of the neocortex region rather than overall brain size — for primates⁷ and other taxa⁸. Yet, as Ashton and colleagues acknowledge, analyses of large databases often provide conflicting results. When many variables differ between species, cross-species comparisons can lack robustness, because compensating for the differences can make a study so unwieldy that

it undermines reliable testing of a hypothesis⁹.

Ashton and colleagues turned instead to intraspecies comparisons. They studied 56 magpies, which were ringed to enable identification, from 14 different territorial groups that ranged in size from 3 to 12 birds (Fig. 1). Rather than measuring brain size, the authors conducted cognitive-performance tests in which the birds encountered wooden or plastic devices that tested problem-solving skills; successful birds received a mozzarella-cheese treat. Four different devices each tested a specific skill, including spatial memory and the ability to learn new associations between stimuli and rewards.

The authors report that group size is linked to cognitive performance. Birds living in a larger group displayed better performance at the population level on each of the tests than did birds living in smaller groups. At the individual level, exceptions to this trend could be found — some birds from smaller groups outperformed birds from larger groups, and vice versa.

The authors recorded the reproductive success of individuals by counting the average number of hatched clutches of eggs per year, and found that birds that performed well on the tests had greater reproductive success than



Figure 1 | Australian magpies in Guildford, Western Australia. Wild Australian magpies (*Cracticus tibicen dorsalis*, also known as *Gymnorhina tibicen dorsalis*) are territorial and live in groups. Ashton *et al.*² analysed the relationship between the birds' group size and cognitive performance to test the long-debated idea¹ that life in complex social groups can select for intelligence. At the population level, larger groups of birds performed better than smaller groups in cognitive-performance tests, and cognitive performance was also linked to reproductive success.

BEN ASHTON

birds that performed poorly. Evidence for a connection between test performance and biological fitness could not have been assessed by the earlier approaches based on interspecies comparisons.

For any given individual, the bird's performance on each of the four skill tests was correlated. A principal-components statistical analysis, which identifies the number of factors accounting for variance in an array of scores, showed that a single unknown factor accounted for 65% of the variance in test scores. The authors refer to this factor as 'general intelligence', analogous to the 'g factor' used to assess general intelligence in humans. However, it is worth noting that the magpie tests assess learning abilities rather than testing the capacity to invent creative solutions to problems — a talent sometimes considered to be a defining characteristic of animal or human intelligence.

Humphrey proposed that intelligence evolved in response to the pressures of social complexity. Ashton and colleagues, however, did not directly address this evolutionary hypothesis; instead, they investigated the relationship between social-group size and the development of cognition in the birds' early life, a linkage that was observed to emerge by the time the birds were 200 days old. Nevertheless, the link between cognitive prowess and fitness identified by Ashton and colleagues has major implications for connecting the social-intellect hypothesis to an underlying evolutionary mechanism, and it suggests that selection is acting on a relationship between sociality and cognition.

Group size is, of course, a crude index of social complexity, just as brain size is a crude indicator for the complexities of cognition being selected for. Indeed, group size itself cannot be the key causal factor — the immensity of a wildebeest herd, for example, is unlikely to select strongly for intellect. And even three individuals can suffice to create a high level of social complexity, as demonstrated in the humorous account provided by Jerome K. Jerome's 1889 book *Three Men in a Boat*, or documented in an analysis³ of three adult chimpanzees that repeatedly shifted alliances in a way that allowed each to be supreme for a while in their 'game of thrones'. Ashton and colleagues can only speculate on how magpies' cognitive powers relate to social-group size and number of offspring, and suggest that some kind of political skill, such as the ability to successfully handle or avoid conflicts, might be involved.

Which types of intelligence deserve closer attention in future studies of the social-intelligence hypothesis? Some substantially different ideas exist regarding which form of intelligence might be selected for⁴. One such contrast is between whether social complexity selects for overall intelligence across many different contexts (also known

as domain-general intelligence), or for specialized forms of intelligence, such as the social skill of understanding what others might be thinking. This might sound like a tall order for a magpie. But there is evidence¹⁰ for such sophisticated behaviour in the crow family — a western scrub-jay (*Aphelocoma californica*) might make a theft-prevention manoeuvre by relocating hidden food elsewhere if it spots that another bird observed where the food was hidden. Social cognition has numerous other manifestations^{11,12}. Yet, what Ashton *et al.*² tested was essentially non-social cognition. What now begs to be fleshed out is the nature of both the social and non-social intelligence skills that may have been at work in the phenomena these authors observed. ■

Andrew Whiten is in the Centre for Social Learning and Cognitive Evolution, School of Psychology and Neuroscience, University of St Andrews, St Andrews KY16 9JP, UK.

e-mail: a.whiten@st-andrews.ac.uk

1. Humphrey, N. K. in *Growing Points in Ethology* (eds Bateson, P. P. G. & Hinde, R. A.) 303–317 (Cambridge Univ. Press, 1976).
2. Ashton, B. J., Ridley, A. R., Edwards, E. K. & Thornton, A. *Nature* **554**, 364–367 (2018).
3. de Waal, F. B. M. *Chimpanzee Politics: Power and Sex Among Apes* (Cape, 1982).
4. Byrne, R. W. & Whiten, A. *Machiavellian Intelligence: Social Complexity and the Evolution of Intellect in Monkeys, Apes and Humans* (Oxford Univ. Press, 1988).
5. Seyfarth, R. M. & Cheney, D. L. *Anim. Behav.* **103**, 191–202 (2015).
6. Dunbar, R. I. M. *J. Hum. Evol.* **28**, 287–296 (1995).
7. Dunbar, R. I. M. & Shultz, S. *Science* **317**, 1344–1347 (2007).
8. Perez-Barberia, F. J., Shultz, S. & Dunbar, R. I. M. *Evolution* **61**, 2811–2821 (2007).
9. Powell, L. E., Isler, K. & Barton, R. A. *Proc. R. Soc. B* **284**, 20171765 (2017).
10. Clayton, N. S., Dally, J. M. & Emery, N. J. *Phil. Trans. R. Soc. B* **362**, 507–522 (2007).
11. Emery, N. J., Clayton, N. S. & Frith, C. D. *Phil. Trans. R. Soc. B* **362**, 485–488 (2007).
12. Whiten, A. & van de Waal, E. *Neurosci. Biobehav. Rev.* **82**, 58–75 (2017).

This article was published online on 7 February 2018.

NEUROSCIENCE

Burst firing sets the stage for depression

Salvos of neuronal activity in the brain's lateral habenula, regulated by astrocyte cells, drive depression-like behaviours in rodents. The finding might help us to understand one antidepressant and to develop more. [SEE ARTICLES P.317 & P.323](#)

WILLIAM M. HOWE & PAUL J. KENNY

Opposing forces shape our everyday lives — for instance, stimuli can encourage us to move or stop, and events can make us happy or sad. Accordingly, our brains are designed with 'yin-yang' systems that guide our actions and influence our feelings. Neurons in the brain's mesolimbic system promote reward-seeking behaviour and help to process information about actions that result in pleasurable outcomes^{1–3}. By contrast, neurons in the lateral habenula (LHb) encode information related to noxious outcomes and suppress reward-seeking^{4–6}. Unbalancing these opposing systems might therefore affect our behaviour. Indeed, emerging evidence⁷ suggests that LHb hyperactivity contributes to mood disorders such as major depression. Two papers^{8,9} in *Nature* now shed light on the mechanisms that underlie LHb hyperactivity, and on how the antidepressant drug ketamine modulates this state.

In the first paper, Yang and colleagues⁸ (page 317) assessed the firing activity of LHb neurons in two rat models of depression. Neuronal firing involves depolarization of the

electrical potential across the cell membrane (in a resting state, the inside of the cell is negatively charged relative to the extracellular space around it). Hyperpolarization, in which the cell interior becomes more negative than normal, is typically associated with neuronal inhibition.

By studying brain slices *ex vivo*, Yang and co-workers showed that LHb neurons were more likely to fire in a pattern of rapid bursts in the 'depressed' rats than in control animals. They also observed that, when the LHb neurons were hyperpolarized, this increased the likelihood that these cells would fire in bursts rather than steady volleys. The researchers went on to show that they could increase depression-like behaviours in rats using a genetic manipulation to drive hyperpolarization, and so burst firing, in LHb neurons.

Next, the group investigated the signals that regulate this burst firing. In other brain regions¹⁰, burst firing is controlled by N-methyl-D-aspartate receptors (NMDARs) — membrane-spanning channel proteins whose activation leads to an influx of positively charged calcium ions into neurons, resulting in depolarization and neuronal firing. Yang

and colleagues found that burst firing of LHB neurons required the activity of NMDARs and of another class of protein, T-type voltage-sensitive calcium channels (T-VSCCs).

Could inhibition of NMDARs prevent bursting? Ketamine is an NMDAR inhibitor and a promising, rapid-acting antidepressant in humans (taking effect in as little as 30 minutes)¹¹ that is currently in clinical trials for the treatment of major depressive disorder with imminent risk of suicide. The mechanisms by which ketamine acts have been a puzzle to scientists. Strikingly, Yang *et al.* found that local infusion of ketamine into the LHB elicited antidepressant-like responses in depression-prone rats. These findings suggest that the therapeutic actions of ketamine might relate, at least in part, to its ability to block burst firing in the LHB.

In the second paper, Cui *et al.*⁹ (page 323) turned their attention to the mechanisms by which LHB neurons become skewed to firing in burst mode during depression. The authors performed a large-scale analysis of differentially expressed proteins in the LHB. This revealed that the expression of Kir4.1, a component of potassium-ion (K^+) channels, was increased in the LHB of depression-prone rats compared with that of controls.

Kir4.1 is expressed in astrocytes, cells that interact with neurons to influence their activity state¹² (although the functional relevance of such interactions is still being defined). The researchers showed that overexpression of Kir4.1 in LHB astrocytes increased the burst firing of local neurons and precipitated depression-like behaviours in mice. Conversely, reducing Kir4.1 expression in depression-prone rats reduced the burst firing of LHB neurons, and attenuated the animals' depression-like behaviours.

How do Kir4.1-containing channels in astrocytes regulate the activity of neurons? Neurons can pump K^+ from their cytoplasm into the extracellular space to cause hyperpolarization. Cui *et al.* provide evidence that astrocytic K^+ channels in the LHB help to clear away extracellular K^+ . This facilitates the ability of LHB neurons to enter a hyperpolarized state, and hence to fire in bursts (Fig. 1). Future studies will be required to understand whether LHB astrocytes interact with neurons in other ways to influence their patterns of activity.

Together, these two papers provide crucial insights into a depression-associated pattern of cell firing in the LHB and its regulation by ketamine. However, exactly why burst firing of LHB neurons increases depression-like behaviours in rodents remains unclear. One potential explanation, put forward by Yang *et al.*, is the inhibitory influence that LHB neurons exert over reward-associated dopamine neurons in the mesolimbic system and mood-associated serotonin neurons in the midbrain. Perhaps burst firing of LHB neurons alters the activity of these downstream neurotransmitter systems in a manner that reduces their positive effects

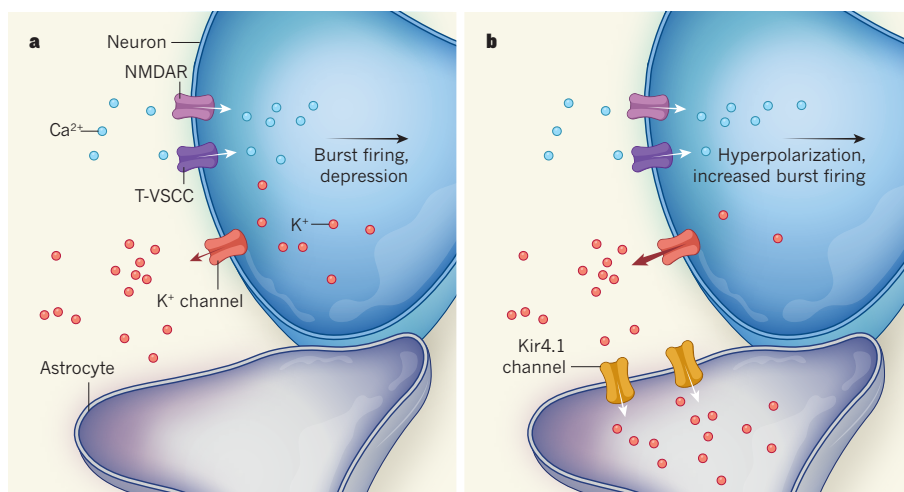


Figure 1 | Burst firing in depression. **a**, The activation of membrane-spanning N-methyl-D-aspartate receptors (NMDARs) leads to an influx of calcium ions (Ca^{2+}) that depolarizes neurons (the insides of which are negative relative to the outside in resting conditions), and causes firing. Ca^{2+} influx also leads to an efflux of potassium ions (K^+) through K^+ -channel proteins. Yang *et al.*⁸ show that, in the brain's lateral habenula (LHB), coordinated activity of NMDARs and T-type voltage-sensitive calcium channels (T-VSCCs) causes neuron firing to occur in a pattern of rapid bursts, and that such firing leads to depression-like symptoms in rats through unknown mechanisms. **b**, Cui *et al.*⁹ demonstrate that K^+ ions are rapidly cleared away by nearby cells called astrocytes, which express K^+ channels containing the protein Kir4.1. This facilitates rapid K^+ efflux from the neuron and its entry into a state of hyperpolarization, which increases the likelihood of burst firing⁸.

on mood, thereby increasing vulnerability to depression. Testing this possibility, and other potential mechanisms, will require further experimentation. The potential involvement of subpopulations of dopamine and serotonin neurons that encode aversion-relevant stimuli must also be considered¹³.

The current studies have several therapeutic implications. First, Cui and colleagues' data show that astrocytes might have a key role in regulating a brain system involved in mood and motivation. Previous studies linking astrocyte function to disease states have focused mostly on neurodegenerative and developmental disorders^{14,15}, but the current papers suggest that modulating the activity of these cells might be a way to treat psychiatric disorders.

Second, Yang *et al.* showed that a T-VSCC blocker delivered directly into the LHB had antidepressant-like effects, similar to those of ketamine. This raises the exciting possibility that T-VSCC blockers, or other compounds that suppress LHB burst firing, could be effective antidepressants.

Finally, the papers shed light on the possible mechanisms by which ketamine elicits rapid antidepressant effects in humans. Ketamine and its metabolites stimulate the formation of synaptic connections between neurons in the brain^{16–18}, a process that is thought to be important for the drug's therapeutic effects. The findings suggest that another property of the drug — its ability to inhibit burst firing in a brain region implicated in aversion and negative mood — also contributes to its efficacy and explains its rapid onset of action. This

knowledge might facilitate the development of next-generation ketamine-related antidepressants that specifically target LHB activity and that might eliminate two major side effects of ketamine and other NMDAR blockers: their abuse potential and the induction of a transient, schizophrenia-like, psychotic state. ■

William M. Howe and Paul J. Kenny are in the Department of Neuroscience, Icahn School of Medicine at Mount Sinai, New York, New York 10029, USA.
e-mail: paul.kenny@mssm.edu

- Berridge, K. C. & Robinson, T. E. *Brain Res. Brain Res. Rev.* **28**, 309–369 (1998).
- Di Chiara, G. & Bassareo, V. *Curr. Opin. Pharmacol.* **7**, 69–76 (2007).
- Schultz, W. *Neuron* **36**, 241–263 (2002).
- Christoph, G. R., Leonzio, R. J. & Wilcox, K. S. *J. Neurosci.* **6**, 613–619 (1986).
- Ji, H. & Shepard, P. D. *J. Neurosci.* **27**, 6923–6930 (2007).
- Matsumoto, M. & Hikosaka, O. *Nature* **447**, 1111–1115 (2007).
- Sartorius, A. *et al. Biol. Psychiatry* **67**, e9–e11 (2010).
- Yang, Y. *et al. Nature* **554**, 317–322 (2018).
- Cui, Y. *et al. Nature* **554**, 323–327 (2018).
- Grace, A. A., Floresco, S. B., Goto, Y. & Lodge, D. J. *Trends Neurosci.* **30**, 220–227 (2007).
- Berman, R. M. *et al. Biol. Psychiatry* **47**, 351–354 (2000).
- Halassa, M. M. & Haydon, P. G. *Annu. Rev. Physiol.* **72**, 335–355 (2010).
- Lammel, S., Ion, D. I., Roeper, J. & Melenka, R. C. *Neuron* **70**, 855–862 (2011).
- Molofsky, A. V. *et al. Genes Dev.* **26**, 891–907 (2012).
- Ransom, B., Behar, T. & Nedergaard, M. *Trends Neurosci.* **26**, 520–522 (2003).
- Autry, A. E. *et al. Nature* **475**, 91–95 (2011).
- Zanos, P. *et al. Nature* **533**, 481–486 (2016).
- Li, N. *et al. Science* **329**, 959–964 (2010).

Working memory freed from the past

Working memory is influenced by past experiences. An area of the rat brain has now been identified that represents recent history — silencing this area can remove biases from working memory and decision-making. [SEE LETTER P.368](#)

LAURA BUSSE

Our natural environment is characterized by statistical regularities in both space and time — for example, it does not consist of randomly distributed light, but frequently contains objects that have elongated vertical and horizontal contours¹ and predictable motion². These regularities are exploited by our brains to interpret the often-ambiguous information that reaches our senses, to improve perception, decision-making and working memory. Although, in the natural world, past experiences can thus have a vital role in information processing and cognition, past experiences can impair performance in laboratory experiments that involve random structure. On page 368, Akrami *et al.*³ take advantage of this difference to identify an area of the rat brain that holds recent sensory history, and show that temporarily silencing this area removes history-related biases in memory-guided decision-making.

More than a century ago, the cognitive psychologist Harry Hollingworth identified a phenomenon called contraction bias⁴, in which the representation of a stimulus in working memory is systematically biased towards the average of recent past observations. As an example of contraction bias, consider Hollingworth's historic experiment, in which participants were asked to judge the sizes of different cards. Subjects tended to overestimate the size of memorized cards if they were smaller than others used in the experiment, and to underestimate the size of memorized cards that were relatively large.

Akrami *et al.* first set out to show that, like these findings in humans, contraction bias governs the behaviour of rats. They trained rats in an auditory working-memory task, in which the animals had to determine which of two tones, delivered several seconds apart, was louder. This task requires rats to hold the loudness of the first tone in working memory during the delay period between the two tones, to enable comparison with the second (Fig. 1).

The authors used a custom-built, high-throughput facility for automated rat training and testing, allowing them to collect data from almost half a million trials. Analysis of the rats'

behaviour revealed that, in trials in which the first tone was the fainter, performance was improved if the previous trial had contained a pair of relatively faint tones, and hampered if it had contained louder tones. The group fitted powerful computational models to the rats' behaviour that captured the animals' recent sensory history. The models demonstrated that these systematic patterns of performance are predicted by contraction bias, which pulls the representation of the first tone (held in working memory) towards the recently experienced tones. In doing so, contraction bias facilitates or impedes the comparison of the two tones.

In a search for the site of working memory

in the rat brain, Akrami *et al.* next made a truly exceptional observation. They temporarily silenced a brain region called the posterior parietal cortex (PPC), which has been implicated in working memory⁵, and found that overall task performance was improved by this intervention, particularly when the PPC was silenced during the delay period. This observed cognitive enhancement is clearly inconsistent with the idea that the PPC maintains the working-memory trace during the delay period, because silencing the PPC would erase the trace and hence lead to performance breakdown.

What underlies this remarkable improvement in performance during PPC silencing? Akrami and colleagues fitted their computational model to the rats' behaviour during PPC silencing, and found that the improvement was due to a markedly reduced influence of past recent experience. Previous sensory information can distort working-memory representations. Therefore, in the randomized world of laboratory experiments, it makes sense that silencing a brain area that holds traces of sensory history can lead to more bias-free working-memory content and thus to behaviours more aligned with reality.

To directly test how PPC neurons encode the recent past, Akrami *et al.* recorded PPC

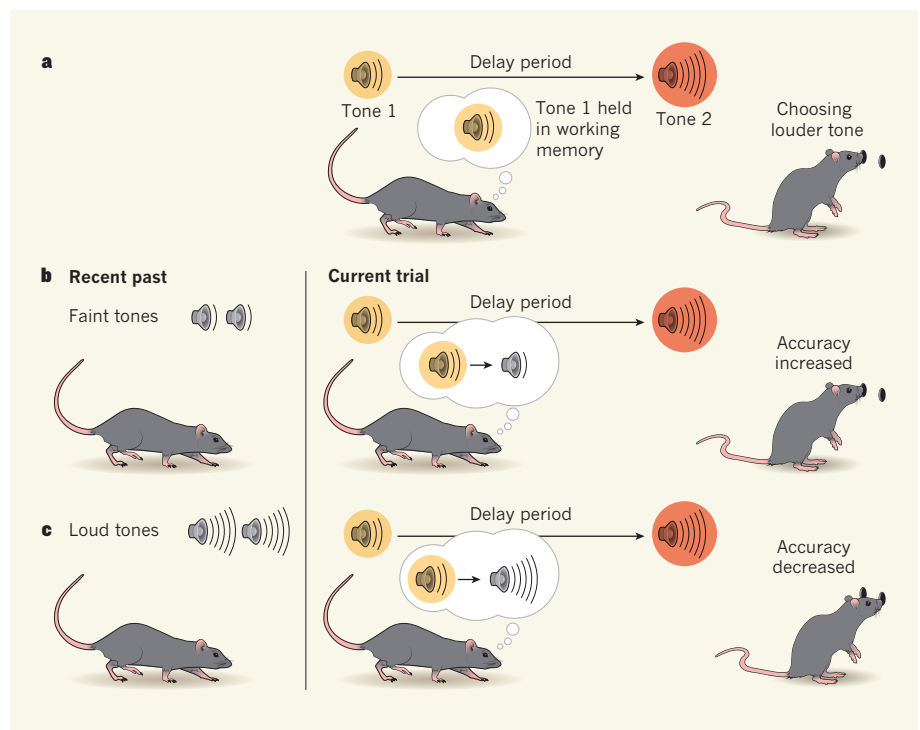


Figure 1 | Biasing the working memory of rats. **a**, Akrami *et al.*³ trained rats in a working-memory task, in which the animals listened to two tones separated by a delay of a few seconds, and had to indicate, through a nose poke, which was the louder. The task requires the first tone to be held in working memory during the delay period. **b**, The authors investigated how recent sensory history affected trials (here, trials in which the first tone was the fainter). If the animal had recently been exposed to faint tones, it remembered the first sound as fainter than it really was, improving its ability to compare the two tones. **c**, By contrast, the animal's judgement was hampered if it had recently been exposed to loud tones, because it remembered the first tone as louder than it really was. Thus, the rat's recent sensory history impinged on how it held the first tone in working memory.

activity during task performance. Consistent with their other results, the group found that, during the delay period, PPC neurons carried more information about the recent past than about the current tone held in working memory. Furthermore, across rats, the percentage of neurons holding such history-related information was tightly correlated with the level of history-induced bias in each animal's performance.

It has long been recognized that even simple perceptual decisions are not isolated, static computations — rather, they are dynamic processes embedded in a stream of past information⁶. Akrami and colleagues have taken a crucial step towards understanding these processes, by identifying a node in the brain network that influences working-memory performance by holding a representation of recent history. That their discovery was made in an animal model offers the exciting possibility that future studies could investigate, at the cellular level, precisely which neurons in the PPC represent recent history, how this representation arises, and where and how it is integrated with sensory information to guide memory-based decision-making.

Statistical regularities not only influence working memory, but can also bias motor outputs and the encoding and decoding of sensory information⁷. It is therefore likely that history-related biases are implemented across many nodes of the decision-making brain network in addition to the PPC, through various mechanisms. Long-term mechanisms, on evolutionary and developmental scales, include the adaptation of neurons in sensory areas to the statistics of the natural environment. For example, the over-representation of vertical and horizontal contours in our visual environments is paralleled by an over-representation in the brain of neurons that respond preferentially to horizontal and vertical orientations⁸, and a biased ability to perceive these orientations⁹. Dynamic, short-term mechanisms occurring on a scale of milliseconds to seconds probably involve activity in long-range feedback or neuromodulatory circuits that adjust sensory areas¹⁰, the decision-making network¹¹ and motor areas¹². Elucidating the interplay between these mechanisms is just one of the remaining challenges in the quest to understand the powerful role of past experience in working memory. ■

Laura Busse is in the Division of Neurobiology, Department Biology II, LMU Munich, Munich 82152, Germany. e-mail: busse@bio.lmu.de

5. Harvey, C. D., Coen, P. & Tank, D. W. *Nature* **484**, 62–68 (2012).
6. Gold, J. I. & Stocker, A. A. *Annu. Rev. Vis. Sci.* **3**, 227–250 (2017).
7. Kiyonaga, A., Scimeca, J. M., Bliss, D. P. & Whitney, D. *Trends Cogn. Sci.* **21**, 493–497 (2017).
8. Coppola, D. M., White, L. E., Fitzpatrick, D. & Purves, D. *Proc. Natl Acad. Sci. USA* **95**, 2621–2623 (1998).
9. Girshick, A. R., Landy, M. S. & Simoncelli, E. P.

- Nature Neurosci.* **14**, 926–932 (2011).
10. St. John-Saaltink, E., Kok, P., Lau, H. C. & de Lange, F. P. *J. Neurosci.* **36**, 6186–6192 (2016).
11. Akaishi, R., Umeda, K., Nagase, A. & Sakai, K. *Neuron* **81**, 195–206 (2014).
12. Pape, A.-A. & Siegel, M. *Nature Commun.* **7**, 13098 (2016).

This article was published online on 7 February 2018.

CONDENSED-MATTER PHYSICS

The two faces of a magnetic honeycomb

Quantum spin liquids are long-sought exotic states of matter that could transform quantum computing. Signatures of such a state have now been observed in a compound comprising iridium ions on a honeycomb lattice. SEE LETTER P.341

MARTIN MOURIGAL

Scientists are searching for elusive forms of magnetism in which spins — atomic-scale ‘compass needles’ associated with electrons — perpetually dance to an intrinsic quantum beat. On page 341, Kitagawa *et al.*¹ describe the synthesis and properties of a remarkable quantum magnet in which the ballet of spins persists down to a temperature of 0.05 kelvin. Such behaviour might be associated with exotic magnetic excitations that are of great fundamental interest and are sought for quantum-computing technologies.

Quantum magnets are often found in electrically insulating crystals. In such materials, unpaired electrons are arranged on a periodic lattice, which allows the spins of the electrons to interact with those of their neighbours. At low temperatures, these spins usually organize into symmetrical and regular patterns.

In rare cases, however, quantum fluctuations prevent the spins from becoming ordered. Instead, the spins enter a quantum superposition — a concerted and perpetual dance in which the spins are entangled, meaning that they are inseparable and share a common quantum state. Many flavours of such states, called quantum spin liquids, have been predicted². At first sight, these states resemble paramagnetic materials, in which spins are disordered in the absence of an external magnetic field. However, whereas spins behave as independent entities in paramagnets, those in quantum spin liquids are entangled with one another, even if separated by long distances.

Experimental physicists have long pondered how to obtain and detect quantum spin liquids in real materials³. Much has been learnt from the study of one-dimensional quantum magnets — in particular, from chains of spins that exhibit antiferromagnetism⁴, whereby each spin is aligned in the opposite direction to that

of its neighbours. For instance, a by-product of long-range entanglement is the presence of magnetic excitations that have fractional quantum numbers (fractions of quantities such as electric charge and spin). These excitations have been shown to leave distinct fingerprints in measurements of a material's thermodynamic and magnetic properties. Furthermore, the presence or absence of an excitation gap (a lack of excitations that have particular energies) often reveals whether the underlying entanglement is short- or long-range, respectively.

However, in spite of these breakthroughs, finding two- and three-dimensional quantum spin liquids has been a daunting task⁵. One approach has been to use geometric frustration³, in which there is an incompatibility between the spatial arrangement of spins and their interactions. This causes many spin configurations to have the same energy, which jump-starts entanglement. Kitagawa and colleagues used a different materials-science strategy, and focused on a quantum spin liquid that was proposed by the theoretical physicist Alexei Kitaev⁶ in 2006.

In Kitaev's model, spins on a honeycomb lattice are forced to interact in seemingly unnatural ways. The resulting quantum spin liquid has two types of exotic magnetic excitation: Majorana fermions, which have fractional quantum numbers, lack an excitation gap and can propagate on the lattice; and other excitations that have a small excitation gap and remain localized.

In a seminal paper⁷, it was demonstrated that the ingredients of Kitaev's model might exist in real materials, accompanied by more-conventional spin interactions called Heisenberg interactions. It was later suggested⁸ that the model could be realized in materials that have two key properties. The first is a strong coupling between the motion of electrons and their spin — a feature present in the

1. Burton, G. J. & Moorhead, I. R. *Appl. Opt.* **26**, 157–170 (1987).
2. Dong, D. W. & Atick, J. J. *Netw. Comput. Neural Syst.* **6**, 345–358 (1995).
3. Akrami, A., Kopec, C. D., Diamond, M. E. & Brody, C. D. *Nature* **554**, 368–372 (2018).
4. Hollingworth, H. L. *J. Phil. Psychol. Sci. Methods* **7**, 461–469 (1910).

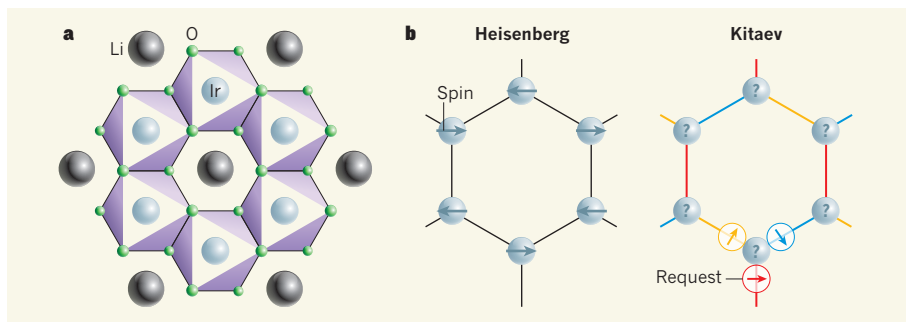


Figure 1 | The structure and spin interactions of $\text{H}_3\text{LiIr}_2\text{O}_6$. **a**, Kitagawa *et al.*¹ report that, unlike other magnetic materials, the compound $\text{H}_3\text{LiIr}_2\text{O}_6$ does not show magnetic ordering at temperatures close to absolute zero (H, hydrogen; Li, lithium; Ir, iridium; O, oxygen). A single unit of a layer of the compound is shown here. Octahedra (purple) formed from iridium and oxygen ions cause the iridium ions to be arranged on a honeycomb lattice. **b**, The magnetic properties of $\text{H}_3\text{LiIr}_2\text{O}_6$ suggest that at least two types of interaction are at play between the spins (magnetic moments) of neighbouring iridium ions. The first are Heisenberg interactions (black lines), which cause spins to align in the opposite direction to that of their neighbours. The second are Kitaev interactions (coloured lines), which predispose neighbouring spins to co-align in one of three possible orientations, depending on which bond of the lattice is considered. Each line colour corresponds to a different preferred orientation. Because each lattice site participates in three distinct bonds, a given spin receives contradictory requests from its neighbours, which prevents magnetic ordering.

outer electron shells of some transition-metal ions. The second is a specific bonding geometry, which is achieved when octahedra formed from metal and oxygen ions share their edges to form a honeycomb lattice. Compounds such as lithium iridate⁹ (Li_2IrO_3), sodium iridate (Na_2IrO_3) and ruthenium chloride¹⁰ (RuCl_3) fulfil these requirements. However, all of these compounds become magnetically ordered below a few kelvin, which excludes them as genuine realizations of Kitaev's model.

Using an approach known as soft chemistry, in which materials are modified under mild temperature conditions (here, at 120 °C), Kitagawa *et al.* replaced inter-layer lithium ions of Li_2IrO_3 with hydrogen ions, while preserving the overall structure of the magnetic-honeycomb layers. The authors found that the resulting compound, $\text{H}_3\text{LiIr}_2\text{O}_6$, has low-temperature properties that are spectacularly different from those of Li_2IrO_3 . In particular, they observed no magnetic ordering in $\text{H}_3\text{LiIr}_2\text{O}_6$ down to a temperature of 0.05 K, and used nuclear magnetic resonance to confirm these findings down to 1 K (see Figure 2 of the paper¹). The complex interplay between Kitaev and Heisenberg interactions¹¹ is probably key to stabilizing this quantum state (Fig. 1). The authors discovered that the compound's thermodynamic and magnetic properties are highly unusual, and interpreted these measurements in terms of exotic magnetic excitations that lack an excitation gap and perhaps have fractional quantum numbers.

$\text{H}_3\text{LiIr}_2\text{O}_6$ is a remarkable compound: it is the first iridium-based honeycomb magnet that does not become magnetically ordered at temperatures below a few kelvin. However, its overall behaviour and unusual thermodynamic properties indicate that it is governed by microscopic ingredients that differ substantially from those of Kitaev's model. This

is not a curse, but a blessing: understanding exotic magnetic phases is often achieved by studying related materials and models¹². Future experimental work in which, for example, large crystals of $\text{H}_3\text{LiIr}_2\text{O}_6$ are grown, or particles such as neutrons or photons are scattered off $\text{H}_3\text{LiIr}_2\text{O}_6$, could reveal whether the compound's excitations have fractional quantum numbers — the ultimate experimental proof of a quantum spin liquid.

MEDICAL RESEARCH

On the trail of invasive cells in breast cancer

During breast-cancer progression, tumour cells that arise in the milk duct spread elsewhere in the breast. The origin of these invasive tumour cells is now revealed by an analysis of spatially defined single cells.

DOUGLAS S. MICALIZZI
& SHYAMALA MAHESWARAN

In the early-stage breast cancer called ductal carcinoma *in situ* (DCIS), a cluster of cancer cells arises in the milk duct and remains confined there. The recorded incidence of DCIS has risen since the late 1980s, probably due to an increase in its detection through more widespread breast-cancer screening¹. Up to 40% of cases of DCIS progress to invasive ductal carcinoma (IDC), in which tumour cells invade other regions of the breast^{2–4}. IDC requires clinical treatment. Moreover, because it is not possible to predict which people with DCIS are at risk of progressing to IDC, the standard treatment

The soft-chemistry approach used by Kitagawa *et al.* offers great promise for controlling the properties of layered quantum magnets. However, with regard to oxide materials, there are challenges associated with the presence of chemical disorder and heterogeneities. For instance, the layered structure of $\text{H}_3\text{LiIr}_2\text{O}_6$ is prone to faults associated with the stacking of the layers¹³. In the future, it will be exciting to see chemists and physicists join forces to develop a deeper understanding of how material defects influence, and potentially even favour, entangled magnetic matter. ■

Martin Mourgial is in the School of Physics, Georgia Institute of Technology, Atlanta, Georgia 30332, USA.
e-mail: mourgial@gatech.edu

1. Kitagawa, K. *et al.* *Nature* **554**, 341–345 (2018).
2. Savary, L. & Balents, L. *Rep. Prog. Phys.* **80**, 016502 (2016).
3. Imai, T. & Lee, Y. *Phys. Today* **69**, 30 (2016).
4. Lake, B. *et al.* *Phys. Rev. Lett.* **111**, 137205 (2013).
5. Lee, P. A. *Science* **321**, 1306–1307 (2008).
6. Kitaev, A. *Ann. Phys.* **321**, 2–111 (2006).
7. Jackeli, G. & Khaliullin, G. *Phys. Rev. Lett.* **102**, 017205 (2009).
8. Chaloupka, J., Jackeli, G. & Khaliullin, G. *Phys. Rev. Lett.* **105**, 027204 (2010).
9. Singh, Y. *et al.* *Phys. Rev. Lett.* **108**, 127203 (2012).
10. Plumb, K. W. *et al.* *Phys. Rev. B* **90**, 041112 (2014).
11. Rau, J. G., Lee, E. K. & Kee, H. Y. *Phys. Rev. Lett.* **112**, 077204 (2014).
12. Banerjee, A. *et al.* *Nature Mater.* **15**, 733–740 (2016).
13. Bette, S. *et al.* *Dalton Trans.* **46**, 15216–15227 (2017).

for patients who have DCIS is surgery, often followed by radiotherapy⁵. Therefore, understanding how DCIS progresses to IDC might enable the selective treatment of those at high risk of developing IDC. A paper in *Cell* by Casasent *et al.*⁶ reveals the origin of DCIS and its progression to IDC.

Casasent and colleagues obtained frozen samples of breast-cancer tissue gathered from patients. The authors used single-cell DNA sequencing of cells from DCIS and IDC regions in the same section of tissue to create molecular maps of patients' breast cancers, in an approach they call topographic single-cell sequencing. They stained the samples to identify tumour cells and noted the location of each selected cell in the regions of DCIS and IDC. A

MEDICAL RESEARCH

On the trail of invasive cells in breast cancer

During breast-cancer progression, tumour cells that arise in the milk duct spread elsewhere in the breast. The origin of these invasive tumour cells is now revealed by an analysis of spatially defined single cells.

DOUGLAS S. MICALIZZI
& SHYAMALA MAHESWARAN

In the early-stage breast cancer called ductal carcinoma *in situ* (DCIS), a cluster of cancer cells arises in the milk duct and remains confined there. The recorded incidence of DCIS has risen since the late 1980s, probably due to an increase in its detection through more widespread breast-cancer screening¹. Up to 40% of cases of DCIS progress to invasive ductal carcinoma (IDC), in which tumour cells invade other regions of the breast^{2–4}. IDC requires clinical treatment. Moreover, because it is not possible to predict which people with DCIS are at risk of progressing to IDC, the standard treatment for patients who have DCIS is surgery, often followed by radiotherapy⁵. Therefore, understanding how DCIS progresses to IDC might enable the selective treatment of those at high risk of developing IDC. A paper in *Cell* by Casasent *et al.*⁶ reveals the origin of DCIS and its progression to IDC.

Casasent and colleagues obtained frozen samples of breast-cancer tissue gathered from patients. The authors used single-cell DNA sequencing of cells from DCIS and IDC regions in the same section of tissue to create molecular maps of patients' breast cancers, in an approach they call topographic single-cell sequencing. They stained the samples to identify tumour cells and noted the location of each selected cell in the regions of DCIS and IDC. A technique called laser capture microdissection enabled the separation of a selected cell from its neighbours by tracing a laser beam around the cell. This was combined with an approach termed laser catapulting, in which energy from an ultraviolet laser propels a microdissected cell into a collection tube for subsequent DNA analysis. These laser-based techniques are used in other contexts, including forensic science and studies of plant physiology⁷.

The authors analysed 1,293 of these individually isolated tumour cells from 10 patients with breast cancer. They assessed whether the cells isolated from each patient

contained alterations in the number of copies of genes, a type of change that sometimes drives tumour formation and growth. A comparison of these alterations in tumour cells from an individual can identify distinct populations of cells (clones). Analysis of the patterns of genetic alterations can reveal a clone's cellular origin and its relationship with other clones. Combining this information with knowledge of a cell's location offers a way to track the progression of DCIS to IDC.

Casasent *et al.* observed that the tumours of four patients had formed from a single clone, and that those of the other six patients consisted of between 2 and 5 clones. The clones of each patient with multiclonal tumours shared a set of genomic aberrations, which suggests that all tumour cells in each of those patients had descended from a single cell, with genetic divergence between the various clones arising

from the acquisition of further alterations.

In patients with multiclonal tumours, all of the individual's clones were present in both DCIS and IDC regions (Fig. 1). This points to a model in which clones arise and evolve in the milk duct and then escape to establish IDC elsewhere in the breast, such as in regions containing stromal cells. The various clones had a wide distribution across breast tissue, with certain clones being evenly distributed between milk ducts and regions of tumour invasion, and others being enriched in either the invaded regions or the milk ducts.

The authors conducted additional analysis by sequencing the protein-coding regions of the tumour cells' DNA — detecting an average of 23 mutations per patient. This analysis confirmed that there were striking similarities between specific clones in a given patient, regardless of whether the clonal tumour cell was part of a DCIS or an IDC region. The transition from DCIS to IDC was not associated with a notable increase in the number of mutations in the clones or in the number of independent clones. A few mutations specific to DCIS or IDC regions were identified, and, although these warrant further study, the authors' main finding is the remarkable genetic similarity of a patient's tumour cells in these two distinct disease states. The observation that genomic evolution of tumour cells occurs in the milk duct before invasion proceeds suggests that a transient period of genome instability is an early event in breast-cancer initiation.

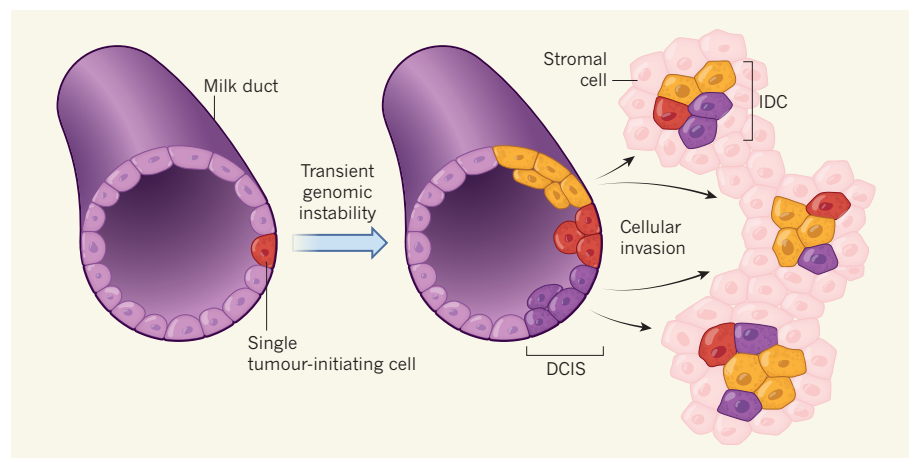


Figure 1 | Tracking the cellular origins of breast cancer. Casasent *et al.*⁶ report the development of a technique for spatially resolved analysis of individual breast-cancer cells in tissue samples obtained from patients. This enabled them to determine the cellular origin of a non-invasive breast cancer called ductal carcinoma *in situ* (DCIS), in which tumour cells form in the milk duct. The authors reveal that DCIS arises from a single tumour-initiating cell and its descendants. Some of these tumour cells might diverge from each other during a period of transient genomic instability to form several different cellular populations, or clones (distinct clones shown as red, yellow or dark purple). DCIS sometimes progresses to an invasive stage in which tumour cells migrate to other areas of the breast tissue, such as regions containing stromal cells, where tumour growths known as invasive ductal carcinoma (IDC) form. The identity of the cells that give rise to IDC has been debated. Casasent and colleagues found that all the tumour clones present in regions of DCIS are also present in areas of IDC.

Casasent and colleagues' model, in which breast cancer arises in the milk duct from a single initiating cell that gives rise to several clones in the duct that then invade the rest of the breast tissue, contrasts with two alternative models of IDC development^{8–10}. The independent-lineage model^{8,9} proposes that DCIS and IDC evolve independently from different tumour-initiating cells. The other model¹⁰, called an evolutionary bottleneck, proposes that a single initiating cell in the milk duct gives rise to several clones, only one of which successfully escapes the milk duct to invade the rest of the tissue.

Many questions remain. What triggers the genetic alterations in the tumour-initiating cell in DCIS? Do other potential tumour-initiating cells arise at the earliest stage of the disease, of which only one gives rise to DCIS and the others are eliminated? A better understanding is needed of how tumour cells escape the milk duct through the breakdown of the duct's outer layer (the basement membrane), and how some cells from all the clones present in DCIS manage to exit the duct.

The genetic similarity between tumour cells in the DCIS and IDC regions of a given individual raises the question of what differences enable some cells to give rise to invasive disease. A clearer definition of the differences between low-risk DCIS that does not advance to IDC and high-risk DCIS that does, might enable the accurate prediction of disease-progression risk. Addressing this will probably require single-cell comparisons of gene-transcription profiles or the assessment of modifications known as epigenetic changes, which alter the protein–DNA complex of chromatin and can affect gene expression.

Casasent and colleagues' approach could be used to study different cancers in which spatially resolved insight into tumour growth cannot be obtained by conventional methods. For example, using this technique to investigate abnormal cellular growths that eventually progress to a malignant state would be a good choice for future studies into the origin and clonal heterogeneity of tumour cells. It is unclear how widely this method is likely

to be applied, considering the technical and financial requirements. Nevertheless, Casasent *et al.* have demonstrated that their approach has the potential to provide useful insight into the dynamics of tumour clones during the progression of breast cancer. ■

Douglas S. Micalizzi and Shyamala Maheswaran are at Massachusetts General Hospital Center for Cancer Research, Harvard Medical School, Massachusetts 02129, USA. e-mail: maheswaran@helix.mgh.harvard.edu

1. Virnig, B. A., Tuttle, T. M., Shamliyan, T. & Kane, R. L. *J. Natl Cancer Inst.* **102**, 170–178 (2010).
2. Sanders, M. E., Schuyler, P. A., Dupont, W. D. & Page, D. L. *Cancer* **103**, 2481–2484 (2005).
3. Sanders, M. E., Schuyler, P. A., Simpson, J. F., Page, D. L. & Dupont, W. D. *Mod. Pathol.* **28**, 662–669 (2015).
4. Collins, L. C. *et al. Cancer* **103**, 1778–1784 (2005).
5. Shah, C. *et al. JAMA Oncol.* **2**, 1083–1088 (2016).
6. Casasent, A. K. *et al. Cell* **172**, 205–217 (2018).
7. Schütze, K., Niyaz, Y., Stich, M. & Buchstaller, A. *Methods Cell Biol.* **82**, 649–673 (2007).
8. Sontag, L. & Axelrod, D. E. *J. Theor. Biol.* **232**, 179–189 (2005).
9. Miron, A. *et al. Cancer Res.* **70**, 5674–5678 (2010).
10. Cowell, C. F. *et al. Mol. Oncol.* **7**, 859–869 (2013).

Genomics of the origin and evolution of *Citrus*

Guohong Albert Wu¹, Javier Terol², Victoria Ibanez², Antonio López-García², Estela Pérez-Román², Carles Borredá², Concha Domingo², Francisco R. Tadeo², Jose Carbonell-Caballero³, Roberto Alonso³, Franck Curk⁴, Dongliang Du⁵, Patrick Ollitrault⁶, Mikeal L. Roose⁷, Joaquin Dopazo^{3,8}, Frederick G. Gmitter Jr⁵, Daniel S. Rokhsar^{1,9,10} & Manuel Talon²

The genus *Citrus*, comprising some of the most widely cultivated fruit crops worldwide, includes an uncertain number of species. Here we describe ten natural citrus species, using genomic, phylogenetic and biogeographic analyses of 60 accessions representing diverse citrus germ plasms, and propose that citrus diversified during the late Miocene epoch through a rapid southeast Asian radiation that correlates with a marked weakening of the monsoons. A second radiation enabled by migration across the Wallace line gave rise to the Australian limes in the early Pliocene epoch. Further identification and analyses of hybrids and admixed genomes provides insights into the genealogy of major commercial cultivars of citrus. Among mandarins and sweet orange, we find an extensive network of relatedness that illuminates the domestication of these groups. Widespread pummelo admixture among these mandarins and its correlation with fruit size and acidity suggests a plausible role of pummelo introgression in the selection of palatable mandarins. This work provides a new evolutionary framework for the genus *Citrus*.

The genus *Citrus* and related genera (*Fortunella*, *Poncirus*, *Eremocitrus* and *Microcitrus*) belong to the angiosperm subfamily Aurantioideae of the Rutaceae family, which is widely distributed across the monsoon region from west Pakistan to north-central China and south through the East Indian Archipelago to New Guinea and the Bismarck Archipelago, northeastern Australia, New Caledonia, Melanesia and the western Polynesian islands¹. Native habitats of citrus and related genera roughly extend throughout this broad area (Extended Data Fig. 1a and Supplementary Table 1), although the geographical origin, timing and dispersal of citrus species across southeast Asia remain unclear. A major obstacle to resolving these uncertainties is our poor understanding of the genealogy of complex admixture in cultivated citrus, as has recently been shown². Some citrus are clonally propagated apomictically³ through nucellar embryony, that is, the development of non-sexual embryos originating in the maternal nucellar tissue of the ovule, and this natural process may have been co-opted during domestication; grafting is a relatively recent phenomenon⁴. Both modes of clonal propagation have led to the domestication of fixed (desirable) genotypes, including interspecific hybrids, such as oranges, limes, lemons, grapefruits and other types.

Under this scenario, it is not surprising that the current chaotic citrus taxonomy—based on long-standing, conflicting proposals^{5,6}—requires a solid reformulation consistent with a full understanding of the hybrid and/or admixture nature of cultivated citrus species. Here we analyse genome sequences of diverse citrus to characterize the diversity and evolution of citrus at the species level and identify citrus admixtures and interspecific hybrids. We further examine the network of relatedness among mandarins and sweet orange, as well as the pattern of the introgression of pummelos among mandarins for clues to the early stages of citrus domestication.

Diversity and evolution of the genus *Citrus*

To investigate the genetic diversity and evolutionary history of citrus, we analysed the genomes of 58 citrus accessions and two outgroup genera (*Poncirus* and *Severinia*) that were sequenced to high coverage, including recently published sequences^{2,3,7} as well as 30 new genome sequences described here. For our purpose, we do not include accessions related by somatic mutations. These sequences represent a diverse sampling of citrus species, their admixtures and hybrids (Supplementary Tables 2, 3 and Supplementary Notes 1, 2). Our collection includes accessions from eight previously unsequenced and/or unexamined citrus species, such as pure mandarins (*Citrus reticulata*), citron (*Citrus medica*), *Citrus micrantha* (a wild species from within the subgenus *Papeda*), Nagami kumquat (*Fortunella margarita*, also known as *Citrus japonica* var. *margarita*), and *Citrus ichangensis* (also known as *Citrus cavaleriei*; this species is also considered a *Papeda*), as well as three Australian citrus species (Supplementary Notes 3, 4). For each species, we have sequenced one or more pure accessions without interspecific admixture.

Local segmental ancestry of each accession can be delineated for both admixed and hybrid genotypes, based on genome-wide ancestry-informative single-nucleotide polymorphisms (Supplementary Note 5). Comparative genome analysis further identified shared haplotypes among the accessions (Supplementary Notes 6, 7). In particular, we demonstrate the F1 interspecific hybrid nature of Rangpur lime and red rough lemon (two different mandarin–citron hybrids), Mexican lime (a *micrantha*–citron hybrid) and calamondin (a kumquat–mandarin hybrid), and confirm, using whole-genome sequence data, the origins of grapefruit (a pummelo–sweet orange hybrid), lemon (a sour orange–citron hybrid) and eremorange (a sweet orange and *Eremocitrus glauca* (also known as *Citrus glauca*) hybrid). We also verified the parentage of Cocktail grapefruit, with low-acid pummelo as the seed parent and

¹US Department of Energy Joint Genome Institute, Walnut Creek, California, USA. ²Centro de Genómica, Instituto Valenciano de Investigaciones Agrarias (IVIA), Moncada, Valencia, Spain.

³Computational Genomics Department, Centro de Investigación Príncipe Felipe (CIPF), Valencia, Spain. ⁴AGAP Research Unit, Institut National de la Recherche Agronomique (INRA), San Giuliano, France. ⁵Citrus Research and Education Center (CREC), Institute of Food and Agricultural Sciences (IFAS), University of Florida, Lake Alfred, Florida, USA. ⁶AGAP Research Unit, Centre de Coopération Internationale en Recherche Agronomique pour le Développement (CIRAD), Petit-Bourg, Guadeloupe, France. ⁷Department of Botany and Plant Sciences, University of California, Riverside, Riverside, California, USA. ⁸Functional Genomics Node, Spanish National Institute of Bioinformatics (ELIXIR-es) at CIPF, Valencia, Spain. ⁹Department of Molecular and Cell Biology and Center for Integrative Genomics, University of California, Berkeley, Berkeley, California, USA. ¹⁰Molecular Genetics Unit, Okinawa Institute of Science and Technology Graduate University, Onna, Okinawa 904-0495, Japan.

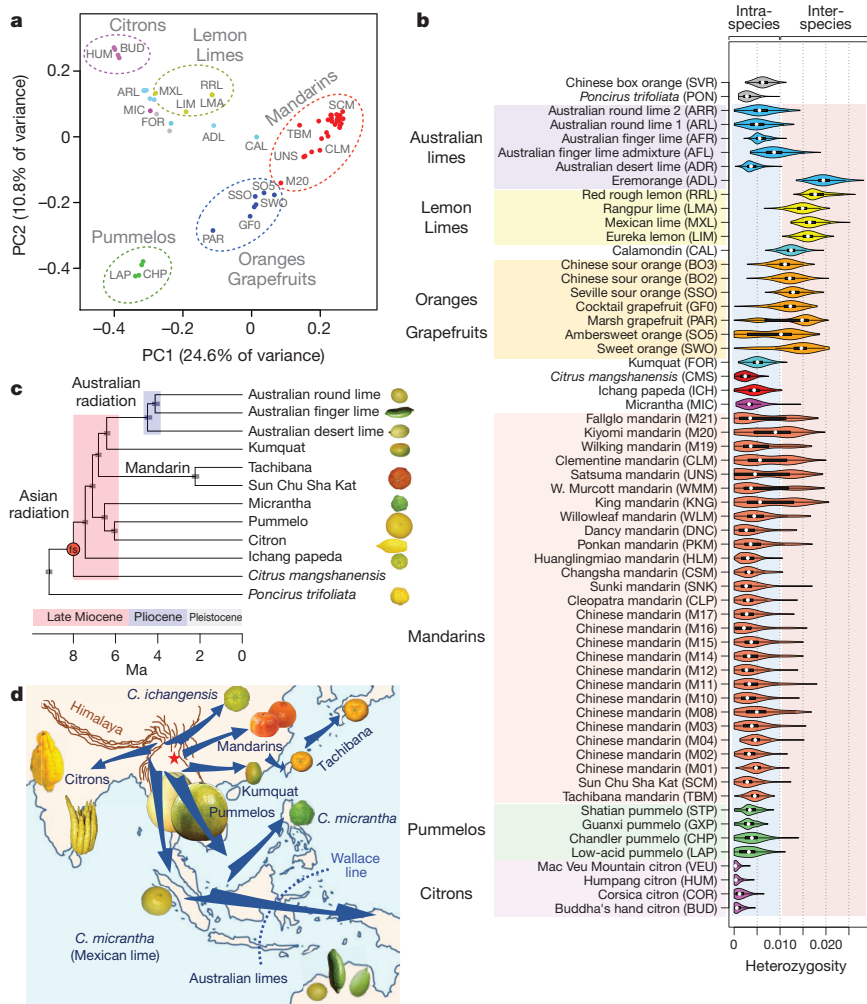


Figure 1 | Genetic structure, heterozygosity and phylogeny of *Citrus* species. **a**, Principal coordinate analysis of 58 citrus accessions based on pairwise nuclear genome distances and metric multidimensional scaling. The first two axes separate the three main citrus groups (citrons, pummelos and mandarins) with interspecific hybrids (oranges, grapefruit, lemon and limes) situated at intermediate positions relative to their parental genotypes. **b**, Violin plots of the heterozygosity distribution in 58 citrus accessions, representing 10 taxonomic groups as well as 2 related genera, *Poncirus* (*Poncirus trifoliata*, also known as *Citrus trifoliata*) and Chinese box orange (*Severinia*). White dot, median; bar limits, upper and lower quartiles; whiskers, $1.5 \times$ interquartile range. The bimodal separation of intraspecific (light blue) and interspecific (light pink) genetic diversity is manifested among the admixed mandarins and across different genotypes including interspecific hybrids. Three-letter codes are listed in parenthesis with additional descriptions in Supplementary Table 2. **c**, Chronogram of citrus speciation. Two distinct and temporally well-separated phases of species radiation are apparent, with the southeast Asian citrus radiation followed by the Australian citrus diversification. Age calibration is based on the citrus fossil *C. linczangensis*¹⁶ from the Late Miocene (denoted by a filled red circle). The 95% confidence intervals are derived from 200 bootstraps. Bayesian posterior probability is 1.0 for all nodes. **d**, Proposed origin of citrus and ancient dispersal routes. Arrows suggest plausible migration directions of the ancestral citrus species from the centre of origin—the triangle formed by northeastern India, northern Myanmar and northwestern Yunnan. The proposal is compatible with citrus biogeography, phylogenetic relationships, the inferred timing of diversification and the paleogeography of the region, especially the geological history of Wallacea and Japan. The red star marks the fossil location of *C. linczangensis*. Citrus fruit images in **c** and **d** are not drawn to scale.

King and Dancy mandarins as the two grandparents on the paternal side. The origin of the Ambersweet orange is similarly confirmed to be a mandarin–sweet orange hybrid with Clementine as a grandparent. We have previously shown that sour orange (cv. Seville) (*Citrus aurantium*) is a pummelo–mandarin hybrid, and have analysed the more complex origin of sweet orange (*Citrus sinensis*)². Re-analysing sequences from ten cultivars of sweet orange³ shows that they are all derived from the same genome by somatic mutations, and were thus not included in our study.

We identified ten progenitor citrus species (Supplementary Note 4.1) by combining diversity analysis (Extended Data Table 1), multidimensional scaling and chloroplast genome phylogeny (Extended Data Fig. 1b). The first two principal coordinates in the multidimensional scaling (Fig. 1a) separate three ancestral (sometimes called ‘fundamental’) *Citrus* species associated with commercially important types^{8,9}—citrons (*C. medica*), mandarins (*C. reticulata*) and pummelos (*Citrus maxima*)—and display lemons, limes, oranges and grapefruits as hybrids involving these three species. The nucleotide diversity distributions (Fig. 1b) show distinct scales for interspecific divergence and intraspecific variation, and reflect the genetic origin of each accession. Hybrid accessions (sour orange, calamondin, lemon and non-Australian limes) with ancestry from two or more citrus species are readily identified on the basis of their higher segmental heterozygosity (1.5–2.4%) relative to intraspecific diversity (0.1–0.6%). Other citrus accessions show bimodal distributions in heterozygosity (sweet orange, grapefruits and some highly heterozygous mandarins) due to interspecific admixture, a process that generally involves complex backcrosses. Among the pure genotypes without interspecific admixture, citrons

show significantly lower intraspecific diversity (around 0.1%) than the other species (0.3–0.6%). The reduced heterozygosity of citrons, a mono-embryonic species, is probably due to the cleistogamy of its flowers¹⁰, a mechanism that promotes pollination and self-fertilization in unopened flower buds, which in turn reduces heterozygosity.

The identification of a set of pure citrus species provides new insights into the phylogeny of citrus, their origins, evolution and dispersal. Citrus phylogeny is controversial^{1,5,6,11,12}, in part owing to the difficulty of identifying pure or wild progenitor species, because of substantial interspecific hybridization that has resulted in several clonally propagated and cultivated accessions. Some authors assign separate binomial species designations to clonally propagated genotypes^{1,6}. Our nuclear genome-based phylogeny, which is derived from 362,748 single-nucleotide polymorphisms in non-genic and non-pericentromeric genomic regions, reveals that citrus species are a monophyletic group and establishes well-defined relationships among its lineages (Fig. 1c and Supplementary Note 8). Notably, the nuclear genome-derived phylogeny differs in detail from the chloroplast-derived phylogeny (Extended Data Fig. 1). This is not unexpected, as chloroplast DNA is a single, non-recombining unit and is unlikely to show perfect lineage sorting during rapid radiation (Supplementary Note 8.3).

The origin of citrus has generally been considered to be in southeast Asia¹, a biodiversity hotspot¹³ with a climate that has been influenced by both east and south Asian monsoons¹⁴ (Supplementary Note 9). Specific regions include the Yunnan province of southwest China¹⁵, Myanmar and northeastern India in the Himalayan foothills¹. A fossil specimen from the late Miocene epoch of Lincang in Yunnan, *Citrus linczangensis*¹⁶, has traits that are characteristic of current major citrus

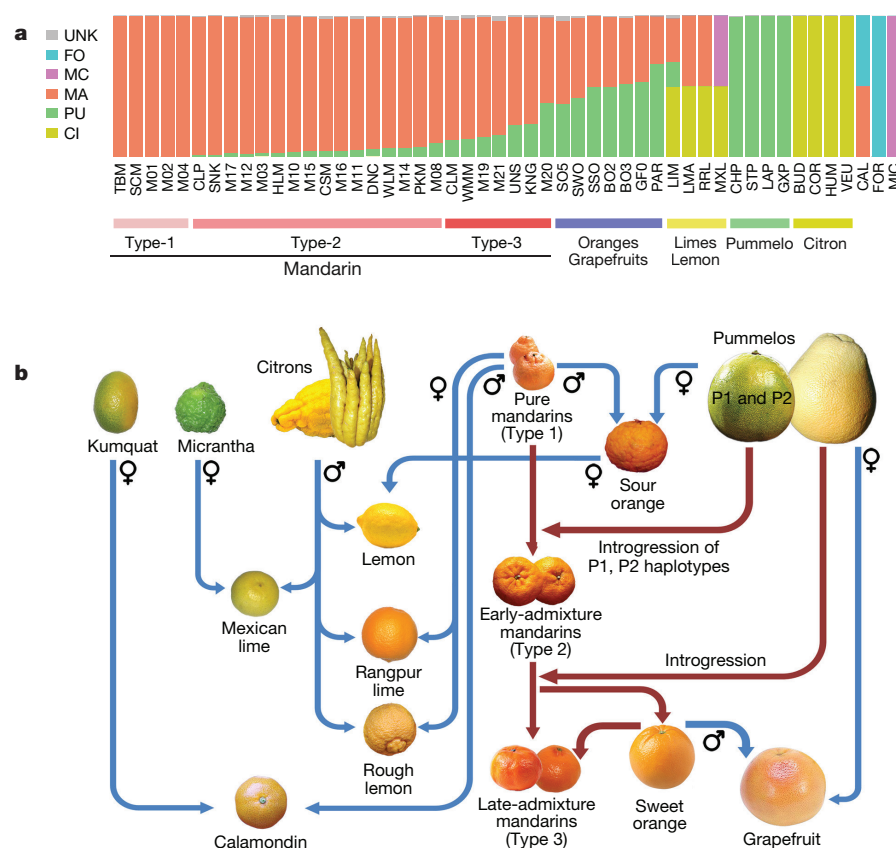


Figure 2 | Admixture proportion and citrus genealogy. **a**, Allelic proportion of five progenitor citrus species in 50 accessions. CI, *C. medica*; FO, *Fortunella*; MA, *C. reticulata*; MC, *C. micrantha*; PU, *C. maxima*; UNK, unknown. The pummelos and citrons represent pure citrus species, whereas in the heterogeneous set of mandarins, the degree of pummelo introgression subdivides the group into pure (type-1) and admixed (type-2 and -3) mandarins. Three-letter code as in Fig. 1, see Supplementary Table 2 for details. **b**, Genealogy of major citrus genotypes. The five progenitor species are shown at the top. Blue lines represent simple crosses between two parental genotypes, whereas red lines represent more complex processes involving multiple individuals, generations and/or backcrosses. Whereas type-1 mandarins are pure species, type-2 (early-admixture) mandarins contain a small amount of pummelo admixture that can be traced back to a common pummelo ancestor (with P1 or P2 haplotypes). Later, additional pummelo introgressions into type-2 mandarins gave rise to both type-3 (late-admixture) mandarins and sweet orange. Further breeding between sweet orange and mandarins or within late-admixture mandarins produced additional modern mandarins. Fruit images are not to scale and represent the most popular citrus types. See Supplementary Note 1.1 for nomenclature usage.

groups, and provides definite evidence for the existence of a common *Citrus* ancestor within the Yunnan province approximately 8 million years ago (Ma).

Our analysis establishes a relatively rapid Asian radiation of citrus species in the late Miocene (6–8 Ma; Fig. 1c, d), a period coincident with an extensive weakening of monsoons and a pronounced climate transition from wet to drier conditions¹⁷. In southeast Asia, this marked climate alteration caused major changes in biota, including the migration of mammals¹⁸ and rapid radiation of various plant lineages^{19,20}. Australian citrus species form a distinct clade that was proposed to be nested with citrons¹², although distinct generic names (*Eremocitrus* and *Microcitrus*) were assigned in botanical classifications by Swingle^{1,5}. Both molecular dating analysis²¹ and our whole-genome phylogenetic analysis do not support an Australian origin for citrus²². Rather, citrus species spread from southeast Asia to Australasia, probably via trans-oceanic dispersals. Our genomic analysis indicates that the Australian radiation occurred during the early Pliocene epoch, around 4 Ma. This is contemporaneous with other west-to-east angiosperm migrations from southeast Asia^{23,24}, presumably taking advantage of the elevation of Malesia and Wallacea in the late Miocene and Pliocene^{25,26} (Supplementary Note 9).

The nuclear and chloroplast genome phylogenies indicate that there are three Australian species in our collection. One of the two Australian finger limes shows clear signs of admixture with round limes (Supplementary Note 5.4). The closest relative to Australian citrus is *Fortunella*, a species that has been reported to grow in the wild in southern China²⁷. Australian citrus species are diverse, and found natively in both dry and rainforest environments in northeast Australia, depending on the species²⁸. Our phylogeny shows that the progenitor citrus probably migrated across the Wallace line, a natural barrier for species dispersal from southeast Asia to Australasia, and later adapted to these diverse climates.

The results also show that the Tachibana mandarin, naturally found in Taiwan, the Ryukyu archipelago and Japan²⁹, split from mainland

Asian mandarins (Fig. 1c, d) during the early Pleistocene (around 2 Ma), a geological epoch with strong glacial maxima³⁰. Tachibana, as did other flora and fauna in the region, very probably arrived in these islands from the adjacent mainland³¹ during the drop in the sea level of the South China Sea and the emergence of land bridges^{32,33}, a process promoted by the expansion of ice sheets that repetitively occurred during glacial maxima (Supplementary Note 9).

Although Tachibana^{5,6} has been assigned its own species (*Citrus tachibana*), sequence analysis reveals that it has a close affinity to *C. reticulata*^{34,35} and does not support its taxonomic position as a separate species (Supplementary Note 4.1). However, both chloroplast genome phylogeny (Extended Data Fig. 1b) and nuclear genome clustering (Fig. 1a) clearly distinguish Tachibana from the mainland Asian mandarins. This suggests that Tachibana should be designated a subspecies of *C. reticulata*. By contrast, the wild Mangshan ‘mandarin’ (*Citrus mangshanensis*)⁷ represents a distinct species, with comparable distances to *C. reticulata*, pummelo and citron² (Extended Data Table 1).

Pattern of pummelo admixture in the mandarins

Using 588,583 ancestry-informative single-nucleotide polymorphisms derived from three species, *C. medica*, *C. maxima* and *C. reticulata*, we delineate the segmental ancestry of 46 citrus accessions (Extended Data Fig. 2 and Supplementary Note 5). Pummelo admixture is found in all but 5 of the 28 sequenced mandarins, and the amount and pattern of pummelo admixture, as identified by phased pummelo haplotypes (Fig. 2a and Supplementary Note 6), suggests the classification of the mandarins into three types.

Type-1 mandarins represent pure *C. reticulata* with no evidence of interspecific admixture and include Tachibana, three unnamed Chinese mandarins (M01, M02, M04)³ and the ancient Chinese cultivar Sun Chu Sha Kat reported here, a small tart mandarin commonly grown in China and Japan, and also found in Assam. This cultivar is likely described in Han Yen-Chih’s AD 1178 monograph ‘Chü Lu’³⁶, which

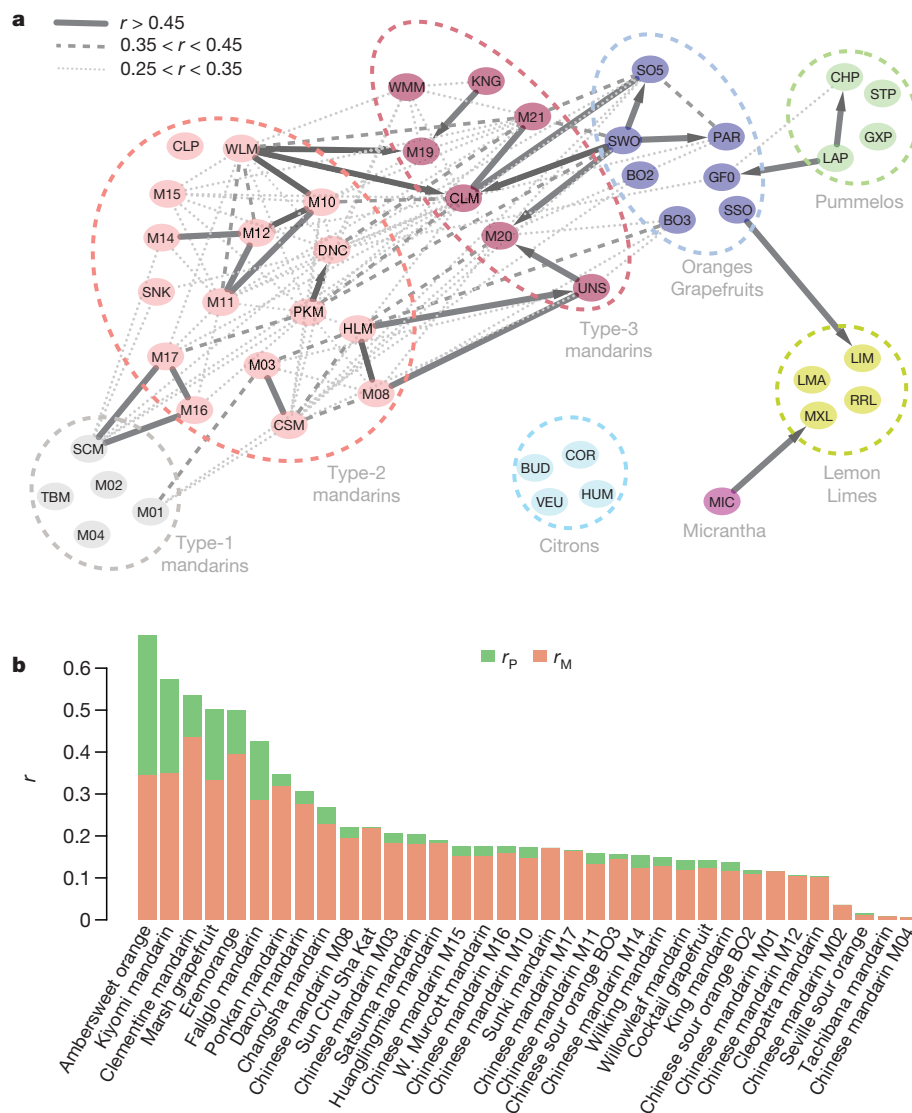


Figure 3 | Citrus relatedness network and haplotype sharing with sweet orange.

a, Genetic relatedness among 48 citrus accessions derived from four progenitor species including citrons, pummelos, pure mandarins and micrantha. Solid lines connect pairs with coefficient of relatedness $r > 0.45$, with parent–child pairs denoted by arrows pointing from parent to child. Dashed and dotted lines correspond to $0.35 < r < 0.45$ and $0.25 < r < 0.35$, respectively. Mandarins are distinguished from other taxonomic groups by an extensive relatedness network, indicating shared haplotypes in the ancestral gene pool. Three-letter code as in Fig. 1, see Supplementary Table 2 for details. **b**, Shown in decreasing order are the values of coefficient of relatedness between sweet orange and other accessions, with *C. maxima* (r_P) and *C. reticulata* (r_M) components in green and light salmon, respectively. There is significant haplotype sharing between sweet orange and all mandarins, except for three of the type-1 mandarins. Five accessions (Clementine and Kiyomi mandarins, eremorange, Marsh grapefruit, and Ambersweet orange) have sweet orange as the male parent.

includes references to citrus cultivated during the reign of Emperor Ta Yu (2205–2197 BC). Sixteen of the twenty-eight mandarins belong to type-2 mandarins, which have a small amount of pummelo admixture (1–10% of the length of the genetic map; Fig. 2a), usually in the form of a few short segments distributed across the genome. Although the lengths and locations of these admixed segments may be distinct in different mandarins, they share one or two common pummelo haplotypes (designated as P1 and P2) (Extended Data Fig. 3). By contrast, the seven remaining mandarins (type-3) contain higher proportions of pummelo alleles (12–38%; Fig. 2a) in longer segments. Although the P1 and P2 pummelo haplotypes are also detectable among type-3 mandarins, other more extensive pummelo haplotypes dominate the pummelo admixture in type-3 mandarins (Fig. 2b and Extended Data Table 2).

These observations suggest that the initial pummelo introgression into the mandarin gene pool may have involved as few as one pummelo tree (carrying both P1 and P2 haplotypes), the contribution of which was diluted by repeated backcrosses with mandarins (Supplementary Note 6.3). The introgressed pummelo haplotypes became widespread and gave rise to type-2 (early-admixture) mandarins (Fig. 2b). We propose that later, additional pummelo introgressions gave rise to type-3 (late-admixture) mandarins and sweet orange, and that some modern type-3 mandarins were derived from hybridizations among existing mandarins and sweet orange. This late-admixture model for type-3 mandarins is consistent with the historical records for Clementine and

Kiyomi (both mandarin–sweet orange hybrids), and for W. Murcott, Wilking and Fallglo (hybrids involving other type-3 mandarins), whereas definitive records for the remaining two late-admixture mandarins (King and Satsuma) are not available.

Domestication of mandarins and sweet orange

Citrus domestication probably began with the identification and asexual propagation of selected, possibly hybrid or admixed individuals, rather than recurrent selection from a breeding population as for annual crops^{37,38}. Additional diversity was obtained by capturing somatic mutations that occur within a relatively few basic genotypes. Therefore, conventional approaches to identifying selective pressures under recurrent breeding³⁹ cannot be applied. We can, however, use genome sequences to infer some features of the early stages of citrus domestication. Here we focus on mandarins, a class of citrus comprising small and easily peeled fruits that are of high commercial value.

All 28 mandarin accessions, except for Tachibana, exhibit an extensive network of relatedness (with a coefficient of relatedness, $r > 1/8$), and all but four mandarins (three of the four are pure or type-1 mandarins) show second degree or higher relatedness ($r > 1/4$) to at least one (mean = 7) other mandarin (Fig. 3a and Supplementary Note 7). By contrast, sequenced pummelos and citrons appear to be independent selections from relatively large populations. In the

absence of historical records for most mandarins, the actual kinships are difficult to infer, owing to extensive haplotype sharing among the ancestors, although some parent–child pairs can be identified. In addition to confirming, using the whole-genome sequence, the parentage of Wilking (King–Willowleaf), Kiyomi (Satsuma–sweet orange) and Fallglo (one grandparent is Clementine), we find parent–child relationships between two pairs of mandarins (Ponkan is a parent of Dancy; Huanglingmiao (a somatic mutant of Kishu) is a parent of Satsuma)³⁴, in addition to the previously established parent–child pair of Willowleaf and Clementine mandarins². Additional parent–child pairs involving the recently sequenced Chinese mandarins³ are also identified (Supplementary Note 7.3). A few cultivar types in this network (Satsuma, Dancy, Clementine, Kiyomi, Fallglo and the Chinese cultivar BTJ mandarins) have marked signs of inbreeding, indicated by runs of homozygosity (Extended Data Fig. 4a) as a result of shared haplotypes between their parents. The high degree of relatedness among mandarins implies extensive sharing of *C. reticulata* haplotypes.

Sweet orange also shows extensive haplotype sharing at the level of $r > 0.1$ with 25 of the 28 sequenced mandarins (except for three pure or type-1 mandarins; Fig. 3b and Extended Data Fig. 4b). Two late-admixture mandarins (Clementine and Kiyomi) are direct offspring of sweet orange. Among the early-admixture (type-2) mandarins, Ponkan shows the highest affinity to sweet orange² with $r \approx 0.36$. Even the pure mandarin, Sun Chu Sha Kat has $r \approx 0.23$, equivalent to second degree relatedness to sweet orange. We can rule out the scenario that sweet orange is the common ancestor of the mandarins, because of a lack of pummelo haplotypes (derived from sweet orange) among the mandarins. Rather, the extensive *C. reticulata* haplotype sharing between sweet orange and mandarins suggests that the mandarin parent of sweet orange was part of an expansive network of relatedness among mandarins.

Because our collection of mandarins represents a diverse set of both ancient and modern varieties, including economically important accessions with mostly unknown parentage, the presence of an extensive relatedness network was not anticipated a priori. The shared *C. reticulata* haplotypes are suggestive of and consistent with signatures of the human selection process, during which mandarins with desirable traits were necessarily maintained through clonal propagation (nucellar polyembryony or grafting). Although one cannot preclude the possibility that the relatedness network was initiated before domestication from a small number of founder trees, human selection of accessions resulting from natural hybridization probably had a key role in the process of domestication that eventually led to the extensive relatedness network observed today. For example, modern mandarins, such as Clementine and W. Murcott, are known to be selections from chance seedlings found in Algeria⁴⁰ and Morocco², at the onset and middle of the last century, respectively.

Pummelo admixture is correlated with fruit size and acidity, suggesting a role for pummelo introgression in citrus domestication. As both fruit size and acidity profile for the most recently sequenced accessions³ are not described, we used 37 citrus accessions in this analysis. We find that the fruit sizes of mandarins, oranges, grapefruit and pummelos show a strong positive correlation (Pearson correlation coefficient $r = 0.88$) with pummelo admixture proportion (Extended Data Fig. 5a, b and Supplementary Note 10.1). In addition to fruit size, a pivotal driver of fruit domestication is palatability, a characteristic that in citrus requires low to moderate levels of acidity. In mandarins, palatability appears to be linked to pummelo introgression at a major locus at the start of chromosome 8 (0.3–2.2 Mb), where all nine known palatable mandarins, but none of the four known acidic mandarins, show pummelo admixture in at least part of the genomic region (Extended Data Fig. 3). This locus is also found to be significant in a genome scan for palatability association (Extended Data Fig. 5c, d and Extended Data Table 3) and contains several potentially relevant genes (Supplementary Note 10.2). Among these genes is a gene encoding

the mitochondrial NAD⁺-dependent isocitrate dehydrogenase (*IDH*) which regulates citric-acid synthesis⁴¹ (Extended Data Table 4).

Our study finds that domesticated citrus fruit crops, such as mandarins and sweet orange, experienced a complex history of admixture, conceptually similar to those well-recognized in annual crops, such as rice⁴² and maize⁴³, and in other fruit trees, such as apple⁴⁴ and grape⁴⁵, for which the current genomic diversity is linked to widespread ancient introgression. Other cultivated citrus groups, the interspecific F1 hybrids in particular, originated from hybridizations of two pure parental species. Several of these involve *C. medica* (citron), including limes and lemons¹⁰. A unique and critical characteristic of the three pivotal species (*C. maxima*, *C. reticulata* and *C. medica*) that gave rise to most cultivated citrus fruits is the occurrence of a complex floral anatomy (Extended Data Fig. 6), thus leading to the development of more complex fruit. Other species were also involved in hybridizations, including *Fortunella* and *C. micrantha*. Distinct from the mandarin lineages, these hybrids are characterized by their acidic fruit, and their selection must have been made on the basis of other characteristics, such as a sweet edible peel and aroma², respectively.

Conclusion

On the basis of genomic, phylogenetic and biogeographic analyses of 60 diverse citrus and related accessions, we propose that the centre of origin of citrus species was the southeast foothills of the Himalayas, in a region that includes the eastern area of Assam, northern Myanmar and western Yunnan. Our analyses suggest that the ancestral citrus species underwent a sudden speciation event during the late Miocene. This radiation coincided with a pronounced transition from wet monsoon conditions to a drier climate, as observed in nearby areas in many other plant and animal lineages. The Australian citrus species and Tachibana, a native Japanese mandarin, split later from mainland citrus during the early Pliocene and Pleistocene, respectively. By distinguishing between pure species, hybrids and admixtures, we could trace the genealogy and genetic origin of the major citrus commercial cultivars. Both the extensive relatedness network among mandarins and sweet orange, and the association of pummelo admixture with desirable fruit traits suggest a complex domestication process.

Our work challenges previous proposals for citrus taxonomy. For example, we find that several named genera (*Fortunella*, *Eremocitrus* and *Microcitrus*) are in fact nested within the citrus clade. These and other distinct clades that we have identified are therefore more appropriately considered species within the genus *Citrus*, on a par with those that formerly were referred to as the three ‘true’ or ‘biological’ species (*C. reticulata*, *C. maxima* and *C. medica*). Additionally, the related genus, *Poncirus*, a subject of continuous controversy since it was originally proposed to be within the genus *Citrus*^{12,46}, is clearly a distinct clade that is separate from *Citrus* based on sequence divergence and whole-genome phylogeny.

In summary, this work presents insights into the origin, evolution and domestication of citrus, and the genealogy of the most important wild and cultivated varieties. Taken together, these findings draw a new evolutionary framework for these fruit crops, a scenario that challenges current taxonomic and phylogenetic thoughts, and points towards a reformulation of the genus *Citrus*.

Online Content Methods, along with any additional Extended Data display items and Source Data, are available in the online version of the paper; references unique to these sections appear only in the online paper.

Received 15 November 2016; accepted 10 December 2017.

Published online 7 February 2018.

- Swingle, W. T. & Reece, P. C. in *The Citrus Industry, revised 2nd edn, History, World Distribution, Botany, and Varieties* Vol. 1 (eds Reuther, W. et al.) 190–430 (Univ. California, 1967).

2. Wu, G. A. *et al.* Sequencing of diverse mandarin, pummelo and orange genomes reveals complex history of admixture during citrus domestication. *Nat. Biotechnol.* **32**, 656–662 (2014).
3. Wang, X. *et al.* Genomic analyses of primitive, wild and cultivated citrus provide insights into asexual reproduction. *Nat. Genet.* **49**, 765–772 (2017).
4. Mudge, K., Janick, J., Scofield, S. & Goldschmidt, E. E. A history of grafting. *Hortic. Rev. (Am. Soc. Hortic. Sci.)* **35**, 437–493 (2009).
5. Swingle, W. in *The Citrus Industry, History Botany and Breeding* Vol. 1 (eds Webber, H. J. & Batchelor, L. D.) 129–474 (Univ. California Press, 1943).
6. Tanaka, T. *Species Problem in Citrus* (Japanese Society for Promotion of Science, 1954).
7. Xu, Q. *et al.* The draft genome of sweet orange (*Citrus sinensis*). *Nat. Genet.* **45**, 59–66 (2013).
8. Barrett, H. & Rhodes, A. A numerical taxonomic study of affinity relationships in cultivated *Citrus* and its close relatives. *Syst. Bot.* **1**, 105–136 (1976).
9. Scora, R. W. On the history and origin of *Citrus*. *Bull. Torrey Bot. Club* **102**, 369–375 (1975).
10. Curk, F. *et al.* Phylogenetic origin of limes and lemons revealed by cytoplasmic and nuclear markers. *Ann. Bot.* **117**, 565–583 (2016).
11. Nicolosi, E. *et al.* Citrus phylogeny and genetic origin of important species as investigated by molecular markers. *Theor. Appl. Genet.* **100**, 1155–1166 (2000).
12. Bayer, R. J. *et al.* A molecular phylogeny of the orange subfamily (Rutaceae: Aurantioideae) using nine cpDNA sequences. *Am. J. Bot.* **96**, 668–685 (2009).
13. Jacques, F. M. *et al.* Late Miocene southwestern Chinese floristic diversity shaped by the southeastern uplift of the Tibetan Plateau. *Palaeogeogr. Palaeoclimatol. Palaeoecol.* **411**, 208–215 (2014).
14. Jacques, F. M. *et al.* Quantitative reconstruction of the Late Miocene monsoon climates of southwest China: a case study of the Lincang flora from Yunnan Province. *Palaeogeogr. Palaeoclimatol. Palaeoecol.* **304**, 318–327 (2011).
15. Gmitter, F. G. & Hu, X. L. The possible role of Yunnan, China, in the origin of contemporary citrus species (Rutaceae). *Econ. Bot.* **44**, 267–277 (1990).
16. Xie, S., Manchester, S. R., Liu, K., Wang, Y. & Sun, B. *Citrus lincangensis* sp. n., a leaf fossil of Rutaceae from the late Miocene of Yunnan, China. *Int. J. Plant Sci.* **174**, 1201–1207 (2013).
17. Clift, P. D., Wan, S. & Blusztajn, J. Reconstructing chemical weathering, physical erosion and monsoon intensity since 25 Ma in the northern South China Sea: a review of competing proxies. *Earth Sci. Rev.* **130**, 86–102 (2014).
18. Valdiya, K. S. Emergence and evolution of Himalaya: reconstructing history in the light of recent studies. *Prog. Phys. Geogr.* **26**, 360–399 (2002).
19. Wen, J., Zhang, J. Q., Nie, Z. L., Zhong, Y. & Sun, H. Evolutionary diversifications of plants on the Qinghai-Tibetan Plateau. *Front. Genet.* **5**, 4 (2014).
20. Favre, A. *et al.* The role of the uplift of the Qinghai-Tibetan Plateau for the evolution of Tibetan biotas. *Biol. Rev. Camb. Philos. Soc.* **90**, 236–253 (2015).
21. Pfeil, B. E. & Crisp, M. D. The age and biogeography of *Citrus* and the orange subfamily (Rutaceae: Aurantioideae) in Australasia and New Caledonia. *Am. J. Bot.* **95**, 1621–1631 (2008).
22. Beattie, G. A. C., Holford, P., Mabblerley, D. J., Haigh, A. M. & Broadbent, P. in *On the origins of Citrus, Huanglongbing, Diaphorina citri and Trioza erytreae. International Conference of Huanglongbing* (eds Gottwald, T. R. & Graham, J. H.) 25–57 (Plant Management Network, 2009).
23. Thomas, D. C. *et al.* West to east dispersal and subsequent rapid diversification of the mega-diverse genus *Begonia* (Begoniaceae) in the Malesian archipelago. *J. Biogeogr.* **39**, 98–113 (2012).
24. Richardson, J. E., Costion, C. M. & Muellner, A. N. in *Biotic Evolution and Environmental Change in Southeast Asia* Ch. 6 (eds Gower, D. *et al.*) 138–163 (Cambridge Univ. Press, 2012).
25. van Welzen, P. C., Slik, J. W. F. & Alahuhta, J. Plant distribution patterns and plate tectonics in Malesia. *Biol. Skr.* **55**, 199–217 (2005).
26. Hall, R. Southeast Asia's changing palaeogeography. *Blumea* **54**, 148–161 (2009).
27. Zhang, W. *Thirty years achievements in citrus varietal improvement in China in Proc. International Citrus Congress* (ed. Matsumoto, K.) 51–53 (International Society of Citriculture, 1982–1983).
28. Brophy, J. J., Goldsack, R. J. & Forster, P. I. The leaf oils of the Australian species of *Citrus* (Rutaceae). *J. Essent. Oil Res.* **13**, 264–268 (2001).
29. Tanaka, T. The discovery of *Citrus tachibana* in Formosa, and its scientific and industrial significance. *Studia Citrologica* **5**, 1–20 (1931).
30. Gibbard, P. & Cohen, K. M. Global chronostratigraphical correlation table for the last 2.7 million years. *Episodes* **31**, 243–247 (2008).
31. Chiang, T.-Y. & Schaal, B. A. Phylogeography of plants in Taiwan and the Ryukyu Archipelago. *Taxon* **55**, 31–41 (2006).
32. Voris, H. K. Maps of Pleistocene sea levels in southeast Asia: shorelines, river systems and time durations. *J. Biogeogr.* **27**, 1153–1167 (2000).
33. Huang, S.-F. Hypothesizing origin, migration routes and distribution patterns of gymnosperms in Taiwan. *Taiwania* **59**, 139–163 (2014).
34. Shimizu, T. *et al.* Hybrid origins of citrus varieties inferred from DNA marker analysis of nuclear and organelle genomes. *PLoS ONE* **11**, e0166969 (2016).
35. Hirai, M., Mitsue, S., Kita, K. & Kajiuira, I. A survey and isozyme analysis of wild mandarin, *Tachibana* (*Citrus tachibana* (Mak.) Tanaka) growing in Japan. *J. Jpn. Soc. Hortic. Sci.* **59**, 1–7 (1990).
36. Hagerly, M. J. Han Yen-Chih's Chü lu (monograph on the oranges of Wên-chou, Chekiang). *Toung Pao* **22**, 63–96 (1923).
37. Miller, A. J. & Gross, B. L. From forest to field: perennial fruit crop domestication. *Am. J. Bot.* **98**, 1389–1414 (2011).
38. Gaut, B. S., Díez, C. M. & Morrell, P. L. Genomics and the contrasting dynamics of annual and perennial domestication. *Trends Genet.* **31**, 709–719 (2015).
39. Hamblin, M. T., Buckler, E. S. & Jannink, J. L. Population genetics of genomics-based crop improvement methods. *Trends Genet.* **27**, 98–106 (2011).
40. Trabut, J. L'hybridation des Citrus: une nouvelle tangérine 'la Clémentine'. *Revue Horticole* **10**, 232–234 (1902).
41. Meléndez-Hevia, E., Waddell, T. G. & Cascante, M. The puzzle of the Krebs citric acid cycle: assembling the pieces of chemically feasible reactions, and opportunism in the design of metabolic pathways during evolution. *J. Mol. Evol.* **43**, 293–303 (1996).
42. Gross, B. L. & Zhao, Z. Archaeological and genetic insights into the origins of domesticated rice. *Proc. Natl Acad. Sci. USA* **111**, 6190–6197 (2014).
43. Hufford, M. B. *et al.* The genomic signature of crop-wild introgression in maize. *PLoS Genet.* **9**, e1003477 (2013).
44. Cornille, A. *et al.* New insight into the history of domesticated apple: secondary contribution of the European wild apple to the genome of cultivated varieties. *PLoS Genet.* **8**, e1002703 (2012).
45. Myles, S. *et al.* Genetic structure and domestication history of the grape. *Proc. Natl Acad. Sci. USA* **108**, 3530–3535 (2011).
46. Nesom, G. L. *Citrus trifoliata* (Rutaceae): review of biology and distribution in the USA. *Phytoneuron* **46**, 1–14 (2014).

Supplementary Information is available in the online version of the paper.

Acknowledgements Please see Supplementary Note 11 for funding information.

Author Contributions M.T., D.S.R. and G.A.W. developed the project and acted as project coordinators and provided scientific leadership; G.A.W. developed methods for admixture analysis and interspecific phasing, and performed comparative genome analysis. J.T., V.I., A.L.-G., E.P.-R., C.B., C.D., F.R.T., J.C.-C., R.A., J.D. and M.T. contributed 26 genomes; J.T., J.C.-C., R.A. and J.D. provided bioinformatics support; J.T. and E.P.-R. contributed to the study of the *IDH* gene; V.I., E.P.-R. and C.B. contributed to the variant analysis of candidate genes using genome-wide association studies; A.L.-G. and C.B. assisted in the biogeographic study; A.L.-G. and F.G.G. contributed to the description of citrus accessions and discriminatory characteristics; P.O. and F.C. contributed to germplasm, admixture analysis and hypothesis on the origin of cultivated citrus species; D.D. and F.G.G. contributed one citrus genome; M.L.R. contributed seven citrus genomes; F.G.G. contributed perspective garnered from more than 35 years of experience working on the genetic improvement of citrus; G.A.W., M.T., D.S.R. and F.G.G. wrote the manuscript; G.A.W. and M.T. contributed the hypothesis on the origin and dispersal of citrus.

Author Information Reprints and permissions information is available at www.nature.com/reprints. The authors declare no competing financial interests. Readers are welcome to comment on the online version of the paper. Publisher's note: Springer Nature remains neutral with regard to jurisdictional claims in published maps and institutional affiliations. Correspondence and requests for materials should be addressed to G.A.W. (gwu@lbl.gov), D.S.R. (dsroksar@gmail.com) or M.T. ([talón_man@gva.es](mailto:talon_man@gva.es)).

Reviewer Information Nature thanks J. Ross-Ibarra, P. Wincker and the other anonymous reviewer(s) for their contribution to the peer review of this work.



This work is licensed under a Creative Commons Attribution 4.0 International (CC BY 4.0) licence. The images or other third party material in this article are included in the article's Creative Commons licence, unless indicated otherwise in the credit line; if the material is not included under the Creative Commons licence, users will need to obtain permission from the licence holder to reproduce the material. To view a copy of this licence, visit <http://creativecommons.org/licenses/by/4.0/>.

METHODS

Sample collection and sequencing. Whole-genome sequences from a total of 60 accessions were analysed: 58 citrus accessions with different geographical origins and two representative outgroup genera. Twelve of these genomes, including five mandarins, four pummelos, two oranges and a wild Mangshan mandarin (*C. mangshanensis*) were reanalysed from previous works^{2,7}. We also reanalysed 19 genomes from Chinese collections, including 15 unnamed mandarins, 2 Chinese sour oranges, Ambersweet orange and Cocktail grapefruit (a hybrid resembling grapefruit) that have been previously reported³.

The 30 accessions that were newly sequenced came from citrus germ-plasm banks and collections at IVIA, Valencia, Spain; SRA, Corse, France; UCR, Riverside and FDACS/DPI, Florida and included nine mandarins, two limes, one rough lemon, one grapefruit, one lemon, four citrons, one Australian desert lime, one eremorange, two Australian finger limes, two Australian round limes, one kumquat, one calamondin, one micrantha, one Ichang papeda, one trifoliate orange and one Chinese box orange (Supplementary Note 1).

DNA libraries were constructed using standard protocols with some modifications. Library insert sizes range from 325 to 500 bp. Sequencing was performed on HiSeq2000/2500 instruments using 100-bp paired-end reads. Primary analysis of the data included quality control on the Illumina RTA sequence analysis pipeline (Supplementary Note 2).

Variant calls and *Citrus* species diversity. Illumina paired-end reads were aligned to the haploid Clementine reference sequence² and the sweet orange chloroplast genome assembly⁴⁷ using bwa-mem⁴⁸. PCR duplicates were removed using Picard. Raw variants were called using GATK HaplotypeCaller⁴⁹ with subsequent filtering based on read map quality score, base quality score, read depth and so on (Supplementary Note 3.1).

Interspecific admixtures versus pure citrus species were distinguished based on sliding window analysis of heterozygosity and pairwise genetic distance D (Supplementary Note 4). Genome-wide ancestry informative markers for the progenitor species were derived using pure accessions. Admixture analysis was carried out in sliding windows using ancestry informative markers (Supplementary Notes 5).

Citrus relatedness and haplotype sharing. Interspecific phasing was used to extract admixed haplotypes. Identical-by-descent sharing was calculated for each of the non-overlapping sliding windows across the genome and used to estimate coefficient of relatedness among citrus accessions (Supplementary Notes 6, 7).

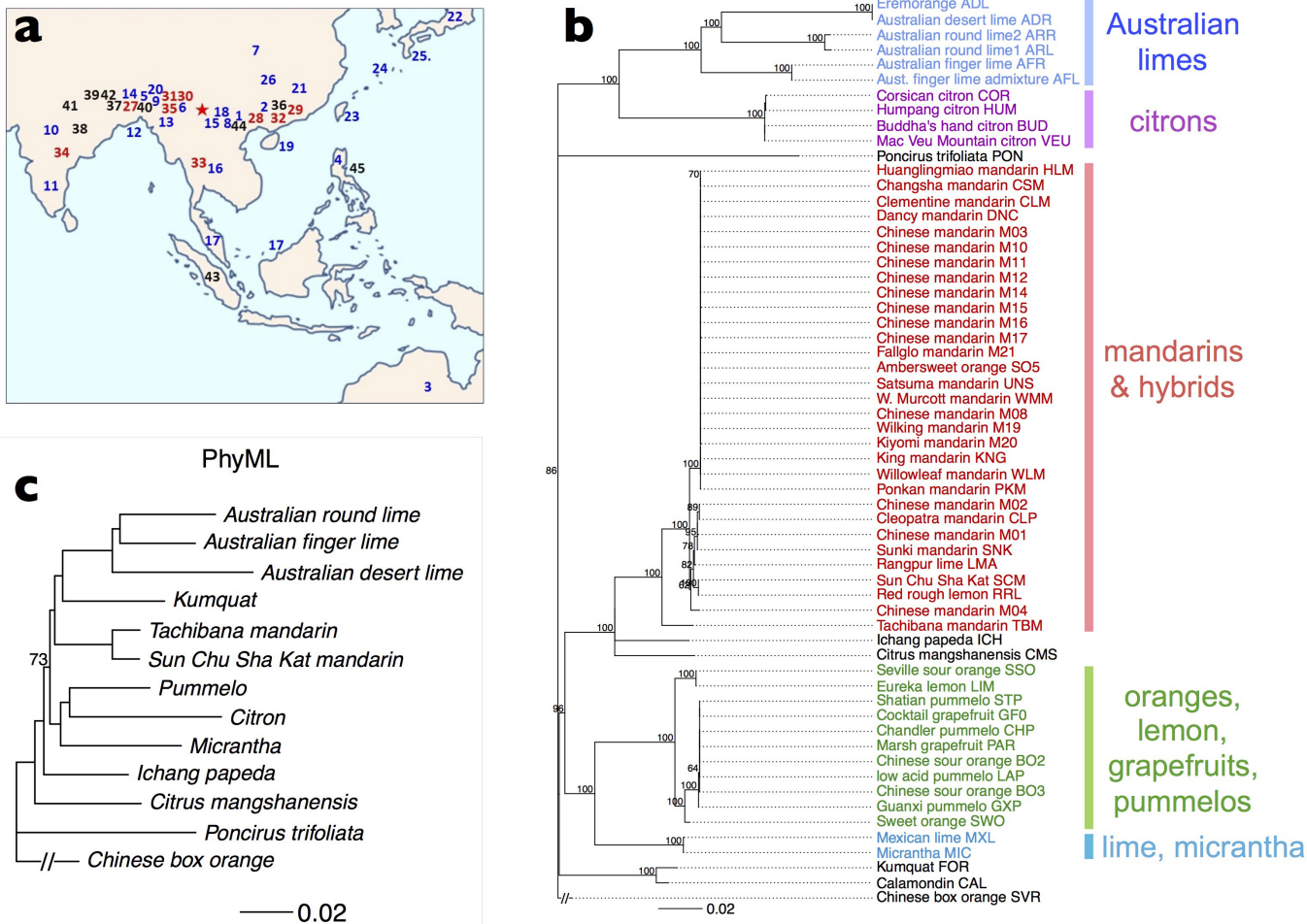
Phylogeny and speciation dating. We used Chinese box orange (genus *Severinia*) as an outgroup. Time calibration is based on the *C. linczangensis*¹⁶ fossil from Lincang, Yunnan, China. MrBayes⁵⁰ was used for whole genome Bayesian

phylogenetic inference, and corroborated with a PhyML⁵¹ reconstructed maximum likelihood tree. A penalized likelihood method⁵² as implemented in APE⁵³ was used to construct the chronogram (Supplementary Note 8).

Genome scan of palatability association. We used a mixed linear model as implemented in gemma⁵⁴ for a case-control study of citrus acidity and palatability with 37 citrus accessions. A conservative Bonferroni correction was used to select significant genomic loci, with subsequent manual examination of each candidate variant in all accessions to identify most discriminatory loci for fruit palatability (Supplementary Note 10).

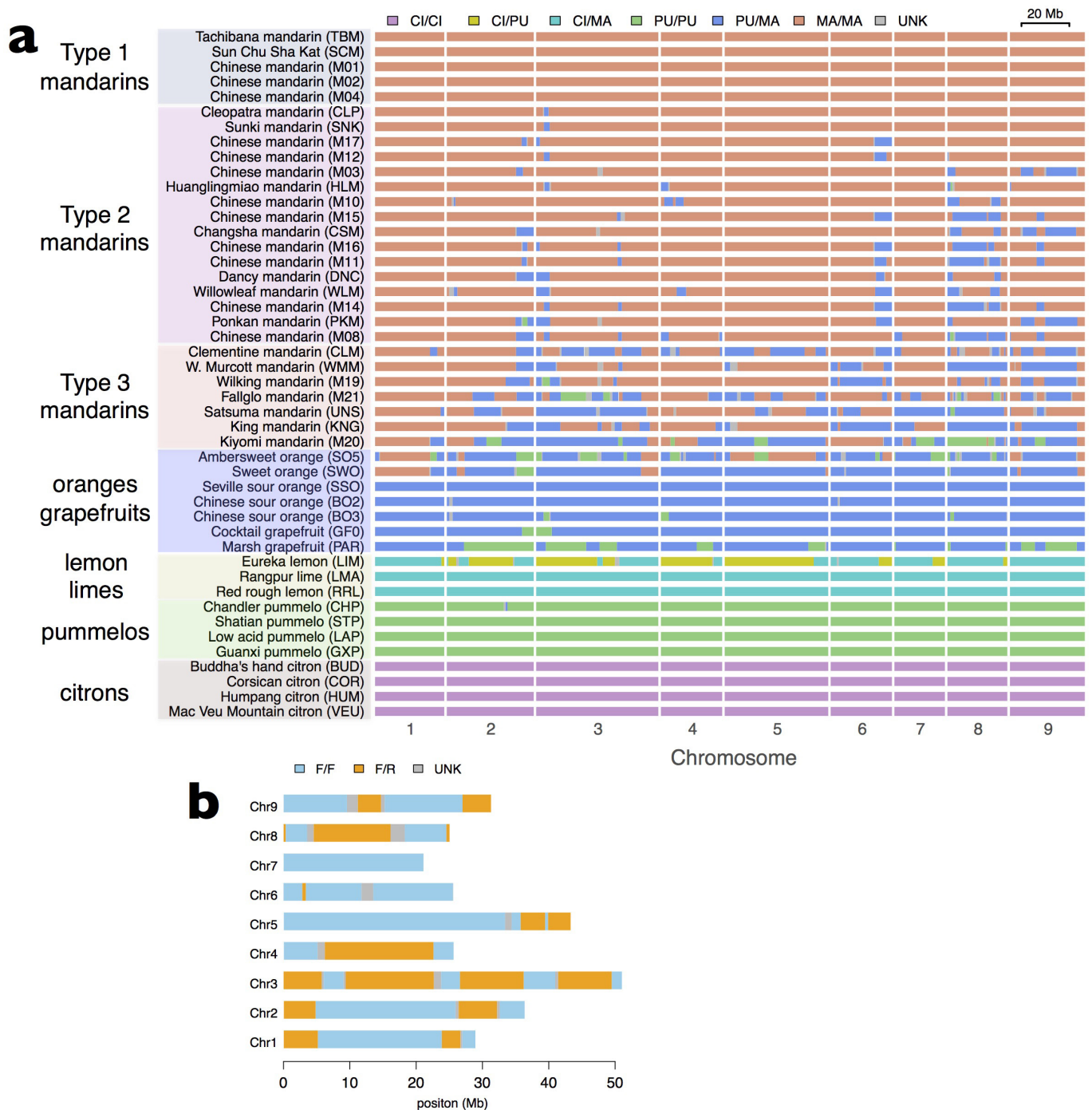
Data availability. Whole-genome shotgun-sequencing data generated in this study have been deposited at NCBI under BioProject PRJNA414519. Prior resequencing data analysed here can be accessed under BioProject accession numbers PRJNA320985 (mandarins) and PRJNA321100 (oranges), and also under the NCBI Sequence Read Archive accession codes SRX372786 (sour orange), SRX372703 (sweet orange), SRX372702 (low-acid pummelo), SRX372688 (Chandler pummelo), SRX372685 (Willowleaf mandarin), SRX372687 (W. Murcott mandarin), SRX372665 (Ponkan mandarin) and SRX371962 (Clementine mandarin). The Clementine reference sequence used here is available at <https://phytozome.jgi.doe.gov/>.

47. Bausher, M. G., Singh, N. D., Lee, S. B., Jansen, R. K. & Daniell, H. The complete chloroplast genome sequence of *Citrus sinensis* (L.) Osbeck var 'Ridge Pineapple': organization and phylogenetic relationships to other angiosperms. *BMC Plant Biol.* **6**, 21 (2006).
48. Li, H. & Durbin, R. Fast and accurate long-read alignment with Burrow-Wheeler transform. *Bioinformatics* **26**, 589–595 (2010).
49. McKenna, A. *et al.* The Genome Analysis Toolkit: a MapReduce framework for analyzing next-generation DNA sequencing data. *Genome Res.* **20**, 1297–1303 (2010).
50. Ronquist, F. *et al.* MrBayes 3.2: efficient Bayesian phylogenetic inference and model choice across a large model space. *Syst. Biol.* **61**, 539–542 (2012).
51. Guindon, S. *et al.* New algorithms and methods to estimate maximum-likelihood phylogenies: assessing the performance of PhyML 3.0. *Syst. Biol.* **59**, 307–321 (2010).
52. Sanderson, M. J. Estimating absolute rates of molecular evolution and divergence times: a penalized likelihood approach. *Mol. Biol. Evol.* **19**, 101–109 (2002).
53. Paradis, E., Claude, J. & Strimmer, K. APE: analyses of phylogenetics and evolution in R language. *Bioinformatics* **20**, 289–290 (2004).
54. Zhou, X. & Stephens, M. Genome-wide efficient mixed-model analysis for association studies. *Nat. Genet.* **44**, 821–824 (2012).
55. Frost, H. B. & Soost, R. K. in *The Citrus Industry* Vol. 2 (eds Reuther, W. *et al.*) 290–324 (1968).

Extended Data Figure 1 | *Citrus* biogeography and phylogeny.

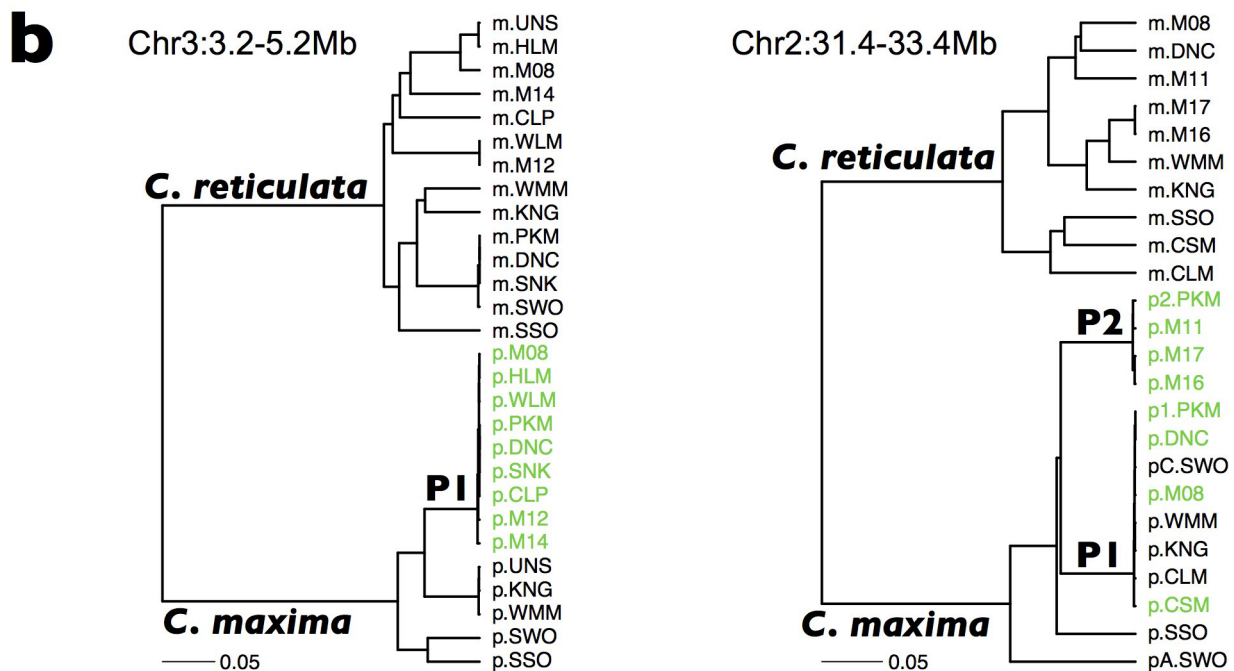
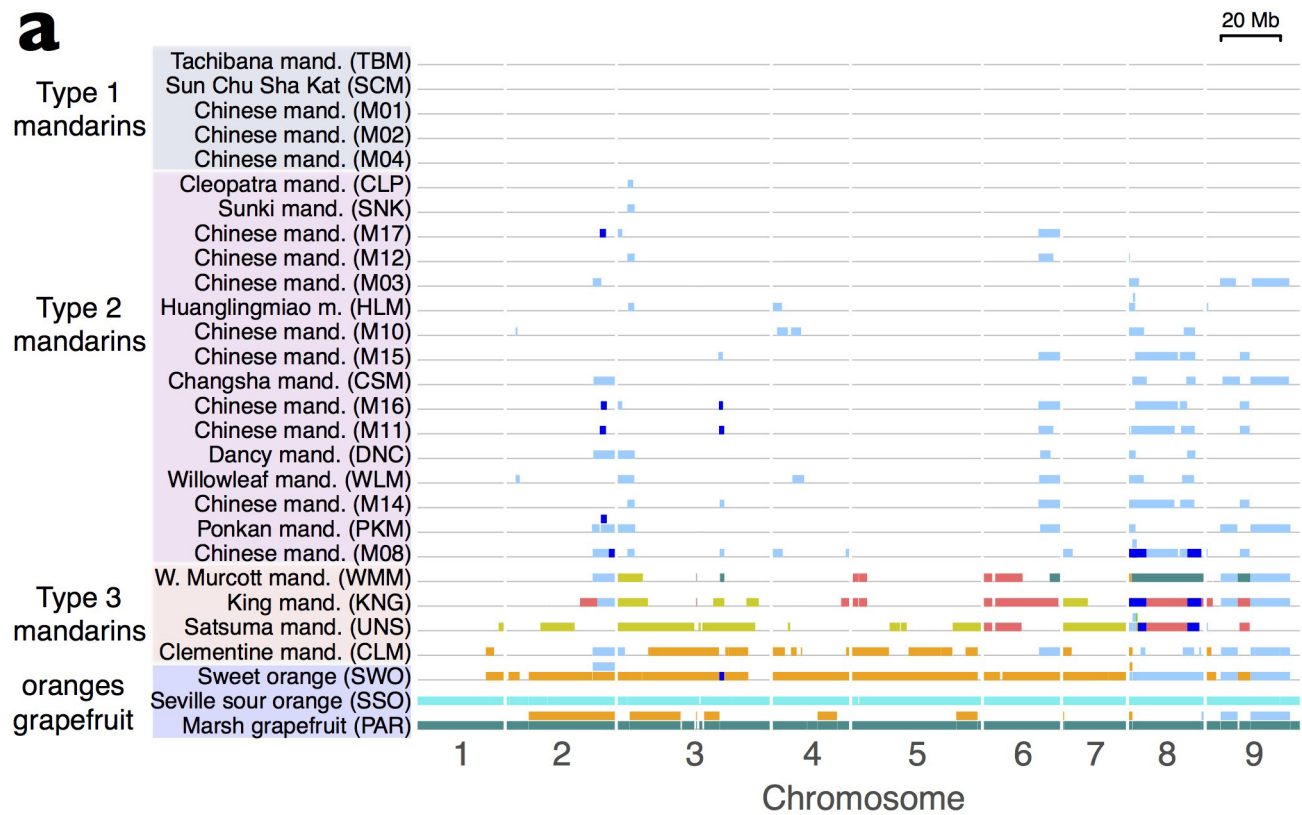
a, Geographical distribution of the genus *Citrus* in southeast Asia and Australia. Distribution is based on documented reports on the presence of wild genotypes representative of pure citrus species (blue numbers), admixtures (red numbers) and relevant interspecific hybrids (black numbers), growing freely in non-cultivated areas. Numbers are as in Supplementary Table 1. 1, 2, *Fortunella* spp. ; 3, Australian citrus (*E. glauca*; *Microcitrus australasica*; *Microcitrus australis*); 4, *C. micrantha*; 5–8, *C. ichangensis*; 9–15, *C. medica*; 16–19, *C. maxima*; 20–22, *C. reticulata* (Sun Chu Sha Kat); 23–25, *C. tachibana*; 26, *C. mangshanensis*; 27–29, *Citrus* spp. (mandarins); 30–33, *C. sinensis*; 34, 35, *Citrus limon* (probably not truly wild genotypes); 36, 37, *Citrus limonia*; 38, *Citrus jambhiri*; 39–42, *C. aurantium*; 43, *Citrus aurantifolia* (probably not truly wild

genotypes); 44, 45, *Fortunella* and *C. reticulata* hybrid. The red star indicates the location of the *C. lincangensis* fossil from the Late Miocene of Lincang¹⁶. **b**, Citrus chloroplast genome phylogeny rooted with *Severinia*. The analysis was performed on 58 citrus accessions and 2 outgroup genera, *Poncirus* and *Severinia*. The maximum likelihood tree as inferred from PhyML is shown. Percentage statistical support for the nodes is based on 200 bootstrap replicates. **c**, Citrus nuclear genome phylogeny rooted with *Severinia*. Both Bayesian and maximum likelihood trees yield the same topology with highly supported branches. The maximum likelihood tree reconstructed from PhyML is shown. Branch statistical support is based on 1,000 bootstraps and is shown if it is less than 100%. All branches have posterior probability 1.0 with Bayesian inference using MrBayes (not shown).



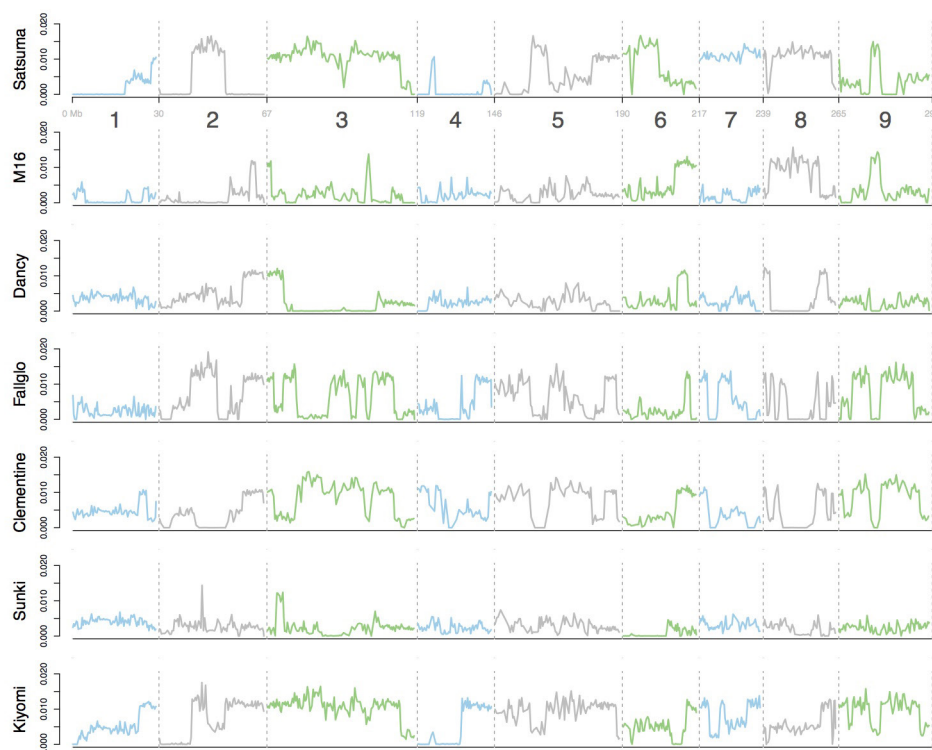
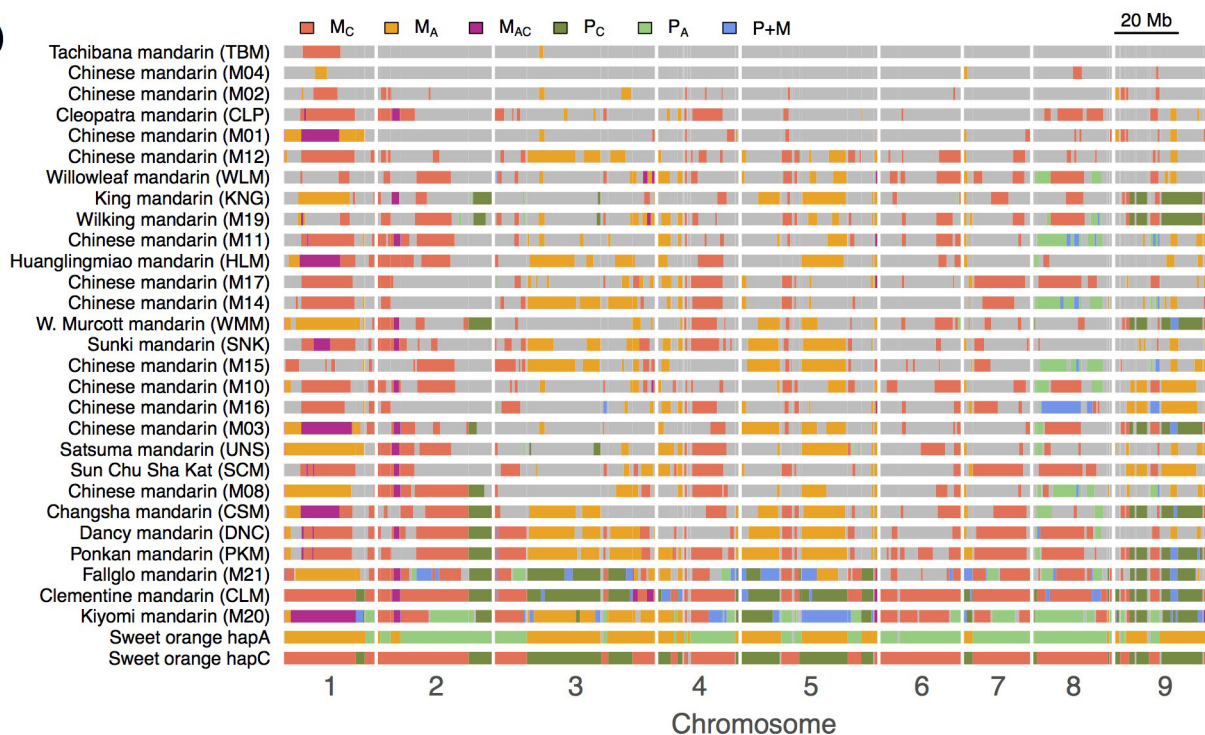
Extended Data Figure 2 | Segmental ancestry and admixture in citrus.
a, Segmental ancestry of 46 citrus accessions derived from the three progenitor species of *C. medica* (CI), *C. maxima* (PU) and *C. reticulata* (MA). UNK, unknown. Mandarins are divided into three types with type-1 representing pure mandarins. Types 2 and 3 are determined by the

pummelo admixture pattern. **b**, Segmental ancestry of an Australian finger lime. Blue segments denote pure finger lime (genotype: F/F), and orange segments have Australian round lime admixture (genotype: F/R). Genomic regions are coloured in grey if segmental ancestry cannot be determined.



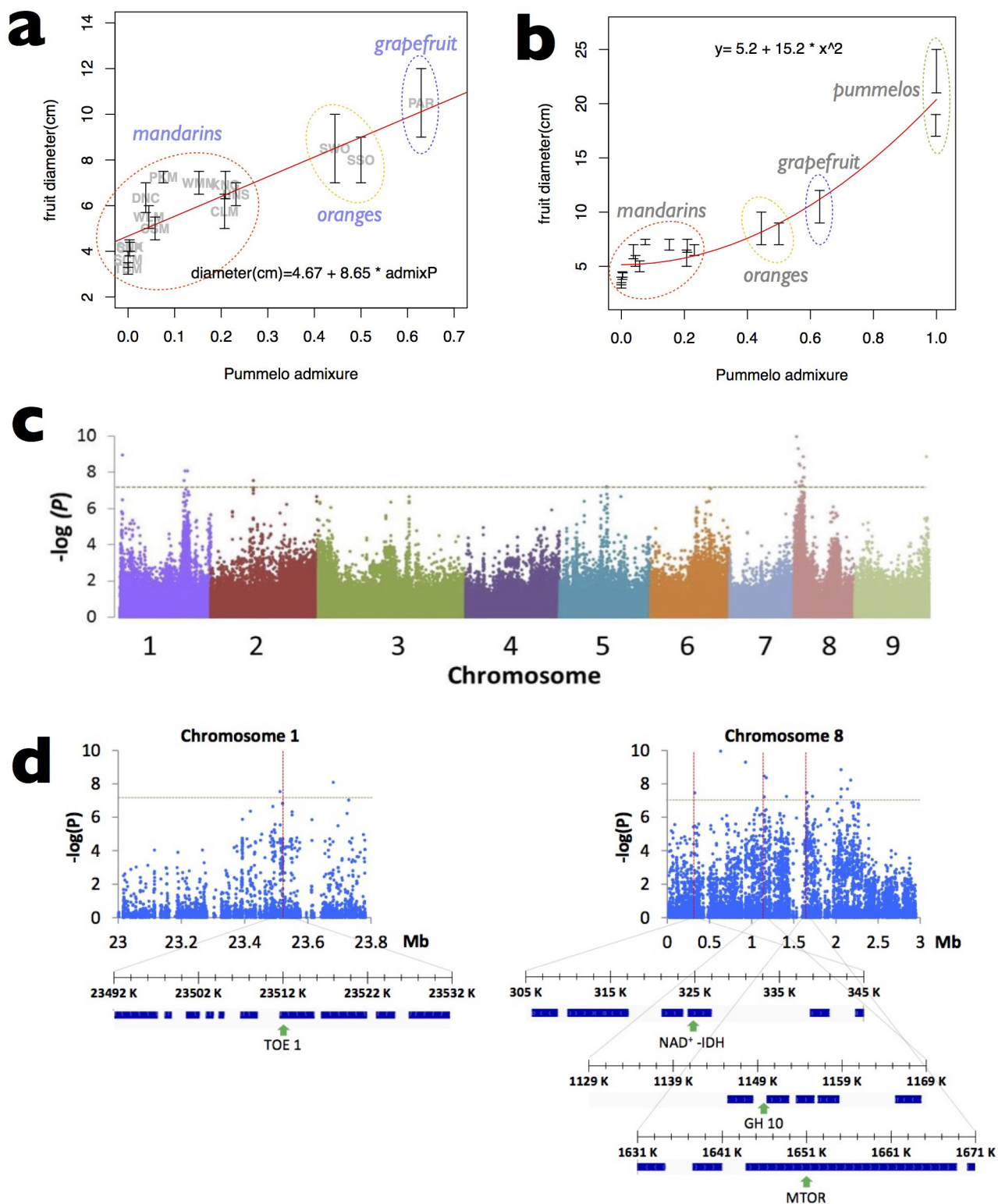
Extended Data Figure 3 | Pattern of pummelo introgression in mandarins. **a**, Distinct admixed pummelo haplotypes among mandarins, oranges and grapefruit are shown in different colours; the *C. reticulata* haplotypes are masked. The admixture pattern separates the mandarins into three groups, with type-1 representing pure mandarins. Type-2 mandarins contain a small amount of pummelo admixture derived from two *C. maxima* haplotypes: P1 (light blue colour) and P2 (dark blue), suggesting as few as one common pummelo ancestor in the distant past. Type-3 mandarins are characterized by both marked pummelo admixture and additional pummelo haplotypes besides P1 and P2. **b**, Haplotype trees for two chromosome segments where pummelo haplotypes of

type-2 mandarins are in green. Left, haplotype tree for chr3:3.2–5.2 Mb. Sweet orange, sour orange, and twelve of the sequenced mandarins are interspecific hybrids, and their phased *C. maxima* and *C. reticulata* haplotypes are denoted by prepending, respectively, 'p' and 'm' to the corresponding accession codes. The nine type-2 mandarins share the same pummelo haplotype (P1). Right, the haplotype tree for chr2:31.4–33.4 Mb. Two pummelo haplotypes (P1, P2) are shared among seven type-2 mandarins, with Ponkan mandarin containing both P1 and P2. Sweet orange also carries two pummelo haplotypes at this locus, denoted by pC.SWO (shared with Clementine) and pA.SWO (alternate haplotype).

a**b**

Extended Data Figure 4 | Haplotype sharing in mandarins. a, Runs of homozygosity in mandarins. Heterozygosity is plotted in non-overlapping windows of 200 kb along the nine chromosomes of 7 mandarin accessions with the highest degree of inbreeding. Runs of homozygosity correspond to regions with zero heterozygosity as a result of haplotype sharing between the parents. **b,** Haplotype sharing between sweet orange and mandarins. The two haplotypes of sweet orange are denoted by hapC (transmitted to Clementine) and hapA (alternate), respectively. The hapC haplotype is coloured in red (denoted by M_C) or dark green (denoted

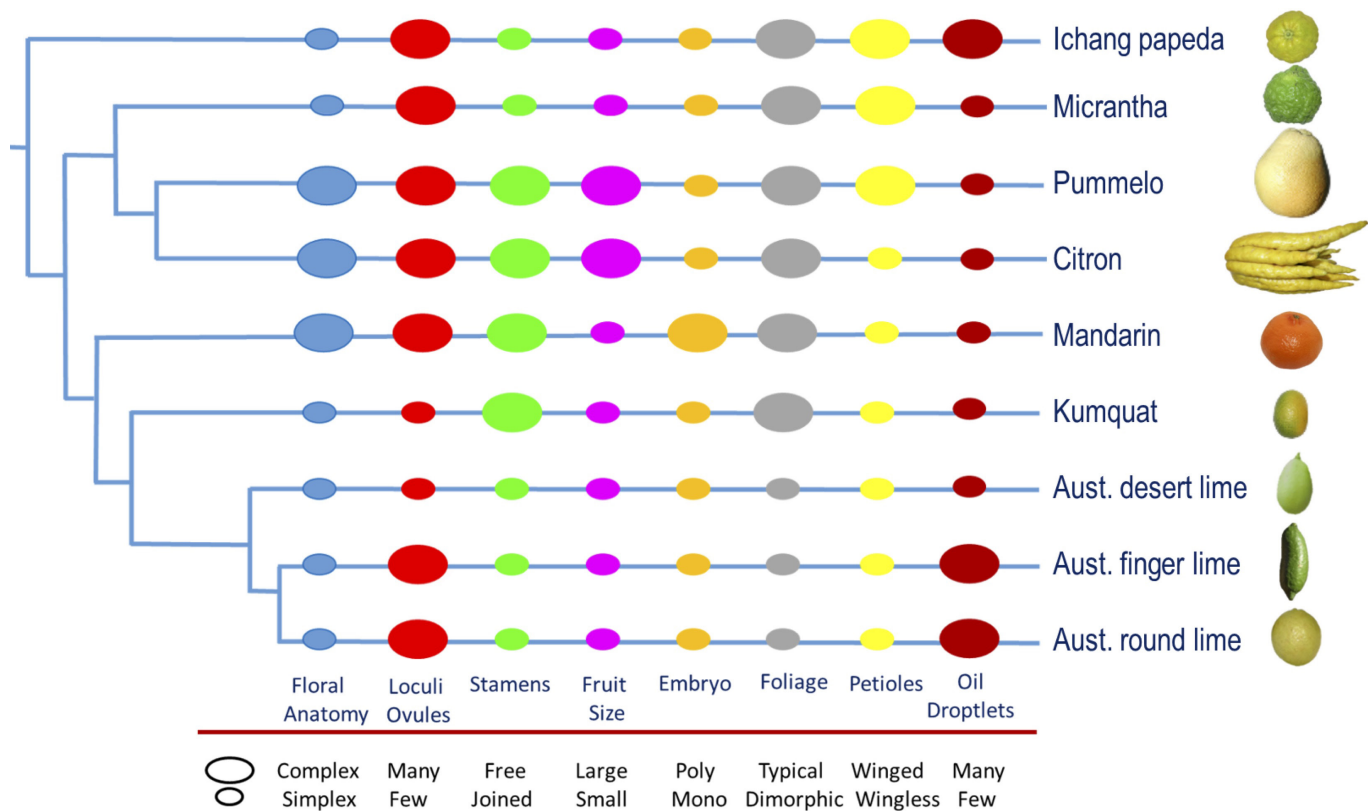
by P_C) if its genetic ancestry is *C. reticulata* or *C. maxima*, respectively. Similarly, hapA can take the form of *C. reticulata* (M_A in orange colour) or *C. maxima* (P_A in light green) depending on its genetic ancestry. Shared sweet orange haplotypes in mandarins are coloured accordingly, except when both haplotypes of sweet orange are shared (IBD2) either as two *C. reticulata* haplotypes (M_{AC} , dark red) or as interspecific hybrid ($P + M$, blue). Regions coloured in grey denote the absence of haplotype sharing between sweet orange and mandarin.



Extended Data Figure 5 | See next page for caption.

Extended Data Figure 5 | Fruit size and acidity correlated with pummelo introgression. **a**, Fruit size strongly correlated with pummelo admixture. The diameters of mandarins, oranges and grapefruit are plotted against the corresponding pummelo admixture proportions. A simple linear regression is shown in red. The strong correlation (Pearson correlation coefficient $r = 0.88$) between fruit size and pummelo admixture is apparent, especially among the three taxonomic groups of mandarins, oranges and grapefruit. The outliers (Ponkan mandarin and four acidic mandarins) suggest that certain genomic loci could be more important than others in fruit size determination. Accessions without size information are not included. Data are mean \pm s.d. from a set of 25 measurements for each of the 15 accessions. **b**, Fruit size correlation with pummelo allelic proportion with the addition of two pummelos. A polynomial regression provides a better fit than simple linear regression (adjusted $R^2 = 0.92$). Data are mean \pm s.d. from a set of 25 measurements for each of the 17 accessions. **c**, Genome scan of

significant loci associated with citrus acidity. Manhattan plot of a case-control analysis of a genome-wide association study (GWAS) of $n = 37$ citrus accessions with known acidity profile. The horizontal dashed line denotes the conservative Bonferroni-corrected P value of 7.9×10^{-8} for genome-wide significance ($\alpha = 0.05$). **d**, Manual inspection of candidate regions identified by GWAS ($n = 37$ accessions) demonstrates that in addition to the locus at chr1:23512067, single-nucleotide polymorphisms located in chromosome 8 are discriminatory for acidity. Shown are 40-kb zoom windows containing focal single-nucleotide polymorphisms (red vertical lines and green arrows) and gene models depicted by blue boxes in these two regions. *TOE1*, target of EGR1 protein 1 (Ciclev10007611; <https://phytozome.jgi.doe.gov/pz/portal.html>); NAD $^{+}$ -IDH, NAD $^{+}$ -dependent isocitrate dehydrogenase (*IDH*, Ciclev10028714); GH10, glycosyl hydrolase family 10 protein (Ciclev10028121) and MTOR, serine/threonine protein kinase (Ciclev10027661).



Extended Data Figure 6 | Species characteristics of citrus. Reproductive and vegetative characteristics among several species of the genus *Citrus* and related genera according to refs 1 and 55. The tree topology represented is that of the chronogram shown in Fig. 1c and citrus fruit images are not drawn to scale. Most mandarins in our collection are polyembryonic, though a few are monoembryonic, including Clementine. Other exceptions to the generalized description concerning embryo numbers, in kumquat and other citrus species, can also be found.

Extended Data Table 1 | Citrus interspecies divergence and intraspecies diversity

ADR	AFR	ARL	BUD	LAP	SCM	MIC	FOR	ICH	CMS	PON	SVR	
4.291	13.85	15.19	21.64	18.64	18.11	20.23	18.61	17.87	19.34	24.4	36.76	Aus. desert lime
	6.246	11.37	18.92	15.76	16.96	17.67	15.97	15.31	16.36	21.84	34.4	Aus. finger lime
		5.483	21.98	17.85	20.14	20.59	18.82	18.22	18.02	24.97	37.12	Aus. round lime
			1.092	15.66	19.88	18.84	18.9	17.46	17.68	24.27	36.24	Citron
				3.786	15.44	14.71	14.6	12.77	14.45	19.85	32.46	Pummelo
					3.678	18.51	15.86	14.66	14.87	22.33	34.17	Mandarin
						3.893	17.28	16.02	16.57	23.24	35.56	Micrantha
							5.836	14.32	14.49	21.39	34.01	<i>Fortunella</i>
								4.758	13.16	19.79	32.77	Ichang papeda
									3.082	18.8	32.55	<i>C. mangshanensis</i>
										3.16	36.31	<i>Poncirus</i>
											6.479	<i>Severinia</i>

Average pairwise sequence divergences between ten citrus species and two out groups (*Poncirus* and *Severinia*) are listed, in unit of 10^{-3} . Each citrus species is represented by one diploid genotype free from interspecific admixture. Intraspecies variation is measured by the nucleotide diversity (that is, mean sequence divergence between the two haploid sequences of a diploid), and is represented along the diagonal in units of 10^{-3} . The species names and the codes of the representative accessions are given in the last column and first row, respectively. Note the wide separation between interspecies divergence and intraspecies variation. See Supplementary Table 2 for details and definitions.

Extended Data Table 2 | Admixture proportions of 50 citrus accessions derived from five progenitor species

	Code	PU/PU	PU/MA	MA/MA	UNK
Type-1 mandarins	TBM,SCM,M01,M02,M04	0	0	1	0
Type-2 mandarins	CLP	0.000	0.019	0.977	0.004
	SNK	0.000	0.025	0.975	0.000
	M17	0.000	0.045	0.949	0.006
	M12	0.000	0.047	0.944	0.009
	M03	0.000	0.055	0.937	0.007
	HLM	0.008	0.043	0.928	0.021
	M10	0.000	0.063	0.934	0.003
	M15	0.000	0.080	0.915	0.005
	CSM	0.000	0.081	0.901	0.017
	M16	0.000	0.082	0.911	0.007
	M11	0.000	0.088	0.894	0.018
	DNC	0.000	0.114	0.882	0.004
	WLM	0.000	0.118	0.870	0.012
	M14	0.000	0.120	0.868	0.013
	PKM	0.010	0.124	0.863	0.003
	M08	0.015	0.173	0.804	0.008
Type-3 mandarins	CLM	0.000	0.237	0.737	0.027
	WMM	0.000	0.252	0.732	0.016
	M19	0.031	0.214	0.747	0.008
	M21	0.015	0.281	0.672	0.032
	UNS	0.018	0.411	0.563	0.008
	KNG	0.000	0.471	0.519	0.009
	M20	0.099	0.565	0.327	0.009
Sweet orange	SWO	0.044	0.743	0.200	0.013
Ambersweet or.	SO5	0.104	0.543	0.318	0.035
Sour oranges	SSO,BO2	0.000	1.000	0.000	0.000
	BO3	0.046	0.942	0.000	0.012
Grapefruit	PAR	0.328	0.670	0.000	0.002
Cocktail grapef.	GF0	0.067	0.933	0.000	0.000
Pummelos	CHP	0.990	0.005	0.000	0.005
	LAP,GXP,STP	1	0	0	0
	Code	CI/CI	CI/PU	CI/MA	UNK
Rangpur lime	LMA	0	0	1	0
Rough lemon	RRL	0	0	1	0
Lemon	LIM	0	0.364	0.620	0.016
Citrons	BUD,COR,HUM,VEU	1	0	0	0
	Code	CI/CI	CI/MC	MC/MC	UNK
Micrantha	MIC	0	0	1	0
Mexican lime	MXL	0	1	0	0
	Code	MA/MA	MA/FO	FO/FO	UNK
Kumquat	FOR	0	0	1	0
Calamondin	CAL	0	1	0	0

These five species are *C. medica* (CI), *C. maxima* (PU), *C. reticulata* (MA), *C. micrantha* (MC), *Fortunella* (FO). Estimates based on genetic map lengths. UNK, unknown.

Extended Data Table 3 | Alleles of candidate single-nucleotide polymorphisms associated with citrus palatability

Code	1:415175	1:23512067	1:23679916	1:24219222	2:15484525	2:15702160	5:35094706	5:35098538	8:325527	8:631678	8:927020	8:1149577	8:1149586	8:1174414	8:1413967	8:1651338	8:1655701	8:1722788	8:2058824	8:2060290	8:2063416	8:2137063	8:2174360	9:30789594
NON-ACIDIC VARIETIES																								
CLM	C	C	C	A	G	G	G	C	A/G	T/C	C/T	G/T	C/T	T/A	A	G	G	T	C	T	T	G	C	T
KNG	C	C/T	C/A	A/G	G/T	G/T	G	C	A/G	T/C	C/T	G/T	C/T	T/A	A/G	G/A	G/T	T/C	C/T	T/C	T/C	G/C	C/T	T
PKM	C	C	C	A	G/T	G/T	G	C	A/G	T/C	C/T	G/T	C/T	T/A	A/G	G/A	G/T	T/C	C/T	T/C	T/C	G/C	C/T	T
DNC	C	C	C	A	G/T	G/T	G	C	A/G	T/C	C/T	G/T	C/T	T/A	A/G	G/A	G/T	T/C	C/T	T/C	T/C	G/C	C/T	T
CSM	C	C	C	A	G/T	G/T	G	C	G	C	C/T	G/T	C/T	T/A	A/G	G/A	G/T	T/C	C/T	T/C	T/C	G/C	C/T	T
WMM	C	C	C	A	G/T	G/T	G	C	A/G	T/C	C/T	G/T	C/T	T/A	A/G	G/A	G/T	T/C	C/T	T/C	T/C	G/C	C/T	T
HLM	C	C	C	A	G/T	G/T	G	C	A/G	T/C	C/T	G	C	T	G	A	T	C	T	C	C	C	T	T
UNS	C	C	C	A	G/T	G/T	G/A	C/T	A/G	T/C	C/T	G	C	T	G	A	T	C	T	C	C	C	T	T
WLM	C	C	C	A	G/T	G	G/A	C/T	A/G	T/C	C/T	G	C	T	A	A/G	G/A	G/T	T/C	C/T	T/C	T/C	G/C	C/T
SWO	C	C	C	A	G/T	G/T	G/A	C/T	A	T	C	G	C	T	A/G	G/A	G/T	T/C	C/T	T/C	T/C	G/C	C/T	T/C
CHP	T	C	C	A	T	T	A	T	A/G	T	C	G/T	C/T	T	G	A	T	C	C/T	T/C	C	C	T	C
LAP	T	C	C	A	T	T	A	T	A/G	T	C	G/T	C/T	T	G	A	T	C	T	C	C	C	T	C
GXP	T	C	C	A	T	T	A	T	A	T	C	G/T	C/T	T	G	A	T	C	T	C	C	C	T	C
STP	T	C	C	A	T	T	A	T	A	T	C	G	C	T	G	A	T	C	T	C	T/C	G/C	T	C
PAR	C/T	C	C	A	T	T	A	T	A/G	T	C	G	C	T	A/G	G/A	G/T	T/C	C/T	T/C	T/C	G/C	C/T	C
ACIDIC VARIETIES																								
SNK	T	C/T	C	A/G	T	T	G/A	C/T	G	C	T	T	T	A	A	G	G	T	C	T	T	G	C	C
TBM	T	T	C/A	A/G	T	T	A	T	G	C	T	T	T	A	A	G	G	T	C	T	T	G	C	C
CLP	T	C/T	C/A	A/G	T	T	A	T	G	C	T	T	T	A	A	G	G	T	C	T	T	G	C	C
SCM	C/T	C/T	C/A	A/G	T	T	A	T	G	C	T	T	T	A	A	G	G	T	C	T	T	G	C	C
SSO	T	C/T	C/A	A/G	T	T	A	T	G	C	C/T	T	T	T/A	A/G	G/A	G/T	T	C	T	T	G	C/T	C
RRL	C/T	T	C/A	A/G	T	T	A	T	G	C	T	T	T	A	A	G	G	T	C	T	T	G	C	T/C
LMA	T	C/T	C/A	A/G	T	T	A	T	G	C	T	T	T	A	A	G	G	T	C	T	T	G	C	C
LIM	T	T	C/A	A/G	T	T	A	T	G	C	T	T	T	A	A	G	G	T	C	T	T	G	C	C
CAL	T	T	C/A	A/G	T	T	A	T	G	C	T	T	T	A	A	G	G	T	C	T	T	G	C	C
FOR	T	T	C	A	T	T	A	T	G	C	T	T	T	A	A	G	G	T	C	T	T	G	C	C
MIC	T	T	C	A	T	T	A	T	G	C	T	T	T	A	A	G	G	T	C	T	T	G	C	C
MXL	T	T	C	A	T	T	A	T	G	C	T	T	T	A	A	G	G	T	C	T	T	G	C	C
COR	T	T	C	A	T	T	A	T	G	C	T	T	T	A	A	G	G	T	C	T	T	G	C	C
VEU	T	T	C	A	T	T	A	T	G	C	T	T	T	A	A	G	G	T	C	T	T	G	C	C
BUD	T	T	C	A	T	T	A	T	G	C	T	T	T	A	A	G	G	T	C	T	T	G	C	C
HUM	T	T	C	A	T	T	A	T	G	C	T	T	T	A	A	G	G	T	C	T	T	G	C	C
ICH	T	T	C	A	T	T	A	T	G	C	T	T	T	A	A	G	G	T	C	T	T	G	C	C
AFL	T	T	C	A	T	T	A	T	G	C	T	T	T	A	A	G	G	T	C	T	T	G	C	C
ARL	T	T	C	A	T	T	A	T	G	C	T	T	T	A	A	G	G	T	C	T	T	G	C	C
AFR	T	T	C	A	T	T	A	T	G	C	T	T	T	A	A	G	G	T	C	T	T	G	C	C
ARR	T	T	C	A	T	T	A	T	G	C	T	T	T	A	A	G	G	T	C	T	T	G	C	C
ADR	T	T	C	A	T	T	A	T	G	C	T	T	T	A	A	G	G	T	C	T	T	G	C	C

The association study is based on a case-control GWAS analysis of 37 accessions with known palatability. Grey, ancestral alleles detected in *Severinia* and *Poncirus*; red, derived alleles; yellow, heterozygous single-nucleotide polymorphisms.

Extended Data Table 4 | The *IDH* gene variants

Species	Cultivar	Code	SNP position		
			Exon 1	Exon 4	Exon 4
			8:324328	8:326594	8:326608
NON-ACIDIC VARIETIES					
<i>Citrus maxima</i>	Chandler pummelo	CHP	T/T	G/G	C/C
<i>Citrus maxima</i>	Low-acid pummelo/	LAP	T/T	G/G	C/C
<i>Citrus maxima</i>	Guanxi pummelo	GXP	T/T	G/G	C/C
<i>Citrus maxima</i>	Shatian pummelo	STP	T/T	G/G	C/C
<i>Citrus sinensis</i>	Sweet orange	SWO	T/T	G/G	C/C
<i>Citrus paradisi</i>	Marsh grapefruit	PAR	T/T	G/G	C/C
<i>Citrus reticulata</i>	Ponkan mandarin	PKM	T/T	G/T	C/G
<i>Citrus clementina</i>	Clementine mandarin	CLM	T/T	G/T	C/G
<i>Citrus tangerina</i>	Dancy mandarin	DNC	T/T	G/T	C/G
<i>Citrus deliciosa</i>	Willowleaf mandarin	WLM	T/T	G/T	C/G
<i>Citrus unshiu</i>	Satsuma mandarin	UNS	T/T	G/A	C/G
<i>Citrus reticulata</i>	Huanglingmiao mandarin	HLM	T/T	G/A	C/G
<i>Citrus nobilis</i>	King mandarin	KNG	T/G	G/A	C/G
<i>Citrus reticulata</i>	Changsha mandarin	CSM	T/T	A/T	G/G
<i>Citrus reticulata</i>	W. Murcott mandarin	WMM	T/G	G/A	C/G
ACIDIC VARIETIES					
<i>Citrus aurantium</i>	Sour orange	SSO	T/G	G/A	C/G
<i>Citrus sunki</i>	Sunki mandarin	SNK	T/T	A/T	G/G
<i>Citrus reshni</i>	Cleopatra mandarin	CLP	T/G	A/A	G/G
<i>Citrus ichangensis</i>	Ichang papeda	ICH	T/G	A/A	G/G
<i>Citrus limon</i>	Eureka lemon	LIM	T/T	A/A	G/G
<i>Citrus micrantha</i>	Micrantha	MIC	A/A	A/A	G/G
<i>Citrus aurantifolia</i>	Mexican lime	MXL	A/A	A/A	G/G
<i>Fortunella margarita</i>	Kumquat. Nagami	FOR	T/A	A/A	G/G
<i>Citrus limonia</i>	Rangpur lime	LMA	T/A	A/A	G/G
<i>Citrus madurensis</i>	Calamondin	CAL	T/A	A/A	G/G
<i>Citrus medica</i>	Mac Veu Montain Citron	VEU	T/T	A/A	G/G
<i>Citrus medica</i>	Corsican citron	COR	T/T	A/A	G/G
<i>Citrus medica</i>	Buddha's hand citron	BUD	T/T	A/A	G/G
<i>Citrus medica</i>	Humpang citron	HUM	T/T	A/A	G/G
<i>Microcitrus australasica</i>	Australian finger lime (BC2)	AFL	G/G	A/A	G/G
<i>Microcitrus australis</i>	Australian round lime (Pure)	ARL	G/G	A/A	G/G
<i>Microcitrus australasica</i>	Australian finger lime (Pure)	AFR	G/G	A/A	G/G
<i>Microcitrus australis</i>	Australian round lime (Pure)	ARR	G/G	A/A	G/G
<i>Eremocitrus glauca</i>	Australian desert line	ADR	G/G	A/A	G/G
<i>Citrus jambhiri</i>	Red rough lemon	RRL	T/T	A/T	G/G
<i>Citrus reticulata</i>	Sun Chu Sha Kat mandarin	SCM	T/T	T/T	G/G
<i>Citrus tachibana</i>	Tachibana mandarin	TBM	G/G	A/A	G/G

Alleles of non-synonymous single-nucleotide polymorphisms of the NAD⁺-dependent isocitrate dehydrogenase (*IDH*) gene (Ciclev10028714) in 37 citrus accessions with known palatability.

Ketamine blocks bursting in the lateral habenula to rapidly relieve depression

Yan Yang^{1,2*}, Yihui Cui^{1,2*}, Kangning Sang^{1,2*}, Yiyan Dong^{1*}, Zheyi Ni¹, Shuangshuang Ma¹ & Hailan Hu^{1,2}

The *N*-methyl-*D*-aspartate receptor (NMDAR) antagonist ketamine has attracted enormous interest in mental health research owing to its rapid antidepressant actions, but its mechanism of action has remained elusive. Here we show that blockade of NMDAR-dependent bursting activity in the ‘anti-reward center’, the lateral habenula (LHb), mediates the rapid antidepressant actions of ketamine in rat and mouse models of depression. LHb neurons show a significant increase in burst activity and theta-band synchronization in depressive-like animals, which is reversed by ketamine. Burst-evoking photostimulation of LHb drives behavioural despair and anhedonia. Pharmacology and modelling experiments reveal that LHb bursting requires both NMDARs and low-voltage-sensitive T-type calcium channels (T-VSCCs). Furthermore, local blockade of NMDAR or T-VSCCs in the LHb is sufficient to induce rapid antidepressant effects. Our results suggest a simple model whereby ketamine quickly elevates mood by blocking NMDAR-dependent bursting activity of LHb neurons to disinhibit downstream monoaminergic reward centres, and provide a framework for developing new rapid-acting antidepressants.

The discovery of the rapid antidepressant effects of the NMDAR antagonist ketamine is arguably the most important advance in the field of psychiatry in the past half century¹. A single administration of ketamine elicits fast (in as little as half an hour) and sustained antidepressant effects both in humans^{1,2} and in animal models of depression^{3–6}. It also has a fast metabolic turnover rate, with a half-life of three hours⁷. This rapid ‘hit-and-go’ temporal profile suggests that ketamine is likely to act on a system that has ongoing activity with open NMDAR channels⁸.

The LHb has recently been implicated in the coding of negative emotion^{9–13} and the pathophysiology of major depression^{14–18}. The LHb hosts primarily glutamatergic neurons¹⁹, but it inhibits the brain’s reward centres (including the dopaminergic ventral tegmental area (VTA) and the serotonergic dorsal raphe nucleus (DRN), hypoactivity of which has been implicated in depression^{20,21}) either through a relay at the γ -aminobutyric acid (GABA)ergic rostromedial tegmental nucleus (RMTg) or via local interneurons within the VTA and DRN^{9,12,22–24}. Although there is accumulating evidence that aberrant overactivity in the LHb is crucial to depression^{14–18}, it remains unknown how the spike patterns of LHb neurons are altered during depression and what role this may play in the aetiology of depression and the fast antidepressant effects of ketamine.

Blockade of LHb NMDARs is antidepressant

We found that congenitally learned helpless (cLH) rats^{15–17}, which model several aspects of depression, showed an antidepressant response to systemic injection of ketamine (25 mg kg^{−1}) in the forced swim test (FST; Extended Data Fig. 1a). To assess whether ketamine exerts its antidepressant effects through the LHb, we performed bilateral infusion of ketamine into the LHb through dual-guide cannulae (Fig. 1a). Local infusion of ketamine (25 μ g, 1 μ l each side, Fig. 1b) into the LHb of cLH rats was sufficient to quickly rescue the depression-like behaviours, including behavioural despair (as measured by immobile time in the FST; Fig. 1c) and anhedonia (as measured by the sucrose preference test (SPT); Fig. 1d), one hour after infusion. These antidepressant effects

were dosage-dependent (Fig. 1c, d). Liquid chromatography–tandem mass spectrometry (LC–MS/MS, Extended Data Fig. 1e–g) revealed that infusion of 25 μ g ketamine through cannulae into the LHb resulted in a local ketamine concentration of $5.2 \pm 1.3 \mu\text{M}$, in a similar range to that caused by intraperitoneal injection of 25 mg kg^{−1} ketamine ($11.0 \pm 1.7 \mu\text{M}$, Fig. 1e).

Local bilateral infusion of the specific NMDAR antagonist 2-amino-5-phosphonopentanoic acid (AP5; 40 nmol, Fig. 1f) into the LHb effectively reduced the immobile time in the FST (Fig. 1g) and increased the sucrose preference in the SPT (Fig. 1h), similar to the effects of ketamine. Neither ketamine nor AP5 infusion changed general locomotion, as measured by the open field test (OFT; Extended Data Fig. 1b, c). Notably, infusion of the AMPAR (α -amino-3-hydroxy-5-methyl-4-isoxazole propionic acid receptor) antagonist NBQX (1,2,3,4-tetrahydro-6-nitro-2,3-dioxo-benzo[f]quinoxaline-7-sulfonamide; 1 nmol or 5 nmol, Fig. 1i) into the LHb did not cause significant antidepressant effects (Fig. 1j).

Increased LHb burst firing in depression

To investigate the activity patterns of LHb neurons, we performed whole-cell patch-clamp on neurons in LHb coronal slices and recorded spontaneous neuronal activity under current clamp at resting conditions ($I = 0$ pA). As previously shown^{25,26}, LHb neurons were intrinsically active and fell into three categories: silent, tonic-firing and burst-firing (Fig. 2a–c). Tetrodotoxin (TTX; 1 μM) abolished action potentials but left a plateau potential in the bursting neurons (Fig. 2c), indicating that the ionic component of this plateau potential is not sodium, but might be calcium²⁵. The three classes of neurons were distributed among different sub-nuclei of the LHb with no clear regional enrichment (Fig. 2f). The resting membrane potentials (RMPs) of LHb neurons were on average more depolarized than those in the hippocampus or cortex²⁶ (Fig. 2d, e). Notably, bursting neurons had significantly more hyperpolarized RMPs than silent or tonic-firing neurons (Fig. 2d, e). Moreover, the frequencies of the intra-burst spikes, but not of the inter-burst spikes, correlated with the degree of hyperpolarization (Extended Data Fig. 2c, d).

¹Center for Neuroscience, Key Laboratory of Medical Neurobiology of the Ministry of Health of China, School of Medicine, Interdisciplinary Institute of Neuroscience and Technology, Qiushi Academy for Advanced Studies, Zhejiang University, Hangzhou 310058, China. ²Mental Health Center, School of Medicine, Zhejiang University, Hangzhou 310013, China.

*These authors contributed equally to this work.

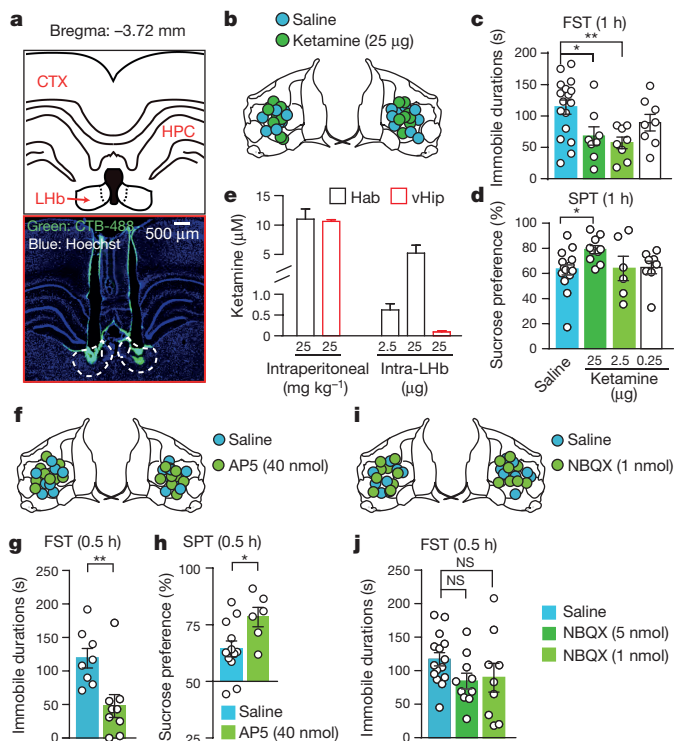


Figure 1 | Local blockade of NMDARs in LHB is sufficient to elicit rapid antidepressant effects. **a**, Illustration of bilateral implantation of cannulae in the LHB of cLH rats. CTX, cortex; HPC, hippocampus. Bottom: white dashed lines indicate location of habenula. **b–d**, Rapid antidepressant effects of local bilateral infusion of ketamine into the LHB (**b**, 25, 2.5 or 0.25 µg, 1 µl each side) in the FST (**c**) and the SPT (**d**). **e**, Concentration of ketamine in habenula (Hab) or ventral hippocampus (vHip) 1 h after intraperitoneal (i.p.) injection or intra-LHB infusion of ketamine, as measured by LC–MS/MS. **f–j**, Acute effects of local bilateral infusion of AP5 (40 nmol, 1 µl each side, **f–h**) or NBQX (1 or 5 nmol, 1 µl each side, **i, j**) into the LHB on the FST (**g, i**) and SPT (**h, j**). Infusion sites of drugs verified by CTB (cholera toxin subunit B) (**b, f, i**). Data are mean \pm s.e.m. * $P < 0.05$, ** $P < 0.01$, NS, not significant. See Supplementary Table 1 for statistical analysis and n numbers.

Although basic membrane properties, such as input resistance, and I – V relationships, and the average duration of bursts were indistinguishable between neurons from cLH and wild-type rats (Extended Data Fig. 2), the percentage of bursting neurons increased significantly from 7% in wild-type controls to 23% in cLH rats ($P = 0.003$, Fig. 2g). The percentage of spikes in the bursting mode also increased from 7% in control to 43% in cLH rats (Fig. 2h). The inter-spike intervals (ISIs) of LHB neurons in cLH rats exhibited a clear bimodal distribution with an extra sharp and condensed cluster of high frequency events centred around 14 ms (corresponding to about 71 Hz), indicating a significant weight increase of burst firings (Fig. 2i).

To test whether enhanced bursting is universal in depression-like states, we used a second animal model of depression, mice with chronic restraint stress (CRS) (Extended Data Fig. 3). Patch-clamp recording of LHB neurons from these mice revealed similar phenomena: namely, a marked increase in both the percentage of bursting cells and the percentage of spikes in bursting mode (Extended Data Fig. 3g–i), and an extra peak at 20 ms in the ISI distribution (Extended Data Fig. 3j). Notably, acute systemic injection of ketamine at antidepressant dosages reduced bursting back to control levels in both cLH rats (Fig. 2g, h) and CRS mice (Extended Data Fig. 3h, i).

To test whether bursting also occurs *in vivo* in the LHB and whether it is bidirectionally modulated by depression-like state and ketamine, we performed *in vivo* multi-tetrode recording in the LHB of freely behaving mice (Fig. 2j, Extended Data Fig. 4). LHB neurons from CRS

mice showed a notable increase in bursting activity (Fig. 2k, l) but not tonic firing (Extended Data Fig. 4f), compared with neurons from naive control mice. As a consequence, the mean firing rate was also higher in CRS mice than in control mice (Extended Data Fig. 4f). Injection of ketamine (10 mg kg⁻¹, intraperitoneal, 1 h before recording) significantly suppressed LHB bursting activity ($P < 0.0001$, Fig. 2m and Extended Data Fig. 4i) and overall firing rate (Extended Data Fig. 4h). The cumulative frequency distributions of ISIs, which clearly differed between CRS and control mice, were significantly shifted towards the control level by ketamine ($P < 0.0001$, Fig. 2n).

Burst firing is known to increase network synchronization²⁷. We therefore tested whether LHB network synchronization was altered in the CRS mice. We calculated the spike-triggered averages (STAs) of local field potentials (LFPs), which revealed oscillatory synchronization between spikes and LFPs (see Methods). In control mice, the distribution of the power spectra of STAs was relatively flat (Extended Data Fig. 4j), indicating a lack of synchronization. In CRS mice, there emerged a dominant frequency of 7 Hz in the power spectra of STAs (Extended Data Fig. 4j), indicating that spikes tended to phase-lock with LFPs in the theta-band range. Consistently, CRS mice showed significantly higher spike-field coherence (SFC, reflecting the normalized power spectra of STAs) in the theta band range compared with control mice ($P = 0.022$, Fig. 2o). These changes in LHB network synchronization were reversed to control level 1 h after intraperitoneal injection of ketamine (10 mg kg⁻¹, Fig. 2o and Extended Data Fig. 4j).

LHB bursts require NMDARs

Given that NMDAR-mediated calcium influx plays a pivotal role in burst generation in several brain regions^{28–30}, and in light of our finding that systematic injection of ketamine suppressed bursting activity (Fig. 2), we tested whether NMDARs are directly required for the bursting activity in the LHB. NMDAR currents were detected in LHB neurons (Extended Data Fig. 5a, b). Bath application of ketamine (100 µM) to LHB brain slices did not change the neuronal RMPs (Extended Data Fig. 5c) or miniature excitatory postsynaptic potentials (EPSCs; Extended Data Fig. 5h–j), but completely eliminated spontaneous burst firing within seconds of application (Fig. 3a). Lowering the concentration of ketamine to 10 µM or 1 µM, close to the effective antidepressant concentration (Fig. 1e), also completely blocked bursting, but with a longer delay (Fig. 3b, c). Bath application of the specific NMDAR antagonist AP5 (100 µM) also stopped burst firing (Fig. 3d). Notably, consistent with the modest behavioural effects of cannular infusion (Fig. 1j), full blockade of AMPARs with NBQX (10 µM) reduced bursts only moderately (Fig. 3e). Application of the classical specific serotonin reuptake inhibitor (SSRI) antidepressant fluoxetine did not affect LHB bursts at this rapid time scale (Fig. 3f). Furthermore, perfusion of brain slices with NMDA (20 µM) in artificial cerebrospinal fluid (ACSF) with no Mg²⁺ induced strong bursting activity in 10 out of 13 originally silent LHB neurons (Fig. 3g, h). Again this bursting activity was blocked by additional bath application of ketamine (Fig. 3h).

LHB bursts depend on RMP and T-VSCCs

Given the correlation between RMPs and firing modes of LHB neurons²⁶ (Fig. 2d, e), we next tested whether changing RMPs can alter the pattern of spiking activity in the LHB. By applying a transient ramp-like current injection that enabled RMPs to change progressively²⁶ from around –80 to –40 mV (Extended Data Fig. 6a), we found that in 90% ($n = 48$) of rat and 93% ($n = 26$) of mouse LHB neurons, the hyperpolarization current injection was able to evoke high frequency bursts of action potentials. The intra-burst frequencies of the ramp-evoked bursts were positively correlated with the hyperpolarization of membrane potentials (Extended Data Fig. 6b). The duration of bursts tended to decrease with increased hyperpolarization (Extended Data Fig. 6c). Consequently, the number of spikes in each burst, which is the product of the intra-burst frequency and burst duration, were normally distributed from –80 mV to –40 mV and peaked at

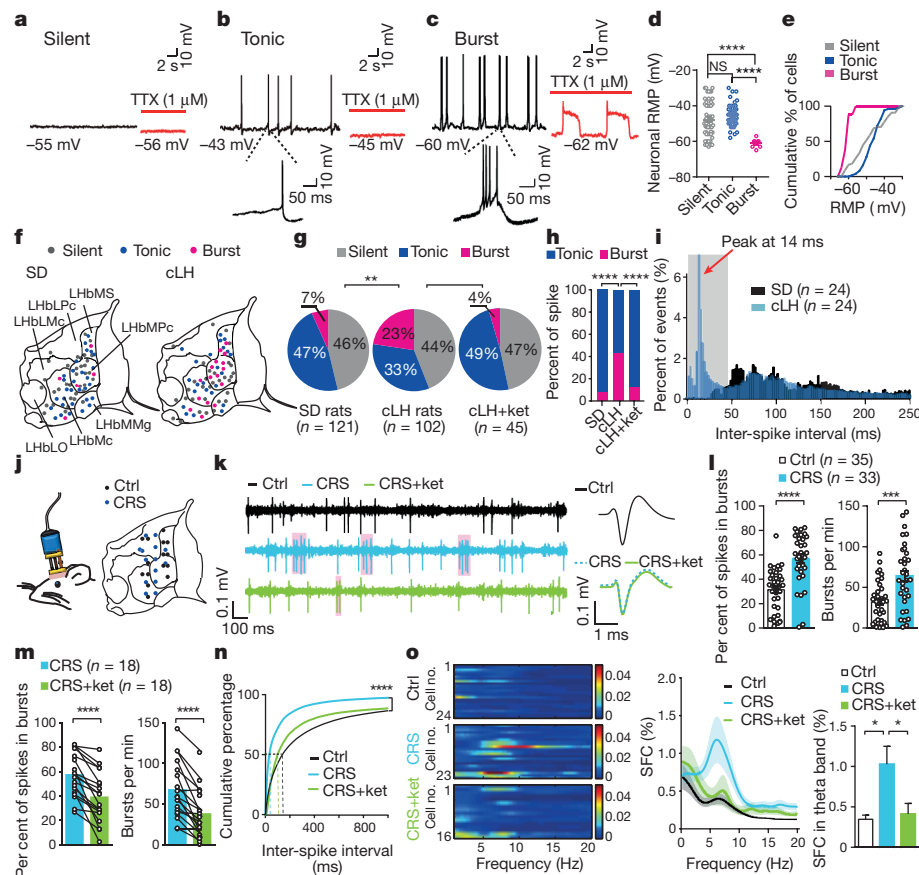


Figure 2 | Ketamine suppresses enhanced LHB bursting activity and theta-band synchronization in animal models of depression.

a–c, Representative traces showing spontaneous activity of silent (**a**), tonic-firing (**b**), and burst-firing (**c**) LHB neurons recorded with whole-cell patch-clamp. Red traces are responses of the same neurons after TTX treatment. **d**, **e**, Scattered plots (**d**) and cumulative curves (**e**) denoting the mean and distribution of RMPs. **f–i**, Burst firing is significantly increased in cLH rats, and this increase is reversed by ketamine (i.p., 25 mg kg^{−1}). **f**, Recording sites across different subregions of LHB. **g**, Pie charts illustrating the per cent abundance of the three types of LHB neurons. **h**, Bar graph illustrating the percentage of burst- and tonic-type spikes in all spikes recorded. **i**, Histogram of ISI distribution. **j**, Recording sites of each tetrode track in the LHbs of CRS and control mice. **k**, Example traces

(left) and averaged spike waveform (right) of recorded neurons from the LHbs of control (top) and CRS mice (middle) and the same CRS unit after ketamine injection (bottom). Bursts (grey shades) are identified by the ISI method (see Methods). **l**, **m**, Per cent of spikes in bursting mode and number of bursts per minute of neurons recorded from control mice, CRS mice (**l**), and the same unit in CRS mice 1 h before and after ketamine injection (**m**). **n**, Cumulative distribution of ISIs. Dashed lines indicate the 50th percentile of ISI. **o**, Spike-field coherence (SFC) of neurons recorded from control and CRS mice, and from CRS mice after ketamine injection. Left, SFC of each unit; middle, average SFC; right, per cent SFC in theta band (4–10 Hz). Data are mean ± s.e.m. **P* < 0.05, ***P* < 0.01, ****P* < 0.001, *****P* < 0.0001, NS, not significant. See Supplementary Table 1 for statistical analysis and *n* numbers.

about −56 to −60 mV (Extended Data Fig. 6d), close to the average RMPs observed in spontaneous bursting LHB neurons (Fig. 2d, e). This voltage-dependent transition of firing mode also occurred in spontaneously spiking LHB neurons: by delivering a hyperpolarizing current injection (−10 to −20 pA), 75% (*n* = 20) of originally tonic-firing neurons were transformed to burst-firing (Extended Data Fig. 6e); vice versa, a depolarizing current injection (10–20 pA), transformed 100% (*n* = 7) of originally bursting neurons to tonic-firing mode (Extended Data Fig. 6f).

The pacemaker channel T-VSCC, unlike other types of voltage-sensitive calcium channel, is inactivated quickly after opening at depolarized membrane potentials, but can be de-inactivated to initiate burst firing when the membrane potential is hyperpolarized for longer than 100 ms³¹. We detected T-VSCC currents in both rat and mouse LHB neurons³² (Extended Data Fig. 7a, b). Bath application of the specific T-VSCC blocker mibefradil (10 μM) onto the LHB brain slices effectively decreased the bursting probability and reduced the amplitude of the plateau potentials of spontaneous bursts (Fig. 4a), without significantly changing RMPs (Extended Data Fig. 5f). ZD7288 (50 μM), an antagonist of another pacemaker channel (hyperpolarization-activated cyclic nucleotide-gated (HCN) channel), had a significant but much smaller effect on bursts than mibefradil (*P* = 0.018, Fig. 4b).

To understand how NMDARs and T-VSCCs work synergistically to mediate LHB burst firing, we constructed a minimal biophysical model that successfully recapitulated the key characteristics of the LHB bursts, including the voltage dependency and the *in silico* knockout effects of T-VSCCs or NMDAR (Extended Data Fig. 8; see Methods).

Although AMPAR blockade reduced LHB burst probability only slightly (Fig. 3e), application of AMPA onto LHB neurons or increased AMPAR current increased the burst frequency in electrophysiology recording or modelling experiments, respectively (Extended Data Figs 8h, 9a). Blockade of GABA receptors (GABARs) also increased burst firing (Extended Data Fig. 9b). Thus, burst generation in the LHB relies on intrinsic cellular properties and is modulated by network synaptic inputs.

The above results predict that drugs that block T-VSCCs may also have rapid antidepressant effects. Indeed, both systematic injection of the T-VSCC blocker 2-ethyl-2-methylsuccinimide (ethosuximide), which can cross the blood–brain barrier, in CRS mice and bilateral infusion of mibefradil (10 nmol) into the LHB of cLH rats caused rapid antidepressant effects in both the FST and the SPT (Fig. 4c–g), without inducing significant changes in total distance travelled in the OFT (Extended Data Fig. 1b, d).

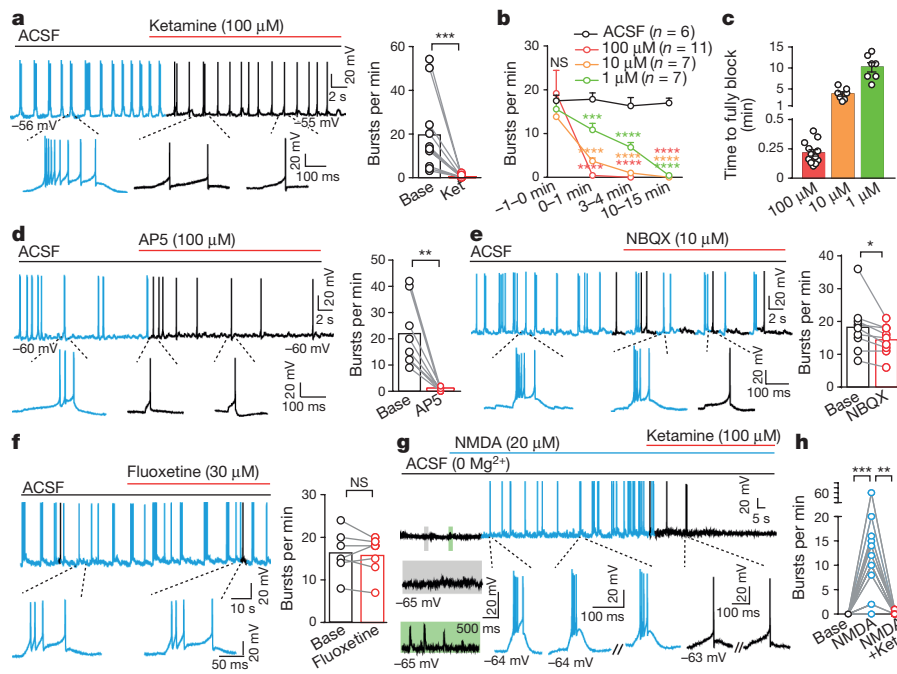


Figure 3 | LHB bursting requires activation of NMDARs. **a, d–f**, Example traces (left) and statistics (right, sampled within 3 min before and 1 min after drug application) showing effects of ketamine (**a**), AP5 (**d**), NBQX (**e**) and fluoxetine (**f**) on spontaneous bursts in the LHB of wild-type and cLH rats. Spikes in bursting and tonic-firing mode are shown in blue and black, respectively. **b**, Blockade of spontaneous LHB burst by different dosages of ketamine. Bursts per minute are calculated before (–1 to 0 min) and after (0–1 min, 3–4 min and 10–15 min) ketamine perfusion. **c**, Average time

required to fully block LHB bursts by different concentrations of ketamine. **g**, Example trace of an originally silent LHB neuron induced to burst by NMDA perfusion and returned to silence after ketamine application. Note that NMDA markedly enhances both EPSPs (green shading) and burst firing. **h**, Summary of effects of NMDA perfusion and ketamine on bursts. Data are mean \pm s.e.m., * $P < 0.05$, ** $P < 0.01$, *** $P < 0.001$, **** $P < 0.0001$, NS, not significant. See Supplementary Table 1 for statistical analysis and n numbers.

LHB bursts drive depression

To test whether increased burst activity is sufficient to induce depression-like behaviours, we used optogenetic tools to drive bursting activity in the LHB. We first used a variant of channelrhodopsin 2 (ChR2), oChIEF, which is optimized to follow high-frequency stimulation. However, LHB neurons expressing oChIEF could not follow pulsed 100-Hz light stimulation (Extended Data Fig. 10a). Consistently, no depression-like behaviours were induced with this protocol (Extended Data Fig. 10b–d).

On the basis of the observation that a hyperpolarization ramp current could induce burst firing in the LHB (Extended Data Fig. 6a), we devised a protocol involving a transient (100-ms) hyperpolarization current injection, which induced NMDAR- and T-VSCC-dependent rebound bursts in LHB brain slices with 100% success (Extended Data Fig. 6g–k). We therefore used an inhibitory opsin, eNpHR3.0 (an enhanced variant of halorhodopsin), to drive rebound bursts in the LHB (Fig. 5a). Yellow light pulses (1 Hz, 100 ms at 589 nm) reliably elicited robust rebound bursts in *in vitro* slice recordings with a

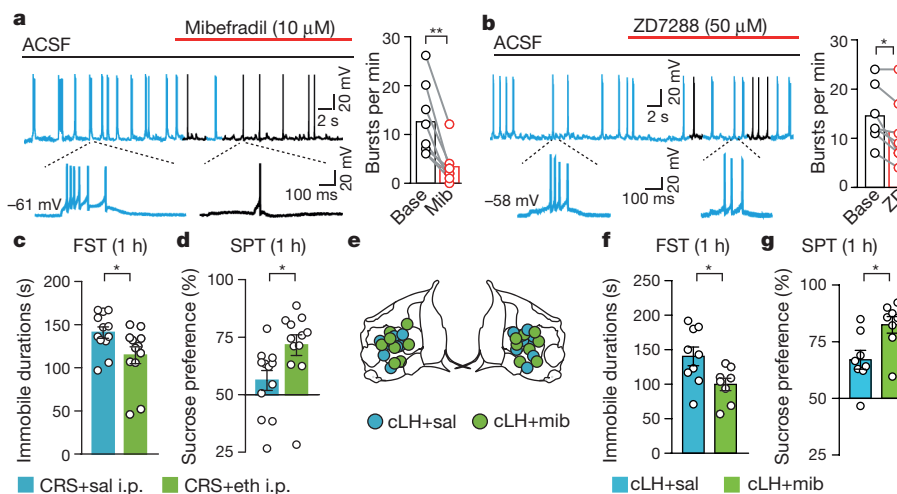


Figure 4 | Antagonists of T-VSCCs block LHB bursts and cause rapid antidepressant. **a, b**, Example traces (left) and statistics (right, sampled within 3 min before and 1 min after drug application) showing effects of mibefradil (**a**) or ZD7288 (**b**) on spontaneous bursts in the LHB of wild-type and cLH rats. **c–g**, Antidepressant effects caused by systemic

ethosuximide injection (200 mg kg^{-1} , i.p.; **c, d**) or local bilateral infusion of mibefradil into the LHB (**e–g**) in the FST (**c, f**) and SPT (**d, g**) 1 h after treatment. Infusion sites verified by CTB (**e**). Data are mean \pm s.e.m., * $P < 0.05$, ** $P < 0.01$. See Supplementary Table 1 for statistical analysis and n numbers.

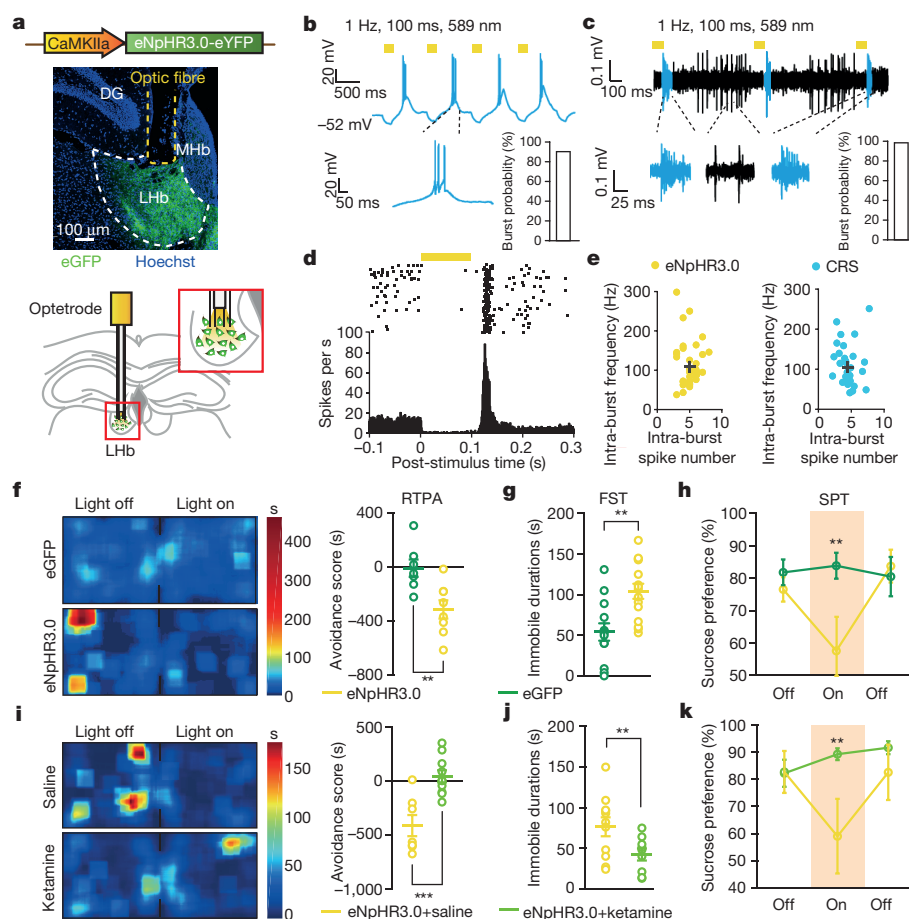


Figure 5 | eNpHR3.0-induced rebound bursting drives behavioural aversion and depression-like symptoms that are reversible by ketamine.

a, Construct of AAV2/9-eNpHR3.0 (top), example site of viral injection and optic fibre implantation (middle), and illustration of optrode recording (bottom). **b, c**, Representative traces showing rebound bursts reliably elicited by pulsed yellow light in LHB brain slices *in vitro* (**b**) and *in vivo* (**c**) from mice infected with AAV2/9-eNpHR3.0. Spikes in bursting and tonic-firing mode are shown in blue and black, respectively. Percentage of successfully induced bursts is shown at bottom right. **d**, Raster plots (top) and post-stimulus time histogram (bottom) of an example LHB neuron responding to 100-ms yellow light stimulation from

in vivo optrode recording. **e**, Distribution of intra-burst frequencies and intra-burst spike numbers of eNpHR3.0-driven rebound bursts (left) are comparable to those recorded from CRS mice (right). Means are represented by black crosses. **f, i**, RTPA (**f**) induced by eNpHR3.0-driven bursts reversed by ketamine (i.p. injection, 1 h before test, **i**). Left, representative heat maps of RTPA; right, quantitative aversion score (see Methods). **g, h, j, k**, Depression-like behaviours in the FST (**g**) and SPT (**h**) induced by eNpHR3.0-driven bursts reversed by ketamine (i.p. injection, 1 h before test, **j, k**). Data are represented as mean \pm s.e.m., ** $P < 0.01$, *** $P < 0.001$. See Supplementary Table 1 for statistical analysis and n numbers.

high intra-burst frequency and 90% success rate (Fig. 5b). Optrode recording *in vivo* revealed that the intra-burst frequency and intra-burst number of spikes produced by this rebound burst protocol were comparable to those detected in depressed CRS mice (Fig. 5c–e).

We then tested whether rebound bursts in the LHB could acutely drive aversion and depression-like symptoms in freely behaving mice. In the real-time place aversion (RTPA) assay, 1 Hz yellow light photostimulation significantly reduced the time spent in the light-paired chamber in mice injected with an adenoviral vector encoding eNpHR3.0 but not in those injected with a vector encoding eGFP ($P = 0.0064$, Fig. 5f), without changing velocity (Extended Data Fig. 10j). Furthermore, 1 Hz yellow light photostimulation of mice expressing eNpHR3.0 significantly increased immobility in the FST ($P = 0.0049$, Fig. 5g) without altering locomotion in the OFT (Extended Data Fig. 10k), and decreased sucrose preference (Fig. 5h). A stimulation protocol (5 Hz on AAV-oChIEF injected mice) that yields the same overall firing rate as the rebound burst protocol (Extended Data Fig. 10e) did not cause depression-like phenotypes (Extended Data Fig. 10f–h), indicating that it is the pattern of burst firing rather than a mere increase in spikes that is important for the induction of depression-like behaviours. Notably, ketamine reversed both rebound burst-induced RTPA and depression-like behaviours (Fig. 5i–k).

Discussion

We have provided multiple lines of evidence to support the idea that a depression-like state depends critically on a bursting mode of firing in the LHB, and that the rapid antidepressant effects of ketamine are induced largely by targeting this burst firing. Burst firing can reduce synaptic transmission failure, enhance the signal-to-noise ratio, facilitate synaptic plasticity or promote neuropeptide release³³. Thus, enhanced bursting in the LHB may provide a stronger output than tonic firing onto the downstream inhibitory RMTg or onto inhibitory interneurons within the VTA or DRN, to suppress the activity of dopaminergic, serotonergic or glutamatergic neurons in the reward centres of the brain. By blocking NMDAR-dependent LHB bursts, ketamine can then release this inhibition brake onto the reward centres to elicit its rapid antidepressant effects. Although our data addresses how ketamine can act so rapidly, the mechanism for the long-term effects of ketamine remains unclear; it might involve upregulation of brain-derived neurotrophic factor (BDNF)⁵ or synaptogenesis⁴.

Given the importance of LHB bursting activity for the depressive state, it is plausible that entry into this mode should be carefully controlled. We found no significant changes in T-VSCC currents in the LHB of animal models of depression (Extended Data Fig. 7c, d). Instead, the RMPs of LHB neurons in these models were more

hyperpolarized (by 5–6 mV) than those of control animals (Extended Data Fig. 7e, f). Considering that hyperpolarization can convert silent or tonic-firing neurons to bursting mode (Extended Data Fig. 6e), we hypothesize that a molecular mechanism that lowers the RMPs of LHb neurons to the level at which T-VSCCs can be de-inactivated may account for the increase of LHb bursting in depression-like states. In the accompanying paper³⁴, we show that increased levels of astrocytic Kir4.1 and potassium buffering may be responsible for the hyperpolarization of RMPs and for the increased bursting of LHb neurons in depression.

Online Content Methods, along with any additional Extended Data display items and Source Data, are available in the online version of the paper; references unique to these sections appear only in the online paper.

Received 18 May 2017; accepted 9 January 2018.

- Berman, R. M. *et al.* Antidepressant effects of ketamine in depressed patients. *Biol. Psychiatry* **47**, 351–354 (2000).
- Zarate, C. A. Jr *et al.* A randomized trial of an *N*-methyl-D-aspartate antagonist in treatment-resistant major depression. *Arch. Gen. Psychiatry* **63**, 856–864 (2006).
- Maeng, S. *et al.* Cellular mechanisms underlying the antidepressant effects of ketamine: role of α -amino-3-hydroxy-5-methylisoxazole-4-propionic acid receptors. *Biol. Psychiatry* **63**, 349–352 (2008).
- Li, N. *et al.* mTOR-dependent synapse formation underlies the rapid antidepressant effects of NMDA antagonists. *Science* **329**, 959–964 (2010).
- Autry, A. E. *et al.* NMDA receptor blockade at rest triggers rapid behavioural antidepressant responses. *Nature* **475**, 91–95 (2011).
- Zanos, P. *et al.* NMDAR inhibition-independent antidepressant actions of ketamine metabolites. *Nature* **533**, 481–486 (2016).
- Clements, J. A., Nimmo, W. S. & Grant, I. S. Bioavailability, pharmacokinetics, and analgesic activity of ketamine in humans. *J. Pharm. Sci.* **71**, 539–542 (1982).
- Homayoun, H. & Moghaddam, B. NMDA receptor hypofunction produces opposite effects on prefrontal cortex interneurons and pyramidal neurons. *J. Neurosci.* **27**, 11496–11500 (2007).
- Matsumoto, M. & Hikosaka, O. Lateral habenula as a source of negative reward signals in dopamine neurons. *Nature* **447**, 1111–1115 (2007).
- Lammel, S. *et al.* Input-specific control of reward and aversion in the ventral tegmental area. *Nature* **491**, 212–217 (2012).
- Shabel, S. J., Proulx, C. D., Trias, A., Murphy, R. T. & Malinow, R. Input to the lateral habenula from the basal ganglia is excitatory, aversive, and suppressed by serotonin. *Neuron* **74**, 475–481 (2012).
- Stamatakis, A. M. & Stuber, G. D. Activation of lateral habenula inputs to the ventral midbrain promotes behavioral avoidance. *Nat. Neurosci.* **15**, 1105–1107 (2012).
- Stephenson-Jones, M. *et al.* A basal ganglia circuit for evaluating action outcomes. *Nature* **539**, 289–293 (2016).
- Morris, J. S., Smith, K. A., Cowen, P. J., Friston, K. J. & Dolan, R. J. Covariation of activity in habenula and dorsal raphe nuclei following tryptophan depletion. *Neuroimage* **10**, 163–172 (1999).
- Shumake, J., Edwards, E. & Gonzalez-Lima, F. Opposite metabolic changes in the habenula and ventral tegmental area of a genetic model of helpless behavior. *Brain Res.* **963**, 274–281 (2003).
- Li, B. *et al.* Synaptic potentiation onto habenula neurons in the learned helplessness model of depression. *Nature* **470**, 535–539 (2011).
- Li, K. *et al.* β CaMKII in lateral habenula mediates core symptoms of depression. *Science* **341**, 1016–1020 (2013).
- Lecca, S. *et al.* Rescue of GABAB and GIRK function in the lateral habenula by protein phosphatase 2A inhibition ameliorates depression-like phenotypes in mice. *Nat. Med.* **22**, 254–261 (2016).
- Aizawa, H., Kobayashi, M., Tanaka, S., Fukui, T. & Okamoto, H. Molecular characterization of the subnuclei in rat habenula. *J. Comp. Neurol.* **520**, 4051–4066 (2012).
- Tye, K. M. *et al.* Dopamine neurons modulate neural encoding and expression of depression-related behaviour. *Nature* **493**, 537–541 (2013).
- Hu, H. Reward and aversion. *Annu. Rev. Neurosci.* **39**, 297–324 (2016).
- Jhou, T. C., Fields, H. L., Baxter, M. G., Saper, C. B. & Holland, P. C. The rostromedial tegmental nucleus (RMTg), a GABAergic afferent to midbrain dopamine neurons, encodes aversive stimuli and inhibits motor responses. *Neuron* **61**, 786–800 (2009).
- Tian, J. & Uchida, N. Habenula lesions reveal that multiple mechanisms underlie dopamine prediction errors. *Neuron* **87**, 1304–1316 (2015).
- Zhou, L. *et al.* Organization of functional long-range circuits controlling the activity of serotonergic neurons in the dorsal raphe nucleus. *Cell Reports* **18**, 3018–3032 (2017).
- Chang, S. Y. & Kim, U. Ionic mechanism of long-lasting discharges of action potentials triggered by membrane hyperpolarization in the medial lateral habenula. *J. Neurosci.* **24**, 2172–2181 (2004).
- Weiss, T. & Veh, R. W. Morphological and electrophysiological characteristics of neurons within identified subnuclei of the lateral habenula in rat brain slices. *Neuroscience* **172**, 74–93 (2011).
- McCormick, D. A. & Bal, T. Sleep and arousal: thalamocortical mechanisms. *Annu. Rev. Neurosci.* **20**, 185–215 (1997).
- Grillner, S., McClellan, A., Sigvardt, K., Wallén, P. & Wilén, M. Activation of NMDA-receptors elicits “fictive locomotion” in lamprey spinal cord *in vitro*. *Acta Physiol. Scand.* **113**, 549–551 (1981).
- Schiller, J., Major, G., Koester, H. J. & Schiller, Y. NMDA spikes in basal dendrites of cortical pyramidal neurons. *Nature* **404**, 285–289 (2000).
- Zhu, Z. T., Munhall, A., Shen, K. Z. & Johnson, S. W. NMDA enhances a depolarization-activated inward current in subthalamic neurons. *Neuropharmacology* **49**, 317–327 (2005).
- Cheong, E. & Shin, H. S. T-type Ca^{2+} channels in normal and abnormal brain functions. *Physiol. Rev.* **93**, 961–992 (2013).
- Huguenard, J. R., Gutnick, M. J. & Prince, D. A. Transient Ca^{2+} currents in neurons isolated from rat lateral habenula. *J. Neurophysiol.* **70**, 158–166 (1993).
- Lisman, J. E. Bursts as a unit of neural information: making unreliable synapses reliable. *Trends Neurosci.* **20**, 38–43 (1997).
- Cui, Y. *et al.* Astroglial Kir4.1 in the lateral habenula drives neuronal bursts in depression. *Nature* <https://doi.org/10.1038/nature25752> (2018).

Supplementary Information is available in the online version of the paper.

Acknowledgements We thank L.-S. Yu and J. Pan for performing LC–MS/MS; S.-M. Duan, X.-H. Zhang, X.-W. Chen, Y.-S. Shu, X. Ju, C. Lohmann and W. Yang for advice on experimental design and comments on the manuscript; and N. Lin, L. Zhang and K.-F. Liu for consultation on *in vivo* recording. This work was supported by grants from the National Key R&D Program of China (2016YFA0501000), the National Natural Science Foundation of China (91432108, 31225010, and 81527901) to H.H. and (81600954) to Y.Y., and the 111 project (B13026) to H. H.

Author Contributions H.H., Y.C. and Y.Y. designed the study. Y.C. performed the *in vitro* patch-clamp experiments. Y.Y. and S.M. conducted the behavioural pharmacology experiments. K.S. performed the *in vivo* recordings. Y.D. and K.S. performed the optogenetic behaviour experiments. Z.N. established the biophysical model. H.H. conceived the project and wrote the manuscript with the assistance of Y.C., Y. Y. and Z.N.

Author Information Reprints and permissions information is available at www.nature.com/reprints. The authors declare competing financial interests; details are available in the online version of the paper. Readers are welcome to comment on the online version of the paper. Publisher's note: Springer Nature remains neutral with regard to jurisdictional claims in published maps and institutional affiliations. Correspondence and requests for materials should be addressed to H.H. (huhailan@zju.edu.cn).

Reviewer Information *Nature* thanks P. Kenny, H.-S. Shin and the other anonymous reviewer(s) for their contribution to the peer review of this work.

METHODS

Animals. Male cLH rats (8–16 weeks of age) and age-matched male Sprague Dawley rats (SLAC Laboratory Animal Co.) were used. The cLH rats were screened using the learned helplessness test^{17,35} for breeding as previously described³⁵. Male adult (8–16 weeks of age) C57BL/6 mice (SLAC) were used for establishing the chronic restraint stress (CRS) depression model. Rats were group-housed two per cage and mice were housed four per cage under a 12-h light–dark cycle (light on from 7 a.m. to 7 p.m.) with free access to food and water *ad libitum*. All animal studies and experimental procedures were approved by the Animal Care and Use Committee of the animal facility at Zhejiang University.

Systemic drug delivery for antidepressant. All drugs were dissolved in 0.9% saline, and administered intraperitoneally (i.p.). Concentrations were as follows: ketamine (Gutian Pharma Co.) 25 mg/kg for rats³⁶ and 10 mg/kg for mice⁶; ethosuximide (2-ethyl-2-methylsuccinimide; a T-VSCC blocker, which can cross the blood–brain barrier³⁷, Selleck) 200 mg/kg for mice. One hour after drug delivery, animals were used for behavioural or *in vivo* electrophysiology studies, or killed for *in vitro* electrophysiology studies.

Cannula infusion experiment. A 26-gauge double guide cannulae (centre-to-centre distance 1.4 mm, Plastics One) was placed at a 2° angle to the coronal plane (without the 2° rotation, we found it difficult to hit both sides of the LHb) and inserted bilaterally into the LHb (AP, −3.7 mm from bregma; ML, ±0.7 mm; DV, −4.05 mm from the brain surface) of cLH rats. A 33-gauge double dummy cannulae (Plastics One), secured with a dust cap, was inserted into the guide cannula to prevent clogging during the recovery period. After rats had recovered for at least 7 days, drugs were microinjected with a 33-gauge double injector cannulae, which has a 0.6-mm extension beyond the tip of the guide cannula, while cLH rats were anaesthetized with isoflurane on an anaesthetic machine. The extensions were manually sharpened before insertion.

Ketamine (25 µg/µl, IC₅₀ = 5.35 µM³⁸), AP5 (40 nmol/µl, IC₅₀ = 30 µM³⁹), NBQX (1 or 5 nmol/µl, IC₅₀ = 0.15 µM⁴⁰) or mibefradil (10 mol/µl, IC₅₀ = 2.7 µM⁴¹) were dissolved in 0.9% saline. Before the local drug infusion, tip-sharpened 33-gauge double injector cannulae were inserted into the guide cannulae to ensure clear passage and then pulled out. One microlitre of drug was infused (0.1 µl/min) into each side through another set of tip-sharpened 33-gauge double injector cannulae, which were connected to the microsyringe. The injector cannulae were left in place for an additional 10 min to minimize spread of the drug along the injection track. The FST or SPT was performed 1 h after the injection of ketamine or mibefradil and 0.5 h after the injection of AP5 or NBQX. To verify the drug infusion sites, rats were injected with 1 µl CTB-488 to each side of the LHb after all behavioural tests. For immunostaining, rats were then euthanized 30 min after CTB injection and processed as described¹⁷. Brain slices were counterstained with Hoechst before mounting on the slides. Fluorescent image acquisition was performed with an Olympus VS120 virtual microscopy slide scanning system. Only data from rats with correctly sited injections were used.

LC–MS/MS measurement of ketamine concentration. Male cLH rats were anaesthetized by isoflurane and subsequently decapitated 1 h after drug administration (i.p. or LHb cannulae infusion). Habenular or ventral hippocampal tissues (about 4 mg) were immediately dissected from the brain with Brain Matrix (RWD). The tissues were rinsed with PBS and immediately frozen in liquid nitrogen and stored at −80 °C until analysis. After samples were thawed, 100 µl solution (ddH₂O: acetonitrile = 9:1, v/v) and steel balls were added to homogenize samples for 2 min at 60 Hz with a tissue grinder. Ten microlitres of fluvoxamine solution (0.5 µg/ml) was then added for vortex mixing, followed by the addition of 100 µl supersaturated sodium carbonate. After vortex mixing for 10 s, the samples were extracted by liquid–liquid extraction with 800 µl methyl tert-butyl ether under continuous shaking for 2 min at room temperature. After centrifugation for 10 min at 13,000 r.p.m. at 4 °C, 640 µl of the upper layer was removed into a centrifugal concentrator (CentriVap, LABCONCO) to spin at 1,725 r.p.m. and 30 °C for 45 min, then vortexed with 40 µl solution (ddH₂O: acetonitrile = 1:1, v/v). After centrifugation for 5 min at 13,000 r.p.m. and 4 °C, the upper layer was injected into the chromatographic system.

The concentrations of (R,S)-ketamine in habenular and hippocampal tissue were determined by achiral LC–MS/MS following a previously described method^{6,42} with slight modifications. The analysis was accomplished using an Agilent Extend-C18 column (3.0 mm × 100 mm ID, 1.8 µm; Varian). The mobile phase consisted of 0.1% methanoic acid buffer (pH 2.67) as component A and acetonitrile as component B at a flow rate of 0.3 ml/min, temporized at 10 °C (injection volume: 7 µl). A linear gradient was run as follows: 0–0.2 min, 10% B; 0.2–1.5 min, from 10% B increased to 90% B; 1.5–3.0 min, 90% B; 3.0–3.1 min, from 90% B decreased to 10% B; 3.1–4.0 min, 10% B. Ten microlitres of (R,S)-ketamine of different concentrations (0.1, 1, 5, 10, 50, 100, 200 ng/ml) was mixed with 90 µl brain tissue to establish the standard calibration curve. The quantification of (R,S)-ketamine was accomplished by calculating area ratios using fluvoxamine

(10 µl of 0.5 µg/ml solution loaded) as the internal standard. The MS/MS analysis was performed using a triple quadrupole mass spectrometer model AB SCIEX 4000 plus (AB Company). The data were acquired and analysed using MutiQuant 3.0.2. Positive electrospray ionization data were acquired using multiple reaction monitoring (MRM) using the following transitions for (R,S)-ketamine studies: 238 → 125.

Viral vectors. AAV2/9-CaMKIIa-eNpHR3.0-eYFP (titre: 7.45×10^{12} vector genome (v.g.)/ml, dilution: 1:5, 0.1 µl unilateral into LHb, Taitool Bioscience), AAV2/9-Ubi-eGFP (titre: 2.5×10^{13} v.g./ml, 1:30, 0.1 µl unilateral into LHb, University of Massachusetts, Guangping Gao Laboratory), and AAV2/9-hSyn-oChIEF-tdTomato (titre: 6.29×10^{12} v.g./ml, 1:5, 0.1 µl unilateral into LHb, Obio Technology) were aliquoted and stored at −80 °C until use.

Behavioural assays. All behavioural assays were performed on animals 12–16 weeks old. Most behaviours were performed during the light phase except for the sucrose preference test, which was performed during the dark phase to maximize the consumption of solution, and the open field test for CRS mice. Behavioural analysis was performed blinded to experimental conditions.

Chronic restraint stress (CRS). Mice were subjected to chronic-restraint stress by placement in 50-ml conical tubes with holes for air flow for 2–3 h per day for 14 consecutive days⁴³.

Open field test (OFT). Animals were placed in the centre of an arena (40 cm × 40 cm × 40.5 cm for mice and 100 cm × 100 cm × 50 cm for rats) in a room with dim light for 10 min. A video camera positioned directly above the arena was used to track the movement of each animal (Any-maze, Stoelting). For optogenetic manipulations, mice were allowed to move freely throughout the arena for 9 min, with laser stimulation occurring during the middle 3-min epoch.

Forced swim test (FST). Animals were individually placed in a cylinder (12 cm diameter, 25 cm height for mice; 20 cm diameter, 50 cm height for rats) of water (23–25 °C) and swam for 6 min under normal light⁴⁴. Water depth was set to prevent animals from touching the bottom with their tails or hind limbs. Animal behaviours were videotaped from the side. The immobile time during the last 4-min test was counted offline by an observer blinded to animal treatment. Immobile time was defined as time when animals remained floating or motionless with only movements necessary for keeping balance in the water. For rats, an additional pre-test was conducted 24 h before the test, during which rats were individually placed in a cylinder of water with conditions described above for 15 min. For optogenetic manipulations, laser stimulation was delivered immediately after mice were placed in the water and lasted for 6 min. In order to minimize the impact of the optogenetic cable on swimming behaviour, the cable length was adjusted to allow the cable to just touch the water surface.

Sucrose preference test (SPT). Animals were single housed and habituated with two bottles of water for 2 days, followed by two bottles of 2% sucrose for 2 days⁴⁴. Animals were then water deprived for 24 h and then exposed to one bottle of 2% sucrose and one bottle of water for 2 h in the dark phase. Bottle positions were switched after 1 h (for 2 h test). Total consumption of each fluid was measured and sucrose preference was defined as the average sucrose consumption ratio during the first and second hours. Sucrose consumption ratio was calculated by dividing the total consumption of sucrose by the total consumption of both water and sucrose. For optogenetic manipulations, mice were gently placed in a white arena containing normal bedding and allowed to move freely in the arena. During the 90-min test, light was delivered during 30–60 min. Sucrose preference scores were measured for every 30 min. Only animals that had a baseline sucrose preference greater than 30% during the first 30-min session proceeded to the next session. Otherwise they were tested later on a different day²⁰.

Real-time place aversion (RTPA). Mice were placed in a white open chamber (52 cm × 26 cm × 23 cm) consisting of two chambers, and allowed to freely move between chambers for 20 min to assess their baseline place preference⁴⁵. During the following 20-min test, we assigned a stimulated side in a counterbalanced manner. Laser stimulation was delivered as soon as mice entered the stimulated side and terminated once mice crossed to the non-stimulated side. A video camera positioned above the chamber recorded each trial. Mouse locations and velocity were tracked and analysed using Any-maze software (Stoelting). Avoidance score was calculated as (Time in stimulated side – Time in non-stimulated side)_{test} – (Time in stimulated side – Time in non-stimulated side)_{baseline}.

Optogenetic light delivery and protocols. For mice expressing eNpHR3.0⁴⁶ and eGFP, a 589-nm yellow light laser was delivered at 1 Hz, 100 ms pulse. Light intensity was calculated to be 16 mW, which was estimated at 3.5 mm from optic patch cable tip with a ceramic sleeve. For the SPT experiment, laser intensity during eNpHR3.0 stimulation was adjusted to 10 mW because LHb neurons could not follow 16 mW stimulation for longer than 10 min (amplitude of bursting spikes declines to noise level). For mice expressing oChIEF⁴⁷ and eGFP, a 473-nm blue light laser was used; light intensity was calculated to be 25 mW. The blue light delivery paradigm was either 5 ms pulse, 5 pulses per s for the pulsed 100-Hz

protocol, or 20 Hz, tonic 5-ms pulses for the 20-Hz protocol, or 5 Hz, tonic 5-ms pulses for the 5-Hz protocol.

LHb brain slice preparation. Animals (postnatal day (P)45–70 rats and P65–75 mice) were anaesthetized with isoflurane and 10% chloral hydrate, and then perfused with 20 ml ice-cold ACSF (oxygenated with 95% O₂ + 5% CO₂) containing (mM): 125 NaCl, 2.5 KCl, 25 NaHCO₃, 1.25 NaH₂PO₄, 1 MgCl₂ and 25 glucose, with 1 mM pyruvate added. The brain was removed as quickly as possible after decapitation and put into chilled and oxygenated ACSF. Coronal (for most of experiments if not specified) or sagittal slices containing the habenula (350 µm and 300 µm thickness for rats and mice, respectively) were sectioned in cold ACSF using a Leica2000 vibratome and then transferred to ACSF at 32 °C for incubation and recovery. ACSF was continuously gassed with 95% O₂ and 5% CO₂. Slices were allowed to recover for at least 1 h before recording. For cLH rats, as a very high percentage (90%) of cLH offspring are learned helpless, we did not perform a learned helplessness test before taking them for brain slice recording. For CRS mice, both CRS and wild-type control mice went through an FST before brain slice recording. We then used the CRS animals that showed high immobility scores (immobile time >140 s) and control mice that showed low immobility (immobile time <110 s) in the FST for slice recording.

In vitro electrophysiological recordings. For LHb neuron recordings, currents were measured under whole-cell patch-clamp using pipettes with a typical resistance of 5–6 MΩ filled with internal solution containing (mM) 105 K-gluconate, 30 KCl, 4 Mg-ATP, 0.3 Na-GTP, 0.3 EGTA, 10 HEPES and 10 Na-phosphocreatine, with pH set to 7.35. The external ACSF solution contained (in mM) 125 NaCl, 2.5 KCl, 25 NaHCO₃, 1.25 NaH₂PO₄, 1 MgCl₂ and 25 glucose. Cells were visualized with infrared optics on an upright microscope (BX51WI, Olympus). A MultiClamp 700B amplifier and pCLAMP10 software were used for electrophysiology (Axon Instruments). The series resistance and capacitance were compensated automatically after a stable Gigaseal was formed. Recordings were typically performed between 3 and 6 min after break-in. The spontaneous neuronal activity was recorded under current clamp ($I = 0$ pA).

LHb neurons show three modes of spontaneous activity at resting conditions. Silent cells showed no spike activity during recording. Tonic cells spontaneously generated tonic trains of action potentials at frequencies between 0.1 and 10 Hz, rarely up to 10–20 Hz. Burst-firing cells spontaneously generated clusters of spikes with an initially high but progressively declining intra-burst firing frequency in each burst. For bursting neurons, 99% (from $n = 50$ bursting neurons) of their spikes occurred within bursts. The inter-spike intervals (ISI) of neurons represent the duration of the silent periods between two neighbouring single spikes. A typical bursting neuron shows a bimodal distribution of ISIs since it is composed of relatively large inter-burst intervals and small intra-burst intervals. By contrast, tonic-firing neurons show a more homogenous Poisson distribution of ISIs.

Evoked NMDAR EPSCs were recorded under voltage clamp from –50 mV to –80 mV in sagittal LHb slices by stimulating the input stria medullaris fibre in a modified extracellular ACSF solution⁴⁸ with the AMPAR blocker NBQX, GABAR blocker picrotoxin and 0 Mg²⁺ and isolated currents were confirmed to be NMDAR currents because they could be abolished by AP5 (Extended Data Fig. 5a, b). Evoked T-type VSCC currents were recorded under voltage clamp starting from a holding potential of –50 mV before being increased to conditioning potential (–100 mV) for 1 s preceding the command steps (5 mV, 0.1 Hz per step increment). LHb T-VSCC currents were obtained by subtraction of recorded traces in the presence or absence of mibefradil⁴⁹ (Extended Data Fig. 7a–d).

Pharmacological characterization of burst and neuronal RMP. Ketamine (100 µM, 10 mM and 1 µM, Gutian Pharma Co.)⁵, AP5 (100 µM, Sigma)⁵⁰, NBQX (10 µM, Sigma)⁵¹, mibefradil (10 µM, Sigma)⁵², ZD7288 (50 µM, Tocris)⁵³, TTX (1 µM, Sigma)¹⁸, picrotoxin (100 µM, Sigma)⁵⁰, NMDA (20 µM, Sigma)⁵⁴, AMPA (1 µM, Sigma)⁴⁸ and fluoxetine (30 µM, Sigma)^{55,56} were used for electrophysiology. Drugs were dissolved in water, aliquoted at 1,000× final concentration and stocked at –80 °C before use. Recordings were performed between 3 and 6 min after whole cell break-in. During recordings, baselines of spontaneous or rebound bursts and RMPs were recorded for at least 3 min before drugs were perfused. The start of drug perfusion was precisely indicated by a bubble that was added before the transition from normal ACSF to ACSF with drug.

The effect of ketamine (100 µM) on mEPSCs was tested under voltage clamp (the cells were held at –60 mV) in the presence of TTX (1 µM) and picrotoxin (100 µM) in ACSF. The intracellular solution contained CsMeSO₃ 115 mM, CsCl 20 mM, HEPES 10 mM, MgCl₂ 2.5 mM, Na₂-ATP 4 mM, Na-GTP 0.4 mM, Na-phosphocreatine 10 mM, and EGTA 0.6 mM. Data were filtered at 2 kHz and sampled at 10 kHz using Digidata1550. The baseline was recorded for 5 min. Ketamine was then perfused for 10 min. mEPSCs were analysed from 2 to 4 min before and 5 to 7 min after the start of ketamine perfusion. Data were analysed by Mini Analysis Program (Synaptosoft) with an amplitude threshold of 5 pA.

In vivo electrophysiology. For *in vivo* recording experiments, a custom-made microdrive array consisting of eight tetrodes (impedance 250–500 KΩ, California fine wire)⁵⁷ was implanted into the LHb (AP, –1.72 mm; ML, 0.46 mm; DV, –2.44 mm from the brain surface) of control or CRS mice. Stainless steel wires were attached to two screws on the skull as ground. The microdrive was secured to the skull with dental cement. After recovery for 2 weeks, mice were allowed to adapt to the recording headstage for 10 min per day for 2–3 days. Spontaneous spiking activity (digitized at 40 kHz, band-pass filtered between 300 and 6,000 Hz) and LFP (digitized at 1 kHz sampling rate, low-pass filtered up to 250 Hz) were recorded simultaneously for 30 min during the still period of the mice in their home cages with a gain of 5,000×. A single channel without a detectable unit was assigned as a reference electrode. The tetrodes were lowered in steps of 70 µm after each recording session, followed by at least a 2-day recovery. For CRS mice, data were recorded for 30 min before and 1 h after ketamine treatment (10 mg/kg, i.p.). If mice received a second ketamine injection, at least a 2-week interval was introduced before the next recording session. All procedures were performed during the light phase. The positions of the electrodes were verified by electrolytic lesions (30 µA, 10–15 s) at the end of all experiments.

Spike sorting. All waveforms recorded from each tetrode were imported in Offline Sorter V3 (Plexon Inc.). Single units were manually identified by threshold crossing and principal component analysis (PCA). Spikes with inter-spike interval (ISI) less than the refractory period (1.4 ms) were excluded. Cross correlograms were plotted to ensure that no cell was discriminated more than once on overlapping tetrodes. Only units with a signal-to-noise ratio larger than 2 were used.

Data analysis. Data analysis was conducted by Neuroexplorer4 (Plexon Inc.) and MATLAB. For criteria to identify *in vivo* bursts in the LHb, we analysed intra-spike intervals from 120 spontaneous bursts (from 10 neurons) recorded in LHb brain slices (Extended Data Fig. 4c). All bursts began with a maximal inter-spike interval of 20 ms and ended with a maximal inter-spike interval of 100 ms (Extended Data Fig. 4c). Accordingly, we defined *in vivo* bursting as clusters of spikes beginning with a maximal inter-spike interval of 20 ms and ending with a maximal inter-spike interval of 100 ms (Extended Data Fig. 4d). The minimum intra-burst interval was set at 100 ms (Extended Data Fig. 4d) and the minimum number of spikes in a burst was set at 2. Burst events per minute, the percentage of spike firing within bursts, intra and inter-burst intervals and average spike numbers in a burst were analysed.

The raw LFPs were filtered between 1 and 200 Hz using a fourth-order Butterworth filter. To measure the synchronization between spikes and local field potential oscillations, we calculated spike-triggered averages (STAs)^{58,59} by averaging all LFP segments at ±300 ms around all spikes under one experimental condition, and normalized STAs by spike number. Only STAs of spikes and LFPs recorded from separate electrodes were used. We then quantified STAs using spike-field coherence (SFC)^{58,59}. The spectrum of the STA (fSTA) was calculated using the multitaper method (Chronux 2.0) with seven tapers. The average of these individual frequency spectra results in the spike triggered power (STP). The SFC was calculated as $SFC(f) = [fSTA(f)/STP(f)]$. SFC in the theta band was calculated as the average SFC in the theta frequency domain (4–10 Hz).

In vivo optoretro recordings. To validate the effects of optogenetic stimulation on neuron firing, optoretro recording was applied on mice injected with AAV2/9-CaMKIIa-eNpHR3.0-eYFP into the LHb. Mice were anaesthetized with isoflurane (5% for induction and 1% for maintenance). An optrode consisted of four tetrodes and an optical fibre in the centre was lowered into the LHb (AP, –1.72 mm; ML, 0.46 mm; DV, –2.62 mm from the brain surface). The tip of the optical fibre was 200 µm above the tip of the tetrodes. For optical stimulation, the optical fibre was connected to a 589 nm laser. 100 ms light pulses at 1 Hz were delivered to evoke rebound bursting. The light intensity was identical to that used in behavioural tests. Single units were recorded and sorted as described above.

Surgery for optogenetics. Mice (P50–80) were deeply anaesthetized and placed in a stereotaxic frame (RWD Instruments). Virus (0.1 µl) was injected into the LHb one side (AP, –1.72 mm from bregma; ML, ±0.46 mm; DV, –2.62 mm from the brain surface) using a pulled glass capillary with a pressure microinjector (Picospritzer III, Parker) at a rate of 0.1 µl/min. The injection needle was withdrawn 10 min after the end of the injection. After surgery, mice recovered from anaesthesia on a heat pad.

For optic fibre implantation, a 200-µm fibre-optic cannula (Plastics one) was placed 300 µm above the centre of viral injection site, and cemented onto the skull using dental cement.

Biophysics modelling. Our single compartment model of a LHb neuron was constructed using the following equations:

$$dV/dt = (I_{inj} - I_T - I_K - I_{Na} - I_{Kleak} - I_{NaLeak} - I_{AMPA} - I_{NMDA} - I_{GABA})/c$$

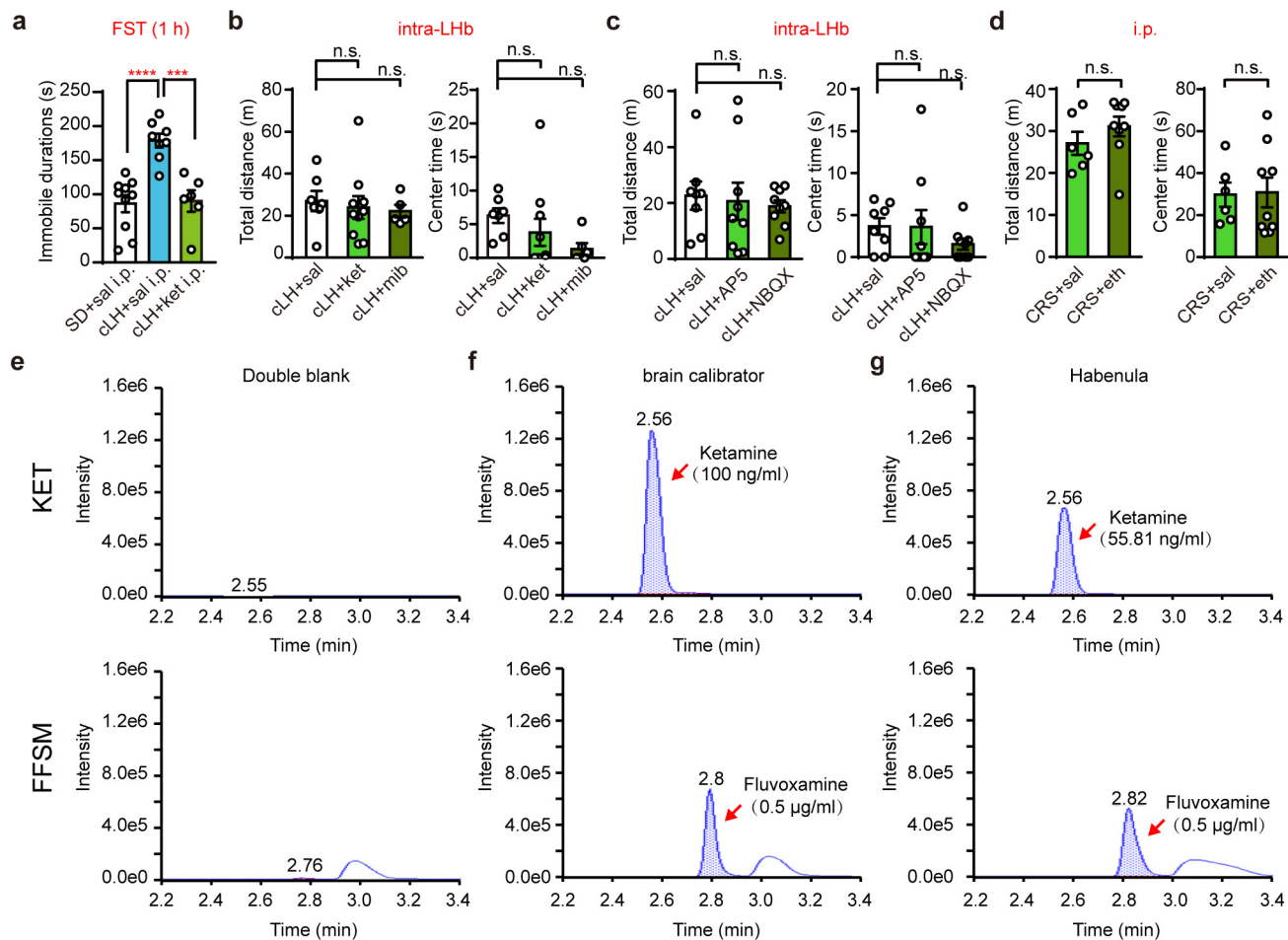
where V is the membrane potential and c is the capacitance of the membrane. Only currents absolutely necessary were included in the model. I_{inj} is the external current

applied to the cell; I_T is the low-threshold Ca^{2+} current mediated by T-VSCCs; I_{Na} and I_K are the fast Na^+ and K^+ currents of action potentials; I_{Kleak} and I_{Naleak} are responsible for the resting membrane potential; I_{AMPA} , I_{NMDA} and I_{GABA} are the synaptic currents mediated by AMPA, NMDA and GABA receptors respectively. See Supplementary Information for detailed formulae.

Statistical analysis. Required sample sizes were estimated on the basis of our past experience performing similar experiments. Mice were randomly assigned to treatment groups. Analyses were performed in a manner blinded to treatment assignments in all behavioural experiments. Statistical analyses were performed using GraphPad Prism software v6. By pre-established criteria, values were excluded from analyses if the viral injection or drug delivery sites were out of the LHb. All statistical tests were two-tailed, and significance was assigned at $P < 0.05$. Normality and equal variances between group samples were assessed using the D'Agostino & Pearson omnibus normality test and Brown–Forsythe tests, respectively. When normality and equal variance between sample groups was achieved, one-way ANOVA (followed by Bonferroni's multiple comparisons test), or t -test were used. Where normality or equal variance of samples failed, Kruskal–Wallis one-way ANOVA (followed by Dunn's correction), Mann–Whitney U test, or Wilcoxon matched-pairs signed rank test were performed. Linear regression test, Chi-square test, Fisher's exact test or two-way ANOVA (followed by Bonferroni's multiple comparisons test) were used in appropriate situations. The sample sizes, specific statistical tests used, and main effects of our statistical analyses for each experiment are reported in Supplementary Information Table 1.

Data availability. The data that support the findings of this study are available from the corresponding author upon reasonable request.

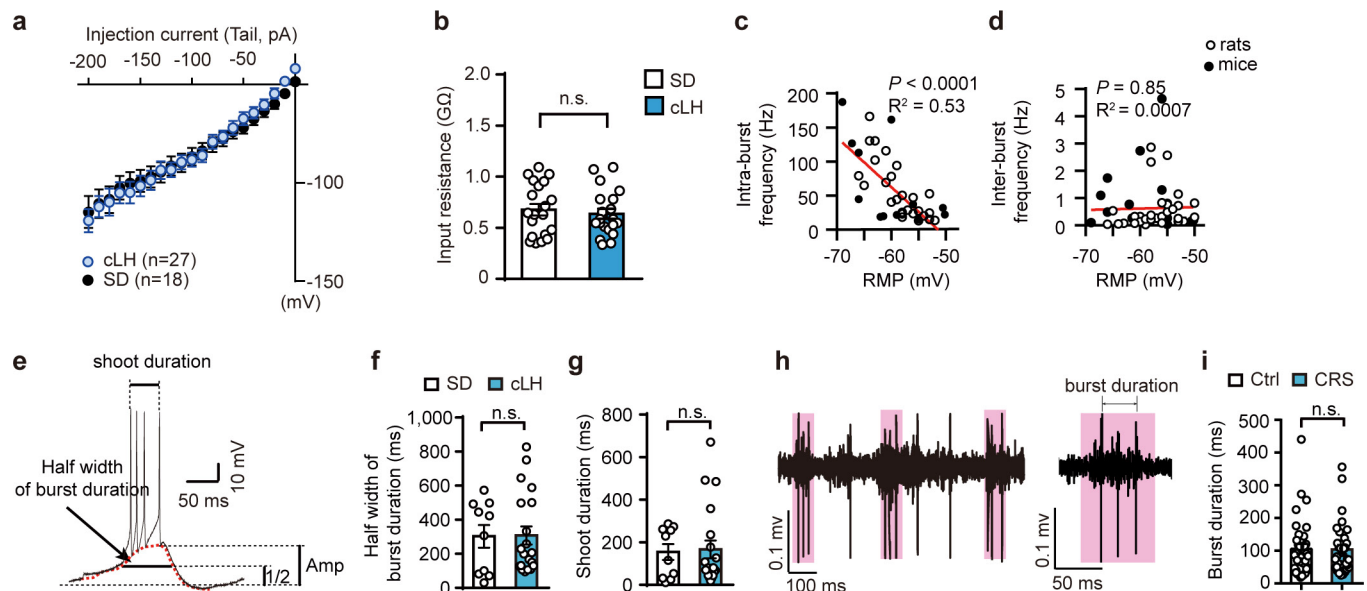
35. Henn, F. A. & Vollmayr, B. Stress models of depression: forming genetically vulnerable strains. *Neurosci. Biobehav. Rev.* **29**, 799–804 (2005).
36. Gigliucci, V. *et al.* Ketamine elicits sustained antidepressant-like activity via a serotonin-dependent mechanism. *Psychopharmacology (Berl.)* **228**, 157–166 (2013).
37. Gören, M. Z. & Onat, F. Ethosuximide: from bench to bedside. *CNS Drug Rev.* **13**, 224–239 (2007).
38. Gideons, E. S., Kavalali, E. T. & Monteggia, L. M. Mechanisms underlying differential effectiveness of memantine and ketamine in rapid antidepressant responses. *Proc. Natl Acad. Sci. USA* **111**, 8649–8654 (2014).
39. Ambert, N. *et al.* Computational studies of NMDA receptors: differential effects of neuronal activity on efficacy of competitive and non-competitive antagonists. *Open Access Bioinformatics* **2**, 113–125 (2010).
40. Endo, M., Kurachi, Y. & Mishina, M. *Pharmacology of Ionic Channel Function: Activators and Inhibitors* Vol. 147 (Springer Science & Business Media, 2012).
41. Mehrke, G., Zong, X. G., Flockerzi, V. & Hofmann, F. The Ca^{++} -channel blocker Ro 40-5967 blocks differently T-type and L-type Ca^{++} channels. *J. Pharmacol. Exp. Ther.* **271**, 1483–1488 (1994).
42. Hasan, M. *et al.* Quantitative chiral and achiral determination of ketamine and its metabolites by LC-MS/MS in human serum, urine and fecal samples. *J. Pharm. Biomed. Anal.* **139**, 87–97 (2017).
43. Kim, K. S. & Han, P. L. Optimization of chronic stress paradigms using anxiety- and depression-like behavioral parameters. *J. Neurosci. Res.* **83**, 497–507 (2006).
44. Powell, T. R., Fernandes, C. & Schalkwyk, L. C. Depression-related behavioral tests. *Curr. Protoc. Mouse Biol.* **2**, 119–127 (2012).
45. Zhu, Y., Wienecke, C. F., Nachtrab, G. & Chen, X. A thalamic input to the nucleus accumbens mediates opiate dependence. *Nature* **530**, 219–222 (2016).
46. Gradinaru, V. *et al.* Molecular and cellular approaches for diversifying and extending optogenetics. *Cell* **141**, 154–165 (2010).
47. Lin, J. Y., Lin, M. Z., Steinbach, P. & Tsien, R. Y. Characterization of engineered channelrhodopsin variants with improved properties and kinetics. *Biophys. J.* **96**, 1803–1814 (2009).
48. Ren, M., Cao, V., Ye, Y., Manji, H. K. & Wang, K. H. Arc regulates experience-dependent persistent firing patterns in frontal cortex. *J. Neurosci.* **34**, 6583–6595 (2014).
49. Coulter, D. A., Huguenard, J. R. & Prince, D. A. Calcium currents in rat thalamocortical relay neurones: kinetic properties of the transient, low-threshold current. *J. Physiol. (Lond.)* **414**, 587–604 (1989).
50. Shabel, S. J., Proulx, C. D., Piriz, J. & Malinow, R. Mood regulation. GABA/glutamate co-release controls habenula output and is modified by antidepressant treatment. *Science* **345**, 1494–1498 (2014).
51. Valentinova, K. & Mameli, M. mGluR-LTD at excitatory and inhibitory synapses in the lateral habenula tunes neuronal output. *Cell Reports* **16**, 2298–2307 (2016).
52. Zhu, Z. T., Munhall, A., Shen, K. Z. & Johnson, S. W. Calcium-dependent subthreshold oscillations determine bursting activity induced by *N*-methyl-D-aspartate in rat subthalamic neurons *in vitro*. *Eur. J. Neurosci.* **19**, 1296–1304 (2004).
53. Rateau, Y. & Ropert, N. Expression of a functional hyperpolarization-activated current (I_h) in the mouse nucleus reticularis thalami. *J. Neurophysiol.* **95**, 3073–3085 (2006).
54. Bon, C. L., Paulsen, O. & Greenfield, S. A. Association between the low threshold calcium spike and activation of NMDA receptors in guinea-pig substantia nigra pars compacta neurons. *Eur. J. Neurosci.* **10**, 2009–2015 (1998).
55. Zhong, P. & Yan, Z. Differential regulation of the excitability of prefrontal cortical fast-spiking interneurons and pyramidal neurons by serotonin and fluoxetine. *PLoS One* **6**, e16970 (2011).
56. Caiati, M. D. & Cherubini, E. Fluoxetine impairs GABAergic signaling in hippocampal slices from neonatal rats. *Front. Cell. Neurosci.* **7**, 63 (2013).
57. Lin, L. *et al.* Large-scale neural ensemble recording in the brains of freely behaving mice. *J. Neurosci. Methods* **155**, 28–38 (2006).
58. Fries, P., Roelfsema, P. R., Engel, A. K., König, P. & Singer, W. Synchronization of oscillatory responses in visual cortex correlates with perception in interocular rivalry. *Proc. Natl Acad. Sci. USA* **94**, 12699–12704 (1997).
59. Rutishauser, U., Ross, I. B., Mamelak, A. N. & Schuman, E. M. Human memory strength is predicted by theta-frequency phase-locking of single neurons. *Nature* **464**, 903–907 (2010).



Extended Data Figure 1 | Representative ion chromatograms of separation of ketamine by LC-MS/MS and OFT results for different drug treatments.

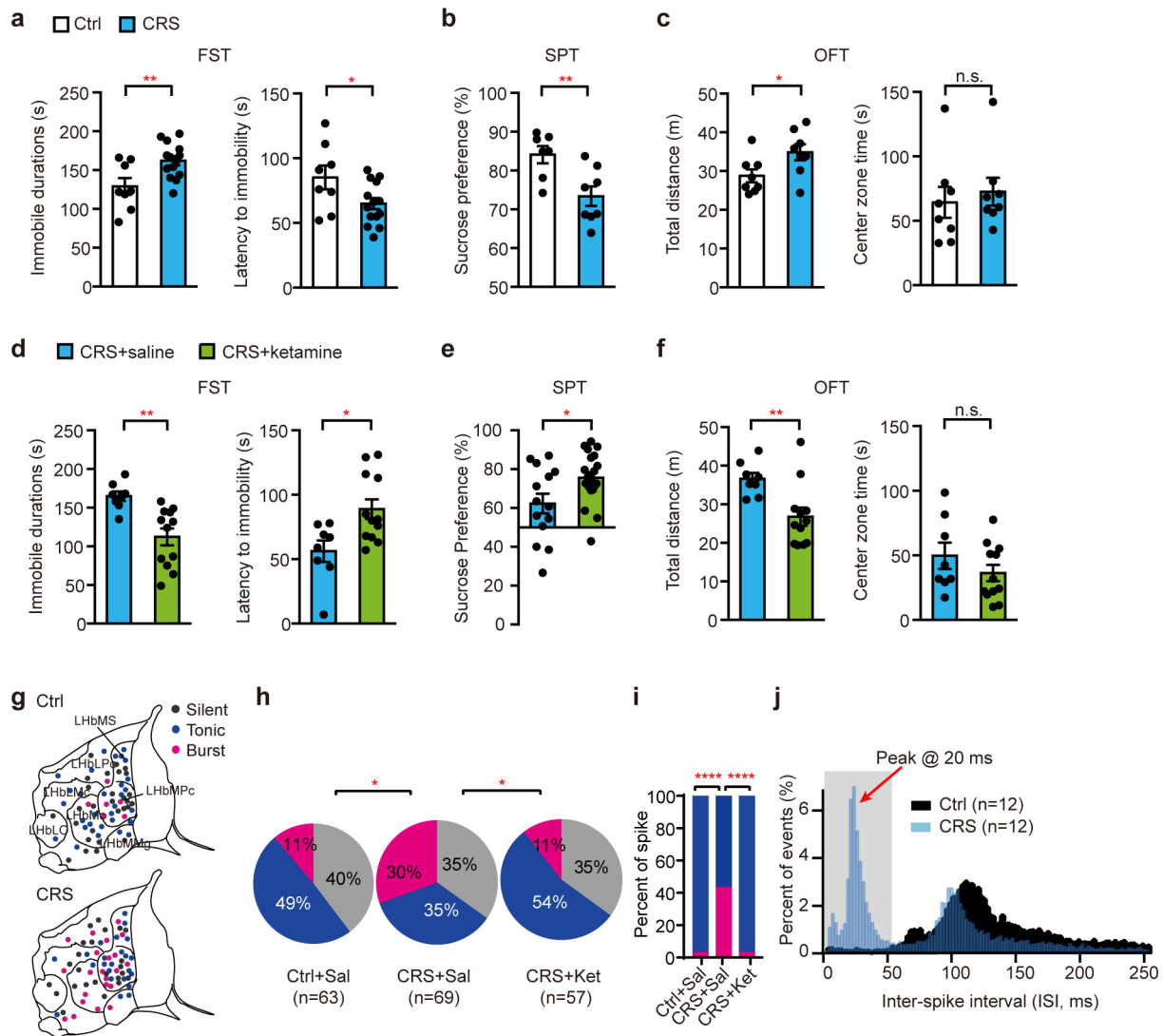
a, Antidepressant response to systemic ketamine injection (25 mg kg^{-1} , i.p.) in FST 1 h after treatment in cLH rats. $n = 10$, 8, 6 for wild-type rats injected with saline, cLH rats injected with saline, and cLH rats injected with ketamine, respectively. **b**, **c**, OFT of cLH rats after bilateral infusion of ketamine ($25 \mu\text{g}$, $1 \mu\text{l}$ each side) or mibefradil (10 nmol , $1 \mu\text{l}$ each side; **b**), AP5 (40 nmol , $1 \mu\text{l}$ each side) or NBQX (1 nmol , $1 \mu\text{l}$ each side; **c**) into the LHb. $n = 7$, 10, 6 rats (**b**) and 8, 9, 9 rats (**c**) for saline, ketamine and mibefradil, respectively. **d**, OFT of CRS

mice 1 h after intraperitoneal injection of saline or ethosuximide. $n = 6$, 9 mice for saline and ethosuximide, respectively. **e–g**, Representative ion chromatograms of separation of ketamine including double blank (**e**), brain calibrator spiked with 100 ng ml^{-1} ketamine (KET) (**f**) and a habenular sample from a cLH rat bilaterally infused with $25 \mu\text{g} \mu\text{l}^{-1}$ ketamine into the LHb 1 h earlier (**g**). Fluvoxamine (FFSM) is used as the internal standard. Data are mean \pm s.e.m.; *** $P < 0.001$, **** $P < 0.0001$; n.s., not significant. One-way ANOVA (**a–c**), two-tailed Mann–Whitney test and unpaired t -test (**d**).



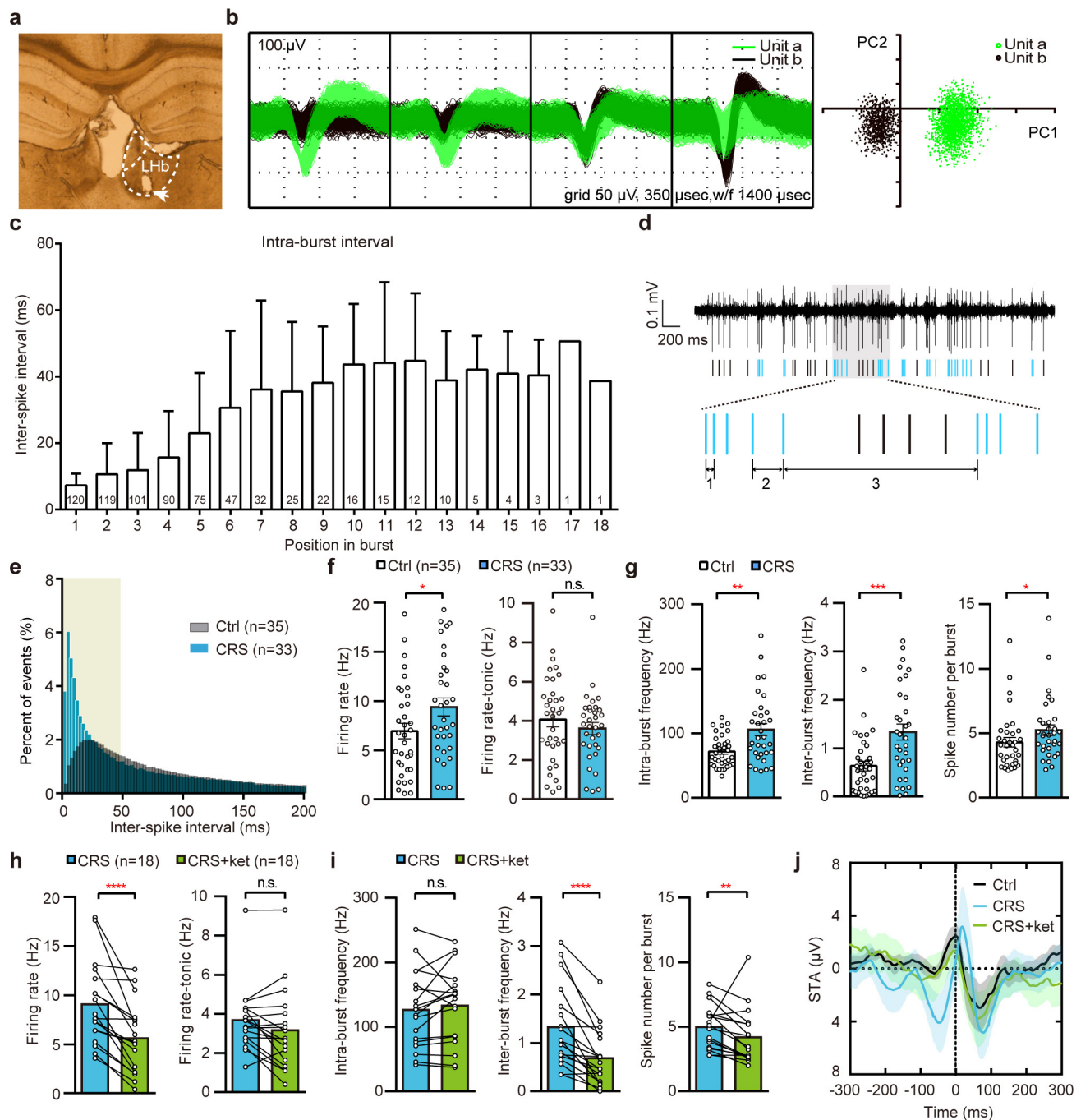
Extended Data Figure 2 | *I*-*V* relationship, input resistance and burst duration are not changed in animal models of depression. **a-d**, *I*-*V* plots (**a**), input resistance (**b**), intra-burst frequency (**c**) and inter-burst frequency (**d**) for LHB neurons in brain slices from mice and rats. Note that intra-burst frequency (**c**) but not inter-burst frequency (**d**) reversely correlates with RMPs. $n = 20$ neurons per group, 5 wild-type and 3 cLH rats (**b**); $n = 53$ neurons, 8 mice and 12 rats (**c**, **d**). **e-i**, Burst duration in animal models of depression recorded in brain slices *in vitro* (**e-g**) and in behaving animals *in vivo* (**h**, **i**). **e**, Representative trace of a typical burst in an *in vitro* recording. It consists of a depolarizing wave and a high-frequency train of action potentials. The duration of the line indicated by the black arrow at half-maximum amplitude of the area under the red dash

line is defined as the half width of burst duration; the duration between the first and last shoots (intra burst spikes) within one burst is defined as the shoot duration. **f**, **g**, Half widths of burst duration (**f**) and shoot duration (**g**) do not differ between cLH and wild-type rats. $n = 10$, 20 neurons, 7 wild-type and 5 cLH rats. **h**, Representative trace of an LHB neuron (pink shades indicate burst events) recorded *in vivo*. An enlarged view of a typical burst on the right shows the definition of burst duration, which is the time interval between the first and last spike within the same burst. **i**, Burst duration of LHB neurons from *in vivo* recording do not differ between control and CRS mice. $n = 35$, 33 neurons, 5 control and 5 CRS mice. Data are mean \pm s.e.m.; n.s., not significant. Two-tailed unpaired *t*-test (**b**, **f**, **g**) and Mann-Whitney test (**i**).



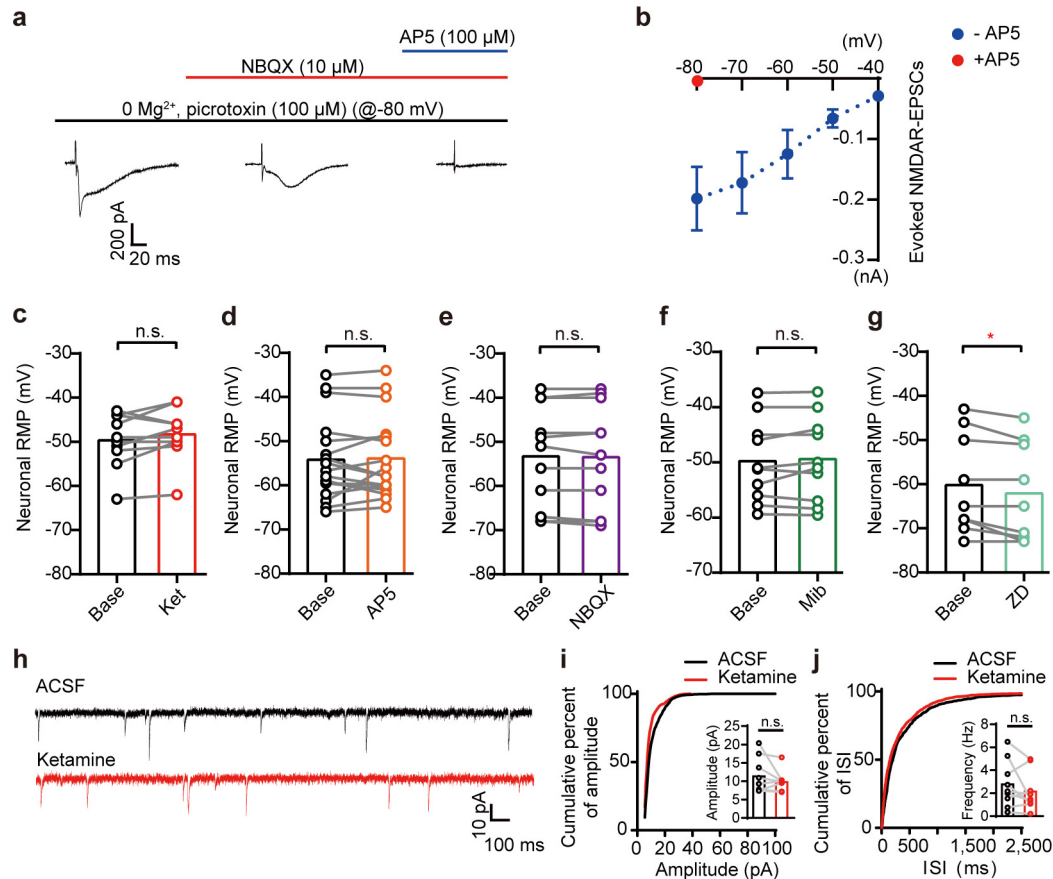
Extended Data Figure 3 | Chronic restraint stress induces reliable depression-like phenotypes and increased burst firing, which can be reversed by ketamine. **a, b**, CRS induces increased immobility and decreased latency to immobility in the FST (**a**) and decreases sucrose preference in the SPT (**b**). $n = 8, 14$ mice (**a**) and $7, 8$ mice (**b**) for control and CRS group, respectively. **c**, CRS increases locomotion in the OFT. $n = 8$ mice per group. **d, e**, Ketamine suppresses immobility of CRS mice in the FST (**d**) and increases sucrose preference (**e**) in CRS mice. **f**, Ketamine decreases locomotion of CRS mice in the OFT. $n = 8, 12$ mice (**d, f**) and $14, 21$ mice (**e**) for saline and ketamine groups, respectively. **g–j**, Burst firing is significantly increased in CRS mice, and this increase

is reversed by ketamine (i.p., 10 mg kg^{-1}). **g**, Whole-cell patch-clamp recording sites across different subregions of LHb in mice. **h**, Pie charts illustrating the per cent abundance of the three types of LHb neurons in all spikes recorded. **i**, Bar graph illustrating the percentage of burst- and tonic-type spikes in all spikes recorded. **j**, Histogram of distribution of inter-spike intervals (ISIs). $n = 63, 69, 57$ neurons, 4 control, saline-treated mice, 3 CRS, saline-treated mice and 5 CRS, ketamine-treated mice. Data are mean \pm s.e.m.; * $P < 0.05$, ** $P < 0.01$, **** $P < 0.0001$, n.s., not significant. Two-tailed Mann–Whitney test and unpaired t -test (**a–f**), Chi-square test (**h**), Fisher's exact test (**i**).



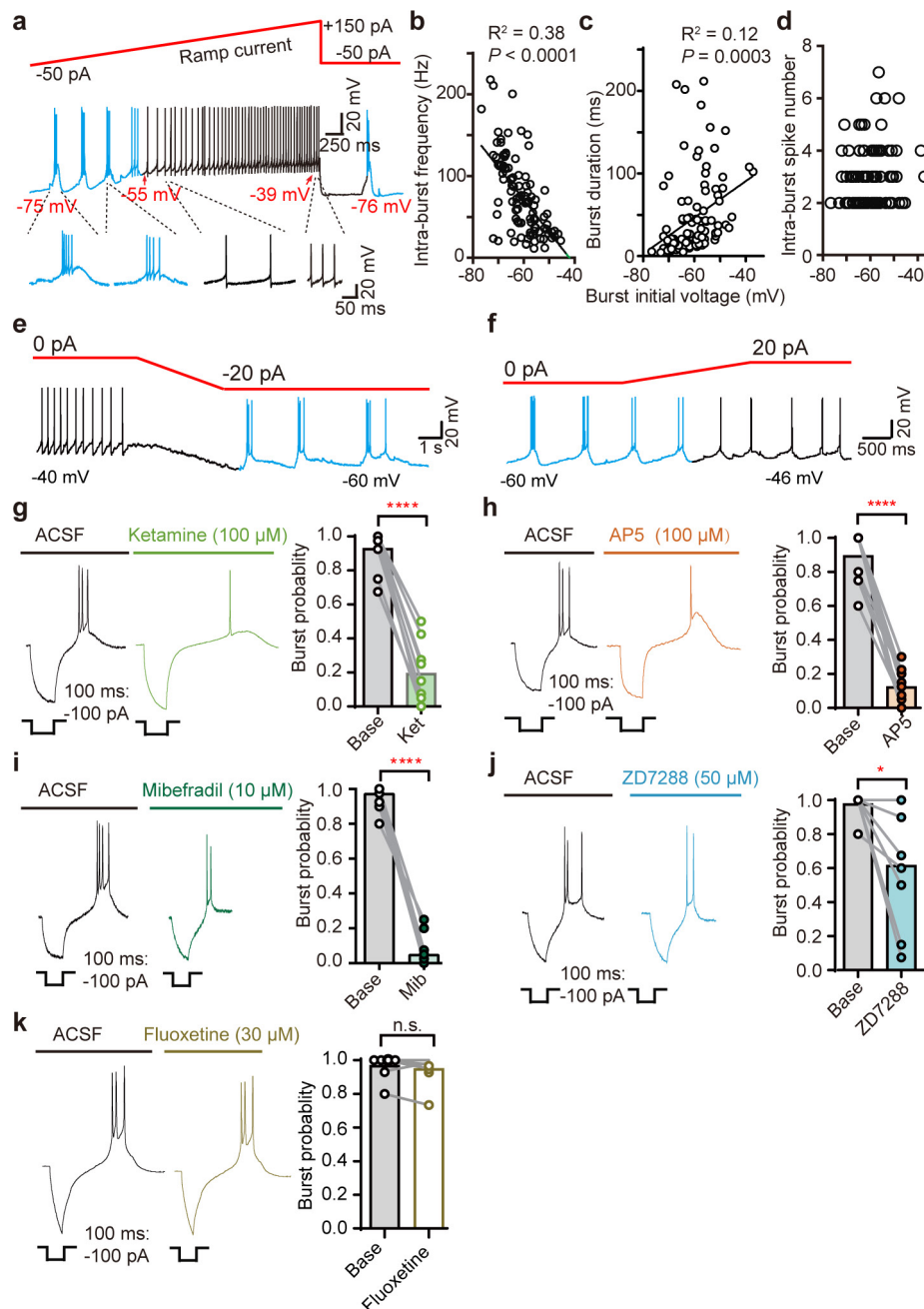
Extended Data Figure 4 | Ketamine suppresses LHB bursting activity *in vivo*. **a**, Histology of recording site. Arrowhead indicates the electrical lesion by tetrodes. **b**, Representative waveform clusters of two isolated LHB units in the respective four channels of a tetrode (left) and principal-component analysis (PCA) clustering display of these two units (right). **c**, ISIs between consecutive spikes in relation to their positions within the burst (120 bursts from *in vitro* recording). **d**, Example recording trace (upper) and spike train (bottom) of an irregular-firing LHB neuron from an *in vivo* recording. Bursts (blue sticks) are identified by ISI method (see Methods for details): 1, ISI to start burst; 2, ISI to end burst; 3, inter-burst interval. **e**, Histogram of ISI distribution (bin, 2.5 ms) from *in vivo* recording. **f–i**, Mean of total and tonic firing rates (**f**, **h**), intra- and

inter-burst frequencies, and number of spikes per burst (**g**, **i**) of neurons recorded *in vivo* from control mice, CRS mice and CRS mice 1 h before and after ketamine injection (i.p., 10 mg kg⁻¹). *n* = 35, 33 neurons (**f**, **g**) and 18, 18 neurons (**h**, **i**), 5 control and 5 CRS mice. **j**, STAs of neurons recorded *in vivo* from control mice, CRS mice, and CRS mice after ketamine injection (i.p., 10 mg kg⁻¹). Note that the distance between the neighbouring troughs is around 140 ms (corresponding to 7 Hz) in CRS mice. Data are mean ± s.e.m.; **P* < 0.05, ***P* < 0.01, ****P* < 0.001, *****P* < 0.0001, n.s., not significant. Two-tailed Mann–Whitney test and unpaired *t*-test (**f**, **g**), two-tailed Wilcoxon matched-pairs signed rank test and paired *t*-test (**h**, **i**).



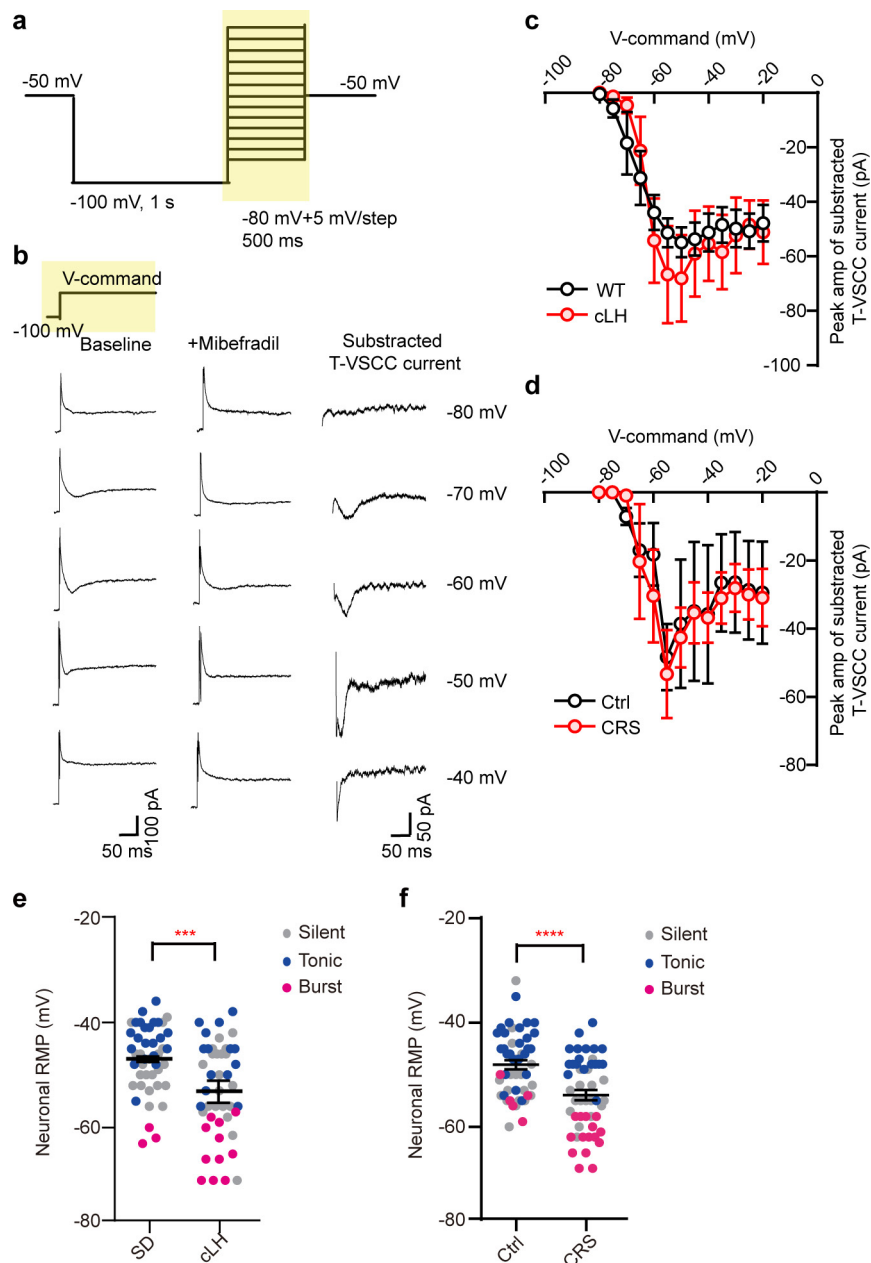
Extended Data Figure 5 | Drug effects on NMDAR currents, RMPs and miniature EPSCs of LHb neurons. **a**, Example traces showing evoked EPSCs when cells were held at -80 mV. NMDAR EPSCs were isolated by application of picrotoxin ($100 \mu\text{M}$) and NBQX ($10 \mu\text{M}$) in Mg^{2+} -free ACSF, and confirmed by AP5 ($100 \mu\text{M}$) blockade. **b**, Amplitudes of NMDAR EPSCs under different voltages (EPSCs are recorded under 0Mg^{2+} , picrotoxin and NBQX). Note that isolated NMDAR EPSCs are completely blocked by AP5. **c–f**, Ketamine (c), AP5 (d), NBQX (e) and mibefradil (f) do not affect RMPs of LHb neurons. $n = 10$ neurons, 5 rats (c); $n = 17$ neurons, 6 rats (d); $n = 11$ neurons, 6 rats (e); $n = 10$ neurons, 3 rats (f).

g, ZD7288 causes a small but significant hyperpolarization of LHb neurons. $n = 9$ neurons, 4 rats. **h**, Example mEPSC traces before (black) and after (red) perfusion of ketamine ($100 \mu\text{M}$, see Methods) measured in a whole-cell configuration (cells were held at -60 mV) from LHb neurons. **i, j**, Cumulative distribution of mEPSC amplitude (i) or mEPSC inter-events interval and average frequency (j) of neurons before (black) or after (red) ketamine treatment. Each line represents values before or after treatment with ketamine from the same LHb neuron. $n = 9$ neurons, 2 rats. Data are mean \pm s.e.m.; $*P < 0.05$, n.s., not significant. Two-tailed paired t -test.



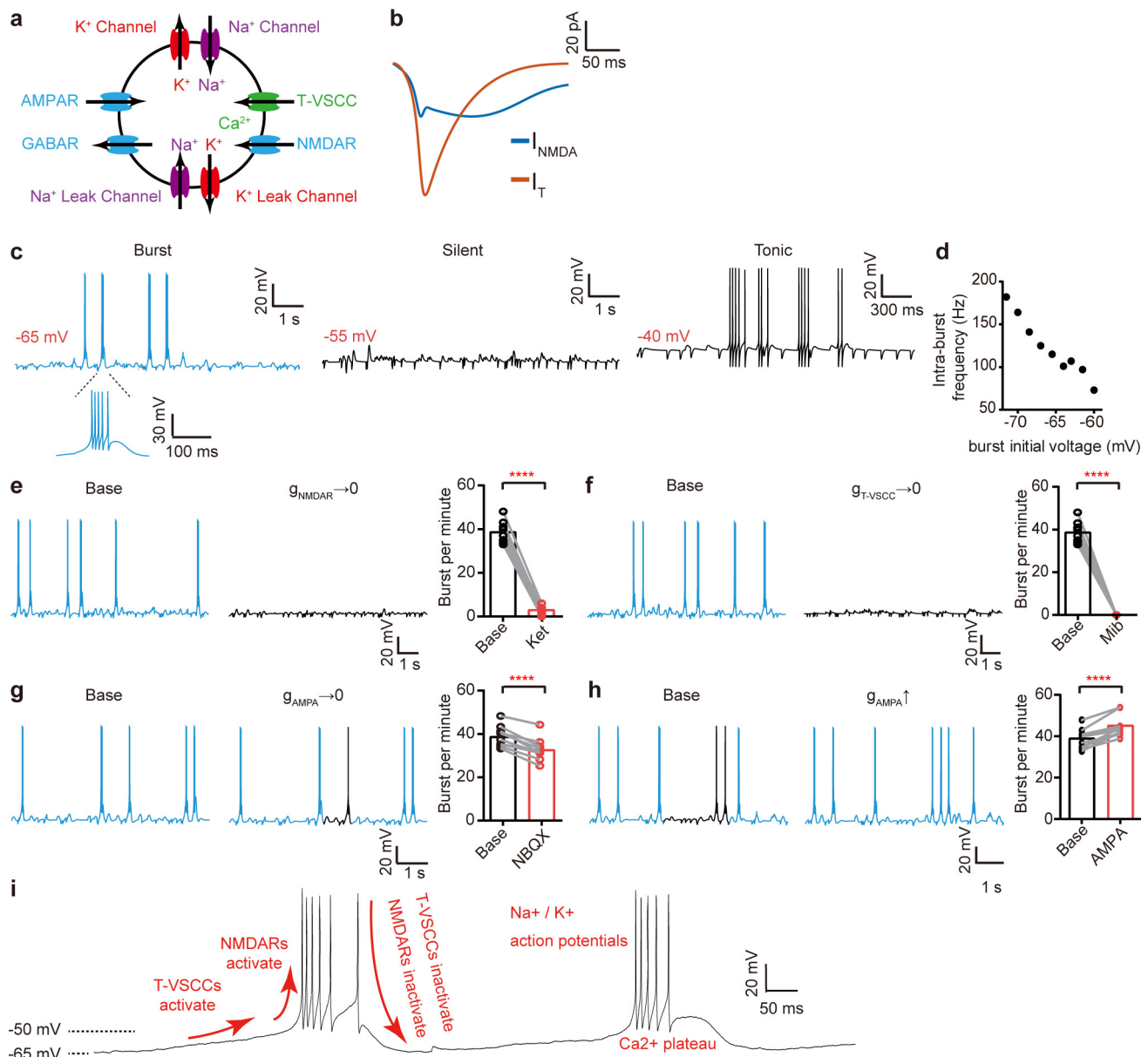
Extended Data Figure 6 | Voltage dependency of LHB bursts and pharmacological manipulation of hyperpolarization-triggered rebound bursts in LHB. **a**, Representative trace of an LHB neuron transformed from bursting to tonic-firing mode with a ramp-like current injection, showing bursting at more hyperpolarized potentials and tonic firing at more depolarized potentials. Spikes in bursting and tonic-firing mode are shown in blue and black, respectively. **b–d**, Correlations of membrane potential with intra-burst frequency (**b**), burst duration (**c**) and intra-burst spike number (**d**) generated by current ramps. $n = 104$ neurons, 14 rats. **e, f**, Example traces of a spontaneously tonic-firing neuron transformed to

burst-firing mode by hyperpolarization (**e**), and a spontaneously bursting neuron transformed to tonic-firing mode by depolarization (**f**). **g–k**, Example traces (left) and statistics (right) showing effects of ketamine (**g**), AP5 (**h**), mibefradil (**i**), ZD7288 (**j**) and fluoxetine (**k**) on rebound bursts induced by a transient hyperpolarizing current step. Current injection steps are illustrated under the bottom of the trace. $n = 9$ neurons, 2 rats (**g**); $n = 12$ neurons, 5 rats (**h**); $n = 14$ neurons, 2 rats (**i**); $n = 8$ neurons, 3 rats (**j**); $n = 6$ neurons, 2 rats (**k**). Data are mean \pm s.e.m.; * $P < 0.05$, **** $P < 0.0001$, n.s., not significant. Two-tailed paired t -test.



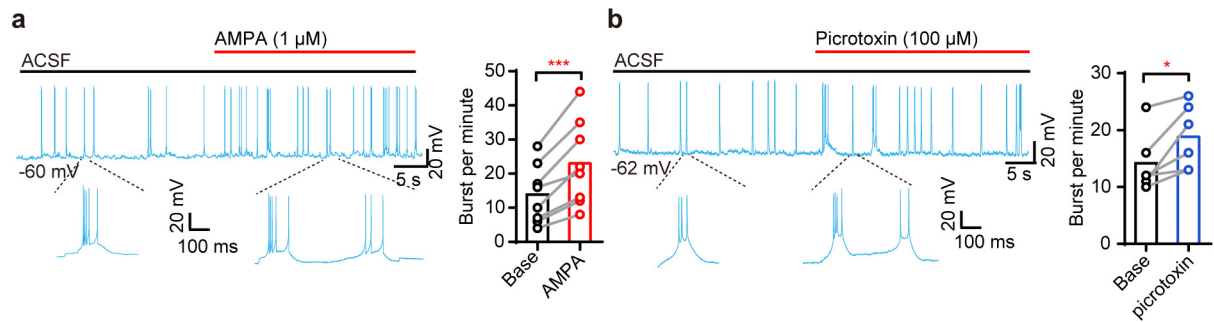
Extended Data Figure 7 | T-VSCC currents and RMPs of LHb neurons in animal models of depression. **a**, Voltage steps used to isolate T-VSCC currents, starting from a holding potential of -50 mV before being increased to conditioning potential (-100 mV) for 1 s preceding the command steps (5 mV, 0.1 Hz per step increment). **b**, LHb T-VSCC currents (right column) are obtained by subtraction of recorded traces without (left) mibefradil from those with mibefradil ($10 \mu\text{M}$, middle). The maximum of isolated T-VSCC current is obtained at -50 mV.

c, d, No difference in LHb T-VSCC currents is detected between wild-type and cLH rats (c) or control and CRS mice (d). $n = 4$ neurons per group from 2 wild-type and 2 cLH rats (c); $n = 5$ neurons per group from 2 control and 2 C57 mice (d). **e, f**, Scatter plots showing that neuronal RMPs are more hyperpolarized in cLH rats (e) and CRS mice (f) than in controls. $n = 45$ neurons per group from 5 wild-type and 4 cLH rats (e); $n = 50$ neurons per group from 4 control and 3 C57 mice (f). Data are mean \pm s.e.m.; *** $P < 0.001$, **** $P < 0.0001$. Two-tailed unpaired t -test (e, f).



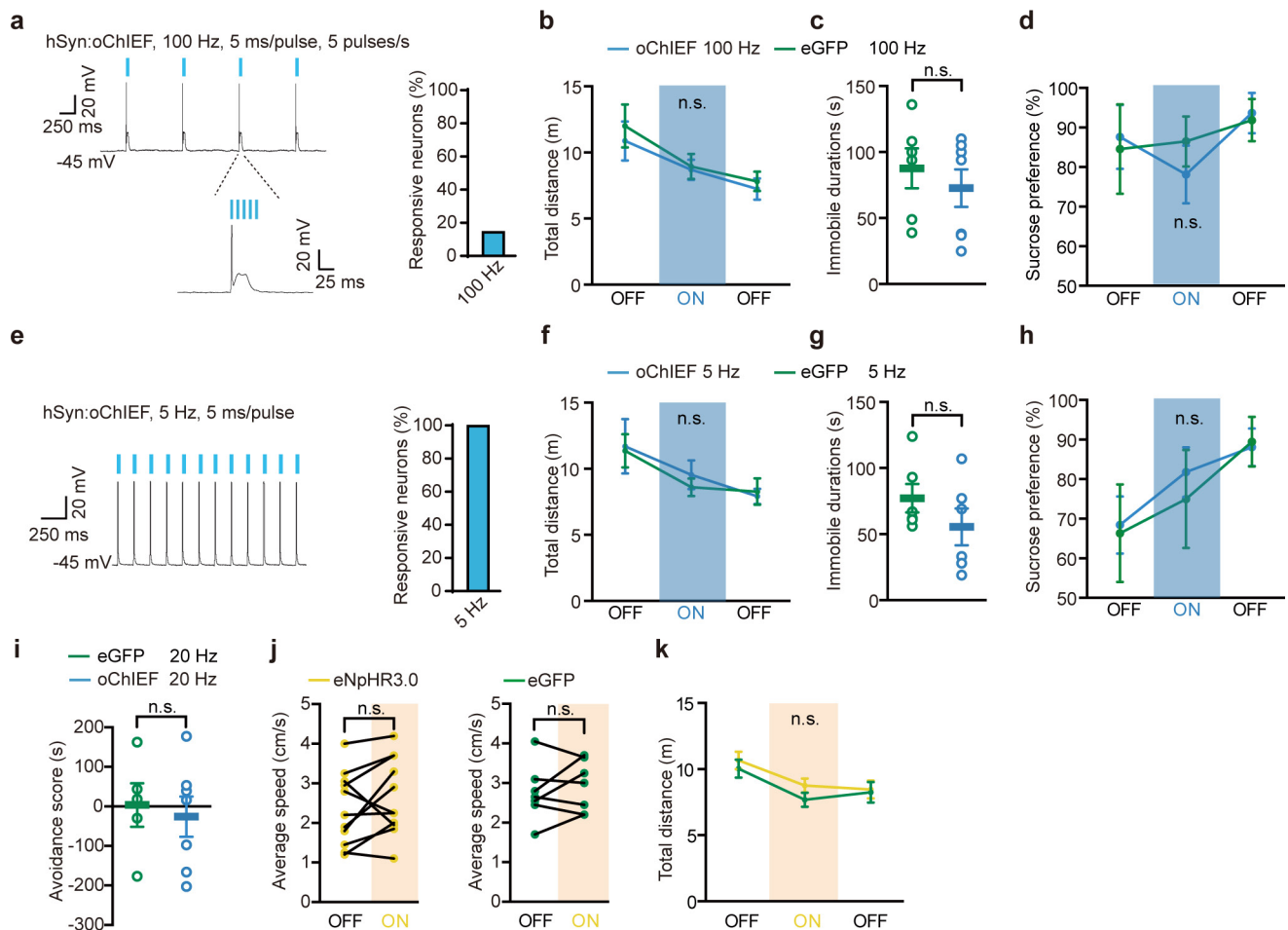
Extended Data Figure 8 | Simulation of Lhb neurons incorporating T-VSCCs and NMDAR channels. **a**, Scheme of a single compartment model of an Lhb neuron (see Methods). **b**, The contribution of NMDAR current I_{NMDA} and T-VSCC current I_{T} during bursts derived from simulation. **c**, RMP-dependent firing mode of the Lhb model neuron. Spikes in bursting mode are shown in blue. Spikes in tonic and silent firing mode are shown in black. **d**, The correlation between RMPs and intra-burst frequencies of the Lhb model neuron. **e**, **f**, Example trace (left) and statistics (right) showing *in silico* effects of ketamine (set NMDAR conductance $g_{\text{NMDAR}} = 0$, **e**) or mibefradil ($g_{\text{T-VSCC}} = 0$, **f**) on spontaneous bursts in the Lhb model neuron. The bursting probability was evaluated across ten independent trials with simulated synaptic inputs. Note that *in silico* knockout of NMDAR or T-VSCC current from the model abolished the bursts, which matched experimental observations (Fig. 3a, d, 4a). **g**, **h**, Example trace (left) and statistics (right) showing *in silico* effects of

NBQX ($g_{\text{AMPA}} = 0$, **g**) or AMPA (g_{AMPA} increased from 8 to $15 \mu\text{S cm}^{-2}$, **h**) on spontaneous bursts in the Lhb model neuron. $n = 10$ simulations (**e**–**h**). **i**, An example trace summarizing the ionic components and channel mechanisms involved in Lhb bursting: hyperpolarization of neurons to membrane potentials negative to -55 mV slowly de-inactivates T-VSCC. I_{T} continues to grow as the de-inactivated T-VSCCs increase, leading to a transient Ca^{2+} plateau potential. The Ca^{2+} plateau helps remove the magnesium blockade of NMDARs while T-VSCC inactivates rapidly during the depolarization. After the Ca^{2+} plateau reaches approximately -45 mV, I_{NMDA} dominates the driving force to further depolarize RMP to the threshold for Na spike generation. As RMP falls back to below -55 mV it de-inactivates I_{T} and results in the intrinsic propensity of Lhb neurons to generate the next cycle of bursting. Data are mean \pm s.e.m.; **** $P < 0.0001$. Two-tailed paired *t*-test.



Extended Data Figure 9 | AMPA or picrotoxin increases LHB burst frequency. **a, b**, Example traces (left) and statistics (right, sampled within 3 min before and 1 min after drug application) showing effects of AMPA

(**a**) or picrotoxin (**b**) on spontaneous bursts in the LHB. $n = 8$ neurons, 2 rats (**a**); $n = 6$ neurons, 3 rats (**b**). Data are mean \pm s.e.m.; * $P < 0.05$, *** $P < 0.001$. Two-tailed paired t -test.



Extended Data Figure 10 | Additional behavioural results of eNpHR3.0- or oChIEF-based photostimulation. **a**, Representative trace showing that LHB neurons can follow only the first of the five 100-Hz pulsed blue light stimulations in a pulsed 100-Hz protocol in LHB brain slices infected with AAV2/9-oChIEF. Percentage of responsive neurons shown on the right. **b–d**, Pulsed 100-Hz photostimulation of mice expressing oChIEF does not change locomotion in the OFT (**b**), and does not induce depressive phenotypes in the FST (**c**) or SPT (**d**). $n = 6, 7$ mice (**b, c**) and $5, 5$ mice (**d**) for oChIEF and eGFP groups, respectively. **e**, Representative trace showing LHB neurons following a 5-Hz tonic blue light stimulation protocol in LHB brain slices infected with AAV2/9-oChIEF. Percentage of responsive neurons shown on the right. **f–h**, 5-Hz photostimulation of LHB in mice expressing oChIEF does not change locomotion in the OFT (**f**) and does

not induce depressive phenotypes in the FST (**g**) or SPT (**h**). $n = 7, 6$ mice (**f**); $6, 6$ mice (**g**) and $5, 12$ mice (**h**) for oChIEF and eGFP groups, respectively. **i**, 20-Hz tonic photostimulation of the LHB in mice expressing oChIEF does not cause RTPA. Note that this result is different from 20-Hz optogenetic stimulation of a presynaptic input from the entopeduncular nucleus into the LHB, which caused aversion¹¹. $n = 5, 7$ mice for oChIEF and eGFP group. **j, k**, eNpHR3.0-driven burst does not change speed of movement in RTPA (**j**) or affect locomotion in the OFT (**k**). $n = 11, 7$ mice (**j**) and $13, 21$ mice (**k**) for NpHR and eGFP group, respectively. Data are mean \pm s.e.m.; n.s., not significant. Two-way ANOVA (**b, d, f, h, k**), two-tailed unpaired t -test (**c, g, i**) and paired t -test (**j**).

Astroglial Kir4.1 in the lateral habenula drives neuronal bursts in depression

Yihui Cui^{1,2}, Yan Yang^{1,2}, Zheyi Ni¹, Yiyan Dong¹, Guohong Cai³, Alexandre Foncelle^{4,5}, Shuangshuang Ma¹, Kangning Sang¹, Siyang Tang¹, Yuezhou Li¹, Ying Shen¹, Hugues Berry^{4,5}, Shengxi Wu³ & Hailan Hu^{1,2}

Enhanced bursting activity of neurons in the lateral habenula (LHb) is essential in driving depression-like behaviours, but the cause of this increase has been unknown. Here, using a high-throughput quantitative proteomic screen, we show that an astroglial potassium channel (Kir4.1) is upregulated in the LHb in rat models of depression. Kir4.1 in the LHb shows a distinct pattern of expression on astrocytic membrane processes that wrap tightly around the neuronal soma. Electrophysiology and modelling data show that the level of Kir4.1 on astrocytes tightly regulates the degree of membrane hyperpolarization and the amount of bursting activity of LHb neurons. Astrocyte-specific gain and loss of Kir4.1 in the LHb bidirectionally regulates neuronal bursting and depression-like symptoms. Together, these results show that a glia–neuron interaction at the perisomatic space of LHb is involved in setting the neuronal firing mode in models of a major psychiatric disease. Kir4.1 in the LHb might have potential as a target for treating clinical depression.

A major breakthrough in neuroscience was the discovery that astrocytes interact intimately with neurons to support and regulate essential functions and thereby foster information processing in the brain^{1–8}. Many investigations have focused on astroglia–neuron interactions at tripartite synapses, where astrocyte processes wrap tightly around presynaptic and postsynaptic sites⁹. By contrast, less attention has been placed on astroglia–neuron interactions in proximity to the neuronal soma. In particular, how astrocytes regulate the intrinsic firing patterns of neurons, and what structural basis may underlie this regulation, have been much less explored.

Despite the surging interest in the role of the LHb in depression^{10–18}, only limited attention has been given to the influence of astrocyte malfunction in the LHb on the aetiology of depression¹⁹. In an accompanying paper, we show that the bursting activity of LHb neurons is greatly enhanced in animal models of depression²⁰. LHb bursting drives depressive-like behaviours and is a prominent target of the rapid antidepressant ketamine²⁰. However, the cause of this enhanced bursting by LHb neurons remains unknown.

LHb Kir4.1 is upregulated in depression

We used an unbiased, high-throughput, quantitative proteomic screen to compare habenular protein expression between congenitally learned helpless (cLH)²¹ and wild-type Sprague–Dawley rats. Kir4.1 was highly upregulated in the habenulae of cLH rats¹⁴ (1.69-fold of wild-type, Extended Data Fig. 1a). Western blot analysis confirmed that Kir4.1 was significantly increased (1.44-fold, $P = 0.009$) in the membrane protein fraction of habenulae from cLH rats (Fig. 1a). By contrast, another astrocyte-specific protein, glial fibrillary acidic protein (GFAP), showed no change in expression (Extended Data Fig. 1b), indicating that there was no astrogliosis.

To test whether Kir4.1 upregulation is universal in depression, we examined rats in which depression was induced by treatment with lipopolysaccharide (LPS)²². One week of LPS injection (0.5 mg kg^{-1} per day, intraperitoneal (i.p.)) was sufficient to cause strong depressive-like phenotype in three-month-old Wistar rats in the forced swim test (FST; Extended Data Fig. 1c)²² and sucrose preference test (SPT)²².

Rats with LPS-induced depression also showed a significant increase in Kir4.1 in the habenula (1.87-fold, $P < 0.0001$, Fig. 1b). Quantitative real-time PCR revealed an increase (1.2-fold) in *Kir4.1* (also known as *Kcnj10*) mRNA level in habenulae from cLH rats (Extended Data Fig. 1d), suggesting that at least part of the change in protein level is due to transcriptional upregulation.

Kir4.1 is a principal component of the glial Kir channel and is largely responsible for mediating the K^+ conductance and setting the

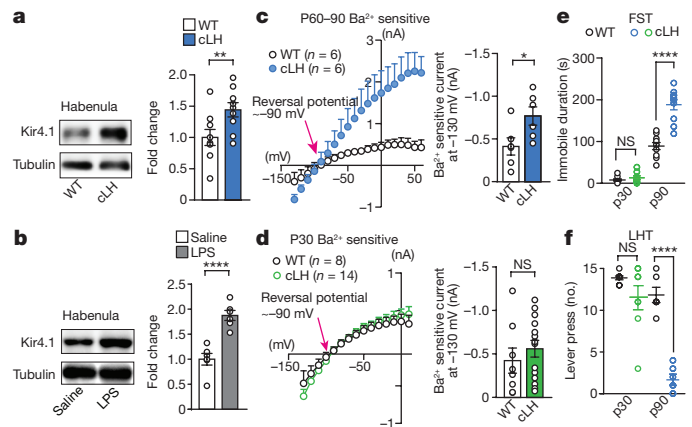


Figure 1 | Kir4.1 is upregulated in the LHb in rat models of depression. a, b, Western blot analysis showing upregulation of Kir4.1 protein in membrane fraction of habenulae of cLH rats ($n = 9$, 9 rats for WT and cLH, respectively, a) and rats with LPS-induced depression ($n = 6$, 6, b). Tubulin is used as loading control. WT, wild-type Sprague–Dawley rats. c, d, $I-V$ plot and bar graph showing Ba^{2+} -sensitive currents in cLH rats and wild-type controls at the age of P60–90 (c) and P30 (d). e, f, Age-dependent FST (e) and LHT (f) phenotypes of cLH rats. $n = 8$, 8 rats for P30, $n = 10$, 10; 6, 6 rats for P90 FST and LHT, respectively. Data are means \pm s.e.m. * $P < 0.05$, ** $P < 0.01$, **** $P < 0.0001$; NS, not significant. Two-tailed paired t -test (a, b), two-tailed unpaired t -test (c, e, f) and Mann–Whitney test (d).

¹Center for Neuroscience, Key Laboratory of Medical Neurobiology of the Ministry of Health of China, School of Medicine, Interdisciplinary Institute of Neuroscience and Technology, Qiushi Academy for Advanced Studies, Zhejiang University, Hangzhou 310058, China. ²Mental Health Center, School of Medicine, Zhejiang University, Hangzhou 310013, China. ³Department of Neurobiology, School of Basic Medicine, Fourth Military Medical University, Xi'an 710032, China. ⁴INRIA, Lyon, F-69603, France. ⁵University of Lyon, UMR 5205, CNRS, LIRIS, F-69622, France.

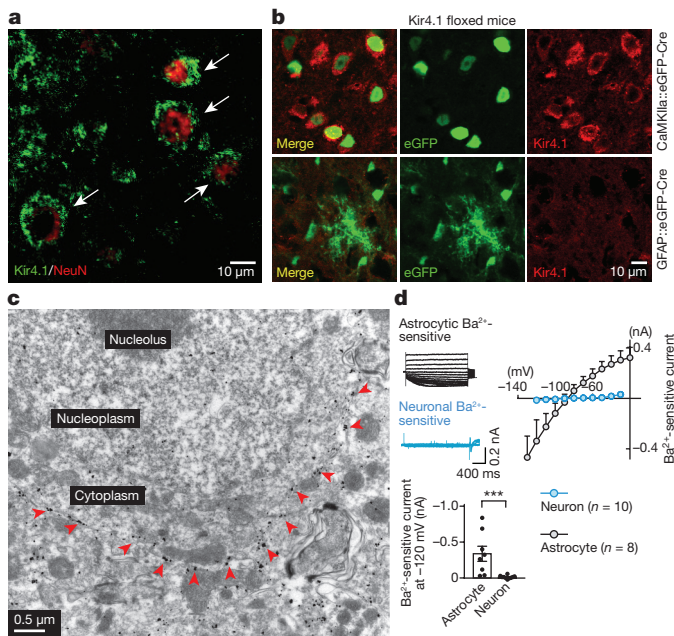


Figure 2 | Kir4.1 is expressed on astrocytic processes that wrap tightly around neuronal somata in LHB. **a**, Immunohistochemistry signals of Kir4.1 envelope neuronal somata as indicated by white arrows (three independent experiments). **b**, The pan-soma Kir4.1 signals remain intact in the LHB of Kir4.1 floxed mice injected with AAV-CaMKIIa::eGFP-Cre, but are eliminated in mice injected with AAV-GFAP::eGFP-Cre (three independent experiments). **c**, Immunogold electron microscopy of Kir4.1. Red arrows indicate gold signals surrounding a neuronal soma (three independent experiments). **d**, I - V plots of the Ba^{2+} -sensitive Kir4.1 current recorded in LHB astrocytes and neurons. Top left, representative traces; bottom left, bar graph of current recorded when cells are held at -120 mV. Two-tailed Mann-Whitney test. Data are means \pm s.e.m. *** $P < 0.001$.

resting membrane potential (RMP) in astrocytes^{23–25}. To confirm that Kir4.1 function is indeed upregulated in rat models of depression, we performed whole-cell patch-clamp recordings onto LHB astrocytes from cLH or wild-type rats. Astrocytes were distinguished from neurons by their small (5 – $10\ \mu\text{m}$), oval somata and electrophysiological features (Extended Data Fig. 2a–d; see Methods). Biocytin filling and the absence of NeuN co-staining confirmed that cells fitting the above criteria were indeed astrocytes (Extended Data Fig. 3). We then bath-applied Ba^{2+} (BaCl_2 , $100\ \mu\text{M}$), which selectively blocks Kir channels at sub-millimolar concentrations, to isolate Kir4.1 current²⁴ (Extended Data Fig. 2a, c). The Ba^{2+} -sensitive current displayed a reversal potential close to the equilibrium potential of K^+ (E_K) (-90 mV)^{23,24} (Fig. 1c, d), indicating that it represents the K^+ conductance. We found that Ba^{2+} -sensitive currents in LHB astrocytes were almost doubled in astrocytes from cLH (Fig. 1c) and LPS-treated rats (Extended Data Fig. 2f) at postnatal days (P)60–90.

Notably, the increase in Kir4.1 current and protein level was not obvious in cLH rats at P30 (Fig. 1d, Extended Data Fig. 1e). At this age, cLH rats did not yet show depression-like phenotypes in either the FST (Fig. 1e) or the learned helplessness test (LHT; Fig. 1f), suggesting that the upregulation of Kir4.1 is concomitant with the developmental onset of the depression-like symptoms.

Kir4.1 on astrocytes encircles neuronal soma

As an inwardly rectifying K^+ channel, Kir4.1 has been strongly implicated in buffering excess extracellular K^+ in tripartite synapses^{25–28}. The conventional model of K^+ buffering suggests that Kir4.1 is highly expressed in astrocytic endfeet surrounding synapses^{29,30}. Unexpectedly, immunohistochemical staining for Kir4.1 in the LHB appeared to overlap with the neuronal marker NeuN at low

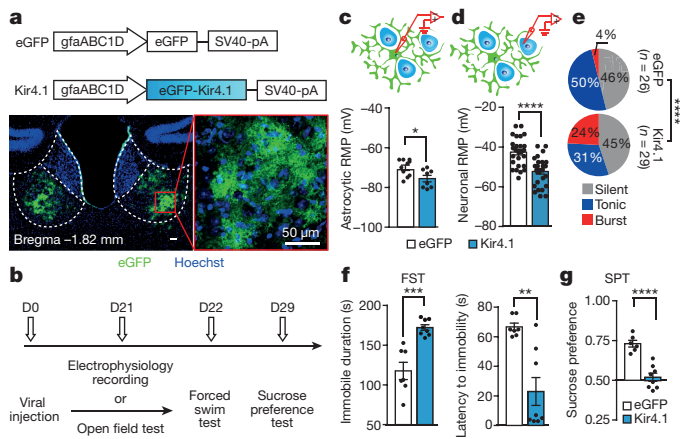


Figure 3 | Astrocytic kir4.1 overexpression increases neuronal bursts in the LHB and causes depression-like phenotypes. **a**, Top, schematics of AAV vectors engineered to overexpress Kir4.1 or eGFP control under a GFAP promoter. Bottom, illustration of bilateral viral injection of AAV-GFAP::Kir4.1 in mouse LHB (stained with antibody against GFP and Hoechst) (four independent experiments). **b**, Experimental paradigm for electrophysiology and behavioural testing. **c–e**, Astrocytic overexpression of Kir4.1 decreases RMPs of both astrocytes ($n = 10$, 8 astrocytes from 4, 3 mice for eGFP and Kir4.1, respectively, **c**) and neurons ($n = 26$, 29 neurons from 6, 6 mice, **d**) and increases the bursting population in neurons (**e**). **f, g**, Behavioural effects of expression of various viral constructs in the LHB in the FST ($n = 7$, 8 mice, **f**) and SPT ($n = 6$, 8 mice, **g**). Data are means \pm s.e.m. * $P < 0.05$, ** $P < 0.01$, *** $P < 0.001$, **** $P < 0.0001$. Two-tailed unpaired t -test (**c, d, f, g**) and χ^2 test (**e**).

magnification ($20\times$; Extended Data Fig. 4a), although in the same brain slice Kir4.1 staining in the hippocampus showed a typical astrocytic appearance (Extended Data Fig. 4b). However, higher magnification imaging with single-layer scanning ($0.76\ \mu\text{m}$ per layer) revealed that Kir4.1 staining enveloped NeuN signals (Fig. 2a). To confirm that Kir4.1 was located within astrocytes but not neurons in the LHB, we separately knocked it out in either neurons or astrocytes by injecting AAV viruses expressing the Cre recombinase under either the neuronal *Camk2a* promoter or the glial GFAP promoter (gfaABC1D)^{7,31} into Kir4.1 floxed (*Kcnj10*^{fl/fl}) mice²⁴. Neuronal knockout of Kir4.1 expression did not change the pattern of Kir4.1 staining, but astrocytic knockout completely eliminated it (Fig. 2b). Electron microscopy imaging revealed that Kir4.1-positive gold particles encircled the membrane of neuronal cell bodies (Fig. 2c, Extended Data Fig. 5a, b) as well as synapses (Extended Data Fig. 5c). Consistently, whole-cell patch-clamp recordings showed that Ba^{2+} -sensitive currents were absent from neurons but abundant in astrocytes in the LHB (Fig. 2d, Extended Data Fig. 6). Together these results suggest that Kir4.1 is mainly expressed in astrocytic processes that wrap tightly around neuronal somata and synapses in the LHB.

Kir4.1 gain-of-function causes depression

To test the consequences of Kir4.1 upregulation in the LHB, we used adeno-associated viruses of the 2/5 serotype (AAV2/5), which preferentially target astrocytes⁷, together with the human GFAP (gfaABC1D) promoter^{7,31} to deliver eGFP-tagged Kir4.1 channel (AAV-GFAP::Kir4.1) or eGFP alone (AAV-GFAP::eGFP) as a control (Fig. 3a). Twenty-one days after bilateral injection into the LHB at P50, AAV2/5-mediated viral transfection led to expression of Kir4.1 and eGFP in astrocytes throughout the LHB (Fig. 3a). The specificity of the viral infection in astrocytes was verified by co-immunostaining of NeuN and eGFP: only 0.3% of NeuN⁺ cells ($n = 2,668$) were infected by this virus (Extended Data Fig. 7a). We made whole-cell patch-clamp recordings from either astrocytes or neurons surrounding the virally transfected astrocytes in coronal LHB slices (Fig. 3b–e). The RMPs of

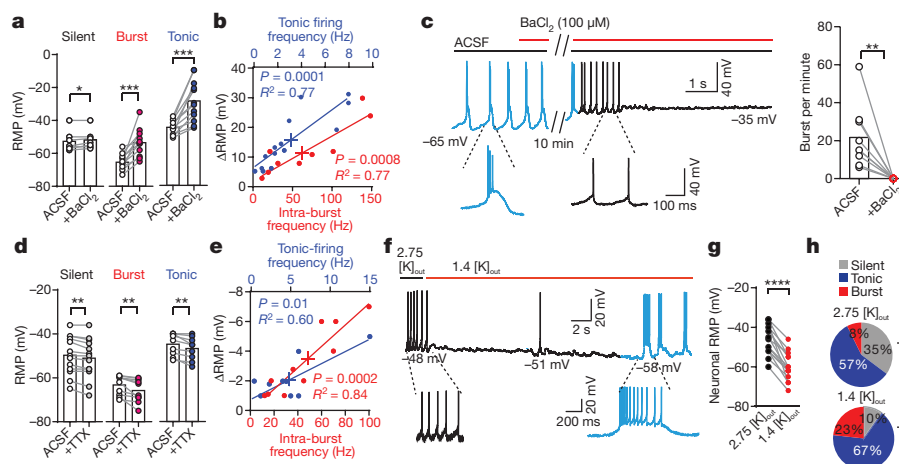


Figure 4 | Kir4.1-dependent potassium buffering regulates neuronal RMP and bursting in LHB. **a, d,** Changes in neuronal RMPs caused by BaCl₂ (100 μ M, $n = 7, 11, 12$ neurons from 3, 3, 3 rats for silent, bursting and tonic, respectively, **a**) or TTX (1 μ M, $n = 13, 9, 9$ neurons from 2, 2, 2 rats, **d**) in different neuronal types. RMPs were measured 15 min or 5 min after perfusion with BaCl₂ or TTX, respectively, when the RMPs had stabilized. **b, e,** Changes in neuronal RMPs after BaCl₂ ($n = 14, 9$ neurons from 3, 3 rats for tonic and burst group, respectively, **b**) or TTX ($n = 9, 9$ neurons from 2, 2 rats, **e**) treatment correlate with original firing rates of tonic-firing neurons (blue) or intra-burst frequencies of bursting neurons (red). **c,** Representative trace (left) and bar graph (right, 9 neurons from

3 rats) showing effect of BaCl₂ (15 min after drug perfusion) on bursting neurons. Spikes in bursting and tonic firing modes are shown in blue and black, respectively. **f,** Example of LHB neurons transforming from tonic-firing to burst-firing mode after [K]_{out} is reduced from normal (2.75 mM) by 50% (to 1.4 mM). **g, h,** Reducing [K]_{out} by 50% decreases neuronal RMPs ($n = 15$ neurons from 4 rats, sampled 1 min after change in [K]_{out}, **g**) and increases bursting neural population ($n = 33, 40$ neurons from 4, 6 rats for normal and reduced [K]_{out}, respectively, **h**). Data are means \pm s.e.m. * $P < 0.05$, ** $P < 0.01$, *** $P < 0.001$, **** $P < 0.0001$. Two-tailed paired t -test (**a, c, d, g**), χ^2 test (**h**) and linear regression test (**b, e**).

both astrocytes and neurons were more hyperpolarized (Fig. 3c, d) and the percentage of bursting neurons was significantly higher (Fig. 3e, $P < 0.0001$) in mice infected with AAV-GFAP::Kir4.1 than in mice infected with AAV-GFAP::eGFP.

We then assayed depression-like phenotypes and found that mice with AAV-GFAP::Kir4.1 infection in the LHB displayed severe depression-like behaviours, including increased immobile duration and decreased latency to immobility in the FST (Fig. 3f), and decreased sucrose preference in the SPT (Fig. 3g), while general locomotion was unchanged (Extended Data Fig. 7c, d).

Kir4.1 regulates neuronal RMP and bursting

How does an astrocytic K⁺ channel regulate the RMP and burst firing of LHB neurons? We hypothesize that within the highly confined extracellular space between neuronal somata and Kir4.1-positive astrocytic processes (Fig. 2), the constantly released K⁺ from intrinsically active LHB neurons is quickly cleared by astrocytes through a Kir4.1-dependent mechanism. Accordingly, we predict that blockade of Kir4.1 should compromise spatial buffering of K⁺, resulting in increased extracellular K⁺ ([K]_{out}), and according to the Nernst equation, depolarized neuronal RMPs (modelled in Extended Data Fig. 8). Consistent with this prediction, blockade of Kir4.1 by bath perfusion with BaCl₂ for about 10 min depolarized the RMPs of LHB neurons (Fig. 4a). The degree of change in RMP positively correlated with the original firing rates of neurons (Fig. 4b), indicating that the more active the neuron is, the larger contribution the K⁺ buffering makes to its RMP. A similar amount of RMP change was induced when BaCl₂ was applied in the presence of synaptic transmission blockers (picrotoxin, 1,2,3,4-tetrahydro-6-nitro-2,3-dioxo-benzo[f]quinoxaline-7-sulfonamide (NBQX) and 2-amino-5-phosphonopentanoic acid (AP5); Extended Data Fig. 9a–c), suggesting that Kir4.1-dependent regulation of RMP in LHB neurons occurs mostly at neuronal cell bodies instead of at synapses. Consequent to the RMP change and accumulation of [K]_{out}, perfusion with BaCl₂ caused either a shift in the spiking pattern from bursting to tonic firing and eventually to cessation of neuronal activity (5 of 9 neurons; Fig. 4c), or a prolonged plateau potential within a burst and eventually cessation of bursting firing (4 of 9 neurons; Extended Data Fig. 9d).

By contrast, upregulation of Kir4.1 or prevention of neuronal firing should decrease [K]_{out} and hyperpolarize neuronal RMPs. Indeed, overexpression of Kir4.1 in astrocytes (Fig. 3d) or blockage of neuronal action potentials by tetrodotoxin (TTX; Fig. 4d, e) caused hyperpolarization of LHB neurons. Overexpression of Kir4.1 in astrocytes also increased neuronal bursting (Fig. 3e). Finally, to assess a causal relationship between [K]_{out} and firing mode, we made current-clamp recordings from LHB neurons while lowering [K]_{out} by 50% (from 2.75 mM to 1.4 mM, Fig. 4f). This led to a reduction in neuronal RMP of 13.7 ± 0.5 mV (Fig. 4g) and a direct shift of originally tonic-firing neurons (8 out of 15) into bursting mode. Consequently, the percentage of bursting neurons was increased from 8% to 23% (Fig. 4h). Thus, by increasing astrocytic Kir4.1 expression or decreasing extracellular K⁺ concentration, we were able to phenocopy in wild-type animals several key neuronal properties observed in the LHB of animal models of depression, namely hyperpolarized RMPs and enhanced bursts. These results indicate that enhanced extracellular K⁺ clearance resulting from overexpression of Kir4.1 might underlie the neuronal hyperpolarization required for burst initiation.

Kir4.1 loss-of-function rescues depression

To determine whether loss-of-function of Kir4.1 in the LHB could reduce neuronal bursts and reverse depressive phenotypes, we devised two strategies. We used AAV2/5 viral vectors to express either a short hairpin RNA (shRNA) to knock down the level of Kir4.1, or a dominant-negative construct to block its function, in the LHB of cLH rats (Fig. 5a). We tested six shRNAs that specifically targeted the Kir4.1 transcript in cell culture and chose the one with highest knockdown efficiency (Fig. 5b and Extended Data Fig. 10a) for viral packaging. To avoid an off-target effect of the shRNA, we also used a dominant-negative form of Kir4.1 (dnKir4.1), which contains a GYG-to-AAA point mutation at the channel pore, which blocks K⁺ channels³² (Fig. 5a, c, Extended Data Figs 7b, 10b). We first examined the effect of Kir4.1-shRNA on glial and neural electrophysiological properties. In astrocytes infected with AAV-H1::Kir4.1-shRNA, we observed a marked change in the current–voltage (I – V) relationship (Fig. 5d) and a depolarization of 41 mV compared with astrocytes infected with control shRNA (Fig. 5e), consistent with previous findings that Kir4.1 is mainly responsible for

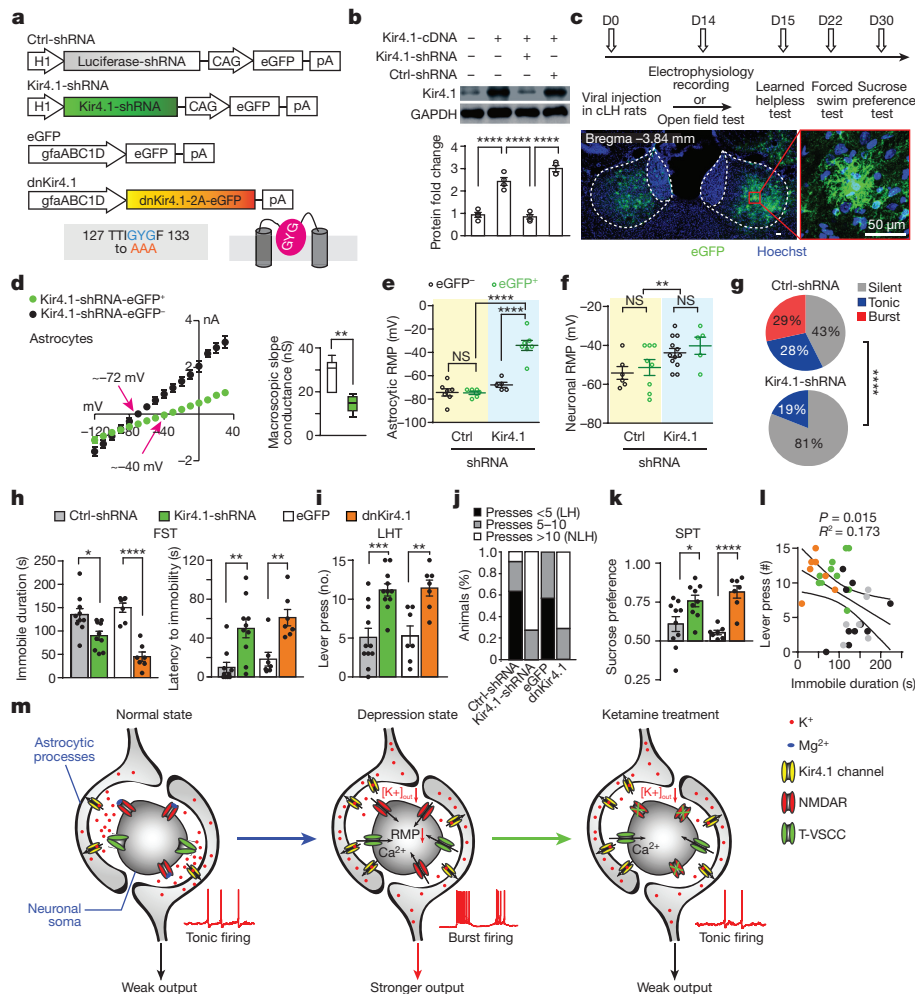


Figure 5 | Loss of function of Kir4.1 in LHb decreases neuronal bursting and rescues depression-like phenotypes of cLH rats. **a**, Schematics of the AAV vector engineered to overexpress shRNA or dominant-negative Kir4.1. H1, human H1 promoter; CAG, CMV early enhancer/chicken *Actb* promoter. Three point mutations in the dnKir4.1 and their locations in the channel pore are shown below. **b**, Western blot and quantification showing efficient knockdown of Kir4.1 by shRNA in HEK293T cells. **c**, Top, experimental paradigm for behavioural testing; bottom, illustration of bilateral expression of AAV-GFP::dnKir4.1 in LHb (stained with antibodies against GFP and Hoechst). **d–g**, AAV-Kir4.1-shRNA caused a shift in reversal potential from -72 to -40 mV in astrocytes (**d**), depolarized astrocytes (**e**) and neurons in viral infected region (**f**), and abolished neuronal bursting (**g**). Floating bars for membrane slope conductance in **d** are calculated from the I - V plots (between -120 and

$+40$ mV). **h–k**, Behavioural effects of expression of various viral constructs in the LHb of cLH rats in the FST (**h**), LHT (**i**, **j**) and SPT (**k**). **j**, Percentage of rats in each category. LH, learned helpless rats with <5 lever presses; NLH, non-learned helpless rats with >10 lever presses. **l**, FST immobility is highly correlated with learned helplessness phenotype. **m**, A model for mechanisms of depression and ketamine treatment in the LHb. Upregulation of Kir4.1 on astrocytic processes surrounding neuronal somata leads to enhanced K^+ buffering at the tight neuron–glia junction, decreased $[K]_{out}$ and hyperpolarized neuronal RMP. Consequently, de-inactivation of T-VSCCs initiates NMDAR-dependent bursts, causing a stronger output of LHb to trigger depression. Ketamine blockade of NMDARs stops bursting and relieves depression. Data are means \pm s.e.m. $*P < 0.05$, $**P < 0.01$, $***P < 0.001$, $****P < 0.0001$, NS, not significant. (See Supplementary Table 1 for statistical analysis and n numbers.)

setting astrocytic RMPs²⁴. The RMPs of neurons infected with AAV-H1::Kir4.1-shRNA did not differ from those of neighbouring non-infected neurons (because neurons do not express Kir4.1 endogenously, Fig. 5f). However, the RMPs of neighbouring LHb neurons in AAV-H1::Kir4.1-shRNA-infected brain slices were overall more depolarized than the RMPs of neurons from rats infected with the control shRNA (Fig. 5f), suggesting that knock-down of Kir4.1 in astrocytes had a widespread impact on the RMPs of neighbouring neurons. Similar effects were observed in LHb slices infected with AAV-GFAP::dnKir4.1 (Extended Data Fig. 10c–f). Notably, bursting activity in the LHb of cLH rats was eliminated by infection with AAV-H1::Kir4.1-shRNA (Fig. 5g) or AAV-GFAP::dnKir4.1 (Extended Data Fig. 10f).

Behaviourally, infection with AAV-H1::Kir4.1-shRNA or AAV-GFAP::dnKir4.1 caused a pronounced reduction in the depression-like phenotypes of cLH rats in three depression paradigms: it reduced immobility in the FST (Fig. 5h), increased bar pressing number

in the LHT (Fig. 5i, j), and increased sucrose preference in the SPT (Fig. 5k). The behaviour scores in the LHT correlated with those in the FST (Fig. 5l).

Concluding remarks

Here we describe an important function of Kir4.1 in regulating neuronal RMP and firing pattern at the highly specialized neuron–glia interface in the LHb. During depression, upregulation of Kir4.1 may cause enhanced extracellular K^+ clearance, leading to a decrease in $[K]_{out}$ and neuronal hyperpolarization (Fig. 5m). As demonstrated in the accompanying publication²⁰, neuronal hyperpolarization may de-inactivate T-type voltage-sensitive calcium channels (T-VSCCs), which in turn initiate NMDAR-dependent bursts and thereby increase suppression of downstream monoaminergic centres (Fig. 5m). These results may inspire the development of new treatments for major depression targeting maladaptive neuron–glia interactions in the LHb.

We also expect that the perisomatic K^+ buffering mechanism described here may have a more widespread function.

Online Content Methods, along with any additional Extended Data display items and Source Data, are available in the online version of the paper; references unique to these sections appear only in the online paper.

Received 19 May 2017; accepted 12 January 2018.

- Volterra, A. & Meldolesi, J. Astrocytes, from brain glue to communication elements: the revolution continues. *Nat. Rev. Neurosci.* **6**, 626–640 (2005).
- Attwell, D. *et al.* Glial and neuronal control of brain blood flow. *Nature* **468**, 232–243 (2010).
- Giaume, C., Koulakoff, A., Roux, L., Holcman, D. & Rouach, N. Astroglial networks: a step further in neuroglial and gliovascular interactions. *Nat. Rev. Neurosci.* **11**, 87–99 (2010).
- Halassa, M. M. & Haydon, P. G. Integrated brain circuits: astrocytic networks modulate neuronal activity and behavior. *Annu. Rev. Physiol.* **72**, 335–355 (2010).
- Molofsky, A. V. *et al.* Astrocytes and disease: a neurodevelopmental perspective. *Genes Dev.* **26**, 891–907 (2012).
- Woo, D. H. *et al.* TREK-1 and Best1 channels mediate fast and slow glutamate release in astrocytes upon GPCR activation. *Cell* **151**, 25–40 (2012).
- Tong, X. *et al.* Astrocyte Kir4.1 ion channel deficits contribute to neuronal dysfunction in Huntington's disease model mice. *Nat. Neurosci.* **17**, 694–703 (2014).
- Khakh, B. S. & Sofroniew, M. V. Diversity of astrocyte functions and phenotypes in neural circuits. *Nat. Neurosci.* **18**, 942–952 (2015).
- Araque, A., Parpura, V., Sanzgiri, R. P. & Haydon, P. G. Tripartite synapses: glia, the unacknowledged partner. *Trends Neurosci.* **22**, 208–215 (1999).
- Sartorius, A. *et al.* Remission of major depression under deep brain stimulation of the lateral habenula in a therapy-refractory patient. *Biol. Psychiatry* **67**, e9–e11 (2010).
- Li, B. *et al.* Synaptic potentiation onto habenula neurons in the learned helplessness model of depression. *Nature* **470**, 535–539 (2011).
- Lammel, S. *et al.* Input-specific control of reward and aversion in the ventral tegmental area. *Nature* **491**, 212–217, (2012).
- Shabel, S. J., Proulx, C. D., Trias, A., Murphy, R. T. & Malinow, R. Input to the lateral habenula from the basal ganglia is excitatory, aversive, and suppressed by serotonin. *Neuron* **74**, 475–481 (2012).
- Li, K. *et al.* β CaMKII in lateral habenula mediates core symptoms of depression. *Science* **341**, 1016–1020 (2013).
- Proulx, C. D., Hikosaka, O. & Malinow, R. Reward processing by the lateral habenula in normal and depressive behaviors. *Nat. Neurosci.* **17**, 1146–1152 (2014).
- Shabel, S. J., Proulx, C. D., Piriz, J. & Malinow, R. Mood regulation. GABA/glutamate co-release controls habenula output and is modified by antidepressant treatment. *Science* **345**, 1494–1498 (2014).
- Lecca, S. *et al.* Rescue of GABAB and GIRK function in the lateral habenula by protein phosphatase 2A inhibition ameliorates depression-like phenotypes in mice. *Nat. Med.* **22**, 254–261 (2016).
- Yang, Y., Wang, H., Hu, J. & Hu, H. Lateral habenula in the pathophysiology of depression. *Curr. Opin. Neurobiol.* **48**, 90–96 (2017).
- Cui, W. *et al.* Glial dysfunction in the mouse habenula causes depressive-like behaviors and sleep disturbance. *J. Neurosci.* **34**, 16273–16285 (2014).
- Yang, Y. *et al.* Ketamine blocks bursting in the lateral habenula to rapidly relieve depression. *Nature* <http://doi.org/10.1030/nature25509> (2018).
- Henn, F. A. & Vollmayr, B. Stress models of depression: forming genetically vulnerable strains. *Neurosci. Biobehav. Rev.* **29**, 799–804 (2005).
- Adzic, M. *et al.* The contribution of hypothalamic neuroendocrine, neuroplastic and neuroinflammatory processes to lipopolysaccharide-induced depressive-like behaviour in female and male rats: Involvement of glucocorticoid receptor and C/EBP- β . *Behav. Brain Res.* **291**, 130–139 (2015).
- Ransom, C. B. & Sontheimer, H. Biophysical and pharmacological characterization of inwardly rectifying K^+ currents in rat spinal cord astrocytes. *J. Neurophysiol.* **73**, 333–346 (1995).
- Djukic, B., Casper, K. B., Philpot, B. D., Chin, L. S. & McCarthy, K. D. Conditional knock-out of Kir4.1 leads to glial membrane depolarization, inhibition of potassium and glutamate uptake, and enhanced short-term synaptic potentiation. *J. Neurosci.* **27**, 11354–11365 (2007).
- Olsen, M. L. & Sontheimer, H. Functional implications for Kir4.1 channels in glial biology: from K^+ buffering to cell differentiation. *J. Neurochem.* **107**, 589–601 (2008).
- Newman, E. & Reichenbach, A. The Müller cell: a functional element of the retina. *Trends Neurosci.* **19**, 307–312 (1996).
- Amédée, T., Robert, A. & Coles, J. A. Potassium homeostasis and glial energy metabolism. *Glia* **21**, 46–55 (1997).
- Neusch, C. *et al.* Lack of the Kir4.1 channel subunit abolishes K^+ buffering properties of astrocytes in the ventral respiratory group: impact on extracellular K^+ regulation. *J. Neurophysiol.* **95**, 1843–1852 (2006).
- Newman, E. A. Inward-rectifying potassium channels in retinal glial (Müller) cells. *J. Neurosci.* **13**, 3333–3345 (1993).
- Rojas, L. & Orkand, R. K. K^+ channel density increases selectively in the endfoot of retinal glial cells during development of *Rana catesbeiana*. *Glia* **25**, 199–203 (1999).
- Shigetomi, E. *et al.* Imaging calcium microdomains within entire astrocyte territories and endfeet with GCaMPs expressed using adeno-associated viruses. *J. Gen. Physiol.* **141**, 633–647 (2013).
- Hibino, H. *et al.* Inwardly rectifying potassium channels: their structure, function, and physiological roles. *Physiol. Rev.* **90**, 291–366 (2010).

Supplementary Information is available in the online version of the paper.

Acknowledgements We thank K. McCarthy for Kir4.1 floxed mice; B. Khakh for the GFAP-Kir4.1 plasmid; T. Xue for advice on dn-Kir4.1 design; Y.-Y. Liu for technical support on electromicroscopy; C. Liu and C.-J. Shen for help with immunohistochemistry; S.-M. Duan, Y.-D. Zhou, J.-W. Zhao, X.-H. Zhang and B. MacVicar for advice on experimental design; and C. Giaume and P. Magistretti for comments on the manuscript. This work was supported by grants from the National Key R&D Program of China (2016YFA0501000), the National Natural Science Foundation of China (91432108, 31225010, and 81527901 to H.H., 81701335 to Y.C., and 81730035 to S.W.), the Strategic Priority Research Program (B) of the Chinese Academy of Sciences (XDB02030004) and 111 project (B13026) to H.H.

Author Contributions Y.C. performed the *in vitro* patch recordings; Y.Y. performed the biochemistry and immunohistochemistry experiments; Y.C., Y.Y., Y.D. and K.S. performed viral injections and behavioural experiments; Z.N., A.F. and H.B. established the biophysical model; S.M. assisted with cell culture experiments; G.C. and S.W. conducted the electron microscopy experiments; Y.S. contributed Kir4.1 floxed mice; S.T. and Y.L. constructed plasmids; H.H. and Y.C. designed the study; and H.H. wrote the manuscript with the assistance of Y.C., Y.Y. and Z.N.

Author Information Reprints and permissions information is available at www.nature.com/reprints. The authors declare no competing financial interests. Readers are welcome to comment on the online version of the paper. Publisher's note: Springer Nature remains neutral with regard to jurisdictional claims in published maps and institutional affiliations. Correspondence and requests for materials should be addressed to H.H. (huhailan@zju.edu.cn).

Reviewer Information Nature thanks P. Kenny and the other anonymous reviewer(s) for their contribution to the peer review of this work.

METHODS

Animals. Male cLH rats (3–4 weeks or 8–12 weeks of age) and age-matched male Sprague Dawley rats (SLAC Laboratory Animal Co.) were used. The cLH rats were screened using the learned helplessness test^{14,21} for breeding as previously described²¹. Male Wistar rats (SLAC Laboratory Animal Co, 12 weeks) were used for establishing the LPS-induced depressive-like rat model. Male adult (7–8 weeks of age) C57BL/6 mice (SLAC) were used for virus injection in the behaviour experiments. Kir4.1 floxed (*Kcnj10^{fl/fl}*) mice (originally obtained from K. McCarthy at University of North Carolina) were used for virus injection in the immunohistochemistry experiments. Animals were group-housed two per cage for rats and four per cage for mice under a 12-h light–dark cycle (light on from 7 a.m. to 7 p.m.) with access to food and water *ad libitum*. All animal studies and experimental procedures were approved by the Animal Care and Use Committee of the animal facility at Zhejiang University.

Western blotting. The habenular membrane fraction and whole proteins were extracted as previously described¹⁴. Animals were anaesthetized using isoflurane, and habenular tissue was quickly dissected from the brain and homogenized in lysis buffer (320 mM sucrose, 4 mM HEPES pH 7.4, 1 mM MgCl₂ and 0.5 mM CaCl₂, 5 mM NaF, 1 mM Na₃VO₄, EDTA-free, protease inhibitor cocktail tablets (Roche) on ice. The lysis buffer used for extracting the total protein of HEK293TN cells contained 50 mM Tris (pH 7.4), 150 mM NaCl, 1% Triton X-100, 1% sodium deoxycholate, 0.1% SDS and protease inhibitor cocktail tablets (Roche). After protein concentration measurement by BCA assay, 10–20 µg protein for each lane was separated on a 10% SDS–PAGE gel and transferred for western blot analysis. Rabbit anti-Kir4.1 intracellular peptide (1:1,000, Alomone labs), mouse anti-GFAP (1:1,000, Sigma), mouse anti-α-tubulin (1:5,000, Sigma) and mouse anti-GAPDH–HRP (1:5,000, KangChen Bio-tech Inc.) antibodies, and high-sensitivity ECL reagent (GE Healthcare) were used. All the bands were analysed with Quantity One or Image J.

Immunohistochemistry. Animals were anaesthetized using 10% chloral hydrate, and then perfused transcardially with ice-cold PBS (pH 7.4) followed by 4% paraformaldehyde. After overnight post fix in 4% paraformaldehyde solution, brains were cryoprotected in 30% sucrose for 1 day (for mice) or 3 days (for rats). Coronal sections (40 µm) were cut on a microtome (Leica) and collected in PBS and stored at 4 °C for further use. The antibodies used were rabbit anti-Kir4.1 extracellular peptide (1:200, Alomone labs), mouse anti-GFAP (1:500, Sigma), mouse anti-NeuN (1:500, Millipore), rabbit anti-NeuN (1:500, Millipore), mouse anti-S100B (1:500, Sigma), chicken anti-GFP (1:1,000, Abcam), mouse anti-Flag (1:1,000, Beyotime), Alexa Fluor 488 goat anti-rabbit IgG, Alexa Fluor 488 goat anti-chicken IgG, Alexa Fluor 546 goat anti-mouse IgG (all 1:1,000, Invitrogen). Specifically, for Kir4.1 staining, the rabbit anti-Kir4.1 extracellular peptide antibody was incubated for 48–72 h and the other primary antibodies were incubated for 36–48 h. For the antibody absorption experiments, the rabbit anti-Kir4.1 extracellular peptide antibody was pre-adsorbed with the Kir4.1 extracellular antigen by mixing at a weight ratio of 1:2 for 24 h. Slices for checking the injection site were counterstained with Hoechst in the final incubation step. Fluorescent image acquisition was performed with an Olympus Fluoview FV1000 confocal microscope and a Nikon A1 confocal microscope.

Cell transfection and cell culture. Human embryonic kidney (HEK293) cells (gift from J. Luo) were used for the electrophysiology recording and HEK293TN cells (Taitool Bioscience) were used for western blot analysis. Cells used in this study were authenticated and checked for mycoplasma contamination. The plasmids used were pAAV-Ubi-Kir4.1-2A-eGFP, pAAV-Ubi-dnKir4.1 (GYG to AAA)-2A-eGFP, pAAV-CAG-eGFP, pAAV-H1-Kir4.1-shRNA-CAG-eGFP and pAAV-H1-Luciferase-shRNA-CAG-eGFP. HEK293 or HEK293 TN cells were grown in DMEM (HyClone) with 10% FBS (HyClone) at 37 °C and 5% CO₂. Cells were transfected with appropriate constructs 24 h after plating using Lipofectamine 2000 (Invitrogen) according to the manufacturer's instructions. Culture medium was replaced 5–6 h after transfection. Cells were cultured for another 48 h before western blotting or electrophysiology experiments.

Plasmid constructs. The pAAV-Ubi-Kir4.1-2A-eGFP plasmid was assembled by homologous recombination of an AAV backbone linearized from the AAV-Ubi-CaMKIIA-2A-eGFP plasmid¹⁴ by PCR and Kir4.1 amplified from a pZac2.1-gfaABC1D-eGFP-Kir4.1 plasmid (AddGene). The pAAV-Ubi-dnKir4.1 (GYG to AAA)-2A-eGFP plasmid was made by PCR-based mutagenesis using pAAV-Ubi-Kir4.1-2A-eGFP as a backbone (fw: 5'-ACCATTGCGCCGCC TTCCGCTACATCAGCGA-3'; rev: 5'-GGCGGCGGCAATGGTGGTCTGG GATTGAGGGA-3'). The pAAV-gfaABC1D-dnKir4.1 (GYG to AAA)-2A-eGFP plasmid was assembled by homologous recombination of a pZac2.1-gfaABC1D backbone linearized from the pZac2.1-gfaABC1D-eGFP-Kir4.1 plasmid (AddGene) by PCR and a Kir4.1dn-2A-eGFP sequence amplified from the pAAV-Ubi-dnKir4.1 (GYG to AAA)-2A-eGFP plasmid. The pAAV-H1-Kir4.1-shRNA-CAG-eGFP plasmid was constructed using a vector (Taitool Bioscience), which

contains a CAG promoter driving eGFP and an H1 promoter driving shRNA expression. We designed six shRNA sequences using RNAi designer online software (<http://rnaidesigner.thermofisher.com/rnaexpress/>; Invitrogen) as indicated below:

- 1) 5'-GGACGACCTTCATTGACAT-3'
- 2) 5'-GCTACAAGCTTCTGCTCTTCT-3'
- 3) 5'-GCTCTTCTCGCCACCTTTAC-3'
- 4) 5'-CCGGAACCTTCCTTGCAA-3'
- 5) 5'-GCGTAAGAGTCTCCTCATTGG-3'
- 6) 5'-GCCCTTAGTGTGCGCATT-3'

We then tested the knockdown efficiency by western blot of Kir4.1 from HEK293TN cells which were co-transfected with Flag-tagged-Kir4.1 plasmid (pAAV-CMV-betaGlobin-Kir4.1-eGFP-3Flag) and each of the six shRNA plasmids. Based on our western blot result (Extended Data Fig. 10a), we chose the fifth sequence, 5'-GCGTAAGAGTCTCCTCATTGG-3', for the Kir4.1-shRNA virus package.

Electron microscopic immunohistochemistry. Four mice were deeply anaesthetized with 1% sodium pentobarbital intraperitoneally (50 mg/kg body weight) and perfused transcardially with 20 ml saline, followed by 40 ml ice-cold mixture of 4% paraformaldehyde and 0.05% glutaraldehyde in 0.1 M PB for 1 h. Brainstems were removed and postfixed by immersion in the same fixative for 4 h at 4 °C. Serial coronal sections of 50 µm thickness were prepared with a vibratome (VT 1000S, Leica), and approximately 18–20 sections, including the LHb region, were collected from each brain.

Kir4.1 was detected by immunogold-silver staining. In brief, sections were blocked with blocking buffer (5% BSA, 5% NGS and 0.05% Triton X-100 in PBS), and then incubated overnight with primary antibodies (rabbit anti-Kir4.1 extracellular peptide; 1:200, Alomone labs) diluted with solution containing 1% BSA, 1% NGS and 0.05% Triton X-100. The secondary antibody was anti-rabbit IgG conjugated to 1.4-nm gold particles (1:100, Nanoprobes) for 4 h. After rinsing, sections were post fixed in 2% glutaraldehyde in PBS for 45 min. Silver enhancement was performed in the dark with HQ Silver Kit (Nanoprobes) for visualization of Kir4.1 immunoreactivity. Before and after the silver enhancement step, sections were rinsed several times with deionized water.

Immunolabelled sections were fixed with 0.5% osmium tetroxide in 0.1 M PB for 1 h, dehydrated in graded ethanol series and then in propylene oxide, and finally flat-embedded in Epon 812 between sheets of plastic. After polymerization, acrylic sheets were then peeled from the polymerized resin, and flat-embedded sections were examined under the light microscope. Three to four sections containing Kir4.1 immunoreactivity in the LHb were selected from each brain, trimmed under a stereomicroscope, and glued onto blank resin stubs. Serial ultrathin sections were cut with an Ultramicrotome (Leica EM UC6, Germany) using a diamond knife (Diatome) and mounted on formvar-coated mesh grids (6–8 sections per grid). They were then counterstained with uranyl acetate and lead citrate, and observed under a JEM-1230 electron microscope (JEOL) equipped with a CCD camera and its application software (832 SC1000).

Stereotaxic surgery and virus injection. cLH rats (P50–60) were deeply anaesthetized using 4% pentobarbital. Mice (P50–60 days) were deeply anaesthetized using ketamine (100 mg/kg of body weight) and xylazine (8 mg/kg). Animals were placed on a stereotaxic frame (RWD Instruments). A small volume of virus was injected into the LHb bilaterally (for rats LHb: AP, –3.7 mm from bregma; ML, ±0.7 mm; DV, –4.55 mm from the brain surface; for mice: AP, –1.72 mm from bregma; ML, ±0.46 mm; DV, –2.62 mm from the brain surface) using a pulled glass capillary with a pressure microinjector (Picospritzer III, Parker) at a slow rate of 0.1 µl/min. After the injection was completed, the capillary was left for an additional 10 min before it was then slowly withdrawn completely. After surgery, animals were allowed to recover from anaesthesia under a heat pad.

The following vectors were used: AAV-CaMKIIA::eGFP-Cre (AAV2/1-CaMKIIA-HI-eGFP-Cre, 0.2 µl, bilateral into LHb, University of Pennsylvania vector core), AAV-GFAP::eGFP-Cre (AAV2/5-gfaABC1D-eGFP-Cre, titre: 4.74×10^{12} v.g./ml, dilution: 1:2, 0.2 µl, bilateral into LHb, Taitool Bioscience), AAV-GFAP::Kir4.1 (AAV2/5-gfaABC1D-eGFP-Kir4.1, titre: 9.19×10^{12} v.g./ml, dilution: 1:5, 0.2 µl, bilateral into LHb, Taitool Bioscience), AAV-GFAP::eGFP (AAV2/5-gfaABC1D-eGFP, titre: 1.61×10^{13} v.g./ml, dilution: 1:5, 0.2 µl, bilateral into LHb, University of Massachusetts, Gao Laboratory), AAV-H1::Kir4.1-shRNA (AAV2/5-H1-Kir4.1-shRNA-CAG-eGFP, titre: 3.04×10^{13} v.g./ml, dilution: 1:10, 0.2 µl, bilateral into LHb, Taitool Bioscience), AAV-H1::Ctrl-shRNA (AAV2/5-H1-Luciferase-shRNA-CAG-eGFP, titre: 1.46×10^{13} v.g./ml, dilution: 1:5, 0.2 µl, bilateral into LHb, Taitool Bioscience), AAV2/5-gfaABC1D-dnKir4.1-2A-eGFP (GYG to AAA) (titre: 4.15×10^{13} v.g./ml, 0.2 µl, bilateral into LHb, Taitool Bioscience). All viral vectors were aliquotted and stored at –80 °C until use.

Depression model and behaviour assay. LPS-induced depression. The LPS-induced depression model was used as previously described²². Wistar male rats

(3 months) were used for the experiments. LPS (Sigma, L-2880) dissolved in sterile 0.9% saline was intraperitoneally injected into Wistar rats, at a dosage of 0.5 mg/kg. This dosage was used to stimulate a subclinical infection without inducing obvious inflammation and other apparent impairments in animals. Saline or LPS was injected between 09:30 and 10:30 a.m. daily for 7 days. The forced swim test was performed 24 h after the last injection. The habenular tissue was dissected 24 h after the behavioural test for western blotting or electrophysiology experiments.

Learned helplessness test (LHT). Male juvenile (P30) or adult (P90) cLH rats were tested in a lever-pressing task to evaluate the learned helplessness (LH) phenotype¹⁴. A cue-light-illuminated lever in the shock chamber was presented, which terminated the shock when rats pressed the lever. Fifteen escapable shocks (0.8 mA) were delivered with a 24-s inter-shock interval. Each shock lasted up to 60 s unless the rat pressed the lever to terminate the shock. Out of the 15 trials, rats that failed to press the lever for more than ten trials were defined as learned helpless (LH), and rats with fewer than five failures were defined as non-learned helpless (NLH).

Forced swim test (FST). Animals were individually placed in a cylinder (12 cm diameter, 25 cm height for mice; 20 cm diameter, 50 cm height for rats) of water (23–25 °C) and swam for 6 min under normal light³³. Water depth was set to prevent animals from touching the bottom with tails or hind limbs. Animal behaviours were videotaped from the side. The immobility time during the last 4 min of the test was counted offline by an observer blinded to the animal treatments. Immobility was defined as time when animals remained floating or motionless with only movements necessary for keeping balance in the water. For rats, an additional pre-test was conducted 24 h before the test, during which rats were individually placed in a cylinder of water under the conditions described above for 15 min. **Sucrose preference test (SPT).** Animals were single housed and habituated with two bottles of water for 2 days, followed by two bottles of 2% sucrose for 2 days³³. Animals were then water deprived for 24 h and then exposed to one bottle of 2% sucrose and one bottle of water for 2 h in the dark phase. Bottle positions were switched after 1 h. Total consumption of each fluid was measured and sucrose preference was defined as the average sucrose consumption ratio during the first and second hours. Sucrose consumption ratio was calculated by dividing total consumption of sucrose by total consumption of both water and sucrose.

Open field test (OFT). Animals were placed in the centre of an arena (40 cm × 40 cm × 40.5 cm for mice; 100 cm × 100 cm × 40 cm for rats) in a room with dim light for 10 min. A video camera positioned directly above the arena was used to track the movement of each animal (Any-maze, Stoelting).

LHb brain slice preparation. Rats (P25–30 or P60–90) and mice (P90) were anaesthetized with isoflurane and 10% chloral hydrate, and then perfused with 20 ml ice-cold ACSF (oxygenated with 95% O₂ + 5% CO₂) containing (mM): 125 NaCl, 2.5 KCl, 25 NaHCO₃, 1.25 NaH₂PO₄, 1 MgCl₂ and 25 glucose, with 1 mM pyruvate added. The brain was removed as quickly as possible after decapitation and put into chilled and oxygenated ACSF. Coronal slices containing the habenula (350 μm and 300 μm thickness for rats and mice, respectively) were sectioned in cold ACSF with a Leica 2000 vibratome, transferred to ASCF at 32 °C for incubation and recovery for 1 h and then transferred to room temperature. ACSF was continuously gassed with 95% O₂ and 5% CO₂. Slices were allowed to recover for at least 1 h before recording.

In vitro electrophysiological recording. For LHb neuron recordings, currents were measured under whole-cell patch-clamp recordings using pipettes with a typical resistance of 5–6 MΩ filled with internal solution containing (mM) 105 K-gluconate, 30 KCl, 4 Mg-ATP, 0.3 Na-GTP, 0.3 EGTA, 10 HEPES and 10 Na-phosphocreatine, with pH set to 7.35. For the biocytin filling, 5 mg/ml biocytin was added in the internal solution. The external ACSF solution contained (in mM) 125 NaCl, 2.5 KCl, 25 NaHCO₃, 1.25 NaH₂PO₄, 1 MgCl₂ and 25 glucose. Cells were visualized with infrared optics on an upright microscope (BX51WI, Olympus). A MultiClamp 700B amplifier and pCLAMP10 software were used for electrophysiology (Axon Instruments). The series resistance and capacitance were compensated automatically after a stable Gigaseal was formed. Spontaneous neuronal activity was recorded under current-clamp ($I = 0$ pA) for 60 s consecutively. RMP was determined during the silent period of neuronal spontaneous activity.

To test the effects of TTX (1 μM, Sigma) and BaCl₂ (100 μM, Sigma) on neuronal RMP and spontaneous activity, baselines were recorded for at least 3 min. Then the drug was perfused into the medium with the arrival of the drug being precisely indicated with a bubble that was added before the transition from normal ACSF to ACSF with drug. The effect of TTX on the RMP and spontaneous activity of LHb neurons stabilized after a few minutes, whereas the effect of BaCl₂ took more than 10 min to stabilize. We thus analysed the effects of TTX and BaCl₂ at 5 and 15 min after perfusion started, respectively.

Astrocytic whole-cell patch-clamp recordings and Kir4.1 current isolation. Astrocytes were distinguished from neurons by their small (5–10 μm), oval somata

and distinct electrophysiological features: a hyperpolarized RMP (-74 ± 1 mV), a low input resistance R_{in} (47 ± 6 MΩ), a linear $I-V$ relationship and an absence of action potentials in response to increased injection currents^{34,35}. BaCl₂ (100 μM, Sigma) was applied to isolate Kir4.1 current, which was subtracted from the $I-V$ curve recorded from -120 mV to 0 mV. Biocytin (Sigma, 5 mg/ml) was dissolved into the patch-clamp pipette solution. After electrophysiological characterization, cells were held for at least 30 min in voltage clamp and constantly injected with a hyperpolarization current (500 ms, 50 pA, 0.5 Hz, 30 min) to allow biocytin filling (performed at 34 °C). Subsequently, slices were fixed overnight in 4% paraformaldehyde at 4 °C. The antibodies used were rabbit anti-NeuN (1:500, Millipore), Alexa Fluor 546 donkey anti-rabbit IgG (1:1,000, Invitrogen) and Cy2-conjugated streptavidin (1:1,000, Jackson ImmunoResearch). Fluorescent image acquisition was performed with a Nikon A1 confocal microscope.

Tri-compartment model. A tri-compartment model was constructed including the neuron, the astrocyte and the extracellular space. The model was based on ionic fluxes between these three compartments. Na⁺ and K⁺ voltage-gated channels, and leak channels were recruited into the neuron as $dV_N/dt = (I_{app} - I_K - I_{Na} - I_{Leak,N})/C_N$, where V_N is the neuronal membrane potential, C_N is the neuronal capacitance, I_{app} is an external current applied to the neuron, I_{Na} and I_K are the fast Na⁺ and K⁺ currents of the action potentials, respectively, and $I_{Leak,N}$ is responsible for the neuronal resting membrane potential. To trigger an action potential, we applied an external step current of amplitude 5 nA and duration 0.1 ms. Kir4.1 channels on the extracellular and vessel side and leak channels were recruited into the astrocyte as $dV_A/dt = (-I_{Kir} - I_{Kir,vess} - I_{Leak,A})/C_A$, where V_A is the astrocytic membrane potential, C_A is the astrocytic capacitance, I_{Kir} and $I_{Kir,vess}$ account for the K⁺ flow on the side of the neuron and vessel, respectively (I_{Kir} is outward during the resting state, and becomes inward when K⁺ equilibrium potential exceeds the astrocytic membrane potential), and $I_{Leak,A}$ is responsible for the astrocytic resting membrane potential.

The dynamics for K⁺ in the three compartments are described by:

$$d[K^+]_O/dt = (I_{Kir} + I_K)/(F \times Vol_O) - 2(i_{pump,N} + i_{pump,A}) - d_{K_O}([K^+]_O - K_{O_0})$$

$$d[K^+]_N/dt = -I_K/(F \times Vol_N) + 2i_{pump,N} \times Vol_O/Vol_N - d_{K_N}([K^+]_N - K_{N_0})$$

$$d[K^+]_A/dt = (-I_{Kir} - I_{Kir,vess})/(F \times Vol_A) + 2i_{pump,A} \times Vol_O/Vol_A - d_{K_A}([K^+]_A - K_{A_0})$$

where $[K^+]_O$, $[K^+]_N$ and $[K^+]_A$ are the extracellular, neuronal and astrocytic K⁺ concentrations, respectively; F is the Faraday constant; Vol_O , Vol_A and Vol_N are the volumes of the extracellular, astrocytic and neuronal compartments, respectively; and $i_{pump,N}$ and $i_{pump,A}$ are the fluxes through the Na⁺/K⁺ pump of the neuron and astrocyte membranes, respectively. The term $d([X] - [X_0])$ describes the diffusion of K⁺ in the considered compartment, where d_{K_O} , d_{K_N} and d_{K_A} are the rates of extracellular, neuronal and astrocytic K⁺ effective flux; K_{O_0} , K_{N_0} and K_{A_0} are the extracellular, neuronal and astrocytic K⁺ concentrations expected at equilibrium, respectively. The extracellular K⁺ is mainly contributed by I_K . Released extracellular K⁺ from the neuron is taken up by Kir4.1 channels and Na⁺/K⁺ pumps.

The dynamics for Na⁺ in the three compartments are described by:

$$d[Na^+]_O/dt = I_{Na}/(F \times Vol_O) + 3(i_{pump,N} + i_{pump,A}) - d_{Na_O}([Na^+]_O - Na_{O_0})$$

$$d[Na^+]_N/dt = -I_{Na}/(F \times Vol_N) - 3i_{pump,N} \times Vol_O/Vol_N - d_{Na_N}([Na^+]_N - Na_{N_0})$$

$$d[Na^+]_A/dt = -3i_{pump,A} \times Vol_O/Vol_A - d_{Na_A}([Na^+]_A - Na_{A_0})$$

See Supplementary Information (Model Description and Supplementary Table 2) for detailed formulae.

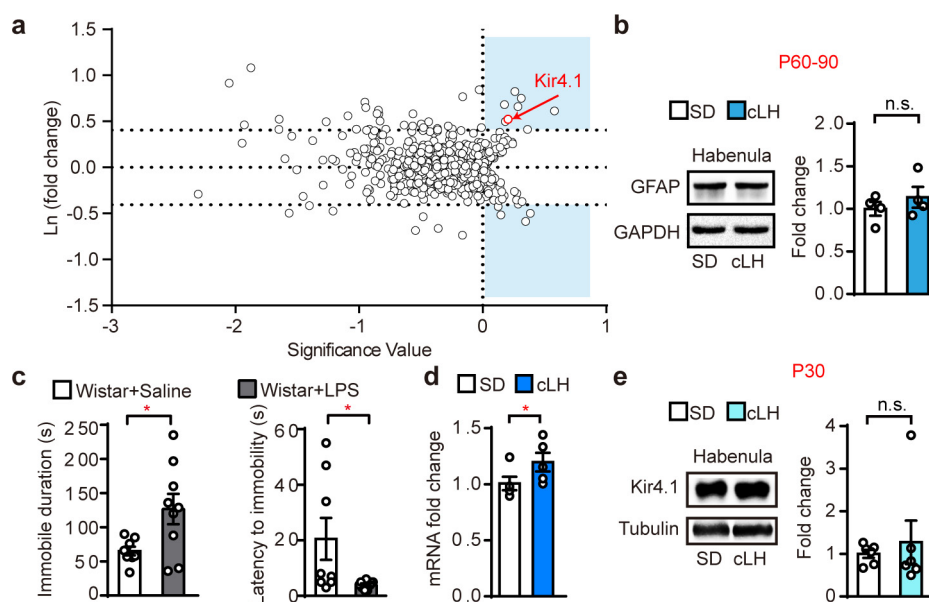
Statistical analyses. The required sample sizes were estimated on the basis of our past experience performing similar experiments. Animals were randomly assigned to treatment groups. Analyses were performed blinded to treatment assignments in all behavioural experiments. Statistical analyses were performed using GraphPad Prism software v6. By pre-established criteria, values were excluded from the

analyses if the viral injection or drug delivering sites were out of the LHb. All statistical tests were two-tailed, and significance was assigned at $P < 0.05$. Normality and equal variances between group samples were assessed using the D'Agostino and Pearson omnibus normality test and Brown–Forsythe tests, respectively. When normality and equal variance between sample groups was achieved, one-way ANOVAs (followed by Bonferroni's multiple comparisons test) or t -tests were used. Where normality or equal variance of samples failed, Mann–Whitney U tests were performed. Linear regression tests and χ^2 tests were used in appropriate situations. The sample sizes, specific statistical tests used,

and main effects of our statistical analyses for each experiment are reported in Supplementary Table 1.

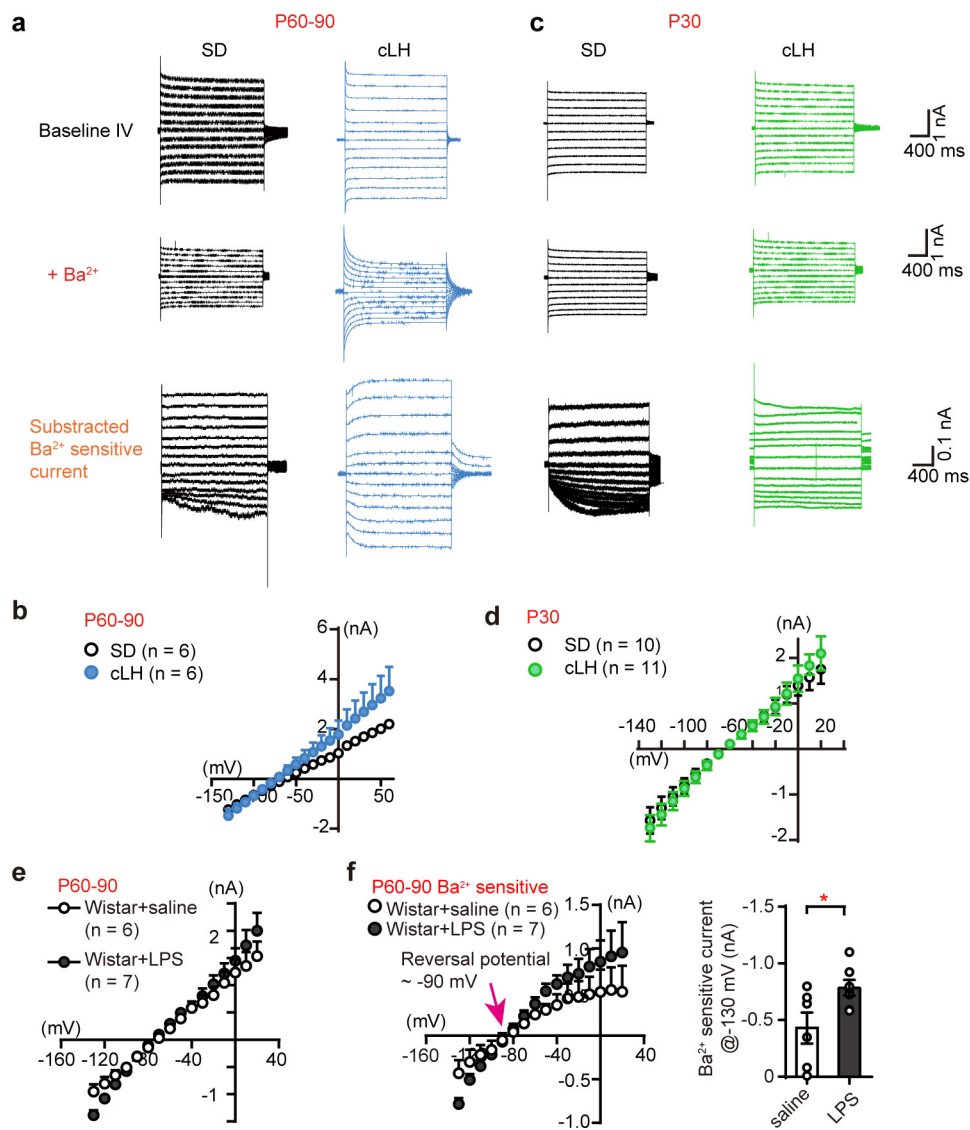
Data availability. The data that support the findings of this study are available from the corresponding author upon reasonable request.

33. Powell, T. R., Fernandes, C & Schalkwyk, L. C. *Depression-Related Behavioral Tests* (John Wiley & Sons, 2011).
34. Verkhratskii, A. N & Butt, A. *Glial Neurobiology: a Textbook* (John Wiley & Sons, 2007).
35. Kettenmann, H & Ransom, B. R. *Neuroglia* 3rd edn (Oxford Univ. Press, 2013).



Extended Data Figure 1 | Habenular protein expression in rat models of depression. **a**, Volcano plot of high-throughput proteomic screen identifies proteins that are differentially expressed in the habenulae of cLH rats versus wild-type rats. Ln (fold change) is ln-transformed value of the normalized protein ratio of cLH and control¹⁴. Significance value was calculated as the average normalized ratio minus two folds of s.d.¹⁴. Proteins in the shaded areas have more than 50% significant change. Kir4.1 is one of the eight upregulated proteins identified¹⁴. Dashed lines indicate fold change of 50%. **b**, Western blot analysis showing no change in

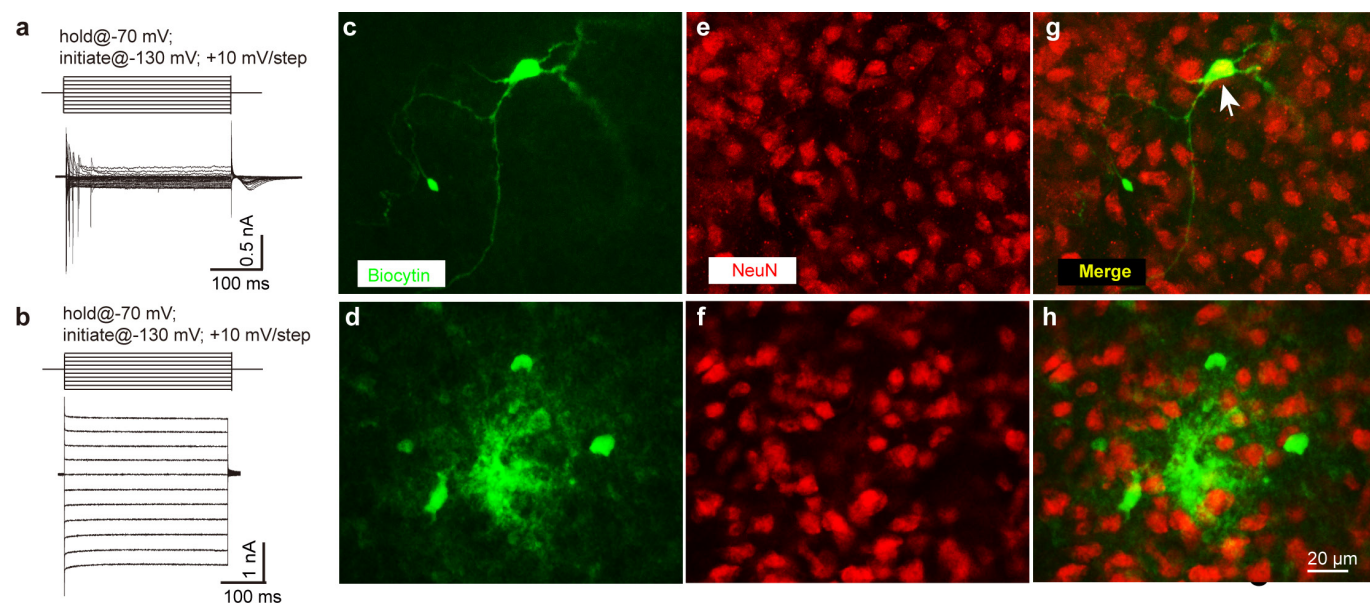
GFAP protein in habenulae of cLH rats at P60–90. $n = 4$, 4 rats for control and cLH, respectively. **c**, LPS injection ($500 \mu\text{g kg}^{-1}$ i.p. for 7 days) induces increased immobile time and decreased latency to immobility in the FST. $n = 8$, 9 rats for saline and LPS, respectively. **d**, QPCR analysis of Kir4.1 mRNA in habenulae. Two-tailed paired t -test. $n = 5$, 5 rats for control and cLH, respectively. **e**, Western blot analysis showing no change in Kir4.1 protein in membrane fraction of habenulae in cLH rats at P30. $n = 6$, 6. Data are means \pm s.e.m., * $P < 0.05$, n.s., not significant. Two-tailed paired t -test (**b**, **d**, **e**); two-tailed unpaired t -test (**c**).



Extended Data Figure 2 | Ba²⁺-sensitive Kir4.1 current is upregulated in LHb of adult cLH rats and adult LPS-injected Wistar rats.

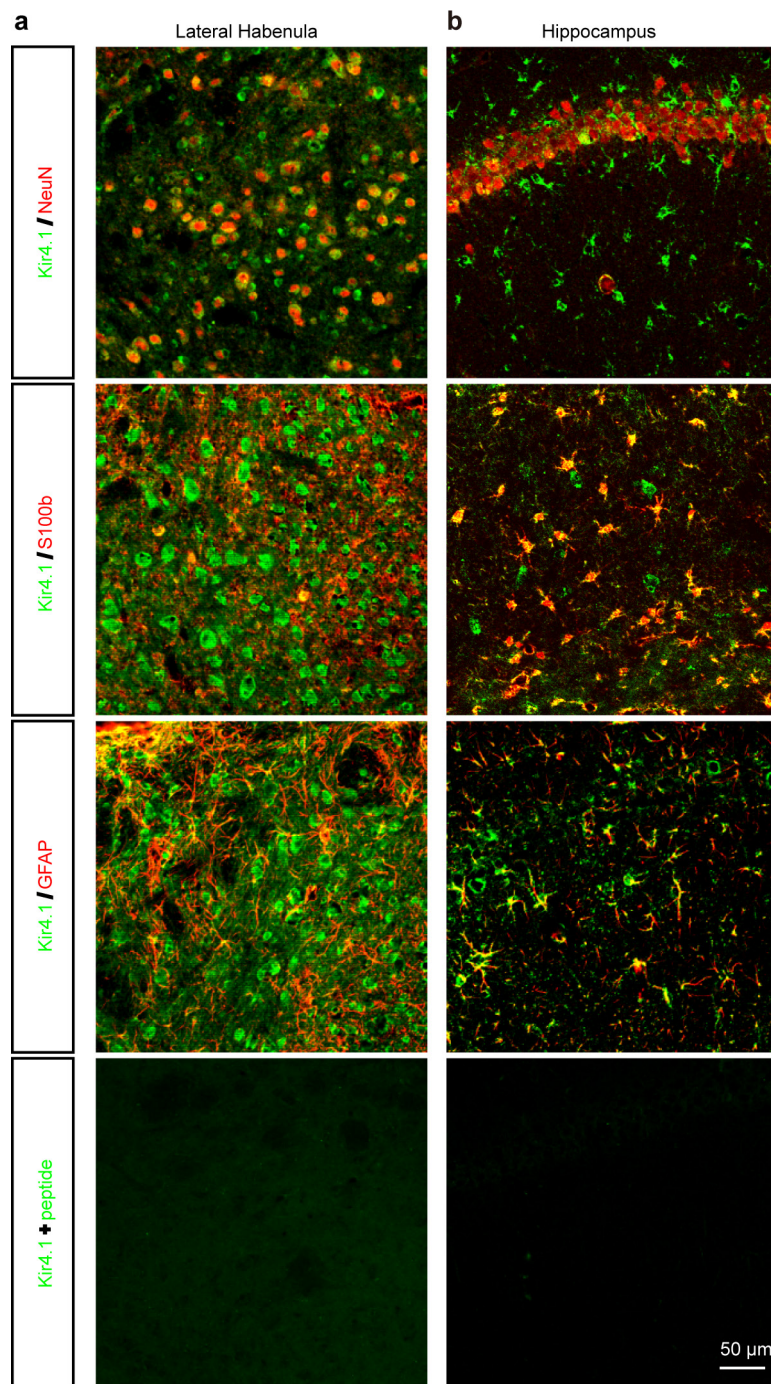
a, c, Representative traces showing linear *I*-*V* curve in a typical astrocyte before (upper) and after (middle) Ba²⁺ perfusion under voltage steps (-130 mV to -30 mV, step by 10 mV, 2 s duration, holding at -70 mV). Subtraction of the two led to Ba²⁺-sensitive Kir current (bottom) at P60-90 (**a**) and P30 (**c**) in cLH rats. **b, d,** *I*-*V* plots of astrocytes in cLH rats

and controls at P60-90 (**b**) and P30 (**d**). **e,** *I*-*V* plots of astrocytes in LPS-injected Wistar rats and saline controls at P60-90. **f,** *I*-*V* plot and bar graph showing Ba²⁺-sensitive currents in LPS-injected Wistar rats and saline-injected controls at P60-90. Two-tailed unpaired *t*-test. *n* = 7, 6 astrocytes from 2, 2 rats for saline and LPS, respectively. Data are means ± s.e.m., **P* < 0.05.



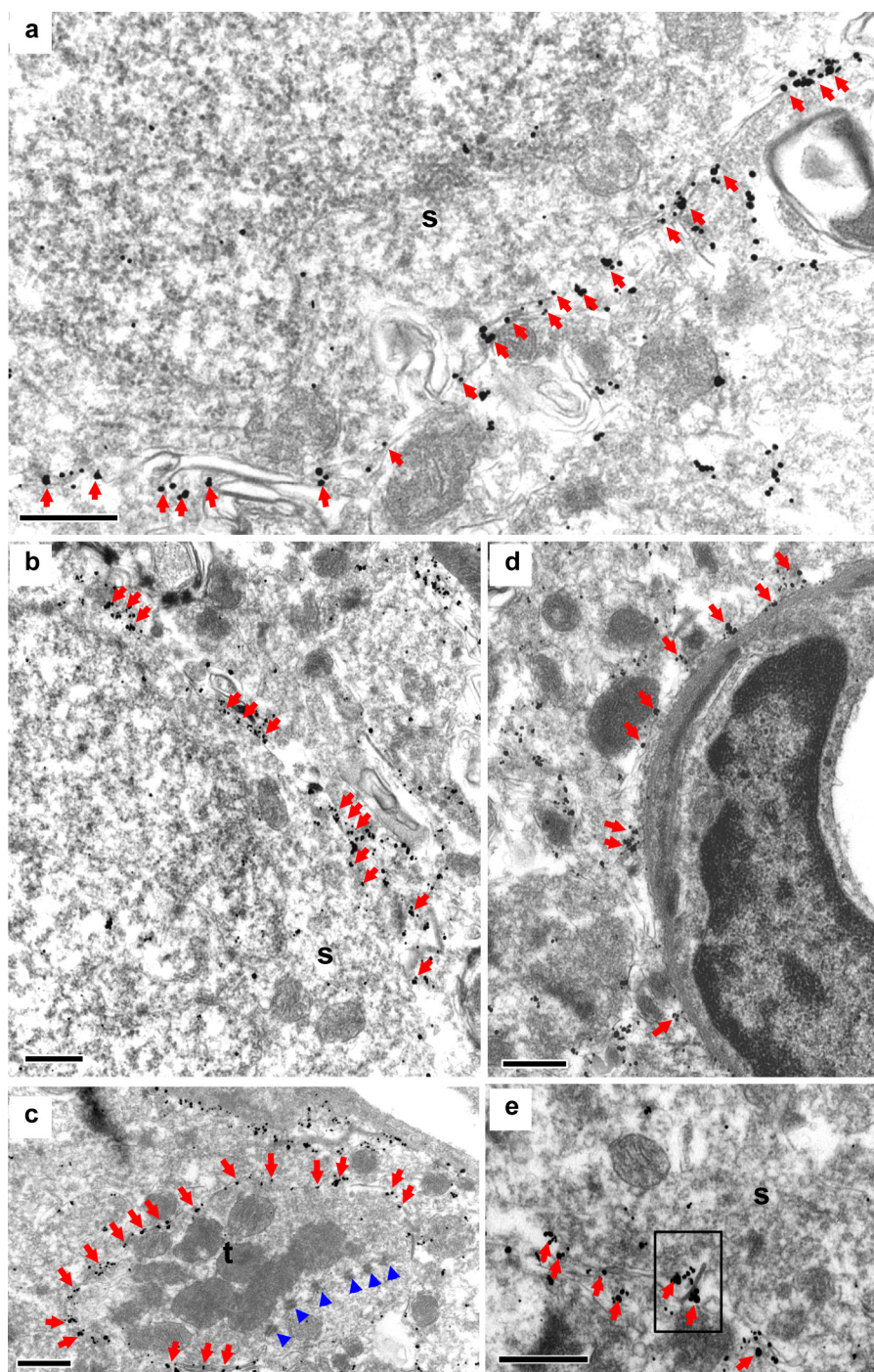
Extended Data Figure 3 | Biocytin intercellular filling and double staining with NeuN confirm the identity of electrophysiologically identified neurons and astrocytes. **a, b**, A neuron (**a**) and an astrocyte (**b**) in LHb slices were first identified on the basis of their specific morphology (astrocytes: 5–10 μ m diameter; neurons: \sim 15 μ m diameter) and physiological properties. The neuron fires at a depolarizing voltage step (**a**), whereas the astrocyte shows a steady-state I – V relationship and a lack of spiking activity (**b**). After electrophysiological characterization, cells were held for at least 30 min in voltage clamp and constantly injected with a hyperpolarization current (500 ms, 50 pA, 0.5 Hz, 30 min) to allow biocytin

filling. **c–h**, Biocytin-labelled neurons and astrocytes subsequently confirmed by co-labelling with NeuN. **c, d**, Biocytin signals in a single neuron (**c**) or a group of astrocytes owing to diffusion through gap junctions (**d**) (four independent experiments). **e, f**, NeuN signals (four independent experiments). **g, h**, Colabelling of NeuN with the neuron (indicated by white arrow, **g**) but not astrocytes (**h**) (four independent experiments). Note that all biocytin-filled neurons ($n = 18$) colabel with NeuN and all biocytin-filled astrocytes ($n = 11$) do not colabel with NeuN.



Extended Data Figure 4 | Expression pattern of Kir4.1 in the LHb and hippocampus. a, b, Kir4.1 co-immunostaining with neuronal marker (NeuN) or astrocytic marker (S100b and GFAP) in the LHb (a) or

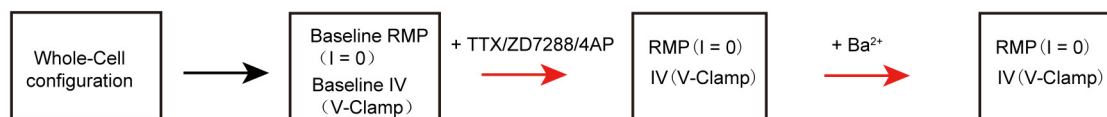
hippocampus (b). Bottom two panels show staining with the same Kir4.1 antibody pre-incubated with the antigen peptide, demonstrating the specificity of the Kir4.1 antibody (two independent experiments).



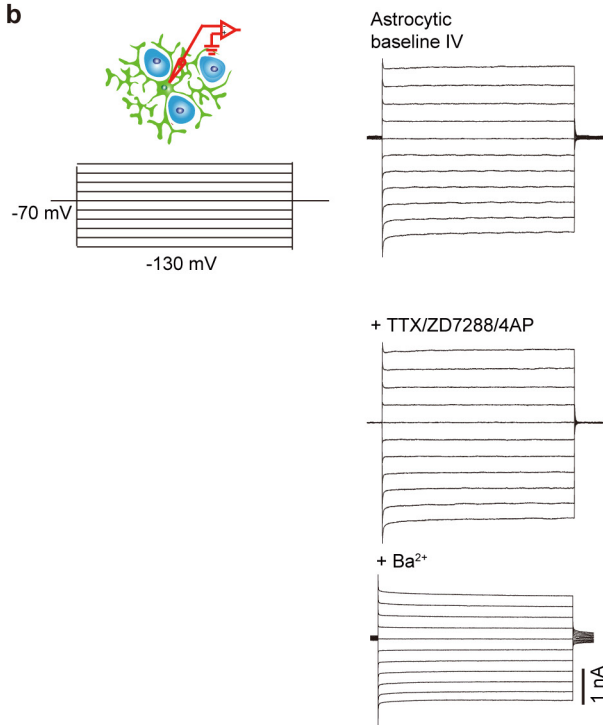
Extended Data Figure 5 | Electron microscopy immunohistochemistry of Kir4.1 staining. **a, b,** Many Kir4.1 immunograin (arrows) surround the neuronal soma. **c,** Kir4.1 grains (arrows) also surround axon–dendrite synapses, but are rare near the synaptic zones as indicated by

the postsynaptic densities (arrowheads). **d,** Kir4.1 immunograin are also detected surrounding a vascular endothelial cell. **e,** Inset shows Kir4.1 immunograin near a gap junction. s, neuronal soma; t, axon terminal. Scale bars, 0.5 μ m. Three independent experiments.

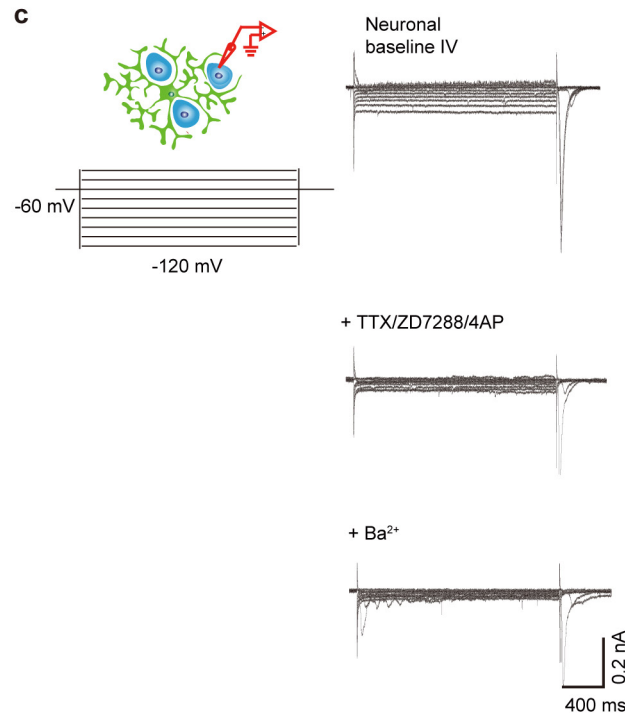
a



b

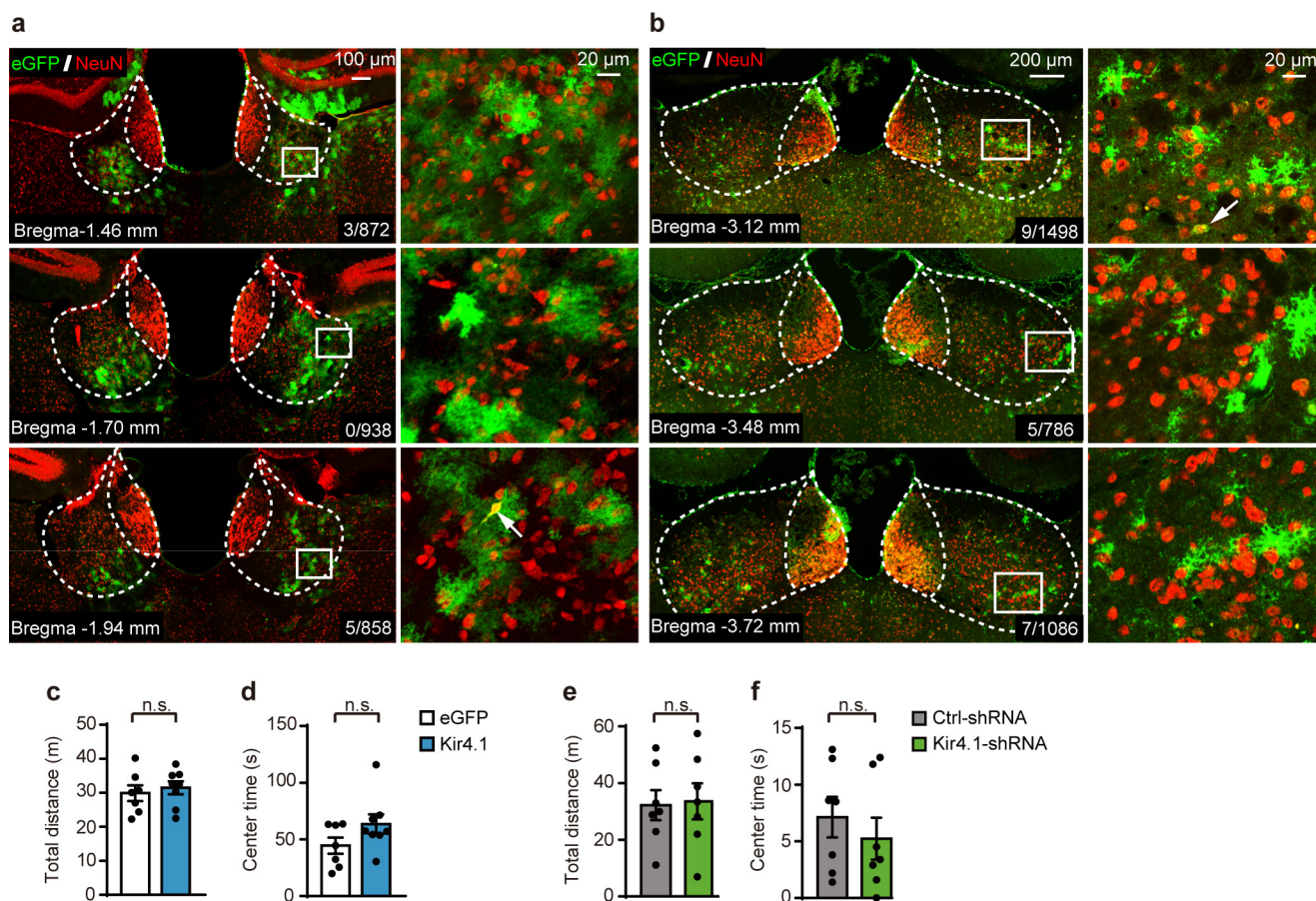


c



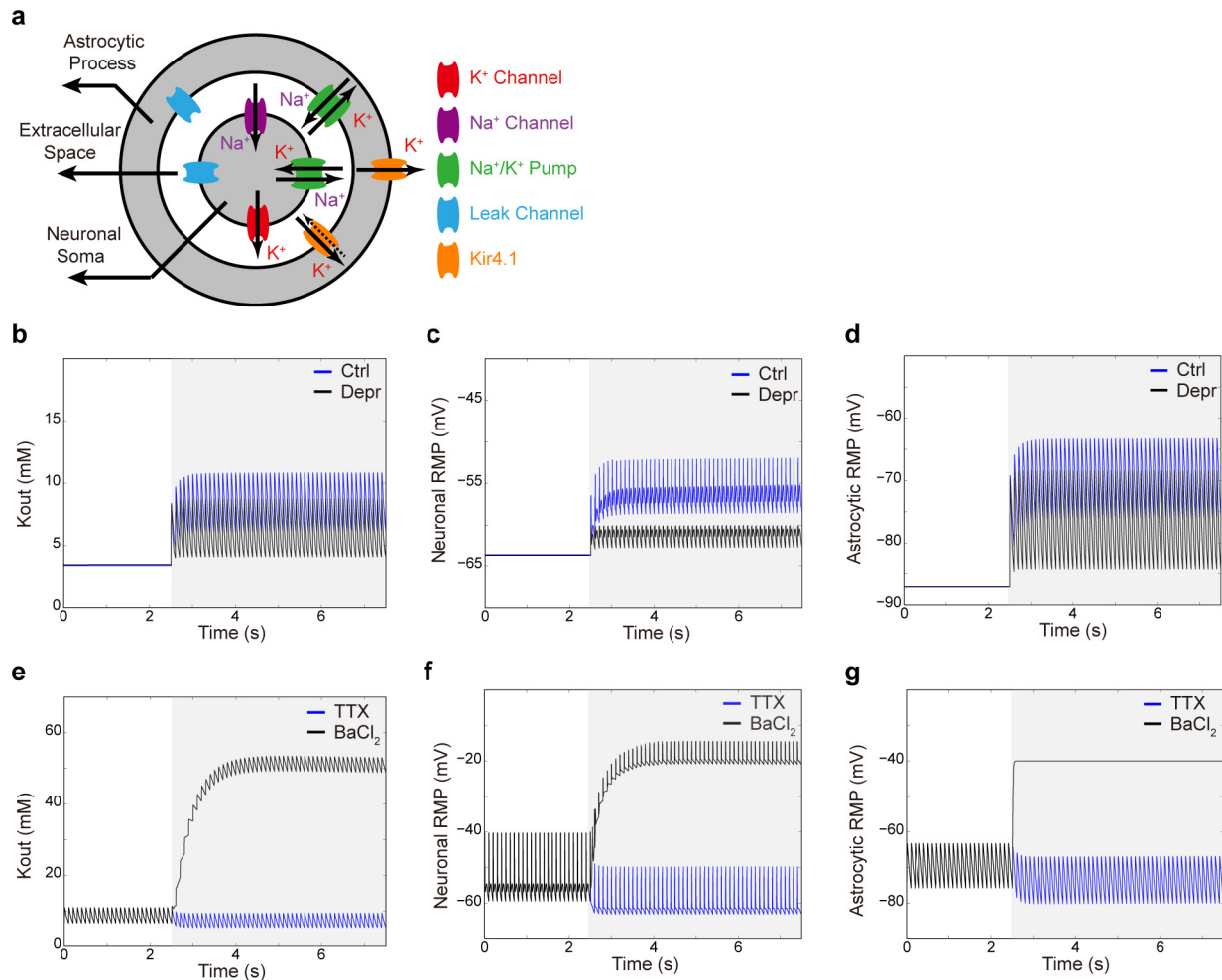
Extended Data Figure 6 | Kir4.1 is expressed in astrocytes but not neurons in the LHB. **a**, Schematics showing sequence of drug application and recording after a neuron or astrocyte is patched. **b**, Representative traces showing a linear I - V curve in a typical astrocyte under voltage steps (-130 mV to -30 mV, step by 10 mV, 2 s duration, holding at -70 mV, protocol demonstrated on left, upper panel). I - V curves of the same cell after addition of TTX (1 μ M), 4-aminopyridine (4AP, 1 mM) and

4-(*N*-ethyl-*N*-phenylamino)-1,2-dimethyl-6-(methylamino) pyrimidinium chloride (ZD7288, 50 μ M) (middle) and further addition of Ba^{2+} (100 μ M, bottom) are shown below. **c**, Representative traces showing a nonlinear I - V curve in a typical neuron under voltage steps (-120 mV to -40 mV, step by 10 mV, 2 s duration, holding at -60 mV, protocol demonstrated on left, upper panel). I - V curves of the same cell after addition of TTX, ZD7288 and 4AP (middle) and further addition of Ba^{2+} (bottom) are shown below.



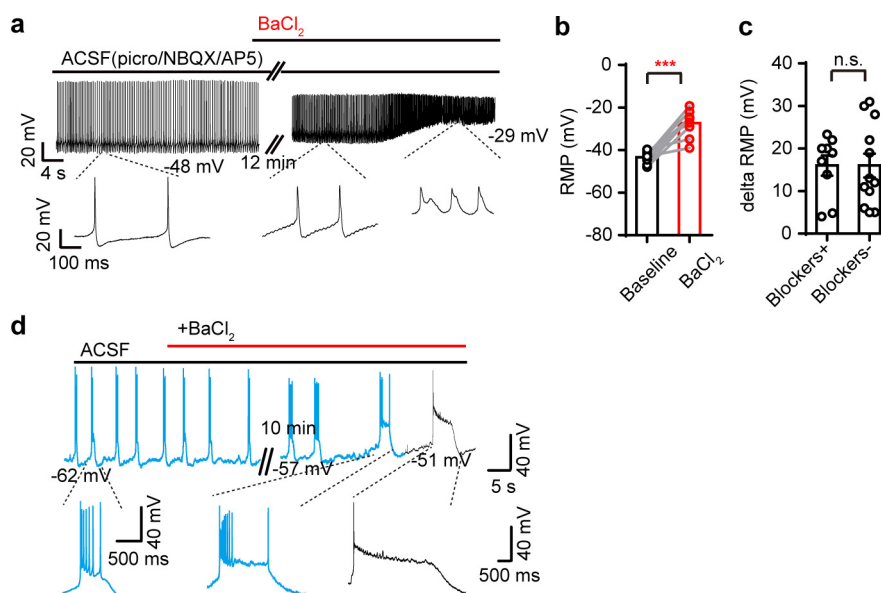
Extended Data Figure 7 | Characterization of cell-type specificity of GFAP promoter, and locomotion. **a, b**, Double immunofluorescence for NeuN (red) and eGFP (green) in the coronal section of LHb brain slices infected with AAV-GFAP::Kir4.1 (AAV2/5-gfaABC1D-eGFP-Kir4.1) virus in mice (three independent experiments, **a**) or AAV-GFAP::dnKir4.1 (AAV2/5-gfaABC1D-dnKir4.1-2A-eGFP) virus in cLH rats (two independent experiments, **b**). Left, examples of anterior, middle and posterior coronal sections of LHb. Numbers in the bottom right corner are the number of merged cells/number of NeuN⁺ cells in the virus-infected

area. Right, zoomed-in images of the white square area in left. Note that there is only one infected neuron, as indicated by the white arrow, in all three fields of view. **c, d**, Overexpression of Kir4.1 in the LHb of C57 mice does not affect locomotion. $n = 7, 8$ mice for eGFP and Kir4.1, respectively. **e, f**, Overexpression of Kir4.1-shRNA in the LHb of cLH rats does not affect locomotion activities. $n = 7, 7$ rats for control and Kir4.1 shRNA, respectively. Data are means \pm s.e.m; n.s., not significant. Two-tailed unpaired *t*-test (**c-f**).



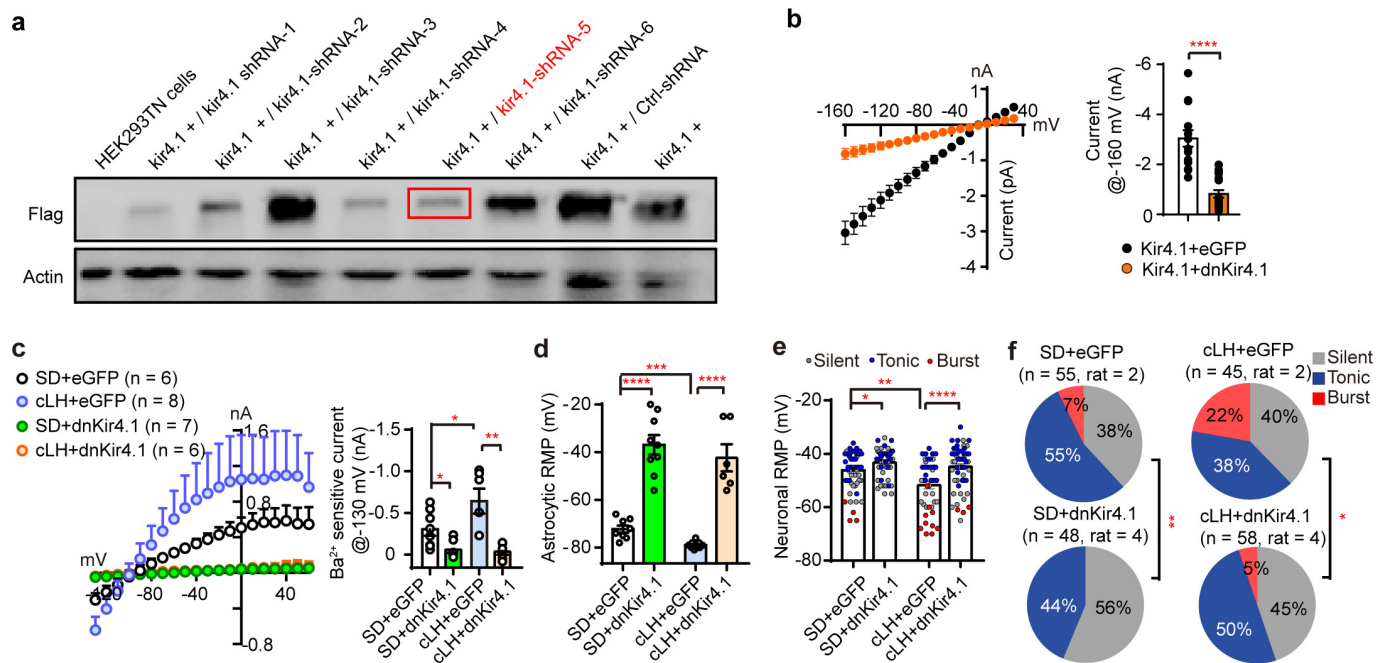
Extended Data Figure 8 | Simulation of the dynamic potassium buffering effect of Kir4.1 in the tri-compartment model. **a**, Schematic representation of a tri-compartment model involving neuron, astrocyte and extracellular space (see Methods for details). **b–d**, Effects of increasing Kir4.1 expression on $[K]_{out}$ (**b**), neuronal membrane potential (**c**) and astrocytic membrane potential (**d**). Ctrl, control condition with $1 \times$ Kir4.1 conductance; Depr, depression condition with $2 \times$ Kir4.1 conductance. Grey shaded areas indicate application of 10 Hz tonic stimulation to neurons. Note that under this neuronal firing condition, $[K]_{out}$ is lower,

and neuron and astrocyte are more hyperpolarized in the depression condition than the control. **e–g**, Effects of *in silico* TTX (blocking action potentials, $g_{Na} = 0$) or Ba^{2+} (blocking Kir4.1, $g_{Kir4.1} = 0$) treatments on $[K]_{out}$ (**e**), neuronal membrane potential (**f**) and astrocytic membrane potential (**g**) when neurons are under 10 Hz tonic stimulation. Grey shaded areas indicate *in silico* application of drugs. Note that TTX and Ba^{2+} cause opposite changes to $[K]_{out}$, neuronal membrane potential and astrocytic membrane potential. Neuronal spikes are not shown for clarity of presentation.



Extended Data Figure 9 | BaCl_2 caused depolarization of neuronal RMP in the presence of synaptic transmitter blockers. **a, b**, Representative trace (**a**) and bar graph ($n = 9$ neurons from 3 rats; **b**) showing effect of BaCl_2 ($100 \mu\text{M}$) perfusion onto tonic-firing neurons that have been bathed with transmitter blockers ($100 \mu\text{M}$ picrotoxin, $10 \mu\text{M}$ NBQX and $100 \mu\text{M}$ AP5). **c**, Bar graph showing the level of RMP depolarization caused by BaCl_2 in the presence or absence of transmitter blockers.

$n = 9$, 12 neurons from 3, 3 rats for with and without blockers, respectively. **d**, Representative trace showing effect of BaCl_2 (sampled 15 min after drug perfusion) on bursting neurons ($n = 4$ out of 9 neurons from 3 rats). Spikes in bursting and tonic-firing mode are shown in blue and black, respectively. Data are means \pm s.e.m., *** $P < 0.001$, n.s., not significant. Two-tailed paired t -test (**b**) and two-tailed unpaired t -test (**c**).



Extended Data Figure 10 | Characterization of Kir4.1 loss-of-function constructs. **a**, Flag-tagged-Kir4.1 plasmid (pAAV-CMV-betaGlobin-Kir4.1-eGFP-3Flag) was co-transfected with pAAV-vector expressing six different shRNAs (see Methods) of Kir4.1 or the negative control (shRNA of luciferase) into HEK293 TN cells. On the basis of knockdown efficiency as shown in the western blot, Kir4.1-shRNA-5 was chosen for viral package (two independent experiments). **b**, I-V plot showing Kir4.1 currents recorded in HEK293 cells transfected with pAAV-Kir4.1 together with negative control pAAV-eGFP or pAAV-dnKir4.1 plasmid. Bars represent the current values recorded at -160 mV. $n = 18, 15$ HEK293 cells

for eGFP and dnKir4.1, respectively. **c**, I-V plot and bar graph showing Ba²⁺-sensitive currents blocked by AAV-dnKir4.1 in both cLH and wild-type rats. **d-f**, AAV-dnKir4.1 caused depolarization of RMP in astrocytes ($n = 9, 8, 9, 6$ astrocytes from 2, 4, 2, 4 rats for wild-type eGFP, wild-type dnKir4.1, cLH eGFP and cLH dnKir4.1, respectively; **d**) and neurons in viral infected area ($n = 54, 48, 45, 58$ neurons from 2, 4, 2, 4 rats, **e**), and abolished neuronal bursting (**f**) in both cLH and wild-type rats. Data are means \pm s.e.m.; * $P < 0.05$, ** $P < 0.01$, *** $P < 0.001$, **** $P < 0.0001$. Two-tailed unpaired t -test (**b-e**) and χ^2 test (**f**).

Teneurin-3 controls topographic circuit assembly in the hippocampus

Dominic S. Berns^{1,2,3}, Laura A. DeNardo^{1,2}, Daniel T. Pederick^{1,2} & Lihun Luo^{1,2}

Brain functions rely on specific patterns of connectivity. Teneurins are evolutionarily conserved transmembrane proteins that instruct synaptic partner matching in *Drosophila* and are required for vertebrate visual system development. The roles of vertebrate teneurins in connectivity beyond the visual system remain largely unknown and their mechanisms of action have not been demonstrated. Here we show that mouse teneurin-3 is expressed in multiple topographically interconnected areas of the hippocampal region, including proximal CA1, distal subiculum, and medial entorhinal cortex. Viral-genetic analyses reveal that teneurin-3 is required in both CA1 and subicular neurons for the precise targeting of proximal CA1 axons to distal subiculum. Furthermore, teneurin-3 promotes homophilic adhesion *in vitro* in a splicing isoform-dependent manner. These findings demonstrate striking genetic heterogeneity across multiple hippocampal areas and suggest that teneurin-3 may orchestrate the assembly of a complex distributed circuit in the mammalian brain via matching expression and homophilic attraction.

The hippocampal region is critical for the acquisition of declarative memory and the neural representation of space^{1–4}. The connections between hippocampal subregions and adjacent cortex are topographically organized along both the dorsal–ventral and proximal–distal axes⁵. Along the proximal–distal axis, proximal CA1, distal subiculum, and medial entorhinal cortex (MEC) neurons are specifically interconnected, as are distal CA1, proximal subiculum, and lateral entorhinal cortex (LEC) neurons^{6,7}. These two parallel circuits may be preferentially used for processing spatial and object-related information, respectively⁸. Genetic heterogeneity that could contribute to the observed anatomical and functional differentiation along the proximal–distal axis in CA1 has been reported⁹. However, the mechanisms that control the exquisite wiring specificity remain unknown.

Since the proposal of the chemoaffinity hypothesis for establishing specific neuronal connections¹⁰, many cell surface and secreted proteins have been discovered that guide developing axons to target regions and recognize specific synaptic partners^{11,12}. Members of the teneurin family of type II transmembrane proteins exhibit matching expression in pre- and postsynaptic partners and instruct synaptic partner choice in the *Drosophila* olfactory and neuromuscular systems, probably through homophilic attraction^{13,14}. Teneurins are evolutionarily conserved, with four members in mammals¹⁵ that are dynamically expressed during brain development¹⁶. Human teneurins are risk loci in bipolar disorder^{17–20} and schizophrenia²¹, and are implicated in other neurological disorders^{22,23}. Teneurin-3 (Ten3) is required for proper dendrite morphogenesis and axon targeting in the vertebrate visual system^{24–27}. Although Ten3 has been hypothesized to function as a homophilic attractant, no cellular or molecular mechanisms have been demonstrated. Furthermore, conflicting evidence exists as to whether vertebrate teneurins interact *in trans* in a homophilic manner^{28–30}, and heterophilic *trans* interactions with the adhesion-type G-protein-coupled receptors latrophilins have been demonstrated^{30–32}. Here, we examine the role of Ten3 in the development of specific connections within the hippocampal region, and shed new light on its mechanism of action during mammalian neural development.

Ten3 expression in hippocampal regions

Using a custom antibody against a cytoplasmic epitope (Extended Data Fig. 1a), we found that Ten3 was expressed in highly specific regions of the postnatal brain. In particular, Ten3 was expressed in restricted domains of the developing hippocampal region (Fig. 1a), including proximal CA1, distal subiculum, and MEC. A second Ten3 antibody against an extracellular epitope recapitulated this staining pattern (Extended Data Fig. 1a, d). Staining with both antibodies was abolished in *Ten3* knockout mice (*Ten3*^{Δ4/Δ4})²⁴ (Extended Data Fig. 1b–e). Ten3 was most prominent in synaptic layers, including stratum lacunosum-moleculare of CA1 and the molecular layer of subiculum, consistent with Ten3 being present in the synaptic cleft³³. Ten3 was also present in axons, dendrites, and cell bodies (Extended Data Fig. 1f–i). *In situ* hybridization revealed that *Ten3* mRNA was expressed in all regions where Ten3 protein was observed (Fig. 1b and Extended Data Fig. 1j). In both CA1 and subiculum, *Ten3* mRNA showed a graded distribution along the proximal–distal axis, peaking in proximal CA1 and distal subiculum (Fig. 1c and Extended Data Fig. 2).

Remarkably, Ten3 protein and mRNA expression patterns corresponded to the known topography of multiple connections in the hippocampal region. MEC neurons send axons to proximal CA1 and distal subiculum^{34–36}, proximal CA1 neurons project to distal subiculum^{37,38} and MEC^{6,7}, and distal subicular neurons project to MEC^{6,39}. All of these regions highly expressed Ten3 protein and mRNA (Fig. 1a–c). By contrast, LEC neurons are interconnected with distal CA1 and proximal subiculum^{6,7,34–40}, all of which expressed low or no Ten3. To further examine the relationship between Ten3 expression and topographic projections, we injected an anterograde viral tracer into MEC, and found that MEC axons and Ten3 protein clearly overlapped in the molecular layers of proximal CA1 and distal subiculum (Fig. 1d). By contrast, LEC axons projected to distal CA1 and proximal subiculum, regions of low Ten3 expression (Fig. 1e).

In summary, Ten3 expression matches with topographic connectivity between entorhinal cortex, CA1, and subiculum (Fig. 1f). Ten3 protein and mRNA were also specifically expressed in subregions of the presubiculum, parasubiculum, medial mammillary nucleus, and anteroventral thalamic nucleus that are topographically connected

¹Howard Hughes Medical Institute, Stanford University, Stanford, California 94305, USA. ²Department of Biology, Stanford University, Stanford, California 94305, USA. ³Neurosciences Graduate Program, Stanford University, Stanford, California 94305, USA.

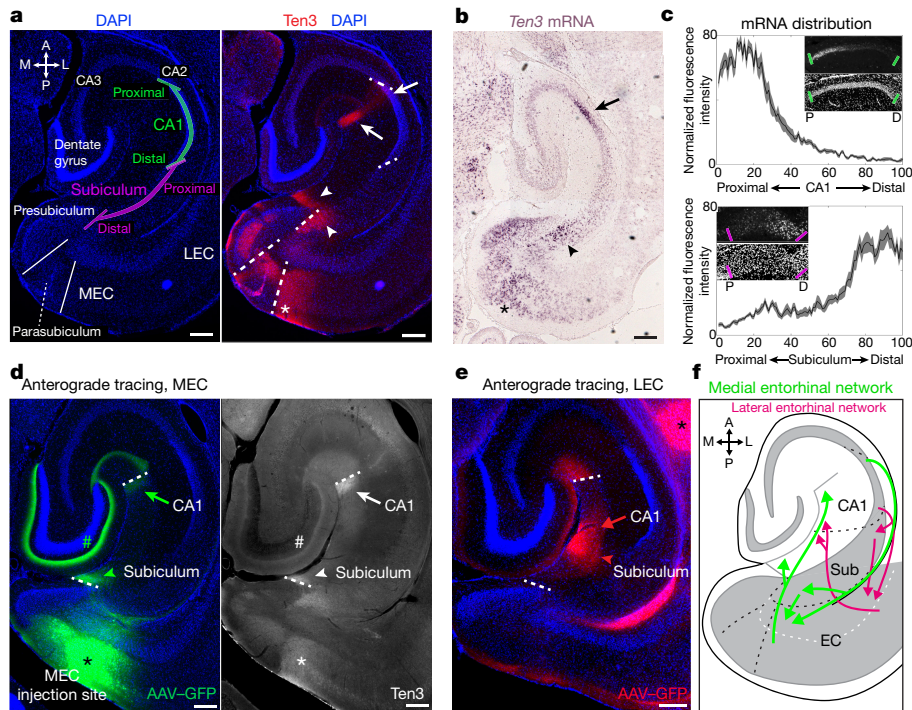


Figure 1 | *Ten3* expression in the developing hippocampal region.

a, Left: diagram of the hippocampal region on a horizontal section of P10 mouse brain. A, anterior; P, posterior; M, medial; L, lateral. Right: same section with *Ten3* immunostaining. **b**, *In situ* hybridization for *Ten3* mRNA on a P9 horizontal section. In **a** and **b**, arrows denote proximal CA1; arrowheads, distal subiculum; asterisk, MEC. **c**, Quantification of *Ten3* mRNA along the proximal–distal (P–D) axis of CA1 ($n = 12$ sections, four mice) and subiculum ($n = 14$ sections, four mice) of P10 horizontal sections. Insets: *Ten3* mRNA (top) and DAPI (4',6-diamidino-2-phenylindole) staining (bottom). The x axis represents bin along the proximal–distal axis of CA1 or subiculum. Shaded curves, mean \pm s.e.m.

with subiculum or entorhinal cortex (Extended Data Fig. 3). Given the function of *Drosophila* teneurins in synaptic partner matching^{13,14}, we hypothesized that *Ten3* may act as a homophilic attractant to control the development of these precise wiring patterns.

Ten3 knockout analysis

To test the function of *Ten3* in hippocampal circuit development, we focused on the projection from CA1 to subiculum, where proximal CA1 neurons (*Ten3*-high) send axons to distal subiculum (*Ten3*-high), and distal CA1 neurons (*Ten3*-low) project to proximal subiculum (*Ten3*-low) (Fig. 2a–c). We generated a *Ten3* knock-in *cre* allele (*Ten3*^{cre}, Extended Data Fig. 4a), which functioned as a protein null and allowed us to visualize neurons that normally express *Ten3* in a mutant background (Extended Data Fig. 4b–d). We injected the anterograde tracer *Phaseolus vulgaris* leucoagglutinin (PHA-L)⁴¹ into proximal CA1 of the dorsal hippocampus of *Ten3* heterozygous (*Ten3*^{cre/+}, hereafter *Ten3*^{Het}) and knockout (*Ten3*^{cre/ Δ 4}, hereafter *Ten3*^{KO}) mice, and analysed the distribution of labelled CA1 axons in subiculum (Fig. 2c–g). In *Ten3*^{Het} mice, proximal CA1-restricted injections labelled axons that arborized densely in distal subiculum, confirming the topography described in the rat^{37,38} (Fig. 2c). In *Ten3*^{KO} mice, however, similarly placed injections in proximal CA1 labelled axons that spread significantly more proximally in subiculum (Fig. 2d, e), with increased overall width (Fig. 2f) and a proximal shift in the mean position (Fig. 2g) of the projection. Middle and distal CA1 injections revealed that the overall topography of the CA1 \rightarrow subiculum projection was less sharp in *Ten3*^{KO} mice (Extended Data Fig. 5). Thus, *Ten3* is required for the precise projections of proximal CA1 axons to distal subiculum.

d, Labelling of MEC axons projecting to hippocampus in P70 brain after AAV1-CMV-GFP injection in MEC (asterisk) (left) and *Ten3* staining on the same section (right). GFP in layer III MEC axons overlaps with *Ten3* in proximal CA1 (arrows) and distal subiculum (arrowheads); GFP in layer II MEC axons also overlaps with *Ten3* in dentate gyrus (#). **e**, Labelling of LEC axons in P55 brain projecting to distal CA1 (arrow) and proximal subiculum (arrowhead). Asterisk identifies track to the more ventral injection site. **f**, Summary of topographic connections between MEC, proximal CA1, and distal subiculum (Sub) (green arrows), and between LEC, distal CA1, and proximal subiculum (red arrows). Scale bars, 200 μ m.

We next recorded excitatory postsynaptic currents (EPSCs) from proximal and distal subicular cells in hippocampal slices from *Ten3*^{+/+} (*Ten3*^{WT}) and *Ten3*^{KO} mice in response to electrical stimulation of the CA1 \rightarrow subiculum axon bundles (Fig. 2h). In *Ten3*^{WT} slices, stimulation reliably evoked EPSCs in proximal and distal subicular neurons (Fig. 2i). In *Ten3*^{KO} mice, evoked EPSC amplitudes in distal but not proximal subicular neurons were strongly reduced, consistent with the anatomical defect in *Ten3*^{KO} mice (Fig. 2i, j). The paired pulse ratio was unaffected in proximal subicular neurons but was increased in distal subicular knockout cells, indicating a lower baseline release probability in *Ten3* mutants (Fig. 2k). Given that, in knockout mice, some proximal CA1 axons still reached distal subiculum (Fig. 2d, e), the marked physiological changes suggest that *Ten3* may also be required for formation or function of the synapses between proximal CA1 and distal subicular neurons, consistent with the persistent expression of *Ten3* in adults (Fig. 1d) and the function of *Drosophila* teneurins in synapse formation^{14,42}.

CA1 conditional knockout analysis

To distinguish whether *Ten3* is required in CA1, subiculum, or both, for the CA1 \rightarrow subiculum projection, we generated a conditional *Ten3* allele (*Ten3*^f) that allowed us to delete *Ten3* in cells expressing Cre recombinase (Extended Data Fig. 6). Because the CA1 \rightarrow subiculum projection develops postnatally (Extended Data Fig. 7), we injected cre-expressing lentivirus into either CA1 or subiculum at postnatal day 0 (P0) to generate area-specific *Ten3* knockouts.

For CA1 conditional knockout, we injected a Cre-dependent anterograde tracer into proximal CA1 of adults to visualize axons only from Cre-expressing neurons (Fig. 3a). In *Ten3*^{WT} controls, proximal CA1

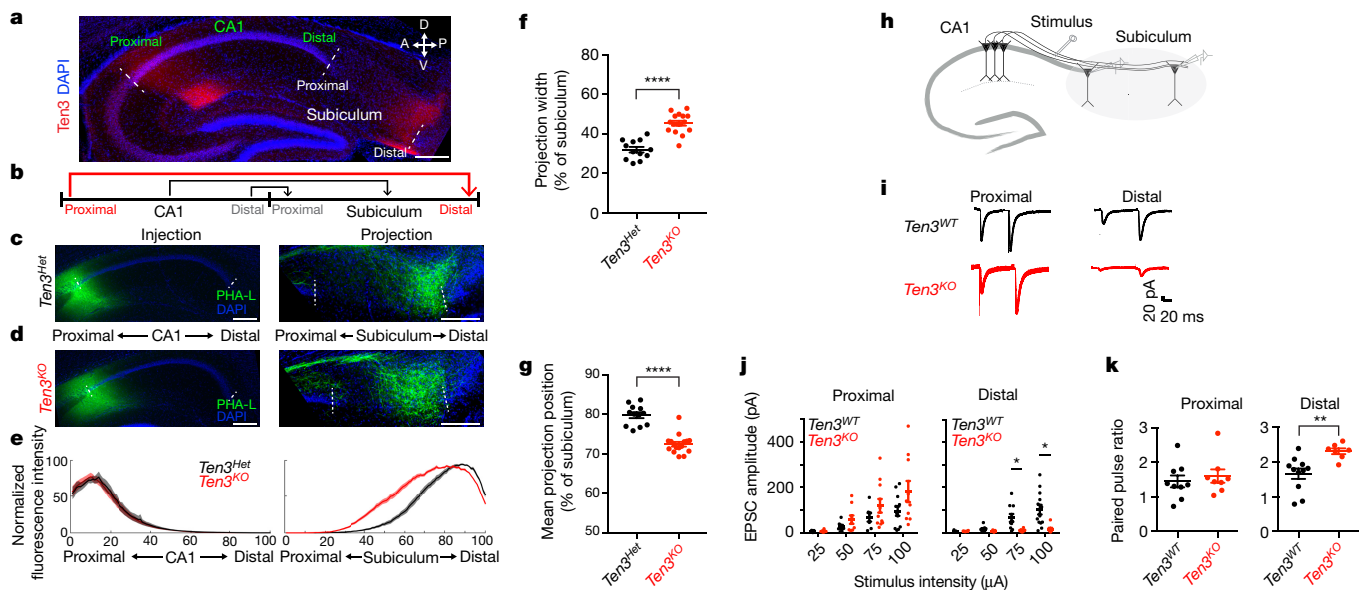


Figure 2 | Ten3 is required for the precise CA1→subiculum projection.

a, Sagittal section of P11 hippocampus, showing Ten3 expression in proximal CA1 and distal subiculum. A, anterior; P, posterior; D, dorsal; V, ventral. **b**, Diagram of the CA1→subiculum topographic projection, with Ten3-high regions and axons in red. **c, d**, PHA-L (green) injections in proximal CA1 and corresponding projections in subiculum of *Ten3*^{Het} (**c**) or *Ten3*^{KO} (**d**) mice. **e**, Averaged normalized fluorescence intensity traces for proximal injections in CA1 (left) and corresponding projections in subiculum (right) for *Ten3*^{Het} (black, *n* = 12 mice) and *Ten3*^{KO} (red, *n* = 16 mice). The *x* axis represents bin along the proximal–distal axis of CA1 or subiculum. Shaded curves represent mean \pm s.e.m. at each bin. **f, g**, Projection width-at-half-maximum (**f**) and mean position (**g**) for *Ten3*^{Het} and *Ten3*^{KO}. *****P* < 0.0001 (*Ten3*^{Het}, *n* = 12; *Ten3*^{KO}, *n* = 16;

two-tailed *t*-test). **h**, Diagram of stimulating electrode and recording sites. **i**, EPSC traces from proximal and distal subicular cells in *Ten3*^{WT} and *Ten3*^{KO} mice. **j**, Average EPSC amplitude in proximal (left) and distal (right) subicular cells from *Ten3*^{WT} and *Ten3*^{KO} mice at increasing stimulation intensities. Proximal: *Ten3*^{WT}, *n* = 12 cells; *Ten3*^{KO}, *n* = 11 cells; *P* > 0.05 for all stimulation intensities. Distal: *Ten3*^{WT}, *n* = 14 cells, 6 mice; *Ten3*^{KO}, *n* = 9 cells, 7 mice; 75 μ A stimulation, *P* = 0.035; 100 μ A stimulation, *P* = 0.022, adjusted *P* values from two-tailed *t*-tests with Holm–Šidák’s correction. **k**, Paired pulse ratio for proximal (left) and distal (right) subicular cells from *Ten3*^{WT} and *Ten3*^{KO} mice. (Proximal: *Ten3*^{WT}, *n* = 9 cells, 6 mice; *Ten3*^{KO}, *n* = 8 cells, 7 mice; *P* = 0.5566. Distal: *Ten3*^{WT}, *n* = 11 cells, 6 mice; *Ten3*^{KO}, *n* = 7 cells, 7 mice; *P* = 0.0049, two-tailed *t*-test.) Scale bars, 200 μ m. Error bars, mean \pm s.e.m.

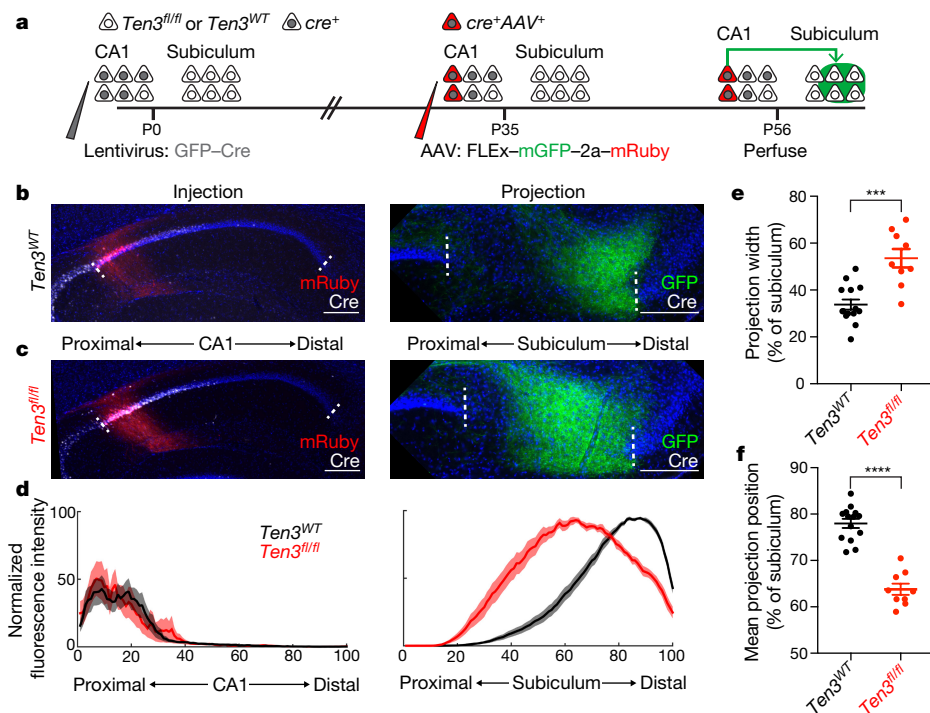


Figure 3 | Ten3 conditional knockout in CA1. **a**, Experimental scheme. **b, c**, Adeno-associated virus (AAV) injections in proximal CA1 (left) and corresponding projections in subiculum (right) of *Ten3*^{WT} (**b**) and *Ten3*^{fl/fl} (**c**) mice. Red, injections; green, projections; white, Cre staining. **d**, Average normalized fluorescence intensity traces for proximal CA1

injections (left) and corresponding subicular projections (right) for control (black, *n* = 14) and CA1 conditional knockout (red, *n* = 9) mice. **e, f**, Projection width-at-half-maximum (**e**) and mean position (**f**) for control and knockout mice. ****P* = 0.0001, *****P* < 0.0001, two-tailed *t*-tests. Scale bars, 200 μ m. Error bars, mean \pm s.e.m.

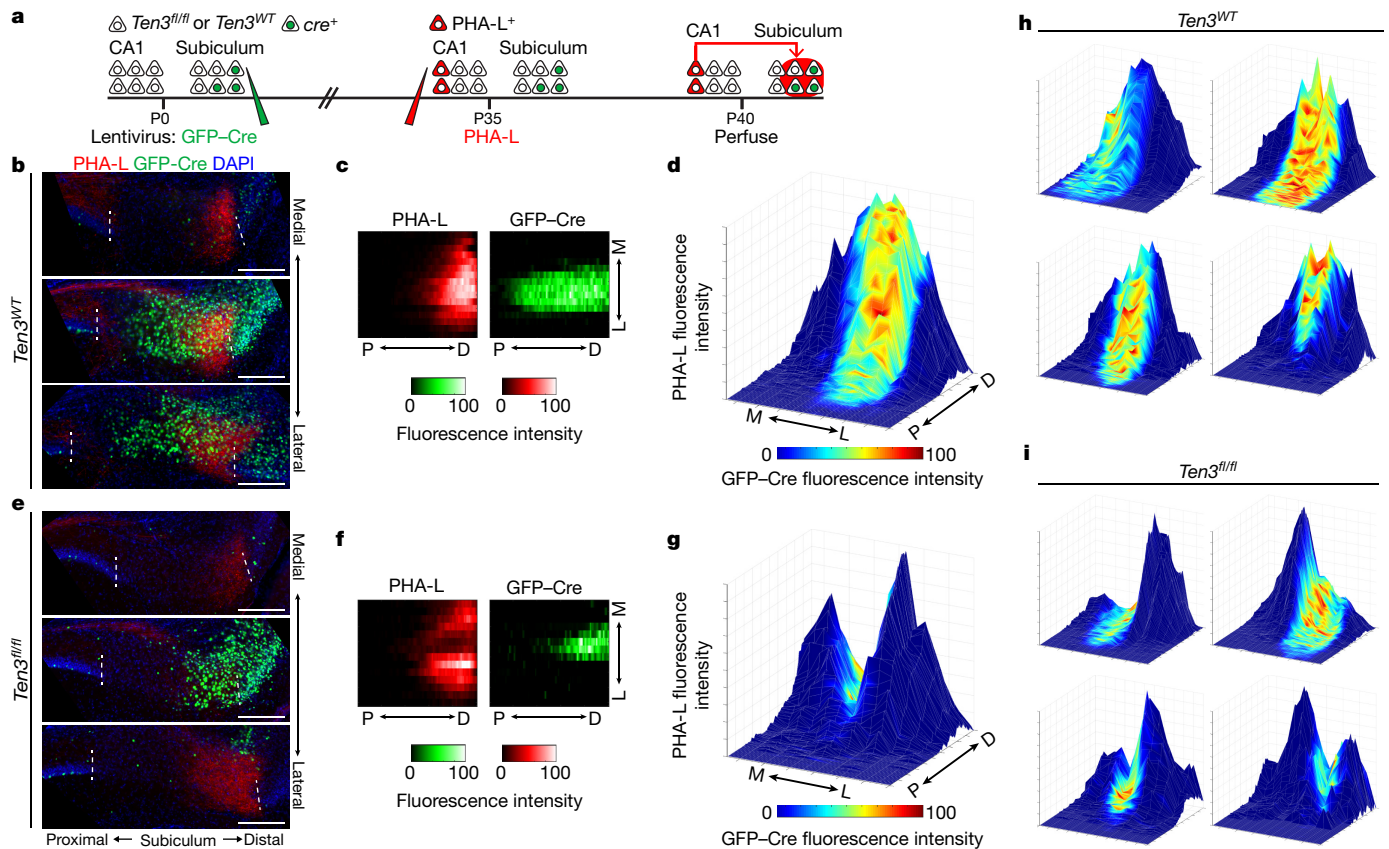


Figure 4 | *Ten3* conditional knockout in subiculum. **a**, Experimental scheme. **b**, **e**, Example images from *Ten3^{WT}* (**b**) and *Ten3^{fl/fl}* (**e**) mice, showing axons from proximal CA1 PHA-L injection in red, and GFP-Cre in subiculum in green. Three 60- μ m sections are arranged from medial to lateral, 480–600 μ m between sections. Scale bars, 200 μ m. **c**, **f**, Heatmaps showing normalized PHA-L fluorescence intensity

neurons sent axons to distal subiculum as expected (Fig. 3b, d). In *Ten3^{fl/fl}* mice, however, proximal CA1 axons covered most of subiculum, with their intensity peaking near the centre (Fig. 3c, d). The width of the projection was significantly increased in *Ten3^{fl/fl}*, and the mean position shifted proximally (Fig. 3d–f). Thus, *Ten3* is required in CA1 neurons for their precise axon targeting in subiculum.

Subiculum conditional knockout analysis

To test whether *Ten3* is also required in subicular cells for CA1 axon targeting, we injected *cre*-expressing lentivirus into subiculum at P0, the anterograde tracer PHA-L into proximal CA1 at P35, and analysed the position of CA1 axons in subiculum (Fig. 4a). Because Cre expression covered a small region of subiculum relative to the target field of labelled CA1 axons, we asked whether CA1 axons targeted differently within Cre-expressing regions versus nearby Cre-negative regions. In *Ten3^{WT}* controls, CA1 axons were unaffected when projecting into Cre-expressing subicular areas, as analysed in serial histological sections (Fig. 4b, c and Extended Data Fig. 8a, c). In *Ten3^{fl/fl}* mice, however, labelled CA1 axons appeared to avoid the patch of Cre-expressing, *Ten3*-deleted subicular cells (Fig. 4e, f and Extended Data Fig. 8b, d).

To visualize the relationship between the CA1→subiculum axon projections and GFP-Cre expression in the target, we plotted the intensities of CA1 axons and GFP-Cre on the same graph as height and colour, respectively. While Cre expression ('hot' coloured) did not affect the projection strength (height) in *Ten3^{WT}* controls (Fig. 4d, h and Extended Data Fig. 8c), the projection strength was severely diminished in Cre-expressing patches in *Ten3^{fl/fl}* mice (Fig. 4g, i and Extended Data Fig. 8d). Because we only made a focal deletion of *Ten3* in subiculum

(red, left) and normalized GFP-Cre intensity (green, right) in subiculum, same mice as **b** and **e**. Each row is one section, 120 μ m between rows. **d**, **g**, Surface plots showing normalized PHA-L intensity as height, and normalized GFP-Cre intensity as colour, same data as **b**, **c** and **e**, **f**, respectively. **h**, **i**, Surface plots from additional *Ten3^{WT}* (**h**) and *Ten3^{fl/fl}* (**i**) mice. See Extended Data Fig. 8 for all mice analysed.

with the lentivirus injection, there were many *Ten3*-expressing cells in nearby regions of distal subiculum. The simplest interpretation for this drastic phenotype is that *Ten3*-high proximal CA1 axons destined for the *Ten3*-deleted patch mistargeted to nearby *Ten3*-high distal regions, consistent with *Ten3* in distal subiculum acting as an attractant for proximal CA1 axons (Fig. 5f).

Ten3 promotes homophilic adhesion

If *Ten3* functions as a homophilic cell adhesion molecule as previously proposed^{28,29,43}, it could directly mediate the recognition of *Ten3*-expressing target cells by *Ten3*-expressing axons. *Ten3* has alternatively spliced isoforms that differ by the inclusion or exclusion of exon 12 and exon 20 (at splice sites A and B, hereafter) encoding 9- and 7-amino-acid peptides in the extracellular epidermal growth factor-like (EGF-like) and NCL-1, HT2A, and Lin-41 (NHL) repeats, respectively^{44,45} (Fig. 5a, b). We denote the splicing at site A as *A*₀ (exon 12 excluded) or *A*₁ (exon 12 included), and at site B as *B*₀ (exon 20 excluded) or *B*₁ (exon 20 included). We sequenced *Ten3* cDNA clones from CA1 or subiculum at P8, a time when the CA1→subiculum projection was still developing (Extended Data Fig. 7). We found two additional alternative splicing variants at site A (termed *A*₂ and *A*₃) that were computationally predicted⁴⁶; the inclusion of these exons (12.1 or 12.2) would add six or seven additional amino acids to exon-12-containing variants (Fig. 5a, b). Overall, CA1 and subiculum expressed similar splicing isoforms, most of which included inserts at sites A and B (Fig. 5c).

We next performed cell aggregation experiments, and found that all isoforms tested promoted homophilic adhesion except *A*₀*B*₀, which

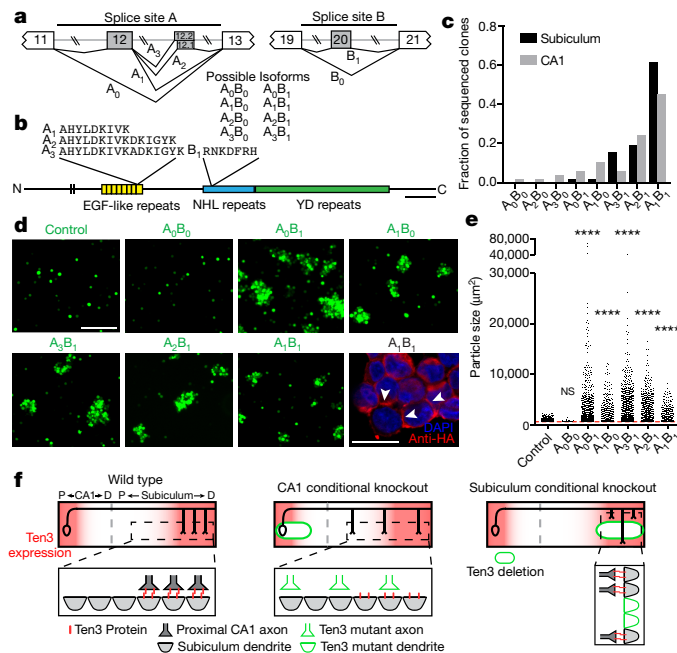


Figure 5 | *Ten3* promotes homophilic adhesion in a splicing isoform-dependent manner. **a**, Partial *Ten3* genomic regions (top) highlighting alternatively spliced exons (grey boxes) and constitutive exons (white boxes). Splice variant names are next to corresponding splicing pattern. **b**, Locations of alternative splicing sites A and B in *Ten3* protein, and amino acid sequences produced. YD, tyrosine and aspartate. Scale bar, 200 amino acids. **c**, Summary of cDNA sequencing from P8 subiculum ($n = 52$ clones) and CA1 ($n = 49$ clones). **d**, Aggregation of K562 cells expressing different *Ten3* isoforms and GFP. Scale bar, 200 μm . Bottom right: A_1B_1 aggregate stained for the N-terminal haemagglutinin (HA) tag (red). Arrowheads highlight membrane-localized *Ten3* at cell–cell junctions. Scale bar, 20 μm . **e**, Quantification of aggregate sizes pooled from three biological replicates. Dotted red line shows size cutoff at 600 μm^2 . NS, not significant; **** $P \leq 0.0001$, adjusted P values from Dunn's multiple comparisons test after Kruskal–Wallis test, comparing all conditions to GFP. GFP, $n = 1449$ particles above threshold; A_0B_0 , $n = 26$; A_0B_1 , $n = 1179$; A_1B_0 , $n = 411$; A_3B_1 , $n = 1268$; A_2B_1 , $n = 628$; A_1B_1 , $n = 336$. **f**, Summary of data (top) and working model (bottom). KO, knockout. See Discussion for details.

lacks all alternatively spliced exons (Fig. 5d, e). A_0B_0 was functionally expressed because it promoted adhesion with latrophilin-3-expressing cells (Extended Data Fig. 9), as previously reported for other teneurin and latrophilin family proteins³⁰. The A_0B_0 isoform occurred in only one out of 101 sequenced clones, indicating that most *Ten3* isoforms present in CA1 and subiculum were capable of interacting in *trans* to promote homophilic adhesion. When the three highest-expressed isoforms of *Ten3* were tested in a mixed cell aggregation assay, all aggregates were mixed, indicating that the major *Ten3* isoforms expressed in the hippocampus can interact with each other in *trans* (Extended Data Fig. 10). Together with the matching expression and conditional knockout phenotypes, these data suggest that homophilic *Ten3* interactions between CA1 axons and subicular cell bodies and dendrites control the targeting specificity of proximal CA1 axons to distal subiculum.

Discussion

A striking feature of neural development is the formation of highly precise connections between neurons. Sensory and motor circuits have been extensively used to characterize the molecular control of wiring specificity^{11,12,47,48}, but relatively little is known about how neurons in complex high-order circuits find appropriate partners. Here, we have shown that *Ten3* acts in both pre- and postsynaptic neurons

in the hippocampus to control the assembly of a precise topographic projection. Loss-of-function phenotypes support a homophilic attraction mechanism: when *Ten3* is lost from CA1 neurons, proximal CA1 axons spread throughout the entire subiculum, instead of projecting only to distal, *Ten3*-high targets; when *Ten3* is lost from a subset of distal subicular cells, *Ten3*-high proximal CA1 axons do not target these areas and instead innervate nearby *Ten3*-high regions (Fig. 5f). Our *in vitro* data further show that *Ten3* can interact homophilically in *trans*, supporting a model in which *Ten3* on CA1 axons interacts with *Ten3* on subicular targets, leading to contact-mediated attraction or stabilization of proximal CA1 axons by distal subicular target cells. This mechanism of action resembles that of the *Drosophila* teneurins in the development of olfactory and neuromuscular connections, suggesting an evolutionarily conserved mode of teneurin function in neural circuit assembly from insects to mammals. However, whereas *Drosophila* teneurins instruct matching of discrete types of pre- and postsynaptic cell, the graded expression in both CA1 and subiculum suggests that mouse *Ten3* directs continuous topographic mapping along the proximal–distal axis (Fig. 5f).

Our model does not exclude the possibility that interactions of *Ten3* with heterophilic partners have additional roles in circuit assembly. While in many cases we observed *Ten3* expression in both pre- and postsynaptic partners of specific connections, there were also cases where *Ten3* was only observed in axons but not targets (for example, MEC→dentate gyrus–CA3). Further, the A_0B_0 isoform did not exhibit homophilic interactions but did interact heterophilically with latrophilin-3. These observations suggest that interactions between *Ten3* and latrophilins or other potential heterophilic partners may also contribute to wiring specificity.

Our results highlight small regions of *Ten3* that are critical for *trans* interactions. Splice site A corresponds to the most C-terminal of the eight EGF-like repeats, which are thought to mediate *cis*-dimerization of teneurin proteins^{44,49}. Our results suggest that the EGF-like repeats may also participate in *trans* interactions, or that teneurin *cis* interactions may influence *trans* interactions. Splice site B is within the NHL-repeat region, which was implicated in homophilic teneurin interactions using single-cell force spectroscopy²⁹. Our result supports the importance of the NHL repeats, and identifies specific residues that are required for homophilic interactions.

What controls the distal CA1→proximal subiculum projection? Since none of the other three mouse teneurins exhibited differential expression along the proximal–distal axis of the hippocampal formation¹⁶, other differentially expressed proteins might act in parallel with *Ten3* to control the distal CA1→proximal subiculum projection. Axon–axon competition could also contribute, as in retinotopic map development⁵⁰. Indeed, the enhanced severity of the CA1-specific conditional knockout phenotype compared with the whole-animal *Ten3*^{KO} phenotype (Fig. 3d–f versus Fig. 2e–g) may result from *Ten3*-expressing CA1 axons out-competing mutant axons for space in distal subiculum, supporting a role of axon–axon competition in determining CA1→subiculum targeting specificity.

Finally, our findings reveal genetic heterogeneity within many areas of the hippocampal region. Although our genetic analyses focused on the CA1→subiculum projection, *Ten3*-high to *Ten3*-high connectivity was also observed in the entorhinal→hippocampal projections (Fig. 1d–f), and probably exists in additional hippocampus-associated projections (Extended Data Fig. 3). The matching expression of *Ten3* in multiple topographically connected subregions, combined with our loss-of-function and *in vitro* data, suggests that *Ten3* may control the assembly of a widely distributed circuit in mammalian brains.

Online Content Methods, along with any additional Extended Data display items and Source Data, are available in the online version of the paper; references unique to these sections appear only in the online paper.

Received 17 June; accepted 19 December 2017.

Published online 7 February 2018.

1. Scoville, W. B. & Milner, B. Loss of recent memory after bilateral hippocampal lesions. *J. Neurol. Neurosurg. Psychiatry* **20**, 11–21 (1957).
2. Squire, L. R., Stark, C. E. L. & Clark, R. E. The medial temporal lobe. *Annu. Rev. Neurosci.* **27**, 279–306 (2004).
3. O'Keefe, J. & Dostrovsky, J. The hippocampus as a spatial map. Preliminary evidence from unit activity in the freely-moving rat. *Brain Res.* **34**, 171–175 (1971).
4. Hafting, T., Fyhn, M., Molden, S., Moser, M. B. & Moser, E. I. Microstructure of a spatial map in the entorhinal cortex. *Nature* **436**, 801–806 (2005).
5. van Strien, N. M., Cappaert, N. L. M. & Witter, M. P. The anatomy of memory: an interactive overview of the parahippocampal–hippocampal network. *Nat. Rev. Neurosci.* **10**, 272–282 (2009).
6. Tamamaki, N. & Nojyo, Y. Preservation of topography in the connections between the subiculum, field CA1, and the entorhinal cortex in rats. *J. Comp. Neurol.* **353**, 379–390 (1995).
7. Naber, P. A., Lopes da Silva, F. H. & Witter, M. P. Reciprocal connections between the entorhinal cortex and hippocampal fields CA1 and the subiculum are in register with the projections from CA1 to the subiculum. *Hippocampus* **11**, 99–104 (2001).
8. Igarashi, K. M., Ito, H. T., Moser, E. I. & Moser, M. B. Functional diversity along the transverse axis of hippocampal area CA1. *FEBS Lett.* **588**, 2470–2476 (2014).
9. Cembrowski, M. S. *et al.* Spatial gene-expression gradients underlie prominent heterogeneity of CA1 pyramidal neurons. *Neuron* **89**, 351–368 (2016).
10. Sperry, R. W. Chemoaffinity in the orderly growth of nerve fiber patterns and connections. *Proc. Natl Acad. Sci. USA* **50**, 703–710 (1963).
11. Sanes, J. R. & Yamagata, M. Many paths to synaptic specificity. *Annu. Rev. Cell Dev. Biol.* **25**, 161–195 (2009).
12. Kolodkin, A. L. & Tessier-Lavigne, M. Mechanisms and molecules of neuronal wiring: a primer. *Cold Spring Harb. Perspect. Biol.* **3**, 1–14 (2011).
13. Hong, W., Mosca, T. J. & Luo, L. Teneurins instruct synaptic partner matching in an olfactory map. *Nature* **484**, 201–207 (2012).
14. Mosca, T. J., Hong, W., Dani, V. S., Favaloro, V. & Luo, L. Trans-synaptic Teneurin signalling in neuromuscular synapse organization and target choice. *Nature* **484**, 237–241 (2012).
15. Tucker, R. P., Beckmann, J., Leachman, N. T., Schöler, J. & Chiquet-Ehrismann, R. Phylogenetic analysis of the teneurins: conserved features and premetazoan ancestry. *Mol. Biol. Evol.* **29**, 1019–1029 (2012).
16. Li, H., Bishop, K. M. & O'Leary, D. D. M. Potential target genes of EMX2 include *odt/Ten-m* and other gene families with implications for cortical patterning. *Mol. Cell. Neurosci.* **33**, 136–149 (2006).
17. Psychiatric GWAS Consortium Bipolar Disorder Working Group. Large-scale genome-wide association analysis of bipolar disorder identifies a new susceptibility locus near *ODZ4*. *Nat. Genet.* **43**, 977–983 (2011).
18. Green, E. K. *et al.* Replication of bipolar disorder susceptibility alleles and identification of two novel genome-wide significant associations in a new bipolar disorder case-control sample. *Mol. Psychiatry* **18**, 1302–1307 (2013).
19. Mühleisen, T. W. *et al.* Genome-wide association study reveals two new risk loci for bipolar disorder. *Nat. Commun.* **5**, 3339 (2014).
20. Croarkin, P. E. *et al.* Genetic risk score analysis in early-onset bipolar disorder. *J. Clin. Psychiatry* **78**, 1337–1343 (2017).
21. Ivorra, J. L. *et al.* Replication of previous genome-wide association studies of psychiatric diseases in a large schizophrenia case-control sample from Spain. *Schizophr. Res.* **159**, 107–113 (2014).
22. Aldahmesh, M. A., Mohammed, J. Y., Al-Hazaa, S. & Alkuraya, F. S. Homozygous null mutation in *ODZ3* causes microphthalmia in humans. *Genet. Med.* **14**, 900–904 (2012).
23. Alkelai, A. *et al.* A role for *TENM1* mutations in congenital general anosmia. *Clin. Genet.* **90**, 211–219 (2016).
24. Leamey, C. A. *et al.* *Ten-m3* regulates eye-specific patterning in the mammalian visual pathway and is required for binocular vision. *PLoS Biol.* **5**, e241 (2007).
25. Dharmaratne, N. *et al.* *Ten-m3* is required for the development of topography in the ipsilateral retinocollicular pathway. *PLoS ONE* **7**, e43083 (2012).
26. Antinucci, P., Nikolaou, N., Meyer, M. P. & Hindges, R. Teneurin-3 specifies morphological and functional connectivity of retinal ganglion cells in the vertebrate visual system. *Cell Reports* **5**, 582–592 (2013).
27. Antinucci, P., Suleyman, O., Monfries, C. & Hindges, R. Neural mechanisms generating orientation selectivity in the retina. *Curr. Biol.* **26**, 1802–1815 (2016).
28. Rubin, B. P., Tucker, R. P., Brown-Luedi, M., Martin, D. & Chiquet-Ehrismann, R. Teneurin 2 is expressed by the neurons of the thalamofugal visual system in situ and promotes homophilic cell-cell adhesion in vitro. *Development* **129**, 4697–4705 (2002).
29. Beckmann, J., Schubert, R., Chiquet-Ehrismann, R. & Müller, D. J. Deciphering teneurin domains that facilitate cellular recognition, cell-cell adhesion, and neurite outgrowth using atomic force microscopy-based single-cell force spectroscopy. *Nano Lett.* **13**, 2937–2946 (2013).
30. Boucard, A. A., Maxeiner, S. & Südhof, T. C. Latrophilins function as heterophilic cell-adhesion molecules by binding to teneurins: regulation by alternative splicing. *J. Biol. Chem.* **289**, 387–402 (2014).
31. Silva, J.-P. *et al.* Latrophilin 1 and its endogenous ligand Lasso/teneurin-2 form a high-affinity transsynaptic receptor pair with signaling capabilities. *Proc. Natl Acad. Sci. USA* **108**, 12113–12118 (2011).
32. O'Sullivan, M. L. *et al.* FLRT proteins are endogenous latrophilin ligands and regulate excitatory synapse development. *Neuron* **73**, 903–910 (2012).
33. Loh, K. H. *et al.* Proteomic analysis of unbound cellular compartments: synaptic clefts. *Cell* **166**, 1295–1307 (2016).
34. Steward, O. Topographic organization of the projections from the entorhinal area to the hippocampal formation of the rat. *J. Comp. Neurol.* **167**, 285–314 (1976).
35. van Groen, T., Miettinen, P. & Kadish, I. The entorhinal cortex of the mouse: organization of the projection to the hippocampal formation. *Hippocampus* **13**, 133–149 (2003).
36. Muraoka, D., Katsuyama, Y., Kikkawa, S. & Terashima, T. Postnatal development of entorhinodentate projection of the Reeler mutant mouse. *Dev. Neurosci.* **29**, 59–72 (2007).
37. Tamamaki, N. & Nojyo, Y. Disposition of the slab-like modules formed by axon branches originating from single CA1 pyramidal neurons in the rat hippocampus. *J. Comp. Neurol.* **291**, 509–519 (1990).
38. Amaral, D. G., Dolorfo, C. & Alvarez-Royo, P. Organization of CA1 projections to the subiculum: a PHA-L analysis in the rat. *Hippocampus* **1**, 415–435 (1991).
39. Honda, Y. & Ishizuka, N. Topographic distribution of cortical projection cells in the rat subiculum. *Neurosci. Res.* **92**, 1–20 (2015).
40. Witter, M. P. & Groenewegen, H. J. The subiculum: cytoarchitectonically a simple structure, but hodologically complex. *Prog. Brain Res.* **83**, 47–58 (1990).
41. Gerfen, C. R. & Sawchenko, P. E. An anterograde neuroanatomical tracing method that shows the detailed morphology of neurons, their axons and terminals: immunohistochemical localization of an axonally transported plant lectin, *Phaseolus vulgaris* leucoagglutinin (PHA-L). *Brain Res.* **290**, 219–238 (1984).
42. Mosca, T. J. & Luo, L. Synaptic organization of the *Drosophila* antennal lobe and its regulation by the Teneurins. *eLife* **3**, e03726 (2014).
43. Leamey, C. A. *et al.* Differential gene expression between sensory neocortical areas: potential roles for *Ten-m3* and *Bcl6* in patterning visual and somatosensory pathways. *Cereb. Cortex* **18**, 53–66 (2008).
44. Ohashi, T. *et al.* Mouse *Ten-m/Odz* is a new family of dimeric type II transmembrane proteins expressed in many tissues. *J. Cell Biol.* **145**, 563–577 (1999).
45. Ben-Zur, T., Feige, E., Motro, B. & Wides, R. The mammalian *Odz* gene family: homologs of a *Drosophila* pair-rule gene with expression implying distinct yet overlapping developmental roles. *Dev. Biol.* **217**, 107–120 (2000).
46. O'Leary, N. A. *et al.* Reference sequence (RefSeq) database at NCBI: current status, taxonomic expansion, and functional annotation. *Nucleic Acids Res.* **44** (D1), D733–D745 (2016).
47. Luo, L. & Flanagan, J. G. Development of continuous and discrete neural maps. *Neuron* **56**, 284–300 (2007).
48. Bonanomi, D. & Pfaff, S. L. Motor axon pathfinding. *Cold Spring Harb. Perspect. Biol.* **2**, a001735 (2010).
49. Feng, K. *et al.* All four members of the *Ten-m/Odz* family of transmembrane proteins form dimers. *J. Biol. Chem.* **277**, 26128–26135 (2002).
50. Triplett, J. W. *et al.* Competition is a driving force in topographic mapping. *Proc. Natl Acad. Sci. USA* **108**, 19060–19065 (2011).

Supplementary Information is available in the online version of the paper.

Acknowledgements We thank C. Guo and the Howard Hughes Medical Institute/Janelia Research Campus for producing the *Ten3^{cre}* and *Ten3^{fl}* alleles, M. Sur for providing the *Ten3^{Δ4}* allele, the Neuroscience Gene Vector and Virus Core at Stanford for producing viruses, K. DeLoach for technical assistance, T. Mosca and W. Hong for advice and inspiration, members of the Luo laboratory for discussion and support, P. Thomas for the dual transcription unit vector, T. Südhof for advice and the latrophilin-3 construct, and K. Shen, L. Giocomo, T. Mosca, H. Li, J. Li, J. Lui, E. Richman and A. Shuster for critiques of the manuscript. D.S.B. was supported by a National Institute on Deafness and Other Communication Disorders predoctoral fellowship (F31DC013240), L.A.D. was supported by an National Institute of Neurological Disorders and Stroke postdoctoral fellowship (F32NS087860) and L.L. is an investigator of Howard Hughes Medical Institute. This work was supported by a National Institutes of Health grant (R01-NS050580 to L.L.).

Author Contributions D.S.B. performed all the experiments and analysed the data except the electrophysiology experiments. L.A.D. performed the electrophysiology experiments and analysed the data. D.T.P. assisted in aggregation assays. L.L. supervised the project. D.S.B. and L.L. wrote the paper.

Author Information Reprints and permissions information is available at www.nature.com/reprints. The authors declare no competing financial interests. Readers are welcome to comment on the online version of the paper. Publisher's note: Springer Nature remains neutral with regard to jurisdictional claims in published maps and institutional affiliations. Correspondence and requests for materials should be addressed to L.L. (lluo@stanford.edu).

Reviewer Information *Nature* thanks M. Witter and the other anonymous reviewer(s) for their contribution to the peer review of this work.

METHODS

Statistics and reproducibility. All statistical analyses were performed in Prism 7 (GraphPad). No statistical methods were used to determine sample size. The experiments were not randomized. Experimenters were blind to genotype during injections and analysis of axon tracing, but not for electrophysiology or other experiments. Images of Ten3 immunostaining and *in situ* hybridization (Figs 1a, b and 2a and Extended Data Figs 1b–j, 3a–g, 4b–d and 6b–d) are representative of at least three separate experiments in all cases. Images of entorhinal cortex axon tracing (Fig. 1d, e) are representative of three injections. For developmental tracing, images shown are representative of three (P2 and P4) or two (P6 and P8) experiments. For subiculum conditional knockout (Fig. 4 and Extended Data Fig. 8), results from all experiments are shown in Extended Data Fig. 8.

Mice. All animal procedures followed animal care guidelines approved by Stanford University's Administrative Panel on Laboratory Animal Care. Both male and female mice were used, and mice were group housed. CD-1 mice from Charles River Laboratories were used for all wild-type expression studies. *Ten3*^{Cre} mice²⁴ were provided by M. Sur and maintained on a CD-1 background. *Ten3*^{Cre} and *Ten3*^{fl} were maintained on mixed CD-1, C57BL/6, and 129 backgrounds. *Ten3*^{Cre} mice used in this study still had the neomycin resistance cassette (Neo) in the genome. *Ten3*^{fl} mice were crossed to a germline-active GFP-FlpO line⁵¹ to delete the Neo. Both Neo-deleted and Neo-containing *Ten3*^{fl} mice were used for Figs 3 and 4.

Generation of *Ten3*^{Cre} and *Ten3*^{fl} mice. Mice were generated by the Gene Targeting and Transgenics core at Janelia Research Campus. *Ten3*^{Cre} was generated by homologous recombination in embryonic stem cells using standard procedures. *Ten3*^{fl} was generated by co-injection of the targeting construct with *Cas9* mRNA and guide RNAs targeted just outside the *loxP* sites. Target sequences for gRNAs were GGGTGTCTAGAAAGTCAGTG AGG and AAAGTCCTTCATGGGCT TGC AGG. Targeting was verified in embryonic stem cells by long-arm PCR. After microinjection, chimaeras were bred with CD-1 females and F₁ offspring were screened by long-arm PCR and Southern blot to identify mice with germline transmission of the correctly targeted construct.

Generation and affinity purification of Ten3 antibodies. Rabbit polyclonal antibodies (produced by YenZym Antibodies) were raised to the following peptides: Ten3IC (used in main figures), amino acids 163–176 (C)ENRSDSESEQPSNN; Ten3EC, amino acids 346–364 (C)DTFENGKVNSDTVPTNTVS. Affinity purification from serum was performed using target peptides immobilized on SulfoLink columns (Thermo Fisher, 44999). Peptides were coupled to columns following the manufacturer's instructions. After blocking and washing, 2 ml antiserum mixed with 2 ml PBS, pH 7.4, was added to the column, and left on a nutator overnight at 4°C. The next day, columns were washed with 40 ml PBS pH 7.4, 40 ml PBS pH 7.4 + 0.5 M NaCl, and 40 ml PBS pH 7.4, all by gravity flow. Columns were eluted with 20 ml 100 mM glycine pH 2.5. Fractions (1 ml) were collected into tubes containing 60 µl 1 M Tris-HCl pH 8.8 for neutralization. All washes and elutions were performed at room temperature. Antibody concentration was measured using A_{280 nm} on a NanoDrop 1000, immunoglobulin-G setting. Fractions containing protein were combined and dialysed against PBS, pH 7.4, using Slide-a-lyzer cassettes (Thermo Fisher, 66380). Antibody concentration was measured again using A_{280 nm}, and BSA (Thermo Fisher, 15561020) was added to raise total protein concentration to 1 mg ml⁻¹. Aliquots were snap frozen in liquid nitrogen and stored at -80°C.

Immunostaining. Mice were given an overdose of 2.5% Avertin and were perfused transcardially with PBS followed by 4% paraformaldehyde (by weight) in PBS. For Ten3 immunostaining, brains were dissected, post-fixed in 4% paraformaldehyde for 1 h, and cryoprotected for 24–48 h in 30% sucrose. For all other immunostaining, brains were dissected, post-fixed in 4% paraformaldehyde for 12–24 h, and placed in 30% sucrose for 24–48 h. They were then embedded in Optimum Cutting Temperature (OCT, Tissue-Tek) on dry ice and stored at -80°C until sectioning. Floating sections (60 µm) were collected into PBS. Sections were incubated in the following solutions at room temperature unless otherwise indicated: 1 × 5–10 min in PBS, 1 h in 0.3% PBS/Triton X-100 (PBST) and 10% normal donkey serum (NDS), two to four nights in primary antibody at 4°C in 5% NDS in PBST, 2 × 15 min in PBST, 2 h in secondary antibody in 5% NDS in PBST, 2 × 15 min in PBST, 30 min in DAPI (1:10,000 of 5 mg ml⁻¹, Sigma-Aldrich) in PBS, and 5–10 min in PBS. Sections were mounted on Superfrost Plus slides and coverslipped with Fluoromount-G (SouthernBiotech). For adult Ten3 staining, tissue was fixed overnight. Antigen retrieval on sections was performed in 10 mM sodium citrate, pH 8.5, at 80°C for 30 min. Tissue was allowed to cool, washed three times with PBS, then blocked and immunostained as above. Primary antibodies used were rabbit anti-Ten3IC (1:1,000, four nights in primary antibody); rabbit anti-Ten3EC (1:200, four nights in primary antibody), mouse anti-Cre (1:1,000, Millipore, MAB3120), rabbit anti-PHA-L (1:1,000, Vector Labs, AS-2300, two nights in primary), chicken anti-GFP (1:2,500, Aves Labs, GFP-1020), and

rat anti-mCherry (1:1,000, Thermo Fisher, M11217). Secondary antibodies conjugated to Alexa 488, Alexa 647, or Cy3 (Jackson ImmunoResearch) were used at 1:500 from 50% glycerol stocks. For Biotinylated Dextran Amine (BDA) axon tracing, sections were washed for 5 min in PBS, incubated in PBST for 30 min, 1:200 streptavidin-Cy3 in PBST overnight, washed 3 × 15 min in PBST, and stained with DAPI and mounted as described above. Sections were imaged on Zeiss epifluorescence and 780 confocal microscopes and on a Leica Ariol automated fluorescence slide scanning system. Images were processed in FIJI to stitch multiple fields-of-view of single sections and to adjust contrast and brightness of each channel. Images presented together were processed identically.

In situ hybridization. *In situ* hybridization was performed as previously described⁵² with the following modifications. Cryosections (12–16 µm) were collected on Superfrost Plus slides. *Ten3* probe containing base pairs 4124–4953 of *Ten3* mRNA (located in exon 23; mRNA accession number NM_011857.3) was PCR amplified from genomic DNA using the following primers: 5'-GTGGCTAAAAGCCCACTGTTGCC-3', 5'-GAATGGCC CACTGACCTCGCG-3'. PCR product was cloned into pCR4-TOPO (K457502). RNA probes were transcribed using T3 or T7 RNA polymerases. For colorimetric development (Fig. 1d), Sigma-FAST NBT/BCIP (Sigma, B5655) was used. For combined *in situ* hybridization with immunostaining (Extended Data Fig. 1j) hybridized slides were incubated overnight with alkaline phosphatase-conjugated anti-DIG antibody (1:1,000, Roche Applied Science, 1093274) and rabbit anti-PCP4 (1:200, Sigma, HPA005792). Signals were developed using Fast Red TR/ Naphthol As-MX (Sigma-Aldrich, F4523) and 488 donkey anti-rabbit secondary (1:200, Jackson ImmunoResearch). Sections were imaged on Zeiss epifluorescence and 780 confocal microscopes. For fluorescent *in situ* hybridization for quantification, 12 µm sections of P10 brain were used. Sagittal sections were taken from dorsal hippocampus, and horizontal sections were from middle levels of the dorsal-ventral axis. After hybridization, washing, and blocking, slides were incubated with alkaline phosphatase-conjugated anti-DIG antibody (1:1,000) for 1 h and developed with Fast Red TR/Naphthol As-MX for 45 min. Sections were imaged at 10× magnification on a Zeiss epifluorescence scope. Fluorescence intensity measurements were taken on unprocessed images in FIJI and data were processed using custom MATLAB scripts. For CA1 quantifications, a 45-pixel-wide segmented line with spline fit was drawn along CA1, from proximal to distal. Intensity values along the CA1 line were measured using the Plot Profile command. For quantification of subiculum, a 125-pixel-wide segmented line with spline fit was drawn along subiculum, from proximal to distal. The bottom of the line was aligned to the superficial border of the subicular pyramidal cell layer; the proximal border of subiculum was defined in the same way as the distal border of CA1: that is, the point where the compact CA1 cell body layer ended. The distal subiculum border was defined by the increase in cell density of presubiculum layer 2. Because of the narrowing of the distal subicular cell layer, the line was drawn until the *Ten3* fluorescent signal became narrower than the 125-pixel line, to avoid averaging areas with zero signal. This resulted in the exclusion of a small portion of the *Ten3* signal in the most distal subiculum. Identical background subtraction was performed on all intensity traces, on the basis of the signal in sense control slides. The intensity traces were binned into 100 bins from proximal to distal, and the traces for individual sections were normalized to a peak of 100. Traces for individual sections were then averaged to produce intensity plots. Numbers of sections were as follows: sagittal and horizontal CA1, 12 sections, 4 mice; sagittal and horizontal subiculum, 14 sections, 4 mice.

Electrophysiology. At P14–P19, the brain was removed and placed in ice-cold carbonated slicing artificial cerebrospinal fluid that contained (in mM) 83 NaCl, 2.5 KCl, 1 NaH₂PO₄, 26.2 NaHCO₃, 22 glucose, 72 sucrose, 0.5 CaCl₂, and 3.3 MgSO₄. Coronal sections (300 µm) were cut on a Leica vibratome. Slices were allowed to recover at 31°C for 40 min and then at 23–25°C for 30 min to 6 h. Slices were then placed in carbonated recording artificial cerebrospinal fluid (119 NaCl, 2.5 KCl, 26 NaHCO₃, 1 NaH₂PO₄, 1.5 MgSO₄, 2.5 CaCl₂, and 11 glucose, all in mM) that contained 50 µM picrotoxin (Sigma). Signals were recorded with a 5× gain, low-pass filtered at 2 kHz, digitized at 10 kHz (Molecular Devices Multiclamp 700B), and analysed with pClamp 10 (Molecular Devices). Whole-cell recordings were made using 3–5 MΩ pipettes filled with an internal solution that contained (in mM) 123 caesium gluconate, 8 NaCl, 1 CaCl₂, 10 EGTA, 10 HEPES, and 10 glucose, pH 7.3, with CsOH, 280–290 mOsm. Series resistance (*R_s*) and input resistance (*R_{in}*) were monitored throughout the experiment by measuring the capacitive transient and steady-state deflection, respectively, in response to a -5 mV test pulse. *R_s* and *R_{in}* did not differ across experimental conditions (proximal subiculum recordings: *R_s* wild type = 4.397 ± 0.157 MΩ, *n* = 12; Ten3 knockout = 4.865 ± 0.417 MΩ, *n* = 11; *P* = 0.289, Student's *t*-test; *R_{in}* in wild type = 201.6 ± 18.7 MΩ, *n* = 12; Ten3 knockout = 253.1 ± 28.64 MΩ, *n* = 11; *P* = 0.141, Student's *t*-test; distal subiculum recordings: *R_s* wild type = 4.409 ± 0.114 MΩ, *n* = 14; Ten3

knockout = $4.561 \pm 0.213 \text{ M}\Omega$, $n = 9$; $P = 0.502$, Student's t -test; R_{in} wild type = $221.8 \pm 29.57 \text{ M}\Omega$, $n = 14$; Ten3 knockout = $254.6 \pm 34.83 \text{ M}\Omega$, $n = 9$; $P = 0.486$, Student's t -test). Responses were evoked by a platinum two-contact cluster electrode (FHC) placed in the stratum oriens–alveus above distal CA1, at the stimulation intensities listed in the figure. Cells were clamped at -60 mV to measure GluA (AMPA-receptor)-mediated EPSC. Analysis was based on the average of ten sweeps. The inter-stimulus interval for paired pulse ratio measurements was 50 ms.

Stereotactic surgery. For stereotactic injections in neonatal mice, hypothermia was used for anaesthesia. Coordinates were zeroed from lambda. For CA1, coordinates used were 1 mm lateral, 1.1 mm anterior, 0.85 mm ventral from skull. For subiculum, coordinates were 1.1 mm lateral, 0.3 mm anterior, 0.8 mm ventral from skull. For developmental axon tracing, BDA (Thermo Fisher D1956, 5% in PBS) was iontophoretically injected into CA1 using a Digital Midgard Precision Current Source (Stoelting, 51595), pulled glass micropipettes (World Precision Instruments, 1B120F4) with tips broken to outer diameter of $10 \mu\text{m}$, and current parameters $5 \mu\text{A}$, alternating 7-s on, 7-s off, for 2 min. Mice were perfused between 2 and 8 days post-injection for histology as above. For conditional knockout experiments, 100 nl of lentivirus containing *Ub-GFP-cre* (4.6×10^8 to 6.8×10^8 infectious units per microlitre, Neuroscience Gene Vector and Virus core, Stanford University) was injected at 100 nl min^{-1} . Subsequent injections of PHA-L or AAV8-hSyn1-FLEX-mGFP-2a-synaptophysin-mRuby⁵³ were performed at P35–P40. For whole-animal knockout studies, PHA-L was injected between P30 and P45. Mice were anaesthetized with ketamine-xylazine (Lloyd Laboratories) or isoflurane and immobilized in stereotactic apparatus (Kopf). Coordinates were proximal CA1 (from bregma) 1.4 mm lateral, 1.25–1.3 mm posterior, 1.1–1.2 mm ventral from brain surface; distal CA1 1.4 mm lateral, 1.8–2 mm posterior, 1.1 mm ventral. For PHA-L iontophoresis, 2.5% (by weight) PHA-L (Vector Labs, L-1110) solution in PBS, pH 8, was iontophoretically injected using current parameters $2 \mu\text{A}$, alternating 7-s on, 7-s off, for 1 min with pipette tips broken to an outer diameter of 6–12 μm . For AAV iontophoresis, current parameters were $2 \mu\text{A}$, 7-s on, 7-s off, for 2 min. Mice were perfused 5 (PHA-L) or 21 (AAV) days later and processed for PHA-L and Cre, or Cre, GFP, and mCherry immunostaining as described above. For entorhinal cortex axon tracing, CD-1 mice aged P40–P55 were used. AAV1-CMV-GFP (40–50 nl) was injected at 20 nl min^{-1} into the coordinates (from bregma): medial entorhinal 2.8 mm lateral, 4.75 mm posterior, 2.75 mm ventral from brain surface; lateral entorhinal 4.6 mm lateral, 3.5 mm posterior, 3 mm ventral from brain surface. Mice were perfused 2 weeks later.

Imaging and data analysis for CA1 axon tracing. For whole-animal mutant tracing, every other 60- μm parasagittal section was stained and analysed. Images of injections were taken at $5\times$ magnification on a Zeiss epiFluorescence scope and projections were imaged at $10\times$. Mice with labelling too faint to image or with retrogradely labelled cells were excluded. Images were acquired at identical gain and offset settings, but because injection and projection intensities varied between mice, exposure times were adjusted to avoid saturation. Fluorescence intensity measurements were taken on unprocessed images in FIJI and data were processed using custom MATLAB scripts. For quantification of injections, a 30-pixel-wide segmented line with spline fit was drawn along CA1, from proximal to distal. DAPI and Cre signals (from *Ten3^{Cre}*) were used to identify the proximal end of CA1, and DAPI signal was used to identify the distal end of CA1. Intensity values along the CA1 line were measured using the Plot Profile command. For quantification of projections, a 180-pixel-wide segmented line with spline fit was drawn along the subiculum, from proximal to distal. The bottom of the line was aligned to the superficial border of subiculum pyramidal cell layer; the proximal border of subiculum was defined in the same way as the distal border of CA1: that is, the point where the compact CA1 cell body layer ended. The distal border of the subiculum was defined as the point where layer 2 of the presubiculum became obvious as an increase in DAPI density in the superficial cell body layer. The 180-pixel-wide curved line was straightened using the Straighten function under Selection. For injections that labelled CA2 and CA1, axons from CA2 were present near the distal border of CA1. Area selections were drawn around these axons and intensities were set to zero using the Clear function. Pixel values at each position were imported into MATLAB, and the 180 pixels for each point along the proximal–distal axis were averaged to give the fluorescence intensity at that coordinate of the proximal–distal axis. From this point forward, injections and projections were processed in the same way. A manual background subtraction was performed by selecting a value corresponding to an area of the trace that was only background signal, and this value was subtracted from all points on the trace. Any intensity values below zero after subtraction were set to 0. The length of the CA1 or subiculum axis was divided into 100 equally sized bins and intensity values were averaged within each bin. For each injection or projection, the three sections with the highest total labelling were combined by summing the three intensity values at each binned position. This summed intensity trace was then normalized to a peak value of 100.

The mean position of the trace was calculated by multiplying the intensity value by the bin position, summing across the entire axis, and dividing by the sum of the intensity values. The width of the trace was defined as the full width-at-half-maximum. Traces were averaged across mice to produce the plots in Fig. 2e and Extended Data Fig. 5c, d, and the shaded error traces represent the standard error of the mean fluorescence intensity at that bin. For mean and width quantifications in Fig. 2f, g, the means were compared using two-tailed t -tests. For quantification of tracing across the proximal–distal axis of CA1 (Extended Data Fig. 5), injections and projections were processed as above. Values were combined into five groups for analysis and averaging based on the injection mean positions to the right of Extended Data Fig. 5d. Projection widths were compared using two-way analysis of variance (ANOVA) followed by a Šidák multiple comparisons test; multiplicity-adjusted P values are reported. Projection mean regression lines were generated and compared using Prism 7 (GraphPad). All statistical analyses were performed in Prism 7 (GraphPad).

Data analysis for conditional knockout experiments. Tissue processing and imaging for CA1 and subiculum conditional knockout experiments were the same as for whole-animal mutants, with the following modifications. For subiculum conditional knockout, mice were excluded if lentivirus–GFP–Cre cells spread into the proximal half of CA1 (more than two cells in proximal CA1 per section, or if any PHA-L⁺ cells were GFP–Cre⁺). Some mice had GFP–Cre expression in the distal CA1; however, because these cells express low to no Ten3, these mice were included as subiculum conditional knockouts. GFP–Cre signal in subiculum was measured and quantified along with the PHA-L labelling intensity. Heatmaps were generated in MATLAB using the 'imagesc' function, and three-dimensional plots were generated in MATLAB using the 'surf' function. For CA1 conditional knockout, mice were excluded if lentivirus–GFP–Cre cells spread into the distal half of subiculum. The mRuby signal from AAV8-hSyn1-FLEX-mGFP-2a-synaptophysin-mRuby was used for injection quantifications and the mGFP for projection quantifications. In addition, we stained for Cre in the 647 nm channel instead of using the GFP–Cre signal, because of the presence of mGFP. mGFP and GFP–Cre signal could be unambiguously distinguished by staining for Cre. In cases where the GFP–Cre signal overlapped with the mGFP signal, the Cre staining in the 647 nm channel was used to mask out Cre⁺ pixels, so the GFP–Cre signal was not counted as mGFP from CA1 axons. Analysis and quantification for CA1 conditional knockout projection mean and width was identical to the whole-animal knockout. For both CA1 and subiculum conditional knockouts, mice were excluded that had injection mean positions greater than 30 in CA1.

Hippocampus cDNA sequencing. Freshly dissected brains from P8 CD-1 mice were sliced horizontally into 1 mm slices using a tissue slicer. CA1 and subiculum were microdissected from individual slices using tungsten needles. Tissue from five mice was pooled, and total RNA was extracted using TRIzol reagent (Thermo Fisher, 15596018) and chloroform followed by purification using an RNeasy kit (Qiagen). DNA was removed by on-column digestion with DNase (Qiagen) for 15 min. cDNA was produced using a Superscript III First-Strand Synthesis System (Thermo Fisher, 18080-051) and a gene-specific primer located 3' of splice site B (5'-ATCAGAGACGTACAAATCTCCGG-3') followed by PCR for 30 cycles with Q5 polymerase (NEB) using the same primer and a primer located 5' of splice site A: 5'-TGTAATCAGAGAGCTTGCCACC-3'. PCR products were cloned into pCR-Blunt II-TOPO (Thermo Fisher, 450245), individual colonies were minipreped and sequenced using T7 and SP6 sequencing primers (Sequetech), and the status at splice sites A and B was assigned to individual clones using Geneious 10 software.

DNA constructs. Full-length mouse *Ten3* cDNA was obtained from Source Bioscience, clone identifier IRCKp5014M2020Q (accession number BC145284.1). This sequence lacks all alternatively spliced exons (corresponding to isoform A₀B₀). Haemagglutinin-tag was added and cDNA was cloned into pCDNA3.1(–) (Thermo Fisher, V79520) in two steps using a NEBuilder HiFi Assembly Kit (NEB, E2621) and NEB Stable competent cells (NEB, C3040H). Phusion Taq polymerase (NEB M0530) was used to amplify the 5' portion for *Ten3* cDNA, adding a 5' haemagglutinin-tag and Kozak sequence. Primers were as follows: 5'-TAGACTCGAGCGGCCGCCACCATGTACCCATACGATGTTCCAGATTACGCTGATGTGAAGGAACGCAGG-3' and 5'-TGGAAATTCTGCAGATATCTCTGAGGATCAGGCAA-3'. NEBuilder HiFi Assembly mix was used to insert this PCR fragment into pCDNA3.1(–) digested with EcoRV and NotI. The assembled product was subsequently digested with EcoRV and KpnI, and the HiFi Assembly mix was used to insert the 3' end of *Ten3* cDNA, amplified using the following primers: 5'-CCTGATCTCTCAGGATATCATTTAG-3' and 5'-TTAAACTTTAAGCTTGGTACCTTACCTCTTGCCGATCTCA-3'. The assembled product was fully sequenced. Additional isoforms were generated using a Q5 Site-Directed Mutagenesis Kit (NEB E0554S). A₀B₁ was generated from A₀B₀ using the following primers: 5'-TTAGACATAGTAGCAACCCAGCTCACAG-3' and 5'-AATCTTTATTTCTTAGTTCTAAACACTTGTTCACATTC-3'. A₁B₀ and A₁B₁ were generated from A₀B₀ and A₀B₁, respectively, using the following primers:

5'-AAGATAGTTAAAGAGGGTTGCCCGGGCTTGT-3' and 5'-ATCCAAATAGTGAGCAATTGTGCAGTCTCCGTC-3'. A₂B₁ was generated from A₁B₁ using the following primers: 5'-GATATAAGAGGGTTGCCCGGGCTTGT 3' and 5' CTATCTTGTCTTTAACTATCTTATCCAAATAGTGAGCAAT TGTGCAG-3'. A₃B₁ was generated from A₁B₁ using the following primers: 5'-GGATATAAGAGGGTTGCCCGGGCTTGT-3' and 5'-TATCTTGTCTGCTTTAACTATCTTATCCAAATAGTGAGCAATTGTGCAG-3'.

All the haemagglutinin-tagged *Ten3*-isoform open reading frames were then cloned into a dual transcription unit vector under the Efl α promoter. The vector also contained mCherry or GFP under the CMV promoter. Primers for amplifying the haemagglutinin-tagged open reading frames were 5'-TACAAAAA GCAGGTGCCACCGTCGACATGACCATACGATGTC-3' and 5'-TTGTA CAAGAAAGCTGGGTGGATCCTTACCTCTTGCCGATC-3'. NEBuilder HiFi Assembly mix was used to insert this PCR fragment into the destination vector digested with BamHI and SalI. CMV-mCherry and CMV-GFP were generated by cloning eGFP and mCherry into NheI and HindIII-digested pCDNA3.1(-) using a NEBuilder HiFi Assembly Kit. eGFP and mCherry were amplified from source plasmids using the following primers: 5'-GGAGACCA AGCTGGCTAGCCACCATGGTGAGCAAGGGCGA-3' and 5'-ATCAGCGG TTTAACTTAAGCTTTTACTTGTACAGCTCGTCCA-3'. The expression construct for human latrophilin-3 was published previously⁵⁴ and provided by R. Sando and T. Südhof.

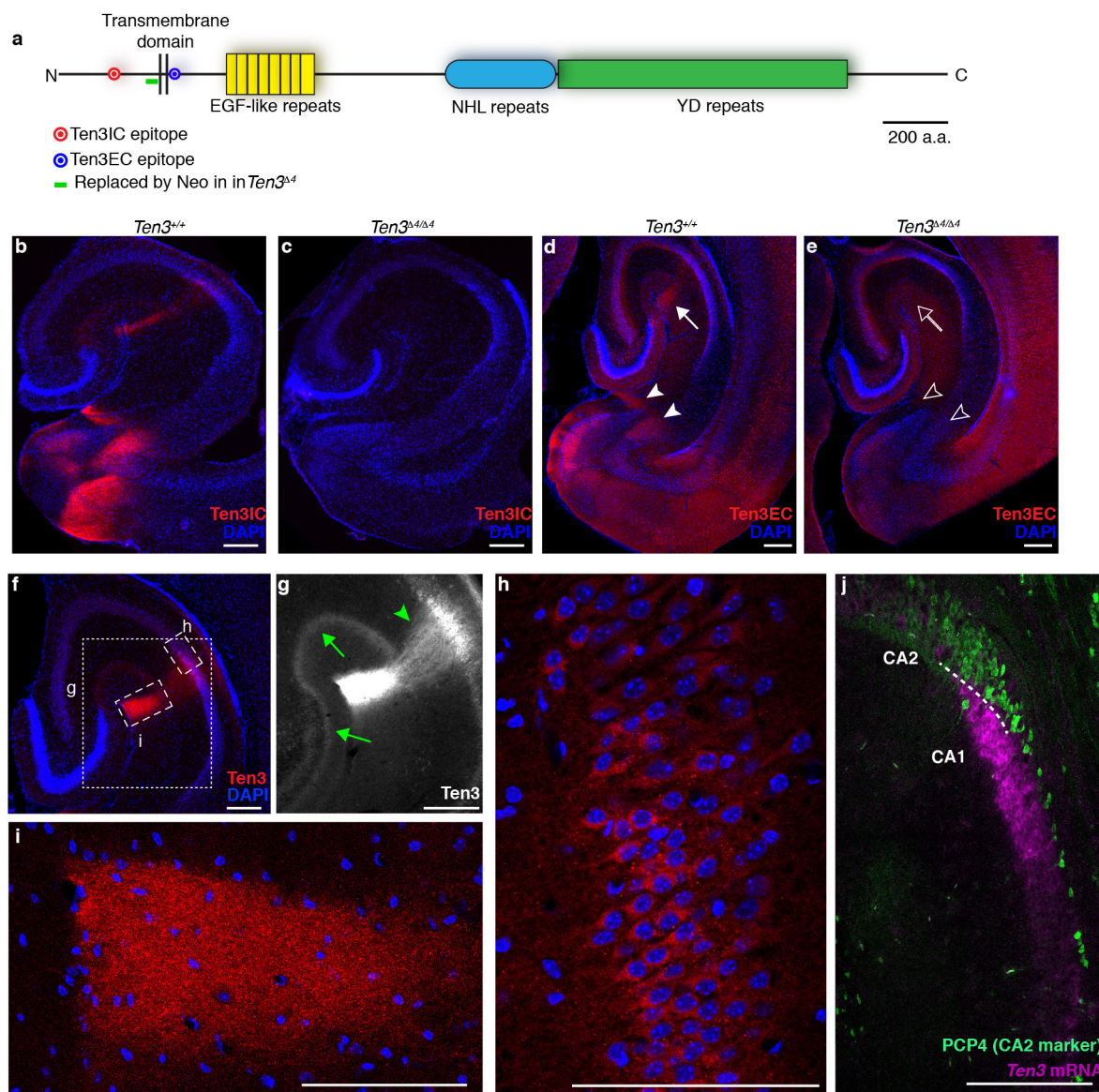
Single isoform K562 cell aggregation assay. K562 cells (American Type Culture Collection (ATCC) CCL-243, lot 61978333) were grown in RPMI-1640 (Gibco 11875-093 with 10% FBS (Gibco A3160501) and 1 \times penicillin-streptomycin (Gibco 15140122)). The lot was authenticated and tested for mycoplasma by ATCC. Cells were electroporated using a Neon Transfection system (Thermo Fisher MPK5000) with 100- μ l tips. DNA was prepared using a HiPure Plasmid Filter MaxiPrep Kit (Thermo Fisher K210017). Fifteen micrograms of the Efl α -*Ten3* CMV-GFP dual transcription unit plasmid expressing a particular isoform were used for each electroporation. For the GFP-only condition, 6.43 μ g of Efl α -empty CMV-GFP along with 8.57 μ g of empty pCDNA3.1 were used. Two million cells were washed once in 5 ml PBS, resuspended in 110 μ l buffer R, mixed with DNA, and electroporated using the following settings: 1,450 V, 10 ms, three pulses, and added to 5 ml of warm RPMI-1640 with 10% FBS. Cells were incubated in six-well plates at 37°C and 5% CO₂. Sixteen to 20 h later, cells were centrifuged at 200g for 3 min, resuspended in 1 ml RPMI-1640 + 10% FBS, and incubated for 15 min at 37°C with 0.1 mg ml⁻¹ DNase (Worthington LS002060). Cells were washed twice with RPMI-1640 + 10% FBS, then resuspended in aggregation medium. Aggregation medium was neural growth medium: Neurobasal-A, 4% B27, 2 mM glutamine, 10% FBS, 20 mM HEPES. Cells were passed through a 40- μ m cell strainer, counted, and added to wells of a 24-well plate at 4 \times 10⁵ cells per millilitre in 1 ml aggregation medium, and the plate was placed on a nutator at 37°C for 1.5 h. After 1.5 h, cells were gently transferred to 2 ml of aggregation media in a six-well plate and imaged with a Nikon Eclipse Ti microscope using a 4 \times lens. Five images were taken for each well. Images were thresholded in FIJI, and Analyze Particles was used to measure particle number and size. Particle sizes from three separate experiments were combined, and particles below 600 μ m², the size of a large GFP⁺ cell in control wells, were filtered out to remove single cells. Combined particle sizes were then compared with GFP-only control using a Kruskal-Wallis test followed by Dunn's multiple comparisons test. A family-wide significance level was set to 0.05, and multiplicity-adjusted *P* values were reported. For haemagglutinin immunostaining following aggregation, cells were fixed in 4% paraformaldehyde for 15 min, centrifuged for 3 min at 200g, rinsed once with PBS, and resuspended in 30% sucrose in PBS. Cells were spun onto Superfrost Plus slides using a cytospin⁵⁵ then incubated in the following solutions, at room temperature except for primary antibody: 2 \times 5 min in PBS, 10 min in 0.1% Triton X-100 in PBS, 3 \times 5 min in PBS, 30 min in 10% NDS in PBS, overnight in primary antibody (Ms anti-haemagglutinin, Covance MMS-101R) at 4°C in 5% NDS in PBS, 3 \times 5 min in PBS, 2 h in secondary antibody (Donkey Alexa 647 anti-mouse, Jackson ImmunoResearch) in 5% NDS in PBS, 3 \times 5 min in PBS, 5 min in DAPI, and 5 min in PBS. Aggregates were imaged at 40 \times magnification on a Zeiss 780 confocal microscope.

K562 mixed cell aggregation assay. For the *Ten3* isoform mixing assay (Extended Data Fig. 10), electroporations and aggregation assay were performed as above with the following modifications. The mCherry versions of the dual promoter constructs were used where appropriate. The two populations of cells were mixed at 2 \times 10⁵ each in 1 ml aggregation media, for a final cell concentration of 4 \times 10⁵ cells per millilitre. Phase-contrast images of the cells and aggregates were also taken. For quantification, aggregates were identified from the phase image, then identified as mixed, GFP-only, or mCherry-only, on the basis of the merged fluorescence image. Mixed aggregates had to contain at least three cells of each colour, to avoid identifying single population aggregates as mixed because of chance overlap with a single cell in the other channel. At least 100 aggregates across three separate experiments were counted. For the latrophilin-3 and *Ten3* mixing experiment, conditions and analysis differed as described below. For each electroporation, 5 μ g CMV-GFP DNA was co-electroporated with 12 μ g CMV-*Ten3* or 12 μ g empty pCDNA3.1, or 5 μ g CMV-mCherry and 1.75 μ g CMV-latrophilin-3. Aggregation media were the same as above except with 1.25% FBS rather than 10%. After 1.5 h of mixing, 3 μ l aliquots were taken from the wells, spotted onto slides, and imaged at 5 \times magnification on a Zeiss epifluorescence scope. Three or four aliquots were taken per well, and two images were taken per aliquot. For aggregate size quantification, the GFP and mCherry channels were thresholded, combined, and Analyze Particles was used on the combined binary image to measure particle number and size. Particle sizes from three separate experiments were combined, and particles below a 600 μ m², the size of a large GFP⁺ cell in control wells, were filtered out to remove single cells. Combined particle sizes were then compared with latrophilin-3 and GFP-only control using a Kruskal-Wallis test followed by Dunn's multiple comparisons test. A family-wide significance level was set to 0.05, and multiplicity-adjusted *P* values were reported.

Code availability. Custom MATLAB scripts used in analysing data are available from the corresponding author upon reasonable request.

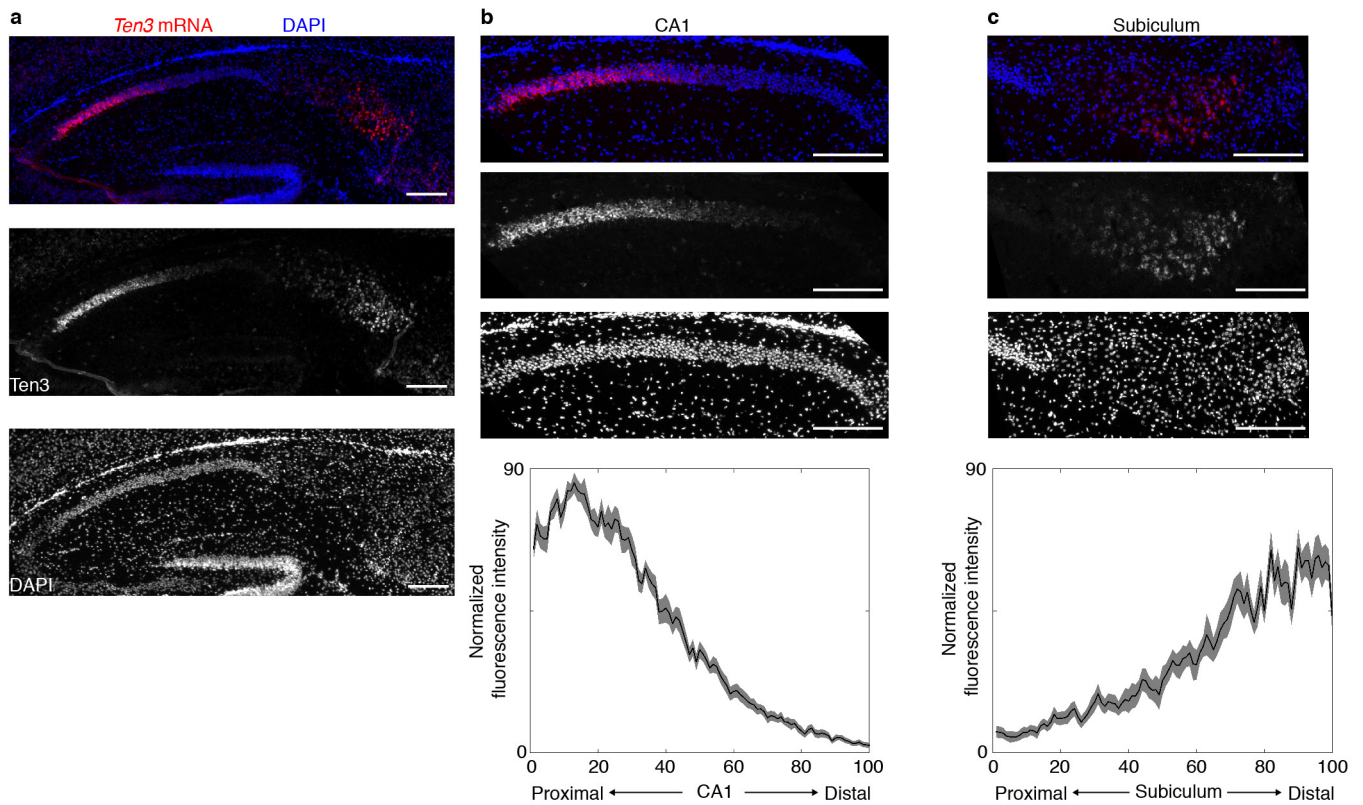
Data availability. All data supporting the findings reported in this study are available from the corresponding author upon reasonable request. The *Ten3* isoform cDNA sequences have been deposited in GenBank under accession numbers MG387139-MG387146.

- Tasic, B. *et al.* Site-specific integrase-mediated transgenesis in mice via pronuclear injection. *Proc. Natl Acad. Sci. USA* **108**, 7902–7907 (2011).
- Weissbourd, B. *et al.* Presynaptic partners of dorsal raphe serotonergic and GABAergic neurons. *Neuron* **83**, 645–662 (2014).
- Beier, K. T. *et al.* Circuit architecture of VTA dopamine neurons revealed by systematic input-output mapping. *Cell* **162**, 622–634 (2015).
- Lu, Y. C. *et al.* Structural basis of latrophilin-FLRT-UNC5 interaction in cell adhesion. *Structure* **23**, 1678–1691 (2015).
- Sisino, G., Bellavia, D., Corallo, M., Geraci, F. & Barbieri, R. A homemade cytospin apparatus. *Anal. Biochem.* **359**, 283–284 (2006).
- Witter, M. in *The Mouse Nervous System* (eds Watson, C., Paxinos, G. & Puelles, L.) 112–139 (Elsevier, 2012).
- Kohara, K. *et al.* Cell type-specific genetic and optogenetic tools reveal hippocampal CA2 circuits. *Nat. Neurosci.* **17**, 269–279 (2014).
- Caballero-Bleda, M. & Witter, M. P. Regional and laminar organization of projections from the presubiculum and parasubiculum to the entorhinal cortex: an anterograde tracing study in the rat. *J. Comp. Neurol.* **328**, 115–129 (1993).
- Honda, Y. & Ishizuka, N. Organization of connectivity of the rat presubiculum: I. efferent projections to the medial entorhinal cortex. *J. Comp. Neurol.* **473**, 463–484 (2004).
- O'Reilly, K. C., Gulden Dahl, A., Ulsaker Kruge, I. & Witter, M. P. Subicular-parahippocampal projections revisited: development of a complex topography in the rat. *J. Comp. Neurol.* **521**, 4284–4299 (2013).
- Wright, N. F., Vann, S. D., Erichsen, J. T., O'Mara, S. M. & Aggleton, J. P. Segregation of parallel inputs to the anteromedial and anteroventral thalamic nuclei of the rat. *J. Comp. Neurol.* **521**, 2966–2986 (2013).
- Meibach, R. C. & Siegel, A. Efferent connections of the hippocampal formation in the rat. *Brain Res.* **124**, 197–224 (1977).
- Ishizuka, N. Laminar organization of the pyramidal cell layer of the subiculum in the rat. *J. Comp. Neurol.* **435**, 89–110 (2001).
- Wright, N. F., Erichsen, J. T., Vann, S. D., O'Mara, S. M. & Aggleton, J. P. Parallel but separate inputs from limbic cortices to the mammillary bodies and anterior thalamic nuclei in the rat. *J. Comp. Neurol.* **518**, 2334–2354 (2010).



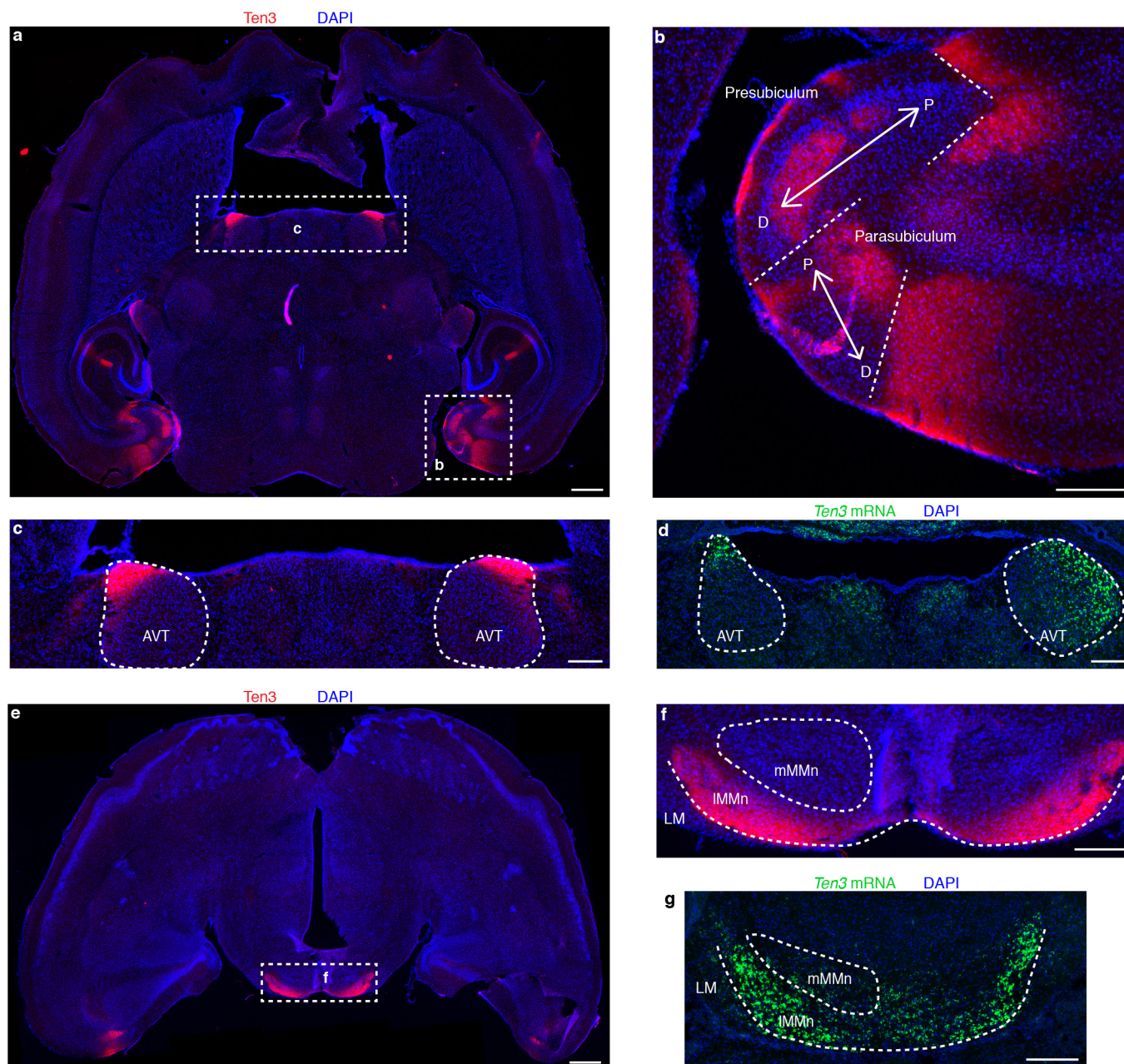
Extended Data Figure 1 | Ten3 staining details and controls. **a**, Diagram of Ten3 protein showing location of antibody epitopes, specific domains, and region deleted in the *Ten3*^{Δ4} mutant. In *Ten3*^{Δ4}, a neomycin resistance cassette (Neo) replaces 110 base pairs of sequence directly N-terminal to the transmembrane domain. The Ten3IC antibody was used for all Ten3 stainings in the paper except **d** and **e** of this figure. Scale bar, 200 amino acids. **b**, **c**, Ten3IC staining (red) on P9 horizontal sections of *Ten3*^{WT} (**b**) and mutant *Ten3*^{Δ4/Δ4} (**c**) brains, showing loss of staining in *Ten3* mutants. Note that the Ten3IC epitope is located N-terminal to Δ4, suggesting that in *Ten3*^{Δ4/Δ4} either the mRNA undergoes nonsense-mediated decay or the truncated protein is not stable. **d**, **e**, Ten3EC staining on P10 horizontal sections of *Ten3*^{WT} (**d**) and mutant *Ten3*^{Δ4/Δ4} (**e**) brains. Staining has a higher background than Ten3IC antibody, but signal is present in proximal CA1 (arrow) and distal subiculum (arrowheads), similar to Ten3IC, which is absent in the knockout (open arrow/arrowheads). **f**, Ten3 staining

(red) on P10 horizontal section with boxes around regions magnified in **g**–**i**. **g**, Ten3 staining in dentate gyrus from **f**, CA3, and CA1. Intensity was increased to highlight Ten3 signal in axons and dendrites. Ten3 in stratum radiatum of proximal CA1 (arrowhead) is most probably from CA1 dendrites, since CA3 cells, the major source of axons in this layer, did not express *Ten3* mRNA (Fig. 1b). Ten3 in the molecular layers of dentate gyrus and CA3 (arrows) is probably contributed by the axons of MEC layer II neurons⁵⁶, since dentate gyrus and CA3 neurons did not express *Ten3* mRNA (Fig. 1b). **h**, Proximal CA1 pyramidal cell layer from **f**, showing Ten3 signal in cell bodies. **i**, Proximal CA1 stratum lacunosum-moleculare from **f**, showing Ten3 signal in the region where MEC axons synapse onto CA1 pyramidal neuron dendrites. **j**, *In situ* hybridization on P9 horizontal section for *Ten3* mRNA (magenta) combined with immunostaining for PCP4 (green), a marker of CA2 neurons⁵⁷. No overlap between Ten3 and PCP4 was observed. Scale bars, 200 μm in **b**–**g**, **j**, and 100 μm in **h**, **i**.



Extended Data Figure 2 | Distribution of *Ten3* mRNA in sagittal sections. **a**, *In situ* hybridization for *Ten3* mRNA on sagittal section of P10 brain. Top, merged image with *Ten3* mRNA signal in red and DAPI in blue; middle, *Ten3* mRNA signal alone; bottom: DAPI signal alone. **b**, Top: magnified image of *Ten3* *in situ* hybridization in CA1; bottom: quantification of *Ten3* mRNA along the proximal–distal axis of CA1 ($n = 12$ sections, four mice), showing a graded signal that peaks in proximal CA1 and decreases to a minimum in distal CA1. Proximal–distal axis is divided into 100 bins, with 1 being most proximal and 100 most

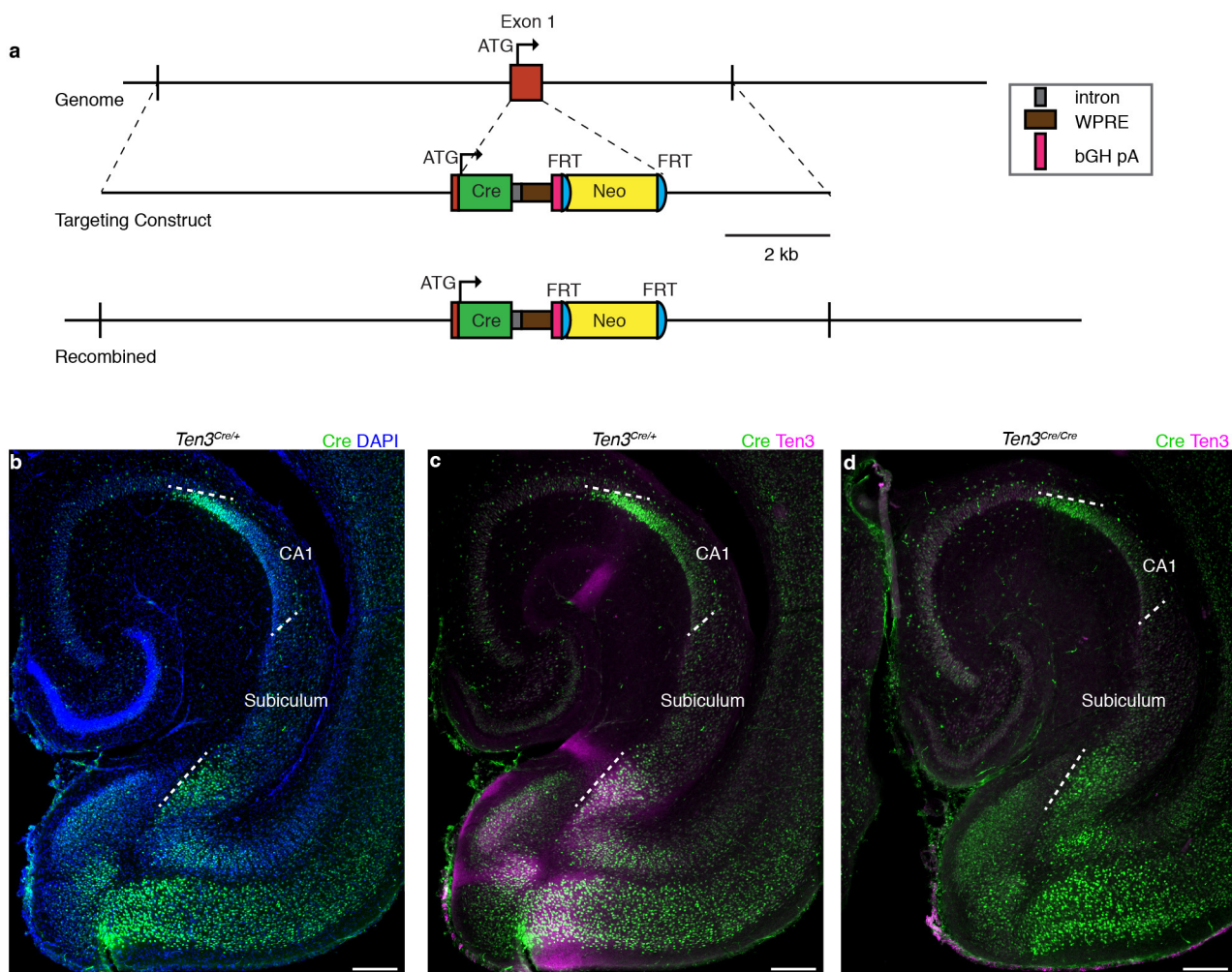
distal. Shaded curves represent mean \pm s.e.m. **c**, Top: magnified image of *Ten3* *in situ* hybridization in subiculum; bottom: quantification of *Ten3* mRNA along the proximal–distal axis of subiculum ($n = 14$ sections, four mice) showing a graded signal that peaks in distal subiculum and decreases to a minimum in proximal subiculum. The distributions in CA1 and subiculum are similarly shaped but reversed along the proximal–distal axis, reflecting the graded topographic connections along this axis (see Fig. 2 and Extended Data Fig. 5c). Scale bars, 200 μ m in all panels.



Extended Data Figure 3 | Ten3 expression and topography details.

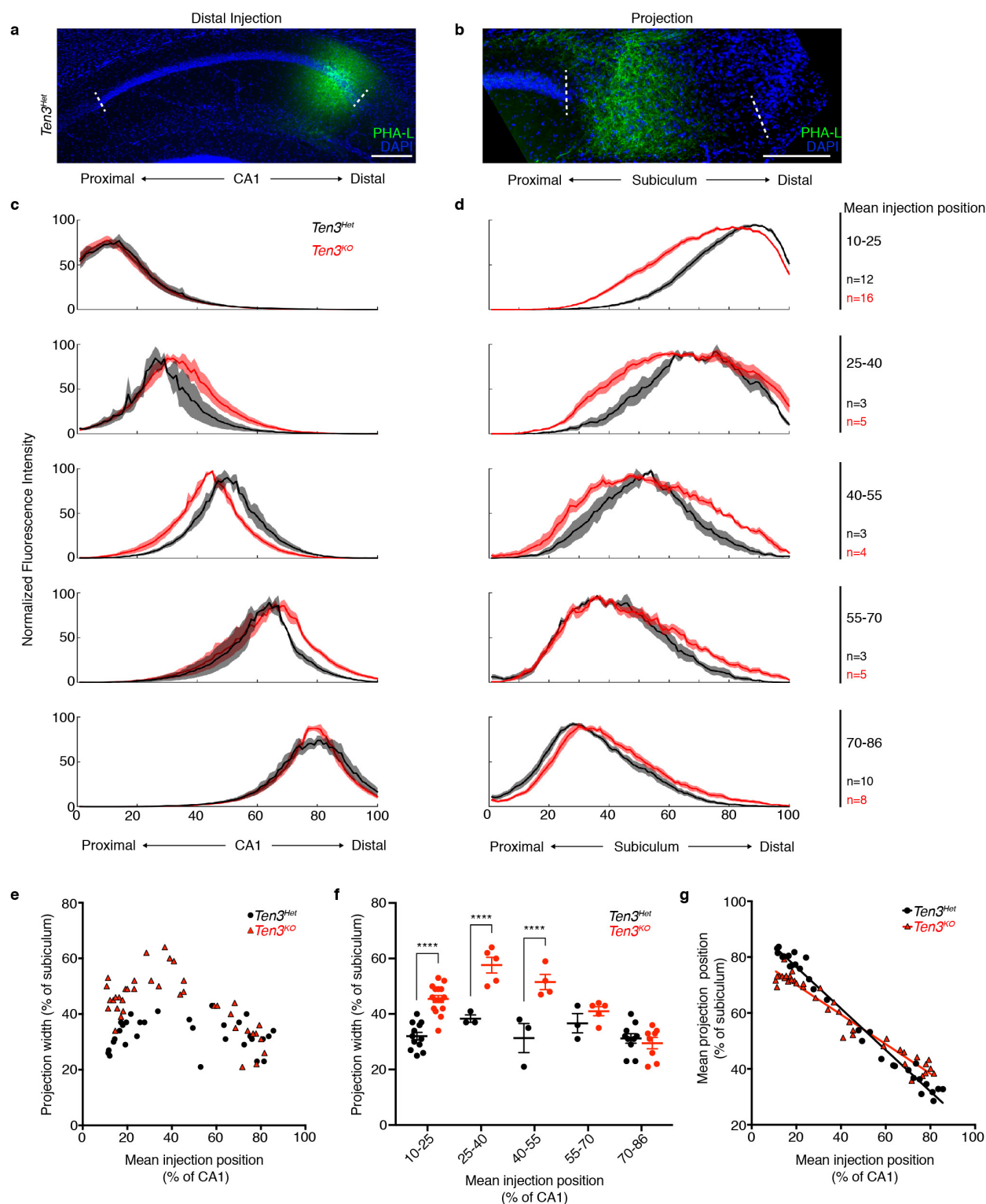
a, Ten3 staining (red) on P10 horizontal section. Dotted rectangles highlight staining in the hippocampal region and anteroventral thalamic nucleus, which are magnified in **b** and **c**. **b**, The parahippocampal region from **a**, showing expression of Ten3 relative to the proximal–distal (P–D) axes (arrows) in the presubiculum and parasubiculum. The connectivity of these regions is complex^{58,59}, but seems to be consistent with preferential connectivity between Ten3-expressing subregions. Ten3 is expressed in distal presubiculum (close to parasubiculum), which projects to MEC near the parasubicular border⁵⁹, and receives projections from distal subiculum⁶⁰, both Ten3-high subregions. Ten3 is also expressed in proximal parasubiculum, which projects to MEC⁵⁸ and receives projections from distal subiculum⁶⁰, again both Ten3-high subregions. **c**, The anteroventral thalamus from **a**, showing intense Ten3 staining in the anterior and lateral division of the anteroventral thalamic nucleus (AVT, outlined). Distal subiculum, another Ten3-high region, projects to the anteroventral thalamic nucleus, whereas proximal subiculum projects to the anteromedial thalamus⁶¹. **d**, *In situ* hybridization for Ten3 mRNA (green) on P9 horizontal section from similar location as **c**.

e, Ten3 staining (red) on P10 horizontal section, more ventral than **a**. Dotted rectangle highlights intense staining in the medial mammillary nucleus, which is magnified in **f**. **f**, Medial mammillary nucleus from **e**, showing Ten3 labelling in the lateral division of the medial mammillary nucleus (lMMn). Outlines show location of lateral mammillary nucleus (LM), lateral division of the medial mammillary nucleus (lMMn), and medial division of the medial mammillary nucleus (mMMn). Proximal subicular neurons project to the medial division of the medial mammillary nucleus, whereas Ten3-high distal subicular neurons project to the Ten3-high lateral division^{40,62–64}. The neurons of the lateral division project to the Ten3-high anteroventral thalamic nucleus, while medial division neurons project to the anteromedial thalamus⁶¹. **g**, *In situ* hybridization for Ten3 mRNA (green) on P9 horizontal section from similar location as **f**. Scale bars, 500 μ m in **a** and **e**; 200 μ m elsewhere. In summary, the pattern of Ten3-high to Ten3-high connectivity observed for CA1, subiculum, and entorhinal cortex seems to extend to many of the topographic projections formed between these subregions and the presubiculum, parasubiculum, thalamus, and mammillary nucleus.



Extended Data Figure 4 | Generation and characterization of *Ten3^{cre}*.
a, Design of *Ten3^{cre}*. Top: region of chromosome 8 containing *Ten3* exon 1, which contains the start codon (ATG). Middle: targeting construct with *cre* open reading frame inserted directly after the *Ten3* start codon. *cre* is followed by a synthetic intron, woodchuck hepatitis virus post-transcriptional regulatory element (WPRE), and bovine growth hormone polyadenylation sequence (bGH pA) (see key on right). Neo includes a phosphoglycerate kinase (PGK) promoter driving the resistance gene. Bottom: genomic region after homologous recombination.

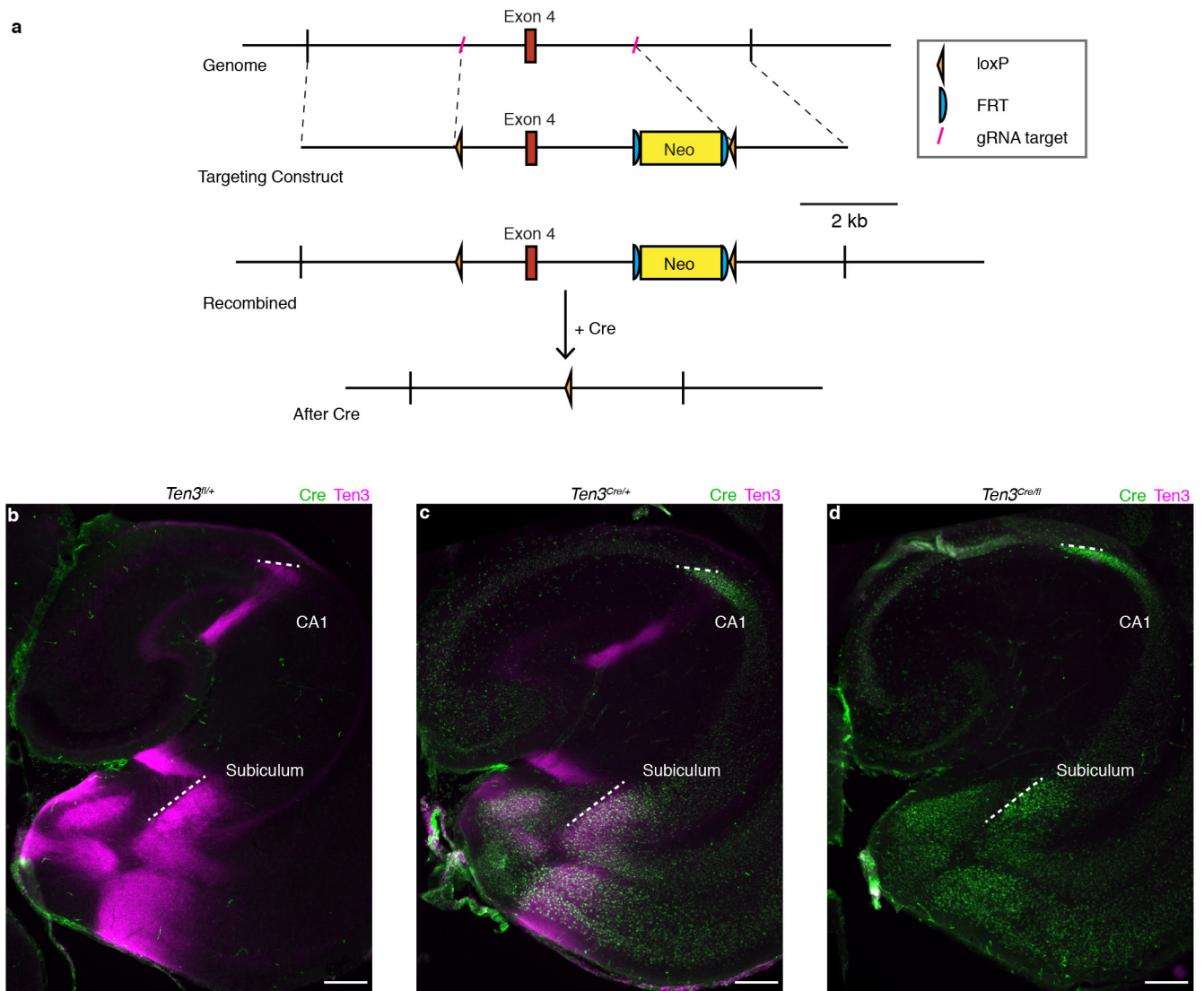
The endogenous exon 1 sequence after the start codon is replaced with *cre*. Neo was not removed by flippase (FLP)-mediated recombination in the mice used in Fig. 2. **b–d**, Cre and Ten3 protein expression in P10 horizontal sections from *Ten3^{cre}* mice. White dotted lines highlight proximal and distal borders of CA1 and subiculum. **b**, **c**, Cre expression (green) mimics the distribution of Ten3 expression (magenta) in *Ten3^{Het}* mice. **d**, In *Ten3^{cre/cre}* mice, Ten3 immunostaining is absent. Scale bars, 200 μ m.



Extended Data Figure 5 | Analysis of CA1→subiculum projections with various injection sites in *Ten3^{Het}* control and *Ten3^{KO}* mice.

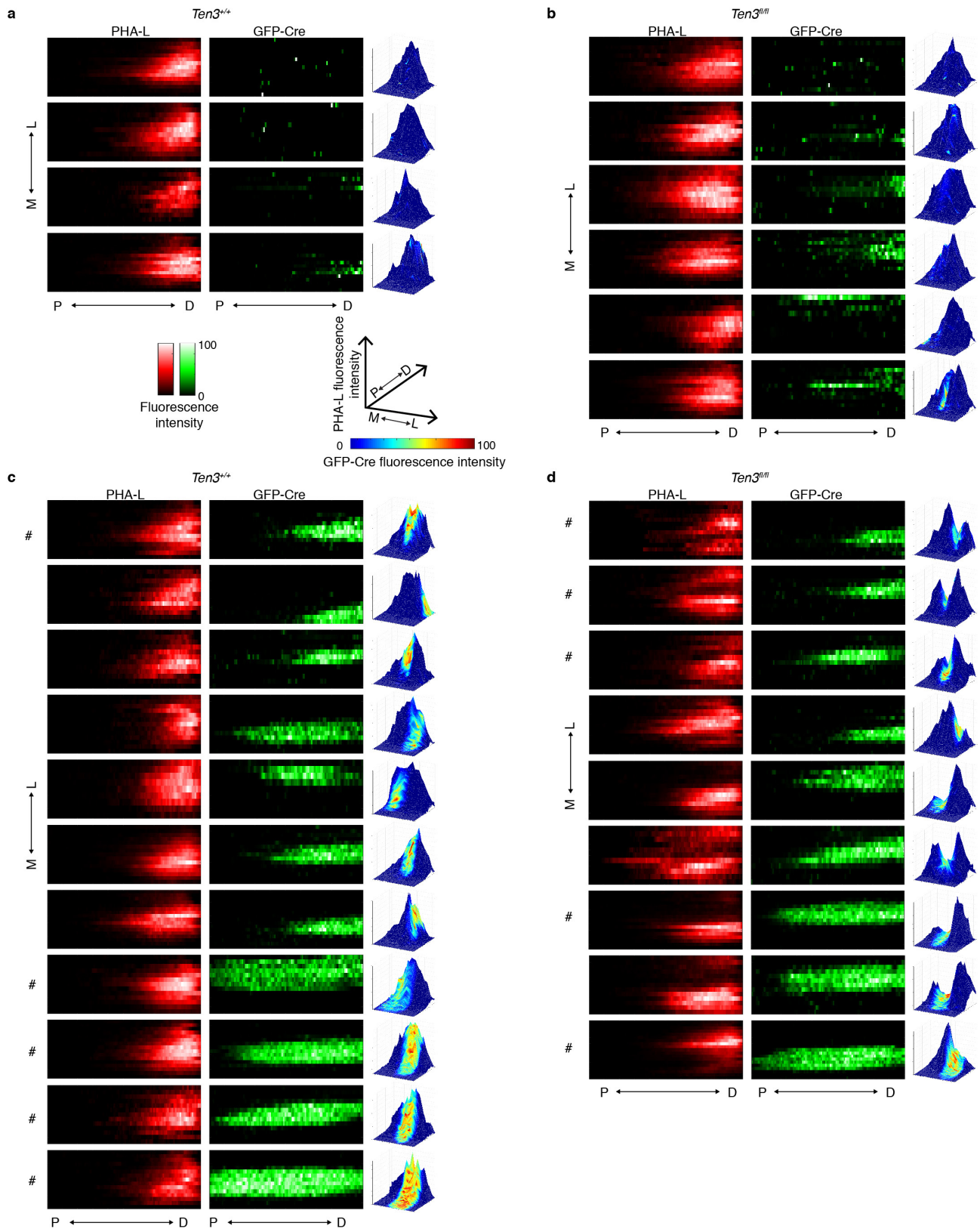
a, b, PHA-L (green) injection in distal CA1 (**a**) and corresponding projection in proximal subiculum (**b**) in *Ten3^{Het}* mouse. Scale bars, 200 μ m. **c, d**, Averaged normalized injection (**c**) and projection (**d**) traces of all *Ten3^{Het}* (black) and *Ten3^{KO}* (red) mice analysed, binned into five groups by the mean position of the injection, and plotted from most proximal (top) to most distal (bottom) injections (bin limits and number of mice per bin listed on the right of **d**). Proximal–distal axis position is numbered from 1 (most proximal) to 100 (most distal). Shaded error curves represent mean \pm s.e.m. at each bin. **e**, Projection width in subiculum versus injection mean position in CA1 for all mice

(*Ten3^{Het}*; $n = 31$, black circles; *Ten3^{KO}*; $n = 38$, red triangles). **f**, Projection width data binned by injection mean. Number of mice per bin same as **d**. Projection width was significantly increased in *Ten3^{KO}* for the three most proximal bins. **** $P < 0.0001$; multiplicity-adjusted P values after two-way ANOVA with Šidák's correction for multiple comparisons. Error bars, mean \pm s.e.m. **g**, Projection mean position in subiculum versus injection mean position in CA1 for all mice used (*Ten3^{Het}*; $n = 31$; *Ten3^{KO}*; $n = 38$), with superimposed linear regression lines (*Ten3^{Het}*; $R^2 = 0.9812$; *Ten3^{KO}*; $R^2 = 0.9515$). The slopes were significantly different ($P < 0.0001$), indicating a less sharp topography in *Ten3^{KO}* mice. Bin 1 data (most proximal, injection mean 10–25) in **c–g** are the same data as in Fig. 2e–g.



Extended Data Figure 6 | Generation and characterization of *Ten3^{fl}*. **a**, Design of *Ten3^{fl}*. Top: region of chromosome 8 containing *Ten3* exon 4, which is 239 base pairs long and encodes 19 of the 21 amino acids in the transmembrane domain. Guide RNA (gRNA) targets shown in red (see key at right). Line 2: targeting construct with *loxP* sites inserted 5' and 3' of exon 4. Neo includes a PGK promoter driving the resistance gene. Line 3: genomic region after homology-directed repair. Bottom: deletion of exon 4 after Cre-mediated recombination between *loxP* sites. Neo was removed by

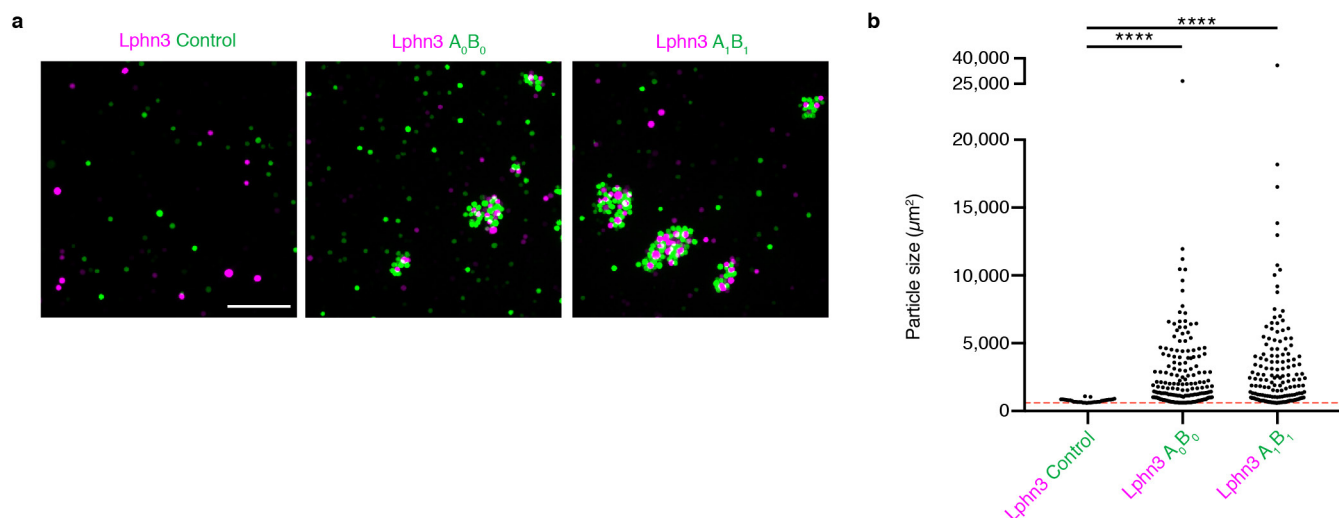
FLP-mediated recombination in some of the mice used in Figs 3 and 4. In addition to deleting exon 4, the reading frame 3' to exon 4 is frame-shifted with respect to the reading frame 5' to exon 4. **b–d**, Cre (green) and *Ten3* (magenta) protein expression in P10 horizontal sections from *Ten3^{fl/+}* (**b**), *Ten3^{Het}* (**c**), and *Ten3^{Cre/fl}* (**d**) mice. *Ten3* staining is absent in *Ten3^{Cre/fl}* mice. White dotted lines highlight proximal and distal borders of CA1 and subiculum. Scale bars, 200 μ m.



Extended Data Figure 8 | Subiculum conditional knockout plots.

a, b, Plots from *Ten3^{WT}* (**a**) and *Ten3^{fl/fl}* (**b**) mice with minimal GFP-Cre expression. Heatmaps show normalized PHA-L fluorescence intensity (red, left) and normalized GFP-Cre intensity (green, middle) in subiculum, same mice. Each row is one section, 120 μ m between rows, colour bars shown below **a**, and proximal–distal position is on the x axis. Surface plots are to the right of the corresponding heatmaps, showing

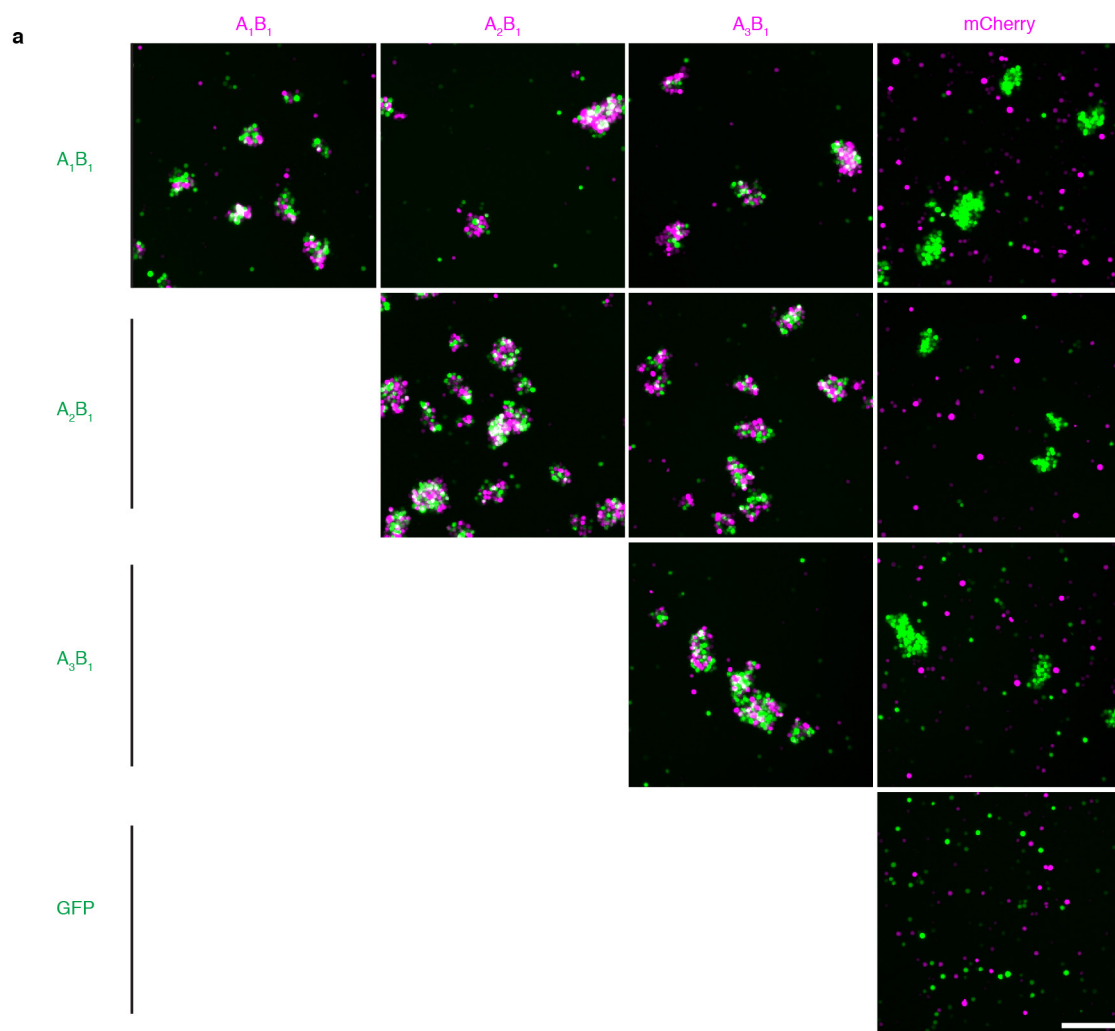
PHA-L fluorescence intensity as height and GFP-Cre fluorescence intensity according to the colour map shown below **a**. P, proximal; D, distal; M, medial; L, lateral. Projections are similar between *Ten3^{WT}* and *Ten3^{fl/fl}*. **c, d,** Plots from *Ten3^{WT}* (**c**) and *Ten3^{fl/fl}* (**d**) mice with high GFP-Cre expression in subiculum. In *Ten3^{fl/fl}* mice, PHA-L signal is decreased in GFP-Cre regions. Number of mice shown in Fig. 4.



Extended Data Figure 9 | Latrophilin-3 and Ten3 aggregation assay.

a, Images from aggregation assay with cells co-transfected with latrophilin-3 (Lphn3) and mCherry (magenta) mixed with cells co-transfected with GFP and empty vector (left), A₀B₀ isoform of Ten3 (middle), or A₁B₁ isoform of Ten3 (right). Scale bar, 200 μm , applies to all images. **b**, Quantification of aggregate sizes pooled from three biological

replicates. Dashed red line shows cutoff at 600 μm^2 , the size of a large GFP⁺ cell from the control images. Asterisks denote significance from Dunn's multiple comparisons test after a Kruskal–Wallis test, comparing all conditions with the Lphn3 and control mix, Lphn3 + control: $n = 32$ particles above threshold; Lphn3 + A₀B₀: $n = 172$; Lphn3 + A₁B₁: $n = 159$. NS, not significant; **** $P \leq 0.0001$, multiplicity-adjusted P values.



b

	mCherry +			
	A ₁ B ₁	A ₂ B ₁	A ₃ B ₁	mCherry only
A ₁ B ₁	100% mixed (110/110)	100% mixed (113/113)	100% mixed (100/100)	97.1% GFP only (102/105) 2.9% mCherry only (3/105)
A ₂ B ₁		100% mixed (110/110)	100% mixed (113/113)	100% GFP only (100/100)
A ₃ B ₁			100% mixed (109/109)	100% GFP only (103/103)
GFP only				0 aggregates observed

Extended Data Figure 10 | Aggregation assays for cells expressing different Ten3 splicing isoforms. **a**, Cell aggregation assay with combinations of K562 cells expressing the A₁B₁, A₂B₁, or A₃B₁ Ten3 isoform along with GFP or mCherry. Scale bar in bottom right panel, 200 μm, applies to all images. **b**, Quantification of aggregates observed in three biological replicates of the aggregation experiment in **a**. At least 100 aggregates were counted across the three replicates in each of the 10 mixing conditions, except for the GFP-alone and mCherry-alone controls,

where no aggregates were observed. One hundred per cent of aggregates were mixed in combinations where both cell populations expressed a Ten3 isoform. No mixed aggregates were observed in combinations of Ten3-expressing cells with cells expressing mCherry alone, confirming that the aggregation is Ten3-dependent and not due to an endogenously expressed interaction partner. Fractions in parentheses indicate aggregates of a particular type out of all aggregates counted in that condition.

A parsec-scale optical jet from a massive young star in the Large Magellanic Cloud

Anna F. McLeod¹, Megan Reiter², Rolf Kuiper³, Pamela D. Klaassen⁴ & Christopher J. Evans⁴

Highly collimated parsec-scale jets, which are generally linked to the presence of an accretion disk, are commonly observed in low-mass young stellar objects^{1,2}. In the past two decades, a few of these jets have been directly (or indirectly) observed from higher-mass (larger than eight solar masses) young stellar objects^{3–7}, adding to the growing evidence that disk-mediated accretion also occurs in high-mass stars^{8–11}, the formation mechanism of which is still poorly understood. Of the observed jets from massive young stars, none is in the optical regime (massive young stars are typically highly obscured by their natal material), and none is found outside of the Milky Way. Here we report observations of HH 1177, an optical ionized jet that originates from a massive young stellar object located in the Large Magellanic Cloud. The jet is highly collimated over its entire measured length of at least ten parsecs and has a bipolar geometry. The presence of a jet indicates ongoing, disk-mediated accretion and, together with the high degree of collimation, implies that this system is probably formed through a scaled-up version of the formation mechanism of low-mass stars. We conclude that the physics that govern jet launching and collimation is independent of stellar mass.

At a distance of 50 kpc, the Large Magellanic Cloud (LMC) is an ideal search location for high-mass ($M > 8M_{\odot}$, where M_{\odot} is the mass of the Sun) young stellar object (YSO) jets. It is close enough to resolve YSOs and their jets; it has a nearly face-on orientation, allowing a convenient viewing angle; it is undergoing active star formation; its low dust content makes it an environment in which the feedback effect of strong ionizing radiation is enhanced¹² and radiation pressure suppressed; and it is a low-metallicity environment, allowing a resolved probe of star formation in conditions similar to those of earlier epochs of the Universe. Current YSO models are based on Milky Way observations, so the LMC allows the analysis of the effect of a different environment on the formation and propagation of jets from YSOs. Until now, only a handful of outflows from massive stars in the LMC^{13,14} have been reported, all of which have been detected in the radio regime with the Atacama Large Millimeter/submillimeter Array (ALMA). The driving sources of these outflows are still deeply embedded in their natal molecular cloud cores and the measured outflows are on sub-parsec scales, with no optical jet counterparts.

The YSO Herbig–Haro (HH) flow¹⁵ reported here was detected in observations of the ionized star-forming region LMC N180 made with the optical integral-field spectrograph Multi Unit Spectroscopic Explorer (MUSE)¹⁶ at the Very Large Telescope (VLT). LMC N180 consists of a classical, bubble-shaped H II region (see Fig. 1) with a radius of about 2.5' (approximately 36 pc). It is located on the border of a giant molecular cloud, it is currently undergoing star formation, and it hosts over 50 stars with masses $M \geq 10M_{\odot}$ – $15M_{\odot}$, as well as several early O-type stars¹⁷.

The jet itself is externally ionized and is detected as blue- and redshifted emission peaks of the H α line. It spans a total of 10 pc and is emerging from a pillar-like structure protruding from the southern

rim of the surrounding ionized star-forming region. The driving source of the jet is probably a MYSO of approximately $12M_{\odot}$ (corresponding to the young stellar object N180-24 in ref. 17), which has formed at the tip of the pillar.

The jet-driving MYSO is optically visible at the origin of the blue and red lobes; this is unusual, as jet-driving MYSOs are usually not visible in the optical wavelength regime owing to the high extinction caused by their embedding material. We suggest that the low dust content of the LMC has aided our investigation by enhancing the ionization feedback from the star on the surrounding matter, thus allowing a situation in which the envelope has been dispersed before the disk and the jet has escaped the pillar.

Although the moderate spectral resolution of MUSE and its limited coverage of blue wavelengths do not allow the determination of

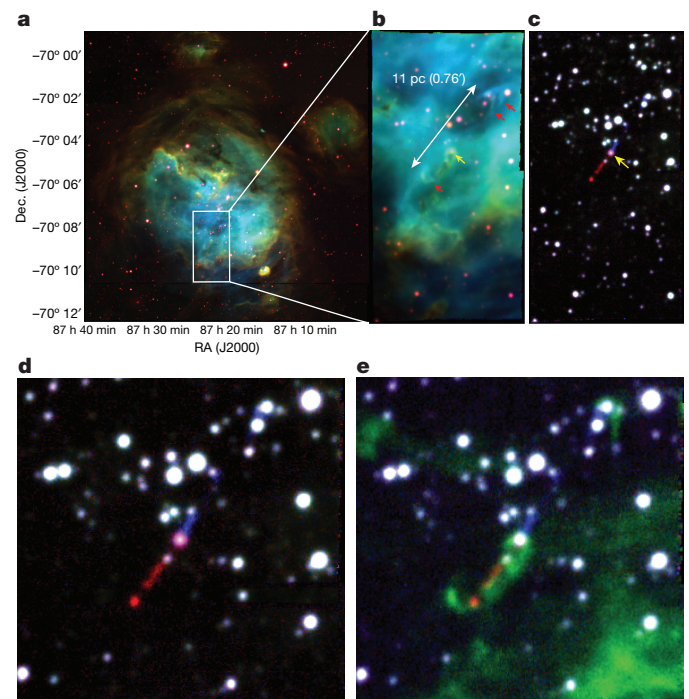


Figure 1 | Three-colour composites of the star-forming region LMC N180 and the jet. **a**, **b**, Three-colour composites of LMC N180 (red, [S II] 6,731 Å; green, H α ; blue, [O III] 5,007 Å). **b**, The red arrows point at the bow shocks and the yellow arrow indicates the jet source. **c**, Three-colour composite of the same region as **b**, where the red and the blue correspond to the red and blue H α emission line peaks, and the green corresponds to the image of the collapsed MUSE data cube. **d**, **e**, Magnified images of the jet shown in **b**. The three-colour composite in **d** is the same as in **a**. In **e**, green corresponds to [S II] 6,731 Å. In all panels, north is up and east is left.

¹School of Physical and Chemical Sciences, University of Canterbury, Christchurch, New Zealand. ²Department of Astronomy, University of Michigan, Ann Arbor, Michigan, USA. ³Institute of Astronomy and Astrophysics, University of Tübingen, Tübingen, Germany. ⁴UK Astronomy Technology Centre, Royal Observatory Edinburgh, Edinburgh, UK.

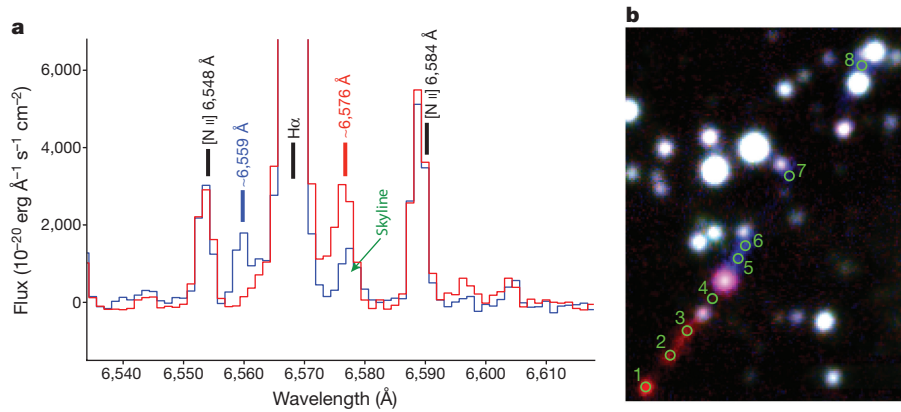


Figure 2 | Spectrum of the red and blue jet lobes. **a**, Co-added spectra of the red and blue jet lobes (colour-coded accordingly), extracted from circular apertures centred on the green circles (labelled 1 for the red lobe and 5 for the blue lobe) in **b**. The estimated signal-to-noise ratios in the spectra were about 92 and 129 for the red and blue lobes, respectively.

the precise spectral type of the star, together with the estimated mass of $12M_{\odot}$ and the absence of He II absorption lines, our observations indicate that the driving source of the jet is an early B-type star (rather than a late O-type star). The jet is associated with HH emission traced by bow-shock structures, where the jet lobes terminate (see Fig. 1). The bow shocks (which, together with the jet, make up the HH 1177 flow) are detected beyond the jet and span 11 pc ($0.76''$) from end to end, making this the second confirmed detection of an HH object beyond our own Galaxy¹⁸, as well as one of the longest jets ever observed.

The detection of emission line peaks together with a spatially resolved continuous structure traced by two distinct velocity components indicates a coherent jet with a spatial orientation in which the red lobe is moving away and the blue lobe is moving towards the observer. The red lobe extends about 3.5 pc ($0.24''$) to the southeast of the pillar, with a position angle of around 144° . The first portion of the red lobe, just below the source (at the position of aperture 4 in Fig. 2), is partly obscured by the dominating pillar emission. It consists of a main segment and a bright terminal knot in close vicinity to the southern bow shock. The blue lobe emerges from the top of the pillar with a position angle of about -32° and spans about 6.5 pc ($0.45''$), although its terminal knot is complicated by the projected vicinity of a star.

The jet is highly collimated along its entire parsec-scale detected length. With an apparent half-width of approximately $R = 0.1$ pc ($0.4''$) throughout, the lower limits for the length-to-half-width ratios are 35 and 65 for the red and blue lobes, respectively. We note that the jet width is an upper limit, as the true width is unresolved in our observations, and the length-to-half-width is therefore a strict lower limit (see Methods). The measured radial velocities that correspond to the wavelength offsets of the red and blue peaks are of the order of $300\text{--}400\text{ km s}^{-1}$, yielding a (non-deprojected) dynamic timescale of the jet in the range $(2.8\text{--}3.7) \times 10^4$ yr. Therefore, despite the short lifetimes of massive stars, the accretion and jet phases are at least of the order of tens of thousands of years.

Figure 2 shows the continuum-subtracted spectra of the red and blue lobes; the red and blue peaks are clearly identified on the right and left of the central H α line. What is seemingly a red peak in the blue spectrum corresponds to an OH skyline doublet¹⁹ at $6,577.183\text{ \AA}$ and $6,577.3863\text{ \AA}$.

From the intensity of the red and blue emission line peaks and the estimated width of the jet body, we compute a mass loss rate of the jet of about $2.9 \times 10^{-6} M_{\odot} \text{ yr}^{-1}$ and a resulting mass accretion rate of around $9.5 \times 10^{-6} M_{\odot} \text{ yr}^{-1}$. These rates are comparable to literature values for embedded MYSOs²⁰, confirming the large mass of the driving source. Furthermore, these values also confirm that the source is young (given that the mass loss and accretion rates are expected to decrease with the

age of the star²⁰), supporting our contention that this is an optically observed jet from an unobscured MYSO.

The total (projected) length of HH 1177 together with the detected bow shocks (about 11 pc) is comparable to some of the largest HH flows observed in the Milky Way^{3,21,22}. However, traditional HH objects are emission-line nebulosities corresponding to shock-excited gas along a protostellar outflow, and direct detection of the jet body is possible with external ionization^{23,24} in massive star-forming regions. In the case of HH 1177, the jet itself is detected, allowing the direct measurement of its length-to-(half) width ratio, extent and velocity, as well as a description of its morphology and spatial orientation. The high degree of collimation and the measured radial velocities of HH 1177 are similar to those found in lower-mass stars^{25,26}. This supports our theoretical knowledge of the connection between accretion disks and magneto-centrifugal ejection, as well as the physics of jet launching and collimation, in which the underlying processes are independent of stellar mass^{4,27,28}. In terms of the accretion–ejection link, the detection of this large-scale MYSO and jet system indicates regular, active disk accretion epochs, which are a key factor in the formation of massive stars. These disk accretion epochs are required to circumvent the radiation pressure problem in the formation of massive stars¹⁰.

Online Content Methods, along with any additional Extended Data display items and Source Data, are available in the online version of the paper; references unique to these sections appear only in the online paper.

Received 14 September; accepted 28 November 2017.

Published online 24 January 2018.

- Reipurth, B., Bally, J. & Devine, D. Giant Herbig–Haro flows. *Astron. J.* **114**, 2708–2735 (1997).
- Frank, A. *et al.* in *Protostars and Planets VI* 451–474 (Univ. Arizona Press, 2014).
- Marti, J. *et al.* HH 80–81: a highly collimated Herbig–Haro complex powered by a massive young star. *Astrophys. J.* **416**, 208–217 (1993).
- Caratti o Garatti, A. *et al.* A near-infrared spectroscopic survey of massive jets towards extended green objects. *Astron. Astrophys.* **573**, L4 (2015).
- Guzmán, A. E. *et al.* Search for ionized jets toward high-mass young stellar objects. *Astrophys. J.* **753**, 51 (2012); erratum **781**, 56 (2014).
- Hirota, T. *et al.* Disk-driven rotating bipolar outflow in Orion Source I. *Nat. Astron.* **1**, 0146 (2017).
- Maud, L. T. *et al.* A distance-limited sample of massive molecular outflows. *Mon. Not. R. Astron. Soc.* **453**, 645–665 (2015).
- Caratti o Garatti, A. *et al.* Disk-mediated accretion bursts in a high-mass young stellar object. *Nat. Phys.* **13**, 276–279 (2017).
- Meyer, D. M.-A. *et al.* On the existence of accretion-driven bursts in massive star formation. *Mon. Not. R. Astron. Soc.* **464**, 90–94 (2017).
- Kuiper, R. *et al.* Circumventing the radiation pressure barrier in the formation of massive stars via disk accretion. *Astrophys. J.* **722**, 1556–1576 (2010).
- Kuiper, R. *et al.* Three-dimensional simulation of massive star formation in the disk accretion scenario. *Astrophys. J.* **732**, 20 (2011).

12. Israel, F. P. *et al.* Carbon monoxide in the Magellanic clouds. *Astrophys. J.* **303**, 186–197 (1986).
13. Fukui, Y. *et al.* High-mass star formation triggered by collision between CO filaments in N159 West in the Large Magellanic Cloud. *Astrophys. J.* **807**, L4 (2015).
14. Shimonishi, T. *et al.* The detection of a hot molecular core in the Large Magellanic Cloud with ALMA. *Astrophys. J.* **827**, 72 (2016).
15. Reipurth, B. & Bally, J. Herbig-Haro flows: probes of early stellar evolution. *Annu. Rev. Astron. Astrophys.* **39**, 403–455 (2001).
16. Bacon, R. *et al.* MUSE commissioning. *The Messenger* **157**, 13–16 (2014).
17. Caulet, A., Gruendl, R. A. & Chu, Y.-H. Young stellar objects in the Large Magellanic Cloud: N63 and N180 H II regions. *Astrophys. J.* **678**, 200–218 (2008).
18. Chu, Y.-H. *et al.* Protostars, dust globules and a Herbig-Haro object in the LMC superbubble N51D. *Astrophys. J.* **634**, L189–L192 (2005).
19. Osterbrock, D. E. *et al.* Night-sky high-resolution spectral atlas of OH and O₂ emission lines for echelle spectrograph wavelength calibration. *Pub. Astr. Soc. Pac.* **108**, 277–308, 1996.
20. Beltrán, M. T. & de Wit, W. J. Accretion disks in luminous young stellar objects. *Astron. Astrophys. Rev.* **24**, 6 (2016).
21. Masqué, J. M. *et al.* Proper motions of the outer knots of the HH 80/81/80N radio-jet. *Astrophys. J.* **814**, 44 (2015).
22. Bally, J. & Devine, D. in *IAU Symposium* (eds Reipurth, B. & Bertout, C.) Vol. 182, 29–38 (Cambridge Univ. Press, 1997).
23. Bally, J. *et al.* Irradiated and bent jets in the Orion nebula. *Astron. J.* **131**, 473–500 (2006).
24. Reipurth, B. *et al.* Protostellar jets irradiated by massive stars. *Nature* **396**, 343–345 (1998).
25. Mundt, R. Observational properties of jets from young stars. In *Proc. 6th Intern. Workshop of the Astron. Observatory of Capodimonte* (eds Errico, L. & Vittone, A. A.) 91–108 (Springer, 1993).
26. Bally, J. *et al.* in *Protostars and Planets V* 215–230 (Univ. Arizona Press, 2007).
27. Pudritz, R. E. *et al.* in *Protostars and Planets V* 277–294 (Univ. Arizona Press, 2007).
28. Königl, A. & Pudritz, R. E. in *Protostars and Planets IV* 759–788 (Univ. Arizona Press, 2000).

Acknowledgements R.K. acknowledges financial support from the Emmy Noether Research Program, funded by the German Research Foundation (DFG) under grant number KU 2849/3-1.

Author Contributions A.F.M. is the Principal Investigator of the MUSE observing programme 096.C-0137(A), which obtained the data used in this work. A.F.M. reduced and analysed the data and wrote the initial manuscript. R.K. provided the theoretical interpretation of the data; C.J.E. analysed the stellar spectrum to determine a first spectral classification. M.R. and P.D.K. provided input concerning the young stellar object jet, pillar observations and jet mass loss rates. All authors commented on the manuscript.

Author Information Reprints and permissions information is available at www.nature.com/reprints. The authors declare no competing financial interests. Readers are welcome to comment on the online version of the paper. Publisher's note: Springer Nature remains neutral with regard to jurisdictional claims in published maps and institutional affiliations. Correspondence and requests for materials should be addressed to A.F.M. (anna.mcleod@canterbury.ac.nz).

Reviewer Information *Nature* thanks A. Guzman and B. Reipurth for their contribution to the peer review of this work.

METHODS

Optical integral-field spectroscopy. The data used for this analysis are optical integral field data from the MUSE instrument¹⁶, which is mounted on the VLT in Chile. MUSE has a field of view of about $1' \times 1'$ and a pixel scale of $0.2''$.

The data were acquired between November and December 2015, and were reduced with the MUSE data reduction pipeline²⁹ in the EsoRex environment using the available standard calibrations for each night. The entire mosaic of region LMC N180 consists of 64 single pointings, each observed twice with a 90° rotation dither pattern and an exposure time of 90 s. The pointings were observed in the MUSE nominal wavelength range (4,650–9,300 Å; resolving power of the spectrograph, 2,000–4,000) and a wide field of view. From the calibrated MUSE data cube, we estimate the noise of the spectra from the continuum flux closest to the analysed lines (from 6,610 Å to 6,660 Å).

Integrated line maps and spectral fitting. The $\text{H}\alpha$, $[\text{S II}]$ 6,731 Å and $[\text{O III}]$ 5,007 Å integrated line maps used to produce the three-colour image of Fig. 1 were obtained with the Python package Spectral Cube (<http://spectral-cube.readthedocs.org>) as for MUSE data of other pillar-like objects^{30,31}. The jet is not visible in the central $\text{H}\alpha$ image; only by searching in the individual slices of the data cube in the region around the $\text{H}\alpha$ line does the jet become evident. We therefore produced integrated line maps centred on the red and blue emission, as for the main emission lines.

To determine the amplitude and central wavelength of the blue- and red-shifted peaks of the $\text{H}\alpha$ line, which trace the two lobes of the bipolar jet, we used the Python package Pyspeckit³² to fit multiple Gaussian components to the emission lines in the region covering the $[\text{N II}]$ and the $\text{H}\alpha$ lines. Because MUSE spectra span approximately 4,600 Å in wavelength, they cover almost all of the nebular emission lines typically found in H II regions, as well as a multitude of skylines, which are particularly dense in the red parts of the spectra. Given the large number of lines, identifying and fitting the continuum across the entire MUSE wavelength range can be challenging and may result in an overestimation of the continuum and a negative baseline after subtraction. We therefore crop the spectra to the range 6,000–6,680 Å to allow a more precise estimate of the local continuum. The fitted spectra are shown in Extended Data Figs 1 and 2. The fit of the blue lobe in apertures 5 and 7 does not appear optimal. Adding a fifth Gaussian component centred between the blue and the $\text{H}\alpha$ lines seems to provide a better fit for the blue peak, but the resulting values of the fit are within the errors of the four-component fit; we therefore do not include the additional component. The best-fit parameters are summarized in Extended Data Tables 1 and 2. Error estimates are taken from the *PySpecKit* fitting routine and correspond to the root mean square of the residuals. For each spectrum shown, we also state the level of noise, which is estimated from the continuum closest to the analysed lines, as described above.

Jet widths and collimation. We measure the (projected) diameter of the two lobes by extracting slices across the jet structure perpendicular to the jet direction at positions 1, 2, 3, 5, 6 and 8 in Fig. 2b (position 4 corresponds to the part of the red lobe covered by the emission from the pillar, and position 7 is contaminated by the emission from a nearby star). We estimate the diameter L of the jet body (and the half-width $R = L/2$) at each position by again fitting Gaussians to the obtained profiles (as shown in Extended Data Fig. 3). These widths are then compared with

the jet length shown in Fig. 1 (see main text). However, owing to a seeing-limited spatial resolution of $0.6''$ (0.15 pc) at the distance of the LMC, the true width of the jet is unresolved and the values obtained from the described fit are strictly upper limits. As a consequence, the resulting length-to-half-width ratios are a strict lower limit.

Mass loss and accretion rate. We compute the mass loss rate by first calculating the electron density n_e from the measured intensity $I_{\text{H}\alpha,\text{red}}$ and $I_{\text{H}\alpha,\text{blue}}$ of the emission line peaks and then combining it with the measured radial velocities V and width L_{pc} of the jet body in parsecs³³:

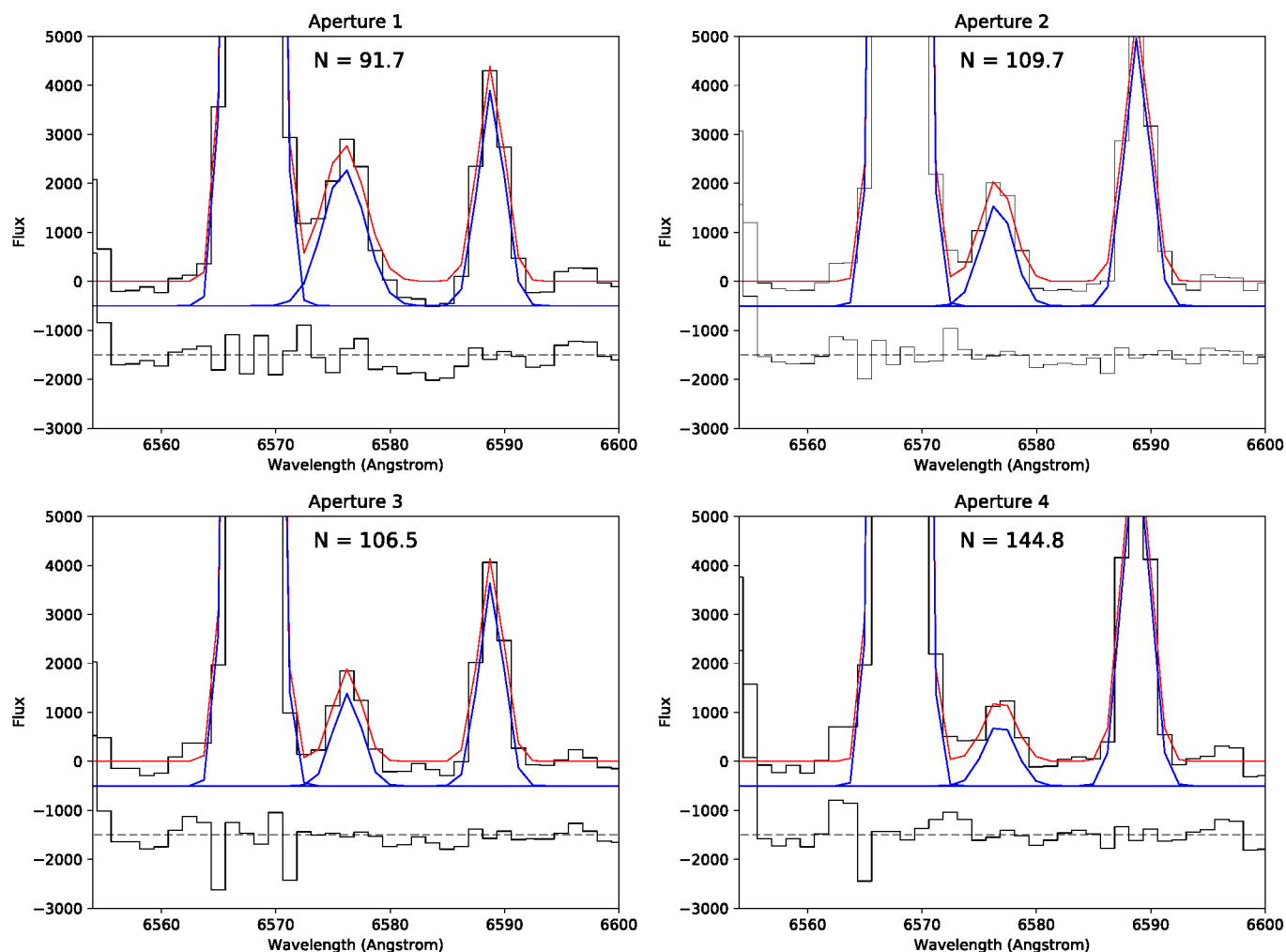
$$n_e = 15.0(I_{\text{H}\alpha}/I_{\text{pc}})^{1/2} \quad (1)$$

$$\dot{M}_{\text{jet}} = \mu m_{\text{H}} n_e V \pi (L/2)^2 f \quad (2)$$

where μ is the mean molecular weight, for which we assume a value of 1.35, m_{H} is the proton mass, V the jet velocity and f a geometric filling factor derived from the morphology of the images. We measure $I_{\text{H}\alpha,\text{red}} \approx (0.224 \pm 0.001) \times 10^{-15} \text{ erg cm}^{-2} \text{ s}^{-1} \text{ arcsec}^{-2}$ from a circular aperture on the terminal red knot (centred on aperture 1) in the integrated intensity map, and use $L \approx (0.08 \pm 0.04) \text{ pc}$ to obtain $n_e \approx (25.13 \pm 0.01) \text{ cm}^{-3}$. Because the width of the jet is not resolved in the MUSE data, we use 0.08 pc as the jet width, which is comparable to that of jet HH 80–81 (from figure 1 in ref. 21), and a large uncertainty of $\pm 50\%$. Together with a radial velocity of $V \approx (363.79 \pm 0.46) \text{ km s}^{-1}$ and $f = 1$, we obtain a mass loss rate of $(1.57 \pm 0.99) \times 10^{-6} M_{\odot} \text{ yr}^{-1}$. Similarly, for the blue lobe, we obtain $I_{\text{H}\alpha,\text{blue}} \approx (0.139 \pm 0.001) \times 10^{-15} \text{ erg cm}^{-2} \text{ s}^{-1} \text{ arcsec}^{-2}$ from aperture 5 and a mass loss rate of $(1.28 \pm 0.81) \times 10^{-6} M_{\odot} \text{ yr}^{-1}$, with $V \approx (376.56 \pm 0.46) \text{ km s}^{-1}$. Finally, we compute the combined mass loss rate to be about $2.85 \times 10^{-6} M_{\odot} \text{ yr}^{-1}$. Assuming a ratio of about 0.3 between the jet mass loss rate and the accretion rate^{34,35}, we obtain a mass accretion rate of about $9.5 \times 10^{-6} M_{\odot} \text{ yr}^{-1}$.

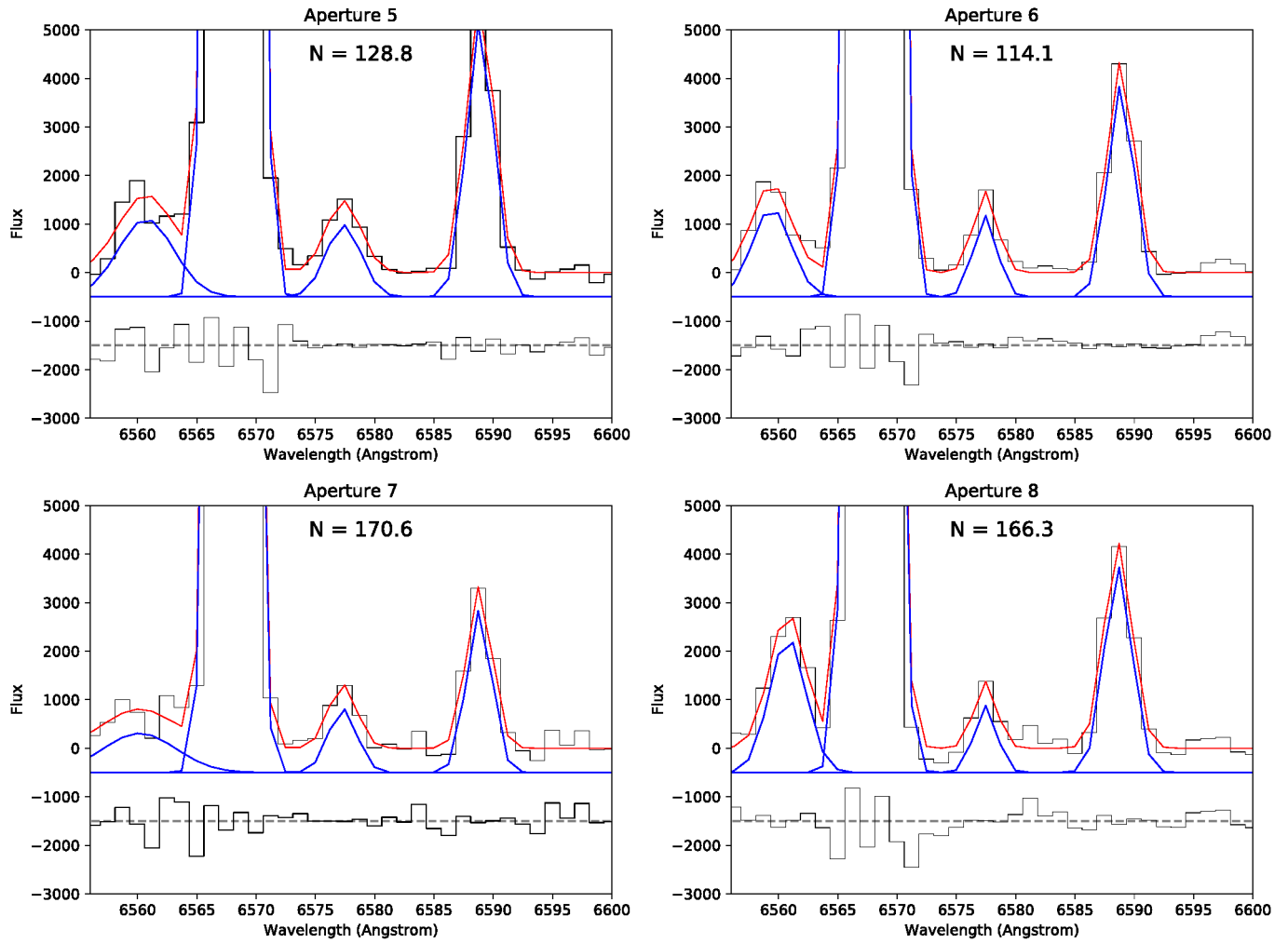
Data availability. The dataset that supports the findings of this study is available in the ESO archive (http://archive.eso.org/eso/eso_archive_main.html) under the observing programme 096.C-0137(A) executed at the VLT (ESO Paranal, Chile). Additional requests can be directed to the corresponding author.

29. Weilbacher, P. Design and capabilities of the MUSE data reduction software and pipeline. *Proc. SPIE* **8451**, 84510B (2012).
30. McLeod, A. F. *et al.* Connecting the dots: a correlation between ionizing radiation and cloud mass-loss rate traced by optical integral field spectroscopy. *Mon. Not. R. Astron. Soc.* **462**, 3537–3569 (2016).
31. McLeod, A. F. *et al.* The Pillars of Creation revisited with MUSE: gas kinematics and high-mass stellar feedback traced by optical spectroscopy. *Mon. Not. R. Astron. Soc.* **450**, 1057–1076 (2015).
32. Ginsburg, A. & Mirocha, J. PySpecKit: Python Spectroscopic Toolkit. *Astrophys. Source Code Lib.* <http://pyspeckit.readthedocs.io> (2011).
33. Smith, N., Bally, J. & Walborn, N. R. HST/ACS $\text{H}\alpha$ imaging of the Carina nebula: outflow activity traced by irradiated Herbig-Haro jets. *Mon. Not. R. Astron. Soc.* **405**, 1153–1186 (2010).
34. Shu, F. *et al.* in *The Origin of Stars and Planetary Systems* (eds Lada, C. J. & Kylafis, N. D.) 193–226 (Springer, 1999).
35. Tomisaka, K. Collapse-driven outflow in star-forming molecular cores. *Astrophys. J.* **502**, L163–L167 (1998).



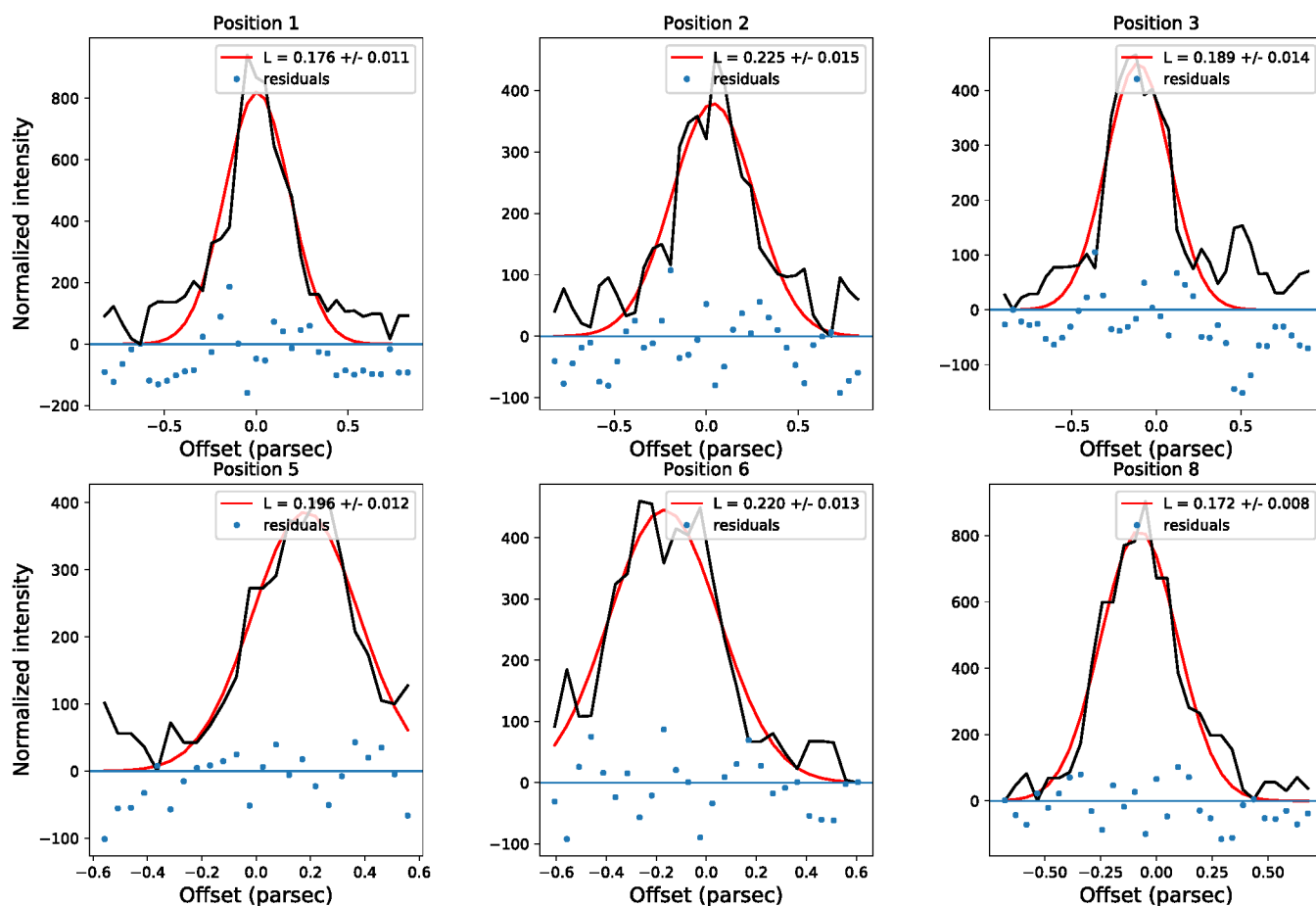
Extended Data Figure 1 | Fitted spectra of the red jet lobe. Co-added spectra of the red lobe of the jet (extracted from a 2-pixel-radius circular aperture centred on the green circles in Fig. 2b), continuum-subtracted and fitted with a three-component Gaussian. The spectrum is shown in black, the fit in red, the single components are plotted in blue and the

residuals of the fit are shown below each spectrum (the latter two are shown with an offset on the y axis for better display). The estimated noise N is stated for each spectrum. The best-fit parameters are summarized in Extended Data Table 1. The flux is in units of $10^{-20} \text{ erg s}^{-1} \text{ \AA}^{-1} \text{ cm}^{-2}$.



Extended Data Figure 2 | Fitted spectra of the blue jet lobe. Co-added spectra of the blue lobe of the jet (extracted from a 2-pixel-radius circular aperture centred on the green circles in Fig. 2b), continuum-subtracted and fitted with a four-component Gaussian. The spectrum is shown in black, the fit in red, the single components are plotted in blue and the

residuals of the fit are shown below each spectrum (the latter two are shown with an offset on the y axis for better display). The estimated noise is stated for each spectrum. The best-fit parameters are summarized in Extended Data Table 2. The flux is in units of $10^{-20} \text{ erg s}^{-1} \text{ \AA}^{-1} \text{ cm}^{-2}$.



Extended Data Figure 3 | Diameter of the jet body. Black curves are the integrated line map intensity profiles along virtual slits perpendicular to the jet axis on the positions of the red (positions 1, 2 and 3) and the blue

lobes (positions 5, 6 and 8) marked in Fig. 2b. Red curves are the best-fit Gaussian profiles; blue diamonds are residuals.

Extended Data Table 1 | Best-fit parameters of the Gaussian fitting to the red lobe

Ap. #	H α			Red peak			[NII]		
	Peak Flux	Centroid	Width	Peak Flux	Centroid	Width	Peak Flux	Centroid	Width
1	82399.0 \pm 416.8	6568.0 \pm 7.5 \times 10 ⁻³	1.2 \pm 7.7 \times 10 ⁻³	3057.0 \pm 331.0	6575.9 \pm 0.3	2.1 \pm 0.3	4649.5 \pm 430.6	6588.8 \pm 0.1	1.1 \pm 0.1
2	99262.3 \pm 570.9	6568.1 \pm 7.5 \times 10 ⁻³	1.15 \pm 7.7 \times 10 ⁻³	2184.6 \pm 466.8	6576.5 \pm 0.4	1.7 \pm 0.4	5604.3 \pm 554.9	6588.8 \pm 0.1	1.2 \pm 0.1
3	80343.2 \pm 429.0	6568.0 \pm 7.2 \times 10 ⁻³	1.2 \pm 7.4 \times 10 ⁻³	2027.6 \pm 390.9	6576.3 \pm 0.3	1.4 \pm 0.3	4281.4 \pm 431.3	6588.8 \pm 0.1	1.1 \pm 0.1
4	140227.0 \pm 735.8	6568.0 \pm 6.5 \times 10 ⁻³	1.1 \pm 6.8 \times 10 ⁻³	1132.7 \pm 485.0	6576.2 \pm 1.2	2.4 \pm 1.2	7338.1 \pm 691.4	6588.7 \pm 0.1	1.2 \pm 0.1

The spectra and fits are shown in Extended Data Fig. 1. Fluxes are in units of 10⁻²⁰ erg s⁻¹ Å⁻¹ cm⁻², centroids and widths are in Å.

Extended Data Table 2 | Best-fit parameters of the Gaussian fitting to the blue lobe

Ap. #	Blue			H α			Sky		
	Peak Flux	Centroid	Width	Peak Flux	Centroid	Width	Peak Flux	Centroid	Width
5	1606.5 \pm 203.2	6560.7 \pm 0.3	2.3 \pm 0.4	159788.0 \pm 295.7	6568.1 \pm 2.4 $\times 10^{-3}$	1.1 \pm 2.5 $\times 10^{-3}$	1484.4 \pm 251.8	6577.4 \pm 0.3	1.5 \pm 0.3
6	1834.4 \pm 210.6	6559.4 \pm 0.2	1.6 \pm 0.2	126890.0 \pm 258.1	6568.1 \pm 2.6 $\times 10^{-3}$	1.1 \pm 2.6 $\times 10^{-3}$	1677.1 \pm 257.4	6577.4 \pm 0.2	1.0 \pm 0.2
7	808.1 \pm 153.9	6560.2 \pm 0.7	3.1 \pm 0.9	85319.3 \pm 249.3	6568.0 \pm 3.7 $\times 10^{-3}$	1.1 \pm 4.0 $\times 10^{-3}$	1317.6 \pm 229.2	6577.3 \pm 0.2	1.2 \pm 0.2
8	2792.7 \pm 261.5	6560.8 \pm 0.2	1.5 \pm 0.2	79684.5 \pm 300.5	6567.9 \pm 5.0 $\times 10^{-3}$	1.2 \pm 5.1 $\times 10^{-3}$	1378.0 \pm 310.8	6577.5 \pm 0.3	0.9 \pm 0.2

The spectra and fits are shown in Extended Data Fig. 2. Fluxes are in units of 10⁻²⁰ erg s⁻¹ Å⁻¹ cm⁻², centroids and widths are in Å (the parameters of the [N II] line are not reported in this table because they are not directly relevant).

Pulsating aurora from electron scattering by chorus waves

S. Kasahara¹, Y. Miyoshi², S. Yokota³, T. Mitani⁴, Y. Kasahara⁵, S. Matsuda², A. Kumamoto⁶, A. Matsuoka⁴, Y. Kazama⁷, H. U. Frey⁸, V. Angelopoulos⁹, S. Kurita², K. Keika¹, K. Seki¹ & I. Shinohara⁴

Auroral substorms, dynamic phenomena that occur in the upper atmosphere at night, are caused by global reconfiguration of the magnetosphere, which releases stored solar wind energy^{1,2}. These storms are characterized by auroral brightening from dusk to midnight, followed by violent motions of distinct auroral arcs that suddenly break up, and the subsequent emergence of diffuse, pulsating auroral patches at dawn^{1,3}. Pulsating aurorae, which are quasiperiodic, blinking patches of light tens to hundreds of kilometres across, appear at altitudes of about 100 kilometres in the high-latitude regions of both hemispheres, and multiple patches often cover the entire sky. This auroral pulsation, with periods of several to tens of seconds, is generated by the intermittent precipitation of energetic electrons (several to tens of kiloelectronvolts) arriving from the magnetosphere and colliding with the atoms and molecules of the upper atmosphere^{4–7}. A possible cause of this precipitation is the interaction between magnetospheric electrons and electromagnetic waves called whistler-mode chorus waves^{8–11}. However, no direct observational evidence of this interaction has been obtained so far¹². Here we report that energetic electrons are scattered by chorus waves, resulting in their precipitation. Our observations were made in March 2017 with a magnetospheric spacecraft equipped with a high-angular-resolution electron sensor and electromagnetic field instruments. The measured^{13,14} quasiperiodic precipitating electron flux was sufficiently intense to generate a pulsating aurora, which was indeed simultaneously observed by a ground auroral imager.

Theories and computer simulations have provided a promising explanation for the origin of electron precipitation: the interaction between electrons and whistler-mode chorus waves near the magnetospheric equator^{7,8,15,16}. After chorus waves are generated at the equator, they propagate towards higher latitudes (grey wavy arrows in Fig. 1) and interact with bouncing, counter-streaming electrons in both hemispheres. As these electrons are scattered by the Lorentz force of the chorus waves, some of them become nearly aligned with the field, fall into the empty electron loss cone (blue open arrow in Fig. 1a), fill it (blue filled arrows in Fig. 1a), and precipitate into the upper atmosphere (top left in Fig. 1a).

Data from the THEMIS (Time History of Events and Macroscale Interactions during Substorms) spacecraft and ground-based imagers have shown a correlation between chorus-wave modulation and auroral patch pulsation^{9,10}. Geosynchronous satellite measurements have revealed a correlation between electron flux modulation and auroral pulsation¹⁷. However, direct evidence of interaction between chorus waves and precipitating electrons at the source region—the connection needed to verify the whistler-mode chorus–electron interaction theory

of pulsating aurorae—has not been obtained. This is principally because of the large acceptance angle of earlier space plasma instruments, which prohibited them from distinguishing small loss cones in the equatorial magnetosphere. Thus, it has been difficult to directly establish the association between precipitating electrons hidden inside loss cones and the chorus waves. The high angular resolution of our instrumentation has enabled us to overcome this limitation.

On 2017 March 27, auroral pulsations were observed by the ground-based auroral All-Sky Imagers (ASIs) of the THEMIS mission¹⁸ (Fig. 2) when a magnetic storm with auroral substorm characteristics developed. Auroral snapshots illustrate the appearance and disappearance of pulsating auroral patches. The ionospheric footprint of the Exploration of energization and Radiation in Geospace (ERG, also called Arase) spacecraft^{13,14}, which was launched in December 2016 and started observations in March 2017, was traced with an empirical magnetic field model¹⁹ and plotted over the auroral images (red crosses in Fig. 2). The model footprint is well within the fields of view of the ASIs in which the auroral pulsations can be clearly detected (see also Supplementary Video 1). Depending on the instantaneous magnetospheric configuration, however, the actual footprint may be displaced from the model by a few degrees in magnetic latitude and longitude²⁰ (fewer than several hundred kilometres in both directions). Therefore, the model footprint should be regarded as approximately located in a wide area where pulsating aurorae were observed (we note that the field of view of an ASI is about 1,000 km across, larger than the mapping uncertainties). Electrons with sufficient energy flux to cause a visible aurora were observed near the equator, closely correlated with chorus waves when the footprint of ERG was located in a region replete with pulsating auroral patches.

During morning hours in magnetic local time, ERG captured a correlation between wave activity and particle flux modulations near the magnetospheric equator. During the 30-min duration of the observation near the equator, waves are seen intermittently in the power spectra of the magnetic (Fig. 3a) and electric fields (Extended Data Fig. 1a) in both the lower-band ($<0.5f_{ce}$) and upper-band ($>0.5f_{ce}$) frequency ranges (where f_{ce} is the electron gyrofrequency). Despite dynamic chorus wave activity, northward-streaming electron fluxes outside the loss cone (with pitch angle, the angle between the particle velocity and the local magnetic field, from 20° to 40°) are relatively stable and do not show any apparent correlation with the waves (Fig. 3c). This is consistent with the absence of correlation between electron flux and chorus waves in previous observations.

Dramatic modulations of the electron flux in concert with chorus waves do occur in the loss cone, however. The northward loss-cone electron flux (Fig. 3b), as measured by the Medium-Energy Particle experiments – electron analyser (MEP-e) onboard ERG with a

¹Department of Earth and Planetary Science, School of Science, University of Tokyo, 7-3-1 Hongo, Bunkyo-ku, Tokyo, Japan. ²Institute for Space-Earth Environmental Research, Nagoya University, Furo-cho, Chikusa-ku, 464-8601 Nagoya, Aichi, Japan. ³Department of Earth and Space Science, Graduate School of Science, Osaka University, 1-1 Machikaneyama-cho, Toyonaka, Osaka, Japan.

⁴Institute of Space and Astronautical Science, 3-1-1 Yoshinodai, Chuo-ku, Sagami-hara, Kanagawa, Japan. ⁵Graduate School of Natural Science and Technology, Kanazawa University, Kakuma-machi, Kanazawa, Ishikawa, Japan. ⁶Graduate School of Science, Tohoku University, 6-3 Aoba, Aramaki, Aoba-ku, Sendai 980-8578 Japan. ⁷Academia Sinica Institute of Astronomy and Astrophysics, 11F Astronomy-Mathematics Building, AS/NTU, No. 1, Sec. 4, Roosevelt Road, Taipei 10617, Taiwan. ⁸Space Sciences Laboratory, University of California, Berkeley, California 94720-7450, USA. ⁹Department of Earth, Planetary and Space Sciences, University of California, Los Angeles, California 90095-1567, USA.

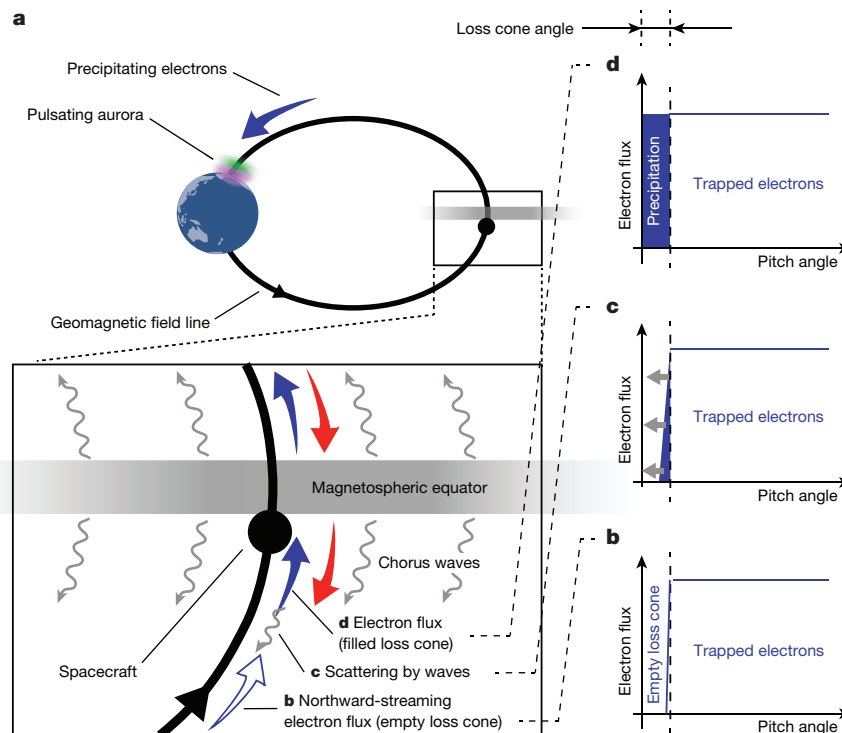


Figure 1 | Schematic of electron scattering by chorus waves, resulting in a pulsating aurora. **a**, The open blue arrow represents northward-streaming electrons with an empty loss cone (**b**) before chorus waves interact with them (**c**). The blue filled arrows represent the same electrons but with a filled loss cone (**d**) after their interaction with chorus waves

(pitch-angle scattering by waves). The red arrows represent loss-cone-filling electrons streaming southwards. The spacecraft location is denoted by a black filled circle. **b–d**, The evolution of the electron PAD. Because chorus activity is intermittent, loss cone filling and depletion are repeated, causing auroral pulsations.

3.5° field of view (full-width at half-maximum), shows repeated enhancements and depletions over a broad energy range from 10 keV to 30 keV, in striking correspondence with bursts of lower-band chorus waves (Fig. 3a).

The correlation between chorus waves and loss-cone electron flux is more clearly presented in Fig. 4, which focuses on the flux of 24.5-keV electrons (selected because of the good loss-cone coverage) and a magnetic wave power spectral density of 0.38–0.64 kHz. This combination of energy and frequency satisfies the cyclotron resonance condition²¹ (thus enabling considerable electron scattering) if we assume an electron density of 3 cm^{-3} , which is typical of this region²², and it is also consistent with the observed frequency of the faint signature of an upper hybrid resonance wave (Extended Data Fig. 1a). The excellent correlation between loss-cone electrons (black solid lines in Fig. 4) and chorus waves (blue dash-dotted lines in Fig. 4) indicates that wave–particle interaction is indeed taking place. Upon close examination of Fig. 4, we see that the loss-cone flux is strongly modulated on a timescale

of 10 s (or less, although the time resolution of the loss-cone measurement is 8 s, and thus shorter periods cannot be resolved), within the typical range of auroral pulsations. As expected from low-altitude observations^{5,11}, the flux is modulated by a factor of 2 to 3. Furthermore, when the loss cone is filled, the measured electron energy flux in the atmosphere is sufficient to excite visible aurorae. Specifically, it is several times $10^9 \text{ keV cm}^{-2} \text{ s}^{-1}$ or several $\text{erg cm}^{-2} \text{ s}^{-1}$ —comparable to, but above, the threshold for visible aurorae²³ (Extended Data Fig. 2 further illustrates the correlation between auroral patch pulsation and the loss-cone electron flux, as well as the chorus waves).

Figure 4 also illustrates that the variability in the quasiparallel flux outside the loss cone (shown by black dashed lines) is nearly stable compared to the dynamic modulation of the loss-cone flux and chorus wave power. This indicates that the observed electron flux just outside the loss cone does not provide clear evidence of precipitation, which explains why previous measurements did not reveal the wave–particle correlation that causes pulsating aurorae.

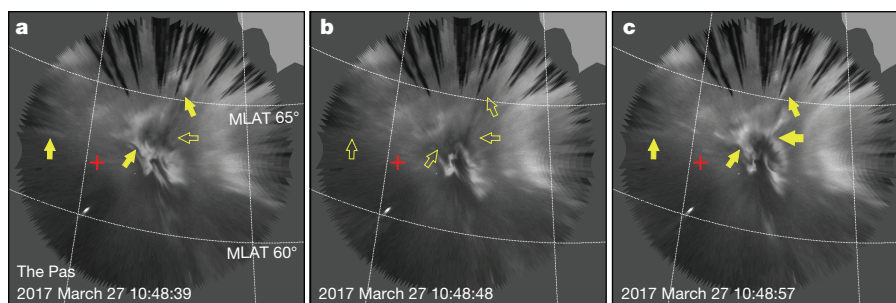


Figure 2 | Auroral snapshots around the footprint of ERG. Successive clear-sky images (10:48:39 to 10:48:57 UT) from a ground station (the Pas). Distinct pulsating patches in the field of view of the Pas are indicated by yellow arrows. The filled and open arrows correspond to pulsations that are ‘on’ (bright aurora) or ‘off’ (no aurora), respectively.

The red crosses show the nominal spacecraft footprint. The dotted lines illustrate magnetic coordinates every 5° in latitude and 15° in longitude, respectively. Supplementary Video 1 shows the full motion of the pulsating auroral patches in a 3-s cadence. MLAT, magnetic latitude.

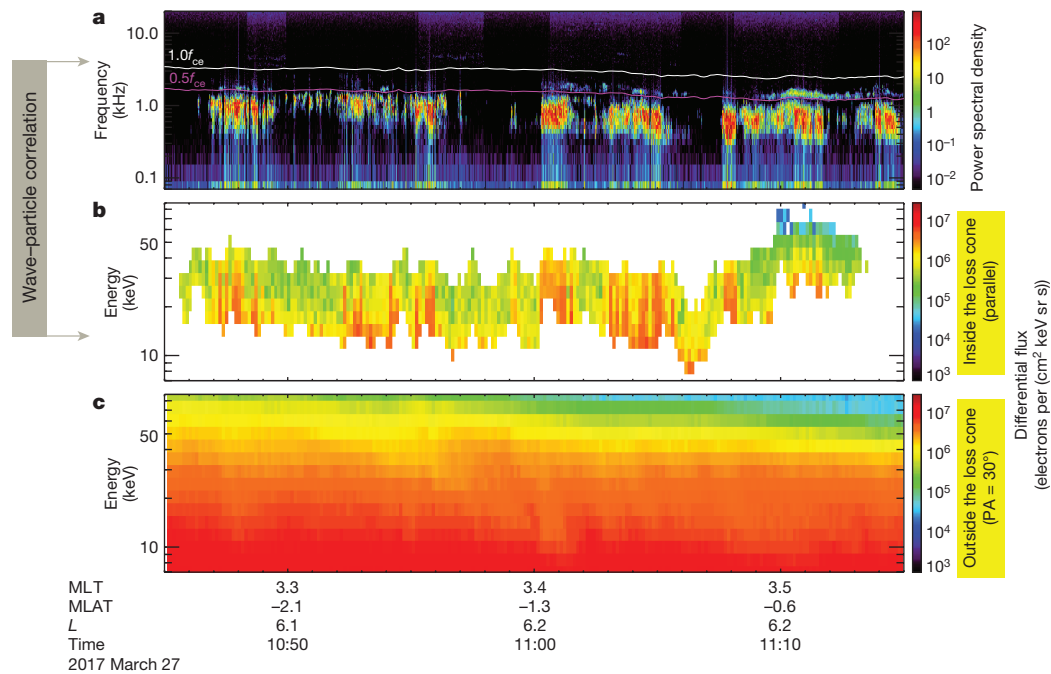


Figure 3 | In situ observations by ERG. **a**, Frequency–time spectrogram of the magnetic field power spectral density (in square picoteslas per hertz), showing chorus waves. The magenta and white lines indicate $0.5f_{ce}$ and $1.0f_{ce}$, respectively, relative to the local magnetic field. **b**, **c**, Energy–time spectrograms for differential fluxes of electrons (expressed in electrons per $\text{cm}^2 \text{ keV sr s}$) in the loss cone (pitch angles $PA < 2^\circ$) (**b**) and outside

the loss cone, but quasiparallel to the magnetic field ($PA = 20^\circ\text{--}40^\circ$) (**c**). In **b**, white areas indicate absence of loss-cone measurements owing to the instrument's limited field of view. MLT, magnetic local time of the spacecraft; L, distance (in Earth radii) where a magnetic field line passing through the spacecraft crosses the magnetospheric equator.

The interpretation of this observation is illustrated in Fig. 1 (bottom left box). The spacecraft was in the Southern Hemisphere but quite close to the magnetospheric equator. The loss cone of the northward-streaming electrons, which is empty during quiet periods, fills with scattered electrons as southward-propagating chorus waves emerge. The evolution of the pitch-angle distribution (PAD) of the northward-streaming electron flux is schematically shown in the right panels of Fig. 1b–d. On the other hand, the electron flux in the southward-streaming loss cone (red arrows) is also seen in the observation (Extended Data Fig. 1d). Although this flux is also modulated (that is,

varies with time), the correlation with the chorus waves is apparently weaker than that of the northward loss-cone flux (Fig. 3b and Extended Data Fig. 1c). For example, chorus waves were absent from 10:56 to 11:00 universal time (UT), while the southward-streaming loss cone continued to be filled. This can be expected because southward-streaming electrons must interact with northward-propagating chorus waves (presumably present in the Northern Hemisphere), which are not necessarily symmetrical with southward-propagating chorus waves.

We determined the location and physical mechanism of electron scattering into the loss cone and subsequent precipitation of energetic

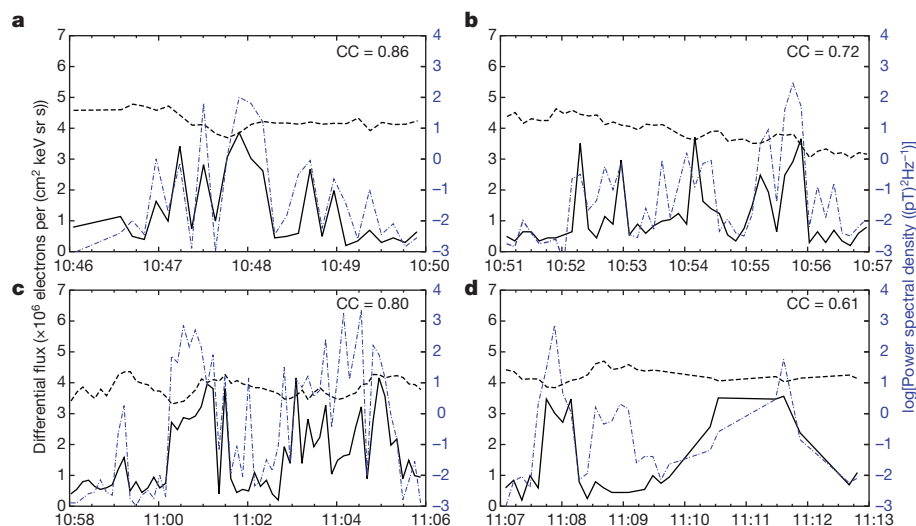


Figure 4 | Correlations between electron flux and wave power spectral density. The black solid line shows the modulation of the loss-cone electron flux ($PA < 2^\circ$); the black dashed line indicates the nearly stable electron flux outside the loss cone ($PA = 20^\circ\text{--}40^\circ$). The blue dashed-dotted line shows the wave magnetic field power spectral density. The electron

energy is 24.5 keV. The frequencies of the power spectral density are 0.64 kHz for **a–c** and 0.38 kHz for **d**, selected according to the resonance condition. The correlation coefficients (CC) between the loss-cone differential flux and the logarithmic power spectral density are shown.

electrons, which results in a pulsating aurora. Whether these results can be generalized across radial distances from Earth, different local times and geomagnetic activity conditions is yet to be determined. Comparing loss-cone fluxes with other potential scattering mechanisms, such as electrostatic electron cyclotron harmonic waves⁷ and large-amplitude parallel electric fields¹², for which the correlated energy range is typically lower than that discussed here, would help to determine whether other wave types make a similar contribution to scattering. The physical process presented here should apply to the aurorae of Jupiter and Saturn, where chorus waves have been detected^{24,25}, and may also operate at other magnetized astrophysical objects.

Online Content Methods, along with any additional Extended Data display items and Source Data, are available in the online version of the paper; references unique to these sections appear only in the online paper.

Received 19 September; accepted 21 December 2017.

1. Akasofu, S. I. *Polar and Magnetospheric Substorms* 22–31, 222–224 (Springer, 1968).
2. Angelopoulos, V. *et al.* Tail reconnection triggering substorm onset. *Science* **321**, 931–935 (2008).
3. Duthie, D. D. & Scourfield, M. W. J. Aurorae and closed magnetic field lines. *J. Atmos. Terr. Phys.* **39**, 1429–1434 (1977).
4. Johnstone, A. D. Pulsating aurora. *Nature* **274**, 119–126 (1978).
5. McEwen, D. J. & Duncan, C. N. A campaign to study pulsating auroras. *Can. J. Phys.* **59**, 1029–1033 (1981).
6. Lessard, M. R. in *Auroral Phenomenology and Magnetospheric Processes: Earth And Other Planets* (eds Keiling, A. *et al.*) 55–68 (American Geophysical Union, 2012).
7. Ni, B. *et al.* Origins of the Earth's diffuse auroral precipitation. *Space Sci. Rev.* **200**, 205–259 (2016).
8. Thorne, R. M., Ni, B., Tao, X., Horne, R. B. & Meredith, N. P. Scattering by chorus waves as the dominant cause of diffuse auroral precipitation. *Nature* **467**, 943–946 (2010).
9. Nishimura, Y. *et al.* Identifying the driver of pulsating aurora. *Science* **330**, 81–84 (2010).
10. Nishimura, Y. *et al.* Multievent study of the correlation between pulsating aurora and whistler mode chorus emissions. *J. Geophys. Res.* **116**, A11221 (2011).
11. Miyoshi, Y. *et al.* Relation between fine structure of energy spectra for pulsating aurora electrons and frequency spectra of whistler mode chorus waves. *J. Geophys. Res. Space Phys.* **120**, 7728–7736 (2015).
12. Mozer, F. S., Agapitov, O. V., Hull, A., Lejosne, S. & Vasko, I. Y. Pulsating auroras produced by interactions of electrons and time domain structures. *J. Geophys. Res. Space Phys.* **122**, 8604–8616 (2017).
13. Miyoshi, Y. *et al.* in *Dynamics of the Earth's Radiation Belts and Inner Magnetosphere* (eds Summers, D. *et al.*) 103–116 (American Geophysical Union, 2012).
14. Miyoshi, Y. *et al.* Geospace exploration project: Arase (ERG). *J. Phys. Conf. Ser.* **869**, 012095 (2017).
15. Kennel, C. F. & Petschek, H. E. Limit on stably trapped particle fluxes. *J. Geophys. Res.* **71**, 1–28 (1966).
16. Trakhtengerts, V. Yu., Tagirov, V. R. & Chernous, S. A. A circulating cyclotron maser and pulsed VLF emissions. *Geomagn. Aeron.* **26**, 77–82 (1986).
17. Jaynes, A. N. *et al.* Pulsating auroral electron flux modulations in the equatorial magnetosphere. *J. Geophys. Res. Space Phys.* **118**, 4884–4894 (2013).
18. Mende, S. *et al.* The THEMIS array of ground-based observatories for the study of auroral substorms. *Space Sci. Rev.* **141**, 357–387 (2008).
19. Tsyganenko, N. A. & Sitnov, M. I. Modeling the dynamics of the inner magnetosphere during strong geomagnetic storms. *J. Geophys. Res.* **110**, A03208 (2005).
20. Nishimura, Y. *et al.* Estimation of magnetic field mapping accuracy using the pulsating aurora-chorus connection. *Geophys. Res. Lett.* **38**, L14110 (2011).
21. Horne, R. B. & Thorne, R. M. Potential waves for relativistic electron scattering and stochastic acceleration during magnetic storms. *Geophys. Res. Lett.* **25**, 3011–3014 (1998).
22. Sheeley, B. W., Moldwin, M. B., Rassoul, H. K. & Anderson, R. R. An empirical plasmasphere and trough density model: CRRES observations. *J. Geophys. Res.* **106**, 25631–25641 (2001).
23. Yahnin, A. G., Sergeev, V. A., Gvozdevsky, B. B. & Vennerstrom, S. Magnetospheric source region of discrete auroras inferred from their relationship with isotropy boundaries of energetic particles. *Ann. Geophys.* **15**, 943–958 (1997).
24. Katoh, Y. *et al.* Whistler mode chorus enhancements in association with energetic electron signatures in the Jovian magnetosphere. *J. Geophys. Res.* **116**, A02215 (2011).
25. Menietti, J. D. *et al.* Saturn chorus intensity variations. *J. Geophys. Res. Space Phys.* **118**, 5592–5602 (2013).

Supplementary Information is available in the online version of the paper.

Acknowledgements The observations presented here were obtained with the help of Mitsubishi Heavy Industries, Ltd, Meisei Electric Co., Ltd, Hamamatsu Photonics Co. Ltd, YS DESIGN Co., Ltd, NIPPI Co. Ltd, Sumitomo Heavy Industries, Ltd and TIERRA TECNICA Co. Ltd. We acknowledge the work of the members of the ERG project team over several years. Y.M. is supported by JSPS Kakenhi (15H05747, 15H05815 and 16H06286). Y. Kasahara is supported by JSPS Kakenhi (16H04056 and 16H01172). H.U.F. is supported by grant AGS-1004736 from the National Science Foundation (NSF) of the USA. I.S. is supported by JSPS Kakenhi (17H06140). We thank NASA for contract NAS5-02099, S. Mende and E. Donovan for use of the ASI data, the Canadian Space Agency for logistical support in fielding and data retrieval from the ground-based observatory stations, and the NSF for support of the Ground-based Imager and Magnetometer Network for Auroral Studies programme through grant AGS-1004736. The ERG (Arase) satellite science data is available from the ERG Science Centre operated by the Institute of Space and Astronautical Science of the Japan Aerospace eXploration Agency and the Institute for Space–Earth Environmental Research of Nagoya University (<https://ergsc.isee.nagoya-u.ac.jp/index.shtml.en>). We are grateful to J. Hohl for assistance in editing the manuscript. We also thank N. Umemura for assistance in source data archiving. S. Kasahara thanks T. Mukai and M. Fujimoto for discussions.

Author Contributions S. Kasahara developed the MEP-e instrument used in this study with S.Y. and T.M., identified the event, analysed the combined dataset and wrote the paper. Y.M. oversaw the production of the combined dataset and discussed its interpretation. Y. Kasahara, S.M. and A.K. provided Plasma Wave Experiment data and discussed the interpretation. A.M. provided MaGnetic Field experiment data. Y. Kazama assisted in the evaluation of MEP-e data through comparison with the Low-Energy Particle experiments – electron analyser. H.U.F. and V.A. provided ASI/THEMIS data and discussed the event and presentation of the results. S. Kurita evaluated the spacecraft footprint with Y.M. and discussed the event. K.K. and K.S. discussed the event and presentation. I.S. oversaw the ERG project and discussed the interpretation of the event. All authors reviewed the manuscript.

Author Information Reprints and permissions information is available at www.nature.com/reprints. The authors declare no competing financial interests. Readers are welcome to comment on the online version of the paper. Publisher's note: Springer Nature remains neutral with regard to jurisdictional claims in published maps and institutional affiliations. Correspondence and requests for materials should be addressed to S. Kasahara (s.kasahara@eps.s.u-tokyo.ac.jp).

METHODS

Electron analyser. The key observation in our dataset is the electron measurement made by the MEP-e sensor onboard the ERG spacecraft. The sensor comprises an electrostatic analyser (ESA) specifically designed for energetic particles²⁶ and avalanche photodiodes²⁷ (APDs). The ESA is an energy filter covering 7–87 keV with an energy resolution of 8%. The angular resolution is determined by combining the focusing property of the ESA with the size of the detector (or the APD). The ESA has a disk-like, 2π -rad field of view divided into 16 narrow elements, each of which corresponds to an APD. Using the spacecraft's spin motion, a full solid angle is swept (with certain dead angles due to gaps between detectors). Depending on the geometry (more specifically, the angle between the spacecraft's spin axis and the magnetic field), MEP-e may see the magnetic field direction (and thus observe the loss cone) once or twice in one spacecraft spin, as in the presented case. The sensor may also miss the magnetic field directions (the magnetic field direction drops at the gaps) or the loss cone may be observed for a longer time (if the spin axis is along the magnetic field direction). Neither of these scenarios occurred in the time period reported here.

Angular resolution. The most important property of the MEP-e sensor for this study—the angular resolution in two orthogonal directions—is shown in Extended Data Fig. 3. These calibration data were obtained by pre-flight laboratory experiments. Profiles are essentially the same for all 16 channels. Here the data are modelled with a Gaussian shape and a full-width at half-maximum of 3.5° for use in the evaluation of the loss-cone determination discussed below.

Loss cone determination. In Figs 3b and 4, as well as in Extended Data Fig. 1c and d, we have plotted the loss-cone electron flux. In these analyses, we used the following criterion for loss-cone measurements: when the angle between the centre of the field of view of the MEP-e and the magnetic field is smaller than 2° , the detected electrons are inside the loss cone. This approach needs caution

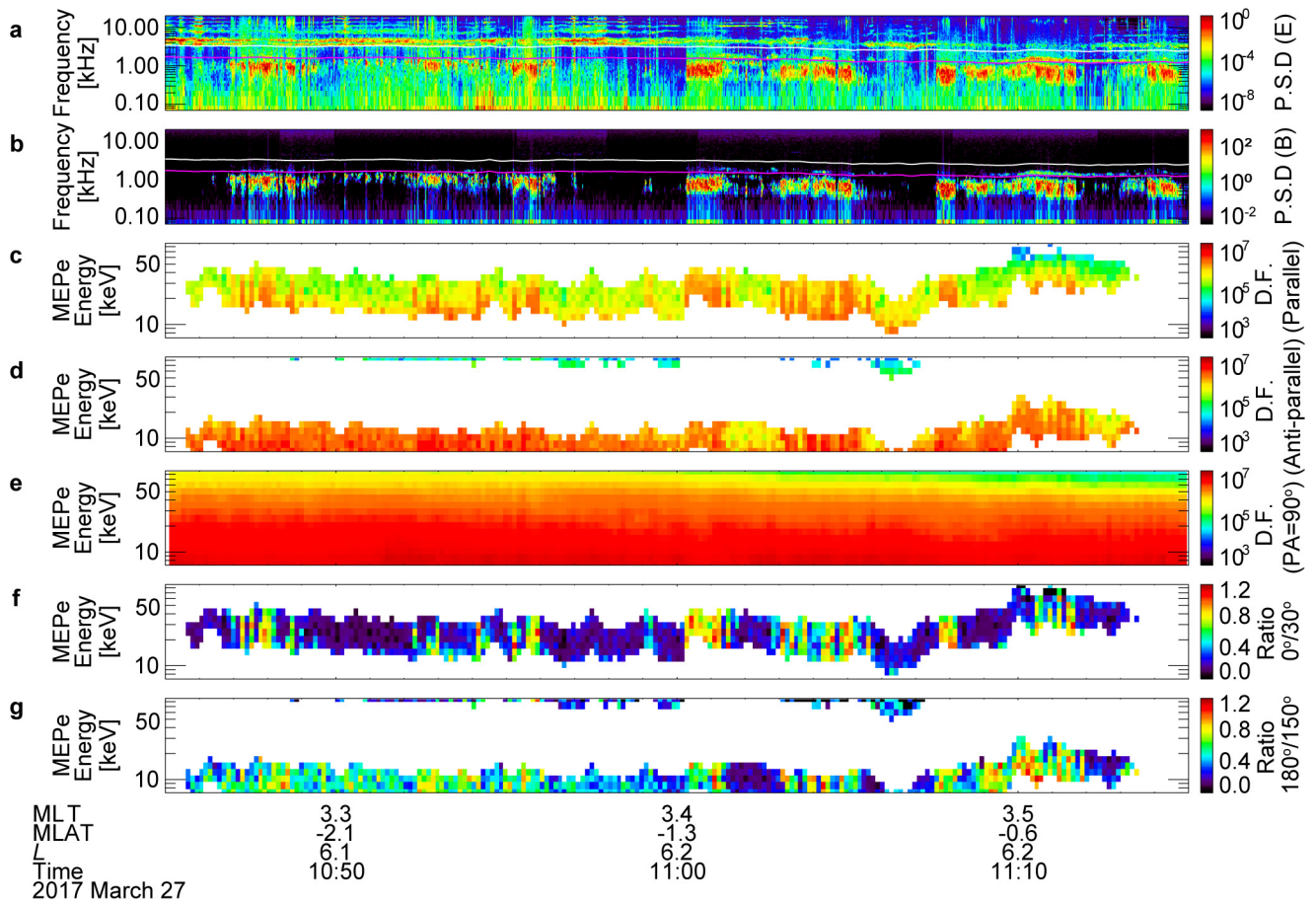
regarding contamination from electrons outside the loss cone, because a fraction of the field of view can extend outside the loss cone. We carefully evaluated this effect (Extended Data Fig. 4) and found it to be insignificant (although not negligible), confirming the robustness of our analyses.

Estimation of precipitating electron energy flux. The downward electron energy flux F at the ionosphere, which contributes to the auroral illumination, is estimated as $F \approx (B_i/B_{eq}) E J_{eq} \Delta\Omega \Delta E$, where the parameters are the magnetic field strength at the ionosphere ($B_i \approx 55,000$ nT) and at the equator (B_{eq}), the electrons' characteristic energy (E), the differential flux at the equator (J_{eq}), the solid angle of the loss cone ($\Delta\Omega$) and the energy range of the precipitating electrons (ΔE). On the basis of our *in situ* observation, we take $B_{eq} \approx 100$ nT, $E \approx 20$ keV, $J_{eq} \approx 4 \times 10^6$ keV cm⁻² sr⁻¹ s⁻¹ keV⁻¹ (here we take the peak value), $\Delta\Omega \approx 6 \times 10^{-3}$ sr and $\Delta E \approx 20$ keV to obtain a downward electron energy flux of about 5×10^9 keV cm⁻² s⁻¹, or 8 erg cm⁻² s⁻¹.

Data availability. The ERG data presented here are publicly available from the ERG science centre website (<https://ergsc.isee.nagoya-u.ac.jp/dataset/2017.1-1001.shtml.en>). THEMIS-ASI data that support the findings of this study are publicly available at http://themis.ssl.berkeley.edu/data_all.shtml.

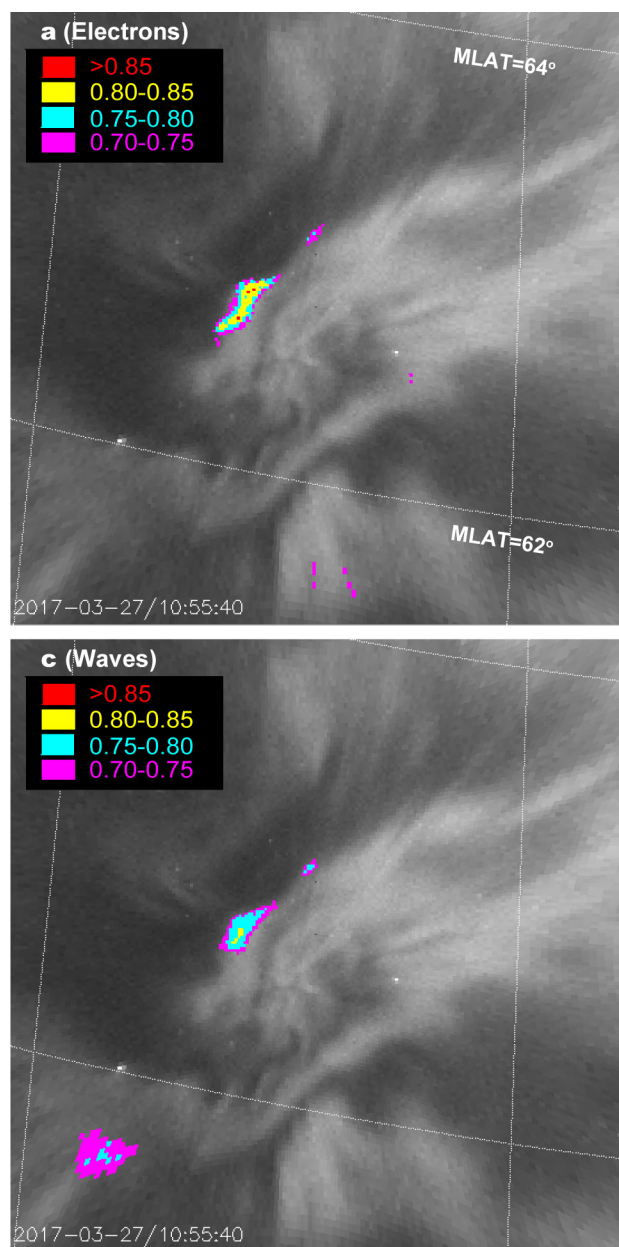
Code availability. The software used to read and analyse the data, part of the publicly available SPEDAS software package, is available at <http://themis.ssl.berkeley.edu/software.shtml> and can be used without any restrictions. All data have a common data file format (<https://cdf.gsfc.nasa.gov/>).

26. Kasahara, S. *et al.* Cusp type electrostatic analyzer for measurements of medium energy charged particles. *Rev. Sci. Instrum.* **77**, 123303 (2006).
27. Kasahara, S., Takashima, T. & Hirahara, M. Variability of the minimum detectable energy of an APD as an electron detector. *Nucl. Instr. Meth. A* **664**, 282–288 (2012).

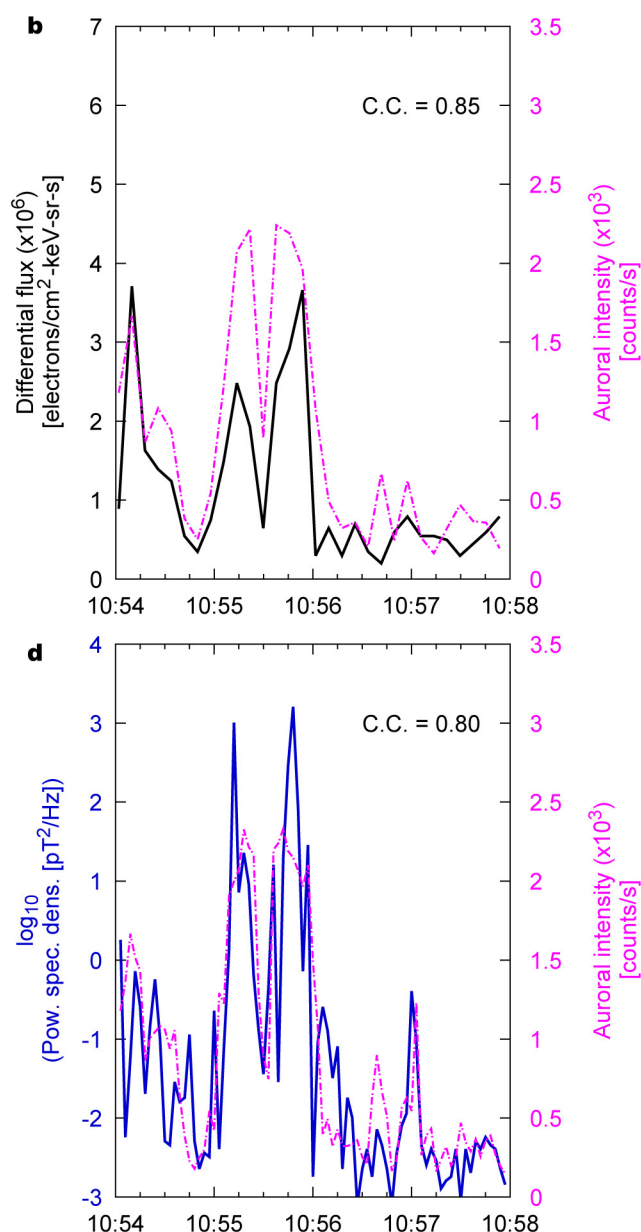


Extended Data Figure 1 | *In situ* observations by ERG with an additional dataset. **a, b**, Frequency–time spectrograms of the power spectral densities of the electric (**a**) and magnetic field (**b**), showing chorus waves. The magenta and white lines indicate $0.5f_{ce}$ and $1.0f_{ce}$, respectively, based on local magnetic field observations. **c–e**, Energy–time spectrograms for differential fluxes of loss-cone electrons parallel (pitch angles $PA < 2^\circ$) (**c**) and anti-parallel ($PA > 178^\circ$) (**d**) to the magnetic field and electrons perpendicular to the magnetic field ($PA = 80^\circ\text{--}100^\circ$) (**e**). Quasiparallel

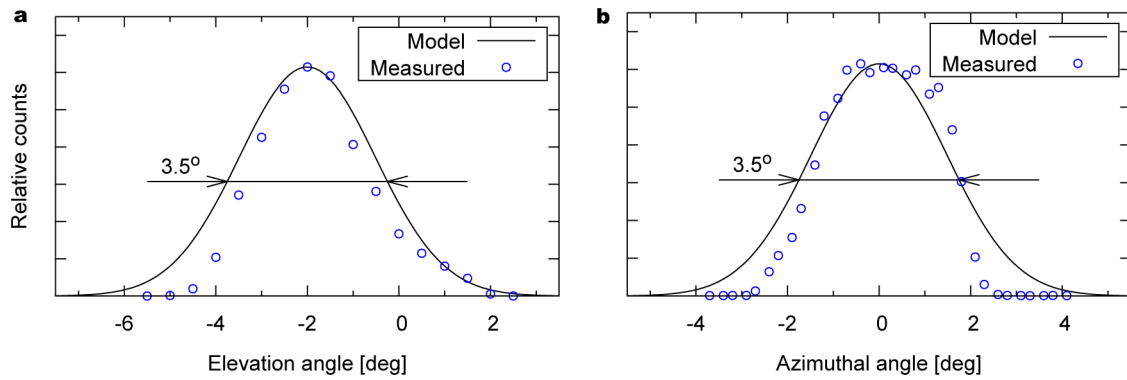
($PA = 20^\circ\text{--}40^\circ$) and quasiantiparallel ($PA = 140^\circ\text{--}160^\circ$) electrons show essentially the same trend as that of the perpendicular flux. **f**, Flux($PA < 2^\circ$)/flux($PA = 20^\circ\text{--}40^\circ$); **g**, flux($PA > 178^\circ$)/flux($PA = 140^\circ\text{--}160^\circ$). The graphs in **b** and **c** are the same as those in Fig. 3a and b, respectively (but replotted here for comparison with **a** and **d**). The faint signature of an upper hybrid resonance wave at 12–16 kHz in **a** at about 11:10 UT is consistent with the assumed density of approximately 3 cm^{-3} .



Extended Data Figure 2 | Correlation coefficients for auroral intensity. **a**, The colours (red, yellow, cyan and magenta) show the correlation coefficients between the auroral intensity and the loss-cone electron flux. **b**, Time series data of the loss-cone electron flux and the auroral intensity at a pixel at which electrons and chorus waves have nearly the highest correlation. The auroral intensity is plotted at the same time resolution as the electrons (about 8 s). **c**, **d**, The same as **a** and **b**, but for the chorus wave intensity. The wave intensity in **d** is plotted at the same time resolution as the auroral intensity (3 s). In **a** and **c**, the background auroral images are magnified around the centre of the field of view of the Pas station. Highest-correlation pixels are consistently located near the centre of both panels, suggesting the spacecraft footprint. The dashed lines in **a** and **c** illustrate magnetic coordinates every 2° in latitude and 5° in longitude. The displacement of the model footprint from the high-correlation pixels is approximately -0.5° and -5° in latitude and longitude, respectively,

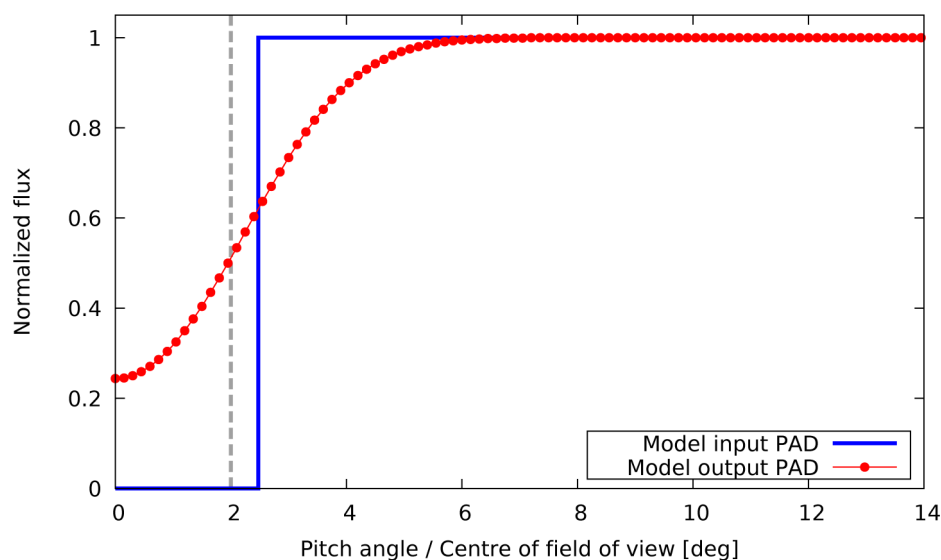


consistent with typical modelling errors²⁰. Cross-correlations were calculated for the period 10:54:00–10:58:00 UT. In other time periods, high-correlation pixels were not commonly obtained, perhaps because of the fine structures of pulsating patches and the equatorial modulation regions near the spacecraft. For example, if the spacecraft leaves the localized modulation region as a result of magnetospheric configuration change, chorus waves and associated electron precipitation disappear at its location, but pulsating patches can continue to be 'on' if the equatorial modulation region still exists. In other words, although the spacecraft's footprint in the ionosphere can leave an illuminated patch owing to spatial reconfiguration of magnetic field line structures or plasma phenomena, the auroral intensity remains high at some pixels. Other reasons that make the above correlations difficult to identify, such as the contribution of soft electron (<10 keV) precipitation to higher-altitude (>100 km) illumination, may be studied in future work.



Extended Data Figure 3 | The angular response of MEP-e in two orthogonal directions. **a**, Sensor response as a function of elevation angle with respect to the sensor's mounting plane. **b**, Response in the sensor's azimuthal direction, which is orthogonal to the elevation angle.

Blue circles, laboratory data; black line, Gaussian model. The model curves were used to obtain the analysis results shown in Extended Data Fig. 4. Profiles for one detector are shown here; similar profiles were obtained for the other 15 detectors.



Extended Data Figure 4 | Results of PAD model taking the sensor's angular resolution into account. Because of the finite angular resolution, contamination from outside the loss cone cannot be completely negligible. The blue line indicates the model input PAD, which is isotropic except for the step-function drop at the loss-cone angle of 2.5° (the nominal loss-cone angle in the event presented in this paper, based on a local magnetic field of about 100 nT). The red curve shows how the electron PAD is modulated by the effect of the sensor's finite angular resolution. The grey dashed line indicates the threshold, 2° , for loss-cone selection (that is, if the angle between the centre of the field of view and the magnetic field is smaller than the threshold, the measured flux is considered to be the

flux inside the loss cone). For this calculation, the sensor's field of view is modelled by a Gaussian cone (full-width at half-maximum, 3.5°), based on the ground calibration. For example, even when the middle of the sensor's field-of-view is centred along the magnetic field line and the actual electron PAD has an ideally empty loss cone, the instrument can inadvertently record about a few tens per cent of the flux from outside the loss cone. In our observations, however, the electron flux in the loss cone most often exhibits a filling ratio larger than 0.5, sometimes about 1, when the precipitation is 'on' (Fig. 4 and Extended Data Fig. 1f and g), too large to be explained by contamination alone. Also, synchronization with chorus waves cannot be produced by this instrumental effect.

A spin–orbital–entangled quantum liquid on a honeycomb lattice

K. Kitagawa^{1*}, T. Takayama^{2*}, Y. Matsumoto², A. Kato¹, R. Takano¹, Y. Kishimoto³, S. Bette², R. Dinnebier², G. Jackeli^{2,4} & H. Takagi^{1,2,4}

The honeycomb lattice is one of the simplest lattice structures. Electrons and spins on this simple lattice, however, often form exotic phases with non-trivial excitations. Massless Dirac fermions can emerge out of itinerant electrons, as demonstrated experimentally in graphene¹, and a topological quantum spin liquid with exotic quasiparticles can be realized in spin-1/2 magnets, as proposed theoretically in the Kitaev model². The quantum spin liquid is a long-sought exotic state of matter, in which interacting spins remain quantum-disordered without spontaneous symmetry breaking³. The Kitaev model describes one example of a quantum spin liquid, and can be solved exactly by introducing two types of Majorana fermion². Realizing a Kitaev model in the laboratory, however, remains a challenge in materials science. Mott insulators with a honeycomb lattice of spin–orbital–entangled pseudospin-1/2 moments have been proposed⁴, including the 5*d*-electron systems α -Na₂IrO₃ (ref. 5) and α -Li₂IrO₃ (ref. 6) and the 4*d*-electron system α -RuCl₃ (ref. 7). However, these candidates were found to magnetically order rather than form a liquid at sufficiently low temperatures^{8–10}, owing to non-Kitaev interactions^{6,11–13}. Here we report a quantum-liquid state of pseudospin-1/2 moments in the 5*d*-electron honeycomb compound H₃LiIr₂O₆. This iridate does not display magnetic ordering down to 0.05 kelvin, despite an interaction energy of about 100 kelvin. We observe signatures of low-energy fermionic excitations that originate from a small number of spin defects in the nuclear-magnetic-resonance relaxation and the specific heat. We therefore conclude that H₃LiIr₂O₆ is a quantum spin liquid. This result opens the door to finding exotic quasiparticles in a strongly spin–orbit-coupled 5*d*-electron transition-metal oxide.

According to the third law of thermodynamics, magnets with many spin degrees of freedom must have zero entropy in the ground state. The conventional way of releasing the entropy is to form a magnetically ordered state. However, there is another way of forming a macroscopically non-degenerate state: through quantum effects, which hinder long-range order. This exotic state of matter is called a quantum spin liquid³. Since the first conjecture of the resonant-valence-bond state¹⁴, geometrically frustrated $S = 1/2$ antiferromagnets (where S is the spin) on a triangular-based lattice have been studied experimentally and theoretically to explore the quantum-spin-liquid state. Although the resonant-valence-bond state is believed to be a quantum superposition of spin singlets, it has not been obtained as an exact solution of any model Hamiltonian. Despite the theoretical challenges, it has been argued on the basis of experiments that certain antiferromagnetic, $S = 1/2$ triangular and kagome materials are quantum spin liquids, including the organic materials κ -(BEDT-TTF)₂Cu₂(CN)₃ (ref. 15) and EtMe₃Sb[Pd(dmit)₂]₂ (refs 16, 17) and the inorganic material ZnCu₃(OH)₆Cl₂ (refs 18–20).

Recently, the simple honeycomb lattice has become important in the exploration of quantum spin liquids, owing to a theoretical breakthrough². Kitaev² proposed a model in which $S = 1/2$ spins on a honeycomb lattice are coupled to their three nearest neighbours by ferromagnetic Ising interactions, with bond-dependent easy axes parallel to the x , y and z axes (Fig. 1a). The orthogonal anisotropy of the three nearest-neighbour bonds creates a conflict between these bonds, giving rise to strong magnetic frustration. By introducing Majorana operators, Kitaev showed rigorously that the ground state of the associated Hamiltonian is a quantum spin liquid. Topological excitations are anticipated, originating from the itinerant Majorana fermions with Dirac dispersion and from the localized Majorana fermions that give rise to Z_2 gauge flux. The Kitaev model provides an alternative pathway to a quantum spin liquid compared to the resonant-valence-bond case, with the advantage that it has an exactly solvable ground state.

The Kitaev model was thought to be a toy model for theorists because pure $S = 1/2$ spins in general do not accommodate strong Ising anisotropy. However, 5*d* transition-metal oxides, in particular Ir⁴⁺ oxides with five *d* electrons, were recently shown to be promising candidates for Kitaev spin liquids. In complex Ir⁴⁺ oxides with octahedral coordination of oxygen ions, a spin–orbital Mott state with pseudospin $J_{\text{eff}} = 1/2$ moments is often formed²¹. If neighbouring IrO₆ octahedra share an edge, then super-exchange interactions give rise to a ferromagnetic Ising interaction of $J_{\text{eff}} = 1/2$ moments with easy axes perpendicular to the Ir–O₂–Ir plane—the essential ingredient of the Kitaev model⁴.

The spin–orbital Mott insulators α -Na₂IrO₃ and α -Li₂IrO₃ crystallize in a layered structure, in which IrO₆ octahedra form a honeycomb network by sharing the three orthogonal edges of an octahedron (Fig. 1b). These honeycomb iridates, and more recently the closely related compound α -RuCl₃, have been studied extensively as possible materializations of the Kitaev model^{5–7}. However, their ground states were found to be magnetically ordered^{8–10} rather than forming quantum spin liquids, although signatures of the existence of Kitaev interactions were captured^{22,23}. It was argued that additional interactions, such as Heisenberg interactions generated by *d*–*d* exchange coupling, compete with Kitaev-type interactions and stabilize the magnetically ordered state^{6,11}. Indeed, the Curie–Weiss temperature θ_{CW} estimated from the magnetic susceptibilities of α -Na₂IrO₃ and α -Li₂IrO₃ is not positive, as would be expected for Kitaev-type ferromagnetic interactions, which points to the presence of additional antiferromagnetic interactions.

The difficulty in realizing a Kitaev spin liquid in the aforementioned candidates motivated us to explore other honeycomb-based Ir⁴⁺ oxides. During this exploration, we discovered a quantum-spin-liquid state in the honeycomb Ir oxide H₃LiIr₂O₆, in which all of the interlayer Li⁺ ions of α -Li₂IrO₃ are replaced with H⁺ ions in an ion-exchange reaction²⁴ (Fig. 1d), but the LiIr₂O₆ honeycomb plane remains as it

¹Department of Physics, University of Tokyo, Bunkyo-ku, Hongo 7-3-1, Tokyo 113-0033, Japan. ²Max Planck Institute for Solid State Research, Heisenbergstrasse 1, 70569 Stuttgart, Germany.

³Graduate School of Integrated Arts and Sciences, Kochi University, Akebonocho 2-5-1, Kochi 780-8520, Japan. ⁴Institute for Functional Matter and Quantum Technologies, University of Stuttgart, Pfaffenwaldring 57, 70569 Stuttgart, Germany.

*These authors contributed equally to this work.

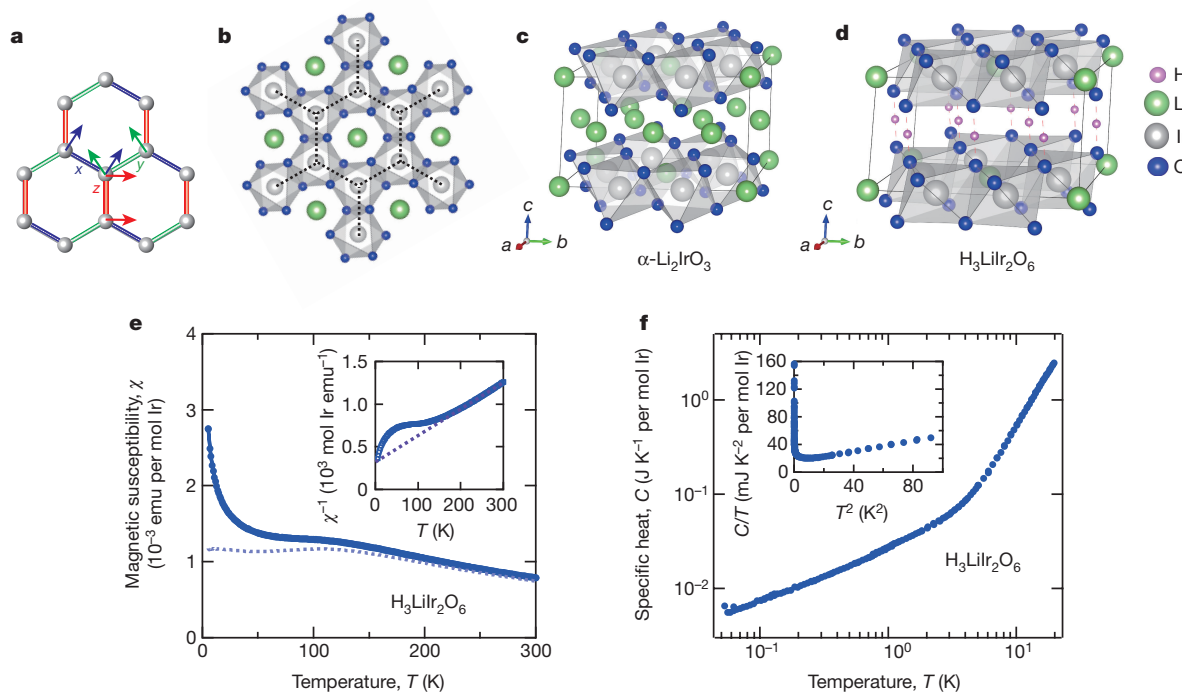


Figure 1 | Crystal structure and basic physical properties of $\text{H}_3\text{LiIr}_2\text{O}_6$. **a**, Kitaev model on a honeycomb lattice. $S = 1/2$ spin moments (indicated by arrows) are present on the honeycomb lattice, coupled by bond-dependent ferromagnetic Ising interactions. The three 120° bonds with orthogonal Ising axes compete with each other, giving rise to strong magnetic frustration and hence a quantum-spin-liquid state. **b**, LiIr_2O_6 layer unit with an edge-shared network of IrO_6 octahedra for $\alpha\text{-Li}_2\text{IrO}_3$ and $\text{H}_3\text{LiIr}_2\text{O}_6$. Ir^{4+} ions with $J_{\text{eff}} = 1/2$ moments form a honeycomb sublattice, as indicated by the dotted lines. The edge-shared $\text{Ir}-\text{O}_2-\text{Ir}$ bond gives rise to ferromagnetic Ising interaction between the neighbouring $J_{\text{eff}} = 1/2$ moments. **c**, Layer stacking of $\alpha\text{-Li}_2\text{IrO}_3$ (ref. 30). **d**, Layer stacking of $\text{H}_3\text{LiIr}_2\text{O}_6$ (ref. 30), in which the interlayer Li^+ ions are replaced with H^+ ions. **e**, Magnetic susceptibility $\chi(T)$ for $\text{H}_3\text{LiIr}_2\text{O}_6$

measured at 1 T. The raw data (solid line and circles) is shown along with the presumed intrinsic χ (dotted line) after numerically subtracting a low-temperature Curie-like contribution, which probably originates from magnetic defects (see also Extended Data Fig. 2a). The inset shows $1/\chi$ as a function of temperature to emphasize the high-temperature Curie-Weiss behaviour of localized $J_{\text{eff}} = 1/2$ moments. The extrapolation to $T = 0$ provides an estimate of the antiferromagnetic Curie-Weiss temperature of $\theta_{\text{CW}} = -105$ K. **f**, Specific heat C as a function of T (main panel) and C/T as a function T^2 (inset) down to 0.05 K, indicating no signature of magnetic ordering. The large non-lattice contribution suggests the presence of low-lying spin excitations. The nuclear Schottky contribution is subtracted (see Methods).

was (Fig. 1b)²⁵. Powder X-ray diffraction indicates the presence of stacking faults between the honeycomb planes (Methods, Extended Data Fig. 1). The presence of magnetic defects with a density of 1%, which probably originate from impurities or vacancies, is indicated by the temperature- and magnetic-field-dependent magnetization $M(T, B)$ and the low-temperature specific heat $C(T, B)$ (Extended Data Fig. 2).

The resistivity $\rho(T)$ of $\text{H}_3\text{LiIr}_2\text{O}_6$ (Extended Data Fig. 3) exhibits insulating behaviour with an activation energy of approximately 0.12 eV. In addition, Curie-Weiss behaviour is observed in the magnetic susceptibility $\chi(T)$ with an effective moment of approximately $1.60\mu_{\text{B}}$ per Ir atom (where μ_{B} is the Bohr magneton) at temperatures above 200 K (Fig. 1e). These findings indicate that $\text{H}_3\text{LiIr}_2\text{O}_6$ is a spin-orbital $J_{\text{eff}} = 1/2$ Mott insulator. We find a negative value for θ_{CW} of -105 K, which implies overall antiferromagnetic interactions, as in other honeycomb Ir oxides^{5,6}. The energy scale of magnetic interactions is of the order of 100 K, but no trace of magnetic ordering is observed in $\chi(T)$ down to 2 K, in sharp contrast to other Kitaev candidates⁵⁻⁷. Accordingly, $C(T)$ down to 0.05 K (Fig. 1f) does not show any signature of a phase transition. These results suggest that the ground state of $\text{H}_3\text{LiIr}_2\text{O}_6$ is a liquid state of $J_{\text{eff}} = 1/2$ moments.

$\chi(T)$ and $C(T)$ are not very sensitive to a weak or glassy magnetic ordering. We therefore conducted ^7Li and ^1H NMR measurements on aligned powders (Fig. 2a, b) to exclude the possibility of any magnetic ordering. The absence of apparent peak splitting or broadening on cooling (see also Extended Data Fig. 4a) clearly indicates that the system remains paramagnetic down to 1 K, roughly 1% of the

energy scale of magnetic interaction. We therefore conclude that a quantum-spin-liquid state is realized in honeycomb $\text{H}_3\text{LiIr}_2\text{O}_6$.

The Knight shift $K(T)$ represents an intrinsic magnetic susceptibility, free from magnetic defects. In Fig. 3a, $K(T)$ is shown for ^7Li with magnetic fields parallel and perpendicular to the honeycomb plane and no indication of magnetic ordering is observed. The sizable anisotropy in the susceptibility of up to around 2 between the two field orientations should originate from spin-orbit coupling, but is not expected for the Kitaev model with equal Ising couplings on the three bonds. Its existence probably implies an anisotropy in the magnitude of the three Ising couplings and/or the presence of off-diagonal interactions^{12,26}. On cooling below about 200 K, $K(T)$ deviates from the Curie-Weiss behaviour that is seen at higher temperatures, exhibiting a broad peak at around 130 K followed by a gradual decrease to a non-zero value. The non-zero susceptibility in the low-temperature limit is analogous to the susceptibilities observed in organic spin liquids^{15,16}, which have been interpreted as evidence for gapless spin excitations. However, spin-orbit coupling can lead to a non-zero susceptibility even in a spin liquid with a finite excitation gap; because the spin-orbit coupling is strong for Ir ($\lambda_{\text{SO}} \approx 0.5$ eV), the non-zero susceptibility does not necessarily imply gapless excitations.

The presence of low-lying spin excitations is captured by the NMR spin relaxation rate T_1^{-1} . In Fig. 3b we plot $(T_1 T)^{-1}$, which measures the density of spin excitations. At a low magnetic field of $B = 1$ T, $(T_1 T)^{-1}$ for ^1H and ^7Li remains non-zero and shows only weak temperature dependence below about 40 K. With increasing B , however, $(T_1 T)^{-1}$ at low temperatures is suppressed and decreases rapidly below a

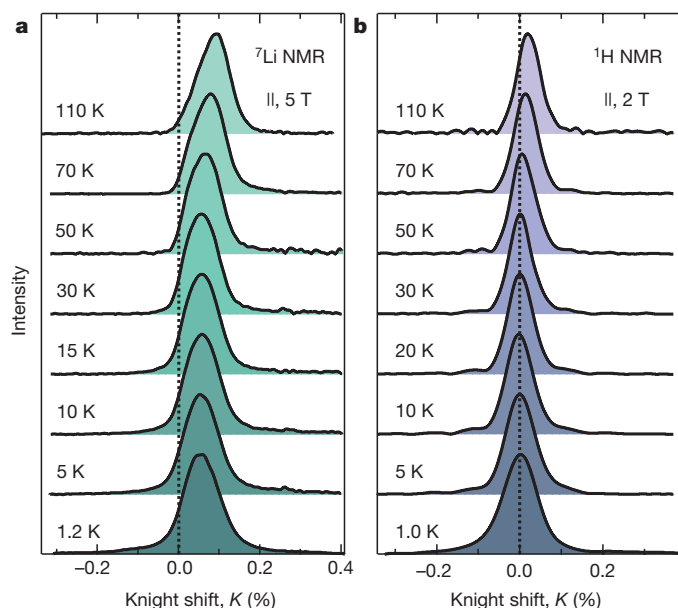


Figure 2 | Evidence from NMR spectroscopy of a spin-liquid ground state in $\text{H}_3\text{LiIr}_2\text{O}_6$ down to 1.0 K. **a**, ${}^7\text{Li}$ (**a**) and ${}^1\text{H}$ (**b**) NMR spectra for a magnetic field $B = 5$ T and 2 T, respectively, applied parallel to the honeycomb plane (\parallel). No appreciable broadening of the peak is observed down to 1.0 K, which provides evidence for intact paramagnetism and hence a spin-liquid state. The dotted vertical line indicates the spectral positions of nuclei without internal fields ($K = 0$). In ${}^7\text{Li}$ NMR, only one peak, assigned to Li ions in the honeycomb layer, is observed, indicating that no Li ions are left in the interlayer sites after the ion-exchange process. The spectra are offset and coloured in various shades for clarity.

characteristic temperature T^* . T^* , at which a knee-like structure is observed, increases linearly with B as $k_B T^* \approx \mu_B B$, where k_B is the Boltzmann constant. This behaviour can be understood as a suppression of low-lying spin excitations with the application of a magnetic field over an energy scale of the Zeeman energy, $\mu_B B$. We note that $K(T)$ does not depend on magnetic field at low temperatures, in marked contrast to the strong B dependence of $(T_1 T)^{-1}$. The temperature-independent and non-zero static susceptibility $K(T)$ at low temperatures must be dominated by different physics from T_1 , indicative of the presence of a duality in the magnetic response.

The low-lying spin excitations are identified also in $C(T)$ at low temperatures (Fig. 4a). On cooling in $B = 0$, C/T does not approach zero and shows a weak power-law increase of $C/T \propto T^{-1/2}$, which suggests the presence of highly degenerate low-lying excitations around energy $E = 0$. With the application of B , a peak emerges in C/T at roughly $T^*(B)/2$, where T^* is the knee temperature in $(T_1 T)^{-1}$. Below the peak, C/T decreases rapidly with decreasing T , almost linearly with T in the low- T limit, consistent with T_1 . $C/T \propto T$ is expected for a V-shaped density of states $D(E) \propto |E|$. The entropy $S(T, B)$ shown in Fig. 4b is calculated from C/T and does not depend appreciably on B above T^* , indicating the weight transfer of the intense low-lying excitations over the energy scale of $\mu_B B$. The field dependence of $S(T, B)$ is linked to the temperature dependence of the magnetization $M(T, B)$ through the Maxwell relationship $(\partial S/\partial B)_T = (\partial M/\partial T)_B$. In $M(T, B)/B$ for the same sample, we observe a Curie-like increase in the low- B limit at low temperatures, which is superposed on the intrinsic and T -independent susceptibility $K(T)$ (Extended Data Fig. 2a). The T -dependent part of $M(T, B)$ —the Curie-like contribution—is well reproduced from the B dependence of $S(T, B)$, which means that the low-lying excitations observed in C originate from the Curie-like contribution in M/B .

We model the observed excitations in terms of an energy-symmetric fermionic density of states $D(E, B)$ (Fig. 4c). In zero magnetic field, the density of states $D(E, 0) = \Gamma|E|^{-1/2}$ (where Γ is a constant) has an $E = 0$ singularity, giving rise to $C/T \propto T^{-1/2}$. At a non-zero field B ,

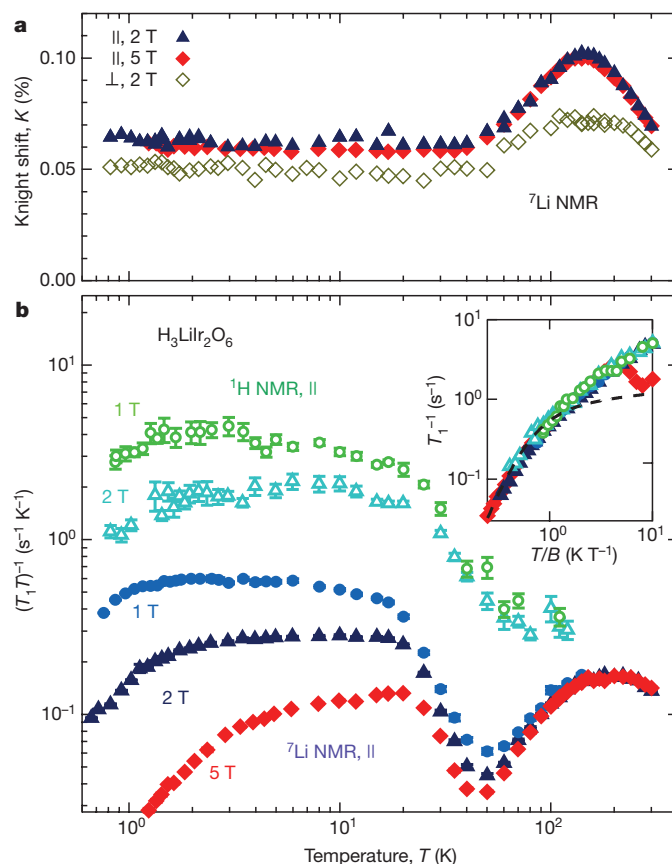


Figure 3 | The Knight shift and relaxation rate for $\text{H}_3\text{LiIr}_2\text{O}_6$ reveal the intrinsic static susceptibility and spin dynamics. **a**, Knight shift K , which represents the intrinsic spin susceptibility, for ${}^7\text{Li}$ at fields $B = 2$ T and 5 T parallel to the honeycomb plane (\parallel) and 2 T perpendicular to the plane (\perp). No appreciable B dependence of K is observed. K remains non-zero and constant from 40 K to below 1 K. **b**, NMR relaxation rate T_1^{-1} plotted as $(T_1 T)^{-1}$ as a function of T , measured for B parallel to the honeycomb plane. $(T_1 T)^{-1}$ measures the momentum \mathbf{q} -averaged imaginary part of susceptibility $\chi''(\mathbf{q}, \omega_0)/\omega_0$ at a very low-energy ω_0 , which reflects the density of low-energy spin excitations. The almost temperature-independent behaviour at low temperatures indicates the presence of a non-zero density of low-lying spin excitations. $(T_1 T)^{-1}$ is particularly suppressed below $T^* \approx \mu_B B/k_B$, which indicates the opening of a B -induced excitation gap on an energy scale of the Zeeman energy. The error bars indicate the standard deviations in the fitting of the nuclear relaxation with a stretched exponential function (see Method). The inset shows a scaling plot: T_1^{-1} versus T/B . The data for ${}^1\text{H}$ (green and light blue) are multiplied by a factor of 0.16 to overlap with those for ${}^7\text{Li}$ (blue, dark blue and red). The dashed line indicates the T_1 calculated for ${}^7\text{Li}$ (see Extended Data Fig. 5) using the density of states model shown in Fig. 4c.

the low-energy region below $\alpha\mu_B B$ ($|E| < \alpha\mu_B B$) (where α is a constant) is replaced with the V-shaped function $D(E, B) = 4\Gamma|E|/(\alpha\mu_B B)^{3/2}$, which represents the excitation gap. Because Γ is a constant, the total number of states is conserved. We found that, by Fermi-averaging over $k_B T$, the simple model $D(E, B)$ with $\alpha = 2.9$ and $\Gamma = 4.3 \times 10^8 \text{ J}^{-1/2}$ per Ir atom reproduces both $C(T, B)$ and $T_1(T, B)$ reasonably well at low temperatures, as indicated by the dashed lines in the insets of Figs 3b and 4a. Incidentally, the presence of an excitation gap scaled by $\alpha\mu_B B$ manifests as a scaling of C , T_1 and M as a function of T/B (Extended Data Figs 2c, 5).

The NMR spin relaxation rate T_1^{-1} clearly captures the same fermionic excitations as C , with an $E = 0$ singularity and a likely particle-hole symmetry, which originates from the Curie-like contribution in M/B . The absence of the Curie-like contribution in $K(T)$ implies that these fermionic excitations are local and produced by magnetic defects embedded in the bulk spin liquid, the density of which

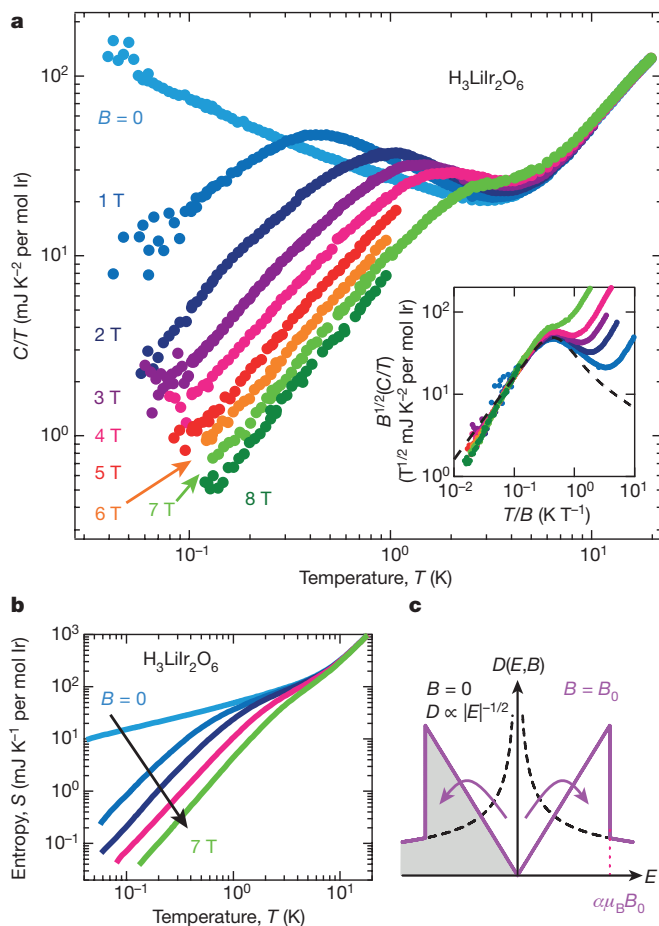


Figure 4 | Low-lying excitations are captured by the specific heat.

a, Specific heat C obtained after subtracting the nuclear contribution, plotted as C/T versus T for various fields B . The $T^{-1/2}$ dependence of C/T at $B = 0$ implies the presence of intense excitations around $E = 0$. With the application of B , the low-temperature C/T below $1/2T^* \approx (\mu_B B/k_B)/2$ is suppressed, which implies that an excitation gap opens over an energy scale of the Zeeman energy. In the $T = 0$ limit, C/T under B shows linear behaviour as a function of T , which suggests the formation of a gap that increases linearly with E . The inset shows a scaling plot: $CB^{1/2}/T$ versus T/B . At low $T/B < 0.5$, all data points (filled circles) measured at different magnetic fields fall onto the universal curve. The dashed line indicates $CB^{1/2}/T$ calculated on the basis of the density of states model shown in **c**; see also Extended Data Fig. 5). $CB^{1/2}/T$ increases rapidly with T/B and deviates from the universal behaviour for large $T/B > 1$, possibly owing to the contribution of the lattice and/or the magnetic excitations in the bulk. **b**, Entropy $S(T, B)$ calculated from the C/T data in **a**. With increasing T (well above T^*), $S(T, B)$ recovers to $S(T, 0)$. **c**, Suggested model of E -symmetric density of states $D(E, B)$. The dashed black line indicates $D(E, 0) = \Gamma|E|^{-1/2}$, which weakly diverges at $E = 0$. In a magnetic field $B = B_0$, a B -induced excitation gap, represented by $D(E, B_0) = 4\Gamma|E|/(\mu_B B_0)^{3/2}$, which is linear in E , is formed for $|E| < \alpha\mu_B B_0$ to conserve the total number of states, as indicated by the solid magenta line. The magenta arrows indicate the transfer of states associated with the formation of the gap. The states for $E < 0$ (shaded area) are occupied. Γ and α are constants.

is estimated to be roughly 1% in our sample. The majority of the nuclear spins are spatially distant from the defects and feel only a negligibly small static dipole field from them, but they have a finite dipole coupling with the local excitations, which governs the nuclear relaxation. Theoretical studies based on the pure Kitaev model indicate that the quantum-spin-liquid state is robust against the presence of a small number of spin vacancies and moderate random bond modulations and that a trapped Z_2 flux gives rise to local magnetic excitations²⁷.

The behaviour of T_1 at high temperatures (Fig. 3b) provides us with information on the interactions among $J_{\text{eff}} = 1/2$ moments.

The relationship $(T_1 T)^{-1} \propto T^{-1}$ around room temperature is consistent with the existence of thermally fluctuating moments. On lowering the temperature below 130 K, where $K(T)$ shows a decrease, $(T_1 T)^{-1}$ for ^7Li shows a pronounced decrease down to 50 K, whereas $(T_1 T)^{-1}$ for ^1H shows a monotonic increase (see also Extended Data Fig. 6a). This marked difference between the behaviour for ^7Li and ^1H comes from the form factors. Li atoms are located symmetrically at the centres of $J_{\text{eff}} = 1/2$ hexagons, where the fluctuating hyperfine fields cancel if antiferromagnetic correlations of $J_{\text{eff}} = 1/2$ moments develop over the hexagon. H atoms are located above the honeycomb layer and near one of the Ir–Ir bonds, where similar cancellation would be observed if nearest-neighbour antiferromagnetic correlations were to develop. The absence of $(T_1 T)^{-1}$ suppression for ^1H therefore implies much reduced antiferromagnetic or possibly ferromagnetic nearest-neighbour correlations as compared with the well-developed antiferromagnetic over-hexagon correlations. This is consistent with the much-discussed superposition of long-ranged antiferromagnetic correlations and Kitaev-type nearest-neighbour ferromagnetic interactions^{6,13,26}. Note that owing to the isotropy of Heisenberg antiferromagnetic interactions, they are multiplied by a factor of three in the mean-field calculation of θ_{CW} for $\chi(T)$ (ref. 26). This enhancement can explain in part why $\chi(T)$ in Fig. 1e shows an antiferromagnetic θ_{CW} .

The data presented here firmly establishes the realization of a quantum-spin-liquid state on the honeycomb lattice in $\text{H}_3\text{LiIr}_2\text{O}_6$. The strong relativistic spin–orbit coupling that is inherent to heavy $5d$ Ir ions and the resultant bond-dependent anisotropic coupling is probably the key to the formation of the liquid phase. Recent numerical calculations for the pure Kitaev model^{28,29} show a sharp peak in C with an entropy of as large as 50% of $k_B \ln(2)$ that originates from the ordering of Z_2 fluxes at very low temperatures, regardless of whether the system is in the gapped or the gapless phase. The observed low-energy excitations captured by C , however, correspond to an entropy of only 1%–2% of $k_B \ln(2)$ at about 5 K (Fig. 4b). Most of the observed entropy can be ascribed to local fermionic excitations associated with magnetic defects. The entropy that originates from the bulk quantum spin liquid should therefore be negligibly small, much less than 1%–2% of $k_B \ln(2)$ at 5 K (Extended Data Fig. 7). This observation might indicate that additional interactions and disorders modify the elementary excitations or even the nature of the liquid from the pure Kitaev case. However, we cannot exclude completely the possibility that the large-flux entropy of the pure Kitaev model is hidden below the lowest temperature that we measured (0.05 K; roughly 10^{-4} times the interaction energy). According to numerical calculations²⁸, flux entropy can be hidden in the Kitaev model with non-equivalent Ising bonds. Experiments at ultralow temperatures and further theoretical calculations with realistic anisotropy, additional interactions and magnetic defects are needed to identify the putative topological excitations in the quantum spin liquid.

Online Content Methods, along with any additional Extended Data display items and Source Data, are available in the online version of the paper; references unique to these sections appear only in the online paper.

Received 18 July; accepted 4 December 2017.

- Geim, A. K. & Novoselov, K. S. The rise of graphene. *Nat. Mater.* **6**, 183–191 (2007).
- Kitaev, A. Anyons in an exactly solved model and beyond. *Ann. Phys.* **321**, 2–111 (2006).
- Balents, L. Spin liquids in frustrated magnets. *Nature* **464**, 199–208 (2010).
- Jackeli, G. & Khaliullin, G. Mott insulators in the strong spin-orbit coupling limit: from Heisenberg to a quantum compass and Kitaev models. *Phys. Rev. Lett.* **102**, 017205 (2009).
- Singh, Y. & Gegenwart, P. Antiferromagnetic Mott insulating state in single crystals of the honeycomb lattice material Na_2IrO_3 . *Phys. Rev. B* **82**, 064412 (2010).
- Singh, Y. et al. Relevance of the Heisenberg–Kitaev model for the honeycomb lattice iridates A_2IrO_3 . *Phys. Rev. Lett.* **108**, 127203 (2012).
- Plumb, K. W. et al. $\alpha\text{-RuCl}_3$: a spin-orbit assisted Mott insulator on a honeycomb lattice. *Phys. Rev. B* **90**, 041112(R) (2014).
- Ye, F. et al. Direct evidence of a zigzag spin-chain structure in the honeycomb lattice: a neutron and X-ray diffraction investigation of single-crystal Na_2IrO_3 . *Phys. Rev. B* **85**, 180403(R) (2012).

9. Williams, S. C. *et al.* Incommensurate counterrotating magnetic order stabilized by Kitaev interactions in the layered honeycomb α -Li₂IrO₃. *Phys. Rev. B* **93**, 195158 (2016).
10. Johnson, R. D. *et al.* Monoclinic crystal structure of α -RuCl₃ and the zigzag antiferromagnetic ground state. *Phys. Rev. B* **92**, 235119 (2015).
11. Chaloupka, J., Jackeli, G. & Khaliullin, G. Kitaev-Heisenberg model on a honeycomb lattice: possible exotic phases in iridium oxides A₂IrO₃. *Phys. Rev. Lett.* **105**, 027204 (2010).
12. Rau, J. G., Lee, E. K. H. & Kee, H. Y. Generic spin model for the honeycomb iridates beyond the Kitaev limit. *Phys. Rev. Lett.* **112**, 077204 (2014).
13. Choi, S. K. *et al.* Spin waves and revised crystal structure of honeycomb iridate Na₂IrO₃. *Phys. Rev. Lett.* **108**, 127204 (2012).
14. Anderson, P. W. Resonating valence bonds: a new kind of insulator? *Mater. Res. Bull.* **8**, 153–160 (1973).
15. Shimizu, Y., Miyagawa, K., Kanoda, K., Maesato, M. & Saito, G. Spin liquid state in an organic Mott insulator with a triangular lattice. *Phys. Rev. Lett.* **91**, 107001 (2003).
16. Itou, T., Oyamada, A., Maegawa, S., Tamura, M. & Kato, R. Quantum spin liquid in the spin-1/2 triangular antiferromagnet EtMe₃Sb[Pd(dmit)₂]₂. *Phys. Rev. B* **77**, 104413 (2008).
17. Yamashita, M. *et al.* Highly mobile gapless excitations in a two-dimensional candidate quantum spin liquid. *Science* **328**, 1246–1248 (2010).
18. Olariu, A. *et al.* ¹⁷O NMR study of the intrinsic magnetic susceptibility and spin dynamics of the quantum kagome antiferromagnet ZnCu₃(OH)₆Cl₂. *Phys. Rev. Lett.* **100**, 087202 (2008).
19. Han, T.-H. *et al.* Fractionalized excitations in the spin-liquid state of a kagome-lattice antiferromagnet. *Nature* **492**, 406–410 (2012).
20. Fu, M., Imai, T., Han, T.-H. & Lee, Y. S. Evidence for a gapped spin-liquid ground state in a kagome Heisenberg antiferromagnet. *Science* **350**, 655–658 (2015).
21. Kim, B. J. *et al.* Phase-sensitive observation of a spin-orbital Mott state in Sr₂IrO₄. *Science* **323**, 1329–1332 (2009).
22. Chun, S. H. *et al.* Direct evidence for dominant bond-directional interactions in a honeycomb lattice iridate Na₂IrO₃. *Nat. Phys.* **11**, 462–466 (2015).
23. Banerjee, A. *et al.* Proximate Kitaev quantum spin liquid behaviour in a honeycomb magnet. *Nat. Mater.* **15**, 733–740 (2016).
24. O'Malley, M. J., Woodward, P. M. & Verweij, H. Production and isolation of pH sensing materials by carbonate melt oxidation of iridium and platinum. *J. Mater. Chem.* **22**, 7782–7790 (2012).
25. Bette, S. *et al.* Solution of the heavily stacking faulted crystal structure of the honeycomb iridate H₃LiIr₂O₆. *Dalton Trans.* **46**, 15216–15227 (2017).
26. Winter, S. M., Li, Y., Jeschke, H. O. & Valentí, R. Challenges in design of Kitaev materials: magnetic interactions from competing energy scales. *Phys. Rev. B* **93**, 214431 (2016).
27. Willans, A. J., Chalker, J. T. & Moessner, R. Site dilution in the Kitaev honeycomb model. *Phys. Rev. B* **84**, 115146 (2011).
28. Nasu, J., Udagawa, M. & Motome, Y. Thermal fractionalization of quantum spins in a Kitaev model: temperature-linear specific heat and coherent transport of Majorana fermions. *Phys. Rev. B* **92**, 115122 (2015).
29. Yoshitake, J., Nasu, J. & Motome, Y. Fractional spin fluctuations as a precursor of quantum spin liquids: Majorana dynamical mean-field study for the Kitaev model. *Phys. Rev. Lett.* **117**, 157203 (2016).
30. Momma, K. & Izumi, F. VESTA: a three-dimensional visualization system for electronic and structural analysis. *J. Appl. Cryst.* **41**, 653–658 (2008).

Acknowledgements We thank Y. Motome, M. Udagawa, R. Valentí, A. Gibbs, Y. B. Kim, A. Smerald and N. Shannon for discussions, and U. Wedig, Y. Ishikuro, T. Nishioka and S. Nakatsuji for experimental support and discussions. This work was partly supported by the Japan Society for the Promotion of Science (JSPS) KAKAENHI (numbers 24224010, 26707018, 15K13523, JP15H05852, JP15K21717 and 17H01140) and the Alexander von Humboldt foundation.

Author Contributions T.T. and A.K. prepared the sample and performed the bulk experiments. K.K., R.T. and Y.K. carried out the NMR measurements. Y.M. carried out the low-temperature specific heat measurements. S.B. and R.D. performed structural analysis. G.J. gave theoretical inputs. T.T., K.K., Y.M. and H.T. wrote manuscript and all authors commented on it. H.T. designed and supervised the experiments.

Author Information Reprints and permissions information is available at www.nature.com/reprints. The authors declare no competing financial interests. Readers are welcome to comment on the online version of the paper. Publisher's note: Springer Nature remains neutral with regard to jurisdictional claims in published maps and institutional affiliations. Correspondence and requests for materials should be addressed to H.T. (h.takagi@kf.fmpg.de).

Reviewer Information *Nature* thanks M. Mourigal and S. Todadri for their contribution to the peer review of this work.

METHODS

Sample synthesis and characterization. Polycrystalline powder of α - Li_2IrO_3 was prepared as a precursor via a solid-state reaction of Li_2CO_3 and IrO_2 . α - Li_2IrO_3 powder was sealed in a Teflon-lined steel autoclave with 4 M H_2SO_4 aqueous solution, and heated at 120 °C for 96 h. The product was washed with distilled water and dried at room temperature. The powder obtained was stable in air. Electrical resistivity and magnetic susceptibility above 2 K were measured by using a Physical Property Measurement System (PPMS) and a Magnetic Property Measurement System (MPMS) (Quantum Design) on cold-pressed pellets.

Structural analysis. The crystal structure of the product was analysed by using powder X-ray diffraction (Extended Data Fig. 1). The diffraction data were collected at room temperature with a Stoe Stadi-P transmission diffractometer (using a primary beam Johann-type Ge(111) monochromator for $\text{Ag K}\alpha_1$ radiation ($\lambda = 0.55941$ Å) and a Mythen-Dectris position-sensitive detector with $12^\circ 2\theta$ opening), with the sample sealed in a glass capillary of 0.5-mm diameter (Hilgenberg, glass No. 50). The sample was spun during measurement for better particle statistics. Rietveld refinement was performed using the program TOPAS version 4.2 (Bruker AXS, 2010).

The presence of stacking disorder makes the diffraction peak extremely asymmetric, which made a precise determination of the detailed structure using the conventional technique extremely difficult. We therefore took a two-step approach²⁵. First, the ideal structure without stacking faults was obtained by eliminating peaks with strong influence of stacking faults in the refinement. The structure obtained is shown in Fig. 1b, d and Extended Data Table 1. With the replacement of Li with H, the interlayer spacing $c = 4.8734(6)$ Å becomes smaller than that of α - Li_2IrO_3 ($c = 5.1219(2)$ Å). This is consistent with the much smaller ionic radius of H^+ than Li^+ . O^{2-} ions in the two adjacent honeycomb layers face each other (Fig. 1d), in contrast to the situation in α - Li_2IrO_3 (Fig. 1c). The location of the H atoms was not included in the refinement because of the very weak scattering from H atoms. However, it is natural that H^+ ions bridge the two facing O^{2-} ions. Site exchanges between Li and H are not considered. ^7Li NMR spectra revealed only one Li site that can be assigned to Li atoms in the honeycomb layer. This means that all of the interlayer Li ions are replaced with H after the ion exchange. Occupation of the Li site in the honeycomb layers by H atoms is very unlikely because of the contrast of ionic size.

The stacking disorder was then treated in the analysis of the powder X-ray diffraction by assuming the faulted stacking of finite-thickness lattice slabs of ideal structure^{25,31}. With a slab thickness of 12 layers, we can reproduce the whole powder X-ray diffraction pattern reasonably. We therefore conclude that the crystal structure of $\text{H}_3\text{LiIr}_2\text{O}_6$ is essentially as given in Extended Data Table 1, but with occasional stacking faults on average every 12 honeycomb layers.

Specific heat measurements. The specific heat C was measured by using a relaxation method in the temperature range 0.3–300 K using a commercial set-up (Quantum Design, PPMS), and separately at very low temperatures of 0.05–1 K using a cell installed in a dilution refrigerator. In the ultralow-temperature measurement, the sample was wrapped in an annealed silver foil (residual resistivity ratio of more than 1,000) and fixed by silver paste to ensure a sufficient thermal link between the sample and the sample stage. The data measured with the dilution refrigerator were analysed using the relaxation method and a quasi-adiabatic method³². The C values obtained by the two methods agree within the experimental resolution, confirming the reliability of the C data obtained. The results were reproducible for two different samples from the same batch of powder.

NMR measurements. NMR measurements were carried out using a standard coherent pulse spectrometer, cryo-cooled preamplifier, double-rotation probe and ^3He -circulation lines. The NMR frequency-swept spectra were acquired using a Fourier-step-sum technique, whereby each Fourier-transformed spectrum shifted with its centre frequency is accumulated during the sweep. The quadrupole splitting for ^6Li nuclei (nuclear spin $I > 1/2$) are negligibly small (less than 20 kHz). The oriented powder sample of $\text{H}_3\text{LiIr}_2\text{O}_6$ was used for the NMR measurements (Extended Data Fig. 8). Preferred orientations were confirmed by the X-ray diffraction pattern and the NMR spectral shape. The oriented powders show a sizable anisotropy in the magnetic susceptibility and Knight shift (Extended Data Fig. 4c).

The integrated spectral intensity of the NMR line corresponds to about 80% of the expected value (Extended Data Fig. 4b). The remaining 20% of nuclei seem to be located close to defect centres, where slow spin dynamics breaks the coherency of NMR signals (short spin-spin relaxation time T_2). Note that the observed behaviour is distinct from the 100% ‘wipe out’ effect that has been widely encountered in the geometrically frustrated materials $\text{SrCr}_8\text{Ga}_4\text{O}_{19}$ (ref. 33), NaCrO_2 (ref. 34), NiGa_2S_4 (ref. 35) and $\text{PbCuTe}_2\text{O}_6$ (ref. 36).

Knight shifts and hyperfine coupling constants. The Knight shift $K(T)$ was determined as the position of the NMR peaks in Fig. 2 and represents an intrinsic susceptibility. The nuclear gyromagnetic ratios $\gamma_n/(2\pi)$ for ^1H , ^6Li and ^7Li that were

used to determine the $K=0$ origins are 42.57639 MHz T^{-1} , 6.265578 MHz T^{-1} and 16.54680 MHz T^{-1} , respectively³⁷. If we subtract the Curie-like term at low temperatures in the bulk susceptibility $\chi(T)$, then $K(T)$ for ^7Li in Fig. 2 and $\chi(T)$ agree reasonably, which gives an estimate of the nearly isotropic hyperfine coupling constant for ^7Li of $A_{\text{hfr}} = 0.44 \text{ T}/\mu_B$ (Extended Data Fig. 4c, d). This agreement confirms that the low-temperature increase in the magnetic susceptibility $\chi(T)$ originates from impurities or defects. $K(T)$ for ^1H appears to have similar temperature dependence to that of ^7Li , but the extremely small shift of less than 100 p.p.m. (see Fig. 2b) does not allow us to estimate the hyperfine coupling for ^1H reliably; a rough estimate of $A_{\text{hfr}} \approx 0.1 \text{ T}/\mu_B$ is obtained from a magnetic dipole calculation. **NMR line width.** Clear broadening of NMR peaks has been observed in the geometrically frustrated spin liquids reported so far^{15,16,18,20} at low temperatures, of the order of 1% of the magnetic coupling J , although no clear peak splitting has been identified. The peak broadening in the geometrically frustrated spin liquids corresponds to the static distribution of a magnetic moment of $(0.01\text{--}0.1)\mu_B$ if the peak width is converted to the unit of magnetic moment using the hyperfine coupling constant A_{hfr} . In the case of $\text{H}_3\text{LiIr}_2\text{O}_6$, the broadening in the unit of magnetic moment is not zero, but is extremely small (at most $0.002\mu_B$ even for the locally less-symmetric H sites). This estimate was made on the basis of the temperature dependence of the half-width at half-maximum (HWHM) of the NMR peak in Extended Data Fig. 4a. The pronounced temperature dependence of the HWHM from room temperature down to 40 K is ascribed to the demagnetization effects. Only the temperature dependence below 40 K (0.2 mT at most) reflects the distribution of static moments, which correspond to $0.00045\mu_B$ and $0.002\mu_B$ for ^7Li and ^1H , respectively. In the conversion to magnetic moment, the isotropic hyperfine coupling constant for ^7Li $A_{\text{hfr}} = 0.44 \text{ T}/\mu_B$ and the mean square of the magnetic dipole interaction for ^1H $|A_{\text{dip}}| \approx 0.1 \text{ T}/\mu_B$ are used. It is not realistic to ascribe such a small moment to any kind of static magnetism.

NMR relaxation rate T_1 . Because the electric quadrupole splitting of $^6,7\text{Li}$ is small, the NMR relaxation rate T_1 for every nucleus was measured by using a comb-shaped-pulse recovery method with an empirical stretched-exponential recovery function, $1 - \exp[-(t/T_1)^\beta]$. T_1^{-1} for ^7Li for B perpendicular to the honeycomb plane was up to 50% larger than that for B parallel to the plane (Extended Data Fig. 6a), which implies stronger fluctuations of the hyperfine fields along the honeycomb plane. The anisotropy of T_1^{-1} is smaller than the field and the temperature dependence and does not affect the main conclusions.

The exponent β for the stretched-exponential recovery function for ^7Li is close to the ideal value of 1 around room temperature, but decreases gradually to about 0.6 with decreasing temperature (Extended Data Fig. 6b). The deviation from 1 can be ascribed to the spatial distribution of internal states, possibly associated with the effect of the specially distributed magnetic defects discussed in the main text. $\beta \approx 0.5$, which corresponds to randomized dipolar hyperfine fields, is commonly observed in frustrated magnets, including quantum spin liquids.

Characteristic timescale of spin fluctuations. $(T_1 T)^{-1}$ is the q -averaged imaginary part of susceptibility $\chi''(\mathbf{q}, \omega_0)/\omega_0$:

$$(T_1 T)^{-1} = 2k_B \left(\frac{\gamma_n}{g\mu_B} \right)^2 \sum_{\mathbf{q}} |A^+(\mathbf{q})|^2 \frac{\chi''(\mathbf{q}, \omega_0)}{\omega_0}$$

where g is the g -factor. We assume that $\chi(\mathbf{q}, \omega_0)$ takes a Lorentz form with a characteristic timescale of fluctuation τ . In the limit of fast fluctuations as compared with NMR frequency ($\omega_0 \ll 1/\tau$), $(T_1 T)^{-1}$ is scaled only by τ and does not depend on ω_0 . However, if extremely slow fluctuations associated with glassy magnetism were present ($\omega_0 \gg 1/\tau$), then $(T_1 T)^{-1} \propto (\omega_0^2 \tau)^{-1}$ and so a ω_0^{-2} dependence of $(T_1 T)^{-1}$ would emerge. To exclude the possibility of such slow spin dynamics dominating $(T_1 T)^{-1}$, we measured T_1^{-1} for ^6Li (Extended Data Fig. 6c). We determined the ratio of T_1^{-1} for ^6Li and ^7Li at 5 T and 10 K to be 0.14 ± 0.01 , in very good agreement with the ratio of γ_n^2 for ^6Li and ^7Li of $(6.27/16.55)^2 = 0.144$ that is expected for the limit of fast fluctuations. This agreement indicates the absence of ω_0 dependence. The magnetic-field-induced suppression of $(T_1 T)^{-1}$ originates from the decrease in the linear slope with respect to ω_0 of $\chi''(\mathbf{q}, \omega_0)$, which corresponds to the opening of a gap in the spin excitations.

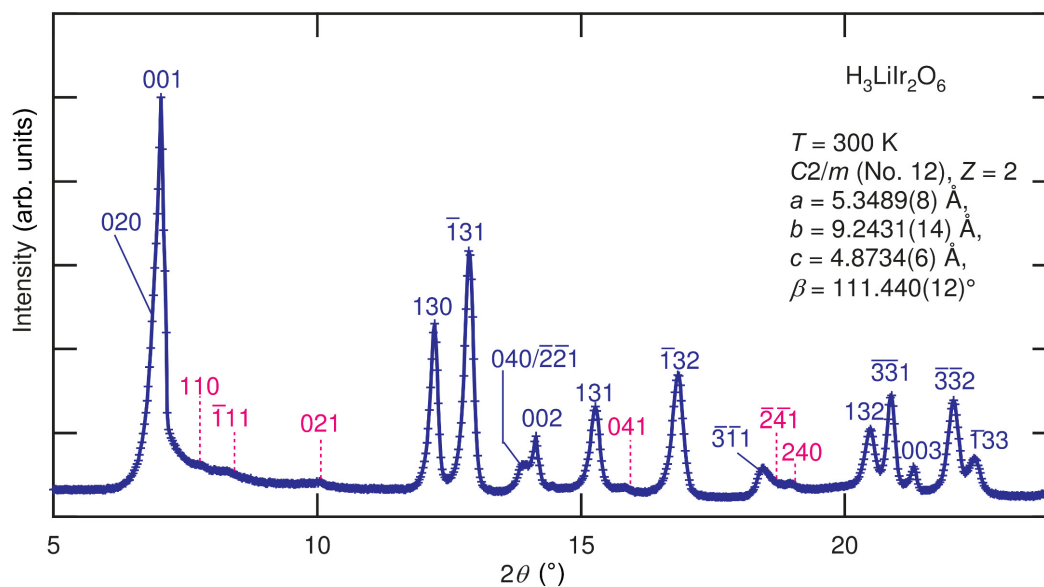
Subtraction of the nuclear contribution to the specific heat. As shown in Extended Data Fig. 9a, the raw specific heat C_{tot}/T without any correction for $B = 0, 1 \text{ T}$ and 3 T exhibits a sharp T^{-3} increase at very low temperatures on cooling, which is expected for a nuclear Schottky contribution. By using the following methods, we obtained the specific heat C/T without the nuclear Schottky contribution shown in Figs 1f and 4. For a low B between 0 T and 3 T, we estimated the nuclear Schottky contribution by fitting the low-temperature C_{tot}/T with $C_{\text{NS}}/T = AT^{-3}$ (broken lines in Extended Data Fig. 9a) and then subtracted C_{NS}/T from C_{tot}/T to obtain the non-nuclear contribution of specific heat C/T . Above 2 T, taking advantage of the very slow relaxation of nuclear contribution, we obtained

the non-nuclear contribution C/T directly by measuring the relaxation with short heating (heating only the non-nuclear contribution; see Extended Data Fig. 9b). In this high-field range, the relaxation of the nuclear contribution becomes extremely slow and is well separated from the fast relaxation from the non-nuclear contribution in the time domain. Note that the extremely slow nuclear decay is consistent with the rapid suppression of ^1H NMR $(T_1 T)^{-1}$ with the application of a magnetic field. We checked the consistency of the two types of analysis (at low B and high B) at an intermediate $B = 3$ T.

Estimate of entropy from the specific heat. The entropy $S(T)$ was estimated by integrating C/T . Below the lowest temperature measured, we extrapolate C/T to $T = 0$ by using a power-law temperature dependence of $T^{-1/2}$ for $B = 0$ and linear T under non-zero magnetic fields.

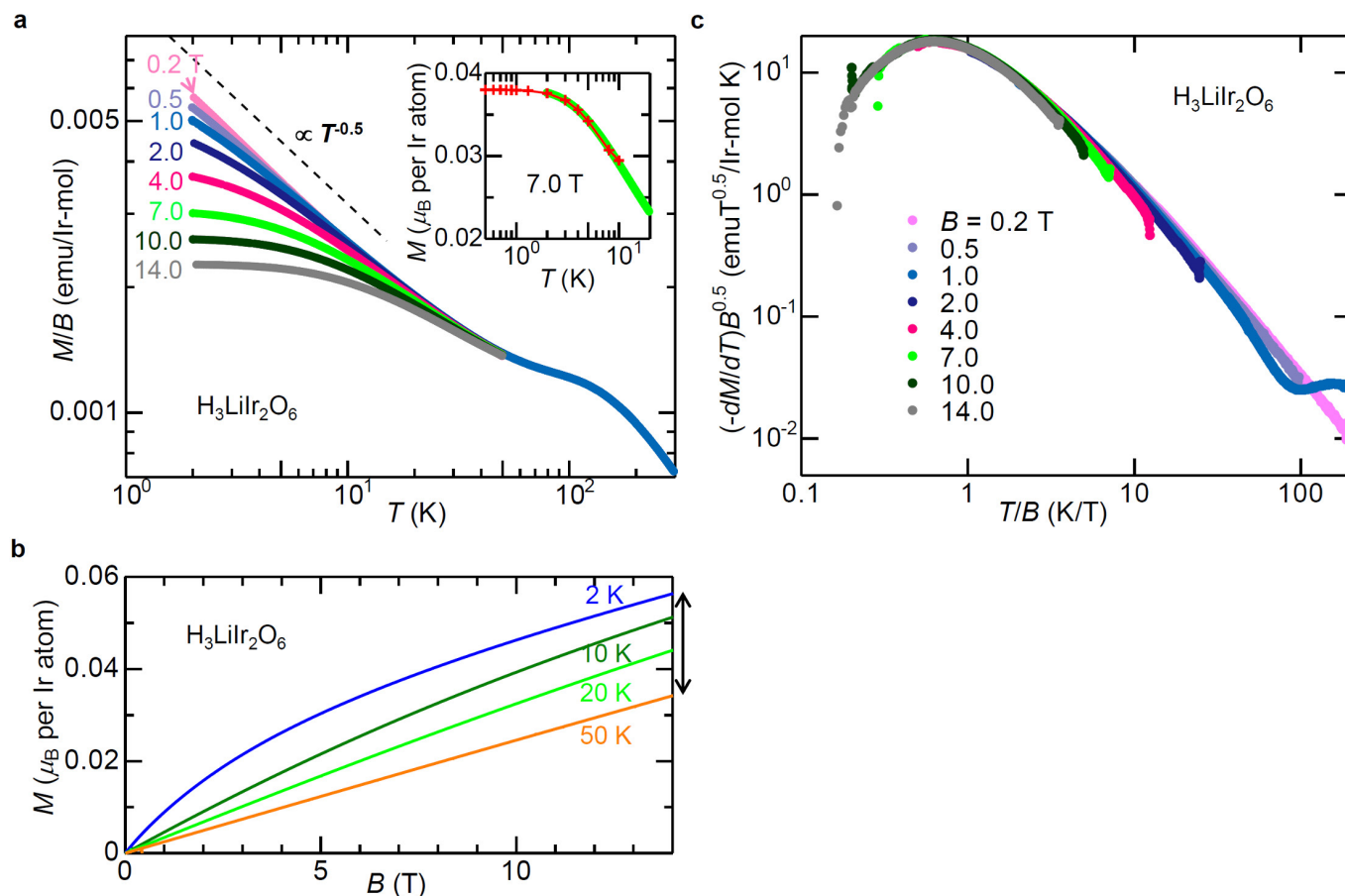
Data availability. The data that support the findings of this study are available from the corresponding author on reasonable request. Source Data for Figs 1, 3 and 4 are provided with the online version of the paper.

31. Bette, S., Dinnebier, R. D. & Freyer, D. Structure solution and refinement of stacking faulted $\text{NiCl}(\text{OH})$. *J. Appl. Cryst.* **48**, 1706–1718 (2015).
32. Tsujii, H., Andraka, B., Muttalib, K. A. & Takano, Y. Distributed τ_2 effect in relaxation calorimetry. *Physica B* **329–333**, 1552–1553 (2003).
33. Mendels, P. *et al.* Ga NMR study of the local susceptibility in kagomé-based $\text{SrCr}_8\text{Ga}_4\text{O}_{19}$: pseudogap and paramagnetic defects. *Phys. Rev. Lett.* **85**, 3496–3499 (2000).
34. Olariu, A. *et al.* Unconventional dynamics in triangular Heisenberg antiferromagnet NaCrO_2 . *Phys. Rev. Lett.* **97**, 167203 (2006).
35. Takeya, H. *et al.* Spin dynamics and spin freezing behavior in the two-dimensional antiferromagnet NiGa_2S_4 revealed by Ga-NMR, NQR and μSR measurements. *Phys. Rev. B* **77**, 054429 (2008).
36. Khuntia, P. *et al.* Spin liquid state in the 3D frustrated antiferromagnet $\text{PbCuTe}_2\text{O}_6$: NMR and muon spin relaxation studies. *Phys. Rev. Lett.* **116**, 107203 (2016).
37. Harris, R. K. *et al.* Further conventions for NMR shielding and chemical shifts (IUPAC recommendations 2008). *Pure Appl. Chem.* **80**, 59–84 (2008).



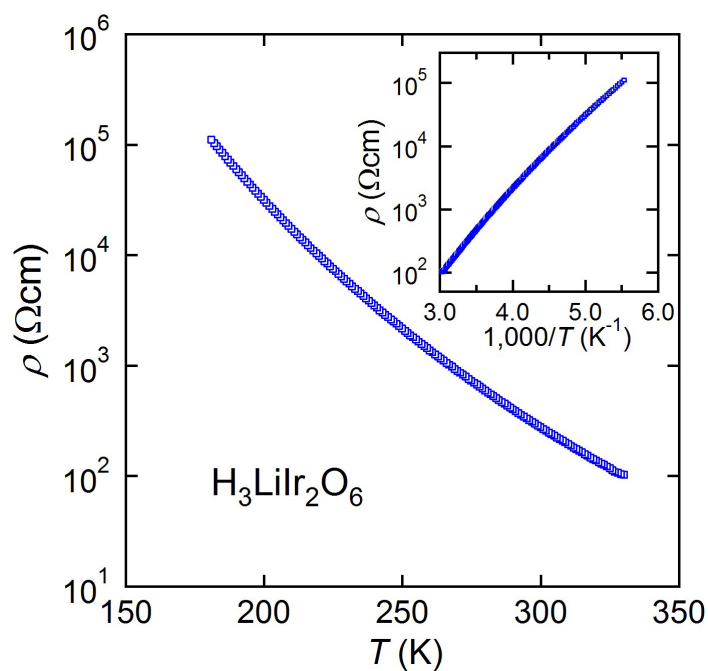
Extended Data Figure 1 | Powder X-ray diffraction pattern. The measured powder X-ray diffraction pattern of $\text{H}_3\text{LiIr}_2\text{O}_6$ at room temperature was recorded with $\text{Ag K}\alpha_1$ radiation; selected reflection

indices based on the $C2/m$ space group symmetry are also shown. The reflections that are vastly broadened owing to stacking faults are indicated in pink.

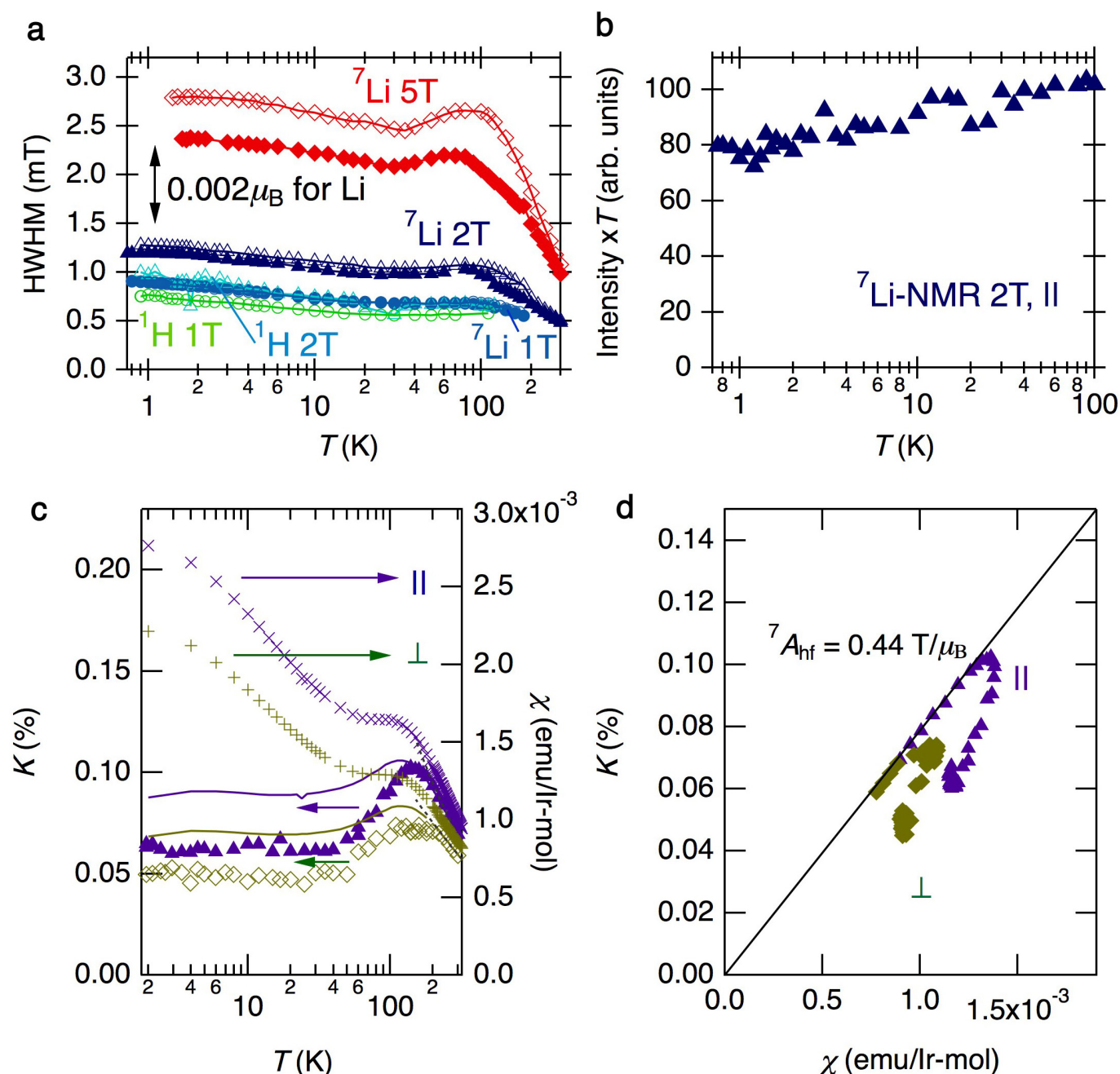


Extended Data Figure 2 | Temperature and magnetic-field dependence of magnetization at low temperatures. **a**, Temperature dependence of magnetization M/B under magnetic fields up to $B = 14$ T for the sample used in the specific heat measurements shown in Fig. 4. The Curie-like contribution that is absent in $K(T)$ is clearly seen, originating from magnetic defects. The dashed line represents a power-law behaviour with $T^{-1/2}$ dependence. The susceptibility in the low-field limit appears to follow the $T^{-1/2}$ dependence better than the conventional Curie–Weiss dependence. At very low temperatures, the Curie-like contribution becomes independent of T for high B fields, implying the saturation of moment from magnetic defects. In the inset, $M(T)$ at $B = 7.0$ T (green line) is compared with that calculated by integrating $\partial M(T, B)/\partial T$, which we obtained from $S(T, B)$ using the Maxwell relation (red pluses).

b, $M(B)$ – B curves at low temperatures. From the offset from the linear magnetization at high fields, we estimate the saturation moment that originates from magnetic defects to be $0.022\mu_B$ (as indicated by the arrow). This corresponds to 2% of the magnetic defects with $g = 2$ and a $S = 1/2$ moment. The Zeeman gap in the density-of-states model in Fig. 4 is $2\alpha\mu_BB$ with $\alpha = 2.9$, suggesting a g -factor of 5.8 for the moment that comes from the magnetic defects. Incorporating $g = 5.8$, the best estimate of the number of magnetic defects with $S = 1/2$ moments is 0.8%. This estimate is consistent with the estimate from the specific heat in Fig. 4, which indicates an entropy $S(T)$ of 1%–2% of $R\ln(2)$ at $T = 5$ K, where R is the gas constant. **c**, $B^{1/2} \times \partial M(T, B)/\partial T$ shows a scaling with T/B similar to that for C and T_1 , indicating that the three probes capture the same excitations.

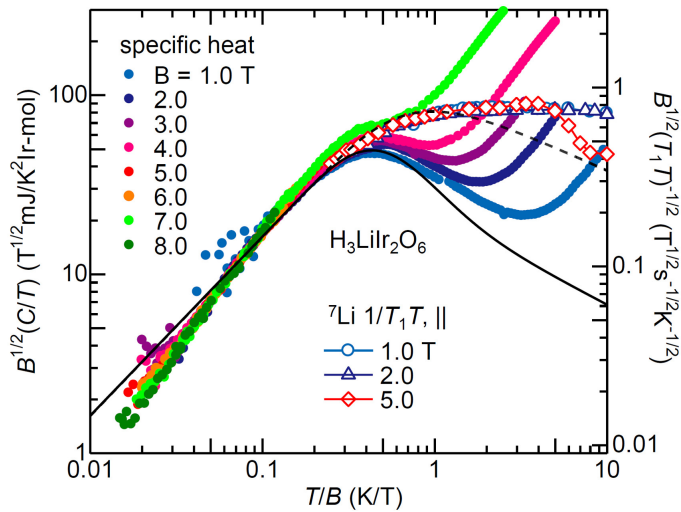


Extended Data Figure 3 | Resistivity versus temperature. The dependence of the resistivity ρ on the insulating temperature T is measured on a polycrystalline pellet of $\text{H}_3\text{LiIr}_2\text{O}_6$. The inset shows the Arrhenius plot of the same data, indicating the transport activation energy of approximately 0.12 eV.



Extended Data Figure 4 | NMR spectral parameters and estimate of the hyperfine coupling constant in $\text{H}_3\text{LiIr}_2\text{O}_6$. **a**, HWHM obtained by performing a Gaussian fit near the top of each peak. The open symbols are for B perpendicular to the honeycomb plane (\perp); the filled symbols are for B parallel to the plane (\parallel). The length of the arrow corresponds to a hyperfine field at a Li site when a moment of $0.002\mu_B$ is placed on the Ir atoms. **b**, The integrated NMR signal intensities after T_1 and T_2 corrections, which is proportional to the number of nuclei under observation. **c**, Bulk magnetic susceptibility $\chi(T)$ of aligned powder at 7 T after the subtraction of core diamagnetism, with B parallel (purple crosses) and perpendicular (green pluses) to the honeycomb plane. The solid lines

represent the intrinsic susceptibility χ_i calculated from χ by subtracting the Curie contribution that originates from the impurities and/or defects. The dotted lines are high-temperature (above 250 K) Curie–Weiss fits, which yield a Curie–Weiss temperature and effective moment in a parallel field of $\theta_{\text{CW}}^{\parallel} = -64$ K and $\mu_{\text{eff}}^{\parallel} = 1.62\mu_B$ per Ir atom, respectively, and in a perpendicular field of $\theta_{\text{CW}}^{\perp} = -175$ K and $\mu_{\text{eff}}^{\perp} = 1.72\mu_B$ per Ir atom. NMR Knight shifts K for ^7Li measured at 2 T (purple triangles and green diamonds) are superposed for comparisons. **d**, K for ^7Li plotted against χ_i . The data in a temperature region $T > 150$ K are well described by the linear relation $K(T) = [A_{\text{hf}}/(N_A\mu_B)]\chi_i$ (solid line), from which we determine the isotropic hyperfine coupling constant $A_{\text{hf}} = 0.44/\mu_B$ T.

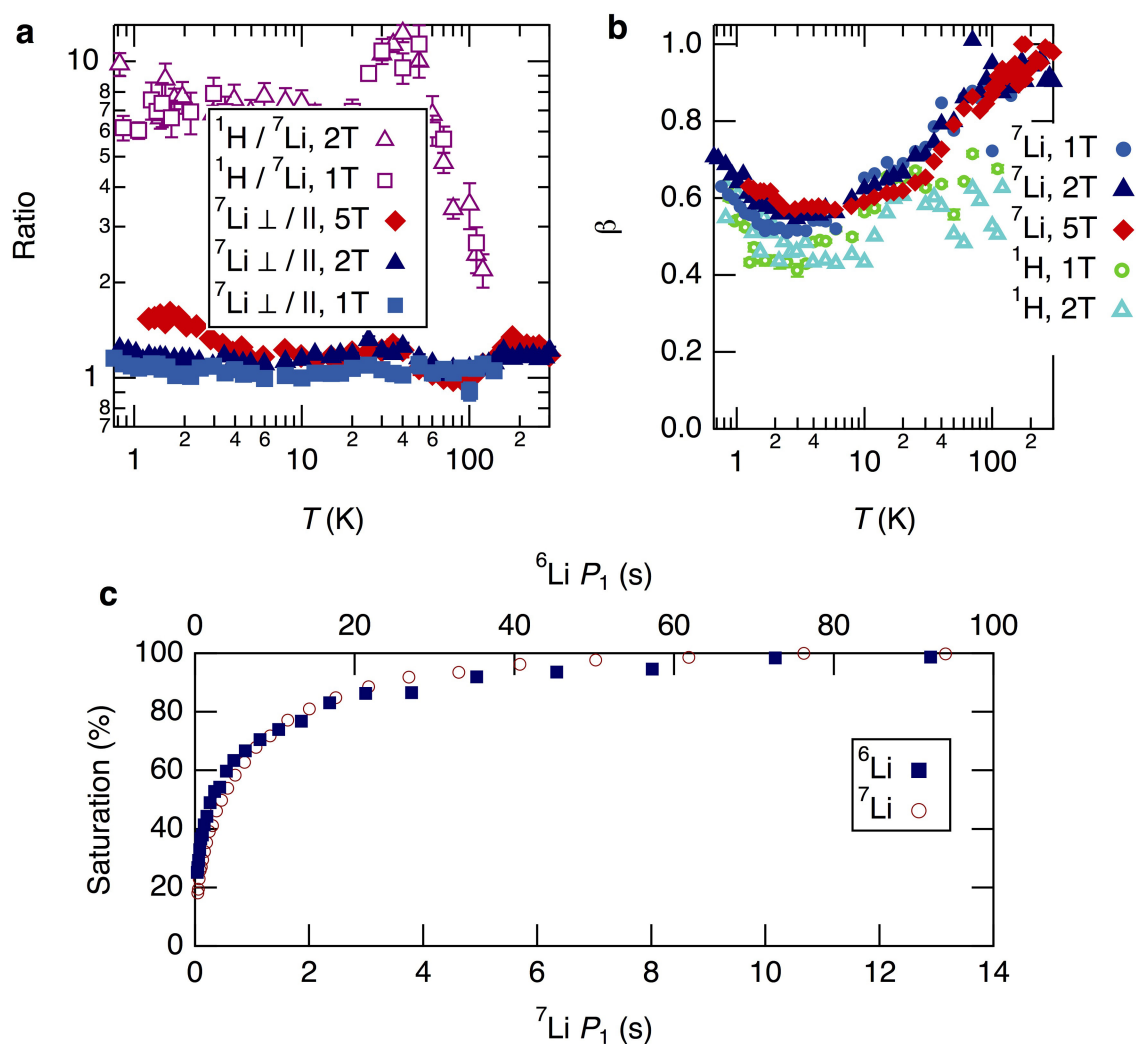


Extended Data Figure 5 | T/B scaling of C and $(T_1T)^{-1}$, and their fitting with the model density of excitations. $B^{1/2}(C/T)$ versus T/B (filled symbols, left axis) and $B^{1/2}(T_1T)^{-1/2}$ versus T/B (open symbols, right axis) under various magnetic fields. All of the $C(T, B)$ data points (closed symbols) and $T_1(T, B)$ data points (open symbols) fall onto the respective universal curves at low T/B , indicating a scaling behaviour. Because $B^{1/2}(T_1T)^{-1/2} = T_1^{-1/2}(T/B)^{-1/2}$, the plot for T_1 is another way of representing the same (T/B) scaling as the inset to Fig. 3b. The physical meaning of $B^{1/2}(T_1T)^{-1/2}$ is the Fermi average of $D(E)$ with a renormalization factor $B^{1/2}$, which is closely related to $B^{1/2}(C/T)$. C/T and $(T_1T)^{-1}$ are given as follows using the standard equations, which express a Fermi averaging of $D(E)$ and $D(E)^2$, respectively:

$$\frac{C}{T} = \frac{1}{T} \int E D(E) \frac{df}{dT} dE = -\frac{1}{T^2} \int E^2 D(E) \frac{df}{dE} dE$$

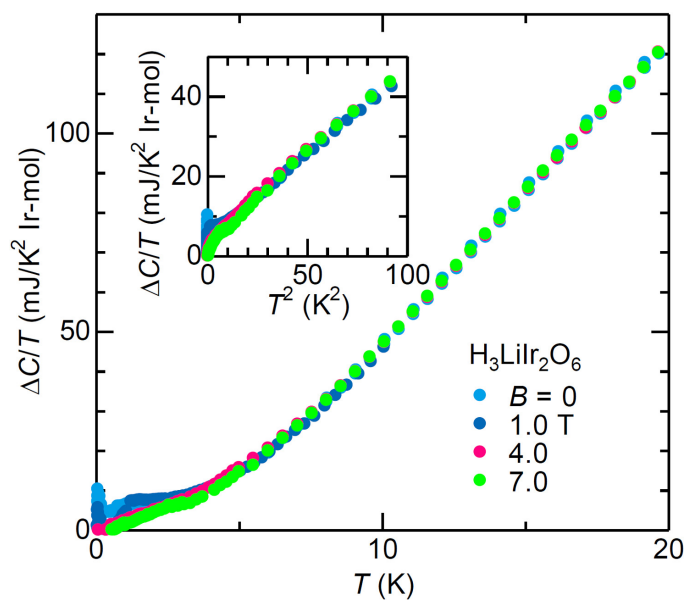
$$\frac{1}{T_1 T} = -4\pi \hbar k_B (\gamma_n A_{\text{hf}})^2 \int D^2(E) \frac{df}{dE} dE$$

Here, $f(T, E) = 1/\{\exp[(E/(k_B T)) + 1]\}$ is Fermi distribution function. The solid and dashed lines indicate $B^{1/2}(C/T)$ and $B^{1/2}(T_1T)^{-1/2}$, respectively, calculated using the above equations for the model for $D(E)$ shown in Fig. 4c. With $\alpha = 2.9$ and $\bar{\Gamma} = 4.3 \times 10^8 \text{ J}^{-1/2}$ per Ir atom, the two scaling curves observed experimentally for $B^{1/2}(C/T)$ and $B^{1/2}(T_1T)^{-1/2}$ are well reproduced by the calculations. $A_{\text{hf}} = 0.44/\mu_B \text{ T}$ and $\gamma_n/2\pi = 16.54680 \text{ MHz T}^{-1}$ were used as known parameters for ^7Li . The calculated $B^{1/2}(C/T)$ and $B^{1/2}(T_1T)^{-1/2}$ show different behaviour at high T/B (greater than about 1), which reflects the different methods of thermal averaging. This difference reasonably accounts for the difference between the two universal curves at high T/B that was observed experimentally.

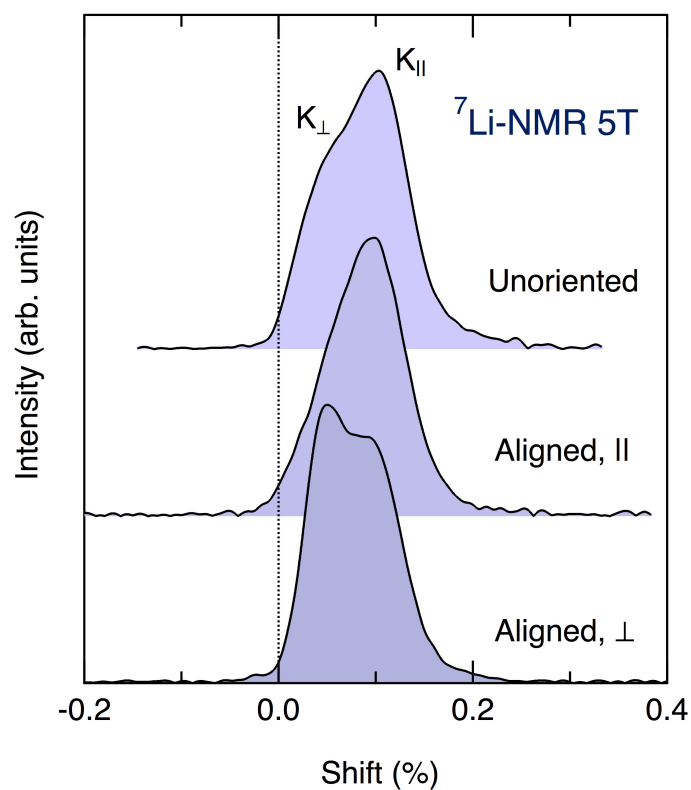


Extended Data Figure 6 | NMR relaxation details. **a**, Ratio of T_1^{-1} for ^1H and ^7Li , and anisotropy of T_1 for ^7Li with perpendicular and parallel fields. The error bars are calculated using the errors in the estimate of T_1 (see Fig. 3b). **b**, Exponent β in the stretched-exponential function describing the NMR relaxation curve as a function of temperature. **c**, Comparison

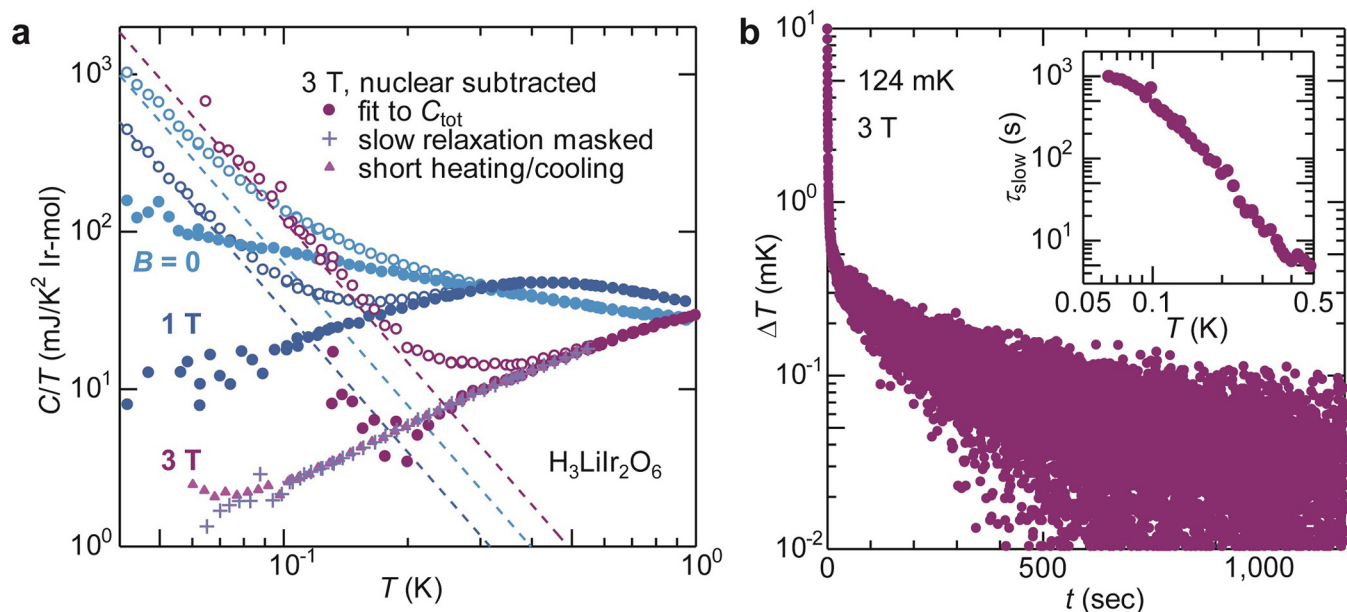
between the relaxation curves of ^6Li and ^7Li at 10 K and 5 T, yielding a ratio of T_1^{-1} for ^6Li and ^7Li of 0.14. P_1 is the time period between a saturation pulse and the echo sequence in the relaxation measurements. This value agrees well with the squares of the gyromagnetic ratios. $\beta = 0.6$ was used in the calculation.



Extended Data Figure 7 | Estimate of the intrinsic specific heat C_i by subtracting the specific heat due to magnetic defects. Fitting the specific heat C in Extended Data Fig. 5 with the model for $D(E)$ in Fig. 4c gives an estimate of the specific heat due to magnetic defects. The best-fitting function, represented dashed line in Extended Data Fig. 5, is subtracted from the total specific heat $C(B, T)$ shown in Fig. 4a. The residual specific heat ΔC is almost independent of B and gives a measure of intrinsic specific heat C_i . $\Delta C/T$ appears to extrapolate almost to zero as the temperature approaches 0 K, within the uncertainty of the estimate of the contribution from magnetic defects. We do not attempt to separate the possible contribution from the bulk spin liquid to ΔC because of the difficulty in estimating the lattice contribution. The inset shows the plot of $\Delta C/T$ as a function of T^2 .



Extended Data Figure 8 | NMR spectra of $\text{H}_3\text{LiIr}_2\text{O}_6$ before and after the alignment of the powder sample. Before the alignment (top), an asymmetric line shape is obtained (reflecting the anisotropy in the Knight shift K_{\parallel} versus K_{\perp} ; Fig. 2a), which represents a powder pattern. The middle and bottom curves shown the line shapes obtained after the alignment for B along the honeycomb plane (the magnetic easy plane) and perpendicular to the plane, respectively. Because of the easy-plane anisotropy of $\text{H}_3\text{LiIr}_2\text{O}_6$, the alignment for the direction perpendicular to the plane is not as complete as that for the direction parallel to the plane.



Extended Data Figure 9 | Subtraction of the nuclear Schottky contribution from the raw specific heat data. **a**, Open circles represent the raw specific heat C_{tot}/T at $B = 0$, 1 T and 3 T . Filled circles represent the non-nuclear specific heat C/T obtained after subtracting the nuclear contribution $C_{\text{NS}}/T \propto T^{-3}$ (dashed lines) from C_{tot}/T . Filled triangles and pluses indicate the non-nuclear C/T obtained directly from a time-domain measurement, either by heating for a short period of 100–200 s and then measuring the short relaxation for a period of 100–200 s (triangles) or by heating for a long period of 1,500–2,500 s and then measuring only the short relaxation for a period of 100–200 s (pluses). The non-nuclear

specific heat C/T at $B = 3\text{ T}$ obtained by the three different methods agree reasonably well, which strongly supports the validity of our analyses. The $C_{\text{NS}}/T \propto T^{-3}$ term for $B = 0\text{ T}$ is slightly larger than that for $B = 1\text{ T}$. The origin of the extra T^{-3} contribution observed in the $B = 0$ data remains elusive. **b**, Example of the relaxation curve at $B = 3\text{ T}$ and $T = 124\text{ mK}$, which indicates the clear separation in the time domain between the fast relaxation due to the non-nuclear contribution and the slow relaxation due to the nuclear contributions. The inset shows the temperature dependence of the slow relaxation time constant at $B = 3\text{ T}$.

Extended Data Table 1 | Refined structural parameters of $\text{H}_3\text{LiIr}_2\text{O}_6$ at 300 K

Atom	site	<i>g</i>	<i>x</i>	<i>y</i>	<i>z</i>	<i>B</i> (Å ²)
Ir(1)	4 <i>g</i>	1	0	0.335(3)	0	0.1(1)
Li(1)	2 <i>a</i>	1	0	0	0	0.1(1)
O(1)	8 <i>j</i>	1	0.404(8)	0.323(3)	0.229(5)	1.7(3)
O(2)	4 <i>i</i>	1	0.417(8)	0	0.220(9)	1.7(3)

The space group is $C2/m$ (number 12), $Z=2$ and the lattice constants are $a=5.3489(8)$ Å, $b=9.2431(14)$ Å, $c=4.8734(6)$ Å and $\beta=111.440(12)^\circ$. *g* and *B* denote the site occupancy and the isotropic temperature factor, respectively. We did not refine the positions of the H atoms because of the small atomic scattering factor. The final *R* index is $R_{\text{wp}}=4.717\%$.

Freezing on a sphere

Rodrigo E. Guerra^{1*}, Colm P. Kelleher^{1*}, Andrew D. Hollingsworth¹ & Paul M. Chaikin¹

The best understood crystal ordering transition is that of two-dimensional freezing, which proceeds by the rapid eradication of lattice defects as the temperature is lowered below a critical threshold^{1–4}. But crystals that assemble on closed surfaces are required by topology to have a minimum number of lattice defects, called disclinations, that act as conserved topological charges—consider the 12 pentagons on a football or the 12 pentamers on a viral capsid^{5,6}. Moreover, crystals assembled on curved surfaces can spontaneously develop additional lattice defects to alleviate the stress imposed by the curvature^{6–8}. It is therefore unclear how crystallization can proceed on a sphere, the simplest curved surface on which it is impossible to eliminate such defects. Here we show that freezing on the surface of a sphere proceeds by the formation of a single, encompassing crystalline ‘continent’, which forces defects into 12 isolated ‘seas’ with the same icosahedral symmetry as footballs and viruses. We use this broken symmetry—aligning the vertices of an icosahedron with the defect seas and unfolding the faces onto a plane—to construct a new order parameter that reveals the underlying long-range orientational order of the lattice. The effects of geometry on crystallization could be taken into account in the design of nanometre- and micrometre-scale structures in which mobile defects are sequestered into self-ordered arrays. Our results may also be relevant in understanding the properties and occurrence of natural icosahedral structures such as viruses^{5,9,10}.

The remarkable predictions of the Kosterlitz–Thouless–Halperin–Nelson–Young (KTHNY)^{1–4} theory of melting on a plane have been verified both by experiment and simulation in systems as diverse as free electrons on liquid He surfaces¹¹, magnetic flux vortices in superconductors¹², and monolayers of paramagnetic colloidal particles interacting through induced magnetic dipoles^{13–15}. This last system is particularly well characterized—its entire phase behaviour can be reduced to a one-dimensional phase diagram parameterized by a single, dimensionless interaction parameter, Γ , defined as the ratio of neighbour magnetic dipole and thermal energies:

$$\Gamma = \frac{(\pi\rho)^{3/2}}{k_B T} A \quad (1)$$

where A quantifies the magnitude of the dipolar pair potential, $U(r) = A/r^3$ (where r is the separation between particles), ρ is the number density of particles, k_B is Boltzmann’s constant, and T is the absolute temperature. Consistent with this definition, the liquid–crystalline hexatic phase that separates the isotropic fluid from the crystalline solid occupies a narrow window of Γ values¹⁵, $67 \lesssim \Gamma \lesssim 70$.

Our system of charged, hydrophobic microspheres adsorbed at oil–aqueous interfaces is accurately described by the same interaction potential^{16,17}. Yet, unlike any system controlled by magnetic fields, these particles are bound to the surface by electrostatic image charge forces (Fig. 1b), and can uniformly decorate the surfaces of spheres, or other curved surfaces, without affecting the form of their interparticle forces (see Supplementary Information section 2). However, the topology of the sphere fundamentally changes the KTHNY picture

of ordering by elimination of defects, since at least twelve 5-coordinated disclinations (particles with pentagonal Voronoi cells and positive topological charge) are required⁵. Furthermore, it has been shown that as the size of the system increases (at constant density) it becomes energetically favourable to decorate these 12 disclinations with dislocations (topologically neutral, 5–7 disclination pairs) organized into linear structures called ‘scars’^{6,8,18,19}. The total number of dislocations in the system—proportional to the length of the scars—grows as R/a , where R is the radius of the sphere and a is the interparticle distance¹⁸. This is unlike other systems, such as superfluid ⁴He (ref. 20) and the two-component plasma²¹, that exhibit a related Kosterlitz–Thouless transition on a sphere, but where all topological defects may be eliminated. Consequently, since dislocations are mobile defects that destroy both crystallinity and rigidity^{4,22}, it is natural to ask whether crystallization of particles confined to the surface of a sphere is possible at all, or whether the proliferation of defects leads to liquid or glassy phases even for the strongest interactions (highest Γ).

Confocal micrographs (top panel of Fig. 1a) show clear differences between droplets with high and low Γ values (for methods see Supplementary Information section 1). First, Voronoi tessellations of these surfaces show that disclinations (particles with topological charge equal to 6 less their coordination number) densely and uniformly cover the liquid-like sample, but are much rarer in the more ordered sample and are clustered in scars (middle panel of Fig. 1a). A similar pattern is shown by the two-dimensional bond-orientational order parameter that measures the orientation and degree of hexagonal order around each particle^{4,14}:

$$\psi_6(\mathbf{r}_i, t) = \frac{1}{N_i} \sum_{j=1}^{N_i} e^{6i\theta_{ij}(t)} \quad (2)$$

Here, N_i is the coordination number of the i th particle, and $\theta_{ij}(t)$ is the angle between the line connecting particle i to its j th neighbour and an arbitrary reference axis. Like the distribution of topological defects (middle panel of Fig. 1a), the time-averaged $|\psi_6(\mathbf{r}_i, t)|$ field, $\langle |\psi_6| \rangle_i$, is homogeneous over the entire sphere, as shown in the bottom panel of Fig. 1a). For the denser samples, $\langle |\psi_6| \rangle_i$ is spatially heterogeneous—the environment around most particles is locally hexagonal for the entire duration of observation, while a small number of particles, in or near the scars, have very low $\langle |\psi_6| \rangle_i$ values.

KTHNY theory postulates that the magnitude of this orientational order—as quantified, for example, by the $|\psi_6(\mathbf{r}_i, t)|$ field averaged over space and time, $\langle |\psi_6| \rangle$ —is intimately related to the distribution of topological defects⁴. Indeed, in flat space the number of topological defects drops precipitously over a narrow range of Γ values centred around $\Gamma \approx 70$, while $\langle |\psi_6| \rangle$ increases rapidly¹⁷. By contrast, while the reduction of defects on spheres with $N \approx 1,500$ particles is accompanied by increasing values of $\langle |\psi_6| \rangle$, the crossover to high- Γ behaviour is broader (especially in the simulations) than what we observe in the flat layers; moreover, the number of topological defects reaches a plateau value much larger than the 12 required by topology (Fig. 1c). In the $\Gamma, N \rightarrow \infty$ limit, the number and clustering of defects has been predicted using continuum elasticity^{6,18}.

¹Center for Soft Matter Research New York University, New York, New York 10003, USA.

*These authors contributed equally to this work.

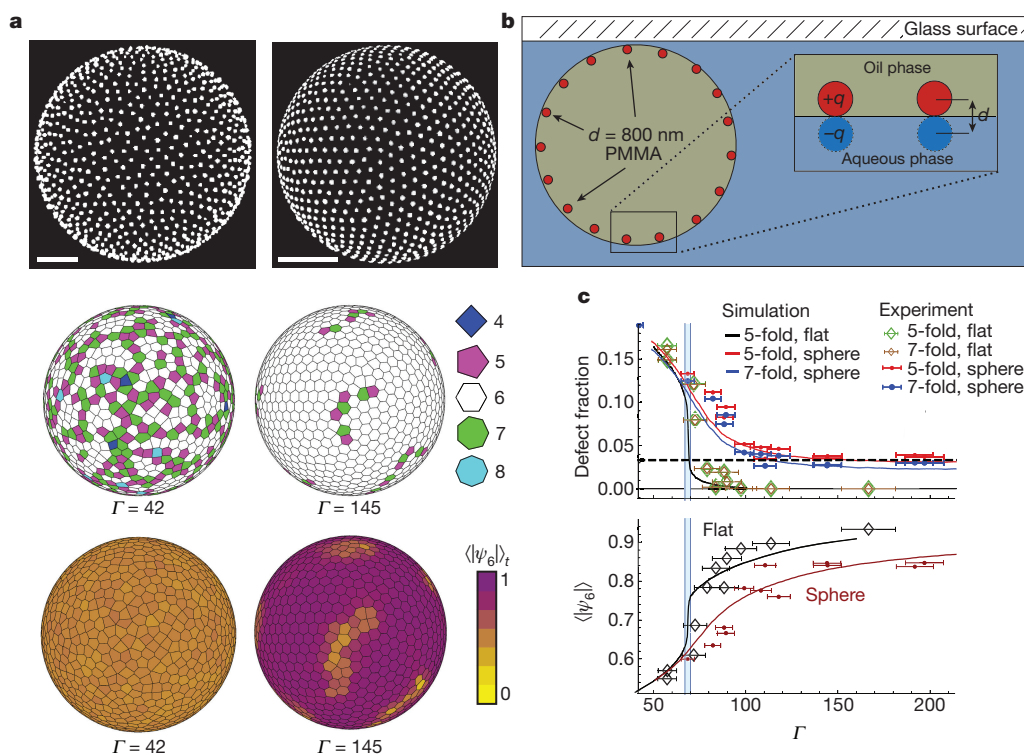


Figure 1 | Defects and order in spherical assemblies. **a**, The top panel shows particles adsorbed on a sphere at low density ($\Gamma=42$, left) appearing disordered. More densely packed particles ($\Gamma=145$, right) exhibit the hexagonal order and lattice lines that are characteristic of flat crystals. Scale bars, $20\mu\text{m}$. The middle panel shows lattice defects uniformly covering the disordered sphere (left), whereas the more ordered sphere (right) is covered mostly by 6-coordinated particles. The bottom panel shows values of the time-averaged bond-orientation order parameter, $\langle|\psi_6(\mathbf{r})|\rangle_t$, of particles on the disordered sphere (left) to be much more uniform than those on the higher- Γ sphere (right). **b**, Image charges generated by the free ions in the aqueous fluid attract hydrophobic poly(methyl methacrylate) (PMMA) particles with charge q and diameter d

to the oil–aqueous interface and induce dipolar repulsive forces between them. **c**, Measurements of defect fractions (top) and $\langle|\psi_6|\rangle$ (bottom) for spheres decorated with $N \approx 1,500$ particles and for similar particles on flat surfaces. Symbols are experimental data points, with error bars defined in Supplementary Information section 2.2, while solid lines are simulation results. Flat surface packings eliminate nearly all defects and attain nearly perfect orientational order over a narrow range of Γ values ($67 \lesssim \Gamma \lesssim 70$, shaded). For spherical packings, the improvement in local order and annihilation of defects with increasing Γ is dramatically hindered, with a finite concentration of defects expected even in the $\Gamma \rightarrow \infty$ limit; this is consistent with predictions based on continuum elasticity (dashed horizontal line).

Yet, although these globally averaged quantities reflect the increasing order of particles with increasing Γ , they do not reflect the clustering of defects that is evident in the micrographs. To understand this clustering better, we compute $g_{55}(r)$, the pair correlation between 5-coordinated defects (Supplementary Information section 4), for experimental and simulated^{23–25} particle configurations over a wide range of Γ . We find that $g_{55}(r)$ is flat for $\Gamma < 70$ —consistent with a random distribution of defects. However, for $\Gamma > 70$, we find a peak in $g_{55}(r)$ at short distances that grows and widens with increasing Γ —indicating the condensation of defects into clusters. More interestingly, additional peaks in $g_{55}(r)$ appear for values of r that correspond to the geodesic distances between the vertices of an icosahedron (Fig. 2a), making it possible to draw a football on the sphere such that most of the defects lie inside its pentagons (Fig. 2b). Nevertheless, this icosahedral ordering of defects develops gradually, and it is difficult to unambiguously identify isolated defect clusters until $\Gamma \gtrsim 120$.

The strong coupling between lattice defects and particle mobility in crystalline solids^{19,22} suggests that the proliferation and spatial segregation of dislocations will also affect the dynamics of our system. To study this we adopt a tool used to describe glasses, labelling particles that move more than a distance λ^* over a time τ^* as ‘mobile’, $Q=1$, and those that do not as ‘caged’, $Q=0$ (Supplementary Information section 6)^{26,27}. For large values of Γ , we observe clustering of mobile particles reminiscent of the clustering of topological defects (Fig. 2c). To investigate the connection between defects and mobility we compute $g_{QD}(r)$, the pair correlation function between mobile particles ($Q=1$)

and disclinations (D , defined as particles with any coordination number other than six). We find that $g_{QD}(r)$ is almost identical to $g_{55}(r)$, confirming that particle mobility is strongly heterogeneous and becomes confined to the same icosahedrally coordinated ‘seas’ that contain the excess lattice defects.

In two dimensions, long-range correlations of orientational order, captured by $g_6(\mathbf{r}) = \langle \psi_6(\mathbf{x}) \psi_6^*(\mathbf{y}) \rangle_{|\mathbf{x}-\mathbf{y}|=r}$, are a clear sign of crystallinity⁴; however, vector transport on the sphere changes angles and complicates the definition of a global reference coordinate system. Nevertheless, the icosahedral ordering of defects suggests that it may be possible to detect crystalline order by explicitly referencing this broken symmetry. We thus define an icosahedral ‘net’ by rotating an icosahedron so that its vertices are aligned with the positions of the defects (Supplementary Information section 8). Projecting the particles onto the faces of the icosahedron and unfolding the structure onto a plane reveals the remarkable global orientational coherence of particle configurations with high Γ (Fig. 3a). We quantify this order using the icosahedrally referenced orientational correlation function:

$$g_6'(r) = \langle \psi_6'(\mathbf{r}_i) \psi_6'^*(\mathbf{r}_j) \rangle_{\cos^{-1}(\mathbf{r}_i \cdot \mathbf{r}_j / R^2) = r} \quad (3)$$

where $\psi_6'(\mathbf{r}_i)$ is the icosahedrally referenced value of the bond-orientational order parameter (Fig. 3b, Supplementary Information section 8.2). We note that randomly oriented icosahedral nets, or nets based on polyhedra with different symmetries, will not produce such coherence (Supplementary Information section 8.5).

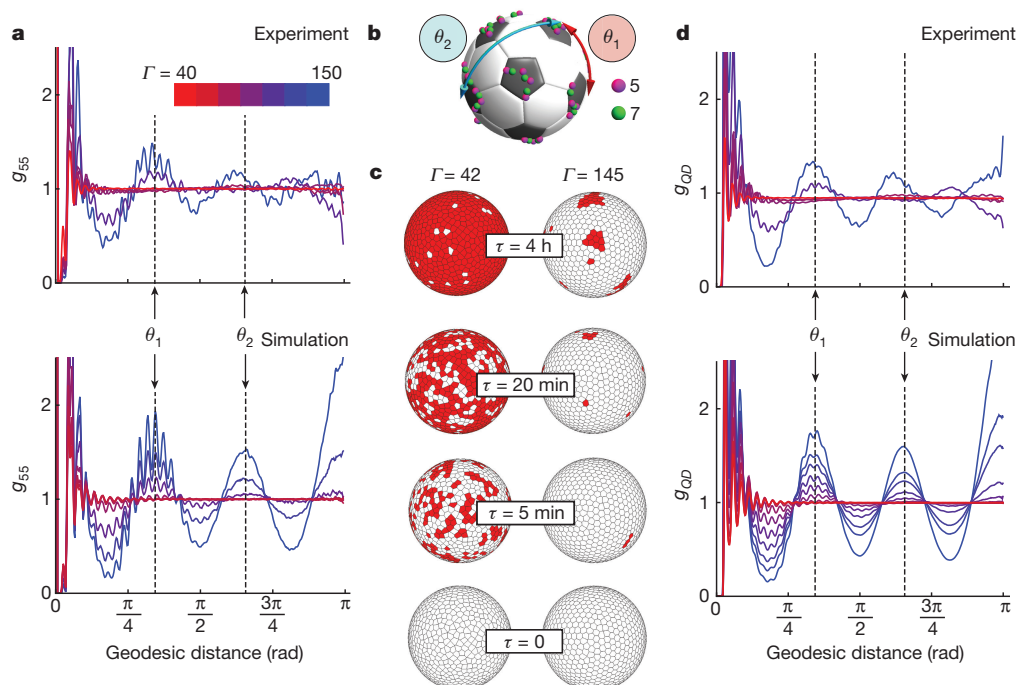


Figure 2 | Emergence of icosahedrally coordinated defect 'seas'. **a**, Pair correlation of 5-coordinated disclinations, g_{55} , for experimental (top) and simulated (bottom) spheres decorated with $N \approx 1,500$ particles. Disordered spheres are uniformly randomly covered with lattice defects, leading to a flat and featureless g_{55} . As order increases so does a coherent defect-density modulation with peaks at $0, \theta_1, \theta_2$ and π , consistent with their segregation into icosahedrally coordinated 'seas'. **b**, Rendering of experimentally determined 5- and 7-fold coordinated lattice defect positions over the surface of a suitably oriented football³⁰ makes the

icosahedral ordering apparent. **c**, Distribution of 'mobile' particles (red, see text) over the surface of spheres with $\Gamma = 42$ and $\Gamma = 145$. After a lag time τ , mobile particles appear randomly over the surface of the disordered sphere (left panels) and quickly cover its surface. Particles on the more ordered sphere (right panels) have far lower absolute mobilities ('caged' particles are white), and the mobile particles that appear are segregated into isolated 'seas'. **d**, Pair cross-correlations of all defects and mobile particles for the same spheres shown in **a** show similar ordering to g_{55} , demonstrating the spatial coincidence of defects and mobility.

The emergence of this new broken symmetry now raises the question of whether the extreme retardation in the growth of $\langle |\psi_6| \rangle$ is a finite-size effect, or arises because the spherical geometry fundamentally changes the form of the freezing transition, perhaps requiring an additional

order parameter to describe it. Consequently, to explore the $N \rightarrow \infty$ limit, we supplement our simulations of spheres decorated with $N = 1,500$ particles, with simulations with $N = 3,000, 6,000$ and $12,000$ particles^{23,25}, and evaluate two order parameters: the icosahedrally

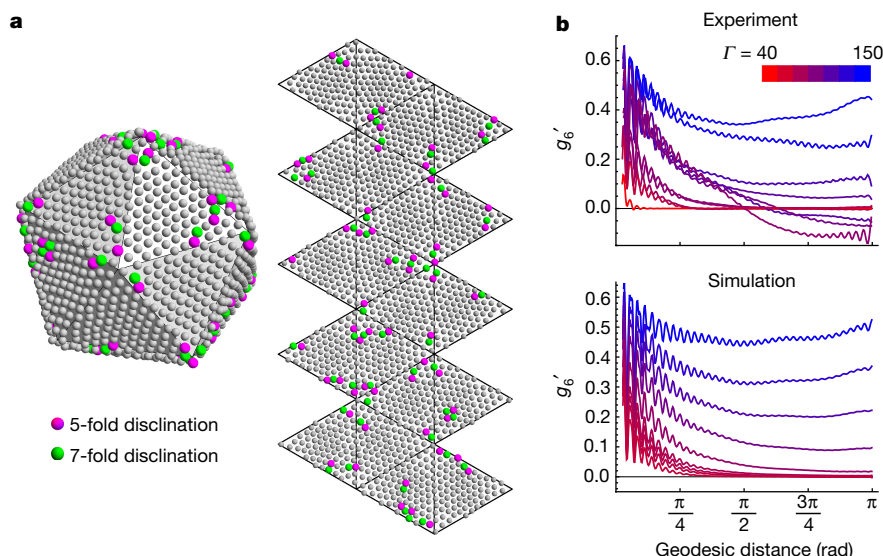


Figure 3 | Icosahedral map projections and long-range order. **a**, The left panel shows a reference icosahedron, oriented by fitting its vertices to the positions of the defect particles. The right panel shows that unfolding this icosahedron reveals long-range order hidden by the extra disclinations. **b**, Orientational correlation functions, $g'_6(r)$, computed using the reference icosahedra (see text and Supplementary Information section 8). For the samples at low Γ , orientational correlations decay rapidly, whereas at high Γ , hexagonal order extends across the entire sphere. At intermediate values of

Γ , the absence of well defined defect clusters means that the correlation of the best-fit icosahedron to the orientational order is low, so many independent configurations must be sampled to produce accurate $g'_6(r)$ curves. Since our experiments sample only a small number of independent configurations, the correlation functions in the top panel of **b** in the range $85 \lesssim \Gamma \lesssim 110$ sometimes reach negative values at large r , whereas simulation results in the bottom panel are consistent with thorough sampling.

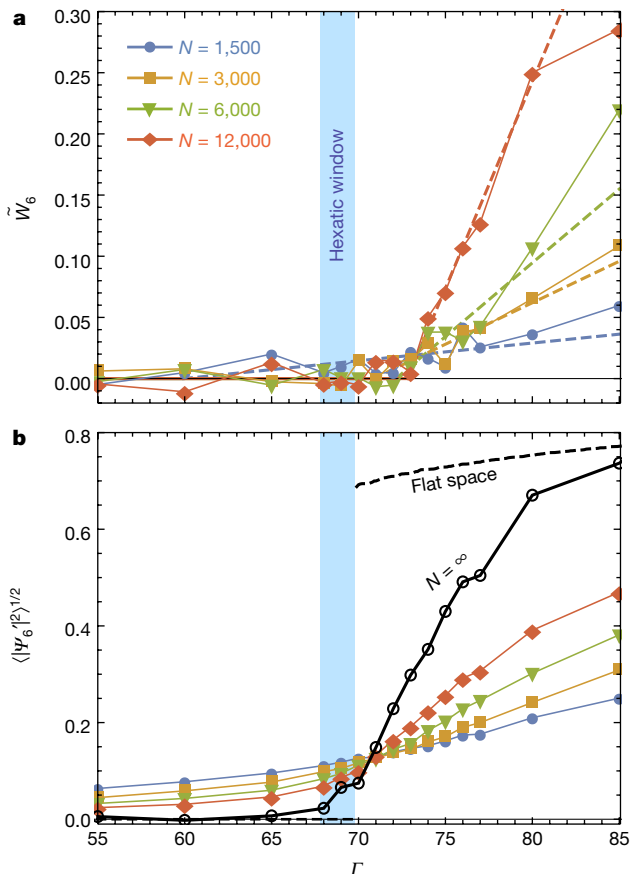


Figure 4 | Icosahedral order and finite size scaling. **a**, Scaling of the normalized, three-body, three-dimensional bond-orientation of the defects, \tilde{W}_6 , with Γ and system size for simulated particle configurations. Icosahedral order grows approximately linearly beyond a critical value of Γ , where the slope of linear fits to the data (dotted lines) appears to diverge as $N \rightarrow \infty$. **b**, Scaling of the average icosahedrally referenced bond order parameter, $\langle |\Psi_6'|^2 \rangle^{1/2}$, with Γ and system size. The rate at which this order parameter grows increases with system size, and its $N \rightarrow \infty$ extrapolated values remain positive for all Γ that correspond to the flat-space solid.

referenced two-dimensional bond-orientation of the particles $\Psi_6' = \frac{1}{N} \sum_i \psi_6'(\mathbf{r}_i)$ and the normalized, three-body, three-dimensional bond-orientation of the defects²⁸ \tilde{W}_6 :

$$\tilde{W}_6 = -\frac{\sqrt{4,199}}{11} \sum_{m_1, m_2, m_3 = -6}^6 \begin{pmatrix} 6 & 6 & 6 \\ m_1 & m_2 & m_3 \end{pmatrix} \frac{\rho_{6m_1} \rho_{6m_2} \rho_{6m_3}}{(\sum_m |\rho_{6m}|^2)^{3/2}} \quad (4)$$

where the first quantity in the summand is the Wigner 3-j symbol and $\rho_{6m} = \sqrt{4\pi} \sum_i Y_{6m}(\theta_i, \phi_i)$ (Y_{6m} are the sixth-order spherical harmonics, and (ϕ_i, θ_i) are the polar coordinates of the i th defect). This order parameter is particularly sensitive to the presence of icosahedral symmetry, and is normalized so that $\tilde{W}_6 = 1$ for a perfect icosahedron.

Plots of these quantities show that increasing the system size increases the rate at which orientational and icosahedral order increase with increasing Γ (Fig. 4a, b). A polynomial extrapolation of $\langle |\Psi_6'|^2 \rangle^{1/2}$ in powers of $1/R \propto 1/\sqrt{N}$ shows that, in the thermodynamic ($N \rightarrow \infty$) limit, $\langle |\Psi_6'|^2 \rangle^{1/2}$ vanishes for $\Gamma < 67$, but remains finite for $\Gamma > 70$, coinciding with the two-dimensional liquid and crystal phase boundaries. Similarly, \tilde{W}_6 is zero for lower Γ , and begins to increase roughly linearly—with a slope approximately proportional to N —above a critical threshold. We note that both of these order parameters $\langle |\Psi_6'|^2 \rangle^{1/2}$ and \tilde{W}_6 exhibit transitions close to the Γ values of the liquid–hexatic and hexatic–solid transitions in flat space as $R \rightarrow \infty$.

The elucidation of order by the unravelling and flattening of an appropriate polyhedral net may be useful in other contexts, such as liquid crystalline orientations on curved surfaces (for example, the tetrahedrally symmetric, baseball-like texture of a nematic confined to a thin shell, Supplementary Information section 8.6²⁹). As in our study, the need for both crystalline and polyhedral order parameters has been invoked in recent models of assembly of icosahedral viral motifs¹⁰. Moreover, the segregation of defects to symmetric sites, and the concomitant mobility near these sites, should prove useful in designing structures where both rigidity and fluidity are desired in specific areas.

Online Content Methods, along with any additional Extended Data display items and Source Data, are available in the online version of the paper; references unique to these sections appear only in the online paper.

Data Availability Source Data for Figs 1–4 are provided with the online version of the paper. Coordinates and trajectories of particles identified from confocal micrographs for every experimental sample referred to in the paper are available from the Open Science Framework repository ‘Freezing on a Sphere’³¹. The same repository contains a snapshot of every simulated dataset referred to in the paper (each stored as an XML file) and corresponding Python scripts, which, together with the HOOMD-blue plugins included in Supplementary Information, can be used to reconstitute all of the simulation data presented here. Raw confocal image data and complete simulation results are available upon request.

Code Availability Numerical simulations were performed using HOOMD-blue v1.3.3 (refs 23, 24) with double-precision arithmetic and custom plug-ins for pairwise interaction potentials and Langevin dynamics integrators. Experimental and simulated datasets were analysed using software written in MATLAB, CUDA, and C. These analysis routines and the HOOMD plug-ins are available in Supplementary Information.

Received 1 June; accepted 29 November 2017.

- Kosterlitz, J. M. & Thouless, D. J. Ordering, metastability and phase transitions in two-dimensional systems. *J. Phys. C* **6**, 1181–1203 (1973).
- Halperin, B. I. & Nelson, D. R. Theory of two-dimensional melting. *Phys. Rev. Lett.* **41**, 121–124 (1978).
- Young, A. P. Melting and the vector Coulomb gas in two dimensions. *Phys. Rev. B* **19**, 1855–1866 (1979).
- Nelson, D. R. *Defects and Geometry in Condensed Matter Physics* Vol. 112 (Cambridge Univ. Press, 2002).
- Caspar, D. L. D. & Klug, A. Physical principles in the construction of regular viruses. *Cold Spring Harb. Symp. Quant. Biol.* **27**, 1–24 (1962).
- Bowick, M. J., Cacciuto, A., Nelson, D. R. & Travesset, A. Crystalline particle packings on a sphere with long-range power-law potentials. *Phys. Rev. B* **73**, 024115 (2006).
- Irvine, W. T. M., Vitelli, V. & Chaikin, P. M. Pleats in crystals on curved surfaces. *Nature* **468**, 947–951 (2010).
- Dodgson, M. J. W. & Moore, M. A. Vortices in a thin-film superconductor with a spherical geometry. *Phys. Rev. B* **55**, 3816–3831 (1997).
- Colson, P. et al. “Megavirales”, a proposed new order for eukaryotic nucleocytoplasmic large DNA viruses. *Arch. Virol.* **158**, 2517–2521 (2013).
- Dharmavaram, S., Xie, F., Klug, W., Rudnick, J. & Bruinsma, R. Orientational phase transitions and the assembly of viral capsids. *Phys. Rev. E* **95**, 062402 (2017).
- Stan, M. A. & Dahm, A. J. Two-dimensional melting: electrons on helium. *Phys. Rev. B* **40**, 8995–9005 (1989).
- Guillamón, I. et al. Direct observation of melting in a two-dimensional superconducting vortex lattice. *Nat. Phys.* **5**, 651–655 (2009).
- Zahn, K., Lenke, R. & Maret, G. Two-stage melting of paramagnetic colloidal crystals in two dimensions. *Phys. Rev. Lett.* **82**, 2721–2724 (1999).
- Gasser, U., Eisenmann, C., Maret, G. & Keim, P. Melting of crystals in two dimensions. *ChemPhysChem* **11**, 963–970 (2010).
- Deuschländer, S., Puertas, A. M., Maret, G. & Keim, P. Specific heat in two-dimensional melting. *Phys. Rev. Lett.* **113**, 127801 (2014).
- Kelleher, C. P. et al. Charged hydrophobic colloids at an oil–aqueous phase interface. *Phys. Rev. E* **92**, 062306 (2015).
- Kelleher, C. P., Guerra, R. E., Hollingsworth, A. D. & Chaikin, P. M. Phase behavior of charged colloids at a fluid interface. *Phys. Rev. E* **95**, 022602 (2017).
- Bausch, A. R. et al. Grain boundary scars and spherical crystallography. *Science* **299**, 1716–1718 (2003).
- Lipowsky, P., Bowick, M. J., Meinke, J. H., Nelson, D. R. & Bausch, A. R. Direct visualization of dislocation dynamics in grain-boundary scars. *Nat. Mater.* **4**, 407–411 (2005).
- Kotsubo, V. & Williams, G. A. Kosterlitz–Thouless superfluid transition for helium in packed powders. *Phys. Rev. Lett.* **53**, 691–694 (1984).
- Ovrt, B. A. & Thomas, S. Theory of vortices and monopoles on a sphere. *Phys. Rev. D* **43**, 1314 (1991).

22. Hirth, J. P. & Lothe, J. *Theory of Dislocations* 2nd edn (John Wiley and Sons, 1982).
23. Anderson, J. A., Lorenz, C. D. & Travesset, A. General purpose molecular dynamics simulations fully implemented on graphics processing units. *J. Comput. Phys.* **227**, 5342–5359 (2008).
24. Glaser, J. *et al.* Strong scaling of general-purpose molecular dynamics simulations on GPUs. *Comput. Phys. Commun.* **192**, 97–107 (2015).
25. Leimkuhler, B. & Matthews, C. Efficient molecular dynamics using geodesic integration and solvent–solute splitting. *Proc. R. Soc. Lond. A* **472**, 20160138 (2016).
26. Parisi, G. Short-time aging in binary glasses. *J. Phys. Math. Gen.* **30**, L765 (1997).
27. Glotzer, S. C., Novikov, V. N. & Schrder, T. B. Time-dependent, four-point density correlation function description of dynamical heterogeneity and decoupling in supercooled liquids. *J. Chem. Phys.* **112**, 509–512 (2000).
28. Steinhardt, P. J., Nelson, D. R. & Ronchetti, M. Bond-orientational order in liquids and glasses. *Phys. Rev. B* **28**, 784–805 (1983).
29. Vitelli, V. & Nelson, D. R. Nematic textures in spherical shells. *Phys. Rev. E* **74**, 021711 (2006).
30. Michael E2. 3D graphic of soccer ball. <https://mathematica.stackexchange.com/questions/118604> (version 2016–06–19, Mathematica Stack Exchange, 2016).
31. Kelleher, C. P. & Guerra, R. E. Freezing on a sphere. <https://osf.io/2d38z/> (Open Science Framework, 2017).

Supplementary Information is available in the online version of the paper.

Acknowledgements We thank M. J. Bowick and A. Travesset for discussions. This research was primarily supported by the National Science Foundation (NSF) under grant DMR 1105417 and grant GBMF3849 from the Gordon and Betty Moore Foundation. This work was supported partially by the Materials Research Science and Engineering Center (MRSEC) Program of the NSF under award number DMR-1420073 and by the National Aeronautics and Space Administration (NASA) under grant NNX13AR67G. This work has used the NYU IT High Performance Computing resources and services.

Author Contributions C.P.K. performed the experiments. A.D.H. synthesized the samples. R.E.G. performed the simulations. C.P.K., R.E.G. and P.M.C. designed the research, analysed the data and wrote the paper. P.M.C. conceived and directed the project.

Author Information Reprints and permissions information is available at www.nature.com/reprints. The authors declare no competing financial interests. Readers are welcome to comment on the online version of the paper. Publisher's note: Springer Nature remains neutral with regard to jurisdictional claims in published maps and institutional affiliations. Correspondence and requests for materials should be addressed to P.M.C. (chaikin@nyu.edu).

Reviewer Information *Nature* thanks D. A. Vega and the other anonymous reviewer(s) for their contribution to the peer review of this work.

Southern Hemisphere climate variability forced by Northern Hemisphere ice–sheet topography

T. R. Jones¹, W. H. G. Roberts², E. J. Steig³, K. M. Cuffey⁴, B. R. Markle³ & J. W. C. White⁵

The presence of large Northern Hemisphere ice sheets and reduced greenhouse gas concentrations during the Last Glacial Maximum fundamentally altered global ocean–atmosphere climate dynamics¹. Model simulations and palaeoclimate records suggest that glacial boundary conditions affected the El Niño–Southern Oscillation^{2,3}, a dominant source of short-term global climate variability. Yet little is known about changes in short-term climate variability at mid- to high latitudes. Here we use a high-resolution water isotope record from West Antarctica to demonstrate that interannual to decadal climate variability at high southern latitudes was almost twice as large at the Last Glacial Maximum as during the ensuing Holocene epoch (the past 11,700 years). Climate model simulations indicate that this increased variability reflects an increase in the teleconnection strength between the tropical Pacific and West Antarctica, owing to a shift in the mean location of tropical convection. This shift, in turn, can be attributed to the influence of topography and albedo of the North American ice sheets on atmospheric circulation. As the planet deglaciated, the largest and most abrupt decline in teleconnection strength occurred between approximately 16,000 years and 15,000 years ago, followed by a slower decline into the early Holocene.

During glacial–interglacial transitions, the coupled ocean–atmosphere system shifts between stable states, driven by large climate forcings, including Milankovitch orbital cycles, greenhouse gas concentrations, and the decay of continental ice sheets¹. The state changes are observed in palaeoclimate proxy archives such as ice cores at high latitudes, and lake sediments and speleothems in the tropics and mid-latitudes. The state of the tropical Pacific is particularly important because this region affects the generation and communication of climate anomalies between the low and high latitudes^{4,5}.

Whether the nature of the El Niño–Southern Oscillation (ENSO) changed between the Last Glacial Maximum (LGM) and the Holocene is an important question^{3,6}. Proxy studies of ENSO variability during the LGM are contradictory^{7,8}, and the results of modelling studies are similarly ambiguous². One obstacle to understanding past ENSO variability is disentangling changes in ENSO itself from changes in its influence on climate outside the tropics, that is, the strength of ENSO-related teleconnections, which can vary over time⁹.

Tropical Pacific climate variability is an important driver of interannual to multidecadal climate variability in West Antarctica^{4,5}. Warm sea surface temperatures (SSTs) in the tropical Pacific drive the propagation of atmospheric Rossby waves towards the high latitudes, affecting weather systems that develop over the Amundsen Sea^{4,5}. Variability in the Amundsen Sea region dominates climate variability over the adjacent West Antarctic Ice Sheet (WAIS)^{5,10,11}. Over longer timescales, the influence of tropical climate variability on the Amundsen Sea may have implications both for the stability of the ice sheet¹² and for the ventilation of carbon dioxide from the Southern Ocean¹³.

The influence of tropical variability on the climate of West Antarctica is reflected in ice core records from the WAIS. In particular, the oxygen

and hydrogen isotope ratios of water are sensitive to temperature and atmospheric circulation anomalies associated with large ENSO events¹⁴. Such records might therefore yield important insights about changes in tropical climate variability and tropical-to-extratropical teleconnections during glacial–interglacial transitions. In this study, we use a high-resolution hydrogen isotope (δD) record from the WAIS Divide ice core (WDC) to investigate about 31,000 years (31 kyr) of high-frequency climatic variability. The data were produced using laser absorption spectroscopy coupled with a continuous flow analysis system¹⁵. The record is the longest continuously measured water isotope record ever recovered, with an effective sample resolution of 5 mm and a maximum difference in age between consecutive samples of 0.33 years (Extended Data Fig. 1e).

We use spectral techniques (see Methods) on the WDC δD record to analyse West Antarctic climate variability (Fig. 1). Periods longer than 3 yr are preserved throughout the 31-kyr record (Extended Data Fig. 1a). To account for attenuation of the δD signal by diffusion in the firn column and solid ice¹⁶, we apply a diffusion correction on consecutive 500-yr data windows (see Methods; Extended Data Figs 1b, 2c). We isolate the amplitude of 3–7-yr and 4–15-yr δD variations by averaging power density over these frequency ranges. The 3–7-yr range is typical of a high-frequency spectral peak seen in observations of the Southern Oscillation Index (Extended Data Fig. 1c), while the 4–15-yr range is less affected by diffusion (Extended Data Fig. 1a) and captures the decadal variability observed in the Southern Oscillation Index (Extended Data Fig. 1c), tropical Pacific coral isotope records¹⁷, and in modern observations in West Antarctica^{5,14}.

We find that the mean amplitudes of the diffusion-corrected variability in the 3–7-yr and 4–15-yr bands are elevated in the Late Glacial (16–31 kyr ago) period relative to the Holocene (0–10 kyr ago) (Fig. 1c, d). An approximately 50% decrease in amplitude occurs from about 16 kyr to 10 kyr ago in both time series. This decline occurs in two steps: an abrupt decrease about 16 kyr ago followed by a second but less pronounced decline during the period 13–10 kyr ago. Neither time series reveal other substantial changes in variability during the Holocene or during the Late Glacial. We use an objective algorithm (see Methods) to detect an initial statistically significant ($P < 0.05$) decline in the diffusion-corrected 4–15-yr time series based on 500-yr data windows (Extended Data Fig. 2a, b). We find that the decline began 16.44 ± 0.30 kyr ago (all ages are given relative to the present, 1950 AD). Identical results are obtained using the 3–7-yr time series. The timing of the initial decline is robust among different detection techniques. Using a subset of 100-yr data windows for the diffusion-corrected 4–15-yr time series (Extended Data Fig. 2c, d), the decline occurs 16.24 ± 0.17 kyr ago. The timing of the decline is not an artefact of the diffusion correction. Using the raw data in the 4–15-yr band for 500-yr data windows (Fig. 1d), an approximately 40% decrease in amplitude occurs from about 16 kyr to 10 kyr ago, with an initial decline occurring

¹Institute of Arctic and Alpine Research, University of Colorado, Boulder, Colorado 80309-0450, USA. ²Bristol Research Initiative for the Dynamic Global Environment and Bristol Glaciology Centre, School of Geographical Sciences, University of Bristol, Bristol BS8 1SS, UK. ³Department of Earth and Space Sciences, University of Washington, Seattle, Washington 98195-1310, USA.

⁴Department of Geography, University of California, Berkeley, California 94720, USA. ⁵Institute of Arctic and Alpine Research and Department of Geological Sciences, University of Colorado, Boulder, Colorado 80309-0450, USA.

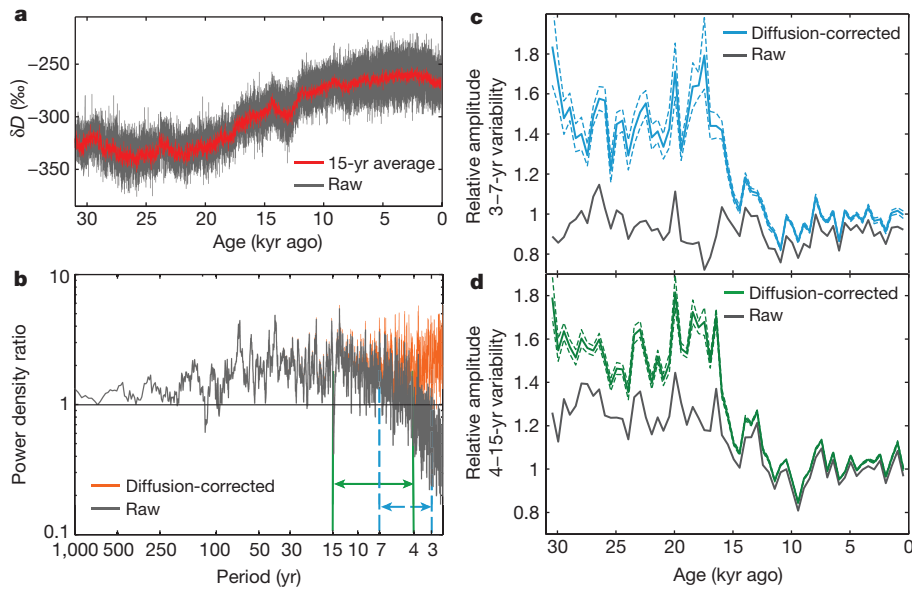


Figure 1 | WDC high-frequency signal strength. **a**, The raw, high-resolution WDC δD water isotope record (grey) and a 15-yr average (red). **b**, Power density ratio for 15 kyr before and after the primary shift in WDC variability (that is, 16–31 kyr ago relative to 0–15 kyr ago); raw data in grey and diffusion-corrected data in orange. For centennial periodicities, the mean ratio is 1.3, whereas the mean ratio for raw and diffusion-corrected periods for the 4–15-yr band is 1.9 and 2.5, respectively. The blue and

green intervals show 3–7-yr and 4–15-yr variability, respectively. The raw data ratio is lower than one at <3 yr owing to increased mean diffusion in the glacial period relative to the Holocene¹⁶. Periods >4 yr are not substantially influenced by diffusion (Extended Data Fig. 1a). **c**, **d**, Plots of diffusion-corrected relative amplitudes using 500-yr data windows, normalized to the most recent value, for 3–7-yr variability (**c**) and 4–15-yr variability (**d**). Dashed lines show 1σ uncertainties (see Methods).

15.94 ± 0.30 kyr ago. Conservatively, this places the decline in WDC variability between 16.74 kyr to 15.64 kyr ago, with a central estimate of 16.24 kyr ago.

The climate shift about 16 kyr ago coincides with large-scale geologic events observed in proxy records across the globe. A substantial

lowering of the Laurentide Ice Sheet surface is estimated to have occurred 16 kyr ago (from ^{14}C dating)¹⁸, corresponding to the Heinrich Event 1 iceberg discharge event in the Northern Hemisphere (Fig. 2). The Heinrich Event 1 ice-rafted debris is of Laurentide origin¹⁹, indicating abrupt changes in ice mass and the topography of the Laurentide Ice

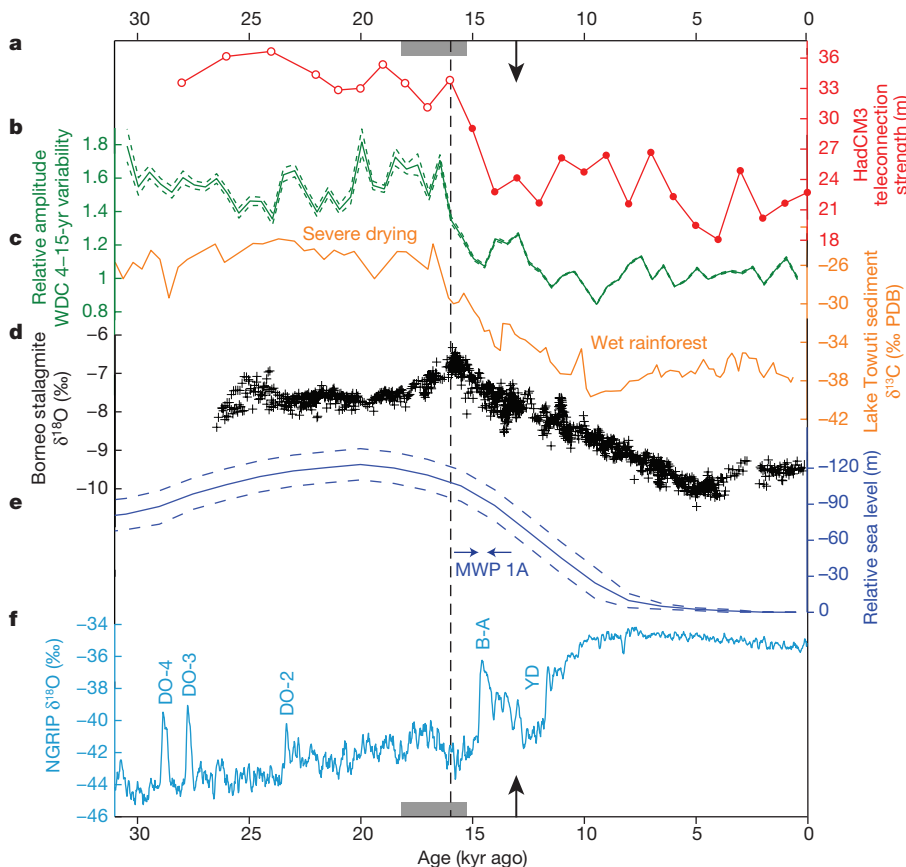


Figure 2 | Indicators of oceanic and atmospheric variability. **a**, Tropical Pacific–West Antarctic teleconnection strength from HadCM3 (see Fig. 3). The open red dots indicate when the teleconnection strength is 95% significantly different from the pre-industrial period using a two-tailed Student's t -test. **b**, WDC diffusion-corrected 4–15-yr variability; dashed lines are 1σ uncertainties (see Methods). **c**, **d**, Hydrologic variability recorded in an Indonesian lake sediment core²¹ (**c**) and Bornean stalagmites²⁶ (**d**). **e**, Relative sea level (solid line) and confidence interval (dashed lines)²⁸, with the estimated duration of melt water pulse (MWP) 1A²⁴. **f**, The NGRIP ice core $\delta^{18}\text{O}$ record²⁷ from central Greenland, showing the Younger Dryas (YD), Bölling–Allerød (B-A), and Dansgaard–Oeschger (DO) events 2–4. The dashed black line represents the maximum about 16 kyr ago in North Atlantic ice-rafted debris, corresponding to a massive freshwater discharge during Heinrich Event 1¹⁸. The grey block is the estimated duration of Heinrich Event 1²⁹. The black arrow is the estimated timing of the flooding of the Sunda Shelf^{21,23,24}.

Sheet. The Cordilleran ice sheet also declined rapidly at this time²⁰, and the lowering of the combined Laurentide–Cordilleran ice sheets (LCIS) has been suggested as a possible forcing mechanism for the transition from dry to wet conditions in Indonesia²¹ (Fig. 2c). Taken together, the similarity in timing of these various records suggests a common link.

To investigate the mechanisms responsible for changing high-frequency variability at WDC, we use the HadCM3 fully coupled ocean–atmosphere model to simulate climate in thousand-year steps from 28 kyr to 0 kyr ago²² (see Methods). We assess variability in both the Amundsen Sea region and the tropical Pacific Ocean. Since the isotopic composition of ice at WDC is indicative of atmospheric circulation in the Amundsen Sea region¹⁴ (Fig. 3a), we examine the mid-level flow in the model, represented by the 500-hPa geopotential height field. The amplitude of the simulated variability in the mean 500-hPa geopotential height field (Z_{ASL}) of the Amundsen Sea Low (ASL) region (55°–70° S, 195°–240° E) follows the same trend as the observations from WDC: more variability during the LGM, less variability during the Holocene, and a decline in variability 16 kyr ago (Fig. 4a). We examine the tropical Pacific influence (Z_{pac}) on the modelled Z_{ASL} by linearly removing the effect of the basin-wide (150°–270° E, 5° N–5° S) tropical Pacific SST (SST_{pac}) from the Z_{ASL} time series (Fig. 4e, f). The amplitude of the residual ASL variability (Z_{local}) is essentially constant over the past 28 kyr (Fig. 4a), demonstrating that the change in the ASL is connected to tropical variability.

The increased Z_{ASL} variability at the LGM could be the result of either increased tropical variability or a change in efficiency of the teleconnection between the tropics and the high latitudes, forced by a change in the tropical mean state. To separate these processes, we compute the strength of the teleconnection between the tropics and ASL by constructing composite maps. These composites show the average response of the 500-hPa geopotential height field to ENSO events in the tropical Pacific (see Methods). We use a composite that imposes both an upper and lower limit on the size of SST_{pac} (± 1.25 to 2.5 times the pre-industrial standard deviation) to eliminate the possible influence of stronger or weaker ENSO events during the glacial period. Composites with or without this upper limit are indistinguishable. The results demonstrate that, in our HadCM3 experiments, the change in Z_{ASL} variability is the result of a more efficient teleconnection, rather than a change in ENSO variability (see Methods). A time series of the strength of the simulated teleconnection over the past 28 kyr (Figs 2a, 4b) shows that the teleconnection is stronger through the LGM until 16 kyr ago, at which time it rapidly decreases. This is in agreement with the modelled change in variability in Z_{ASL} and the observed timing of change in the WDC record. A change in the LGM teleconnection strength is also evident in eight out of eleven of the models of the Paleoclimate Model Intercomparison Project (PMIP2/3) (Extended Data Fig. 7). This is remarkable given the diversity of the response of the tropical climate of these models to LGM forcing²³.

The stronger teleconnection in the glacial period in our simulations suggests a change in the tropical Pacific mean state. Such a change could result from the lowered greenhouse gas concentrations, the altered orbital forcing, or the presence of continental ice sheets. In HadCM3, we test each of these boundary conditions individually to evaluate their impact (see Methods). The greenhouse gas concentrations and orbital forcing cause a negligible change, whereas the influence of continental ice sheets is statistically significant ($P < 0.05$). Two processes associated with continental glaciation may be important for changing the teleconnection: the lowering of sea level, leading to the exposure of the shelf seas in the West Pacific^{23,24}, and the topographic and albedo forcing of the LCIS. When considered separately, the lowered sea level causes a small change in the teleconnection that is statistically significant ($P < 0.05$) only to the north of the ASL region (Fig. 3e). Since flooding of West Pacific shelf seas is thought to have occurred about 13 kyr ago²¹, this may be a possible cause of the decline in WDC variability between about 13–10 kyr ago, but cannot explain the larger step change about 16 kyr ago.

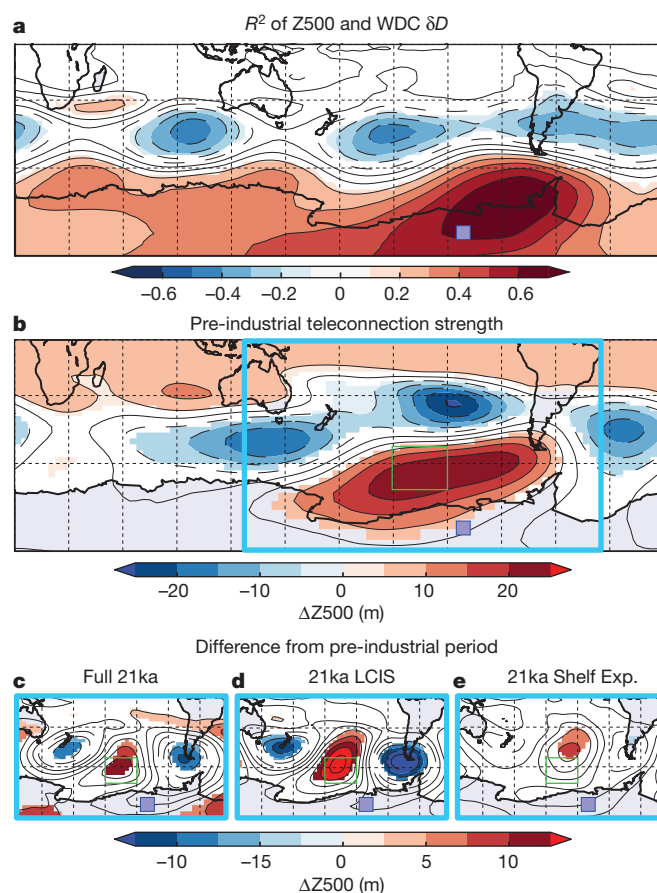


Figure 3 | HadCM3 teleconnection strength. **a**, Map of the correlation coefficient R^2 for the 500-hPa geopotential height (Z_{500}) and WAIS Divide δD , using the isotope-enabled HadCM3 model for the pre-industrial period. Contours are filled (not white) when the statistical significance exceeds 95%. **b–e**, Composite maps of the annual average 500-hPa height anomaly (ΔZ_{500}) for ENSO events, including the pre-industrial (**b**), and the differences between three different model experiments and the pre-industrial (**c–e**). Contours are filled (non-white) when statistical significance exceeds 95% using a Monte Carlo test. The green box is the Amundsen Sea region over which we calculate the teleconnection strength from the mean 500-hPa height anomaly. The purple square is the WAIS Divide ice core site. The blue box in **b** indicates the area shown in **c–e**. The contour interval is 5 m in **b** and 2.5 m in **c**. Negative contours are dashed.

The topography and albedo of the LCIS force a large change to the teleconnection strength about 16 kyr ago, which is statistically significant ($P < 0.05$) across the ASL region (Fig. 3d). This timing is consistent with major deglacial changes to the LCIS¹⁸. To separate the effects of topography and albedo, we perform two tests. First, using pre-industrial settings, we introduce the LGM–LCIS albedo and topographic effects into the model. In this case we find that almost the full LGM teleconnection strength change is realized (Fig. 3d). Second, we remove the LGM–LCIS topographic effect, while keeping the albedo effect. Here, the teleconnection pattern changes, but is not statistically significant in the ASL region. Our results therefore demonstrate a link between the topography of the LCIS and multi-year to decadal climate variations in West Antarctica—a previously undocumented inter-polar teleconnection mechanism.

When the LCIS surface is high, the circulation in the North Pacific changes, with a persistent annual mean Aleutian Low that is deeper and farther south, a response that is consistent amongst climate models²⁵. This weakens the mean winds in the West Pacific, causing the warm pool to expand eastward, as occurs during an El Niño event.

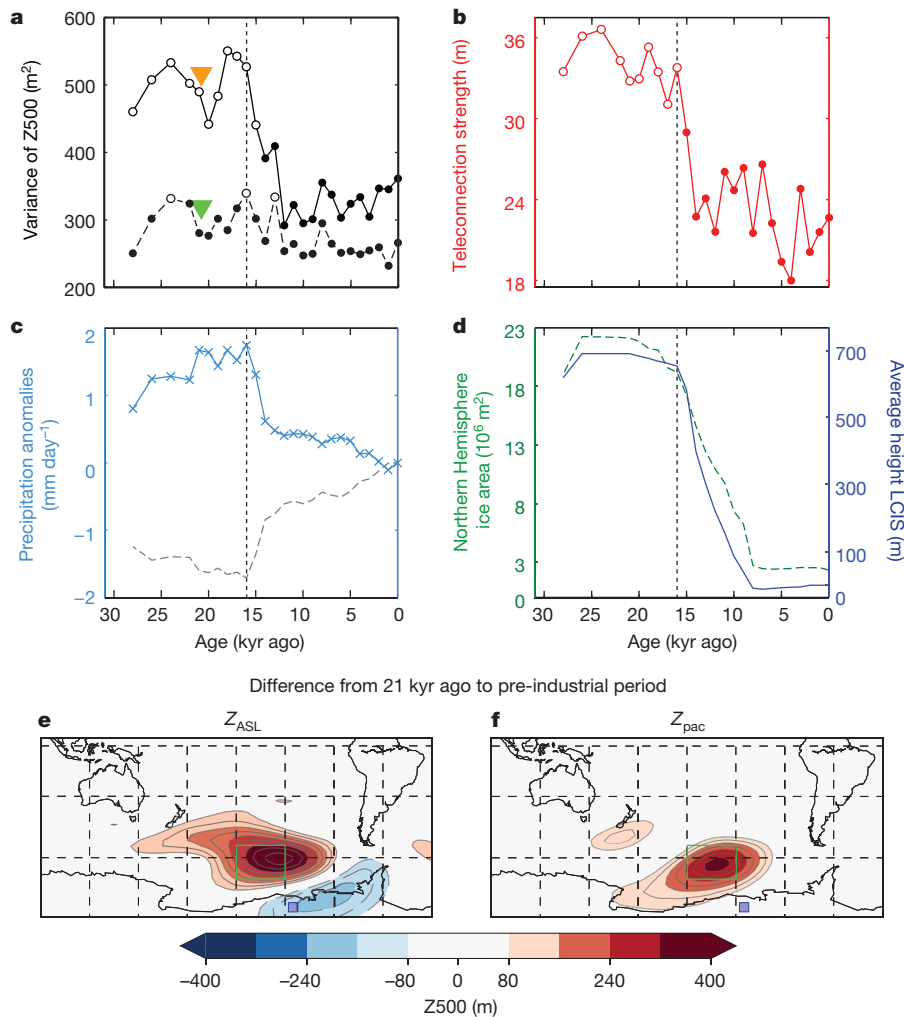


Figure 4 | HadCM3 mechanistic attribution. **a**, The variance of the height of the 500-hPa pressure surface (Z500) for the Z_{ASL} (solid line) and Z_{local} (dashed line) indices, computed from monthly mean data that is filtered with a 4–15-yr band pass filter. The markers are unfilled if the variance of Z_{ASL} at each time slice is 95% significantly different (F -test) to that of 0 kyr ago. At 21 kyr ago, the orange triangle shows Z_{ASL} for the ‘21ka LCIS only’ scenario, and the green triangle shows Z_{ASL} for the ‘21ka Shelf Exp.’ scenario (that is, the effect of sea level change in the Maritime Continent region). Each of these scenarios is defined in Supplementary Data. **b**, The modelled teleconnection strength between the tropical Pacific and West Antarctica (solid red line; open red dots indicate statistically significant differences from pre-industrial). **c**, The simulated difference in mean annual rainfall between the central Pacific and the Maritime Continent (average of 20° N–20° S, 145°–190° E minus

average of 20° N–20° S, 100°–145° E), shown as an anomaly relative to the pre-industrial period (light blue line). Also shown are the precipitation anomalies over the Maritime Continent only (dashed grey line). **d**, Northern Hemisphere ice area³⁰ (dashed green line) and average height of the LCIS³⁰ (blue line). In all panels, the dashed vertical line shows 16 kyr ago, as in Fig. 2. **e**, Map of the change in the 500-hPa height field variance between 21 kyr ago and the pre-industrial period. **f**, As in **e**, except for the Z_{pac} variability that is linearly related to ENSO (that is, the part removed from Z_{ASL} to yield Z_{local}). The green box is the Amundsen Sea region over which we calculate the indices in **a**. The purple square is the WAIS Divide ice core site. The contour interval is 40 m², with colours changing every 80 m². Negative contours are dashed. Colours are plotted for 95% statistical significance using a Monte Carlo test.

The atmospheric convection moves with the warmer waters away from the Maritime Continent (the part of Southeast Asia comprising Indonesia, the Philippines, Papua New Guinea and nearby countries) (Fig. 4c); hence, rainfall decreases in this region, consistent with the LGM drying inferred from lake sediments in Indonesia²¹ (Fig. 2c) and stalagmites in Borneo²⁶ (Fig. 2d). The shifted convection then causes a change in the location of the atmospheric heating that occurs during ENSO events. Changing the location of this heating alters the structure of the extra-tropical Rossby waves that are excited during ENSO events, so that, when the LCIS is present, there are additional circulation anomalies in the Southern Hemisphere high latitudes. Although there are large changes in how the Rossby waves are forced from the tropics, there is no change in how they propagate within the Southern Hemisphere. Since Rossby waves are the primary mechanism responsible for the tropical Pacific–West Antarctic teleconnection^{4,5}, the LCIS can force a change in West Antarctic climate variability. Hence, when an ENSO

event occurred during the LGM—even if it were no bigger than during the modern era—it had a larger impact on West Antarctic climate than during the modern era.

Our results identify an influence of Northern Hemisphere ice-sheet topography on the climate system. By altering the coupled ocean–atmosphere circulation, the decay of the LCIS affected the strength of interactions between the tropical Pacific and high southern latitudes, reducing interannual and decadal variability in West Antarctica by nearly half. Although several abrupt climate events occur during the past 31 kyr, including Dansgaard–Oeschger events, the Bølling–Allerød, the Younger Dryas and melt water pulse 1A^{24,27} (Fig. 2e, f), the interannual and decadal climate variability in West Antarctica and the patterns of rainfall in the tropical West Pacific do not appear to be affected. Instead, the initial reduction in West Antarctic variability at about 16 kyr ago corresponds to a maximum in North Atlantic ice-rafted debris layers during Heinrich Event 1¹⁸. It was this ice-sheet purge

that probably reduced LCIS topography beyond a critical threshold, altering the interhemispheric climate dynamics of the Pacific basin, even as separate abrupt climate events continued to occur in the Atlantic basin and further afield.

Online Content Methods, along with any additional Extended Data display items and Source Data, are available in the online version of the paper; references unique to these sections appear only in the online paper.

Received 22 February; accepted 19 October 2017.

Published online 5 February 2018.

- Broecker, W. S. & Denton, G. H. The role of ocean-atmosphere reorganizations in glacial cycles. *Geochim. Cosmochim. Acta* **53**, 2465–2501 (1989).
- Zheng, W., Braconnot, P., Guiliardi, E., Merkel, U. & Yu, Y. ENSO at 6ka and 21ka from ocean-atmosphere coupled model simulations. *Clim. Dyn.* **30**, 745–762 (2008).
- Tudhope, A. W. *et al.* Variability in the El Niño-Southern Oscillation through a glacial-interglacial cycle. *Science* **291**, 1511–1517 (2001).
- Lachlan-Cope, T. & Connolley, W. Teleconnections between the tropical Pacific and the Amundsen-Bellinghousen Sea: role of the El Niño/Southern Oscillation. *J. Geophys. Res.* **D 111**, D23101 (2006).
- Ding, Q., Steig, E. J., Battisti, D. S. & Küttel, M. Winter warming in West Antarctica caused by central tropical Pacific warming. *Nat. Geosci.* **4**, 398–403 (2011).
- Turney, C. S. M. *et al.* Millennial and orbital variations of El Niño/Southern Oscillation and high-latitude climate in the Last Glacial Period. *Nature* **428**, 306–310 (2004).
- Sadekov, A. Y. *et al.* Palaeoclimate reconstructions reveal a strong link between El Niño-Southern Oscillation and tropical Pacific mean state. *Nat. Commun.* **4**, 2692 (2013).
- Ford, H. L., Ravelo, A. C. & Polissar, P. J. Reduced El Niño-Southern Oscillation during the Last Glacial Maximum. *Science* **347**, 255–258 (2015).
- Merkel, U., Prange, M. & Schulz, M. ENSO variability and teleconnections during glacial climates. *Quat. Sci. Rev.* **29**, 86–100 (2010).
- Steig, E. J. *et al.* Warming of the Antarctic ice-sheet surface since the 1957 International Geophysical Year. *Nature* **457**, 459–462 (2009).
- Nicolas, J. P. & Bromwich, D. H. Climate of West Antarctica and influence of marine air intrusions. *J. Clim.* **24**, 49–67 (2011).
- Steig, E. J., Ding, Q., Battisti, D. S. & Jenkins, A. Tropical forcing of Circumpolar Deep Water Inflow and outlet glacier thinning in the Amundsen Sea Embayment, West Antarctica. *Ann. Glaciol.* **53**, 19–28 (2012).
- Anderson, R. F. *et al.* Wind-driven upwelling in the Southern Ocean and the deglacial rise in atmospheric CO₂. *Science* **323**, 1443–1448 (2009).
- Steig, E. J. *et al.* Recent climate and ice-sheet changes in West Antarctica compared with the past 2,000 years. *Nat. Geosci.* **6**, 372–375 (2013).
- Jones, T. R. *et al.* Improved methodologies for continuous-flow analysis of stable water isotopes in ice cores. *Atmos. Meas. Tech.* **10**, 617–632 (2017a).
- Jones, T. R. *et al.* Water isotope diffusion in the WAIS Divide ice core during the Holocene and last glacial. *J. Geophys. Res. Earth Surf.* **122**, 290–309 (2017b).
- Urban, F. E., Cole, J. E. & Overpeck, J. T. Influence of mean climate change on climate variability from a 155-year tropical Pacific coral record. *Nature* **407**, 989–993 (2000).
- Stern, J. V. & Lisiecki, L. E. North Atlantic circulation and reservoir age changes over the past 41,000 years. *Geophys. Res. Lett.* **40**, 3693–3697 (2013).
- Dyke, A. S. *et al.* The Laurentide and Innuitian ice sheets during the Last Glacial Maximum. *Quat. Sci. Rev.* **21**, 9–31 (2002).
- Porter, S. C. & Swanson, T. W. Radiocarbon age constraints on rates of advance and retreat of the Puget Lobe of the Cordilleran Ice Sheet during the last glaciation. *Quat. Res.* **50**, 205–213 (1998).
- Russell, J. M. *et al.* Glacial forcing of central Indonesian hydroclimate since 60,000 y BP. *Proc. Natl Acad. Sci. USA* **111**, 5100–5105 (2014).
- Singarayer, J. S. & Valdes, P. J. High-latitude climate sensitivity to ice-sheet forcing over the last 120kyr. *Quat. Sci. Rev.* **29**, 43–55 (2010).
- DiNezio, P. N. & Tierney, J. E. The effect of sea level on glacial Indo-Pacific climate. *Nat. Geosci.* **6**, 485–491 (2013).
- Deschamps, P. *et al.* Ice-sheet collapse and sea-level rise at the Bølling warming 14,600 years ago. *Nature* **483**, 559–564 (2012).
- Yanase, W. & Abe-Ouchi, A. A numerical study on the atmospheric circulation over the midlatitude north Pacific during the Last Glacial Maximum. *J. Clim.* **23**, 135–151 (2010).
- Partin, J. W., Cobb, K. M., Adkins, J. F., Clark, B. & Fernandez, D. P. Millennial-scale trends in west Pacific warm pool hydrology since the Last Glacial Maximum. *Nature* **449**, 452–455 (2007).
- Johnsen, S. J. *et al.* Oxygen isotope and palaeotemperature records from six Greenland ice-core stations: Camp Century, Dye-3, GRIP, GISP2, Renland and NorthGRIP. *J. Quat. Sci.* **16**, 299–307 (2001).
- Waelbroeck, C. *et al.* Sea-level and deep water temperature changes derived from benthic foraminifera isotopic records. *Quat. Sci. Rev.* **21**, 295–305 (2002).
- Hemming, S. R. Heinrich events: massive Late Pleistocene detritus layers of the North Atlantic and their global climate imprint. *Rev. Geophys.* **42**, RG1005 (2004).
- Peltier, W. R. Global glacial isostasy and the surface of the ice-age Earth: the ICE-5G (VM2) model and GRACE. *Annu. Rev. Earth Planet. Sci.* **32**, 111–149 (2004).

Supplementary Information is available in the online version of the paper.

Acknowledgements This work was supported by US National Science Foundation (NSF) grants 0537593, 0537661, 0537930, 0539232, 1043092, 1043167, 1043518 and 1142166. Field and logistical activities were managed by the WAIS Divide Science Coordination Office at the Desert Research Institute, USA, and the University of New Hampshire, USA (NSF grants 0230396, 0440817, 0944266 and 0944348). The NSF Division of Polar Programs funded the Ice Drilling Program Office (IDPO), the Ice Drilling Design and Operations (IDDO) group, the National Ice Core Laboratory (NICL), the Antarctic Support Contractor, and the 109th New York Air National Guard. W.H.G.R. was funded by a Leverhulme Trust Research Project Grant. All HadCM3 model simulations were carried out using the computational facilities of the Advanced Computing Research Centre, University of Bristol (<http://www.bris.ac.uk/acrc/>). We thank P. J. Valdes and J. S. Singarayer for providing their model simulations, as well as the groups that provided climate model data as part of the PMIP2/3.

Author Contributions T.R.J., W.H.G.R. and E.J.S. designed the project and led the writing of the paper. T.R.J., J.W.C.W., E.J.S. and B.R.M. contributed water isotope measurements. W.H.G.R. conducted HadCM3 simulations and led model analysis. T.R.J., K.M.C., E.J.S. and J.W.C.W. developed the diffusion-correction calculations. B.R.M. contributed change point detection algorithms and power density ratio calculations. All authors discussed the results and contributed input to the manuscript.

Author Information Reprints and permissions information is available at www.nature.com/reprints. The authors declare no competing financial interests. Readers are welcome to comment on the online version of the paper. Publisher's note: Springer Nature remains neutral with regard to jurisdictional claims in published maps and institutional affiliations. Correspondence and requests for materials should be addressed to T.R.J. (tyler.jones@colorado.edu).

METHODS

Water isotope data. The WDC water isotope record (Fig. 1a) was analysed on a continuous flow analysis system¹⁵ using a cavity ring-down spectroscopy instrument (Picarro Inc. model L2130-i). The data are reported in delta notation relative to Vienna Standard Mean Ocean Water (VSMOW, $\delta^{18}\text{O} = \delta D = 0\text{‰}$), normalized to the Standard Light Antarctic Precipitation ($\delta^{18}\text{O} = -55.5\text{‰}$, $\delta D = -428.0\text{‰}$) scale. WDC is annually dated, with accuracy better than 0.5% of the age in the range 0–12 kyr ago, and better than 1% of the age in the range 12–31 kyr ago^{31,32}.

Frequency domain analyses. Spectral conversion. We use the MultiTaper method fast Fourier transform technique to calculate spectral power densities^{33,34} of the measured water isotope time series. As in other palaeoclimate studies³⁵, we use the pmtm.m routine of P. Huybers (<http://www.people.fas.harvard.edu/~phuybers/Mfiles/>). Before spectral analysis, the isotope data are linearly interpolated at a uniform time interval of 0.05 yr.

High-frequency signal attenuation. High-frequency water isotope information in ice cores is attenuated by diffusion in the firn column and deep ice^{16,36–40}. Frequency spectra reveal the amount of signal attenuation as declines in the amplitude of a given frequency through time, relative to lower frequencies (Extended Data Fig. 1a). For WDC, the annual signal (1 yr) is indiscernible at ages >14 kyr ago. The 2-yr signal is indistinguishable from 17–19 kyr ago. Signals >3 yr are detectable throughout the past 31 kyr, while signals >4 yr are not substantially attenuated by diffusion (Extended Data Fig. 1a).

Gaussian determination of diffusion lengths. The quantitative effects of diffusion can be represented by the convolution of a Gaussian filter with the original water-isotope signal deposited at the surface and subsequently strained by ice deformation and firn compaction^{36,39} (Extended Data Fig. 1b). The power density spectrum observed in the ice core record, $P(f)$, after diffusion, is $P(f) = P_0(f) \exp[-(2\pi f \sigma_z)^2]$, where $P_0(f)$ represents the power spectrum of the undiffused signal, $f = 1/\lambda$ is the frequency, λ is the signal wavelength, z is the depth, and σ_z is the diffusion length. Fitting a Gaussian to $P(f)$ defines a standard deviation σ_f with units of per metre. The conversion $\sigma_z = 1/2\pi\sqrt{2} \times 1/\sigma_f$ then yields the diffusion length σ_z in units of metres¹⁶. The diffusion length expressed in metres of time is $\sigma_t = \sigma_z/\lambda_{\text{avg}}$, where λ_{avg} is the mean annual layer thickness (in metres per year) at a given depth (Extended Data Figs 1f, 2c). The diffusion length quantifies the statistical vertical displacement of water molecules from their original position in the ice sheet. In the present study, we use our previously published WDC diffusion lengths, calculated for 500-yr data windows throughout the interval 0–29 kyr ago¹⁶.

Natural logarithm determination of diffusion length. The variable σ_f can also be determined by using the slope of the linear regression of $\ln[P(f)]$ versus f^2 . This provides a means of estimating diffusion-length uncertainty¹⁶. Here, $\sigma_f = \sqrt{1/[2|(m_{\ln})|]}$, where m_{\ln} is the slope of the linear regression over the interval from 0.01 (cycles per metre)² to the value at which systematic noise from the ice core analysis system overwhelms the physical signal. The point where noise dominates appears as a 'kink' or 'bend' in the decay of $\ln[P(f)]$. A maximum and minimum slope is fitted within the standard deviation of the linear regression to determine an uncertainty range for σ_f .

Power density diffusion correction. Diffusion of a water isotope signal in an ice sheet reduces the power of high-frequencies, so $P(f)$ takes the form of quasi-red noise. Given that WDC Holocene spectra show constant power density in the frequencies largely unperturbed by diffusion (periods >4 yr), we use a white-noise normalization to estimate the original, pre-diffusion power density spectrum. Specifically, we calculate $P_0(f) = P \exp(4\pi^2 f^2 \sigma_z^2)$, where P is the observed power density (in units of $\text{‰}^2 \text{yr}$), f the frequency (in units of per year), and σ_z is the diffusion length (in units of years). We report the average power density for the diffusion-corrected 3–7-yr, 4–15-yr, and 3–30-yr bands (Fig. 1c, d, Extended Data Fig. 1d) calculated as the integral of power density divided by the frequency range. The uncertainty on these power density diffusion corrections is determined using the uncertainty range for diffusion lengths discussed in the section 'Natural logarithm determination of diffusion length'.

Change point detection. We fit linear regressions to windows of data within the 3–7-yr and 4–15-yr relative amplitude time series, using window sizes of 2,500 yr to 10,000 yr. We calculate the P value for the F -test to determine whether the slope of the regression in each window is statistically different from zero (Extended Data Fig. 2b). We make no a priori assumptions about the timing or size of statistically significant change and take an a posteriori confidence level equivalent to 95%: $\alpha = 1 - 0.95^{1/n}$, where n is the number of statistical test realizations³¹. The first statistically significant change occurs 16,440 yr ago for the 4–15-yr diffusion-corrected data (all ages are given relative to the present, 1950 AD). The 3–7-yr diffusion-corrected data yields identical results. The first statistically significant change in the 4–15-yr raw data (not corrected for diffusion) occurs 15,940 yr ago.

Uncertainty in the timing of initial change includes the spectral window resolution of 500 ± 250 yr and the WDC14 age scale ($\pm 1\%$ for ages >12 kyr ago³²). For the initial change centred at 16.4 kyr ago and 15.9 kyr ago, the age scale imposes an uncertainty of ± 164 yr and ± 159 yr, respectively. Adding the above in quadrature yields initial timing uncertainties of just less than ± 300 yr. We also estimate the change point visually using a subset of 4–15-yr diffusion-corrected data, calculated using 100-yr non-overlapping windows between 16.64 kyr ago and 15.54 kyr ago. The initial decline occurs 16.24 kyr ago, with uncertainty on the window length of ± 50 yr and a dating uncertainty of ± 162 yr. Added in quadrature, this gives an uncertainty value of ± 170 yr.

HadCM3 model simulations. Model setup. We use the fully coupled ocean–atmosphere model HadCM3^{41,42}. This model has been shown to simulate the climate in the tropical Pacific very well, including in its response to glacial forcing²³. We simulate the climate over the past 28 kyr in a series of snapshots run every thousand years²². For each snapshot, we prescribe the orbital forcing⁴³, greenhouse gas concentration^{44,45}, and ice-sheet topography and sea level³⁰. We use a suite of simulations to test the sensitivity of the model to individual boundary conditions, including 'Full 28–0ka', 'Full 21ka', '21ka Orbit + GHG' (where GHG is greenhouse gas), '21ka Ice Sheets', '21ka LCIS' (where LCIS is the combined Laurentide–Cordilleran ice sheets), '21ka Shelf Exp.' and '21ka LCIS albedo'. Each of these simulations is defined in Supplementary Data. All simulations are run for at least 500 yr with analysis made on the final 200 yr of each simulation. (The term 'ka' refers to 'kyr ago'.)

Long-term evolution of ASL variability. The variability in the WDC water isotope record on interannual and longer timescales is related to changes in the large-scale atmospheric circulation, particularly in the Amundsen Sea Basin¹⁴ (Fig. 3a). These changes in the circulation can be characterized by the ASL^{46,47}. To assess the amount of variability in the ASL, we compute an ASL index of monthly mean 500-hPa height averaged from 55° – 70° S and 195° – 240° E (Z_{ASL}). We use a 4–15-yr band pass filter to isolate variability on the same timescale as the WDC record. Extended Data Fig. 3 shows the variance of Z_{ASL} within each snapshot of a thousand years, using the 'Full 28–0ka' simulations. From 28 kyr until around 15 kyr ago, the ASL is more variable than during the Holocene (95% significant, F -test). Both the magnitude and timing of the decrease are comparable to those observed in the WDC water isotope record.

Internal versus forced variability of ASL. To assess how much of the change in the simulated Z_{ASL} is due to the tropics, we linearly remove the average of SST across 5° N– 5° S and 150° – 270° E (SST_{pac}) from the Z_{ASL} . This operation is performed by regressing Z_{ASL} onto SST_{pac} as shown by the equation $Z_{\text{pac}} = \text{SST}_{\text{pac}} \times \text{regress}(\text{SST}_{\text{pac}}, Z_{\text{ASL}})$. We then subtract Z_{pac} from Z_{ASL} to obtain the component of Z_{ASL} that is unrelated to the tropical Pacific: $Z_{\text{local}} = Z_{\text{ASL}} - Z_{\text{pac}}$. The variance of Z_{local} is plotted in Extended Data Fig. 3. The results show that there is no statistically significant change in the ASL variability that is unrelated to tropical Pacific SST over the deglaciation (95% significance, F -test). We compare these results, obtained with the 4–15-yr band pass filtered data of monthly mean model output, to the annual mean data with no filtering (Extended Data Fig. 3a,b). We obtain very similar results for both outputs. The tests described below use the annual mean data.

The tropical Pacific-to-ASL teleconnection. The tropical Pacific-to-ASL teleconnection has been well documented^{48,49}. To show this teleconnection in HadCM3, we construct composite maps of 500-hPa height for years when the annual SST_{pac} anomaly exceeds $\pm 0.81^\circ\text{C}$ (Extended Data Fig. 4). This threshold is chosen so that SST_{pac} anomalies exceed 1.25 standard deviations in a pre-industrial simulation. We include cold ENSO events by multiplying the 500-hPa height field by (-1) . Note that computing SST_{pac} over the entire tropical Pacific basin eliminates biases that may arise from changes in the pattern of SST variability, either in response to forcing or as a result of intrinsic ENSO variability.

The pre-industrial composite pattern that we obtain for the atmospheric response to tropical Pacific SST shows greatest amplitude in the Amundsen Sea region, with a positive height anomaly for warm ENSO events (Extended Data Fig. 4a). A similar pattern is obtained from reanalysis data using either regression analysis⁴⁸ or compositing^{48,50}. The composite is statistically significant across the Southern Hemisphere.

Using HadCM3, we find a similar composite pattern for the pre-industrial period (Extended Data Fig. 4a) and for the 'Full 21ka' simulation (Extended Data Fig. 4b). The difference between the two patterns is shown in Extended Data Fig. 4c; a Rossby-wave response emanating from the western tropical Pacific is evident. This response is consistent with other studies that show the tropical Pacific-to-ASL teleconnection^{4,5,48,51}. Using each snapshot in the 'Full 28–0ka' simulations, we evaluate the amplitude of the tropical Pacific-to-ASL teleconnection as the mean of the composite averaged over 55° – 70° S and 195° – 240° E (Extended Data Fig. 5). There is a dramatic decrease in the strength of the teleconnection around 16 kyr ago.

Teleconnection changes resulting from ENSO changes using HadCM3. We find that the simulated variance of SST_{pac} anomalies 21 kyr ago ($\sigma = 0.78^\circ\text{C}$) is increased by 40% compared to the pre-industrial period ($\sigma = 0.65^\circ\text{C}$). To determine the effect of SST variability on the teleconnection strength, we re-compute the composites using SST_{pac} anomalies in the range $\pm 0.81^\circ\text{C} < \text{SST}_{\text{pac}} < \pm 1.63^\circ\text{C}$, corresponding to SST_{pac} at 0 kyr ago of $\pm 1.25\sigma$ to $\pm 2.5\sigma$. By imposing both an upper and lower bound, the atmospheric response in the 500-hPa height composites is unaffected by the amplitude of simulated ENSO events. Furthermore, any change in the frequency of ENSO events is rendered unimportant by taking an average composite of events.

The composite patterns for all simulations from 28 kyr to 0 kyr ago, as well as how they differ from the pre-industrial period, are unchanged by imposing the upper and lower bound, while the amplitude of the composites is slightly reduced. For the 'Full 21ka' simulation, the average amplitude of the Z_{ASL} is 32 m without the upper bound, and 30 m with the upper bound imposed (Extended Data Fig. 6). Therefore, even though HadCM3 simulates an increase in the strength of ENSO during the LGM, this is not the primary cause for the change in Z_{ASL} variability. Rather, the increased Z_{ASL} variability occurs because the atmospheric response to SST_{pac} during the glacial period is stronger than during the pre-industrial period. *Teleconnection changes resulting from ENSO changes using the PMIP.* For a subset of PMIP2/3 simulations (those for which sufficient data was available⁵²), we follow the same procedure as outlined above to construct composites of 500-hPa height response to SST_{pac} anomalies. We include both the lower and upper SST_{pac} bounds. The composites are computed for the 'Pre-industrial' and 'Full 21ka' simulations (Extended Data Fig. 7). A change in the tropical Pacific-to-ASL teleconnection is apparent in many of the models. Since each model has a different teleconnection in the pre-industrial, the response of the models to boundary conditions 21 kyr ago is also different.

In the LGM simulations, PMIP2/3 models with enhanced SST_{pac} variance do not display a consistently different teleconnection compared to models with reduced SST_{pac} variance. This confirms that changes in the tropical Pacific-to-ASL teleconnection strength are not driven by changes in the amplitude of SST_{pac} anomalies (that is, ENSO). Indeed, in comparison to HadCM3, the most similar change in the teleconnection occurs in FGOALS-1.0g simulations, part of the PMIP2/3 model suite. FGOALS-1.0g shows a large decrease in ENSO strength at 21 kyr ago, compared to the HadCM3 increase. The FGOALS-1.0g positive geopotential height anomaly is shifted eastward, consistent with the location of the regional low-pressure centre in the pre-industrial simulations.

Boundary condition changes responsible for the teleconnection change. In 'Full 21ka' simulations, a number of the climate forcings are substantially changed compared to the pre-industrial period. These include insolation, the greenhouse gas concentrations, and the size of the ice sheets (Extended Data Fig. 8a). We investigate the impact of each of these boundary condition changes on the teleconnection. The '21ka Orbit + GHG' simulation does not cause a significant change (Extended Data Fig. 8b). In the '21ka Ice Sheets' simulation, which includes reduced sea level, enhanced albedo in the higher latitudes, and altered topography over North America, Europe, Antarctica, and the Southern Andes, there is a large change in the amplitude of the teleconnection (Extended Data Fig. 8c). Prior modelling simulations have explored other aspects of the topographic effects of Northern Hemisphere ice sheets⁵³, including their influence on glacial climate⁵⁴, abrupt glacial climate change⁵⁵, the Atlantic Meridional Overturning Circulation⁵⁶, and Heinrich events⁵⁷.

The '21ka LCIS only' simulation displays a statistically significant ($P < 0.05$) change in the teleconnection strength, similar in magnitude to the 'Full 21ka' simulation (Extended Data Fig. 8e). The '21ka LCIS albedo' simulation (that is, albedo only) displays a statistically significant change in the teleconnection, but its effect is much smaller than that of topography and albedo combined (Extended Data Fig. 8f). Although we cannot isolate the effect of topography alone, our results suggest that topography is the dominant mechanism acting to change the teleconnection strength. This agrees with the WDC shift in variability about 16 kyr ago, which is concurrent with the abrupt lowering of the LCIS¹⁸.

It has been proposed that lowered sea level in the West Pacific at the LGM can have a large impact on tropical Pacific climate by exposing the continental shelves^{23,58}. We test this by changing only the land-sea mask in the West Pacific in the '21ka Shelf Exp.' simulation (Extended Data Fig. 8d). This results in a change to Z_{ASL} that is 3 to 4 times smaller than that seen in the '21ka LCIS only' simulation. There is also a statistically significant change in the composite map only to the north of the ASL. In the WDC diffusion-corrected variability (3–7-yr and 4–15-yr bands), there appears to be a step-change that occurs at about 13 kyr ago. This timing is consistent with the flooding of the continental shelves in the West Pacific^{24,59}. Therefore, it is possible that the WDC data are detecting flooding of the continental shelves, but this effect is secondary to the abrupt change at approximately 16 kyr ago.

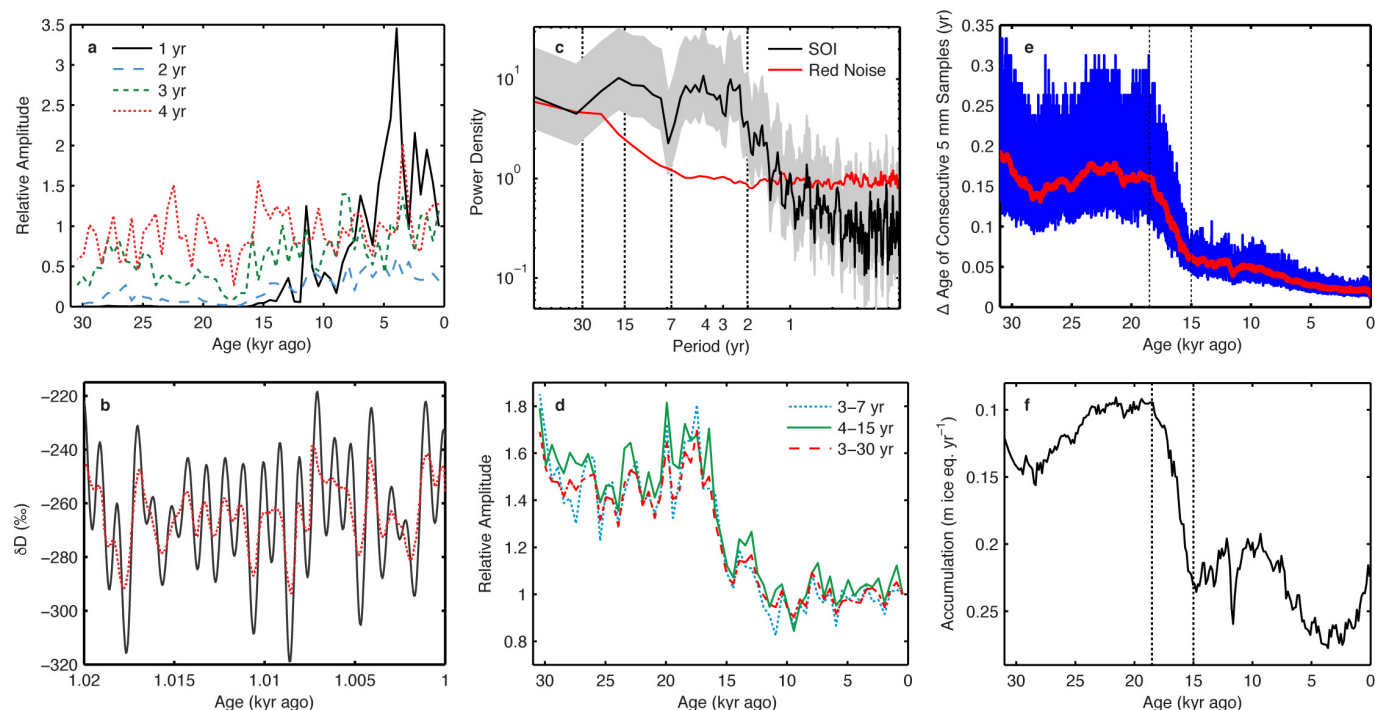
Climatic changes associated with the teleconnection change. The tropical Pacific-to-ASL teleconnection can be considered as a Rossby Wave response to diabatic heating in the western tropical Pacific⁶⁰. The location of this diabatic heating will depend upon the mean state. To understand how the mean state changes, we analyse how the patterns of precipitation and SST change in the '21ka' simulations relative to the pre-industrial period. Extended Data Fig. 9a shows the precipitation difference between the 'Full 21ka' simulation and the 'Pre-industrial' simulation. There is a prominent decrease in precipitation over the Maritime Continent, and an increase in precipitation over the Indian Ocean and the western and central tropical Pacific. This is consistent with proxy evidence^{21,23,61}. In Extended Data Fig. 9b, the '21ka Ice Sheets' simulation accounts for the majority of the precipitation changes in the 'Full 21ka' simulation. When we decompose this effect, the '21ka LCIS only' simulation accounts for most of the precipitation changes in the western and central tropical Pacific (Extended Data Fig. 9c), while the '21ka Shelf Exp.' simulation accounts for most of the precipitation changes over the Maritime Continent and in the Indian Ocean (Extended Data Fig. 9d). We find that there is a much larger change in West Pacific diabatic heating (as shown by the precipitation field) in the '21ka LCIS only' simulation than in the '21ka Shelf Exp.' simulation. Since the ASL responds to diabatic heating anomalies in the West Pacific, rather than the Indian Ocean, this is consistent with our interpretation that the LCIS dominates the tropical Pacific-to-ASL teleconnection strength change. The timing of the change in the precipitation pattern is shown in Fig. 4c. Around 16 kyr ago, the location of the tropical precipitation moves westward from its glacial position to its pre-industrial position in the far West Pacific.

The location of diabatic heating is ultimately a response to the winds and SST. Extended Data Fig. 9 shows that the SST patterns for the 'Full 21ka', '21ka Ice Sheets', and '21ka LCIS only' simulations are all similar. Although the global mean SST is much cooler in the 'Full 21ka' simulation (Extended Data Fig. 9a), it is the spatial structure of the SST that determines the climatic response⁶². Therefore it is not surprising that all three simulations alter the teleconnection in a similar way. Furthermore, the SST pattern is consistent across most of the LGM PMIP2/3 simulations, indicating a robust SST response to an ice sheet. The SST pattern in the 'Full 21ka' simulation is associated with cyclonic flow in the North Pacific that is forced by the presence of the LCIS. Prior modelling has shown that this wind response to the LCIS could result from a summertime weakening of the sub-tropical high and a wintertime deepening of the Aleutian Low⁵³.

Data availability. The WDC water isotope data that support the findings of this study are available at <http://gcmd.gsfc.nasa.gov/search/Metadata.do?entry=NSF-ANT10-43167#metadata>. Additional supporting data, including model results, are provided in Supplementary Data and Extended Data Figs 1–9.

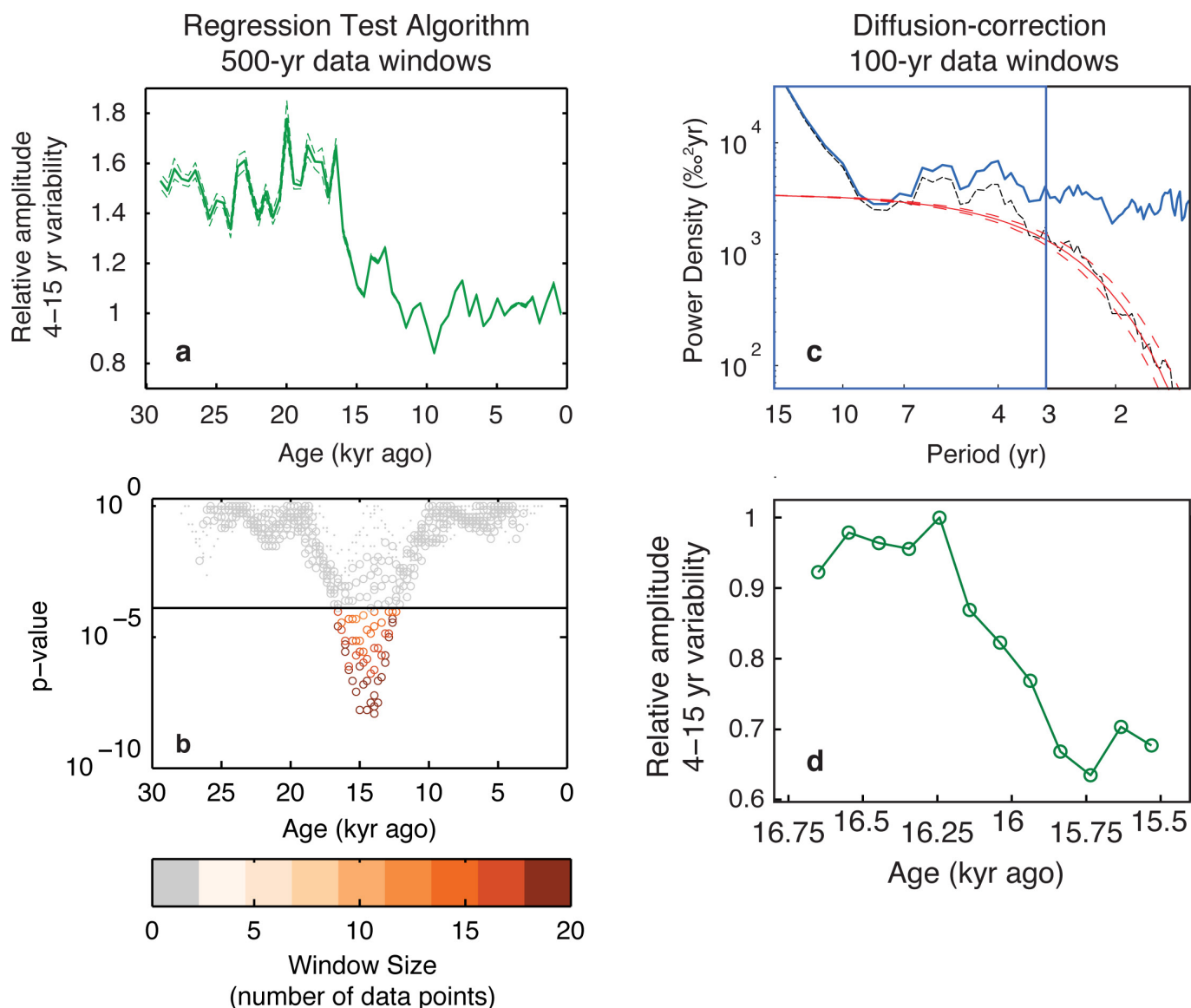
1. WAIS Divide Project Members. Onset of deglacial warming in West Antarctica driven by local orbital forcing. *Nature* **500**, 440–444 (2013).
2. Sigl, M. et al. The WAIS Divide deep ice core WD2014 chronology—Part 2. Annual-layer counting (0–31 ka BP). *Clim. Past* **12**, 769–786 (2016).
3. Thomson, D. J. Spectrum estimation and harmonic analysis. *Proc. IEEE* **70**, 1055–1096 (1982).
4. Percival, D. B. & Walden, A. T. *Spectral Analysis for Physical Applications* 1–583 (Cambridge Univ. Press, 1993).
5. Markle, B. R. et al. Global atmospheric teleconnections during Dansgaard-Oeschger events. *Nat. Geosci.* **10**, 36–40 (2017).
6. Johnsen, S. J. Stable isotope homogenization of polar firn and ice. In *Proc. Symp. on 'Isotopes and Impurities in Snow and Ice'* Vol. 118, 210–219 http://hydrologie.org/redbooks/a118/iahs_118_0210.pdf (IAHS AISH Publ, 1977).
7. Whillans, I. M. & Grootes, P. M. Isotopic diffusion in cold snow and firn. *J. Geophys. Res.* **90**, 3910–3918 (1985).
8. Cuffey, K. M. & Steig, E. J. Isotopic diffusion in polar firn: implications for interpretation of seasonal climate parameters in ice-core records, with emphasis on central Greenland. *J. Glaciol.* **44**, 273–284 (1998).
9. Johnsen, S. J. et al. Diffusion of stable isotopes in polar firn and ice: the isotope effect in firn diffusion. *Phys. Ice Core Rec.* **159**, 121–140 (2000).
10. Gkinis, V., Simonsen, S. B., Buchardt, S. L., White, J. W. C. & Vinther, B. M. Water isotope diffusion rates from the NorthGRIP ice core for the last 16,000 years—glaciological and paleoclimatic implications. *Earth Planet. Sci. Lett.* **405**, 132–141 (2014).
11. Gordon, C. et al. The simulation of SST, sea ice extents and ocean heat transports in a version of the Hadley Centre coupled model without flux adjustments. *Clim. Dyn.* **16**, 147–168 (2000).
12. Valdes, P. J. et al. The BRIDGE HadCM3 family of climate models: HadCM3@Bristol v1.0. *Geosci. Model Dev.* **10**, 3715–3743 (2017).
13. Berger, A. & Loutre, M. F. Insolation values for the climate of the last 10 million years. *Quat. Sci. Rev.* **10**, 297–317 (1991).
14. Spahni, R. et al. Atmospheric methane and nitrous oxide of the Late Pleistocene from Antarctic ice cores. *Science* **310**, 1317–1321 (2005).
15. Loulergue, L. et al. Orbital and millennial-scale features of atmospheric CH₄ over the last 800,000 years. *Nature* **453**, 383–386 (2008).
16. Fogt, R. L. & Bromwich, D. H. Decadal variability of the ENSO teleconnection to the high-latitude south Pacific governed by coupling with the Southern Annular Mode*. *J. Clim.* **19**, 979–997 (2006).

47. Fogt, R. L., Bromwich, D. H. & Hines, K. M. Understanding the SAM influence on the South Pacific ENSO teleconnection. *Clim. Dyn.* **36**, 1555–1576 (2011).
48. Schneider, D. P., Okumura, Y. & Deser, C. Observed Antarctic interannual climate variability and tropical linkages. *J. Clim.* **25**, 4048–4066 (2012).
49. Ding, Q. & Steig, E. J. Temperature change on the Antarctic Peninsula linked to the tropical Pacific. *J. Clim.* **26**, 7570–7585 (2013).
50. Welhouse, L. J., Lazzara, M. A., Keller, L. M., Tripoli, G. J. & Hitchman, M. H. Composite analysis of the effects of ENSO events on Antarctica. *J. Clim.* **29**, 1797–1808 (2016).
51. Ding, Q., Steig, E. J., Battisti, D. S. & Wallace, J. M. Influence of the tropics on the Southern Annular Mode. *J. Clim.* **25**, 6330–6348 (2012).
52. Braconnot, P. *et al.* Results of PMIP2 coupled simulations of the Mid-Holocene and Last Glacial Maximum—Part 2. Feedbacks with emphasis on the location of the ITCZ and mid- and high latitudes heat budget. *Clim. Past* **3**, 279–296 (2007).
53. Abe-Ouchi, A. *et al.* Ice-sheet configuration in the CMIP5/PMIP3 Last Glacial Maximum experiments. *Geosci. Model Dev. Discuss.* **8**, 3621–3637 (2015).
54. Ullman, D. J., LeGrande, A. N., Carlson, A. E., Anslow, F. S. & Licciardi, J. M. Assessing the impact of Laurentide Ice Sheet topography on glacial climate. *Clim. Past* **10**, 487–507 (2014).
55. Zhang, X., Lohmann, G., Knorr, G. & Purcell, C. Abrupt glacial climate shifts controlled by ice sheet changes. *Nature* **512**, 290–294 (2014).
56. Zhu, J., Liu, Z., Zhang, X., Eisenman, I. & Liu, W. Linear weakening of the AMOC in response to receding glacial ice sheets in CCSM3. *Geophys. Res. Lett.* **41**, 6252–6258 (2014).
57. Roberts, W. H. G., Valdes, P. J. & Payne, A. J. Topography's crucial role in Heinrich Events. *Proc. Natl Acad. Sci. USA* **111**, 16688–16693 (2014).
58. Di Nezio, P. N. *et al.* The climate response of the Indo-Pacific warm pool to glacial sea level. *Paleoceanography* **31**, 866–894 (2016).
59. Hanebuth, T. Rapid flooding of the Sunda Shelf: a late-glacial sea-level record. *Science* **288**, 1033–1035 (2000).
60. Trenberth, K. E. *et al.* Progress during TOGA in understanding and modeling global teleconnections associated with tropical sea surface temperatures. *J. Geophys. Res. Oceans* **103**, 14291–14324 (1998).
61. Carolin, S. A. *et al.* Varied response of western Pacific hydrology to climate forcings over the Last Glacial Period. *Science* **340**, 1564–1566 (2013).
62. Yin, J. H. & Battisti, D. S. The importance of tropical sea surface temperature patterns in simulations of Last Glacial Maximum climate. *J. Clim.* **14**, 565–581 (2001).
63. Fudge, T. J. *et al.* Variable relationship between accumulation and temperature in West Antarctica for the past 31,000 years. *Geophys. Res. Lett.* **43**, 3795–3803 (2016).



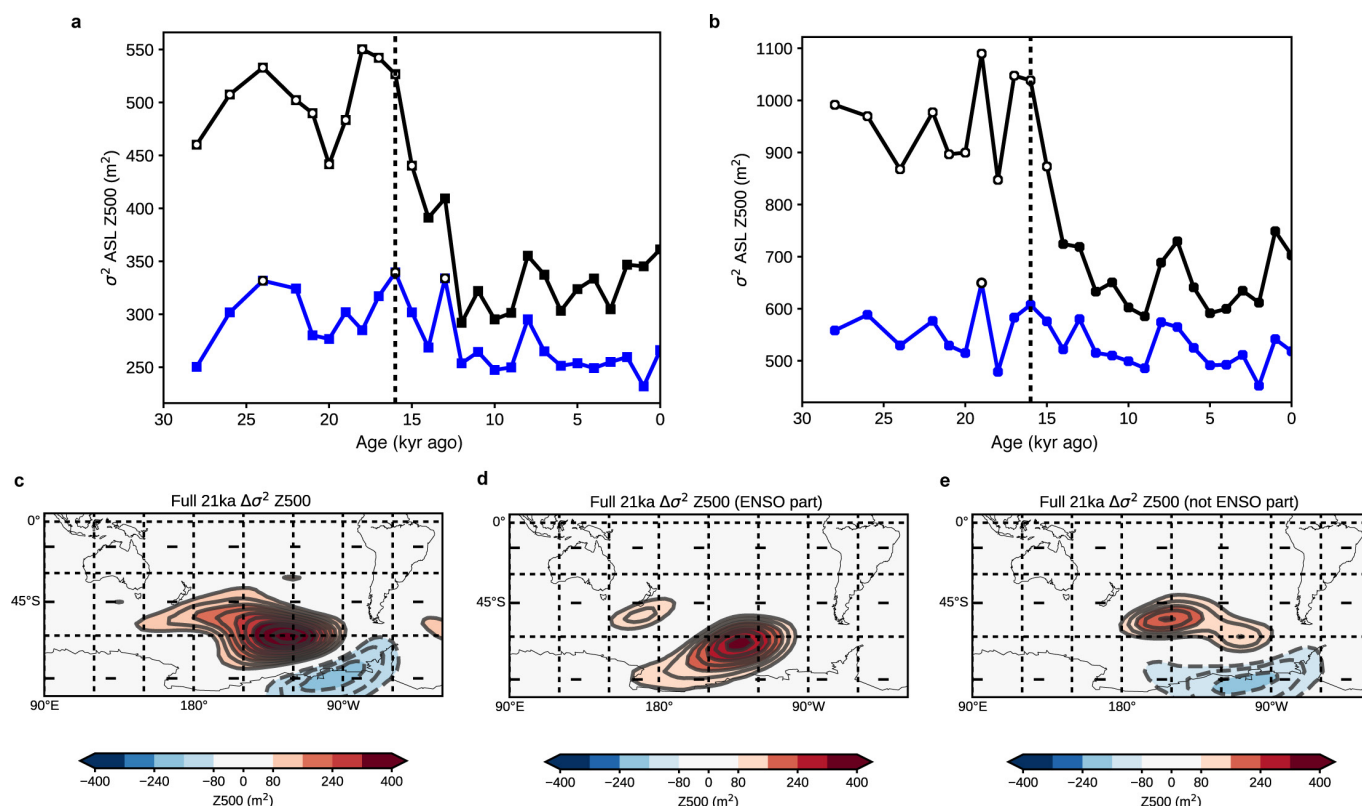
Extended Data Figure 1 | Signal detection. **a**, Relative amplitudes for 1-yr, 2-yr, 3-yr and 4-yr periods calculated for 500-yr spectral data windows, normalized to the value for the annual signal in the most recent data window. Both the climate and diffusion affects the amplitude of these high-frequency signals. However, it is mainly the effects of diffusion that cause the loss of the annual signal at >14 kyr ago. Similarly, the 2-yr period is lost between 17 kyr ago and 19 kyr ago, when the rate of diffusion for WDC was highest¹⁶. Periods >3 yr survive diffusion throughout the past 31 kyr. **b**, An example of a deconvolution calculation showing the observed δD water isotope record (that is, raw data; dotted red line), and the diffusion-corrected record (black line). Although this calculation was not used for the data presented in this paper, it serves as a visual aid in understanding how the diffusion-corrected water isotope record would look in the time domain. We performed all diffusion-correction calculations in the frequency domain to reduce uncertainty. **c**, The power density spectrum for the Southern Oscillation Index from 1951 to 2017 (black; 95% confidence intervals in grey), compared with a red noise null

hypothesis (red) calculated from the average of 100 power spectrums of synthetic data that have the same autocorrelation and variance as the Southern Oscillation Index. The Southern Oscillation Index has power greater than the red noise across a broad spectral peak between 2 and 17 yr, which can be subdivided into a 2–7-yr high-frequency peak and an 8–17-yr peak. Owing to the limited temporal span of modern observations, multi-decadal spectral estimates of the Southern Oscillation Index cannot be adequately defined. **d**, Diffusion-corrected relative amplitudes using 500-yr windows of WDC water isotope data. **e**, The difference in age of consecutive 5-mm WDC water isotope samples (blue) and a 500-yr sliding average (red). **f**, The WDC accumulation rate⁶³, inverted. The accumulation (in metres of ice equivalent per year), and by extension the difference in age of consecutive 5-mm WDC water isotope samples in **e**, undergoes large changes during the deglaciation at around 18.5 kyr ago, occurring 2.5 kyr before the change point in teleconnection strength at about 16 kyr ago.



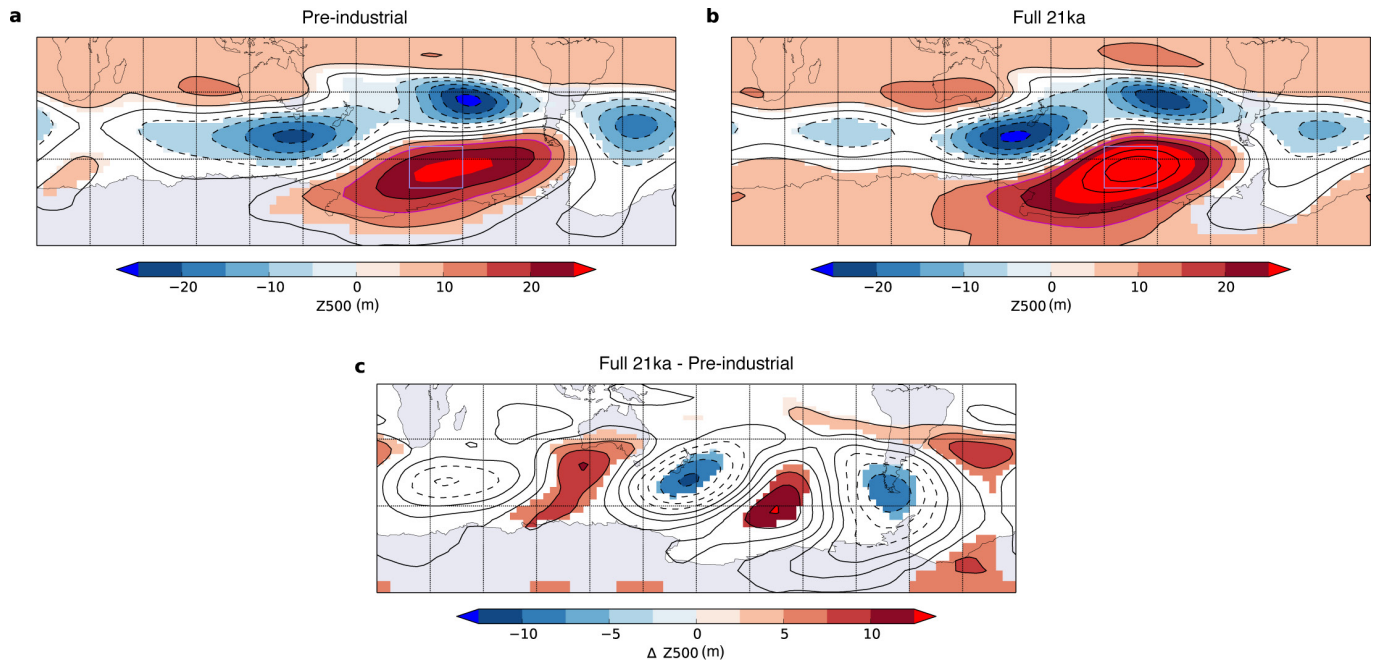
Extended Data Figure 2 | Change point detection. **a**, WDC 4–15-yr variability for 500-yr data windows (dashed lines are 1σ uncertainties; see Methods). **b**, Regression test algorithm to determine the first significant change in the WDC 4–15-yr variability in **a**. The first coloured data point below the P -value significance threshold occurs 16.44 kyr ago. **c**, Example of the diffusion-correction calculation for a 100-yr data window centred

on 15.54 kyr ago; raw data (black), diffusion-corrected data (blue), Gaussian fit (red) with dashed 1σ uncertainty bounds (see Methods). The same calculation is made for 500-yr data windows. **d**, The subset of diffusion-corrected 4–15-yr amplitudes (green) calculated at 100-yr resolution. The values are normalized to the amplitude value at 16.24 kyr ago, which represents the change point towards smaller amplitudes.



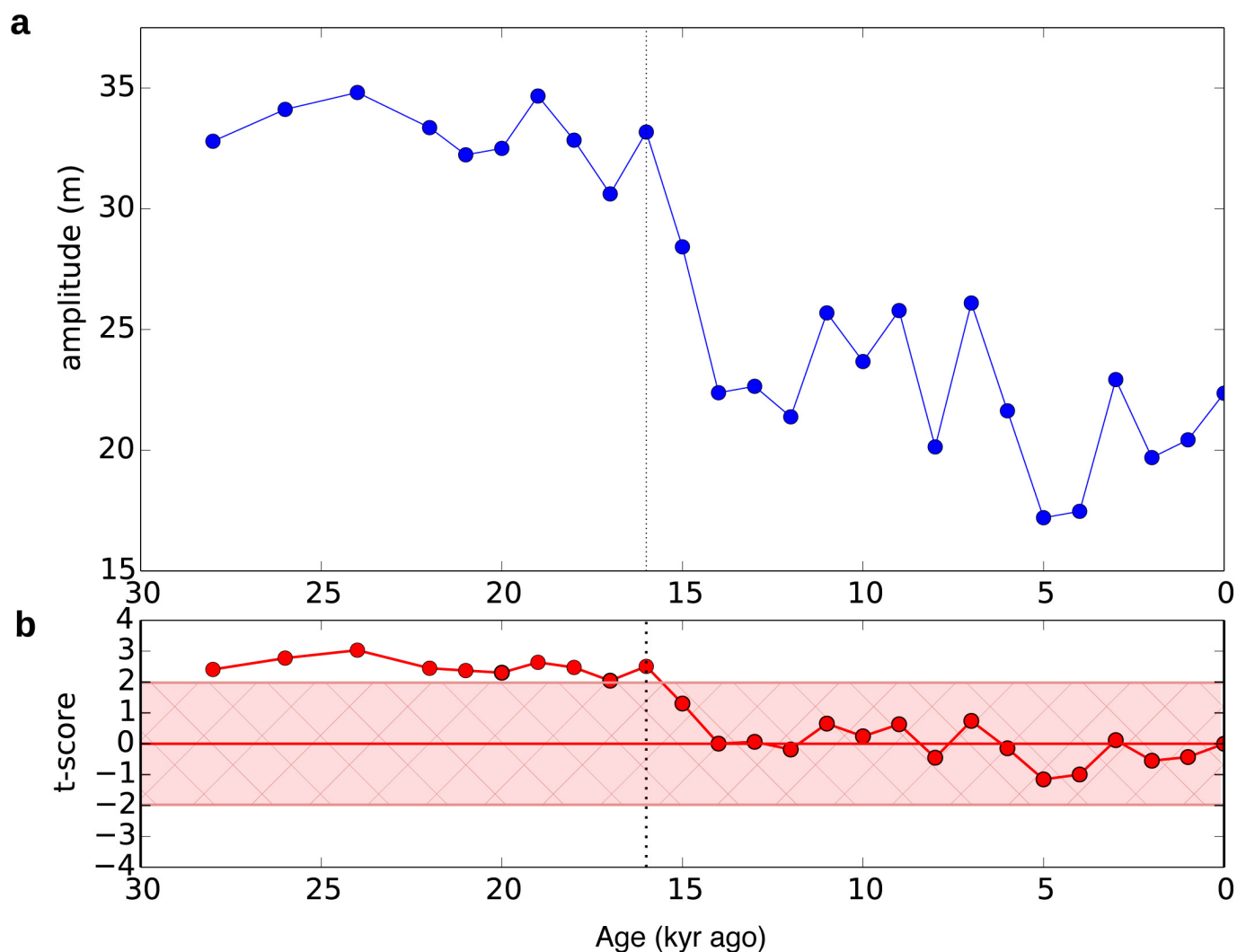
Extended Data Figure 3 | ASL variability. Panels **a** and **b** show the variance σ^2 of the indices Z_{ASL} (black) and Z_{local} (blue). **a**, The indices are computed from monthly mean data, then filtered with a 4–15-yr band pass filter. **b**, The indices are computed from annual mean output. We compute Z_{ASL} as the mean 500-hPa height in the region 55°–70° S and 195°–240° E. The blue lines show Z_{ASL} after linearly removing the SST_{pac} time series from the 500-hPa height field; this is the ASL variability unrelated to the tropical Pacific (Z_{local} ; see Methods). The markers are unfilled if the variance of Z_{ASL} at each time slice is 95% significantly different (F -test)

to that of the pre-industrial period. **c**, Map of the change in the variance of the 500-hPa height field between 21 kyr ago and the pre-industrial period. **d**, The variability that is linearly related to ENSO, Z_{pac} (this is the part removed from Z_{ASL} to yield Z_{local}). **e**, The variability with the effect of ENSO linearly removed (see Methods; this is the equivalent of Z_{local}). Changes not attributable to ENSO occur to the north of the Amundsen Sea, while changes over the Amundsen Sea are related to ENSO. In **c–e** the contour intervals are 40 m^2 , with colours changing every 80 m^2 . Negative contours are dashed.



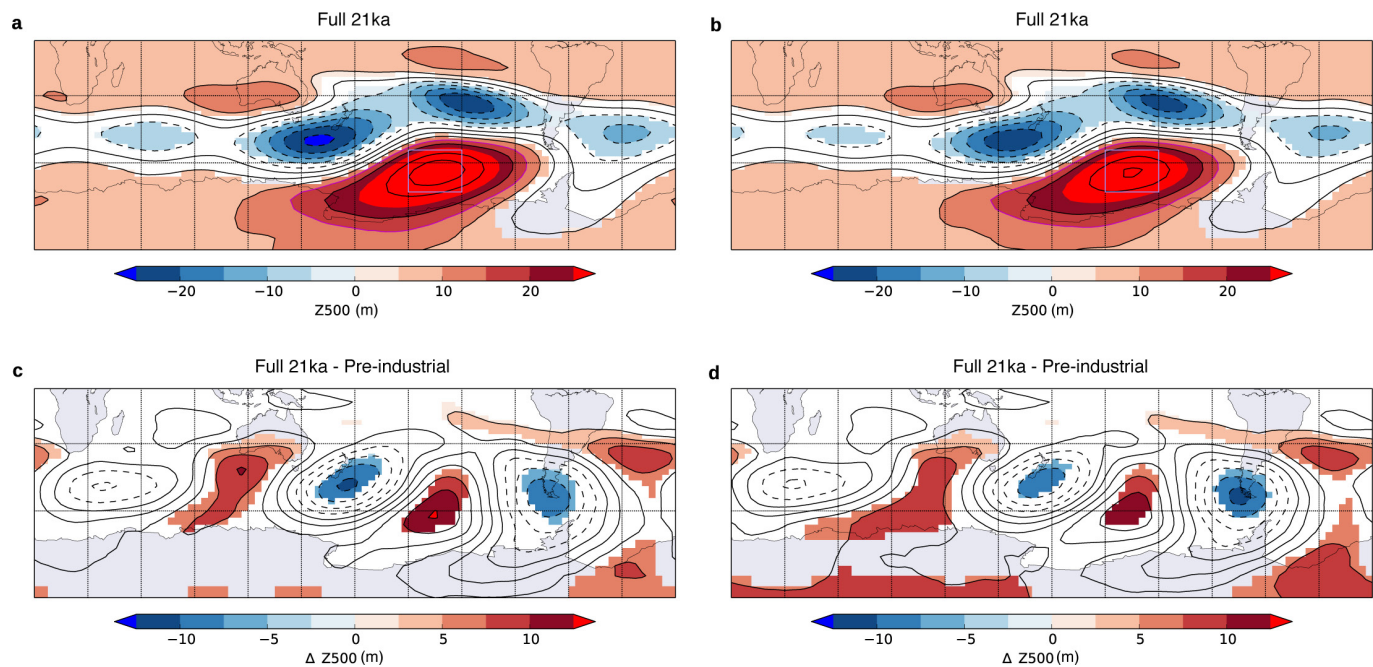
Extended Data Figure 4 | Composites of the 500-hPa height field for ENSO events. a–c, Composite for the ‘Pre-industrial’ (a), ‘Full 21ka’ (b) and the difference between the ‘Full 21ka’ and ‘Pre-industrial’ simulations (c). Contours are filled (not white) when statistical significance exceeds

95% using a Monte Carlo test. Negative contours are dashed. In **a** and **b** the contours are plotted every 5 m and colours saturate at ± 25 m. The thin blue box shows where the ASL index is computed. In **c** contours are plotted every 2.5 m and colours saturate at ± 12.5 m.



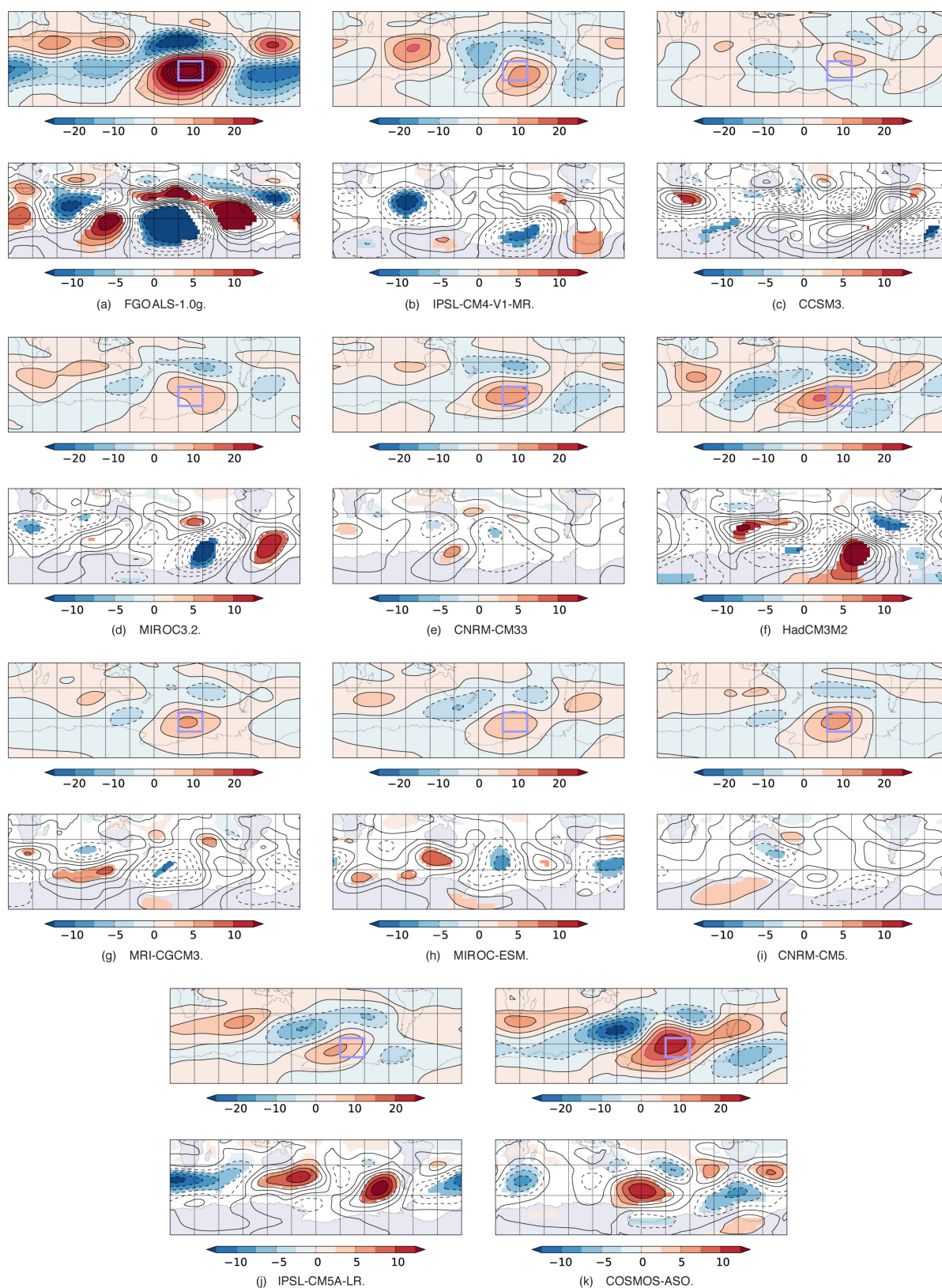
Extended Data Figure 5 | Tropical Pacific-to-ASL teleconnection strength, computed using the ‘Full 28–0ka’ simulations. a, Average 500-hPa geopotential height anomaly in the Amundsen Sea region, computed within the purple box shown in Extended Data Fig. 4. These

values are derived from composites constructed using only the lower limits on the size of ENSO events (see main text and Methods). **b,** The t -score is indicated by the red line. Values outside the shaded red region are 95% statistically different from the pre-industrial value.



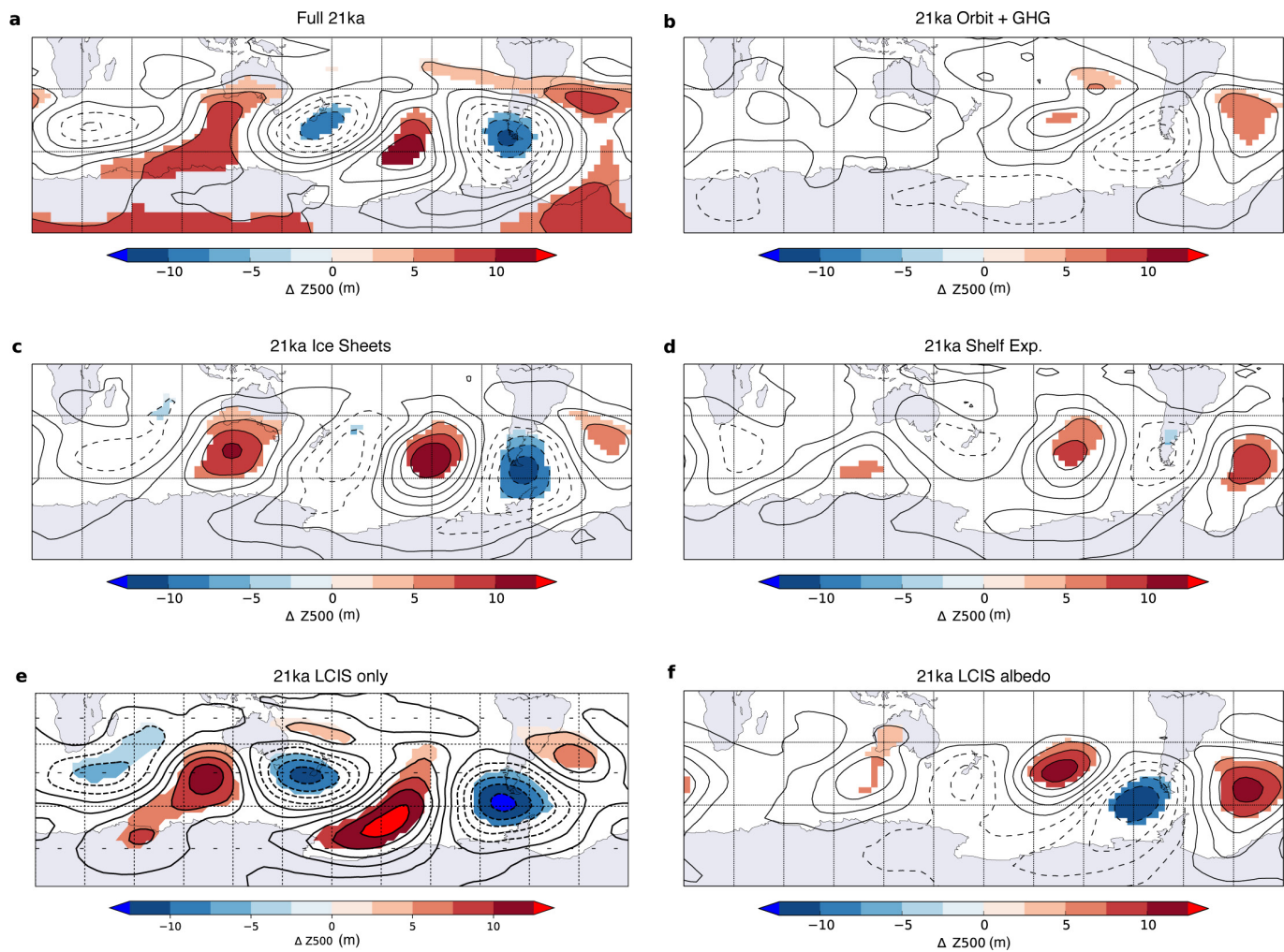
Extended Data Figure 6 | Composites of the 500-hPa height field for ENSO events with and without upper bound. a, The teleconnection without upper limit using the 'Full 21ka' simulation. **b,** The teleconnection with upper limit using the 'Full 21ka' simulation. **c,** The difference in teleconnection between the 'Full 21ka' simulation and the 'Pre-industrial' simulation without upper limit. **d,** The same difference as c with upper

limit. In all panels, negative contours are dashed, and contours are filled (not white) when statistical significance exceeds 95% using a Monte Carlo test. In **a** and **b**, the contours are plotted every 5 m and colours saturate at ± 25 m. In **c** and **d**, contours are plotted every 2.5 m and colours saturate at ± 12.5 m.



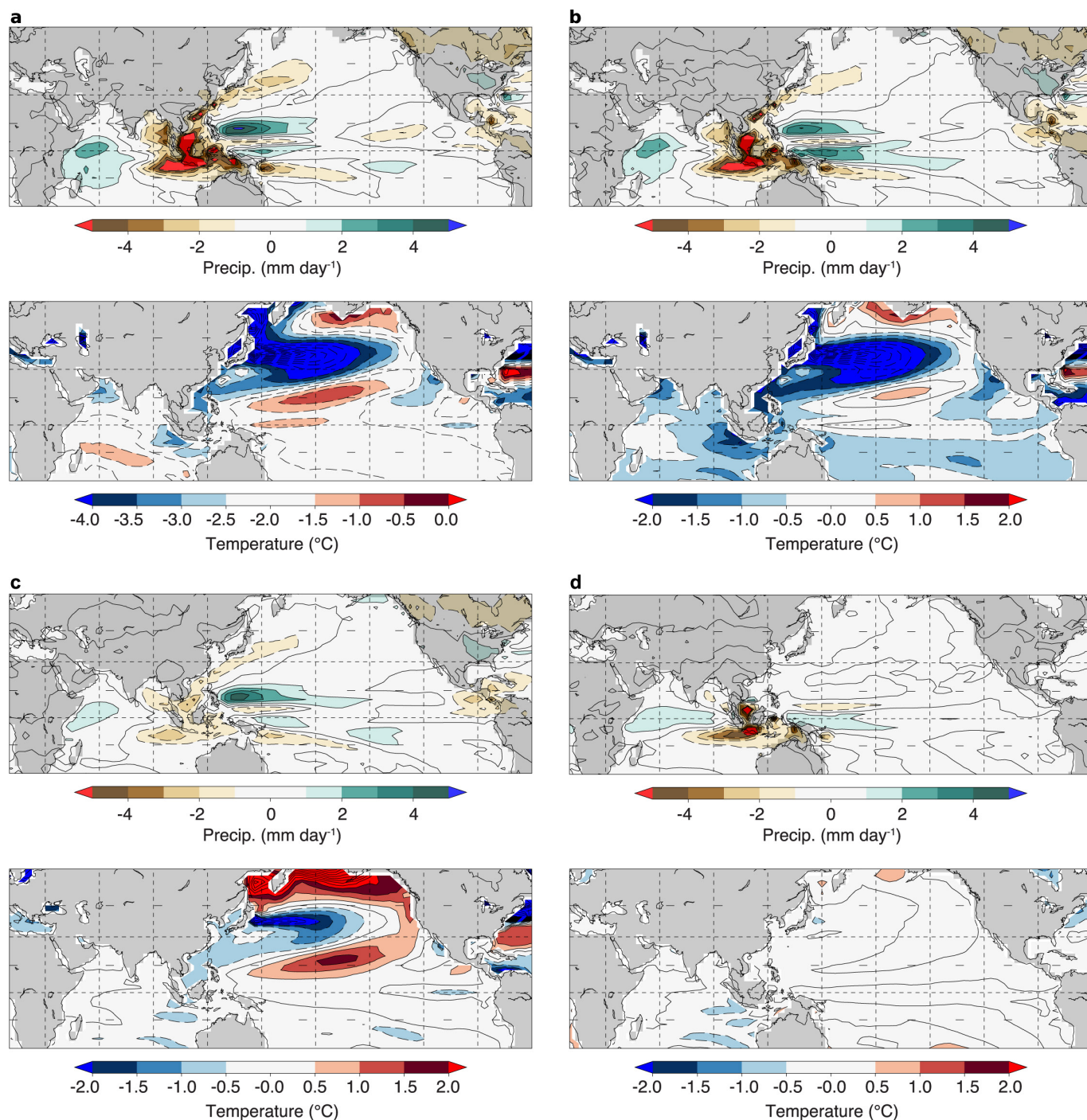
Extended Data Figure 7 | Composite maps of the 500-hPa height field for ENSO events in the PMIP2/3 models. For each model in a–k, the top panel shows the ‘Pre-industrial’ composite and the bottom panel the difference between the ‘Full 21ka’ and ‘Pre-industrial’ simulations. In the bottom panel, contours are filled (non-white) when statistical significance exceeds 95% using a Monte Carlo test. In the top panels, contours are

plotted at 5-m intervals, with colours saturating at 25 m. In the bottom panels, contours are plotted at 2.5-m intervals, with colours saturating at ± 12.5 m. Negative contours are dashed. The reduced statistical significance in these panels compared to those shown in Extended Data Figs 4, 6, 8 and 9 is due to the shorter data series available in the PMIP2/3 archives.



Extended Data Figure 8 | Sensitivity of composite maps to different sets of boundary conditions 21 kyr ago. All plots show the difference between 21-kyr and 0-kyr composites. The composites are constructed using both upper and lower limits on the size of ENSO events. Contours are plotted every 2.5 m (negative contours are dashed) and colours saturate at ± 12.5 m. Contours are filled (not white) when statistical significance

exceeds 95% using a Monte Carlo test. **a**, 'Full 21ka' simulation. **b**, '21ka Orbit + GHG' simulation. **c**, '21ka Ice Sheets' simulation. **d**, '21ka Shelf Exp.' simulation. **e**, '21ka LCIS only' simulation. **f**, '21ka LCIS albedo' simulation. Each of these simulations is fully defined in Supplementary Data.



Extended Data Figure 9 | Annual mean anomalies of precipitation and sea surface temperature. Maps of anomalies 21 kyr ago relative to the pre-industrial period. **a**, 'Full 21ka' simulation. **b**, '21ka Ice Sheets' simulation. **c**, '21ka LCIS only' simulation. **d**, '21ka Shelf Exp.' simulation. Annual means are calculated from 100 years of output. Contour intervals for

precipitation are 1 mm per day, and for sea surface temperature are 0.5 °C. Land areas are shown in grey. Note that the temperature colour scale in **a** ranges from -4 °C to 0 °C. This accounts for the mean greenhouse gas cooling that is seen in the 'Full 21ka' simulation.

Global patterns of declining temperature variability from the Last Glacial Maximum to the Holocene

Kira Rehfeld^{1,2}, Thomas Münch^{1,3}, Sze Ling Ho^{1,4} & Thomas Laepple¹

Changes in climate variability are as important for society to address as are changes in mean climate¹. Contrasting temperature variability during the Last Glacial Maximum and the Holocene can provide insights into the relationship between the mean state of the climate and its variability^{2,3}. However, although glacial–interglacial changes in variability have been quantified for Greenland², a global view remains elusive. Here we use a network of marine and terrestrial temperature proxies to show that temperature variability decreased globally by a factor of four as the climate warmed by 3–8 degrees Celsius from the Last Glacial Maximum (around 21,000 years ago) to the Holocene epoch (the past 11,500 years). This decrease had a clear zonal pattern, with little change in the tropics (by a factor of only 1.6–2.8) and greater change in the mid-latitudes of both hemispheres (by a factor of 3.3–14). By contrast, Greenland ice-core records show a reduction in temperature variability by a factor of 73, suggesting influences beyond local temperature or a decoupling of atmospheric and global surface temperature variability for Greenland. The overall pattern of reduced variability can be explained by changes in the meridional temperature gradient, a mechanism that points to further decreases in temperature variability in a warmer future.

There is scientific consensus that the mean global temperature has been rising over the instrumental era⁴. However, whether this warming has caused surface temperatures to become more⁵ or less^{6,7} variable, and how this variability will change in a warmer future, remain topics of debate. Here we use palaeoclimate proxy data to quantify changes in temperature variability before and after the last major transition in global mean climate: the 3–8 °C warming⁸ from the Last Glacial Maximum (LGM, around 21,000 years (21 kyr) ago) to the current warm period of the Holocene (Fig. 1). The magnitude of temperature change during this transition is in the same range as that projected for the coming centuries⁴.

The global spatial pattern of the mean LGM-to-Holocene temperature change has been established through numerous studies^{8–10}. However, except for some studies on changes in interannual climate variability in the tropics¹¹, our current understanding of changes in variability is largely based on the stable oxygen isotope records of the high-resolution central Greenland ice cores¹². The isotope records, which are interpreted as a proxy for temperature¹³, show that the last glacial period appears to have been not only cold but also highly variable on decadal to millennial timescales^{2,3}. This finding is not limited to the magnitude of distinct events, such as the Heinrich stadials (that is, cold periods in Greenland) or the abrupt transitions into the Dansgaard–Oeschger interstadials; it also holds for the background variability during the LGM (Fig. 1b).

Consequently, glacial climate has been characterized as highly variable^{2,3}, whereas the Holocene is commonly described as a stable and quiescent period³. The large reduction in variability was proposed to have supported human dispersal throughout Europe¹⁴ and cultural evolution¹⁵. However, the evidence for an exclusively stable Holocene climate—beyond that of Greenland ice-core records—is unclear,

particularly because other proxy records for temperature in and outside of Greenland suggest considerable variability during the Holocene^{16,17}.

In this study, we derive a quantitative estimate for global and regional change in temperature variability between the LGM (27–19 kyr ago) and the Holocene (8–0 kyr ago) based on high-resolution palaeoclimate proxy records for temperature (Fig. 1a). These time periods represent rather stable boundary conditions with minimal changes in ice-sheet size and sea level. Furthermore, our LGM time window contains only one small Dansgaard–Oeschger event, thereby enabling us to focus our analysis on the glacial background state. We compile two global datasets (Methods). The first (‘joint’) dataset contains 28 records that cover both the LGM and the Holocene. We estimate the change in variability from the ratio of LGM to Holocene variance separately for each record and thus independently of calibration uncertainties, as long as the calibrations are constant over time. This is a reasonable assumption because state-dependent calibrations have been proposed only for Greenlandic ice cores¹⁸, and we take this into account. Analysing variance ratios from single cores also minimizes site-specific effects on the variance estimates, such as the ecological preferences of the organisms that record the climate signal or the extent of bioturbation, which affects marine proxies in sediments (Methods). The second (‘separate’) dataset is more extensive, containing 88 records for the Holocene and 39 for the LGM. In this case, we first derive zonal mean estimates of temperature variability for each time slice and then form the ratio. All proxy types for which multiple calibrations exist were recalibrated using a single temperature relationship for each proxy type and region. For both the joint and the separate dataset, we quantify the change in variability as the ratio of variance at timescales between 500 and 1,750 years in the spectral domain using a method that is insensitive to changes in the temporal sampling. We correct the ratio for the effects of non-climate variability in the proxy records using independent estimates of the signal-to-noise ratio of the proxies (Methods).

All three Greenlandic ice-core records display large changes in variability, with an average LGM-to-Holocene variance ratio $R = V_{\text{LGM}}/V_{\text{Hol}}$ of 73 (90% confidence interval of 50–112; Fig. 2a). In contrast to this marked reduction, the area-weighted average change in variability for the rest of the globe is far lower: the separate estimate indicates a decrease in variability by a factor of 7.0 (90% confidence interval, 2.2–16). The large uncertainty range is due to the combination of many different proxy records which are affected by potential site-specific effects such as differing seasonal responses. The magnitude of change is confirmed by the joint dataset, which offers a more precise estimate of $R = 4.4$ (90% confidence interval, 2.5–6.6) by circumventing these complications. Together, these datasets suggest a significantly lower ($P \leq 0.01$) change in variability outside of Greenland than is found in Greenlandic ice-core records. The discrepancy also cannot be reconciled by considering a potentially lower quality of marine-based temperature reconstructions (Methods). This observation suggests that Greenlandic ice-core records should not be used as a sole reference for climate variability, particularly concerning the amplitude of change.

¹Alfred Wegener Institute Helmholtz Centre for Polar and Marine Research, Telegrafenberg A43, 14473 Potsdam, Germany. ²British Antarctic Survey, High Cross, Madingley Road, Cambridge CB3 0ET, UK. ³Institute of Physics and Astronomy, University of Potsdam, Karl-Liebknecht-Strasse 24-25, 14476 Potsdam, Germany. ⁴University of Bergen and Bjerknes Centre for Climate Research, Allégaten 41, 5007 Bergen, Norway.

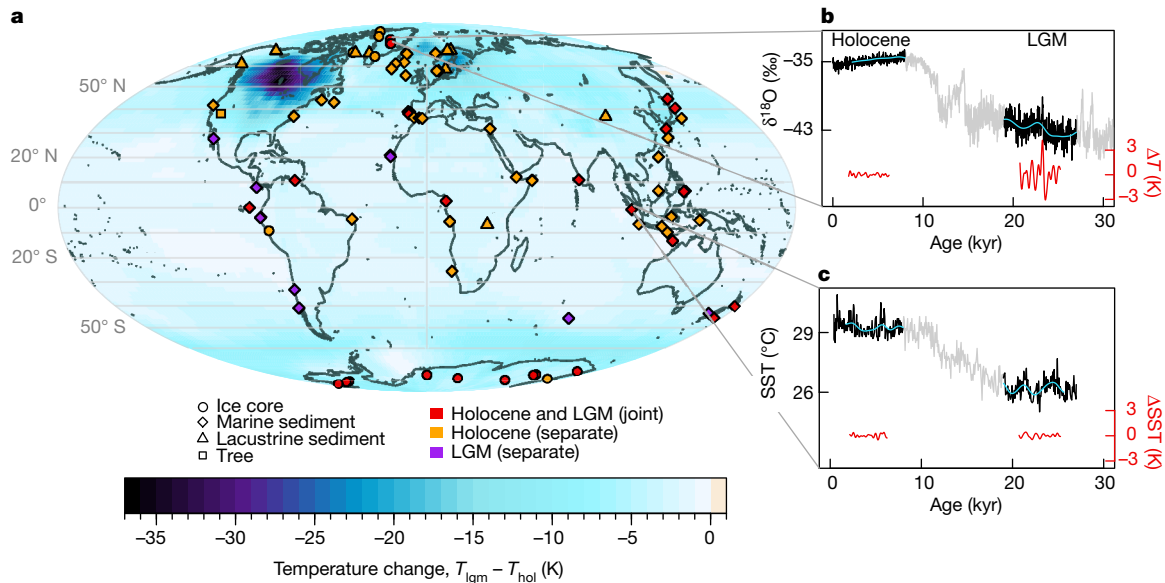


Figure 1 | Proxy records for temperature. **a**, Site locations (symbols) and mean LGM-to-Holocene temperature change ($T_{\text{LGM}} - T_{\text{hol}}$; background), estimated from climate model and proxy data⁹. The pre-industrial (AD 1850) temperature is used as a surrogate for the Holocene time slice because we are interested in only the first-order pattern of the deglaciation. **b**, North Greenland Ice Core Project (NGRIP) ice-core $\delta^{18}\text{O}$

data for Greenland (ref. 12; black, expressed in ‰ with respect to Vienna Standard Mean Ocean Water) with millennial trend (blue) and bandpass-filtered temperature (ΔT ; 0.5–1.75 kyr⁻¹; red) for Holocene and LGM (grey lines in background show the full record). **c**, Sea-surface temperature (SST) inferred from Mg/Ca ratios from tropical marine sediment record SO189-39KL³¹; colours as in **b**.

The spatial pattern of variability change (Fig. 2b–d) shows a distinct latitude dependence (Fig. 3a). A small, yet statistically significant, change can be found in the tropics (20° S–20° N; $R = 2.1$;

90% confidence interval, 1.6–2.8). The mid-latitudes (20–50° S and 20–50° N) show a moderate decrease in variability from the glacial period to the Holocene by a factor of 5.4 (90% confidence interval,

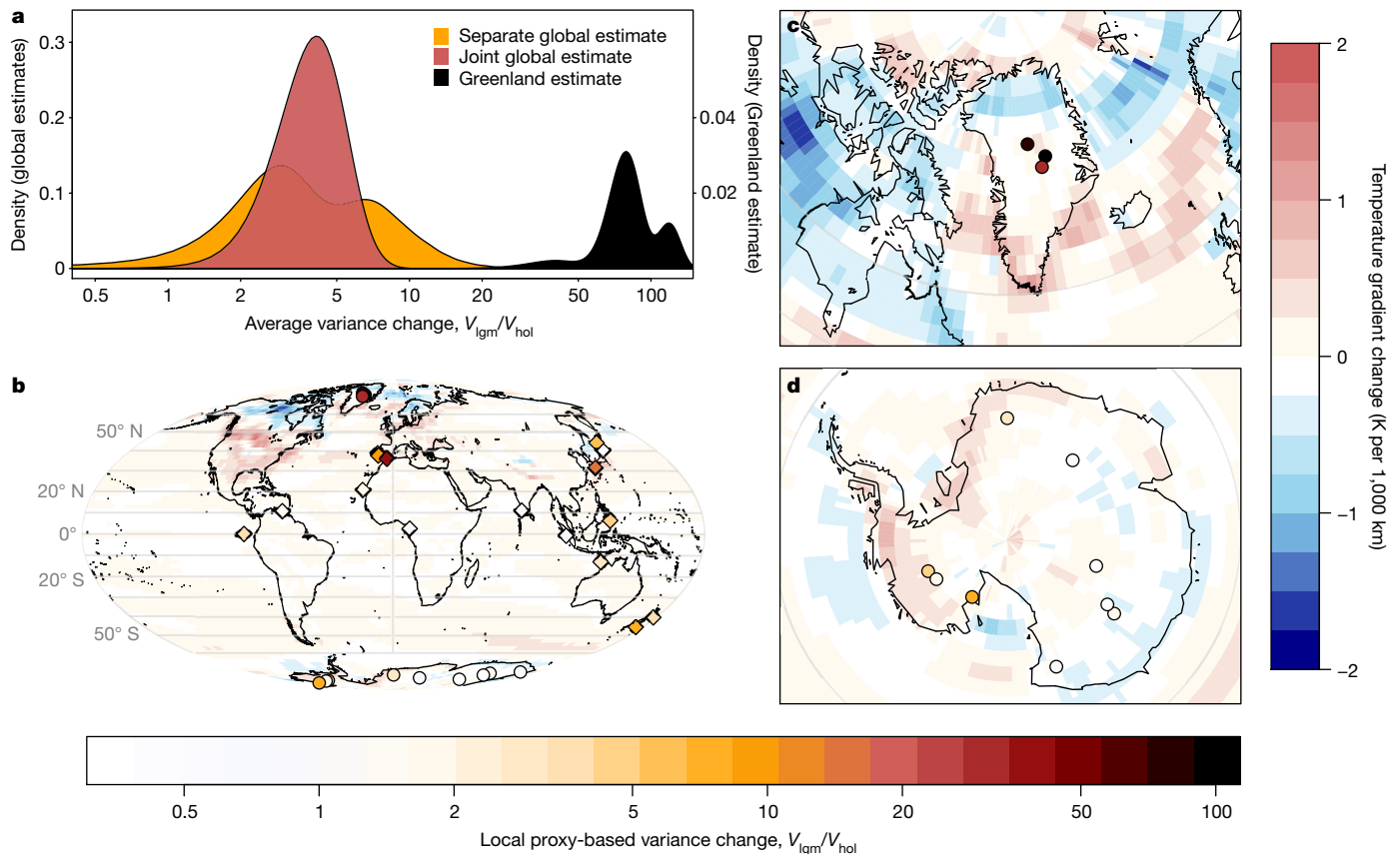


Figure 2 | Global LGM-to-Holocene change in variability and temperature gradient. **a**, Distribution of the globally averaged area-weighted LGM-to-Holocene variance ratio ($V_{\text{LGM}}/V_{\text{hol}}$; without Greenland; red denotes the joint dataset, orange the separate dataset) and the regional Greenland variance ratio (black). Note that for visibility the Greenland

density estimates are on a separate y axis. **b–d**, LGM-to-Holocene proxy-derived variance ratios (symbols, bottom colour scale) and modelled change in temperature gradient⁹ (background, right colour scale; details in Methods) for the globe (**b**), Greenland (**c**) and Antarctica (**d**).

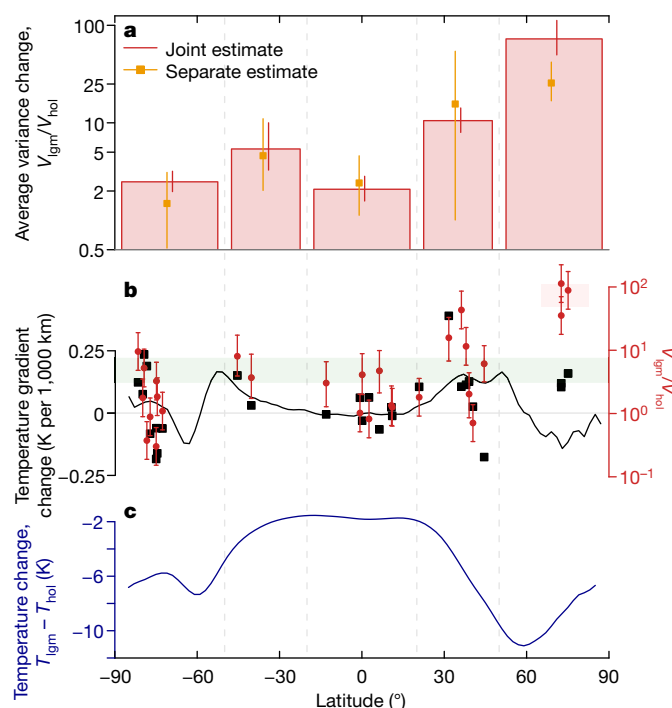


Figure 3 | Latitudinal structure of LGM-to-Holocene variability and mean changes. **a**, Zonal-mean change in variability from the proxy compilations (red bars denote the joint estimate, orange points the separate estimate). **b**, Latitude dependence of the equator-to-pole change in temperature gradient. The five-point smoothed zonal-mean change in gradient (black line) is shown together with the change in gradient at the proxy locations (black squares), compared to the individual proxy estimates of the change in variability (red circles). Red and green shading denotes the 90% confidence interval of the global-mean change in variance without Greenland and of the mean change in variance for Greenland, respectively. **c**, Zonal-mean change in temperature⁹. All error bars are 90% confidence intervals.

3.3–10) and 11 (90% confidence interval, 8.0–14), respectively. The polar regions (50–90° S and 50–90° N) are represented by only Greenlandic and Antarctic ice-core records and reveal an asymmetric pattern: the Greenland change is the highest globally, whereas Antarctica displays only a small change ($R = 2.5$; 90% confidence interval, 2.0–3.2), comparable to that in the tropical ocean. West Antarctic ice cores show a stronger variability change than do ice cores from East Antarctica (Fig. 2d), a finding that is similar to the west–east contrast in the response to anthropogenic forcing¹⁹. The estimated pattern of variability change is similar for multicentennial and millennial timescales (Extended Data Fig. 1), which demonstrates that our finding is not limited to one specific frequency band. This result further suggests that the Dansgaard–Oeschger event included in the LGM time slice has only a minor influence.

The equator-to-pole surface air temperature gradient in the LGM was larger than in the Holocene, because the high latitudes have warmed more than the tropics since the LGM¹⁰ (Figs 1a, 2b). Furthermore, the land–sea contrast in mid- to high latitudes was stronger in the LGM because a relatively warm open ocean contrasted with the partly ice-covered land, and changing sea-ice cover affected both the meridional and zonal temperature gradients²⁰. Atmospheric temperature gradients are a primary driver of local temperature variability on synoptic timescales. Accordingly, changes in spatial gradients due to mean climate changes have been proposed to control changes in variability^{21,22}. Hence, steeper temperature gradients in the LGM may have led to increased synoptic variability. Describing climate variability as the linear response to stochastic weather forcing integrated by the slow components of the climate system, such as the ocean²³, increased synoptic variability relates directly to an increase in variability on interannual

to millennial timescales²⁴. Contrasting the change in the atmospheric equator-to-pole temperature gradient—as estimated from a combined model–data temperature reconstruction⁹—with the estimated change in variability (Fig. 3b, Extended Data Fig. 2) indeed reveals a consistent pattern on a global scale (Spearman's rank correlation coefficient $r = 0.43$, $P = 0.03$, $n = 28$), although the high variability reconstructed for Greenland appears as an outlier (Fig. 3b). This relationship between temperature gradient and variability change also holds for the heterogeneous pattern of temperature variability change over Antarctic land surfaces (Fig. 2d), although the quality of the gradient estimates on this regional scale is unclear. In addition, a reconfiguration of the large-scale oceanic circulation could also drive changes in temperature variability. Perturbation experiments in climate models suggest that the Atlantic meridional overturning circulation (AMOC) may have been less stable in the LGM than in the Holocene²⁵, and the temperature response to a varying AMOC that modulates the oceanic poleward heat flux shows a first-order pattern²⁵ that is consistent with our estimated changes in variability (Fig. 3). However, there is no evidence that the imprint of AMOC modulations should be greater on Greenlandic air temperatures than on any other North Atlantic region.

The general meridional pattern is thus consistent with both synoptic atmospheric and oceanic contributions to the change in variability. However, neither contribution can explain the considerably stronger variability change found in the oxygen isotope records from Greenlandic ice cores, which is 18 times stronger than the global mean—a polar-to-global change in variance that is much larger than the observed polar amplification during the twentieth century⁴. In addition, the resultant asymmetry between Greenlandic and Antarctic variability change contrasts with the rather symmetric polar amplification that is simulated by climate models for past and future climate states²⁶. The specific discrepancy for the Greenlandic records thus points either to a decoupling of Greenlandic temperature variability from global surface temperature variability, for example owing to the altitude of the ice sheet representing close to mid-tropospheric atmospheric conditions, or to strong influences on the isotopic composition of Greenlandic ice cores beyond the local site temperature.

Sea-ice changes have been linked to temperature variability changes on interannual to decadal timescales⁷, and may also contribute to the uniqueness of the Greenlandic variability estimates. The sea-ice extent during the glacial period was larger than at present²⁰, and the increased area favoured increased sea-ice variability on centennial timescales, a change that is corroborated by proxy-based sea-ice reconstructions (Extended Data Table 1). A large sea-ice lid shields more ocean heat from the atmosphere, reduces the effective heat capacity at the surface and thus also renders local temperatures more volatile under the same forcing. Additionally, a larger sea-ice area can change more, which amplifies temperature variability on the Greenland ice sheet through atmospheric feedbacks²⁷. Changes in sea-ice extent also influence the seasonality of snow accumulation on the central Greenland ice sheet²⁸, which can strongly affect the isotopic composition recorded in ice cores²⁹. Furthermore, changes in the moisture pathways as an atmospheric response to the large Northern Hemisphere ice sheets could also have caused changes in isotope variability that are unrelated to local temperatures³⁰.

On the interannual to multidecadal scale, the surface temperature variability ratio in coupled model simulations from PMIP3 confirms the overall reduction in temperature variability from the LGM to the Holocene (Methods, Extended Data Fig. 3). The spatial pattern is similar, but the magnitude of change is smaller ($R = 1.28$; 90% confidence interval, 1.25–1.30), suggesting either a difference in the partitioning of variability between fast and slow timescales, or that the models suppress long-term climate variability¹⁷ and so do not display realistic variability changes. The tendency of coupled climate models to underestimate changes in the meridional temperature gradient²⁶ might also contribute to this discrepancy. To establish to what extent variability change is uniform across timescales, as predicted by linear

energy balance models^{23,24}, or is specific to certain timescales related to dynamic modes in the climate system, variability estimates at decadal to centennial scales are needed. Possibilities include annually laminated sediment records or a better understanding of non-climate effects on ice-core records to enable reliable high-resolution reconstructions. The PMIP3 climate model results also suggest that the temperature variability change in Greenland is not larger than elsewhere. Therefore, it is paramount to establish whether the Greenlandic variability change is indeed a change in local temperature variability or specific to the oxygen isotope proxy for temperature. The representativeness of Greenlandic isotope variability for Arctic and global temperature variability could be clarified using non-stable-water-isotope proxies for temperature in Greenland¹⁶, more data from across the Arctic and climate modelling with embedded water-isotope tracers.

Our results have implications for the understanding of past and future climate variability. The reconstruction reveals that temperature variability decreased globally by a factor of four for a warming of 3–8°C from the LGM to the Holocene. This decrease is small compared with the reduction by a factor of 73 estimated for Greenland and indicates that the change in variability recorded by Greenlandic ice cores is not representative of changes in variability across the globe. In terms of the magnitude of variability, these iconic datasets thus do not provide a reference for global climate changes as is often implicitly assumed. Consequently, we have to rethink the notion of an unstable glacial period and a very stable Holocene and the implications for societal evolution. Although a direct extrapolation from the glacial period to the future would not be prudent, it is reasonable to assume that the relationship between mean change and variability change holds, given our mechanistic understanding of the drivers and the direction of future changes in the temperature gradient. Our findings therefore add support to climate modelling studies that predict a reduction in winter temperature variability under global warming via reduced spatial gradients^{21,22}. Our results further suggest that this variability (which dominates annual-mean temperature variability), might also translate to a reduction in multidecadal and slower variability⁷. More high-resolution records of glacial climate, continued quantification of recording and preserving processes of palaeoclimate signals, and an extension of similar analyses to other climate states will help to further constrain the mean-state dependence of climate variability.

Online Content Methods, along with any additional Extended Data display items and Source Data, are available in the online version of the paper; references unique to these sections appear only in the online paper.

Received 24 August; accepted 12 December 2017.

Published online 5 February 2018.

- Katz, R. W. & Brown, B. G. Extreme events in a changing climate: variability is more important than averages. *Clim. Change* **21**, 289–302 (1992).
- Ditlevsen, P. D., Svensmark, H. & Johnsen, S. Contrasting atmospheric and climate dynamics of the last-glacial and Holocene periods. *Nature* **379**, 810–812 (1996).
- Shao, Z.-G. & Ditlevsen, P. D. Contrasting scaling properties of interglacial and glacial climates. *Nat. Commun.* **7**, 10951 (2016).
- IPCC. *Climate Change 2013: The Physical Science Basis. Contribution of Working Group I to the Fifth Assessment Report of the Intergovernmental Panel on Climate Change* (Cambridge Univ. Press, 2013).
- Hansen, J., Sato, M. & Ruedy, R. Perception of climate change. *Proc. Natl Acad. Sci. USA* **109**, E2415–E2423 (2012).
- Rhines, A. & Huybers, P. Frequent summer temperature extremes reflect changes in the mean, not the variance. *Proc. Natl Acad. Sci. USA* **110**, E546 (2013).
- Huntingford, C., Jones, P. D., Livina, V. N., Lenton, T. M. & Cox, P. M. No increase in global temperature variability despite changing regional patterns. *Nature* **500**, 327–330 (2013).
- Shakun, J. D. & Carlson, A. E. A global perspective on Last Glacial Maximum to Holocene climate change. *Quat. Sci. Rev.* **29**, 1801–1816 (2010).
- Annan, J. D. & Hargreaves, J. C. A new global reconstruction of temperature changes at the Last Glacial Maximum. *Clim. Past* **9**, 367–376 (2013).
- MARGO Project Members. Constraints on the magnitude and patterns of ocean cooling at the Last Glacial Maximum. *Nat. Geosci.* **2**, 127–132 (2009).
- Koutavas, A. & Joannides, S. El Niño–Southern Oscillation extrema in the Holocene and Last Glacial Maximum. *Paleoceanography* **27**, PA4208 (2012).

- NGRIP members. High-resolution record of Northern Hemisphere climate extending into the last interglacial period. *Nature* **431**, 147–151 (2004).
- Masson-Delmotte, V. *et al.* GRIP deuterium excess reveals rapid and orbital-scale changes in Greenland moisture origin. *Science* **309**, 118–121 (2005).
- Gamble, C., Davies, W., Pettitt, P. B. & Richards, M. Climate change and evolving human diversity in Europe during the last glacial. *Phil. Trans. R. Soc. Lond. B* **359**, 243–254 (2004).
- Richerson, P. J., Boyd, R. & Bettinger, R. L. Was agriculture impossible during the Pleistocene but mandatory during the Holocene? A climate change hypothesis. *Am. Antiq.* **66**, 387–411 (2001).
- Kobashi, T. *et al.* High variability of Greenland surface temperature over the past 4000 years estimated from trapped air in an ice core. *Geophys. Res. Lett.* **38**, L21501 (2011).
- Laepple, T. & Huybers, P. Ocean surface temperature variability: large model–data differences at decadal and longer periods. *Proc. Natl Acad. Sci. USA* **111**, 16682–16687 (2014).
- Jouzel, J. *et al.* Validity of the temperature reconstruction from water isotopes in ice cores. *J. Geophys. Res.* **102**, 26471–26487 (1997).
- Bromwich, D. H. *et al.* Central West Antarctica among the most rapidly warming regions on Earth. *Nat. Geosci.* **6**, 139–145 (2013).
- de Vernal, A. *et al.* Comparing proxies for the reconstruction of LGM sea-surface conditions in the northern North Atlantic. *Quat. Sci. Rev.* **25**, 2820–2834 (2006).
- Schneider, T., Bischoff, T. & Plotka, H. Physics of changes in synoptic midlatitude temperature variability. *J. Clim.* **28**, 2312–2331 (2015).
- Holmes, C. R., Woollings, T., Hawkins, E. & de Vries, H. Robust future changes in temperature variability under greenhouse gas forcing and the relationship with thermal advection. *J. Clim.* **29**, 2221–2236 (2016).
- Hasselmann, K. Stochastic climate models part I. Theory. *Tellus* **28**, 473–485 (1976).
- Rypdal, K., Rypdal, M. & Fredriksen, H.-B. Spatiotemporal long-range persistence in earth's temperature field: analysis of stochastic–diffusive energy balance models. *J. Clim.* **28**, 8379–8395 (2015).
- Sévellec, F. & Fedorov, A. V. Unstable AMOC during glacial intervals and millennial variability: the role of mean sea ice extent. *Earth Planet. Sci. Lett.* **429**, 60–68 (2015).
- Masson-Delmotte, V. *et al.* Past and future polar amplification of climate change: climate model intercomparisons and ice-core constraints. *Clim. Dyn.* **26**, 513–529 (2006).
- Li, C., Battisti, D. S., Schrag, D. P. & Tziperman, E. Abrupt climate shifts in Greenland due to displacements of the sea ice edge. *Geophys. Res. Lett.* **32**, L19702 (2005).
- Rhines, A. & Huybers, P. J. Sea ice and dynamical controls on preindustrial and Last Glacial Maximum accumulation in central Greenland. *J. Clim.* **27**, 8902–8917 (2014).
- Laepple, T., Werner, M. & Lohmann, G. Synchronicity of Antarctic temperatures and local solar insolation on orbital timescales. *Nature* **471**, 91–94 (2011).
- Wunsch, C. Abrupt climate change: an alternative view. *Quat. Res.* **65**, 191–203 (2006).
- Mohtadi, M. *et al.* North Atlantic forcing of tropical Indian Ocean climate. *Nature* **509**, 76–80 (2014).

Supplementary Information is available in the online version of the paper.

Acknowledgements This study was supported by the Initiative and Networking Fund of the Helmholtz Association grant no. VG-900NH. K.R. acknowledges funding by the German Science Foundation (DFG, code RE 3994/1-1). This project has received funding from the European Research Council (ERC) under the European Union's Horizon 2020 research and innovation programme (grant agreement no. 716092). We acknowledge P. Huybers, L. Sime, M. Holloway and T. Kunz for comments on the manuscript. We thank all original data contributors who made their proxy data available, and acknowledge the World Climate Research Programmes Working Group on Coupled Modelling, which is responsible for CMIP, and thank the climate modelling groups for producing and making available their model output. The US Department of Energy Programme for Climate Model Diagnosis and Intercomparison provided coordinating support for CMIP5 and led development of software infrastructure in partnership with the Global Organization for Earth System Science Portals. The PMIP3 data archives are supported by CEA and CNRS.

Author Contributions K.R. and T.L. designed the research; T.M. established the ice database and signal-to-noise ratio correction. S.L.H. established the marine database. K.R. and T.L. developed the methodology. K.R. performed the data analysis and wrote the first draft of the manuscript. K.R., T.M., S.L.H. and T.L. contributed to the interpretation and to the preparation of the final manuscript.

Author Information Reprints and permissions information is available at www.nature.com/reprints. The authors declare no competing financial interests. Readers are welcome to comment on the online version of the paper. Publisher's note: Springer Nature remains neutral with regard to jurisdictional claims in published maps and institutional affiliations. Correspondence and requests for materials should be addressed to K.R. (krehfeld@awi.de).

Reviewer Information *Nature* thanks P. Ditlevsen and the other anonymous reviewer(s) for their contribution to the peer review of this work.

METHODS

Proxy data for variability estimates. For the variability analyses we collected all available proxy records for temperature that fulfilled the following sampling criteria. To be included, a record had to (1) be associated with an established, published calibration to temperature and (2) cover at least 4 kyr in the interval of the Holocene (8–0 kyr ago) and/or the LGM (27–19 kyr ago) at (3) a mean sampling frequency of $1/225 \text{ yr}^{-1}$ or higher. Our definition for the LGM time slice, based on previously published starting³² and end¹⁰ times, covers the coldest part of the last glacial with the most stable boundary conditions while maintaining the same period duration as for the Holocene section. All proxy time series which fulfil the sampling criteria for both time intervals are included in our primary ‘joint’ dataset. All time series which fulfil the criteria for only one of the two intervals are included only for this period (‘separate’ dataset). This dataset consequently also includes all records from the joint dataset. All selected records are listed in Supplementary Information along with the time intervals for which they were included. Extended Data Table 2 summarizes the individual variance ratio estimates for the joint dataset.

Model-based estimates for the temperature gradient and variability change. Changes in temperature gradient between the LGM and the Holocene were estimated on the basis of an LGM-to-pre-industrial temperature anomaly⁹ based on proxy and model data from the Paleoclimate Model Intercomparison Project Phase 2 (PMIP2). The equator-to-pole temperature gradient change was calculated from the temperature anomaly differences between adjacent grid-boxes in the poleward direction (north relative to south), divided by the meridional gridbox extent (222 km) and normalized to 1,000 km. The model-based LGM-to-Holocene variability change estimate was derived from surface (2 m) air temperature output for the LGM and pre-industrial simulations available through PMIP Phase 3 (PMIP3-CMIP5) archives. Model simulations were included from the CCSM4, CNRM-CM5, FGOALS-g2, GISS-E2-R, IPSL-CM5A-LR, MIROC-ESM, MPI-ESM-P and MRI-CGCM3 models. For each model, the last 100 years of the archived simulations were used to estimate temperature variance fields. The fields of the ratio of variances were then re-gridded to a common T63 resolution to form the model-mean ratio of variances (Extended Data Fig. 3). We use the pre-industrial model results as a reasonable surrogate for the Holocene time slice because we are interested in the first-order patterns of the gradient and variability changes, which are governed by the deglaciation.

Temperature recalibration of proxy records. Marine and ice-core records were recalibrated using a single temperature relationship for each proxy type and region to minimize the calibration-dependent uncertainty for variability estimates based on the separate dataset. Terrestrial records based on lacustrine sediments, pollen and tree data were not recalibrated owing to the lack of a suitable global calibration for these proxy types.

Recalibration of ice-core records. For the calibration of ice-core stable isotope data to temperature (isotope-to-temperature slope in $^{\circ}\text{C}$ per ‰) two distinct methods exist: based on either the relationship of observed present-day spatial gradients in surface snow isotopic composition and temperature (spatial slope) or temporal gradients observed at a single site (temporal slope).

For Greenland, temporal slopes appear to lie consistently above the spatial slope, depending on the timescale, probably owing to changes in moisture origin and seasonality of precipitation¹⁸. For the Holocene temporal slope we used a borehole temperature calibration³³ of 2.1°C per ‰, with an estimated uncertainty of $\pm 0.4^{\circ}\text{C}$ per ‰ based on the slopes reported by other studies^{34–39}. The LGM temporal slope is a factor of 1–2 greater than the Holocene slope^{37,38,40–42}; as a best guess we used a factor of 1.5.

For Antarctica, direct estimations of temporal slopes are difficult. However, the difference between spatial and temporal slopes as well as the timescale dependence of the latter is expected to be small⁴³. Here, we adopted reported spatial slopes⁴⁴ of 1.25°C per ‰ for $\delta^{18}\text{O}$ and 0.16°C per ‰ for $\delta^2\text{H}$, with an uncertainty of 20% for recalibrating the Antarctic ice-core data.

For tropical ice cores, we adopted a constant calibration slope for $\delta^{18}\text{O}$ of 1.49°C per ‰⁴⁵.

Recalibration of marine records. Marine proxy records were recalibrated if the proxy type occurred more than once in our data collection and a suitable global calibration existed. Most of the Mg/Ca records in our compilation are based on planktic foraminifera *Globigerinoides ruber*, converted to temperatures using the calibration⁴⁶ $\text{Mg/Ca} = b \times \exp(a \times \text{SST})$, with $a = 0.09 \text{ mmol mol}^{-1} ^{\circ}\text{C}^{-1}$, $b = 0.38 \text{ mmol mol}^{-1}$, and standard errors $s_a = 0.003 \text{ mmol mol}^{-1} ^{\circ}\text{C}^{-1}$ and $s_b = 0.02 \text{ mmol mol}^{-1}$. For consistency, we recalibrated other *G. ruber* Mg/Ca records to the same calibration even though it is established using sediment trap samples and hence not a global calibration. For species other than *G. ruber*, that is, *Globigerina bulloides* (two records from different regions) and *Neoglobobulimina pachyderma* (left-coiling; one record), we kept the Mg/Ca records as published. Similarly, temperature records based on the transfer function of diatom,

radiolarian and foraminifera assemblages were kept as published. All $U^{K'}_{37}$ -based records were recalibrated using the calibration⁴⁷ $U^{K'}_{37} = a \times \text{SST} + b$, with $a = 0.033^{\circ}\text{C}^{-1}$, $b = 0.044$, $s_a = 0.001^{\circ}\text{C}^{-1}$ and $s_b = 0.016$. All TEX_{86} and TEX_{86}^H records were recalibrated to the subsurface TEX_{86}^H calibration⁴⁸ $T = a \times \text{TEX}_{86}^H + b$ with $a = 40.8^{\circ}\text{C}$, $b = 22.3^{\circ}\text{C}$, $s_a = 4.37^{\circ}\text{C}$ and $s_b = 2.19^{\circ}\text{C}$, because marine surface and subsurface temperature variability are on average similar⁴⁸.

Timescale-dependent variance and variance ratio estimation. The records were interpolated onto a regular time axis given by their individual mean sampling frequency in the LGM or the Holocene, following a previously reported procedure¹⁷. To minimize aliasing, data were first linearly interpolated to ten times the target resolution, low-pass filtered using a finite response filter with a cut-off frequency of 1.2 divided by the target time step, and then resampled at the target resolution. Linear interpolation of a process that has been unevenly sampled reduces the variance near the Nyquist frequency, but the sampling rate of our records relative to the timescale of the variance estimates is high enough to minimize this effect (Extended Data Fig. 4). Timescale-dependent variance estimates were obtained by integrating the raw periodogram⁴⁹ in the frequency band (f_1, f_2) using $f_1 = 1/500 \text{ yr}^{-1}$ and $f_2 = 1/1,750 \text{ yr}^{-1}$ to capture multicentennial- to millennial-scale temperature variability. All spectra are shown in Extended Data Fig. 4. Tests with surrogate records on the original time axes demonstrate that our estimates are largely unbiased (Extended Data Fig. 5). Furthermore, our results are robust to changes in the sampling criteria (Extended Data Fig. 1).

Confidence intervals for the variance estimates were derived from the χ^2 distribution with d degrees of freedom, in which d is given by twice the number of spectral power estimates in the frequency band (f_1, f_2). Confidence intervals for variance ratios were derived accordingly from the F distribution with the degrees of freedom of the variance estimates.

For the joint dataset, zonally averaged variance ratios were derived from the bias-corrected individual ratio estimates as

$$\bar{R} = \frac{1}{N} \sum_{i=1}^N \frac{d_{\text{hol},i} - 2}{d_{\text{hol},i}} R_i$$

in which $R_i = V_{\text{lgm},i}/V_{\text{hol},i}$ is the noise-corrected variance ratio of the i th record. For the separate dataset, zonally averaged variance ratios were derived from the ratio of the zonal-mean variances with subsequent noise correction.

For both datasets, global-mean variance ratios were derived from the area-weighted zonal means. To obtain the ratio distributions (Fig. 2a), we sample 50,000 times with replacement from the proxy estimates (joint, ratios; separate, variances). For each realization, we form the zonal-mean estimates of the variance change (for the joint dataset), or of the mean Holocene and LGM variance and then take the ratio (for the separate dataset). We then form the area-weighted global mean for the variance change. Confidence intervals for the global-mean estimate are derived as quantiles from the realizations. The ratio distribution for Greenland is estimated using the same method but considering only the three Greenlandic ice cores. Kernel density estimates are shown (Fig. 2a) using a Gaussian smoothing kernel with a bandwidth of $1/10$ of the mean ratio, so 0.4 for the global mean and 7 for Greenland.

Noise correction. We determine the effect of noise on the estimated variance ratio R' between two climate periods,

$$R' = \frac{\text{var}(X_1)}{\text{var}(X_0)} \quad (1)$$

Here, X_1 and X_0 are the proxy time series of the investigated (LGM) and reference (Holocene) climate periods, respectively. Each proxy time series contains noise. Assuming additive noise, and that the climate signal and noise are uncorrelated on each timescale covered, we can split the variances in equation (1) into contributions from the signal S and the noise ε :

$$R' = \frac{\text{var}(S_1) + \text{var}(\varepsilon_1)}{\text{var}(S_0) + \text{var}(\varepsilon_0)} = \frac{\text{var}(S_1)}{\text{var}(S_0)[1 + \text{SNR}^{-1}]} + \frac{\text{var}(\varepsilon_1)}{\text{var}(S_0)[1 + \text{SNR}^{-1}]}$$

in which we have introduced the reference-period signal-to-noise variance ratio, $\text{SNR} = \text{var}(S_0)/\text{var}(\varepsilon_0)$. Identifying the true climate variance ratio, $R = \text{var}(S_1)/\text{var}(S_0)$, and denoting the noise variance ratio by $F_\varepsilon = \text{var}(\varepsilon_1)/\text{var}(\varepsilon_0)$, we obtain

$$R' = \frac{\text{SNR}}{1 + \text{SNR}} R + \frac{F_\varepsilon}{1 + \text{SNR}}$$

Solving for R yields

$$R = R' \frac{1 + \text{SNR}}{\text{SNR}} - \frac{F_\varepsilon}{\text{SNR}} \quad (2)$$

Because R cannot be negative, the parameters must always satisfy the condition $F_e/(1 + \text{SNR}) \leq R'$. For any $R' \geq F_e$, the effect of noise dampens the true ratio ($R \geq R'$; Extended Data Fig. 6a).

To correct for the effect of noise on the LGM-to-Holocene variance ratio, we apply equation (2) both to every individual variance ratio estimated for the joint dataset and to the zonal-mean variance ratios derived from the separate dataset. A reasonable assumption is that the noise level is independent of the climate period ($F_e = 1$), which we adopt for all analyses. For the joint dataset, we assume a signal-to-noise ratio of 1.5 for the Greenland records and of 1 for all other records. To correct the zonal-mean variance ratios derived from the separate dataset, we adopt a signal-to-noise ratio of 1.

Testing the effect of the noise correction on the variability change difference. The signal-to-noise ratio is a considerable source of uncertainty for the noise correction. Signal-to-noise ratios can be estimated, among other approaches, by direct forward modelling of the proxy¹⁷ or by correlation of nearby records^{17,50–52}. An overview of signal-to-noise ratios for the regions and proxies of interest is given in Extended Data Fig. 6c. We tested the effect of the noise correction on the difference between the Greenland ice-core-based variance ratio estimates and those from the proxy records outside Greenland. To bring the variance ratios into agreement, the signal-to-noise ratio of proxies outside Greenland would have to be less than 0.05 (Extended Data Fig. 6b), which is one order of magnitude below published estimates for marine proxy¹⁷ and Antarctic isotope records⁵². It is therefore unlikely that the observed variability difference can be attributed to Greenland ice cores being better recorders (that is, having a higher signal-to-noise ratio) than marine sediment or Antarctic ice-core records.

Potential effect of ecological adaption and bioturbational mixing on marine variance ratios. Variability derived from biological proxies, that is, recorded by marine organisms, are possibly muted relative to the actual environmental changes owing to the tendency of organisms to adapt and seek their ecological niche (for example, of a certain temperature or nutrient range)⁵³. Our results are based on the ratio of variability and not on absolute variability estimates. Therefore, for ecological adaptation to affect our results, LGM variability needs to be muted to a much larger extent than that for the Holocene. In the simple conceptual ecological model⁵³, given the same temperature preference, larger variability would result in a stronger damping. However, the largest part of the variability seen by marine organisms is the seasonal and vertical temperature range in the depth habitat. This spread is controlled by insolation and stratification and not primarily by the climate state. The interannual to millennial variability, which we find to be larger in the LGM, contributes only a small fraction to the total variability and so should not be a primary control of the damping strength affecting the proxy records. Our oceanic temperature variability estimates for the joint dataset (containing both Holocene and LGM) are based on alkenone-based $U^{K'}$ (nine sites) and the Mg/Ca of planktic foraminifera *G. ruber* (six sites), the latter from tropical sites. Unlike planktic foraminifera, which have a preferred temperature niche, the known major producers of alkenones such as the coccolithophore *Emiliana huxleyi* occur throughout the global ocean from the tropics to the polar waters. Their abundance is mostly controlled by nutrient and light availability, which do not always co-vary with temperature. Most of our *G. ruber* Mg/Ca records are from the tropics, with Holocene temperatures (such as 29°C at SO189-39KL; Fig. 1c) close to the warm end of their temperature niche (15–29°C; ref. 54), whereas LGM temperatures (such as 26°C at SO189-39KL; Fig. 1c) are closer to the mean of the range. Therefore, if there is ecological adaptation, it is more likely to occur near the extremes (that is, the Holocene) rather than in the middle of the range. This would result in an amplified variance ratio between the Holocene and the LGM.

Bioturbational mixing in marine sediments reduces the absolute variability preserved in marine sediments⁵⁵. However, here we focus our analysis on variability changes and thus largely circumvent this problem, because both the glacial and the Holocene part of the core are affected by bioturbation. Bioturbation can be approximated as a linear filter⁵⁵ and so the ratio of variances is not affected as long as the sedimentation rate and bioturbation strength that define the filter are similar in both time periods or do not change systematically between climate states. Our dataset shows no evidence of a systematic change in sedimentation rate with 7 of the 16 marine cores in our joint dataset showing higher and 9 lower sedimentation rates in the Holocene (with a statistically insignificant change in mean sedimentation rate of 20%). The changes also show no detectable latitudinal dependency. There is also no evidence of a systematic change in largely unconstrained bioturbation strength between the time periods in the manuscripts that describe the datasets.

Despite not being effects of climate, the ecological preference of the organisms that record the climate signal and bioturbational mixing of the sediment can affect variability estimates and may thus add to site-specific variability changes. But the aforementioned arguments demonstrate that their effect is expected to be very small compared to the orders of magnitude difference between tropics and mid-latitudes and between marine cores and ice cores.

Testing the effect of the proxy sampling locations on zonal-mean variance estimates. The proxy locations are not randomly distributed in space, which could lead to sampling biases. To test for a potential sampling bias we analyse the 2-metre temperature field of the past 7,000 years from the coupled atmosphere ocean TraCE-21K simulation⁵⁶. The time period is chosen to focus on the continuum of climate variability and to minimize the effect of the deglaciation. The temperature variance field for centennial and longer timescales is derived by estimating the variance at every grid point after applying a low-pass finite response filter with a cut-off frequency of $1/100 \text{ yr}^{-1}$.

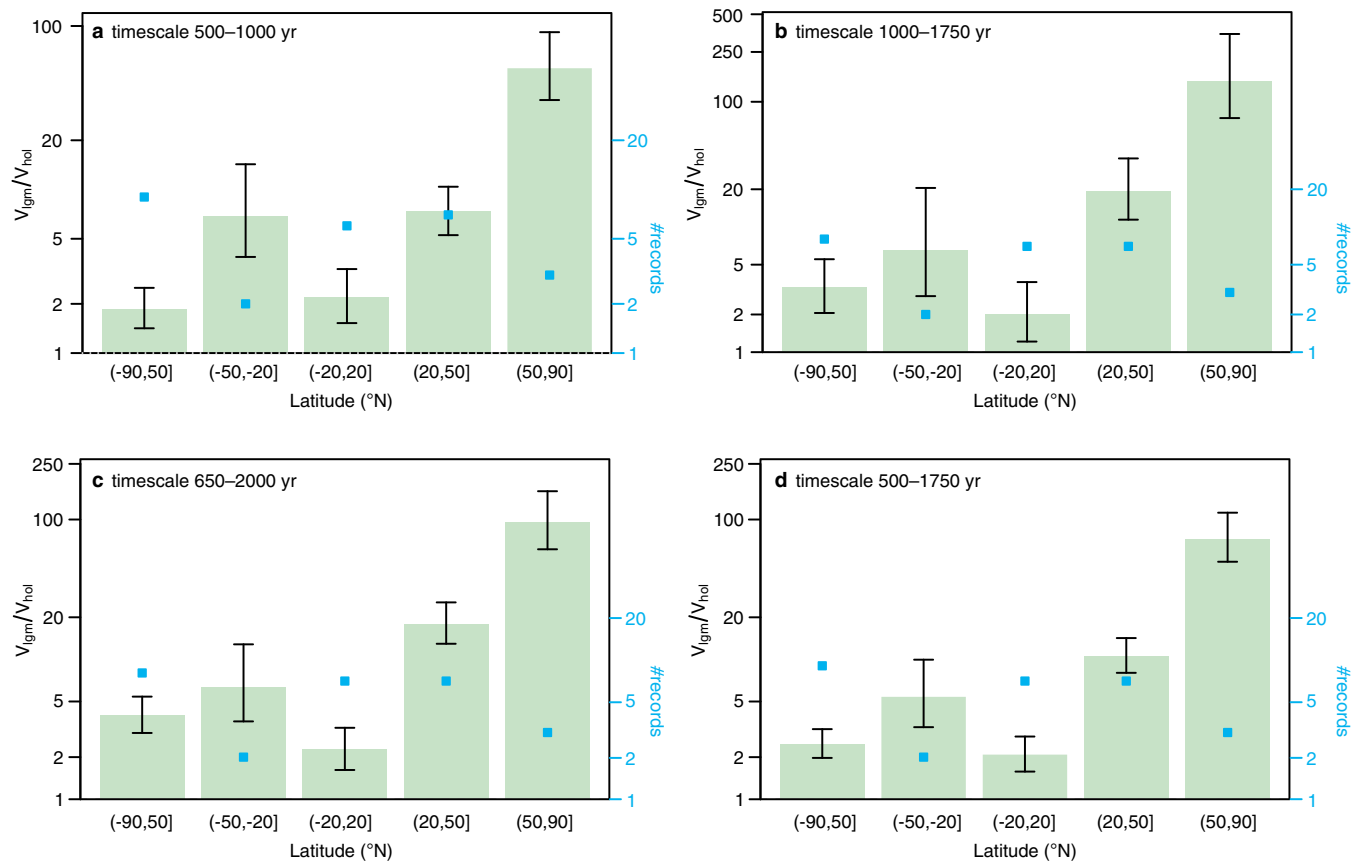
We sample the variance field at the actual proxy locations and average the results into the same latitude bands as for the proxy-based variance ratio estimates. To estimate the expected distribution of mean values from unbiased locations, we sample N random locations at each latitude band, where N corresponds to the number of actual records in each band. We form the mean of this random sample and repeat the procedure 10,000 times, from which we report the 90% quantiles. The results (Extended Data Fig. 7) show that the mean values from the actual proxy locations are always inside the expected distribution. This result holds when using the full dataset and when restricting the analysis to the records that cover both the LGM and the Holocene.

Code availability. Code is available on request from the authors.

Data availability. All data that support the findings of this study are available within the paper, given references or Supplementary Information. Source Data for Figs 2 and 3 are provided with the paper.

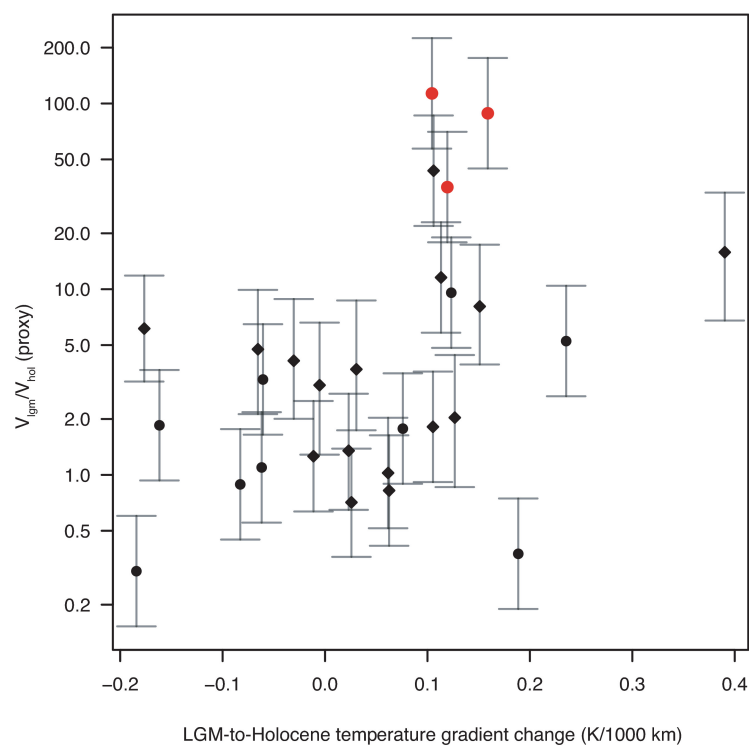
32. Rasmussen, S. O. *et al.* Synchronization of the NGRIP, GRIP, and GISP2 ice cores across MIS 2 and palaeoclimatic implications. *Quat. Sci. Rev.* **27**, 18–28 (2008).
33. Vinther, B. M. *et al.* Holocene thinning of the Greenland ice sheet. *Nature* **461**, 385–388 (2009).
34. Shuman, C. A. *et al.* Temperature and accumulation at the Greenland Summit: comparison of high-resolution isotope profiles and satellite passive microwave brightness temperature trends. *J. Geophys. Res.* **100**, 9165–9177 (1995).
35. Beltrami, H. & Taylor, A. E. Records of climatic change in the Canadian Arctic: towards calibrating oxygen isotope data with geothermal data. *Global Planet. Change* **11**, 127–138 (1995).
36. Cuffey, K. M., Alley, R. B., Grootes, P. M., Bolzan, J. M. & Anandakrishnan, S. Calibration of the $\delta^{18}\text{O}$ isotopic paleothermometer for central Greenland, using borehole temperatures. *J. Glaciol.* **40**, 341–349 (1994).
37. Cuffey, K. M. & Clow, G. D. Temperature, accumulation, and ice sheet elevation in central Greenland through the last deglacial transition. *J. Geophys. Res.* **102**, 26383–26396 (1997).
38. Johnsen, S. J. *et al.* The $\delta^{18}\text{O}$ record along the Greenland Ice Core Project deep ice core and the problem of possible Eemian climatic instability. *J. Geophys. Res.* **102**, 26397–26410 (1997).
39. Sjolte, J. *et al.* Modeling the water isotopes in Greenland precipitation 1959–2001 with the meso-scale model REMO-iso. *J. Geophys. Res.* **116**, D18105 (2011).
40. Johnsen, S. J., Dahl-Jensen, D., Dansgaard, W. & Gundestrup, N. Greenland palaeotemperatures derived from GRIP bore hole temperature and ice core isotope profiles. *Tellus B* **47**, 624–629 (1995).
41. Cuffey, K. M. *et al.* Large arctic temperature change at the Wisconsin-Holocene glacial transition. *Science* **270**, 455–458 (1995).
42. Kindler, P. *et al.* Temperature reconstruction from 10 to 120 kyr b2k from the NGRIP ice core. *Clim. Past* **10**, 887–902 (2014).
43. Jouzel, J. Magnitude of isotope/temperature scaling for interpretation of central Antarctic ice cores. *J. Geophys. Res.* **108**, 4361 (2003).
44. Masson-Delmotte, V. *et al.* A review of Antarctic surface snow isotopic composition: observations, atmospheric circulation, and isotopic modeling. *J. Clim.* **21**, 3359–3387 (2008).
45. Thompson, L. G. *et al.* Late glacial stage and Holocene tropical ice core records from Huascarán, Peru. *Science* **269**, 46–50 (1995).
46. Anand, P., Elderfield, H. & Conte, M. H. Calibration of Mg/Ca thermometry in planktonic foraminifera from a sediment trap time series. *Paleoceanography* **18**, 1050 (2003).
47. Müller, P. J., Kirst, G., Ruhland, G., von Storch, I. & Rosell-Melé, A. Calibration of the alkenone paleotemperature index $U^{K'}$ based on core-tops from the eastern South Atlantic and the global ocean (60° N–60° S). *Geochim. Cosmochim. Acta* **62**, 1757–1772 (1998).
48. Ho, S. L. & Laepple, T. Flat meridional temperature gradient in the early Eocene in the subsurface rather than surface ocean. *Nat. Geosci.* **9**, 606–610 (2016).
49. Chatfield, C. *The Analysis of Time Series: An Introduction* 6th edn (Chapman & Hall/CRC, 2004).
50. Fisher, D. A., Reeh, N. & Clausen, H. B. Stratigraphic noise in time series derived from ice cores. *Ann. Glaciol.* **7**, 76–83 (1985).
51. Steen-Larsen, H. C. *et al.* Understanding the climatic signal in the water stable isotope records from the NEEM shallow firn/ice cores in northwest Greenland. *J. Geophys. Res.* **116**, D06108 (2011).
52. Münch, T., Kipfstuhl, S., Freitag, J., Meyer, H. & Laepple, T. Constraints on post-depositional isotope modifications in East Antarctic firn from analysing temporal changes of isotope profiles. *Cryosphere* **11**, 2175–2188 (2017).

53. Mix, A. in *North America and Adjacent Oceans during the Last Deglaciation* (eds Ruddiman, W. F. & Wright, H. E.) 111–135 (Geological Society of America, 1987).
54. Hilbrecht, H. *Extant Planktic Foraminifera and the Physical Environment in the Atlantic and Indian Oceans: An atlas based on CLIMAP and Levitus (1982) data*. Technical Report (Eidgenössische Technische Hochschule und Universität Zürich, 1996).
55. Berger, W. H. & Heath, G. R. Vertical mixing in pelagic sediments. *J. Mar. Res.* **26**, 134–143 (1968).
56. Liu, Z. *et al.* Transient simulation of last deglaciation with a new mechanism for Bølling–Allerød warming. *Science* **325**, 310–314 (2009).
57. Müller, J. & Stein, R. High-resolution record of late glacial and deglacial sea ice changes in Fram Strait corroborates ice–ocean interactions during abrupt climate shifts. *Earth Planet. Sci. Lett.* **403**, 446–455 (2014).
58. Hoff, U., Rasmussen, T. L., Stein, R., Ezat, M. M. & Fahl, K. Sea ice and millennial-scale climate variability in the Nordic seas 90 kyr ago to present. *Nat. Commun.* **7**, 12247 (2016).



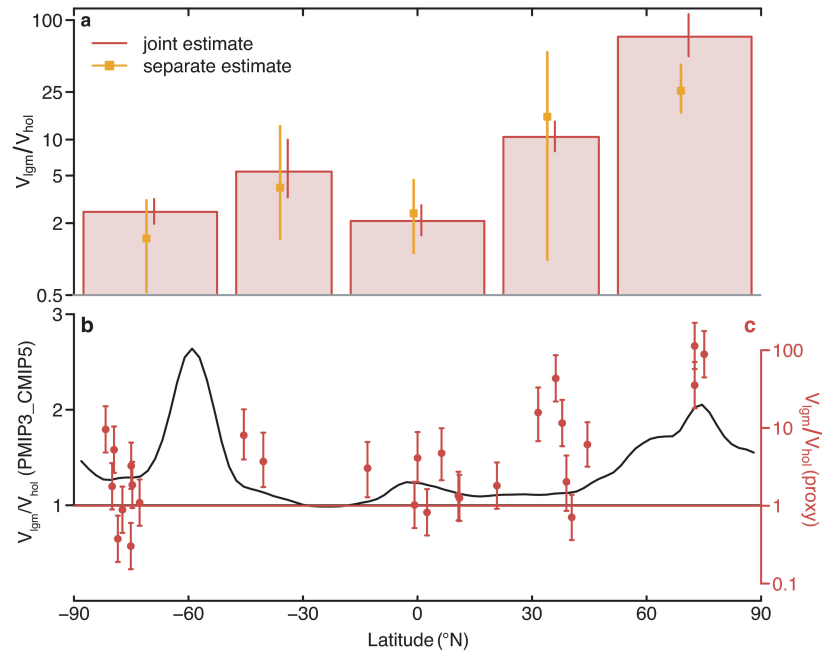
Extended Data Figure 1 | Zonal variability change pattern for different timescales and length requirements. a–d, Results for the estimated zonal-mean variance ratios based on the joint dataset are shown as a function of the timescale considered and the minimum number of data points in the time period: 500–1,000-year timescale with a minimum of 25 data points (a); 1,000–1,750-year timescale with a minimum of 25 data points (b);

650–2,000-year timescale with a minimum of 20 data points (c); and 500–1,750-year timescale with a minimum of 25 data points (d), which corresponds to the results shown in the main text. The number of records for each zonal-mean ratio is indicated by blue points. The total number of records varies depending on the timescale constraints. Error bars denote the 90% confidence intervals of the zonal mean.



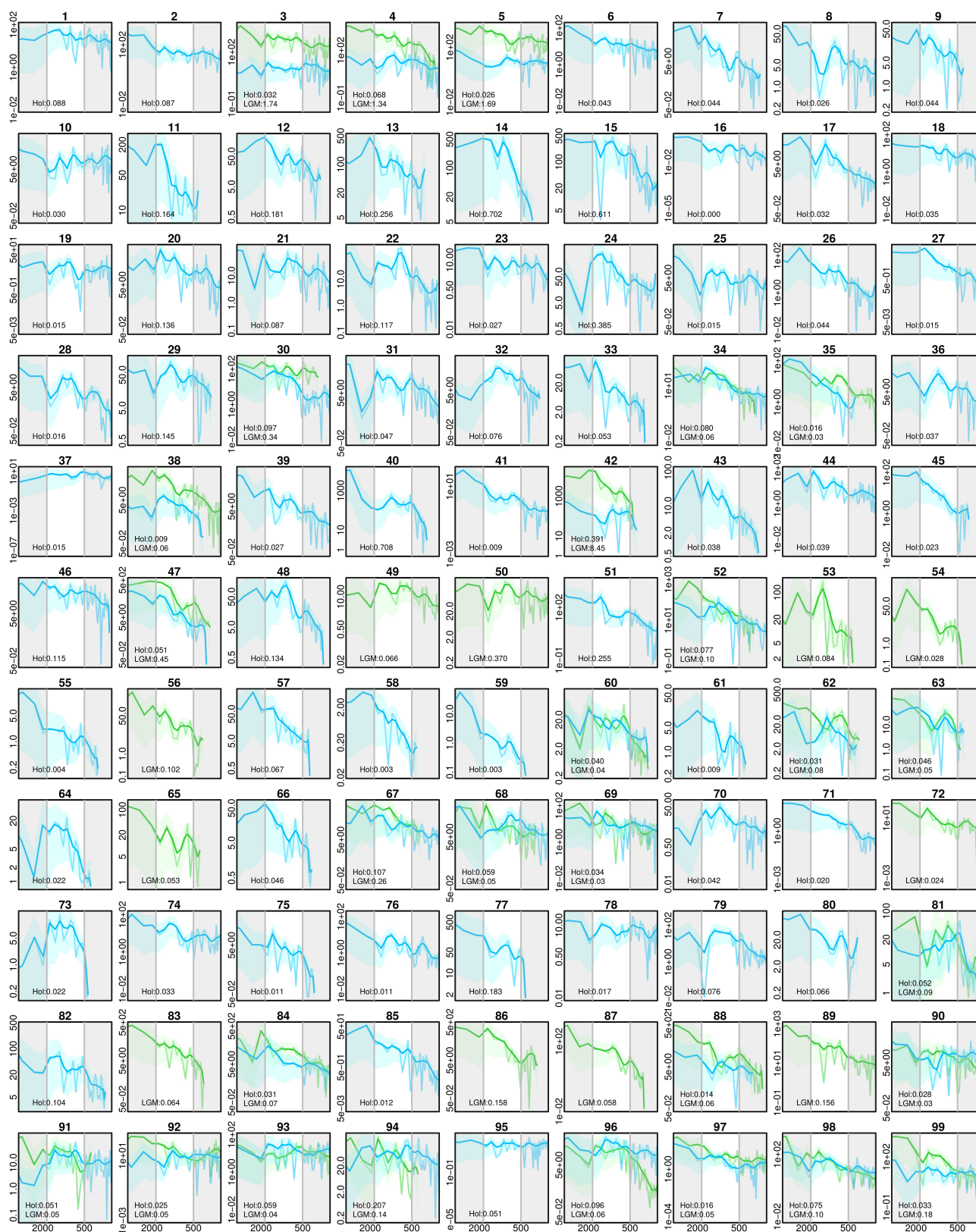
Extended Data Figure 2 | Temperature gradient versus variability change. Scatter plot of the model-based equator-to-pole temperature gradient change at the proxy locations versus the variability change estimated from the proxy records. Filled circles correspond to ice-core records (red, Greenland; black, other) and filled diamonds to marine

records. Error bars denote the 90% confidence interval of the estimated variance ratios. The data have a Spearman's rank correlation coefficient of 0.43 ($P \leq 0.03$, $n = 28$) when including the Greenland ice cores and of 0.35 ($P \leq 0.09$, $n = 25$) when excluding them.



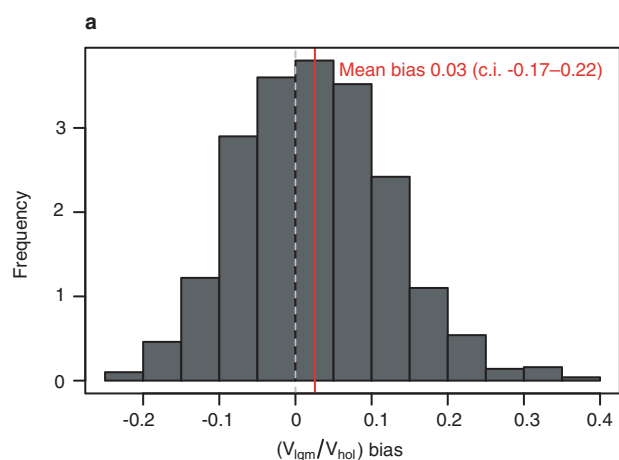
Extended Data Figure 3 | Proxy- versus model-based variability change. **a**, Zonal-mean LGM-to-Holocene variability change from the proxy compilations (red bars denote the joint estimate, orange points the separate estimate). **b**, Interannual to multidecadal zonal-mean variability change based on the PMIP3-CMIP5 simulations for the LGM and the

pre-industrial period. **c**, Individual variability change at the proxy locations from the joint dataset. Error bars in **a** show the 90% confidence interval of the mean; error bars in **c** show the 90% confidence interval of the individual variance ratios.

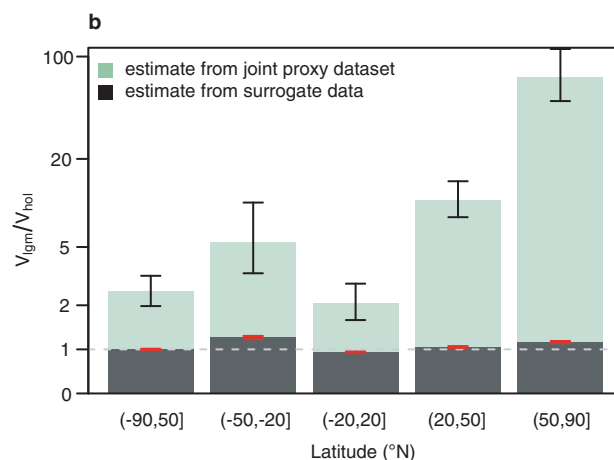


Extended Data Figure 4 | Raw periodograms of all records. Thin blue lines show the spectra of the Holocene time slice; thin green lines show the spectra of the LGM time slice. Logarithmically smoothed spectra are given as thick lines with 90% confidence intervals as shading. Grey areas indicate the frequency response outside the bandwidth used for the timescale-

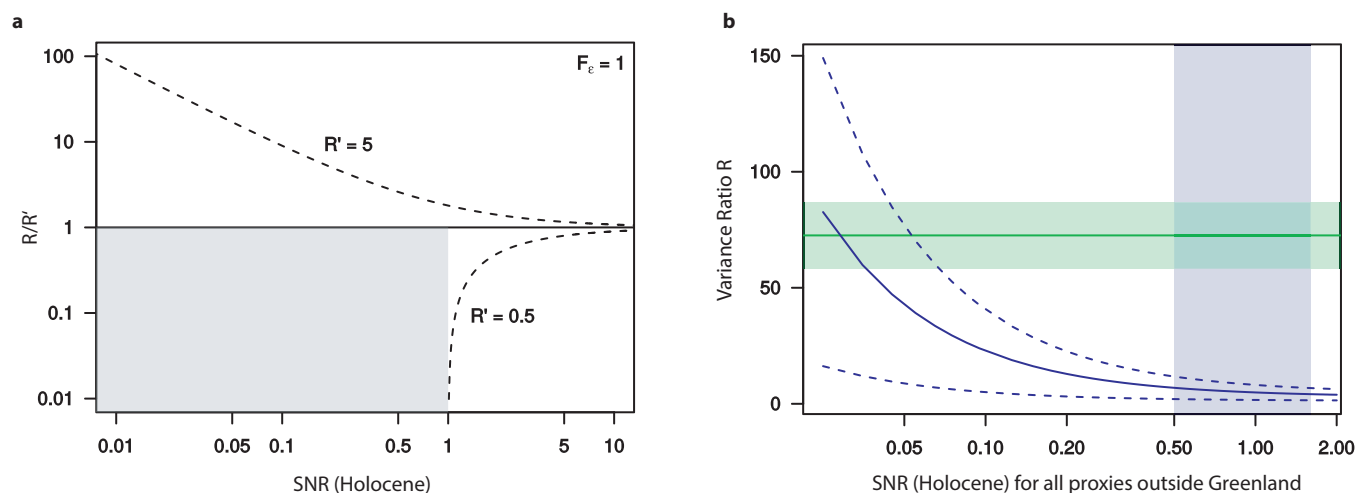
dependent variance ratio estimate. x -axis scaling is in periods in years; y -axis scaling denotes power spectral density. Text insets give the time-slice variances for the LGM and the Holocene ('Hol') in K^2 ; variance ratios for the records from the joint dataset are listed in Extended Data Table 2.



Extended Data Figure 5 | Surrogate tests for the magnitude of variance change. The magnitude of potential biases in the variance ratio estimates were derived using 1,000 realizations of power-law noise (slope $\beta = 1$) of constant variance on the original time axes of the records. Analyses for variability quantification were performed as for the primary analyses and described in Methods. **a**, Histogram of the bias of the variance ratio estimated from the surrogate data. The mean of the distribution (red line)



is not significantly different from zero (c.i., confidence interval). **b**, Estimated zonal-mean ratios from the surrogate data. The individual surrogate zonal-mean ratios (black bars) are all close to 1 and show no latitudinal pattern, in contrast to the zonal-mean ratios from the proxy data (joint dataset, green bars). Error bars show the 90% confidence interval for the proxy data and ± 2 times the standard error of the zonal mean for the surrogate data ($n = 1,000$).



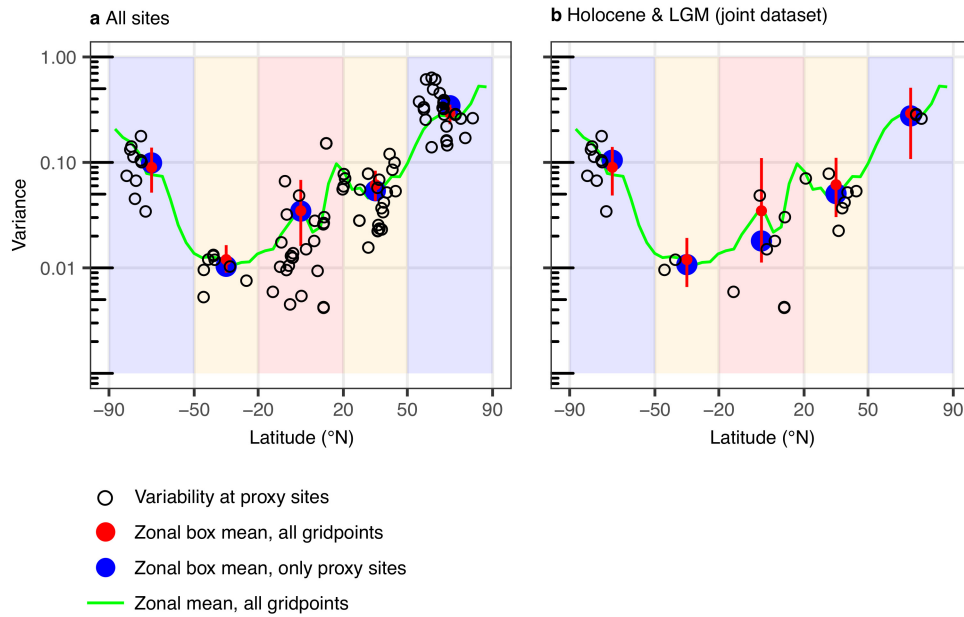
c

Domain	Estimate (CI)	Method	Timescale	Ref.
Central Greenland (Milcent & Crete)	1.25 (0.6)	correlation	interannual	[50]
Central Greenland (NEEM)	2.7	correlation	interannual	[51]
Marine Mg/Ca (global)	0.5	forward model	centennial	[17]
Marine UK'37 (global)	1.6	forward model	centennial	[17]
East Antarctica (EDML)	1.0 (0.5)	correlation	seasonal	[52]

Extended Data Figure 6 | Effect of the Holocene signal-to-noise ratio of proxy records on the noise correction of the variance ratios estimated.

a, Noise correction as a function of the Holocene signal-to-noise ratio (SNR). The ratio of the true variance ratio to the estimated one, R/R' , is displayed for $R' = 0.5$ and $R' = 5$ (dashed lines) for a noise variance ratio of $F_e = 1$. The shaded area denotes the region where for $R' = 0.5$, no $R/R' \geq 0$ exists. **b**, Test for the comparability of marine and Greenland ice-core variance ratios as a function of the signal-to-noise ratio. The expected value of R for the mean over all records of the joint dataset below 70° N is shown under the assumption of a wide range of signal-to-noise ratios

(solid blue line), with uncertainty (dashed lines) of ± 2 s.e.m. ($n = 25$). Within the realistic range of Holocene signal-to-noise ratios (shaded blue area, based on the published estimates listed in **c**), the noise-corrected global variance ratio (excluding Greenland) ranges from 1.7 to 11.4, which cannot be brought into agreement with the mean variance ratio of the Greenland ice cores (horizontal green line; shading denotes full uncertainty including the range of Greenland signal-to-noise ratios (**c**) used in the noise correction). **c**, Overview of published^{17,50–52} proxy signal-to-noise ratio estimates for the Holocene. Greenlandic and Antarctic estimates refer to $\delta^{18}\text{O}$. CI, confidence interval.



Extended Data Figure 7 | Representativeness of the proxy data locations. The centennial temperature variability in the TraCE-21K simulation, sampled at the proxy locations (black circles), the zonal-mean variability (green line) and the mean of the variability in the zonal box, either formed only from the variance at the proxy sites (blue) or formed using all grid points (red), are shown. The red vertical lines show the 90%

quantiles from the mean of N random samples of the variance field, where N is the number of proxy sites in the zonal box. **a**, Results when sampling from the proxy locations of the separate dataset. **b**, Results when sampling from the joint dataset. In all cases the mean of the proxy sites is inside the distribution of random samples, which demonstrates that under the assumption of this variance field the proxy estimates are unbiased.

Extended Data Table 1 | North Atlantic sea-ice variability ratios

Site	Lat. (°N)	Lon. (°E)	Proxy	R (90 % c.i.)	Ref.
MSM5-5-712-2	78.9	6.8	PBIP25	2.1 (1.1–4.1)	[57]
MSM5-5-712-2	78.9	6.8	IP25	11.2 (5.6–22.1)	[57]
JM11-FI-19PC	62.8	−3.9	PBIP25	14.1 (5.8–35.8)	[58]

The variance ratios *R* are listed, based on sea-ice reconstructions^{57,58} from three North Atlantic records (two sites, one based on two different sea ice proxies).

Extended Data Table 2 | Individual variability ratio estimates for all records from the joint dataset

No.	Record	R_{est}	R_{calib} (lower)	R_{calib} (upper)	R_{est} (5 % quantile)	R_{est} (95 % quantile)	R_{raw}
3	NGRIP	88.6	28.8	103.8	44.7	175.8	53.6
4	GISP2	35.5	11.7	42	17.9	70.4	21.7
5	GRIP	113.4	36.8	132.6	57.1	224.9	68.4
30	MD01-2412	6.1	3.2	4	3.2	11.8	3.6
34	PC-6	0.7	0.8	1	0.4	1.4	0.9
35	MD03-2699	2	1.3	1.7	0.9	4.4	1.5
38	MD01-2444	11.6	5.6	7.1	5.8	22.9	6.3
42	ODP976-4	43.5			21.9	86.2	22.2
47	MD98-2195	15.8	7.4	9.5	6.8	33.1	8.4
52	ODP658C-Zhao	1.8	1.2	1.6	0.9	3.6	1.4
60	SK237-GC04	1.3	1	1.3	0.6	2.5	1.1
62	ODP1240	4.1			2	8.8	2.6
63	PL07-39PC	1.3	1	1.3	0.6	2.7	1.2
67	MD98-2181	4.7	2.5	3.3	2.1	9.9	2.9
68	MD03-2707	0.8	0.8	1	0.4	1.6	0.9
69	SO189-39KL	1	0.9	1.2	0.5	2	1
81	MD01-2378	3	1.8	2.3	1.3	6.6	2
84	MD97-2121	3.7	2.1	2.7	1.7	8.7	2.4
88	MD97-2120	8.1	4	5.1	3.9	17.4	4.5
90	Talos Dome	1.1	0.5	2.4	0.6	2.2	1
91	Dome C	1.9	0.6	3.2	0.9	3.7	1.4
92	EPICA DML	3.3	0.9	4.8	1.6	6.5	2.1
93	EPICA Dome C	0.3	0.3	1.5	0.2	0.6	0.7
94	Dome F	0.9	0.4	2.1	0.4	1.8	0.9
96	Vostok	0.4	0.3	1.5	0.2	0.7	0.7
97	WAIS Divide	5.3	1.4	7	2.7	10.4	3.1
98	Byrd	1.8	0.6	3.1	0.9	3.5	1.4
99	Siple Dome	9.6	2.4	11.9	4.8	19	5.3

The estimate used throughout this paper is the noise-corrected variance ratio R_{est} (first data column). R_{calib} (lower/upper) denotes the results for the variance ratios when using the calibration parameters with the lower/upper limits of the calibration uncertainty for the LGM and the upper/lower calibration uncertainty limits for the Holocene. Data columns four and five give the 5% and 95% quantiles of the estimate used (R_{est}). Data column six gives the raw, uncorrected ratio (R_{raw}). Numbers (first column) refer to the list of records given in Supplementary Information. For ODP976-4 and ODP1240, no calibration uncertainty estimate is available.

Fluctuating interaction network and time-varying stability of a natural fish community

Masayuki Ushio^{1,2,3,4}, Chih-hao Hsieh^{5,6,7}, Reiji Masuda⁸, Ethan R Deyle⁹, Hao Ye^{9,10}, Chun-Wei Chang⁶, George Sugihara⁹ & Michio Kondoh¹

Ecological theory suggests that large-scale patterns such as community stability can be influenced by changes in interspecific interactions that arise from the behavioural and/or physiological responses of individual species varying over time^{1–3}. Although this theory has experimental support^{2,4,5}, evidence from natural ecosystems is lacking owing to the challenges of tracking rapid changes in interspecific interactions (known to occur on timescales much shorter than a generation time)⁶ and then identifying the effect of such changes on large-scale community dynamics. Here, using tools for analysing nonlinear time series^{6–9} and a 12-year-long dataset of fortnightly collected observations on a natural marine fish community in Maizuru Bay, Japan, we show that short-term changes in interaction networks influence overall community dynamics. Among the 15 dominant species, we identify 14 interspecific interactions to construct a dynamic interaction network. We show that the strengths, and even types, of interactions change with time; we also develop a time-varying stability measure based on local Lyapunov stability for attractor dynamics in non-equilibrium nonlinear systems. We use this dynamic stability measure to examine the link between the time-varying interaction network and community stability. We find seasonal patterns in dynamic stability for this fish community that broadly support expectations of current ecological theory. Specifically, the dominance of weak interactions and higher species diversity during summer months are associated with higher dynamic stability and smaller population fluctuations. We suggest that interspecific interactions, community network structure and community stability are dynamic properties, and that linking fluctuating interaction networks to community-level dynamic properties is key to understanding the maintenance of ecological communities in nature.

The dynamics of ecological communities are influenced by interspecific interactions occurring at multiple temporal and spatial scales. Earlier studies have focused mainly on long-term effects; specifically those that focus on the timescale of the birth–death process (for example, predator–prey interactions)^{10–13} or those that relate community stability to gross properties of the interaction network such as mean interaction strength, preponderance of weak interactions and species diversity^{10,14,15}. However, more recent theoretical and experimental studies have revealed that temporally variable ecological and/or biological responses (including physiological and behavioural responses) can have considerable effects on community dynamics^{1,2,4}. In other words, short-term responses such as adaptive resource choice, inter-habitat movement or physiological metabolic responses can in principle generate rapid changes in interaction strength, influence population dynamics and even reverse the classic relationship between community complexity and stability¹.

Although the arguments are compelling, evidence is lacking for whether and how short-term fluctuations in interspecific interactions influence the overall stability of ecological communities in nature. There are two main challenges here: (1) quantifying fluctuating interspecific interactions and (2) evaluating fluctuating community stability. First, there is the practical challenge of measuring rapidly changing multiple interactions as they occur in nature. Traditional approaches such as direct observation and experimental manipulations (for example, species exclusions) have provided insights into species interactions and their consequences for community dynamics^{2,16,17}. For example, manipulative experiments have shown that the interactions of species are often variable and that this variability can strongly influence the dynamics of a local community^{5,17}. However, as has

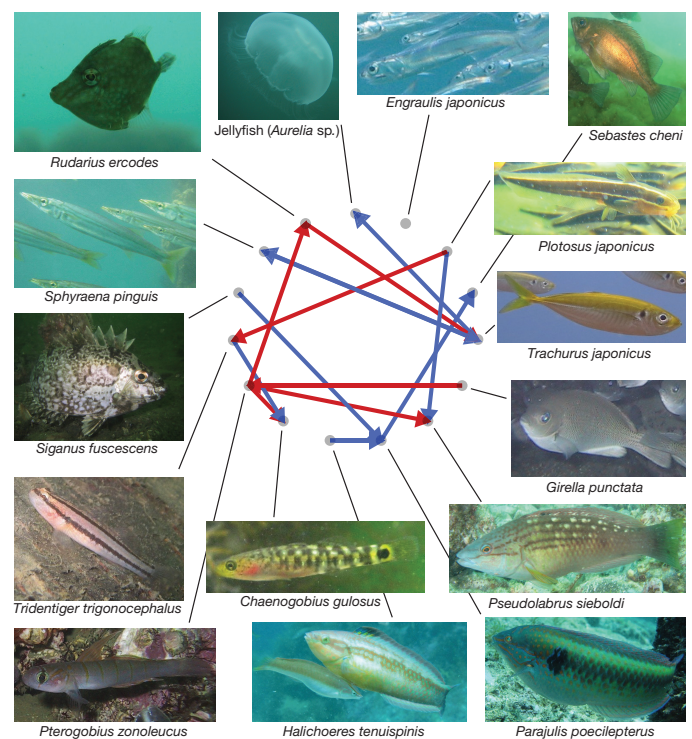


Figure 1 | Reconstructed interaction network of a subset of the Maizuru Bay fish community. Arrows indicating interspecific interactions are assigned on the basis of the results of convergent cross mapping (Extended Data Table 1). Blue and red colours indicate positive and negative interactions, respectively, calculated by the S-map method based on the 12-year average. All fish images by R.M.

¹Department of Environmental Solution Technology, Faculty of Science and Technology, Ryukoku University, Otsu 520-2194, Japan. ²Joint Research Center for Science and Technology, Ryukoku University, Otsu 520-2194, Japan. ³Center for Ecological Research, Kyoto University, Otsu 520-2113, Japan. ⁴PRESTO, Japan Science and Technology Agency, Kawaguchi 332-0012, Japan.

⁵Institute of Oceanography, Institute of Ecology and Evolutionary Biology, and Department of Life Science, National Taiwan University, Taipei 10617, Taiwan. ⁶Taiwan International Graduate Program (TIGP)–Earth System Science Program, Academia Sinica and National Central University, Taipei 11529, Taiwan. ⁷National Center for Theoretical Science, Taipei 10617, Taiwan.

⁸Maizuru Fisheries Research Station, Field Science Education and Research Center, Kyoto University, Maizuru, Kyoto 625-0086, Japan. ⁹Scripps Institution of Oceanography, University of California at San Diego, La Jolla, California 92093, USA. ¹⁰Department of Wildlife Ecology and Conservation, University of Florida, Gainesville, Florida 32611, USA.

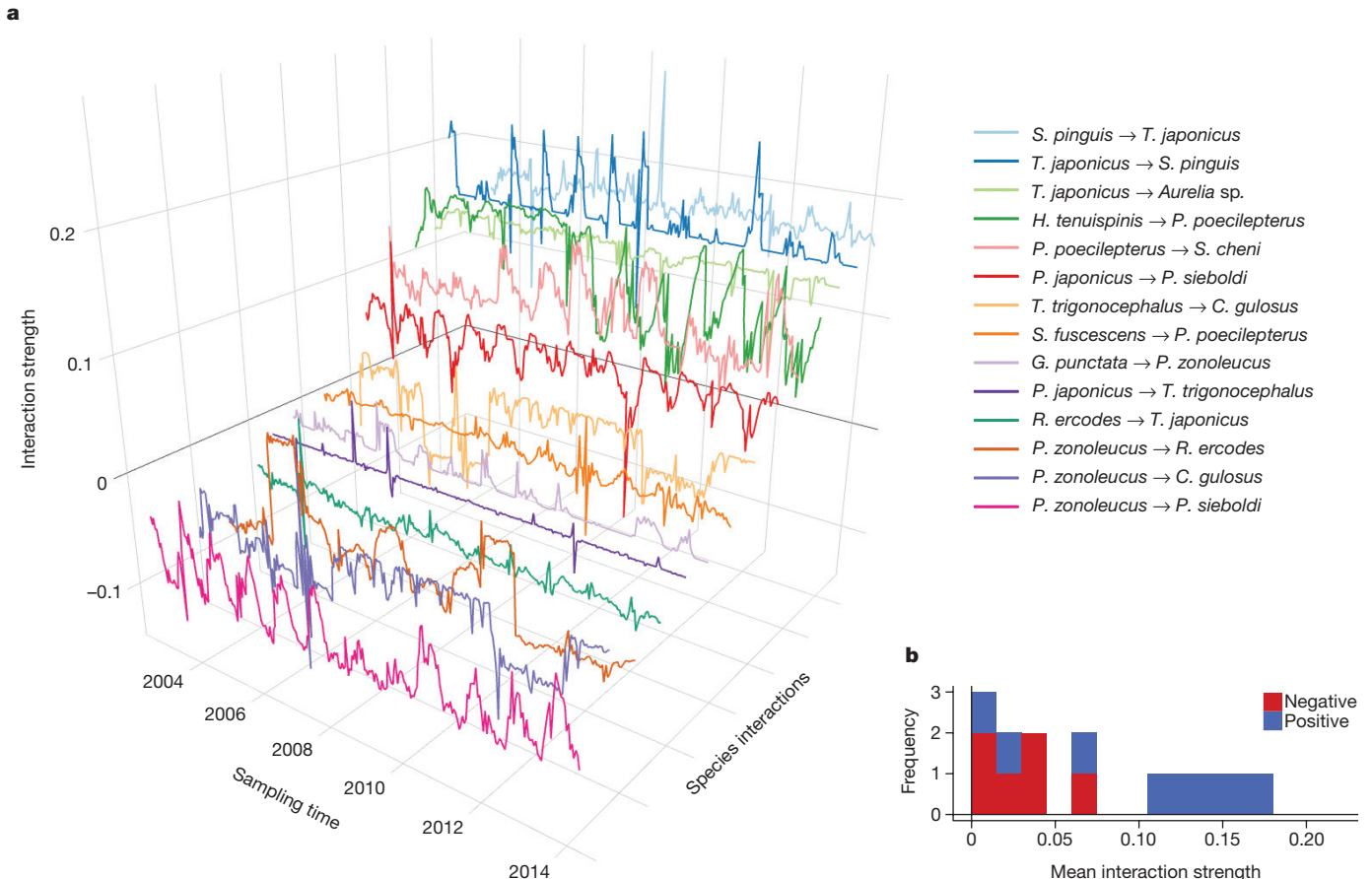


Figure 2 | Time-varying interspecific interactions in a subset of the Maizuru fish community. **a**, Fourteen interspecific interactions quantified by the S-map method. The x axis indicates the sampling time (2-week

intervals) from 2002 to 2014. **b**, The distribution of average interaction strengths over the 12-year sampling period.

previously been shown⁶, these approaches are labour-intensive and are not feasible for studying large ecological communities in nature. Second, because interspecific interactions vary over time, the resultant community stability also varies³; this means that evaluating community stability is not at all straightforward. Natural ecosystems do not typically exhibit equilibrium dynamics^{7–9,18} that would accommodate a standard calculation of stability. Thus, for non-equilibrium systems that possess intrinsic variability (that is, systems that exhibit nonlinear dynamics) the magnitude of population fluctuations (for example, coefficient of variation of abundance) may not be a good indicator of community stability or resilience, because there exists the potential for confounding effects. Here we look instead at a measure that accounts for nonlinear dynamics and that tracks community stability as it varies through time. Relating fluctuating interaction networks to community stability is crucial for understanding how natural ecological communities are maintained.

Fluctuating ecological interaction networks can be identified and measured with empirical dynamic modelling^{6–9,18,19}—tools based on attractor reconstruction that are specifically designed for analysing nonlinear dynamical systems from their time series^{6–9,18,19} (see Extended Data Fig. 1, Methods and Supplementary Information section 1).

We begin by applying convergent cross mapping⁷, an empirical dynamic modelling causality test, to identify the linkages defining the interaction network for the fish community in Maizuru Bay, a 12-year-long monitoring study that collected observations once every two weeks²⁰ (Extended Data Fig. 2). Overall, we identify 14 interspecific interactions among the 15 dominant fish species (Fig. 1, Extended Data Fig. 3 and Extended Data Table 1). Most of the detected interactions

are ecologically interpretable (Supplementary Information section 2), and all the species—except *Engraulis japonicus*—have at least one interaction, which indicates that interspecific interactions have a non-trivial role in the community dynamics.

The attractor for a set of causally related fish species is constructed by plotting their abundances as a point in a coordinate space in which the axes are the set of causally related species (see Methods), and tracing the position forward in time to delineate a trajectory⁷ (<https://youtu.be/fevurdpIRYg>). As the system travels along its attractor, S-maps (sequential locally weighted global linear maps) can be used to compute sequential Jacobian matrices⁹, the elements of which are partial derivatives that describe the changing interactions between species⁶; this is known as the multivariate S-map method^{6,9,18} (see Methods).

Figure 2a shows that interactions in the Maizuru Bay fish community are not static; this contradicts a common assumption of ecological research. Instead, they change over time, as expected for a system with nonlinear dynamics (Extended Data Table 2). Of the 14 interspecific interactions, on average 8 are negative and 6 are positive. The right-skewed distribution of mean interaction strengths in Fig. 2b shows that the interaction network is dominated by weak links; this domination is hypothesized to be a stabilizing property^{14,15}. There is also a clear seasonal pattern at the community level; weak interactions become more dominant during summer months than during winter months (Fig. 3), with a lower median:maximum interaction strength ratio (as this index decreases, weak interactions become more dominant). These fluctuations in interaction strengths could be driven by a number of mechanisms acting independently or together; these include time-varying behavioural and/or physiological responses^{1–3}, fluctuations in species diversity²¹, or a weakening of interactions among fish species due to

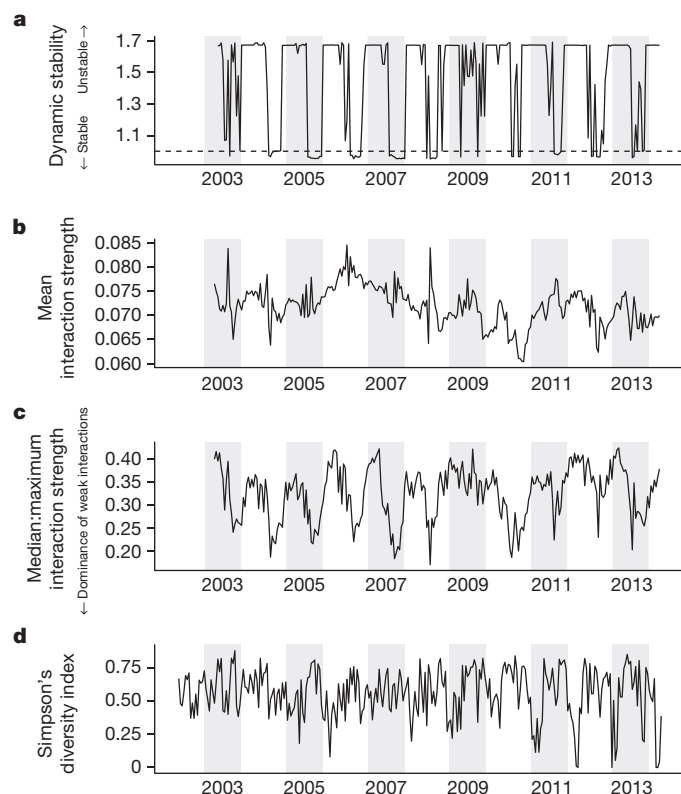


Figure 3 | Time-varying stability, interaction strength and Simpson's diversity index. **a**, The dynamic stability of the fish community. Dynamic stability is computed as the absolute value of the real part of the dominant eigenvalue of the interaction matrix at each time point. The fish community tends to recover from perturbations if the dynamic stability is lower than 1 (dashed line). **b–d**, Mean interaction strength (**b**), weak interaction index (median interaction strength:maximum interaction strength ratio; a lower ratio indicates increasing dominance of weak interactions) (**c**) and Simpson's diversity index (**d**) of the fish community. White or grey shading delineate each 1-year interval (from January to December).

higher primary productivity during the summer that results in higher fish abundance²⁰.

Community stability at each time point is evaluated by computing the dominant eigenvalue of the time-varying interaction matrix: this sequentially computed 'local Lyapunov stability' is hereafter referred to as 'dynamic stability' (see Methods). Our analysis reveals that dynamic stability varies in a non-random way (Extended Data Table 2); community dynamics are mainly stable in the summer (that is, the dynamic stability is less than 1.0; Fig. 3a), and unstable in the winter (that is, the dynamic stability is more than 1.0; Fig. 3a). Sensitivity analyses show that dynamic stability is robust when including less abundant species in the analysis, as well as when incorporating observation errors in the census data (Extended Data Fig. 4 and Supplementary Information sections 3, 4). Finally, we find that the stable time period (dynamic stability < 1.0) contains smaller variations in population abundances than the unstable period (Extended Data Fig. 5 and Supplementary Information section 5), and this supports the proposition that population fluctuations reflect community stability in the Maizuru Bay fish community, given that the level of stochastic noise through time is relatively constant.

We identify two large-scale properties as being responsible for the fluctuation in dynamic stability (Fig. 4a–c; see also Extended Data Figs 6, 7): overall interspecific interaction strength and species diversity. Figure 4d shows that the dominance of weak interactions is the strongest driver of dynamic stability, with the largest absolute

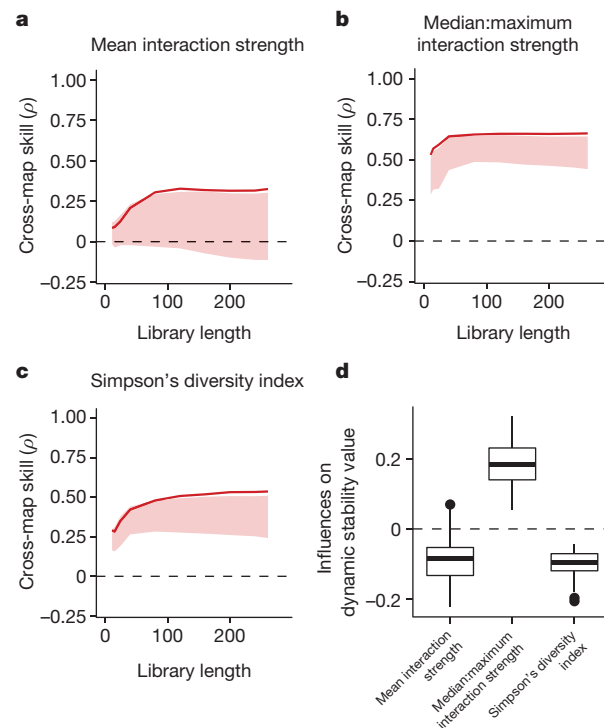


Figure 4 | Causal influences between dynamic stability, interaction strength and Simpson's diversity index. **a–c**, Convergent cross mapping between dynamic stability and properties of the interspecific interaction network (**a**, **b**), and Simpson's diversity index (**c**). Solid lines indicate cross-map skill (ρ) from dynamic stability to another variable, which represents the causal influence of that variable on dynamic stability. Shaded regions indicate 95% confidence intervals of 100 surrogate time series. Cross-map skills (ρ) reported in **a–c** were all significant. **d**, Influences of mean interaction strength, weak interaction index and diversity on dynamic stability ($n = 240$ calculated partial derivatives for each index). Midline, box limits, whiskers and points indicate median, upper and lower quartiles, $1.5 \times$ interquartile range and outliers, respectively. Note that smaller values of dynamic stability are indicative of stability (see Fig. 3 and Methods).

effect. Therefore, the co-occurrence of weaker interactions and stable conditions during summer (Fig. 3a, c) seems to reflect a true causal relationship. This provides empirical support for the theory that weak interactions are stabilizing^{14,22}. The analysis also identifies species diversity (Simpson's diversity index) as a stabilizing factor (Fig. 4c), supporting recent findings from manipulative experiments²³ and addressing the long-standing question of how species diversity influences community dynamics^{1,11,23,24}. Our results show that the Maizuru Bay fish community tends to recover faster from perturbations when species diversity is higher. In fact, higher species diversity seems to be a necessary condition for the dominance of weak interactions (Extended Data Fig. 8) and more stable communities (Fig. 4d). Because diversity seems to be a weaker driver of stability than interaction strength, it is likely that the latter is a more proximate driver of dynamic stability. Further investigations drawing on additional observational time series could reveal whether and how different interspecific interactions—for example, diet choice, anti-predator defence and inter-habitat movement—are involved in the maintenance of the Maizuru Bay fish community.

Here we present a framework based on attractor reconstruction from observational time series that quantifies the dynamic nature of the community interaction network and provides an estimate of dynamic stability. Although the exact individual-level behaviour that gives rise to the interspecific effect cannot be addressed by this analysis, the analysis does enable quantitative identification of the essential interactions that

influence community dynamics. Further applications of this framework to ecological time series in different geographical regions—for example, Arctic and tropical regions³—will enable tests of the generality of the present results, and aid in identifying other critical patterns in the dynamic stability of natural ecological communities. Such applications of empirical dynamic modelling could also clarify the relationships between interaction strengths, properties of the distribution (for example, the dominance of weak interactions, skewness and standard deviations), network structure (for example, arrangements and topologies) and community dynamics (such as the relationship between dynamic stability and population variation observed in this study), enabling a more in-depth investigation of the mechanisms by which dynamic interactions and species diversity govern the behaviour of a wide range of natural ecosystems.

Online Content Methods, along with any additional Extended Data display items and Source Data, are available in the online version of the paper; references unique to these sections appear only in the online paper.

Received 13 February 2017; accepted 9 January 2018.

Published online 7 February 2018.

- Kondoh, M. Foraging adaptation and the relationship between food-web complexity and stability. *Science* **299**, 1388–1391 (2003).
- Reynolds, P. L. & Bruno, J. F. Multiple predator species alter prey behavior, population growth, and a trophic cascade in a model estuarine food web. *Ecol. Monogr.* **83**, 119–132 (2013).
- McMeans, B. C., McCann, K. S., Humphries, M., Rooney, N. & Fisk, A. T. Food web structure in temporally-forced ecosystems. *Trends Ecol. Evol.* **30**, 662–672 (2015).
- Gratton, C. & Denno, R. F. Seasonal shift from bottom-up to top-down impact in phytophagous insect populations. *Oecologia* **134**, 487–495 (2003).
- Navarrete, S. A. & Berlow, E. L. Variable interaction strengths stabilize marine community pattern. *Ecol. Lett.* **9**, 526–536 (2006).
- Deyle, E. R., May, R. M., Munch, S. B. & Sugihara, G. Tracking and forecasting ecosystem interactions in real time. *Proc. R. Soc. Lond. B* **283**, 20152258 (2016).
- Sugihara, G. *et al.* Detecting causality in complex ecosystems. *Science* **338**, 496–500 (2012).
- Sugihara, G. & May, R. M. Nonlinear forecasting as a way of distinguishing chaos from measurement error in time series. *Nature* **344**, 734–741 (1990).
- Sugihara, G. Nonlinear forecasting for the classification of natural time series. *Philos. Trans. R. Soc. A* **348**, 477–495 (1994).
- Allesina, S. *et al.* Predicting the stability of large structured food webs. *Nat. Commun.* **6**, 7842 (2015).
- May, R. M. Will a large complex system be stable? *Nature* **238**, 413–414 (1972).
- Tang, S., Pawar, S. & Allesina, S. Correlation between interaction strengths drives stability in large ecological networks. *Ecol. Lett.* **17**, 1094–1100 (2014).
- Mougi, A. & Kondoh, M. Diversity of interaction types and ecological community stability. *Science* **337**, 349–351 (2012).
- McCann, K., Hastings, A. & Huxel, G. R. Weak trophic interactions and the balance of nature. *Nature* **395**, 794–798 (1998).

- Wootton, K. L. & Stouffer, D. B. Many weak interactions and few strong; food-web feasibility depends on the combination of the strength of species' interactions and their correct arrangement. *Theor. Ecol.* **9**, 185–195 (2016).
- Wootton, J. T. & Emmerson, M. Measurement of interaction strength in nature. *Annu. Rev. Ecol. Syst.* **36**, 419–444 (2005).
- Berlow, E. L. Strong effects of weak interactions in ecological communities. *Nature* **398**, 330–334 (1999).
- Dixon, P. A., Milicich, M. J. & Sugihara, G. Episodic fluctuations in larval supply. *Science* **283**, 1528–1530 (1999).
- Ye, H. *et al.* Equation-free mechanistic ecosystem forecasting using empirical dynamic modeling. *Proc. Natl Acad. Sci. USA* **112**, E1569–E1576 (2015).
- Masuda, R. *et al.* Fish assemblages associated with three types of artificial reefs: density of assemblages and possible impacts on adjacent fish abundance. *Fishery Bull.* **108**, 162–173 (2010).
- Allesina, S. & Tang, S. Stability criteria for complex ecosystems. *Nature* **483**, 205–208 (2012).
- Bascompte, J., Melián, C. J. & Sala, E. Interaction strength combinations and the overfishing of a marine food web. *Proc. Natl Acad. Sci. USA* **102**, 5443–5447 (2005).
- Downing, A. L., Brown, B. L. & Leibold, M. A. Multiple diversity–stability mechanisms enhance population and community stability in aquatic food webs. *Ecology* **95**, 173–184 (2014).
- Hector, A. *et al.* General stabilizing effects of plant diversity on grassland productivity through population asynchrony and overyielding. *Ecology* **91**, 2213–2220 (2010).

Supplementary Information is available in the online version of the paper.

Acknowledgements We thank members of the Kondoh laboratory in Ryukoku University; F. Grziwotz, A. Telschow and T. Miki for discussions; S.-I. Nakayama for advice on the twin surrogate method; and T. Yoshida and M. Kasada for providing time series of the algae–rotifer system. This research was supported by CREST, grant number JPMJCR13A2, Japan Science and Technology Agency; KAKENHI grant number 15K14610 and 16H04846, Japan Society for the Promotion of Science; Foundation for the Advancement of Outstanding Scholarship (Ministry of Science and Technology, Taiwan); DoD-Strategic Environmental Research and Development Program 15 RC-2509; Lenfest Ocean Program 00028335; NSF DBI-1667584; NSF DEB-1655203; the McQuown Fund and the McQuown Chair in Natural Sciences (University of California, San Diego).

Author Contributions M.U., C.H. and M.K. designed the research programme; R.M. collected fish monitoring data; M.U. and G.S. conceived the idea of computing local Lyapunov stability from S-maps; M.U. performed analysis with help from C.H., E.R.D., H.Y. and C.-W.C.; M.U., C.H. and M.K. wrote the first draft of the paper; and all authors were involved in interpreting the results, and contributed to the final draft of the paper.

Author Information Reprints and permissions information is available at www.nature.com/reprints. The authors declare no competing financial interests. Readers are welcome to comment on the online version of the paper. Publisher's note: Springer Nature remains neutral with regard to jurisdictional claims in published maps and institutional affiliations. Correspondence and requests for materials should be addressed to M.U. (ong8181@gmail.com) or M.K. (kondohmjp@icloud.com).

Reviewer Information *Nature* thanks J. Bascompte, U. Brose and K. McCann for their contribution to the peer review of this work.

METHODS

Fish community time-series data. Long-term time-series data of the fish community were obtained by underwater direct visual census conducted approximately once every two weeks along the coast of the Maizuru Fishery Research Station of Kyoto University (Nagahama, Maizuru: 35° 28' N, 135° 22' E) from 1 January 2002 to 2 April 2014 (285 time points during approximately 12 years)²⁰. This high-frequency census enables the detection of short-term interspecific interactions. The area was within 50 m of the shore and at a water depth of 1–10 m. A 600-m visual transect line, composed of three parts, was set: each transect line was 200 m long with a 2-m-width survey area. Each transect included a rocky reef, brown algae macrophyte and filamentous epiphyte vegetation, live oysters (*Crassostrea gigas*) and their shells, a sandy or muddy silt bottom and an artificial vertical structure that functioned as a fish reef. The vegetation in the area was dominated by *Sargassum tortile* and *Sargassum thunbergii* on the rocky substrate and patches of *Zostera marina* on the shallow (1–2 m) sandy bottom substrate.

Species and sizes of individual fish observed within 1 m of each census line (thus triplicated in the survey area) were recorded on waterproof paper. Each census was conducted on a sunny day and commenced around 12:00 with high tide of 2–3 h. The census was undertaken by diving using scuba equipment. Water temperature was measured near the surface and at the deepest point of the census line (10-m depth) during the diving. Visibility ranged from 1 to 15 m but was normally 3–5 m. Daily observations at 10:00 revealed that surface water temperature and salinity in the area ranged from 1.2 to 30.8 °C and from 4.14 to 34.09 parts per thousand, respectively. The mean \pm s.d. surface salinity was 30.0 ± 2.9 ($n = 1,753$) and did not show clear seasonality. Importantly, the same scientist conducted this field survey throughout the 12-year research term. Thus, inconsistency in fish identification and counting is diminished in the time series.

We selected dominant fish species (that is, with a total observation count that was larger than 1,000) for analyses, because rare species that were not observed during most of the census term (that is, with many zero values) were not suitable for the time-series analysis. We used time series of 14 fish species and 1 jellyfish species (Extended Data Fig. 2). Jellyfish data were included because jellyfish are abundant in this region, and are thought to have notable influences on the community dynamics of fishes²⁵. Including less abundant species in the analyses does not change the conclusion (see Extended Data Fig. 4). Before the analyses, the time series were normalized to unit mean and variance²⁶.

Convergent cross mapping. Convergent cross mapping (CCM) was performed to determine the causal relationships among the 15 dominant species in Maizuru Bay. CCM is based on Takens's theorem for nonlinear dynamical systems. For multi-variable dynamical systems in which only some of variables are observable, Takens's theorem²⁷—with several extensions (for example, ref. 28 and references therein)—proves that it is possible to represent the system dynamics in a state space by substituting time lags of the observable variables for the unknown variables. The information in the unobserved variables is encoded in the observed time series, and a single time series can therefore be used to reconstruct the original state space. This gives a time-delayed coordinate representation (or embedding) of the system trajectories, and this operation is sometimes referred to as state space reconstruction.

An important consequence of the state space reconstruction theorems²⁷ is that if two variables X and Y are part of the same dynamical system, then the reconstructed state spaces of X and Y will topologically represent the same attractor (with a one-to-one mapping between the reconstructed attractors of X and Y). Therefore, it is possible to predict the current state of variable X using time lags of variable Y . We can look for the signature of a cause variable (for example, X) in the time series of an effect variable (for example, Y) by testing whether there is a correspondence between their reconstructed state spaces (that is, cross mapping)⁷. In this study, cross mapping from one variable to another was performed using simplex projection⁸. In the simplex projection, a set of neighbouring points of $Y(t)$ that have similar historical processes to those of $Y(t)$ can find their time-corresponding points of X . If the time-corresponding set in X is also the neighbouring points of $X(t)$, then it is possible to estimate $X(t)$ accurately by cross-mapping. The cross-mapping skill (that is, predictability) can be evaluated using the correlation coefficient (ρ) between cross-map estimates and observations. Significant skill of the cross mapping is one necessary condition for the detection of causality (see the test for significance in 'Phase-lock twin surrogate method').

In addition, the cross-map skill will increase as the library length (that is, the number of points in the reconstructed state space of an effect variable) increases if two variables are causally coupled⁷ (that is, convergence). As the number of points in the state space increases (that is, the time series becomes longer), the trajectory defining the attractor fills in, which results in closer nearest neighbours and declining estimation error (a higher correlation coefficient). Therefore, convergence is another necessary condition for the detection of causality. Practical criteria for the causality are described later (see 'Phase-lock twin surrogate method').

CCM results are sensitive to the choice of embedding dimension (that is, how many time-lag coordinates are used for state space reconstruction). Therefore, the embedding dimension (E) should be carefully determined. In this study, E was determined by evaluating out-of-sample predictability through trials of different embedding dimension, using univariate simplex projection⁸ as previously described²⁹. In brief, the value for E that gives maximum predictability was chosen, which ensured that E was sufficiently large to capture the dynamics of the system without including extraneous dimensions. Predictability can be measured using mean absolute error, root mean squared error or correlation (ρ) between predictions and observations. To determine the best E value we used mean absolute error, as described previously²⁹. The best E value was examined from 1 to 24, as our dataset came from a census conducted once every two weeks (24 points per year), which allows for the influence of previous populations (up to one year prior). After the determination of the best E value, CCM was applied to the normalized abundance time-series data of the dominant fishes.

Phase-lock twin surrogate method. Most of our data show strong seasonality (Extended Data Figs 2, 6), and time-series data with strong seasonality often exhibit a high cross-map skill even when there is no causal relationship between variables (Extended Data Fig. 3). This means that synchronization driven by seasonality can lead to misidentification of causality (that is, false positives). To deal with this problem, we developed the phase-lock twin surrogate method, which takes seasonality into account. This new method is modified from the twin surrogate method³⁰, which generates time series that preserve the shape of an attractor but exhibit no causal relationship with a target time series.

The twin surrogate time series is generated by the following steps: (1) construction of a recurrence matrix, (2) identification of twin points on the recurrence matrix, (3) selection of the starting point of the surrogate, and (4) generation of the surrogate time series by switching trajectories at the twin points. In brief, the recurrence matrix is constructed using the following equation:

$$R_{i,j} = \Theta(\delta - \|\mathbf{x}(i) - \mathbf{x}(j)\|)$$

in which Θ denotes the Heaviside function ($\Theta(a)$ is 1 if a is positive and 0 otherwise), $\|\cdot\|$ indicates the maximum norm, δ is a predefined threshold and $\mathbf{x}(i)$ denotes the system state at time i . We initially set $\delta = 0.125$. Results do not change significantly for δ values between 0.05 and 0.20³⁰. By coding $R_{i,j} = 1$ in the matrix as black dots and $R_{i,j} = 0$ as white dots, we obtained recurrence plots. The recurrence plot contains all topological information about the attractor. In the recurrence plot there can be identical columns; that is, $R_{k,i} = R_{k,j} \forall k$, called twins. These two points are not only neighbours but also share the same neighbourhood. Twins are special points of the time series that are indistinguishable in the recurrence plot, but have different pasts and futures in time series. After identifying the twins in the recurrence plot, we randomly chose an entry (l) of the original time series ($\mathbf{x}(l)$), as the starting point of the surrogate time series, $\mathbf{x}^s(1)$. Then, we followed the trajectory in the state space— $\mathbf{x}^s(1) = \mathbf{x}(l)$, $\mathbf{x}^s(2) = \mathbf{x}(l+1)$, $\mathbf{x}^s(3) = \mathbf{x}(l+2)$ and so on—in order to generate the surrogate. If we suppose that entry m of the surrogate $\mathbf{x}^s(m)$ may be given by entry j of the original time series ($\mathbf{x}(j)$), if $\mathbf{x}(j)$ has no twins we set $\mathbf{x}^s(m+1) = \mathbf{x}(j+1)$. If $\mathbf{x}(k)$ is a twin of $\mathbf{x}(j)$, we set $\mathbf{x}^s(m+1) = \mathbf{x}(j+1)$ or $\mathbf{x}^s(m+1) = \mathbf{x}(k+1)$ with equal probability. This step is iterated until the surrogate time series reaches the same length as the original time series. By performing the above steps, the twin surrogate time series preserves only the nonlinearity (that is, the shape of the attractor), but not any of the remaining causal influences.

To take seasonality into account, we added another constraint to the twin surrogate method: twins in the recurrence plot must also be from the same season (that is, phase-locking). In our dataset, there are 24 points per year; therefore, if a reconstructed state represents an observation in early January, only observations in early January (from a different year) can be considered for switching of the trajectory. With this constraint, the surrogate time series preserves both the seasonality and the shape of the attractor (Extended Data Fig. 3b).

To evaluate the phase-lock twin surrogate method, we generated artificial time series with seasonality by using the following equations:

$$X_0(t+1) = X_0(t)\{4 - 3X_0(t) + \beta_{yx}Y_0(t)\}$$

$$Y_0(t+1) = Y_0(t)\{3.8 - 3.8Y_0(t) + \beta_{xy}X_0(t)\}$$

$$X(t+1) = X_0(t+1) + a_x \text{ seasonality}$$

$$Y(t+1) = Y_0(t+1) + a_y \text{ seasonality}$$

in which β_{xy} and β_{yx} indicate interspecific interactions, and α_x and α_y indicate the strength of the seasonality. 'Seasonality' is defined by a sine curve. In this analysis, the time-series length is 288 (that is, equivalent to a 12-year census with

24 observations per year). To examine the effects of seasonality on the cross-map skill (ρ) and convergence, we set $\beta_{xy} = \beta_{yx} = 0$ (no causality between $X(t)$ and $Y(t)$) and $a_x = a_y = 0.3$ (moderate seasonality). We found that even a moderate strength of seasonality resulted in a relatively high predictability and convergence of cross-map skill (a false positive) (Extended Data Fig. 3a).

The phase-lock twin surrogate method generates time series with the same non-linearity and seasonality (Extended Data Fig. 3b). Intuitively, $\alpha_x = \alpha_y = 1.0$ indicates strong seasonality in the time series (Extended Data Fig. 3b and Supplementary Information section 6). By changing α_x and α_y from 0 to 2.0, we examined the performance of the new surrogate method under various strengths of seasonality. We examined conditions of no interaction between X and Y ($\beta_{xy} = \beta_{yx} = 0$), unidirectional interaction from X to Y and bidirectional interactions between X and Y (Extended Data Fig. 3e–h).

Analyses of model simulations show that the phase-lock twin surrogate method gives a conservative criteria (that is, low possibility of false positives) for detecting causality among time series that exhibit seasonality (Extended Data Fig. 3). In this study, the CCM was regarded as significant if the following two criteria were satisfied: (1) cross-mapping for the real time series showed higher skill (ρ) than 95% confidence intervals of phase-lock twin surrogate data (that is, significant predictability), and (2) the difference between the cross-map skill at the smallest and largest library sizes ($\Delta\rho$) was larger than 0.1 (that is, convergence). Although $\Delta\rho > 0$ is a minimum and simpler criterion for convergence, observation error can cause fluctuations in ρ and $\Delta\rho$, and we therefore used a more conservative criterion instead.

The multivariate S-map method. The multivariate S-map method enables quantification of dynamic (that is, time-varying) interactions^{6,9}. If we consider a system that has E different interacting species, and the state space at time t is given by $\mathbf{x}(t) = \{x_1(t), x_2(t), \dots, x_E(t)\}$, for each target time point t^* , the S-map method produces a local linear model \mathbf{C} that predicts the future value $x_i(t^* + p)$ from the multivariate reconstructed state-space vector $\mathbf{x}(t^*)$. That is,

$$\hat{x}_i(t^* + p) = C_0 + \sum_{j=1}^E C_j x_j(t^*)$$

The linear model is fit to the other vectors in the state space. However, points that are close to the target point $\mathbf{x}(t^*)$ are given greater weighting. The model \mathbf{C} is the singular value decomposition solution to the equation $\mathbf{B} = \mathbf{A} \cdot \mathbf{C}$, in which \mathbf{B} is an n -dimensional vector (n is the number of observations) of the weighted future values of $x_i(t_i)$ for each historical point t_i , given by

$$B_i = w(|\mathbf{x}(t_i) - \mathbf{x}(t^*)|) x_i(t_i + p)$$

\mathbf{A} is then the $n \times E$ dimensional matrix given by

$$A_{ij} = w(|\mathbf{x}(t_i) - \mathbf{x}(t^*)|) x_j(t_i)$$

The weighting function w is defined by

$$w(d) = \exp\left(-\frac{\theta d}{\bar{d}}\right)$$

which is tuned by the nonlinear parameter $\theta \geq 0$ and normalized by the average distance between $\mathbf{x}(t^*)$ and the other historical points,

$$\bar{d} = \frac{1}{n} \sum_{j=1}^n |\mathbf{x}(t_j) - \mathbf{x}(t^*)|$$

The Euclidian distance between two vectors in the E -dimensional state space is given by $|\mathbf{x} - \mathbf{y}|$. Note that the model \mathbf{C} is separately calculated (and thus potentially unique) for each time point t . The coefficients of the local linear model (\mathbf{C}) are a proxy for the interaction strength between variables⁶; these interaction strengths, defined as partial derivatives in a multidimensional state space, quantify the population-level interaction between two species and do not assume any particular form of interaction, such as mutualism or competition. Instead, one might be able to infer the type of interactions after calculating the interaction strength.

Evaluations of the multivariate S-map method. Here we also show that the long-term averaged interaction strength estimated from the multivariate S-map method is equivalent to the interaction coefficient, β_{ij} in the following equations (Extended Data Fig. 1). These equations provide the explicit system of equations for the two-species model:

$$X(t+1) = X(t)\{r_x + s_x X(t) + \beta_{yx} Y(t)\}$$

$$Y(t+1) = Y(t)\{r_y + s_y Y(t) + \beta_{xy} X(t)\}$$

in which r_x and s_x (for species x) or r_y and s_y (for species y) represent an intrinsic growth rate and a self-regulation term, respectively. β_{yx} is an effect of Y on X and β_{xy} is an effect of X on Y .

In a unidirectional two-species model, β_{yx} was set to 0 and β_{xy} was set to -0.31 . Other parameters were set as follows: $r_x = 4$, $s_x = -3$, $r_y = 3.1$ and $s_y = -3.1$. The length of the time series was 1,000 and the initial abundances of X and Y were set at 0.5. Before the multivariate S-map analysis, the time series were normalized to unit mean and variance. We used a fully multivariate embedding, $\{X(t), Y(t)\}$, to reconstruct the attractor.

In a bidirectional two-species model, β_{yx} was changed from -0.5 to 0.2 , with an interval of 0.1 . β_{xy} was changed from -0.5 to 0.25 , with an interval of 0.005 . Other parameters were set as follows: $r_x = 3.8$, $s_x = -3.8$, $r_y = 3.5$ and $s_y = -3.5$. The length of the time series was 1,000 and the initial abundances of X and Y were set at 0.5. The attractor was reconstructed using a fully multivariate embedding.

To further test the effectiveness of the S-map method, we applied it to experimental systems in which signs of interactions were known on the basis of biological background knowledge about organisms. We applied the S-map method to two experimental systems; one was a classic predator–prey system, and the other was a more complex rotifer–algae system.

The data of the classic *Paramecium*–*Didinium* protozoan prey–predator system have previously been published³¹ and can also be found at <http://robjhyndman.com/tsdldata/data/veilleux.dat> (Extended Data Fig. 1e). A previous study³² identified conditions that produced sustained oscillations in predators (*Didinium nasutum*) and prey (*Paramecium aurelia*). Initial densities of *Paramecium* and *Didinium* in medium were 15 and 5 individuals per millilitre, respectively. Abundance measurements were taken every 12 h. The first 10 data points were removed to eliminate transient behaviour in the initial period of the experiment. The time series were then normalized to unit mean and variance before analysis.

The data of the rotifer–chlorella system were from an experimental predator–prey system³³. The predator–prey system consisted of *Brachionus calyciflorus* (an asexually reproducing predatory rotifer) and *Chlorella vulgaris* (an asexually reproducing algal prey) (Extended Data Fig. 1g). One type of algal clone has a higher population growth rate, whereas another type of algal clone is more defensive against rotifer predation (hereafter algae r and algae K, respectively). The changes in clonal frequency in the algal population (that is, natural selection in the population) were quantified using the allele-specific quantitative PCR technique. Detailed experimental protocols were as described³³.

Among the 63 data points, 7 were not available (days 10, 14, 17, 18, 26, 57 and 59). The missing data were estimated using simple linear interpolation. Before quantifying interaction strengths between the species, CCM was performed to detect causality. CCM detected causalities between all pairs in the system; thus, there are six causal relationships in the system. We then quantified interaction strength using the S-map method. The S-map method was performed using full multivariate embedding that is, $\{\text{Rotifer}(t), \text{Algae}_r(t), \text{Algae}_K(t)\}$. To forecast the abundance of the rotifer, algae r and algae K, nonlinear parameters (θ) were set as 0.1, 1.8 and 1.2, respectively.

Reconstruction of the dynamic interaction matrix of the fish community. CCM with the phase-lock twin surrogate method identified 14 causal links among the fish species (Fig. 1 and Extended Data Table 1). To approximate the interaction matrix (Jacobian matrix) of the fish interaction network at each time point, we used the multivariate S-map method^{6,9}.

The estimation of interaction strengths by the multivariate S-map method is sensitive to the choice of variables included in state space reconstruction, and these variables should therefore be determined carefully. In the analysis of the Maizuru fish community, variables included in the state space reconstruction were as follows: if species x_1 is causally influenced by x_2 and x_3 , and if the best E of x_1 is 5 (determined by the simplex projection; see ‘Convergent cross mapping’), the state space is reconstructed by $\{x_1(t), x_2(t), x_3(t), x_1(t-1), x_1(t-2)\}$. That is, the number of variables used to reconstruct the attractor must be equal to the best E : to fulfil this requirement, the time lags of the target variable were included in the embedding space when the number of candidate species was smaller than E . This was done to capture fully the dynamics of the system without including extraneous dimensions. The best nonlinear parameter (θ) was chosen for the multivariate embedding on the basis of the mean absolute error, as previously described²⁹. In this study, the coefficients of the local linear model for $x_2(t)$ and $x_3(t)$ were regarded as interspecific interaction strengths, and other coefficients (that is, for $x_1(t)$, $x_1(t-1)$ and $x_1(t-2)$) were not interspecific and thus excluded from the calculations for indices of interspecific interactions (see later).

Dynamic stability of the fish community and indices of interspecific interactions. The interaction strength quantified by the multivariate S-map method is an approximation of the partial derivative for each time point. Thus,

using the multivariate S-map method, population dynamics including time-lag effects are described as

$$\hat{x}_i(t+1) = \frac{\partial x_i(t+1)}{\partial x_1(t)} x_1(t) + \frac{\partial x_i(t+1)}{\partial x_2(t)} x_2(t) + \frac{\partial x_i(t+1)}{\partial x_3(t)} x_3(t) + \dots + \frac{\partial x_i(t+1)}{\partial x_1(t-1)} x_1(t-1) + \frac{\partial x_i(t+1)}{\partial x_1(t-2)} x_1(t-2) + \dots + C_0$$

in which \hat{x}_i indicates the predicted abundance of species i in the community (\hat{x}_1 for species 1, in this example), and C_0 indicates the intercept. Note that the partial derivatives and intercept are calculated using the S-map method as described earlier⁶. For simplicity, here we describe a case in which $\hat{x}_i(t+1)$ includes only one time lag ($x_1(t-1)$), but the following descriptions can easily be extended to cases that include more time-lag terms. In a matrix notation, the community dynamics are described as

$$X(t+1) = J_1 X(t) + J_2 X(t-1) + C \quad (1)$$

in which X indicates the n -dimensional vector of the abundance of n species, J_1 is the $n \times n$ -dimensional matrix of partial derivatives (interaction strengths), and C is the n -dimensional vector of the intercepts. If we write the unity matrix, zero matrix and zero vector as I , O and $\mathbf{0}$, respectively, then we can describe $X(t)$ as

$$X(t) = I X(t) + O X(t-1) + \mathbf{0} \quad (2)$$

By combining equations (1) and (2), we get the following:

$$\begin{pmatrix} X(t+1) \\ X(t) \end{pmatrix} = \begin{pmatrix} J_1 & J_2 \\ I & O \end{pmatrix} \begin{pmatrix} X(t) \\ X(t-1) \end{pmatrix} + \begin{pmatrix} C \\ \mathbf{0} \end{pmatrix} \quad (3)$$

If we write

$$\begin{pmatrix} X(t) \\ X(t-1) \end{pmatrix} = W(t), \begin{pmatrix} J_1 & J_2 \\ I & O \end{pmatrix} = A \text{ and } \begin{pmatrix} C \\ \mathbf{0} \end{pmatrix} = B,$$

Then equation (3) can be written as:

$$W(t+1) = A W(t) + B \quad (4)$$

Assuming that W^* is the abundance of the steady state (note that assuming W^* here does not assume the existence of the local stable equilibrium of the community dynamics), equation (4) can be written as

$$W^* = A W^* + B \quad (5)$$

$$(I - A) W^* = B \quad (6)$$

By substituting equation (5) from equation (4), we get

$$W(t+1) - W^* = A(W(t) - W^*)$$

For the purpose of convenience, we write $W(t+1) - W^*$ as $Z(t+1)$, and then equation (4) can be written as:

$$Z(t+1) = A Z(t)$$

Therefore, the stability of this system can be examined by investigating eigenvalues of the interaction matrix A , which correspond to the Lyapunov exponents. In this study, for the purpose of convenience, we describe the local Lyapunov stability as the absolute value of the real part of the dominant eigenvalue of the interaction matrix A , and this stability is called 'dynamic stability'. A dynamic stability value of less than 1 indicates that the community tends to recover faster from perturbations, if the interspecific interaction strengths (off-diagonal elements in the interaction matrix J_1) and self-regulation effects (diagonal elements in the interaction matrix J_1 and J_2) are kept constant. Although our analysis may be analogous to local stability analyses, the calculation of dynamic stability does not require an assumption of a locally stable equilibrium: because the multivariate S-map method actually generates a state-dependent (and hence time-varying) interaction matrix, it is applicable to non-equilibrium systems and reflects whether the trajectories at any particular time are converging or diverging⁶. In addition, we computed several properties of the interaction network structure including mean, weak interaction index (indicated by the median interaction strength: maximum interaction strength ratio), standard deviations and skewness, using the absolute value of off-diagonal elements in J_1 . Previous theoretical studies have suggested that these indices are potential drivers of community stability^{10,15,16}.

Sensitivity of the dynamic stability to the inclusion of subdominant species. In the main analyses, we included only a subset of the whole community; only

dominant species were selected. To test the robustness of our analysis to the inclusion of a less abundant species, we performed a sensitivity analysis to look at how the dynamic stability is affected. In this sensitivity analysis, four subdominant species were chosen. These were *Ditrema temminckii*, *Pseudoblennius cottoides*, *Takifugu niphobles* and *Takifugu poecilonotus*. The total abundance of each of these species during the census term is between 1,000 and 100; furthermore, they do not show too many '0' observations during the census period. Each of the subdominant species was added separately in reconstructing an interaction network. The same procedure described in the above sections was applied to the network reconstruction, quantification of interaction strength and calculation of the dynamic stability.

Sensitivity of the dynamic stability to observation errors. To test the sensitivity of the dynamic stability to observation errors in the visual census data, we calculated the dynamic stability after artificial observation errors were added to the visual census data. In this analysis, we assumed that observation errors are proportional to the number of observed fish individuals. More specifically, observation errors were added using the following R script: `error <- rnorm(1, mean=0, sd=error_percent * data)`. Error_percent represents the magnitude of observation errors added to the original value, and data indicates the number of fish individuals at a particular time point.

Calculations of coefficient of variation. To compare the dynamic stability in this study and coefficient of variation (CV) of the fish community, we calculated mean values of CV of fish populations (that is, 15 fish species). First, we determined a target time point and selected three time points before and after the target point, which generated a three-month window. Then, we calculated the mean value, standard deviations and CV for each species within the window. The mean CV was calculated at each window by taking the average of the CVs of the 15 fish species. This procedure was repeated throughout the census period.

Relationships between dynamic stability and other variables. Using CCM and the phase-lock twin surrogate method, we investigated the following possible causal drivers of dynamic stability: (1) measures of the strength of interspecific interactions such as mean interaction strength and weak interaction index (Fig. 4a, b); (2) diversity indices (such as species richness and Simpson's diversity index) (Fig. 4c and Extended Data Fig. 6); (3) water temperature and total fish abundance (Extended Data Fig. 6); and (4) measures of the distribution of interspecific interactions such as s.d. and skewness (Extended Data Fig. 6).

Abundance-based stability index. An alternative and more intuitively understandable measure of stability of the community dynamics would be the Euclidean distance of the species abundance between time point t and $t+1$, $\|W(t+1) - W(t)\|$. Here we show that this abundance-based stability index is directly related to the eigenvalue-based stability (that is, dynamic stability). From equation (4), the abundance-based stability can be written as

$$W(t+1) - W(t) = (A - I)W(t) + B \quad (7)$$

Using equation (6), equation (7) can be written as

$$W(t+1) - W(t) = (A - I)W(t) + (I - A)W^*$$

$$W(t+1) - W(t) = (A - I)(W(t) - W^*) \quad (8)$$

Equation (8) indicates that the abundance-based stability can be expressed as the product of $(A - I)$ and $(W(t) - W^*)$; this $(W(t) - W^*)$ describes the difference between the steady state and the abundance at time t . It is important to note that assuming W^* does not assume the existence of the local stable equilibrium of the community dynamics. Equation (8) indicates how the difference between the steady state and the abundance at time t will be amplified in the next time step. In other words, $(W(t+1) - W(t))$, $(A - I)$ and $(W(t) - W^*)$ indicate the community-level fluctuation, the potential to change the abundance of each population and how the present state differs from the steady state, respectively. The interspecific interactions caused an abundance-based stability index $(W(t+1) - W(t))$ (Extended Data Fig. 7), which suggests that interspecific interactions also drive fluctuations in the realized population abundance.

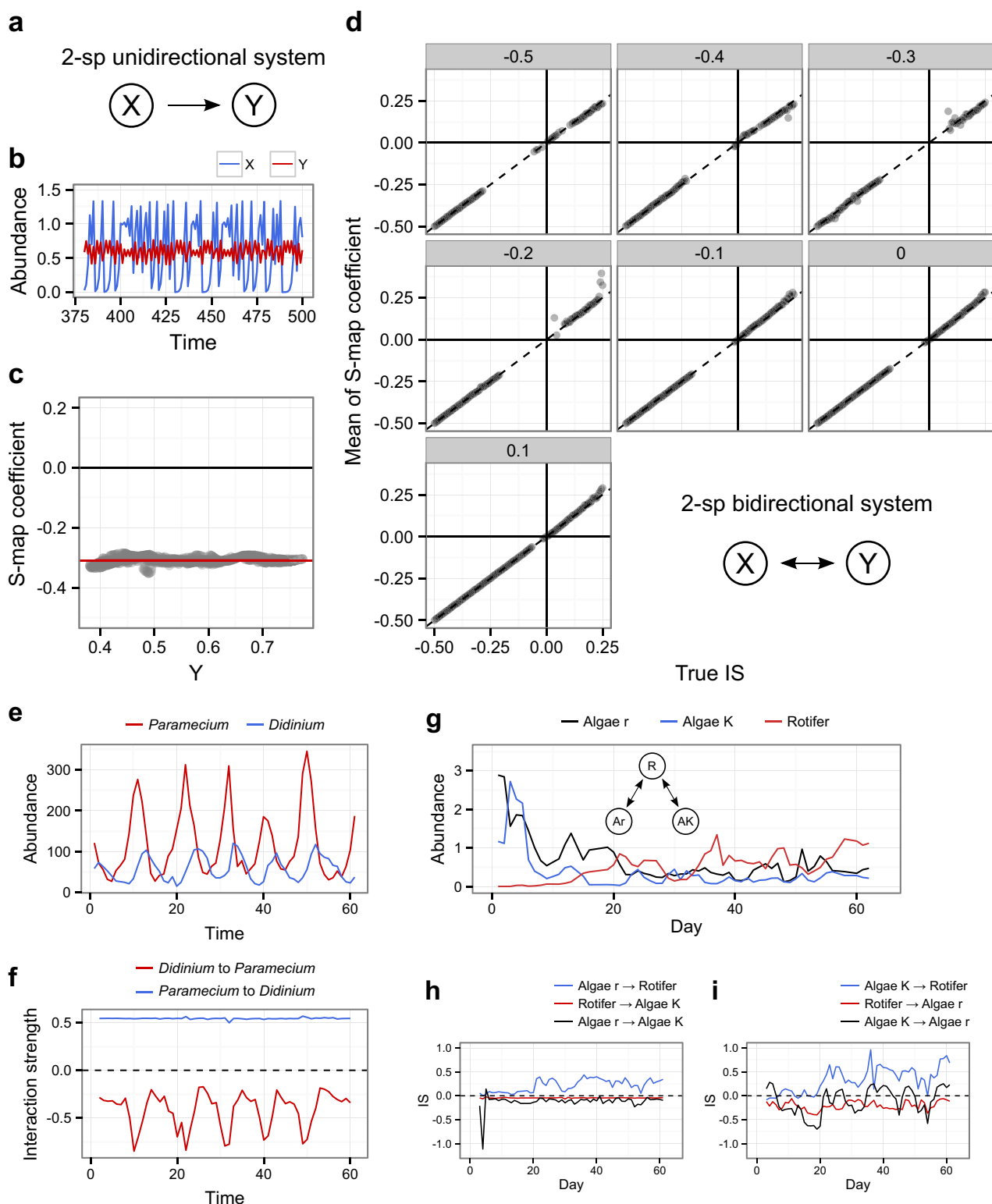
Effects of interspecific interactions and species diversity on the dynamic stability. To determine how interspecific interactions and species diversity affect dynamic stability, we quantified the causal effect using the multivariate S-map method (Fig. 4d), which is described above. Before the analysis, all data were normalized. When using the multivariate S-map method, we used fully multivariate embedding (reconstructed state space = {DynamicStability(t), MeanInteractionStrength(t), WeakInteractionIndex(t), Simpson'sDiversity(t), and time-lag terms}), and the partial derivatives were then calculated.

Computation. Simplex projection, the S-map method and CCM were performed using the 'rEDM' package (version 0.2.4)¹⁹, and all statistical analyses were performed in the statistical environment R v.3.2.1³⁴.

Code availability. The R scripts used for the main analyses are available at <https://doi.org/10.5281/zenodo.1039387>.

Data availability. Time-series data of the Maizuru fish community are available at <https://doi.org/10.5281/zenodo.1039387>. All other data are available from the corresponding author(s) upon reasonable request.

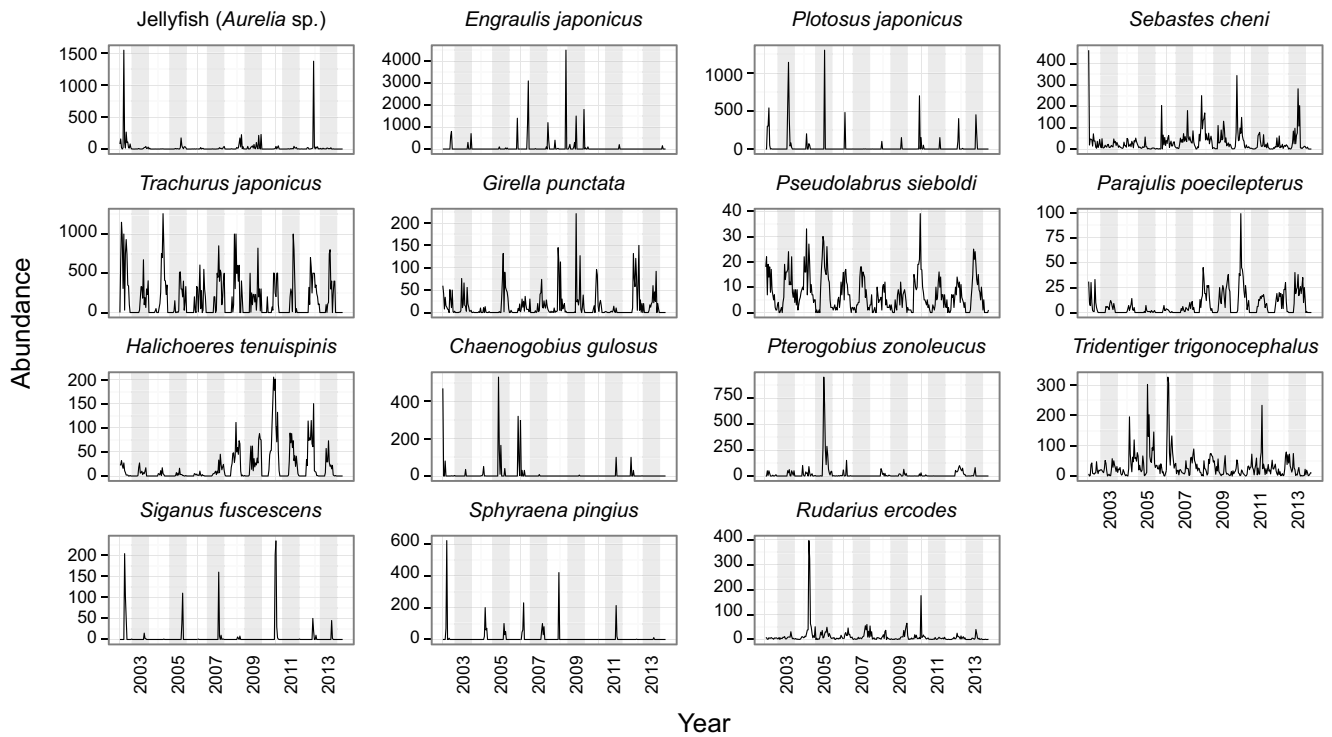
25. Masuda R. Ontogeny of swimming speed, schooling behaviour and jellyfish avoidance by Japanese anchovy *Engraulis japonicus*. *J. Fish Biol.* **78**, 1323–1335 (2011).
26. Chang, C.-W., Ushio, M. & Hsieh, C. Empirical dynamic modeling for beginners. *Ecol. Res.* **32**, 785–796 (2017).
27. Takens, F. in *Dynamical Systems and Turbulence* (eds Rand, D. A. & Young, L.-S.) 366–381 (Springer, 1981).
28. Deyle, E. R. & Sugihara, G. Generalized theorems for nonlinear state space reconstruction. *PLoS ONE* **6**, e18295 (2011).
29. Deyle, E. R. *et al.* Predicting climate effects on Pacific sardine. *Proc. Natl Acad. Sci. USA* **110**, 6430–6435 (2013).
30. Thiel, M., Romano, M. C., Kurths, J. & Rofs, M. R. K. Twin surrogates to test for complex synchronisation. *Europhys. Lett.* **75**, 535–541 (2006).
31. Veilleux, B. G. *The Analysis of a Predatory Interaction between Didinium and Paramecium*. MSc thesis, Univ. Alberta (1976).
32. Jost, C. & Ellner, S. P. Testing for predator dependence in predator–prey dynamics: a non-parametric approach. *Proc. R. Soc. Lond. B* **267**, 1611–1620 (2000).
33. Kasada, M., Yamamichi, M. & Yoshida, T. Form of an evolutionary tradeoff affects eco-evolutionary dynamics in a predator–prey system. *Proc. Natl Acad. Sci. USA* **111**, 16035–16040 (2014).
34. R Core Team. *R: A Language and Environment for Statistical Computing*; <http://R-project.org/> (R Foundation for Statistical Computing, 2015).



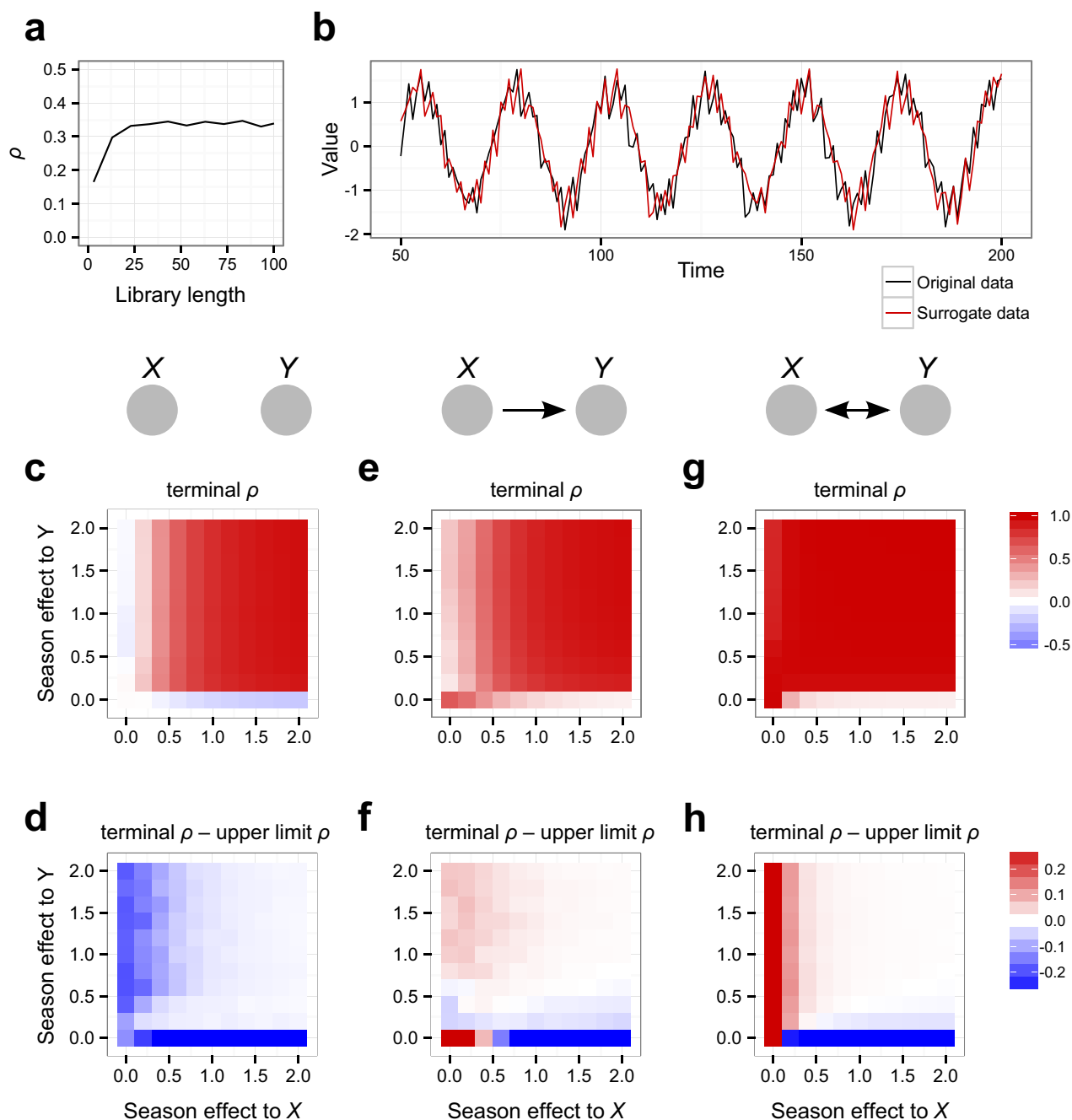
Extended Data Figure 1 | Effectiveness of the S-map method examined in two-species model systems and laboratory experiment systems.

a, Illustration of the unidirectional two-species model system. X has a direct influence on Y, but Y does not have an influence on X. **b**, An example of the dynamics of the two-species system. The interaction strength from X to Y was set at -0.31 in this example. **c**, The estimation of interaction strength using the S-map method. True interaction strength is -0.31 , whereas the mean of the S-map coefficients is -0.309 . The length of the time series used for the analysis was 1,000. **d**, Test of the S-map method in a two-species bidirectional system. Interaction strength from Y to X was fixed for each panel (as denoted in the header of each panel), and interaction strength from X to Y was changed (x axis). The length of

the time series used for each analysis was 1,000 (see Methods). Dashed lines indicate 1:1 lines. Dynamics that show strong linearity (for example, limit cycle and equilibrium) were excluded from the analysis; that is, regions around the origin were excluded. **e**, Population dynamics of *Didinium* (predator) and *Paramecium* (prey). **f**, Estimation of interaction strength between *Didinium* and *Paramecium*. **g**, Population dynamics of the rotifer (predator) and two types of algae (prey). Inset illustrates the three-species experimental system. R, Ar and AK indicate rotifers, r-strategy algae and K-strategy algae, respectively. Units for the y axis are 10^6 cells per ml for the algae, and 10 individual females per ml for the rotifer. **h**, **i**, Estimation of pair-wise interaction strength among r-strategy algae, K-strategy algae and rotifers.



Extended Data Figure 2 | Time series of dominant fish species and jellyfish in Maizuru Bay in Japan. During a 12-year census (2002–2014), 285 surveys were conducted. The width of the grey region corresponds to a 1-year interval that runs from January to December (24 observations per year).



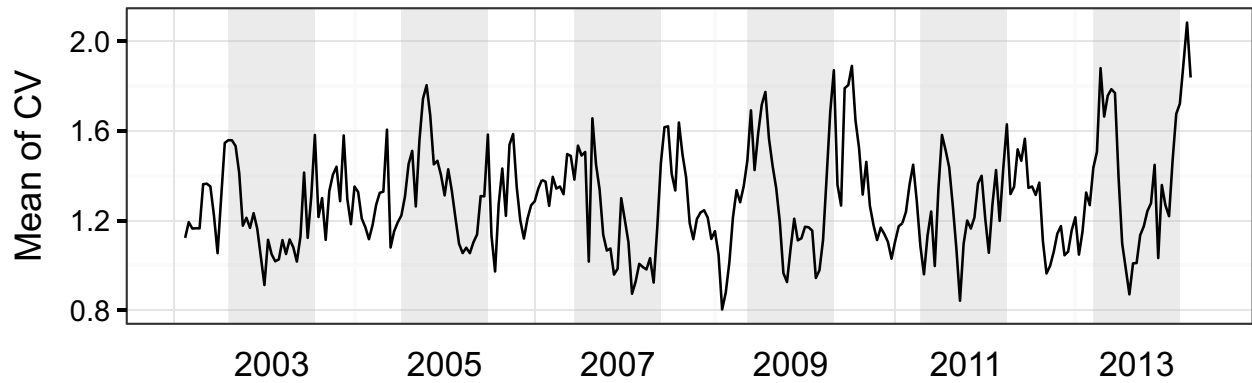
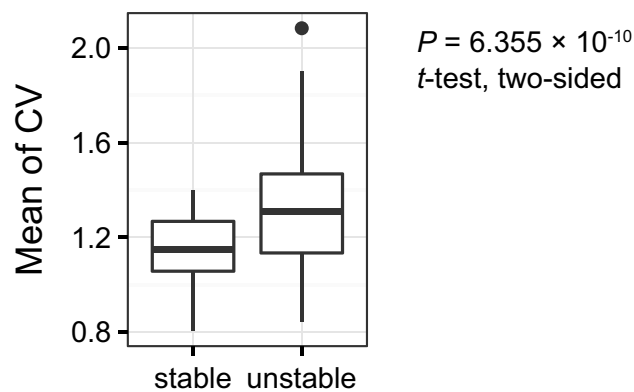
Extended Data Figure 3 | Evaluation of the phase-lock twin surrogate

method. **a**, A false high cross-map skill and convergence, owing to seasonality. We set $\beta_{xy} = \beta_{yx} = 0$ (no causality between $X(t)$ and $Y(t)$) and $a_x = a_y = 0.3$ (moderate seasonality). **b**, An example of the phase-lock twin surrogate time series. The original time series with strong seasonality is shown as a black solid line ($Y(t)$; $\beta_{xy} = -0.3$, $\beta_{yx} = 0$, $\alpha_x = 1.0$ and $\alpha_y = 1.0$). The surrogate time series, with the same seasonality and

nonlinearity as the original data, is shown as a solid red line. **c–h**, Cross-map skill (terminal ρ) and terminal ρ – 95% upper limit; ρ of 100 surrogate data by CCM between X and Y , when X and Y have no interaction (**c**, **d**), unidirectional interaction (**e**, **f**) and bidirectional interaction (**g**, **h**). The length of the time series used for the evaluation was 288 (equivalent to a 12-year census with 24 observations per year).

Extended Data Figure 4 | Sensitivity to the inclusion of subdominant species and observation errors. **a–d**, Relationship between the dynamic stability calculated from the community of 15 dominant species versus that of a 16-species community. A subdominant species (*D. temminckii* (**a**), *P. cottoides* (**b**), *T. niphobles* (**c**) or *T. poecilonotus* (**d**)) was added to the community of 15 dominant species, and the dynamic stability was calculated by the procedure described in the Methods. Inset shows the interaction network structures of the 16-species community. Solid black line indicates the 1:1 line. Red circle indicates the newly included subdominant species. Blue and red arrows indicate positive and negative time-averaged interactions, respectively, associated with the subdominant species. Grey arrows and circles indicate the edges and

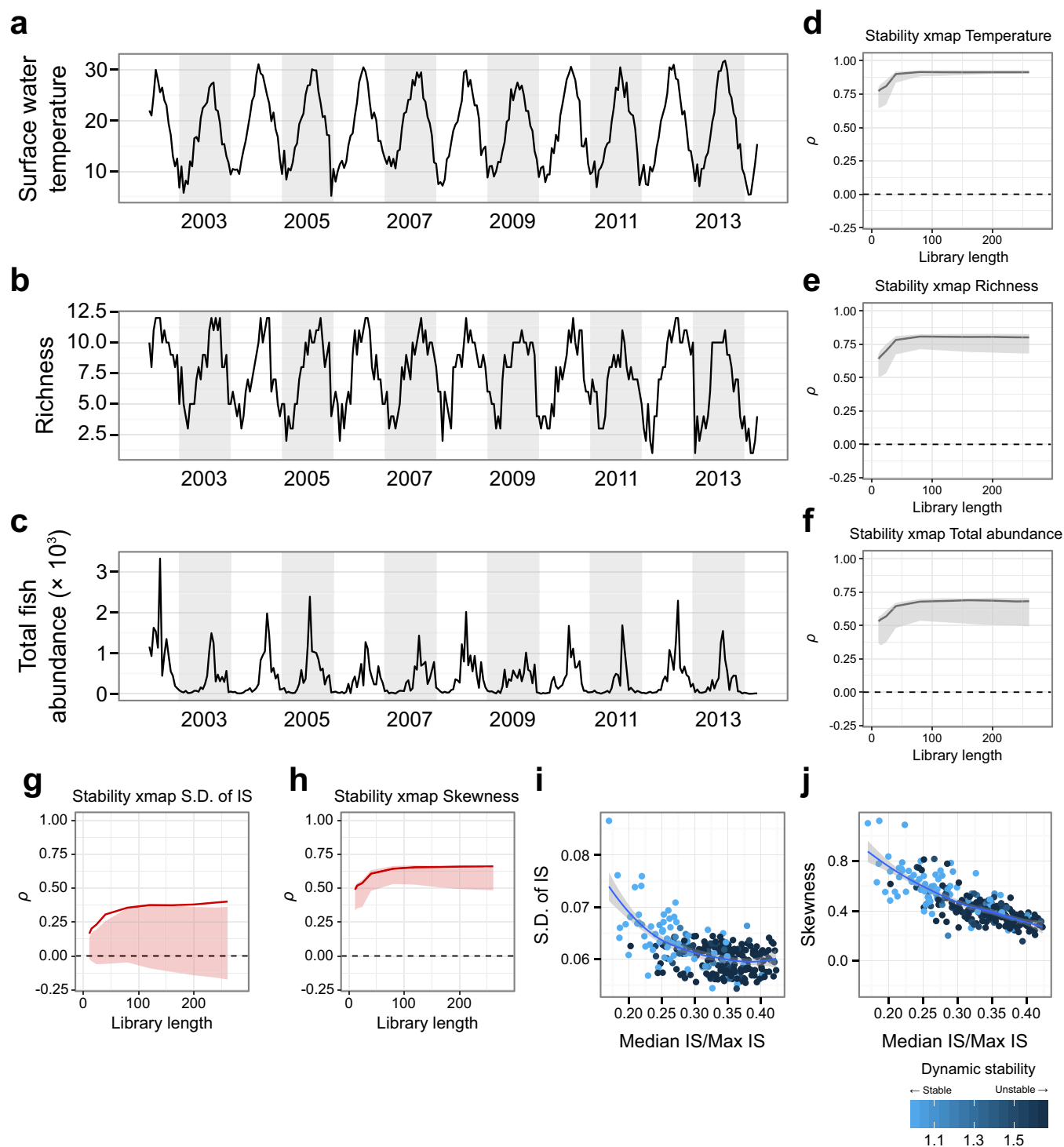
nodes, respectively, of the original community of 15 dominant species. **e–j**, Effects of observation errors on the calculations of the dynamic stability. **e**, Observation errors were added to the original time series (see Methods), R^2 was calculated between the original dynamic stabilities and those calculated from the time series with an added error. This procedure was repeated 100 times for each error magnitude (%). Midline, box limits, whiskers and points indicate median, upper and lower quartiles, $1.5 \times$ interquartile range and outliers, respectively ($n = 100$ for each box). **f–j**, Examples illustrating the relationships between the original dynamic stabilities versus those calculated after the addition of 1% (**f**), 5% (**g**), 10% (**h**), 20% (**i**) and 30% (**j**) observation errors. The solid line indicates the 1:1 line. The dashed line indicates the dynamic stability = 1.0.

a**b**

Condition of community stability

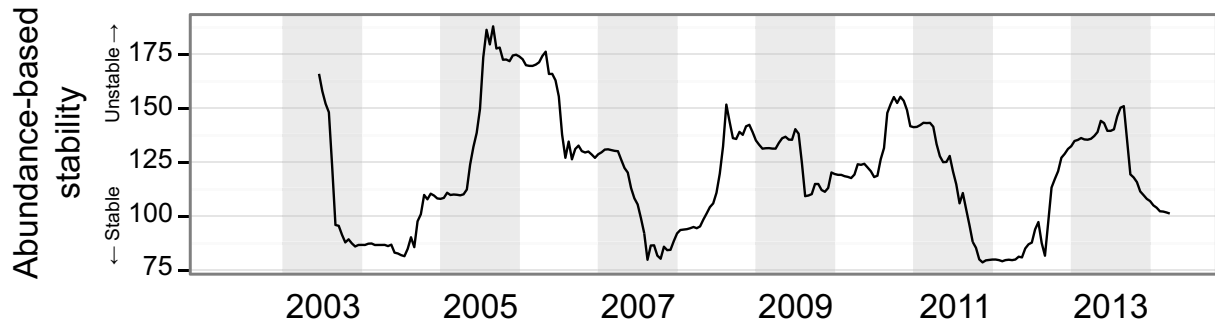
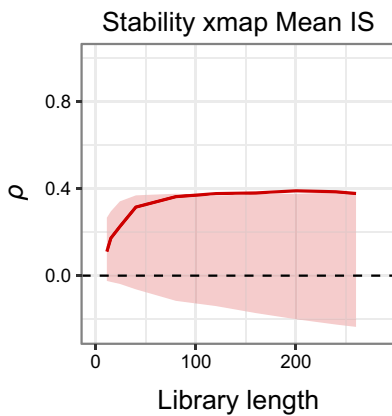
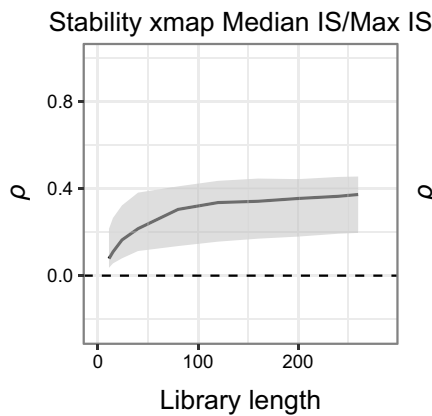
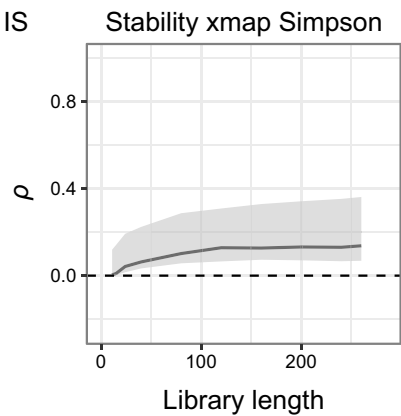
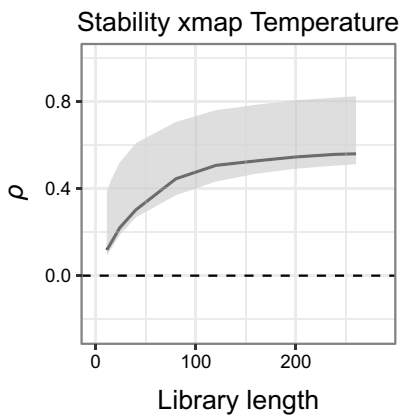
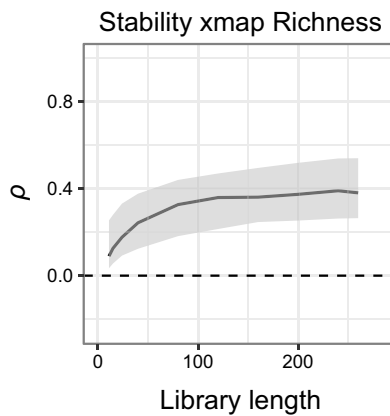
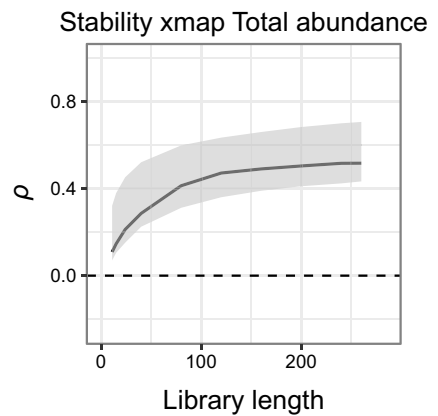
Extended Data Figure 5 | Relationship between dynamic stability and coefficient of variation of fish abundance. **a**, Time series of mean values of CV. CV was calculated using a moving window (window width = 6 time points; 3 months) for population dynamics of each fish species. Mean values of CV were then calculated by averaging CV values of the 15 fish species. **b**, Comparison of CV between stable and unstable periods

($n = 56$ for stable conditions and $n = 203$ for unstable conditions). Under stable conditions (dynamic stability < 1.0), the CV is significantly lower than it is under unstable conditions ($P < 0.0001$, two-sided t -test). Midline, box limits, whiskers and points indicate median, upper and lower quartiles, $1.5 \times$ interquartile range and outliers, respectively.



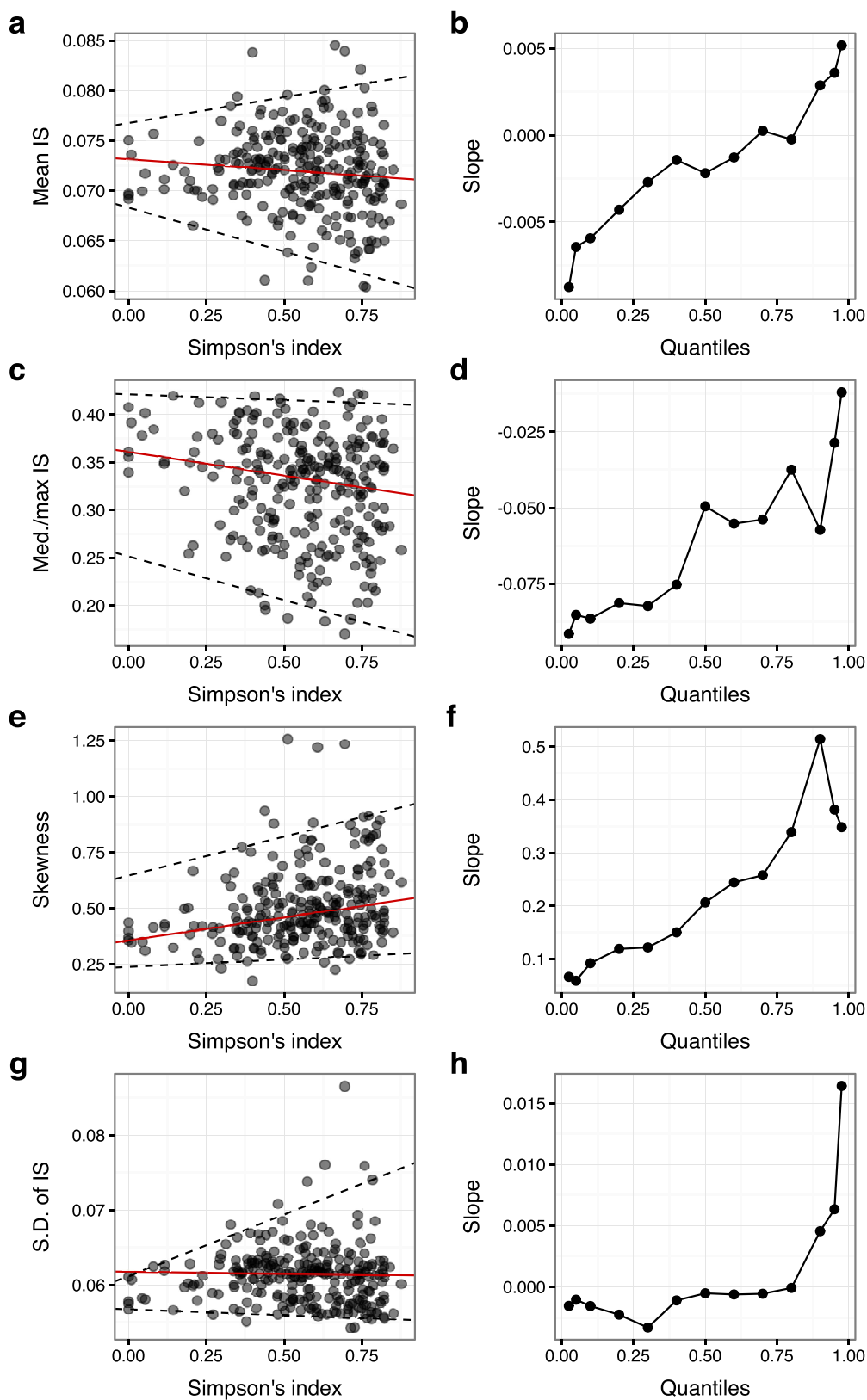
Extended Data Figure 6 | CCM between dynamic stability and surface water temperature, species richness, total fish abundance and the s.d. and skewness of the interaction strength distribution. **a–c**, Time series of surface water temperature (**a**), richness of dominant fish species (**b**) and total abundance of dominant fish species (**c**). The width of the grey region corresponds to a 1-year interval (24 observations per year). **d–f**, Results of CCM analysis between dynamic stability and surface water temperature (**d**), species richness (**e**) and total fish abundance (**f**). **g–h**, Results of CCM between the dynamic stability and s.d. of interaction strength (**g**) and skewness of the interaction strength distribution (**h**). Dark solid lines

indicate cross-map skill (ρ) from dynamic stability to another variable. Shaded regions indicate 95% confidence intervals of 100 surrogate time series. Significant cross-map skills (ρ) are highlighted in red (**d–h**). **i, j**, Correlations between median:maximum interaction strength (IS) (weak interaction index) and s.d. of interaction strength (**i**) and the skewness (**j**) ($n = 261$ for each panel). The dynamic stability is indicated in blue. The weak interaction index and s.d. and skewness of interaction strength were predominantly linearly correlated, which suggests that the s.d. and skewness of interaction strength are alternative representations of the weak interaction index in our data.

a**b****c****d****e****f****g**

Extended Data Figure 7 | Abundance-based stability index of the fish community. **a**, Temporal dynamics of the abundance-based stability index. Euclidean distance between $W(t+1)$ and $W(t)$ was calculated (see Methods for the definition of $W(t)$). Note that the abundance of each fish species was standardized before calculating the Euclidean distance. **b–g**, Results of CCM between the abundance-based stability and

interspecific interactions, species richness, diversity and surface water temperature. Dark solid lines indicate cross-map skill (ρ) from the abundance-based stability to another variable. Shaded regions indicate 95% confidence intervals of 100 surrogate time series. Significant cross-map skills (ρ) are highlighted in red.



Extended Data Figure 8 | Results of quantile regressions between Simpson's diversity index and properties of the distributions of interaction strengths. **a–h**, Quantile regressions and their regression coefficients of the mean IS (**a**, **b**), median:maximum interaction strength (**c**, **d**), skewness (**e**, **f**) and s.d. of interaction strength (**g**, **h**) were

plotted against Simpson's diversity index. The solid red line indicates the 50% quantile and the dashed black lines enclose the 2.5% and 97.5% quantiles (**a**, **c**, **e**, **g**; $n = 261$ for each panel). Regression coefficients (slopes) were plotted against quantiles (**b**, **d**, **f**, **h**), and show that all coefficients exhibit an increasing trend as the quantile increases.

Extended Data Table 1 | Result of CCM for the dominant fish species in Maizuru Bay

	Jellyfish	<i>Engraulis</i>	<i>Plotosus</i>	<i>Sebastes</i>	<i>Trachurus</i>	<i>Girella</i>	<i>Pseudolabrus</i>	<i>Parajulis</i>
Jellyfish	-	-0.003	0.030	0.012	0.131	0.169	0.035	0.097
<i>Engraulis japonicus</i>	-0.005	-	-0.003	0.046	0.067	0.125	0.144	-0.030
<i>Plotosus japonicus</i>	0.077	-0.030	-	0.197	0.263	0.028	0.333	0.195
<i>Sebastes cheni</i>	0.044	-0.022	0.112	-	0.311	0.339	0.269	0.334
<i>Trachurus japonicus</i>	0.391	0.133	0.309	0.269	-	0.481	0.447	0.552
<i>Girella punctata</i>	0.168	0.090	0.243	0.191	0.421	-	0.296	0.358
<i>Pseudolabrus sieboldi</i>	0.418	-0.030	0.417	0.342	0.643	0.546	-	0.594
<i>Parajulis poecilepterus</i>	0.188	0.029	0.071	0.570	0.370	0.425	0.359	-
<i>Halichoeres tenuispinis</i>	0.215	0.110	0.072	0.360	0.394	0.324	0.319	0.688
<i>Chaenogobius gulosus</i>	0.101	-0.058	0.049	-0.026	0.043	0.037	0.071	0.023
<i>Pterogobius zonoleucus</i>	0.009	-0.086	0.062	0.087	0.287	0.138	0.408	-0.008
<i>Tridentiger trigonocephalus</i>	0.022	-0.131	-0.002	0.075	0.142	0.103	-0.029	0.186
<i>Siganus fuscescens</i>	0.078	0.018	0.175	-0.018	0.215	0.180	0.180	0.328
<i>Sphyaena pinguis</i>	0.048	-0.045	0.004	-0.010	0.340	0.154	0.028	0.153
<i>Rudarius ercodes</i>	0.092	0.056	0.069	-0.005	0.411	0.149	0.284	0.117

	<i>Halichoeres</i>	<i>Chaenogobius</i>	<i>Pterogobius</i>	<i>Tridentiger</i>	<i>Siganus</i>	<i>Sphyaena</i>	<i>Rudarius</i>
Jellyfish	0.019	0.019	0.032	-0.025	0.064	0.032	0.077
<i>Engraulis japonicus</i>	-0.043	-0.061	-0.042	0.141	-0.059	-0.024	0.145
<i>Plotosus japonicus</i>	0.019	0.064	0.053	0.337	0.047	-0.010	0.123
<i>Sebastes cheni</i>	0.285	0.117	0.102	0.127	0.229	0.003	0.257
<i>Trachurus japonicus</i>	0.415	0.190	0.296	0.215	0.266	0.465	0.499
<i>Girella punctata</i>	0.229	-0.022	0.353	0.105	0.244	0.047	0.224
<i>Pseudolabrus sieboldi</i>	0.567	0.336	0.371	0.339	0.401	0.204	0.530
<i>Parajulis poecilepterus</i>	0.656	0.119	0.200	0.270	0.336	-0.042	0.313
<i>Halichoeres tenuispinis</i>	-	0.209	0.236	0.182	0.312	-0.027	0.374
<i>Chaenogobius gulosus</i>	0.005	-	0.005	0.044	0.069	-0.027	0.091
<i>Pterogobius zonoleucus</i>	0.095	0.243	-	0.002	0.086	-0.047	0.551
<i>Tridentiger trigonocephalus</i>	0.232	0.325	0.125	-	0.084	0.130	0.241
<i>Siganus fuscescens</i>	0.209	-0.014	-0.016	0.133	-	0.014	0.100
<i>Sphyaena pinguis</i>	0.014	0.090	0.003	0.104	-0.021	-	0.153
<i>Rudarius ercodes</i>	0.148	0.131	0.081	0.061	0.028	0.127	-

The significance of the CCM was judged using two criteria: (1) the terminal ρ is higher than the 95% confidence intervals of phase-lock twin surrogate, and (2) the initial ρ minus the terminal ρ ($\Delta\rho$) is larger than 0.1.

Extended Data Table 2 | Dimensionality and nonlinearity of the stability index and interaction strength

Index or interspecific interactions		Best embedding dimension (E)	Best nonlinear parameter (θ)
Dynamic stability		≥ 24	2
Individual interspecific interactions			
Cause species	Effect species		
<i>Trachurus japonicus</i>	<i>Aurelia</i> sp.	2	1.3
<i>Parajulis poecilepterus</i>	<i>Sebastes cheni</i>	10	0.8
<i>Sphyræna pinguis</i>	<i>Trachurus japonicus</i>	12	0.8
<i>Rudarius ercodes</i>	<i>Trachurus japonicus</i>	7	1.9
<i>Plotosus japonicus</i>	<i>Pseudolabrus sieboldi</i>	≥ 24	0.8
<i>Pterogobius zonoleucus</i>	<i>Pseudolabrus sieboldi</i>	6	2.4
<i>Halichoeres tenuispinis</i>	<i>Parajulis poecilepterus</i>	5	1.5
<i>Siganus fuscescens</i>	<i>Parajulis poecilepterus</i>	5	2.3
<i>Pterogobius zonoleucus</i>	<i>Chaenogobius gulosus</i>	6	1.2
<i>Tridentiger trigonocephalus</i>	<i>Chaenogobius gulosus</i>	7	0
<i>Girella punctata</i>	<i>Pterogobius zonoleucus</i>	4	1.2
<i>Plotosus japonicus</i>	<i>Tridentiger trigonocephalus</i>	≥ 24	0
<i>Trachurus japonicus</i>	<i>Sphyræna pinguis</i>	8	1.6
<i>Pterogobius zonoleucus</i>	<i>Rudarius ercodes</i>	3	0

Embedding dimension was examined from $E = 1$ to 24, and the best nonlinear parameter was examined from $\theta = 0$ to 10.

Cognitive performance is linked to group size and affects fitness in Australian magpies

Benjamin J. Ashton¹, Amanda R. Ridley¹, Emily K. Edwards¹ & Alex Thornton²

The social intelligence hypothesis states that the demands of social life drive cognitive evolution^{1–3}. This idea receives support from comparative studies that link variation in group size or mating systems with cognitive and neuroanatomical differences across species^{3–7}, but findings are contradictory and contentious^{8–10}. To understand the cognitive consequences of sociality, it is also important to investigate social variation within species. Here we show that in wild, cooperatively breeding Australian magpies, individuals that live in large groups show increased cognitive performance, which is linked to increased reproductive success. Individual performance was highly correlated across four cognitive tasks, indicating a ‘general intelligence factor’ that underlies cognitive performance. Repeated cognitive testing of juveniles at different ages showed that the correlation between group size and cognition emerged in early life, suggesting that living in larger groups promotes cognitive development. Furthermore, we found a positive association between the task performance of females and three indicators of reproductive success, thus identifying a selective benefit of greater cognitive performance. Together, these results provide intraspecific evidence that sociality can shape cognitive development and evolution.

The social environment is commonly assumed to generate important cognitive challenges. According to the social intelligence (or social brain) hypothesis, these challenges, including the need to form and maintain social bonds, track third-party relationships and anticipate the actions of others, are the central drivers of cognitive evolution^{1–3}. This argument receives widespread support from studies that link variation in social factors, such as group size or mating systems, with differences in cognitive performance or neuroanatomy across species of birds and mammals (for example, see refs 3–6). However, comparative analyses are subject to ecological and phylogenetic confounding effects, and have yielded conflicting results, with recent work calling into question the importance of social factors^{8–10}. To understand the role of sociality in cognitive evolution, it is critical to examine the causes and fitness consequences of cognitive variation within species^{11,12}.

For species that live in stable social groups, within-population variation in group size could generate differences in information-processing demands and so influence the expression of cognitive traits¹³. Measurements of brain structure correlate with group size in humans, captive cichlids (*Neolamprologus pulcher*) and captive macaques (*Macaca mulatta*)^{13–15}, but the relationship between group size and cognition in wild animals is unknown. Furthermore, the potential for group-size-dependent cognitive traits to come under selection is not understood, as their fitness consequences have not been investigated. To address these critical gaps in our knowledge, we examined whether group size predicts individual variation in cognitive performance (controlling for morphological, nutritional and behavioural factors) within a population of wild, cooperatively breeding Australian magpies (Western Australian subspecies, *Cracticus tibicen dorsalis*, also known as *Gymnorhina tibicen dorsalis*). We quantified

individual cognitive performance in 56 birds from 14 groups, which ranged in size from 3 to 12 individuals, using a variety of cognitive tasks designed to measure inhibitory control (the ability to inhibit prepotent responses), associative learning, reversal learning and spatial memory (Extended Data Fig. 1). These four domain-general cognitive processes are thought to have an important role in a range of fitness-related behaviours in both social and asocial contexts^{11,16} (see Methods for details).

Group size was the strongest predictor of adult performance across all four tasks (Supplementary Tables 1–4), with individuals from larger groups performing better than those from smaller groups (Fig. 1). Individual performance was significantly positively correlated across all four tasks (Supplementary Table 5), suggestive of an underlying general intelligence factor akin to what has been reported in human psychometric studies¹⁷. A principal component analysis revealed that performance in all four tasks positively contributed to the first principal component (PC1; eigenvalue >1). This component (referred to hereafter as ‘general cognitive performance’) accounted for 64.6% of the total variance in task performance (Extended Data Table 1), a substantially higher proportion than has previously been shown for cognitive tasks in other species^{18–22}. Group size was also the strongest predictor of PC1 (Fig. 2 and Supplementary Table 6). To confirm that our tasks provided robust measurements of individual cognitive performance, we ran a second set of cognitive tasks two weeks later using causally identical, but visually distinct, tasks (see Methods). Individual performance was highly repeatable in all four tasks: inhibitory control ($r = 0.806$, $P < 0.0001$), associative learning ($r = 0.97$, $P < 0.0001$), reversal learning ($r = 0.975$, $P < 0.0001$) and spatial memory ($r = 0.932$, $P < 0.0001$) (Extended Data Table 2).

To examine the development of the relationship between group size and cognition, we repeatedly tested juveniles at 100, 200 and 300 days after fledging. There was no evidence of general cognitive performance at 100 days after fledging (see Supplementary Discussion); however, much like adults, there was strong evidence for general cognitive performance at 200 (PC1 accounted for over 64% of total variance in task performance; Extended Data Table 3 and Supplementary Table 7) and 300 days after fledging (more than 80% of total variance explained by PC1; Extended Data Table 4 and Supplementary Table 8). There was no relationship between group size and cognitive performance at 100 days (Supplementary Tables 9, 10), but PC1 was strongly positively correlated with group size at 200 and 300 days (Fig. 3, Supplementary Tables 11, 12; see Supplementary Discussion for discussion of influential data points). When analysed longitudinally, an interaction between age tested and group size was the best predictor of cognitive performance (Extended Data Fig. 2 and Supplementary Tables 13–18).

The emergence of a positive association between group size and cognitive performance through early life supports the possibility that living in large groups helps to drive cognitive development. Manipulations of group size would be required to demonstrate an unequivocal causal effect, which in wild populations would lead to

¹Centre for Evolutionary Biology, School of Biological Sciences, University of Western Australia, 35 Stirling Highway, Crawley, Western Australia 6009, Australia. ²Centre for Ecology and Conservation, University of Exeter, Penryn Campus, Treliever Road, Penryn TR10 9FE, UK.

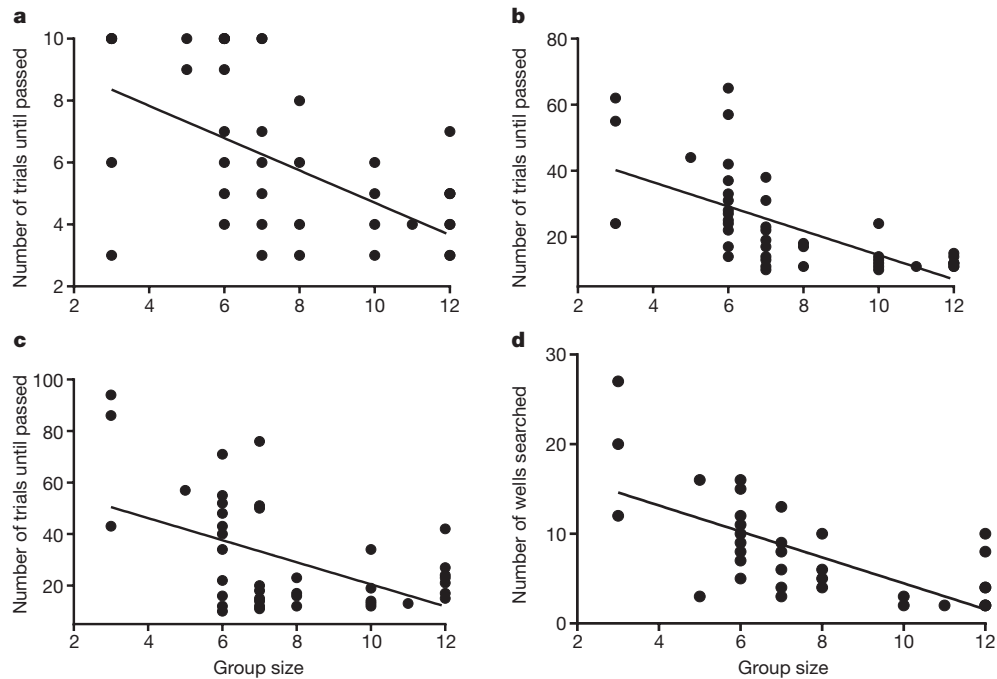


Figure 1 | The relationship between group size and cognition.

a–d, The relationship between group size and cognitive performance in an inhibitory control task (**a**; $n = 56$ individuals), associative learning task (**b**; $n = 48$ individuals), reversal learning task (**c**; $n = 48$ individuals)

and spatial memory task (**d**; $n = 49$ individuals). Lines represent best fit. Performance is measured as either the number of trials taken to succeed with the task, or the number of locations searched, so lower scores indicate better performance.

strong logistical and ethical challenges (see Supplementary Discussion). However, our analyses allow us to address key alternative explanations. First, the increased cognitive performance of birds in large groups is unlikely to be explained by reduced nutritional constraints on cognitive development²³, because we found no effect of group size on offspring provisioning rates (Supplementary Table 19), and no relationship between body size and cognitive performance in either adults or juveniles (Supplementary Tables 1–4, 9–12). We also found no relationship between foraging efficiency and cognitive performance in adults (Supplementary Tables 1–4; foraging efficiency data were not available for juveniles). Second, the positive effects of group size cannot result from a reduced need for vigilance or reduced neophobia (the fear of something new): we recorded no anti-predator behaviour during any task presentations and neophobia was unrelated to performance on any tasks, except juveniles' performance on the spatial memory task at 100 days after fledging (adults: Supplementary Tables 1–4; juveniles: Supplementary Tables 9–12). There was also no

relationship between group size and the time that test subjects spent interacting with tasks (see Supplementary Discussion). Third, a link between cognitive performance and group size could potentially arise if magpies preferentially joined groups containing individuals with similar traits, but life-history data collected over more than four years provided no evidence of such social assortment (see Supplementary Discussion). Moreover, we found a clear difference in the frequency distribution of cognitive phenotypes between small and large groups (Extended Data Fig. 3), so it is not simply the case that larger groups have a wider distribution of cognitive phenotypes, and are therefore more likely to contain some high-performing individuals by chance. Instead, we propose that, as suggested by captive studies^{13,15}, living in larger groups presents wild animals with information-processing challenges that promote the development of cognitive traits. Determining precisely what those challenges are is a priority for future research. An important next step will be to determine whether individual cognitive development is specifically linked to the quantity and quality of their relationships within their social networks, as might be expected if the need to establish and maintain multiple relationships within groups places cognitive demands on individuals³.

To determine whether the group-size-dependent cognitive variation that we have identified may be subject to selection, we examined the relationship between individual cognitive performance and three measures of reproductive success. General intelligence has been linked to fitness-related traits in humans²⁴, but few studies have examined the fitness consequences of cognitive variation in wild animals¹¹, and the two studies that have used rigorous psychological tests found no effects^{19,25}. In our magpie population, exceptionally high rates of extra-group paternity²⁶ mean that we were only able to reliably identify the mother of the brood (female reproductive skew in our population is low, and all females attempt to breed). Variation in female reproductive success was strongly linked to cognitive performance: general cognitive performance and foraging efficiency were the best predictors of the average number of hatched clutches per female per year (Fig. 4a, b and Supplementary Table 20), and general cognitive performance was the best predictor of the average number of fledglings produced and the

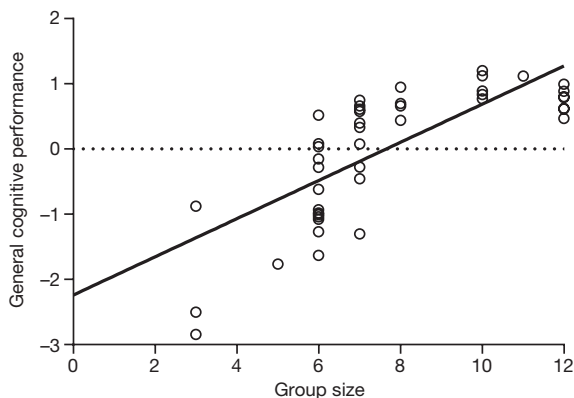


Figure 2 | The relationship between group size and general cognitive performance. Individual measurements of general cognitive performance derived from principal components analysis. $n = 46$ individuals.

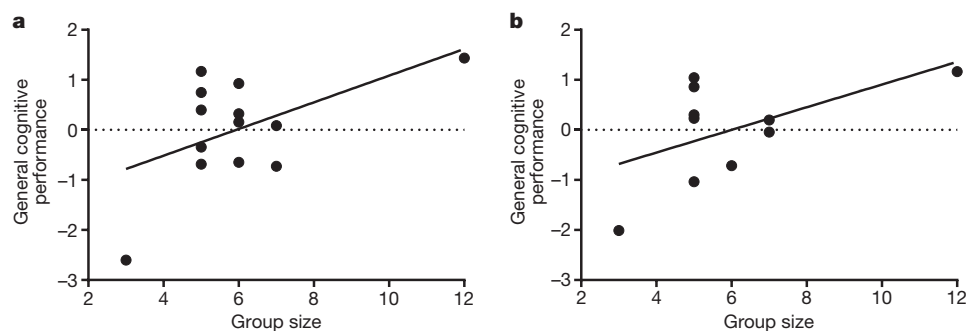


Figure 3 | The relationship between general cognitive performance and group size in juveniles. a, b, The relationship between general cognitive performance and group size at 200 days after fledging

(a; $n = 15$ individuals) and 300 days after fledging (b; $n = 10$ individuals). General cognitive performance could not be computed at 100 days after fledging.

average number of fledglings surviving to independence per female per year (Fig. 4c, d and Supplementary Tables 21, 22). These effects were independent of group size (Supplementary Tables 20–22), indicating that fitness benefits arise as a direct consequence of increased cognitive performance and are not simply the result of the non-cognitive advantages of living in larger groups. These results provide the evidence of a potential selective benefit of high levels of general cognitive performance in a wild population of non-human animals. Precisely how these benefits arise, and whether increased cognitive performance incurs any costs²⁷, has yet to be determined. General cognitive performance and foraging efficiency are not correlated in female magpies ($r = 0.06$, $P = 0.791$, $n = 22$), but it is possible that cognitively adept females may boost their reproductive success through improvements not in the quantity, but in the quality or variety of food given to offspring²⁸. Additional, non-mutually exclusive explanations for the relationship between cognition and reproductive success could include enhanced abilities to defend young by avoiding inter- and intraspecific conflict²⁹, or heritable cognitive abilities that promote offspring survival³⁰. It is also possible that the fitness benefits of cognitive performance may account for the relation between group size and cognition, if females with increased cognitive performance produce large numbers of

cognitively adept offspring. However, this explanation is unlikely, given that group size is stable over time (see Methods), and the extraordinarily high rates of extra-group paternity²⁶ are likely to preclude substantial genetic differentiation between groups.

Since its inception, the social intelligence hypothesis has focused on cognitive differences between species that result from selection in response to the challenges of social life. Our results indicate that social factors can also have developmental effects on cognition within species, with important consequences for individual fitness. In summary, we have shown that wild Australian magpies living in larger groups show increased cognitive performance, which is associated with increased reproductive success. The association between group size and cognition emerges through early life and cannot be explained by food intake, body size, neophobia, attention to tasks or social assortment. Although we cannot rule out the possibility that some other, unmeasured factor could have a role in driving the relationship, our findings strongly suggest that the social environment has developmental effects on fundamental, domain-general cognitive traits. Furthermore, we provide rare evidence that cognitive performance provides benefits for female reproductive success. Recent comparative studies have brought into question the notion that variation in social structure drives cognitive

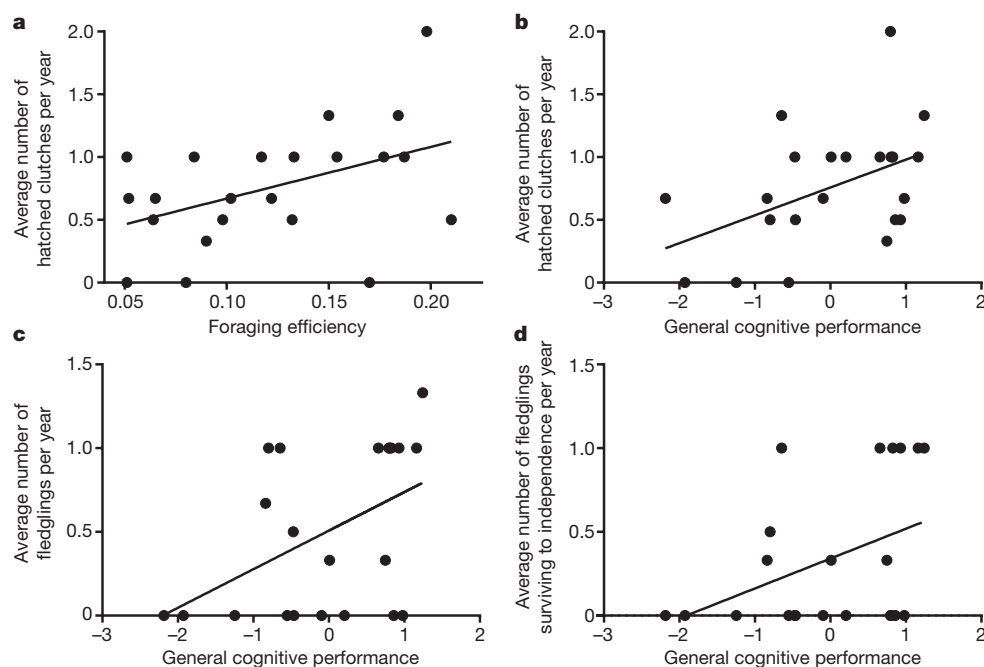


Figure 4 | The relationship between female traits and reproductive success. a–d, The relationship between foraging efficiency and the average number of hatched clutches per female per year (a), general cognitive performance and the average number of hatched clutches per female

per year (b), general cognitive performance and the average number of fledglings per female per year (c) and general cognitive performance and the average number of fledglings surviving to independence per female per year (d). $n = 22$ individuals.

evolution^{9,10}. However, our work highlights the critical importance of considering intraspecific variation, which is typically overlooked by comparative analyses. Together, our results point to a major role for the social environment in driving both the development and evolution of cognitive traits.

Online Content Methods, along with any additional Extended Data display items and Source Data, are available in the online version of the paper; references unique to these sections appear only in the online paper.

Received 20 September 2017; accepted 8 January 2018.

Published online 7 February 2018.

- Humphrey, N. in *Growing Points in Ethology* (eds Bateson, P. P. G. & Hinde, R. A.) 303–317 (Cambridge Univ. Press, 1976).
- Byrne, R. W. & Whiten, A. *Machiavellian Intelligence: Social Expertise and the Evolution of Intellect in Monkeys, Apes, and Humans* (Clarendon, 1988).
- Shultz, S. & Dunbar, R. I. The evolution of the social brain: anthropoid primates contrast with other vertebrates. *Proc. R. Soc. B* **274**, 2429–2436 (2007).
- Bond, A. B., Kamil, A. C. & Balda, R. P. Social complexity and transitive inference in corvids. *Anim. Behav.* **65**, 479–487 (2003).
- Street, S. E., Navarrete, A. F., Reader, S. M. & Laland, K. N. Coevolution of cultural intelligence, extended life history, sociality, and brain size in primates. *Proc. Natl Acad. Sci. USA* **114**, 7908–7914 (2017).
- Forss, S. I. F., Willems, E., Call, J. & van Schaik, C. P. Cognitive differences between orang-utan species: a test of the cultural intelligence hypothesis. *Sci. Rep.* **6**, 30516 (2016).
- Fox, K. C. R., Muthukrishna, M. & Shultz, S. The social and cultural roots of whale and dolphin brains. *Nat. Ecol. Evol.* **1**, 1699–1705 (2017).
- Holekamp, K. E. Questioning the social intelligence hypothesis. *Trends Cogn. Sci.* **11**, 65–69 (2007).
- DeCasien, A. R., Williams, S. A. & Higham, J. P. Primate brain size is predicted by diet but not sociality. *Nat. Ecol. Evol.* **1**, 0112 (2017).
- Sayol, F. *et al.* Environmental variation and the evolution of large brains in birds. *Nat. Commun.* **7**, 13971 (2016).
- Morand-Ferron, J., Cole, E. F. & Quinn, J. L. Studying the evolutionary ecology of cognition in the wild: a review of practical and conceptual challenges. *Biol. Rev. Camb. Philos. Soc.* **91**, 367–389 (2016).
- Thornton, A. & Lukas, D. Individual variation in cognitive performance: developmental and evolutionary perspectives. *Phil. Trans. R. Soc. B* **367**, 2773–2783 (2012).
- Sallet, J. *et al.* Social network size affects neural circuits in macaques. *Science* **334**, 697–700 (2011).
- Kanai, R., Bahrami, B., Roylance, R. & Rees, G. Online social network size is reflected in human brain structure. *Proc. R. Soc. B* **279**, 1327–1334 (2012).
- Fischer, S., Bessert-Nettelbeck, M., Kotrschal, A. & Taborsky, B. Rearing-group size determines social competence and brain structure in a cooperatively breeding cichlid. *Am. Nat.* **186**, 123–140 (2015).
- MacLean, E. L. *et al.* The evolution of self-control. *Proc. Natl Acad. Sci. USA* **111**, E2140–E2148 (2014).
- Plomin, R. The genetics of G in human and mouse. *Nat. Rev. Neurosci.* **2**, 136–141 (2001).
- Chandra, S. B., Hosler, J. S. & Smith, B. H. Heritable variation for latent inhibition and its correlation with reversal learning in honeybees (*Apis mellifera*). *J. Comp. Psychol.* **114**, 86–97 (2000).
- Isden, J., Panayi, C., Dingle, C. & Madden, J. Performance in cognitive and problem-solving tasks in male spotted bowerbirds does not correlate with mating success. *Anim. Behav.* **86**, 829–838 (2013).
- Shaw, R. C., Boogert, N. J., Clayton, N. S. & Burns, K. C. Wild psychometrics: evidence for 'general' cognitive performance in wild New Zealand robins, *Petroica longipes*. *Anim. Behav.* **109**, 101–111 (2015).
- Hopkins, W. D., Russell, J. L. & Schaeffer, J. Chimpanzee intelligence is heritable. *Curr. Biol.* **24**, 1649–1652 (2014).
- Galsworthy, M. J. *et al.* Assessing reliability, heritability and general cognitive ability in a battery of cognitive tasks for laboratory mice. *Behav. Genet.* **35**, 675–692 (2005).
- Buchanan, K. L., Grindstaff, J. L. & Pravosudov, V. V. Condition dependence, developmental plasticity, and cognition: implications for ecology and evolution. *Trends Ecol. Evol.* **28**, 290–296 (2013).
- Plomin, R. & Deary, I. J. Genetics and intelligence differences: five special findings. *Mol. Psychiatry* **20**, 98–108 (2015).
- Boogert, N. J., Anderson, R. C., Peters, S., Searcy, W. A. & Nowicki, S. Song repertoire size in male song sparrows correlates with detour reaching, but not with other cognitive measures. *Anim. Behav.* **81**, 1209–1216 (2011).
- Hughes, J. M. *et al.* High levels of extra-group paternity in a population of Australian magpies *Gymnorhina tibicen*: evidence from microsatellite analysis. *Mol. Ecol.* **12**, 3441–3450 (2003).
- Kotrschal, A. *et al.* Artificial selection on relative brain size in the guppy reveals costs and benefits of evolving a larger brain. *Curr. Biol.* **23**, 168–171 (2013).
- Arnold, K. E., Ramsay, S. L., Donaldson, C. & Adam, A. Parental prey selection affects risk-taking behaviour and spatial learning in avian offspring. *Proc. R. Soc. B* **274**, 2563–2569 (2007).
- Silk, J. B., Alberts, S. C. & Altmann, J. Social bonds of female baboons enhance infant survival. *Science* **302**, 1231–1234 (2003).
- Croston, R., Branch, C. L., Kozlovsky, D. Y., Dukas, R. & Pravosudov, V. V. Heritability and the evolution of cognitive traits. *Behav. Ecol.* **26**, 1447–1459 (2015).

Supplementary Information is available in the online version of the paper.

Acknowledgements We thank E. Russell and the late I. Rowley for access to their life-history records, and for allowing us to continue work on their Guildford magpie population; A. Wolton for help with fieldwork; R. Lymbery for help with statistical analyses; and N. Boogert and A. Young for helpful comments and discussion. This work was funded by an ARC Discovery grant awarded to A.R.R., A.T. and M. B. V. Bell, and a University of Western Australia International Postgraduate Research Scholarship and Endeavour Research Fellowship awarded to B.J.A. A.T. received additional support from a BBSRC David Phillips Fellowship (BB/H021817/1).

Author Contributions B.J.A., A.R.R. and A.T. conceived and designed the study. B.J.A. wrote the manuscript. B.J.A. and E.K.E. carried out data collection. All authors discussed results and commented on the manuscript.

Author Information Reprints and permissions information is available at www.nature.com/reprints. The authors declare no competing financial interests. Readers are welcome to comment on the online version of the paper. Publisher's note: Springer Nature remains neutral with regard to jurisdictional claims in published maps and institutional affiliations. Correspondence and requests for materials should be addressed to B.J.A. (benjamin.ashton@research.uwa.edu.au), A.R.R. (amanda.ridley@uwa.edu.au) and A.T. (alex.thornton@exeter.ac.uk).

Reviewer Information *Nature* thanks T. Bugnyar and the other anonymous reviewer(s) for their contribution to the peer review of this work.

METHODS

Data reporting. No statistical methods were used to predetermine sample size. The experiments were not randomized and the investigators were not blinded to allocation during experiments and outcome assessment.

Study site and species. The study took place in Guildford, Western Australia, between September 2013 and February 2016. The study population consists of 14 groups of ringed, habituated Australian magpies (Western Australian subspecies *Cracticus tibicen dorsalis*), with groups ranging in size from 3 to 12 individuals (for composition of study population, see Supplementary Table 23). The Western Australian subspecies breeds cooperatively and lives in territorial groups, in which the number of adults remains stable (individuals within our study population have remained in the same group since research commenced in 2013, and there have been no recordings of ringed birds moving between groups)^{26,31}. Individuals exhibit a range of cooperative behaviours such as territory defence and alloparental care³². Reproductive skew among females is very low, with all adult females typically attempting to breed each year³³, but extra-group paternity is the highest recorded for any bird species (>82%)²⁶, indicating high gene flow between groups. All of the group territories for our study population are located in urban parklands. Although individuals have access to food from anthropogenic sources, it is worth noting that all territories cover similar habitats and none contain dumps or landfills that could provide a glut of food sources.

The majority of birds within our study population are colour-ringed and habituated to close human observation, allowing us to present cognitive tests to most individuals. Individuals are trained to hop onto electronic top-pan scales in return for a crumb of mozzarella cheese, allowing us to collect daily records of individual body mass. Mozzarella was also used as the food reward in the cognitive tests. Weekly behavioural focal follows are carried out on all individuals in the study population³³, from which foraging efficiency is calculated (defined as the mass of food (in grams), caught per foraging minute; biomass of food items was calculated using ref. 33).

Adult cognitive test battery. We carried out a series of cognitive tests on 56 adult Australian magpies. The battery consisted of four tasks designed to measure inhibitory control, associative learning, reversal learning and spatial memory (Extended Data Fig. 1a–c). All individuals were tested on the tasks in this order. We chose these tasks, because (i) they target well-understood and widely studied cognitive traits spanning cognitive domains^{11,20,34} and (ii) they are likely to be highly ecologically relevant: spatial memory is likely to be important in remembering locations of resources and territory boundaries³⁵, while associative and reversal learning enable the acquisition and flexible readjustment of predictive contingencies between cues in the environment, including learning from conspecifics' behaviour^{11,34,36,37}. Finally, inhibitory control, the ability to inhibit prepotent responses, has been implicated in adaptive decision-making in both social and asocial contexts^{16,25,38}.

Inhibitory control. To quantify individuals' ability to inhibit ineffective prepotent responses towards food, we presented individuals with a detour reaching task²⁵. This consisted of a transparent open-ended cylinder (13 cm length, 5 cm diameter; Extended Data Figs 1a, 4a) in which a food reward was placed in the centre. Test subjects were presented with the task such that the open ends of the cylinder were facing away from the individual's direction of gaze. A trial was deemed successful if the test subject inhibited the prepotent response of pecking the transparent cylinder, and detoured around to the open ends of the cylinder to gain access to the food reward. Once an individual successfully detoured to the open ends of the cylinder without pecking the transparent walls three times in a row, it was considered to have succeeded at the inhibitory control task. The number of trials taken to succeed was the measure of success. Trials were carried out at one-minute intervals with a maximum of 10 trials, and when possible, all trials were carried out on the same day. Individuals that failed to pass were assigned the maximum score of 10 for statistical analyses. Other studies using the detour reaching task commonly include a training phase in which test subjects are presented with an opaque tube before being exposed to the transparent tube (for example, ref. 25). We did not include the opaque phase in our study, because it generates difficulties in interpretation: success in the transparent condition could be linked to inhibitory control, or could result from the continued application of a learned rule: pecking at the open ends of the cylinder was rewarded in the opaque condition, so individuals may persist with this behaviour in the transparent condition.

Associative learning. To test associative learning, we used a colour-discrimination task consisting of a wooden foraging grid (31 × 9 × 4 cm) containing two wells (3.5 cm diameter, 2.5 cm deep; Extended Data Fig. 1b). The presence of only two wells allowed experimental trials to be carried out quickly, reducing the chance of non-focal birds detecting and approaching the task. The wells were covered with PVC lids that fitted exactly into the wells, and were held in place by elastic bands that were threaded through drilled holes in the lids and fastened to either side of the well (Extended Data Fig. 5). This created an axis on which the lids could swivel when pecked. Birds were first trained to search the wells using a shaping

procedure similar to what is described in ref. 39: magpies could gain access to a food reward (a small amount of grated mozzarella cheese) by first being exposed to the wells without any lids covering them, second with the lids partially covering the well, and third with the lid fully covering the well. Lid colour in the training phase was yellow, a colour not used in any of the experimental trials. Once a bird had successfully searched the wells when fully covered by lids three times in a row, it moved onto the experimental trials of the associative learning task.

During experimental trials, the wells were covered by either a dark-blue or light-blue lid. One of these two colours was randomly assigned to be the rewarded colour for each of the test subjects. We used dark and light shades of one colour, rather than distinct colours (for example, red versus yellow), in order to minimize any potential effects of past experience with particular colours on task performance⁴⁰. Following ref. 20, test subjects were allowed to search both wells in the first trial to demonstrate that only one of the wells contained a food reward. In all subsequent trials, the bird was only allowed to search one well before the task was removed. Test subjects had a maximum of one minute to complete the task. There was a minimum interval of one minute between trials (mean ± s.d. = 1.06 ± 0.35 min; range = 1–6 min) with a maximum of 50 trials per individual per day; differences in inter-trial interval were unrelated to group size (Spearman's correlation, $r_s = 0.048$, $P = 0.121$, $n = 1,027$ trials). If the maximum number of trials was reached on one day, trials were continued the following day. To ensure that the colour was the cue being associated with a food reward, rather than location, the position of the baited well was pseudo-randomized and was never on the same side of the foraging grid for more than three consecutive trials. Furthermore, both wells were wiped with cheese to control for olfactory cues. Following ref. 20, an individual was considered to have succeeded at the task when it pecked the rewarded colour in at least 10 out of 12 consecutive trials (10/12 correct represents a significant deviation from random binomial probability; binomial test: $P = 0.039$). The number of trials taken to reach this criterion (including the final 12 trials) was the associative learning score.

Reversal learning. Twenty-four hours after the completion of the associative learning task, individuals were tested on a reversal learning task. The same foraging grid was presented; the only difference being the colour of the rewarded lid was reversed from that of the associative learning task. Otherwise the experimental protocol and the criteria for passing were the same as the associative learning task described above.

Spatial memory. The spatial memory task consisted of a wooden foraging grid (40 × 36 × 4.5 cm), containing eight wells (3.5 cm diameter, 2.5 cm deep). The wells were equidistant from one another (6 cm between wells) and were arranged in three rows, with the first row containing two wells, the second row four wells and the third row two wells (Extended Data Fig. 1c). The wells were covered with light-blue lids that were the same as those used in the associative and reversal learning experiments, so no training phase was necessary. Following the protocol described in ref. 20, the experiment consisted of five phases. One of the eight wells was randomly chosen to be the baited well, containing a food reward in all phases of the experiment. The first phase was a 'baseline' trial in which individuals searched the foraging grid for the baited well. Once the test subject had located and eaten the food reward, the foraging grid was removed. Five minutes after the baseline trial, the second 'training' phase was carried out, during which the same well was baited, and the test subjects had to search for the food reward again. The third and fourth phases were test trials in which subjects were presented with the foraging grid 24 and 48 h after the training phase, respectively. The cumulative number of wells searched before locating the rewarded well in the third and fourth phases of the experiment was the spatial memory score, thus higher scores indicate worse performance. To control for olfactory cues, the foraging grid was presented a fifth time as an unrewarded 'probe' trial²⁰ (five minutes after the 48-h post-training phase trial), in which the grid was rotated 180 degrees, and without a baited well. The foraging grid would appear identical to the magpie, but the position of the previously baited well would be on the opposite side of the grid compared to the other phases of the experiment. If the test subject had remembered the location of the rewarded well in the experimental phases, one would predict that it would search the well opposite the previously baited well. If the test subjects were using olfactory cues to locate the rewarded well, one would predict that the previously baited well would be searched first. To investigate whether birds were using olfactory cues to locate the food reward a paired *t*-test was carried out to see whether there was a difference between the number of wells searched in the 48-h post-training phase trial and the fifth trial (see Supplementary Discussion for results). The number of wells searched in the fifth presentation did not count towards the spatial memory score.

To ensure that we tested individual performance, and to control for the potentially confounding effect of social learning or social interference, all trials were carried out in conditions as close as possible to social isolation. This was achieved by ensuring that no other birds were within 10 m of the bird being tested. This was

possible as magpies often forage over 10 m away from each other. If another bird approached during an experimental trial, the trial was discontinued. To investigate whether individual performance was affected by social learning, we included 'test order' as an explanatory term in the analyses investigating factors affecting performance. This allowed us to verify that individuals tested later within a group (who could therefore have had opportunities to observe previous group members being tested) did not perform better than those tested earlier. Tasks were placed directly in front of the test subjects. Experiments were run between 05:00 and 10:00 and were recorded live by the observers (B.J.A. and E.K.E.). One observer recorded individual performance, while the other recorded neophobia (defined as the time elapsed between the test subject first came within 5 m of the apparatus and first touching the apparatus), the time spent interacting with the task, and anti-predator behaviour within the group.

Individual consistency in adult performance—repeatability testing. Apparent individual differences in cognitive performance in a single round of testing could simply result from stochastic variation or extraneous confounding variables⁴¹. To determine whether individuals were consistent in their performance, we carried out a second test battery two weeks after the first test battery to test the repeatability of adult cognitive performance. To ensure that individuals could not simply use memory of visual cues from the first round of testing to solve tasks in the second round, we changed the visual appearance of each task, while keeping the causal structure of the task the same. In the associative and reversal learning task the colour of lids was changed to dark green and light green. In the spatial memory task, the location of the rewarded well was changed from the first test battery. In the inhibitory control task, rather than using an open-ended cylinder, we presented food rewards behind a transparent curved wall (30 cm length, 10 cm height; Extended Data Fig. 4d). Other than these changes in the appearance of the tasks, the protocol and criteria for passing were exactly the same as the first cognitive test battery.

Juvenile cognitive test battery. Juveniles were presented with a battery of four cognitive tasks at three ages: 100, 200 and 300 days after fledging (Extended Data Fig. 4). Cognitive testing commenced at 100 days after fledging, because by this time, individuals spend most of their time foraging independently³¹. The same four cognitive traits (inhibitory control, associative learning, reversal learning and spatial memory) were quantified at each age by presenting individuals with cognitive test batteries containing causally identical but visually distinct versions of each of the four tasks (Extended Data Fig. 4). This ensured the same cognitive traits were tested at each age, while making sure the tasks were not the same in appearance, minimizing the potentially confounding effect of memory.

To quantify inhibitory control at 100 days after fledging, we presented individuals with the same detour reaching task used in the adult cognitive test battery (Extended Data Figs 1a, 4a), and used the same experimental protocols and criteria for succeeding at the task. At 200 days after fledging, rather than using a transparent open-ended cylinder, food rewards were presented behind a transparent curved wall (32 cm length, 12 cm height; Extended Data Fig. 4d). At 300 days after fledging, individuals were presented with a detour reaching task consisting of a transparent 'umbrella'; the food reward could be accessed by detouring underneath the transparent Perspex dome (55 cm circumference, 8 cm height; Extended Data Fig. 4g). Regardless of the differences in appearance, the criteria for passing the inhibitory control tasks at 200 and 300 days after fledging were the same as for the first detour reaching task presented at 100 days after fledging.

Spatial memory was quantified at 100 days after fledging by presenting individuals with a wooden foraging grid (40 × 26 × 4 cm) containing six wells (3.5 cm diameter, 2.5 cm deep) covered with lids as used for the associative and reversal learning tasks (Extended Data Fig. 4c). One of the six wells was randomly assigned to be the rewarded location for all phases of the experiment. The spatial memory experiment consisted of two phases; first the grid was presented in a baseline trial, in which individuals were able to search for the rewarded location. A memory trial was carried out five minutes later, during which individuals were presented with the foraging grid in the exact same arrangement a second time. The number of wells searched before locating the food reward in the memory trial was the spatial memory score. At 200 and 300 days after fledging the same experiment was carried out, although we ensured that a different well was randomly assigned as the rewarded location (Extended Data Fig. 4f, i).

We were unable to quantify individual performance in associative and reversal learning at 100 days after fledging, because individuals took a prohibitive amount of trials to complete the tasks (no individuals succeeded within 20 trials). Associative learning was quantified at 200 days after fledging by presenting test subjects with a wooden foraging grid (41 × 35 × 4 cm) containing 20 wells (3.5 cm diameter, 2.5 cm deep), covered with 20 plastic lids; 10 a light-blue colour and 10 a dark-blue colour (Extended Data Fig. 4e). Wells covered with lids of one colour were randomly assigned to be rewarded for the duration of the trials, when these lids were pecked, a food reward could be accessed. Test subjects were considered to have passed the

associative learning task when they chose the rewarded well in eight out of the first nine wells searched; this represents a significant deviation from binomial probability (binomial test: $P = 0.039$). The number of trials taken to reach this criterion was the associative learning score. Individuals received a maximum of 10 trials; those that failed to pass were assigned a score of 10 for statistical analyses. At 300 days after fledging rather than light- and dark-blue lids, light- and dark-green lids were used (Extended Data Fig. 4h). Other than the change in lid colour, all protocols and criteria for passing remained the same.

At each developmental stage (200 and 300 days after fledging), reversal learning was quantified 24 h after the successful completion of the associative learning task. The protocol and criteria for passing the reversal learning tasks were the same as the associative learning task, except that the previously unrewarded colours were now rewarded.

Similar to the cognitive testing carried out on adults, all trials were carried out on juveniles in isolation. This was achievable because by 100 days after fledging, juveniles are foraging independently.

Life-history data collection. To obtain measures of reproductive success for individual birds, we collected life-history data on the study population over three years. This was collected through a combination of behavioural focal follows on individuals, brood observations and ad libitum data collected while watching the whole group (for details see refs 31, 33). The extensive life-history database developed from these observations allowed us to determine the number of hatched clutches, the number of nestlings that fledged and the number of fledglings surviving to independence for each adult female in the study population per annum. In addition, the behavioural focal observations, brood observations and ad libitum data allowed us to quantify the amount of food adults provisioned to young. Fledglings were considered to have survived to independence when they reached three months after fledging. At this age, magpies forage independently and are fed by adults infrequently³¹. In addition to these three proxies of fitness, we also recorded the number of breeding attempts by females—a breeding attempt was considered to have occurred if a female was observed incubating on a nest. The mother was assumed to be the bird incubating at the nest (there is no evidence of egg-dumping or shared incubation in this subspecies, so there was only ever one female incubating a given nest). Groups were visited at least once a week during the breeding season, providing accurate measurements of the number of breeding attempts made per female, and accurate hatch and fledge dates for all nests. Clutches were considered to have hatched when adults started bringing food to the nest, or if we could see young in the nest. As many nests were upwards of 20 m high, we were unable to accurately determine clutch size to use as an additional measure of reproductive success.

All methods were performed in accordance with the guidelines and regulations of the University of Western Australia, and were approved by the University of Western Australia Animal Ethics Office (RA/3/100/1272).

Statistical analyses. Adult cognitive performance. To determine the factors influencing individual variation in cognitive ability, we analysed cognitive performance using generalized linear mixed models (GLMM) with either a Poisson distribution with a logarithmic link (inhibitory control) or a negative binomial distribution with a logarithmic link to account for overdispersion (associative learning, reversal learning and spatial memory). Cognitive performance was measured as the number of trials taken to pass the task. In addition to the potential cognitive demands of living in larger social groups, it is possible that indirect effects of group size on energy intake and task attention could generate group-size effects on cognitive performance^{41,42}. We therefore included neophobia (defined as the time taken to interact with the task once being within 5 m of it), body mass and foraging efficiency as explanatory terms in the analysis, as well as sex, the sex ratio of males to females in the group, the order tested within the group and group size. Group identity was included as a random term in all models.

To determine whether body condition (body mass, accounting for skeletal size) could explain the variation in cognitive performance, we included mass (in grams) and tarsus size (in mm; a common analysis of skeletal size in birds) as covariates in an additional analysis on a subset of individuals for which both of these morphometric analyses were available ($n = 27$). Dominance status was not included as an explanatory variable, because there is no clear dominance hierarchy within magpie groups. Adult age and immigration status were not included as explanatory variables, because the fledge date and natal origins of some of the adults in our population is unknown (Australian magpies are very long-lived, living up to 25 years in the wild³²). We note that among the birds for which the complete life-history is known ($n = 19$ individuals), there has been no movement between groups.

We analysed our data using a model selection process; terms were ranked in order of their corrected quasi-information criterion (QICc) values (the lowest QICc value has the greatest explanatory power⁴³). If a term was more than two QICc units smaller than any other term, then this was judged to explain the observed

relationship in the data better than any other term. If there was more than one term with $\Delta QICc < 2$ from the 'best' term, had confidence intervals that did not intersect zero and explained more variation than the basic model (the model containing no predictors, just the constant and the random terms), then model averaging was carried out on this top set of models as described in ref. 44. All statistical analyses were carried out using IBM SPSS Statistics software (v.22).

To examine the relationship in performance across tasks, we conducted Spearman's rank pairwise correlations between all four tasks. To determine whether a general cognitive factor explained cognitive performance across all four tasks, we performed a principal component analysis with a varimax rotation. Only principal components with an eigenvalue > 1 were extracted from the analysis. A general intelligence factor has been argued to exist when all four tasks positively contributed to the first principal component and explain $> 30\%$ of total task variance²². Following ref. 20, to assess whether the tasks were associated with the first principal component by chance, we compared the mean and standard deviation of the first component factor weights to the 95% confidence intervals of the means and standard deviations of the first component factor weights from 10,000 simulations. For each simulation, performance within each task was randomized between individuals (using the `randomizeMatrix` function in the `picante` R package⁴⁵), a principal component analysis was performed, and the mean and standard deviation of the first component factor weights were obtained. The 95% confidence intervals were then calculated from the stored means and standard deviations from all the simulations.

Statistical analyses used to calculate estimates of repeatability in cognitive performance between the first and second cognitive test batteries were carried out in R (v.3.1.1, <http://www.r-project.org>) with the `rptR` package⁴⁶ using a linear mixed model repeatability estimate, with a restricted maximum likelihood function (REML).

Juvenile cognitive performance. A series of GLMMs were carried out to determine which factors affect cognitive performance in each task. Model selection (using the same approach as for analyses on adult cognitive performance) was then used to determine the most significant predictors of performance in each of the cognitive tasks⁴³.

At 100 days after fledging, the response terms used were cognitive performance, in the detour reaching task this was the number of trials until passed and in the spatial memory task it was the number of wells searched. As these were count data, GLMMs with a Poisson distribution were used. The relationship between performance in the detour reaching task and the spatial memory task were examined using a Spearman rank correlation. At 200 and 300 days after fledging, we found evidence of general cognitive performance in juvenile magpies (Extended Data Tables 3, 4); this parameter was therefore used as the response term for analyses investigating factors affecting cognitive performance at 200 and 300 days after fledging.

Explanatory terms included in the models were neophobia, body mass, the stage of the breeding season (early or late), the presence or absence of siblings (from the same brood), group size and the sex ratio of adult males to females in the group. We were unable to include provisioning rate from adults to fledglings as an explanatory term in analyses as these data were only available for a small subset of individuals. Group ID was included as a random term in all models.

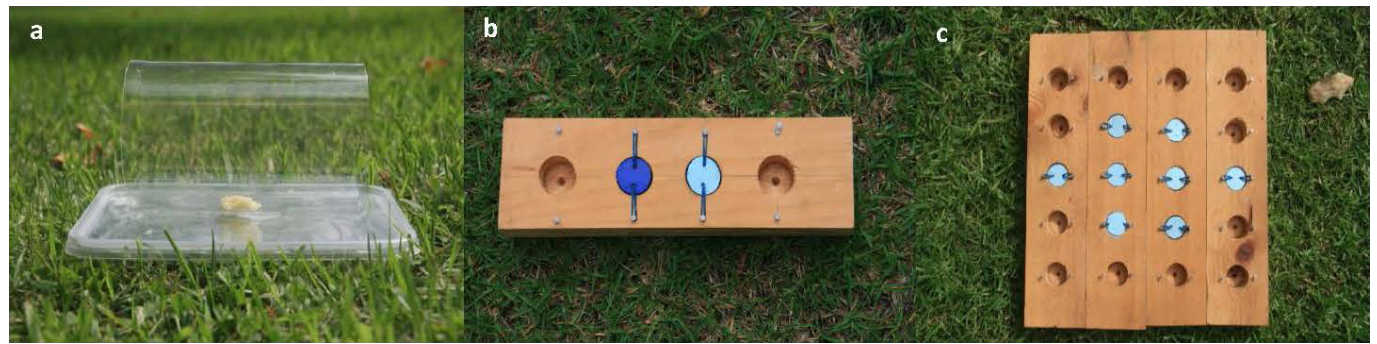
Factors affecting performance across all ages were analysed for each of the four cognitive traits quantified, using GLMMs. Four separate analyses were carried out, with cognitive performance used as the response term. Two additional analyses were carried out. First, to determine factors affecting performance across all ages for both inhibitory control and spatial memory (associative and reversal learning were omitted from this analysis as we only quantified performance at 200 and 300 days after fledging for these traits). Second, we investigated factors affecting

general cognitive performance measured at 200 and 300 days after fledging. Group ID and individual ID were included as random terms. Explanatory terms included were those used for the previous analyses. A model-selection approach was used to determine the most significant terms affecting performance.

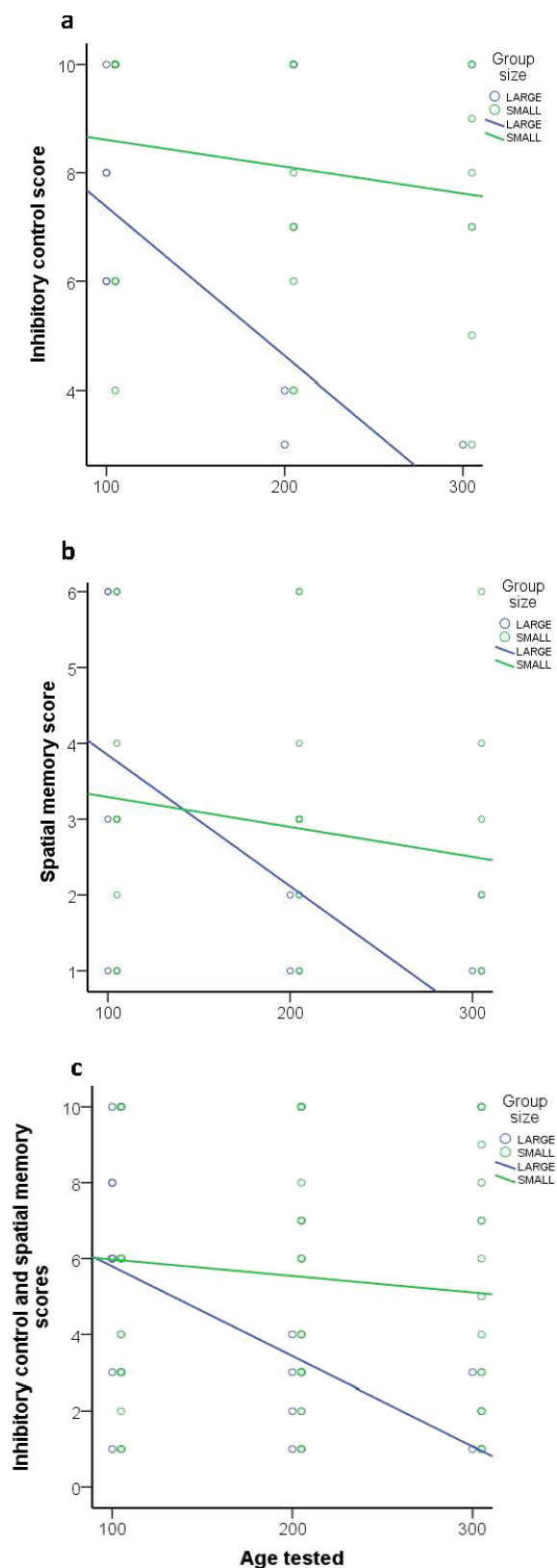
Relationship between cognitive performance and measures of reproductive success. We carried out three separate analyses to determine the factors affecting three measures of reproductive success: the average number of hatched clutches per year, the average number of nestlings fledged per year and the average number of fledglings surviving to independence per year. We carried out GLMMs, with the analysis of reproductive success as the response term, and group ID was included as a random term. Explanatory terms included in the analyses were body mass, foraging efficiency, group size, the sex ratio of the group and general cognitive performance. General cognitive performance was used as an explanatory term for cognitive performance, because the principal component analysis revealed robust evidence for its existence within females (PC1 accounted for $> 70\%$ of total variance in female task performance, Supplementary Table 25). We did not include age, because we do not know the exact fledge date for the majority of adult females in the population.

Data availability. The data that support the findings of this study have been deposited in the Dryad Digital Repository (<https://doi.org/10.5061/dryad.ph3h8>). Source Data have been provided for Figs 1–4 and Extended Data Figs 2, 3.

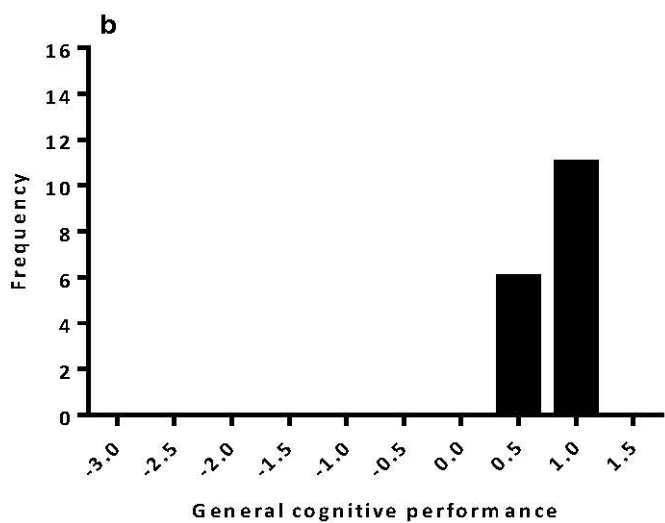
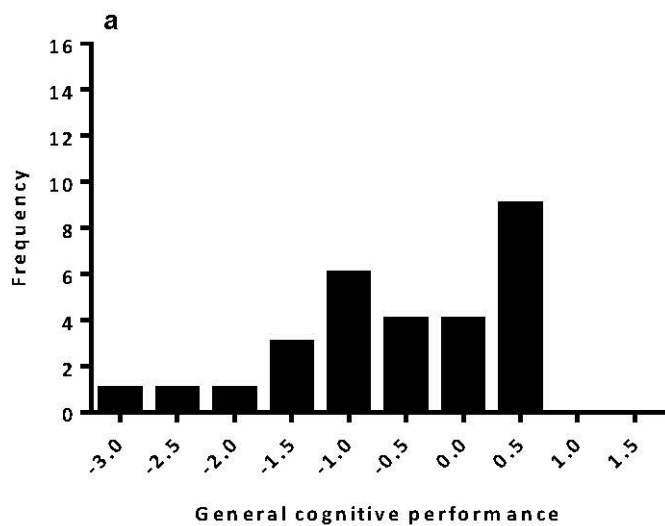
31. Pike, K. N. *How much do Helpers help? Variation in Helper Behaviour in the Cooperatively Breeding Western Australian Magpie*. MSc Thesis, Univ. Western Australia (2016).
32. Kaplan, G. *Australian Magpie: Biology and Behaviour of an Unusual Songbird* (CSIRO Publishing, 2004).
33. Edwards, E. K., Mitchell, N. J. & Ridley, A. R. The impact of high temperatures on foraging behaviour and body condition in the Western Australian Magpie *Cracticus tibicen dorsalis*. *Ostrich* **86**, 137–144 (2015).
34. Morand-Ferron, J. Why learn? The adaptive value of associative learning in wild populations. *Curr. Opin. Behav. Sci.* **16**, 73–79 (2017).
35. Sherry, D. F. in *Cognitive Ecology: the Evolutionary Ecology of Information Processing and Decision Making* (ed. Dukas, R.) 261–296 (Univ. Chicago Press, 1998).
36. Lotem, A. & Halpern, J. Y. Coevolution of learning and data-acquisition mechanisms: a model for cognitive evolution. *Phil. Trans. R. Soc. B* **367**, 2686–2694 (2012).
37. Leadbeater, E. What evolves in the evolution of social learning? *J. Zool.* **295**, 4–11 (2015).
38. Amici, F., Aureli, F. & Call, J. Fission–fusion dynamics, behavioral flexibility, and inhibitory control in primates. *Curr. Biol.* **18**, 1415–1419 (2008).
39. Boogert, N. J., Giraldeau, L.-A. & Lefebvre, L. Song complexity correlates with learning ability in zebra finch males. *Anim. Behav.* **76**, 1735–1741 (2008).
40. Rowe, C. & Healy, S. D. Measuring variation in cognition. *Behav. Ecol.* **25**, 1287–1292 (2014).
41. Griffin, A. S. & Guez, D. Innovative problem solving in nonhuman animals: the effects of group size revisited. *Behav. Ecol.* **26**, 722–734 (2015).
42. Nowicki, S., Searcy, W. & Peters, S. Brain development, song learning and mate choice in birds: a review and experimental test of the "nutritional stress hypothesis". *J. Comp. Physiol. A* **188**, 1003–1014 (2002).
43. Burnham, K. P. & Anderson, D. R. *Model Selection and Multimodel Inference: A Practical Information-Theoretic Approach* (Springer, 2002).
44. Symonds, M. R. E. & Moussalli, A. A brief guide to model selection, multimodel inference and model averaging in behavioural ecology using Akaike's information criterion. *Behav. Ecol. Sociobiol.* **65**, 13–21 (2011).
45. Kembel, S. W. *et al.* `Picante`: R tools for integrating phylogenies and ecology. *Bioinformatics* **26**, 1463–1464 (2010).
46. Nakagawa, S. & Schielzeth, H. Repeatability for Gaussian and non-Gaussian data: a practical guide for biologists. *Biol. Rev. Camb. Philos. Soc.* **85**, 935–956 (2010).



Extended Data Figure 1 | Adult cognitive test set. a–c, The cognitive test series used to quantify individual variation in inhibitory control (a), associative and reversal learning (b) and spatial memory (c).



Extended Data Figure 2 | Developmental trajectory of cognitive performance. a, b, The developmental trajectory of Australian magpies at 100, 200 and 300 days after fledging for two cognitive traits: behavioural inhibition (**a**; $n = 48$ trials) and spatial memory (**b**; $n = 46$ trials). **c,** Developmental trajectory for behavioural inhibition and spatial memory combined ($n = 94$ trials). Green dots, individuals from small groups (containing 1–7 individuals); blue dots, individuals from large groups (≥ 8 individuals). Scores are measured as either the number of trials taken to succeed at the task or the number of locations searched, so lower scores indicate better performance.



Extended Data Figure 3 | Frequency distribution of general cognitive performance in relation to group size. a, b, Frequency distribution of general cognitive performance among individuals in small groups (a; containing <8 individuals, $n = 29$ individuals) and large groups (b, >8 individuals, $n = 17$ individuals).



Extended Data Figure 4 | Juvenile cognitive test batteries. a–i, Cognitive test batteries presented to individuals at 100 (a–c), 200 (d–f) and 300 (g–i) days after fledging, containing four tasks designed to quantify inhibitory control (a, d, g), associative and reversal learning (b, e, h) and spatial memory (c, f, i). b is shown in black and white, because individuals were

unable to complete the associative and reversal learning tasks at 100 days after fledging. Red circles indicate that individuals had to search a different location at each age tested in order to obtain the food reward in the spatial memory task.



Extended Data Figure 5 | Example of the lids used in the cognitive tasks. The lids used in the associative learning, reversal learning and spatial memory tasks. The lids were held firmly in place by elastic bands,

and swivelled when pecked, allowing individuals to search wells for their contents.

Extended Data Table 1 | Principal component analysis (adults)

Task	PC1
Inhibitory control	0.703
Associative learning	0.789
Reversal learning	0.870
Spatial memory	0.841
Eigenvalue	2.582
% of total variance explained	64.56

Results of the principal component analysis for adult magpies that completed all four tasks.
All four tasks positively contributed to the first principal component extracted with an eigenvalue
>1. $n = 46$ individuals.

Extended Data Table 2 | Repeatability of cognitive performance

Task	Repeatability	SE	Confidence intervals	P
Inhibitory control	0.806	0.049	0.691, 0.882	<0.0001
Associative learning	0.970	0.01	0.946, 0.983	<0.0001
Reversal learning	0.975	0.008	0.954, 0.986	<0.0001
Spatial memory	0.932	0.021	0.879, 0.963	<0.0001

Estimations of repeatability for the first and second series of cognitive tests. Inhibitory control, $n = 56$ individuals; associative learning, $n = 46$ individuals; reversal learning, $n = 46$ individuals; spatial memory, $n = 46$ individuals.

Extended Data Table 3 | Principal component analysis (200 days after fledging)

Task	PC1
Inhibitory control	0.571
Associative learning	0.916
Reversal learning	0.941
Spatial memory	0.737
Eigenvalue	2.593
% of total variance explained	64.837

Results of the principal component analysis for magpies that completed all four tasks at 200 days after fledging. All four tasks positively contributed to the first principal component extracted with an eigenvalue > 1. *n* = 15 individuals.

Extended Data Table 4 | Principal component analysis (300 days after fledging)

Task	PC1
Inhibitory control	0.675
Associative learning	0.947
Reversal learning	0.972
Spatial memory	0.957
Eigenvalue	3.215
% of total variance explained	80.363

Results of the principal component analysis for magpies that completed all four tasks at 300 days after fledging. All four tasks positively contributed to the first principal component extracted with an eigenvalue >1 . $n = 10$ individuals.

Posterior parietal cortex represents sensory history and mediates its effects on behaviour

Athena Akrami^{1,2,3}, Charles D. Kopec^{1,2}, Mathew E. Diamond⁴ & Carlos D. Brody^{1,2,3}

Many models of cognition and of neural computations posit the use and estimation of prior stimulus statistics^{1–4}: it has long been known that working memory and perception are strongly impacted by previous sensory experience, even when that sensory history is not relevant to the current task at hand. Nevertheless, the neural mechanisms and regions of the brain that are necessary for computing and using such prior experience are unknown. Here we report that the posterior parietal cortex (PPC) is a critical locus for the representation and use of prior stimulus information. We trained rats in an auditory parametric working memory task, and found that they displayed substantial and readily quantifiable behavioural effects of sensory-stimulus history, similar to those observed in humans^{5,6} and monkeys⁷. Earlier proposals that the PPC supports working memory^{8,9} predict that optogenetic silencing of this region would impair behaviour in our working memory task. Contrary to this prediction, we found that silencing the PPC significantly improved performance. Quantitative analyses of behaviour revealed that this improvement was due to the selective reduction of the effects of prior sensory stimuli. Electrophysiological recordings showed that PPC neurons carried far more information about the sensory stimuli of previous trials than about the stimuli of the current trial. Furthermore, for a given rat, the more information about previous trial sensory history in the neural firing rates of the PPC, the greater the behavioural effect of sensory history, suggesting a tight link between behaviour and PPC representations of stimulus history. Our results indicate that the PPC is a central component in the processing of sensory-stimulus history, and could enable further neurobiological investigation of long-standing questions regarding how perception and working memory are affected by prior sensory information.

Finding long-term regularities in the environment, and exploiting them, is a critical brain function in a complex yet structured world. However, little is known about the neural mechanisms involved in estimating these regularities or their impact on memory. The history of sensory stimuli affects working memory^{10,11} and many other tasks involving sensory percepts^{12,13}. One salient example, discovered over a century ago¹⁴ and repeatedly observed in human cognition^{5,14,15}, is contraction bias, in which the representation of a stimulus held in working memory shifts towards the centre of the distribution of stimuli observed in the past (the prior distribution). Despite the ubiquity of this phenomenon, and much psychophysical and theoretical research into the use and effects of prior stimulus distributions^{2,3}, the neural mechanisms of contraction bias have not been identified.

On the basis of previous work using somatosensory stimuli⁶, and inspired by parametric working memory (PWM) tasks in primates⁷, we developed a computerized protocol to train rats, in high-throughput facilities, to perform a novel auditory PWM task (behavioural shaping code at <http://brodylab.org/auditory-pwm-task-code>). PWM tasks involve the sequential comparison of two graded (that is, analogue) stimuli separated by a delay of a few seconds. Here we used auditory

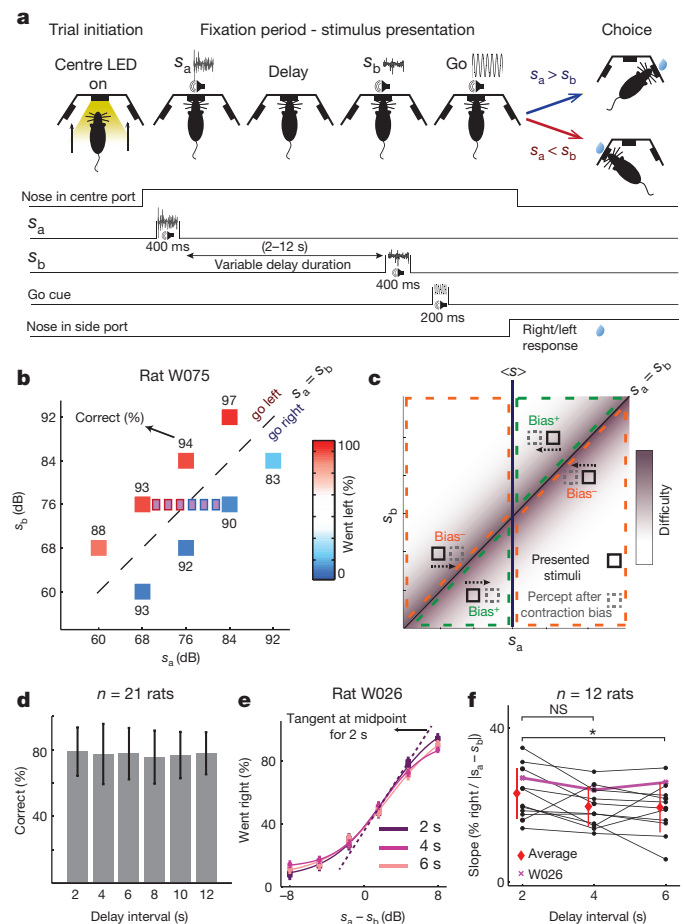


Figure 1 | Rat performance and contraction bias. **a**, Rats compared two sequentially presented auditory stimuli s_a and s_b , separated by a delay, and were rewarded for correctly reporting, through their choice of inserting their nose into the left or right ports, which stimulus was louder. **b**, Set of (s_a, s_b) pairs used in a session. In each trial, one randomly selected pair was presented. The small purple squares represent stimuli used in a subset of sessions to assess performance at the psychometric threshold. **c**, Contraction bias proposes that the presented stimuli (black boxes) drive behaviour as if s_a were closer (dashed boxes) to the average stimulus $\langle s \rangle$ (vertical midline) than its actual value. For some (s_a, s_b) pairs, this decreases their difference, and thus impairs performance (bias⁺, red), whereas for others it has the opposite effect (bias⁻, green). **d**, Overall average performance as a function of delay duration ($n = 21$ rats, mean \pm s.d. over subjects). **e**, Psychometric curves for one example rat ($n = 120$ sessions, mean \pm s.e.m. over sessions), fits to a four-parameter logistic function; see Methods). **f**, Midpoint tangent line slopes for the psychometric curves for each of 12 rats. These are significantly greater (reflecting better performance) at delays of 2 s compared with 6 s (two sample t -test: 2 versus 4 s: $P = 0.051$; 2 versus 6 s: $P = 0.045$; 4 versus 6 s: $P = 0.86$). The mean and s.d. of the 12 rats are shown in red; the results for rat W026 are shown in magenta. NS, not significant.

¹Princeton Neuroscience Institute, Princeton University, Princeton, New Jersey 08544, USA. ²Department of Molecular Biology, Princeton University, Princeton, New Jersey 08544, USA. ³Howard Hughes Medical Institute, Princeton University, Princeton, New Jersey 08544, USA. ⁴Tactile Perception and Learning Laboratory, International School for Advanced Studies (SISSA), 34136 Trieste, Italy.

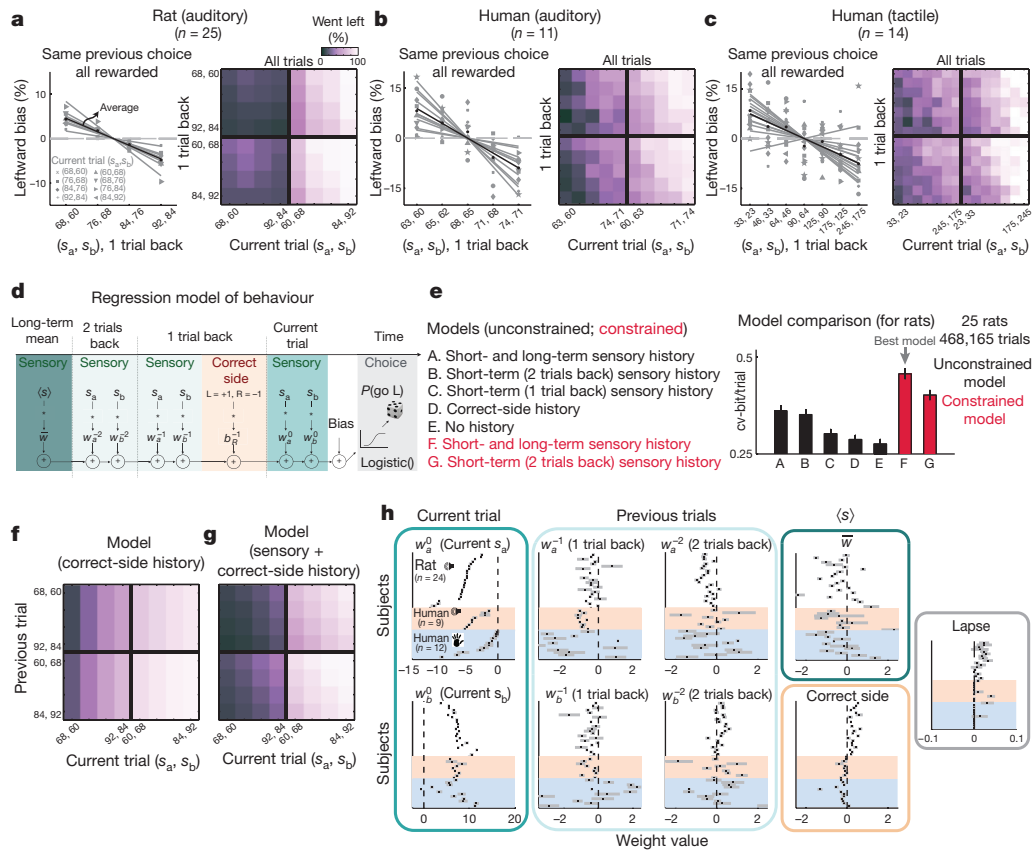


Figure 2 | Sensory history biases behaviour. **a**, Rat auditory trials. Left, percentage of trials in which rats went left minus the average value of left choices, as a function of the stimuli of the previous trial, for fixed previous trial response choice and reward. Right, percentage of trials in which rats went left for each combination of current and previous stimuli; vertical modulation indicates the previous-trial effect. **b**, As in **a**, but for human subjects in the auditory PWM task. **c**, As in **a**, but for human tactile trials. **d**, A linear weighted sum of 9 regressors is used to predict the probability ratio $\log(P_{\text{go left}}/P_{\text{go right}})$; weights are fit to best-match training data, and are evaluated on left-out cross-validation data (see Methods). Regressors: averaged stimuli over the last 20–50 trials (excluding the last two); stimuli from last two trials; correct side on last trial (that is, the side baited with a reward; when b_R^{-1} is positive, this increases the probability of going towards the previously baited side, that is, win-stay/lose-shift); current trial stimuli; overall side bias. **e**, Evaluation of model variants with different regressors

pink noise stimuli, denoted s_a and s_b ; rats were rewarded for correctly reporting which of the two was louder (Fig. 1a). Following ref. 16, the set of (s_a, s_b) pairs used across trials in a session was chosen so that neither stimulus alone contained sufficient information to solve the task (Fig. 1b). As with any magnitude-discrimination task, the smaller the difference between the stimuli, the harder the task (Fig. 1c). Classical contraction bias⁵ argues that during the delay, the memory of the magnitude of s_a drifts towards the mean of all stimuli presented (Fig. 1c, vertical line $\langle s \rangle$). Consequently, for those pairs in which s_a drifts away from the high-difficulty $s_a = s_b$ diagonal, s_a becomes more distinct from s_b in memory, so contraction bias would improve performance (bias⁺, Fig. 1c). In pairs for which s_a drifts towards the diagonal, performance would decrease (bias⁻).

This predicted pattern is observed in the behaviour of the rats during our experiments (Fig. 1b, high percentage correct for bias⁺ stimulus pairs ($s_a = 84, s_b = 92$) and ($s_a = 68, s_b = 60$), lower percentage correct for bias⁻ stimulus pairs ($s_a = 60, s_b = 68$) and ($s_a = 92, s_b = 84$)). The same pattern has been observed in monkeys⁷ and humans (Extended Data Fig. 1d, e, and refs 5, 6, 17). History-dependent effects are probably adaptive in the natural world, in which there are many long-term

(see Methods; Extended Data Fig. 6). The best model has the regressors shown in **d**. Model A has all regressors shown in **d**; in models B to E, the following regressors are progressively removed: long-term sensory history (B); stimuli of the last two trials (short-term history, C and D); previous trial correct side (E)—model E therefore has no history information. The next two models (F and G, shown in red) have the same regressors as A and B, respectively, but the weights on the s_a of the current trial plus all previous sensory-stimuli weights are constrained to sum to 1, removing one free parameter. cv, cross validation. **f**, A poor match to the data in **a** is found from the predictions of a model with the current trial and previous trial's correct side regressors only. **g**, As in **f**, but now including sensory-history regressors, which greatly improves the match to the data. **h**, Summaries of best-fit parameters over all subjects, from model F in **e**, with additional 'lapse' term. Black ticks, best-fit parameter values, per subject; grey bars, 95% confidence intervals. All panels sorted based on value of w_a^0 .

regularities. But in our laboratory task, in which each trial is generated independently, such biases, on average, produce suboptimal performance. The overall performance of the rats was robust and similar across delay intervals from 2–12 s (Fig. 1d; see Extended Data Fig. 1b, c for performance over learning). In some sessions, we used stimulus pairs that were closely spaced along s_a (Fig. 1b) to measure the psychometric discrimination threshold. This worsened slightly, but significantly, at longer delay periods (Fig. 1e, f).

Whereas variation of the delay interval resulted in small effects on overall performance (Fig. 1d), sensory history, by contrast, had a strong effect on performance. As quantified below, this effect was greater than the well-documented influence of previous rewards and choices^{18–20} (see also Extended Data Fig. 1g–i). In the trials that followed a rewarded, rightwards choice—thus holding previous choice and reward fixed—it was found that the smaller the stimuli of the previous trial, the greater the percentage of leftwards choices in the current trial (Fig. 2a, left; slope = -3.06% per decibel, linear fits to percentage leftwards minus average, $P < 0.0001$; see Extended Data Fig. 5a for slopes from $n = 1$ –7 trials back). This is consistent with a contraction bias in which the estimate of $\langle s \rangle$ is weighted towards recent stimuli¹⁷, because recent

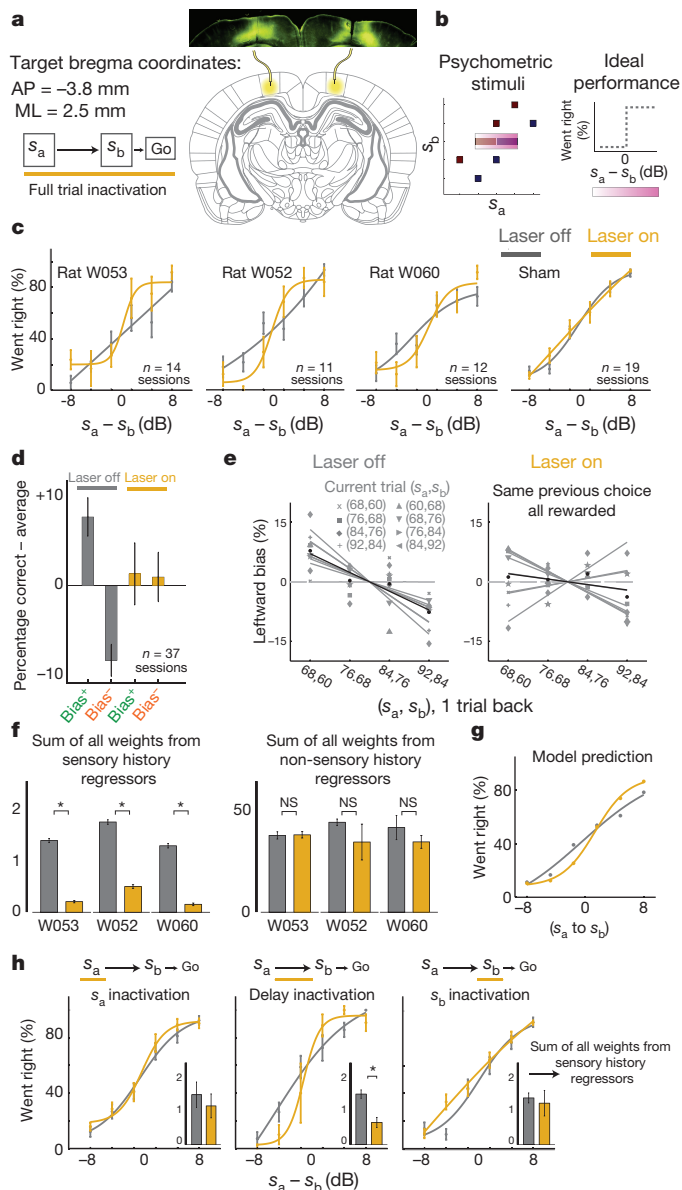


Figure 3 | The PPC is specifically necessary for the behavioural effect of previous sensory stimuli. **a**, Schematic of virus injection and full trial inactivations (delay = 2 s). The atlas panel is taken from ref. 31. AP, anteroposterior; ML, mediolateral. **b**, Left, the stimuli included our standard (s_a, s_b) set (black) plus psychometric pairs (purple); right, the ideal psychometric performance. **c**, Psychometric curves for all rats were closer to ideal during PPC inactivation (yellow) trials than during control (grey) trials. Far right, sham inactivation in rats with optic fibres but without virus had no effect ($n = 2$). Error bars show s.e.m. **d**, Percentage correct averaged across all bias⁺ or all bias⁻ trials (Fig. 1c), relative to overall average performance. PPC inactivation eliminates the difference between bias⁺ and bias⁻ trials, or versus overall average (*t*-test, bias⁺ - bias⁻ significantly different from zero, laser off, $P < 0.00001$; laser on, $P = 0.706$; laser off versus on, $P < 0.01$; two-way analysis of variance, interaction of laser on/off and bias⁺/bias⁻: $P < 0.01$). Error bars show s.e.m. **e**, The bias induced by previous stimuli is reduced under PPC inactivation (laser off: slope of -4.74, $P = 0.0017$; laser on: slope of -1.36, $P = 0.42$; laser on versus off: $P = 0.044$). **f**, Left, PPC inactivation selectively reduces sensory-history weights in the regression model shown in Fig. 2d. Error bars show 95% confidence interval ($n = 600$, 200 iterations of threefold cross-validation; $*P < 0.01$, one-sided *t*-test). Right, sum of all other weights. See Extended Data Fig. 9 for individual weights. **g**, Reducing sensory-history weights in the model is sufficient to improve psychometric performance, comparable to experimental data (c). **h**, Similar to c, for inactivation during either s_a (left), delay (middle) or s_b (right). The insets show the sum of all sensory-history regressors, as in f ($n = 600$). Only inactivation of the PPC during the delay produces a significant effect (permutation test, s_a , laser off versus on: $P = 0.17$; delay: $P < 0.0001$; s_b : $P = 0.18$; s_a versus delay: $P = 0.03$, s_b versus delay: $P = 0.02$).

that constraining the sum of regression weights on the s_a stimulus of the current trial plus weights on previous sensory stimuli to equal one—thus removing one free parameter from the model—produced the best performance on cross-validation data (Fig. 2e, red; see Extended Data Fig. 6 for all models and comparisons; the best-fitting model, for every individual rat, had the regressors in Fig. 2d). Sensory history was essential in accounting for behaviour (Fig. 2f, g): examining the weights in the regression model (Fig. 2h) shows that those for sensory history are significantly larger than those for correct side history ($P < 0.001$), and have a greater impact on behaviour (Extended Data Fig. 6g).

It has been proposed that the PPC is critical for working memory (refs 8, 9, 28, but see also refs 29, 30), and therefore we examined its role in our task. We injected bilaterally an AAV virus that drives expression of the light-activated inhibitory opsin halorhodopsin eNpHR3.0, under the CaMKII α promoter (centre of injection, anteroposterior -3.8 mm and mediolateral 2.5 mm from the bregma, Fig. 3a, Extended Data Fig. 7a). Sharp optical fibres were inserted at the centres of injection sites to deliver laser illumination, and we inactivated the PPC during a randomly chosen 20% of trials. To best probe for any small effects, we included psychometric stimuli (Figs 1b and 3b).

Expecting a performance impairment⁸, we were surprised to instead observe an improvement in psychometric performance in all rats tested (Fig. 3c). However, the effect was not simply an overall performance improvement: looking beyond the psychometric stimuli, although performance was indeed improved with respect to control on bias⁻ trials, PPC silencing instead impaired performance on bias⁺ trials (Fig. 3d). Moreover, the difference between bias⁺ and bias⁻ trials was eliminated, as was their difference from control average performance (Fig. 3d, Extended Data Fig. 9a). Similarly, bias as a function of the stimuli of the previous trial was markedly reduced (Fig. 3e, laser off: $P = 0.42$; laser on: $P = 0.0017$; laser on versus off: $P = 0.044$, see Extended Data Fig. 8 for effect on history matrices). Fitting our regression model separately to the set of laser on versus off trials, we found that PPC inactivation significantly reduced sensory-history regression weights (Fig. 3f), and no other regression terms were significantly affected (individual weights in Extended Data Fig. 9). A model with reduced sensory-history effects as in Fig. 3f was sufficient to reproduce the experimental data (Fig. 3g). Therefore, PPC silencing appeared to have no impact on working memory, but specifically and substantially

small values make it more likely that the current s_a is perceived as small, increasing the likelihood of an $s_a < s_b$ (leftwards) response. Figure 2a, right shows that the same effect occurred across all combinations of current and previous trial stimuli from our standard stimulus set ($|s_a - s_b|$ fixed at 8 dB; see Extended Data Fig. 3 for $n = 1-5$ trials back, and Extended Data Fig. 4 for controlling for action and reward). Similar effects were found in human auditory (Fig. 2b) or tactile (Fig. 2c) versions of the task, and increased for larger delay intervals^{21,22} (Extended Data Fig. 2). To simultaneously take into account effects across several previous trials of the history of rewards, choices and stimuli, we fit logistic regression models with these variables as regressors, and compared the performance of a variety of such models on cross-validation data (Fig. 2d, Methods, Extended Data Fig. 6). Consistent with human data¹⁷, short-term (previous two trials) sensory history had a strong effect on behaviour. In addition, our large dataset revealed a smaller but nevertheless important effect of longer-term (average of previous few tens of trials) sensory history (Fig. 2e, Extended Data Fig. 5b). It has been suggested^{21,23-27} that sensory history does not add a behavioural bias independent of working memory, but instead produces a value of s_a in working memory that is a weighted average of the current stimulus and sensory history. In weighted averages, the weights sum to one. Consistent with that suggestion, we found

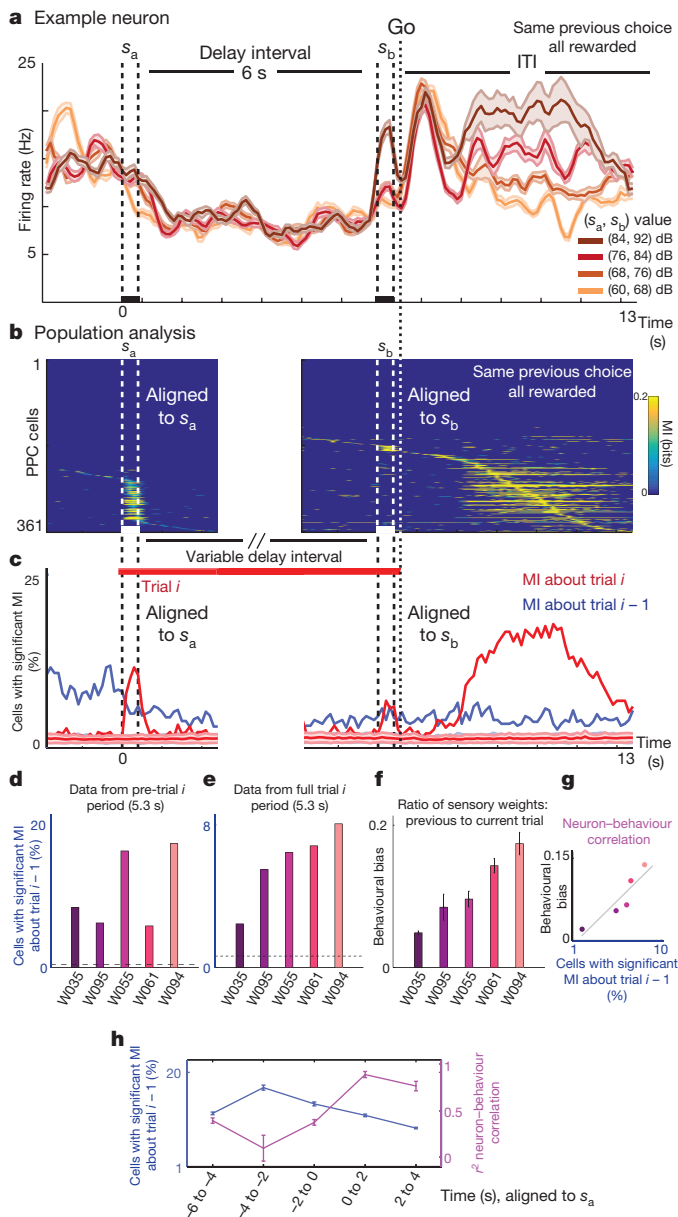


Figure 4 | PPC neurons carry more information about previous-trial sensory stimuli than about current trial stimuli, which predicts behavioural bias. **a**, Firing rate of example neuron in response to different s_a values. For clarity, the graph shows only trials in which the rat responded left after the 'go' cue, was rewarded, and the delay interval was 6 s. **b**, Mutual information (MI) between the firing rate of each neuron and stimulus pair (s_a, s_b) as a function of time. Data are from trials with delay intervals of 2–6 s. Left, aligned to the start of s_a ; right, aligned to the start of s_b . Only mutual information values significantly larger than the shuffled distribution ($P < 0.005$) are included; non-significant values are dark blue. To control for reward and choice, mutual information values were calculated using only trials with fixed choice and reward (see Methods). **c**, Summary of population analysis, showing the percentage of cells with significant coding of stimuli from trial i (red), or trial $i - 1$ (blue). **d**, Percentage of cells with significant mutual information about the previous trial, for each of five recorded rats, calculated over 5.3 s during the ITI before a new trial. The horizontal dashed line indicates the percentage of cells expected by chance from shuffled data (see Methods). **e**, As in **d**; data from 5.3 s of the new trial. **f**, Behavioural bias for individual rats, calculated as relative sensory-history weights (to weights for s_a and s_b regressors of trial i) from the best model fit. **g**, Neuron-behaviour correlation; data from **f** plotted against data from **e**, Spearman's rank correlation $r = 1.0$, $P < 0.01$, $n = 5$ rats. **h**, Calculation as in **d–g**, using 2-s windows. High neuron-behaviour correlation appears concurrently with the s_a of the new trial. Error bars show s.d. of the mean over $n = 1,000$ bootstrap samples with replacement.

reduced sensory-history effects. This reduction did not persist into future trials (Extended Data Fig. 8), and occurred with PPC inhibition during the working memory delay, but not during s_a or s_b (Fig. 3h), suggesting a focused role for the PPC in the interaction between the previous stimuli and the working memory of the current trial.

To examine whether signatures of sensory history are present in the region in which inactivation appears to cancel history effects, we made extracellular recordings that targeted the PPC during task performance, recording from 936 units in 5 rats implanted with microwire arrays. Neurons with a mean firing rate of below 2 Hz were discarded (Methods), leaving 361 units for the analysis. Most cells gave results similar to those of the example cell in Fig. 4a; their firing rates during the working memory delay did not distinguish between values of s_a held in memory, and therefore did not carry information about them. Instead, robust information about the sensory stimulus pair appeared approximately 1 s after the trial had terminated, during the inter-trial interval (ITI). We used mutual information (Methods) to quantify the amount of information, in neuronal firing rates, about which (s_a, s_b) sensory-stimulus pair was presented (Fig. 4b, c; see Extended Data Fig. 10 for mutual information about other components, including current and previous choices, rewards and s_a alone). During the ITI before a new trial, a large fraction of PPC neurons carried significant information about the previous trial stimuli (22% of analysed neurons; Fig. 4c). A smaller fraction of cells continued to code the stimuli of the previous trial both into the start of the new trial and throughout the working memory delay of the new trial (Fig. 4c, Extended Data Fig. 10b). We computed the fraction of neurons with significant mutual information about the stimuli of the previous trial, during the ITI (Fig. 4d) or the current trial (Fig. 4e), and compared this to the strength of the sensory history behavioural bias of the rat (Fig. 4f). During the new trial, but not during the ITI, these two measures were perfectly correlated (Fig. 4g, Spearman's rank correlation $r = 1$, $P < 0.01$ during current trial; $r = 0.3$, $P = 0.68$ during ITI; $P < 0.00001$ ITI versus full current trial from Steiger's Z-test). This suggests two things: first, a tight link between sensory history representations in the PPC and history biases, and second, that the PPC history representation is used during or shortly after the presentation of the new s_a (Fig. 4h), consistent with the idea that contraction bias affects the working memory representation of s_a .

Parametric working memory tasks, with their quantifiable behaviour, are well suited to investigating the effect of sensory history on perception and behaviour. Rodent versions of these tasks, with semi-automated training, are an efficient platform for causal and cellular-resolution investigation of neural mechanisms. By using this platform, we identified the PPC as an essential node in both the representation and causal effects of sensory-stimulus history. This represents a step towards a cellular-resolution understanding of long-standing questions about how sensory-stimulus history affects working memory and perception. Important issues that may now be addressed include how history representations in the PPC interact with current stimulus representations to modulate perception, how history information reaches the PPC, and which brain regions connected to the PPC are also essential nodes of the circuit.

Online Content Methods, along with any additional Extended Data display items and Source Data, are available in the online version of the paper; references unique to these sections appear only in the online paper.

Received 10 August 2017; accepted 9 January 2018.

Published online 7 February 2018.

1. Steyvers, M., Griffiths, T. L. & Dennis, S. Probabilistic inference in human semantic memory. *Trends Cogn. Sci.* **10**, 327–334 (2006).
2. Chater, N., Tenenbaum, J. B. & Yuille, A. Probabilistic models of cognition: conceptual foundations. *Trends Cogn. Sci.* **10**, 287–291 (2006).
3. Pouget, A., Beck, J. M., Ma, W. J. & Latham, P. E. Probabilistic brains: knowns and unknowns. *Nat. Neurosci.* **16**, 1170–1178 (2013).
4. Schapiro, A. & Turk-Browne, N. in *Brain Mapping: An Encyclopaedic Reference* Vol. 3, (ed. Toga, A. W.) 501–506 (Academic, 2015).

5. Ashourian, P. & Loewenstein, Y. Bayesian inference underlies the contraction bias in delayed comparison tasks. *PLoS ONE* **6**, e19551 (2011).
6. Fassihi, A., Akrami, A., Esmaeili, V. & Diamond, M. E. Tactile perception and working memory in rats and humans. *Proc. Natl Acad. Sci. USA* **111**, 2331–2336 (2014).
7. Romo, R. & Salinas, E. Flutter discrimination: neural codes, perception, memory and decision making. *Nat. Rev. Neurosci.* **4**, 203–218 (2003).
8. Harvey, C. D., Coen, P. & Tank, D. W. Choice-specific sequences in parietal cortex during a virtual-navigation decision task. *Nature* **484**, 62–68 (2012).
9. Carandini, M. & Churchland, A. K. Probing perceptual decisions in rodents. *Nat. Neurosci.* **16**, 824–831 (2013).
10. Visscher, K. M., Kahana, M. J. & Sekuler, R. Trial-to-trial carryover in auditory short-term memory. *J. Exp. Psychol. Learn. Mem. Cogn.* **35**, 46–56 (2009).
11. Lockhead, G. R. & King, M. C. A memory model of sequential effects in scaling tasks. *J. Exp. Psychol. Hum. Percept. Perform.* **9**, 461–473 (1983).
12. Ernst, M. O. & Banks, M. S. Humans integrate visual and haptic information in a statistically optimal fashion. *Nature* **415**, 429–433 (2002).
13. Körding, K. P. & Wolpert, D. M. Bayesian integration in sensorimotor learning. *Nature* **427**, 244–247 (2004).
14. Hollingworth, H. L. The central tendency of judgment. *J. Philos. Psychol. Sci. Methods* **7**, 461–469 (1910).
15. Karim, M., Harris, J. A., Langdon, A. & Breakspear, M. The influence of prior experience and expected timing on vibrotactile discrimination. *Front. Neurosci.* **7**, 255 (2013).
16. Hernández, A., Salinas, E., García, R. & Romo, R. Discrimination in the sense of flutter: new psychophysical measurements in monkeys. *J. Neurosci.* **17**, 6391–6400 (1997).
17. Raviv, O., Ahissar, M. & Loewenstein, Y. How recent history affects perception: the normative approach and its heuristic approximation. *PLoS Comput. Biol.* **8**, e1002731 (2012).
18. Busse, L. *et al.* The detection of visual contrast in the behaving mouse. *J. Neurosci.* **31**, 11351–11361 (2011).
19. Abrahamyan, A., Silva, L. L., Dakin, S. C., Carandini, M. & Gardner, J. L. Adaptable history biases in human perceptual decisions. *Proc. Natl Acad. Sci. USA* **113**, E3548–E3557 (2016).
20. Hwang, E. J., Dahlen, J. E., Mukundan, M. & Komiyama, T. History-based action selection bias in posterior parietal cortex. *Nat. Commun.* **8**, 1242 (2017).
21. Olkkonen, M., McCarthy, P. F. & Allred, S. R. The central tendency bias in color perception: effects of internal and external noise. *J. Vis.* **14**, 5 (2014).
22. Fritsche, M., Mostert, P. & de Lange, F. P. Opposite effects of recent history on perception and decision. *Curr. Biol.* **27**, 590–595 (2017).
23. Lu, Z. L., Williamson, S. J. & Kaufman, L. Behavioral lifetime of human auditory sensory memory predicted by physiological measures. *Science* **258**, 1668–1670 (1992).
24. Sinclair, R. J. & Burton, H. Discrimination of vibrotactile frequencies in a delayed pair comparison task. *Percept. Psychophys.* **58**, 680–692 (1996).
25. Preuschhof, C., Schubert, T., Villringer, A. & Heekeren, H. R. Prior information biases stimulus representations during vibrotactile decision making. *J. Cogn. Neurosci.* **22**, 875–887 (2010).
26. Papadimitriou, C., Ferdoash, A. & Snyder, L. H. Ghosts in the machine: memory interference from the previous trial. *J. Neurophysiol.* **113**, 567–577 (2015).
27. Fischer, J. & Whitney, D. Serial dependence in visual perception. *Nat. Neurosci.* **17**, 738–743 (2014).
28. Pasternak, T. & Greenlee, M. W. Working memory in primate sensory systems. *Nat. Rev. Neurosci.* **6**, 97–107 (2005).
29. Erlich, J. C., Brunton, B. W., Duan, C. A., Hanks, T. D. & Brody, C. D. Distinct effects of prefrontal and parietal cortex inactivations on an accumulation of evidence task in the rat. *eLife* **4**, e05457 (2015).
30. Raposo, D., Kaufman, M. T. & Churchland, A. K. A category-free neural population supports evolving demands during decision-making. *Nat. Neurosci.* **17**, 1784–1792 (2014).
31. Paxinos, G. & Watson, C. *The Rat Brain in Stereotaxic Coordinates* 5th edn (Elsevier, 2004).

Supplementary Information is available in the online version of the paper.

Acknowledgements We thank C. Duan, R. Low, A. Piet, L. Pinto, B. Scott and I. Witten for their comments on the manuscript. We thank K. Osorio and J. Teran for animal and laboratory support.

Author Contributions A.A. and C.D.B. conceived the project. A.A. carried out all experiments and analysed the data, with the optogenetic inactivations carried out with assistance from C.D.K. A.A. gathered human tactile data in M.E.D.'s laboratory. A.A. and C.D.B. wrote the manuscript, based on a first draft by A.A., with extensive comments from C.D.K. and M.E.D.

Author Information Reprints and permissions information is available at www.nature.com/reprints. The authors declare no competing financial interests. Readers are welcome to comment on the online version of the paper. Publisher's note: Springer Nature remains neutral with regard to jurisdictional claims in published maps and institutional affiliations. Correspondence and requests for materials should be addressed to A.A. (aakrami@princeton.edu) or C.D.B. (brody@princeton.edu).

Reviewer Information *Nature* thanks L. Busse and J. de la Rocha for their contribution to the peer review of this work.

METHODS

Rat subjects. A total of 33 male Long–Evans rats (*Rattus norvegicus*) between the ages of 6 and 24 months were used for this study. Of these, 25 rats were used for behavioural assessments, 6 were used for neural recordings, and 7 for optogenetic inactivations. All rats were assigned randomly to different experimental conditions. All statistical tests were performed between groups with similar sample sizes. No statistical methods were used to predetermine sample size. Investigators were not blinded to experimental groups during data collection or analysis. Animal use procedures were approved by the Princeton University Institutional Animal Care and Use Committee and carried out in accordance with National Institutes of Health standards.

Human subjects (auditory). 11 human subjects (8 males and 3 females, aged 22–40) were tested and all gave their informed consent. Participants were paid to be part of the study and were naive to the main conclusions of the study. The consent procedure and the rest of the protocol were approved by the Princeton University Institutional Review Board.

Human subjects (tactile). 14 human subjects (8 males and 6 females, aged 22–35) were tested. Protocols conformed to international norms and were approved by the Ethics Committee of the International School for Advanced Studies (Trieste, Italy). Subjects signed informed consent.

Rat behaviour. We developed a computerized protocol to train rats, in high-throughput facilities, to perform an auditory delayed comparison task, adapted from a tactile version⁶. All training takes place in three-port operant conditioning chambers, in which ports are arranged side-by-side along one wall, with two speakers placed above the left and right nose ports. Figure 1a shows the task structure. A visible light-emitting diode in the centre port signals the availability of each trial. Rat subjects initiate a trial by inserting their nose into the centre port, which causes the centre light to turn off. Rats must keep their nose in the centre port (fixation period), until an auditory ‘go’ cue (a 6-kHz pure tone for 200 ms) signals the end of fixation. Only after the ‘go’ cue can subjects withdraw and orient to one of the side ports in order to receive a reward of water. During the fixation period two auditory stimuli, s_a and s_b , separated by a variable delay, are played for 400 ms, with short delay periods of 250 ms inserted before s_a and after s_b . The stimuli consist of broadband noise (2,000–20,000 Hz), generated as a series of sound pressure level (SPL) values sampled from a zero-mean normal distribution. The overall mean intensity of sounds varies from 60–92 dB. Rats should judge which out of the two stimuli, s_a and s_b , had the greater SPL standard deviation. If $s_a > s_b$, the correct action is to poke the nose into the right-hand nose port in order to collect the reward, and if $s_a < s_b$, rats should orient to the left-hand nose port. Trial durations are independently varied on a trial-by-trial basis, by varying the delay interval between the two stimuli, which can be as short as 2 s or as long as 12 s. Rats progressed through a series of shaping stages before the final version of the delayed comparison task, in which they learned to: associate light in the centre poke with the availability of trials; associate special sounds from the side pokes with reward; maintain their nose in the centre poke until they hear an auditory ‘go’ signal; and compare the two s_a and s_b stimuli.

Although a substantial amount of data has been collected on all delay intervals from 2 to 12 s, in this manuscript we focus on delay durations of 2, 4 and 6 s, as most of the rats were consistently trained on these values. Training began when rats were two months old, and typically required three to four months for rats to display stable performance on the complete version of the task.

Human auditory behaviour. Similar auditory stimuli to those used for rats were used in the human version of the task. In this experiment, subjects received, in each trial, a pair of sounds played from ear-surrounding noise-cancelling headphones (brand 233621-H501). The subject self-initiated each trial by pressing the space bar on the keyboard. The first sound was then presented together with a green square on the left side of a computer monitor in front of the subject. This was followed by a delay period, indicated by ‘WAIT!’ on the screen, then the second sound was presented together with a red square on the right side of the screen. At the end of the second stimulus and after the go cue, subjects were required to compare the two sounds and decide which one was louder, then indicate their choice by pressing the ‘k’ key with their right hand (second was louder) or the ‘s’ key with their left hand (first was louder). Written feedback about the correctness of their response was provided on the screen, for individual trials as well as the average performance updated every ten trials.

Human tactile behaviour. In a separate set of experiments, run at the International School For Advanced Studies (SISSA), human subjects performed the tactile version of the task. The details of this task have been previously described and the behaviour has been characterized⁶. In brief, at each trial two noisy vibration stimuli, interleaved with a variable delay interval, were delivered to the subject’s fingertip on their left hand. Subjects viewed a computer monitor and wore headphones that presented acoustic noise and eliminated ambient sounds. To start a trial, the subject pressed the keyboard up arrow with their right hand. This triggered presentation

of the two stimuli. After a post-stimulus delay, a blue panel was illuminated on the monitor, and the subject pressed the left or right arrow on the keyboard, signifying selection of the first or the second stimulus as greater, respectively. They received feedback (correct/incorrect) on each trial via the monitor. Human experiments were controlled using LabVIEW software (National Instruments).

Stimulus set. If the first stimulus, s_a , was fixed across all trials and only the second stimulus, s_b , changed, subjects might solve the task by ignoring the first stimulus and applying a constant threshold to the second stimulus. Likewise, if the second stimulus was fixed, subjects might apply a constant threshold on the first stimulus. To prevent such alternative strategies, it is necessary to vary both s_a and s_b , and use a set of stimuli composed of pairs of s_a and s_b that guarantee that, across trials, the same value of SPL standard deviation is randomly presented for the first stimulus or the second stimulus. The stimuli along the diagonal in Fig. 1b represent such a stimulus set. A minimum of eight pairs of stimuli span a wide range of SPL standard deviation values (Fig. 1b). Using this stimulus set, if the subject were to ignore either s_a or s_b , then the maximum performance would be 63%. The mean amplitudes of stimuli were evenly distributed in a logarithmic scale (linear in dB). The diagonal line represents $s_a = s_b$; all of the stimulus pairs on one side of the diagonal are associated with the same action, and all have the same ratio of s_a to s_b . For each trial, one of these eight pairs of stimuli is randomly selected to determine s_a and s_b . **Psychometric curves.** In some sessions, we used stimulus pairs that were closely spaced along s_a (Fig. 1b) to measure the psychometric discrimination threshold. Psychometric plots (as shown in Fig. 1e and Fig. 3c) show the probability of the subject responding leftward as a function of the difference between s_a and s_b when s_b is fixed. The fits were to a four-parameter logistic function of the form

$$y(x) = y_0 + \frac{a}{1 + e^{\left(\frac{-(x-x_0)}{b}\right)}}$$

where y_0 is the left endpoint, $y_0 + a$ is the right endpoint, x_0 is the bias, and $a/4b$ is the slope. Fits were performed using the nonlinear least square regression method (nlinfit.m function) in MATLAB 2013.

Regression model of behaviour. Our semi-automated training protocol facilitated the generation of a behavioural dataset comprising 468,165 trials from 25 trained rats, which in turn enabled statistical characterization of the decision-making process. To quantify the behaviour of the rats, we carried out an analysis to weight the contributions of s_a and s_b on the current trial and several trials in the past, as well as the contributions of the history of choice and reward on the rat’s choice in the current trial. Using the data generated by concatenating several training sessions, we fit the rat’s choice with a logistic regression model that allows for the linear combinations of s_a and s_b and other desired factors. The linear combination is then mapped non-linearly into the rat’s choice; that is, the probability of trials in which the subject judged $s_a > s_b$, through a logistic function as:

$$P(\text{left}) = \text{lapse} + \frac{1 - 2\text{lapse}}{1 + e^{(-A)}}$$

where

$$A = \sum_{t=0}^n (s_a^{-t} W_a^{-t} + s_b^{-t} W_b^{-t} + b_R^{-1} + \beta)$$

where W_a^{-t} and W_b^{-t} are coefficients of the s_a and s_b regressors, respectively, from t trials back. b_R^{-1} is the correct side on the previous trial: left = +1, right = −1. This regressor captures the win-stay/lose-switch strategy. β is the baseline regressor that captures the overall (stimulus-independent) bias of the subject in calling $s_a > s_b$ (for instance, a bias against turning right, the side associated with the judgment of $s_a > s_b$). The absolute values of all of the regressors are normalized between 0 and 1. We used the log-likelihood as the cost function C :

$$C = -y \log(p) - (1 - y) \log(1 - p) = -\frac{1}{m} \sum_i^m [y_i \log(p_i) + (1 - y_i) \log(1 - p_i)]$$

The model was fit using a gradient-descent algorithm to minimize the negative log-likelihood cost function. We used the sqp algorithm in the fmincon function from MATLAB 2013. Weights were calculated using L2-regularization to prevent overfitting. The hyperparameter value (λ) was selected independently for each rat using evidence optimization, on the basis of fivefold cross-validation. Different variants of the model, which systematically study the relevance of various sensory and reward history factors^{18,19,32}, capturing not only win-stay/lose-switch but also perseveration, are discussed in Extended Data Fig. 6.

Model comparison and cross-validation. All models were fit separately for each individual rat ($n = 25$), using 200 runs of fivefold cross-validation. For each run

we calculated the log-likelihood of the test dataset given the best-fit parameters on the training set ($\log l$). We also calculated the log-likelihood of the test dataset for the mean value of %Left (the experimentally measured fraction of trials in which the rat went left). This gives us a null log-likelihood reference value ($\log l_0$). In order to quantify the efficiency of each model we defined the cross-validated bit/trial (CV-bit/trial) as the trial-averaged excess likelihood of the model compared to the null model³³:

$$\frac{(\log l - \log l_0)/n_{\text{trials}}}{\log(2)}$$

For each model, we first chose the optimal regularization value (λ) that would maximize the CV-bit/trial. To compare different models, we calculated the median value of CV-bit/trial across 10,000 fits for each subject. Because in this method we measure the log-likelihood using the cross-validated data, it automatically addresses the overfitting problem, such that if additional parameters of one model result in overfitting in the training set, it would penalize it in the cross-validated test set.

Optogenetic virus injection and fibre implantation. For optogenetic perturbation experiments, the general surgery techniques and fibre etching follow previous reports³⁴, except that we began the construction with a standard off-the-shelf 50/125 μm LC-LC duplex fibre cable (<http://www.fibercables.com>), instead of the usual FC-FC duplex fibre cables. The cable jacket, strengthening fibres and outer plastic coating (typically white or orange) were fully removed, leaving 1 cm of the fibre-optic cable and the inner plastic coating (typically clear) intact. Then 2 mm of the fibre tip (with the final layer of plastic coating still attached) was submerged in 48% hydrofluoric acid topped with mineral oil for 85 min, followed by water for 5 min (submerging 5 mm), and acetone for 2 min to soften the plastic. The plastic coating was then gently cut with a razor and removed with tweezers to reveal a 1-mm sharp-etched fibre tip. Sufficient plastic was removed, depending on the depth of the targeted site, to ensure that only the glass fibre optic would be inserted into the brain.

For viral injections, 2 μl of adeno-associated virus (AAV) (AAV5-CaMKII α -eNpHR3.0-eYFP), which drives expression of the light-activated inhibitory opsin halorhodopsin eNpHR3.0, under the CaMKII α promoter, coupled to eYFP, was lightly dyed with fast green powder and front-loaded into a glass pipette mounted to a Nanoject (Drummond Scientific) prefilled with mineral oil. The pipette tip was manually cut to a diameter of approximately 30 μm . Five closely spaced injection tracts were used for each rat. For the central injection tract (anteroposterior -3.8 mm and mediolateral 2.5 mm from the bregma, Fig. 3a; brain image from Paxinos and Watson³¹), one injection of 23 nl was administered every 100 μm in depth, starting 100 μm below the brain surface of the PPC, to a total depth of 1.5 mm. Four additional injection tracts were completed, using procedures identical to those for the central tract, with one injection at 500 μm anterior, posterior, medial and lateral from the central tract. Each injection was followed by a 10-s pause, with 1 min after the final injection in a tract before the pipette was removed. A total of 1.5 μl of virus was injected over a 30-min period consisting of approximately 160 separate injections. A chemically sharpened fibre optic (50 μm core, 125 μm cladding) was then lowered down the central injection tract to a depth of 1 mm. The craniotomy was filled with kwik-sil (World Precision Instruments), allowed to set for 10 min, and the fibre optic was secured to the skull with C&B Metabond and dental acrylic. Dental acrylic covered the entire incision site and allowed only the LC connector to protrude. Halorhodopsin expression was allowed to develop for six weeks before the behavioural testing began.

Optogenetic perturbation. The implant in the rat was connected to a 1-m patch cable attached to a single-fibre rotary joint (Princeton) mounted on the ceiling of the behavioural chamber. This was connected to a 200 mW, 532 nm laser (OEM Laser Systems) operating at 25 mW, which was triggered with a 5 V transistor-transistor logic pulse. Laser illumination occurred on 20% of randomly selected trials. See Extended Data Fig. 7 for physiological confirmation of optogenetic inactivation effects in an anesthetized rat. On the basis of our previous quantifications of optogenetic effects³⁴, we estimate that using eNpHR3.0 we can inhibit, almost entirely, neurons in a radius of approximately 750 μm from the tip of the optic fibre, amounting to a sphere of around 1,500 μm in diameter.

Recordings. Six rats were implanted with microwire arrays in their left or right PPC ($n = 3$ in lPPC, $n = 3$ in rPPC, see Extended Data Fig. 7 for histological localization of electrodes). The target region was accessed by craniotomy, using standard stereotaxic techniques (centred 3.8 mm posterior to the bregma and 2.5 mm lateral to the midline). Dura mater was removed over the entire craniotomy with a small syringe needle. The remaining pia mater, even if not usually considered to be resistant to penetration, nevertheless presents a barrier to the entry of the micro-electrode arrays, owing to the high-density arrangement of electrodes in the multi-channel electrode arrays. This dimpling phenomenon, when the electrodes are

pushing the brain cortex down without penetrating, is more pronounced for arrays with larger numbers of electrodes. In addition to potentially injuring the brain tissue, dimpling is a source of error in the determination of depth measurements. Ideally, if dimpling could be eliminated, the electrodes would move in relation to the pial surface, allowing for effective and accurate electrode placement. To overcome the dimpling problem, we implemented the following procedure. After the craniotomy was made, and the dura was carefully removed over the entire craniotomy, a petroleum-based ointment (such as bacitracin ointment or sterile petroleum jelly (Puralube Vet Ointment)) was applied to the exact site of electrode implantation. The cyanoacrylate adhesive (Vetbond Tissue Adhesive) was then applied to the zone of the pia surrounding the penetration area. This procedure fastens the pia mater to the overlying bone and the resulting surface tension prevents the brain from compressing under the advancing electrodes. Once the polymerization of cyanoacrylate adhesive was complete, over a period of few minutes, the petroleum ointment at the target site was removed, and the 32-electrode microwire array (Tucker-Davis Technologies) was inserted by slowly advancing a Narishige hydraulic micromanipulator. After inserting the array(s), the remaining exposed cortex was covered with biocompatible silicone (kwik-sil), and the microwire array was secured to the skull with C&B Metabond and dental acrylic.

During the ten-day recovery period, rats had unlimited access to water and food. Recording sessions in the apparatus began thereafter, using Neuralynx acquisition systems. Extracellular activity of the PPC neurons was manually sorted into single units and multi units, on the basis of the spike waveform and the refractory period observed in the interspike interval histogram, using SpikeSort3D software. In total 1,081 single or multi units were recorded in the PPC of 6 rats. Only neurons for which the overall mean firing rate within the session was at least 2 Hz were included in the analysis, giving a total of 456.

Neural analysis. Mutual information. To quantify the type and amount of information that the PPC neurons carry about various task parameters, we computed Shannon's mutual information³⁵. In this formulation, the amount of information that can be extracted from the firing rate of a neuron R , about the task-related parameter X can be computed as:

$$I(X, R) = \sum_x P(x) \sum_r P(r, x) \log_2 \frac{P(r|x)}{P(r)}$$

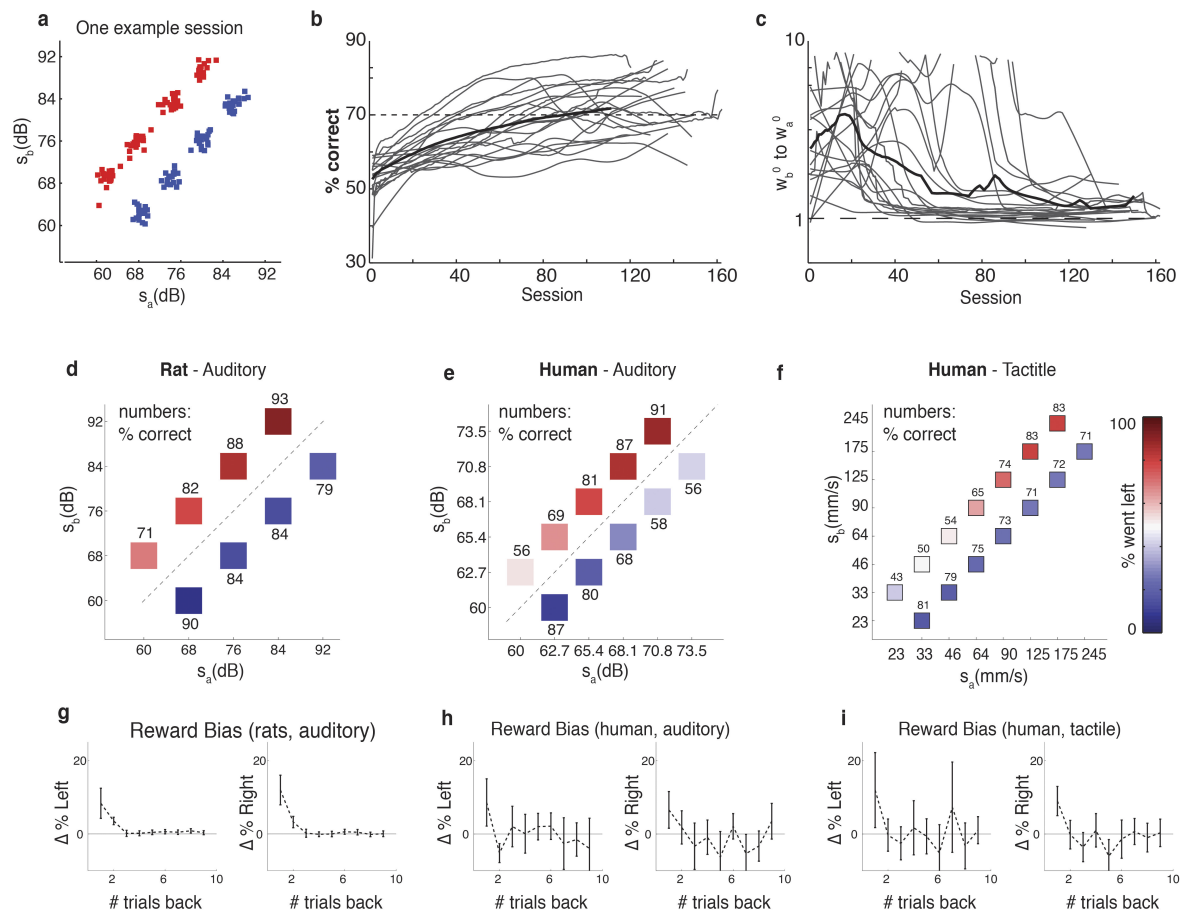
where $P(r|x)$ is the conditional probability of observing a neuronal response r given the presentation of the task parameter x , $P(r)$ is the marginal probability of occurrence of neuronal response r among all possible responses, and $P(x)$ is the probability of task parameter x . Information measured in this way quantifies how well an ideal observer can discriminate between members of a stimulus set on the basis of the neuronal responses of a single trial³⁶. For each trial, neuronal response was defined as the rate of spiking during a time window of 100 ms. The conditional probability in the above formula is not known a priori and must be estimated empirically from a limited number, N , of experimental trials for each stimulus. Limited sampling of response probabilities can lead to an upward bias in the estimate of mutual information³⁷. In order to correct for this bias, we used a combination of two techniques. First we estimated and corrected the bias based on the quadratic extrapolation method³⁸, which assumes that the bias can be accurately approximated as second order expansions in $1/N$. Then we used a bootstrap procedure (shuffling) that consists of many rounds of pairing stimuli and responses at random in order to destroy all the information that the responses carry about the stimulus. Owing to limited data sampling, the information computed using the bootstrapped responses may still be positive. The average value of the bootstrapped information was then used to estimate the residual bias of the information calculation, and was subtracted out. Moreover, the distribution of bootstrapped information values was used to build a non-parametric test of whether the corrected information computed using quadratic extrapolation method is significantly different from zero³⁹.

Using the mutual information distribution from a shuffled dataset, at each time bin, in which trials are randomly labelled, we first calculated the bin-by-bin estimate of the percentage of cells with significant value of mutual information expected by chance (Fig. 4c, shuffled data). We then computed the average over the ITI or the duration of trial i to find the mean values depicted by dashed lines in Fig. 4d, e. To control for reward and choice, mutual information values were calculated using only trials with fixed choice and reward, and only then averaged across different, separately calculated reward and choice groups.

Code availability. All software used for behavioural training is available on the Brody laboratory website at <http://brodylab.org/auditory-pwm-task-code>. Software used for data analysis is available from the corresponding authors upon reasonable request.

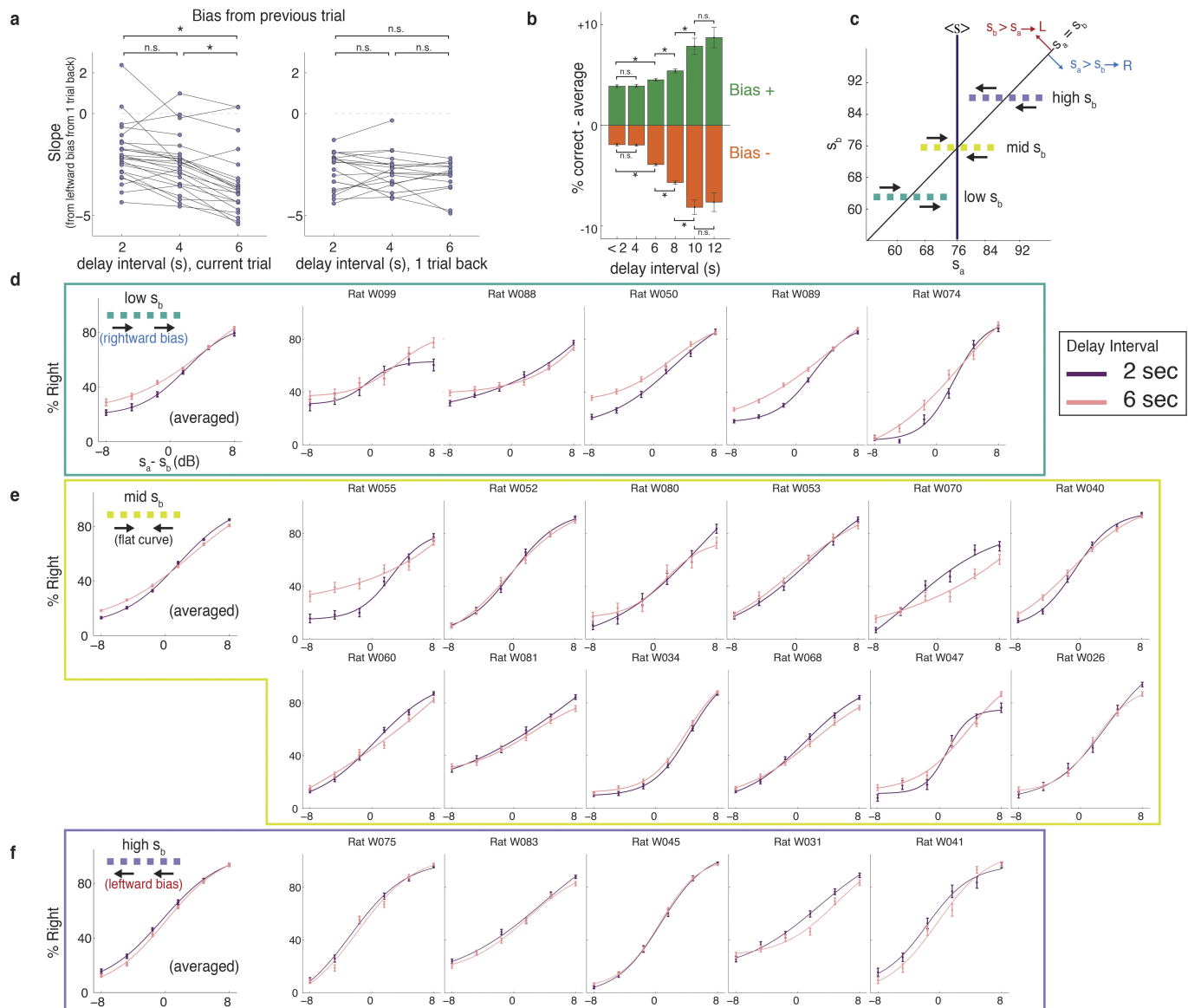
Data availability. Raw and processed data are available from the corresponding authors upon reasonable request.

32. Nogueira, R. *et al.* Lateral orbitofrontal cortex anticipates choices and integrates prior with current information. *Nat. Commun.* **8**, 14823 (2017).
33. Paninski, L., Shoham, S., Fellows, M. R., Hatsopoulos, N. G. & Donoghue, J. P. Superlinear population encoding of dynamic hand trajectory in primary motor cortex. *J. Neurosci.* **24**, 8551–8561 (2004).
34. Hanks, T. D. *et al.* Distinct relationships of parietal and prefrontal cortices to evidence accumulation. *Nature* **520**, 220–223 (2015).
35. Shannon, C. E. A mathematical theory of communication. *Bell Syst. Tech. J.* **27**, 379–423 (1948).
36. Rieke, F., Warland, D. & Bialek, W. Coding efficiency and information rates in sensory neurons. *Europhys. Lett.* **22**, 151–156 (1993).
37. Treves, A. & Panzeri, S. The upward bias in measures of information derived from limited data samples. *Neural Comput.* **7**, 399–407 (1995).
38. Nemenman, I., Bialek, W. & de Ruyter van Steveninck, R. Entropy and information in neural spike trains: progress on the sampling problem. *Phys. Rev. E* **69**, 056111 (2004).
39. Ince, R. A. A., Mazzoni, A., Petersen, R. S. & Panzeri, S. Open source tools for the information theoretic analysis of neural data. *Front. Neurosci.* **4**, 62–70 (2010).



Extended Data Figure 1 | Full stimulus set, learning curves, mean performance and reward bias. **a**, Each stimulus is composed of a series of SPL values sampled from a zero-mean normal distribution, and standard deviation of s . For each trial, SPL values are randomly drawn and therefore, owing to sampling statistics, the actual standard deviation value of the stimulus always differed slightly from its designated value. The coordinates of each small box represent the actual joint values of (s_a, s_b) for one sample training session. **b**, Individual grey lines show learning curves presented as the change in percentage correct over months of training, for $n = 25$ rats. An average rat (black line) reaches 70% of performance after 90 sessions. **c**, Learning curve presented as the ratio of the best fit weights for the second stimulus, s_b , to the first stimulus, s_a , using the model described in Fig. 2e (three-parameter, no-history version). **d**, Rat auditory working memory performance, data from 21 rat subjects (total of 468,165 trials) are grouped according to (s_a, s_b) pair but averaged across subjects and over different delay durations (2–8 s). **e**, Human auditory working memory

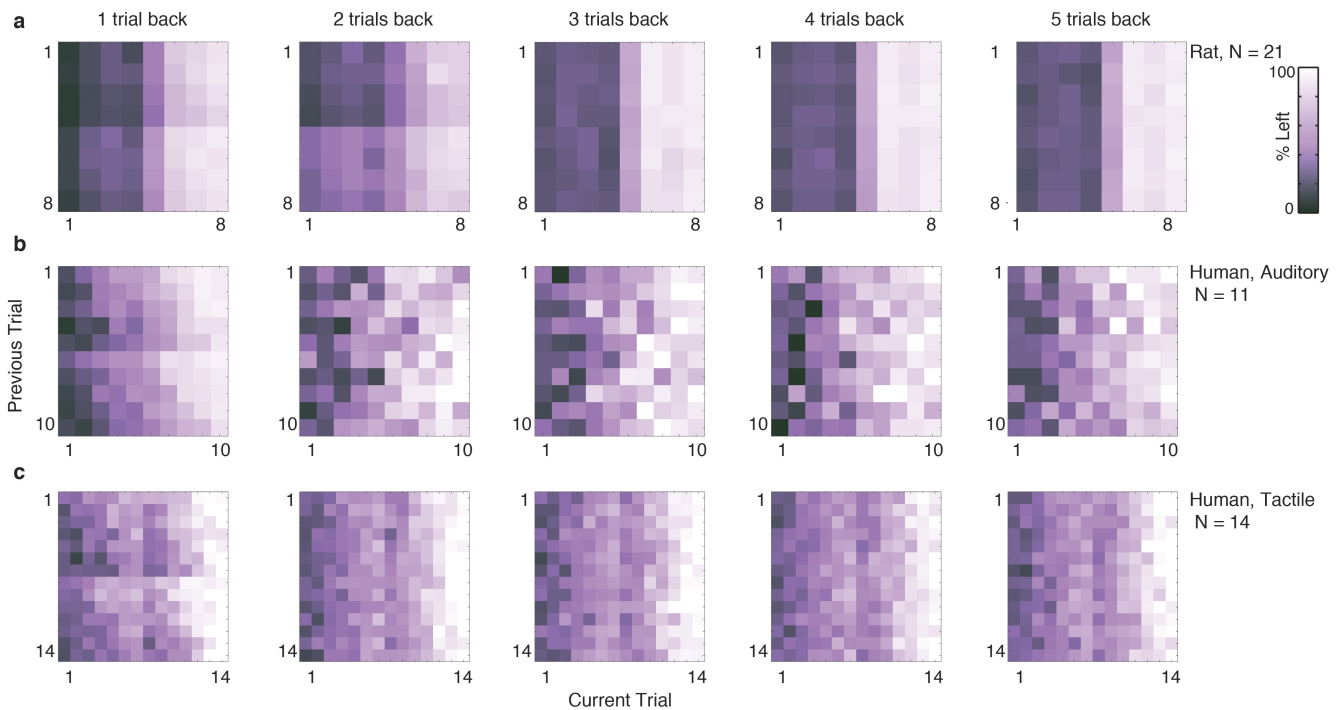
performance. For humans, the interstimulus delay varied randomly from 2 s to 6 s. (11 subjects, 12,623 trials). **f**, Human tactile working memory performance; similar to **e** but for humans engaged in the tactile version of the task. In this task, the interstimulus delay varied randomly from 2 s to 8 s. Data from 14 human subjects (total of 4,694 trials) are pooled together. **g**, Reward history bias. Left, the y axis shows, for turn-left trials and as a function of k , the percentage of subjects that went left when the k^{th} trial back was rewarded on the left, minus the percentage that went left when the k^{th} trial back was rewarded on the right. Right, the complementary plot for turn-right trials: the percentage that went right when the k^{th} trial back was rewarded on the right, minus the percentage that went right when the k^{th} trial back was rewarded on the left. Data from $n = 21$ rats. Each point shows the mean value of the bias over subjects. Error bars show 95% confidence intervals. **h**, **i**, Similar to **g** for human auditory (**h**, $n = 11$ subjects) and tactile (**i**, $n = 14$ subjects) PWM tasks.



Extended Data Figure 2 | Contraction bias grows as a function of the working memory delay interval of the current trial. **a**, Slopes from linear fits to the percentage leftward bias (as in Fig. 2a), for rats that were each trained on delay intervals of 2, 4 and 6 s ($n = 21$). The plot on the left shows the behavioural bias (percentage that went left minus the average) as a function of working memory delay interval of the current trial. The plot on the right shows the behavioural bias as a function of working memory delay interval from one trial back. Each dot represents a rat; lines connect the different delay intervals for each rat. Left: from a one-sided paired t -test, 2 versus 4 s: $P = 0.012$, 2 versus 6 s: $P < 0.001$; 4 versus 6 s: $P < 0.001$ * $P < 0.001$, one-sided paired t -test. Right: 2 versus 4 s: $P = 0.76$, 2 versus 6 s: $P = 0.37$; 4 versus 6 s: $P = 0.65$. The behavioural bias increases with greater current working memory delay period, but no significant dependence on the working memory delay period of the previous trial is found²⁶. **b**, Percentage correct averaged across all bias⁺ trials or all bias⁻ trials, relative to overall average performance, as a function of working memory delay interval on the current trial. Data are pooled from a dataset in which different rats were trained on different sets of delay intervals; data for each delay interval may therefore contain different rats than data for other delay intervals ($n = 25$ rats total). Error bars show s.d. As in **a**, behavioural effect grows as a function of the current working memory

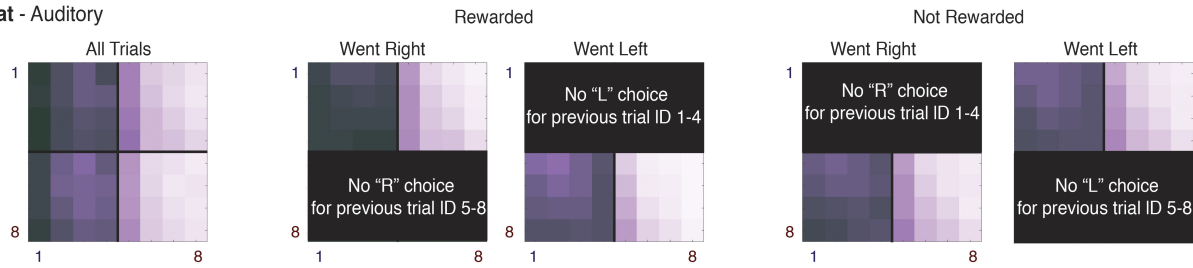
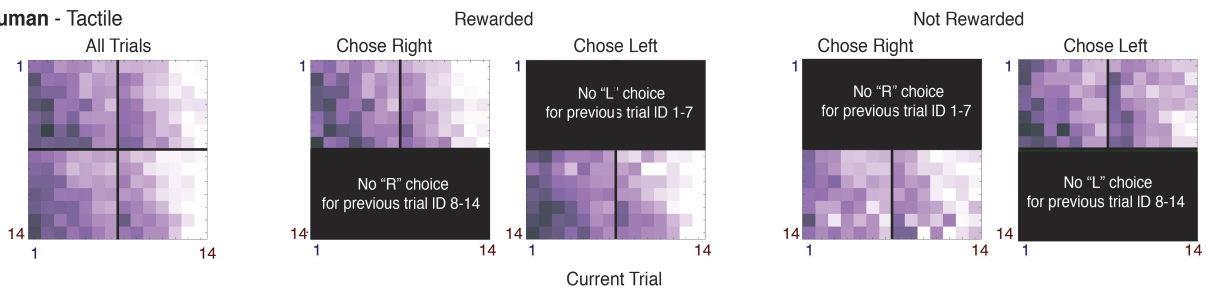
delay period. * $P < 0.001$, one-sided t -test.

c, Schematics of stimuli used for three different psychometric curves: high s_b , in which contraction bias would lead all the s_a stimuli to be treated as lower than they actually were (indicated by the leftward arrows), producing a rightward shift of the psychometric curve; mid s_b , in which contraction bias would lead all the s_a stimuli to be treated as closer to s_b than they actually were, producing a flattening of the psychometric curve; and low s_b , in which contraction bias would lead all the s_a stimuli to be treated as higher than they actually were, producing a leftward shift of the psychometric curve. **d**, Psychometric curves for low- s_b trials, averaged across rats and separately for each individual rat, for trials with a 2-s working memory delay interval, and for trials with a 6-s working memory delay interval. Curves are fits to a four-parameter logistic function (see Methods). As the working memory delay interval grows, the leftward shift predicted by contraction bias shift is more pronounced. For each individual rat, $n = 120$ sessions of data were used. Error bars show the s.e.m. over sessions. **e**, as in **d** but for the mid- s_b trials. As the working memory delay interval grows, the flattening predicted by contraction bias is more pronounced. **f**, as in **d** but for the high- s_b trials. As the working memory delay interval grows, the rightward shift predicted by contraction bias is more pronounced.



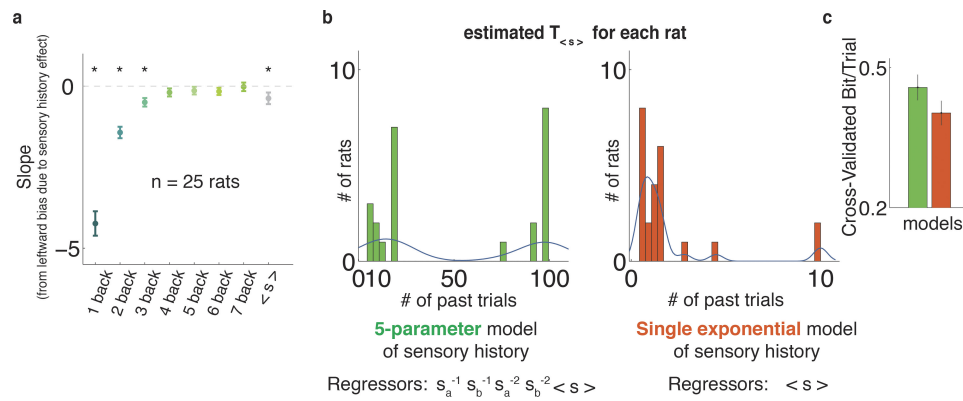
Extended Data Figure 3 | Sensory-history matrix, from one to five trials back. **a**, Stimulus-history matrix, as described in Fig. 2a, when percentage left is shown given any combination of the stimuli in the current trial (x axis) and n -trials back (y axis), $n = 1, 2, 3, 4, 5$. Trial numbers indicate pairs of (s_a, s_b), values in dB. 1: (68, 60); 2: (76, 68); 3: (84, 76); 4: (92, 84); 5: (60, 68); 6: (68, 76); 7: (76, 84); 8: (92, 84). Data from $n = 21$ rats, comprising a total of 468,165 trials used in this analysis. **b**, Similar to **a**,

for the human auditory task. Trial numbers, with values in dB: 1: (62.7, 60); 2: (65.4, 62.7); 3: (68.1, 65.4); 4: (70.8, 68.1); 5: (73.5, 70.8); 6: (60, 62.7); 7: (62.7, 65.4); 8: (65.4, 68.1); 9: (68.1, 70.8); 10: (70.8, 73.5). **c**, Similar to **a**, for the human tactile task. Trial numbers, in mm s^{-1} : 1: (33, 23); 2: (46, 33); 3: (64, 46); 4: (90, 64); 5: (125, 90); 6: (175, 125); 7: (245, 175); 8: (23, 33); 9: (33, 46); 10: (46, 64); 11: (64, 90); 12: (90, 125); 13: (125, 175); 14: (245, 175).

a. Rat - Auditory**b. Human - Auditory****c. Human - Tactile**

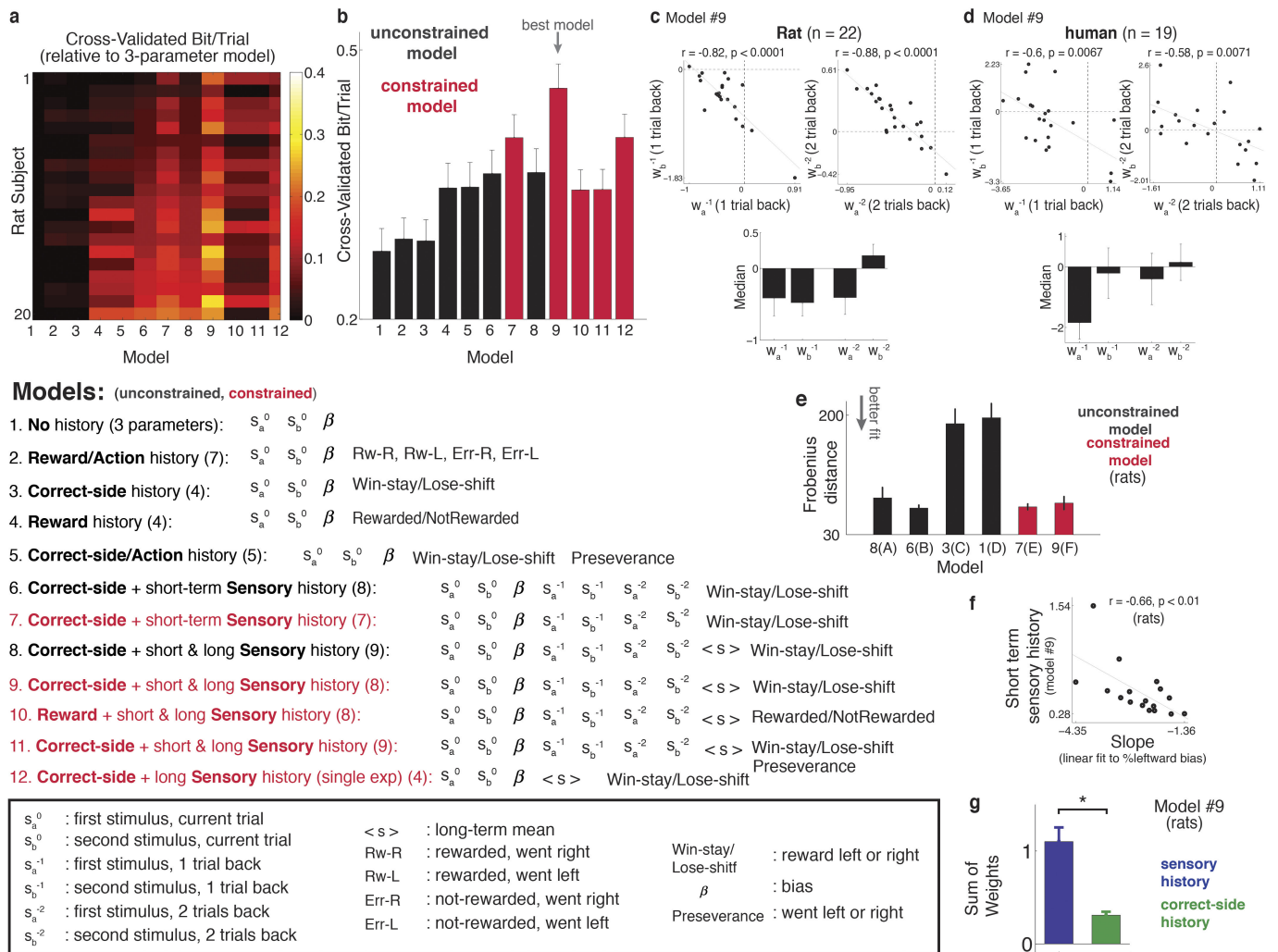
Extended Data Figure 4 | Sensory-history matrix, controlled for reward and choice. Similar to Extended Data Fig. 2, except that in this plot only trials for which the previous trial resulted in the same action and reward

status are included. Therefore, modulation by previous trial cannot be due to action history or reward history. Trial numbers are similar to those in Extended Data Fig. 3.



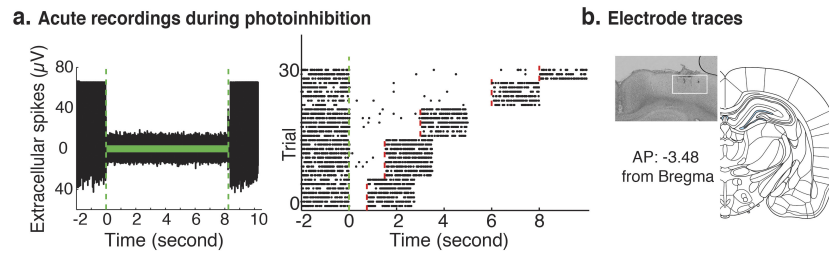
Extended Data Figure 5 | Short-term and long-term sensory history, and estimating the optimal window of $\langle s \rangle$. **a**, Slopes from linear fits to the percentage leftward bias from n -back trials ($n = 1-7$, as in Fig. 2a where $n = 1$ was used), and also $\langle s \rangle$ which is a window of 17 trials, from $n = 4$ to $n = 20$, in grey. Each point shows the mean of the slope values over $n = 25$ rats. Error bars show 95% confidence intervals. **b**, For each rat the optimal exponential window over the past trials was estimated such that it would maximize the cross-validation bit/trial measurement. Two models are compared here: green shows the distribution of τ values from a model that has five regressors to account for the sensory history—the first and second

stimulus from the two trials back and a separate exponential window over the remaining past trials (Fig. 2d). The results shown in orange are from a model containing only one regressor: a single exponential window over all the past trials accounts for the sensory history. In the single-exponential model, the best-fit value of τ is very small, practically as if only past one or two trials back are inducing most of the effect. **c**, The five-parameter model of sensory history outperforms the single-exponential model. Two hundred iterations of fivefold cross validation were used to calculate the cross-validated bit/trial (see Methods). Accordingly, each bar shows the mean of $n = 1,000$ data points. Error bars denote s.d.



Extended Data Figure 6 | Model comparison. **a**, Model comparisons, 200 runs of fivefold cross validation were performed, on data from each rat, in order to find the best fit parameters and to compare different model fits using the cross-validated bit/trial quantity defined as the relative value of the log likelihood of each model, to the null log likelihood, normalized in log2. Removing one parameter by constraining the regression weights on the s_a stimulus of the current trial plus the weights on previous sensory stimuli to add to 1 (constrained model, in red) improved performance on cross-validated data compared to the unconstrained model (in black). A total of 12 different variants of the model are compared. Regressors are described in the box. **b**, Mean value of cross-validated bit/trial for different variants of the model as in **a**, over $n = 20$ rats. Error bars show s.e.m. Unconstrained models are shown in black, constrained models are shown in red. **c**, Top, raster plots of W_a^{-t} versus W_b^{-t} ($t = 1, 2$, from model 9). Each dot represents a subject. Pearson correlation values (r), and corresponding two-sided P values are shown for each plot. Bottom, median value of W_a^{-t} and W_b^{-t} ($t = 1, 2$), across rats. Error bars show median absolute deviation. **d**, Similar to **c**, for human subjects (auditory and tactile tasks are pooled together). Similar to rat subjects, model 9 shows the best performance for human subjects as well (data not shown). **e**, To compare the sensory-history matrix from the real data to the ones predicted from the best model fits (Fig. 2f, g), Frobenius distance norm was used, defined as the

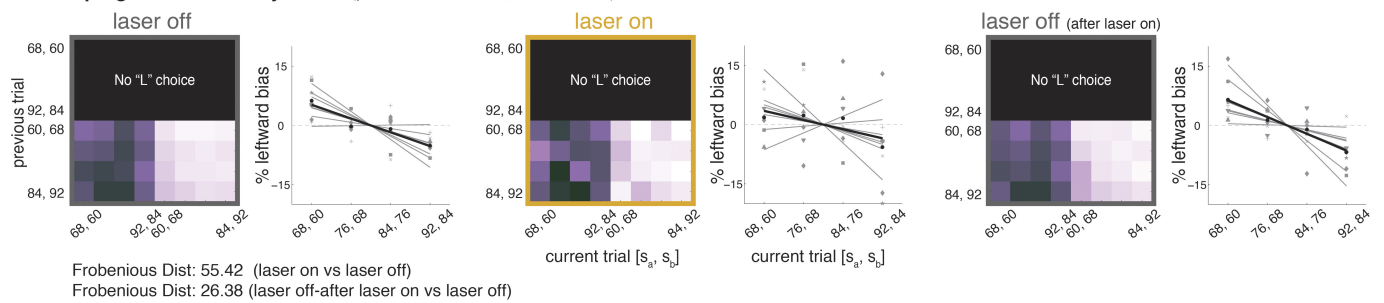
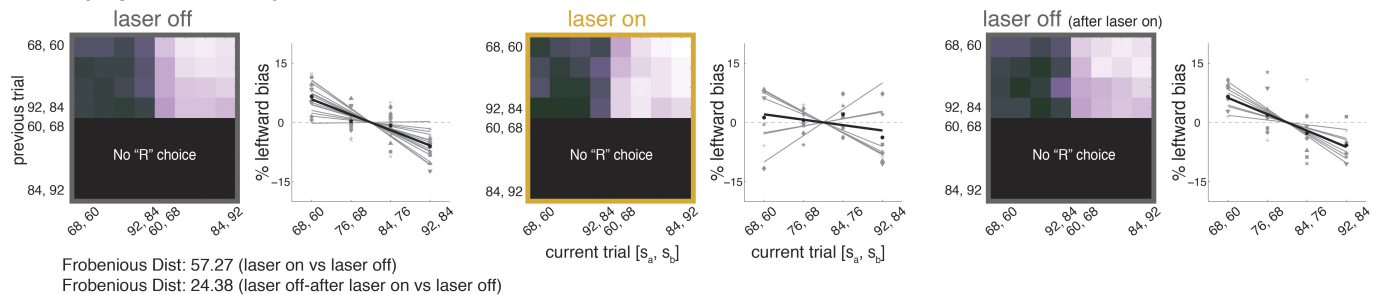
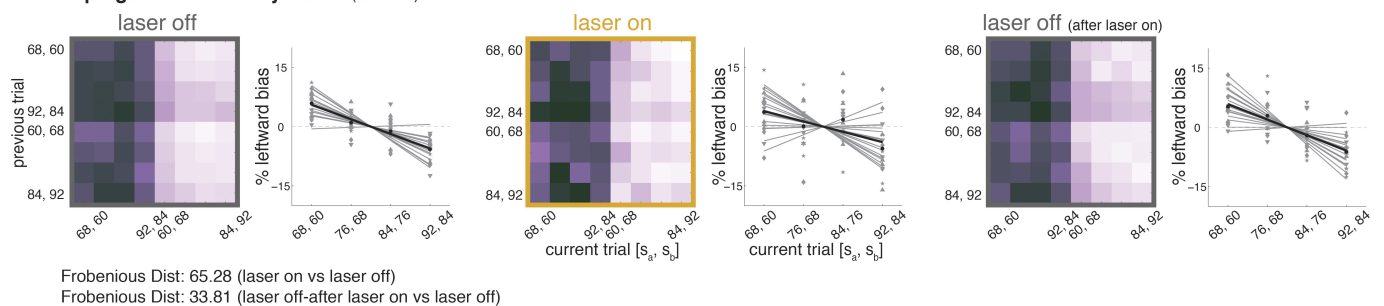
square root of the sum of the absolute squares of the difference between elements of two matrices. Frobenius distance is a measure of similarity, and the smaller the value, the more similar the two matrices. Frobenius distance is calculated separately for individual rats and each bar shows its mean value over $n = 20$ rats. Error bars show s.e.m. Models are models A–F from Fig. 2e. **f**, Scatter plot of slopes from linear fits to percentage leftward bias (Fig. 2a) versus short-term sensory history (that is, sum of weights for $s_a^{-1}, s_b^{-1}, s_a^{-2}$ and s_b^{-2}) from model 9. This plot shows significant correlation between the two measurements (Pearson correlation, $r = -0.66$, two-sided $P = 0.0084$, $n = 17$ rats), suggesting that when our logistic fit coefficients are particularly large, the subjects also have a particularly large contraction bias. **g**, Examining the weights in regression model 9, which is determined to be the best model, shows that the weights for sensory-history terms are significantly larger than those for the correct-side history term (paired-sample t -test, $P < 0.0001$, $n = 22$ rats). Data from individual rats are used to fit the model and bars show the mean value of sensory-history weights (in blue), and correct-side history weight (in green), over fit values from $n = 22$ rats. Error bars show s.e.m. Moreover, the sensory history regressor term, that is, sum of sensory-history weights \times regressors produces larger variance over trials (0.38) compared to the correct-side regressor (0.11), indicating a bigger impact on trial-by-trial behaviour.



Extended Data Figure 7 | Physiological and histological confirmations.

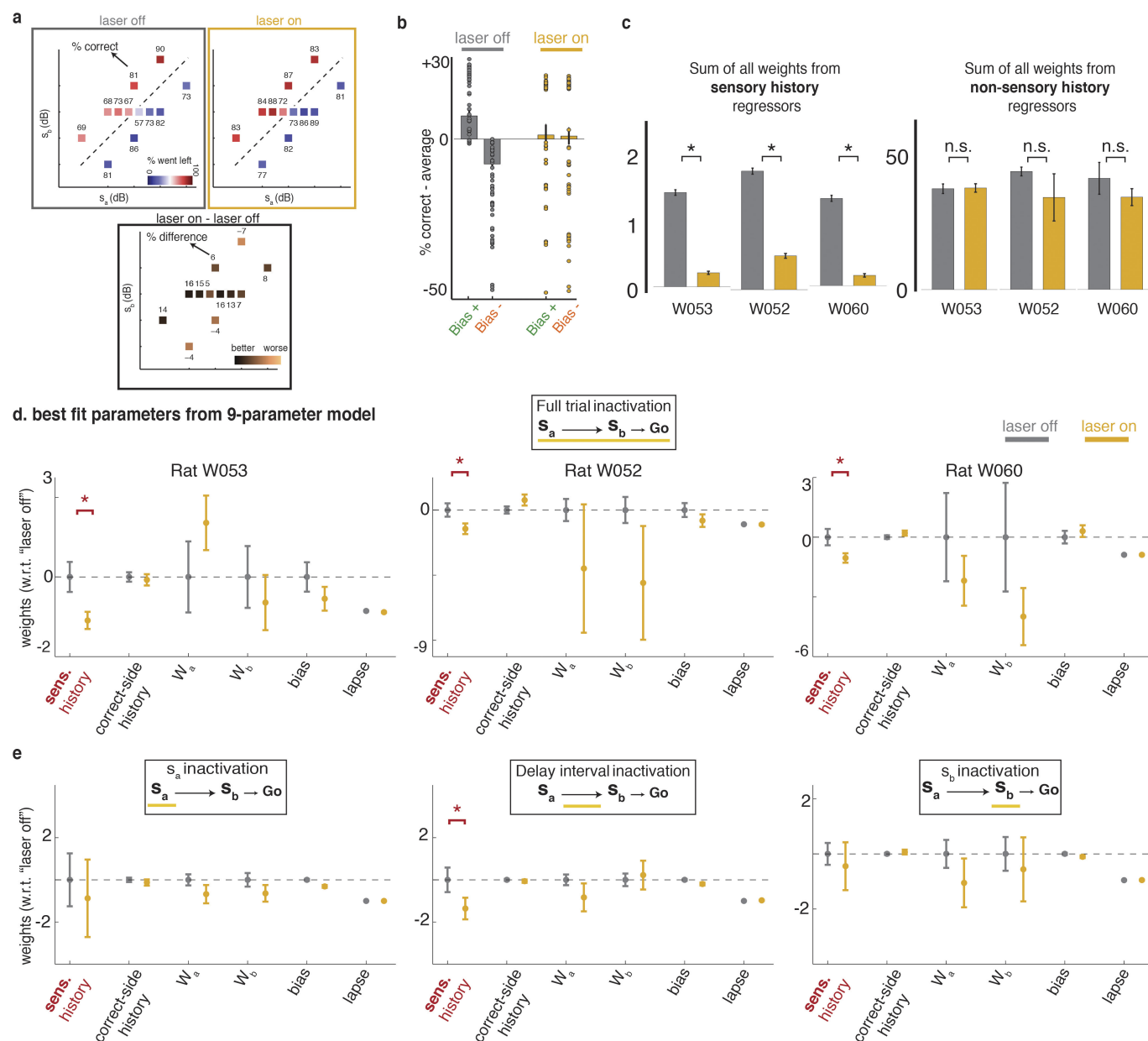
a, Physiological confirmation of optogenetic inactivation effect in an anesthetized rat. Left, single trace of acute extracellular activity of an example cell in the PPC, expressing eNpHR3.0, is shown in response to light stimulation. Laser illumination period (8 s) is marked by the light green bar. Right, raster-plot for 32 trials, for variable durations of light stimulation. The green vertical dashed line indicates the start of the laser illumination. The laser was on for variable durations of 750,

1,500, 3,000, 6,000 or 8,000 ms. The laser turning off is indicated by the vertical red dashed line. Recordings continued for 2 s after the laser was turned off. **b**, Histological localization of electrodes targeting the PPC. The inset shows an example of electrode locations in a coronal slice at anteroposterior = 3.48 from the bregma. In all cases, the electrode and fibre placements in the PPC were within between 2.8 and 4 mm posterior the bregma and between 2 and 3.5 mm lateral to the midline. Atlas panel is taken from Paxinos and Watson, 2004 (ref. 31).

a. Optogenetics - History Matrix (previous Left choice, all rewarded)**b. Optogenetics - History Matrix** (previous Right choice, all rewarded)**c. Optogenetics - History Matrix** (all trials)

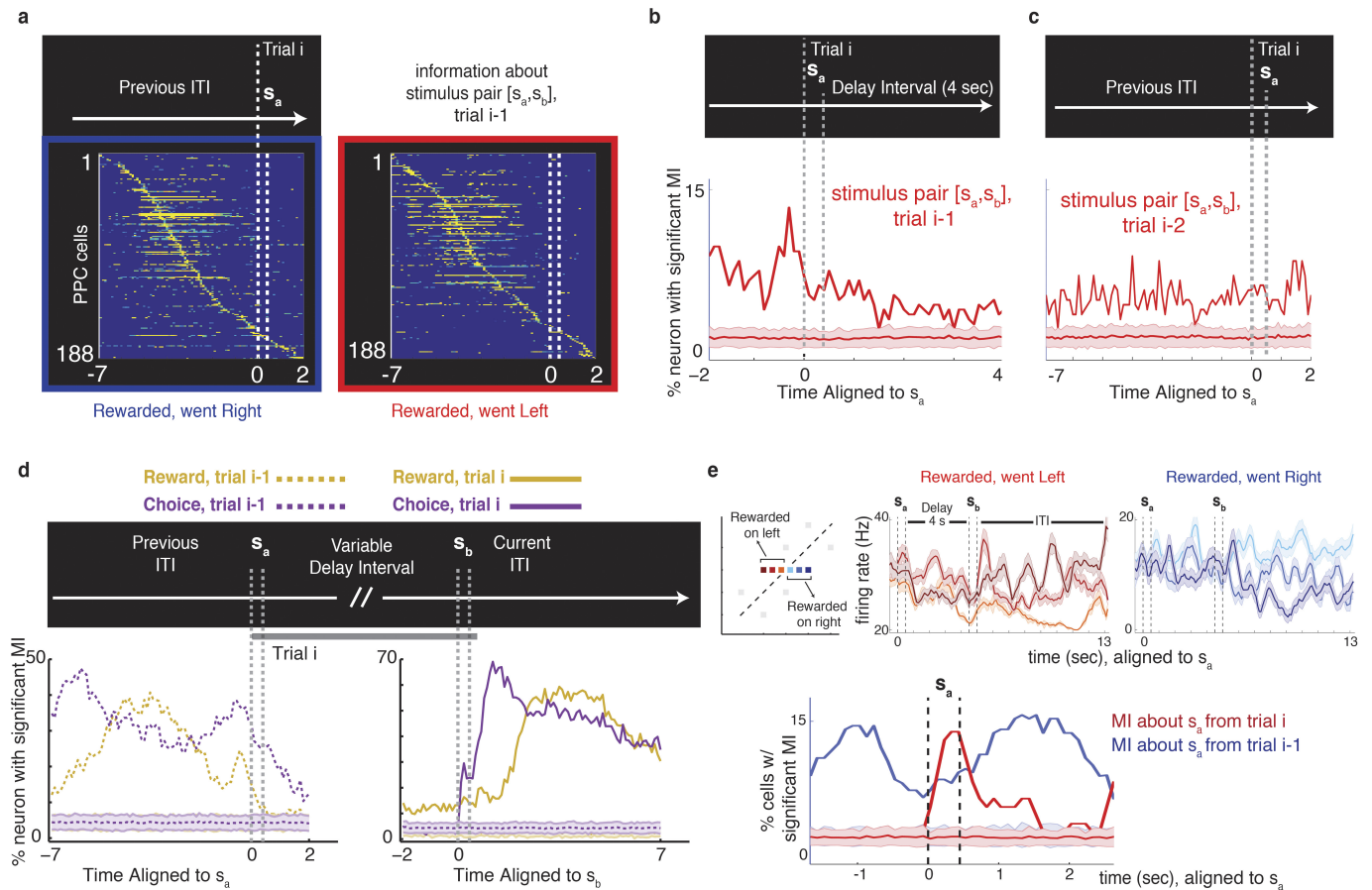
Extended Data Figure 8 | Optogenetics: PPC inhibition reduces leftward bias owing to past sensory stimuli. **a.** Sensory-history matrix and leftward biases due to past sensory stimuli, similar to Fig. 2a–c, but now for three types of trials: laser-off trials (two leftmost panels) that consist of trials with no PPC inactivation on either the current or the previous trial; laser-on trials (two middle panels) that consist of trials with PPC inactivation on the current trial; and laser-off-after-laser-on trials (two rightmost panels) that consist of trials immediately after the laser-on

trials. This last set controls for number of trials, as it contains equal numbers of trials to the laser-on condition. Modulation along the vertical indicates a previous trial effect behavioural bias as a function of the stimuli of the previous trial, for trials for which rats went left, and were rewarded, therefore history of reward and choice is held fixed. Grey lines are different current trial (s_a, s_b) pairs, the black line is the average over pairs. **b.** Similar to **a**, for trials for which rats went right and were rewarded. **c.** Similar to **a** for all combinations of current and previous stimuli.



Extended Data Figure 9 | Optogenetics: impact on contraction bias on the full stimulus set, individual data points and best fit parameters for non-sensory-history weights. **a**, Stimulus set and performance during optogenetic inhibition sessions, averaged over 37 sessions from 3 rats (delay interval of 2 s). Trials are grouped based on laser-off (left) and laser-on (right) conditions. The boxes represent the set of (s_a , s_b) pairs used in a session, with the colour representing the percentage that went left and the numbers above each box indicating the percentage correct. The plot in the bottom shows the difference between laser-off and laser-on conditions, with positive values indicating improved performance in laser-on conditions and negative values indicating impaired performance. **b**, **c**, Similar to Fig. 3d–f, with all data points overlaid on the bar plots.

For **b**, $n = 37$ for each bar plot (equal to the total number of inactivation sessions); for **c**, $n = 600$, from 200 iterations of threefold cross-validation data; $*P < 0.01$ from one sided t -test. **d**, Best-fit parameter values for all weights from the nine-parameter model (short-term sensory-history model, constrained version, Fig. 2d, e). Values are plotted as their mean once the average value from the laser-off condition is subtracted. Except for the sensory history, none of the other weights were significantly affected by optogenetic inactivation of the PPC. Error bars show s.d. ($n = 600$, 200 iterations of threefold cross-validation; $*P < 0.01$ from one sided t -test). **e**, Similar to **d**, for period-selective optogenetic inhibitions, in which the PPC is selectively inhibited during the first stimulus s_a (left), delay interval (middle) or second stimulus s_b (right).



Extended Data Figure 10 | Mutual information. **a**, Sensory-history coding, one trial back, population analysis, each row represents the time course of significant values of mutual information between the firing rate of a cell and the stimulus pair (s_a , s_b) presented on the previous trial. Data from all trials with variable delay duration (minimum of 2 s) were pooled and plots are aligned to the beginning of s_a . Data from $n = 5$ rats, and only cells with significant values of mutual information values are included. When estimating the mutual information, spurious information values can be attributed to the inherent correlations between task parameters, such as sensory stimuli and choice. To overcome this, conditional mutual information was calculated only when trials with same previous choice and reward status were considered, and sensory inputs were the only variable. Left, on the previous trial rats went right and were rewarded. Right, on the previous trial rats went left and were rewarded. **b**, Sensory-history coding, one trial back, percentage of cells with significant coding of stimuli presented on the previous trial (trial $i - 1$), aligned to the start of trial i . Only trials with a delay interval larger than 4 s are included in this analysis. **c**, Sensory-history coding, two trials back, percentage of cells with significant coding of stimuli presented two trials in the past (trial $i - 2$), aligned to the start of trial i . Shaded horizontal areas show the mean \pm s.d. of the percentage of neurons with significant mutual information (MI), calculated from random sets built by shuffling the firing rates of neurons and conditions. **d**, Percentage of cells with significant coding of a rat's choice and reward status, on both the current trial (solid lines) and previous trial (dashed lines), when time is aligned to the

current trial, either s_a (left), or s_b (right). Shaded horizontal areas show the mean \pm s.d. of the percentage of neurons with significant mutual information, calculated from random sets built by shuffling the firing rates of neurons and conditions. **e**, In the standard stimulus set (Fig. 1b), (s_a , s_b) pairs along the diagonal lines, knowledge of the rat's choice of side, whether it was rewarded or not, and one of either s_a or s_b enables unique identification of the other stimulus (s_b or s_a). Therefore, in order to probe whether neurons carried information for different values of s_a itself (as opposed to a combination of choice, reward and s_b), we ran recording sessions with psychometric stimuli added to the standard stimulus set (top left). In this way, three different values of s_a are assigned to one fixed value of s_b and one fixed action (left in different shades of red, and right in different shades of blue). The firing rate of an example neuron is shown in response to different values of s_a , only for trials in which the rat responded by going left (middle graph) or right (right graph) after the 'go' cue, was rewarded, and the delay interval was 4 s. Even though choice, reward and s_b are fixed, firing rates clearly differentiate values of s_a . The bottom graph shows a summary of population analysis from psychometric recording sessions (as in the examples in the graphs above), showing the percentage of cells with significant coding of s_a from trial i (red) or trial $i - 1$ (blue, $n = 142$ cells). Shaded horizontal areas show the mean \pm s.d. of the percentage of neurons with significant mutual information, calculated from random sets built by shuffling the firing rates of neurons and conditions.

c-MAF-dependent regulatory T cells mediate immunological tolerance to a gut pathobiont

Mo Xu^{1*}, Maria Pokrovskii^{1*}, Yi Ding², Ren Yi³, Christy Au^{1,4}, Oliver J. Harrison⁵, Carolina Galan¹, Yasmine Belkaid^{5,6}, Richard Bonneau^{3,7,8} & Dan R. Littman^{1,4}

Both microbial and host genetic factors contribute to the pathogenesis of autoimmune diseases^{1–4}. There is accumulating evidence that microbial species that potentiate chronic inflammation, as in inflammatory bowel disease, often also colonize healthy individuals. These microorganisms, including the *Helicobacter* species, can induce pathogenic T cells and are collectively referred to as pathobionts^{4–6}. However, how such T cells are constrained in healthy individuals is not yet understood. Here we report that host tolerance to a potentially pathogenic bacterium, *Helicobacter hepaticus*, is mediated by the induction of ROR γ ⁺FOXP3⁺ regulatory T (iT_{reg}) cells that selectively restrain pro-inflammatory T helper 17 (T_H17) cells and whose function is dependent on the transcription factor c-MAF. Whereas colonization of wild-type mice by *H. hepaticus* promoted differentiation of ROR γ -expressing microorganism-specific iT_{reg} cells in the large intestine, in disease-susceptible IL-10-deficient mice, there was instead expansion of colitogenic T_H17 cells. Inactivation of c-MAF in the T_{reg} cell compartment impaired differentiation and function, including IL-10 production, of bacteria-specific iT_{reg} cells, and resulted in the accumulation of *H. hepaticus*-specific inflammatory T_H17 cells and spontaneous colitis. By contrast, ROR γ inactivation in T_{reg} cells had only a minor effect on the bacteria-specific T_{reg} and T_H17 cell balance, and did not result in inflammation. Our results suggest that pathobiont-dependent inflammatory bowel disease is driven by microbiota-reactive T cells that have escaped this c-MAF-dependent mechanism of iT_{reg}-T_H17 homeostasis.

We chose *H. hepaticus* as a model to investigate host–pathobiont interactions. Blockade of IL-10RA induced inflammation of the large intestine in *H. hepaticus*-colonized *Il23r*^{GFP} reporter mice^{5,6}, increasing the proportion of green fluorescent protein-positive (GFP⁺) cells (predominantly T_H17 cells) from approximately 10% to 50% of large intestine CD4⁺ T cells (Extended Data Fig. 1a). We therefore sought to determine why *H. hepaticus*-induced T cells do not cause disease in wild-type mice at the steady state. To address this question, we first identified the T cell receptor (TCR) sequences and cognate epitopes of *H. hepaticus*-induced T_H17 cells that expand during inflammation, and subsequently traced the fate of these cells at the steady state.

We cloned individual TCR sequences from colitogenic IL-23R-GFP⁺ T cells (Extended Data Fig. 1b) and found that nine out of twelve clonotypic TCRs were *H. hepaticus*-specific (Extended Data Fig. 1c). We subsequently identified^{7,8} a *H. hepaticus*-unique protein, HH_1713, that contains two immunodominant epitopes. The E1 peptide epitope, presented by I-A^b, was recognized by *H. hepaticus*-specific TCR HH5-1, whereas E2 was recognized by TCR HH5-5, HH6-1 and HH7-2 (Extended Data Fig. 1c). We next developed two complementary

approaches to track *H. hepaticus*-specific T cells *in vivo*^{9,10}, HH7-2 and HH5-1 TCR transgenic mice (HH7-2tg and HH5-1tg) and a major histocompatibility complex (MHC) class II tetramer loaded with E2 peptide (HH-E2 tetramer) (Extended Data Fig. 1d–g).

To track what happens to *H. hepaticus*-specific T cells in healthy mice, we simultaneously transferred naive T cells from HH7-2tg and 7B8tg (segmented filamentous bacteria (SFB)-specific TCRtg control)⁸ mice into wild-type mice that were stably colonized with *H. hepaticus* and SFB (Fig. 1a). Two weeks after adoptive transfer, HH7-2tg donor cells were enriched in the large intestinal lamina propria (LILP) and caecal patch, whereas 7B8tg cells predominated in the small intestinal lamina propria (SILP) and Peyer's patches (Extended Data Fig. 2a, b), consistent with colonization of *H. hepaticus* in the large intestine and SFB in the small intestine. As previously reported, 7B8 cells developed into T_H17 cells that were largely positive for ROR γ t and negative for FOXP3⁸ (Fig. 1b, c, Extended Data Fig. 2c, d). By contrast, HH7-2tg cells in the LILP were mostly iT_{reg} cells that express both ROR γ t and FOXP3 (approximately 60% of total donor-derived HH7-2tg cells)^{11,12}, rather than T_H17 cells (less than 10% of total HH7-2tg cells) (Fig. 1b, c, Extended Data Fig. 2c, d). Notably, two other colonic T_{reg} cell markers, GATA3 and ST2, were not expressed on HH7-2tg cells¹³ (Extended Data Fig. 2e). 7B8tg and HH7-2tg T cells that expressed neither ROR γ t nor FOXP3 were mostly T follicular helper (T_{FH}) cells and were enriched in the Peyer's patches and caecal patch (Fig. 1b, c, Extended Data Fig. 2c, d). Breeding HH7-2tg mice onto the *Rag1*^{−/−} background excluded the possibility that HH7-2tg iT_{reg} cells detected after adoptive transfer were contaminated by thymus-derived natural T_{reg} (nT_{reg}) cells or were influenced by the presence of dual TCRs (Extended Data Fig. 3a–c). Adoptively transferred HH5-1tg and HH-E2-tetramer-positive cells had differentiation profiles similar to HH7-2tg cells (Fig. 1d, e, Extended Data Figs 2f and 3d, e). These results indicate that the host responds to *H. hepaticus* by generating immunotolerant iT_{reg} cells rather than pro-inflammatory T_H17 cells.

To examine whether the iT_{reg} cell-dominant differentiation of *H. hepaticus*-specific T cells is altered during intestinal inflammation, we co-transferred naive HH7-2tg and control 7B8tg T cells into colonized *Il10*^{−/−} recipients. Notably, only a small proportion of the transferred HH7-2tg T cells expressed FOXP3 in the LILP. Instead, most of them differentiated into pro-inflammatory T_H17 cells with T_H1-like features, characterized by the expression of both ROR γ t and T-bet and high levels of IL-17A and IFN γ upon re-stimulation¹⁴ (Fig. 2a–f, Extended Data Fig. 4a, c, d). These results were recapitulated with HH5-1tg T cell adoptive transfer and endogenous HH-E2 tetramer⁺ T cells (Extended Data Fig. 4e–g). By comparison, disruption of IL-10-mediated immune tolerance did not result in deviation of

¹Molecular Pathogenesis Program, The Kimmel Center for Biology and Medicine of the Skirball Institute, New York University School of Medicine, New York, New York 10016, USA. ²Department of Pathology and Laboratory Medicine, University of Rochester Medical Center, Rochester, New York 14642, USA. ³Courant Institute of Mathematical Sciences, Computer Science Department, New York University, New York, New York 10003, USA. ⁴The Howard Hughes Medical Institute, New York University School of Medicine, New York, New York 10016, USA. ⁵Mucosal Immunology Section, Laboratory of Parasitic Diseases, National Institute of Allergy and Infectious Diseases, NIH, Bethesda, Maryland 20892, USA. ⁶NIAID Microbiome Program, NIH, Bethesda, Maryland 20892, USA. ⁷Center for Genomics and Systems Biology, Department of Biology, New York University, New York, New York 10003, USA. ⁸Center for Computational Biology, Flatiron Institute, Simons Foundation, New York, New York 10010, USA.

*These authors contributed equally to this work.

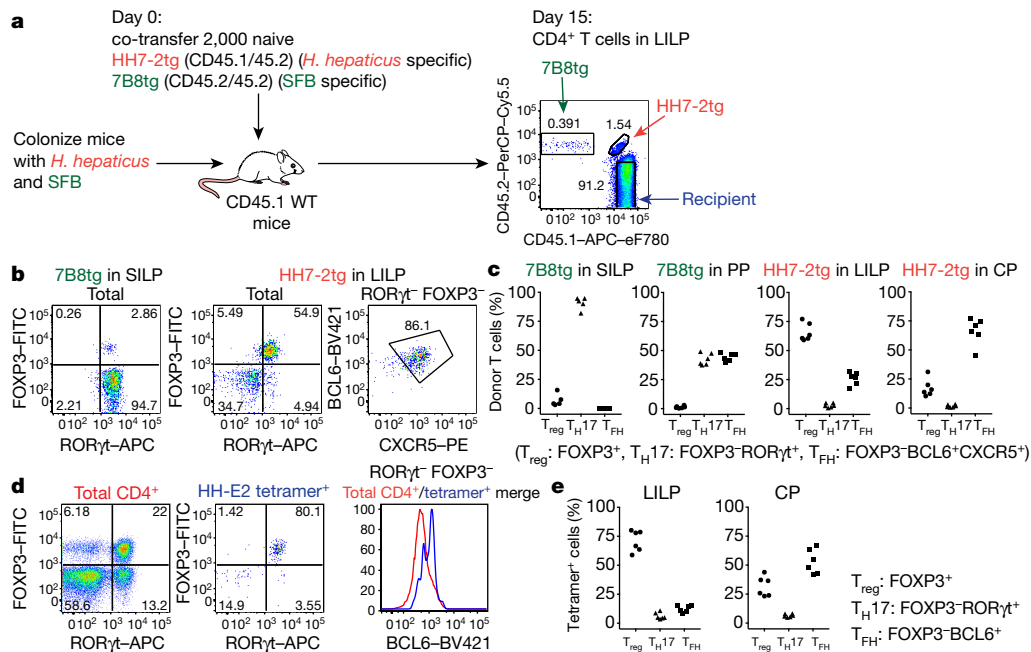


Figure 1 | *H. hepaticus* induces RORγt⁺ T_{reg} and T_{FH} cell responses under steady state. **a**, Experimental scheme for co-transfer of congenic isotype-labelled HH7-2tg and 7B8tg cells into wild-type (WT) mice colonized with *H. hepaticus* and SFB. **b**, **c**, RORγt, FOXP3, BCL6 and CXCR5 expression (**b**) and frequencies of T_{reg} (FOXP3⁺), T_H17 (FOXP3⁺RORγt⁺) and T_{FH} (BCL6⁺CXCR5⁺) (**c**) among donor-derived T cells in indicated tissues. Data are from 1 of 3 experiments, with *n* = 15 in the 3 experiments. CP, caecal patch; PP, Peyer's patches. APC (allophycocyanin), Cy5.5, eF780, FITC, PE (phycoerythrin) and PerCP denote fluorochrome labels. **d**, **e**, Wild-type mice (*n* = 6) were colonized with *H. hepaticus* for 3–4 weeks and analysed for RORγt, FOXP3 and BCL6 expression in total CD4⁺ (red) and HH-E2 tetramer⁺ (blue) T cells from the LILP (**d**) and frequencies of T_{reg} (FOXP3⁺), T_H17 (FOXP3⁺RORγt⁺) and T_{FH} (BCL6⁺) cells among HH-E2 tetramer⁺ T cells in the LILP and caecal patch (**e**). Data summarize two independent experiments.

SFB-specific T_H17 cells to the inflammatory T_H17–T_H1 cell phenotype (Fig. 2c, d, Extended Data Fig. 4a–d). Furthermore, we observed similar deviated T cell responses to *H. hepaticus* in models of T cell transfer colitis and *Citrobacter rodentium*-induced colonic inflammation, but not in dextran sulfate sodium (DSS) colitis, an innate immunity-dependent model (Extended Data Fig. 5a–h). Commensal microorganism-specific T cells can thus acquire pro-inflammatory phenotypes

during enteric infection¹⁵, although the high frequency of such infections suggests the existence of a mechanism to re-establish gut tolerance. Our observations of *H. hepaticus*-specific iT_{reg}–T_H17 skewing during colitis are consistent with a contemporaneous study using two different *Helicobacter* species¹⁶. These findings indicate that dysregulated T cell tolerance to pathobionts may be a general hallmark of inflammatory bowel disease.

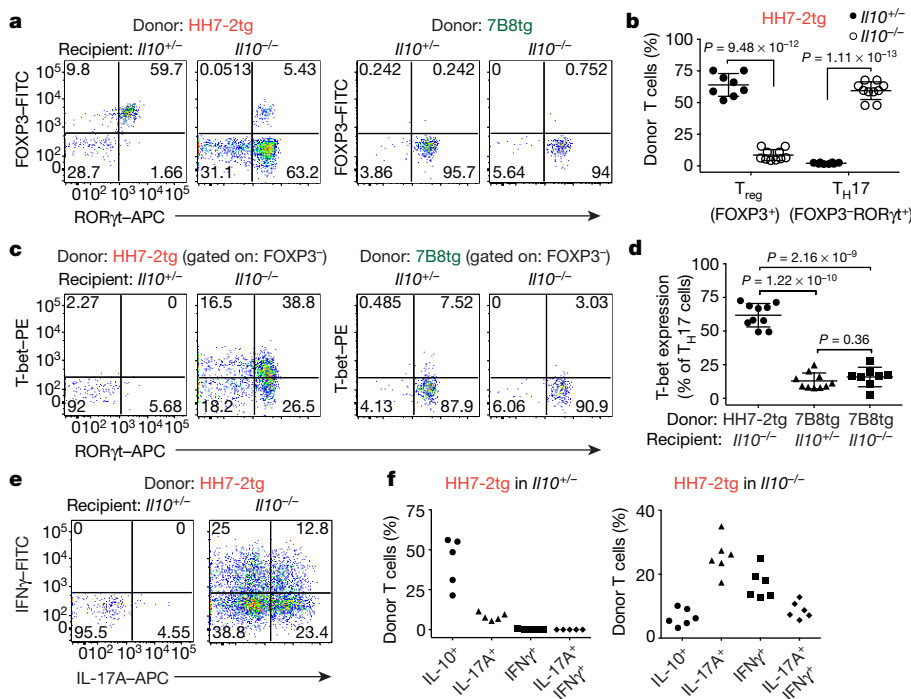


Figure 2 | *H. hepaticus* predominantly induces inflammatory T_H17 cells in IL-10 deficiency-dependent colitis. **a–d**, LILP HH7-2tg and SILP 7B8tg donor-derived cells in IL10^{+/+} (*n* = 8) and IL10^{-/-} (*n* = 10) mice were analysed for FOXP3 and RORγt expression (**a**), frequencies of T_{reg} (FOXP3⁺) and T_H17 (FOXP3⁺RORγt⁺) cells (**b**), RORγt and T-bet co-expression (**c**), and frequencies of T-bet expression among T_H17 (FOXP3⁺RORγt⁺) cells (**d**). Data are from four independent experiments. **e**, **f**, IL-17A and IFNγ expression (**e**) and frequencies of IL-10⁺, IL-17A⁺ and IFNγ⁺ cells (**f**) among LILP HH7-2tg donor-derived cells in IL10^{+/+} (*n* = 5) and IL10^{-/-} (*n* = 6) mice after re-stimulation. Data summarize two independent experiments. All statistics were calculated by unpaired two-sided Welch's *t*-test. Error bars denote mean ± s.d. *P* values are indicated on the figure.

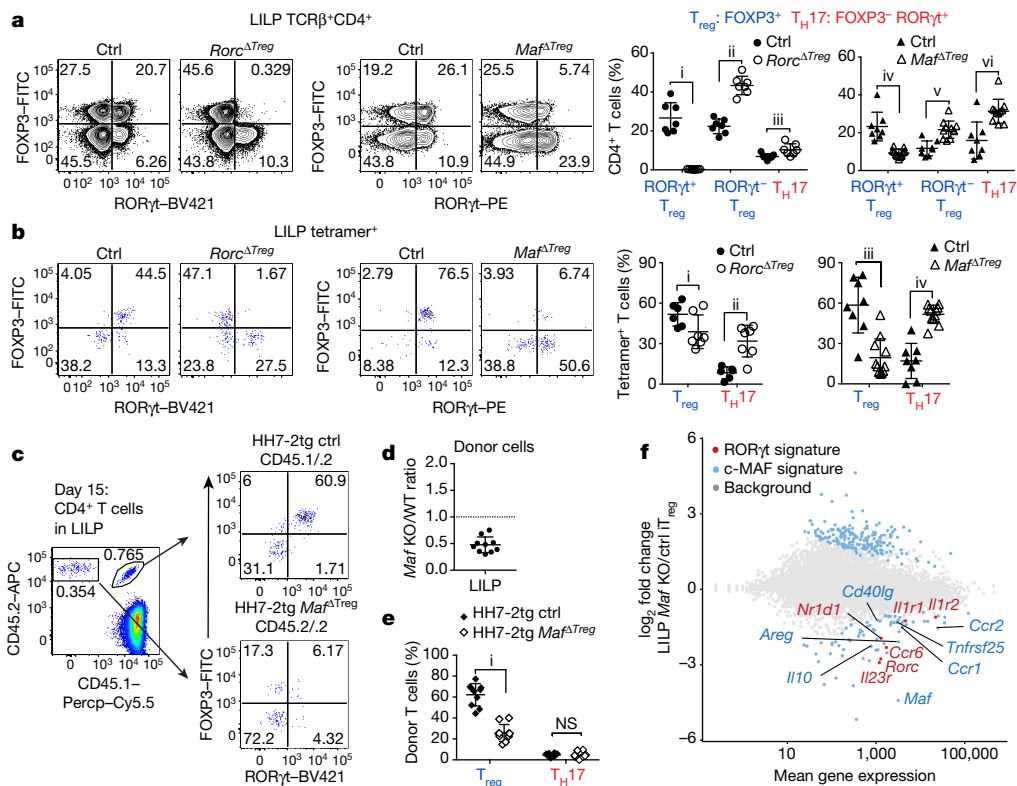


Figure 3 | c-MAF is required for the differentiation and function of induced T_{reg} cells in the gut. **a, b,** Transcription factor staining in total CD4⁺ (**a**) and HH-E2 tetramer⁺ (**b**) T cells from the LILP of indicated mice. Left, RORγt and FOXP3 expression. Right, frequencies of indicated T_{reg} (FOXP3⁺) and T_H17 (FOXP3[−]RORγt⁺) cell subsets. Mice were colonized with *H. hepaticus* for 5–6 weeks before analysis. Data summarize 3 independent experiments for *Rorc*^{ΔTreg} (*n* = 7) and littermate controls (*n* = 7 for **a**, *n* = 6 for **b**), and 4 independent experiments for *Maf*^{ΔTreg} (*n* = 10) and littermate controls (*n* = 8). **c–e,** Co-transfer of *Maf*^{ΔTreg} and control HH7-2tg T cells into wild-type *H. hepaticus*-colonized mice. **c,** Left, donor cell composition in the LILP of recipient mice. Right, RORγt and FOXP3 expression in indicated donor-derived cells. **d,** Ratios of *Maf*^{ΔTreg} (knockout, KO) versus control (WT) HH7-2tg donor-derived cells in the LILP. Dashed line represents ratio of co-transferred cells before transfer. **e,** Frequencies of T_{reg} (FOXP3⁺) and T_H17 (FOXP3[−]RORγt⁺)

cells among donor-derived cells. Data are a summary of 10 mice from 2 independent experiments. **a, b, e,** Statistics were calculated by unpaired two-sided Welch's *t*-test. Error bars denote mean ± s.d. *P* values are as follows: **a,** i = 1.21×10^{-6} , ii = 8.82×10^{-7} , iii = 0.016, iv = 6.38×10^{-4} , v = 8.06×10^{-4} and vi = 9.89×10^{-7} . **b,** i = 0.056, ii = 7.48×10^{-4} , iii = 7.64×10^{-7} and iv = 6.01×10^{-6} . **e,** i = 6×10^{-14} . NS = 0.86. **f,** MA plot depicting RNA-seq comparison of donor naive T cell-derived *Maf*^{ΔTreg} versus control FOXP3[−]YFP⁺ iT_{reg} cells (mean of two biologically independent experiments). Blue dots indicate 190 upregulated and 75 downregulated genes in the c-MAF-dependent signature. Highlighted blue dots represent downregulated genes related to T_{reg} cell function, and highlighted red dots indicate genes that are also downregulated in RORγt[−]. Differentially expressed genes were calculated in DESeq2 using the Wald test with Benjamini–Hochberg correction to determine the false discovery rate (FDR) (FDR < 0.1 and log₂ fold change > 1.5).

We next wished to determine whether RORγt⁺ T_{reg} cells are critical for immune tolerance to gut pathobionts. The transcription factor c-MAF attracted our attention as it was highly enriched in these cells^{11,17} (Extended Data Fig. 6a) and known to promote an anti-inflammatory program, for example, IL-10 expression in other T helper cell subsets^{18,19}. We therefore deleted *Maf* with *Foxp3*^{cre} (*Maf*^{ΔTreg}) mice, despite incomplete depletion of c-MAF protein (Extended Data Fig. 6b), there was a marked decrease in the proportion of RORγt⁺ but not RORγt[−] T_{reg} cells among CD4⁺ T cells in the large intestine, and a concomitant increase in T_H17 cell frequency (Fig. 3a). *Maf*^{ΔTreg} mice also had expanded numbers of total CD4⁺ T cells in the large intestine, reflected by a pronounced accumulation of T_H17 cells, but notably not RORγt⁺ T_{reg} cells (Extended Data Fig. 6c). By contrast, after *H. hepaticus* colonization, T_H17 cell expansion was less striking in *Rorc*^{ΔTreg}; *Foxp3*^{cre} (*Rorc*^{ΔTreg}) mice (Fig. 3a, Extended Data Fig. 6c), and neither a decrease of RORγt⁺ T_{reg} cells nor an expansion of T_H17 cells was observed in *Gata3*^{ΔTreg}; *Foxp3*^{cre} (*Gata3*^{ΔTreg}) mice (Extended Data Fig. 6d, e). The altered frequency of RORγt⁺ T_{reg} and T_H17 cell subsets led us to test whether the fate of *H. hepaticus*-specific T cells would be affected in the *Maf*^{ΔTreg} and *Rorc*^{ΔTreg} mice. Notably, HH-E2 tetramer⁺ cells were predominantly T_H17 in *Maf*^{ΔTreg} mice, but mostly RORγt⁺ T_{reg} in control mice (Fig. 3b, Extended Data Fig. 6f). By contrast, although

Rorc^{ΔTreg} mice also had an increased proportion of *H. hepaticus*-specific T_H17 cells, most tetramer⁺ cells were T_{reg} cells (Fig. 3b, Extended Data Fig. 6f). Collectively, these results suggest that pathobiont-specific RORγt⁺ iT_{reg} cells are required for the suppression of inflammatory T_H17 cell accumulation. Although RORγt expression contributes to gut iT_{reg} cell function, c-MAF has a more substantial role in the differentiation and/or function of these cells. *H. hepaticus*-specific T_{reg} cell differentiation in the caecal patch did not seem to be affected in *Maf*^{ΔTreg} mice (Extended Data Fig. 6g). Notably, as in IL-10-deficient mice, SFB-specific T_H17 cells neither expanded nor adopted a T_H1-like phenotype in *Maf*^{ΔTreg} mice (Extended Data Fig. 6h, i). A potential explanation is that SFB- and *H. hepaticus*-specific T_H17 responses are instructed by different innate immune pathways^{20,21}.

To investigate how c-MAF regulates the gut RORγt⁺ iT_{reg}–T_H17 cell axis, we co-transferred equal numbers of naive *Maf*^{ΔTreg}; *Foxp3*^{cre} (control) and *Maf*^{ΔTreg}; *Foxp3*^{cre} HH7-2tg cells into *H. hepaticus*-colonized wild-type mice (Extended Data Fig. 7a, b). Two weeks after adoptive transfer, the *Maf*^{ΔTreg}; *Foxp3*^{cre} HH7-2tg cells were markedly underrepresented compared to control cells in the LILP, mesenteric lymph nodes (mLNs) and spleen, and were unable to form iT_{reg} cells (Fig. 3c–e and Extended Data Fig. 7c, d). Importantly, at homeostasis, mutant donor-derived cells did not give rise to a high frequency of T_H17 cells (Fig. 3e). Transcriptomics analysis revealed that the c-MAF-deficient

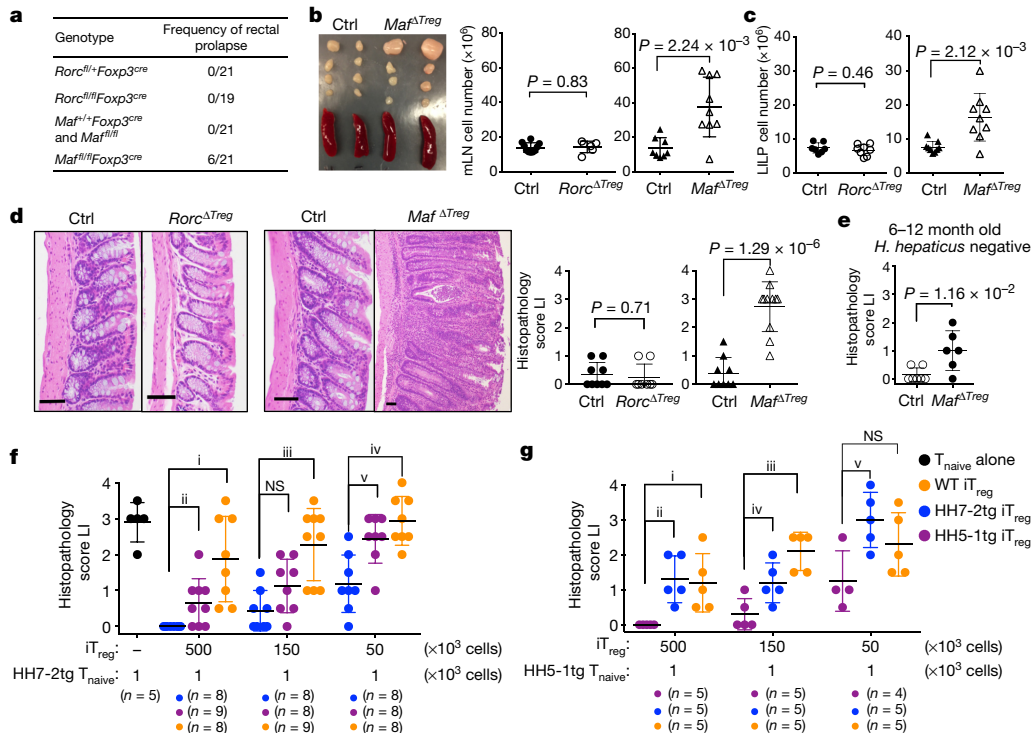


Figure 4 | ROR γ t⁺ iT_{reg} cells are required to maintain gut homeostasis.

a, Frequency of rectal prolapse by genotype. **b**, Left, spleens and mLN from *Maf^{ΔTreg}* and littermate controls. Right, total cell numbers in mLN. Data summarize three independent experiments for *Rorc^{ΔTreg}* ($n = 6$) and littermate controls ($n = 7$), and four independent experiments for *Maf^{ΔTreg}* ($n = 9$) and littermate controls ($n = 8$). **c**, Number of leukocytes in the LILP. Data summarize three independent experiments for *Rorc^{ΔTreg}* ($n = 7$) and littermate controls ($n = 8$), and four independent experiments for *Maf^{ΔTreg}* and littermate controls ($n = 9$). **d**, Representative histology of large intestine (LI) sections (left) and colitis scores (right) of mice with indicated genotypes. *Rorc^{ΔTreg}* ($n = 8$) and littermate controls ($n = 9$). *Maf^{ΔTreg}* ($n = 11$) and littermate controls ($n = 9$). Scale bars, 50 μ m.

iT_{reg} cells were functionally impaired, as indicated by defective expression of *Il10* and other T_{reg} cell signature genes, as well as of ROR γ t-dependent genes¹¹ (Fig. 3f, Extended Data Fig. 7e–h). Taken together, these findings show that c-MAF is a crucial cell-intrinsic factor for both the generation and function of microorganism-specific iT_{reg} cells. Notably, the vast majority of accumulated T_H17 cells in *Maf^{ΔTreg}* mice expressed c-MAF, indicating that the bulk of these cells did not arise from T_{reg} cells in which c-MAF was deleted (Extended Data Fig. 7i). Thus, suppression of T_H17 cell expansion is mediated by these iT_{reg} cells *in trans*.

ROR γ t expression in iT_{reg} cells has been implicated in the maintenance of gut immune homeostasis under different challenges^{11,12}. However, spontaneous gut inflammation in *Rorc^{ΔTreg}* mice has not been described. We noticed that *Maf^{ΔTreg}*, but not *Rorc^{ΔTreg}* or control littermates, were prone to rectal prolapse (Fig. 4a). *Maf^{ΔTreg}* mice (8–12 weeks old) colonized with *H. hepaticus* for 5–6 weeks had enlarged large intestine-draining mLN, and increased cellularity of mLN and the large intestine (Fig. 4b, c). Histopathological analysis of the large intestine of these mice revealed mixed acute and chronic inflammation (Fig. 4d). Without *H. hepaticus* colonization, aged (6–12 months old) *Maf^{ΔTreg}* mice also exhibited mild spontaneous colitis (Fig. 4e). Notably, none of the above changes was observed in *Rorc^{ΔTreg}* mice (Fig. 4b–d). Thus, c-MAF but not ROR γ t expression in iT_{reg} cells is crucial for the suppression of spontaneous inflammation. Indeed, the transcriptional profile of *H. hepaticus*-specific T effector (T_{eff}) cells from *Maf^{ΔTreg}* mice with spontaneous colitis was highly similar to that of pathogenic T_H17 cells in IL-10RA blockade-induced

e, Colitis scores in aged *H. hepaticus*-negative *Maf^{ΔTreg}* ($n = 6$) and littermate control ($n = 7$) mice. **f**, **g**, Suppression of *H. hepaticus*-specific TCRtg cell-mediated transfer colitis by *in vitro* differentiated iT_{reg} cells. Data summarize two independent experiments with indicated sample size (n) in total. Colitis scores for *Rag1^{-/-}* mice that received the indicated TCRtg naive T cells and iT_{reg} combinations. All statistics were calculated by unpaired two-sided Welch's *t*-test. Error bars denote mean \pm s.d. *P* values are indicated on the figure or as follows: **f**, i = 5.34×10^{-4} , ii = 1.24×10^{-2} , iii = 3.64×10^{-4} , iv = 3.26×10^{-4} and v = 4.54×10^{-3} . NS = 0.056. **g**, i = 0.013, ii = 2.50×10^{-3} , iii = 4.59×10^{-4} , iv = 0.024, and v = 0.016. NS = 0.12.

colitis, but differed markedly from homeostatic T_H17 cells (which are predominantly SFB-specific) (Extended Data Fig. 8a–f).

Similar to the *Maf^{ΔTreg}* strain, mice with inactivation of STAT3 in the T_{reg} compartment or impaired TGF β signalling in CD4⁺ T cells also lacked ROR γ t⁺ T_{reg} cells and developed spontaneous colitis^{12,22,23} (Extended Data Fig. 9a, b). Consistent with these findings, c-MAF expression in T_{reg} cells required a combination of both TGF β and STAT3 signals *in vitro* and *in vivo*, as it does in other CD4⁺ T cells^{18,19} (Extended Data Fig. 9a–c). This suggests that c-MAF integrates anti-inflammatory TGF β receptor signals with microorganism-induced cytokine-dependent STAT3 activation to mediate ROR γ t⁺ T_{reg} induction.

Although c-MAF is also expressed, albeit at a lower level, in nT_{reg} cells, c-MAF-deficient and -sufficient nT_{reg} cells showed equivalent activity in inhibiting T_{eff} cell proliferation *in vitro*, as well as in suppressing pathogenesis in a model of T cell transfer colitis *in vivo* (Extended Data Fig. 10a, b). We therefore wondered why, despite their increased numbers (Extended Data Fig. 6c), nT_{reg} cells were not sufficient to establish gut homeostasis in *Maf^{ΔTreg}* mice. Adoptive transfer of 1,000 naive HH7-2tg or HH5-1tg cells into *H. hepaticus*-colonized *Rag1^{-/-}* mice led to colitis. Taking advantage of this system, we compared the suppressive function of iT_{reg} cells differentiated *in vitro* from naive HH7-2tg, HH5-1tg and polyclonal T cells. We found that epitope-specific iT_{reg} were better at suppressing colitis, providing a potential explanation for why pathobiont-specific iT_{reg} cells are required in addition to nT_{reg} cells to maintain gut homeostasis²⁴ (Fig. 4f, g).

Our results reveal a mechanism for how a healthy individual can host a 'two-faced' commensal pathobiont such as *H. hepaticus* without developing inflammatory disease. Our findings suggest that T_{reg} cell induction serves as a strategy to establish commensalism, not only by helping the microorganisms to colonize their niche²⁵, but also by protecting the host from inflammation. A similar requirement for iT_{reg} cells has also been reported in the establishment of food tolerance²⁶. Our observations in *Maif^{ΔTreg}* mice are linked to and help explain the expansion of colitogenic T_H17 cells in mice with T_{reg}-specific inactivation of STAT3²³. Like c-MAF, STAT3 is probably required for the differentiation and/or function of microbiota-induced RORγt⁺ iT_{reg} cells¹². Moreover, microorganism-specific iT_{reg} cells, compared with non-specific nT_{reg} cells, can better suppress inflammatory T_{eff} cells by recognizing the same epitopes. This result raises the prospect of harnessing the mechanisms of pathobiont-specific iT_{reg} cell responses to re-establish homeostasis in patients with inflammatory bowel disease, for example, by engineering non-pathogenic T_{reg} cell-inducing microorganisms²⁷ to express pathobiont antigens.

Online Content Methods, along with any additional Extended Data display items and Source Data, are available in the online version of the paper; references unique to these sections appear only in the online paper.

Received 20 April 2017; accepted 2 January 2018.

Published online 7 February 2018.

- Round, J. L. & Mazmanian, S. K. The gut microbiota shapes intestinal immune responses during health and disease. *Nat. Rev. Immunol.* **9**, 313–323 (2009).
- Hooper, L. V., Littman, D. R. & Macpherson, A. J. Interactions between the microbiota and the immune system. *Science* **336**, 1268–1273 (2012).
- Kamada, N., Seo, S. U., Chen, G. Y. & Núñez, G. Role of the gut microbiota in immunity and inflammatory disease. *Nat. Rev. Immunol.* **13**, 321–335 (2013).
- Chow, J., Tang, H. & Mazmanian, S. K. Pathobionts of the gastrointestinal microbiota and inflammatory disease. *Curr. Opin. Immunol.* **23**, 473–480 (2011).
- Kullberg, M. C. *et al.* IL-23 plays a key role in *Helicobacter hepaticus*-induced T cell-dependent colitis. *J. Exp. Med.* **203**, 2485–2494 (2006).
- Hue, S. *et al.* Interleukin-23 drives innate and T cell-mediated intestinal inflammation. *J. Exp. Med.* **203**, 2473–2483 (2006).
- Sanderson, S., Campbell, D. J. & Shastri, N. Identification of a CD4⁺ T cell-stimulating antigen of pathogenic bacteria by expression cloning. *J. Exp. Med.* **182**, 1751–1757 (1995).
- Yang, Y. *et al.* Focused specificity of intestinal T_H17 cells towards commensal bacterial antigens. *Nature* **510**, 152–156 (2014).
- Kearney, E. R., Pape, K. A., Loh, D. Y. & Jenkins, M. K. Visualization of peptide-specific T cell immunity and peripheral tolerance induction *in vivo*. *Immunity* **1**, 327–339 (1994).
- Moon, J. J. *et al.* Naive CD4⁺ T cell frequency varies for different epitopes and predicts repertoire diversity and response magnitude. *Immunity* **27**, 203–213 (2007).
- Sefik, E. *et al.* Individual intestinal symbionts induce a distinct population of RORγt⁺ regulatory T cells. *Science* **349**, 993–997 (2015).
- Ohnmacht, C. *et al.* The microbiota regulates type 2 immunity through RORγt⁺ T cells. *Science* **349**, 989–993 (2015).
- Schiering, C. *et al.* The alarmin IL-33 promotes regulatory T-cell function in the intestine. *Nature* **513**, 564–568 (2014).
- Hirota, K. *et al.* Fate mapping of IL-17-producing T cells in inflammatory responses. *Nat. Immunol.* **12**, 255–263 (2011).
- Hand, T. W. *et al.* Acute gastrointestinal infection induces long-lived microbiota-specific T cell responses. *Science* **337**, 1553–1556 (2012).
- Chai, J. N. *et al.* *Helicobacter* species are potent drivers of colonic T cell responses in homeostasis and inflammation. *Sci. Immunol.* **2**, eaal5068 (2017).
- Yang, B. H. *et al.* Foxp3⁺ T cells expressing RORγt represent a stable regulatory T-cell effector lineage with enhanced suppressive capacity during intestinal inflammation. *Mucosal Immunol.* **9**, 444–457 (2016).
- Ciofani, M. *et al.* A validated regulatory network for Th17 cell specification. *Cell* **151**, 289–303 (2012).
- Apetoh, L. *et al.* The aryl hydrocarbon receptor interacts with c-Maf to promote the differentiation of type 1 regulatory T cells induced by IL-27. *Nat. Immunol.* **11**, 854–861 (2010).
- Hoshi, N. *et al.* MyD88 signalling in colonic mononuclear phagocytes drives colitis in IL-10-deficient mice. *Nat. Commun.* **3**, 1120 (2012).
- Ivanov, I. I. *et al.* Specific microbiota direct the differentiation of IL-17-producing T-helper cells in the mucosa of the small intestine. *Cell Host Microbe* **4**, 337–349 (2008).
- Gorelik, L. & Flavell, R. A. Abrogation of TGFβ signaling in T cells leads to spontaneous T cell differentiation and autoimmune disease. *Immunity* **12**, 171–181 (2000).
- Chaudhry, A. *et al.* CD4⁺ regulatory T cells control T_H17 responses in a Stat3-dependent manner. *Science* **326**, 986–991 (2009).
- Haribhai, D. *et al.* A requisite role for induced regulatory T cells in tolerance based on expanding antigen receptor diversity. *Immunity* **35**, 109–122 (2011).
- Round, J. L. *et al.* The Toll-like receptor 2 pathway establishes colonization by a commensal of the human microbiota. *Science* **332**, 974–977 (2011).
- Kim, K. S. *et al.* Dietary antigens limit mucosal immunity by inducing regulatory T cells in the small intestine. *Science* **351**, 858–863 (2016).
- Atarashi, K. *et al.* T_{reg} induction by a rationally selected mixture of Clostridia strains from the human microbiota. *Nature* **500**, 232–236 (2013).

Supplementary Information is available in the online version of the paper.

Acknowledgements We thank S. Y. Kim and the NYU Rodent Genetic Engineering Laboratory (RGEL) for generating TCR transgenic mice, A. Heguy and colleagues at the NYU School of Medicine's Genome Technology Center (GTC) for preparation of RNA-seq libraries and RNA sequencing, the NIH Tetramer Core Facility for generating MHC class II tetramers, K. Murphy for providing the 58αβ⁺ hybridoma line, D. E. Levy for providing the *Stat3^{fl/fl};Cd4^{cre}* mice, J. Fox for providing the *H. hepaticus* strain, P. Dash and P. G. Thomas for advice on single-cell TCR cloning, and J. A. Hall, J. Muller and J. Lafaille for suggestions on the manuscript. The Experimental Pathology Research Laboratory of NYU Medical Center is supported by National Institutes of Health Shared Instrumentation grants S10OD010584-01A1 and S10OD018338-01. The GTC is partially supported by the Cancer Center Support grant P30CA016087 at the Laura and Isaac Perlmutter Cancer Center. This work was supported by the Irvington Institute fellowship program of the Cancer Research Institute (M.X.); the training program in Immunology and Inflammation 5T32AI100853 (M.P.); the Helen and Martin Kimmel Center for Biology and Medicine (D.R.L.); the Colton Center for Autoimmunity (D.R.L.); and National Institutes of Health grant R01DK103358 (R.B. and D.R.L.). D.R.L. is an Investigator of the Howard Hughes Medical Institute.

Author Contributions M.X. and M.P. designed and performed all experiments and analysed the data. Y.D. performed blinded histology scoring on colitis sections. C.A. and C.G. assisted with *in vivo* and *in vitro* experiments. R.Y. and M.P. performed RNA-seq analysis. O.J.H. and Y.B. analysed the *Gata3^{ΔTreg}* mouse phenotype. R.B. supervised RNA-seq analysis. M.X., M.P. and D.R.L. wrote the manuscript with input from the co-authors. D.R.L. supervised the research and contributed to experimental design.

Author Information Reprints and permissions information is available at www.nature.com/reprints. The authors declare no competing financial interests. Readers are welcome to comment on the online version of the paper. Publisher's note: Springer Nature remains neutral with regard to jurisdictional claims in published maps and institutional affiliations. Correspondence and requests for materials should be addressed to D.R.L. (dan.littman@med.nyu.edu).

Reviewer Information Nature thanks C. Ohnmacht and the other anonymous reviewer(s) for their contribution to the peer review of this work.

METHODS

Mice. Mice were bred and maintained in the animal facility of the Skirball Institute (New York University School of Medicine) and the National Institute of Allergy and Infectious Diseases (NIAID) in specific pathogen-free conditions. C57BL/6 mice were obtained from Jackson Laboratories or Taconic Farm. *Il10*^{tm1Cgn/J} mice were purchased from Jackson Laboratories and bred with wild-type C57BL/6 mice, which subsequently generated *Il10*^{+/-} and *Il10*^{-/-} littermates by heterozygous breeding. CD4-dnTGFβRII mice²² were purchased from Jackson Laboratories, and bred with wild-type C57BL/6 mice to generate CD4-dnTGFβRII and wild-type littermates. *Cd4*^{cre} (*Tg(Cd4-cre)1Cwi/Bflu*) and *Cd45.1* (*B6.SJL-Ptprca Pepcb/BoyJ*) mice were purchased from Jackson Laboratories. *Foxp3*^{creYFP} mice were previously described and obtained from Jackson Laboratories²⁸. *Il23*^{gfp} and *Mafigf*^{gfp} strains were previously described^{29,30} and provided by M. Oukka and C. Birchmeier, respectively. *Stat3*^{gfp}/*gfp*, *Cd4*^{cre} mice were provided by D. E. Levy. *Gata3*^{gfp}/*gfp*, *Foxp3*^{creYFP} mice were bred at the NIAID. Littermates with matched sex (both males and females) were used. Except the aged mice (6–12 months old) analysed in the experiments of Fig. 4e, mice in all the experiments were 6–12 weeks old at the starting point of treatments. Animal sample size estimates were determined using power analysis (power = 90% and $\alpha = 0.05$) based on the mean and standard deviation from our previous studies and/or pilot studies using 4–5 mice per group. All animal procedures were performed in accordance with protocols approved by the Institutional Animal Care and Usage Committee of New York University School of Medicine or the NIAID as applicable.

Antibodies, intracellular staining and flow cytometry. The following monoclonal antibodies were purchased from eBiosciences, BD Pharmingen or BioLegend: CD3 (145-2C11), CD4 (RM4-5), CD25 (PC61), CD44 (IM7), CD45.1 (A20), CD45.2 (104), CD62L (MEL-14), CXCR5 (L138D7), NPR-1 (3E12), ST2 (RMST2-2), TCRβ (H57-597), TCR Vβ6 (RR4-7), TCR Vβ8.1/8.2 (MR5-2), TCR Vβ14 (14-2), BCL6 (K112-91), c-MAF (T54-853), FOXP3 (FJK-16s), GATA3 (TWAJ), Helios (22F6), RORγt (B2D or Q31-378), T-bet (eBio4B10), IL-10 (JES5-16E3), IL-17A (eBio17B7) and IFNγ (XM61.2). 4',6-diamidino-2-phenylindole (DAPI) or Live/dead fixable blue (ThermoFisher) was used to exclude dead cells.

For transcription factor staining, cells were stained for surface markers, followed by fixation and permeabilization before nuclear factor staining according to the manufacturer's protocol (FOXP3 staining buffer set from eBioscience). For cytokine analysis, cells were incubated for 5 h in RPMI with 10% FBS, phorbol 12-myristate 13-acetate (PMA) (50 ng ml⁻¹; Sigma), ionomycin (500 ng ml⁻¹; Sigma) and GolgiStop (BD). Cells were stained for surface markers before fixation and permeabilization, and then subjected to intracellular cytokine staining according to the manufacturer's protocol (Cytofix/Cytoperm buffer set from BD Biosciences).

Flow cytometric analysis was performed on an LSR II (BD Biosciences) or an Aria II (BD Biosciences) and analysed using FlowJo software (Tree Star).

Isolation of lymphocytes. Intestinal tissues were sequentially treated with PBS containing 1 mM DTT at room temperature for 10 min, and 5 mM EDTA at 37 °C for 20 min to remove epithelial cells, and then minced and dissociated in RPMI containing collagenase (1 mg ml⁻¹ collagenase II; Roche), DNase I (100 μg ml⁻¹; Sigma), dispase (0.05 U ml⁻¹; Worthington) and 10% FBS with constant stirring at 37 °C for 45 min (small intestine) or 60 min (large intestine). Leukocytes were collected at the interface of a 40%/80% Percoll gradient (GE Healthcare). The Peyer's patches and caecal patch were treated in a similar fashion except for the first step of removal of epithelial cells. Lymph nodes and spleens were mechanically disrupted.

Single-cell TCR cloning. *Il23*^{gfp/+} mice were maintained in SFB-free conditions to guarantee low T_H17 background levels. To induce a robust T_H17 cell response, the mice were orally infected with *H. hepaticus* and injected intraperitoneally with 1 mg anti-IL-10RA (clone 1B1.3A, Bioxcell) every week from the day of infection. After two weeks, large intestine GFP⁺ CD4⁺ T cells were sorted on the BD Aria II and deposited at one cell per well into 96-well PCR plates pre-loaded with 5 μl high-capacity cDNA reverse transcription mix (Thermo Fisher) supplemented with 0.1% Triton X-100 (Sigma-Aldrich). Immediately after sorting, whole plates were incubated at 37 °C for 2 h, and then inactivated at 85 °C for 10 min for cDNA preparation. A nested multiplex PCR approach described previously was used to amplify the CDRα and CDRβ TCR regions separately from the single cell cDNA³¹. PCR products were cleaned up with ExoSap-IT reagent (USB) and Sanger sequencing was performed by Macrogen. Open reading frame nucleotide sequences of the TCRα and TCRβ families were retrieved from the IMGT database (<http://www.imgt.org>)³².

Generation of TCR hybridomas. The NFAT-GFP 58α⁺β⁻ hybridoma cell line was provided by K. Murphy³³. To reconstitute TCRs, cDNA of TCRα and TCRβ were synthesized as gBlocks fragments by Integrated DNA Technologies (IDT), linked with the self-cleavage sequence of 2A (TCRα-p2A-TCRβ), and shuttled into a modified MigR1 retrovector in which IRES-GFP was replaced with IRES-mCD4 (mouse CD4) as described previously⁸. Then retroviral vectors were transduced

into Phoenix E packaging cells using TransIT-293 (Mirus). Hybridoma cells were transduced with viral supernatants in the presence of polybrene (8 μg ml⁻¹) by spin infection for 90 min at 32 °C. Transduction efficiencies were monitored by checking mCD3 surface expression three days later.

Assay for hybridoma activation. Splenic dendritic cells were used as antigen-presenting cells (APCs). B6 mice were injected intraperitoneally with 5 × 10⁶ FLT3L-expressing B16 melanoma cells to drive APC proliferation as previously described³⁴. Splenocytes were prepared 10 days after injection, and positively enriched for CD11c⁺ cells using MACS LS columns (Miltenyi). 2 × 10⁴ hybridoma cells were incubated with 10⁵ APCs and antigens in round bottom 96-well plates for two days. GFP induction in the hybridomas was analysed by flow cytometry as an indicator of TCR activation.

Construction and screen of whole-genome shotgun library of *H. hepaticus*.

The shotgun library was prepared with a procedure modified from previous studies^{7,8}. In brief, genomic DNA was purified from cultured *H. hepaticus* with DNeasy PowerSoil kit (Qiagen). DNA was partially digested with MluCI (NEB), and the fraction between 500 and 2,000 base pairs (bp) was ligated into the EcoRI-linearized pGEX-6P-1 expression vector (GE Healthcare). Ligation products were transformed into ElectroMAX DH10B competent Cells (Invitrogen) by electroporation. To estimate the size of the library, we cultured 1% and 0.1% of transformed bacteria on lysogeny broth (LB) agar plates containing 100 μg ml⁻¹ Ampicillin for 12 h and then quantified the number of colonies. The library is estimated to contain 3 × 10⁶ clones. To ensure the quality of the library, we sequenced the inserts of randomly picked colonies. All the sequences were mapped to the *H. hepaticus* genome, and their sizes were 700 to 1,200 bp. We aliquoted the bacteria into 96-well deepwell plates (Axygen) (~30 clones per well) and grew with AirPort microporous cover (Qiagen) in 37 °C. The expression of exogenous proteins was induced by 1 mM isopropylthiogalactoside (IPTG, Sigma) for 4 h. Then bacteria were collected in PBS and heat-killed by incubating at 85 °C for 1 h, and stored at -20 °C until use. Two screening rounds were performed to identify the antigen-expressing clones. For the first round, pools of heat-killed bacterial clones were added to a co-culture of splenic APCs and hybridomas. Clones within the positive pools were subsequently screened individually against the hybridoma bait. Finally, the inserts of positive clones were subjected to Sanger sequencing. The sequences were blasted against the genome sequence of *H. hepaticus* (ATCC51449) and aligned to the annotated open reading frames. Full-length open reading frames containing the retrieved fragments were cloned into pGEX-6P-1 to confirm their activity in the T cell stimulation assay.

Epitope mapping. We cloned overlapping fragments spanning the entire HH_1713 coding region into the pGEX-6P-1 expression vector, and expressed these in *Escherichia coli* BL21 cells. The heat-killed bacteria were used to stimulate relevant hybridomas. This process was repeated until we mapped the epitope to a region containing 30 amino acids. The potential MHC class II epitopes were predicted with online software RANKPEP³⁵. Overlapping peptides spanning the predicted region were further synthesized (Genescript) and verified by stimulation of the hybridomas.

Generation of TCRtg mice. TCR sequences of HH5-1 and HH7-2 were cloned into the pTα and pTβ vectors provided by D. Mathis³⁶. TCR transgenic mice were generated by the Rodent Genetic Engineering Core at the New York University School of Medicine. Positive pups were genotyped by testing TCR Vβ8.1/8.2 (HH5-1tg) or Vβ6 (HH7-2tg) expression on T cells from peripheral blood.

MHC class II tetramer production and staining. HH-E2 tetramer was produced by the NIH Tetramer Core Facility³⁷. In brief, QESPRIAAAYTIKGA (HH_1713-E2), an immunodominant epitope validated with the hybridoma stimulation assay, was covalently linked to I-A^b via a flexible linker, to produce pMHCII monomers. Soluble monomers were purified, biotinylated, and tetramerized with phycoerythrin- or allophycocyanin-labelled streptavidin. SFB-specific tetramer (3340-A6 tetramer) was described previously⁸. To stain endogenous T cells, mononuclear cells from SILP, LILP or caecal patch were first resuspended in MACS buffer with FcR block, 2% mouse serum and 2% rat serum. Then tetramer was added (10 nM) and incubated at room temperature for 60 min, and cells were re-suspended by pipetting every 20 min. Cells were washed with MACS buffer and followed by regular surface marker staining at 4 °C.

Adoptive transfer of TCRtg cells. Recipient mice were colonized with *H. hepaticus* and/or SFB by oral gavage seven days before adoptive transfer (The method for oral infection of SFB has been previously described⁸). Spleens from donor TCRtg mice were collected and mechanically dissociated. Red blood cells were lysed using ACK lysis buffer (Lonza). For TCRtg mice in wild-type background, naive Tg T cells were sorted as CD4⁺CD3⁺CD44^{lo}CD62L^{hi}CD25⁻Vβ6⁺ (HH7-2tg), Vβ8.1/8.2⁺ (HH5-1tg) or Vβ14⁺ (7B8tg) on the Aria II (BD Biosciences). For HH7-2tg mice bred to the *Foxp3*^{creYFP} background, naive transgenic T cells were sorted as CD4⁺CD3⁺CD44^{lo}CD62L^{hi}FOXP3^{creYFP}-Vβ6⁺. Cells were resuspended in PBS on ice and transferred into congenic isotype-labelled recipient mice by retro-orbital injection. Cells from indicated tissues were analysed two weeks after transfer.

***H. hepaticus* culture and oral infection.** *H. hepaticus* was provided by J. Fox (MIT). Frozen stock aliquots of *H. hepaticus* were stored in Brucella broth with 20% glycerol and frozen at -80°C . The bacteria were grown on blood agar plates (TSA with 5% sheep blood, Thermo Fisher). Inoculated plates were placed into a hypoxia chamber (Billups-Rothenberg), and anaerobic gas mixture consisting of 80% nitrogen, 10% hydrogen, and 10% carbon dioxide (Airgas) was added to create a micro-aerobic atmosphere, in which the oxygen concentration was 3–5%. The micro-aerobic jars containing bacterial plates were left at 37°C for 5 days before animal inoculation. For oral infection, *H. hepaticus* was resuspended in Brucella broth by application of a pre-moistened sterile cotton swab applicator tip to the colony surface. The concentration of bacterial inoculation dose was determined by the use of a spectrophotometric optical density (OD) analysis at 600 nm, and adjusted to OD_{600 nm} readings between 1 and 1.5. 0.2 ml bacterial suspension was administered to each mouse by oral gavage. Mice were inoculated every 5 days for a total of two doses.

***H. hepaticus*-specific TCRtg cell-mediated transfer colitis.** Naive T (T_{naive}) cells were isolated from the spleens of HH7-2tg mice as $\text{CD4}^{+}\text{CD3}^{+}\text{CD44}^{\text{lo}}\text{CD62L}^{\text{hi}}\text{CD25}^{-}\text{V}\beta 6^{+}$ by FACS. The sorted cells (1×10^3) were administered by retro-orbital injection into *H. hepaticus*-colonized $\text{Rag1}^{-/-}$ mice. After two weeks, cells from the large intestine were isolated and analysed by flow cytometry.

***C. rodentium*-mediated colon inflammation.** *C. rodentium* strain DBS100 (ATCC51459; American Type Culture Collection) was used for all inoculations. Bacteria were grown at 37°C in LB broth to OD_{600 nm} reading between 0.4 and 0.6. Mice were inoculated with 200 μl of a bacterial suspension (1×10^9 – 2×10^9 colony-forming units (CFU)) by way of oral gavage. After 15 days, cells from the large intestine were isolated, stained for HH-E2 tetramer and other markers as indicated and analysed by flow cytometry.

DSS-induced colitis. Mice were colonized with *H. hepaticus* 5 days before DSS treatment. To induce colitis, mice were given 2% DSS (50,000MW, Affymetrix/USB) in drinking water for 2 cycles, with each exposure for 7 days with 5 days of untreated water in between. Control mice were given drinking water for the same period. Cells from the large intestine were then isolated, stained for HH-E2 tetramer and other marks as indicated and analyzed by flow cytometry. Animal weights were monitored daily during the entire experiment.

T cell culture. Naive CD4^{+} T cells were purified from spleen and lymph nodes of mice with indicated genotypes. In brief, CD4^{+} T cells were positively selected from organ cell suspensions by magnetic-activated cell sorting using CD4 beads (MACS, Miltenyi) according to the product protocol, and then isolated as $\text{CD4}^{+}\text{CD3}^{+}\text{CD44}^{\text{lo}}\text{CD62L}^{\text{hi}}\text{CD25}^{-}$ (polyclonal) or $\text{CD4}^{+}\text{CD3}^{+}\text{CD44}^{\text{lo}}\text{CD62L}^{\text{hi}}\text{CD25}^{-}\text{V}\beta 6^{+}$ (HH7-2tg) or $\text{V}\beta 8.1/8.2^{+}$ (HH5-1tg) by FACS. T cells were cultured at 37°C in RPMI (Hyclone) supplemented with 10% heat-inactivated FBS (Hyclone), 50 U penicillin–streptomycin (Hyclone), 2 mM glutamine (Hyclone), 10 mM HEPES (Hyclone), 1 mM sodium pyruvate (Hyclone) and 50 μM β -mercaptoethanol (Gibco).

To generate iT_{reg} cells for transfer colitis experiments (see below), wild-type, HH7-2tg or HH5-1tg cells were seeded at 1×10^6 cells in 1.5 ml per well in 12-well plates pre-coated with an anti-hamster IgG secondary antibody (MP Biomedicals), and cultured for 72 h. The culture was supplemented with soluble anti-CD3 ϵ (0.25 $\mu\text{g ml}^{-1}$, Bioxcell, clone 145-2C11) and anti-CD28 (1 $\mu\text{g ml}^{-1}$, Bioxcell, clone 37.51) for TCR stimulation, and anti-IL-4 (1 $\mu\text{g ml}^{-1}$, Bioxcell, clone 11B11), anti-IFN γ (1 $\mu\text{g ml}^{-1}$, Bioxcell, clone XMG1.2), human TGF β 1 (20 ng ml^{-1} , Peprotech), human IL-2 (500 U ml^{-1} , Peprotech) and all-trans retinoic acid (100 nM, sigma) for optimal iT_{reg} cell polarization. Aliquots of cultured cells were analysed for intracellular FOXP3 staining by flow cytometry. After they were confirmed to be more than 98% FOXP3 $^{+}$, the remaining live cells (DAPI negative) were FACS sorted for adoptive transfer.

To test the conditions inducing c-MAF expression, 200 μl naive T cells isolated from $\text{Maf}^{\text{fl/fl}}$, $\text{Maf}^{\text{fl/fl}};\text{Cd4}^{\text{cre}}$ or $\text{Stat3}^{\text{fl/fl}};\text{Cd4}^{\text{cre}}$ mice were seeded at 1×10^5 cells per well in 96-well plates pre-coated with the anti-hamster IgG secondary antibody, and cultured for 48 h. The culture was supplemented with soluble anti-CD3 ϵ (0.25 $\mu\text{g ml}^{-1}$) and anti-CD28 (1 $\mu\text{g ml}^{-1}$) for TCR stimulation. Combinations of the following antibodies or cytokines were added as indicated in Extended Data Fig. 9c: anti-TGF β 1 (1 $\mu\text{g ml}^{-1}$, Bioxcell, 1D11.16.8), human TGF β 1 (0.3 or 20 ng ml^{-1} , Peprotech), human IL-2 (500 U ml^{-1} , Peprotech), mouse IL-6 (20 ng ml^{-1} , Thermo), mouse IL-10 (100 ng ml^{-1} , Peprotech), mouse IL-27 (25 ng ml^{-1} , Thermo), mouse IL-12 (10 ng ml^{-1} , Peprotech), mouse IL-1 β (10 ng ml^{-1} , Peprotech), mouse IL-4 (10 ng ml^{-1} , R&D systems), mouse IFN γ (10 ng ml^{-1} , Peprotech), and all-trans retinoic acid (100 nM, sigma).

T_{reg} cell in vitro suppression assay. T_{naive} cells with the phenotype $\text{CD4}^{+}\text{CD3}^{+}\text{CD44}^{\text{lo}}\text{CD62L}^{\text{hi}}\text{CD25}^{-}$ were isolated from the spleen and lymph nodes of CD45.1 wild-type B6 mice by FACS and labelled with carboxyfluorescein diacetate succinimidyl ester (CFSE). nT_{reg} (CD45.2) cells with the phenotype

$\text{CD4}^{+}\text{CD3}^{+}\text{FOXP3}^{\text{creYFP}}\text{NRP1}^{+}$ were isolated from the spleen and lymph nodes of $\text{Foxp3}^{\text{creYFP}}$ or $\text{Maf}^{\Delta T_{\text{reg}}}$ mice by FACS. B cells were isolated from the spleen and lymph nodes of CD45.2 wild-type B6 mice by positive enrichment for B220 $^{+}$ cells using MACS LS columns (Miltenyi). 2.5×10^4 CFSE-labelled T_{naive} cells were cultured for 72 h with B cell APCs (5×10^4) and anti-CD3 (1 $\mu\text{g ml}^{-1}$) in the presence or absence of various numbers of nT_{reg} cells as indicated. The cell division index of responder T cells was assessed by dilution of CFSE using FlowJo software (Tree Star).

Suppression of adoptive transfer colitis with T_{reg} cells. To compare the suppressive function of c-MAF-sufficient and -deficient nT_{reg} cells, $\text{CD4}^{+}\text{CD3}^{+}\text{CD25}^{-}\text{CD45RB}^{\text{hi}}$ T_{eff} cells were isolated by FACS from B6 mouse spleens and $\text{CD4}^{+}\text{CD3}^{+}\text{FOXP3}^{\text{creYFP}}\text{NRP1}^{+}$ nT_{reg} were isolated from spleen of *H. hepaticus*-colonized $\text{Foxp3}^{\text{creYFP}}$ or $\text{Maf}^{\Delta T_{\text{reg}}}$ mice. T_{eff} cells (5×10^5) were administered by retro-orbital injection into *H. hepaticus*-colonized $\text{Rag1}^{-/-}$ mice alone, or simultaneously with 4×10^5 nT_{reg} cells as previously described³⁸. Animal weights were measured weekly.

To compare the suppressive function of TCRtg and polyclonal T_{reg} cells, T_{naive} cells with the phenotype $\text{CD4}^{+}\text{CD3}^{+}\text{CD44}^{\text{lo}}\text{CD62L}^{\text{hi}}\text{CD25}^{-}$ and $\text{V}\beta 6^{+}$ (HH7-2tg) or $\text{CD4}^{+}\text{CD3}^{+}\text{CD44}^{\text{lo}}\text{CD62L}^{\text{hi}}\text{CD25}^{-}$ and $\text{V}\beta 8.1/8.2^{+}$ (HH5-1tg) were isolated from spleens of TCRtg mice. 1,000 naive HH7-2tg or HH5-1tg cells were co-transferred with different numbers (500,000, 150,000 or 50,000 as indicated in Fig. 4f, g) of *in vitro* polarized (see T cell culture, above) HH7-2tg, HH5-1tg or polyclonal iT_{reg} cells into *H. hepaticus*-colonized $\text{Rag1}^{-/-}$ mice by retro-orbital injection.

Co-housed littermate recipients were randomly assigned to different treatment groups such that each cage contained all treatment conditions. After four to five weeks (for nT_{reg} cell comparisons) or eight weeks (for the transgenic T cell comparisons), large intestines were collected and fixed with 10% neutral buffered formalin (Fisher). Samples were sectioned and stained with haematoxylin and eosin (H&E) by the Histopathology Core at the New York University School of Medicine.

Histology analysis. The H&E slides from each sample were examined in a blinded fashion. Samples of proximal, mid and distal colon were graded semi-quantitatively from 0 to 4 as described previously³⁹. Scores from proximal, mid and distal sites were averaged to obtain inflammation scores for the entire colon.

Cell isolation for RNA-seq experiment. A T cell reconstitution system was designed to purify c-MAF-sufficient or -deficient iT_{reg} cells from compatible microenvironments. In brief, T_{naive} cells were isolated from the spleen of CD45.2 $\text{Foxp3}^{\text{creYFP}}$ or $\text{Maf}^{\Delta T_{\text{reg}}}$ mice as $\text{CD4}^{+}\text{CD3}^{+}\text{CD44}^{\text{lo}}\text{CD62L}^{\text{hi}}\text{FOXP3}^{\text{creYFP}}$ and T_{reg} cells were isolated from the spleens of CD45.1 wild-type B6 mice as $\text{CD4}^{+}\text{CD3}^{+}\text{CD25}^{+}$ by FACS. T_{naive} cells (2×10^5) and T_{reg} cells (8×10^5) were simultaneously administered by retro-orbital injection into *H. hepaticus*-colonized $\text{Rag1}^{-/-}$ mice. Two weeks after transfer, c-MAF-sufficient or -deficient iT_{reg} cells were purified from the large intestine of reconstituted mice as $\text{CD4}^{+}\text{CD3}^{+}\text{CD45.1}^{-}\text{CD45.2}^{+}\text{FOXP3}^{\text{creYFP}}$ by FACS and collected into FBS. 20% of the sorted cells were stained for ROR γ t and FOXP3 and the remaining cells were saved in TRIzol (Invitrogen) for RNA extraction.

To isolate *H. hepaticus*-specific colitogenic T_{eff} cells, HH7-2tg; $\text{Maf}^{\Delta T_{\text{reg}}}$ and HH7-2tg; $\text{Foxp3}^{\text{cre}}$ mice were colonized with *H. hepaticus*. HH7-2tg; $\text{Foxp3}^{\text{cre}}$ mice were further injected intraperitoneally with 1 mg anti-IL-10RA antibody (clone 1B1.3A, Bioxcell) weekly from the day of colonization. HH7-2 T_{eff} cells ($\text{CD3}^{+}\text{CD4}^{+}\text{TCRV}\beta 6^{+}\text{FOXP3}^{-}\text{YFP}^{-}$) were sorted from the LILP two weeks after colonization. Homeostatic IL-23R-GFP $^{+}$ T cells ($\text{CD3}^{+}\text{CD4}^{+}\text{IL-23R-GFP}^{+}$) were sorted from both SILP and LILP of $\text{Il23r}^{\text{GFP/+}}$ mice stably colonized with SFB.

RNA-seq library preparation. Total RNA was extracted using TRIzol (Invitrogen) followed by DNase I treatment and cleanup with RNeasy MinElute kit (Qiagen). T_{reg} cell RNA-seq libraries were prepared with the SMART-Seq v4 Ultra Low Input RNA Kit (Clontech 634899 and 634888). $T_{\text{H}}17$ cell RNA libraries were prepared using the Nugen Ovation Ultralow Library Systems V2 (7102 and 0344). All sequencing was performed using the Illumina NextSeq. RNA-seq libraries were prepared and sequenced by the Genome Technology Core at New York University School of Medicine.

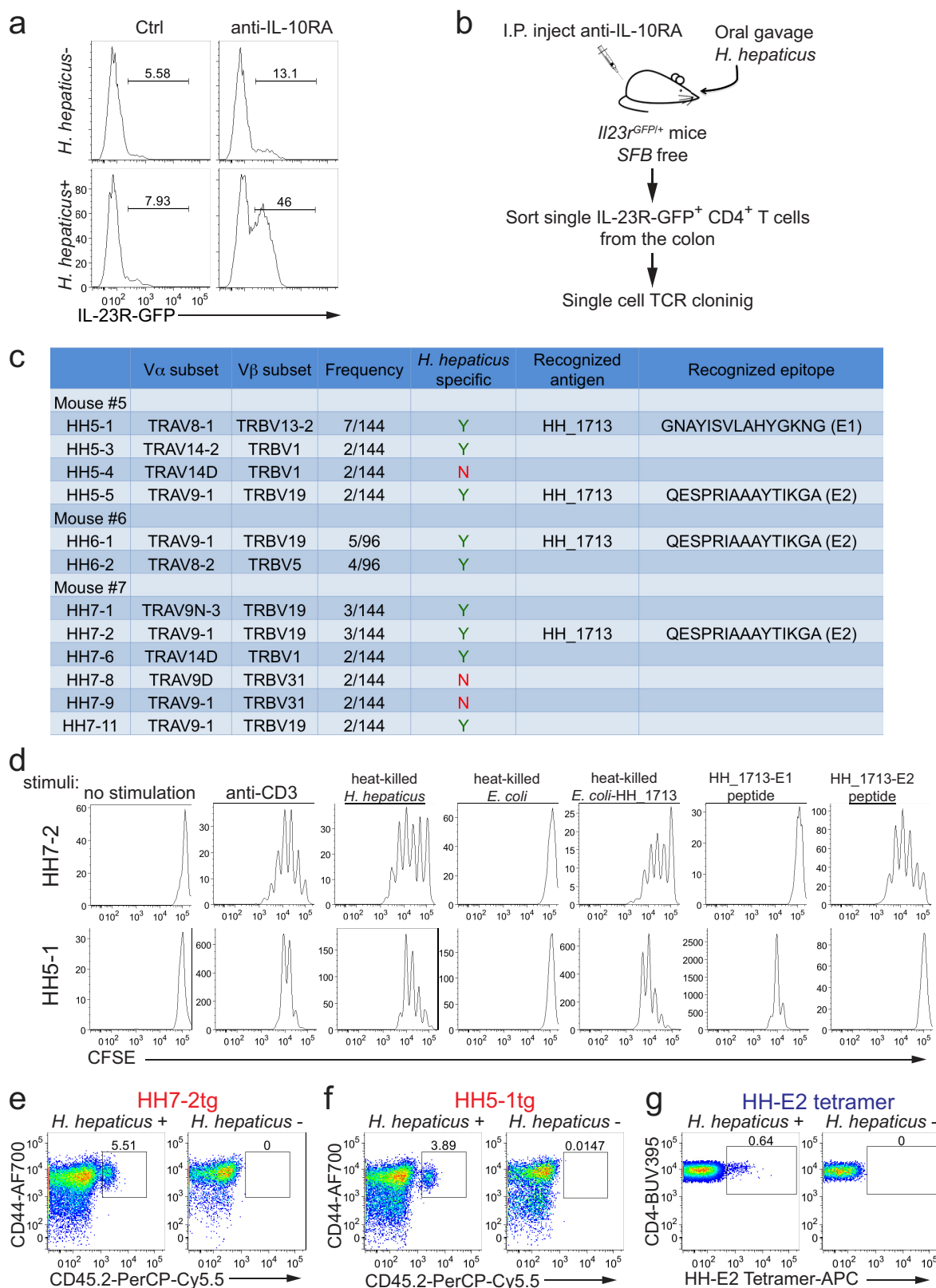
Data processing of RNA-seq. RNA-seq reads were mapped to the *Mus musculus* genome Ensembl annotation release 87 with STAR (v2.5.2b)⁴⁰. Uniquely mapped reads were counted using featureCounts⁴¹ with parameters: -p -Q 20. DESeq2⁴² was used to identify differentially expressed genes across conditions with experimental design: ~condition + gender. Read counts were normalized and transformed by functions varianceStabilizingTransformation and rlog in DESeq2 with the following parameter: blind=FALSE. Gender differences were considered as batch effect, and were corrected by ComBat⁴³. Downstream analysis and data visualization were performed in R⁴⁴.

Statistical analysis. For animal studies, mutant and control groups did not always have similar standard deviations and therefore an unpaired two-sided Welch's *t*-test was used. Error bars represent \pm s.d. Animal sample size estimates were determined using power analysis (power = 90% and $\alpha = 0.05$) based on the mean and s.d.

from our previous studies and/or pilot studies using 4–5 mice. No samples were excluded from analysis. For RNA-seq analysis, differentially expressed genes were calculated in DESeq2 using the Wald test with Benjamini–Hochberg correction to determine the FDR. Genes were considered differentially expressed with FDR < 0.1 and log₂ fold change > 1.5. Enriched disease pathways in pathogenic HH7-2 T_H17 were determined using Ingenuity Pathway Analysis (<https://www.ingenuity.com>). Gene set enrichment analysis (GSEA, <http://www.broad.mit.edu/gsea/>) on Maf-deficient or -sufficient iT_{reg} cells was performed using a gene set of 33 ROR γ t-dependent genes in NRP1[−] colonic T_{reg} cells (*Rorc*, *Ccr6*, *Idua*, *Il1rn*, *C2cd4b*, *Nxt1*, *Tmem176b*, *Cxcr3*, *Tnfrsf1a*, *Adams7*, *Pik3ip1*, *Rrad*, *Crmp1*, *Irak3*, *Fam129b*, *Ppcs*, *Tbxa2r*, *Avpi1*, *Serpib1a*, *Alkbh7*, *Nckipd*, *Havcr2*, *Il23r*, *Txnip*, *Igj* (also known as *Jchain*), *Trim16*, *Pigp*, *Rras*, *Samd10*, *Il1r2*, *F2rl1*, *Maff* and *Ly6c1*)¹¹.

Data availability. cDNA sequences of *H. hepaticus*-specific TCRs yielding data that support the findings of this study have been deposited in GenBank with the accession codes KY964547–KY964570. RNA-seq data have been deposited in the Sequence Read Archive (SRA) with accession code SRP126932, and in the Gene Expression Omnibus (GEO) with accession code GSE108184. All other data are available from the corresponding author upon reasonable request.

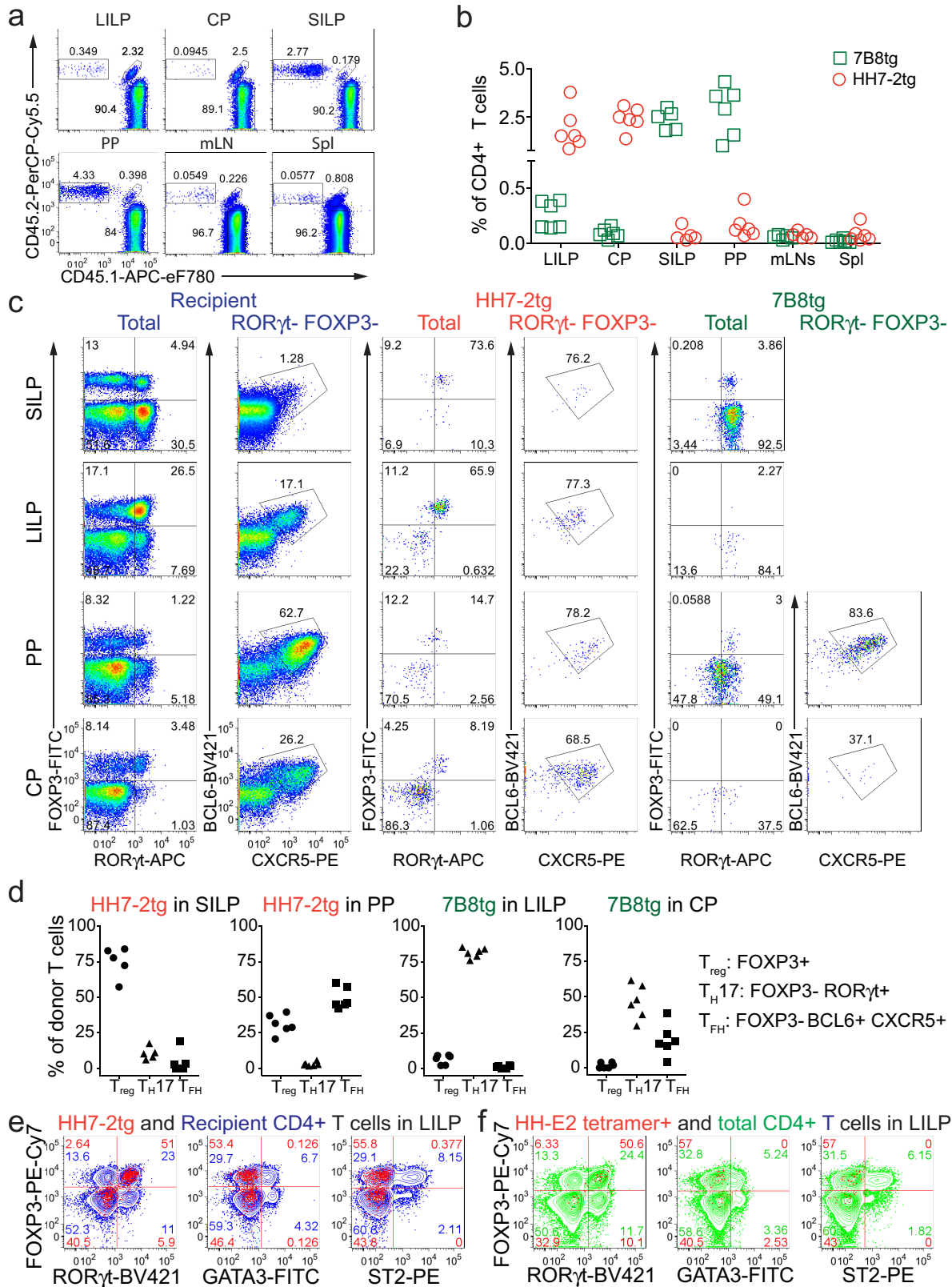
28. Rubtsov, Y. P. *et al.* Regulatory T cell-derived interleukin-10 limits inflammation at environmental interfaces. *Immunity* **28**, 546–558 (2008).
29. Wende, H. *et al.* The transcription factor c-Maf controls touch receptor development and function. *Science* **335**, 1373–1376 (2012).
30. Awasthi, A. *et al.* Cutting edge: IL-23 receptor GFP reporter mice reveal distinct populations of IL-17-producing cells. *J. Immunol.* **182**, 5904–5908 (2009).
31. Dash, P. *et al.* Paired analysis of TCR α and TCR β chains at the single-cell level in mice. *J. Clin. Invest.* **121**, 288–295 (2011).
32. Lefranc, M. P. *et al.* IMGT, the international ImMunoGeneTics information system. *Nucleic Acids Res.* **37**, D1006–D1012 (2009).
33. Ise, W. *et al.* CTLA-4 suppresses the pathogenicity of self antigen-specific T cells by cell-intrinsic and cell-extrinsic mechanisms. *Nat. Immunol.* **11**, 129–135 (2010).
34. Mach, N. *et al.* Differences in dendritic cells stimulated in vivo by tumors engineered to secrete granulocyte-macrophage colony-stimulating factor or Flt3-ligand. *Cancer Res.* **60**, 3239–3246 (2000).
35. Reche, P. A. & Reinherz, E. L. Prediction of peptide–MHC binding using profiles. *Methods Mol. Biol.* **409**, 185–200 (2007).
36. Kouskoff, V., Signorelli, K., Benoist, C. & Mathis, D. Cassette vectors directing expression of T cell receptor genes in transgenic mice. *J. Immunol. Methods* **180**, 273–280 (1995).
37. Altman, J. D. *et al.* Phenotypic analysis of antigen-specific T lymphocytes. *Science* **274**, 94–96 (1996).
38. Ostani, D. V. *et al.* T cell transfer model of chronic colitis: concepts, considerations, and tricks of the trade. *Am. J. Physiol. Gastrointest. Liver Physiol.* **296**, G135–G146 (2009).
39. Read, S., Malmström, V. & Powrie, F. Cytotoxic T lymphocyte-associated antigen 4 plays an essential role in the function of CD25⁺CD4⁺ regulatory cells that control intestinal inflammation. *J. Exp. Med.* **192**, 295–302 (2000).
40. Dobin, A. *et al.* STAR: ultrafast universal RNA-seq aligner. *Bioinformatics* **29**, 15–21 (2013).
41. Liao, Y., Smyth, G. K. & Shi, W. featureCounts: an efficient general purpose program for assigning sequence reads to genomic features. *Bioinformatics* **30**, 923–930 (2014).
42. Love, M. I., Huber, W. & Anders, S. Moderated estimation of fold change and dispersion for RNA-seq data with DESeq2. *Genome Biol.* **15**, 550 (2014).
43. Johnson, W. E., Li, C. & Rabinovic, A. Adjusting batch effects in microarray expression data using empirical Bayes methods. *Biostatistics* **8**, 118–127 (2007).
44. R Development Core Team. *R: A Language And Environment For Statistical Computing*; <https://www.r-project.org/> (R Foundation for Statistical Computing, Vienna, Austria, 2016).



Extended Data Figure 1 | Cloning and characterization of *H. hepaticus*-specific T_H17 TCRs, and generation of TCRtg mice and MHC class II tetramers.

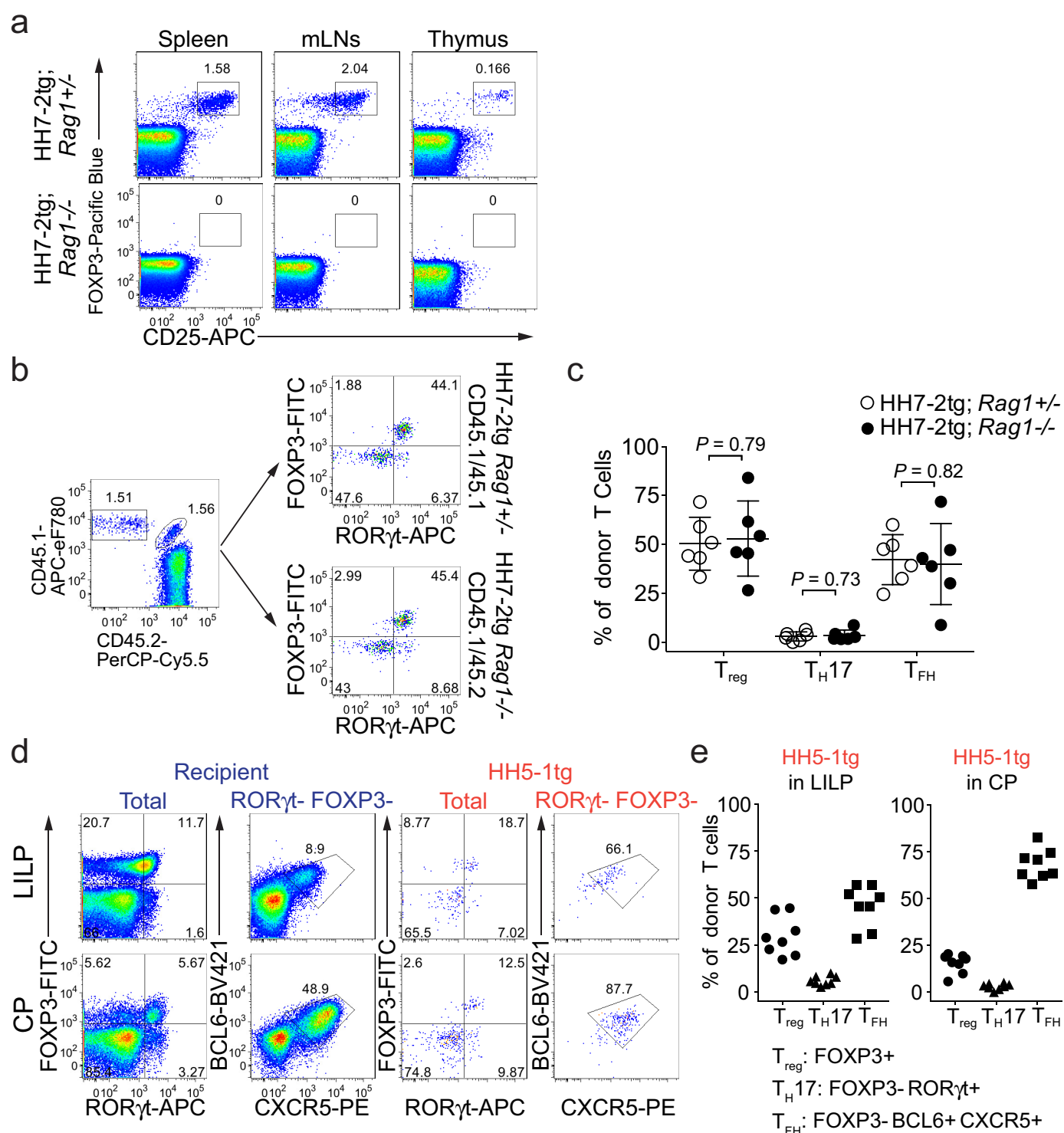
a, IL-23R-GFP expression in CD4⁺ T cells from the large intestines of mice with and without *H. hepaticus* colonization and after IL-10RA blockade. Data are from one of five independent experiments. **b**, Experimental scheme for cloning *H. hepaticus*-induced single IL-23R-GFP⁺ (predominantly T_H17) cell TCRs under IL-10RA blockade. **c**, Summary of the 12 dominant *H. hepaticus*-induced T_H17 TCRs.

d, *In vitro* activation of CFSE-labelled naive HH7-2tg and HH5-1tg cells by indicated stimuli in the presence of antigen-presenting cells. Data are from one of two independent experiments. **e**, **f**, Expansion of donor-derived HH7-2tg (**e**) and HH5-1tg (**f**) (CD45.2) cells in the large intestine of *H. hepaticus*-colonized or -free CD45.1 mice, gated on total CD4⁺ T cells. Data are from one of three independent experiments. **g**, HH-E2 tetramer staining of CD4⁺ T cells from the large intestine of *H. hepaticus*-colonized or -free mice. Data are from one of six independent experiments.



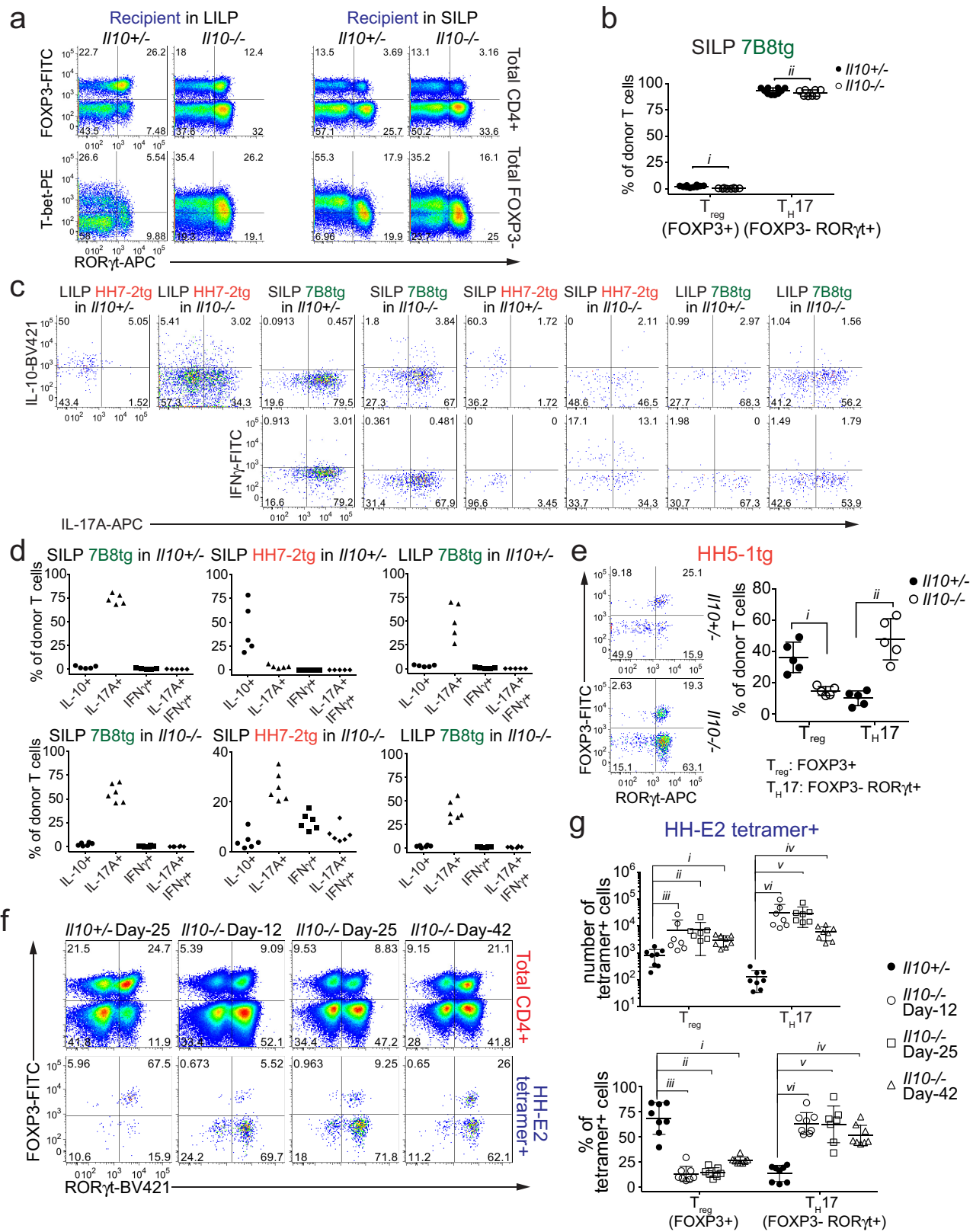
Extended Data Figure 2 | Extended characterization of SFB- and *H. hepaticus*-specific T cells in distinct anatomical sites in bacteria-colonized wild-type mice. **a**, Representative flow cytometry plots of donor-derived HH7-2tg (CD45.1/45.2) and 7B8tg (CD45.2/45.2) T cells in indicated tissues of mice colonized with SFB and *H. hepaticus*, gated on total CD4⁺ T cells (CD4⁺CD3⁺) ($n = 15$). **b**, Proportions of donor-derived HH7-2tg and 7B8tg T cells among total CD4⁺ T cells in indicated tissues. Data in **a** and **b** are from 1 of 3 experiments, with a total of 15 mice in the 3 experiments. **c**, Representative flow cytometry plots of RORγt, FOXP3, BCL6 and CXCR5 expression in CD4⁺ T cells from the host and from

HH7-2tg and 7B8tg donors in different tissues ($n = 15$). **d**, Frequencies of T_{reg} (FOXP3⁺), T_{H17} (FOXP3⁺ RORγt⁺) and T_{FH} (BCL6⁺ CXCR5⁺) cells among donor-derived HH7-2tg and 7B8tg cells in different tissues. Data are from 1 of 3 experiments, with a total of 15 mice in the 3 experiments. **e**, Representative flow cytometry plots of FOXP3, RORγt, GATA3 and ST2 expression in CD4⁺ T cells from the host (blue) and from HH7-2tg donors (red) in the LILP ($n = 5$). **f**, Representative flow cytometry plots of FOXP3, RORγt, GATA3 and ST2 expression in total CD4⁺ (green) and HH-E2 tetramer⁺ (red) T cells in the LILP ($n = 5$). Spl, spleen.



Extended Data Figure 3 | Extended characterization of *H. hepaticus*-specific TCRtg cell differentiation. **a**, HH7-2tg; *Rag1*^{−/−} mice do not develop T_{reg} cells in the thymus. Representative flow cytometry plots of T_{reg} (FOXP3⁺CD25⁺) frequency in indicated tissues of *H. hepaticus*-free HH7-2tg; *Rag1*^{+/−} (*n* = 3) or HH7-2tg; *Rag1*^{−/−} (*n* = 3) mice. **b**, **c**, HH7-2tg; *Rag1*^{+/−} and HH7-2tg; *Rag1*^{−/−} donor-derived T cells differentiated into equal frequencies of RORγt⁺ T_{reg} cells in the large intestine of wild-type mice. Equal numbers (2,000) of congenic isotype-labelled HH7-2tg; *Rag1*^{+/−} (CD45.1/45.1) and *Rag1*^{−/−} (CD45.1/45.2) naive T cells were co-transferred into *H. hepaticus*-colonized wild-type B6 mice. Cells from the LILP were analysed two weeks after transfer. Data summarize two independent experiments (*n* = 6). **b**, Representative flow cytometry plots of donor and recipient T cell frequency (left), and RORγt and FOXP3 expression (right) (*n* = 6). **c**, Frequencies of T_{reg}

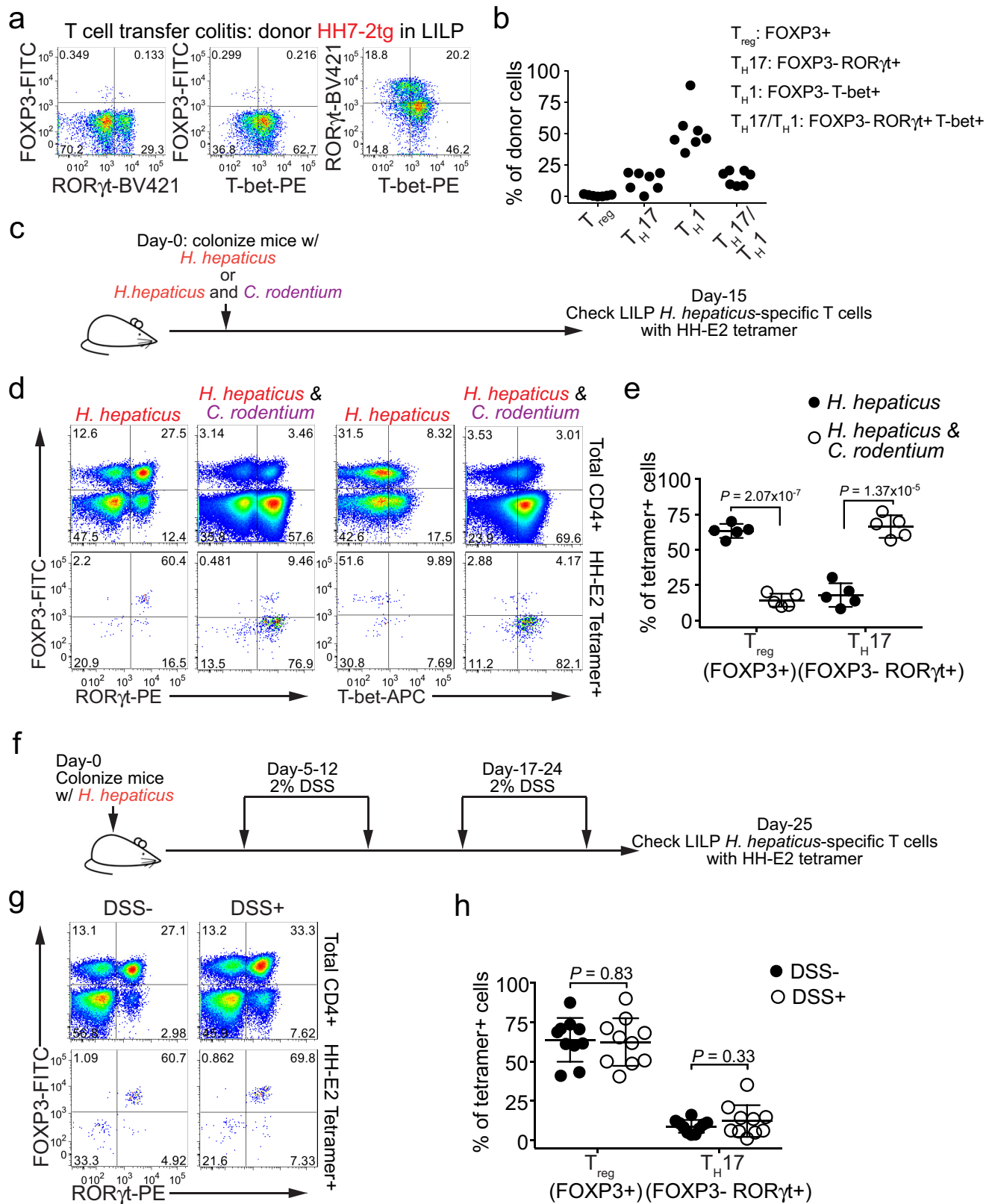
(FOXP3⁺), T_{H17} (FOXP3[−]RORγt⁺) and T_{FH} (BCL6⁺CXCR5⁺) cells among HH7-2tg *Rag1*^{+/−} (*n* = 6) and *Rag1*^{−/−} (*n* = 6) donor-derived T cells. **d**, **e**, Approximately 2,000 naive HH5-1tg cells (CD45.1/45.2) were adoptively transferred into wild-type B6 mice (CD45.2/45.2) colonized with *H. hepaticus*. Cells from LILP and the caecal patch were analysed two weeks after transfer. **d**, Representative flow cytometry plots are shown for RORγt, FOXP3, BCL6 and CXCR5 expression in donor-derived and recipient CD4⁺ T cells in the indicated tissues. **e**, Frequencies of T_{reg} (FOXP3⁺), T_{H17} (FOXP3[−]RORγt⁺) and T_{FH} (BCL6⁺CXCR5⁺) among HH5-1tg donor T cells (*n* = 8). Data are a summary of eight mice from two independent experiments. All statistics were calculated by unpaired two-sided Welch's *t*-test. Error bars denote mean ± s.d. *P* values are indicated on the figure.



Extended Data Figure 4 | See next page for caption.

Extended Data Figure 4 | Differentiation of SFB- and *H. hepaticus*-specific T cells in *Il10*^{+/-} and *Il10*^{-/-} mice. **a–d**, Equal numbers (10,000) of congenic isotype-labelled HH7-2tg (CD45.1/45.2) and 7B8tg (CD45.1/45.1) T cells were co-transferred into *Il10*^{-/-} and *Il10*^{+/-} mice (CD45.2/45.2) colonized with both *H. hepaticus* and SFB. Intestinal T cells were examined two weeks later. **a**, Representative flow cytometry plots of FOXP3, RORγt and T-bet expression in total and FOXP3⁻ host CD4⁺ T cells in the SILP and LILP of *Il10*^{+/-} (*n* = 10) and *Il10*^{-/-} (*n* = 8) mice that received TCR transgenic T cell transplants. **b**, Frequencies of T_{reg} (FOXP3⁺) and T_H17 (FOXP3⁻RORγt⁺) cells among SILP 7B8tg donor-derived cells in *Il10*^{+/-} (*n* = 10) and *Il10*^{-/-} (*n* = 8) mice. Data for **a** and **b** are a summary of four independent experiments. **c**, Representative flow cytometry plots of IL-10, IL-17A and IFNγ expression in transferred 7B8tg and HH7-2tg cells from LILP and SILP of *Il10*^{+/-} and *Il10*^{-/-} mice after re-stimulation (*n* = 5 or 6). **d**, Proportions of transferred 7B8tg and HH7-2tg cells in the SILP and LILP of *Il10*^{+/-} and *Il10*^{-/-} mice that express IL-10, IL-17A and IFNγ after re-stimulation (*n* = 5 or 6). Data for

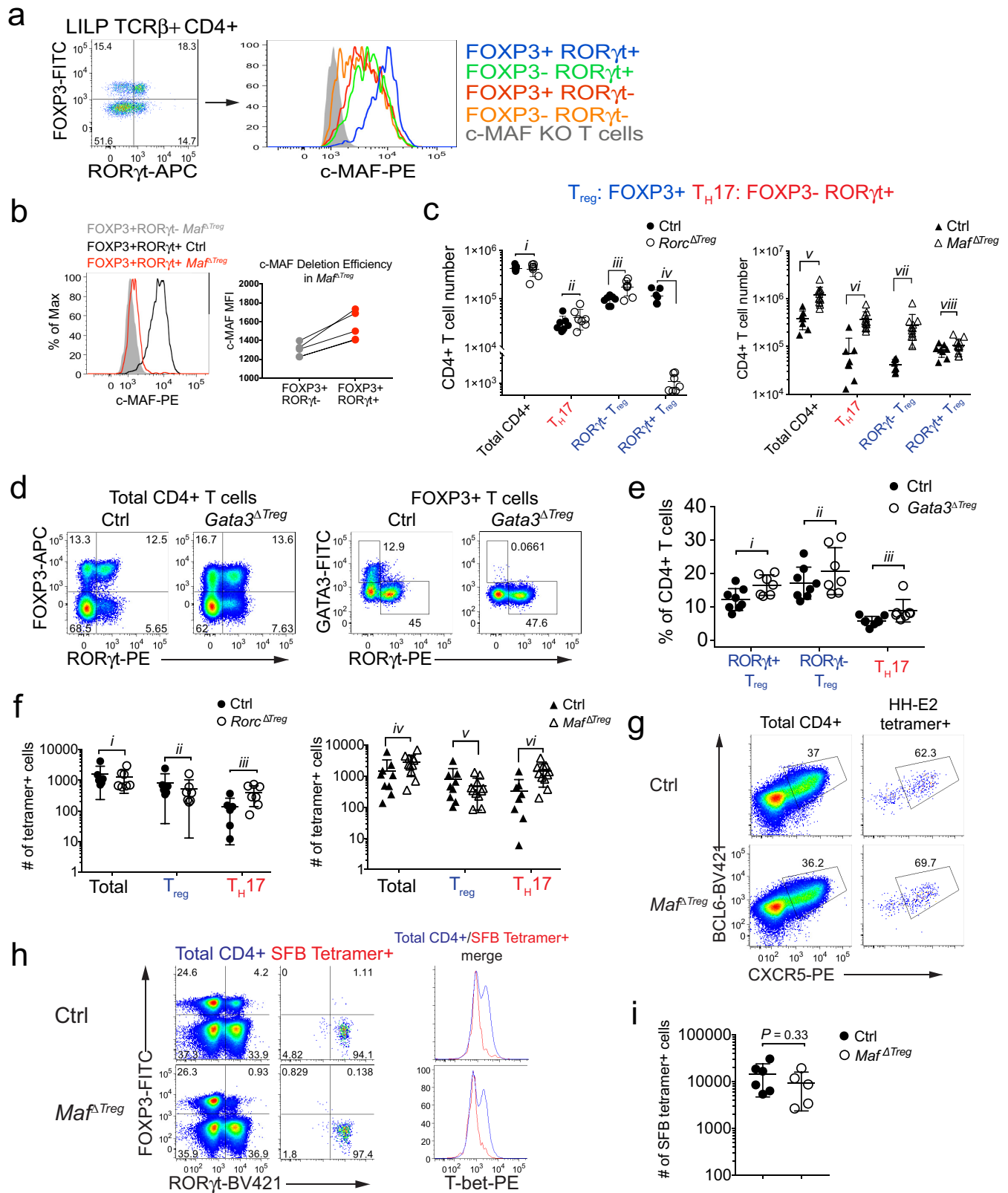
c and **d** are a summary of two independent experiments. **e**, 2,000 naive HH5-1tg cells (CD45.1/45.2) were adoptively transferred into *Il10*^{+/-} and *Il10*^{-/-} mice colonized with *H. hepaticus*. Cells from the LILP were analysed two weeks after transfer (*n* = 5). Representative flow cytometry plots of RORγt and FOXP3 expression in HH5-1tg donor cells are shown (left), along with a compilation of frequencies of T_{reg} (FOXP3⁺) and T_H17 (FOXP3⁻RORγt⁺). **f**, **g**, RORγt and FOXP3 expression in total CD4⁺ and HH-E2 tetramer⁺ T cells (**f**) and frequencies (above) and absolute numbers (below) of T_{reg} (FOXP3⁺) and T_H17 (FOXP3⁻RORγt⁺) cells among HH-E2 tetramer⁺ T cells (**g**) in the LILP of *Il10*^{+/-} (day 25, *n* = 8) and *Il10*^{-/-} (day 12 *n* = 8, day 25 *n* = 7, day 42 *n* = 8) mice colonized with *H. hepaticus* for indicated times. All statistics were calculated by unpaired two-sided Welch's *t*-test. Error bars denote mean ± s.d. *P* values are as follows: **b**, i = 0.062 and ii = 0.063. **e**, i = 1.46×10^{-3} and ii = 3.10×10^{-4} . **g**, Top, i = 7.82×10^{-4} , ii = 0.014, iii = 0.088, iv = 1.48×10^{-4} , v = 1.47×10^{-3} and vi = 0.016; bottom, i = 3.85×10^{-6} , ii = 9.63×10^{-7} , iii = 1.31×10^{-6} , iv = 8.91×10^{-7} , v = 1.15×10^{-5} and vi = 1.56×10^{-7} .



Extended Data Figure 5 | See next page for caption.

Extended Data Figure 5 | Differentiation of *H. hepaticus*-specific T cells in colitis models. **a, b**, Naive HH7-2tg T cells were adoptively transferred into *H. hepaticus*-colonized *Rag1*^{-/-} mice to induce colitis ($n = 7$). Data summarize two independent experiments. Representative expression of FOXP3, ROR γ t, and T-bet (**a**), and a compilation of frequencies of T_{reg} (FOXP3⁺), T_H17 (FOXP3⁻ROR γ t⁺), T_H1 (FOXP3⁻T-bet⁺) and T_H17/T_H1 (FOXP3⁻ROR γ t⁺T-bet⁺) cells in HH7-2tg donor-derived cells in the LILP of recipient mice was analysed 4 weeks after transfer. **c–e**, Analysis of *H. hepaticus*-specific T cell differentiation during *C. rodentium*-induced colonic inflammation. Data summarize two independent experiments. **c**, Schematic of experimental design. **d, e**, Representative flow cytometry plots of FOXP3, ROR γ t and T-bet expression in total CD4⁺ and HH-E2

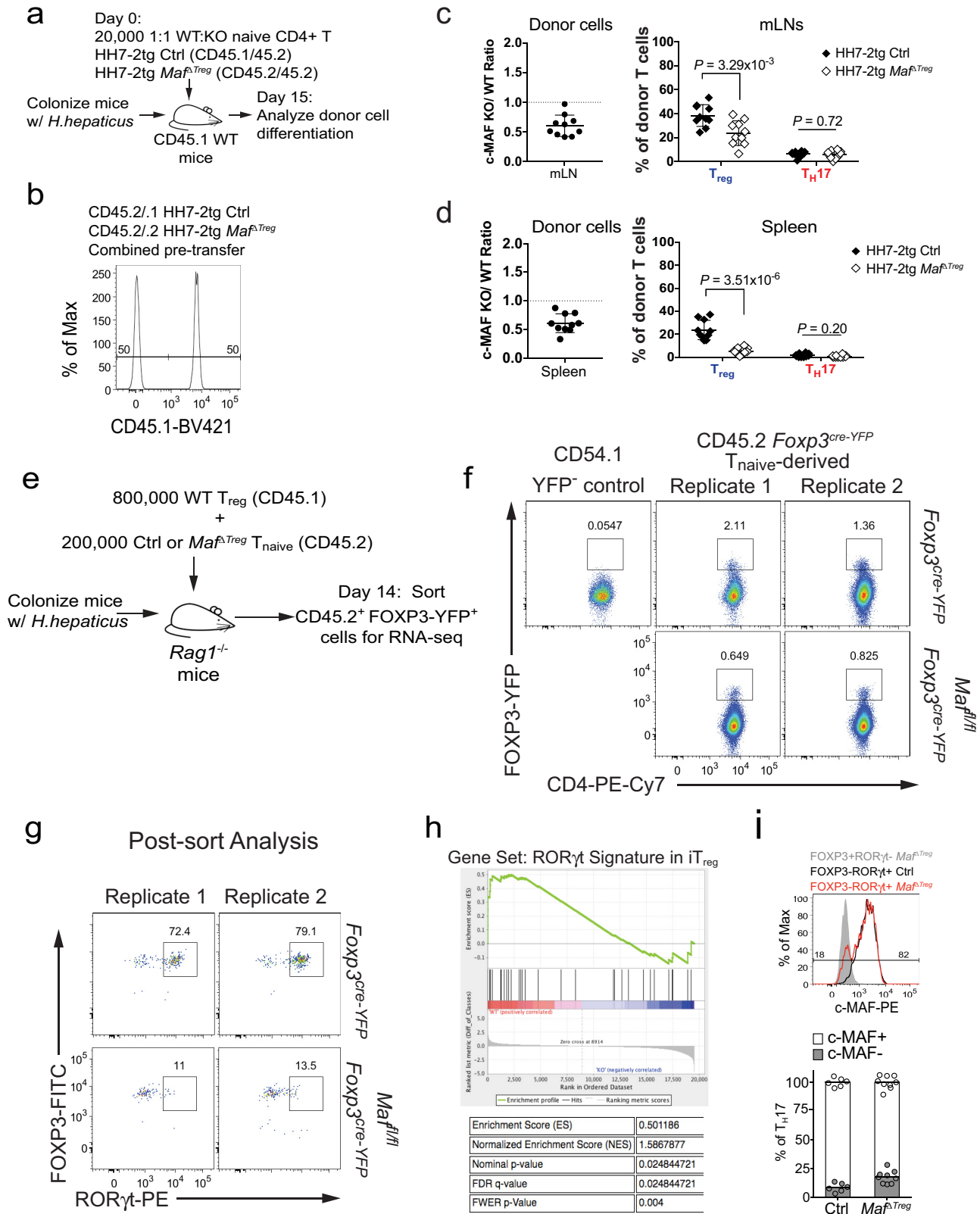
tetramer⁺ T cells (**d**) and frequencies of T_{reg} (FOXP3⁺) and T_H17 (FOXP3⁻ROR γ t⁺) cells among HH-E2 tetramer⁺ T cells (**e**) in the LILP of *C. rodentium*-infected ($n = 5$) and -uninfected mice ($n = 5$). **f–h**, Analysis of *H. hepaticus*-specific T cell differentiation during DSS-induced colitis. Data are a summary of two independent experiments. **f**, Schematic of experimental design. **g, h**, Representative flow cytometry plots of FOXP3, ROR γ t and T-bet expression in total CD4⁺ and HH-E2 tetramer⁺ T cells (**g**) and a compilation of frequencies of T_{reg} (FOXP3⁺) and T_H17 (FOXP3⁻ROR γ t⁺) cells among HH-E2 tetramer⁺ cells (**h**) in the LILP of DSS-treated ($n = 10$) and -untreated mice ($n = 10$). All statistics were calculated by unpaired two-sided Welch's *t*-test. Error bars denote mean \pm s.d. *P* values are indicated on the figure.



Extended Data Figure 6 | See next page for caption.

Extended Data Figure 6 | Extended characterization of *Maf* ^{Δ Treg}, *Rorc* ^{Δ Treg} and *Gata3* ^{Δ Treg} mice. **a**, Expression of c-MAF in the indicated CD4⁺ T cell subsets in the LILP. **b**, Incomplete depletion of c-MAF protein in ROR γ t⁺ T_{reg} cells in *Maf* ^{Δ Treg} mice shown by a representative flow cytometry graph from 3 independent experiments (left), and a compilation of mean fluorescence intensities (MFI) in ROR γ t⁺ T_{reg} cells and residual ROR γ t⁺ T_{reg} cells (right). **c**, Absolute numbers of indicated CD4⁺ T cell populations in the LILP of indicated mice. Data are a summary of 3 independent experiments for *Rorc* ^{Δ Treg} ($n=7$) and littermate controls ($n=7$) and 4 independent experiments for *Maf* ^{Δ Treg} ($n=11$) and littermate controls ($n=8$). **d, e**, Representative flow cytometry plots of FOXP3, ROR γ t and GATA3 expression in total and FOXP3⁺ CD4⁺ T cells (**d**) and a compilation of frequencies of ROR γ t⁺ and ROR γ t⁺ T_{reg} (FOXP3⁺) cells and T_H17 (FOXP3⁺ ROR γ t⁺) cells among total CD4⁺ T cells (**e**) in the LILP of *Gata3* ^{Δ Treg} ($n=8$) and littermate controls ($n=7$). Data summarize two independent experiments. **f**, Absolute numbers of indicated HH-E2 tetramer⁺ T cell populations in the LILP of indicated

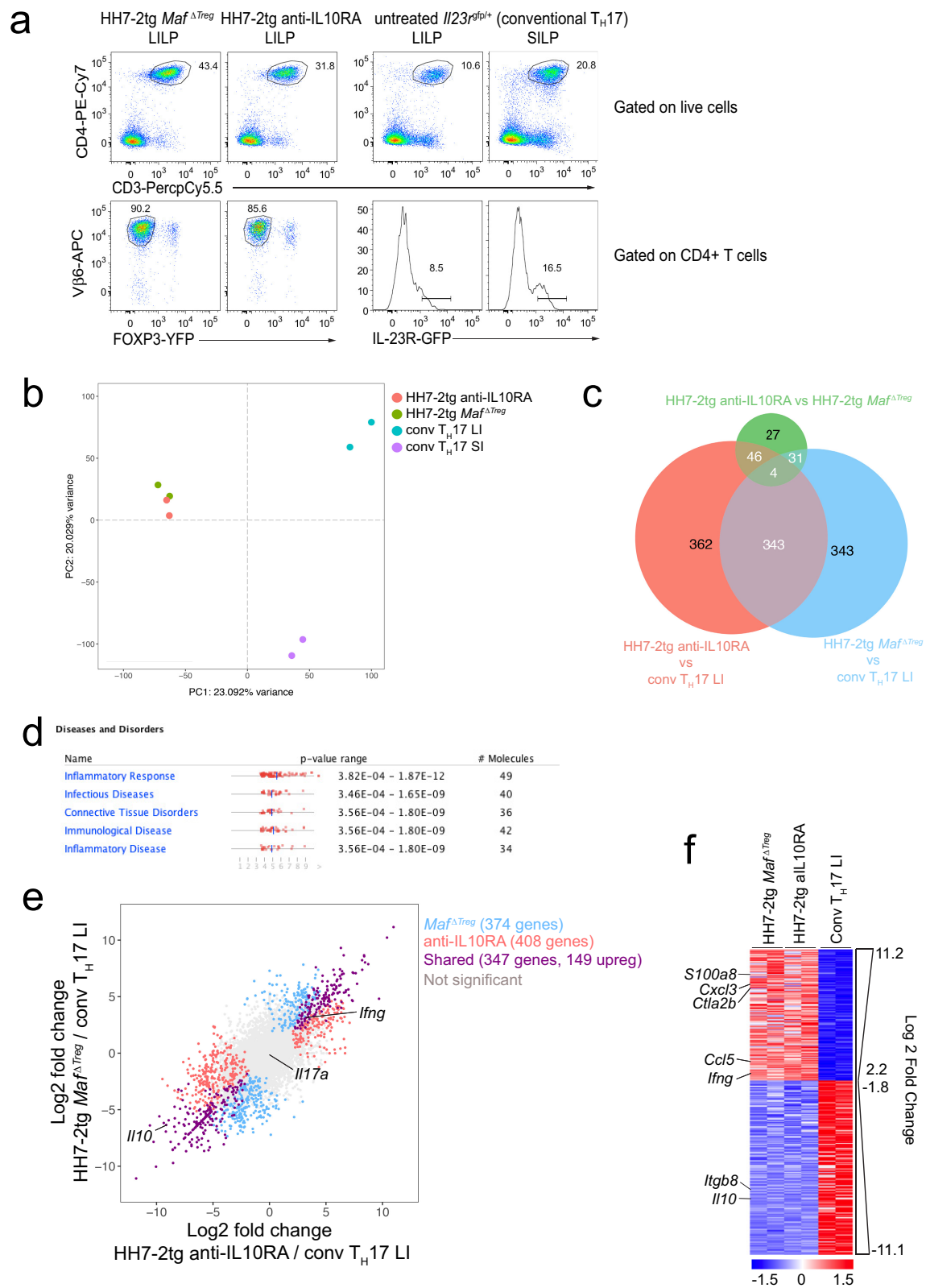
mice. Data are a summary of 3 independent experiments for *Rorc* ^{Δ Treg} ($n=7$) and littermate controls ($n=6$) and 4 independent experiments for *Maf* ^{Δ Treg} ($n=11$) and littermate controls ($n=8$). **g**, Representative flow cytometry plots of T_{HH} markers BCL6 and CXCR5 among total CD4⁺ and HH-E2 tetramer⁺ cells from the caecal patch of *Maf* ^{Δ Treg} mice and littermate controls ($n=4$). **h, i**, SFB-specific T cells did not adopt the pro-inflammatory T_H17–T_H1 phenotype or expand in *Maf* ^{Δ Treg} mice. Data summarize two experiments, *Maf* ^{Δ Treg} ($n=5$) and littermate controls ($n=6$). Representative flow cytometry plots of FOXP3, ROR γ t and T-bet expression in total CD4⁺ and SFB-tetramer⁺ T cells (**h**) and absolute number of SFB-tetramer⁺ cells (**i**) in the SILP. All statistics were calculated by unpaired two-sided Welch's *t*-test. Error bars denote mean \pm s.d. *P* values are indicated on the figure or as follows: **c**, $i=0.42$, $ii=0.73$, $iii=6.38 \times 10^{-3}$, $iv=2.28 \times 10^{-4}$, $v=7 \times 10^{-11}$, $vi=7.10 \times 10^{-3}$, $vii=2.99 \times 10^{-2}$ and $viii=0.83$. **e**, $i=0.081$, $ii=0.102$ and $iii=0.16$. **f**, $i=0.65$, $ii=0.41$, $iii=0.045$, $iv=0.12$, $v=0.29$ and $vi=6.28 \times 10^{-3}$.



Extended Data Figure 7 | See next page for caption.

Extended Data Figure 7 | Analysis of c-MAF function in ROR γ t⁺ iT_{reg} cells. **a–d**, Equal numbers of congenic isotype-labelled naive *Maf*^{fl/+}; *Foxp3*^{cre} (ctrl, CD45.1/45.2) and *Maf*^{fl/fl}; *Foxp3*^{cre} (CD45.2/45.2) HH7-2tg cells were co-transferred into *H. hepaticus*-colonized wild-type CD45.1 mice. Cells from the LILP, mLN and spleen were analysed 15 days after transfer. **a**, Schematic of experimental design. **b**, Flow cytometry plot depicting ratio of pooled co-transferred naive T cells before transfer. **c, d**, Left, ratios of *Maf*^{ΔTreg} versus control HH7-2tg donor-derived cells in the mLN and spleen ($n = 10$). Dashed line represents ratio of co-transferred cells before transfer. Right, frequencies of T_{reg} (FOXP3⁺) and T_H17 (FOXP3[−]ROR γ t⁺) cells among donor-derived cells ($n = 10$). Statistics were calculated by unpaired two-sided Welch's *t*-test. Error bars denote mean \pm s.d. *P* values are indicated on the figure. **e–h**, Isolation of *Maf*-deficient and -sufficient iT_{reg} cells for RNA-seq through a

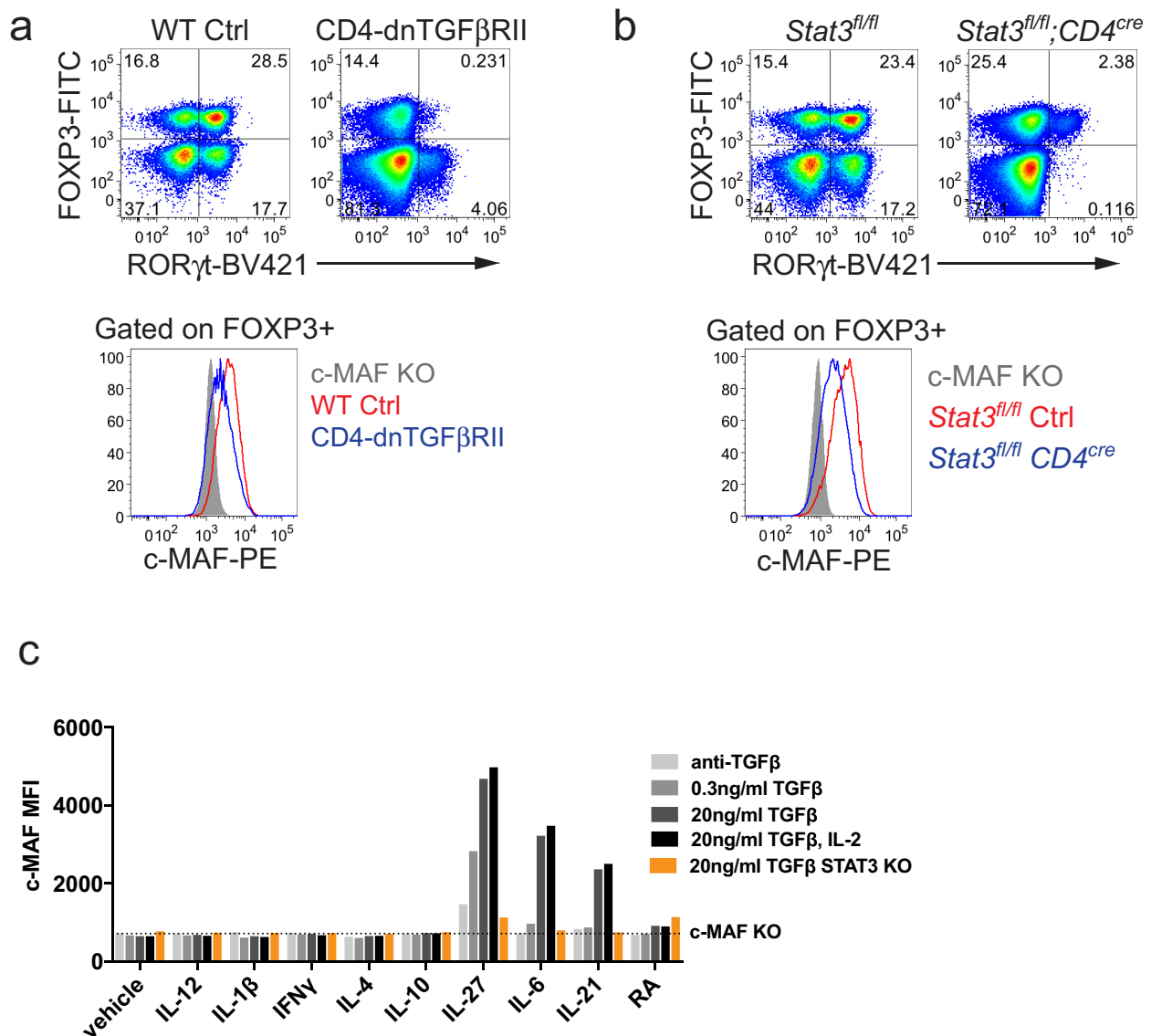
T cell reconstitution system. Two replicates represent two independent experiments. **e**, Schematic of experimental design. **f**, Flow cytometry plots indicating the sorting gates from two independent experiments. **g**, Flow cytometry plots showing FOXP3 and ROR γ t expression in sorted FOXP3[−]YFP⁺ cells from two independent experiments. **h**, Gene set enrichment analysis performed on RNA-seq dataset of c-MAF-sufficient versus -deficient iT_{reg} (FOXP3[−]YFP⁺) cells ($n = 2$ independent experiments) with a gene set of 33 ROR γ t-dependent transcripts identified previously¹¹. **i**, Top, representative flow cytometry plot of c-MAF expression in T_H17 cells (FOXP3[−]ROR γ t⁺) from LILP of control (black) and *Maf*^{ΔTreg} (red) mice. The c-MAF negative population is defined by gating on FOXP3⁺ROR γ t[−] T_{reg} cells from *Maf*^{ΔTreg} mice (solid grey). Bottom, frequency of c-MAF expression in T_H17 cells in control ($n = 6$) and *Maf*^{ΔTreg} ($n = 9$) mice from 3 independent experiments.



Extended Data Figure 8 | See next page for caption.

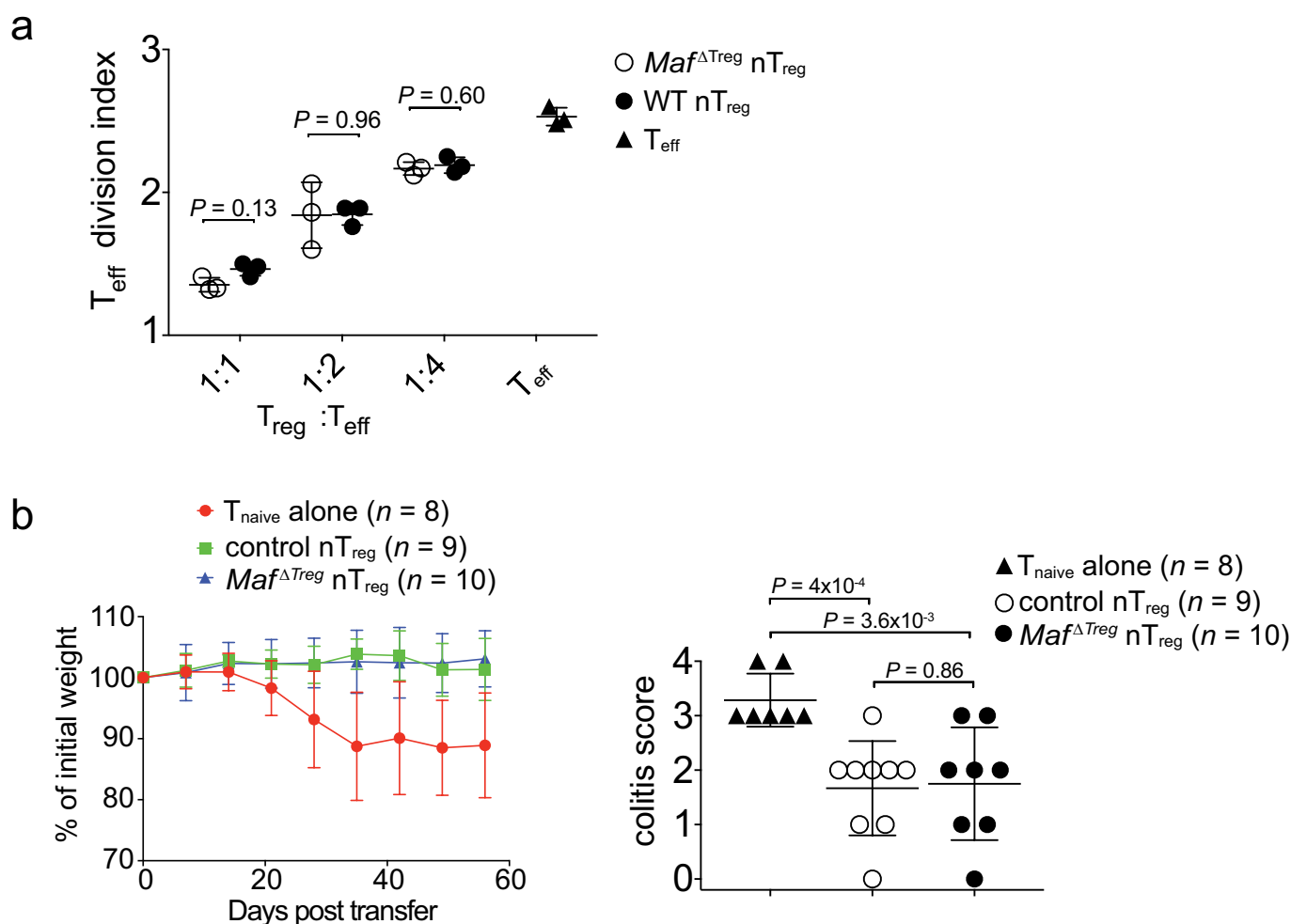
Extended Data Figure 8 | Transcriptional profiling of conventional T_H17 and *H. hepaticus*-specific T effector cells. **a–f**, RNA-seq was performed on 2 biological replicates of each indicated condition. **a**, Flow cytometry analysis of HH7-2tg T_{eff} cells from *H. hepaticus*-colonized mice and conventional IL-23R-GFP⁺ (predominantly SFB-specific T_H17) cells from SFB-colonized mice. GFP⁺ gates in the bottom panel were used for sorting to perform RNA-seq. **b**, Principal component analysis of RNA-seq data from sorted cell populations. Coloured dots represent individual samples ($n = 2$). **c**, **e**, **f**, Differentially expressed genes were calculated in DESeq2 using the Wald test with Benjamini–Hochberg correction to determine the FDR. Genes were considered differentially expressed when FDR < 0.1 and log₂ fold change > 1.5. **c**, Venn diagram depicting differentially expressed genes between indicated comparisons.

d, Significantly enriched disease pathways in the set of 149 shared genes upregulated in HH7-2tg *Maf*^{ΔTreg} and HH7-2tg from anti-IL-10RA-treated mice compared to conventional large intestine T_H17 cells. *P* values calculated by ingenuity pathway analysis using Fisher's exact test. **e**, Comparison of transcriptomes of *H. hepaticus*-specific T_H17 cells from mice treated with IL-10RA blockade or *Maf*^{ΔTreg} and conventional T_H17 cells. Scatter plot depicting log₂ fold change of gene expression. Blue, red and purple dots indicate significant differences. **f**, Heat map depicting the 347 shared genes differentially expressed between pathogenic HH7-2 and conventional T_H17 cells (purple dots in **e**). Data for each condition are the mean of 2 biological replicates. Scale bar represents z-scored variance stabilized data (VSD) counts.



Extended Data Figure 9 | STAT3 and TGFβ signal synergistically to promote c-MAF expression. **a**, Top, representative flow cytometry plots depicting RORγt and FOXP3 expression in CD4⁺ T cells in the LILP of mice with a dominant-negative mutant of TGFβ receptors (CD4-dnTGFβRII) and littermate controls ($n = 3$). Bottom, representative plot of c-MAF expression in FOXP3⁺ cells from the indicated mice in the top panel. **b**, Top, representative flow cytometry plots depicting RORγt and FOXP3 expression in CD4⁺ T cells in the LILP of *Stat3^{fl/fl};Cd4^{cre}* and

Stat3^{fl/fl} littermate controls ($n = 4$). Bottom, representative plot of c-MAF staining in FOXP3⁺ cells from indicated mice in the top panel. **c**, Mean fluorescence intensity of c-MAF staining in *in vitro* differentiated CD4⁺ T cells. Naive CD4⁺ T cells from wild-type, *Stat3^{fl/fl};Cd4^{cre}* and *Mafl^{fl/fl};Cd4^{cre}* mice were activated for 48 h with anti-CD3ε/anti-CD28 antibodies under indicated conditions. Dashed line represents the MFI of c-MAF in *Mafl^{fl/fl};Cd4^{cre}* T cells. Data are from one of two independent experiments.



Extended Data Figure 10 | c-MAF-deficient nT_{reg} cells retain suppressive function. **a**, Equivalent inhibitory function of nT_{reg} cells from *Maf*^{ΔTreg} and control mice in the *in vitro* proliferative response of CD4⁺ T cells (T_{eff}). Three data points are from one of two independent replicates. **b**, Activity of nT_{reg} cells in the transfer-mediated colitis model. Percentage weight change (left) and colitis histology scores (right) of *Rag1*^{-/-} mice

adoptively transferred with naive T cells alone ($n = 8$), or naive T cells in combination with nT_{reg} cells from *Maf*^{ΔTreg} ($n = 10$) or littermate control *Foxp3*^{creYFP} ($n = 9$) mice. Data are a summary of two independent experiments. All statistics were calculated by unpaired two-sided Welch's *t*-test. Error bars denote mean \pm s.d. *P* values are indicated on the figure.

Asparagine bioavailability governs metastasis in a model of breast cancer

Simon R. V. Knott^{1,2,3*}, Elvin Wagenblast^{2,4,5*}, Showkhin Khan^{2,6}, Sun Y. Kim², Mar Soto², Michel Wagner⁷, Marc-Olivier Turgeon⁷, Lisa Fish^{8,9,10}, Nicolas Erard¹, Annika L. Gable², Ashley R. Maceli², Steffen Dickopf², Evangelia K. Papachristou¹, Clive S. D'Santos¹, Lisa A. Carey¹¹, John E. Wilkinson¹², J. Chuck Harrell¹³, Charles M. Perou¹⁴, Hani Goodarzi^{8,9,10}, George Poulgiannis^{7,15} & Gregory J. Hannon^{1,2,6}

Using a functional model of breast cancer heterogeneity, we previously showed that clonal sub-populations proficient at generating circulating tumour cells were not all equally capable of forming metastases at secondary sites¹. A combination of differential expression and focused *in vitro* and *in vivo* RNA interference screens revealed candidate drivers of metastasis that discriminated metastatic clones. Among these, asparagine synthetase expression in a patient's primary tumour was most strongly correlated with later metastatic relapse. Here we show that asparagine bioavailability strongly influences metastatic potential. Limiting asparagine by knockdown of asparagine synthetase, treatment with L-asparaginase, or dietary asparagine restriction reduces metastasis without affecting growth of the primary tumour, whereas increased dietary asparagine or enforced asparagine synthetase expression promotes metastatic progression. Altering asparagine availability *in vitro* strongly influences invasive potential, which is correlated with an effect on proteins that promote the epithelial-to-mesenchymal transition. This provides at least one potential mechanism for how the bioavailability of a single amino acid could regulate metastatic progression.

Most women with breast cancer do not succumb to their primary tumour but instead to metastases that become apparent after the primary lesion has been removed. For cells to contribute to metastases, they must leave the primary site, enter the vasculature, survive in the blood, and then extravasate and colonize secondary sites. Our previous studies of a mouse model of breast tumour heterogeneity identified two clonal 4T1 sub-lines with a strong propensity to form circulating tumour cells (CTCs) through a non-invasive mechanism requiring vascular mimicry (4T1-E and -T)^{1,2}. These two clones differed in their ability to form metastases, with 4T1-T preferentially colonizing brain, liver, and lungs. The distinction between the metastatic potential of the two CTC-forming clones offered the opportunity to identify drivers of metastasis, which exert their effects late in metastatic progression.

To validate the observation that 4T1-T had greater metastatic potential among CTC-proficient clones, we combined equal numbers of 4T1-E and -T cells and introduced these directly into the bloodstream of immune-compromised recipients (NOD-SCID-*Il2rg*^{-/-} (NSG) mice). Although the two clones were initially present in equal abundance (Fig. 1a), when cells were collected from the lung at day 7, clone T predominated, with its relative representation being inversely correlated with the total number of cells injected.

We identified 192 genes with higher expression in 4T1-T than 4T1-E cells (Supplementary Table 1). Their corresponding Gene Ontology

terms were enriched for processes important for metastatic spread (Supplementary Table 2; for example, cell migration and locomotion). A retrospective analysis of patient data showed that genes within the set are more highly expressed in aggressive breast tumour subtypes³ (Extended Data Fig. 1a). They were also more highly expressed in the primary tumours of patients with later relapse to the bone, brain, and lungs compared with primary tumours of relapse-free survivors (Extended Data Fig. 1b for lung).

To identify metastatic drivers, we performed an RNA interference (RNAi) screen, with two arms (Fig. 1b). In total, 26 pools of approximately 40 short hairpin RNAs (shRNAs), targeting protein-coding members of the 192-gene set, were introduced into 4T1-T cells⁴. These were collected onto Matrigel or introduced into NSG mice by tail vein injection. After 24 h, the cells that had invaded through the Matrigel were collected and, after 7 days, lungs were collected from the mice. Using high-throughput sequencing, we identified shRNAs that were depleted from the invaded cell populations or lung metastases, presumably because they targeted genes important for these processes. Strong overlap was observed when the *in vitro* and *in vivo* candidates were compared (Fig. 1c and Supplementary Table 3).

Of the 11 candidate genes that scored in both the *in vitro* and *in vivo* assays, asparagine synthetase (Asns) had the most robust clinical evidence supporting its relevance to disease progression (Extended Data Fig. 1c). Expression levels of the human orthologue, ASNS, were predictive of general and lung-specific relapse in two datasets of patients with breast cancer. Also, when a small collection of matched tumour and lung metastases were transcriptionally profiled, ASNS was found to be more highly expressed in secondary lesions. ASNS is more highly expressed in aggressive tumour subtypes (Extended Data Fig. 1d) and it is more highly expressed in patients with relapse to the lymph node, brain, liver, and lungs compared with relapse-free survivors (Extended Data Fig. 1e). Subsequent analyses identified ASNS as predictive of survival in three additional datasets of patients with breast cancer (Extended Data Fig. 1f). In addition to breast tumours, ASNS is negatively correlated with survival in four out of the ten other solid tumours in The Cancer Genome Atlas (TCGA) Pan-Cancer dataset (Extended Data Fig. 1g) and is a globally predictive biomarker for solid tumours (Extended Data Fig. 1h). Previous research has shown that asparagine is an important regulator of cellular metabolism and adaptation^{5,6}.

To validate Asns as a metastatic driver, we infected 4T1-T cells with two shRNAs targeting Asns or a control and introduced these

¹Cancer Research UK Cambridge Institute, University of Cambridge, Li Ka Shing Centre, Robinson Way, Cambridge CB2 0RE, UK. ²Watson School of Biological Sciences, Howard Hughes Medical Institute, Cold Spring Harbor Laboratory, 1 Bungtown Road, Cold Spring Harbor, New York 11724, USA. ³Center for Bioinformatics and Functional Genomics, Department of Biomedical Sciences, Cedars-Sinai Medical Center, 8700 Beverly Boulevard, Los Angeles, California 90048, USA. ⁴Princess Margaret Cancer Centre, University Health Network, University of Toronto, Toronto, Ontario M5G 1L7, Canada. ⁵Department of Molecular Genetics, University of Toronto, Toronto, Ontario M5G 1L7, Canada. ⁶New York Genome Center, 101 6th Avenue, New York, New York 10013, USA. ⁷Division of Cancer Biology, The Institute of Cancer Research, 237 Fulham Road, London SW3 6JB, UK. ⁸Department of Biochemistry and Biophysics, University of California, San Francisco, San Francisco, California 94158, USA. ⁹Department of Urology, University of California, San Francisco, San Francisco, California 94158, USA. ¹⁰Helen Diller Family Comprehensive Cancer Center, University of California, San Francisco, San Francisco, California 94158, USA. ¹¹Division of Hematology and Oncology, University of North Carolina at Chapel Hill, 170 Manning Drive, CB7305, Chapel Hill, North Carolina 27599, USA. ¹²Department of Pathology, University of Michigan School of Medicine, Ann Arbor, Michigan 48109, USA. ¹³Department of Pathology, Virginia Commonwealth University, Richmond, Virginia 23284, USA. ¹⁴Department of Genetics and Pathology, Lineberger Comprehensive Cancer Center, University of North Carolina at Chapel Hill, Chapel Hill, North Carolina 27599, USA. ¹⁵Division of Computational and Systems Medicine, Department of Surgery and Cancer, Imperial College London, London SW7 2AZ, UK.

*These authors contributed equally to this work.

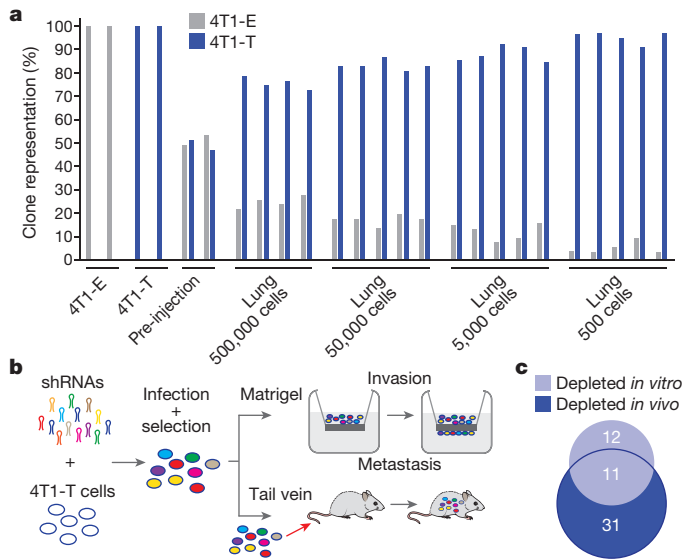


Figure 1 | Identification of metastatic drivers. **a**, Relative proportions of 4T1-E and -T cells extracted from the lungs of NSG mice, into which mixtures of cells were introduced via tail vein at different concentrations. Each bar represents a sample or independent mouse. **b**, RNAi screening scheme to identify drivers of invasion *in vitro* and extravasation and colonization *in vivo* ($n = 5$ mice or $n = 2$ Matrigel six-well invasion chambers per approximately 50-construct shRNA pool, gene-level hit calls with empirical Bayes-moderated t -test false discovery rate < 0.05 and 0.1 for *in vivo* and *in vitro* screens, respectively). **c**, Overlap between genes identified in each arm of the RNAi screen depicted in **b** (hypergeometric test $P < 0.01$).

cells intravenously into NSG mice (Supplementary Table 4). Asns-silenced cells produced significantly fewer lung metastases (Fig. 2a and Extended Data Fig. 2a). Asns-silenced cells also showed poor invasion into Matrigel (Fig. 2b and Extended Data Fig. 2b). Silencing Asns did affect proliferation *in vitro*; however, this defect was minor compared with that observed in the invasion assay (Extended Data Fig. 2c, d). Intracellular free asparagine was reduced by silencing of Asns in 4T1-T cells (Extended Data Fig. 2e), and the abilities to invade and proliferate were increased in Asns-silenced cells when the culture medium was supplemented with asparagine (Extended Data Fig. 2f, g).

When Asns-silenced cells were injected into the mammary fat pad, no significant change in primary tumour formation was observed (Fig. 2c), yet CTCs and lung metastases were reduced (Fig. 2d, e). Although statistically insignificant, metastases initiated by silenced cells were noticeably smaller, hinting at a growth defect at the metastatic site (Fig. 2f). Similar results were obtained with Asns-silenced parental 4T1 cells, indicating that Asns dependency is not a peculiarity of a single clonal line (Extended Data Fig. 3a, b). Enforced Asns expression in parental 4T1 populations did not affect primary tumour growth but did increase metastases both in number and in size (Extended Data Fig. 3c–e). Similar outcomes were observed upon enforced ASNS expression in human MDA-MB-231 breast cancer cells (Extended Data Fig. 3f–i).

To determine whether the observed effects were unique to asparagine, we supplemented the medium separately with other non-essential amino acids (NEAAs) lacking in the culture medium, or with glycine, which is present and acted as a negative control, and assayed cells for invasiveness. 4T1 cells responded uniquely to asparagine supplementation, with an approximately twofold increase in invasiveness (Fig. 3a), although levels of uptake were similar for each of the amino acids with the exception of aspartic and glutamic acids (Extended Data Fig. 4a). More profound effects were observed with MDA-MB-231 cells (Extended Data Fig. 4b, c). Growth was not affected by asparagine supplementation for either cell line during the same period (Extended Data Fig. 4d, e).

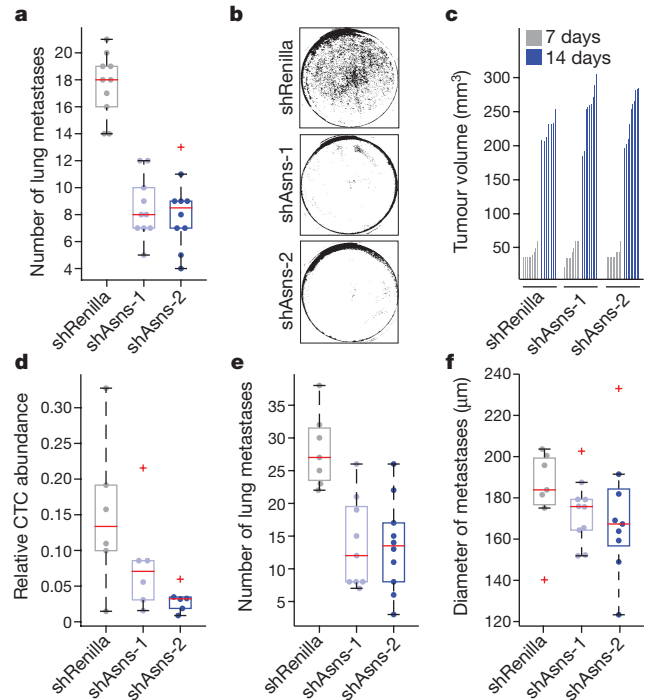


Figure 2 | Validation of Asns as a driver of invasion and metastasis.

a, Quantification of metastases in the lungs of mice intravenously injected with Asns-silenced or -expressing 4T1-T cells ($n = 10$ mice per cell line, edges of the box are the 25th and 75th percentiles, and error bars extend to the values $q_3 + w(q_3 - q_1)$ and $q_1 - w(q_3 - q_1)$, in which w is 1.5 and q_1 and q_3 are the 25th and 75th percentiles, which is also true for **d–f**, rank-sum test $P < 0.001$). **b**, Representative images of collection wells of the Matrigel assay after Asns-silenced and -expressing cells were applied 24 h previously ($n = 3$ invasion chambers per cell line). **c**, Tumour volumes resulting from the orthotopic injection of the cells described in **a** ($n = 10$ mice per cell line). **d**, Relative abundance of CTCs in animals corresponding to the tumours described in **c** ($n = 6$ mice per cell line, rank-sum $P < 0.05$ for shAsns-2). **e**, Quantification of metastases in H&E-stained lung sections, from mice described in **d** (rank-sum $P < 0.0002$). **f**, Average diameters of the metastases of each mouse described in **e**. See Source Data.

Because invasiveness could be modulated either by altering asparagine biosynthetic capacity or by modifying extracellular pools, we investigated whether metastasis could be influenced by treatment with L-asparaginase. This enzyme is used to treat acute lymphoblastic leukaemia, which is generally highly dependent on extracellular asparagine^{7,8}. L-Asparaginase has proved ineffective for treating solid tumours, consistent with Asns silencing not affecting growth at the primary site⁹. NSG mice harbouring orthotopic 4T1 tumours were treated with 60 U L-asparaginase 5 times per week for 19 days, reducing serum asparagine to undetectable levels (Supplementary Table 5). Although no significant difference was detected in primary tumours, compared with controls, a reduction in metastasis was observed (Extended Data Fig. 5a–c).

In TEL-AML1-negative patients with acute lymphoblastic leukaemia, resistance to L-asparaginase is thought to be achieved through increased biosynthetic production of asparagine¹⁰. When Asns-silenced cells were injected orthotopically into mice treated with L-asparaginase, metastases were nearly undetectable (Fig. 3b and Extended Data Fig. 5d). In this case, a reduction of primary tumour volume was also observed (Extended Data Fig. 5e). Similar results were obtained with ASNS-silenced MDA-MB-231 cells (Extended Data Fig. 5f, g).

The availability of extracellular asparagine can also be manipulated by altering asparagine levels in the diet. shRNA-infected 4T1-T cells were orthotopically injected into mice that received a control, low-asparagine, or high-asparagine chow (0.6%, 0%, and 4%, respectively). High-performance liquid chromatography (HPLC)

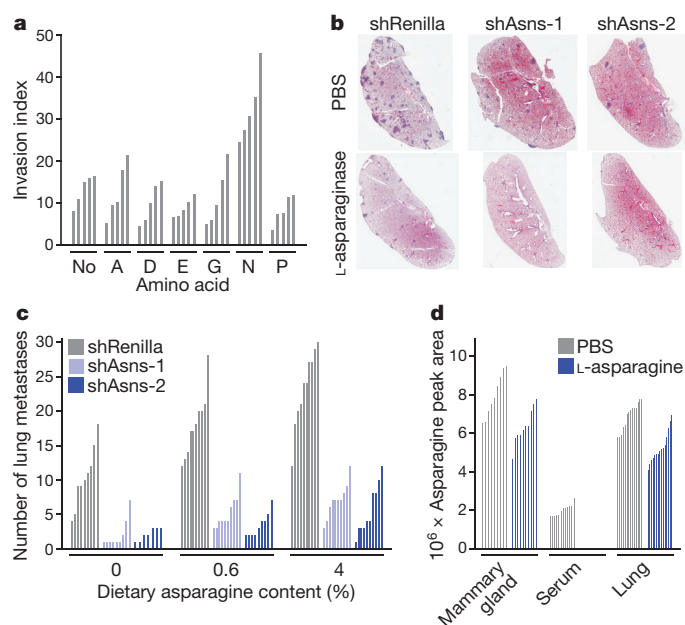


Figure 3 | Extracellular asparagine availability drives invasion and metastasis. **a**, Quantification of parental 4T1 cell invasion rates, as measured by the Matrigel invasion assay, in culture medium supplemented with the indicated NEAAs ($n = 5$ invasion chambers, rank-sum $P < 0.01$). **b**, Representative H&E-stained lung sections from animals injected with Asns-silenced or -expressing 4T1-T cells. Animals were administered L-asparaginase or PBS ($n = 10$ mice per condition). **c**, Quantification of lung metastases in animals injected with Asns-silenced or -expressing 4T1-T cells. Animals were administered a diet with either 0%, 0.6%, or 4% asparagine content for the duration of the experiment ($n = 10$ mice per condition, rank-sum $P < 0.05$ for Asns-silenced versus -expressing cells across all diets, for each cell line with 0% versus 4% diets, for shRenilla and shAsns-1 infected cells with 0% versus 0.6% diet, and for unsilenced cells with 0.6% versus 4% diet). **d**, Mass-spectrometric quantification of the asparagine levels in the mammary gland, blood serum, and lungs of animals administered L-asparaginase or PBS (relative abundance normalized by total metabolite peak area, $n > 8$ tissue sections per condition, rank-sum $P < 0.005$ for PBS versus L-asparaginase across all tissues, rank-sum $P < 0.05$ for mammary gland versus lung, and rank-sum $P < 0.0005$ for serum versus lung and serum versus mammary gland). See Source Data.

confirmed that serum asparagine levels were significantly altered in concordance with dietary intake (Extended Data Fig. 6a). Asparagine restriction did not affect primary tumour growth, regardless of Asns expression status (Extended Data Fig. 6b). By contrast, metastatic burden was decreased in animals that were fed low-asparagine diets and increased in animals given high-asparagine diets (Fig. 3c and Extended Data Fig. 6c). Metastases were nearly undetectable in mice that were injected with Asns-silenced cells and fed a low-asparagine diet. Similar results were obtained when parental 4T1 cells were orthotopically injected into animals fed these same asparagine-controlled diets (Extended Data Fig. 6d–f).

Analyses of the mammary gland, serum, and lungs of mice by mass spectrometry suggested that, under normal physiological conditions, asparagine levels are highest in mammary gland and lowest in serum (Fig. 3d). High asparagine availability in the mammary gland might blunt the effect of Asns silencing or changes in global asparagine levels on primary tumour growth, whereas low levels in the serum may make CTCs susceptible to these manipulations. Overall, asparagine abundance in tissues correlated with Asns expression (Extended Data Fig. 6g). ASNS expression levels follow a similar pattern across human tissues (Extended Data Fig. 6h), raising the possibility of similar effects if asparagine levels were altered in patients¹¹.

To understand the mechanism by which asparagine availability might affect invasion and metastasis, we examined expression changes

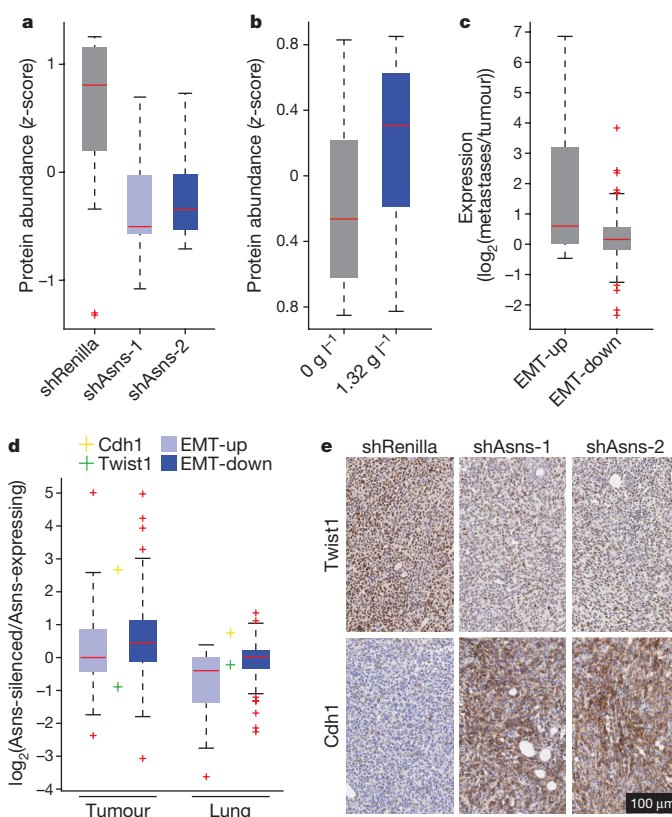


Figure 4 | Asparagine availability regulates EMT. **a**, Relative protein abundances of EMT-up proteins in Asns-silenced and -expressing 4T1-T cells ($n = 3$ replicates per cell line, edges of the box are the 25th and 75th percentiles, and error bars extend to the values $q_3 + w(q_3 - q_1)$ and $q_1 - w(q_3 - q_1)$, in which w is 1.5 and q_1 and q_3 are the 25th and 75th percentiles, which is also true for **b–d**, rank-sum $P < 0.01$). **b**, Relative protein abundances of EMT-up proteins in 4T1-T cells when grown in normal and asparagine-supplemented medium ($n = 3$ replicates per cell line, rank-sum $P < 0.05$). **c**, Relative expression levels of EMT-up and -down genes in lung metastases versus primary tumours derived from orthotopic injection of 4T1-T cells ($n = 4$ mice, rank-sum $P < 5.0 \times 10^{-9}$ for EMT-up genes). **d**, Relative expression levels of Twist1, Cdh1, and EMT-up and -down genes in cells isolated from tumours and lungs derived from Asns-silenced versus -expressing 4T1-T cells ($n = 4$ replicates per condition, rank-sum $P < 5.0 \times 10^{-11}$ for EMT-down genes in the tumour and rank-sum $P < 5.0 \times 10^{-8}$ for EMT-up genes in the lung; Cdh1 was differentially expressed in the tumours and lungs, and Twist1 was differentially expressed in tumours; DESeq false discovery rate < 0.05). **e**, Representative images of immunohistochemistry (IHC) stainings for Twist1 and Cdh1 in orthotopic tumours derived from Asns-silenced and -expressing 4T1-T cells. See Source Data.

induced by Asns silencing, at both the RNA and protein levels. RNA measurements were the strongest predictor of protein-level changes (Extended Data Fig. 7a). Consistent with a previous report of translational pausing at asparagine residues in L-asparaginase-treated cells, we also found asparagine content to be predictive of corresponding protein-level changes¹² (Extended Data Fig. 7a), irrespective of whether they were normalized for RNA levels (Extended Data Fig. 7b).

Among the asparagine-enriched proteins that were depleted on Asns silencing, we found genes whose human orthologues were upregulated after induction of the epithelial-to-mesenchymal transition (EMT)¹³ (Fig. 4a, Extended Data Fig. 7c and Supplementary Table 6; EMT-up proteins). Overall, depleted proteins had 10% higher asparagine content than the analysed proteome as a whole, whereas EMT-up proteins had 19% higher asparagine content (Extended Data Fig. 7c). Human EMT-up proteins were also asparagine-enriched (Extended Data Fig. 7c). A re-analysis of existing ribosomal profiling data revealed high rates of pausing at asparagine residues within EMT-up

genes in L-asparaginase-treated human prostate cancer cells (Extended Data Fig. 7d, e), and these same proteins increased in expression when 4T1-T cells were cultured in elevated asparagine¹² (Fig. 4b). Asparagine enrichment is a globally conserved property of EMT-up proteins, with enrichment being greatest in mammals (Extended Data Fig. 8).

EMT-up genes were also downregulated at the transcriptional level in Asns-silenced cells, and they were increased in their RNA levels when these cells were grown in asparagine-supplemented medium (Extended Data Fig. 9a, b). A re-analysis of existing data also showed reduced expression of EMT-up genes when ATF4, which regulates ASNS transcription, was deleted in haploid cells (Extended Data Fig. 9c), and liver cells from L-asparaginase-treated ATF4-knockout mice were more perturbed in their EMT program than were similarly treated wild-type mice (Extended Data Fig. 9d)^{14,15}. Considered together, these data suggest that asparagine bioavailability might affect metastasis, at least in part, through regulation of EMT.

To examine the role of EMT in metastasis in our model, we orthotopically injected 4T1-T cells in which we had silenced expression of transforming growth factor- β (Tgf- β , also known as Tgfb1), a key driver of EMT¹⁶ (Supplementary Table 4). Primary tumour growth was unaffected by this manipulation (Extended Data Fig. 9e); however, the expression of two prototypical EMT markers (Twist1 and E-cadherin) were altered to indicate a perturbed EMT program (Extended Data Fig. 9f, g). Tgf- β -silenced cells produced fewer metastases from the primary tumour or when intravenously injected (Extended Data Fig. 9h, i).

Although no differences were detected in haematoxylin and eosin (H&E)-stained tumour sections, morphological distinctions were noticeable when shRNA-infected 4T1-T cells were isolated from primary tumours by 6-thioguanine selection, with most Asns-silenced cells displaying an epithelial morphology (Extended Data Fig. 10a, b). Most 6-thioguanine-isolated metastatic cells displayed a mesenchymal morphology, regardless of Asns expression status, and this was matched by an increase in the expression of EMT-up genes (Fig. 4c). Nevertheless, EMT-up genes were downregulated in Asns-silenced versus -expressing metastatic cells, indicating an increased representation of epithelial cells in the silenced populations. Similarly, EMT-down genes were upregulated, and Twist and E-cadherin expression measurements indicated a higher epithelial representation in Asns-silenced primary tumour cell populations (Fig. 4d). These results were validated by qPCR for Twist and E-cadherin in Asns-silenced and -expressing cells that were isolated by fluorescence-activated cell sorting from primary and secondary lesions (Extended Data Fig. 10c, d).

Staining for Twist and E-cadherin proteins confirmed that EMT is perturbed in Asns-silenced tumours, and this same pattern was observed in the corresponding metastases (Fig. 4e and Extended Data Fig. 11a–c). Similar patterns were observed in the primary tumours of mice that had been treated with L-asparaginase (Extended Data Fig. 11d, e) or subjected to dietary asparagine restriction (Extended Data Fig. 11f, g).

Our model of breast tumour heterogeneity has strongly implicated asparagine bioavailability as a regulator of metastatic progression. This also seems to be relevant in human cancers, as high ASNS expression is a marker of poor prognosis for many tumour types. One mechanism underlying our findings is a probable link between asparagine bioavailability and EMT, which can be observed *in vitro* and *in vivo*. In our breast cancer model, the gating step probably occurs in the circulation, where asparagine levels are low and are strongly affected by either L-asparaginase treatment or dietary restriction. Nonetheless, we do see effects on ratios of epithelial- to mesenchymal-like tumour cells at the primary and secondary sites, which could also affect both tumour progression and response to therapy.

Online Content Methods, along with any additional Extended Data display items and Source Data, are available in the online version of the paper; references unique to these sections appear only in the online paper.

Received 5 July 2016; accepted 15 December 2017.

Published online 7 February 2018.

1. Wagenblast, E. *et al.* A model of breast cancer heterogeneity reveals vascular mimicry as a driver of metastasis. *Nature* **520**, 358–362 (2015).
2. Miller, F. R., Miller, B. E. & Heppner, G. H. Characterization of metastatic heterogeneity among subpopulations of a single mouse mammary tumor: heterogeneity in phenotypic stability. *Invasion Metastasis* **3**, 22–31 (1983).
3. Harrell, J. C. *et al.* Genomic analysis identifies unique signatures predictive of brain, lung, and liver relapse. *Breast Cancer Res. Treat.* **132**, 523–535 (2012).
4. Knott, S. R. V. *et al.* A computational algorithm to predict shRNA potency. *Mol. Cell* **56**, 796–807 (2014).
5. Zhang, J. *et al.* Asparagine plays a critical role in regulating cellular adaptation to glutamine depletion. *Mol. Cell* **56**, 205–218 (2014).
6. Krall, A. S., Xu, S., Graeber, T. G., Braas, D. & Christofk, H. R. Asparagine promotes cancer cell proliferation through use as an amino acid exchange factor. *Nat. Commun.* **7**, 11457 (2016).
7. Richards, N. G. & Schuster, S. M. Mechanistic issues in asparagine synthetase catalysis. *Adv. Enzymol.* **72**, 145–198 (1998).
8. Richards, N. G. J. & Kilberg, M. S. Asparagine synthetase chemotherapy. *Annu. Rev. Biochem.* **75**, 629–654 (2006).
9. Tallal, L. *et al.* *E. coli* L-asparaginase in the treatment of leukemia and solid tumors in 131 children. *Cancer* **25**, 306–320 (1970).
10. Stams, W. A. G. *et al.* Asparagine synthetase expression is linked with L-asparaginase resistance in TEL-AML1-negative but not TEL-AML1-positive pediatric acute lymphoblastic leukemia. *Blood* **105**, 4223–4225 (2005).
11. GTEx Consortium *et al.* Genetic effects on gene expression across human tissues. *Nature* **550**, 204–213 (2017).
12. Loayza-Puch, F. *et al.* Tumour-specific proline vulnerability uncovered by differential ribosome codon reading. *Nature* **530**, 490–494 (2016).
13. Taube, J. H. *et al.* Core epithelial-to-mesenchymal transition interactome gene-expression signature is associated with claudin-low and metaplastic breast cancer subtypes. *Proc. Natl Acad. Sci. USA* **107**, 15449–15454 (2010).
14. Gowen, B. G. *et al.* A forward genetic screen reveals novel independent regulators of ULBP1, an activating ligand for natural killer cells. *eLife* **4**, 1876 (2015).
15. Al-Baghdadi, R. J. T. *et al.* Role of activating transcription factor 4 in the hepatic response to amino acid depletion by asparaginase. *Sci. Rep.* **7**, 1272 (2017).
16. McEarchern, J. A. *et al.* Invasion and metastasis of a mammary tumor involves TGF- β signaling. *Int. J. Cancer* **91**, 76–82 (2001).

Supplementary Information is available in the online version of the paper.

Acknowledgements This work was performed with assistance from CSHL Shared Resources, which are funded, in part, by the Cancer Center Support Grant 5P30CA045508. We thank M. Mosquera, M. Cahn, J. Coblenz, and L. Bianco for support with mouse work; K. Cheng, J. Bourbonniere, D. Hoppe, A. Nourjanova, and R. Puzis for support with histology; E. Hodges and E. Lee for support with next-generation sequencing; and J. Johnson for assistance with HPLC. This work was also performed with the assistance of the Cancer Research UK, Cambridge Institute Proteomics Core Facility. S.R.V.K. is supported by a fellowship from The Hope Funds for Cancer Research. E.W. is supported by a long-term fellowship from the Human Frontier Science Program. L.A.C. is supported by the Susan G. Komen Foundation (SAC110006) and the NCI Breast SPORE program (P50-CA58223-09A1). J.C.H. and C.M.P. are supported by funds from the NCI Breast SPORE program (P50-CA58223-09A1), the Breast Cancer Research Foundation, and the Triple Negative Breast Cancer Foundation. H.G. is supported by a grant from the National Institutes of Health (NIH) (NCI R00 CA194077). Work in the G.P. laboratory is supported by the Institute of Cancer Research, London and the Cancer Research UK grand challenge award (C59824/A25044). G.J.H. is the Royal Society Wolfson Research Professor and is supported by core funding from Cancer Research UK, by a Program Project grant from the NIH (5 P01 CA013106-44), and by a grant from the Department of Defense Breast Cancer Research Program (W81XWH-12-1-0300).

Author Contributions S.R.V.K., E.W., and G.J.H. conceived the project, supervised research, and wrote the paper. S.R.V.K. and E.W. analysed experiments. S.R.V.K., E.W., S.K., S.Y.K., and M.S. performed *in vitro* and *in vivo* experiments. N.E., A.L.G., A.R.M., and S.D. assisted with virus production, shRNA cloning, and library preparation. L.A.C., J.C.H., and C.M.P. assisted with human expression data. J.E.W. performed histological analyses. E.K.P. and C.S.D. assisted with proteomic analyses. L.F. and H.G. assisted with ribosomal profiling analyses. M.W., M.T., and G.P. performed metabolite profiling experiments.

Author Information Reprints and permissions information is available at www.nature.com/reprints. The authors declare competing financial interests: details are available in the online version of the paper. Readers are welcome to comment on the online version of the paper. Publisher's note: Springer Nature remains neutral with regard to jurisdictional claims in published maps and institutional affiliations. Correspondence and requests for materials should be addressed to G.J.H. (Greg.Hannon@cruk.cam.ac.uk).

Reviewer Information Nature thanks R. Agami and the other anonymous reviewer(s) for their contribution to the peer review of this work.

METHODS

Cell culture. The mouse mammary tumour cell line 4T1 (American Type Culture Collection, ATCC) and any derived clonal cell line were cultured in DMEM high glucose supplemented with 5% fetal bovine serum, 5% fetal calf serum, MEM NEAA, and penicillin–streptomycin (Thermo Fisher Scientific). The human breast tumour cell line MDA-MB-231 (ATCC) was cultured in DMEM high glucose supplemented with 10% fetal bovine serum, NEAA and penicillin–streptomycin (Thermo Fisher Scientific). The 4T1 and MDA-MB-231 cell lines were tested and authenticated by ATCC. The Platinum-A (Cell BioLabs) and 293FT (Thermo Fisher Scientific) packaging cell lines for virus production were cultured in DMEM high glucose supplemented with 10% fetal bovine serum and penicillin–streptomycin. All cell lines were routinely tested for mycoplasma contamination.

Virus production. Retroviral vectors were packaged using the Platinum-A (Cell BioLabs) cell line and lentiviral vectors were packaged using the 293FT cell line (Thermo Fisher Scientific) as previously described¹.

Animal studies. All mouse experiments were approved by the Cold Spring Harbour Animal Care and Use Committee. The maximal permitted tumour size of 20 mm in any direction was never exceeded. All mouse injections were performed with 6- to 8-week-old female NOD-SCID-*Il2rg*^{-/-} (NSG) mice (JAX). Balb/c mice were not used in this study as the different clonal cell lines have variable GFP levels due to the lentiviral barcode vector. Tail vein injections were performed using 5×10^5 mouse mammary tumour cells, which were re-suspended in 100 μ l of PBS and injected via the tail vein. Orthotopic injections were performed using 1×10^5 mouse mammary tumour cells or 5×10^5 MDA-MB-231 cells. For this, cells were re-suspended in a 1:1 mix of PBS and growth-factor-reduced Matrigel (BD Biosciences). A volume of 20 μ l was injected into mammary gland number 4 for mouse mammary tumour cells and a volume of 40 μ l was injected for MDA-MB-231 cells. Primary tumour volume was measured using the formula $V = \frac{1}{2}(L \times W^2)$, in which L is length and W is width of the primary tumour. For L-asparaginase studies, mice were administered 200 μ l of 60 U L-asparaginase (Abcam) five times per week through intraperitoneal injections. For L-asparagine-adjusted diets, mice were given a control amino-acid diet (0.6% asparagine), an asparagine-deficient diet (0% asparagine), or an asparagine-rich diet (4% asparagine). All diets were isonitrogenous and contained similar calorie densities. Sample size was chosen to give sufficient power for calling significance with standard statistical tests. Tumour and metastasis experiments were performed with ten animals per condition to account for the variability observed in such *in vivo* experiments. Animals were assigned to treatment groups through random cage selection. Mice were excluded from the analysis if the primary tumour engrafted into the peritoneum. All image quantifications were performed in a blinded manner. Source data are available for tumour volume measurements and lung metastases.

Barcode analysis. The barcodes of the 4T1-E and 4T1-T cells were amplified and sequenced as previously described¹.

***In vivo* shRNA lung screen and *in vitro* invasion screen.** shRNAs were predicted on the basis of the Sherwood algorithm described in ref. 4. Pools of approximately 50 shRNAs were packaged in Platinum-A cells. For each pool, 10 million 4T1-T cells were infected at a multiplicity of infection of 0.3. The infected cells were selected with 500 μ g ml⁻¹ hygromycin for 5 days and each pool was injected into five mice each via the tail vein. Two pre-injection pools were collected at the time of injection. After 7 days, mice were euthanized and perfused with PBS to remove blood and non-extravasated cells from the lungs. Lungs were collected and genomic DNA was isolated using phenol chloroform extraction. Genomic DNA of the pre-injection pools was isolated using a QIAamp DNA Blood Mini Kit (Qiagen).

The *in vitro* invasion assays were performed in parallel. Each pool was plated on two six-well BioCoat Matrigel invasion plates (Corning). Six hundred thousand cells were plated on top of each well in cell culture medium without serum. Cells were allowed to invade through the Matrigel into medium containing 5% fetal bovine serum and 5% fetal calf serum for 24 h. Invaded cells were scraped off, washed with PBS, and genomic DNA was isolated using a QIAamp DNA Blood Mini Kit.

The shRNAs were amplified using a two-step PCR protocol previously described in ref. 4 for next-generation sequencing.

First PCR forward primer 1: 5-CAG AAT CGT TGC CTG CAC ATC TTG GAA AC-3 and reverse primer 1: 5-CTG CTA AAG CGC ATG CTC CAG ACT GC-3.

Second PCR forward primer 2: 5-AAT GAT ACG GCG ACC ACC GAG ATC TAC ACT AGC CTG CGC ACG TAG TGA AGC CAC AGA TGT A-3 and reverse primer 2: 5-CAA GCA GAA GAC GGC ATA CGA GAT NNN NNN GTG ACT GGA GTT CAG ACG TGT GCT CTT CCG ATC TCT GCT AAA GCG CAT GCT CCA GAC TGC-3. The reverse primer contained a barcode (NNNNNN) that enabled multiplexing.

Analysis of screening data. shRNA quantification was performed as previously described⁴. For each pool, shRNA quantities in each sample were normalized by their sum and log-fold changes were calculated using the initially infected cell

population as a reference. Fold change values for each pool were then consolidated into a single table and an empirical Bayes-moderated *t*-test was applied to identify depleted molecules. Genes with two or more depleted shRNAs were considered hits in each screen.

Gene Ontology enrichment analysis. Gene Ontology enrichment analysis used the GOrilla web portal¹⁷. The Refseq identifiers of genes identified as overexpressed in 4T1-T cells, compared with 4T1-E cells, were used as foreground and the entire Refseq gene list was used as background.

Expression subtype and relapse analysis. For all clinical data analysis, we used the University of North Carolina '855 patient set', which is available as published data at <https://genome.unc.edu>. All data were derived from an initial matrix that was arranged with patients on the horizontal axis and genes on the vertical axis. Initial normalization involved quantile normalization to ensure that the global expression profile of each patient was similar. Following this, each gene was *z*-score normalized across patients. For Extended Data Fig. 1a, the average expression level of each gene was calculated for each patient subtype. For Extended Data Fig. 1b, the average expression level of each gene was calculated for each gene for patients with and without relapse to each secondary site. For Extended Data Fig. 1d, the level of ASNs in each patient, stratified by subtype, is plotted. For Extended Data Fig. 1e, each boxplot represents the level of ASNs in each patient with and without relapse to each secondary site.

Individual *in vitro* invasion assay. The *in vitro* invasive capacity of cells was measured using six-well BioCoat Matrigel invasion plates. For parental 4T1 cells, 1×10^6 cells were plated on individual wells; for 4T1-T cells, 8×10^5 cells were plated on individual wells; and for MDA-MB-231 cells, 5×10^5 cells were used per individual well. Cells were re-suspended in medium without serum or NEAA and cells invaded into medium with 5% fetal bovine serum and 5% fetal calf serum. For Fig. 3a and Extended Data Fig. 4b, 4T1 and MDA-MB-231 cells were cultured in medium containing 100 \times concentration of the specified amino acid (relative to the concentration achieved by supplementing the medium with $1 \times$ NEAA) for 2 or 3 days, respectively, before starting the invasion assay. After 24 h, non-invaded cells were removed and the invasion wells were washed in PBS, fixed in 2% glutaraldehyde for 2 min, and stained with 0.5% crystal violet for 10 min. The wells were washed in distilled H₂O, air-dried, and scanned using an Odyssey infrared scanner. The signal was quantified using ImageJ (NIH).

Competition and proliferation assay. For Extended Data Fig. 2c, d, cells were grown in medium lacking NEAA. For the mCherry competition assay, shRNA-transduced mCherry-positive cells were admixed with untransduced cells. mCherry fluorescence was quantified on an LSR II flow cytometer (BD Biosciences). The proliferation assay was performed using a CellTrace Violet Cell Proliferation Kit (Thermo Fisher Scientific). For Extended Data Fig. 4d, e, 4T1 and MDA-MB-231 cells were cultured in medium containing 100 \times concentration of the specified amino acid (relative to the concentration that is achieved by supplementing the medium with $1 \times$ NEAA) for 2 or 3 days, respectively, before starting the proliferation assay. Cells were stained with CellTrace violet and then trypsinized and re-suspended in the medium. After 24 h, cells were collected to quantify violet fluorescence intensity using an SH800 flow cytometer (Sony).

Isolation of tumour and lung metastatic cells. Tumour and lung tissues were collected, minced, and digested into single cells as previously reported¹. Cells were either grown in 4T1 cell culture medium containing 60 μ M 6-thioguanine to deplete stromal cells or directly sorted on the basis of mCherry expression using the FACSaria III cell sorter (BD Biosciences).

RNA sequencing library preparation. RNA sequencing libraries from cultured 4T1-T cells were prepared as previously described¹. Each sample was sequenced on an Illumina HiSeq sequencer generating 76-nucleotide single-end reads.

RNA sequencing analysis. Illumina sequencing reads were aligned to the mouse genome (mm10) using Bowtie2 with default parameters¹⁸. Genes were assigned a count using HTseq-count, and differential expression analysis was performed using DESeq^{19,20}.

shRNA knockdown and cDNA overexpression studies. Mouse and human cell lines were transduced with shRNA expressing retroviral or lentiviral constructs, respectively. After infection, 4T1-T cells were selected with 500 μ g ml⁻¹ hygromycin for 5 days and MDA-MB-231 cells were selected with 2 μ g ml⁻¹ puromycin for 4 days. Cell lines infected with cDNA overexpressing retroviral constructs were selected with G418 for 1 week. The parental 4T1 cell line was selected with 600 μ g ml⁻¹ G418 and MDA-MB-231 cells were selected with 1,500 μ g ml⁻¹ G418.

cDNA overexpression genes. Mouse Asns: NM_012055.1. Human ASNS: NM_001673.2.

shRNA knockdown sequences. Mouse shAsns-1: TGCTGTTGACAGTGAGCGCC ACTGCCAATAAGAAAGTATATAGTGAAGCCACAGATGTATATACTTTCT TATTGGCAGTGTTGCCTACTGCCTCGGA.

Mouse shAsns-2: TGCTGTTGACAGTGAGCGCCACTATGAAGTTTGGG TTTATAGTGAAGCCACAGATGTATAAATCCAAAACCTCATAGTGTGCGC TACTGCCTCGGA.

Mouse shTgfb1-1: TGCTGTTGACAGTGAGCGCCAGTATATATGTTCTTCAATAGTGAAGCCACAGATGTATTGAAGAACATATATATAC TGTGCTACTGCTCGGA.

Mouse shTgfb1-2: TGCTGTTGACAGTGAGCGAAGTATATATGTTCTTCAAATAGTGAAGCCACAGATGTATTGAAGAACATATATATACTGTGCC TACTGCTCGGA.

Human shASNS-1: TGCTGTTGACAGTGAGCGCCAGAAGCTAAAGGTC TTGTTATAGTGAAGCCACAGATGTATAACAAGACCTTAGCTTCTGATGC CTACTGCTCGGA.

Human shASNS-2: TGCTGTTGACAGTGAGCGCAGCAATGACAGAAGATGGATATAGTGAAGCCACAGATGTATATCCATCTTCTGTCTTGTCTTG CCTACTGCTCGGA.

Quantitative RT-PCR. Total RNA from cells was purified and DNase treated using an RNeasy Mini Kit (Qiagen). For whole tissues, RNA was isolated using a TRIzol Plus RNA Purification Kit (Thermo Fisher Scientific). The tissue lysate was homogenized using a Dounce homogenizer and passed through a column homogenizer (Thermo Fisher Scientific) to reduce viscosity. RNA integrity (RNA integrity score > 9) was measured on an Agilent Bioanalyzer (RNA nano kit). cDNA was synthesized using SuperScript III Reverse Transcriptase (Sigma). qPCR was performed on an Eppendorf Mastercycler ep realplex. All signals were quantified using the ΔC_t method and were normalized to the levels of Gapdh. For mCherry-positive flow cytometer sorted tumour and lung metastatic cells, cDNA was produced directly from lysed cells using a TaqMan Gene Expression Cells-to-Ct Kit (Thermo Fisher Scientific). qPCR was performed on an CFX96 (Bio-Rad) using TaqMan primer/probe sets and all signals were quantified as described above.

Quantitative RT-PCR primers. Mouse Asns (exon 1–2): 5'-CCT CTG CTC CAC CTT CTC T-3'; 5'-GAT CTT CAT CGC ACT CAG ACA-3'.

Mouse Asns (exon 6–7): 5'-CCA AGT TCA GTATCC TCT CCA G-3'; 5'-CTT CAT GAT GCT CGCTTC CA-3'.

Mouse Tgfb1 (exon 1–2): 5'-CCG AAT GTC TGA CGT ATT GAA GA-3'; 5'-GCG GAC TAC TAT GCT AAA GAG G-3'.

Mouse Tgfb1 (exon 3–4): 5'-GTT ATC TTT GCT GTC ACA AGA GC-3'; 5'-CCC ACT GAT AGC CCT GAG-3'.

Mouse Gapdh (exon 2–3): 5'-AAT GGT GAA GGT CGGTGT G-3'; 5'-GTG GAGTCA TACTGG AAC ATG TAG-3'.

Human ASNS (exon 8–9): 5'-GAGTCA GAC CTT TGT TTA AAG CA-3'; 5'-GGA GTG CTT CAATGT AAC AAG AC-3'.

Human ASNS (exon 12–13): 5'-CTG GAT GAA GTC ATATTT TCC TTG G-3'; 5'-CAG AGA AGATCA CCA CGCTAT C-3'.

Human GAPDH (exon 2–3): 5'-ACA TCG CTC AGA CAC CAT G-3'; 5'-TGT AGT TGA GGT CAA TGA AGG G-3'.

TaqMan probes. Mouse Asns: Mm00803785_m1. Mouse E-cadherin (Cdh1): Mm01247357_m1. Mouse Twist1: Mm00442036_m1. Mouse Gapdh: Mm99999915_g1.

qPCR for CTCs. CTCs were quantified as previously described¹. Genomic DNA was isolated from blood and CTC abundance was quantified using a qPCR assay against mCherry, which was expressed from the retroviral shRNA delivery vectors.

mCherry probes and primers were as follows: primer 1, 5'-GACTACTTGAAGC TGTCCTTCC-3'; primer 2, 5'-CGCAGCTTCACCTTGTAGAT-3'.

HEX probe: 5'-/56-FAM/TTCAAGTGG/ZEN/GAGCGCGTGATG AA/3IABkFQ/-3'.

Housekeeping probes and primers: primer 1, 5'-GACTTGTAACGGGCA GGCAGATTGTG-3'; primer 2, 5'-GAGGTGTGGGTACCTCGACATC-3'.

HEX probe: 5'-/5HEX/CCGTGTGCG/ZEN/TCTGAAGGGCAATAT/ 3IABkFQ/-3'.

Quantification of lung metastasis. For each lung, 5 μ m sections were prepared and stained with a standard H&E protocol. Lung metastatic burden was determined by counting individual lung nodules on one section.

E-cadherin and Twist1 analysis. For immunohistochemistry, primary tumours and lungs were processed as previously described¹. E-Cadherin (24E10) Rabbit mAb (3195, Cell Signaling) was used in a 1:400 dilution and Twist1 (Twist2C1a) Mouse mAb (ab50887, Abcam) was used in a 1:100 dilution. E-cadherin and Twist1 diaminobenzidine-stained (DAB) and haematoxylin stainings were quantified using ImageJ (NIH). For this, images were colour deconvoluted according to ref. 21 and the percentage area of E-cadherin- and Twist1-positive staining was measured.

Free amino-acid quantification using HPLC. Free amino acids were quantified in cultured cells and blood serum. For Extended Data Fig. 2e, 4T1-T cells were cultured under normal medium conditions. For Extended Data Fig. 4a, c, 4T1 and MDA-MB-231 cells were cultured in medium containing 100 \times concentration of the specified amino acid (relative to the concentration achieved by supplementing the medium with 1 \times NEAA) for 2 or 3 days, respectively. All cultured cells were washed in ice-cold PBS, homogenized using a Dounce homogenizer, and the lysate subsequently filtered. Each biological sample was quantified in triplicates using

HPLC and a fluorometric detector. For each replicate, nanomoles of each amino acid were measured.

Proteomic profiling using isobaric tags for relative and absolute protein quantification. All analyses were performed with three biological replicates per treatment. Cell pellets were lysed with 0.1 M triethylammonium bicarbonate, 0.1% SDS buffer, followed by tip sonication and boiling at 90 °C for 5 min. Protein concentration was estimated using a Bradford assay (Bio-Rad, Quick Start), and 90 μ g of total protein per sample were reduced with tris-2-carboxymethyl phosphine (Sigma) for 1 h at 60 °C at a final concentration of 5 mM. Cysteines were blocked for 10 min at room temperature using methyl methanethiosulfonate (Sigma) at a final concentration of 10 mM. Samples were digested overnight at 37 °C with trypsin (Pierce) and peptides were labelled with the TMT10plex reagents according to the manufacturer's instructions (Thermo Fisher Scientific). The TMT mixture was fractionated on a Dionex Ultimate 3000 system at high pH using a XBridge C18 column (3.5 μ m, 2.1 \times 150 mm, Waters). Fractions were analysed on a Dionex Ultimate 3000 UHPLC system coupled with a nano Q-Exactive (Thermo Fisher Scientific) mass spectrometer. Samples were loaded on an Acclaim PepMap 100, 100 μ m \times 2 cm C18, 5 μ m, 100 Å trapping column with the ulPickUp injection method at a loading flow rate of 4 μ l min⁻¹ for 10 min. For peptide separation, an EASY-Spray analytical column 75 μ m \times 25 cm, C18, 2 μ m, 100 Å column was used for multi-step gradient elution. Mobile phase (A) was composed of 2% acetonitrile, 0.1% formic acid, 5% dimethyl sulfoxide (DMSO); mobile phase (B) was composed of 80% acetonitrile, 0.1% formic acid, 5% DMSO. The full scans were obtained at 70,000 resolution and the MS2 scans at 35,000 resolution, with collision energy 33% and isolation window 1.2 Th. Raw data were processed with the SequestHT search engine on Proteome Discoverer 1.4 software. The parameters for the SequestHT node were as follows: precursor mass tolerance 20 p.p.m., fragment mass tolerance 0.02 Da; dynamic modifications were oxidation of M (+15.995 Da), deamidation of N, Q (+0.984 Da); and static modifications were TMT6plex at any N terminus, K (+229.163 Da) and Methylthio at C (+45.988 Da).

For each sample, raw peptide intensities were normalized by their sum. Peptides that had a representation that fell within the bottom quartile based on summed intensities across samples were not analysed further. For the dataset represented in Fig. 4a and Extended Data Fig. 7a, b, proteins were removed from subsequent analysis if fewer than 5 corresponding proteins were identified in any sample. Protein-level differences between treatments were calculated based on the trimmed mean of corresponding peptide log-fold changes (trimming the top and bottom 25% for the experiment represented in Fig. 4a and Extended Data Fig. 7a, b, and the top and bottom 10% for the experiment represented in Fig. 4b). Relative protein abundances were calculated based on the trimmed mean of corresponding log-transformed peptide intensities (trimming the top and bottom 25% and 10% for the experiments representing in Fig. 4a and b, respectively).

Metabolite profiling using LC-MS/MS. Organ tissue samples were placed in 2 ml lysing tubes pre-filled with 1.4-mm ceramic beads for mammary glands or 2.8-mm ceramic beads for lungs and 1 ml of pre-chilled (−80 °C) 80% methanol. Samples were homogenized with a Precellys24 homogenizer (Bertin Instruments) programmed with three 30-s cycles at 6,500 Hz and 4-min pause times. At the end of each cycle, samples were snap-frozen in liquid nitrogen and placed on dry ice. Metabolite extraction of blood serum samples (50 μ l) was performed using 200 μ l of 80% methanol at −80 °C. After centrifugation for 10 min (13,200 revolutions per minute, 4 °C), supernatants were evaporated to dryness and stored at −80 °C until liquid chromatography–tandem mass spectrometry (LC-MS/MS) analysis.

Dried-down extracts were re-suspended in 25 μ l HPLC-grade water, and 1 μ l was analysed using hydrophilic interaction chromatography coupled to tandem mass spectrometry analysis operated in the selected reaction monitoring mode (LC-SRM-MS). Analytical instrumentation consisted of a Nexera X2 (Shimadzu) liquid chromatography system with a XBridge BEH amide 2.1 \times 100 mm, 2.5- μ m column (Waters) and a QTRAP 6500 hybrid triple quadrupole/linear ion trap mass spectrometer (SCIEX) equipped with an electrospray ion source. Raw LC-SRM-MS data were acquired with Analyst 1.6.2 (SCIEX) and peak areas of LC-SRM-MS traces for each metabolite were integrated using MultiQuant 1.1 software (SCIEX).

Amino acid compositional analysis. For Extended Data Fig. 7b, the amino acid representations of genes that showed the greatest decrease in their protein or RNA levels (bottom 25% log-fold change) were compared to those of the analysed gene set, using a rank-sum test. For the amino acid enrichment analysis of protein minus RNA level expression changes, transcriptional- and protein-level log-fold changes were quantile normalized to the same distribution. RNA-level changes were then subtracted from protein-level changes. The amino acid representations of genes whose subsequent values fell within the lowest 25% were then compared to the analysed gene set using a rank-sum test, to identify amino acids whose abundance correlated with the protein-level changes that were not explained by transcriptional changes.

For Extended Data Fig. 7c, the same analysis was performed, this time comparing the proteins of genes that had been detected as upregulated during EMT

compared with all other genes. For the mouse amino-acid enrichment, the EMT-up genes were mouse orthologues of the EMT-up human genes.

For Extended Data Fig. 8, each organism harbouring a minimum of ten genes that were orthologues of the pro-EMT human genes described in Extended Data Fig. 7c were analysed. For each organism, the asparagine percentage of each protein was calculated. Then the asparagine enrichment level for each organism was determined by calculating the ratio of the median asparagine percentage of pro-EMT proteins versus the remaining organism-specific proteins. The statistical significance of enrichment was calculated as described for Extended Data Fig. 7c.

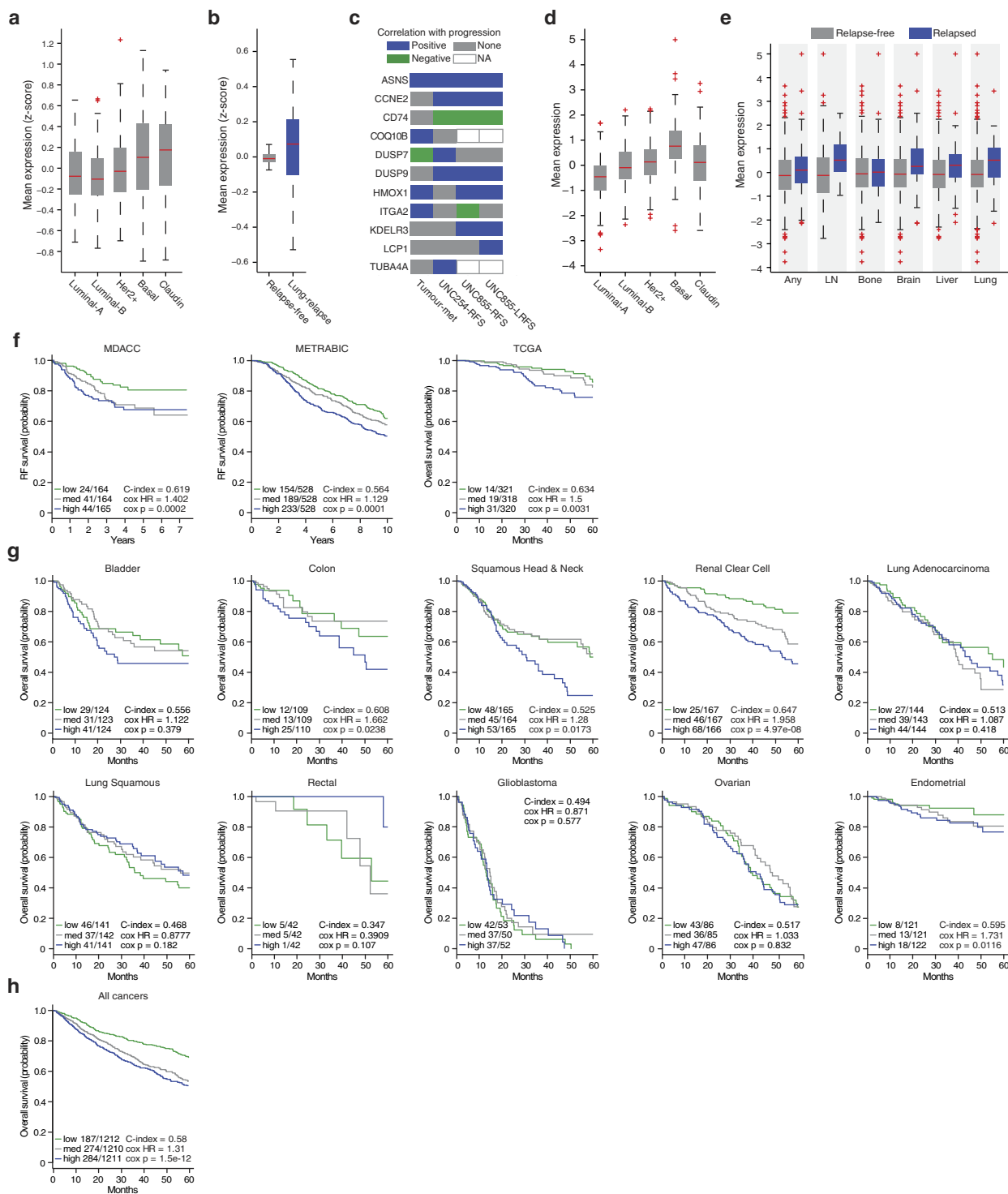
Ribosome profiling analysis. For analysis, quality trimming and sequencing adapter removal was performed using Cutadapt²². Bowtie2 was used to remove reads that mapped to contaminating RNAs (for example, rRNA and tRNA sequences)¹⁸. STAR was subsequently used to map reads of length 29–33 to the human transcriptome²³. The offset was corrected for each read on the basis of read length, and 12 and 15 nucleotides downstream were marked as P and A sites. For each gene, we then calculated the number of events at all positions and aggregated the counts for each codon and subsequently amino acid. Genes with fewer than ten events in any sample were not considered in subsequent analyses.

Code availability. All custom code used during the current study is available from the corresponding author upon reasonable request.

Data availability. All raw and processed high-throughput sequencing data are available at the Gene Expression Omnibus under accession numbers GSE104968

and GSE107109. The mass spectrometry proteomics data have been deposited in the ProteomeXchange consortium via the PRIDE²⁴ partner repository, under the dataset identifier PXD008805. Source Data are available for tumour volume measurements, lung metastases and proteomic measurements. All other datasets generated during and/or analysed during the current study are available from the corresponding author upon reasonable request.

17. Eden, E., Navon, R., Steinfeld, I., Lipson, D. & Yakhini, Z. GOrilla: a tool for discovery and visualization of enriched GO terms in ranked gene lists. *BMC Bioinformatics* **10**, 48 (2009).
18. Langmead, B. & Salzberg, S. L. Fast gapped-read alignment with Bowtie 2. *Nat. Methods* **9**, 357–359 (2012).
19. Anders, S., Pyl, P. T. & Huber, W. HTSeq—a Python framework to work with high-throughput sequencing data. *Bioinformatics* **31**, 166–169 (2015).
20. Anders, S. & Huber, W. Differential expression analysis for sequence count data. *Genome Biol.* **11**, R106 (2010).
21. Ruifrok, A. C. & Johnston, D. A. Quantification of histochemical staining by color deconvolution. *Anal. Quant. Cytol. Histol.* **23**, 291–299 (2001).
22. Martin, M. Cutadapt removes adapter sequences from high-throughput sequencing reads. *EMBnet journal* **17**, 10 (2011).
23. Dobin, A. *et al.* STAR: ultrafast universal RNA-seq aligner. *Bioinformatics* **29**, 15–21 (2013).
24. Vizcaino, *et al.* 2016 update of the PRIDE database and related tools. *Nucleic Acids Res* **44**, D447–D456 (2016).

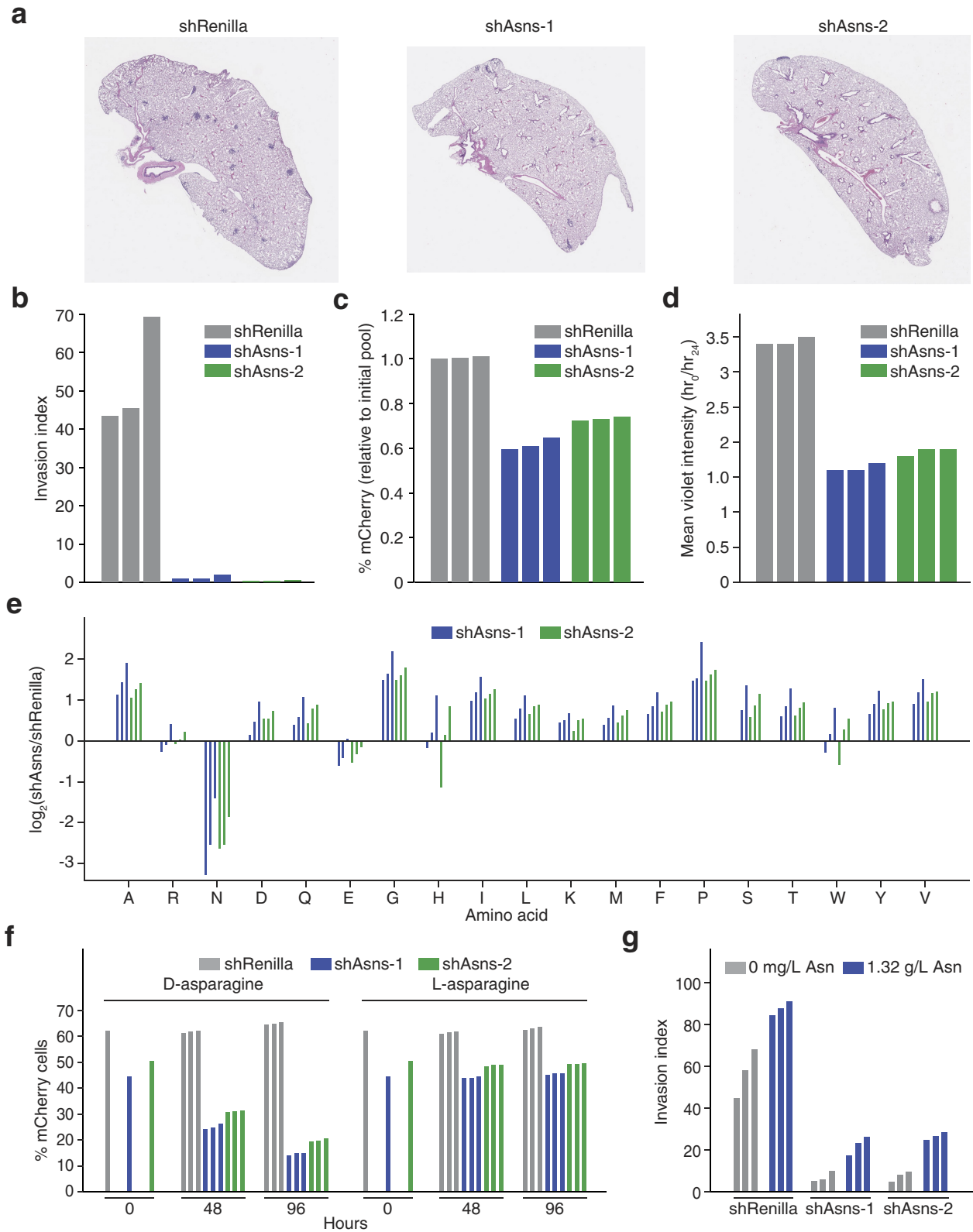


Extended Data Figure 1 | See next page for caption.

Extended Data Figure 1 | Analysis of ASNS expression levels in patient data.

a, Expression level of genes identified as overexpressed in 4T1-T compared with 4T1-E in the primary tumours of patients with different disease subtypes (edges of the box are the 25th and 75th percentiles and error bars extend to the values $q_3 + w(q_3 - q_1)$ and $q_1 - w(q_3 - q_1)$, in which w is 1.5 and q_1 and q_3 are the 25th and 75th percentiles, which is also true for **b**, **d**, and **e**, ANOVA $P < 0.0001$). **b**, Expression level of the same genes in disease-free survivors and patients with relapse to the lung (rank-sum $P < 0.01$). **c**, For each gene that was identified in the screen, a prognostic value was calculated using three different datasets. One consisted of gene expression measurements in three patient-matched basal tumour and metastasis pairs (patients A1, A7, and A11). Here genes were classified as correlated with progression if expression was higher in each of the metastases and negatively correlated if expression was higher in each of the primaries. The other two datasets consisted of primary tumour gene-expression profiles with matched outcomes. For the UNC254 patient dataset, the site of relapse was not available and genes were deemed positively correlated with progression if they had significant (Cox $P < 0.05$) relapse-free survival hazard ratios greater than 1, and

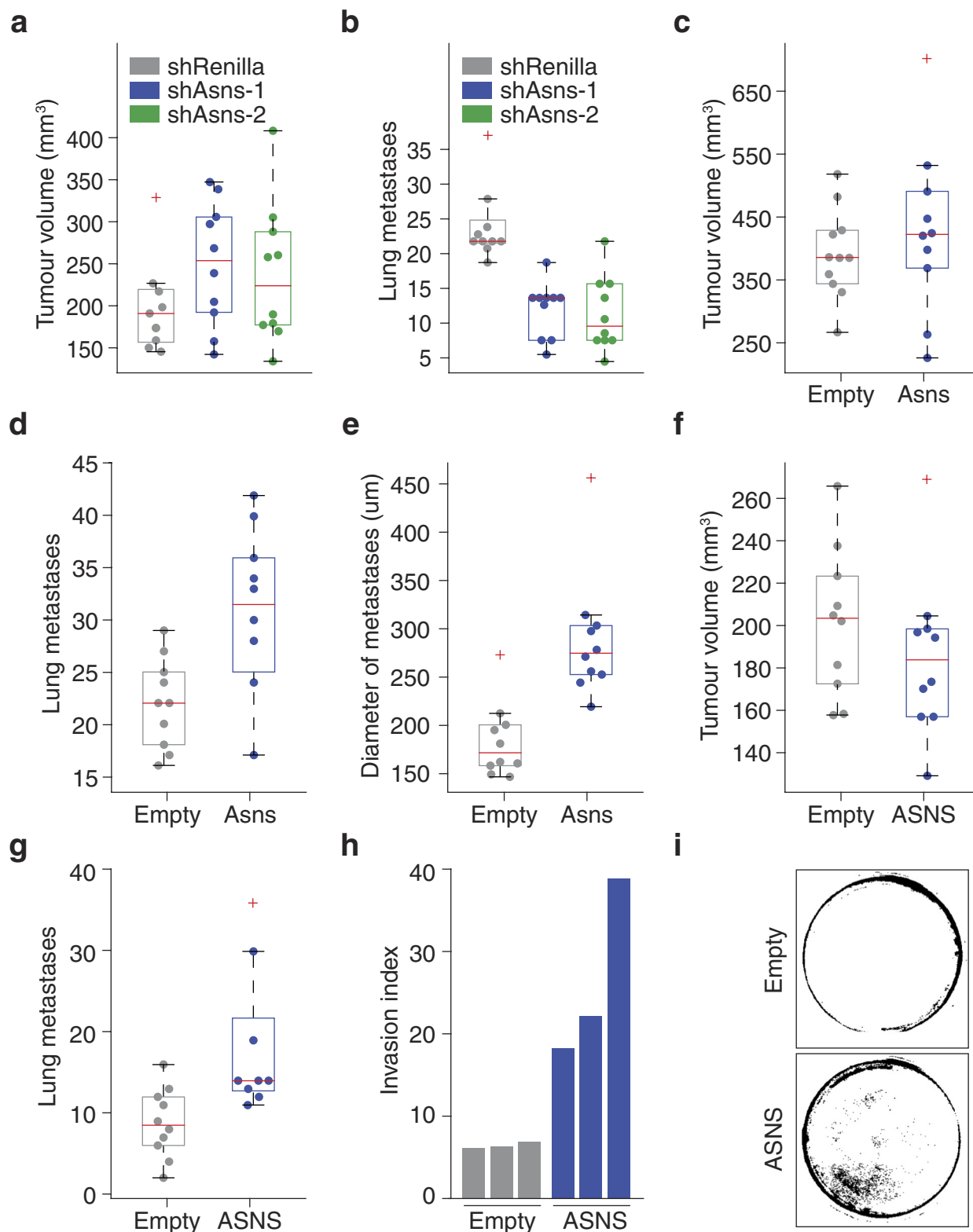
negatively correlated if these ratios were significant (Cox $P < 0.05$) and less than 1. As the UNC855 dataset also had site of relapse information, here both relapse-free and lung relapse-free survival (RFS and LRFS) hazard ratios were used to classify genes as positively or negatively correlated with progression based on the same criteria that were used for the UNC254 data. **d**, Expression level of ASNS in the primary tumours of patients with different disease subtypes (ANOVA $P < 0.0001$). **e**, Expression level of ASNS in the primary tumours of patients with non-specific relapse and relapse to the lymph node, bone, brain, liver, or lung compared with expression levels in patients without relapse to each corresponding site (rank-sum $P < 0.005$). **f**, Analysis of ASNS in three additional sets from patients with breast cancer (MDACC, METRABIC, and TCGA). Shown are survival plots and relevant statistics (Cox $P < 0.01$). **g**, Analysis of ASNS in the TCGA Pan-Cancer expression data. Shown are survival plots and relevant statistics for the ten non-breast solid tumours represented in the dataset (Cox $P < 0.05$ for colon, squamous head and neck, renal clear cell, and endometrial cancers). **h**, Analysis of ASNS across all tumours represented in the TCGA Pan-Cancer dataset (Cox $P = 1.5 \times 10^{-12}$).



Extended Data Figure 2 | See next page for caption.

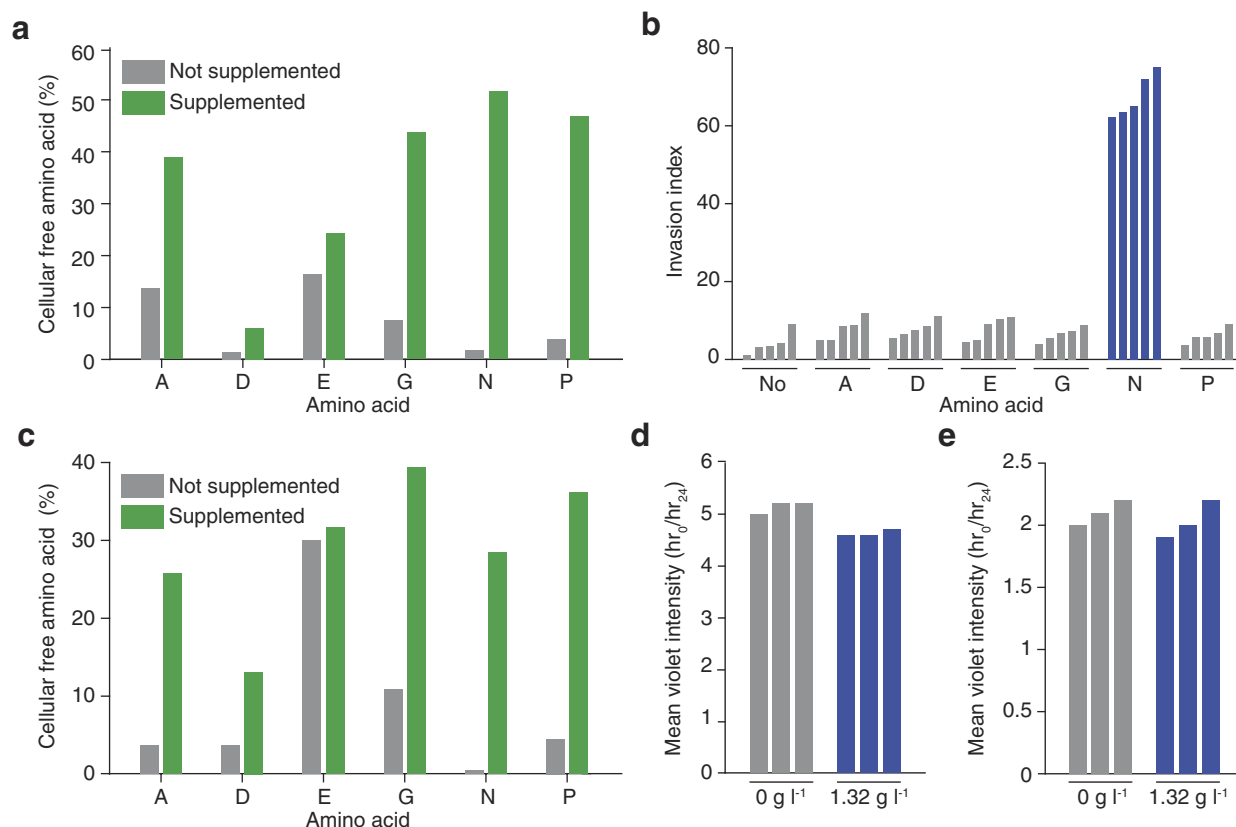
Extended Data Figure 2 | Primary validation of Asns as a driver of invasion and metastasis. **a**, Representative images of the lungs of mice that were intravenously injected with Asns-silenced or -expressing 4T1-T cells as described in Fig. 2a. **b**, Quantification of Matrigel invasion capacity for Asns-silenced and -expressing 4T1-T cells ($n = 3$ replicates per cell line). **c**, Quantification of mCherry-positive 4T1-T cells after roughly 50% of cells were infected with mCherry-expressing constructs harbouring shRNAs targeting *Renilla* luciferase and Asns. Cells were grown during the 24-h period that the Matrigel invasion assay described in Fig. 2b was being performed ($n = 3$ replicates per cell line). **d**, Violet cell-labelling intensity of Asns-silenced and -expressing 4T1-T cells, relative to the initial population. Cells were grown during the 24-h period that the Matrigel

invasion assay described in Fig. 2b was being performed ($n = 3$ replicates per cell line). **e**, Free amino-acid quantification by HPLC for each amino acid in Asns-expressing and -silenced cells. Shown are the log-fold changes for each amino acid ($n = 3$ replicates per cell line). **f**, Quantification of mCherry-positive 4T1-T cells after roughly 50% of cells were infected with mCherry-expressing constructs harbouring shRNAs targeting *Renilla* luciferase and Asns. After infection, cells were grown in medium supplemented with L-asparagine or D-asparagine and mCherry percentages were measured at 48 and 96 h ($n = 3$ replicates per cell line). **g**, Quantification of Matrigel invasion for Asns-silenced and -expressing cells when assayed in medium supplemented with and without L-asparagine ($n = 3$ invasion chambers per cell line).



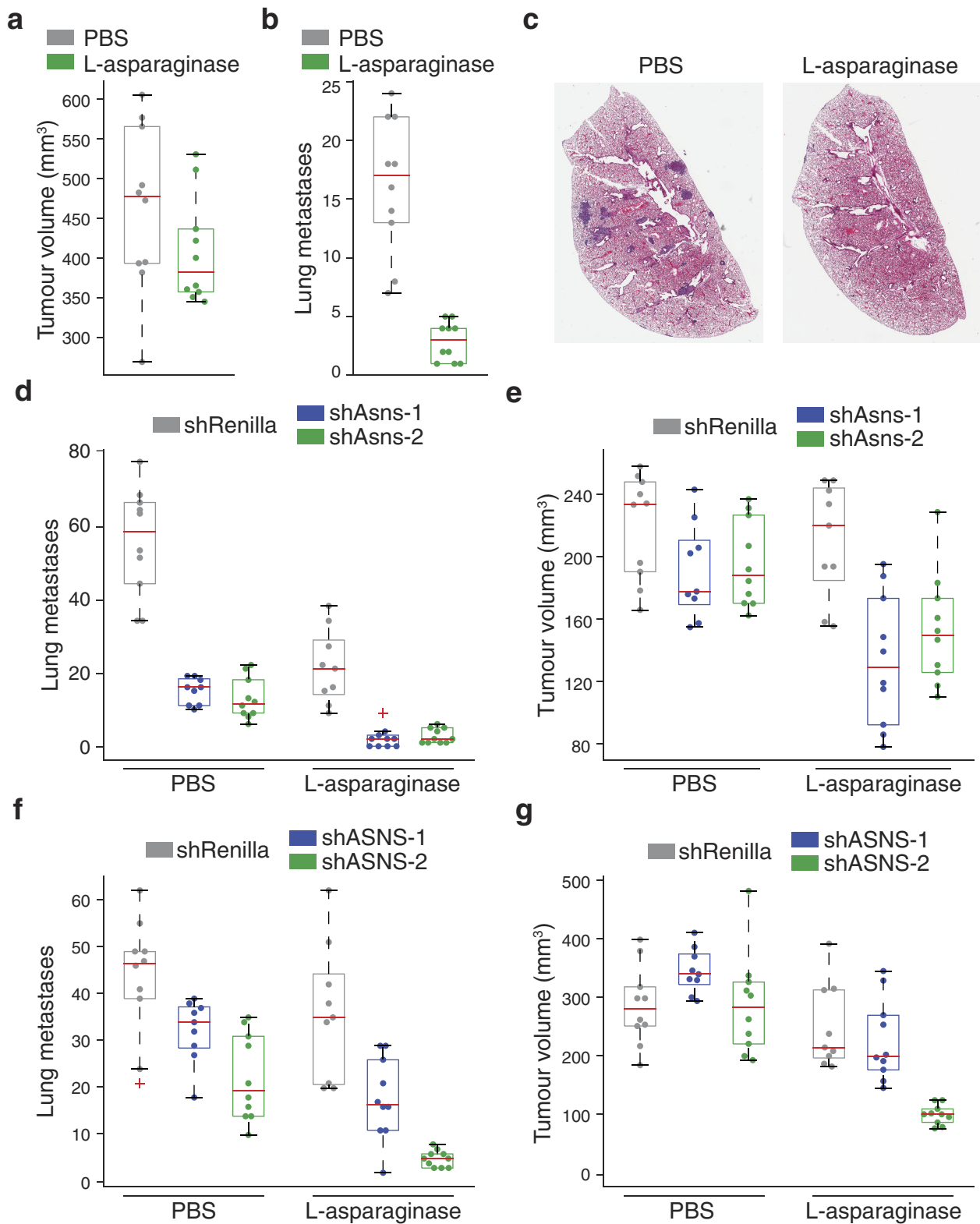
Extended Data Figure 3 | Secondary validation of *Asns* as a driver of invasion and metastasis. **a**, Volume measurements of tumours resulting from orthotopic injection of *Asns*-silenced and -expressing parental 4T1 cells ($n = 10$ mice per cell line, edges of the box are the 25th and 75th percentiles and error bars extend to the values $q_3 + w(q_3 - q_1)$ and $q_1 - w(q_3 - q_1)$, in which w is 1.5 and q_1 and q_3 are the 25th and 75th percentiles, which is also the case for **b–g**). **b**, Quantification of lung metastases corresponding to the tumours described in **a** (rank-sum $P < 0.002$). **c**, Volume measurements of tumours resulting from orthotopic injection of parental 4T1 cells with basal (Empty) or enforced expression of *Asns* ($n = 10$ mice per cell line). **d**, Quantification of lung metastases

corresponding to the tumours described in **c** (rank-sum $P < 5.0 \times 10^{-5}$). **e**, Average diameters of the metastases of each mouse described in **d** (rank-sum $P < 0.001$). **f**, Volume measurements for tumours resulting from orthotopic injection of MDA-MB-231 cells with basal (Empty) or enforced expression of *ASNS* ($n = 10$ mice per cell line). **g**, Quantification of lung metastases corresponding to the tumours described in **f** (rank-sum $P < 0.005$). **h**, Quantification of Matrigel invasion for the MDA-MB-231-derived cell lines described in **f** ($n = 3$ invasion chambers per cell line). **i**, Representative images of the collection wells for the invasion assays described in **h**. See Source Data.



Extended Data Figure 4 | Primary validation that extracellular asparagine availability affects invasion and metastasis. **a**, HPLC quantification of cellular free amino-acid percentages for parental 4T1 cells when the medium is supplemented with each of the NEAAs lacking in the DMEM culture medium ($n = 3$ replicates per cell line). **b**, Quantification of MDA-MB-231 Matrigel invasion rates under the same conditions as described in Fig. 3a ($n = 5$ invasion chambers per condition, rank-sum $P < 0.001$). **c**, HPLC quantification of cellular free amino-acid percentages for MDA-MB-231 cells when cultured in the medium

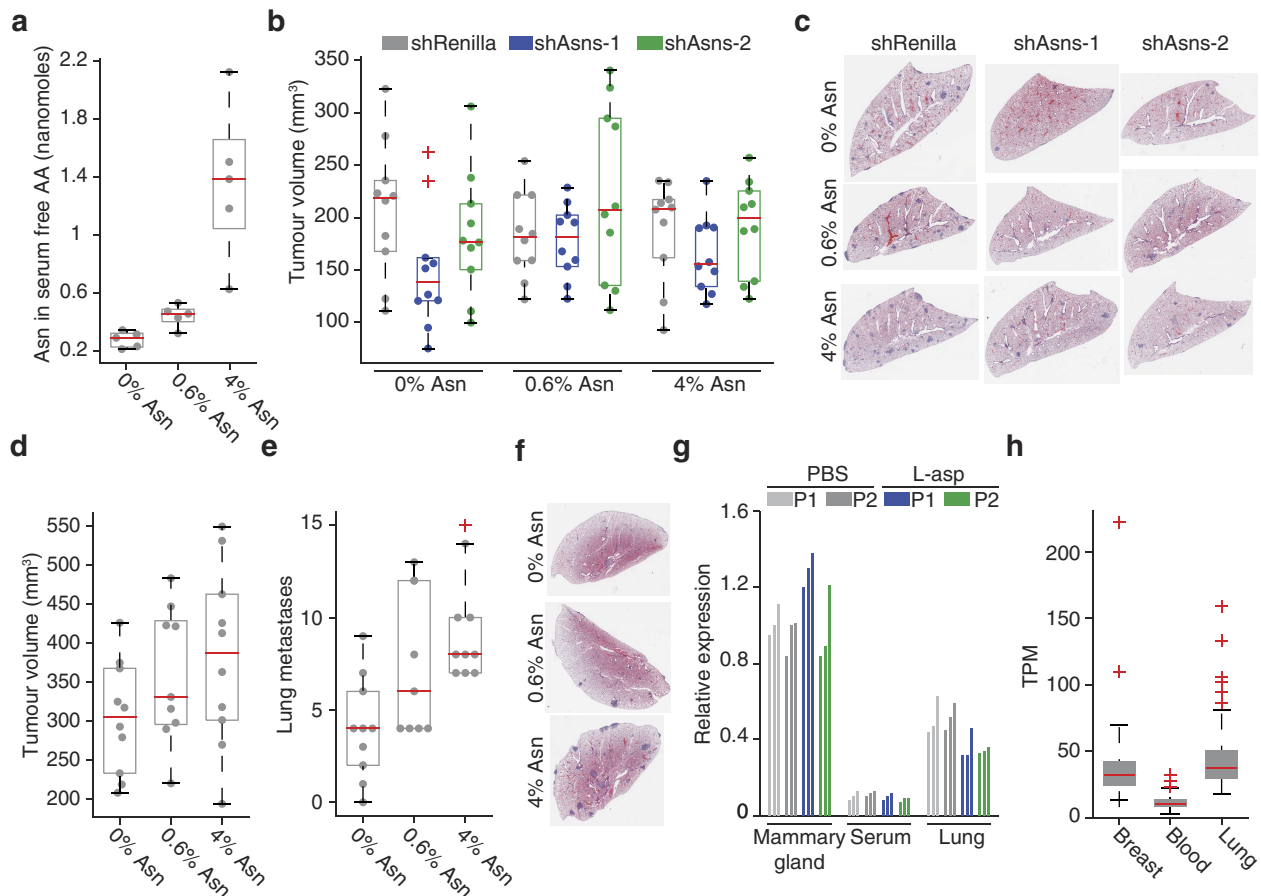
conditions described in **a** ($n = 3$ replicates per cell line). **d**, Violet cell-labelling intensity of parental 4T1 cells when grown in asparagine-lacking or -supplemented medium for the same period that the Matrigel invasion assay described in Fig. 3a was being performed ($n = 3$ replicates per cell line). **e**, Violet cell-labelling intensity of MDA-MB-231 cells when grown in asparagine-lacking or -supplemented medium for the same period that the Matrigel invasion assay described in **b** was being performed ($n = 3$ replicates per cell line).



Extended Data Figure 5 | See next page for caption.

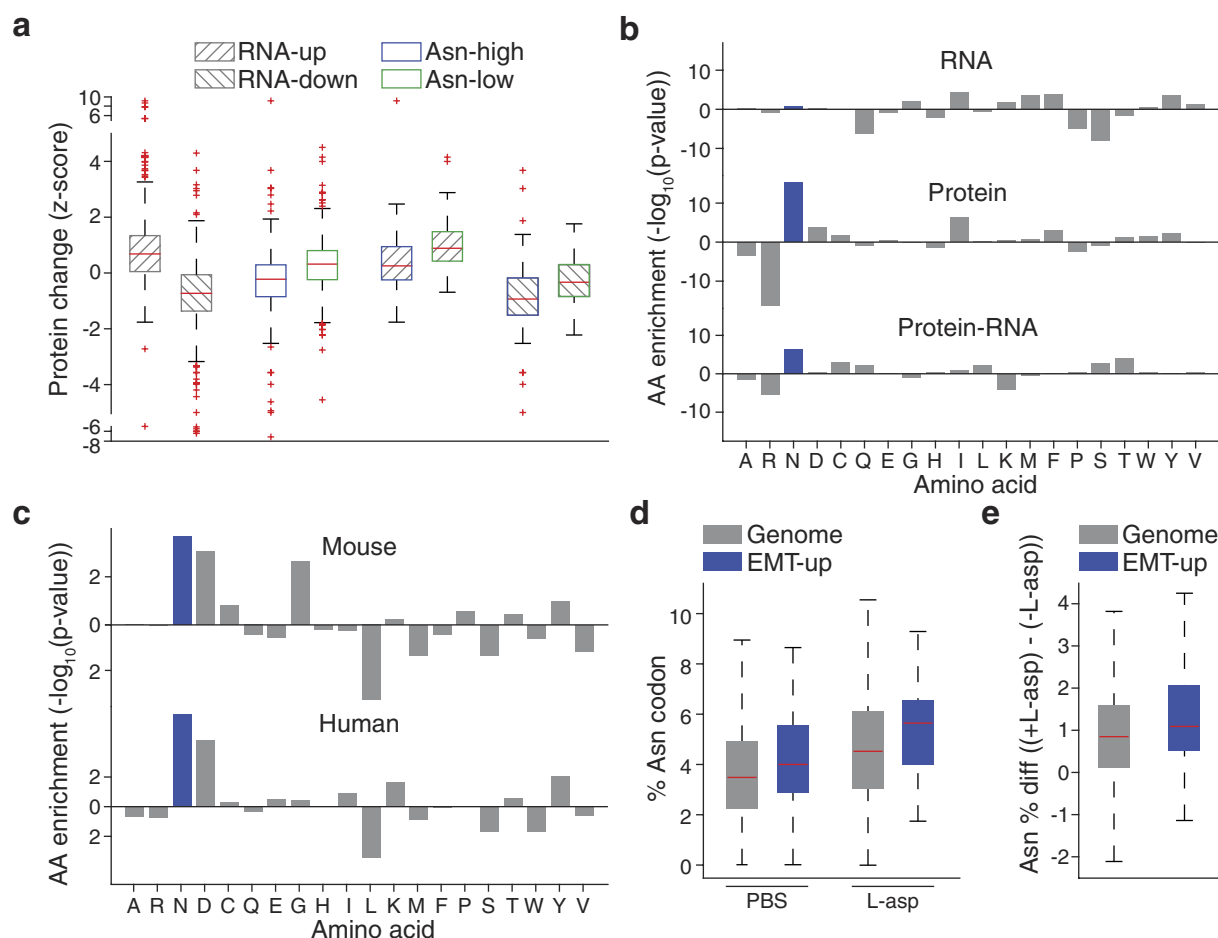
Extended Data Figure 5 | Secondary validation that extracellular asparagine availability affects invasion and metastasis. **a**, Tumour volumes resulting from the orthotopic injection of parental 4T1 cells. Half of the mice received L-asparaginase and the other half received an equivalent volume of PBS at the same injection rate ($n = 10$ mice per condition, edges of the box are the 25th and 75th percentiles and error bars extend to the values $q_3 + w(q_3 - q_1)$ and $q_1 - w(q_3 - q_1)$, in which w is 1.5 and q_1 and q_3 are the 25th and 75th percentiles, which is also the case for **b–g**). **b**, Quantification of lung metastases detected in the animals described in **a** (rank-sum $P < 0.001$). **c**, Representative H&E-stained lung sections as described in **b**. **d**, Quantification of the lung metastases described in Fig. 3b, in which Asns-silenced and -expressing 4T1-T cells were injected into mice. Half of the mice received L-asparaginase and the other half received an equivalent volume of PBS at the same injection rate

($n = 10$ mice per condition, rank-sum $P < 0.0005$ for L-asparaginase versus control for each line and for Asns-silenced versus -unsilenced cells in each drug condition). **e**, Tumour volumes corresponding to the lung metastases described in **d** (rank-sum $P < 0.005$ for Asns-silenced versus -expressing cells in L-asparaginase-treated mice). **f**, Lung metastases resulting from the orthotopic injection of ASNS-silenced and -expressing MDA-MB-231 cells and subsequent treatment of the injected animals with L-asparaginase or PBS ($n = 10$ mice per cell line, rank-sum $P < 0.05$ for ASNS-silenced versus -expressing cells in both conditions and for silenced cells in treated versus untreated mice). **g**, Tumour volumes corresponding to the mice described in **f** (rank-sum $P < 0.05$ for Asns-silenced versus -expressing cells under both treatments and for PBS versus L-asparaginase-treated animals for each cell line). See Source Data.



Extended Data Figure 6 | Tertiary validation that extracellular asparagine availability affects invasion and metastasis. **a**, Asparagine content in the serum free amino-acid pool, for mice fed 0%, 0.6%, or 4% asparagine diets ($n = 5$ mice per diet, edges of the box are the 25th and 75th percentiles and error bars extend to the values $q_3 + w(q_3 - q_1)$ and $q_1 - w(q_3 - q_1)$, in which w is 1.5 and q_1 and q_3 are the 25th and 75th percentiles, which is also the case for **b**, **d**, **e** and **h**, rank-sum $P < 0.05$ between each diet). **b**, Volumes of orthotopic tumours corresponding to the lung metastases described in Fig. 3c, in which Asns-silenced and -expressing 4T1-T cells were orthotopic injected into mice fed with 0%, 0.6%, and 4% asparagine diets ($n = 10$ mice per condition). **c**, Representative images of the lung metastases described for Fig. 3c, which also correspond to the mice described in **b**. **d**, Volumes of tumours

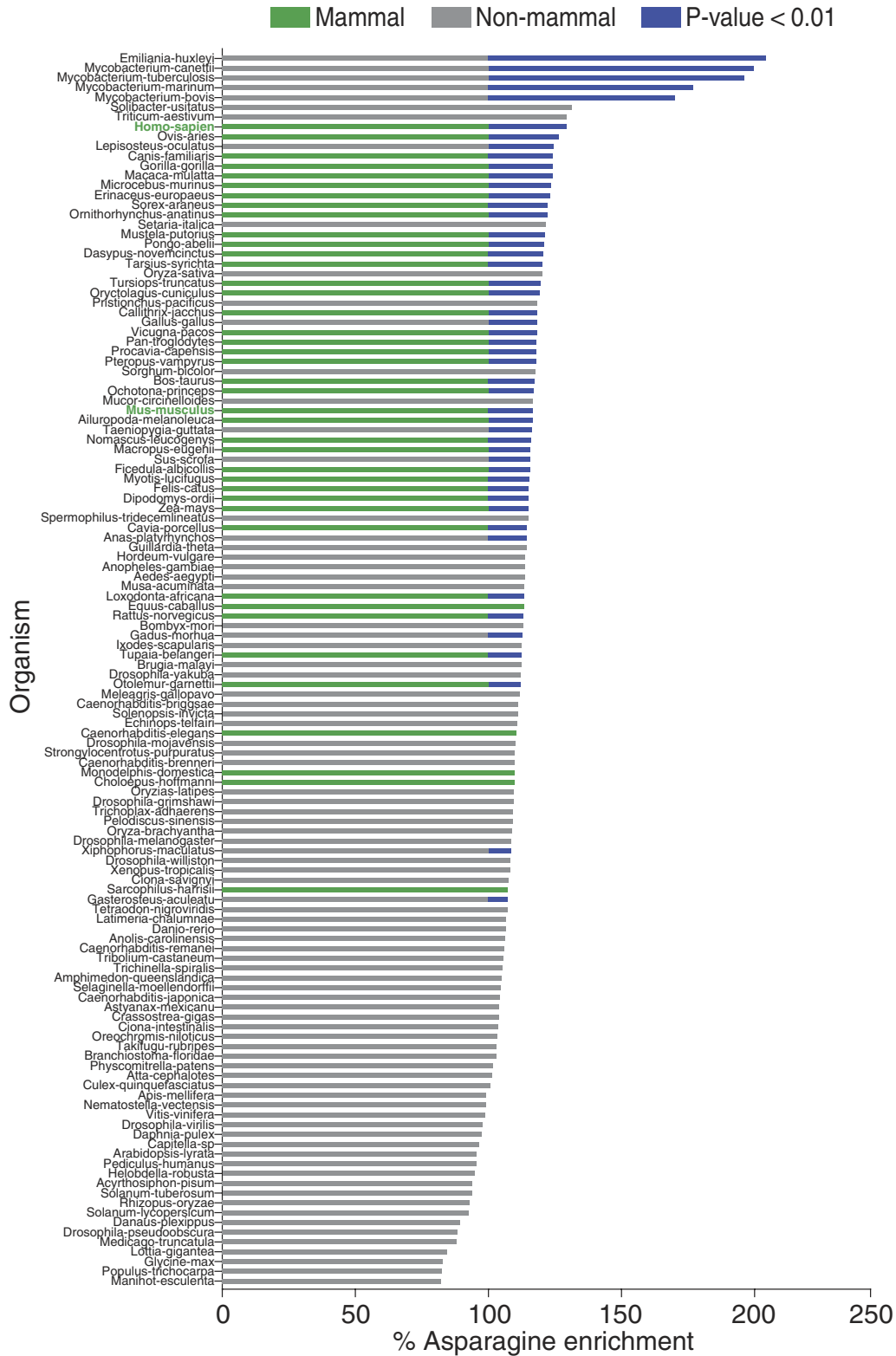
resulting from the orthotopic injection of parental 4T1 cells into mice fed with 0%, 0.6%, or 4% asparagine diets ($n = 10$ mice per diet). **e**, Quantification of metastases in the lungs of the animals described in **d** (rank-sum $P < 0.05$ for mice receiving 0% versus 0.6% and 0% versus 4% diets). **f**, Representative images of H&E-stained sections of the lungs described in **e**. **g**, Relative expression of Asns in the mammary gland, serum, and lungs of mice treated with L-asparaginase or PBS, as measured by qPCR with two primer pairs P1 and P2 ($n = 3$ per condition). **h**, Transcripts per million (TPM) expression measurements for ASNS in human breast, lung, and whole-blood samples ($n > 114$ for each tissue, rank-sum $P < 2.8 \times 10^{-37}$ for blood versus breast and blood versus lung). See Source Data.



Extended Data Figure 7 | Primary validation that asparagine availability regulates EMT. **a**, Protein-level changes between Asns-silenced and -expressing cells when genes are stratified by transcription-level changes (top and bottom 10% of genes based on log-fold change in Asns-silenced cells, gene-up and -down, respectively) and asparagine content (top and bottom 10% of genes based on asparagine content, Asp-high and -low, respectively), edges of the box are the 25th and 75th percentiles and error bars extend to the values $q_3 + w(q_3 - q_1)$ and $q_1 - w(q_3 - q_1)$, in which w is 1.5 and q_1 and q_3 are the 25th and 75th percentiles, which is also the case for **d** and **e**, rank-sum $P < 5.0 \times 10^{-24}$ for both individual variables, and rank-sum $P < 0.005$ for interacting variables). **b**, Amino acid enrichment analysis of downregulated genes (bottom 25% based on log-fold change) on the basis of RNA and protein levels in Asns-expressing versus -silenced 4T1-T cells. Negative correlations indicate the amino acid is depleted in the downregulated genes, whereas positive correlations indicate the amino acid is enriched.

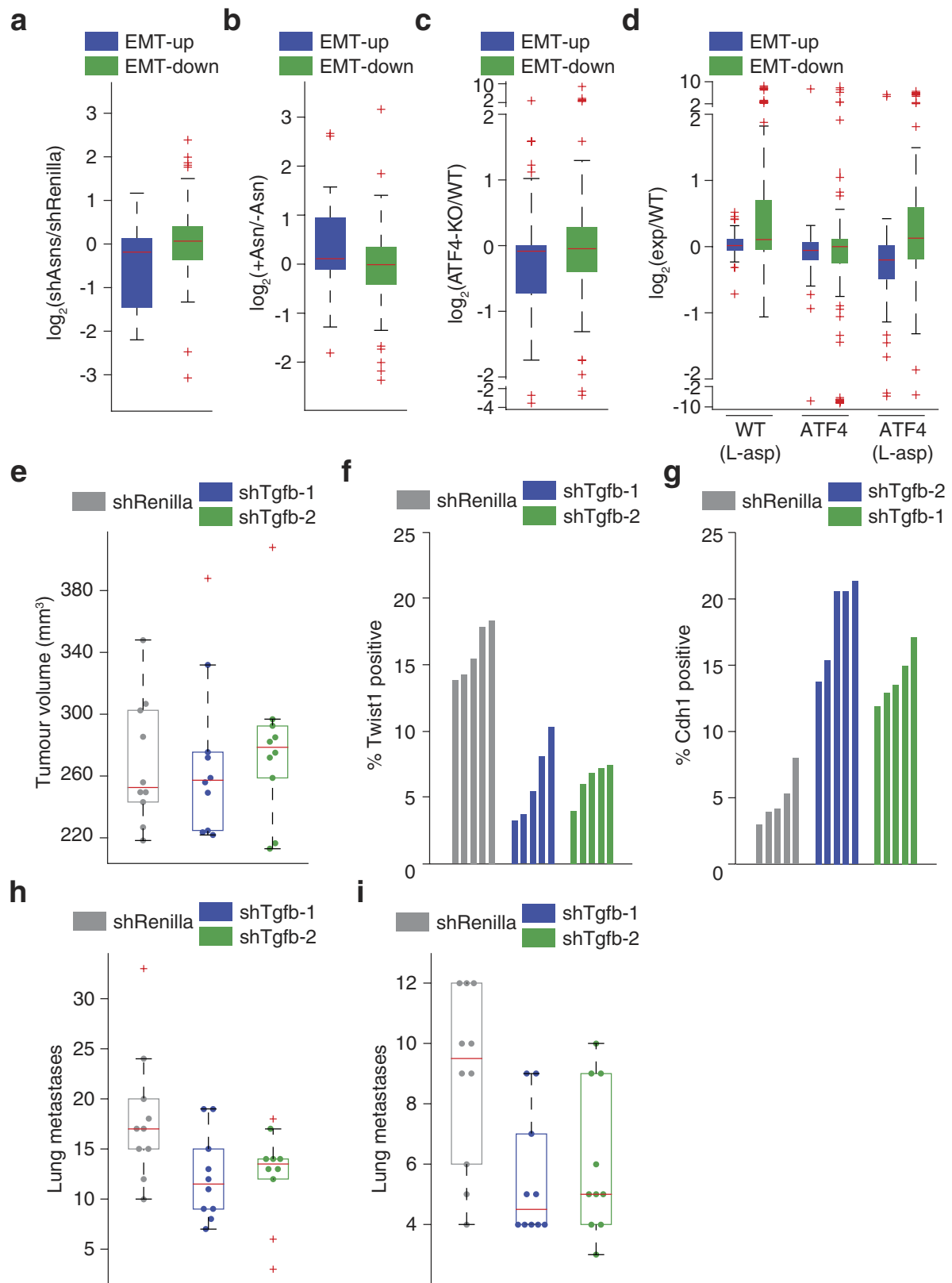
For protein minus RNA level expression changes, amino acids with positive correlations are enriched in proteins in which depletion levels exceed what is predicted by corresponding RNA changes. Negative correlations indicate the amino acid is enriched in proteins in which depletion levels are less than what is predicted by corresponding RNA changes (rank-sum $P < 1.0 \times 10^{-5}$ for asparagine in protein and protein-RNA). **c**, Amino-acid enrichment in mouse and human EMT-up proteins (rank-sum $P < 0.01$ for both human and mouse). **d**, Position 15 asparagine codon enrichment in ribosome protected fragments from PC-3 cells grown with and without L-asparaginase, when all genes or only EMT-up genes are analysed (outliers were not plotted to improve interpretability, which is also the case for **e**, rank-sum $P < 0.05$ for EMT-up versus all genes in both untreated and L-asparaginase-treated cells). **e**, Increase in asparagine codon representation in ribosome protected fragments, when PC-3 cells are grown in L-asparaginase (relative to without), and all genes or EMT-up genes are analysed (rank-sum $P < 0.05$). See Source Data.

Knott et al. 2017, Extended Data Figure 8



Extended Data Figure 8 | Conservation of asparagine enrichment in EMT promoting proteins. Asparagine enrichment analysis of EMT-promoting protein orthologues in the 126 species listed in the Orthologous

MATRIX database that harbour at least 10 orthologues (sign-rank $P < 1.0 \times 10^{-13}$ for all species and rank-sum $P < 9.0 \times 10^{-9}$ for mammals versus other species).

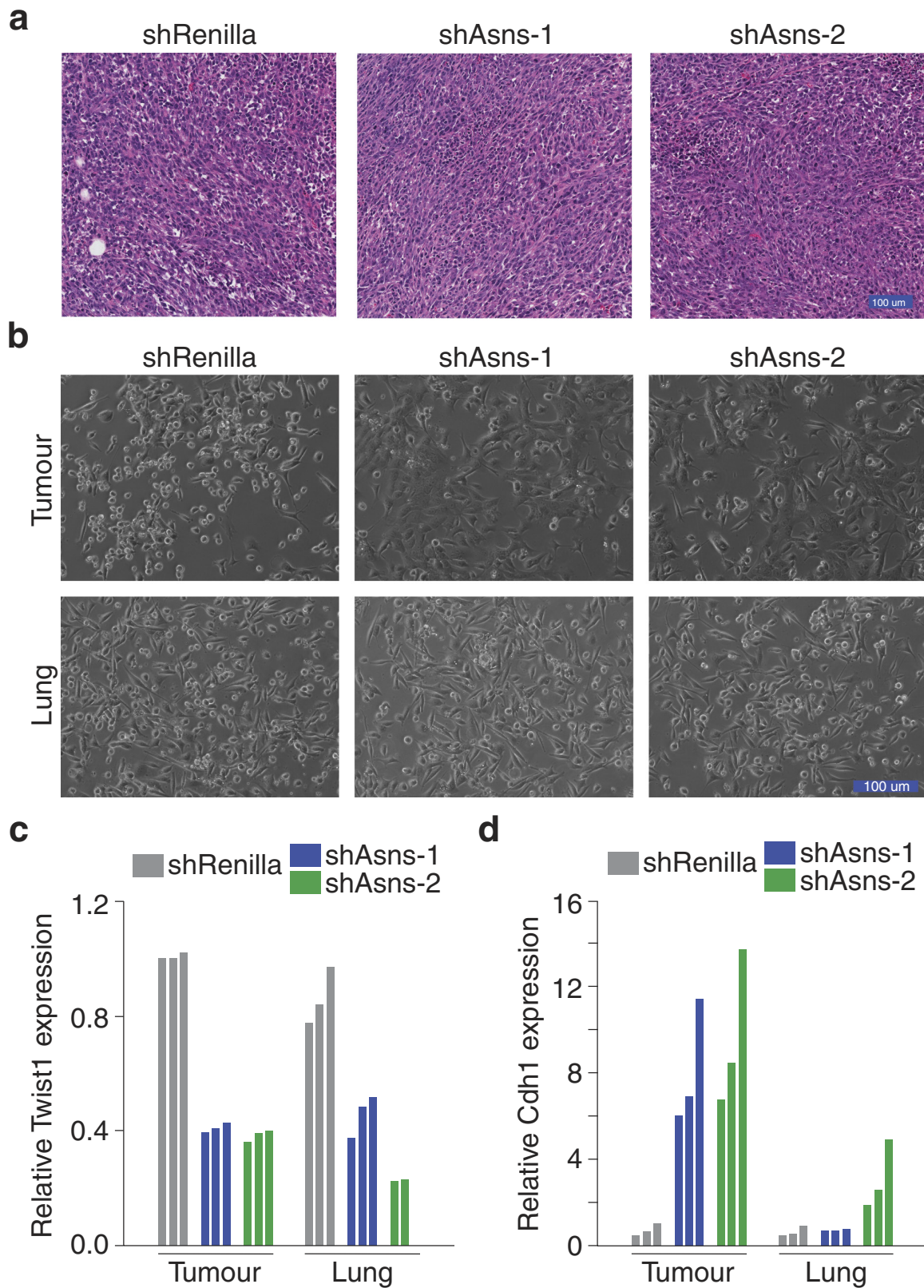


Extended Data Figure 9 | See next page for caption.

Extended Data Figure 9 | Secondary validation that asparagine availability regulates EMT.

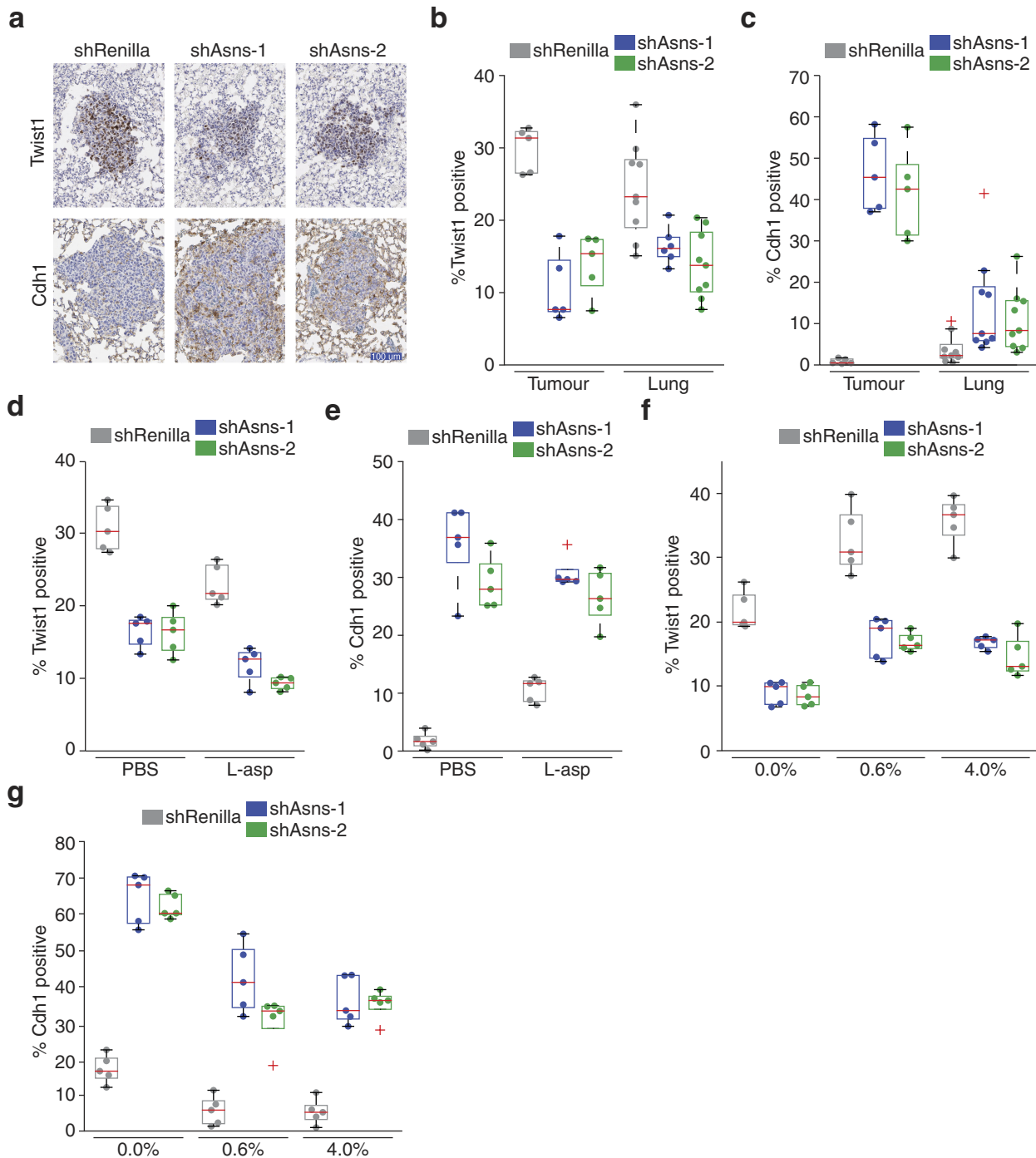
a, Transcription-level changes in EMT-up and -down genes that occur in response to Asns silencing in 4T1-T cells ($n = 2$ replicates per condition, edges of the box are the 25th and 75th percentiles and error bars extend to the values $q_3 + w(q_3 - q_1)$ and $q_1 - w(q_3 - q_1)$, in which w is 1.5 and q_1 and q_3 are the 25th and 75th percentiles, which is also the case for **b–e**, **h** and **i**, rank-sum $P < 0.001$ for EMT-up genes, DESeq false discovery rate < 0.05 for Twist1 and Cdh1). **b**, Transcription-level changes in EMT-up and -down genes that occur in response to the medium of Asns-silenced 4T1-T cells being supplemented with L-asparagine ($n = 2$ replicates per condition, rank-sum $P < 0.005$ for EMT-up genes). **c**, Gene expression changes in EMT-up and -down genes that result from ATF4 knockout in near haploid KBM-7 chronic myelogenous leukaemia (HAP-1 cells, rank-sum $P < 0.05$ for EMT-up genes). **d**, Gene expression changes in EMT-up and -down genes, which result in the liver cells of homozygous

ATF4-deleted mice when treated with L-asparaginase (rank-sum $P < 0.05$ for EMT-down genes in wild-type mice treated with L-asparaginase (WT+L-asp) mice, and both EMT-up and -down genes in ATF4 mice treated with L-asparaginase (ATF4+L-asp) mice). **e**, Volumes of tumours resulting from orthotopic injection of Tgf- β -silenced and -expressing 4T1-T cells ($n = 10$ mice per cell line). **f**, Percentage of Twist1-positive regions based on IHC staining of sections from tumours described in **e** ($n = 5$ tumour sections per cell line, rank-sum $P < 0.01$). **g**, Percentage of Cdh1-positive regions based on IHC staining of sections from tumours described in **e** ($n = 5$ tumour sections per cell line, rank-sum $P < 0.01$). **h**, Quantification of metastases resulting from the tumours described in **e** (rank-sum $P < 0.05$). **i**, Quantification of metastases resulting from intravenous injection of Tgf- β -silenced and -expressing cells ($n = 10$ mice per cell line, rank-sum $P < 0.05$). See Source Data.



Extended Data Figure 10 | Tertiary validation that asparagine availability regulates EMT. **a**, Representative H&E-stained sections of the tumours described in Fig. 2c, in which Asns-silenced and -expressing 4T1-T cells were orthotopically injected into NSG mice. **b**, Images of cultured cells after they were isolated from the tumours and lungs of mice injected orthotopically with Asns-silenced and -expressing 4T1-T cells.

c, Relative Twist1 expression, as measured by qPCR, which were sorted from the tumours and lungs of mice injected orthotopically with Asns-silenced and -expressing 4T1-T cells ($n = 3$ tumours and lungs per cell line). **d**, Relative Cdh1 expression, as measured by qPCR, in the tumours and lungs described in **c** ($n = 3$ tumours and lungs per cell line).



Extended Data Figure 11 | Quaternary validation that asparagine availability regulates EMT. **a**, Representative images of IHC staining for Twist1 and Cdh1 on sections from lungs described in Fig. 4e, in which mice were injected orthotopically with Asns-silenced and -expressing 4T1-T cells. **b**, Quantification of all Twist1 stainings, described in Fig. 4e and **a** ($n = 5$ tumour sections and $n > 5$ lung metastases, edges of the box are the 25th and 75th percentiles and error bars extend to the values $q_3 + w(q_3 - q_1)$ and $q_1 - w(q_3 - q_1)$, in which w is 1.5 and q_1 and q_3 are the 25th and 75th percentiles, which is also the case for **c-g**, rank-sum $P < 0.01$ and $P < 0.05$ for Asns-silenced versus -expressing tumours and metastases, respectively). **c**, Quantification of all Cdh1 stainings, described in **b** ($n = 5$ tumour sections and $n = 9$ lung metastases, rank-sum $P < 0.01$ and $P < 0.05$ for Asns-silenced versus -expressing tumours and metastases, respectively). **d**, Quantification of Twist1-positive regions in the tumours resulting from orthotopic injection of Asns-expressing and -silenced

4T1-T cells into animals treated with PBS or L-asparaginase ($n = 5$ tumour sections per condition, rank-sum $P < 0.01$ for Asns-silenced versus -unsilenced cells and rank-sum $P < 0.05$ for each cell line in treated versus untreated mice). **e**, Quantification of Cdh1-positive regions in the tumours described in **d** ($n = 5$ tumour sections per condition, rank-sum $P < 0.01$ for Asns-silenced versus -unsilenced cells and rank-sum $P < 0.05$ for each cell line in treated versus untreated mice). **f**, Quantification of Twist1-positive regions in tumours resulting from orthotopic injection of Asns-expressing and -silenced cells into mice fed a 0%, 0.6%, or 4% asparagine diet ($n = 5$ tumour sections per condition, rank-sum $P < 0.01$ between Asns-silenced and -expressing cells and between diets). **g**, Quantification of Cdh1-positive regions in the tumours described in **f** ($n = 5$ tumour sections per condition, rank-sum $P < 0.01$ between Asns-silenced and -expressing cells and between diets).

Mitochondria–lysosome contacts regulate mitochondrial fission via RAB7 GTP hydrolysis

Yvette C. Wong¹, Daniel Ysselstein¹ & Dimitri Krainc¹

Both mitochondria and lysosomes are essential for maintaining cellular homeostasis, and dysfunction of both organelles has been observed in multiple diseases^{1–4}. Mitochondria are highly dynamic and undergo fission and fusion to maintain a functional mitochondrial network, which drives cellular metabolism⁵. Lysosomes similarly undergo constant dynamic regulation by the RAB7 GTPase¹, which cycles from an active GTP-bound state into an inactive GDP-bound state upon GTP hydrolysis. Here we have identified the formation and regulation of mitochondria–lysosome membrane contact sites using electron microscopy, structured illumination microscopy and high spatial and temporal resolution confocal live cell imaging. Mitochondria–lysosome contacts formed dynamically in healthy untreated cells and were distinct from damaged mitochondria that were targeted into lysosomes for degradation^{6,7}. Contact formation was promoted by active GTP-bound lysosomal RAB7, and contact untethering was mediated by recruitment of the RAB7 GTPase-activating protein TBC1D15 to mitochondria by FIS1 to drive RAB7 GTP hydrolysis and thereby release contacts. Functionally, lysosomal contacts mark sites of mitochondrial fission, allowing regulation of mitochondrial networks by lysosomes, whereas conversely, mitochondrial contacts regulate lysosomal RAB7 hydrolysis via TBC1D15. Mitochondria–lysosome contacts thus allow bidirectional regulation of mitochondrial and lysosomal dynamics, and may explain the dysfunction observed in both organelles in various human diseases.

Mitochondrial fission has multiple roles including mitochondrial biogenesis and mitochondrial DNA synthesis^{5,8}, and is regulated by the GTPase dynamin-related protein (DRP1), the endoplasmic reticulum, dynamin-2 and actin^{9–16}. By contrast, lysosomal dynamics are regulated by GTP-bound active RAB7, which is recruited to late endosomal–lysosomal membranes but dissociates upon RAB GAP (GTPase-activating protein)-mediated GTP hydrolysis to become inactive, GDP-bound, and cytosolic^{1,17}. Contact sites between mitochondria and lysosomes could thus provide a potential cellular mechanism for simultaneously regulating these dynamics.

Contacts between mitochondria and melanosomes, multi-vesicular bodies and yeast vacuoles have previously been studied^{7,18–20}. Here, we identified contact sites between mitochondria and lysosomes in mammalian cells by performing electron microscopy on untreated HeLa cells. Mitochondria and lysosomes formed contacts (Fig. 1a and Extended Data Fig. 1a–c, yellow arrows) with an average distance between membranes of 9.57 ± 0.76 nm, consistent with other contact sites^{21,22}, and contact length of 198.33 ± 16.73 nm ($n = 55$ contacts from 20 cells; Fig. 1b). Using correlative light electron microscopy (CLEM), we confirmed that lysosomes or late endosomes positive for the acidic organelle label LysoTracker Red contained ultrastructure electron-dense lumens with irregular content and/or multilamellar membrane sheets (Extended Data Fig. 1d) and could simultaneously contact mitochondria and the endoplasmic reticulum (Extended Data Fig. 1e). Three-dimensional super-resolution structured illumination microscopy (N-SIM) of endogenous LAMP1 on late endosomal–lysosomal

membranes, and TOM20 on outer mitochondrial membranes, further demonstrated that mitochondria–lysosome contacts spanned more than 200 nm in the Z-plane ($n = 210$ examples from 26 cells; Fig. 1c (left) and Extended Data Fig. 1f).

We next examined mitochondria–lysosome contacts in live cells using super-resolution N-SIM, and found that vesicles positive for LAMP1 labelled with mGFP (LAMP1–mGFP) and mitochondria expressing TOM20 labelled with mApple (mApple–TOM20) formed contacts in living HeLa cells (Fig. 1c, right). Using confocal microscopy at high spatial and temporal resolutions, mitochondria were found to contact both small (vesicle diameter $< 0.5 \mu\text{m}$) and larger (vesicle diameter $> 1 \mu\text{m}$) LAMP1 vesicles (Extended Data Fig. 2a, b), and LAMP1 vesicles could simultaneously contact multiple mitochondria (Extended Data Fig. 2c) and vice versa (Extended Data Fig. 2d). We also observed multiple examples of mitochondria–lysosome contacts stained for endogenous LAMP1 and TOM20 under confocal microscopy ($n = 341$ examples from 25 cells; Extended Data Fig. 2e).

LAMP1 vesicles and mitochondria remained in stable contact over time (Fig. 1d–g, yellow arrows; Supplementary Video 1), with LAMP1 vesicles approaching mitochondria to form stable contacts (Fig. 1h, yellow arrows), but eventually leaving mitochondria (white arrow) without engulfing them (Extended Data Fig. 2f, g). Contacts observed by confocal microscopy and live cell N-SIM lasted for 10 s or more (Fig. 1i and Extended Data Fig. 3a–c), with about 15% of LAMP1 vesicles in the cell contacting mitochondria at any given time (Fig. 1j). Furthermore, sensitized emission fluorescence resonance energy transfer (SE-FRET) was observed between TOM20–Venus (outer mitochondrial membrane) and LAMP1–mTurquoise2 (lysosomal membrane) at mitochondria–lysosome contacts (Extended Data Fig. 3d, e), further confirming the formation of these contacts in living cells.

Next, we analysed whether mitochondria–lysosome contacts represent sites of bulk protein transfer or mitochondrial degradation, either directly through mitochondrial-derived vesicles (MDVs) fusing with lysosomes⁷ or indirectly through mitophagy⁶. Intermembrane space mitochondrial proteins and mitochondrial matrix proteins (Fig. 1k and Extended Data Fig. 4a–f) were not bulk transferred into lysosomes, and conversely, lysosomal luminal content marked by dextran was not bulk transferred into mitochondria at contact sites (Fig. 1k and Extended Data Fig. 4g–i). Moreover, mitochondria in contact with lysosomes were substantially larger (over 500 nm) than MDVs (about 100 nm)⁷ and contained mitochondrial matrix proteins (Fig. 1k and Extended Data Fig. 4d–f), distinct from previously described TOM20-positive MDVs²³. Mitochondria contacting lysosomes also did not undergo mitophagy, as they were not engulfed by LC3-positive autophagosomes (Extended Data Fig. 4j) or positive for autophagosome biogenesis markers (Extended Data Fig. 4k), suggesting that mitochondria–lysosome contacts do not lead to the bulk transfer of organelle luminal content or bulk mitochondrial degradation.

We then investigated whether mitochondria–lysosome contacts might be modulated by the lysosomal regulator RAB7 GTPase¹. In

¹Department of Neurology, Northwestern University Feinberg School of Medicine, Chicago, Illinois 60611, USA.

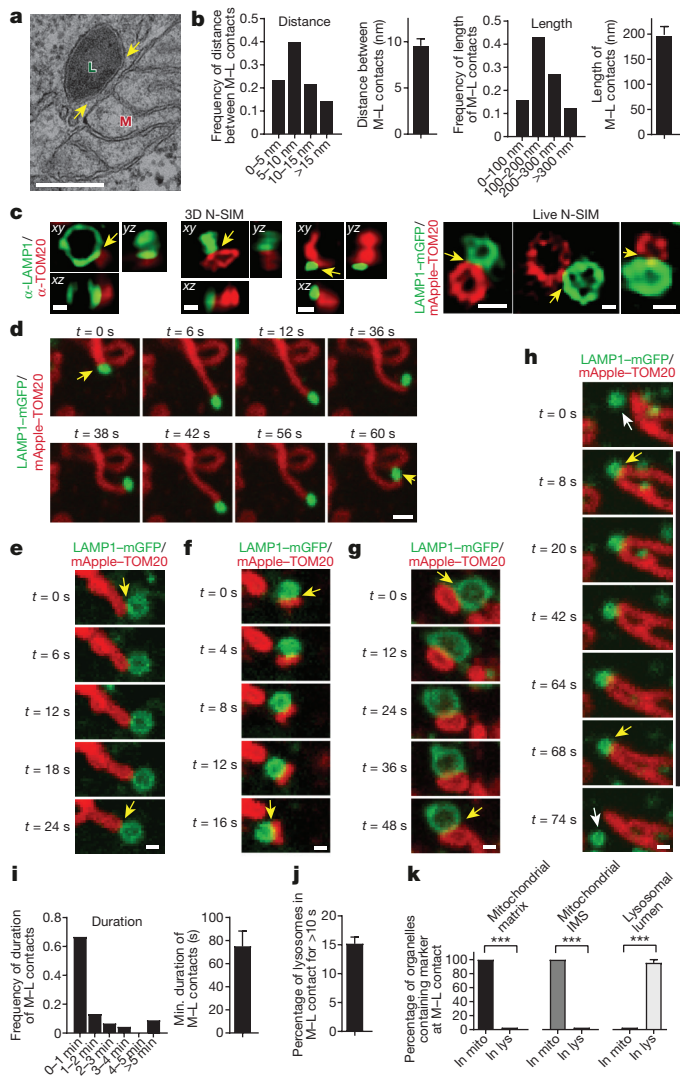


Figure 1 | Mitochondria and lysosomes form stable membrane contact sites. **a**, **b**, Representative electron microscopy image of mitochondria (M) and lysosome (L) contact (yellow arrows) in untreated HeLa cells (**a**) and quantification of distance between contact membranes and length of contact (**b**, $n = 55$ examples from 20 cells). **c**, Representative structured illumination microscopy (N-SIM) images of mitochondria-lysosome contacts (yellow arrows) in fixed HeLa cells stained for endogenous LAMP1 (lysosome) and TOM20 (mitochondria) and imaged in Z-stacks showing contacts extending more than 200 nm in the Z-plane (3D N-SIM; left; $n = 210$ examples from 26 cells) and in living HeLa cells expressing LAMP1-mGFP and mApple-TOM20 (live N-SIM; right; $n = 43$ examples from 10 cells). **d-h**, Representative time-lapse confocal images of stable mitochondria-lysosome contacts (yellow arrows) in living HeLa cells expressing LAMP1-mGFP (lysosomes) and mApple-TOM20 (mitochondria) ($n = 67$ examples from 23 cells). White arrows in **h** mark lysosomes before or after contact tethering to mitochondria. Black line shows duration of contact. **i**, **j**, Quantification of duration of mitochondria-lysosome contacts (**i**) and percentage of lysosomes contacting mitochondria (for >10 s; **j**) from confocal time-lapse images ($n = 45$ examples from 10 cells). **k**, Quantification of percentage of mitochondria (TOM20) or lysosomes (LAMP1) positive for mitochondrial matrix protein (mito-BFP; $n = 104$ events from 23 cells), mitochondrial intermembrane space (IMS) protein (SMAC-EGFP; $n = 57$ examples from 12 cells), or lysosomal lumen marker (pulse-chased dextran; $n = 66$ events from 18 cells) at mitochondria-lysosome contacts in living HeLa cells. Data are means \pm s.e.m. (***) $P < 0.0001$, unpaired two-tailed t -test). Scale bars, 200 nm (**a**); 500 nm (**c**, 3D N-SIM); 500 nm (**c**, Live N-SIM; left, right); 100 nm (**c**, Live N-SIM; middle); 1 μ m (**d**); 0.5 μ m (**e-h**).

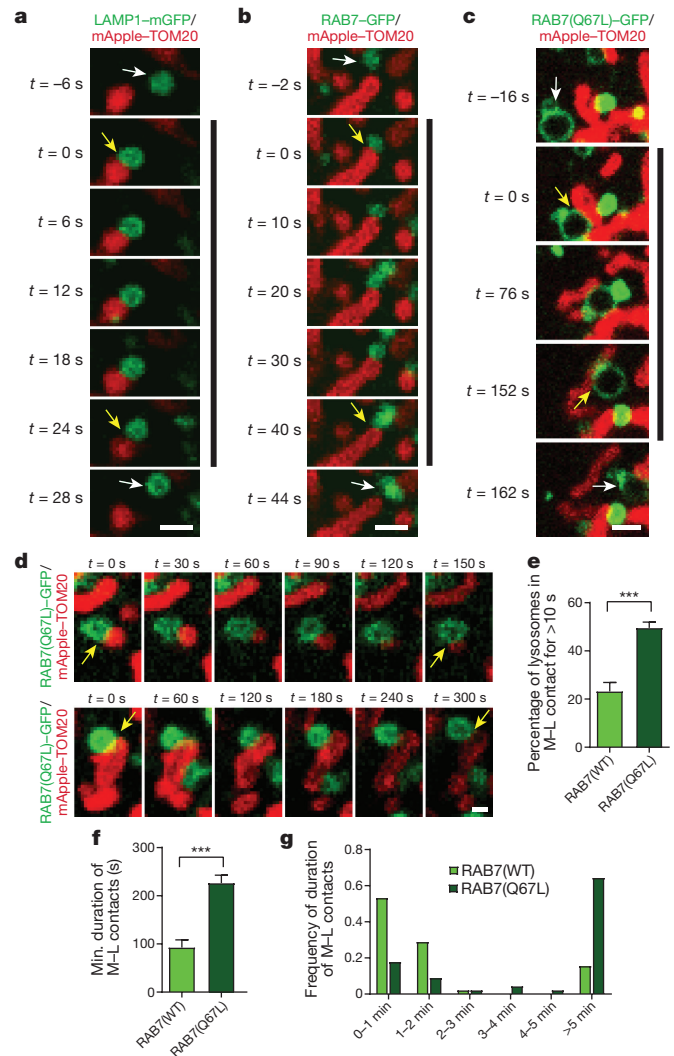


Figure 2 | RAB7 GTP hydrolysis promotes mitochondria-lysosome contact untethering. **a-c**, Representative time-lapse images of lysosome in cytosol (white arrow; top) approaching mitochondria to form a stable contact (yellow arrows; black line) before leaving mitochondria (white arrow; bottom) in living HeLa cells expressing mApple-TOM20 (mitochondria) and lysosomal markers LAMP1-mGFP (**a**), RAB7-GFP (**b**) or constitutively active GTP-bound RAB7(Q67L)-GFP mutant unable to undergo GTP hydrolysis (**c**) ($n = 45$ events from 9 cells per condition). **d**, Representative time-lapse images of mitochondria-lysosome contacts (yellow arrows) lasting more than 150 s in RAB7(Q67L)-GFP cells ($n = 45$ events from 9 cells). **e-g**, Expression of RAB7(Q67L) mutant leads to increased percentage of lysosomes in contacts ($n = 12$ cells per condition), and increased minimum duration of mitochondria-lysosome contacts ($n = 45$ events from 9 cells per condition). Data are means \pm s.e.m. (***) $P < 0.0001$, unpaired two-tailed t -test). Scale bars, 1 μ m (**a-c**); 0.5 μ m (**d**).

contrast to LAMP1-mGFP (Fig. 2a; Supplementary Video 2) or wild-type RAB7-GFP (Fig. 2b), expression of constitutively active GTP-bound mutant RAB7(Q67L)-GFP (Fig. 2c,d; Supplementary Video 3), which localized to lysosomal membranes, markedly increased both the percentage of lysosomes forming stable contacts with mitochondria (Fig. 2e) and mitochondria-lysosome contact duration ($n = 45$ events per condition; Fig. 2f, g). RAB7(Q67L) further resulted in a twofold increase in TOM20-LAMP1 mitochondria-lysosome FRET intensity compared to wild-type RAB7 ($n = 200$ cells per condition; Extended Data Fig. 3f), suggesting that GTP-bound RAB7 promotes contact formation whereas RAB7 GTP hydrolysis may be required for mitochondria-lysosome contact untethering.

We next examined how RAB7 GTP hydrolysis might be regulated at mitochondria–lysosome contacts. TBC1D15 is a RAB7 GAP that is recruited to mitochondria by the mitochondrial protein FIS1^{24,25} to drive RAB7 GTP hydrolysis^{26,27}, potentially allowing mitochondria to regulate both contact untethering and lysosomal RAB7 hydrolysis via TBC1D15. Consistent with previous studies^{24,25}, mitochondrial localization of TBC1D15 was dependent on FIS1 binding (Extended Data Fig. 5a, d–f) but not inhibited by TBC1D15 mutants lacking GAP activity (D397A or R400K in the TBC domain)²⁵ (Extended Data Fig. 5b, c, e). Moreover, expression of mutant TBC1D15 could induce abnormally large lysosomes (Extended Data Fig. 5g), characteristic of inhibiting RAB7 GTP hydrolysis.

Using live cell time-lapse imaging, we found that the GAP mutants TBC1D15(D397A) (Fig. 3a, b and Extended Data Fig. 6a, b; Supplementary Video 4) and TBC1D15(R400K) (Fig. 3c) markedly increased mitochondria–lysosome contact duration compared to wild-type TBC1D15 ($n = 34$ –38 events per condition; Fig. 3d, e) but did not alter the percentage of lysosomes forming contacts with mitochondria (Extended Data Fig. 6c). *TBC1D15*^{−/−} HCT116 cells, generated using transcription activator-like effector nucleases (TALENs) and previously characterized²⁴, also showed a similar increase in contact duration, but no change in contact formation (Extended Data Fig. 6d, e), suggesting that RAB7 GTP hydrolysis induced by TBC1D15 does not regulate contact formation, but rather regulates contact duration by promoting contact untethering upon GTP hydrolysis.

Contact untethering was further dependent on the mitochondrial localization of TBC1D15, as expression of a FIS1(LA) mutant that cannot recruit TBC1D15 to mitochondria²⁵ (Extended Data Fig. 5f) also induced abnormally enlarged lysosomes that contacted mitochondria (Fig. 3f), resulting in an increase in the duration and number of mitochondria–lysosome contacts (Fig. 3f, g and Extended Data Fig. 6f). Consistent with these findings, *FIS1*^{−/−} HCT116 cells²⁴ also showed similar increases in contact duration and number (Extended Data Fig. 6g, h). However, localization of TBC1D15, FIS1 or RAB7 was not restricted to or concentrated at mitochondria–lysosome contact sites (Fig. 2b and Extended Data Fig. 6i, j). Together, these results suggest that RAB7 GTP hydrolysis is regulated at mitochondria–lysosome contacts by the GAP activity of TBC1D15, which is recruited to mitochondria by FIS1. Inhibition of RAB7 GTP hydrolysis leads to both defective lysosomal morphology and mitochondria–lysosome contacts that are unable to untether, and consequently remain in contact for a longer duration.

Finally, we investigated whether mitochondria–lysosome contacts also regulate mitochondrial dynamics. Time-lapse confocal microscopy showed that mitochondria underwent fission events at an average of 1.44 events per min in live HeLa cells. Unexpectedly, sites of mitochondrial fission were predominantly marked by a LAMP1 vesicle (yellow arrow) before the fission event (white arrows) (Fig. 4a–c, Extended Data Fig. 7a–c, Supplementary Videos 5, 6). LAMP1 vesicles contacted mitochondria at 81.5% of mitochondrial fission sites ($n = 44/54$ events from 18 cells), which was significantly greater than expected by random chance (12.6%; *** $P < 0.0001$, Fisher's exact test; Fig. 4d) and greater than the percentage of contacts made by other vesicles such as early endosomes (GFP–EEA1) or peroxisomes (mEmerald–peroxisome) (<20% of fission events) (Fig. 4e). LAMP1 vesicles also localized to mitochondrial fission events at similar rates in other cell types including H4 neuroglioma, HEK293 and HCT116 cells (Extended Data Fig. 7d–g) and upon induction of mitochondrial fragmentation using actinomycin D, staurosporine (STS) or carbonyl cyanide *m*-chlorophenylhydrazone (CCCP) (Extended Data Fig. 8a–d). Mitochondrial fission events marked by lysosomes were also positive for mCherry–DRP1 oligomerization (Extended Data Fig. 9a) and endoplasmic reticulum tubules labelled with the endoplasmic reticulum markers mCherry–ER (100%; $n = 54/54$ events from 16 cells; Extended Data Fig. 9b, c), BFP–KDEL (100%; $n = 24/24$ events from 13 cells) or GFP–SEC61 β (100%; $n = 11/11$ events from 11 cells), demonstrating

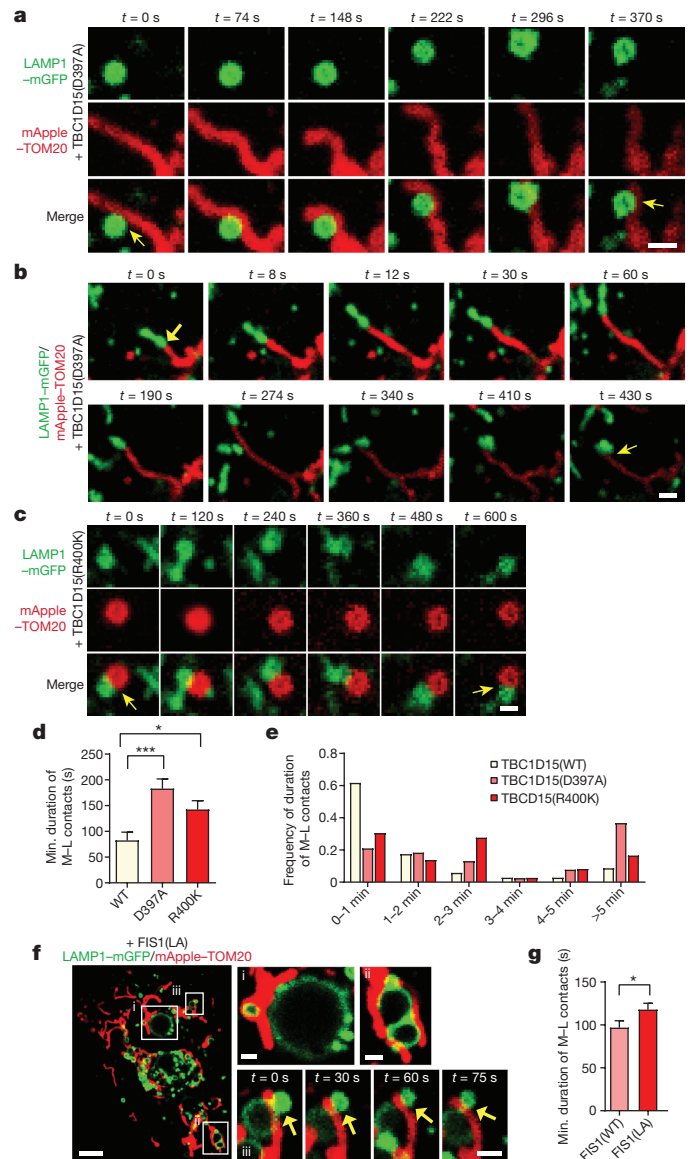


Figure 3 | Mitochondrial recruitment of TBC1D15, a RAB7 GAP, by FIS1 drives RAB7 GTP hydrolysis to promote mitochondria–lysosome contact untethering. a–c, Representative time-lapse images of stable mitochondria–lysosome contacts (yellow arrows) lasting more than 300 s in living HeLa cells expressing mApple–TOM20 (mitochondria), LAMP1–mGFP (lysosome) and TBC domain mutants TBC1D15(D397A) or TBC1D15(R400K) lacking GAP activity. d, Quantification of minimum duration of mitochondria–lysosome contacts, which are increased by TBC domain mutants compared to wild-type TBC1D15 ($n = 34$ events from 12 cells, wild-type; $n = 38$ events from 10 cells, D397A; $n = 36$ events from 11 cells, R400K). * $P = 0.0404$, *** $P = 0.0002$; ANOVA with Tukey's post-hoc test. e, Duration frequencies of mitochondria–lysosome contacts. f, g. Expression of a FIS1(LA) mutant (unable to recruit TBC1D15 to mitochondria) leads to an increase in the minimum duration of mitochondria–lysosome contacts compared to wild-type FIS1 ($n = 45$ events from 9 cells per condition). * $P = 0.049$, unpaired two-tailed t -test. Data are means \pm s.e.m. Scale bars, 1 μ m (a, b); 0.5 μ m (c); 5 μ m (f); 1 μ m (f, insets).

that mitochondria–lysosome contacts mark the sites of DRP1- and endoplasmic reticulum-positive mitochondrial fission events.

As RAB7 GTP hydrolysis regulates mitochondria–lysosome contacts, we investigated whether it also regulates mitochondrial fission. Expression of RAB7(Q67L) markedly reduced the rate of mitochondrial fission (Fig. 4f), resulting in mitochondria that did not undergo fission over time (Extended Data Fig. 10a). In addition, both the GAP

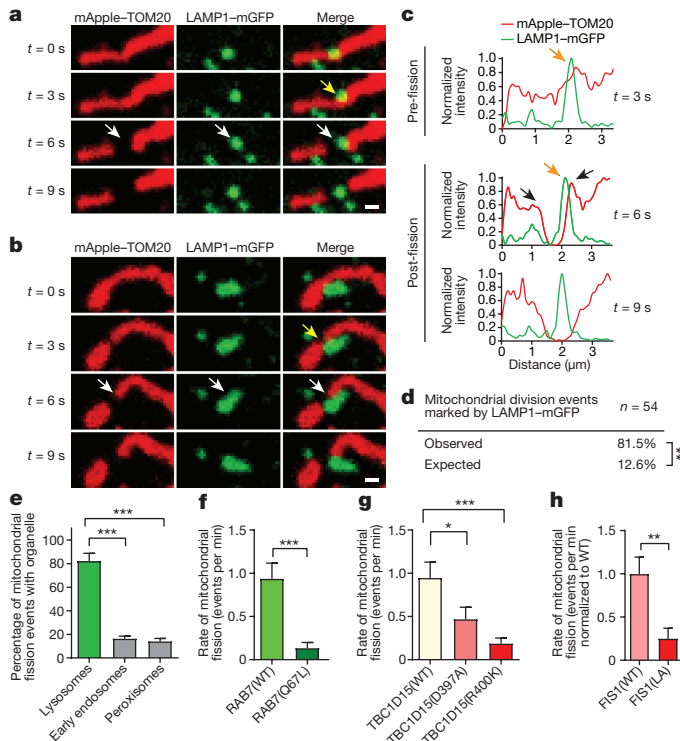


Figure 4 | Mitochondria-lysosome contacts mark sites of mitochondrial fission regulated by RAB7 GTP hydrolysis. **a, b,** Representative time-lapse images of lysosomes contacting mitochondria at the site of mitochondrial division (yellow arrow) before fission (white arrows) in living HeLa cells expressing LAMP1-mGFP (lysosomes) and mApple-TOM20 (mitochondria) ($n = 62$ events from 23 cells). **c,** Linescan corresponding to Fig. 4a showing a lysosome contacting a mitochondrion pre-fission (yellow arrow; top) and remaining in contact post-fission (yellow arrow; middle) after the mitochondria has divided into two daughter mitochondria (grey arrows; middle). **d, e,** Percentage of mitochondrial division events marked by LAMP1 vesicles in living HeLa cells expressing LAMP1-mGFP (lysosomes) and mApple-TOM20 (mitochondria) ($n = 54$ events from 18 cells). Significantly more events were marked by LAMP1 vesicles (81.5%) than expected by random chance (12.6%; $***P < 0.0001$, Fisher's exact test), or by early endosomes (GFP-EEA1) ($n = 45$ events from 17 cells; $***P < 0.0001$) or peroxisomes (mEmerald-peroxisome) ($n = 49$ events from 17 cells; $***P < 0.0001$). **f-h,** RAB7(Q67L) GTP-hydrolysis deficient mutant ($n = 10$ cells, RAB7; $n = 13$ cells, RAB7(Q67L); $***P = 0.0008$), TBC1D15 GAP mutants (D397A or R400K) ($n = 13$ cells per condition; $*P = 0.451$, $***P = 0.001$) or FIS1 (LA) mutant (unable to bind TBC1D15) ($n = 19$ cells, FIS1(WT); $n = 18$ cells, FIS1(LA); $***P = 0.0027$) lead to decreased rates of mitochondrial fission. Data are means \pm s.e.m. ANOVA with Tukey's post-hoc test (**e, g**), unpaired two-tailed t -test (**f, h**). Scale bars, $0.5 \mu\text{m}$ (**a, b**).

mutants TBC1D15(D397A) and TBC1D15(R400K) (Fig. 4g, Extended Data Fig. 10b–e), and FIS1(LA), which disrupts TBC1D15 mitochondrial recruitment (Fig. 4h), markedly reduced mitochondrial fission rates. However, for the few fission events that did occur, the percentage of mitochondrial fission marked by lysosomes or endoplasmic reticulum was not altered by RAB7(Q67L) (Extended Data Fig. 10f, g) or TBC1D15 mutants (Extended Data Fig. 10h, i), further confirming that the majority of fission events are positive for lysosomes and endoplasmic reticulum. Moreover, inhibition of RAB7 GTP hydrolysis by RAB7(Q67L) or TBC1D15 GAP mutants reduced the percentage of cells with normal mitochondrial networks that were not hypertethered or overly elongated (Extended Data Fig. 10j–l). Thus, mitochondrial TBC1D15 recruited by FIS1 promotes RAB7 GTP hydrolysis at mitochondria-lysosome contacts to regulate both lysosomal morphology and mitochondrial fission.

In summary, we propose that mitochondria-lysosome contacts are regulated in two steps: formation and stabilization of contacts promoted by lysosomal GTP-bound RAB7, followed by contact untethering by TBC1D15, a RAB7 GAP recruited to mitochondria by FIS1, which drives RAB7 GTP hydrolysis at contact sites and results in dissociation of GDP-bound RAB7 from the membrane, which can no longer maintain stable contacts.

In addition, our work suggests that mitochondria-lysosome contacts regulate at least two important aspects of mitochondrial and lysosomal dynamics. First, lysosomal RAB7 hydrolysis is regulated by mitochondrial TBC1D15, providing a mechanism for mitochondria to modulate lysosomal dynamics by shutting down active RAB7, which regulates lysosomal transport, fusion and maturation¹. Of note, the distance between TBC1D15's mitochondrial FIS1-binding site²⁵ and its TBC GAP domain for driving lysosomal RAB7 GTP hydrolysis is sufficient to span the distance (about 10 nm) between membranes at mitochondria-lysosome contact sites. This ability to regulate Rab GTP-GDP cycling on the opposing membrane of a target organelle may be similar to that proposed for GEF activation of the Golgi-localized RAB GTPase YPT1P by the TRAPP1 complex on endoplasmic reticulum-derived COPII-coated vesicles²⁸.

Second, mitochondria-lysosome contacts mark sites of mitochondrial fission, conversely allowing lysosomal RAB7 to regulate mitochondrial dynamics. Previous studies examining the role of TBC1D15 in regulating mitochondrial morphology at steady state^{24,25} and that of FIS1 in regulating the mitochondrial fission machinery have been controversial. Although our data suggest that both TBC1D15 and FIS1 indirectly regulate mitochondrial fission events via lysosomal RAB7 GTP hydrolysis, further work examining their mechanistic role in this process will be important. As membrane contact sites mediate multiple forms of inter-organelle communication^{22,29}, we hypothesize that mitochondria-lysosome contacts also function as platforms for metabolic exchanges between the two organelles. Thus, future studies of additional roles and protein tethers involved at these contacts will provide valuable insight into cellular organization and the pathogenesis of multiple diseases linked to both mitochondrial and lysosomal dysfunction^{2–4,30}.

Online Content Methods, along with any additional Extended Data display items and Source Data, are available in the online version of the paper; references unique to these sections appear only in the online paper.

Received 23 March 2017; accepted 3 January 2018.

Published online 24 January 2018.

- Hutagalung, A. H. & Novick, P. J. Role of Rab GTPases in membrane traffic and cell physiology. *Physiol. Rev.* **91**, 119–149 (2011).
- Burté, F., Carelli, V., Chinnery, P. F. & Yu-Wai-Man, P. Disturbed mitochondrial dynamics and neurodegenerative disorders. *Nat. Rev. Neurol.* **11**, 11–24 (2015).
- McDonald, J. M. & Krainc, D. Lysosomal proteins as a therapeutic target in neurodegeneration. *Annu. Rev. Med.* **68**, 445–458 (2017).
- Plotegher, N. & Duchen, M. R. Mitochondrial dysfunction and neurodegeneration in lysosomal storage disorders. *Trends Mol. Med.* **23**, 116–134 (2017).
- Mishra, P. & Chan, D. C. Metabolic regulation of mitochondrial dynamics. *J. Cell Biol.* **212**, 379–387 (2016).
- Pickrell, A. M. & Youle, R. J. The roles of PINK1, parkin, and mitochondrial fidelity in Parkinson's disease. *Neuron* **85**, 257–273 (2015).
- Sugiura, A., McLelland, G. L., Fon, E. A. & McBride, H. M. A new pathway for mitochondrial quality control: mitochondrial-derived vesicles. *EMBO J.* **33**, 2142–2156 (2014).
- Lewis, S. C., Uchiyama, L. F. & Nunnari, J. ER-mitochondria contacts couple mtDNA synthesis with mitochondrial division in human cells. *Science* **353**, aaf5549 (2016).
- Smirnova, E., Griparic, L., Shurland, D. L. & van der Bliek, A. M. Dynamin-related protein Drp1 is required for mitochondrial division in mammalian cells. *Mol. Biol. Cell* **12**, 2245–2256 (2001).
- Friedman, J. R. *et al.* ER tubules mark sites of mitochondrial division. *Science* **334**, 358–362 (2011).
- Korobova, F., Ramabhadran, V. & Higgs, H. N. An actin-dependent step in mitochondrial division mediated by the ER-associated formin INF2. *Science* **339**, 464–467 (2013).

12. Ji, W. K., Hatch, A. L., Merrill, R. A., Strack, S. & Higgs, H. N. Actin filaments target the oligomeric maturation of the dynamin GTPase Drp1 to mitochondrial fission sites. *eLife* **4**, e11553 (2015).
13. Li, S. *et al.* Transient assembly of F-actin on the outer mitochondrial membrane contributes to mitochondrial fission. *J. Cell Biol.* **208**, 109–123 (2015).
14. Manor, U. *et al.* A mitochondria-anchored isoform of the actin-nucleating spire protein regulates mitochondrial division. *eLife* **4**, (2015).
15. Moore, A. S., Wong, Y. C., Simpson, C. L. & Holzbaur, E. L. Dynamic actin cycling through mitochondrial subpopulations locally regulates the fission–fusion balance within mitochondrial networks. *Nat. Commun.* **7**, 12886 (2016).
16. Lee, J. E., Westrate, L. M., Wu, H., Page, C. & Voeltz, G. K. Multiple dynamin family members collaborate to drive mitochondrial division. *Nature* **540**, 139–143 (2016).
17. Zhen, Y. & Stenmark, H. Cellular functions of Rab GTPases at a glance. *J. Cell Sci.* **128**, 3171–3176 (2015).
18. Daniele, T. *et al.* Mitochondria and melanosomes establish physical contacts modulated by Mfn2 and involved in organelle biogenesis. *Curr. Biol.* **24**, 393–403 (2014).
19. Elbaz-Alon, Y. *et al.* A dynamic interface between vacuoles and mitochondria in yeast. *Dev. Cell* **30**, 95–102 (2014).
20. Hönscher, C. *et al.* Cellular metabolism regulates contact sites between vacuoles and mitochondria. *Dev. Cell* **30**, 86–94 (2014).
21. Csordás, G. *et al.* Structural and functional features and significance of the physical linkage between ER and mitochondria. *J. Cell Biol.* **174**, 915–921 (2006).
22. Phillips, M. J. & Voeltz, G. K. Structure and function of ER membrane contact sites with other organelles. *Nat. Rev. Mol. Cell Biol.* **17**, 69–82 (2016).
23. Soubannier, V. *et al.* A vesicular transport pathway shuttles cargo from mitochondria to lysosomes. *Curr. Biol.* **22**, 135–141 (2012).
24. Yamano, K., Fogel, A. I., Wang, C., van der Bliek, A. M. & Youle, R. J. Mitochondrial Rab GAPs govern autophagosome biogenesis during mitophagy. *eLife* **3**, e01612 (2014).
25. Onoue, K. *et al.* Fis1 acts as a mitochondrial recruitment factor for TBC1D15 that is involved in regulation of mitochondrial morphology. *J. Cell Sci.* **126**, 176–185 (2013).
26. Peralta, E. R., Martin, B. C. & Edinger, A. L. Differential effects of TBC1D15 and mammalian Vps39 on Rab7 activation state, lysosomal morphology, and growth factor dependence. *J. Biol. Chem.* **285**, 16814–16821 (2010).
27. Zhang, X. M., Walsh, B., Mitchell, C. A. & Rowe, T. TBC domain family, member 15 is a novel mammalian Rab GTPase-activating protein with substrate preference for Rab7. *Biochem. Biophys. Res. Commun.* **335**, 154–161 (2005).
28. Cai, H. *et al.* TRAPPI tethers COPII vesicles by binding the coat subunit Sec23. *Nature* **445**, 941–944 (2007).
29. Eisenberg-Bord, M., Shai, N., Schuldiner, M. & Bohnert, M. A tether is a tether: tethering at membrane contact sites. *Dev. Cell* **39**, 395–409 (2016).
30. Burbulla, L. F. *et al.* Dopamine oxidation mediates mitochondrial and lysosomal dysfunction in Parkinson's disease. *Science* **357**, 1255–1261 (2017).

Supplementary Information is available in the online version of the paper.

Acknowledgements We thank K. Trajkovic and all members of the Krainc laboratory for advice, F. Korobova for electron microscopy assistance and J. Z. Rappoport and D. Kirichenbuechler for N-SIM assistance. All imaging work was performed at the Northwestern University Center for Advanced Microscopy, supported by NCI CCSG P30 CA060553 awarded to the Robert H Lurie Comprehensive Cancer Center. Structured illumination microscopy was performed on a Nikon N-SIM system, purchased with the support of NIH 1S100D016342-01. The spinning disk confocal system was acquired through a NCRR shared instrumentation grant awarded to V. Gelfand (S10 RR031680-01). *TBC1D15* and *FIS1* constructs were gifts from N. Ishihara. HCT116 wild-type and knockout cells were gifts from R. Youle. This work was supported by NIH/NINDS grants to Y.C.W. (T32 NS041234 and F32 NS101778) and D.K. (R01 NS076054).

Author Contributions Y.C.W. and D.K. designed the overall study, analysed data and wrote the manuscript. Y.C.W. performed cell culture, electron microscopy, correlative light electron microscopy, structured illumination microscopy, confocal live cell imaging and immunofluorescence. D.Y. designed, performed and analysed FRET experiments.

Author Information Reprints and permissions information is available at www.nature.com/reprints. The authors declare no competing financial interests. Readers are welcome to comment on the online version of the paper. Publisher's note: Springer Nature remains neutral with regard to jurisdictional claims in published maps and institutional affiliations. Correspondence and requests for materials should be addressed to D.K. (dkrainc@nm.org).

METHODS

No statistical methods were used to predetermine sample size. For studies involving multiple different experimental conditions in the same cell line, studies were performed on cells originating from the same cell line batch and randomly assigned experimental conditions for transfection. For preliminary analyses, researchers who were either involved or not involved in the study were asked to examine blinded samples for biological effects.

Reagents. The following plasmids were obtained from Addgene: LAMP1–mGFP was a gift from E. Dell’Angelica (Addgene #34831)³¹, LAMP1–RFP was a gift from W. Mothes (Addgene #1817)³², BFP–KDEL, mito–BFP, mCherry–Drp1 and mCherry–RAB7A were gifts from G. Voeltz (Addgene #49150, #49151, #49152, #61804)^{10,33}, EGFP–LC3 was a gift from K. Kirkegaard (Addgene #11546)³⁴, GFP–DFCPI was a gift from N. Mizushima (Addgene #38269)³⁵, pAc–GFP–Sec61 β was a gift from T. Rapoport (Addgene #15108), pCMV3–SMAC–HA–eGFP was a gift from R. Kahn (Addgene #67489), mVenus C1 was a gift from S. Vogel (Addgene #27794)³⁶, pK_{an}CMV–mClover3–mRuby3 was a gift from M. Lin (Addgene #74252)³⁷, EGFP–RAB7A(WT) and EGFP–RAB7A(Q67L) were gifts from Q. Zhong (Addgene #28047, #28049)³⁸, mTagBFP2–Lysosomes–20³⁹, mApple–TOMM20–N–10, mEmerald–TOMM20–C–10, DsRed2–Mito–7, mCherry–ATG5–C–18, mEmerald–ATG12–N–18, mCherry–ER–3, mEmerald–Peroxisome–2 and pmTurquoise2–N1 were gifts from M. Davidson (Addgene #55308, #54955, #54281, #55838, #54995, #54003, #55041, #54228, #60561) and GFP–EEA1 wild type was a gift from S. Corvera (Addgene #42307)⁴⁰. N-terminal HA-tagged TBC1D15 plasmids (wild-type, D397A, R400K and Δ 231–240) and Flag–FIS1 (wild-type and LA mutant) were gifts from N. Ishihara^{25,41}. YFP–TBC1D15 was a gift from R. Youle²⁴. ULK1–GFP was a gift from V. Deretic⁴². The following reagents were also used: dextran cascade blue 10000MW (Thermo Fisher Scientific; D1976), LAMP1 rabbit antibody (Sigma–Aldrich, L1418), TOM20 mouse antibody (BD biosciences, 612278), Flag rabbit antibody (Sigma–Aldrich, F7425), HA rabbit antibody (Cell Signaling, 3724S), HA mouse antibody (Cell Signaling, 2367S) and Alexa fluorophore-conjugated secondary antibodies from Molecular Probes (Invitrogen).

Cell culture and transfection. HeLa cells (gift from M. Schwake (ATCC)) and HEK293 cells (human embryonic kidney cell line 293FT (Life Technologies)) were cultured in Dulbecco’s modified Eagle’s medium (DMEM) (Gibco; 11995-065) supplemented with 10% (vol/vol) FBS, 100 units per ml penicillin, and 100 μ g/ml streptomycin. Wild-type, *FIS1*^{−/−} and *TBC1D15*^{−/−} HCT116 cells were gifts from R. Youle²⁴ and cultured in McCoy’s 5A with L-glutamine (ATCC 30-2007) supplemented with 10% (vol/vol) FBS, 100 units per ml penicillin, and 100 μ g/ml streptomycin and nonessential amino acids. H4 neuroglioma cells⁴³ were cultured in OptiMem + 5% FBS, 200 μ g/ml geneticin and hygromycin and 1% penicillin/streptomycin (Life Technologies), and treated with 1 μ g/ml doxycycline (Sigma) for 3 days. All cells were maintained at 37 °C in a 5% CO₂ incubator and previously verified by cytochrome *c* oxidase subunit I (COI) and short tandem repeat (STR) testing, and were tested and found negative for mycoplasma contamination. Cells were transfected using Lipofectamine 2000 (Invitrogen). Dextran blue was used at 1 mg/ml and pulsed via incubation in medium for 15 min and chased for 4 h, resulting in 95% of LAMP1-positive vesicles containing dextran blue by this time point. For drug treatments, live cells were imaged while being treated for 20 min with actinomycin D (10 μ M) (Sigma–Aldrich; A9415), STS (1 μ M) (Sigma–Aldrich; S6942) or CCCP (20 μ M) (Sigma–Aldrich C2759). For live imaging, cells were grown on glass-bottomed culture dishes (MatTek; P35G-1.5-14-C).

Immunofluorescence. Cells were plated on coverslips and fixed in 3% (vol/vol) paraformaldehyde for 15 min and permeabilized with 2% BSA and 0.1% saponin. Fixed cells were incubated in primary antibody for 1 h, washed three times for 5 min each, incubated in secondary antibody for 1 h, washed three times for 5 min each, and mounted on glass slides with fluorescent mounting medium (Dako).

Confocal microscopy. All non-FRET confocal images were acquired on a Nikon A1R laser scanning confocal microscope with GaAsP detectors using a Plan Apo λ 100x 1.45 NA oil immersion objective (Nikon) using NIS-Elements (Nikon). Live cells were imaged in a temperature-controlled chamber (37 °C) at 5% CO₂ at 1 frame every 2–3 s. Dual-colour videos were acquired as consecutive green–red images, and tricolour videos were acquired as consecutive green–red–blue images.

Electron microscopy. For electron microscopy (EM), cells were grown on coverslips and fixed in a mixture of 2.5% glutaraldehyde and 2% paraformaldehyde in 0.1 M cacodylate buffer for 2–24 h at 4 °C. After post-fixation in 1% osmium tetroxide and 3% uranyl acetate, cells were dehydrated in an ethanol series, embedded in Epon resin and polymerized for 48 h at 60 °C. Ultrathin sections were made using a UCT ultramicrotome (Leica Microsystems) and contrasted with 4% uranyl acetate and Reynolds’s lead citrate. Samples were imaged using a FEI Tecnai Spirit G2 transmission electron microscope (FEI) operated at 80 kV. Images were captured with an Eagle 4k HR 200kV CCD camera. For correlative light

electron microscopy, cells were grown on gridded glass-bottom culture dishes (MatTek; P35G-1.5-14-CGRD) and incubated for 45 min with LysoTracker Red (2 μ M) (Thermo Fisher Scientific) before EM fixation. Fixed cells were imaged on the Nikon A1R laser scanning confocal microscope for LysoTracker staining using Z-stacks with step sizes of 0.2 μ m as described above, and subsequently processed and imaged for EM as described above.

Structured illumination microscopy. Structured illumination microscopy (SIM) super-resolution images were taken on a Nikon N-SIM system with a 100 \times oil immersion objective lens, 1.49 NA (Nikon). Images were captured using Nikon NIS-Elements and reconstructed using slice reconstruction in NIS-elements. Images for live cell imaging (live N-SIM) were taken at a single Z-plane, while images of fixed cells for 3D N-SIM were taken using Z-stacks with step sizes of 0.2 μ m. Cells used for live cell imaging were maintained in a temperature-controlled chamber (37 °C) at 5% CO₂ in a TokaiHit stagetop incubator.

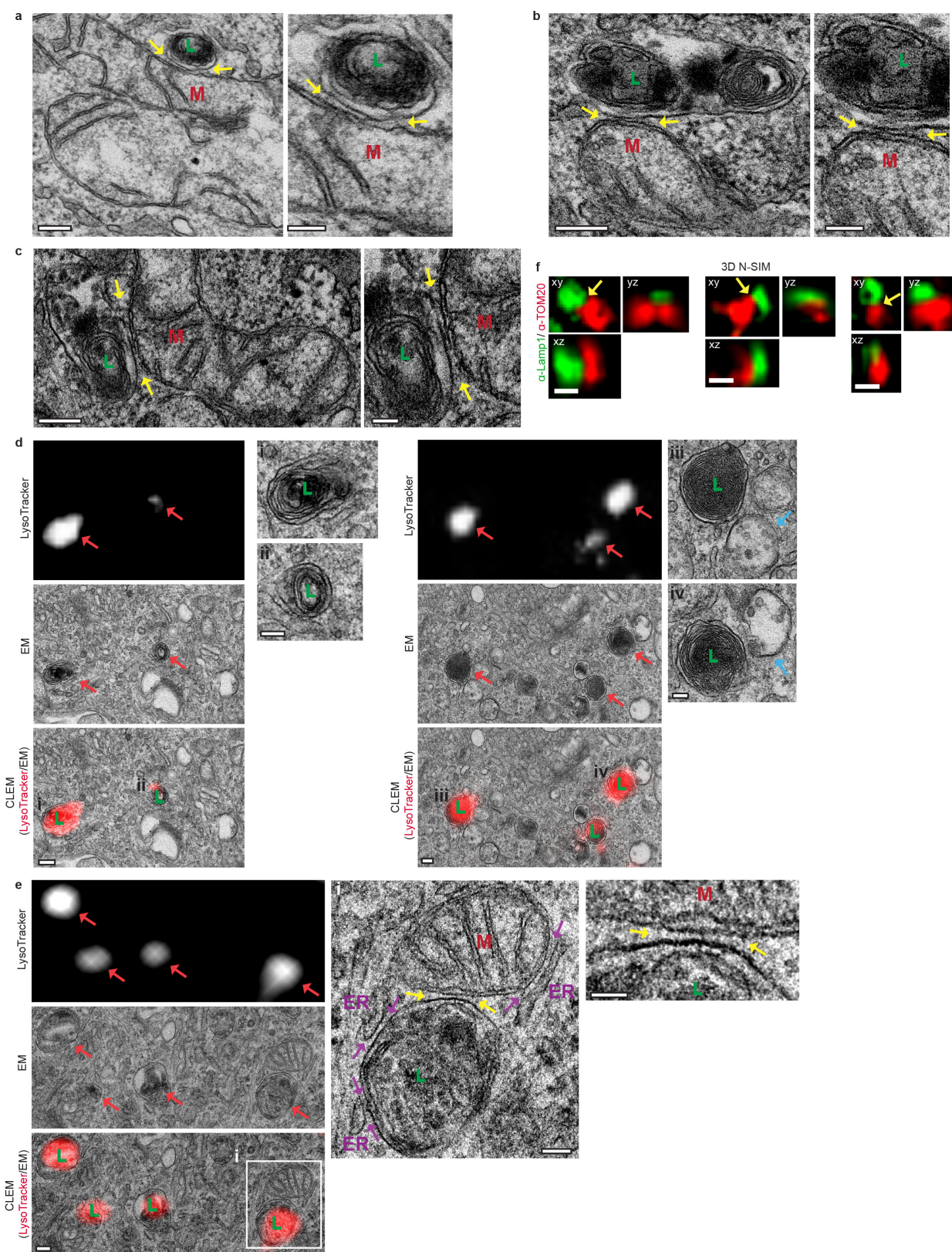
FRET pair generation, imaging and analysis. The outer mitochondrial membrane (TOM20–Venus) and lysosomal membrane (LAMP1–mTurquoise2) FRET pair was generated using mVenus C1 (Addgene #27794) and pmTurquoise2–N1 (Addgene #60561). mRuby3 and RAB7a(Q67L)–mRuby3 were generated using mRuby3 obtained from pK_{an}CMV–mClover3–mRuby3 (Addgene #74252)³⁷. For FRET experiments, HeLa cells were plated on 35-mm 4-chamber glass-bottomed dishes (Cellvis) at a density of 40,000 cells per well. The following day, cells were transfected using lipofectamine with FRET pairs (TOM20–Venus and LAMP1–mTurquoise2) along with mRuby, RAB7a(WT)–mCherry or RAB7a(Q67L)–mRuby3. Images of live HeLa cells were acquired using a Nikon Spinning disk confocal microscope using 20 \times (for FRET intensity calculations) and 60 \times objectives (for representative time-lapse images) at excitation wavelengths of 445 nm, 515 nm, and 561 nm for mTurquoise2, Venus, and mCherry/mRuby3, respectively, in a temperature-controlled chamber (37 °C) at 5% CO₂ using NIS-Elements (Nikon). NIS-Elements (Nikon) was used for FRET analysis to calculate sensitized emission FRET (SE-FRET) and to unbiasedly generate regions of interest (ROI) by tracing individual cells in the red fluorescence view. A total of $n = 200$ cells were analysed per condition for RAB7a(WT) and RAB7a(Q67L) and the FRET intensity was normalized to average SE-FRET values for RAB7a(WT).

Image analysis. Mitochondrial fission events were defined as those that showed clear division of a single mitochondrion into two distinct daughter mitochondria that moved independently of one another after division. The expected probability that a LAMP1 vesicle would be at the site of a mitochondrial division event by random chance was calculated as the density of LAMP1 vesicles in the cytosol from $n = 26$ living cells, using ImageJ (National Institutes of Health (NIH)). Mitochondria–lysosome contacts imaged in living cells were categorized as those that showed mitochondria and lysosomes in close proximity (<0.1 μ m) for >10 s in time-lapse images. All contacts analysed for the minimum duration of contacts were those that had already formed at the beginning of the video. The minimum duration of contact in HeLa cells was quantified as the time before contact termination and dissociation (mitochondria and lysosomes detaching from one another) over a 5-min (300-s) video. Any contacts that lasted throughout the entire 5-min video and were still in contact by the end of the video were categorized as 300 s in bar graphs and as >5 min in histograms for the minimum duration of mitochondria–lysosome contacts. The percentage of lysosomes in contacts was quantified as the percentage of vesicles that formed contacts (defined above) with mitochondria divided by the total number of vesicles in the region of interest. The minimum duration of contact in HCT116 cells was quantified from videos of ≥ 100 s. Mitochondrial networks that did not contain overly elongated mitochondria (>10 μ m length) or hyperfused or hypertethered mitochondria were classified as normal and scored per condition. The rate of mitochondrial fission was calculated per cell by quantifying the number of fission events in the entire cell from videos of ≥ 100 s. The distance between membranes and the length of mitochondria–lysosome contact sites were measured from EM images using ImageJ (NIH). Line scans were generated using ImageJ (NIH) and normalized per protein.

Statistical analysis, graphing and figure assembly. Data were analysed using unpaired two-tailed Student *t*-test (for two datasets) or one-way ANOVA with Tukey’s post hoc test (for multiple datasets). Fisher’s exact test was used to compare the percentage of observed mitochondrial division events with mitochondria–lysosome contacts versus the percentage expected by random chance. Data presented are means \pm s.e.m. (except in histograms). All statistical tests were justified as appropriate and were analysed from $n \geq 9$ cells (see text and figure legends for details) from $n \geq 3$ independent experiments (biological replicates) per condition. Statistics and graphing were performed using Prism 7 (GraphPad) software. All videos and images were assembled using ImageJ 1.51j8 (NIH). All final figures were assembled in Illustrator (Adobe).

Data Availability. All data that support the findings of this study are included in the manuscript or are available from the authors upon reasonable request.

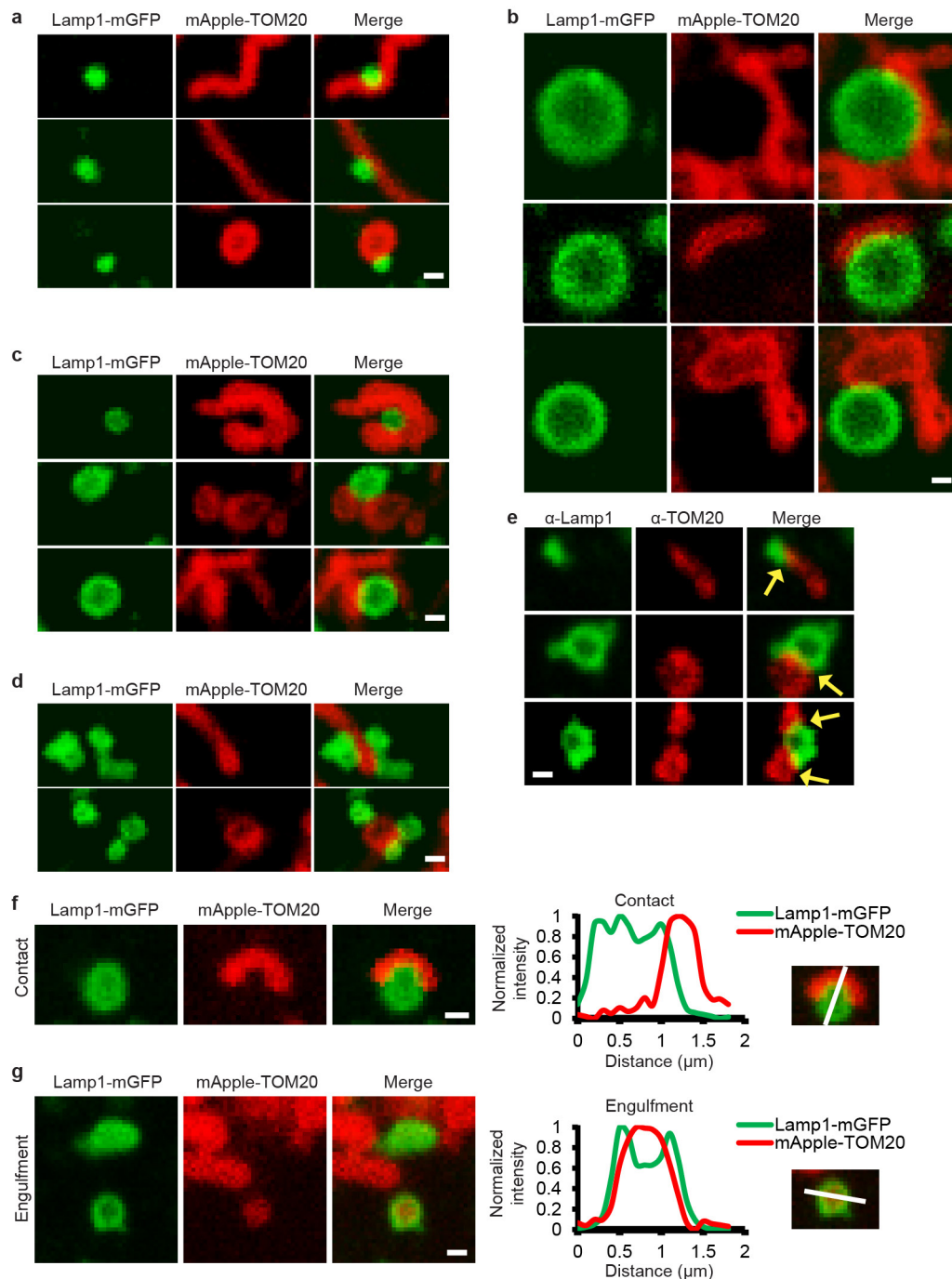
31. Falcón-Pérez, J. M., Nazarian, R., Sabatti, C. & Dell'Angelica, E. C. Distribution and dynamics of Lamp1-containing endocytic organelles in fibroblasts deficient in BLOC-3. *J. Cell Sci.* **118**, 5243–5255 (2005).
32. Sherer, N. M. *et al.* Visualization of retroviral replication in living cells reveals budding into multivesicular bodies. *Traffic* **4**, 785–801 (2003).
33. Rowland, A. A., Chitwood, P. J., Phillips, M. J. & Voeltz, G. K. ER contact sites define the position and timing of endosome fission. *Cell* **159**, 1027–1041 (2014).
34. Jackson, W. T. *et al.* Subversion of cellular autophagosomal machinery by RNA viruses. *PLoS Biol.* **3**, e156 (2005).
35. Itakura, E. & Mizushima, N. Characterization of autophagosome formation site by a hierarchical analysis of mammalian Atg proteins. *Autophagy* **6**, 764–776 (2010).
36. Koushik, S. V., Chen, H., Thaler, C., Puhl, H. L. III & Vogel, S. S. Cerulean, Venus, and VenusY67C FRET reference standards. *Biophys. J.* **91**, L99–L101 (2006).
37. Bajar, B. T. *et al.* Improving brightness and photostability of green and red fluorescent proteins for live cell imaging and FRET reporting. *Sci. Rep.* **6**, 20889 (2016).
38. Sun, Q., Westphal, W., Wong, K. N., Tan, I. & Zhong, Q. Rubicon controls endosome maturation as a Rab7 effector. *Proc. Natl Acad. Sci. USA* **107**, 19338–19343 (2010).
39. Subach, O. M., Cranfill, P. J., Davidson, M. W. & Verkhusha, V. V. An enhanced monomeric blue fluorescent protein with the high chemical stability of the chromophore. *PLoS ONE* **6**, e28674 (2011).
40. Lawe, D. C., Patki, V., Heller-Harrison, R., Lambright, D. & Corvera, S. The FYVE domain of early endosome antigen 1 is required for both phosphatidylinositol 3-phosphate and Rab5 binding. Critical role of this dual interaction for endosomal localization. *J. Biol. Chem.* **275**, 3699–3705 (2000).
41. Jofuku, A., Ishihara, N. & Mihara, K. Analysis of functional domains of rat mitochondrial Fis1, the mitochondrial fission-stimulating protein. *Biochem. Biophys. Res. Commun.* **333**, 650–659 (2005).
42. Mandell, M. A. *et al.* TRIM proteins regulate autophagy and can target autophagic substrates by direct recognition. *Dev. Cell* **30**, 394–409 (2014).
43. Mazzulli, J. R. *et al.* Gaucher disease glucocerebrosidase and α -synuclein form a bidirectional pathogenic loop in synucleinopathies. *Cell* **146**, 37–52 (2011).



Extended Data Figure 1 | Correlative light electron microscopy and 3D structured illumination microscopy of mitochondria-lysosome contacts. **a–c**, Representative electron microscopy images of mitochondria (M) and lysosome (L) contacts (yellow arrows) in untreated HeLa cells (insets shown on right) ($n = 55$ examples from 20 cells).

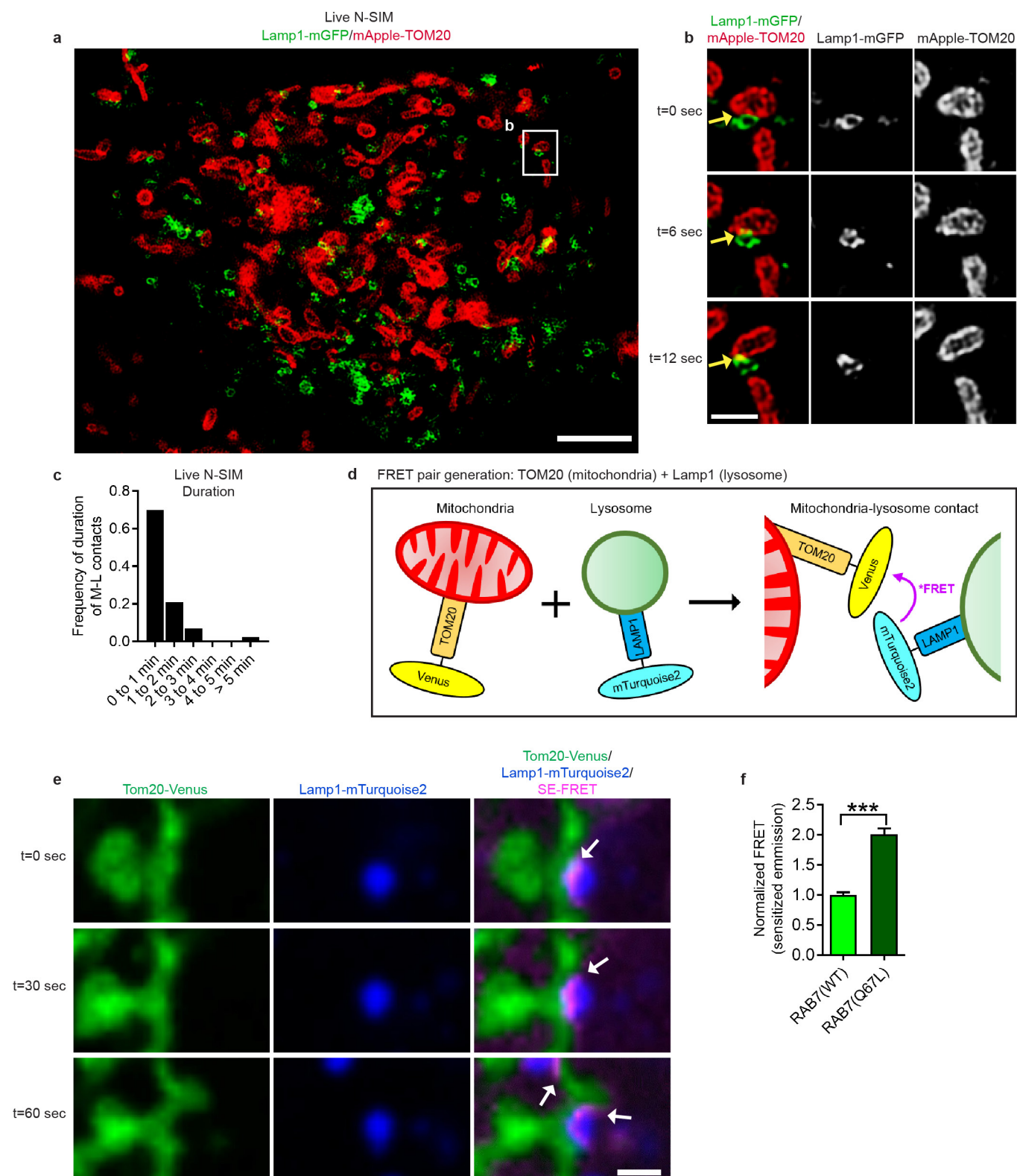
d, e, Representative correlative light electron microscopy and confocal images of HeLa cells (from $n = 14$ images from 6 cells) incubated with LysoTracker Red to label lysosomes or late endosomes (red arrows) that contain electron-dense lumen with irregular content and/or multilamellar membrane sheets (**d**, see insets on right), and form a stable membrane

contact site with mitochondria (**e**, yellow arrows; see inset on right), while simultaneously forming contact sites with the endoplasmic reticulum (**e**, purple arrows). Early endosomes lacking electron-dense lumen are LysoTracker-negative (**d**, blue arrows). **f**, Representative structured illumination microscopy (N-SIM) images of mitochondria-lysosome contacts (yellow arrows) in fixed HeLa cells stained for endogenous LAMP1 (lysosomes) or TOM20 (mitochondria) and imaged in Z-stacks showing contacts extending more than 200 nm in the Z-plane ($n = 210$ examples from 26 cells). Scale bars, 200 nm (**a–d**); 100 nm (**a–d**, insets on right; **e**, right); 50 nm (**e**, left, middle); 500 nm (**f**).



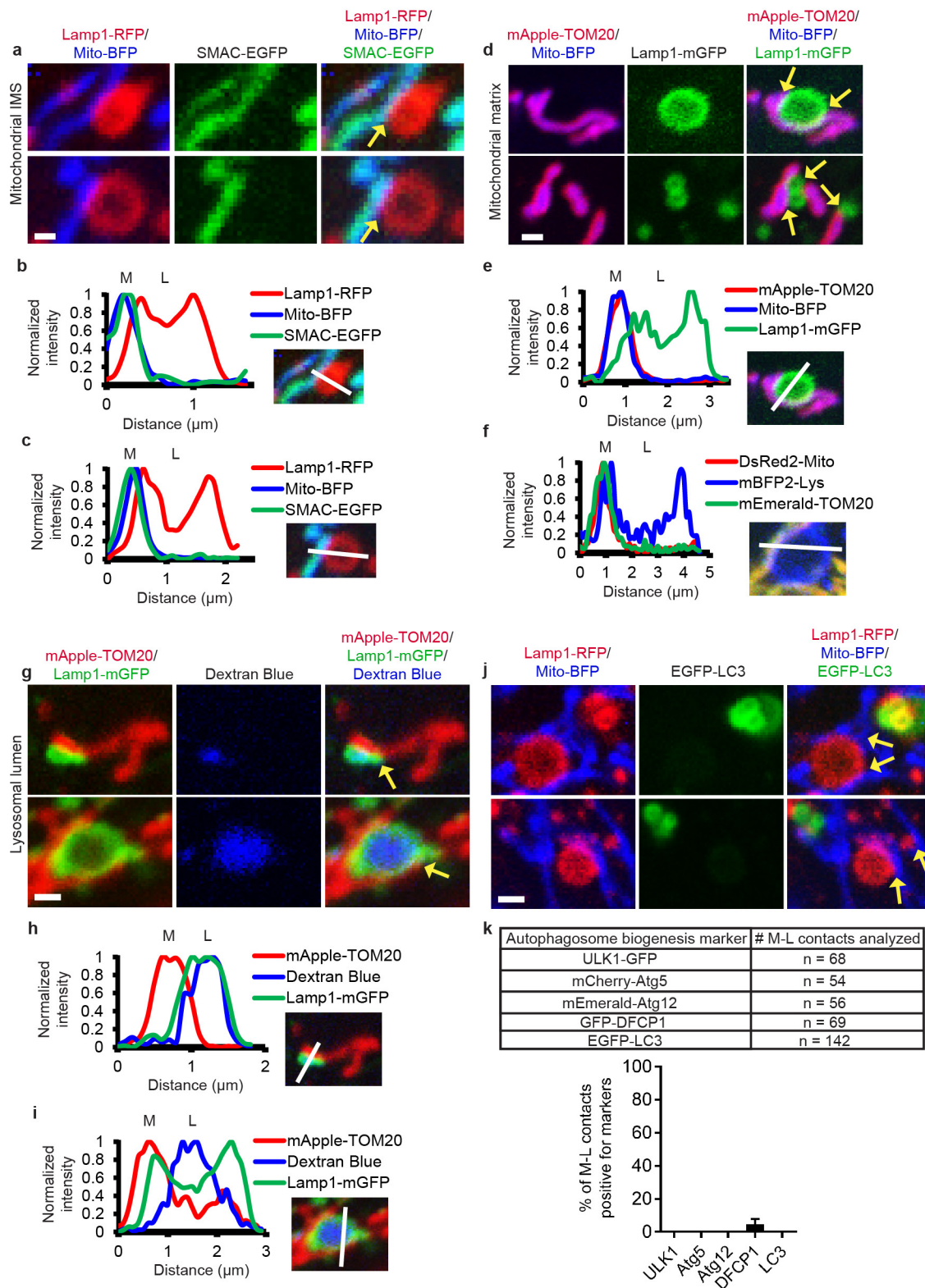
Extended Data Figure 2 | Characterizing mitochondria-lysosome contacts in living cells. **a–d**, Representative images of mitochondria-lysosome contacts (lasting more than 10 s) in living HeLa cells expressing LAMP1-mGFP (lysosomes) and mApple-TOM20 (mitochondria) ($n = 23$ cells). **a**, Examples of small LAMP1 vesicles (vesicle diameter $< 0.5 \mu\text{m}$) contacting mitochondria. **b**, Examples of larger LAMP1 vesicles (vesicle diameter $> 1 \mu\text{m}$) contacting mitochondria. **c**, Examples of a single LAMP1 vesicles contacting multiple mitochondria. **d**, Examples of multiple

LAMP1 vesicles contacting a single mitochondrion. **e**, Representative images of contacts (yellow arrows) in fixed HeLa cells stained for endogenous LAMP1 (green) and TOM20 (red) ($n = 341$ examples from 25 cells). **f**, **g**, Representative images of living HeLa cells ($n = 23$ cells) expressing LAMP1-mGFP (lysosomes) and mApple-TOM20 (outer mitochondrial membrane) with corresponding line scans showing a mitochondria-lysosome contact at close proximity (**f**), distinct from lysosomal engulfment of mitochondrial TOM20 (**g**). All scale bars, $0.5 \mu\text{m}$.



Extended Data Figure 3 | Structured illumination microscopy and FRET imaging of mitochondria-lysosome contacts in living cells. **a–c**, Representative N-SIM images (**a**, **b**) of mitochondria-lysosome contacts (yellow arrows) in living HeLa cells ($n = 43$ examples from 10 cells) expressing LAMP1-mGFP (lysosomes) and mApple-TOM20 (mitochondria) and quantification of duration of mitochondria-lysosome contacts from N-SIM time-lapse images (**c**). **d**, Model of newly generated FRET pairs targeted to the outer mitochondrial membrane (TOM20-Venus) and the lysosomal membrane (LAMP1-mTurquoise2).

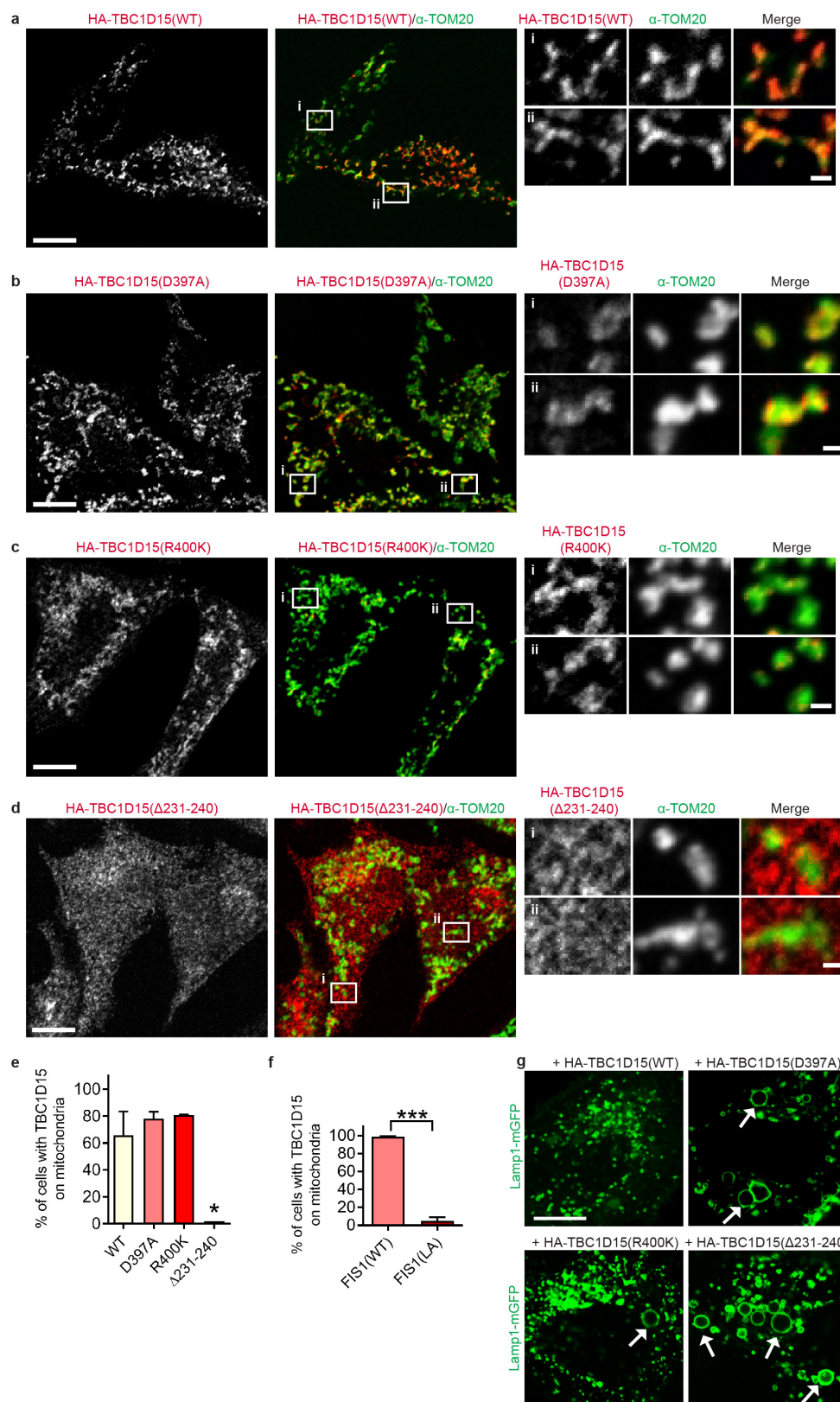
e, Representative time-lapse images of a living HeLa cell ($n = 200$ cells) expressing FRET pairs (TOM20-Venus, LAMP1-mTurquoise2) and RAB7a(Q67L)-mRuby3 demonstrating preferentially increased SE-FRET signal over 60 s at the interface between mitochondria and lysosomes (white arrows). **f**, Quantification of normalized SE-FRET intensity per cell in conditions expressing wild-type RAB7a or RAB7a(Q67L) ($n = 200$ cells per condition) showing an approximately twofold increase in cells expressing RAB7a(Q67L). Data are means \pm s.e.m. *** $P < 0.0001$, unpaired two-tailed t -test (**f**). Scale bars, 4 μ m (**a**); 1 μ m (**b**, **e**).



Extended Data Figure 4 | See next page for caption.

Extended Data Figure 4 | Mitochondria–lysosome contacts are distinct from mitochondria-derived vesicles and mitophagy. **a–c**, Representative images (**a**) of living HeLa cells expressing LAMP1–RFP (lysosomes), mito–BFP (mitochondrial matrix) and SMAC–EGFP (mitochondrial intermembrane space), and corresponding linescans (**b**, **c**) showing that mitochondrial intermembrane space and matrix proteins do not undergo bulk transfer into lysosomes at contacts (yellow arrows) ($n = 57$ events from 12 cells). **d**, **e**, Representative images (**d**) in a living HeLa cell expressing mApple–TOM20 (mitochondrial outer membrane), mito–BFP (mitochondrial matrix) and LAMP1–mGFP (lysosomes) and linescan (**e**, corresponding to top panel in **d**) showing that mitochondria that form contacts with lysosomes (yellow arrows) are positive for mitochondrial matrix protein mito–BFP and are not TOM20-positive MDVs ($n = 104$ events from 23 cells). **f**, Representative linescan in a living HeLa cell expressing mEmerald–TOM20 (mitochondrial outer membrane), DsRed2–Mito (mitochondrial matrix) and mBFP2–Lys (lysosomes) showing that mitochondria that form contacts with lysosomes are positive for mitochondrial matrix protein DsRed2–mito and are not TOM20-

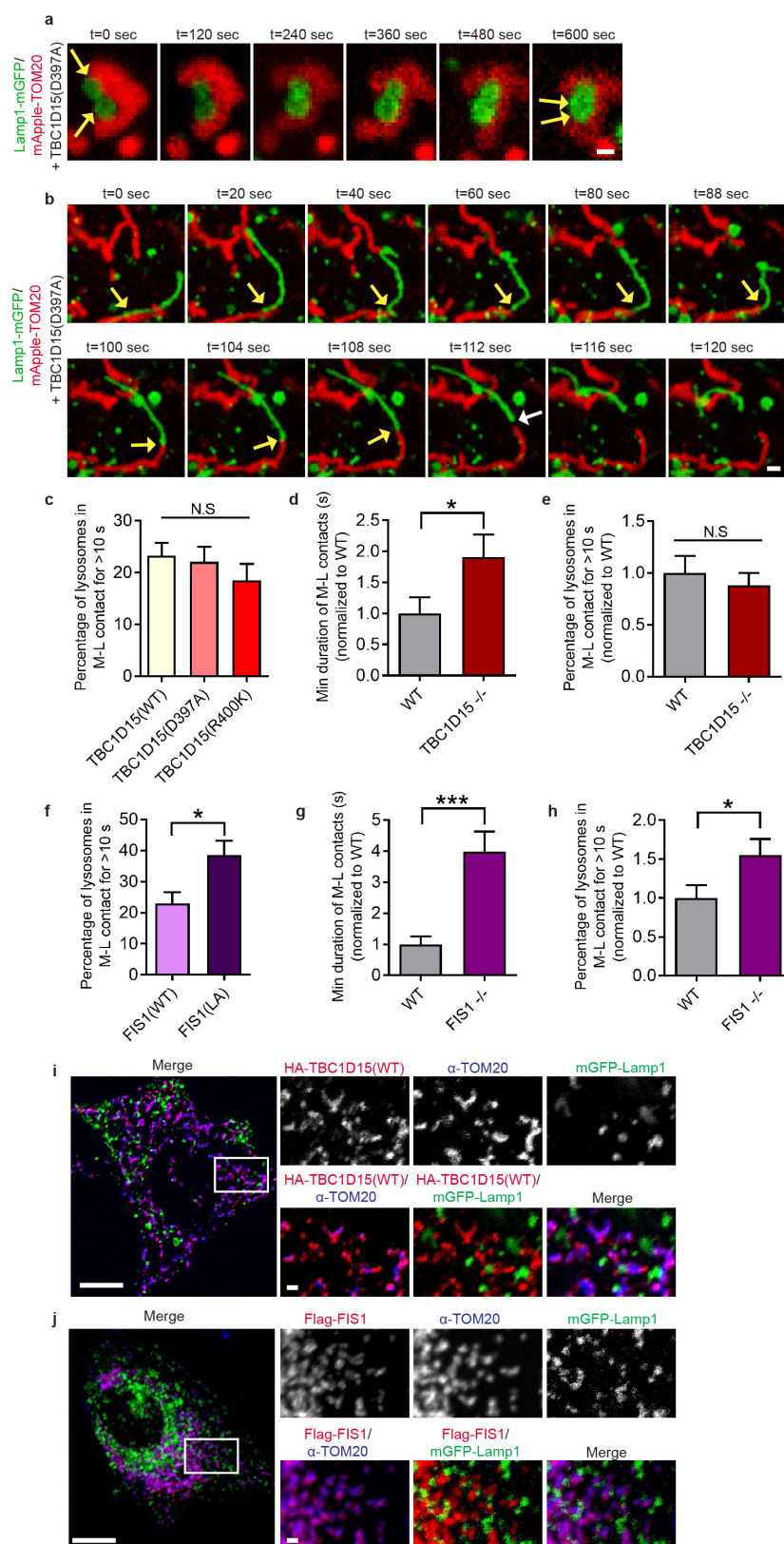
positive MDVs ($n = 94$ events from 16 cells). **g–i**, Representative images (**g**) in a living HeLa cell expressing mApple–TOM20 (outer mitochondrial membrane), LAMP1–mGFP (lysosomal membrane) and fluid-phase marker dextran blue pulse-chased into the lysosomal lumen, and corresponding linescans (**h**, **i**) showing that lysosomal luminal contents (blue) do not undergo bulk transfer into mitochondria at contacts (yellow arrows) ($n = 66$ events from 18 cells). **j**, Representative images in a living HeLa cell expressing LAMP1–RFP (lysosomes), mito–BFP (mitochondrial matrix) and EGFP–LC3 (autophagosome) showing that mitochondria that form contacts with lysosomes (yellow arrows) are not engulfed by autophagosomes (not undergoing mitophagy) ($n = 142$ events from 17 cells). **k**, Autophagosome biogenesis proteins (ULK1–GFP, mCherry–ATG5, mEmerald–ATG12, GFP–DFCP1 and EGFP–LC3) do not mark sites of mitochondria–lysosome contacts in living cells (number of events analysed in $n = 14$ cells (ULK1), $n = 17$ cells (ATG5, ATG12, LC3) or $n = 13$ cells (DFCP1), top; quantification, bottom). Mitochondria (M) and lysosomes (L) are indicated in linescans. Data are means \pm s.e.m. Scale bars, $0.5\ \mu\text{m}$ (**a**); $1\ \mu\text{m}$ (**d**, **g**, **j**).



Extended Data Figure 5 | FIS1 recruits TBC1D15 to mitochondria.

a–e, Representative images and quantification of localization of HA-TBC1D15 to mitochondria (stained with endogenous TOM20) in fixed HeLa cells showing that mitochondrial localization is not disrupted by TBC1D15 GAP mutants (D397A or R400K) but is disrupted by mutating the FIS1-binding site of TBC1D15 (Δ 231–240) ($n = 293$ cells, WT; $n = 228$ cells, D397A; $n = 181$ cells, R400K; $n = 379$ cells, Δ 231–240). Δ 231–240 versus WT ($*P = 0.0178$), D397A ($*P = 0.0131$), and R400K ($*P = 0.0112$), ANOVA with Tukey's post-hoc test. **f**, Quantification showing that

localization of YFP-TBC1D15 to mitochondria is greatly decreased by the Flag-FIS1(LA) mutant (which cannot bind TBC1D15) as compared to wild-type Flag-FIS1 ($n = 290$ cells, FIS1; $n = 281$ cells, FIS1(LA)). *** $P < 0.0001$, unpaired two-tailed t -test. **g**, Examples of HA-TBC1D15 GAP mutants (D397A and R400K) or FIS1-binding mutant (Δ 231–240) inducing enlarged lysosomes (white arrows) (LAMP1-mGFP) not observed in cells expressing wild-type HA-TBC1D15 ($n = 293$ cells, WT; $n = 228$ cells, D397A; $n = 181$ cells, R400K; $n = 379$ cells, Δ 231–240). Data are means \pm s.e.m. Scale bars, 10 μ m (**a–d**, **g**); 1 μ m (**a–d**, insets).

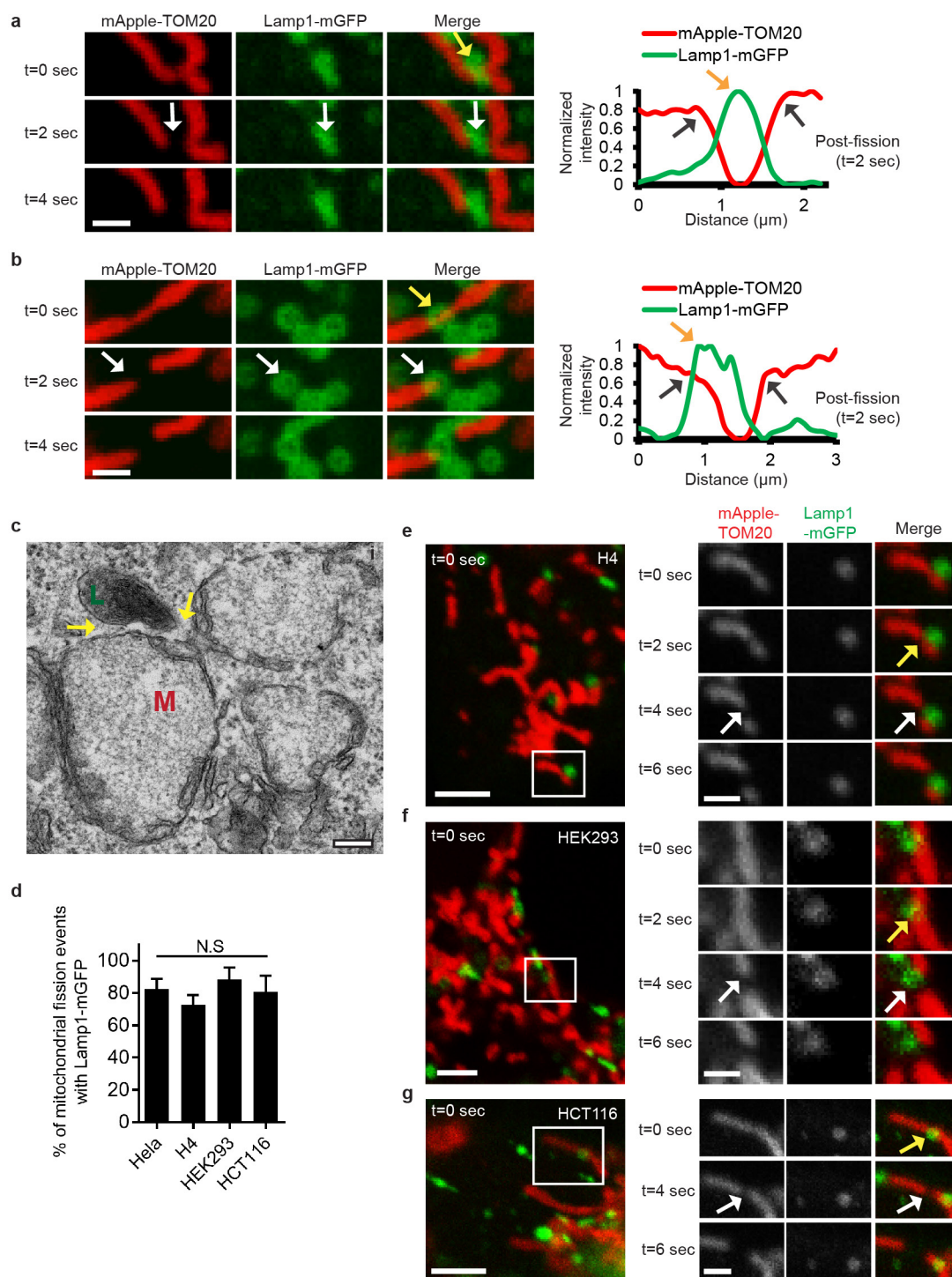


Extended Data Figure 6 | See next page for caption.

Extended Data Figure 6 | Recruitment of TBC1D15 by FIS1 to mitochondria promotes mitochondria-lysosome contact untethering.

a, b, Representative time-lapse images of stable mitochondria-lysosome contacts (yellow arrows) for over 100 s before untethering (white arrow) in living HeLa cells expressing mApple-TOM20 (mitochondria), LAMP1-mGFP (lysosome) and the RAB7 GAP mutant TBC1D15(D397A) ($n = 38$ events from 10 cells). **c**, TBC domain mutants TBC1D15(D397A) and TBC1D15(R400K), which lack GAP activity, do not alter the percentage of lysosomes in contacts ($n = 12$ cells per condition), as compared to wild-type TBC1D15 (N.S., not significant). **d, e**, *TBC1D15*^{-/-} HCT116 cells have increased duration (**d**, $n = 18$ events from 6 cells, WT; $n = 16$ events from 7 cells, *TBC1D15*^{-/-}) but no change in the number of mitochondria-lysosome contacts (**e**, $n = 15$ cells, WT; $n = 14$ cells, *TBC1D15*^{-/-}) compared to wild-type HCT116

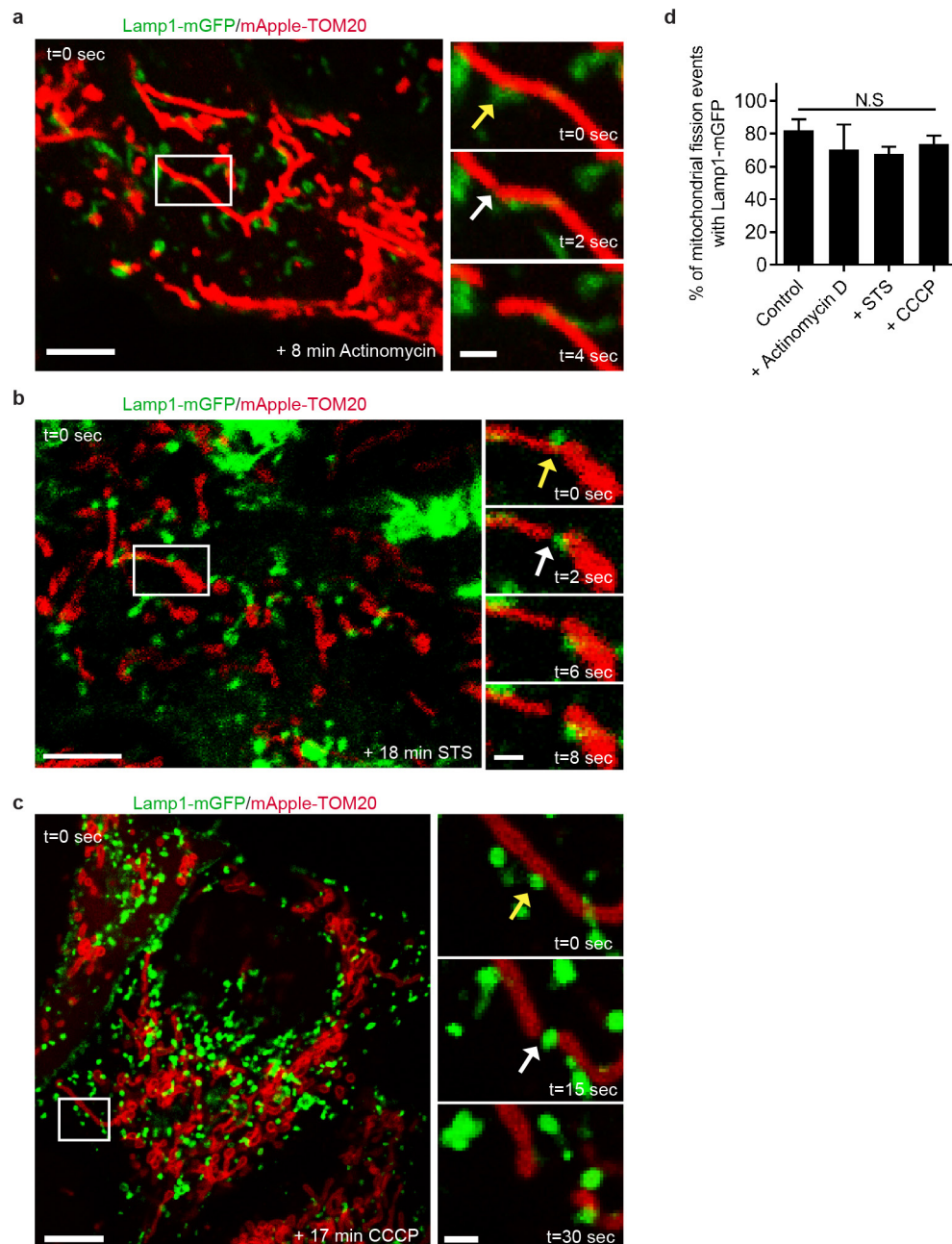
cells ($*P < 0.0491$, N.S., not significant). **f**, Expression of the Flag-FIS1(LA) mutant (unable to bind TBC1D15) increases the percentage of lysosomes in mitochondria-lysosome contacts compared to wild-type FIS1 in living HeLa cells ($n = 18$ cells, FIS1; $n = 16$ cells, FIS1(LA); $*P < 0.0117$). **g, h**, *FIS1*^{-/-} HCT116 cells have an increased duration (**g**, $n = 18$ events from 6 cells, WT; $n = 14$ events from 6 cells, *FIS1*^{-/-}) and number of mitochondria-lysosome contacts (**h**, $n = 15$ cells, WT; $n = 13$ cells, *FIS1*^{-/-}) compared to wild-type HCT116 cells ($*P < 0.0442$, $***P < 0.0001$). **i, j**, Localization of HA-TBC1D15 (**i**, $n = 293$ cells) and Flag-FIS1 (**j**, $n = 272$ cells) to mitochondria in fixed HeLa cells is not restricted to mitochondria-lysosome contacts. Data are means \pm s.e.m. ANOVA with Tukey's post-hoc test (**c**), unpaired two-tailed t test (**d-h**). Scale bars, 0.5 μ m (**a**); 1 μ m (**b, i** (insets), **j** (insets)); 10 μ m (**i, j**).



Extended Data Figure 7 | Mitochondrial fission sites are marked by mitochondria-lysosome contacts in multiple cell types.

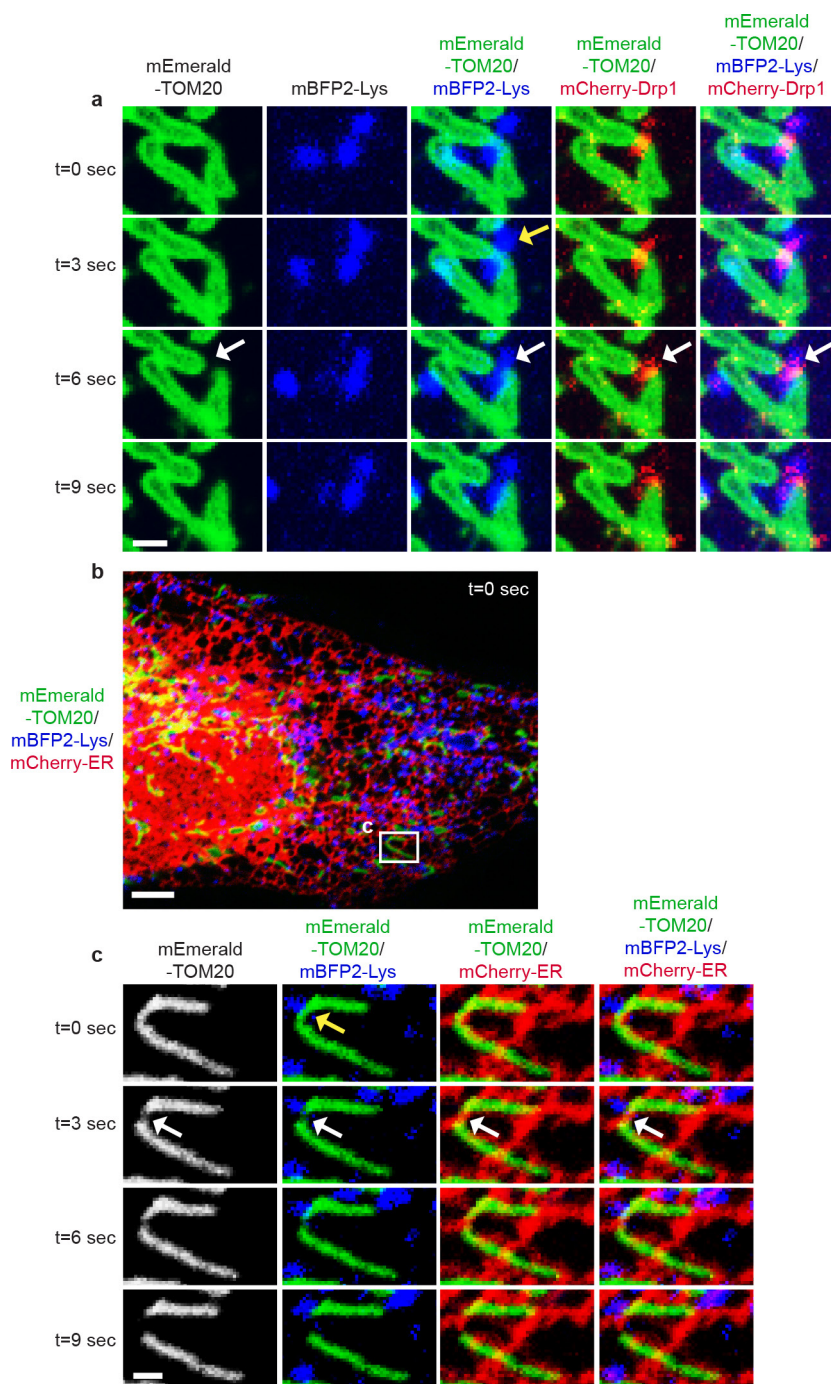
a, b, Representative time-lapse images of lysosomes contacting mitochondria at site of mitochondrial fission (yellow arrow, top) before mitochondrial fission (white arrows, middle) in living HeLa cells expressing mGFP-LAMP1 (lysosomes) and mApple-TOM20 (mitochondria) with corresponding linescans (right) showing lysosomes at the site of fission (yellow arrow; linescan) after mitochondrial division into two daughter mitochondria (grey arrows, linescan) ($n = 62$ events from 23 cells). **c**, Electron microscopy image of mitochondria

(M) in contact (< 30 nm) with a lysosome (L; yellow arrows) at site of mitochondrial constriction in untreated HeLa cells (from $n = 20$ cells imaged). **d–g**, Lysosomes (yellow arrows in **e–g**; mGFP-LAMP1) mark sites of mitochondrial fission (white arrows in **e–g**; mApple-TOM20) at similar rates (**d**) in living H4 neuroglioma, HEK293 and HCT116 cells as in HeLa cells by time-lapse confocal imaging ($n = 49$ events from 10 cells, HeLa; $n = 36$ events from 13 cells, H4; $n = 18$ events from 9 cells, HEK293; $n = 9$ events from 6 cells, HCT116). Data are means \pm s.e.m. N.S., not significant, ANOVA with Tukey's post-hoc test. Scale bars, $1 \mu\text{m}$ (**a, b, e–g**, insets); 200 nm (**c**); $2.5 \mu\text{m}$ (**e–g**).



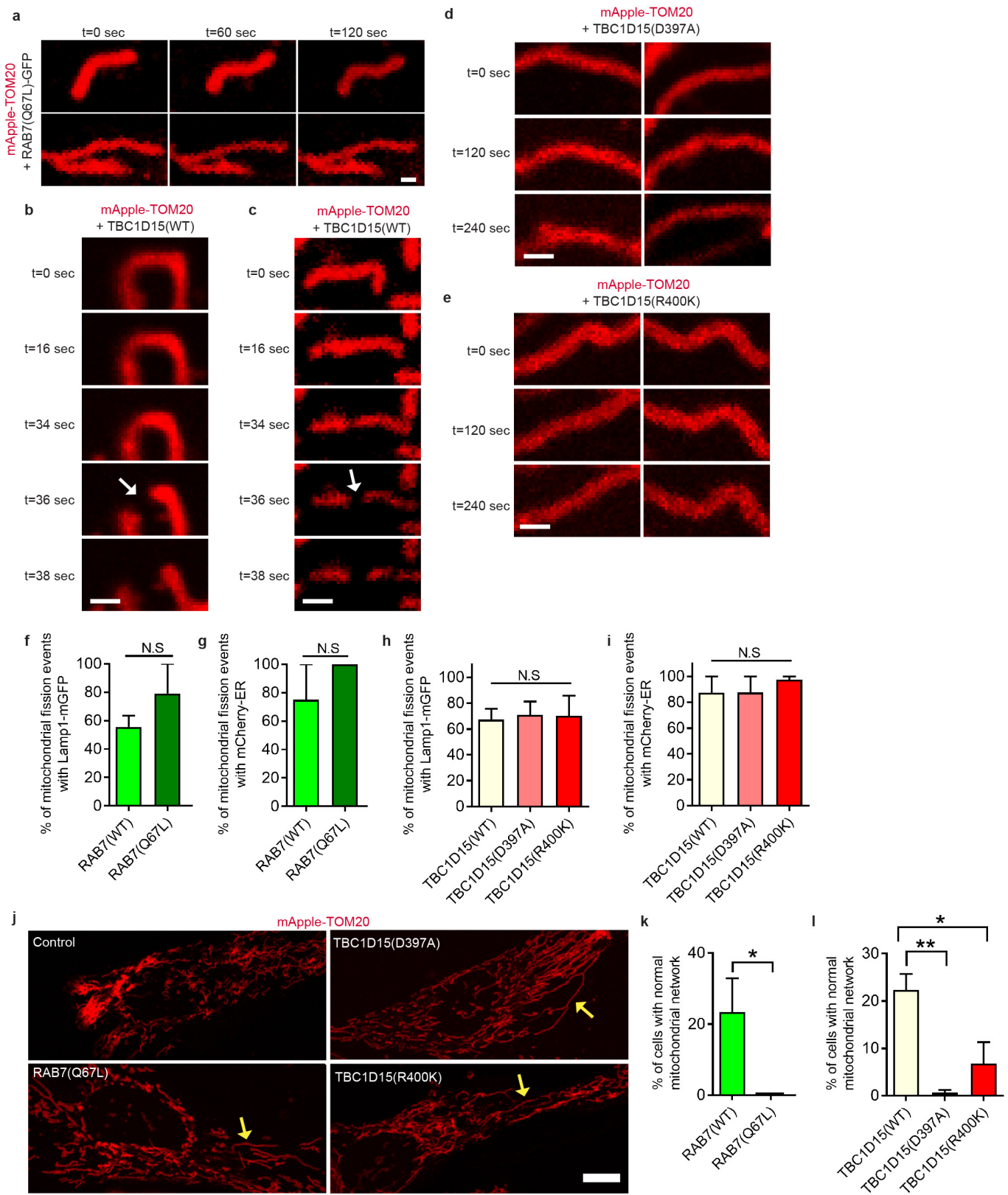
Extended Data Figure 8 | Mitochondria-lysosome contacts mark sites of mitochondrial fission upon induction of mitochondrial fragmentation. a–d, Lysosomes (yellow arrows; mGFP-LAMP1) mark sites of mitochondrial fission (white arrows; mApple-TOM20) at similar rates (d) in untreated living HeLa cells as in cells treated for up to 20 min

with actinomycin D (a), STS (b) or CCCP (c) ($n = 49$ events from 10 cells, control; $n = 29$ events from 14 cells, actinomycin D; $n = 36$ events from 10 cells, STS; $n = 49$ events from 14 cells, CCCP). Data are means \pm s.e.m. N.S., not significant, ANOVA with Tukey's post-hoc test. Scale bars, $5\mu\text{m}$ (a–c); $1\mu\text{m}$ (a–c, insets).



Extended Data Figure 9 | Mitochondrial fission sites marked by lysosomes are positive for DRP1 and endoplasmic reticulum tubules.
a, Representative time-lapse images of a lysosome (mBFP2-Lys) contacting mitochondria (mEmerald-TOM20) at the site of mitochondrial division (yellow arrow) before fission (white arrows) in a living HeLa cell showing mCherry-DRP1 oligomerization at the site of mitochondrial division ($n = 41$ events from 11 cells). **b**, **c**, Representative image (**b**, inset

time-lapse images shown in **c**) of a lysosome (mBFP2-Lys) contacting mitochondria (mEmerald-TOM20) at the site of mitochondrial division (yellow arrow) before fission (white arrows) in a living HeLa cell showing an endoplasmic reticulum tubule (mCherry-ER) at the site of mitochondrial division ($n = 54$ events from 16 cells). Scale bars, $1 \mu\text{m}$ (**a**, **c**); $5 \mu\text{m}$ (**b**).



Extended Data Figure 10 | Regulation of mitochondrial network dynamics by RAB7 GTP hydrolysis. **a**, Examples of mitochondria not undergoing fission for more than 120 s in living HeLa cells expressing mApple-TOM20 (mitochondria) and RAB7(Q67L)-GFP ($n = 13$ cells). **b, c**, Examples of mitochondria undergoing fission (white arrows) after 36 s in living HeLa cells expressing mApple-TOM20 (mitochondria) and wild-type TBC1D15 ($n = 13$ cells). **d, e**, Examples of mitochondria not undergoing fission for more than 240 s in living HeLa cells expressing mApple-TOM20 (mitochondria) and GAP mutants TBC1D15(D397A) (**d**) or TBC1D15(R400K) (**e**) ($n = 13$ cells per condition). **f–i**, The percentage of mitochondrial fission sites marked by lysosomes (mGFP-LAMP1; **f, h**) or endoplasmic reticulum (mCherry-ER; **g, i**) is not disrupted by the RAB7(Q67L) GTP-hydrolysis-deficient mutant (**f, g**; $n = 12$ events from 15 cells) or by TBC1D15 GAP mutants (D397A or

R400K) (**h, i**; $n = 22$ events from 10 cells, WT; $n = 17$ events from 19 cells, D397A; $n = 27$ events from 22 cells, R400K). **j–l**, Examples of RAB7(Q67L) and HA-TBC1D15 GAP mutants (D397A and R400K) inducing elongated mitochondria (**j**, yellow arrows; $>10\ \mu\text{m}$ length) compared to control cells, and quantification of RAB7(Q67L) (**k**; $*P = 0.0321$) and HA-TBC1D15 GAP mutants (D397A and R400K) (**l**; $*P = 0.0297$, $**P = 0.0051$) leading to decreased percentages of cells with normal mitochondrial networks (no elongated mitochondria $>10\ \mu\text{m}$ length or hyperfused or tethered networks) ($n = 47$ cells, RAB7; $n = 72$ cells, RAB7(Q67L); $n = 88$ cells, TBC1D15 WT; $n = 168$ cells, TBC1D15(D397A); $n = 132$ cells, TBC1D15(R400K)). Data are means \pm s.e.m. N.S., not significant; ANOVA with Tukey's post-hoc test (**h, i, l**), unpaired two-tailed t -test (**f, g, k**). Scale bars, $0.5\ \mu\text{m}$ (**a**); $1\ \mu\text{m}$ (**b–e**); $10\ \mu\text{m}$ (**j**).

Structural basis for DNMT3A-mediated *de novo* DNA methylation

Zhi-Min Zhang^{1†*}, Rui Lu^{2,3*}, Pengcheng Wang⁴, Yang Yu⁴, Dongliang Chen^{2,3}, Linfeng Gao⁴, Shuo Liu⁴, Debin Ji⁵, Scott B Rothbart^{3,6}, Yinsheng Wang^{4,5}, Gang Greg Wang^{2,3§} & Jikui Song^{1,4§}

DNA methylation by *de novo* DNA methyltransferases 3A (DNMT3A) and 3B (DNMT3B) at cytosines is essential for genome regulation and development^{1,2}. Dysregulation of this process is implicated in various diseases, notably cancer. However, the mechanisms underlying DNMT3 substrate recognition and enzymatic specificity remain elusive. Here we report a 2.65-ångström crystal structure of the DNMT3A–DNMT3L–DNA complex in which two DNMT3A monomers simultaneously attack two cytosine–phosphate–guanine (CpG) dinucleotides, with the target sites separated by 14 base pairs within the same DNA duplex. The DNMT3A–DNA interaction involves a target recognition domain, a catalytic loop, and DNMT3A homodimeric interface. Arg836 of the target recognition domain makes crucial contacts with CpG, ensuring DNMT3A enzymatic preference towards CpG sites in cells. Haematological cancer-associated somatic mutations of the substrate-binding residues decrease DNMT3A activity, induce CpG hypomethylation, and promote transformation of haematopoietic cells. Together, our study reveals the mechanistic basis for DNMT3A-mediated DNA methylation and establishes its aetiological link to human disease.

Mammalian DNA methylation is an important epigenetic mechanism crucial for gene silencing and imprinting, X-inactivation, genome stability, and cell fate determination³. It is established mainly at CpG dinucleotides by the *de novo* methyltransferases DNMT3A and DNMT3B^{1,2}, and subsequently maintained by DNA methyltransferase 1 (DNMT1) in a replication-dependent manner⁴. The enzymatic function of DNMT3A and DNMT3B is further regulated by DNMT3-like protein (DNMT3L) in germ and embryonic stem (ES) cells^{5–7}. Deregulation of DNMT3A and DNMT3B is associated with various human diseases including haematological cancer^{8–10}. However, the molecular mechanisms underpinning DNMT3A-mediated methylation, especially substrate recognition and catalytic preference towards CpG, remain elusive. Here we generated a productive DNMT3A–DNMT3L–DNA complex using the C-terminal domains of DNMT3A and DNMT3L (Fig. 1a). The DNA molecule consists of a 10-mer central CpG-containing DNA strand annealed to an 11-mer 2′-deoxyzebarine (dZ)-containing strand (target strand), which results in a (CpG)–(dZpG) sequence context and allows formation of stable covalent DNMT3A–DNA complexes (Extended Data Fig. 1a, b). The crystal structure of the DNMT3A–DNMT3L in complex with 10/11-mer DNA, bound to cofactor by-product S-adenosyl-L-homocysteine (AdoHcy), was subsequently determined at 3.1 Å resolution (Extended Data Fig. 1c).

The structure of this DNMT3A–DNMT3L–DNA complex reveals a tetrameric fold arranged in the order of DNMT3L–DNMT3A–

DNMT3A–DNMT3L, reminiscent of its DNA-free form^{11,12} (Extended Data Figs 1d and 2a). Notably, two DNA duplexes, each bound to one DNMT3A monomer, are separated by approximately 15 Å, implying a total of 14-base-pair spacing between the two active sites of DNMT3A (Extended Data Fig. 1d). This finding prompted us to design a longer

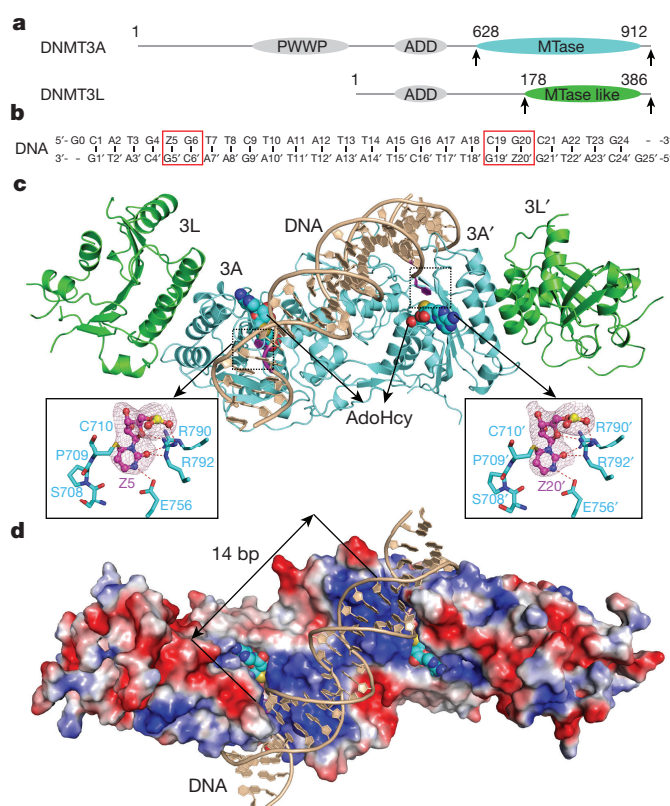


Figure 1 | Structure of the DNMT3A–DNMT3L tetramer in complex with a 25-mer DNA duplex containing two CpG sites. **a**, Domain architectures of DNMT3A and DNMT3L, with the C-terminal domains marked with arrowheads. **b**, DNA sequence used for structural study. Z, zebularine. **c**, **d**, Ribbon (**c**) and surface (**d**) representations of DNMT3A–DNMT3L bound to DNA and AdoHcy. The zebularines anchored at the two active sites are 14 base pairs (bp) away and shown in expanded views, with hydrogen-bonding interactions depicted as dashed lines and the $F_o - F_c$ omit map (pink) of Z5 or Z20′ contoured at the 3σ level.

¹Department of Biochemistry, University of California, Riverside, California 92521, USA. ²The Lineberger Comprehensive Cancer Center, University of North Carolina at Chapel Hill School of Medicine, Chapel Hill, North Carolina 27599, USA. ³Department of Biochemistry and Biophysics, University of North Carolina at Chapel Hill School of Medicine, Chapel Hill, North Carolina 27599, USA. ⁴Environmental Toxicology Graduate Program, University of California, Riverside, California 92521, USA. ⁵Department of Chemistry, University of California, Riverside, California 92521, USA. ⁶Center for Epigenetics, Van Andel Research Institute, Grand Rapids, Michigan 49503, USA. [†]Present address: School of Pharmacy, Jinan University, 601 Huangpu Avenue West, Guangzhou 510632, China.

*These authors contributed equally to this work.

§These authors jointly supervised this work.

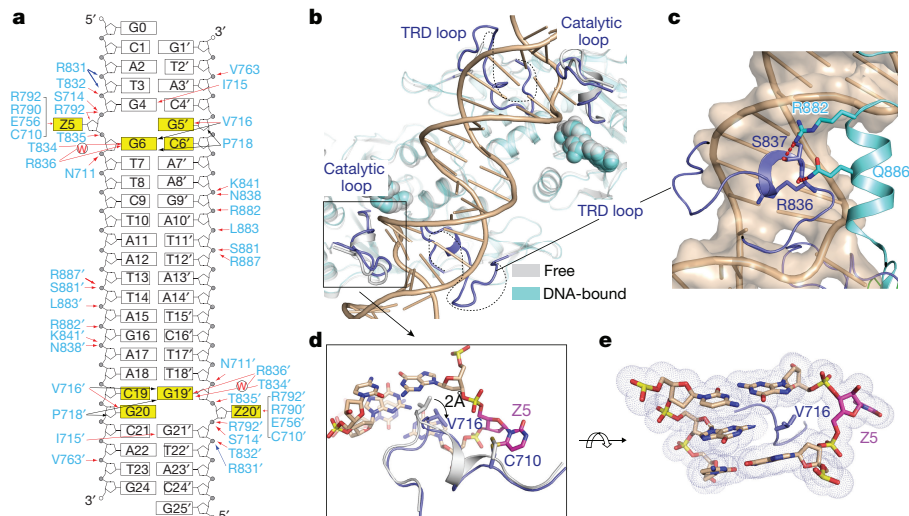


Figure 2 | Structure comparison of free and DNA-bound DNMT3A–DNMT3L tetramer. **a**, Schematic view of the intermolecular interactions between DNMT3A and DNA. The hydrogen-bonding, electrostatic, and van der Waals contacts are represented by red, blue, and black arrows, respectively. Water-mediated hydrogen bonds are labelled with the letter ‘W’. **b**, Structural overlay of free (grey) and DNA-bound (cyan) DNMT3A–

DNMT3L. The disordered TRD loops in free DNMT3A–DNMT3L are depicted as dotted lines. **c**, The TRD loop (blue) in DNA-bound DNMT3A is stabilized by hydrogen-bonding interactions (dashed lines) with R882 and Q886. **d**, Structural overlay of the catalytic loop between free (grey) and DNA-bound (blue) DNMT3A. **e**, DNA intercalation by DNMT3A V716.

DNA substrate involving a self-complementary 25-mer zebularine (Z)-containing DNA, with two (CpG)–(ZpG) sites across 14 base pairs (Fig. 1b). The structure of the DNMT3A–DNMT3L in complex with 25-mer DNA was determined at 2.65 Å resolution (Extended Data Fig. 1c), revealing only one DNA duplex bending towards the DNMT3A–DNMT3L tetramer, with the two CpG sites simultaneously anchored by two DNMT3A monomers (Fig. 1c, d and Extended Data Fig. 2b). Our data thus support the notion that the two DNMT3A monomers can co-methylate two adjacent CpG dinucleotides in one DNA-binding event^{12,13}. Despite being crystallized under different conditions, both DNMT3A–DNMT3L–DNA complexes are well aligned with their DNA-free state, with a root-mean-square deviation of 0.87 Å and 1.12 Å over 790 and 826 C α atoms, respectively (Extended Data Fig. 2a). Notably, in DNMT3A–DNMT3L–DNA complexes, zebularines are flipped out of the DNA helix and inserted deep into DNMT3A catalytic pockets, where they are covalently anchored by the catalytic cysteine C710 and hydrogen bonded to E756, R790, and R792 (Fig. 1c and Extended Data Fig. 1d). Because both structures reveal productive reaction states with consistent protein–DNA interactions, we focus on the structure of DNMT3A–DNMT3L in complex with 25-mer DNA for further analysis.

DNMT3A binding to DNA is mainly mediated by a loop from the target recognition domain (TRD) (residues R831–F848), the catalytic loop (residues G707–K721), and the homodimeric interface of DNMT3A, which together create a continuous DNA-binding surface (Figs 1d and 2a). Accordingly, these segments exhibit the most prominent structural changes upon DNA binding: the TRD loop lacked electron density in the DNA-free structure of DNMT3A–DNMT3L^{11,12}, but became well defined upon DNA binding and penetrated into the DNA major groove for intermolecular contacts (Fig. 2a–c); additionally, the TRD loop is stabilized through hydrogen-bonding interactions with R882, the DNMT3A mutational hotspot among leukaemias^{9,10}, and Q886 from an adjacent helix (Fig. 2c). Meanwhile, the catalytic loop residue V716 moves towards the DNA minor groove by approximately 2 Å, intercalating into the DNA cavity vacated because of zebularine base flipping (Fig. 2d, e). Although no protein–DNA contact was observed for DNMT3L, two DNMT3L-contacting helices of DNMT3A are preceded by DNA-binding loops (Extended Data Fig. 2c), reinforcing the notion that DNMT3L enhances DNMT3A functionality through stabilizing its DNA-binding sites¹².

Recognition of CpG dinucleotides by DNMT3A is mediated by both catalytic and TRD loops. In particular, guanine of the target strand, G6 (G19'), is specified by a hydrogen bond between its O6 atom and the N ϵ atom of R836 from the TRD loop, as well as water-mediated hydrogen bonds between its N7 atom and the N ϵ and O γ atoms of R836 and T834, respectively (Fig. 3a). Meanwhile, the catalytic loop approaches the minor groove, where the backbone carbonyl oxygen of V716 forms a hydrogen bond with the N2 atom of the unpaired guanine G5' (G20) (Fig. 3b). Penetration of the catalytic loop also allows V716 and P718 to engage van de Waals contacts with the base of G6 (G19'), providing additional base-specific recognition (Fig. 3b). No protein interaction was associated with C6' (C19) of the non-target strand, providing an explanation for the observation that DNMT3A does not discriminate hemimethylated against unmethylated DNA². Formation of the DNMT3A–DNA complex is also supported by various protein–DNA interactions flanking CpG, which involve electrostatic and/or hydrogen-bonding interactions of the TRD residues (R831, T832, T835, N838, and K841), catalytic loop residues (N711, S714, and I715) and DNMT3A–DNMT3A homodimeric interface residues (S881, R882, L883, and R887) with various DNA backbone or base sites (Fig. 2a and Extended Data Fig. 3a–f). These DNA-binding residues are highly conserved in DNMT3B (Extended Data Fig. 3g), suggesting a similar substrate engagement mechanism used by the DNMT3 family.

To determine the roles for CpG-engaging residues R836 and V716 in the regulation of DNMT3A activity, we performed mutagenesis followed by enzymatic studies using CpG-, CpA-, or CpT-containing substrates (Fig. 3c and Extended Data Fig. 4a, b). First, wild-type DNMT3A (DNMT3A^{WT}) showed methylation efficiency for CpG-containing DNA more than 20-fold higher than for CpA- or CpT-containing DNA, confirming its well-known CpG specificity¹⁴. By contrast, mutation of R836 to alanine (R836A) enhanced methylation of CpA- and CpT-containing DNA by 5.2- and 4.2-fold, respectively, but, as previously reported¹⁵, only led to slight change in CpG methylation. As a result, the relative CpG/CpA and CpG/CpT preference of the DNMT3A^{R836A} enzyme was reduced by 4.5- and 3.7-fold, respectively, supporting a role for R836 in substrate specificity determination. Consistent with these observations, we solved the structure of the DNMT3A^{R836A}–DNMT3L–DNA complex, which lacks R836-mediated hydrogen bonds to CpG without causing overall structural alterations (Extended Data Fig. 4c). Mutation of V716 to glycine (V716G) abolished methylation

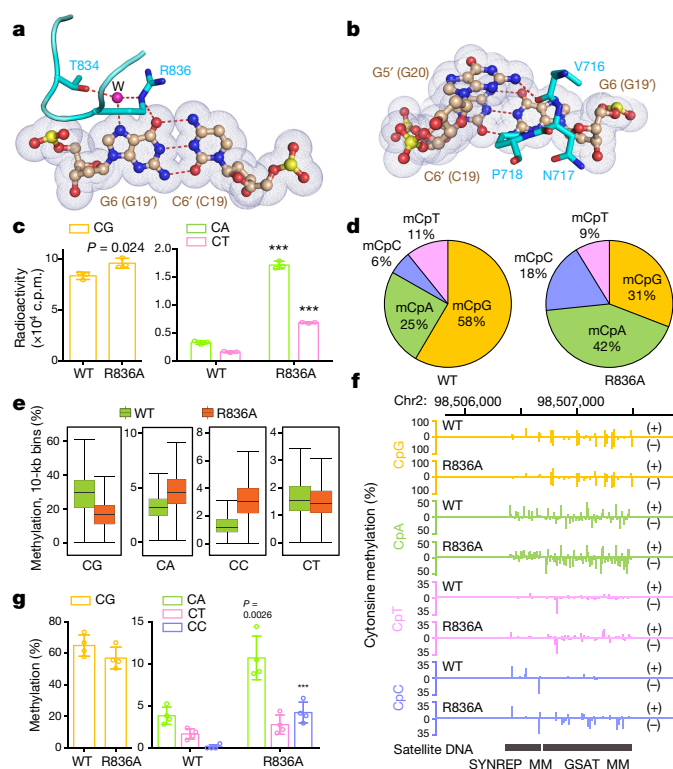


Figure 3 | DNMT3A–CpG interactions. **a, b**, Interactions of R836 (**a**) and V716–P718 (**b**) with one CpG site. The hydrogen bonds and water molecule are shown as dashed lines and a purple sphere, respectively. Nucleotides in the second CpG site are shown in parentheses. **c**, *In vitro* methylation for 40 min using DNMT3A^{WT}–DNMT3L or DNMT3A^{R836A}–DNMT3L complex ($n = 3$ biological replicates); c.p.m., counts per minute. WT, wild type. **d**, Composition of all called methylated cytosines (mC) in TKO ES cells reconstituted with DNMT3A^{WT} or DNMT3A^{R836A}. A methylated cytosine is defined using a binomial distribution-based filter with FDR less than 1% ($n = 21,678,839$ for wild type and $n = 25,272,362$ for R836A). **e, f**, eRRBS revealing averaged CpG and non-CpG methylations, either at global levels (**e**) or at a representative major satellite DNA region (**f**), that are induced by DNMT3A^{WT} versus DNMT3A^{R836A} among three independent lines of TKO ES cells. Shown in **e** are box and whisker plots of 10-kb-bin-averaged methylation levels for each sequence context. Symbols +/–, forward/reverse strand. The box and whiskers depict the interquartile and $1.5 \times$ interquartile ranges, respectively. **g**, Individual bisulfite sequencing detecting the methylation level of CG, CA, CT, or CC sites within a major satellite DNA site at chromosome 2 in TKO cells expressing DNMT3A^{WT} or DNMT3A^{R836A} ($n = 4$). Data are mean \pm s.d. Statistical analysis used two-tailed Student's *t*-test. *** $P < 0.001$.

of all tested substrates (Extended Data Fig. 4d). These observations support the idea that R836-mediated CpG engagement contributes to substrate specificity whereas V716-mediated intercalation is essential for DNMT3A-mediated catalysis. The increased *in vitro* activity of DNMT3A^{R836A} on CpA and CpT suggests that R836 might energetically influence the enzymology of DNMT3A, in addition to target recognition. In the case of CpG DNA, such an influence might be partly compensated by the R836-mediated hydrogen bonds, thereby ensuring the CpG specificity of DNMT3A.

Next, we introduced comparable levels of DNMT3A, either wild type or the above CpG-engagement-defective mutants, into ES cells with compound knockouts of DNMT1, DNMT3A, and DNMT3B (TKO)¹⁶, and detected a global increase in cytosine methylation after rescue with DNMT3A^{WT} or DNMT3A^{R836A}, but not DNMT3A^{V716G} (Extended Data Fig. 4e, f). Furthermore, genome-wide methylation profiling with enhanced reduced representation bisulfite sequencing (eRRBS), followed by calling of methylation using the previously described

binomial model and false discovery rate (FDR)-based threshold^{17,18}, revealed that, in TKO ES cells reconstituted with DNMT3A^{WT}, 58% and 42% of methylated cytosines were presented at CpG and non-CpG sites, respectively (Fig. 3d and Extended Data Fig. 5a–c); by contrast, such a distribution was reversed in cells expressing DNMT3A^{R836A}, with 31% and 69% of methylated cytosines found in CpG and non-CpG contexts (Fig. 3d and Extended Data Fig. 5b, c). Consistently, relative to wild-type controls, the absolute methylation levels were found to be decreased at CpG, but increased at CpA and CpC, sites among cells with DNMT3A^{R836A}, especially at sites showing intermediate-to-high levels of methylation (Fig. 3e and Extended Data Figs 5d and 6a). These changes were persistent among all chromosomes, at both DNA strands and over all annotated genes (Extended Data Fig. 6b–d), as exemplified by those detected at the major satellite DNA repeats (Fig. 3f) and gene-coding regions of *Foxp1* and *Dock1* (Extended Data Fig. 6e). Sanger bisulfite sequencing further validated eRRBS results at major satellite repeats in ES cells¹⁹ (Fig. 3g and Extended Data Fig. 7). DNMT3A^{V716G} abolished both CpG and non-CpG methylations at major satellite DNA (Extended Data Fig. 7b–d). The above observation that DNMT3A^{R836A} decreases overall CpG methylations in TKO cells might be due to competition of non-CpG as a potential substrate for this mutant enzyme. Collectively, we demonstrate that engaging CpG by the R836 side chain ensures DNMT3A substrate specificity in cells.

Notably, heterozygous mutation of DNMT3A at its DNA-binding residues, such as S714, V716, P718, R792, T835, R836, N838, K841, and R882 (Figs 2a and 4a, b), occurs recurrently in haematological cancer^{9,10,20} and overgrowth syndrome²¹. Although recent studies support a dominant-negative effect of the hotspot R882H mutation on DNMT3A-mediated methylation, possibly through affecting DNMT3A tetramerization^{22–25}, our structural observation raises the possibility that interfering with the DNA binding via residue substitution also results in functional impairment of DNMT3A during pathogenesis. Indeed, *in vitro* enzymatic assays showed the significantly reduced activity for all tested DNA-binding mutants, with the most pronounced effect observed for V716D, R792H, and K841E (Fig. 4c and Extended Data Fig. 8a–d). Consistently, expression of these three mutants in TKO ES cells failed to restore global DNA methylation (Extended Data Fig. 8e, f). It is worth noting that, although DNMT3A^{R836W} exhibited modestly reduced overall activities (Extended Data Fig. 8c, f), its activities for non-CpG methylations were found to be significantly increased at the major satellite DNA in TKO cells and in *in vitro* enzymatic assays (Extended Data Fig. 8g, h), suggesting a potential role for R836W in the redistribution of CpG versus non-CpG methylations in diseased cells. Given a largely heterozygous feature of DNMT3A mutations in leukaemia, we also queried whether the DNA-binding-defective mutants of DNMT3A inhibit functionality of DNMT3A^{WT}. To test this, we turned to a co-expression system used previously for studying the dominant-negative DNMT3A^{R882H} mutant²³, and reconstituted wild-type and mutant DNMT3A in equal amounts into TKO ES cells (Fig. 4d). Relative to expression of wild type alone, co-expression of DNMT3A^{V716D}, DNMT3A^{R792H}, or DNMT3A^{K841E} with DNMT3A^{WT} significantly decreased overall cytosine methylation (Fig. 4d). Together, we show that the DNMT3A mutants defective in substrate binding not only decrease activity but also interfere with that of DNMT3A^{WT}.

We further ectopically expressed the above DNMT3A mutants in TF-1 cells, a model used for studying leukaemia-associated gene mutation²⁶. Through DNA methylation array profiling and bisulfite sequencing validation, we observed a significant reduction in overall CpG methylations in TF-1 cells stably expressing DNMT3A^{V716D}, DNMT3A^{R792H} or DNMT3A^{K841E}, relative to control; by contrast, ectopic expression of DNMT3A^{WT} induced hypermethylation (Fig. 4e and Extended Data Fig. 9). There was significant overlap among CpG sites showing hypomethylation due to expression of DNMT3A^{V716D}, DNMT3A^{R792H}, or DNMT3A^{K841E} (Extended Data Fig. 10a), indicating their common effect on epigenomic deregulation. Reduced methylation

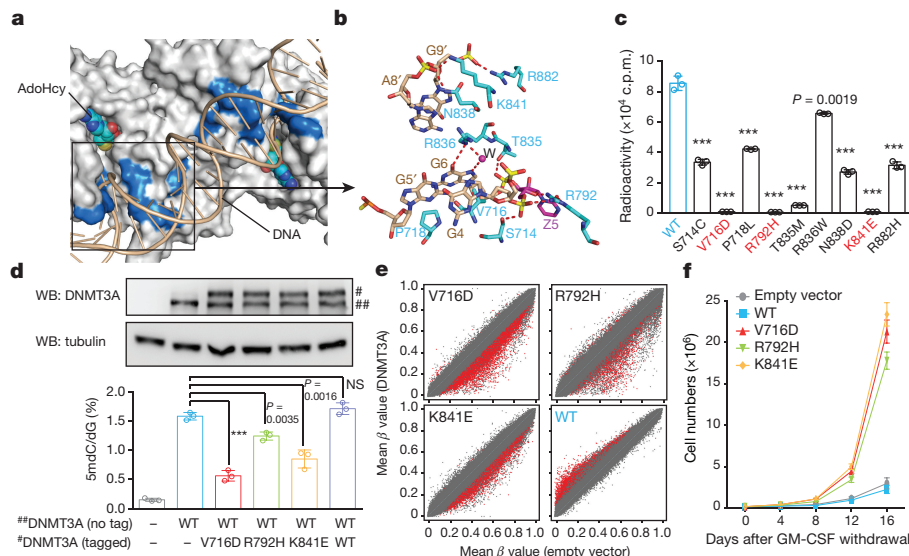


Figure 4 | Haematological cancer-associated mutations of the DNMT3A–DNA interaction residues. **a**, **b**, Surface (**a**) and stick (**b**) views of the DNA-contacting residues in DNMT3A found mutated in haematological cancer. Mutation sites are coloured blue in **a**. The hydrogen-bonding interactions and water molecule are shown as dashed lines and a purple sphere, respectively. **c**, *In vitro* methylation of CpG DNA using DNMT3A^{WT} or its haematological cancer-associated mutants ($n = 3$). **d**, DNMT3A immunoblots (top) and liquid chromatography–tandem mass spectrometry (LC–MS/MS and MS/MS/MS)-based quantification of 5-methyl-2'-deoxycytidine (5-mdC; bottom, $n = 3$ biological replicates) in DNA isolated from TKO ES cells re-expressing

DNMT3A^{WT} alone (##, non-tagged) or together with the equal amount of the indicated DNMT3A mutant (#, tagged). A representative blot of two independent experiments is shown. For gel Source Data, see Supplementary Fig. 1. **e**, Scatter plots showing mean methylation β values of each individual CpG among TF-1 cells with stable expression of the indicated DNMT3A mutant (y axis; $n = 3$ –8 biological replicates) compared with empty vector controls (x axis), with significantly differentially methylated CpGs depicted in red. **f**, Proliferation of the indicated DNMT3A-expressing TF-1 cells under cytokine-poor conditions ($n = 3$). Data are mean \pm s.d. Statistical analysis used two-tailed Student's *t*-test. *** $P < 0.001$.

of these commonly affected sites was also detected after transduction of other leukaemia-associated substrate-binding mutations of DNMT3A (P718L, T835M, R836W, and N838D), although it did not induce hypomethylation globally (Extended Data Fig. 10b, c). Binding of wild-type or mutant DNMT3A was comparable at tested loci showing methylation changes (Extended Data Fig. 10d, e). Given that epigenetic deregulation promotes TF-1 cell transformation characterized by cytokine-independent growth²⁶, we queried whether the DNA-binding-defective mutation of DNMT3A causes a similar transformation of this model. We found that, under cytokine-supporting conditions, TF-1 cells expressing wild-type or mutant DNMT3A exhibited comparable proliferation (Extended Data Fig. 10f). By contrast, those expressing a DNA-binding-defective mutant, but not DNMT3A^{WT}, had significant cytokine-independent growth capability (Fig. 4f and Extended Data Fig. 10g). Collectively, we demonstrate that the DNA-binding residues of DNMT3A are vital for establishing appropriate CpG methylation in haematological cells and that their somatic mutations detected in patients with leukaemia promote transformation.

Online Content Methods, along with any additional Extended Data display items and Source Data, are available in the online version of the paper; references unique to these sections appear only in the online paper.

Received 17 January; accepted 21 December 2017.

Published online 7 February 2018.

- Okano, M., Bell, D. W., Haber, D. A. & Li, E. DNA methyltransferases Dnmt3a and Dnmt3b are essential for *de novo* methylation and mammalian development. *Cell* **99**, 247–257 (1999).
- Okano, M., Xie, S. & Li, E. Cloning and characterization of a family of novel mammalian DNA (cytosine-5) methyltransferases. *Nat. Genet.* **19**, 219–220 (1998).
- Bird, A. DNA methylation patterns and epigenetic memory. *Genes Dev.* **16**, 6–21 (2002).
- Goll, M. G. & Bestor, T. H. Eukaryotic cytosine methyltransferases. *Annu. Rev. Biochem.* **74**, 481–514 (2005).
- Bourc'his, D., Xu, G. L., Lin, C. S., Bollman, B. & Bestor, T. H. Dnmt3L and the establishment of maternal genomic imprints. *Science* **294**, 2536–2539 (2001).

- Chedin, F., Lieber, M. R. & Hsieh, C. L. The DNA methyltransferase-like protein DNMT3L stimulates *de novo* methylation by Dnmt3a. *Proc. Natl. Acad. Sci. USA* **99**, 16916–16921 (2002).
- Hata, K., Okano, M., Lei, H. & Li, E. Dnmt3L cooperates with the Dnmt3 family of *de novo* DNA methyltransferases to establish maternal imprints in mice. *Development* **129**, 1983–1993 (2002).
- Robertson, K. D. DNA methylation and human disease. *Nat. Rev. Genet.* **6**, 597–610 (2005).
- Yang, L., Rau, R. & Goodell, M. A. DNMT3A in haematological malignancies. *Nat. Rev. Cancer* **15**, 152–165 (2015).
- Ley, T. J. et al. DNMT3A mutations in acute myeloid leukemia. *N. Engl. J. Med.* **363**, 2424–2433 (2010).
- Guo, X. et al. Structural insight into autoinhibition and histone H3-induced activation of DNMT3A. *Nature* **517**, 640–644 (2015).
- Jia, D., Jurkowska, R. Z., Zhang, X., Jeltsch, A. & Cheng, X. Structure of Dnmt3a bound to Dnmt3L suggests a model for *de novo* DNA methylation. *Nature* **449**, 248–251 (2007).
- Jurkowska, R. Z. et al. Formation of nucleoprotein filaments by mammalian DNA methyltransferase Dnmt3a in complex with regulator Dnmt3L. *Nucleic Acids Res.* **36**, 6656–6663 (2008).
- Gowher, H. & Jeltsch, A. Enzymatic properties of recombinant Dnmt3a DNA methyltransferase from mouse: the enzyme modifies DNA in a non-processive manner and also methylates non-CpA sites. *J. Mol. Biol.* **309**, 1201–1208 (2001).
- Gowher, H. et al. Mutational analysis of the catalytic domain of the murine Dnmt3a DNA-(cytosine C5)-methyltransferase. *J. Mol. Biol.* **357**, 928–941 (2006).
- Tsumura, A. et al. Maintenance of self-renewal ability of mouse embryonic stem cells in the absence of DNA methyltransferases Dnmt1, Dnmt3a and Dnmt3b. *Genes Cells* **11**, 805–814 (2006).
- Guo, J. U. et al. Distribution, recognition and regulation of non-CpG methylation in the adult mammalian brain. *Nat. Neurosci.* **17**, 215–222 (2014).
- Lister, R. et al. Human DNA methylomes at base resolution show widespread epigenomic differences. *Nature* **462**, 315–322 (2009).
- Chen, T., Tsujimoto, N. & Li, E. The PWWP domain of Dnmt3a and Dnmt3b is required for directing DNA methylation to the major satellite repeats at pericentric heterochromatin. *Mol. Cell. Biol.* **24**, 9048–9058 (2004).
- Forbes, S. A. et al. COSMIC: exploring the world's knowledge of somatic mutations in human cancer. *Nucleic Acids Res.* **43**, D805–D811 (2015).
- Tatton-Brown, K. et al. Mutations in the DNA methyltransferase gene DNMT3A cause an overgrowth syndrome with intellectual disability. *Nat. Genet.* **46**, 385–388 (2014).
- Holz-Schietinger, C., Matje, D. M. & Reich, N. O. Mutations in DNA methyltransferase (DNMT3A) observed in acute myeloid leukemia patients disrupt processive methylation. *J. Biol. Chem.* **287**, 30941–30951 (2012).

23. Kim, S. J. *et al.* A DNMT3A mutation common in AML exhibits dominant-negative effects in murine ES cells. *Blood* **122**, 4086–4089 (2013).
24. Lu, R. *et al.* Epigenetic perturbations by Arg882-mutated DNMT3A potentiate aberrant stem cell gene-expression program and acute leukemia development. *Cancer Cell* **30**, 92–107 (2016).
25. Russler-Germain, D. A. *et al.* The R882H DNMT3A mutation associated with AML dominantly inhibits wild-type DNMT3A by blocking its ability to form active tetramers. *Cancer Cell* **25**, 442–454 (2014).
26. Losman, J. A. *et al.* (R)-2-hydroxyglutarate is sufficient to promote leukemogenesis and its effects are reversible. *Science* **339**, 1621–1625 (2013).

Supplementary Information is available in the online version of the paper.

Acknowledgements We thank X. Cheng for comments on the manuscript, M. Okano, J. Wang, and J.-A. Losman for providing reagents used in the study, and staff members at the Advanced Light Source, Lawrence Berkeley National Laboratory, and at the Advanced Photo Source, Argonne National Laboratory, for access to X-ray beamlines. We are also grateful for the support of University of North Carolina facilities including Genomics Core, which are partly supported by UNC Cancer Center Core Support Grant P30-CA016086. This work was supported by Kimmel Scholar Awards (to J.S. and G.G.W.), the March of Dimes Foundation (1-FY15-345 to J.S.), the DoD Peer-reviewed Cancer Research Program (W81XWH-14-1-0232 to G.G.W.), Gabrielle's Angel Foundation for

Cancer Research (to G.G.W.), Gilead Sciences Research Scholars Program in haematology/oncology (to G.G.W.), University Cancer Research Fund of the N.C. state (to G.G.W.), and the National Institutes of Health (1R35GM119721 to J.S.; R35GM124736 to S.B.R.; 5R21ES025392 to Y.W.; and 1R01CA215284, 1R01CA218600, and 1R01CA211336 to G.G.W.). G.G.W. is a Research Scholar of American Cancer Society and a Junior Faculty Scholar of American Society of Haematology. R.L. was supported by a Lymphoma Research Foundation postdoctoral fellowship.

Author Contributions Z.-M.Z., R.L., P.W., Y.Y., D.C., L.G., S.L., D.J., and J.S. performed experiments. S.B.R. provided technical support. Y.W., G.G.W., and J.S. conceived and organized the study. Z.-M.Z., R.L., G.G.W., and J.S. prepared the manuscript.

Author Information Reprints and permissions information is available at www.nature.com/reprints. The authors declare no competing financial interests. Readers are welcome to comment on the online version of the paper. Publisher's note: Springer Nature remains neutral with regard to jurisdictional claims in published maps and institutional affiliations. Correspondence and requests for materials should be addressed to J.S. (jikui.song@ucr.edu) or G.G.W. (greg_wang@med.unc.edu).

Reviewer Information *Nature* thanks A. Jeltsch, R. Xu and the other anonymous reviewer(s) for their contribution to the peer review of this work.

METHODS

Protein expression and purification. The gene fragments encoding residues 628–912 of human DNMT3A (NCBI accession number NM_022552) and residues 178–386 of human DNMT3L were inserted in tandem into a modified pRFDuet-1 vector (Novagen). The DNMT3A sequence was separated from the preceding His₆-SUMO tag by a ubiquitin-like protease (UPL1) cleavage site. Expression and purification of the DNMT3A–DNMT3L complex followed a previously described protocol²⁷. In brief, the His₆-SUMO–DNMT3A fusion protein and DNMT3L were co-expressed in *Escherichia coli* BL21 DE3 (RIL) cell strains and purified using a Ni²⁺-NTA column. Subsequently, the His₆-SUMO tag was removed through UPL1-mediated cleavage, followed by ion exchange chromatography on a Heparin column. For enzymatic assays, the DNMT3A–DNMT3L complex was further purified through size-exclusion chromatography on a HiLoad 16/600 Superdex 200 pg column (GE Healthcare), and concentrated to 0.1–0.3 mM in a buffer containing 20 mM Tris-HCl (pH 8.0), 100 mM NaCl, 0.1% β-mercaptoethanol, and 5% glycerol. To generate the covalent DNMT3A–DNMT3L–DNA complex, an 11-mer single-stranded DNA that was in-house synthesized to contain 2'-deoxyzebularine²⁸ (5'-CATGdZGCTCTC-3'; dZ, 2'-deoxyzebularine) was annealed with a 10-mer single-stranded DNA (5'-AGAGCGCATG-3') before reaction with the DNMT3A–DNMT3L complex in the presence of 20 mM Tris-HCl (pH 7.5), 50 mM NaCl, 20% glycerol, and 40 mM DTT at room temperature. In addition, a 25-mer zebularine-containing DNA (5'-GCATGZGTCTCTAATTAGAACGCATG-3'; Z, zebularine) was self-annealed and used to form a second DNMT3A–DNMT3L–DNA complex or the DNMT3A^{R836A}–DNMT3L–DNA complex. The reaction products were further purified through a HiTrap Q XL column (GE Healthcare), followed by size-exclusion chromatography on a HiLoad 16/600 Superdex 200 pg column. The final samples for crystallization of the productive DNMT3A–DNMT3L–DNA complexes contained about 0.1–0.2 mM covalent DNMT3A–DNMT3L–DNA complexes, 0.3 mM AdoHcy, 20 mM Tris-HCl (pH 8.0), 100 mM NaCl, 0.1% β-mercaptoethanol, and 5% glycerol.

Crystallization conditions and structure determination. The crystals for the covalent complex of DNMT3A–DNMT3L with the 10/11-mer DNA were generated by the hanging-drop vapour-diffusion method at 23 °C, from drops mixed from 0.5 μl of DNMT3A–DNMT3L–DNA solution and 0.5 μl of precipitant solution (7% PEG4000, 0.1 M Tris-HCl (pH 8.5), 100 mM MgCl₂, 166 mM imidazole (pH 7.0)). The reproducibility and quality of crystals were further improved by the micro-seeding method. The crystals were soaked in cryoprotectant made of mother liquor supplemented with 30% PEG400, before being flash frozen in liquid nitrogen. For the complex of DNMT3A (either wild-type or R836A mutant) with DNMT3L and the 25-mer DNA, crystals were generated by the hanging-drop vapour-diffusion method at 4 °C, from drops mixed from 1.5 μl of the protein solution and 1.5 μl of precipitation solution (0.1 M Tris-HCl (pH 7.0), 200 mM NaH₂PO₄, and 5% PEG4000). The crystals were treated with cryoprotectant containing the precipitation solution and 30% glycerol before collecting.

X-ray diffraction datasets for the covalent DNMT3A–DNMT3L–DNA complexes were collected at selenium peak wavelength on the BL501 or BL502 beamlines at the Advanced Light Source, Lawrence Berkeley National Laboratory, and the dataset for the covalent DNMT3A (R836A)–DNMT3L–DNA complex was collected on the 24-ID-E NE-CAT beamline at the Advanced Photon Source, Argonne National Laboratory. The diffraction data were indexed, integrated, and scaled using the HKL 2000 program²⁹ or the XDS program³⁰. The structures of the productive covalent complexes of DNMT3A–DNMT3L–DNA were solved using the molecular replacement method in PHASER³¹, with the DNA-free structure of DNMT3A–DNMT3L (PDB 2QRV) serving as a search model. Further modelling of the covalent DNMT3A–DNMT3L–DNA complexes was performed using COOT³² and then subject to refinement using the PHENIX software package³³. The same R-free test set was used throughout the refinement. The final models for DNMT3A–DNMT3L complexed with the 25-mer and 10/11-mer DNAs were refined to 2.65 Å and 3.1 Å resolution, respectively. The final model for DNMT3A (R836A)–DNMT3L complexed with the 25-mer DNA was refined to 3.0 Å resolution.

The statistics for data collection and structural refinement of the productive covalent DNMT3A–DNMT3L–DNA complexes are summarized in Extended Data Fig. 1c.

In vitro DNA methylation assay. Synthesized (GAC)₁₂, (AAC)₁₂ and (TAC)₁₂ DNA duplexes were used as CG-, CA- and CT-containing substrates, respectively. The DNA methylation assays were performed in triplicate at 37 °C for 1 h, unless otherwise indicated. In brief, a 20-μl reaction mixture contained 2.5 μM S-adenosyl-L-[methyl-³H]methionine (AdoMet) (specific activity 18 Ci mmol⁻¹, PerkinElmer), 0.3 μM DNMT3A–DNMT3L, 0.75 μM DNA in 59 mM Tris-HCl, pH 8.0, 0.05% β-mercaptoethanol, 5% glycerol, and 200 μg ml⁻¹ BSA. The methylation reactions were stopped by flash freezing in liquid nitrogen, followed by precipitation and incubation on ice for 1 h, in 1 ml of 15% trichloroacetic acid solution plus

40 μg ml⁻¹ BSA. The trichloroacetic acid-precipitated samples were then passed through a GF/C filter (GE Healthcare) using a vacuum-filtration apparatus. After sequential washing with 2 × 5 ml of cold 10% trichloroacetic acid and 5 ml of ethanol, the filters were dried and transferred to scintillation vials filled with 5 ml of ScintiVerse (Fisher), followed by measurement of tritium scintillation with a Beckman LS6500 counter.

Plasmid construction. Full-length human DNMT3A isoform 1 was cloned into the EcoRI site of the pPyCAGIZ vector (a gift from J. Wang). DNMT3A mutation was generated by a QuikChange II XL Site-Directed Mutagenesis Kit (Agilent). To achieve co-expression of the wild-type and mutant DNMT3A at equal levels in cells, we engineered a T2A-based fusion construct consisting of the mutant cDNA, which was added with an N-terminal 3 × Flag-(GGGS)₃-Myc tag to differentiate its protein size from non-tagged wild-type DNMT3A, followed by a T2A peptide sequence at its C terminus and the cDNA of non-tagged wild-type DNMT3A. Myc-tagged full-length human DNMT3A isoform 1 was cloned into MSCV Pac retroviral vector as previously described²⁴. All plasmid sequences were verified by sequencing.

Cell lines and cell culture. *Dnmt3a*, *Dnmt3b*, and *Dnmt1* TKO mouse ES cells (a gift from M. Okano)¹⁶ were cultivated on gelatin-coated dishes in the high-glucose DMEM base medium (Invitrogen) supplemented with 15% of fetal bovine serum (FBS, Invitrogen), 1 × non-essential amino acids (Invitrogen), 0.1 mM β-mercaptoethanol, and 1,000 U ml⁻¹ leukaemia inhibitory factor (ESGRO). The TF-1 human erythroleukaemic cell line was obtained from American Type Culture Collection (ATCC) and cultivated in the RPMI 1640 base medium (Invitrogen) supplemented with 10% of FBS and 2 ng ml⁻¹ of recombinant human granulocyte-macrophage colony-stimulating factor (GM-CSF; R&D Systems). Acquisition of the cytokine-independent growth of TF-1 cells by the introduction of cancer-associated gene mutation was examined and quantified upon GM-CSF removal as previously described²⁶.

Authentication of cell line identities, including those of parental and derived lines, was ensured by the Tissue Culture Facility affiliated to the University of North Carolina at Chapel Hill Lineberger Comprehensive Cancer Center using the genetic signature profiling and fingerprinting analysis previously described³⁴. Every 1–2 months, a routine examination of cell lines in culture for any possible mycoplasma contamination was performed using commercially available detection kits (Lonza Walkersville).

Generation of stable cell lines. TKO ES cells were transfected by Lipofectamine 2000 (Invitrogen) with the pPyCAGIZ empty vector or that carrying wild-type or mutant DNMT3A. Forty-eight hours after transfection, the transduced ES cells were selected out in 50 μg ml⁻¹ Zeocin (Invitrogen) for 10 days. The pooled stable-expression cell lines and independent single-cell-derived clonal lines were continuously maintained in the medium with 25 μg ml⁻¹ zeocin. To generate TF-1 leukaemia cell lines with stable expression of wild-type or mutant DNMT3A, the MSCV-based retrovirus was packaged in HEK293 cells and used for infection as previously described³⁵. Forty-eight hours after infection, TF-1 cells were selected by 2 μg ml⁻¹ puromycin for 4 days and maintained in medium with 1 μg ml⁻¹ puromycin.

Western blotting. Antibodies used for western blotting were anti-MYC (Sigma-Aldrich, 9E10), anti-DNMT3A (Santa Cruz, H-295), anti-β-actin (Santa Cruz, sc-47778), and α-tubulin (Sigma-Aldrich). Total protein samples were prepared by cell lysis with SDS-containing Laemmli sample buffer followed by brief sonication. Extracted samples equivalent to 100,000 cells were loaded to the SDS-PAGE gels for western blot analysis.

Quantification of 5-methyl-2'-deoxycytidine and 2'-deoxyguanosine in genomic DNA. The measurement procedures for 5-methyl-2'-deoxycytidine (5-mdC) and 2'-deoxyguanosine in genomic DNA were described previously^{36,37}. In brief, 1 μg of genomic DNA prepared from cells was enzymatically digested into nucleoside mixtures. Enzymes in the digestion mixture were removed by chloroform extraction, and the resulting aqueous layer was concentrated to 10 μl and subjected directly to LC-MS/MS and LC-MS/MS/MS analysis for quantification of 5-mdC and 2'-deoxyguanosine, respectively. The amounts of 5-mdC and 2'-deoxyguanosine (in moles) in the nucleoside mixtures were calculated from area ratios of peaks found in selected-ion chromatograms for the analytes over their corresponding isotope-labelled standards, the amounts of the labelled standards added (in moles), and the calibration curves. The final levels of 5-mdC, in terms of percentages of 2'-deoxyguanosine, were calculated by comparing the amounts of 5-mdC relative to those of 2'-deoxyguanosine.

eRRBS and data analysis. Genomic DNA of each sample was added with 0.5% of unmethylated lambda DNA (Promega) as a spike-in control and subjected to eRRBS using MethylMidi-seq (Zymo Research) as described before²⁴. In brief, approximately 300 ng of DNA were digested with three restriction enzymes (80 units of MspI, 40 units of BfaI, and 40 units of MseI) to improve genomic DNA fragmentation and coverage. The generated DNA fragments were ligated

to the pre-annealed 5-methyl-cytosine-containing adapters, followed by filling in overhangs and the A extension at the 3' terminus. The DNA fragments were then purified and subjected to bisulfite treatment using an EZ DNA Methylation–Lightning Kit (Zymo Research). After amplification, the quality of eRRBS libraries was checked with Agilent 2200 TapeStation, followed by deep sequencing using an Illumina HiSeq-2000 genome analyser (50 base pairs and paired end as parameters). Obtained reads were aligned to *in silico* bisulfite-converted mouse reference genome mm9 and lambda DNA sequence (GenBank accession number J02459.1) using the Bismark package in a strand-specific manner³⁸. For identification of methylated cytosines, all mapped cytosines were subjected to a binomial distribution model-based methylation calling as described in the section below. To determine distribution of methylation levels, only those high-quality reads with at least 15 times coverage were used. For convenience of data analysis and to increase data complexity, data from all three biological replicates were merged and cytosine sites covered with at least 15 reads in the merged dataset were used for downstream analysis such as averaged methylation levels in 10-kb window sliding and aggregated methylation levels across genes. Data representation and plots were generated with the 'ggplot2' package in R software using custom scripts.

Identification of methylated cytosines. We used a previously described binomial model to identify methylated cytosines^{17,18}. Specifically, with the unmethylated spike-in lambda DNA, we first determined the bisulfite non-conversion rate (probability, *P*) for each cytosine sequence context independently (that is, CpG, CpA, CpC, and CpT). For each mapped cytosine in our eRRBS data, we calculated the binomial *P* value in which methylated reads occurred out of the total read number on the basis of the binomial test, with the bisulfite non-conversion rate as the success probability (*P*). If a *P* value was under a threshold, we defined the cytosine as truly methylated. To determine the FDR for each different threshold, we created a control methylome for each eRRBS sample. In the control methylome, read depth at each cytosine was equal to the real data, and the methylated events were simulated by binomial distribution using the previously defined non-conversion rate (*P*). The FDR was determined by the ratio between the number of identified methylated cytosine sites from the control methylome and that from the real data. For each eRRBS sample, we chose to use a *P* value under which the FDR was less than 1% or 0.1%, as specified in figure legends.

DNA methylation array and data analysis. Genomic DNA was extracted and bisulfite-converted as described above. DNA methylation profiling using an Illumina Infinium HumanMethylation450 BeadChip array was performed by the UNC Genomics Core according to the manufacturer's instructions. Methylation data were then subject to background subtraction and control normalization by executing preprocessIllumina in the R 'minfi' package³⁹. Differentially methylated CpGs were identified using dmpFinder in a categorical mode. Methylation changes were considered significant at a *q*-value of less than 0.05 and a β value difference of more than 0.1. Hierarchical clustering analysis, scatter plots, and density plots were generated in R using 'pheatmap' and 'ggplot2' packages.

Sanger bisulfite sequencing. Sanger bisulfite sequencing was performed as previously described²⁴. In brief, genomic DNA was prepared using a DNeasy Blood and Tissue Kit (Qiagen) and 1 μ g genomic DNA subject to bisulfite conversion using an EZ DNA Methylation Gold Kit according to manufacturer's instructions (Zymo Research). Bisulfite-treated DNA was then used as template in PCR to amplify the target DNA region, followed by cloning of PCR products into pCR2.1-TOPO vector (Invitrogen) for direct sequencing of individual clones. Four biological replicates per cell line were tested, with at least ten clonal sequences per replicate generated. The primers used for amplifying a major satellite DNA sequence located at chromosome 2 were 5'-GGG AAT TTT GGT GGT AGG GT-3' and 5'-AAA AAA CAT CCA CTT AAC TAC TTA AAA A-3'. The primers used for validating 450k array data were, for EIF4G1, 5'-AGG AGA TTG AGG TTT TAG TGA ATA TGT-3' and 5'-CCC TAT ATC AAA TTC TTC CTA CCA TAA-3'; for HDLBP, 5'-GGA GGT GAA GTT ATG GAG ATA TTT TT-3' and 5'-ATC CCA TAC CAA

CAA AAA CTA ACA A-3'; for FOXK2, 5'-TAT GTT TGT ATT TGG GGT GTT TTT T-3' and 5'-CTA AAA AAT CAA AAA CAT TTC CTA CC-3'.

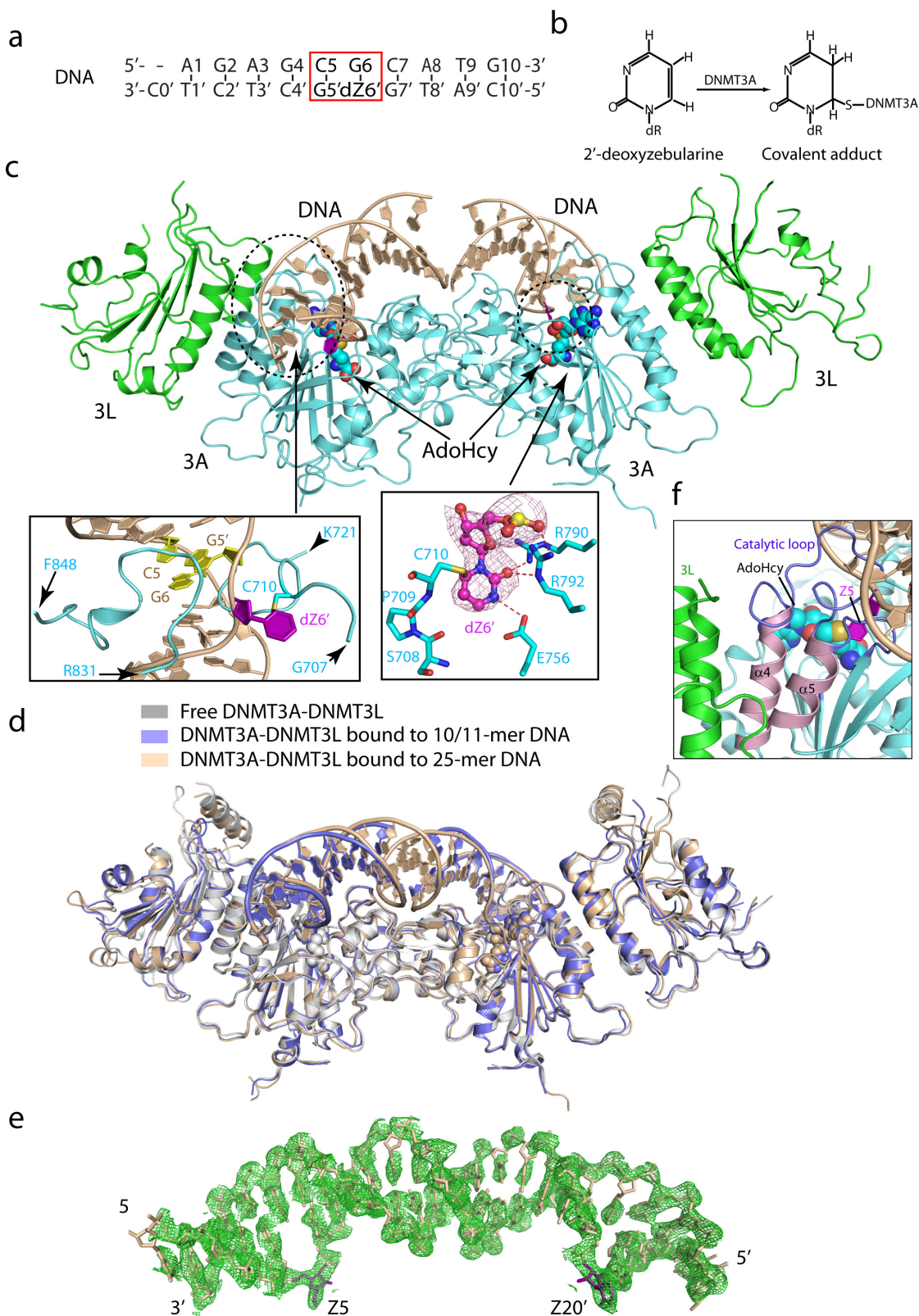
Chromatin immunoprecipitation. Samples used for chromatin immunoprecipitation (ChIP) were prepared as previously described⁸. In brief, chromatin samples extracted from cells expressing Myc-tagged DNMT3A were used for ChIP with the 9E10 anti-Myc antibody (Sigma-Aldrich), with cells expressing empty vector used as negative control. Real-time PCR was performed for detecting DNMT3A binding at sites listed below. The primers for ChIP-PCR at each tested site were as follows: for cg23189692, 5'-TTG GCA TGC TCA CAG AGA GG-3' and 5'-GTC TTC CCA GGC TCA TTG CT-3'; for cg00704780, 5'-AGC AAA ACG GTC AGT AGC CA-3' and 5'-TAC CAG CAA AAG CTG GCA GG-3'; for cg10460657, 5'-GCC TCT GAC CTG CTG TCT AC-3' and 5'-AGG AAA TGC CCC AGA CGT G-3'; for cg07564962, 5'-GGC CGG CAC TAA TGT CTT TC-3' and 5'-TTC CCT GCT CTG TGG GAA GG-3'; for cg13393476, 5'-CCT TGC GAG TGA GTC ACG G-3' and 5'-GAG ATT CTG CCA GGC TCC AC-3'; for cg20509869, 5'-GTG GGA CGC TAA CCC TCT TC-3' and 5'-GGC GGC TGA TTT ATC TGG GT-3'; and for GAPDH transcription start site, 5'-TCT CCC CAC ACA CAT GCA CTT-3' and 5'-CCT AGT CCC AGG GCT TTG ATT-3'.

Statistics. No statistical methods were used to predetermine sample size. The experiments were not randomized. The investigators were not blinded to allocation during experiments and outcome assessment. Data are presented as the mean \pm s.d. of at least three independent experiments. Statistical analysis was performed with a Student's *t*-test for comparing two sets of data with assumed normal distribution. A *P* value of less than 0.05 was considered to be significant.

Code availability. The scripts for genomic data analyses and all other data are available from the corresponding authors upon reasonable request.

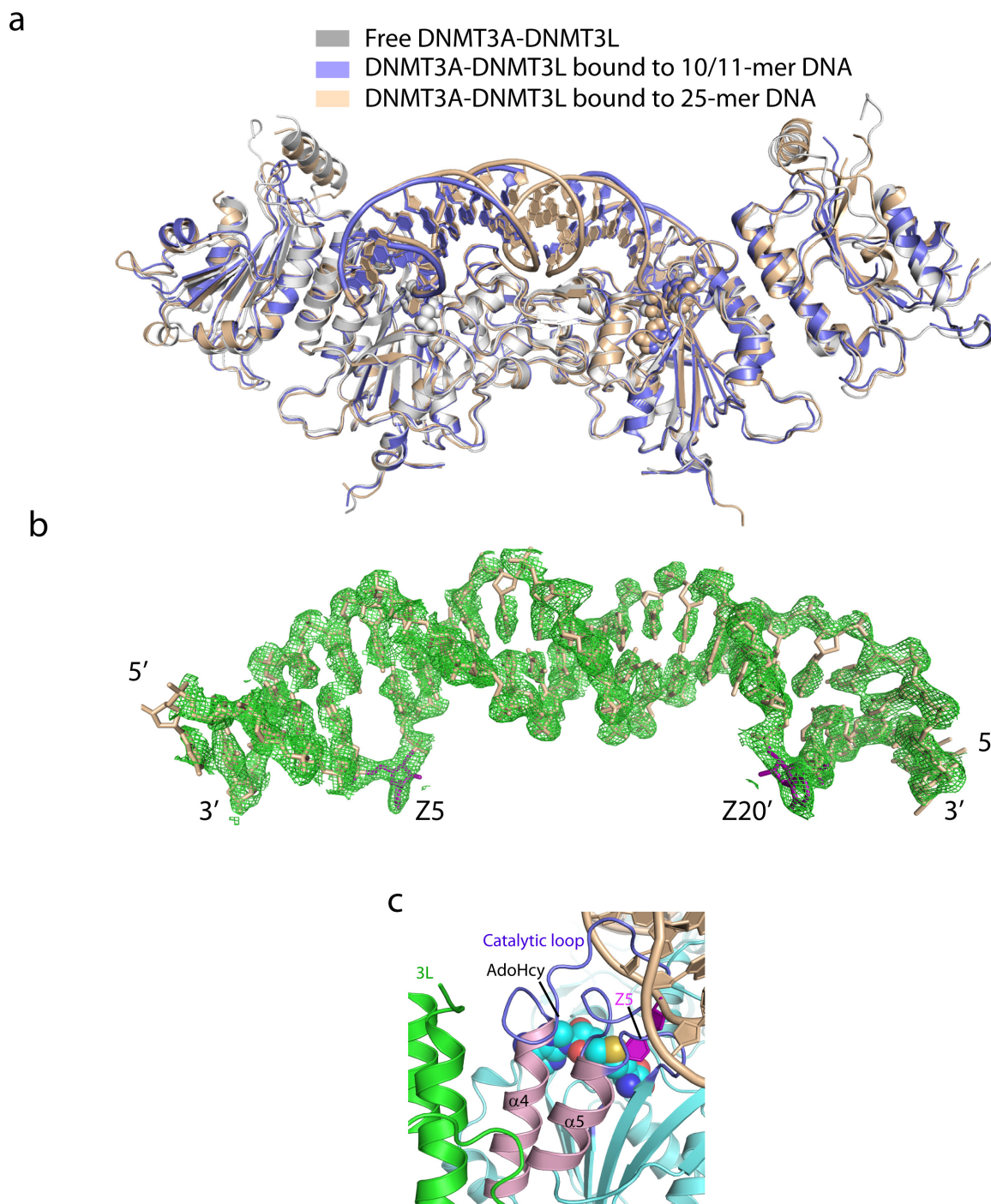
Data availability. Coordinates and structure factors for DNMT3A–DNMT3L in complex with 25-mer DNA, DNMT3A–DNMT3L in complex with 10/11-mer DNA, and DNMT3A (R836A)–DNMT3L in complex with 25-mer DNA have been deposited in the Protein Data Bank under accession numbers 5YX2, 6F57, and 6BRR, respectively. The eRRBS and Illumina Human Methylation 450K array data have been deposited in NCBI Gene Expression Omnibus under accession number GSE99391.

27. Song, J., Rechkoblit, O., Bestor, T. H. & Patel, D. J. Structure of DNMT1-DNA complex reveals a role for autoinhibition in maintenance DNA methylation. *Science* **331**, 1036–1040 (2011).
28. Zhou, L. *et al.* Zebularine: a novel DNA methylation inhibitor that forms a covalent complex with DNA methyltransferases. *J. Mol. Biol.* **321**, 591–599 (2002).
29. Otwinowski, Z. & Minor, W. Processing of X-ray diffraction data collected in oscillation mode. *Methods Enzymol.* **276**, 307–326 (1997).
30. Kabsch, W. Xds. *Acta Crystallogr. D* **66**, 125–132 (2010).
31. McCoy, A. J. *et al.* Phaser crystallographic software. *J. Appl. Crystallogr.* **40**, 658–674 (2007).
32. Emsley, P. & Cowtan, K. Coot: model-building tools for molecular graphics. *Acta Crystallogr. D* **60**, 2126–2132 (2004).
33. Adams, P. D. *et al.* PHENIX: building new software for automated crystallographic structure determination. *Acta Crystallogr. D* **58**, 1948–1954 (2002).
34. Yu, M. *et al.* A resource for cell line authentication, annotation and quality control. *Nature* **520**, 307–311 (2015).
35. Wang, G. G. *et al.* Quantitative production of macrophages or neutrophils *ex vivo* using conditional Hoxb8. *Nat. Methods* **3**, 287–293 (2006).
36. Volz, D. C. *et al.* Tris(1,3-dichloro-2-propyl)phosphate induces genome-wide hypomethylation within early zebrafish embryos. *Environ. Sci. Technol.* **50**, 10255–10263 (2016).
37. Yu, Y. *et al.* Comprehensive assessment of oxidatively induced modifications of DNA in a rat model of human Wilson's disease. *Mol. Cell. Proteomics* **15**, 810–817 (2016).
38. Krueger, F. & Andrews, S. R. Bismark: a flexible aligner and methylation caller for Bisulfite-Seq applications. *Bioinformatics* **27**, 1571–1572 (2011).
39. Aryee, M. J. *et al.* Minfi: a flexible and comprehensive Bioconductor package for the analysis of Infinium DNA methylation microarrays. *Bioinformatics* **30**, 1363–1369 (2014).



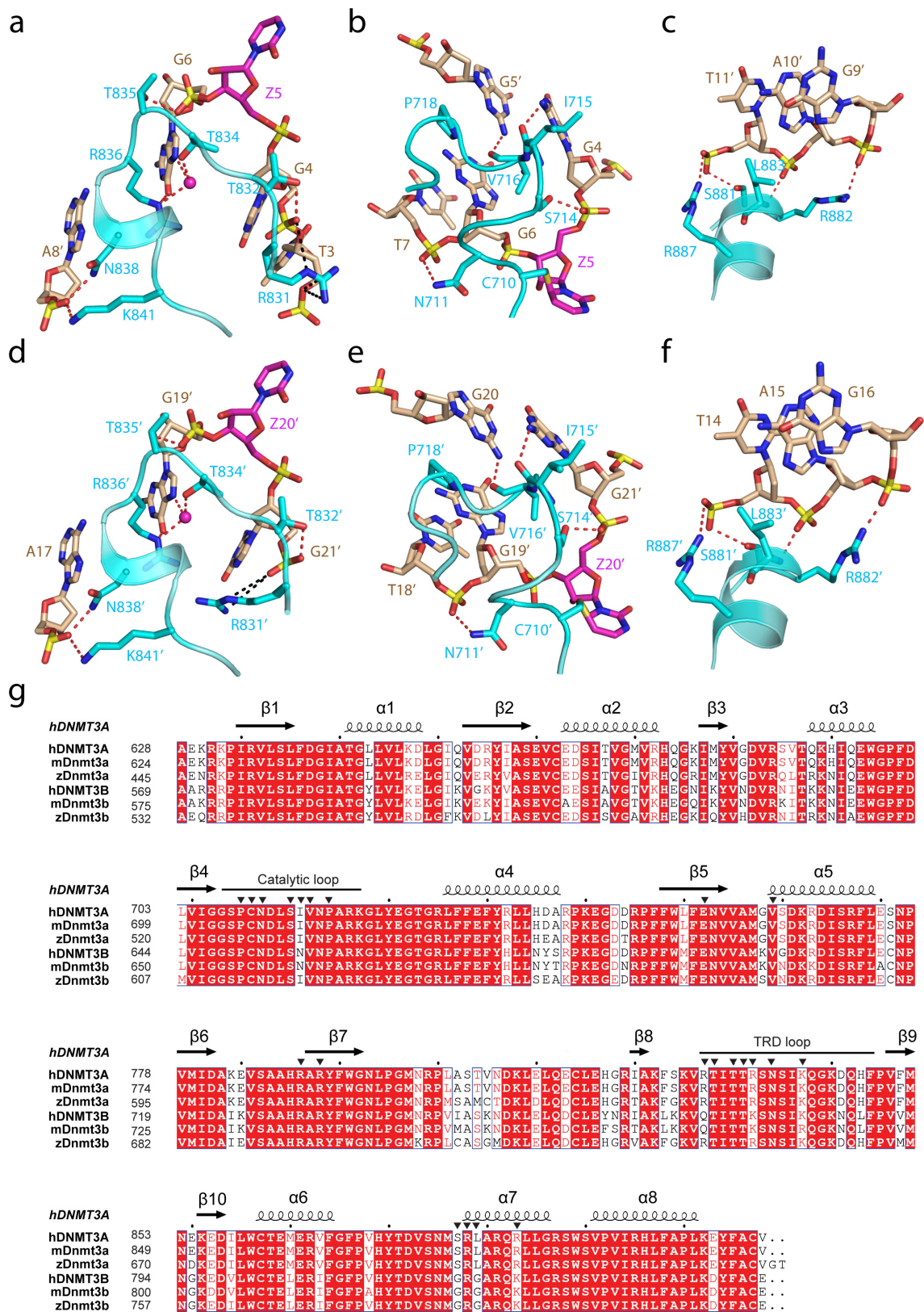
Extended Data Figure 1 | Structures of the DNMT3A-DNMT3L tetramer in complex with the 10/11-mer DNA. **a**, The sequence of the 10/11-mer DNA duplex used for structural study. **b**, Chemical formula of the covalent adduct of DNMT3A and 2'-deoxyzebularine. **c**, Data collection and refinement statistics. Each dataset was collected from a single crystal. **d**, Ribbon representations of the DNMT3A-DNMT3L tetramer in complex with the 10/11-mer DNA duplex and AdoHcy. DNMT3A, DNMT3L, and DNA are coloured in light blue, green, and

wheat, respectively, and AdoHcy shown in sphere representation. The boxed areas show expanded views for the CpG sites (purple and yellow), the DNA-binding TRD and catalytic loops (left box), and the flipped out 2'-deoxyzebularine (dZ6') surrounded by conserved catalytic residues (right box). The $F_o - F_c$ omit map of 2'-deoxyzebularine (pink) is contoured at the 3σ level. The hydrogen-bonding interactions are depicted as dashed lines.



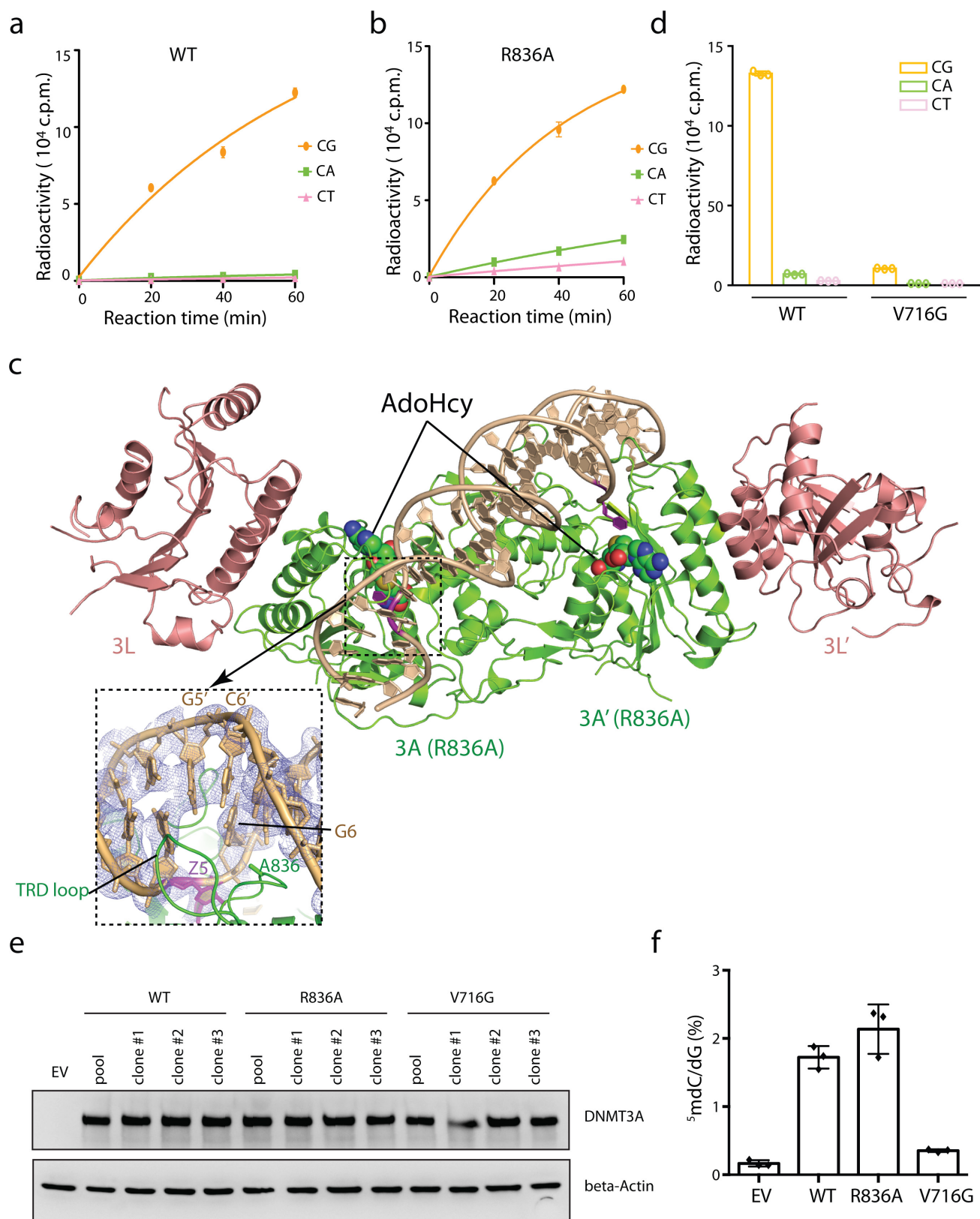
Extended Data Figure 2 | Intermolecular interactions between the DNMT3A–DNMT3L tetramer and DNA. **a**, Structural overlay of free DNMT3A–DNMT3L (PDB 2QRV) with the 10/11-mer DNA and 25-mer DNA-bound states. **b**, Stick representation of the 25-mer DNA duplex bound to the DNMT3A–DNMT3L tetramer, with the $2F_o - F_c$ omit map contoured at the 1σ level. **c**, The two helices of DNMT3A that interact with

DNMT3L (shown in green) are coloured in pink ($\alpha 4$ and $\alpha 5$ in accordance with the numeration in Extended Data Fig. 3g) and preceded by two DNA contact loops, coloured in blue. The flipped out zebularine (Z5) is coloured in purple. The bound AdoHcy molecule is shown in sphere representation.



Extended Data Figure 3 | Various intermolecular interactions between the two DNMT3A monomers and DNA. **a–f**, DNA binding by the first and second DNMT3A monomer (defined as 3A and 3A', respectively, in Fig. 1c) includes the intermolecular interactions between the TRD loop of DNMT3A and the DNA major groove (**a**, **d**), between the catalytic loop of DNMT3A and the DNA minor groove (**b**, **e**), and between the homodimeric interface of DNMT3A and the DNA backbone (**c**, **f**). The hydrogen-bonding interactions are shown as dashed lines.

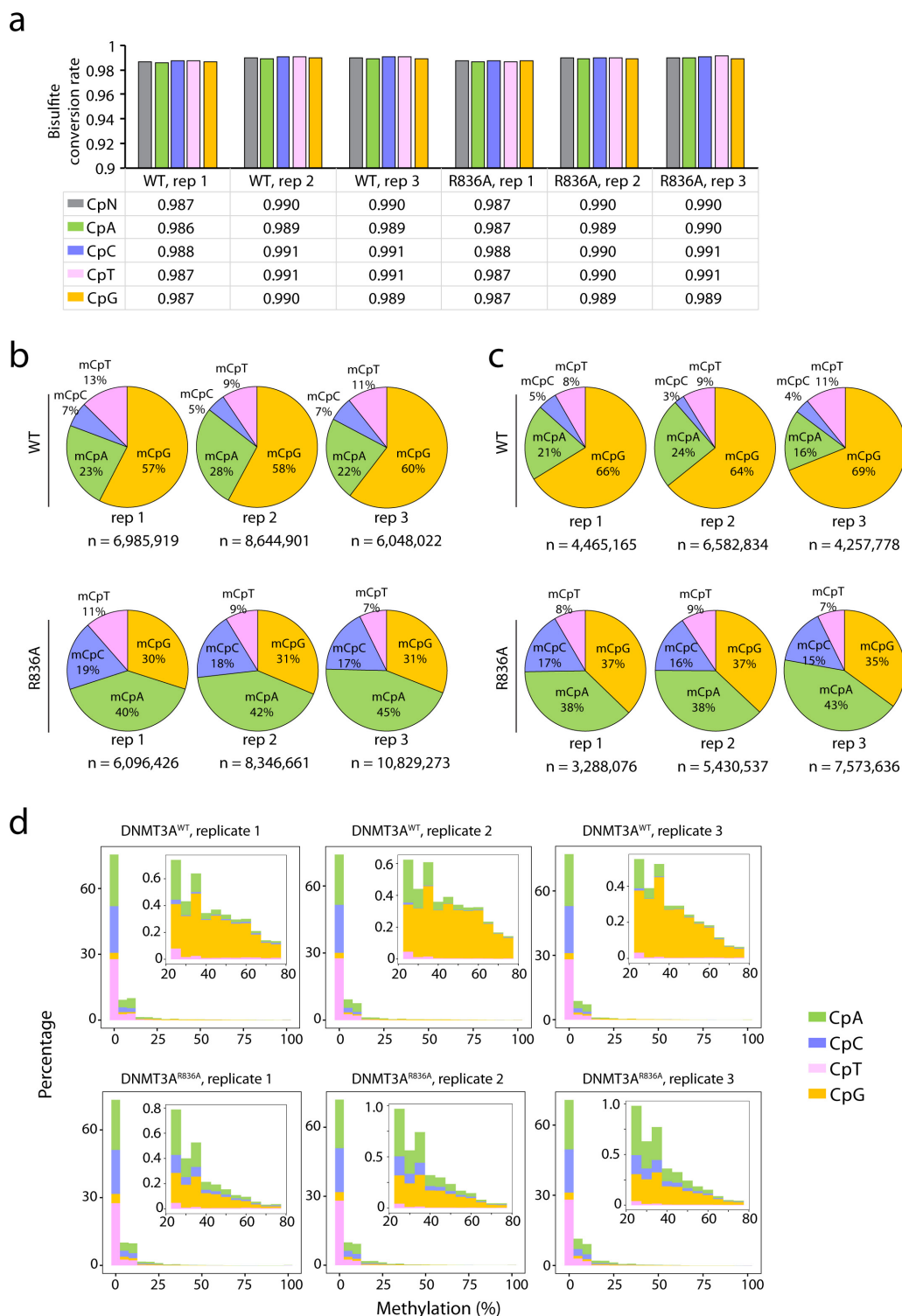
The water molecules are shown as purple spheres. **g**, Structure-based sequence alignment of DNMT3 proteins from human (hDNMT3A and hDNMT3B), mouse (mDnmt3a and mDnmt3b), and zebrafish (zDnmt3a and zDnmt3b). Completely conserved residues are coloured in white and highlighted in red. Partly conserved residues are coloured in red. Secondary structures are shown above the aligned sequences. The DNA-binding residues as revealed by this study are marked with black triangles.



Extended Data Figure 4 | See next page for caption.

Extended Data Figure 4 | The essential roles for the CpG-engaging residues of DNMT3A, R836, and V716 in DNMT3A-mediated CpG versus non-CpG methylations. **a, b**, DNA methylation kinetics analysis of wild-type (DNMT3A^{WT}, **a**) and R836A-mutated (DNMT3A^{R836A}, **b**) DNMT3A using the CpG-, CpA-, or CpT-containing DNA substrates ($n = 3$ biological replicates). Purified DNMT3A–DNMT3L tetramer complex was used for measurements, followed by fitting with a first-order exponential equation. **c**, Ribbon representation of the crystal structure of DNMT3A^{R836A}–DNMT3L tetramer in complex with the 25-mer DNA, with the CpG recognition by one of the DNMT3A monomers shown in expanded view. The $2F_o - F_c$ omit map of DNA was

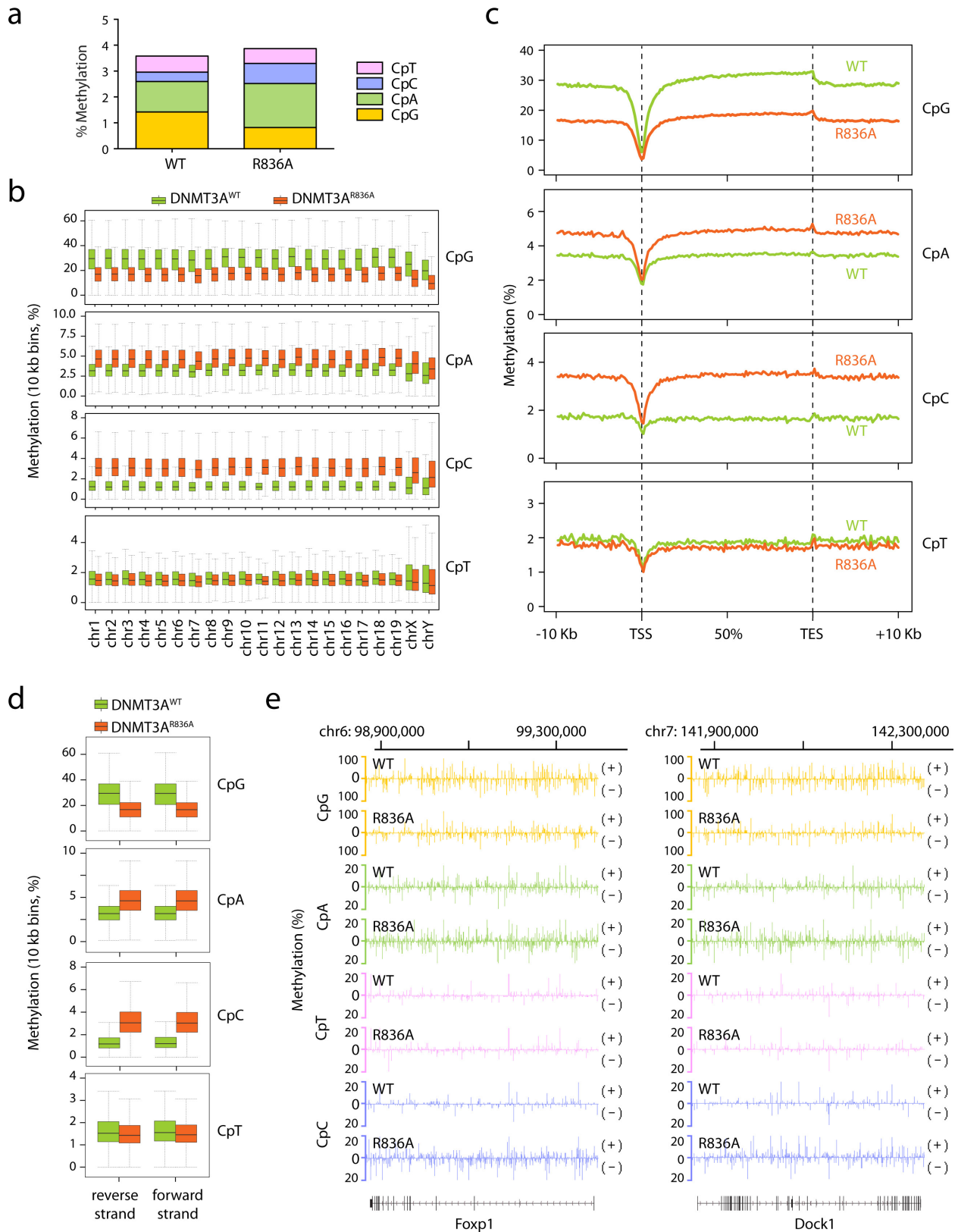
contoured at the 0.8σ level, and coloured in light blue. **d**, Methylation assay using either DNMT3A^{WT} or DNMT3A^{V716G} on CG-, CA-, and CT-containing DNA ($n = 3$ biological replicates). **e**, Immunoblots detect reconstituted expression of the indicated DNMT3A among TKO mouse ES cells, either the pooled stable-expression cell population or single-cell-derived clonal lines. EV, empty vector. A representative blot of two independent experiments is shown. For gel Source Data, see Supplementary Fig. 1. **f**, LC–MS analysis reveals the global 5-methyl-2'-deoxycytidine (5-mdC) levels (calculated as 5-mdC/2'-deoxyguanosine on the y axis) in the TKO ES cells after stable transduction of empty vector or the indicated DNMT3A ($n = 3$ biological replicates). Data are mean \pm s.d.



Extended Data Figure 5 | eRRBS reveals distribution of cytosine methylations in each sequence context among TKO ES cells with reconstituted expression of either DNMT3A^{WT} or DNMT3A^{R836A}.

a, The rates of bisulfite conversion for the indicated sequence context in each sample as determined by the unmethylated lambda DNA spike-in control. CpN, all cytosines. **b**, **c**, Pie charts showing the percentage of methylated cytosines (total number *n* shown at the bottom of each plot) identified among the DNMT3A^{WT}- or DNMT3A^{R836A}-expressing TKO ES

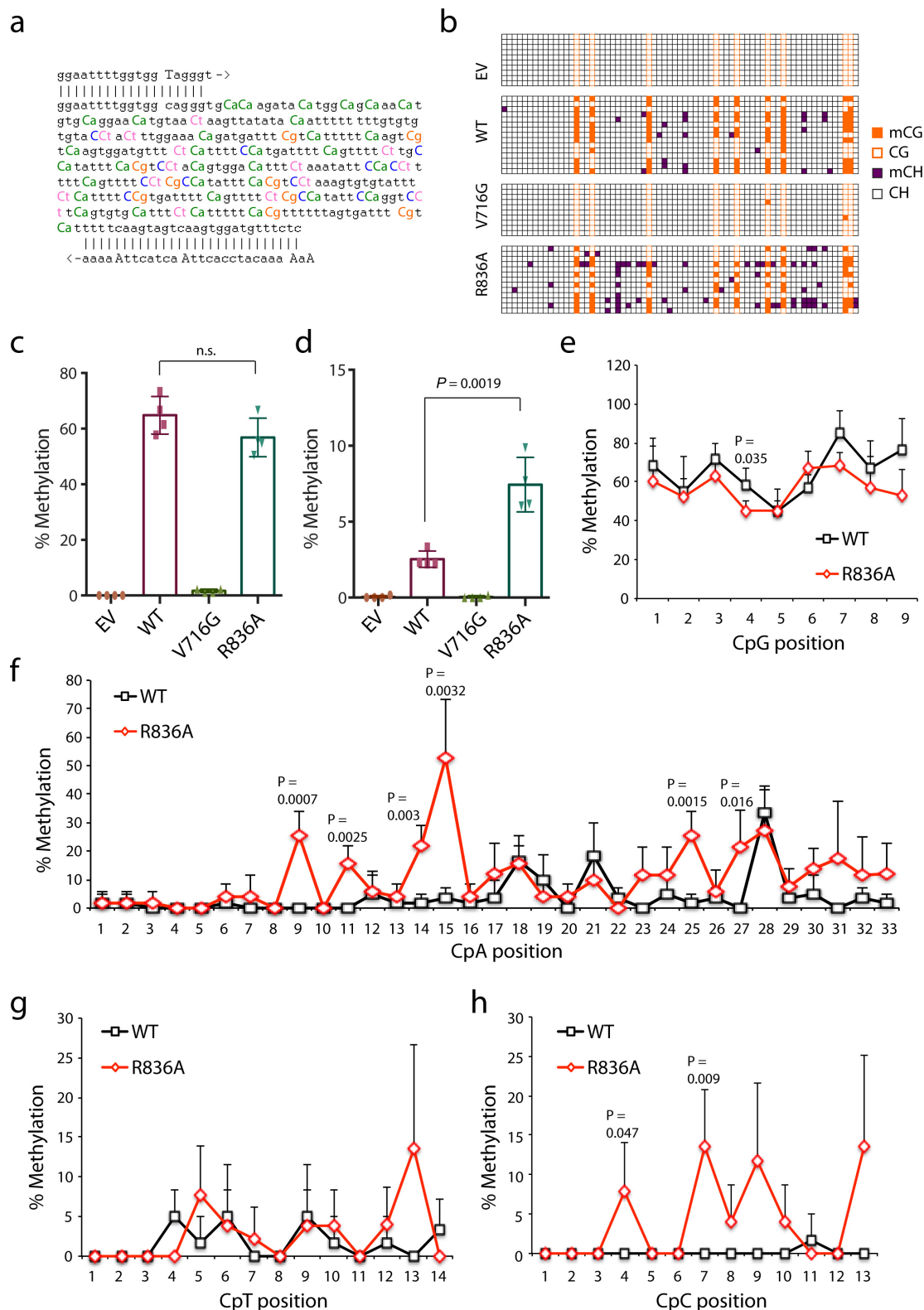
cells in each sequence context. The methylated cytosines were called using a stringent binomial distribution-based filter to eliminate false positives from incomplete bisulfite conversion, with an FDR of 1% and 0.1% set for **b** and **c**, respectively. **d**, Distribution of methylation levels (percentage on *x* axis) for the indicated sequence context. Inserts show a closed view of the distribution at sites with intermediate to high levels of cytosine methylation.



Extended Data Figure 6 | See next page for caption.

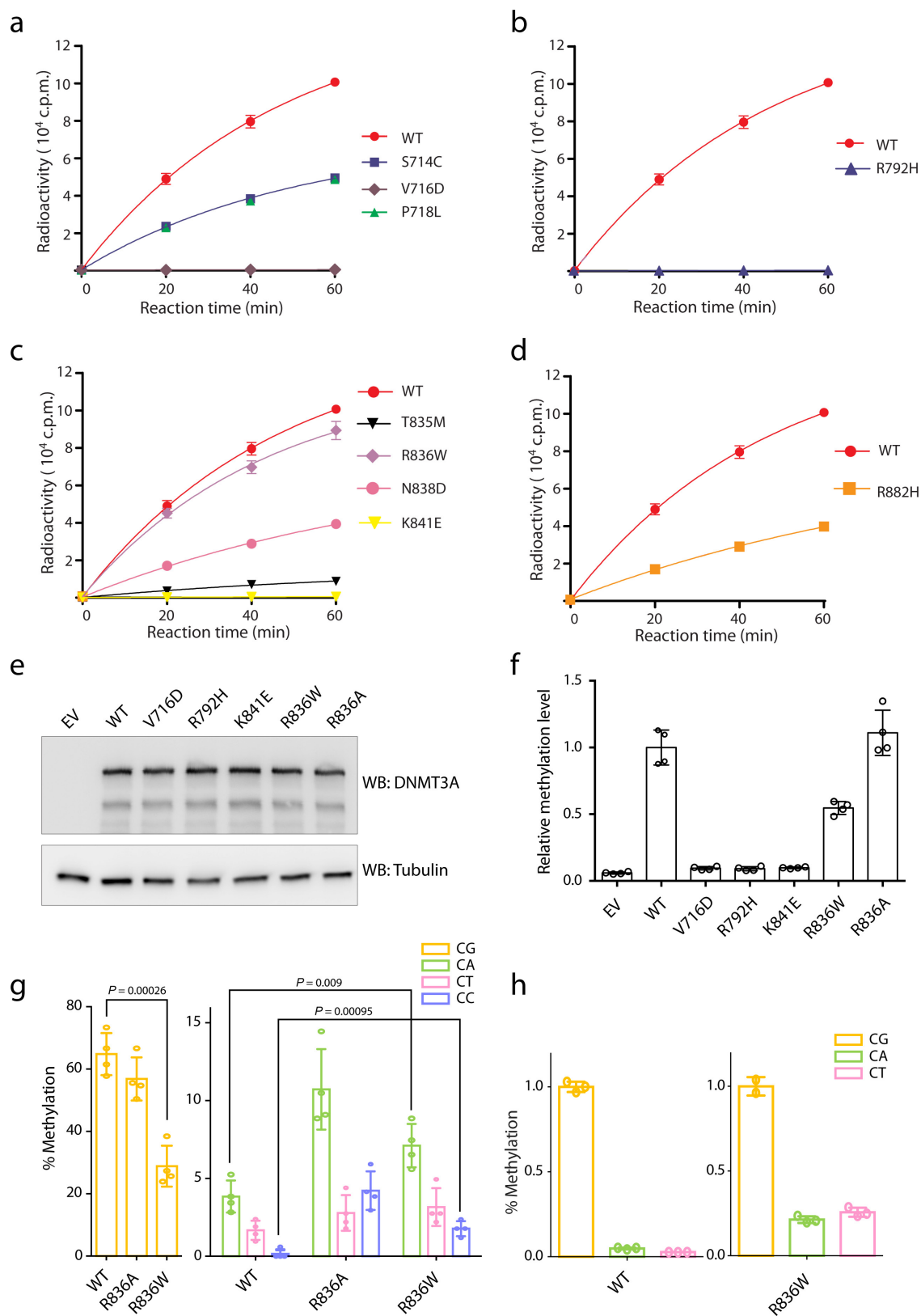
Extended Data Figure 6 | CpG and non-CpG methylations induced by DNMT3A^{WT} versus DNMT3A^{R836A} in the TKO ES cells. **a**, Overall methylation levels of cytosines at four different sequence contexts as detected by eRRBS. On the y axis, the averaged methylation level of all cytosines within the mouse genome is shown, as calculated by normalization of the detected methylation cytosines over total cytosine numbers in the TKO ES cells reconstituted with either DNMT3A^{WT} (left) or DNMT3A^{R836A} (right). **b**, Global levels of CpG and CpH (H = A, C, or T) methylation induced by DNMT3A^{WT} (green) or DNMT3A^{R836A} (red) across the mouse chromosomes of the TKO ES cells. Box and whisker plots of 10-kb-bin-averaged methylation levels of each mouse chromosome are shown. **c**, Global levels of CpG and CpH methylation induced by DNMT3A^{WT} (green) versus DNMT3A^{R836A} (red) across all

annotated genes. Each gene was divided into 100 equally sized bins and the 10-kb flanking region was divided into 50 equally sized bins. Averaged methylation levels were plotted for each bin. TSS, transcription start site; TES, transcription end site. **d**, Global levels of CpG and CpH methylation induced by DNMT3A^{WT} (green) versus DNMT3A^{R836A} (red) on the two opposite DNA strands. Boxplots of 10-kb-bin-averaged CpG, CpA, CpC, and CpT methylation levels of each strand are shown. **e**, Representative gene-wide views of CpG and CpH methylations at *Foxp1* and *Dock1*, which are grouped into either the forward (+) or reverse (−) DNA strand. Cytosines covered by at least 15 reads from eRRBS data are shown, with each site designated by a vertical line. Panels **a–e** use the combined dataset of three biological replicates per group. Box plots depict the interquartile range, and whiskers depict 1.5 × interquartile range.



Extended Data Figure 7 | Sanger bisulfite sequencing to validate the cytosine methylation levels mediated by DNMT3A, either wild type or defective in recognizing the CpG substrate, among the TKO mouse ES cells. **a**, Sequence of the examined major satellite DNA region. Primers used for bisulfite PCR are denoted with 5' and 3' primer pairing. The counts for cytosines, highlighted in colour, are 9 for the CG dinucleotide, 33 for CA, 14 for CT, and 13 for CC. **b**, A representative result for bisulfite sequencing analysis of the major satellite repeat region described above in the TKO cells expressing empty vector, wild-type DNMT3A, or the indicated mutant. Each row represents one DNA clone and each column represents one site of cytosine, either methylated (filled) or unmethylated

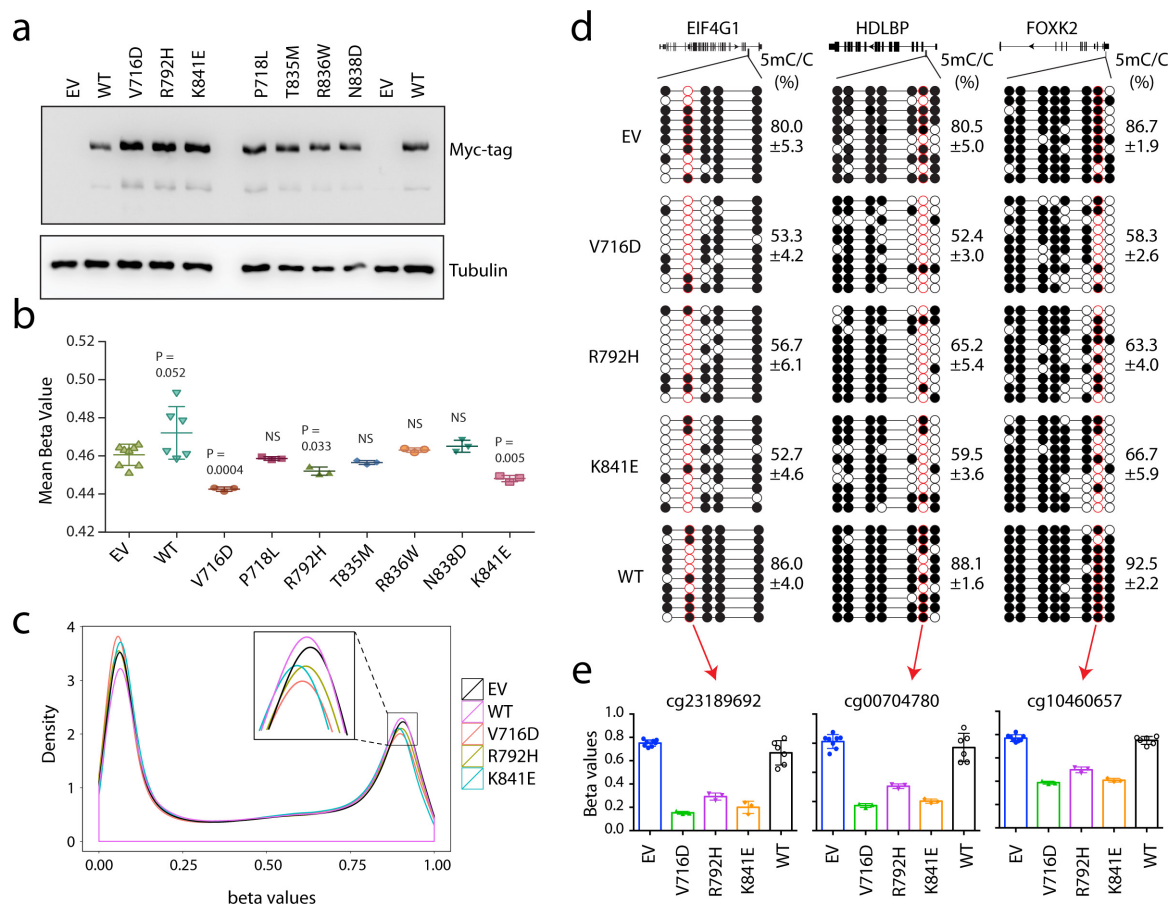
(open). **c**, **d**, Percentage of methylation mediated by DNMT3A or the indicated mutant at CpG (**c**) and non-CpG (**d**) sites within the examined major satellite DNA region in the TKO ES cells. Data are mean \pm s.d.; $n = 4$ independent bisulfite sequencing experiments as shown in **b**. **e**–**h**, Average cytosine methylation levels at each individual site grouped by the CpG (**e**), CpA (**f**), CpT (**g**), or CpC (**h**) context in the examined major satellite DNA among the TKO ES cells reconstituted with DNMT3A^{WT} versus DNMT3A^{R836A} ($n = 4$ biological replicates; mean \pm s.d., with the labelled P values). Statistical analysis used a two-tailed Student's t -test; NS, not significant.



Extended Data Figure 8 | See next page for caption.

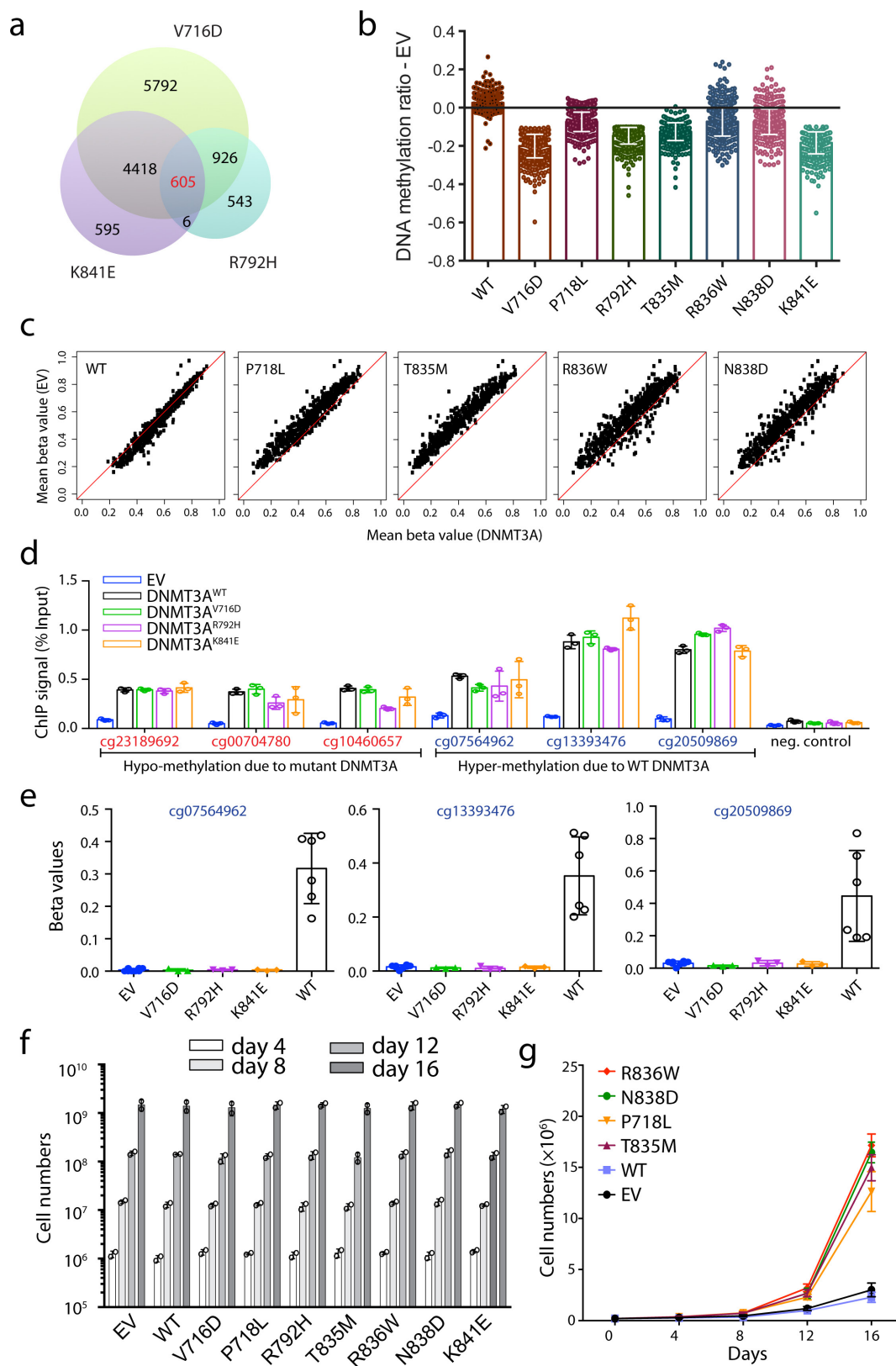
Extended Data Figure 8 | Effect of haematological cancer-associated mutations of DNMT3A on DNA methylation *in vitro* and in mouse TKO ES cells. **a**, Methylation kinetics of DNMT3A with mutations located at the catalytic loop, compared with DNMT3A^{WT}. **b**, Methylation kinetics of DNMT3A with an active site mutation, R792H. **c**, Methylation kinetics of DNMT3A with mutations located at the TRD loop. **d**, Methylation kinetics of DNMT3A with the hotspot mutation R882H. For **a–d**, DNMT3A–DNMT3L complex was used for the measurements ($n = 3$ biological replicates), followed by fitting with a first-order exponential equation. These data were measured independently from those shown in Fig. 4c. **e**, Immunoblot detects stable reconstitution of DNMT3A^{WT} or the indicated DNMT3A mutant in the TKO ES cells. A representative blot of two independent experiments is shown. For gel Source Data, see Supplementary Fig. 1. **f**, LC–MS analysis reveals the global

5-methyl-2'-deoxycytidine (5-mdC) levels (calculated as 5-mdC/2'-deoxyguanosine) in the TKO ES cells after stable transduction of empty vector or the indicated DNMT3A. The methylation levels relative to TKO cells expressing DNMT3A^{WT} are plotted. Data are mean \pm s.d.; $n = 4$ biological replicates. **g**, Individual bisulfate sequencing detects the methylation level of cytosines in each sequence context within a major satellite DNA site at chromosome 2 in the TKO cells reconstituted with DNMT3A^{R836W} (right), compared with DNMT3A^{WT} (left) or DNMT3A^{R836A} (middle; as determined in Fig. 3g) ($n = 4$; mean \pm s.d.). Statistical analysis used a two-tailed Student's *t*-test. **h**, *In vitro* methylation of CG-, CA-, or CT-containing DNA using DNMT3A^{WT} (left) or DNMT3A^{R836W} (right) in complex with DNMT3L, reacted for 40 min ($n = 3$ biological replicates). The methylation levels relative to CG-containing DNA substrates are plotted. Data are mean \pm s.d.



Extended Data Figure 9 | Effect of haematological cancer-associated mutations of DNMT3A on genomic DNA methylation in the TF-1 leukaemia cells. a, Immunoblot of the TF-1 cells stably transduced with Myc-tagged DNMT3A, either wild type or the indicated cancer-associated mutants. EV, empty MSCV vector. A representative blot of two independent experiments is shown. For gel Source Data, see Supplementary Fig. 1. **b**, Profiling of the indicated DNMT3A-expressing TF-1 cell lines with the HumanMethylation_450K BeadChip array reveals the mean methylation β values for all examined CpGs. Each dot represents a biological replicate: that is, an independently derived stable-expression cell line ($n = 3$ –8 biological replicates per group; mean \pm s.d.). Statistical analysis used a two-tailed Student's t -test. **c**, Density plot of methylation β values for all examined CpGs in the indicated DNMT3A-expressing

TF-1 cell lines. The inserted box shows a zoom-in view for densities for highly methylated DNA sites among the indicated samples. Data are mean \pm s.d., with the labelled P values. Statistical analysis used two-tailed Student's t -test. **d**, Sanger bisulfite sequencing of the indicated regions from TF-1 cell lines stably transduced with empty vector, DNMT3A^{WT} or the indicated cancer-associated mutant. Individual CpG sites (circles) are filled with black (methylated) or white (unmethylated). Red circles denote the CpG sites covered by the Illumina Infinium 450K DNA methylation array. Data are mean \pm s.d.; $n = 3$ biological replicates. **e**, Methylation values of the indicated CpG sites (labelled by red circles in **d**) based on the measurements with the Infinium 450K DNA methylation arrays ($n = 3$ –8 biological replicates; mean \pm s.d.).



Extended Data Figure 10 | See next page for caption.

Extended Data Figure 10 | Effect of haematological cancer-associated DNMT3A mutations on DNA hypomethylation and cytokine-independent growth of the TF-1 leukaemia cells. **a**, Venn diagram of CpG sites with hypomethylation induced by either one of the three indicated strong DNA-binding-defective mutants of DNMT3A, V716D, K841E, and R792H. **b**, **c**, Bar plots (**b**) and scatter plots (**c**) showing methylation difference at the 605 commonly hypomethylated CpG sites identified in **a** among the TF-1 cells with stable transduction of either DNMT3A^{WT} or the indicated mutant, compared with empty MSCV vector. A black line in **b** indicates empty vector control ($n = 3-8$ biological replicates per group; mean \pm s.d.). In **c**, mean methylation β values are plotted of each individual CpG in the indicated DNMT3A experimental group (x axis) and control empty vector group (y axis; $n = 3-8$ biological replicates per group). **d**, **e**, Comparable occupancy of DNMT3A and its mutant forms at the indicated genomic loci with affected DNA methylation, as measured by ChIP analysis of the

Myc-tagged DNMT3A^{WT} or mutants in TF-1 stable-expression cell lines. Tested sites by ChIP-qPCR in **d** ($n = 3$ biological replicates; mean \pm s.d.) included three CpG sites showing hypomethylation due to expression of mutant DNMT3A (left; also see Extended Data Fig. 9e), three sites showing hypermethylation due to expression of DNMT3A^{WT} (middle; also see **e**, which shows mean methylation β values from measurements with the Infinium 450K DNA methylation arrays, $n = 3-8$ biological replicates; mean \pm s.d.), and a negative control locus (right; the GAPDH transcription start site). The anti-Myc antibody was used for ChIP and the empty-vector-expressing TF-1 cells used as cell control for unspecific binding. **f**, Proliferation of the indicated DNMT3A stable-expression TF-1 cells in the presence of a supporting cytokine, GM-CSF ($n = 2$ biological replicates; mean \pm s.d.). **g**, Proliferation of the indicated DNMT3A-expressing TF-1 cells after GM-CSF withdrawal ($n = 3$ biological replicates; mean \pm s.d.).

CORRECTIONS & AMENDMENTS

CORRIGENDUM

doi:10.1038/nature25163

Corrigendum: AMPA receptor-mediated regulation of a G_i -protein in cortical neurons

Yizheng Wang, Daniel L. Small, Danica B. Stanimirovic, Paul Morley & Jon P. Durkin

Nature **389**, 502–504 (1997); doi:10.1038/39062

It has come to our attention that Fig. 4 in this Letter presented three events of data duplication. In Fig. 4a the panels in row 1, columns 1 and 7 were the same, in Fig. 4a the panels in row 3, columns 5 and 7 were the same, and in Fig. 4c and e, the panels in columns 1–3 were the same. Given the time elapsed since publication, we could not locate the original raw data. The main conclusion illustrated by Fig. 4, however, of dose-dependent (Fig. 4d) and $G\beta\gamma$ -sensitive (Fig. 4f) activation of $G\alpha i1$ by AMPA in MIN6 cells, which do not express GluR6 (Fig. 4b), remains unaffected. Authors J.P.D. and P.M., now both retired, could not be reached. The original Letter has not been corrected online.

Correspondence should be addressed to Y.W. (yzwang@ion.ac.cn).

CORRECTIONS & AMENDMENTS

ERRATUM

doi:10.1038/nature25445

Erratum: *Runx3* programs CD8⁺ T cell residency in non-lymphoid tissues and tumours

J. Justin Milner, Clara Toma, Bingfei Yu, Kai Zhang, Kyla Omilusik, Anthony T. Phan, Dapeng Wang, Adam J. Getzler, Toan Nguyen, Shane Crotty, Wei Wang, Matthew E. Pipkin & Ananda W. Goldrath

Nature **552**, 253–257 (2017); doi:10.1038/nature24993

In this Letter, owing to errors introduced during the proofreading process, the words ‘infection with’ were missing from the sentence “Furthermore, *Runx3* RNAi also impaired T_{RM} cell differentiation in the context of a localized infection with enteric *Listeria monocytogenes* expressing GP_{33–41} (LM–GP_{33–41}) (Fig. 2b).” In addition, in Fig. 1a, the *x*-axis label for the bottom right graph should have read “Expression change log₂(D7 kid/D7 T_{CM})” rather than “Expression change log₂(D35 kid/D35 T_{CM})”. In Fig. 1e, the arrow pointing from the spleen to T_{CM} should have been enlarged and aligned with the arrow above, and in the heat map in Fig. 1f ‘*Irf4*’ should have been non-italic upright font. These errors have all been corrected in the online versions of the Letter. Supplementary Information to this Corrigendum shows the original uncorrected Fig. 1, for transparency.

Supplementary Information is available in the online version of this Corrigendum.

CORRECTIONS & AMENDMENTS

ERRATUM

doi:10.1038/nature25471

Erratum: Moving beyond microbiome-wide associations to causal microbe identification

Neeraj K. Surana & Dennis L. Kasper

Nature **552**, 244–247 (2017); doi:10.1038/nature25019

In this Letter, errors in Fig. 2c were inadvertently introduced during the production process. The key to the survival graph should state ‘HMb’ for the green line rather than ‘MMb’, ‘HMb^{MMb–1d}’ for the blue line rather than ‘MMb^{HMb–1d}’, and ‘HMb^{MMb–3d}’ for the red line rather than ‘MMb^{HMb–3d}’. The original figure has been corrected online.

CAREERS

GENDER DIFFERENCES How language in job descriptions affects the response **p.395**

BLOG Personal stories and careers counsel
<http://blogs.nature.com/naturejobs>

NATUREJOBS For the latest career listings and advice www.naturejobs.com

DOMINIQUE ROCHE



Marine ecologist Sandra Binning recommends that researchers who are pregnant take a few extra steps of preparation before going out into the field.

WORK-LIFE BALANCE

Child on the horizon

Fieldwork can be tough on a pregnancy — but there are ways to manage.

BY EMILY SOHN

Conservation biologist Amy Dickman had built her career around remote fieldwork in Namibia and Tanzania — extended trips that included close run-ins with wild animals. She had encountered venomous cobras in toilets and bread bins. She had been charged by elephants. And she had been attacked by a cheetah. During her first expedition to Tanzania in 2004, a lion sniffed at her tent and eventually fell asleep on top of it, trapping her arm beneath its body.

The likelihood of such events — both

thrilling and terrifying — was high in her work, which aimed to reduce conflicts between humans and carnivores. So when Dickman learnt in 2013 that she was pregnant, it felt at first as if she might be risking a huge career setback.

She worried that the pregnancy would interfere with her usual field trips to the African wilderness, where she often spent eight months at a stretch doing research that has helped to reduce killings of carnivores by 80% ([see go.nature.com/2guyn1h](http://go.nature.com/2guyn1h)); it has also led to multiple career and funding awards and some 40 publications in peer-reviewed journals. And

she fretted that colleagues, superiors and others might perceive her as professionally weaker — although everyone, including her university, was supportive.

Equally disquieting, she says, was the new equation she faced when making decisions about risks: she was now carrying a tiny person that could not offer its own consent to being plunged into dangerous situations. “You’re directly responsible for someone else within your body,” says Dickman, who has appointments at the University of Oxford, UK, and the University of Vermont in Burlington. And others, she notes, including the baby’s father, ►

► also have a vested interest in risk mitigation.

As academic researchers worldwide struggle with a model that places increasing importance on every publication, grant and keynote talk, many female researchers whose careers hinge on remote or challenging fieldwork agonize over the idea of getting pregnant. They wonder whether they can continue to travel into the field to dig for fossils or scuba dive for data, and whether they will need to change or curtail the type of research they do.

Yet those who have continued with expeditions say they find that the experience can be safe and rewarding, and beneficial for science: their successful field trips show other female researchers, for example, that they, too, can be scientists and also plan a family.

But health in pregnancy is unpredictable, as are conditions in the field. After months of preparing for trips that might involve large teams and complicated logistics, it can be hard to decide whether to go and, once there, to determine how best to deal with pregnancy-related complications or disheartening comments from superiors or others.

Scientists who have balanced pregnancy with remote or otherwise risky fieldwork recommend detailed planning for medical care abroad along with frank communication with superiors and colleagues about their specific fieldwork aims. A willingness to shift gears can be helpful: sometimes, cancelling an excursion can be the right choice. Comparing the length of a pregnancy with the timespan of a typical career can also provide a helpful sense of perspective.

“Over the arc of a career, these are little blips,” says Kim Cobb, a climate scientist at the Georgia Institute of Technology in Atlanta. “The idea that a field trip is make-or-break is kind of folly. You’ll have ample opportunity over the course of your career to participate in field trips.”

DELICATE BALANCE

Some scientists try to make deliberate choices about when to start a family as a way to ease the transition into a new phase of life. As a graduate student at the Scripps Institution of Oceanography in La Jolla, California, Cobb loved having “two surfboards and a career that stretched out in front of me full of possibility, publications and adventure”.

But she wasn’t sure how a pregnancy might affect the feeling of freedom that she so relished. Because she and her husband (also an academic researcher) were based in the United States, which has less-generous parental leave benefits than do many other countries, they decided to delay their first pregnancy until they each felt relatively secure in their jobs. They now have four children, and Cobb resumed trips into the field when each infant was nine or ten months old.

Cobb feels lucky that she could control her family timing in a way that worked out well for her. Some female researchers, whether

for personal or for other reasons, don’t want to wait — or don’t have the option of waiting — until their careers are established before they become pregnant. And sometimes, of course, a pregnancy comes as a surprise. The uncertainties that surround a pregnancy can cause conflicts when an expedition requires detailed planning. As a result, questions about when and how to tell superiors can arise earlier than might be comfortable for some.

Dickman, for example, felt obliged to tell her supervisor about her pregnancy when she was only seven weeks into it, much sooner than many women would share such news, because she would need to shift the timing of a field trip to avoid taking anti-malaria medications in her first trimester. “This is something we shouldn’t feel apologetic about,” she says. Her supervisors were fully supportive of her choices.

It is often best to emphasize the need for confidentiality when informing others about a pregnancy, says Siân Halcrow, a bio-archaeologist at the University of Otago in New Zealand. Early in her first pregnancy in 2004, she learnt that she was not legally obliged to tell her superiors until her second trimester. But she privately shared the news, which was leaked to her department head.

When she opted to tell him herself, he said that he already knew. Although her career was not affected by this breach of confidence, she was still upset by it.

Halcrow also recommends documenting communications. Her plans for a field trip to another country were cancelled once against her will, and she now advises pregnant researchers to put all discussions into writing, and to follow up face-to-face meetings with e-mails that summarize the conversations and underscore the person’s desire to stay involved in fieldwork. “Pregnancy is not a failure,” she says.

RISKS AND RECOMMENDATIONS

Travelling while pregnant raises some health risks, especially when the destination is remote or endemic for specific diseases, such as Zika, which can cause birth defects. The World Health Organization in Geneva, Switzerland, recommends the second trimester as the safest for travel, advises against sleeping at altitudes above 3,000 metres during pregnancy and warns of serious complications if pregnant women contract malaria or viral hepatitis E.

The risk of developing deep-vein thrombosis during flights is five to ten times higher than average, or about 1 in 1,000 to 1 in 500, for pregnant women, according to the US National Institutes of Health (M. Izadi *et al. Adv. Biomed. Res.* 4, 60; 2015). The organization recommends that women who travel during pregnancy pack a medical kit that includes prenatal vitamins, compression hosiery, antiemetic drugs and a blood-pressure monitor.

Physicians can offer important advice about forthcoming field trips, says Cobb. She opted out of a trip during her second pregnancy



Archaeologist Briana Pobiner in the field in Kenya.

after asking her obstetrician about visiting a research site on an isolated Pacific Ocean island, from where it would have taken a week to reach medical care. The obstetrician vetoed the trip, Cobb says. Cancelling doesn’t have to ruin a research project for ever, she adds. For example, she has quickly received ‘no-cost’ grant-funding extensions from the US National Science Foundation, allowing her to postpone fieldwork.

Considering a project’s importance to big-picture goals can help to guide choices, says Sandra Binning, a marine ecologist at the University of Neuchâtel in Switzerland. While pregnant, she travelled to a long-familiar remote field site in Australia near the Great Barrier Reef: the work there was essential to her long-term research and she knew that the local field crew was supportive. But she cancelled a mid-pregnancy trip to Egypt — where she was meant to co-teach a class on field research to graduate students — because she had contracted a food-borne illness on previous trips. A graduate student who was originally scheduled to observe the course for training replaced her, with no repercussions.

Extra preparation can smooth fieldwork trips and mitigate anxiety. Before going to Australia, Binning asked her obstetrician to sign documents that said she was fit to travel, and told field-station directors about her pregnancy in case of complications. She also flew home when she was about seven months pregnant because some airlines can stop

NICK WALTON

women with advanced pregnancies from travelling on long-haul routes (see go.nature.com/2fxptyv). And she called her university, her health-insurance company and each airline that she would be flying with to find out whether she would need a physician's approval to fly home at the end of the trip.

Those who have been pregnant while doing fieldwork recommend researching vetted medical providers and learning about the safety profile of medications that might be necessary in the field. Friends, colleagues and others can answer questions and provide emotional support. Before a two-month trip to Kenya during her pregnancy, Briana Pobiner, an archaeologist at the Smithsonian Institution in Washington DC, got in touch with colleagues and others who she knew had done similar travel. She also contacted the East African chapter of her undergraduate institution's alumni association to learn about the challenges they faced and how they managed them. Those conversations helped her to locate a hospital close to the field site, as well as an obstetrician in nearby Nairobi whom she could see for check-ups.

Such advice from a wider community can be a great help, agrees Suzanne Pilaar Birch, an archaeologist at the University of Georgia in Athens. Soon after she became pregnant in 2016, she was invited to Cyprus to join a field project a few months later. It was an opportunity she would normally have jumped on, but she would have been six months pregnant by then and was unsure whether to go. What if she committed to the trip but suddenly faced complications? And would she have to tell the team that invited her before she agreed?

To seek advice, she started a conversation on Twitter through TrowelBlazers, a network of female archaeologists and Earth scientists that she had helped to create several years earlier, under the hashtag #pregnantinthefield. The torrent of responses from scientists in many disciplines included some tales of pregnancy complications that had kept researchers home. But many more of the anecdotes were positive, and women posted photographs of themselves doing such tasks as measuring iguanas or excavating fossils in countries as varied as Belize, Oman, Croatia and Chile. Ultimately, Birch accepted the invitation to Cyprus, told her hosts about the pregnancy in the initial phone call and went on a smooth trip. She was happy to get in one last drive for data before the baby came.

Seeing other pregnant women in the field can be a major confidence boost, Binning

adds. When she started her career as a marine ecologist, she took a two-week course in Barbados, and one of the three instructors was pregnant at the time. "I had an image of a pregnant woman doing field work, and it didn't seem to present any significant problems for her," she says. "I always had that in my head. When I got pregnant, I never saw it as a barrier. It is so important that other women get these anecdotes and stories and see that it's possible."

And a visible pregnancy can create opportunities to connect with people from another culture. As a female leader of a research team, Dickman says, she had always been treated as an outsider by the women living in native communities near her Tanzanian field site. But when local women on her field staff saw that she was pregnant, they began to quietly bring her extra boiled eggs and more hot water to shower with.

Some researchers find that their attitude to risk changes as a result of being pregnant. While driving through a game reserve in Kenya one night during her pregnancy, Pobiner and a colleague almost hit an elephant on a dirt road. The near miss jolted her into realizing that she could never again afford to be as casual as she once was about health and safety in the field. "I thought, 'Wow, this was scary — it's not just me I have to worry about any more,'" she says.

STAND UP FOR YOURSELF

Pregnancy can be a learning experience that extends beyond the actual physical condition, Cobb says. She was three months pregnant in November 2006 when she travelled from the United States to the Bahamas to consult on a coral-reef filming project. On her physician's advice, she avoided scuba diving with the team. But she boarded the boat every morning to offer advice and support.

On the second day, choppy seas slammed the boat up and down, and Cobb worried that the impact might be harming the fetus. Although she asked the boat captain to slow down, the ride continued to be rough, and she was uneasy that night and beyond.

Cobb's son was born healthy and at full term the following spring. But the experience taught her the value of standing up for herself and of discussing concerns with team members before setting out on an expedition. She now talks to her field teams about speaking up and looking out for each other before they charge ahead on a precious field day. "I explicitly say, 'The field rule is that we are all in this together and there are natural risks to a field expedition, so let's go through them one by one. You need to say, 'I feel uncomfortable' or 'I feel unsafe,'" she says. "You need to be your own advocate." ■

Emily Sohn is a freelance journalist in Minneapolis, Minnesota.

GENDER DIFFERENCES

Language matters

Two studies highlight yet another set of differences between female and male researchers. One suggests that messages that link career success to 'brilliance' in science can discourage some women from pursuing certain career paths or education opportunities. The other finds that women are more likely than men to offer 'honorary authorships' to scientists who might not deserve the accolade — a courtesy that risks obscuring the magnitude of their own contributions.

In the first study (L. Bian *et al.* *J. Exp. Soc. Psychol.* <http://dx.doi.org/doi.org/10.1016/j.jesp.2017.11.006>; 2018), researchers surveyed nearly 200 undergraduates about their interest in hypothetical internships and in studying certain university subjects. Consistently, women were less keen about the possibilities when the descriptions emphasized the importance of brilliance by asking, for example, for an "intellectual firecracker" with a "sharp, penetrating mind". But when descriptions of the same options used language such as "great focus and determination" — highlighting the importance of hard work and dedication — women's interest grew significantly. Conversely, men were generally more interested when descriptions emphasized intelligence over effort.

The gender difference could have real consequences for students and researchers, says lead author Lin Bian, a psychologist at Stanford University in California. "Women are not motivated to pursue fields or jobs that are perceived as requiring intellectual talent or brilliance," she says; rather, she thinks that women are more likely to gravitate towards a field when scientists emphasize other keys to success in it, including hard work. "It's important to de-emphasize the role of brilliance in achieving success."

In a second study (E. A. Fong and A. W. Wilhite *PLoS ONE* **12**, e0187394; 2017), researchers at the University of Alabama in Huntsville looked at survey responses from more than 12,000 US scholars from a wide range of disciplines. Overall, 35.5% of respondents reported giving at least one 'honorary authorship' to a researcher who contributed little to the paper. Women were 38% more likely than men to have felt obliged to give honorary authorships. "Female researchers", the authors conclude, "may be less able to resist pressure to add honorary authors because women are underrepresented in faculty leadership and administrative positions in academia and lack political power." ■

DECOY

The score of a lifetime.

BY ERIC LEWIS

The two thieves stood before the giant vault, fresh out of ideas. “Well?” Braygin prodded, “what do you think?”

Tesca shrugged. “I think the Regent’s not going to be pleased.”

“The Regent’s *never* pleased. When he hears about this he’ll be furious.” Two of the vault’s magnetic locks hung open; those had been easy. But the third... Braygin kicked a box of gear at their feet. “Are you sure you’ve tried everything, little man?”

“Everything! Electronic picks, lockout bypasses — even nanoexplosives didn’t make a scratch. I’ve never seen a system this well guarded.”

“Hmm. Guess that means we’re in the right place,” said Braygin, wiping a bead of sweat from the back of his neck. “Those rumours about Admiral Gnossi hiding her money in the gas oceans of Denovia must’ve been hogwash. But how do we get *in* there?”

Tesca fidgeted in his cumbersome spacesuit. “Whatever we do, it’d better be fast — security system comes back online in 15 minutes, and we’ll need 5 of those to get back to the ship and blast off.”

“Damn. To come so close!” Braygin slammed a fist against the plasteel face of the vault. He could almost *taste* the loot just out of reach. After months of bribing and snooping out the location of the asteroid base, they’d burgled deep inside to rob the Regent’s biggest rival blind. Even a small share of whatever they stole could buy them each a small moon to retire on, but it seemed that the vault had defeated even Tesca’s technocriminal talents. “There’s absolutely nothing you haven’t tried?”

“Nope, nothing. Erm, well...”

“Erm, well what?”

Tesca looked away. “I wasn’t gonna say anything —”

“Say it anyway!”

Tesca knelt and rooted through the box, tossing the various bits of equipment that’d failed them about the dim chamber. He rose holding an awkward, cobbled-together mass of wires and metal. An antimatter symbol emblazoned on the side screamed warning. “It’s just a prototype...”

“A prototype *what*?”

“A portable spatial-displacement-field generator.”



“Spatial... what, like in the engines that move starships?”

“Well, technically, it’s not the ship that moves, it’s space itself —”

“Whatever,” said Braygin. “You mean you built a handheld version? Incredible! You could ‘displace’ us right through the door! Why didn’t you start with that?”

“Like I said, it’s a prototype... also, the parts are highly illegal.”

“Illegal? Tesca, we’re *breaking into Admiral Gnossi’s vault*. Just use the gadget so we can grab the cash and get outta here.”

“But it’s too dangerous! Without a full scan we’ve no idea what’s on the other side. There could be guardbots, automated defences —”

Braygin clapped his partner on the shoulder. “Look, this is the score of a lifetime — I’ll take the risk. Unless *you* want to be the one to bring the Regent the bad news?”

“... all right. Gimme a second to boot it up.”

“Ten minutes and counting.”

While Tesca worked the controls of the device, Braygin again eyed the great circular door, licking his lips with anticipation. “This is it. It’s finally happening, after all these years. My big payoff. No more penny-ante con jobs, no more rackets. No more bowing and scraping before thugs like the

Regent...” He turned back to Tesca. “Hey, how do you work that thing anyway?”

“Hmm? Oh, it’s

pretty simple. You set your field radius, set your displacement vector — say, three metres straight ahead for this door — then hit go. Only enough juice for a couple short jumps so we best go together... there, all set.” Tesca put the device down and went to retrieve his helmet — the atmosphere in the tunnels was thin but breathable and they’d quickly set the protective gear aside. “Better suit up all the way, just in case — *oof!*”

While Tesca’s back was turned, Braygin shoved him hard, and the low-power grav plating sent him tumbling. Braygin grabbed the displacement device and caressed it greedily. “Sorry Tesca, like I said, this is the score of a lifetime, and I find I ain’t willing to split it. Nothing personal; you’d do the same in my place if you had any brains for business. So long, little man!”

“No, Braygin, don’t...!” Tesca watched as Braygin was enveloped in a blue orb, then winked out of existence along with a little section of tunnel floor he’d been standing on. Tesca scrambled for his comm unit. “Braygin! Are you there? Braygin you lying cheat, talk to me!” Nothing.

After a few stunned seconds Tesca heard a low bang emanate from the vault door. From the other side it seemed. Then another, much weaker. Then silence. “Braygin?” He rummaged through his box of gear for a data pad and tried to patch into Braygin’s suit camera. Although the signal was weak through the insulating plasteel, he managed to pick up an image, but no sound. The picture was rotating, slowly. He saw the other side of the door, then a wall of rock. A gloved fist drifted across the camera’s field of view, and when it passed Tesca saw only a field of stars, stark against the blackness of open space.

“Huh,” Tesca muttered to the empty chamber, glancing at Braygin’s helmet left forgotten on the floor. “I guess Admiral Gnossi *does* keep her money on Denovia after all.”

Tesca gathered up his most precious gear and scuttled back to the ship. No, the Regent was most definitely *not* going to be pleased. ■

Eric Lewis is an organic chemist still learning how to be a person again after surviving graduate school. His stories have appeared in Electric Spec, Bards and Sages Quarterly and other online venues.

ON NATURE.COM
Follow Futures:
@NatureFutures
go.nature.com/mtoodm